SOLID MECHANIS AND ITS APPLICATIONS

Alexis Lagarde (Ed.)

IUTAM Symposium on

Advanced Optical Methods and Applications in Solid Mechanics

KLUWER ACADEMIC PUBLISHERS

IUTAM SYMPOSIUM ON ADVANCED OPTICAL METHODS AND APPLICATIONS IN SOLID MECHANICS

SOLID MECHANICS AND ITS APPLICATIONS
Volume 82

Series Editor: G.M.L. GLADWELL
Department of Civil Engineering
University of Waterloo
Waterloo, Ontario, Canada N2L 3GI

Aims and Scope of the Series

The fundamental questions arising in mechanics are: *Why?, How?,* and *How much?* The aim of this series is to provide lucid accounts written bij authoritative researchers giving vision and insight in answering these questions on the subject of mechanics as it relates to solids.

The scope of the series covers the entire spectrum of solid mechanics. Thus it includes the foundation of mechanics; variational formulations; computational mechanics; statics, kinematics and dynamics of rigid and elastic bodies: vibrations of solids and structures; dynamical systems and chaos; the theories of elasticity, plasticity and viscoelasticity; composite materials; rods, beams, shells and membranes; structural control and stability; soils, rocks and geomechanics; fracture; tribology; experimental mechanics; biomechanics and machine design.

The median level of presentation is the first year graduate student. Some texts are monographs defining the current state of the field; others are accessible to final year undergraduates; but essentially the emphasis is on readability and clarity.

IUTAM Symposium on Advanced Optical Methods and Applications in Solid Mechanics

Proceedings of the IUTAM Symposium held in Futuroscope, Poitiers, France August 31st – September 4th 1998

Edited by

Alexis Lagarde
University of Poitiers,
Laboratoire de Mécanique des Solides,
Poitiers, France

Kluwer Academic Publishers

NEW YORK, BOSTON, DORDRECHT, LONDON, MOSCOW

eBook ISBN 0-306-46948-0
Print ISBN 0-792-36604-2

Created in the United States of America

Visit Kluwer Online at: http://www.kluweronline.com
and Kluwer's eBookstore at: http://www.ebooks.kluweronline.com

Nous remercions particulièrement le **Conseil Régional Poitou-Charentes** pour son soutien apporté à l'organisation de ce Symposium par le biais du programme Com'Science.

We thank especially the **Conseil Régional du Poitou-Charentes** for its financial support given to the organisation of this Symposium through the Com'Science program.

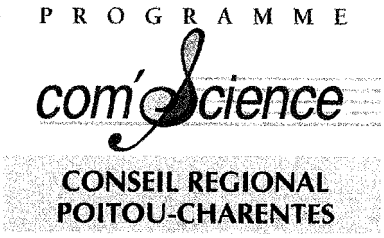

ADVANCED OPTICAL METHODS AND APPLICATIONS IN SOLID MECHANICS

CONTENTS

Strain and displacement measurement

Speckle interferometry

Holography and interferometry

Shearography

Thermomechanics

Hybrid process

TOOLS

Image analysis

Dynamic fracture

Mecanisms analysis

FOREWORD

The request to organize under its patronage at Poitiers in 1998 a Symposium entitled **"Advanced Optical Methods and Applications in Solid Mechanics"** by the International Union of Theoretical and Applied Mechanics (I.U.T.A.M.) was well received for the following two reasons. First, for nearly 20 years no Symposium devoted to optical methods in solids had been organized. Second, recent advances in digital image processing provided many new applications which are described in the following. We have the honour to present here the proceedings of this Symposium.

The Symposium took place from august 31st to September 4th at the **Institut International de la Prospective in Futuroscope** near **Poitiers.**

A significant number of internationally renowned specialists had expressed their wish to participate in this meeting. The Scientific Committee proposed 16 general conferences and selected 33 regular lectures and 17 poster presentations. Papers corresponding to posters are not differentiated in the proceedings from those that were presented orally. It is worth noting that a total of 80 participants, representing 16 countries, registered for this symposium.. The Scientific Committee deserves praise for attracting a significant number of young scientists, both as authors and as participants. Let us add our warm acknowledgements to Professor J.W. Dally and to Professor A.S. Kobayashi who, throughout the symposium preparation time, brought us valuable help.

The proceedings is presented in three parts : ***– the methods,*** which are diverse, and present a conceptual character ***– the tools*** that are numerical, instrumental or purely optical ***– the applications*** in different fields of mechanics.

This Symposium was very rich in new or recently obtained results which cannot be summarised easily. Nevertheless, we shall attempt to highlight a few of the ideas.

Concerning ***the methods,*** we refer to the following :

- three-dimensional photoelasticimetry using optical slicing provides a rapid procedure for optimizing the shape of a piece,
- for large strain, logarithmic measurement proves to be the suitable approach,
- the diffraction of a laser beam by an orthogonal grating marked on a surface provides displacements and strains in static as well as in dynamic situations,
- thermography, with the map of temperatures, reveals damage, fatigue limits, and cracks during cyclical loading,
- by identifying local sources of heat and by using a complete energy balance, we may accurately phenomena of damage and localization study,
- it is possible to implement the methods of moire and speckle interferometry free of thermal disturbances,
- panoramic interferometry permits the determination of the strain state for an axisymetric body,
- a hybrid procedure uses a synergy between optical, numerical and analytical techniques.

Concerning ***the tools,*** we underscore the following :

- the developments of image processing allow the exploitation of the methods quickly and accurately,
- photorefractive crystals provide holography in real time,
- in non destructive evaluation, this process is employed to detect ultrasonic waves on a rough surface,
- novel possibilities based on non linear effect are offered for increasing the amplitude of an optical signal without changing its phase,
- the recording and the reconstruction of the amplitude and the phase of an optical wave without a reference beam provides interesting applications (conception of a laser adapted to micro machining, …),
- a device combining laser impact and interferometric sensors allows flaws detection inside of a solid.

The applications show the interest in optical methods for varied fields :

- shape measurement,
- non-destructive evaluation,
- static and dynamic rupture,
- localization of adiabatic shear bands,
- modelling of the thermomechanical behaviour of materials,
- analysis of the damage process of composites,
- analysis of mechanisms : bearings, prostheses, airbags, …,
- realization of microactuators inserting shape memory materials for microrobotics using stereolithographic apparatus.

The general lectures represent more than a third of the volume of the proceedings ; they give excellent general overviews of the many methods, pointing out the various milestones in the development, and focussing on the many areas of applications.

We cannot finish without noting the evolution of photomechanics since the previous Symposium in 1979. Numerical and experimental analysis are no longer concurrent but complementary. Many methods have integrated numerical tools not only for the treatment of the images in order to extract the best information, but also to implement modern calculus methods ; there is a synergy that comes from the integration of various disciplines.

We are convinced that this publication will be an important and useful tool for future work. The specialist will find it to be a current of the subject. Those of the scientific community in optics, mechanics, physics or engineering who wish to enter this field or study in depth, will find this volume to be a basic tool for the development of major ideas and a complete bibliography.

We invite the reader, scientific or engineer – for professional activity and personal pleasure – to discover here the renewed interest in the optical methods, and the considerable promise evidenced for the future of photomechanics and its implementation in industry.

Finally, we wish to thank the following organizations and societies for their financial assistance so indispensable for the proper preparation and the functioning of the Symposium, but also for the subsidies given to permit the participation of some colleagues :

International Union of Theoretical and Applied Mechanics, European Research Office, Delegation Générale à l'Armement, Centre National de la Recherche Scientifique, Association Universitaire de Mecanique, Université de Poitiers, Faculté des Sciences Fondamentales et Appliquées de Poitiers, Mairie de Poitiers, Conseil Général du Département de la Vienne, Conseil Régional du Poitou-Charentes (programme Com'Science), Peugeot Citroen, Kluwer Academic Publishers.

July 1999
Alexis LAGARDE
Professor, University of Poitiers

This Page Intentionally Left Blank

STATIC AND DYNAMIC STRAIN MEASUREMENT ON A PLANE SURFACE. THREE-DIMENSIONAL PHOTOELASTICITY

A. LAGARDE
Laboratoire de Mécanique des Solides,
Université de Poitiers,
Unité Mixte de Recherche CNRS 6610
SP2MI - Téléport 2 - BP 179, 86960 FUTUROSCOPE CEDEX, FRANCE

Abstract

For small or large strains, using two orthogonal gratings marked upon a plane measurement base, we determine, in its plane, the rotation of the rigid solid and the algebraic values of its principal extensions. An optical setting gives the measure by optical diffraction, without contact and at a distance, within 10^{-5} accuracy by introducing quasi-heterodyne detection. The holographic record permits the extension of the measurement to the whole of a plane surface. For dynamic events, the grating interrogation by a beam laser with angular coding gives not only strains for local measure base but also rigid motions.
In photoelasticity, the optical slicing method is recalled ; then, we introduce a new implementation with a C.C.D. camera which quickly gives isoclinics and isochromatics, and also the isostatics for a model slice bounded by two parallel plane laser beams.

1 INTRODUCTION

The advent of the laser has permitted a spectacular development of the photomechanics. Digitalization of images, their acquisition and their treatment by computer offer new possibilities.
We have selected to present research by our team about two basic procedures in experimental mechanic: the measurement of strains, and three-dimensional photoelasticity.
The measurement of strain on a small plane base uses numerical or optical spectral analysis of an orthogonal grating marked on the surface. Ways of increasing the precision are given in two cases. The chosen optical set up for measurement of strain is insensitive to the out of plane displacement of the piece. Holography allows us to extend the measurements to quasi-plane surfaces. The lecture point by point is executed in retarded time. In dynamics the positions of the diffracted spots permits the determination of the strains and the motion of the local measurement base.

A. Lagarde (ed.),
IUTAM Symposium on Advanced Optical Methods and Applications in Solid Mechanics, 1–16.

In three-dimensional photoelasticity we briefly recall the present practice and the possibilities of non-destructive optical slicing methods, both point-wise and for the whole field. We also recall fundamental results on the propagation of light waves in a weakly anisotropie environment, and their importance for the analysis of thin slices and new modelling concepts. The whole-field optical slicing method is then presented in its recent developments.

2 SMALL AND LARGE STRAIN MEASUREMENT

The idea of creating grids on the surface of a specimen in order to measure its strains is not new. This idea was introduced by Rayleigh [1] in 1874. It was taken up and combined with the Moire phenomenon by Dantu [2] in 1957.
The coherent radiation of a laser beam has permitted the development of the more accurate Moire interferometry [3]. To increase the accuracy, we note the numerous works dealing with interpolation between fringes, the multiplication of fringes [4], and other techniques [5]. The strains are obtained by the help of a differentiation process.
The direct measurement of strains has been realised from the local observation of circles marked on the surface. Orthogonal grids have also been employed. With a smaller pitch the information has been extracted from the grating by optical diffraction either locally [6] or along a line using filtering [7]. The use of a optoelectronic device [8] has allowed automatic calculation of strain distribution. With the recent development of C.C.D. cameras and image processings, these methods are being revived [9-10].
Our purpose is the accurate determination of algebraic values of the principal extensions for large and small strains over the whole of a very small area.

2.1 LOCAL MEASUREMENT OF STRAINS

2.1.1. PRINCIPLE

We use tangent linear application [11] to study deformations of an orthogonal grating of pitch p which is engraved or marked on the local plane surface of a specimen submitted to loadings. This grating is supposed not disturb the deformations of the support. Thus (Fig. 1) an interior point M(X, Y) is transformed to m(x, y) by the following transformation:

$$\begin{cases} x = \dfrac{a_1}{p}\cos\alpha_1\, X + \dfrac{a_2}{p}\cos\alpha_2\, Y \\ y = \dfrac{a_1}{p}\sin\alpha_1\, X + \dfrac{a_2}{p}\sin\alpha_2\, Y \end{cases}$$

The gradient of the transformation tensor F is constant inside the parallelogram.
The Cauchy-Green right tensor $C = {}^tFF$ has the following matrix :

$$C = \begin{pmatrix} \left(\dfrac{a_1}{p}\right)^2 & \dfrac{a_1 a_2}{p^2}\cos(\alpha_2 - \alpha_1) \\ \dfrac{a_1 a_2}{p^2}\cos(\alpha_2 - \alpha_1) & \left(\dfrac{a_2}{p}\right)^2 \end{pmatrix}$$

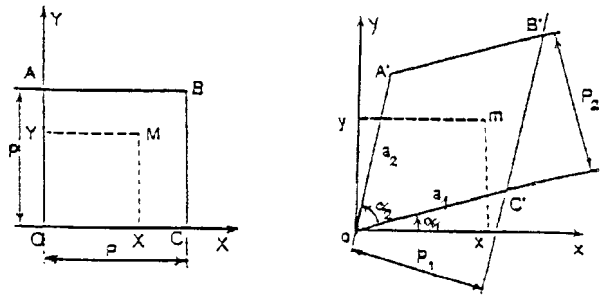

Fig. 1 - Deformation of a square

Using the polar decomposition of F we can express the rigid-body rotation R of the solid:

$$\tan R = \frac{a_2 \cos\alpha_2 - a_1 \sin\alpha_1}{a_2 \sin\alpha_2 + a_1 \cos\alpha_1}$$

We assume the strains are uniform on the measurement base. Thus we obtain the orientation and the value of the principal extensions and the rigid body rotation from a knowledge of four parameters (two pitches p_1 and p_2 and two angles α_1 and α_2). These values are experimentally obtained either by optical Fourier Transform or by numerical Fourier Transform. Optical Fourier Transform gives the strain with an accuracy of 10^{-3} (sec. 2.1.3). For better performance we use the phase shifting technique (sec. 2.2.1). The numerical Fourier Transform requires an adapted interpolation process (sec. 2.2.1).

2.1.2. GRATING REALISATIONS

We use [12] the interference between two laser beams to procedure a gratin on a photosensitive coating. At the surface of some materials (epoxy, steel …), it has possible to engrave a grating, without photosensitive coating, by using the interference between two yag laser beams. We have also use Post's replication technique to obtain a phase grating. All the various techniques give a grating which is disturbed under large strains; so we have developed a technique for making small viscoelastic pavements. Other ways of creating a grating with lines or points involve using transfers, inking pads, mold etc. The choice depend of the size of the measurement base and the nature of the problem.

2.1.3. MEASUREMENT BY OPTICAL DIFFRACTION

The diffraction phenomena of a parallel beam of coherent light passing through a plane grating is well known.
Fig. 2 shows the diffraction image by a grating of parallel crossing lines. We notice that the direction formed by the diffraction points is perpendicular to the orientation of the family of corresponding lines. It is now easy to describe $p_1, p_2, \alpha_1, \alpha_2$ as functions of $d_1, d_2, \delta_1, \delta_2$: (L : distance between the grating and the screen)

$$p_1 = \frac{\lambda\sqrt{L^2 + d_1^2}}{d_1}, \quad p_2 = \frac{\lambda\sqrt{L^2 + d_2^2}}{d_2}, \quad \alpha_1 = \delta_1 + \frac{\pi}{2}, \quad \alpha_2 = \delta_2 - \frac{\pi}{2}$$

In Fig. 2 the diffraction spots are shown in even decreasing size, starting from the central, zeroth order, spot. This is to give an idea of the ever decreasing intensities of the spots. On the actuel diffraction screen all the spots have the same size.

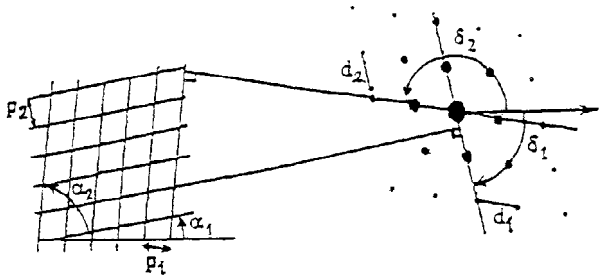

Fig. 2 - Diffraction image by a grating

The diffraction image is recorded by a C.C. D. camera, and the centroïd (x, y) of the spots is computed from an intensity analysis.
The grating analysis using the optical diffraction allows measurement at a distance, and is very convenient for strain determination in a hostile environment. For example, we used this technique to study the evolution of longitudinal and transversal strains determined on a specimen in epoxy resin and subjected to an uniaxial test at the freezing point. The measurement base was 0,5 x 0,5 mm^2, and the line density 300 per millimeter. From this test we can evaluate the strain accuracy to 10^{-3} .
The method has been adapted to dynamics [13] and also, to statics to studies of cylindrical specimens [14].

2.1.4. MEASUREMENT BY SPECTRAL ANALYSIS

The crossed grating is recorded by C.C.D. camera and an algorithm of bidimensional DFT is used.
The location of the 5 peaks of the spectrum (central order and 4 peaks order ± 1) gives the parameters needed for the optical analysis.

2.2. IMPROVEMENT OF ACCURACY

2.2.1. THE TOOLS OF THE ACCURACY

The quasi-heterodyne or phase shifting method [15]
This method is very well known ; we merely mention it.
The spectral interpolation method [16] [17]
Let us consider a periodic function f(x), and its Fourier Transform (F.T.) F(N) ; x and N are respectively spatial and spectral variables. Let T, the period of sampling, satisfy the Shannon condition, M be the number of discretisation points, MT the width of the window limiting the sampling function.

We use the DFT (denoted F_k) with nT and k/MT the reciprocal variables, respectively spatial and spectral. The frequencies of the spectrum of f(nT) are calculated from the peaks of the square modulus of F_k. If the number M of points of discretisation is a multiple of the period of the signal, the DFT is equal at these points to the continuous F.T. The most important peak of coordinate k', corresponds to the fundamental frequency of the signal N = k'/MT. In practice, M is not a multiple of the period of the signal. We show that the fundamental frequency is given by the relations ship.

$$N = \frac{k_s + \beta}{MT} \quad , \quad \beta = Re \frac{F_{k_s-1} - F_{k_s+1}}{2F_{k_s} - F_{k_s-1} - K_{k_s+1}}$$

where k_s is label of the coordonate the nearest to the principal peak.

2.2.2. THE DEVICE

Using a numerical Fourier transform of the grating image, or the optical transform by laser beam diffraction, we find that an out of plane translation between the reference state and the deformed state of the specimen leads to an error in the strain determination. We present a measurement method which can be made at a distance, which is insensitive to translations, and which has better accuracy by the use of quasi-heterodyne detection [17-18]. We consider the diffraction at normal incidence of a laser beam by a parallel equidistant line grating. The optical device (Fig. 3) is made by a cylindrical miror having the same axis as the incident beam. After reflecting, the two diffracted beams of the order ± 1 interfere at the level of the axis of the cylinder. The interference field is composed of parallel fringes and its analysis allows us to characterize the geometry of the grating marked on the piece. The interference field has a depth of several millimeters, depending on the transverse dimension of the diffracted beams where the geometry of the fringes is identical. There is thus no problem of focusing, and out-of-plane displacement of the piece, and therefore of the interference zone, does not lead to an error measurement. To be free from the translation in the plane of the grating, we use a size greater the grating the diameter of the incident beam.

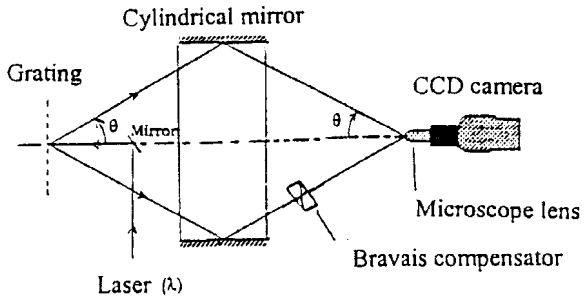

Fig. 3 - Optical device

The interference field can be analysed using numerical spectral interpolation. We have found that the use of the quasi-heterodyne technique gives better results than the previous one. We modulated the phase of one of the diffracted beams by using a Bravais compensator. For an unidimensional signal this technique consists of the use of three

dephasing ψ^k (calculated by Fourier transform) for the determination of the phase ϕ (x), and thus of the value of the period of the signal. The same procedure is applied for a two-dimensional signal. In order to show the performance of the developed optical device, we mention results [19] from an uniaxial traction test on a Plexiglas specimen submitted to step of strain of 2×10^{-5}.

2.3. WHOLE FIELD STRAIN MEASUREMENT

We have developed a whole field strain measurement method [20] which uses the recording of the grating by holography (Fig. 4). The image of the crossed grating illuminated in normal incidence is formed in an optical device that carries out successively two Fourier transforms. In the second Fourier plane we obtain interference between the diffracted beams which create a new grating. A filter located in the fast Fourier plane allows us to eliminate the zero order and the orders other then ± 1. Different orientations of the reference beam are generated to record many object states on the same holographic plate.

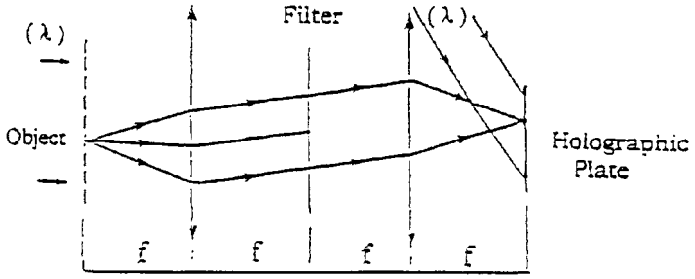

Fig. 4 - Holographic recording device

The figure 5 shows the optical device for the recording of the image of the grating. This device allows us to generate 4 different reference beams.

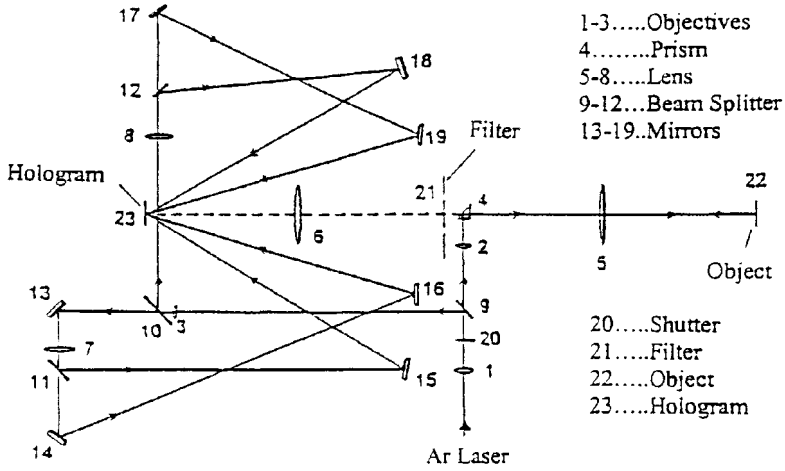

Fig. 5 - Set up for the holographic recording device

At the reconstruction, the illumination of the holographic plate using the reference beam gives the order ± 1 images of each point of the plate. The analysis of the reconstructed grating using device a phase shifting gives the strain components in the whole-field, point by point. It is also possible for the strain determination to employ one part of the set-up for the recording procedure lens and filter are yet positioned. This method has been used for a ductile fracture investigation.

2.4. HIGH SPEED LOCAL STRAIN DETERMINATION

The diameter of the plane measurement base is about 1 mm. The crossed grating, marked on the surface, has a density of 200 lines by millimeter.
The method is always based on the interrogation of a crossed grating by a diffraction phenomenon and we use the five diffracted beams of orders 0 ; ± 1. To separate the spots on the recording (with film or C.C.D. camera) during a dynamic event, we use the angular coding. At each sampled time one cylindrical beam with diameter of about 1 cm lights the crossed grating, as shown in figure 6.
Generally, the unknown quantities are as follows :
- 4 parameters characterising the measure base orientations and paths of the two grating taking into account the pure strains and the rotation of the rigid solid in the plane of that base.
- 2 angular parameters for the orientation of the base.
- 3 parameters defining the position of the base.
- 5 distances from the origin to the position of the spots in the screen.
There are 14 unknown quantities in all.
At each time, one piece of experimental data is the orientation of the incident beam. The measured positions of the corresponding 5 spots on the screen lead to 15 equations.
It can be proved that at each sampled time, the unknown quantities are the solutions of a nonlinear system of fifteen equations characteristic of the five considered beams. Taking into account the given diffraction spots is therefore sufficient for the solution of the problem. Note that the method gives not only the strain tensor components on the measurement base, but also the displacements and rotations of the measurement base. One lecture will deal with it and will detail its performance.

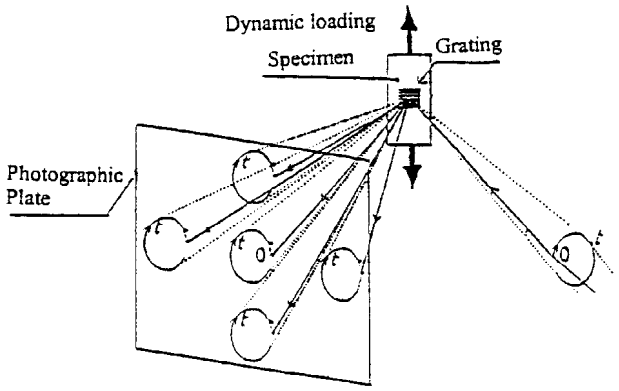

Fig. 6 - Schema of a part of the optical recording device

3 THREE-DIMENSIONAL PHOTOELASTICITY

3.1. PRESENT PRACTICE AND NEW POSSIBILITIES

Photoelasticity still provides research projects, e.g. the study of residual stresses in glass by means of integrated photoelasticity. Mostly, we deal with the study of elasto-static problems for pieces having complex geometry. With the help of the well known frozen stress technique, photoelasticity is still often used in the test and research laboratories of motor vehicle and aeronautical industries.

Photoelasticity provides an efficient procedure ; this efficiency is due to the fact that the model being loaded has the correct boundary conditions. In the last ten years, photoelasticity and numerical simulation have often been used in parallel. Progress in finite element method allowed to solve problems with Poisson's ratio is near 0,5, as it is the case at freezing temperature.

The process consists in first adjusting the boundary conditions in the numerical simulation in order to get the obtained numerical values to coincide with the experimental values, the mechanical parameters being those corresponding to the freezing temperature. Then, the stress distribution inside the prototype is obtained with its own mechanical parameters.

Let us note recent progress : the original, necessary to make the mould, can be realised with help of computer by means of stereolithography. Now, it is even possible to realise the model directly with suitable freezable resin.

The exploitation of the frozen model is executed by mechanical slicing into plane sheets with a thickness from 2 to 4 mm. Each sheet is polished roughly, and analysed in linear and circular polariscopes as in plane photoelasticity. Slicing and analysing of series of parallel sheets requires one qualified technician one week's work. Worktime is reduced if an immension tank is used because it is then unnecessary to polish the slices. The aim is to determine the parameters of interest for engineers : the difference $\sigma' - \sigma''$ of the secondary principal stresses and the angle a giving their directions with reference to the x-axis. Using well known equations, we can use these quantities obtained for three mutually orthogonal planes to integrate the equilibrium equations with known boundary conditions. The most general study, scarcely ever done, requires the making and the slicing of three models. Usually, we restrict ourself to determining the above quantities only in principal planes in order to optimiste the shape of the model.

Over fifteen years ago, we developed and used two optical slicing methods : one point-wise [21 to 25], the other whole-field [24 to 27]. In a three-dimensional medium, these two methods give a non destructive investigatory procedure, based on the scattering light phenomenon. This phenomenon is intensified by introducing fine particles of silica in to the epoxy resin.

The point-wise method of optical slicing offers the possibility of using the light scattering phenomenon as polarizer or as analyser. This method has been automated ; it permits a precise determination, in every point of the sheet, of the three optical parameters leading in general to the determination of α and $\sigma' - \sigma''$ (sec. 3.2.2.). Note that a number of methods have been developed to determine the three optical parameters, more particulary for a thick medium located between a sheet and the model

boundary ; it is analysed in the book by Srinath [28]. Let us mention the iteractive process and the ones using polarizer and analyser rotations and compensator [29].
For example, we have determined the stress tensor along a line in a prismatic bar, under torsion, the cross section of which is an equilateral triangle. The values of the stresses are normalised by the maximum value of the shear of the cross section. So, in the base of a turbine blade, we could determine the values of the equivalent Von Mises stress in the at various points for a tensile load [23] [25].
The whole field optical slicing method is based on limitation of a sheet by two parallel beams emitted from a laser. The model is analysed slice by slice. The scattered rays interfere (Rayleigh's law) on the image plane of the middle of the sheet. The different polarizations depending of optical characteristics of the sheet are taken into account. Two methods have been developed (sec. 3.4.), the aim of which is to demonstrate that it is possible to obtain the isoclinic and isochromatics fringes and to plot the isostatic patterns ; this is a new possibility.
Before presenting the principles of the method, we shall give a new model for light wave propagation in a three dimensional medium with low anisotropy.

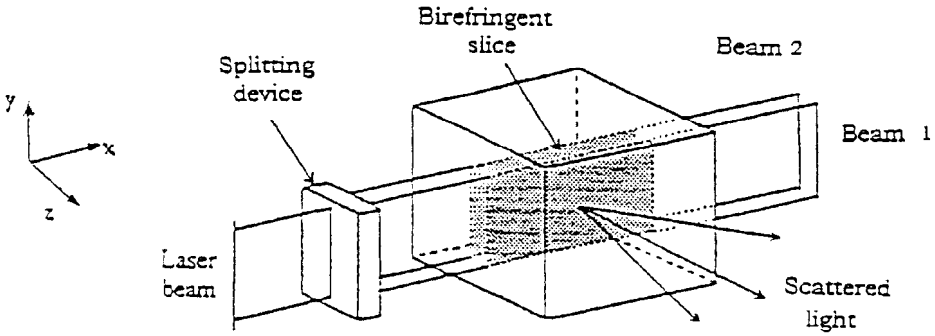

Fig. 7 - Isolation of a slice with two plane laser beams

3.2. PROPAGATION OF LIGHT WAVES THROUGH PHOTOELASTIC MEDIA

To define the light propagating direction in a photoelastic medium we assume that the medium is isotropic, even though current photoelastic materials are slightly anisotropic. It follows that for a ray light propagating along $\vec{z}$ direction, the wave planes are orthogonal to $\vec{z}$, i.e. they are parallel to the (x, y) plane.
It can be shown that the secondary principal directions of the refractive index tensor and the stress tensor coincide, and that we have the following relationship :

$$n' - n_0 = c_1 \sigma' + c_2 (\sigma'' + \sigma_z)$$
$$n'' - n_0 = c_1 \sigma'' + c_2 (\sigma' + \sigma_z)$$

Here n' and n" denote the secondary principal indices in the wave-plane (x,y) and σ', σ'' are corresponding secondary principal stresses ; c_1, c_2 are constants for a photoelastic material.

3.2.1. THE CLASSICAL SCHEME

In three-dimensional photoelasticity it is usually assumed that the directions of secondary principal stresses and their values are constant through the thickness dz of a slice with parallel face normal to $\vec{z}$. This assumption allows us to consider this slice as a birefkingent plate characterized by the following two parameters :

- secondary principal angle $\alpha = (\alpha, \sigma')$ - angular birefkingence $\phi = \frac{2\pi\delta}{\lambda}$,

$\delta = dz\ (n',n'') = C(\sigma', \sigma'')\ dz\ C = c_1 - c_2$ (C is a photoelastic constant).

3.2.2. ABEN SCHEMATISATION

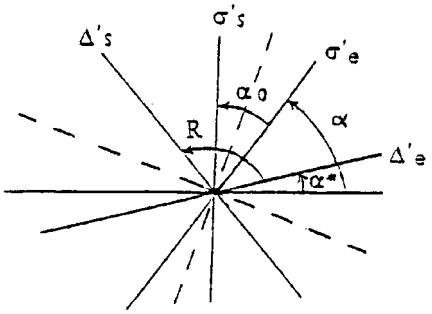

Fig. 8 - Orientation of the characteristic Δ' directions and the σ' directions at the entrance and the emergence

Aben in 1966 showed that when rotation of secondary principal axes was present, there were always two pairs of perpendicular conjugate « characteristic directions » (Fig. 8). He distinguished the primary characteristic directions at the point of entry of the light (Δ'_e, Δ''_e), and the secondary characteristic directions (Δ'_s, Δ''_s) for the light emerging from the medium. The light which is initially linearly polarized along one of the primary directions emerges as linearly polarized along the conjugate secondary direction. We will denote by R the angle determined by two such directions, $R = (\Delta'_e, \Delta'_s)$ and by α^* the angle (x, Δ'_e).

The characteristic directions are generally different from the secondary principal directions of the stress tensor (or those of the index tensor). At entry we have (σ'_e, σ''_e) and at emergence from the medium we have (σ'_s, σ''_s) . We write $\alpha_0 = (\sigma'_e, \sigma'_s)$.

3.2.3. HYPOTHESIS FOR A THIN SLICE

When dx/dz and $\sigma' - \sigma''$ are constant through a thickness, important conclusions follow [30 - 31]:

- The bisecting lines for the angles formed by two associated « characteristic directions » coincide with those for the angles formed by the associated secondary principal directions at the entrance and at the exit, (Fig. 8).

Remark : The bisectors mentioned correspond to the secondary principal directions (mechanical or optical) at mid thickness ; their directions are defined by the angles ± R/2 from the characteristic directions).

- Along two characteristic orthogonal directions the phase difference ϕ^* characteristic of the medium traversed by the light wave is generally different from the angular birefringence ϕ but $\phi^* = \phi$ when the rotation R = 0. The values R, α^*, ϕ^* and α, α_0, ϕ are linked [23 - 27].

Concerning the torsion strain, let us recall that for a bar of equilateral triangular section Aben's scheme gives good agreement between calculated and experimental results for slices inclined at an angle of $\pi/4$ from the axis of the model, with the thickness of the slices being only 2 mm for classical model sizes [23].

3.2.4. DISCRETE ANALYSIS INTO THIN SLICES

This technique approaches the thick medium, in the direction $\vec{z}$ of propagation, by n plane thin slices perpendicular to $\vec{z}$ [31 - 32]. This approach gives more realistic images in comparison with experimental images : in this case, we have variation of the stress difference along the thickness ; Aben's hypothesis does not include this condition. One paper is devoted to this discrete analysis, explains it simply, and discusses the connection with the finite element method.

For a slightly anisotropic medium, with a large thickness, crossed by light, Poincaré's theorem permits us the representation by birefringent plate followed by a rotatory power (or by the inverse position, with the axis rotated of the value of the rotatory power)

3.3. WHOLE-FIELD ANALYSIS WITH A PLANE POLARISCOPE

We present analysis for a light-field polariscope as it used for the whole-field method of optical slicing. There is a similar study for a dark polariscope.

Let us examine a slice (which should be obtained by freezing and slicing) in a plane light-field (rectilinear) polariscope. At each point the slice is represented by a birefringent plate and a rotatory power. Let I_0 denote uniform light-field illumination, and x the polarizing axis of the polarizer ; the light intensity is

$$I = I_0[\cos^2 R - \sin 2\alpha^* \sin 2(\alpha^* + R) \sin^2 \phi^*/2]$$

The extremum values for intensity distribution correspond to the angles :

$$\alpha^* = R/2 + k\pi/4, \quad k = 0, 1, 2, \ldots$$

In order to analyse the fringe patterns we plotted the variations of Imax and Imin, versus ϕ for different values of α_0, following the relationships given in sect. 3.2.3. Fig.9 shows the curves for $\alpha_0 = \pi/9$.

The foregoing analysis indicates that for small values of α_0 ($\alpha_0 < \pi/9$), the maximum intensity Imax shows little modulation. Thus, it characterizes an isoclinic zone which

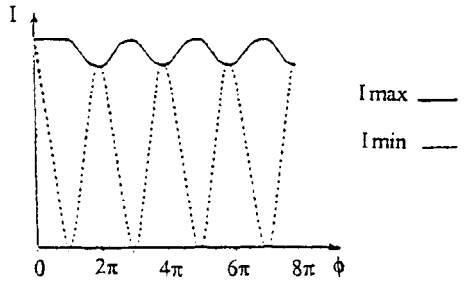

Fig. 9 - Variation of Imax and Imin as a function of $\phi(\alpha_0 = \pi/9)$

permits one to locate the secondary principal stress directions (or those of the indices) in the median plane of a slice. This zone corresponds to $\alpha^* = R/2 \mod \pi/2$ (remark sect. 3.2.3.). The orientation of the polarizer then coincides with one of the secondary principal directions in the median plane. This interesting result is analogous to that established by Hickson [33] for a dark-field polariscope.

It should be emphasized, that in order to avoid errors during the numerical integration procedure, the discretization points should lie in the median plane of a slice.

If α_0 increases, the Imax modulation increases, and becomes very pronounced for $\alpha_0 = \pi/3$. In this case the isoclinic zone disappears, although it should be noticed that the isoclinics are discernible until $\alpha_0 = \pi/6$.

The term Imin, which is strongly modulated for α_0 close to $\pi/6$, characterizes the isochromatic pattern. The extremum values occur for $\phi = k\,\pi (k = 1, 2 ..)$ and it follows that localization of fringes is practically independent of the rotation of secondary principal axes.

We draw a conclusion : investigation of a slice within the plane (rectilinear) polariscope allows one to determine the secondary principal stress directions in the median plane (without resorting to rotatory power measurements), and the angular birefringence ϕ for the multiple π-values when the rotation of the secondary principal axes is less than $\pi/6$. Note that the condition on the orientation of the secondary principal axis is not very limiting, since we can choose the slice-thickness for the non-destructive optical slicing method.

3.4. WHOLE-FIELD OPTICAL SLICING METHOD

We have developed two methods for a sheet bounded by two parallel plane beams emitted from a laser. The scattered radiations interfere (Rayleigh's law) in the image plane of the middle of the sheet. The information concerning isoclinic and isochromatic patterns of the sheet are obtained from the square of the correlation factor γ of the two speckle fields.

We show that the illumination of the speckle field is given by the following basic relation

$$I(x,y) = I_1(x,y) + I_2(x,y) + 2\sqrt{I_1 I_2}\,\gamma \cos(\psi_2 - \psi_1 - \eta)$$

$$\text{with } \gamma^2 = \cos^2 R - \sin 2\alpha^* \sin 2(\alpha^* + R) \sin \phi^*/2$$

ψ_1, ψ_2 random variables, η function of α^*, ϕ^*, R.

The speckle fields interfere in amplitude for $\gamma = 1$; they add in energy for $\gamma = 0$ (it is said that they interfere in energy).

3.4.1. METHOD BASED ON THE CONTRAST MEASUREMENT OF ONE RECORDING INTENSITY FIELD

This method uses only one recording with holographic film. We denote spatial average by <>.

The static study of the speckle field gives the basic relation.

$$\sigma^2 = <[I - <I>]^2> = <I_1>^2 + <I_2>^2 + 2\gamma^2 <I_1><I_2>$$

As the contrast $\rho_i = \dfrac{\sigma_i}{<I_i>}$ is unity for the two speckle fields, we have for the variance

$$\sigma^2 = \sigma_1^2 + \sigma_2^2 + 2\gamma^2 <I_1><I_2>$$

We suppose $<I_1> = <I_2>$, then the square contrast ρ^2 of the recording speckle is $\rho^2 = \dfrac{1+\gamma^2}{2}$ and the maximum of the contrast of the fringes is 1/3.

To increase the contrast of the fringes, we use a polychromatic laser (a laser with variable wave length) [34]. In the regions of the image with $\gamma = 1$, the grain of the speckle are channeled. One pass band filtering gives theoretically a unit contrast ; in practice, the noise of the film somewhat tempers these results.

This method was successfully used in the context of linear fracture mechanics to determine the characteristic parameters K_1 and σ_{on} for a semi-elliptical surface crack loaded in opening in a bar under tension [35].

3.4.2. METHOD BASED ON THE VARIANCE MEASUREMENT OF THE COMBINATION OF THREE RECORDING INTENSITY FIELDS [36 - 37]

The idea of using a C.C.D. camera instead of holographic film was motivated by the consideration of the density of isochromatic patterns. A C.C.D. camera can be used it the speckle grains are large enough (about one pixel) speckle grains. Then C.C.D. is available.

To include the background intensity due to the fluorescence phenomenon of the material and a part of the scattered light not polarized, we add I_{1B}, I_{2B} to the values I_{1S} and I_{2S} corresponding to the Rayleigh laws

$$I_1 = I_{1B} + I_{1S} \qquad I_2 = I_{2B} + I_{2S}$$

and we suppose $k = \dfrac{<I_{1S}>}{<I_1>} = \dfrac{<I_{2S}>}{<I_2>}$

Under these conditions, the basic relation becomes

$$I = I_1 + I_2 + 2\sqrt{I_{1S}}\sqrt{I_{2S}}\,\gamma\cos(\psi_1 + \psi_2 + \eta)$$

and the variance σ^2 of $I - I_1 - I_2$ is $\sigma^2 = 2k^2\gamma^2 < I_1 >< I_2 >$

The recording of the three fields I, I_1, I_2 and the determination of one variance give a value proportional to γ^2. The Fig. 10 shows the comparison of results obtained by this new method and one previous method [27-34].

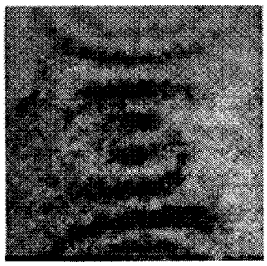

Previous method with holographic film and optical filtering

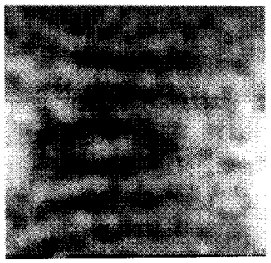

New method with C.C.D. camera and image processing

Fig. 10 - For torsion strain in a bar of square section and a plane slice inclined at an angle of $\pi/4$ from the axis, thickness 8 mm : comparison of the two methods.

3.5. SEPARATION OF ISOCLINIC AND ISOCHROMATIC PATTERNS OF THE SLICE. ISOSTATICS PLOTTING

We recall that the properties of polarization of the scattered light (Rayleigh's law) permits us to realize, with two plane parallel laser beams, the optical slicing giving the analysis of the slice in a light-field polariscope.
In the plane of the slice, we change the orientation of the beams and we record several images of the field (for example, sixteen for a variation of $\pi/2$).

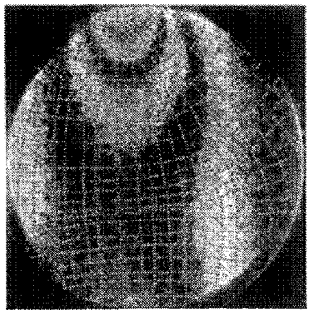

Fig. 11 - Isostatics and isochromatics patterns for one 4mm thickness slice

Then we have sufficient informations characterising a periodic phenomenon and it is possible to calculate in each pixel the Fourier transform of the correlation factor. Filtering in Fourier plane of the zero order gives the isochromatics, and the same operation for the 1 order gives the isoclinic patterns.

When the isoclinic patterns are determined, the isostatics can be plotted to obtain the visualization of the orientations of the secondary principal stress directions.
Figure 11 shows the results for an optical slice in a model loaded by a concentrated force.
This process is important for the shape optimization in mechanical construction.

4 CONCLUSION AND PERSPECTIVES

The optical method based on the grating interrogation on the local plane surface, can make measurements at large distance without contact and without difficulties linked to the use of electrical alimentation of the electrical strain-gages. This is convenient for the control and the measurement in hostile environments. The accuracy is smaller, 10^{-5}, compared to 10^{-6} for strain gages, but the measurement base can be more smaller than that required for rosette strain gage. Holography allows us to extend measurement to quasi-plane surfaces.
Measurement of large strains is limited only by the quality of the marking.
This optical method allow us to extend the metrology in extensometry to domains which are not suitable for electrical strain gages (banded joints, rack, sails, soft materials).
For one dynamic event, the local grating interrogation gives not only the strains but also the rigid motions of the measurement base. Present technical means should permit the extension to large plane surfaces.
Our research on optical slicing methods in three-dimensional photoelasticity with a C.C.D. camera and the means of image processing, show that, for statics, isochromatics and isostatics of a model slice may be determined easily and rapidly.
In the near future, it should be possible to determine the stress tensor in both static and dynamic situations.

References

1. Rayleigh, “Sur la production et la théorie de réseaux de diffraction” Phil. Mag. 47 (8 1) 193-(1874).
2. Dantu M.P., “Utilisation des réseaux pour l'étude des déformations” Annales de l'I.T.B.T.P., n° 12 (reprend une conference du 5 mars 1957) 1958.
3. Post D., “High Sensitivity Displacement Measurement by Moire Interferometry” Pro. 7th . Int. Conf. Exp. Stress Analysis Haïfa Israël 1982.
4. Sciammarella C.A., “Technique of fringe interpolation in Moire patterns” Exp. Mech., pp. 19 A-29 A 7 (11) Novembre 1967.
5. Fu-Pen Chiang, “Techniques of optical spatial filtering applied to the processing of Moire Fringe Patterns” Exp. Mech. pp. 525-526, November 1969.
6. Bell J.F., 1959, “Diffraction grating strain gage” S.E.S.A. Proceeding XVIII (2) 5l-64.
7. Boone P.M., “A method for directly determining surface strain - Fields using diffraction grating” Exp. Mech. 11, Noll (1971).
8. Sevenhuijsen P.J., 1978 “The development of a laser grating method for the measurement of strain distribution in plane, opaque surfaces, V.D.I. Berichte, N°313, pp. 143-147.
9. Brémand F., Lagarde A., “Méthode optique de mesure des déformations utilisant le phénomène de diffraction”. C.R. Acad. Sciences. Paris, 303, série II, 1986, p. 515-520.
10. Brémand F., Lagarde A., “Optical Method of Strain Measurement on a Small Size Area Application” IUTAM Symposium on Yielding, Damage and Failure of Anisotropic Solids, Villars de Lans, Août 1987.
11. Brémand F., Dupré J.C., Lagarde A., “Non-contact and non disturbing local strain measurement methods I Principle”, Eur. J. Mech. A/Solids 11 n°3, pp. 349-366, 1992.
12. Cottron M., Brémand F., Lagarde A., “Non-contact and non-disturbing local strain measurement methods II Applications”, Eur. J. Mech. A/Solids 11 n°3, pp. 367-379.

13. Valle V., Cottron M., Lagarde A., "A new optical method for dynamic strain measurement". 10th International Conference on Experimental Mechanics Lisbon 1994.
14. Meva'a L., Brémand F., Lagarde A., "Optical methods of strain measurement of cylindrical specimen submitted to uniaxial load". 10th International Conference on Experimental Mechanics Lisbon 1994.
15. Cloud G.L., "Optical methods of engineering analysis" Cambridge University Press, pp. 447-491.
16. Rajaona D.R., Sulmont P., "A method of spectral analysis applied to periodic and pseudo-periodic signals", Jour. Comput. Phys., Vol. 61, n°1, pp. 186-193, October 1985.
17. Dupré J.C., "Traitement et analyse d'images pour la mesure de grandeurs cinématiques, déplacements et deformations à partir de la granularité laser et de réseaux croisés, et pour l'étude de couplage thermomécaniques". These de Doctorat de l'université de Poitiers, 1992.
18. Dupré J.C., Lagarde A., "Optical method of the measurement at distance of local strains", XVIII* International Congress of Theoretical and Applied Mechanics, Haïfa, Israël, August 22-28, 1992.
19. Dupré J.C., Cottron M., Lagarde A., "Méthode indépendante des petites translations de l'objet, pour la mesure locale et à distance avec quasi-hétérodynage de l'état de déformations", C.R. Acad. Sci. Paris, Tome 315, Série II, n°4, pp. 393-398, 1992.
20. Wang S.B., Cottron M., Lagarde A, "An holographic grid technic for a whole strain measurement and application to elastoplastic structure". 10th International Conference on Experimental Mechanics Lisbon 1994.
21. Brillaud J., Lagarde A., "Ellipsometry in scatttered light and its application to the determination of optical characteristics of a thin slice in tridimensional photoelasticity". Symposium IUTAM "Optical Methods in Mechanics of Solids", Poitiers, septembre 1979, (Sijthoff Noordoff).
22. Brillaud J., Lagarde A., "Méthode ponctuelle de photoélasticimétrie tridimensionnelle". R.F.M. n° 84, 1982.
23. Brillaud J., "Mesures des paramétres caractéristiques en milieu photoélastique tridimensionnel. Réalisation d'un photoélasticimétrie automatique. Applications". These de Doctorat d'Etat, Poitiers, 1984.
24. Lagarde A., "Non-obstructive Three Dimensional Photoelasticity -Finite strains Applications Photoelasticity". M. Nisida, K Kawata Springer Verlag 1986. Nisida M., Kawata K., Springer Verlag "Photo-elasticity Proceeding" of the International Symposium on Photoelasticity, Tokyo, 1986.
25. Lagarde A., "Dynamic Photoelasticity and Caustics Recent Developments", Springer Verlag, 1987.
26. Desailly R, Lagarde A., "Sur une méthode de photoélasticimétrie tridimensionnelle à champ complet". Journal de Mécanique Appliquée". Vol. 4, n° 1, 1980.
27. Desailly R., "Méthode non-destructive de découpage optique en photoélasticimétrie tridimensionnelle - Application à la mécanique de la rupture". These d'Etat n°336, Poitiers, 1982.
28. Srinath L.S., Torta Mc Graw-Hill, "Scattered Light Photoelasticity". Publishing Company.
29. Srinath L.S., Keshavan S.Y., "A simple method to determine the complete photoelastic parameters using scattered light", Mechanics Research Communications, 5(2), 1978, pp. 85-90.
30. Aben H., "Optical phenomena in photoelastic models by the rotation of principal axes". Expr. Mechanics, Vol. 6, n° 1, 1966.
31. Aben H., Josepson J., "Strange interference blots in the interferometry in inhomogeneous birefringent objects", Applied Optics, vol. 36, n°28, pp. 7172-7179, Oct. 1997.
32. Zénina A., Dupré J.C., Lagarde A., " Découpage optique d'un milieu photoélastique épais pour l'étude des contraintes dans un milieu tridimensionnel", 13ème Congrès Français de Mécanique, Poitiers, France, Vol. 4, pp. 447-450, Sept. 1997.
33. Hickson V.M., "Errors in stress determination at the free boundaries of "Frozen stress" photoelastic model". J. Appl. Phys., Vol. 3, n°6, p. 176-181, 1952.
34. Desailly R, Froehly C., "Whole field method in three dimensional photoelasticity : improvement in contrast fringes". Symposium IUTAM "Optical Methods in Mechanics of Solids", Poitiers, september 1979. Sijthoff Noordhoff.
35. Desailly R., Lagarde A., "Surface Crack Analysis by an Optical Slicing Method of Three Dimensional Photoelasticity" Experimental Stress Analysis Haïfa Israël, août 1982.
36. Dupré J.C., Plouzennec N., Lagarde A., "Nouvelle méthode de découpage optique à champ complet en photoélasticimétrie tridimensionnelle utilisant des moyens numériques d'acquisition et d'analyse des champs de granularité en lumière diffusée", C.R. Acad. Sci, Paris, t, 323, Série II b, pp. 239-245, 1996.
37. Dupré J.C, Lagarde A., "Photoelastic analysis of a three-dimensional specimen by optical slicing and digital image processing", Experimental Mechanics, Vol. 37, n°4, pp. 393-397, Dec. 1997.

Other references can be found in Lagarde A., "Progress in photomechanics". General Lecture 10th International Conference on Experimental Mechanics. Lisbon 1994.

PHASE MEASUREMENT METHOD FOR STRESS ANALYSIS FROM PHOTOELASTIC DATA

J.A. QUIROGA, A. GONZÁLEZ-CANO
Departamento de Óptica. Facultad de CC. Físicas.
Universidad Complutense de Madrid
Ciudad Universitaria s/n. 28040 Madrid (Spain).

Abstract

In recent years, phase measuring techniques have been applied to the problem of extracting information from photoelastic data. In this work, a complete method for stress analysis from photoelastic fringe patterns is presented.

The photoelastic phase maps are obtained with a circular polariscope. For the isoclinics calculation a four-step phase-shift algorithm is used. A white light source is used to avoid problems of low modulation in the fringe pattern. Isochromatics are calculated by a new algorithm developed by us that overcomes the problems associated to low modulation areas produced by isoclinics. The isochromatic parameter can be determined without sign ambiguity. We have also developed a method for analysis of the measurement errors produced by errors in the elements of the polariscope. Finally, using the equilibrium equations, we can obtain the values of the main stresses in the sample from the isoclinic and isochromatic parameters.

1. Introduction

Photoelasticity is a well-established technique for stress analysis and has a wide range of industrial and research applications [1]. Recently, several methods for analyzing photoelastic fringe patterns by means of phase-measuring techniques have been presented [2-7]. The main goal of these techniques is the determination of the distributions of isoclinics and isochromatics in order to be able to analyze the stress distribution in the sample. To develop a complete, fully automated method of stress analysis from photoelastic data, several difficulties must be faced.

First, we must adapt the usual phase-step algorithms to the kind of fringe patterns that appear in photoelasticity. The main problem is that the isoclinic and isochromatic fringe patterns are completely mixed. The modulation of the isoclinic phase map depends on the isochromatics, and vice versa. For that reason, the unwrapping of the corresponding phase maps is difficult because of the appearance of logical inconsistencies associated with low-modulation areas. The methods for the isoclinic calculation proposed in the

A. Lagarde (ed.),
IUTAM Symposium on Advanced Optical Methods and Applications in Solid Mechanics, 17–24.

literature solve this problem adequately, by using of a white light source, instead of a monochromatic one. It is very different with isochromatics. The methods based on phase-measuring techniques that exist in the literature present several problems, the most important being sign ambiguity and dependence on isoclinics. We have developed a new algorithm that avoids sign ambiguity and whose performance is almost independent of the isoclinics, thus overcoming the inconsistencies associated with low-modulation areas produced by them.

Another point to take into account is the different error sources that influence the phase measurement. The error analysis of the phase-shifting algorithms [8,9] must be complemented with a specific study of the contributions of the errors associated with the polariscope. To quantify the errors produced in the determination of the isoclinics and the isochromatics due to this cause we have developed an error analysis [10]. With this method, based on Jones calculus, we are also able to decide in a qualitative way the influence of the different errors in the final measurement.

Finally, we must be able to determine the values of the principal stresses at every point in the sample from the values of the isoclinics and isochromatics. This process is called *stress separation.* To perform this separation we must solve the so-called *equilibrium equations.* When we introduce photoelastic data in these equations we obtain a system of partial differential equations in which the right-hand side is a set of experimental values, which are of course discrete. In this way, the problem of stress separation is reduced to a problem of integration of pairs of difference equations. Different numerical methods have been applied to solve these kind of equations. We propose the use of a multigrid method that is well suited to deal with realistic, noisy sets of data. [11]

The combination of all these techniques (phase-measurement to determine isoclinics and isochromatics, error analysis and multigrid methods to solve the equations for stress separation) permits the complete evaluation of the stress state of a plane sample in few minutes.

2. Isoclinics and isochromatics calculation by phase-measuring techniques

For the isoclinics calculation a circular polariscope is used in the so-called *linear bright field* configuration. The output intensity of the polariscope in this configuration is given by

$$I = 1 - \frac{1}{2} I_0 \sin^2 \frac{\delta}{2} (1 - \cos 4\alpha), \tag{1}$$

where δ and α are the isochromatic and isoclinic parameters respectively. I_0 is the input intensity. We use a four-step phase-shift algorithm where the steps are introduced by rotating the whole polariscope by an angle β. Then, Eqn. (1) takes the form

$$I = I_B + m \cos\left[4(\alpha - \beta)\right] \tag{2}$$

where I_B is a background term and m is the modulation of the isoclinic fringes. Both I_B and m depend on the value of the isochromatic parameter and, because of this, of the wavelength of the used light source. However, the isoclinic parameter does not depend on wavelength. If we take four images with $\beta_i = (i\text{-}1)\pi/8$, $i=1,\ldots,4$, the wrapped isoclinic phase is calculated by

$$W[4\alpha] = \tan^{-1}\left(\frac{I_4 - I_2}{I_3 - I_1}\right) \tag{3}$$

where W is the so-called *wrapping operator,* that denotes the modulo 2π operation.
Eqn. (3) solves the problem of extracting the isoclinic parameter except when modulation is too low. Since m depends on δ, the low-modulation areas depend on wavelength. If a monochromatic light source is used there will be several regions where the value of δ makes m too small. However, this problem can be overcome by simply using a white light source, since then the low-modulation areas corresponding to a given wavelength will be regions of high modulation for another wavelength. Only in the so-called *zero-order isochromatic fringes,* corresponding to the loci of points of the sample for which δ=0, is the modulation very low for every wavelength.
Once $W[4\alpha]$ is determined in this way, we compute the value of the isochromatic parameter that depends on α.
For isochromatics, as we have said, we present a new algorithm. We start now with a general configuration of the circular polariscope. The incident light on the sample is circularly polarized. The output intensity in this case is

$$I = 1 - \sin 2(\psi - \varphi)\cos\delta - \sin 2(\varphi - \alpha)\cos 2(\psi - \varphi)\sin\delta, \tag{4}$$

where α and δ are again the isoclinic and isochromatic parameters and the angles ψ and φ correspond to the orientation of the second quarter-wave plate and the analyzer of the polariscope, respectively.
We take eight images corresponding to different configurations of the circular polariscope, as shown in Table 1.

TABLE 1. Configurations of the polariscope

Configuration	Intensity output	Configuration	Intensity output
1. $P_{90}Q_{45}Q_{45}A_{-45}$	$I_1 = \frac{1}{2}(1 + \cos 2\alpha \sin\delta)$	**5.** $P_{-45}Q_{90}Q_{90}A_0$	$I_5 = \frac{1}{2}(1 + \sin 2\alpha \sin\delta)$
2. $P_{90}Q_{45}Q_{-45}A_{45}$	$I_2 = \frac{1}{2}(1 - \cos 2\alpha \sin\delta)$	**6.** $P_{-45}Q_{90}Q_0A_{90}$	$I_6 = \frac{1}{2}(1 - \sin 2\alpha \sin\delta)$
3. $P_{90}Q_{45}Q_{-45}A_0$	$I_3 = \frac{1}{2}(1 - \cos\delta)$	**7.** $P_{-45}Q_{90}Q_0A_{45}$	$I_7 = \frac{1}{2}(1 - \cos\delta)$
4. $P_{90}Q_{45}Q_{45}A_0$	$I_4 = \frac{1}{2}(1 + \cos\delta)$	**8.** $P_{-45}Q_{90}Q_{90}A_{45}$	$I_8 = \frac{1}{2}(1 + \cos\delta)$

Note: The notation used in the configuration is as follows: *P* stands for *(first) polarizer, Q* stands for *quarter-wave plate* and *A* stands for *analyzer (second polarizer).* The subscript corresponds to the orientation (in degrees) of the element with respect to the chosen x-axis. No reference to the sample (that is placed between the two quarter-wave plates) is included.

From these eight output intensity distributions, the (wrapped) isochromatic phase δ is obtained by

$$W[\delta] = \tan^{-1}\left\{\frac{(I_1 - I_2)\cos 2\alpha + (I_5 - I_6)\sin 2\alpha}{\frac{1}{2}\left[(I_4 - I_3) + (I_8 - I_7)\right]}\right\}. \tag{5}$$

The use of this expression overcomes the usual problems of isochromatic phase extraction, specifically with the problems arising from the existence of low-modulation areas due to isoclinics. From Table 1 we see that I_1-I_2 is modulated by cos 2α and I_5-I_6 by sin 2α. That means that any algorithm that uses only one of these differences, for instance one based on the following equation:

$$W[\delta] = \tan^{-1}\left\{\frac{(I_1 - I_2)}{(I_4 - I_3)\cos 2\alpha}\right\}, \tag{6}$$

would fail in the areas where the value of cos2α is small, since both numerator and denominator would be very small, so there would appear large errors in the phase computation. Obviously, the case will be the same with I_5-I_6, but then the low modulation areas will be associated with low values of sin2α.

We see that the low modulation areas corresponding to the considered differences are in quadrature. That means that if we use both differences, as in Eqn. (5), there will be no regions where both terms in the numerator are small because of the isoclinic parameter. In this way, the modulation of the isochromatic phase map calculated by (5) becomes independent of the value of α, so that a complete separation of the information provided by isochromatics and isoclinics is achieved.

Another advantage of Eqn. (5) is that we work directly with the eight intensity distributions that are smooth functions, suitable to any filtering, since the phase jumps are not affected by this filtering. This is not possible if we work with wrapped phases that are discontinuous by definition.

No sign ambiguity appears in the computation of δ. The algorithm can deal with any number of isochromatic fringes in the field of view, as long as the spatial frequency of the fringes is below the Nyquist limit of the detector. The zero-order isochromatic fringe can be determined by studying the modulation of the isoclinic and isochromatic phase maps.

With this algorithm, both isoclinic and isochromatic wrapped phase maps are good enough for the use of any standard unwrapping algorithm. Unwrapping is necessary if we are going to perform a stress separation process.

3. Error analysis of phase-measuring algorithms applied to photoelasticity

There are many papers in the literature that deal with the problem of error estimation in phase-measuring algorithms. These papers mainly study the effect in the phase calculation of errors in the phase steps, nonlinearities in the detector, additive noise, etc. When applied to photoelasticity, however, a new error source appears for this kind of algorithm, namely the errors associated with the configurations of the polariscope used to obtain the different intensity distributions upon which the phase-measuring algorithms are based. The theoretical expressions for the intensity distributions (e.g., those in Table 1) are valid only for definite orientations of the elements of the polariscope. That means that if we have errors in these orientations the real output intensity of the polariscope does not coincide with the one that is required to obtain the desired phase shifts between intensity distributions, which implies that the calculated phase (e.g., by Eqn. 5) will be in error. The analytical expressions for these intensity distributions cannot be used as a basis of the analysis of the phase error, since they are

true only for the particular configurations of the polariscope for which they are calculated. Therefore, the usual method of error propagation cannot be directly applied to this case.

We have developed a different approach to the error analysis in phase-measuring algorithms applied to photoelasticity based on Jones calculus. To be able to perform simple qualitative and quantitative error analysis our method uses a linear approximation. Instead of using the exact Jones matrices of the error-affected elements, we associate with each element the Jones matrix of the error-free element plus a perturbation Jones matrix that depends linearly on the error. In this way we can calculate the Jones matrix of the whole polariscope, obtaining the Jones matrix of the error-free polariscope and a series of contributions from the different error sources. This "real" Jones matrix can then be used to obtain the output intensity of the error-affected polariscope.

The Jones matrix will be of the form

$$M^* = M + \sum_{j=1}^{5} \varepsilon_j E_j , \tag{7}$$

where M is the "nominal" matrix of the polariscope (i.e., the matrix if all the elements are free of errors) ε_j are the errors corresponding to each error source, and E_j are matrices which can be obtained analytically, and that correspond to the "perturbations" introduced by the errors in the orientation of the elements or the retardation of the plates. Then we can use M to calculate the output intensity

$$I^* = (Ma)^+ Ma, \tag{8}$$

where a is the Jones vector of the initial beam.

We can then use the value of the perturbed intensities I^* in Eqn. (5) to obtain the errors in the isoclinics and the isochromatics. We have developed an error analysis based on the study of the histograms of the distribution of errors for the different values of isoclinics and isochromatics. We have checked the performance of the method by comparing it with experimental results.

4. Stress separation

The determination of the values of the principal stresses at every point in a sample from any kind of direct experimental measurements is called *stress separation.* In photoelastic experiments it is not possible to obtain the values of the principal stresses in every point of the sample directly. What is obtained is the difference of the principal stresses (associated with isochromatics) and their orientations (associated with isoclinics). Therefore, some information must be added to photoelastic data to separate stresses. The method selected by us is the solution of the *equilibrium equations,* which are relationships between the spatial variations of the Cartesian components of the stresses and the value of the shear stress at every point. The connecting point between photoelastic data and the equilibrium equations is shear stress, because it can be directly measured by photoelasticity.

In this way, if σ_x and σ_y are the components of the stress at a given point in a fixed Cartesian system of reference and σ_{xy} is the shear stress, the equilibrium equations, in the absence of body forces, are given by

$$\frac{\partial \sigma_x}{\partial x} + \frac{\partial \sigma_{xy}}{\partial y} = 0, \tag{9}$$

$$\frac{\partial \sigma_y}{\partial y} + \frac{\partial \sigma_{xy}}{\partial x} = 0. \tag{10}$$

The components σ_x and σ_y are related to the isoclinic and isochromatic parameters by

$$(\sigma_x - \sigma_y) = K\delta \cos 2\alpha, \tag{11}$$

$$\sigma_{xy} = \frac{1}{2} K\delta \sin 2\alpha, \tag{12}$$

where

$$K = \frac{\lambda}{2\pi dC}, \tag{13}$$

and λ is the wavelength of the light used, d is the thickness of the sample and C is its photoelastic constant.

From these equations we can obtain a relationship between the sum of stresses $\sigma=\sigma_x+\sigma_y$ and the isoclinic and isochromatic parameters:

$$\frac{\partial \sigma}{\partial x} = -\frac{\partial \Phi}{\partial x} - \frac{\partial \Psi}{\partial y}, \tag{14}$$

$$\frac{\partial \sigma}{\partial y} = \frac{\partial \Phi}{\partial y} - \frac{\partial \Psi}{\partial x},$$

where

$$\Phi = K\delta \cos 2\alpha, \tag{15}$$

and

$$\Psi = K\delta \sin 2\alpha \tag{16}$$

We must then solve (14), a system of partial differential equations in which the right-hand side is a set of experimental values, which are of course discrete. We see that the problem of stress separation is reduced to a problem of integration of pairs of difference equations, which correspond to the discrete version of equation (14). Many numerical methods can be applied for this goal [12]. When dealing with stress separation, these methods must be capable of working with arbitrarily shaped processing areas and of overcoming the problems associated with noise in the data. Noise problems are especially significant, since we measure Φ and Ψ, calculate their partial derivatives and then mix them, so any noise in the experimental data is amplified.

We have adopted a multigrid method to perform stress separation. [11] We can see that σ satisfies Laplace's equation, which can be solved by the well-known Gauss-Seidel relaxation technique. Gauss-Seidel relaxation provides the high-frequency details of the function very quickly, but it propagates this information very slowly, so low-frequency features of the function are difficult to obtain. For this reason, multigrid methods are well suited to improving the efficiency of the Gauss-Seidel relaxation scheme. The key idea of the multigrid approach is to transform the low-frequency components of the solution obtained by a Gauss-Seidel relaxation into high-frequency components on a coarser grid. In a coarser grid, Gauss-Seidel relaxation works very well and we only need to translate the results obtained to the finer grids. A set of grids, each with a double spacing between points can be used, and the information must be transferred first from finer to coarser and then from coarser to finer grids. This is accomplished by the action of two operators, *prolongation* and *restriction.* The algorithm performance is good

5. Experimental results

To show the performance of our method we have chosen a realistic sample, consisting of a plate with a hole and a cut joining the hole with the border (figure 1). A compressive force is applied as indicated in Fig. 1. In Fig. 2 and 3 we show the distribution of isoclinics and isochromatics respectively. Fig. 4 shows the sum of principal stresses calculated by our method. For comparison Fig. 5 shows this sum calculated by a finite element method. For of clarity, contour lines are included. Fig. 6 shows profiles of the σ_1 stress along line *AB* of figure 1, as calculated by our method (line) and the finite element method (circles).

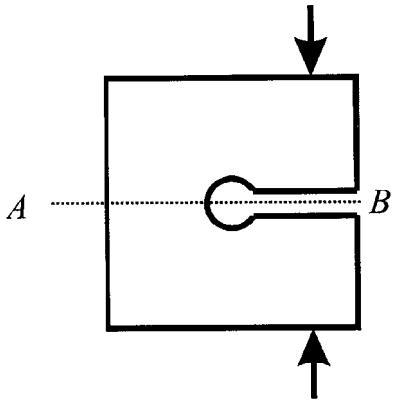

Figure 1. Schematic representation of the sample

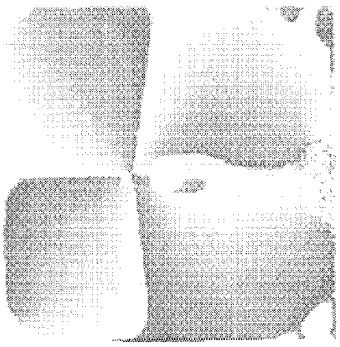

Figure 2. Isoclinics

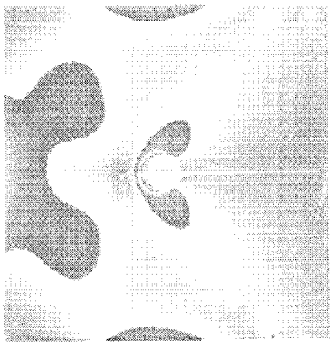

Figure 3. Isochromatics

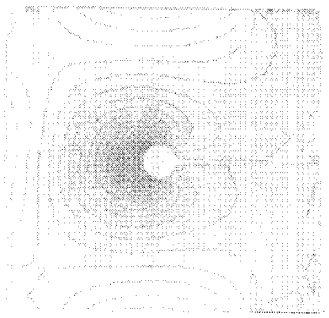

Figure 4. Sum of principal stresses by our method

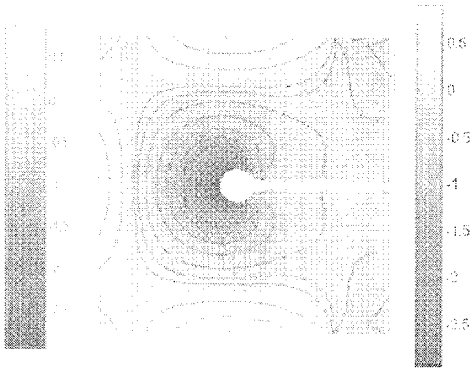

Figure 5. Sum of principal stresses by finite elements

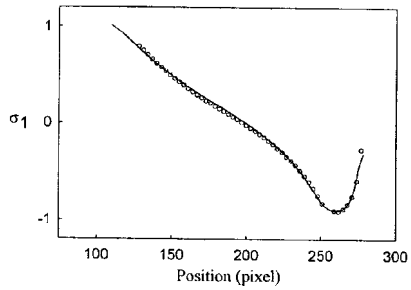

Figure 6. Profile of the σ_1 stress along line *AB*.

References

1. Frocht, M.M., *Photoelasticity,* 2 Vols., John Wiley and Sons, New York, 1941, 1948.
2. Morimoto, Y., Morimoto, Y. Jr., Hayashi, T, Separation of isochromatics and isoclinics using Fourier transform, *Exp. Techn.,* (Sept.-Oct. 1994) 13-16.
3. Buckberry, C., Towers, D., Automatic analysis of isochromatic and isoclinic fringes in photoelasticity using phase-measuring techniques, *Meas. Sci. Technol.,* **6** (1995), 1227-1235.
4. Franz, T., Maidhof, A., Sun, J., "Verfahren und Vorrichtung zur Bestimmung der Isochromatenwerte in der Spannungsoptik", German Patent DE-195 03 851 A1 (August, 10, 1995).
5. Nurse, A.D., Full-field automated photoelasticity by use of a three wavelength approach to phase stepping, *Appl. Opt.,* **36**(1997), 5781-5784.
6. Ng, T.W., Derivation of retardation phase in computer-aided photoelasticity by using carrier fringe phase-shifting, *Appl. Opt.,* **36** (1997) 8259-8263.
7. Quiroga, J.A., González-Cano, A., Phase measuring algorithm for extraction of isochromatics of photoelastic fringe patterns, *Appl. Opt.,* **36** (1997), 8397-8402.
8. Freischlad, K., Koliopoulos, C.L, Fourier description of digital phase-measuring interferometry, *J. Opt. Soc. Am. A* **7** (1990), 542-551.
9. Van Wingerden, K, Frankena, H.J., Smorenburg, C. Linear approximation for measurement errors in phase shifting interferometry, *Appl. Opt.,* **30** (1991), 2718-2729.
10. Quiroga, J.A., González-Cano, A., A method of error analysis for phase-measuring algorithms applied to photoelasticity, *Appl. Opt.,* in press
11. Quiroga, J.A., González-Cano, A., Stress separation from photoelastic data by a multigrid method, *J. Meas. Sci. Technol.,* in press.
12. Press, W.H., Teukolsky S.A., Vetterling, W.T., Flannery, B.P., *Numerical recipes in C. The art of scientific computing,* 2nd ed., Cambridge University Press, Cambridge (UK), 1992.

GENERALIZED PHASE-SHIFTING METHOD FOR MEASURING PHOTOELASTIC FRINGE PARAMETERS AND ITS APPLICATIONS

E. UMEZAKI and Y. NANKA
Department of Mechanical Engineering, Nippon Institute of Technology
4-1 Gakuendai, Miyashiro, Saitama 345-8501, Japan
E-mail: umezaki@nit.ac.jp

Abstract

A generalized phase-shifting method was developed for reducing the influence of noise caused by the variation in light intensity of a light source and so on, and for automatically measuring photoelastic parameters, relative fringe orders and principal-stress directions, in the whole field. The fringe orders obtained using the method were used to measure the stress intensity factor, and the principal-stress directions to extract the zero points. Furthermore the zero points were used to design structural members with holes. The stress intensity factor in a beam with a crack on one side subjected to a three-point bending was accurately obtained from fringe loops multiplied using a technique for drawing a contour map of the fringe order values. The zero points in a T-shaped plate subjected to a compressive load were accurately extracted using a technique for judging the zero points, and were effective to design the plate with holes.

1. Introduction

The photoelastic method is one of the most effective methods for whole-field stress analysis. Photoelastic fringe parameters, fringe orders and principal-stress directions, in the whole field of a model are required in this analysis. There are many available methods for obtaining the fringe parameters[1-10]. Using these methods, the determination of the fringe parameters has been markedly improved. Among these methods, the phase-shifting method, which can be used to obtain the fringe parameters from a combination of several images taken by the rotation of optical components, is promising for the determination of fringe parameters in the whole field. This method has assumed that the time-series light intensity at any point obtained by the rotation of optical components lies exactly on a sinusoidal curve. Actually the light intensity does not lie exactly on such a curve because of noise caused by the variation in the intensity of a light source and by dust on optical components. Such noise has an adverse effect on the results obtained by the phase-shifting method[11]. A method based on Fourier transform[4] has been used to reduce the effect

A. Lagarde (ed.),
IUTAM Symposium on Advanced Optical Methods and Applications in Solid Mechanics, 25–32,

of such noise on the separation of isochromatics and isoclinics from images obtained by rotating the crossed polaroids in a plane polariscope. However, fringe orders were not obtained by the Fourier transform method.

In this study, a generalized phase-shifting method was developed for suppressing such adverse effects and for automatically measuring photoelastic fringe parameters in the whole field, and the parameters were used to measure the stress intensity factors and extract the zero points in a structure member.

2. Generalized Phase-Shifting Method [6, 10]

When the polarizer and analyzer in the dark field and light field are simultaneously rotated by θ from a selected reference, R, the light intensities, I_d, I_l, at any point emerging from the dark-field and light-field plane polariscopes with the monochromatic light source are

$$I_d = I_0 \sin^2 2(\phi - \theta) + I_B \tag{1}$$

$$I_l = -I_0 \sin^2 2(\phi - \theta) + a^2 + I_B \tag{2}$$

where $I_0 = a^2 \sin^2 \pi N$, a is the amplitude of polarized light transmitted through the polarizer, N is the fringe order, ϕ is the direction of principal stress, σ_1, to R, and I_B is the background light intensity.

By applying the Fourier-series expansion to the time-series intensity data, I_{dk} (k=0,1,2,… ,n) obtained according to the rotation of the Polaroids at every angle, $\Delta\theta(=\theta/n)$, from θ=0 to θ=π/2 in a dark-field plane polariscope at each point, I_0, I_B and ϕ in eqs(1) and (2) can be calculated as

$$I_0 = 2\sqrt{a_1^2 + b_1^2} \tag{3}$$

$$I_B = a_0 - \sqrt{a_1^2 + b_1^2} \tag{4}$$

$$\phi = \frac{1}{4}\left[\frac{\pi}{2} - \tan^{-1}\left(\frac{b_1}{a_1}\right)\right] \tag{5}$$

where

$$a_0 = \frac{1}{n}\sum_{m=0}^{n-1} I_{dm}$$

$$a_1 = \frac{2}{n}\sum_{m=0}^{n-1} I_{dm} \cos\left(m\frac{2\pi}{n}\right), \quad b_1 = \frac{2}{n}\sum_{m=0}^{n-1} I_{dm} \sin\left(m\frac{2\pi}{n}\right) \tag{6}$$

In order to measure N, a^2 must be separated from I_0. By applying the Fourier-series expansion to the time-series intensity data, I_{lk} (k=0,1,2,…, n), obtained according to the rotation of polaroids at every angle, $\Delta\theta(=\theta/n)$, from θ=0 to θ=π/2 in a light-field plane

polariscope at each point, a^2 is obtained as

$$a^2 = \frac{I_0}{2} - I_B + \frac{1}{n}\sum_{m=0}^{n-1} I_{lm} \tag{7}$$

Hence the application of a half-angle relation to $I_0 = a^2 \sin^2 \pi N$ gives the relative fringe orders, N

$$N = \frac{1}{2\pi} \cos^{-1}\left(1 - \frac{2I_0}{a^2} \right) \tag{8}$$

where $0 \leqq N \leqq 0.5$

3. **Application**

3.1 MEASUREMENT OF STRESS INTENSITY FACTOR

The fringe orders obtained using the proposed method were used to measure the stress intensity factor in a rectangular plate with a crack at one side under 3-point bending as shown in Fig.1. This specimen was an epoxy resin plate (Arardite-CY230:Hardener-HY956=100:20 in weight ratio) 220 mm long, 50 mm width, 5.8 mm thick, and had a photoelastic sensitivity of 0.076 nun/N. It was subjected to a load of 125.4 N, *P*. The distance between supporting points was 200 mm. The crack length was 6.8 mm.

3.1.1 *Measurement of Fringe Order*

The fringe orders were obtained as follows. Figure 2 shows a polariscope system for measuring the fringe orders. The polarizer and analyzer were simultaneously rotated using the stepper motor driven by the number of pulses transmitted from a personal computer.

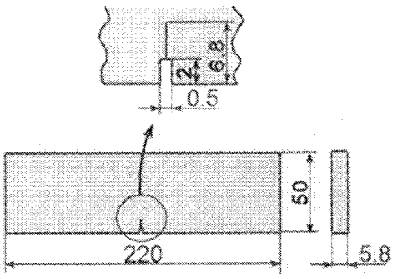

Figure 1. Specimen.

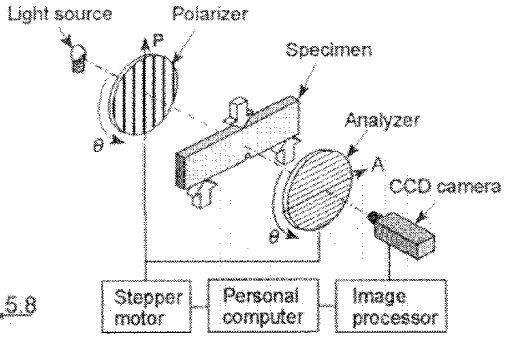

Figure 2. Computerized polariscope.

Images which included both isochromatics and isoclinics were captured using the CCD camera, digitized into 8 bits (256 levels) using the image processor, and stored as a 256 × 256 pixel array in a hard disk for each step of the rotation. In this study, the polarizer and analyzer were rotated with an interval about 0.7 deg, which was obtained by dividing 90 deg into 128 equal angles. As a result, 129 images in the dark and light fields were taken between 0 and 90 deg. A mercury lamp in a plane polariscope was used for obtaining fringe orders.

After the 129 images have been taken in each field, the time-series intensity data were made at each pixel using these images, and stored in a hard disk. The time-series intensity data were used to obtain fringe order at each pixel using the Fourier-series expansion.

Figure 3 shows the isochromatic fringes obtained in a dark-field circular polariscope. Figure 4 shows the relative fringe orders, *N,* obtained by the proposed method. In this figure, the black regions were assigned the value of N=0, and the white ones N=0.5. The regions changed from black to white as the value of N increased from 0 to 0.5.

3.1.2 *Drawing of Fringe Loop*

Fringe loops were drawn from an image with relative fringe orders as follows. First, an image with fringe orders at all pixels in a model, which was obtained using the generalized phase-shifting method, was partitioned into triangles with vertexes *a, b,* and *c,* which were neighboring pixels. Second, the positions at which a fringe loop of a given fringe-order value was passed through on edges *ab, bc,* and *ca* of each triangle were calculated on the basis of linear interpolation of fringe-order values N_a , N_b , and N_c at vertexes *a, b,* and *c*. Third line segments, which were parts of the fringe loop, were drawn between the positions. Finally, the fringe loops were drawn by connecting those line segments.

Figure 5 shows the isochromatic fringes, which were extracted at an interval of fringe order 0.05 between 0 and 0.5. In this figure, the absolute fringe orders were assigned to the extracted fringes. The fringes with integer orders of N=0, 1, 2, … and half orders of N=0.5, 1.5, 2.5, … were not extracted, because the values of N=0 and 0.5 were seldom obtained at the points which were sampled as a 256 × 256 pixel array and digitized into 256 levels used in this study.

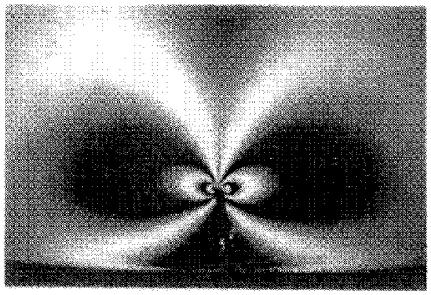

Figure 3. Isochromatics.

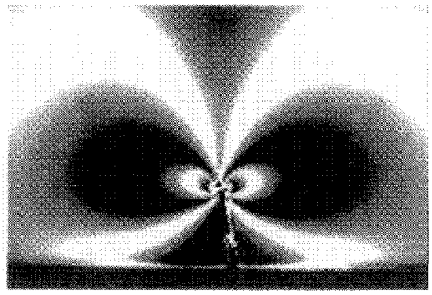

Figure 4. Relative fringe orders obtained using the proposed method.

3.1.3 *Calculation of Stress Intensity Factor*

The fringes shown in Fig.5 were used to calculate the stress intensity factor, $K_{I\,(exp)}$, by the Irwin method[12]. The theoretical stress intensity factor, $K_{I\,(thy)}$, in a rectangular plate with a crack at one side under 3-point bending[13].

Fringes in the vicinity of the crack tip must be used to calculate $K_{I\,(exp)}$ accurately. However, fringes which were located extremely close to the tip were able to be used because they were not drawn accurately due to a large deformation near the tip. Hence, twenty-four fringes with fringe orders 0.85 (L/R), 0.9 (L/R), 0.95 (L/R), 1.05 (L/R),…, 1.45 (L/R), where L/R indicated the fringes at the left and right of the crack shown in Fig.5, were selected to calculate $K_{I\,(exp)}$. Table 1 lists examples of $K_{I\,(exp)}$ obtained by the proposed method. The error in $K_{I\,(exp)}$ measurement decreased as the fringe order increased. The mean errors for four fringes with fringe orders 0.95 (L/R) and 1.05 (L/R) nearest to the 1st-order fringes, which were obtained by conventional techniques such as thinning, and for the twenty-four fringes were 4.3 % and 2.6 %, respectively. The mean error for eighteen fringes with fringe orders 1.05 (L/R), 1.1 (L/R),…, 1.45 (L/R) was 0.9 %. The use of multiple fringes near the crack tip improved the accuracy of the measurement of the stress intensity factor.

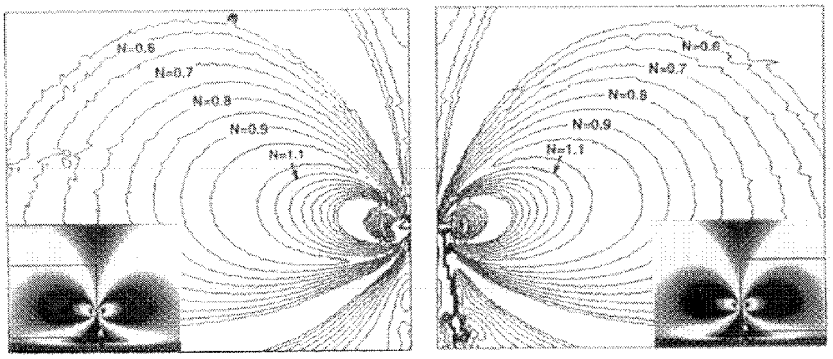

(a) (b)

Figure 5. Cantour maps of fringe order values drawn at intervals of ΔN=0.05.

Table 1. Comparison between experimental and theoretical stress intensity factors, K_{exp} and K_{thy}.

Fringe used to calculate K_{exp}	K_{exp} (MPa · mm$^{1/2}$)	K_{thy} (MPa · mm$^{1/2}$)	Error (%) (= 100 · $\mid K_{exp}$-$K_{thy} \mid /K_{thy}$)
0.9(L/R)*	12.7		8.5
1.1(L/R)	11.9		1.7
1.2 (L/R)	11.7	11.7	0
1.3 (L/R)	11.7		0
1.4 (L/R)	11.7		0

* L/R indicates the fringes at the left and right of the crack shown in Fig. 5.

3.2 EXTRACTION OF ZERO POINT

The principal-stress directions obtained using the proposed method were used to extract the zero points in a T-shaped plate subjected to a compressive load, *P,* of 941N, as shown in Fig.7. Furthermore, the zero points were used to design structural members with holes. This model was made of an epoxy resin plate of 6mm thickness, *t,* 3.6GPa Young's modulus, *E,* 0.36 Poisson's ratio, *v* and 0.1mm/N photoelastic sensitivity, α.

3.2.1 *Measurement of Principal-Stress Direction*

The principal-stress directions were obtained using the same technique as that described in Section 3.1.1 except for use of a white lamp instead of a mercury lamp.

Figure 8 is the image with the principal stress directions used for extracting zero points. In this figure, the black regions were assigned the value of ϕ=0°, and the white ones $|\phi|$=90°. The regions changed from black to white as the value of $|\phi|$ increased from 0° to 90°.

3.2.2 *Judgement of Zero Point*

The extraction of zero points utilized the distribution of principal-stress directions around a zero point which differed from those around a regular point. To extract the positions of zero points, a window was moved on an image with the principal-stress directions, and the distribution around the center of the window was compared with a standard one at a zero point. If the distribution was similar to one of the standard ones, then the center was proposed to be a zero point[14].

Figure 9 shows the zero points superimposed on the isochromatics. The result shows that the location of the zero point extracted by the present method approximately agreed with that of the zero-order isochromatic. Table 2 lists the positions of the zero points extracted using the 11 × 11 pixel window as well as that determined carefully by the naked eye with the aid of a graphic cursor moved on the image. The maximum difference between these coordinates was 1 pixel.

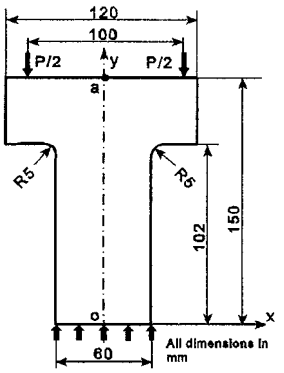

Figure 7. T-shaped plate subjected to compression load.

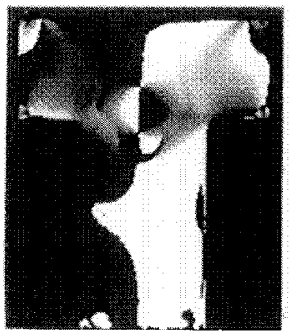

Figure 8. Principal-stress directions.

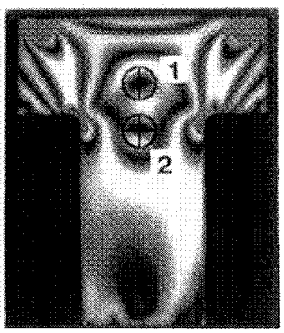

Figure 9. Zero points on isochromatics.

Table 2. CRT coordinates of zero points extracted using a window size of 11x11 pixels and by the naked eye. (Unit:pixel)

Zero ponit no.	Position	
1	127,82	127,83*
2	127,111	127,111*

* By naked eye

3.2.3 *Application of Zero Points to Design of Structural Members*

Holes are frequently made in structural members to decrease the weight of and to pass pipes and wires through these members with an external shape which cannot be changed. The holes should be made at locations at which the stresses in these members are lower than a required value. This is a kind of optimum design. In a plane stress problem, holes at positions where the normal stresses are equal, and the shear stress is zero are desirable. This point is just the zero point.

The stress distributions in structural members with different hole diameters at the zero and other points were analyzed by the finite-element method. The finite-element models had the same shape as that shown in Fig.7 without and with holes and the same material properties, E and v, and thickness, t, as the photoelastic one.

Figure 10 shows the positions of holes in the T-shaped plate. The holes at the zero points and the upper side were called Holes A, B and C, respectively. Hole diameters, D, of 3,5,10 and 15mm were used for each hole. The fringe orders, N, of the simulated isochromatics were obtained by multiplying $(\sigma_1 - \sigma_2)$ obtained from the analysis and αt.

Figure 11 is the relationship between the hole positions and the fringe orders around the holes. The fringe orders around the holes for Holes A and B were approximately constant. The maximum fringe order around the hole was in the case of Hole C. The compressive and tensile stresses alternated around the hole for Hole C, which were different from those in the case of Holes A and B. This implied that the original circular hole became an

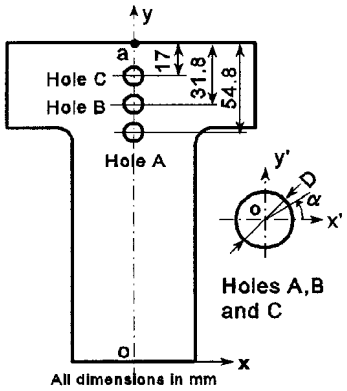

Figure 10. Positions of holes used in analytical models.

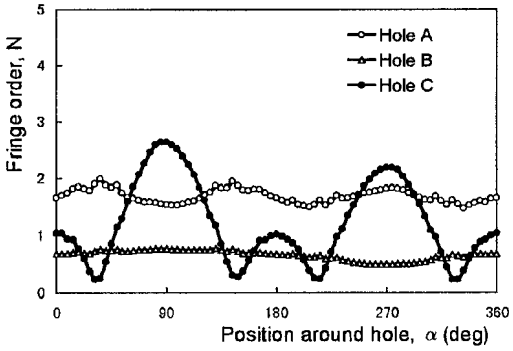

Figure 11. Comparison among fringe orders, N around Holes A, B and C with 3mm diameter.

elliptic one. The T-shaped plate with a hole at the zero point subjected to a compressive load was superior to those with holes at the other points.

The above results showed that the proposed method was effective in designing structural members with holes.

4. Conclusions

A generalized phase-shifting method was developed for reducing the influence of noise caused by the variation in light intensity of a light source and so on, and for automatically measuring photoelastic parameters, relative fringe orders and principal-stress directions, in the whole field. The fringe orders obtained using the method was used to measure the stress intensity factor, and the principal-stress directions to extract the zero points. Furthermore the zero points were used to design structural members with holes. The stress intensity factor was accurately obtained from fringe loops multiplied using a technique for drawing a contour map of the fringe order values. The zero points were accurately extracted using a technique for judging the zero points, and were effective to design a plate with holes.

References

1. Umezaki, E., Tamaki, E., Shimamoto, A., and Takahashi, S. : Whole-field measurement of principal stress directions from photoelastic experiment using image processing system in T.H. Hyde and E. Ollerton (eds.), *Applied Stress Analysis,* Elsevier Applied Science Publishers, London, 1990, pp.526-535.
2. Patterson, E.A., and Wang, Z.F.: Towards full field automated photoelastic analysis of complex components,*Strain,* 27-2 (1991), 49-56.
3. Haake, S. J., and Patterson, E.A.: Photoelastic analysis of frozen stressed specimens using spectral-contents Analysis, *Experimental Mechanics,* 32-3(1992), 266-272.
4. Morimoto, Y., Morimoto, Y. Jr, and Hayashi, T.: Separation of isochromatics and isoclinics using Fourier transform, *Experimental Technics,* 18-5(1994), 13-17.
5. Ajovalasit, A., Barone, S., and Petrucci, G.: Toward RGB photoelasticity: full field automated photoelasticity in white light, *Experimental Mechanics,* 35-3(1995) 29-34.
6. Umezaki, E., Watanabe, H., and Shimamoto, A.: Automatic whole-field measurement of photoelastic fringe orders using generalized phase-shift method, *Post Conf. Proc. VIII Int. Cong. On Experimental Mechanics,* Nashville, 1996, pp. 154-159.
7. Gotoh, J., Yoneyama S., Mawatari, S., and Takashi, M.: Photoelastic analysis from a single piece of image with linearly polarized RGB lights, *Post Conf. Proc. VIII Int. Cong. On Experimental Mechanics,* Nashville, 1996, pp. 160-166.
8. Ramesh, K., and Deshmukh, S.S.: Automation of white light photoelasticity by phase-shifting technique using colour image processing hardware, *Optics and Lasers in Engineering,* 28-1(1997), .47-60.
9. Hoy, D.E.P.: On the use of color imaging in experimental applications, *Experimental Techniques,* 21-4(1997), 17-19.
10. Umezaki, E., and Kawakami, T.: Measurement of principal-stress directions from photoelastic experiment using generalized phase-shift method, *Optical Review,* 4-2(1997), 249-252.
11. Umezaki, E., Koike, H., Shimamoto, A., and Watanabe, H.: Accuracy of measurement of photoelastic fringe orders and principal-stress directions using phase-shift method, J. *Japan Society for Non-Destructive Inspection* (in Japanese), 45-1(1996), 61-67.
12. Takahashi, S., and Nogata, F.: Application of photoelastic method to mechanical engineering (1), *Science of Machine* (in Japanese), 38-1(1986), 82-86.
13. Okamura, H.: *Introduction to linear fracture mechanics* (in Japanese), Baihukan, Tokyo, 1976, pp.21 8-219.
14. Umezaki, E., Watanabe, H., Sirichai, S., and Shimamoto, A.: Extraction of singular points from photoelastic experiment, in J.F.S. Gomes et al. (eds.) *Recent Advances in Experimental Mechanics,* A.A. Balkema, Rotterdam, 1994, pp. 107-112.

INTERFERENCE BLOTS IN INTEGRATED FRINGE PATTERNS

H.ABEN AND L.AINOLA
Institute of Cybernetics,
Tallinn Technical University, 21 Akadeemia tee,
EE0026 Tallinn, Estonia

Abstract. By experiments in integrated photoelasticity it has been observed that besides the usual interference fringes, interference blots may appear. The latter are areas where interference fringes have low contrast or even vanish totally. It has been shown that the cause of the interference blots is rotation of the principal stress axes. Since an arbitrary inhomogeneous birefringent medium is optically equivalent to a system of two birefringent plates, in this paper conditions of the appearance of the interference blots and of the dislocation of integrated fringes is studied using this simple model. Computer generated fringe patterns are compared with the experimentally recorded ones.

1. Introduction

In integrated photoelasticity, a 3-D transparent birefringent specimen is placed in an immersion bath and investigated in a transmission polariscope. Since in the general case both the values of the principal stresses and their directions vary on the light rays, the principle of superposition of birefringence is not valid. Actually, the specimen is an inhomogeneous twisted birefringent medium [1]. Therefore, optical phenomena are much more complicated than in 2-D photoelasticity and can be described by the theory of characteristic directions [1-5].

In the case of strong birefringence, integrated fringe patterns can be recorded. Sometimes these fringe patterns exhibit peculiar features. Figure la shows the integrated fringe pattern of a diametrically loaded sphere in a light-field circular polariscope. Near the points where the load is applied, one can observe dark areas that are similar to fringes but somewhat wider and that cross the basic system of fringes. These are the interference blots.

As another example, Fig. lb shows the integrated fringe pattern of the wall-to-bottom region of a tempered drinking glass. One can observe inter-

A. Lagarde (ed.),
IUTAM Symposium on Advanced Optical Methods and Applications in Solid Mechanics, 33–40.

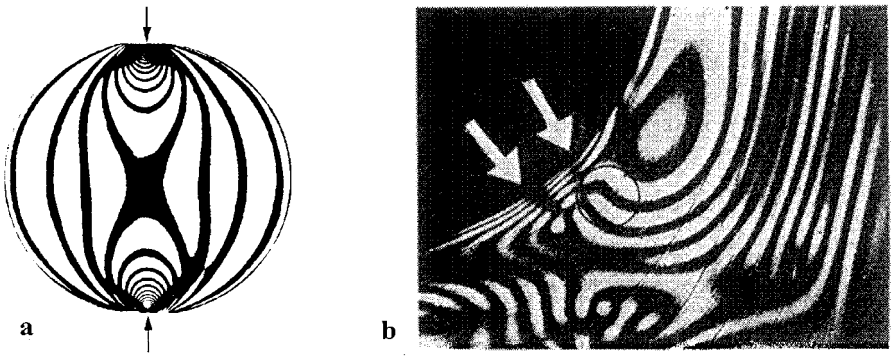

Figure 1. Integrated fringe patterns of a diametrically loaded sphere (a) and of the wall-to-bottom region of a tempered drinking glass (b) in a light-field circular polariscope.

ference blots (shown by arrows) that cross the main fringe system, dislocation of the fringes, etc.

Fringe patterns in Fig. 1 contradict to the conventional theory of fringes in birefringent objects. According to the latter, fringes of different order can never intersect one another, and between the adjacent dark fringes there is always a bright fringe.

Preliminary analysis of the integrated fringe patterns is presented in Refs. 6, 7 and 8. The aim of the present paper is to study in greater detail the reasons of the peculiarities in integrated fringe patterns. This problem is important not only in photoelasticity but also in interferometry and optical tomography of inhomogeneous birefringent phase objects.

According to the Poincaré equivalence theorem [9], an arbitrary inhomogeneous birefringent medium is optically equivalent to a system containing only two birefringent plates, the principal optical axes of which form an angle. Therefore, in this paper the analysis of the interference blots and of fringe dislocations in an inhomogeneous birefringent medium is mostly based on this simple model.

2. Theory of the Fringe Pattern Formation

It is known that the main reason of the complicated optical phenomena in integrated photoelasticity is rotation of the secondary principal stress directions. If the secondary principal stress directions are constant on the ray, integrated optical retardation Δ is expressed through the integral Wertheim law

$$\Delta = C \int (\sigma_1 - \sigma_2) ds, \tag{2.1}$$

where C is photoelastic constant and σ_1, σ_2 are secondary principal stresses.

Light intensity in a dark field circular polariscope is determined by

$$I_1 = I_0 \sin^2 \frac{\Delta}{2}, \tag{2.2}$$

and in a light field circular polariscope by

$$I_2 = I_0 \cos^2 \frac{\Delta}{2}. \tag{2.3}$$

If in the specimen distribution of stress is continuous, integrated fringe patterns determined by Eqs. (2.2) or (2.3) are also continuous, light intensity between fringes varies between 0 and I_0, and no peculiarities in the fringe pattern will occur.

In the case of rotation of the secondary principal directions, in formulas (2.2) and (2.3) instead of Δ appears the characteristic optical retardation Δ_*. The latter is not determined by Eq. (2.1) due to the effect of rotation of the axes, and is related to the stress distribution on the ray in a complicated manner [1,2]. That is the reason of the curious optical phenomena we observe in integrated fringe patterns.

Considering a system of two birefringent plates with optical retardations Δ_1 and Δ_2, and β the angle between the principal axes of the plates, the characteristic retardation can be written as

$$\cos \Delta_* = \cos(\Delta_1 + \Delta_2) \cos^2 \beta + \cos(\Delta_2 - \Delta_1) \sin^2 \beta. \tag{2.4}$$

In rectangular coordinates x and y we have $\Delta_1 = \Delta_1(x, y)$, $\Delta_2 = \Delta_2(x, y)$, $\beta = \beta(x, y)$, and $\Delta_* = \Delta_*(x, y)$. Coordinates x and y are perpendicular to the direction of the wave normal.

If an inhomogeneous birefringent model is investigated in a dark-field circular polariscope, then the light intensity is determined by

$$I_1 = \frac{1}{2} I_0 (1 - \cos \Delta_*), \tag{2.5}$$

and in a light-field circular polariscope by

$$I_2 = \frac{1}{2} I_0 (1 + \cos \Delta_*). \tag{2.6}$$

Consequently, formation of the fringe pattern is completely determined through the function $\cos \Delta_*$. From Eq. (2.4) follows that the function $\cos \Delta_*$ is a complicated function of periodic trigonometric functions of in general aperiodic functions Δ_1, Δ_2 and β.

The distinct fringe structure occurs in regions where one or two of the functions Δ_1, Δ_2 and β change more rapidly than others. Figure 2 shows

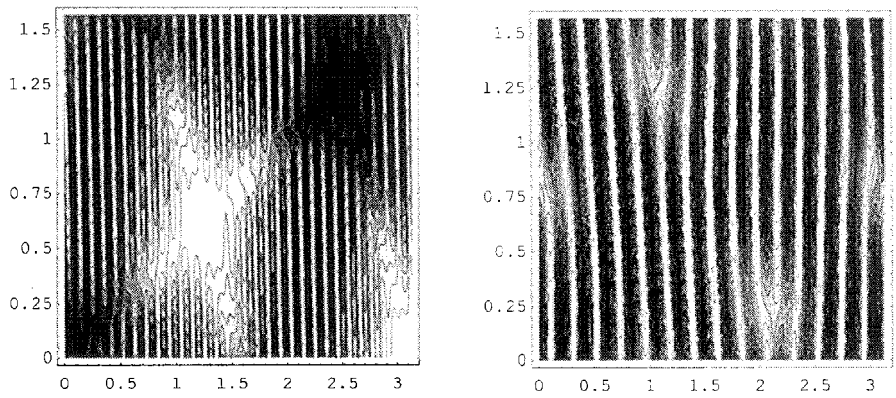

Figure 2. Computer-generated fringe patterns of an optical system containing two birefringent plates: left: $\beta = 30x + y$, $\Delta_1 = x - 2y$, $\Delta_2 = 2x + y$; right: $\beta = x + y$, $\Delta_1 = x - 2y$, $\Delta_2 = 30x + y$.

computer-generated fringe patterns in a dark-field circular polariscope in the cases of different change rates of the functions Δ_1, Δ_2 and β. The distinct fringe patterns can be distorted by two types of irregularities: interference blots [6-8,10] and fringe dislocations [11-13].

3. Interference Blots

We define the interference blot as a region in the fringe pattern where the contrast of fringes is diminished or vanishes completely. This is a region where $\cos \Delta_*$ changes slowly.

Consider the neighborhood of the line $\beta(x, y) = \pi/2$:

$$\beta(x, y) = \pi/2 + \eta(x, y), \tag{3.1}$$

where $|\eta(x, y)| \ll 1$.

In this region we have

$$\cos \beta = -\sin \eta \approx -\eta,$$
$$\sin \beta = \cos \eta \approx 1 - \frac{\eta^2}{2}. \tag{3.2}$$

Therefore, we can write Eq. (2.4) as

$$\cos \Delta_* \approx \cos(\Delta_2 - \Delta_1) - 2\eta^2 \cos \Delta_1 \cos \Delta_2. \tag{3.3}$$

Let us write $\Delta_2 - \Delta_1$ in the form

$$\Delta_2 - \Delta_1 = \pm 2n\pi + \mu(x, y), \tag{3.4}$$

where $|\mu(x, y)| \ll 1$.

Then Eq. (3.3) reveals

$$\cos\Delta_* \approx 1 - \frac{\mu^2}{2} - 2\eta^2\cos^2\Delta_1. \tag{3.5}$$

From Eqs. (2.5) and (3.5) we have

$$I_1 \approx I_0(\frac{1}{4}\mu^2 + \eta^2\cos^2\Delta_1). \tag{3.6}$$

In the same way we obtain

$$\Delta_2 - \Delta_1 = (1 \pm 2n)\pi + \mu,$$
$$I_1 \approx I_0(1 - \frac{1}{4}\mu^2 - \eta^2\cos\Delta_1). \tag{3.7}$$

Consequently, in the neighborhood of the points (x, y) determined by equations

$$\beta(x,y) = \pi/2, \quad \Delta_2(x,y) = \Delta_1(x,y) \pm 2n\pi, \tag{3.8}$$

or

$$\beta(x,y) = \pi/2, \quad \Delta_2(x,y) = \Delta_1(x,y) + (1 \pm 2n)\pi, \tag{3.9}$$

dark or bright areas must appear. The same holds for the neighborhood of the points (x, y) determined by Eqs. (3.8) and (3.9) if $\beta(x, y) = \pi/2 + n\pi$.

Interference blots are seen in Fig. 2 on the left.

4. Fringe Dislocations

Fringe dislocation is an imperfection of the fringe pattern where the normal pattern is distorted by the interposition of one or more extra fringes [11-13]. Using the analogy with crystal structure we can describe the fringe dislocation in terms of the Burgers circuit [11,14]. The Burgers circuit is any fringe-to-fringe path in the fringe pattern cantaining fringe dislocation which forms a closed loop (Fig. 3a). If the same fringe-to-fringe sequence is made in a dislocation-free pattern, the circuit does not close (Fig. 3b). The Burgers vector required to close the circuit describes the magnitude and direction of the slip in the fringe pattern. Notice that to the distance between fringes corresponds the phase shift 2π. Therefore, to the Burgers vector corresponds the phase shift $\pm n2\pi$.

Let us show that fringe dislocations are induced by beat of fringes.

The right side of Eq. (2.4) can be considered as a composite fringe complex which is formed by two sets of fringes (waves) with different frequencies. If we assume that $\Delta_1 \ll \Delta_2$ then the frequencies of the waves are close to each other. In that case the beat phenomena of fringes occurs.

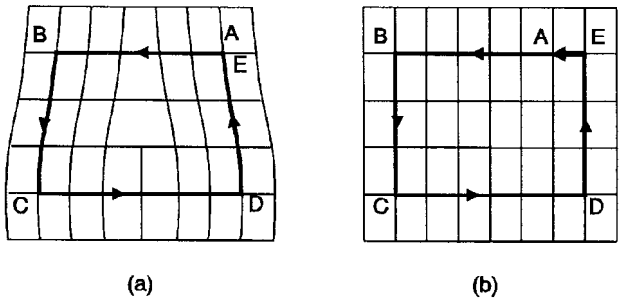

Figure 3. Burgers circuit ABCDE around a fringe dislocation (a); Burgers circuit in a perfect fringe pattern (b).

Equation (2.4) can be written as

$$\cos \Delta_* = A \sin(\Delta_2 + \varphi). \tag{4.1}$$

Here the amplitude and the phase of the composite wave are given by

$$A = \sqrt{\cos^2 2\beta \sin^2 \Delta_1 + \cos^2 \Delta_1}, \tag{4.2}$$

and

$$\tan \varphi = -\frac{\cos \Delta_1}{\cos 2\beta \sin \Delta_1}. \tag{4.3}$$

The amplitude A describes an envelope as a curved surface enclosing the surfaces of fringes (waves). The beat phenomena originate from the low frequency of this envelope.

If in Eq. (4.3) $\cos^2 \beta = \cos \Delta_1 = 0$, we have

$$\tan \varphi = \frac{0}{0}, \tag{4.4}$$

i.e. the phase φ is indeterminate and dislocation of fringes occurs (Fig. 2, right).

5. Boussinesq Problem

Let us consider now optical phenomena in the case of a classical problem of the elasticity theory, the Boussinesq problem, when a vertical concentrated load acts on the surface of a half-space. Integrated fringe patterns in an epoxy cube of 40 × 40 × 40 mm in a light-field circular polariscope for

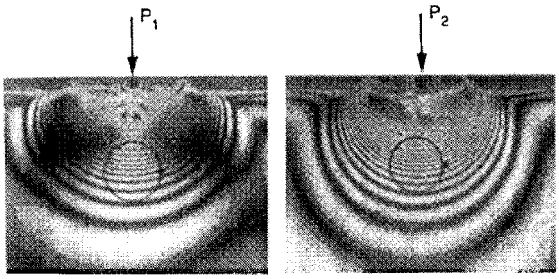

Figure 4. Experimental integrated fringe patterns in a light-field circular polariscope in the case of the Boussinesq problem, $P_2 > P_1$.

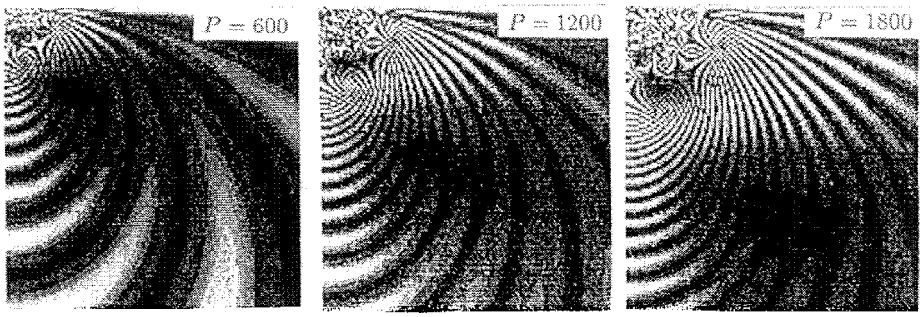

Figure 5. Computer-generated fringe patterns for the Boussinesq problem in a light-field circular polariscope for various loads P (in relative units).

different loads are shown in Fig. 4. In the case of P_1, interference blots are clearly visible. In the case of P_2, interference blots have vanished because of high birefringence. Note that, owing to difficulties in effectuating experimentally a point load, the stress distribution in Fig. 4 deviates to a certain extent from the theoretical one.

To etablish the dependence of the interference blots on the load (or value of the birefringence), integrated fringe patterns for the Boussinesq problem were generated on the computer for different load values (Fig. 5).

In Fig. 5 we see both interference blots and fringe dislocations, similar to those generated above for the optical system containing two birefringent plates. In the fringe pattern for P = 1800, the Burgers vector is 4π.

6. Conclusions

If has been shown both experimentally and numerically that in integrated fringe patterns interference blots and dislocation of fringes may appear. Due to that the fringe order may be ambiguous.

7. Acknowledgements

The authors are thankful to Walter Schumann for his valuable comments and suggestions. Support of the Estonian Science Foundation by grant 2248 is gratefully acknowledged.

References

1. Aben, H.: Characteristic directions in optics of twisted birefringent media, *J. Opt. Soc. Am. A* **3** (1986), 1414-1421.
2. Aben, H.: *Integrated Photoelasticity,* McGraw-Hill, New York *et al.,* 1979.
3. Aben, H.K., Josepson, J.I., and Kell, K-J.E.: The case of weak birefringence in integrated photoelasticity, *Optics and Lasers in Eng.* **11** (1989),145-157.
4. Aben, H., Jdnurm, S., and Puro, A.: Integrated photoelasticity in case of weak birefringence, In: *Proc. of the Ninth Internat. Confer. Exp. Mech.,* Copenhagen. Ashy Tryk, Copenhagen, 1990, **2,** pp. 867-875.
5. Aben, H., and Guillemet, C.: *Photoelasticity of Glass,* Springer-Verlag, Berlin *et al.,* 1993.
6. Josepson, J.: Curious optical phenomena in integrated photoelasticity, In: J.F. Silva Gomes, *et al.* (eds.), *Recent advances in Experimental Mechanics,* A.A. Balkema, Rotterdam, 1994, **1,** pp. 91-94.
7. Aben, H., and Josepson, J.: Nonlinear optical phenomena in integrated photoelasticity, In: *Proc. Internat. Symp. on Advanced Technology in Exp. Mech.,* The Japanese Society of Mechanical Engineers, Tokyo, 1995, pp. 49-54.
8. Aben, H., and Josepson, J.: Strange interference blots in the interferometry of inhomogeneous birefreingent objects, *Appl. Optics* **36** (1997), 7172-7179.
9. Poincaré, H.: *Théorie mathématique de la lumière II.* Paris, 1892.
10. Aben, H., Anton, J., and Josepson, J.: Ambiguity of the fringe order in integrated photoelasticity. In W. Jüptner, W. Osten (eds.), *Proc. 3rd Internat. Workshop on Automatic Processing of Fringe Patterns,* Bremen. Akademie Verlag, Berlin, 1997, pp. 309-317.
11. Nye, J.F., and Berry, M.V.: Dislocations in wave trains, *Proc. Royal Soc. London* **A336** (1974), 165-190.
12. Coullet, P., Gil, L., and Rocca, F.: Optical vortices, *Optics Comm.* **73** (1989), 403-408.
13. Ilyenkov, A.V., Khiznyak, A.I., Kreminskaya, L.V., Soskin, M.S., and Vasnetsov, M.V.: Birth and evolution of wave-front dislocations in a laser beam passed through a photoreactive $LiNbO_3$: Fe crystal, *Appl. Phys.* **B 62** (1996), 465-471.
14. Hull, D., and Bacon, D.J.: *Introduction to Dislocations,* Butterworth–Heinemann, Oxford, 1984.

VISUALISATION OF PHOTOELASTIC FRINGES WITHIN THREE DIMENSIONNAL SPECIMENS USING AN OPTICAL SLICING METHOD

N. PLOUZENNEC*, J-C. DUPRÉ and A. LAGARDE
Université de Poitiers, Laboratoire de Mécanique des Solides, UMR 6610
Bd 3 - Téléport 2 - BP179 - 86960 Futuroscope Cedex - France
**Present address: BAE SYSTEMS, Airbus, Filton, Bristol BS997AR, UK*

Abstract

We show a non destructive method for obtaining the isochromatic and isoclinic fringes in three dimensional photoelastic specimens. The basic idea is to delimit a slice between two plane laser beams. The properties of polarization of the scattered light (Rayleigh law) and the interference possibilities of the diffused beams are used. By introducing speckle pattern properties we can analyse the correlation factor between two scattered beams as we can for the illumination in a plane polariscope in the classical frozen-stress investigation of a slice. We use a monochromatic laser beam, a CCD camera and a PC. As we cannot directly obtain the correlation factor, we do a statistical analysis of the speckle patterns. The variance (a function of the correlation factor) is computed from the light intensities of three images corresponding to the speckle pattern for plane 1 alone, plane 2 alone, and both planes together.

1. Introduction

The experimental study of stress in three-dimensional models remains a problem. The method usually employed is the frozen stress technique coupled with a mechanical slicing and a two dimensional analysis of each slice in a classical polariscope. However, the mechanical slicing of models in different planes takes a lot of time and requires the manufacture of several models for a general study.
To avoid these difficulties, we have developed a non-destructive method of optical slicing using the properties of polarization of the light scattered by a photoelastic material (Rayleigh's law). This phenomenon was used by R. Weller [1] and by many authors for punctual methods [2]-[6]. Our method is based on a whole field technique developed in our laboratory several years ago [7]-[9]. However, this technique, which uses holographic film, polychromatic laser beam, a spectroscope and optical filtering, was very complex, which greatly limited its application. Therefore, we have developed a simpler and faster method using numerical recording and analysis.

A. Lagarde (ed.),
IUTAM Symposium on Advanced Optical Methods and Applications in Solid Mechanics, 41–48.

2. Principle

2.1. INTRODUCTION

The basic idea is to use the properties of polarisation of the scattered light (Rayleigh's law). If one observes along the $\vec{Z}$ vector, perpendicular to the direction of the propagated light beam $\vec{X}$, the scattered light is polarised rectilinearly along $\vec{Z} \wedge \vec{X}$ (fig. 1).

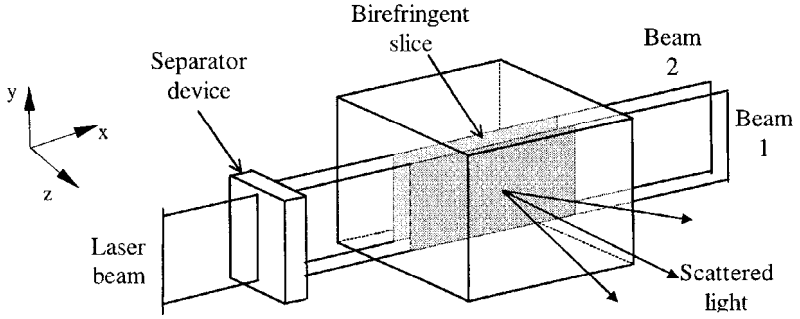

Figure 1. Isolation of a slice with two plane laser beams

The principle of the method is to isolate a slice of the photoelastic model between two parallel plane laser beams (fig. 1). The speckle field observed in the direction perpendicular to the plane of the two illuminated sections is due to the interferences between the light scattered by each section. Their possibilities of interferences depend on the birefringence of the isolated slice. The direct experimental visualisation of the photoelastic fringes is impossible. To obtain this information, we study the characteristics of the scattered light.

2.2. EXPRESSION OF THE SCATTERED LIGHT

The photoelastic model is lit by only one beam (1 or 2), then by both. The scattered light intensities are respectively I_1, I_2 and I. These images are recorded by a CCD camera. The values in grey level of the intensities along one line of these images are plotted on fig. 2.

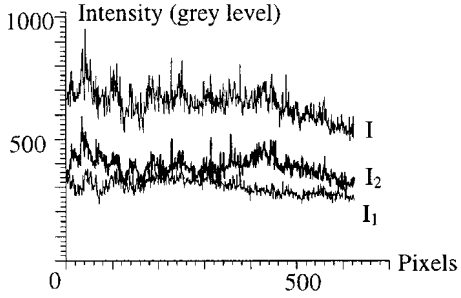

Figure 2. Light intensities profile

By studying one intensity profile (for example I_1), we observe that the speckle field is coupled with a background intensity due to the fluorescence of the specimen, and a part of the scattered light not polarized [10].

The light intensity I_i (i=1 or 2) is expressed as:

$$I_i = I_{iB} + I_{iS} \tag{1}$$

where I_{iB} is the background intensity, I_{iS} is the speckle field intensity.

2.3. SUPERPOSITION OF THE TWO LIGHT FIELDS

The result of the superposition of the two light fields depends on their interference. If they can interfere in a coherent way, they superpose in amplitude ; otherwise, they superpose in intensity [11]. We studied the superposition of I_1 and I_2 using their interference and their statistical properties [12].

The light fields I_{1S} and I_{2S} are due to coherent light, so they superpose in amplitude. The result is

$$I_S = I_{1S} + I_{2S} + 2\,\gamma\sqrt{I_{1S}}\,\sqrt{I_{2S}}\,\cos(\psi_1 - \psi_2 + \eta) \tag{2}$$

where γ is the correlation factor of the two speckle fields, ψ_1, ψ_2 their random phases, η is function of the optical characteristics of the slice.

As the slice is represented by a birefringent plate and a rotatory power, the expression of the correlation factor γ is given by:

$$\gamma^2 = \cos^2 R - \sin 2\alpha \sin 2(\alpha + R) \sin^2 \frac{\varphi}{2} \tag{3}$$

where R is the rotatory power of the slice, α the neutral lines, φ the angular birefringence.

This expression is similar to that usually obtained when analysing a slice (for example by frozen-stress technique and mechanical slicing) between two parallel polarisers. Thus thanks to the correlation factor, the isochromatic and isoclinic fringes of the isolated slice can be visualised.

For thick slices and for a small rotation of the principal secondary stresses (less than 30°), a low modulation of γ corresponds to an isoclinic line where a principal secondary direction is parallel to the polarisation direction, and the isochromatic fringes appear with integer order for maximal values and half order for minimal values [11].

If the rotatory power is negligible (thin slice), equation 3 becomes

$$\gamma^2 = 1 - \sin^2 2\alpha \sin^2 \frac{\varphi}{2} \tag{4}$$

The spatial average of I_S is calculated by the speckle properties [12] of the random variables I_{1S} , I_{2S} , ψ_1 and ψ_2 (ergodicity, stationary, independence of variables...).

$$\langle I_S \rangle = \langle I_{1S} \rangle + \langle I_{2S} \rangle \tag{5}$$

Using the same hypothesis, we calculate the variance of Is.

$$\sigma_S^2 = \sigma_{1S}^2 + \sigma_{2S}^2 + 2\,\gamma^2 \langle I_{1S} \rangle \langle I_{2S} \rangle \tag{6}$$

The light field I_{1B} and I_{2B} are due to incoherent light. So they superpose in intensity. The result is:

$$I_B = I_{1B} + I_{2B} \tag{7}$$

We calculate the spatial average and the variance, and obtain:

$$\langle I_B \rangle = \langle I_{1B} \rangle + \langle I_{2B} \rangle \qquad \text{and} \qquad \sigma_B{}^2 = \sigma_{1B}{}^2 + \sigma_{2B}{}^2 \tag{8}$$

Also, I_B and I_S (or I_{1B} and I_{1S}) (or I_{2B} and I_{2S}) cannot interfere, so we obtain:

$$I = I_B + I_S \qquad \text{and} \qquad \langle I \rangle = \langle I_B \rangle + \langle I_S \rangle \qquad \text{and} \qquad \sigma^2 = \sigma_B{}^2 + \sigma_S{}^2 \tag{9}$$

2.4. PROPERTIES OF THE RESULTING FIELD

The results obtained above give the expression for the global light intensity:

$$I = I_1 + I_2 + 2\,\gamma\sqrt{I_{1S}}\,\sqrt{I_{2S}}\,\cos(\psi_1 - \psi_2 + \eta) \tag{10}$$

Its spatial average is $$\langle I \rangle = \langle I_1 \rangle + \langle I_2 \rangle \tag{11}$$

and its variance $$\sigma^2 = \sigma_1{}^2 + \sigma_2{}^2 + 2\,\gamma^2 \langle I_{1S} \rangle \langle I_{2S} \rangle \tag{12}$$

If we consider that the intensities of the two incident beams are equal and the averages of scattered lights are equivalent, we have

$$\langle I_{1S} \rangle / \langle I_1 \rangle = \langle I_{2S} \rangle / \langle I_2 \rangle = k \tag{13}$$

Here k is a factor, function to the scattered properties of the material ; experimentally it is approximately equal to 1/10.

Equation 12 becomes $$\sigma^2 = \sigma_1{}^2 + \sigma_2{}^2 + 2\,k^2\,\gamma^2 \langle I_1 \rangle \langle I_2 \rangle \tag{14}$$

From this equation, we deduce

$$k^2\gamma^2 = \frac{\sigma^2 - \sigma_1{}^2 - \sigma_2{}^2}{2 \langle I_1 \rangle \langle I_2 \rangle} \tag{15}$$

3. Experimental set-up

The experimental set-up (fig. 3) includes by an argon laser, a separator device and a cylindrical lens in order to obtain two plane laser beams. A CCD camera (perpendicular to the laser beams) and a PC are used for the data acquisition and processing. A Babinet compensator is placed between the lens and the cylindrical lens to minimise the intensities of the Weller fringes (the scattering phenomenon is used like an analyser). These fringes have no influence on the results if their maximal intensities are less than 10 % of the global intensity (this phenomenon has been studied by numerical simulation [13]).

Special care must be taken to choose the CCD captor. The speckle field intensity is very low compared to the background intensity (Fig. 1), so a CCD camera with a low signal-noise ratio is chosen. Some tests are made with a classical camera with 512×512 pixels coded by 256 grey levels. When we took care to have low electronic amplification, with a ratio of 40 dB, we obtained good results. However, the small sensitivity and resolution could limit the tests for all specimens. The CCD camera has a high resolution (1000×1000 pixels coded by 1024 grey levels) and a ratio of 50 dB.

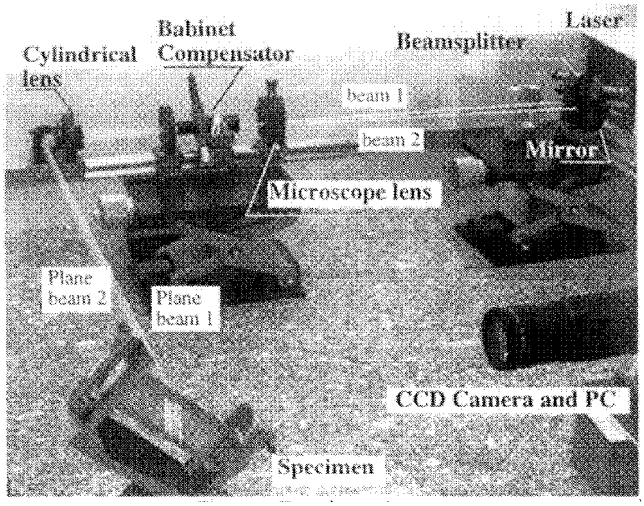

Figure 3. Experimental set-up

4. Obtaining of the photoelastic fringes

The model is placed on the way of the laser beams that are oriented to isolate the slice to study. If the model is not in an optical index liquid tank, the beams have to be perpendicular to the surface of the model to avoid refractions.

Three images, I_1, I_2 and I, corresponding to the speckle patterns for plane 1 alone, plane 2 alone, and both planes together are recorded by the CCD camera and used to calculate a fourth image of $k^2\gamma^2$ using equation (15).

To diminish the calculation time, we first calculate

$$I' = I - I_1 - I_2 \tag{16}$$

Then we calculate the variance of I': σ'^2 ; the expression of $k^2\gamma^2$ becomes

$$k^2\gamma^2 = \frac{\sigma'^2}{2\langle I_1\rangle\langle I_2\rangle} \tag{17}$$

For each pixel (i,j), the different coefficients appearing in equation (17) are calculated with a calculation area of (2N+1)×(2N+1) pixels centred on (i,j).

For i and j varying, the spatial average of I' is calculated by equation 18 :

$$< I'(i,j) >= \left(\sum_{k=-N}^{k=+N} \sum_{l=-N}^{l=+N} I'(i+k, j+l) \right) / (2N+1)^2 \tag{18}$$

When the spatial average is calculated, we can obtained the variance

$$\sigma'^2(i,j) = < [I'(i,j) - < I'(i,j) >]^2 >$$
$$= \left(\sum_{k=-N}^{k=+N} \sum_{l=-N}^{l=+N} [I'(i+k, j+l) - < I'(i+k, j+l) >]^2 \right) / (2N+1)^2 \tag{19}$$

Equation (18) is also used to calculate $\langle I_1 \rangle$ and $\langle I_2 \rangle$, by replacing I' by I_1 and I_2. Then, we use equation (17) to calculate $k_2\gamma_2$ for each pixel (i,j). Thus, we obtain the image of the isoclinic and isochromatic fringes. To eliminate a part of the speckle on the final image, a low-pass filter can be used. The resolution of this image is function of the speckle depth and the size of the calculation area for the spatial average. Using multiple simulations [13], we showed that with a speckle size of 1 pixel and an area of 3 by 3 pixels, the minimal visible period is about 15 pixels. This limitation becomes 30 pixels using a low pass filter (10x10 pixels).

5. Experimental results

The models used for the experimental tests are made in epoxy resin (photoelastic constant: 30 10^{-12} m^2/N).

The first experimental test is for torsion on a bar of square section (34×34 mm^2). The images experimentally obtained correspond to slices inclined at an angle of $\pi/4$ with respect to the axis of the model (fig. 4). Thus, the birefringence and the directions of the principal stresses vary along the observation direction.

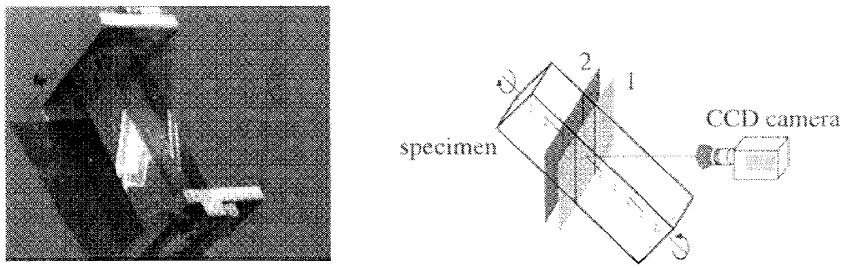

Figure 4.: Torsion strain on a bar of square section

Figure 5 shows the three recorded images I_1 , I_2 and I, for a thickness of the slice equal to 6 mm. In figure 5-c, we can faintly discern the Weller fringes ; their intensity is lower than 10% of the global intensity.

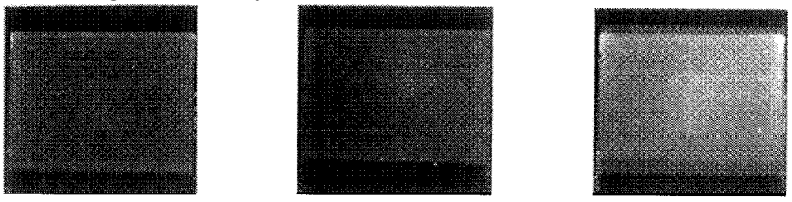

a) I_1 b) I_2 c) I

Figure 5.: Experimental speckle patterns

Using these images, we calculate $k^2\gamma^2$ for an area of 3x3 without a low pass filter (fig. 6-a), and with a low pass filter (fig 6-b). We observe two bright and large isoclinic zones and the isochromatic fringes. The fractional fringe order could be found with a manual procedure, but a full-field automatic calculation seems to be still hard to develop.

a) without low pass filter b) with low pass filter

Figure 6.: Fringe pattern

Our experimental set up allows recording the images for thicknesses varying from 0,5 mm to 10 mm. A small thickness is interesting for studying zones with high stress concentration. For the same loading, the slice thickness varies from the smaller to the higher value. Each time, the three images I_1, I_2 and I are recorded and the correlation factor calculated. These images are shown in figure 7. The number of isochromatic fringes increases with the thickness of the slice, and the isoclinic fringe is constant except when the slice is thick (fig. 7-d); in that case, the isoclinic fringe disappears in the centre of the image where there is a large rotation of the stresses ; we do suppose that the slice is thin. We see continuous isochromatic fringes in the centre.

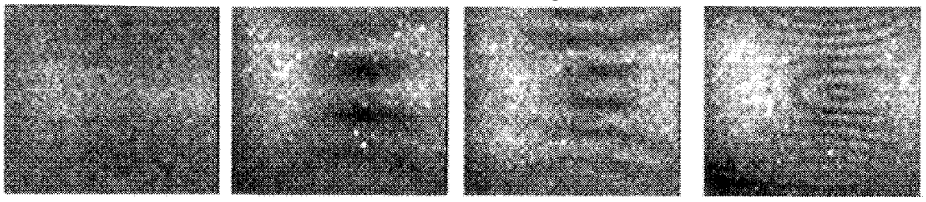

a) 0,5 mm b) 2mm c) 4mm d) mm

Figure 7. Experimental isochromatic and isoclinic fringes for several thickness of slice

The second test is a concentrated loading on the top of a prismatic specimen (section = 60×45 mm^2 and length = 110 mm) (fig. 8). A quick scanning of the model has been realised with 2 mm of translation between each slice. In order to see many fringes, we have chosen a test with slice thickness equal to 6 mm. It is possible to find the stress concentration area and to study a part of it, by zooming in and reducing the thickness of the slice.

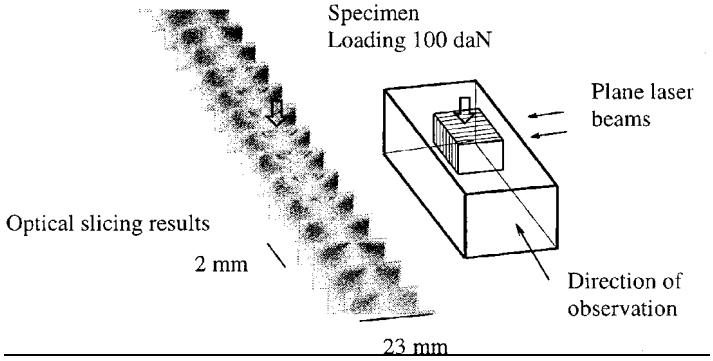

Figure 8. Scanning of a prismatic specimen submitted to a concentrated loading

6. Conclusions

We present a new method using optical slicing coupled with a CCD camera and a PC for rapid visualisation isochromatics and isoclinic fringes of a slice, within a photoelastic material. The slice is delimited by two laser beams, and the scattered light is numerically analysed to obtain the correlation factor. The experimental set up is easy to realise and, once the images are recorded, the calculations are done in few seconds. Our slicing method takes into account the parameters inside the isolated slice, but not the optical path through the specimen. Our set-up allows the thickness slice to vary from 0.5 to 10 mm. In 3D photoelasticity, the rotation of the secondary principal stresses in the thickness of the studied slice cannot be neglected, so the slice is represented by a photoelastic plate and a rotatory power. If the thickness is sufficiently small, the rotatory power has no effect on the isoclinic and isochromatic parameters. The largest studied field is about $150\times150mm^2$ (0.15 mm/pixel) and the smallest $5\times5mm^2$ which permits the study of loaded zone. A model immersed in optical index liquid tank can be examined in different views. For a small size of image, a quasi-real time visualisation can be realised. A rapid study of a specimen can be made in order to visualise the stress concentration and the direction of the secondary principal stresses. On the first industrial applications could be the optimization of the shape of models.

7. References

1 Weller, R., (1941) Three dimensional photoelasticity using. scattered light, Journal of Applied *Physics,* **12,** 610-616.

2 Robert, A. et Guillemet, E., (1963) Nouvelle méthode d'utilisation de la lumière diffusée en photoélasticimétrie à trois dimensions, *Revue Française de Mécanique,* 147-157.

3 Robert, A. et Royer, J., (1980) Photoélasticimétrie tridimensionnelle à lumière diffusée, *Journal de Mécanique Appliquée,* **4,** 445-460.

4 Cheng, Y.F. (1967) A dual observation method for determining photoelastic parameters in scattered light, *Experimental Mechanics,* **7,** 140-144.

5 Brillaud, J. et Lagarde, A., (1982) Méthode ponctuelle de photoélasticité tridimensionnelle. Application, *Revue Française de Mécanique,* 41-49.

6 Srinath, L.S., (1983) *Scattered light Photoelasticity,* Tata McGraw-Hill.

7 Desailly, R., Brillaud, J. et Lagarde, A., (1974) Enregistrement holographique de caractéristiques associées aux formes de lumière du rayonnement diffuse par les milieux transparents biréfringents, *C.R.A.S.,* T. 279, Série B, 391-393.

8 Desailly, R. et Lagarde, A., (1977) Application des propriétés des champs de granularité à la photoélasticimétrie tridimensionnelle, *C.R.A.S.,* T. 284, Série B, 13-46.

9 Desailly, R. et Lagarde, A., (1980) Sur une méthode de photoélasticimétrie tridimensionnelle non destructive à champ complet, *Journal de Mécanique Appliquée,* **4,** 3-30.

10 Brillaud, J. et Lagarde, A., (1975) Mesure des formes de lumière en diffusion et applications, *C.R.A.S.,* T. 281, Série B, 329-332.

11 Desailly, R. et Lagarde, A., (1984) Méthode de découpage optique de photoélasticimétrie tridimensionnelle-Application, *Revue Française de Mécanique,* 47-55.

12 Dainty, J.C., (1975) Laser Speckle and related phenomena, *Topics in Applied Physics,* Springer Verlag,.

13 Dupré, J-C., Plouzennec, N. et Lagarde, A., (1996) Nouvelle méthode de découpage optique à champ complet en photoélasticimétrie tridimensionnelle utilisant des moyens numériques d'acquisition et d'analyse des champs de granularité en lumière diffusée, *C.R.A.Sci.,* T 323, Série II b, 239-245.

OPTICAL APPROACHES OF A PHOTOELASTIC MEDIUM FOR THEORETICAL AND EXPERIMENTAL STUDY OF THE STRESSES IN A THREE-DIMENSIONAL SPECIMEN

A. ZENINA
LMS, Université de Poitiers, CNRS UMR 6610
SP2MI - Téléport 2 - BP 179, 86960 FUTUROSCOPE CEDEX, FRANCE

J.C. DUPRE
LMS, Université de Poitiers, CNRS UMR 6610
SP2MI - Téléport 2 - BP 179, 86960 FUTUROSCOPE CEDEX, FRANCE

A. LAGARDE
LMS, Université de Poitiers, CNRS UMR 6610
SP2MI - Téléport 2 - BP 179, 86960 FUTUROSCOPE CEDEX, FRANCE

Abstract

The aim of this study is to develop a procedure consisting in comparing real photoelastic fringes with the fringe pattern calculated with a theoretical or numerical stress field. This process can be used to validate for example the boundary conditions or mesh of a three-dimensional mechanical problem. We show three optical approaches of a three-dimensional specimen giving the classical photoelastic fringes (isochromatic and isoclinic patterns) from a theoretical stress distribution. So we used a new experimental technique for the study of stress fields in a three-dimensional medium. We show a comparison between these three formulations and experimental results obtained by our non-destructive method of optical slicing.

1 Introduction

The study of the stress state of a three-dimensional specimen may be effected by numerical means (like a finite element method). But for industrial problems, an experimental study is necessary to validate the theoretical and numerical approach as a boundary conditions, shape and mesh. Usually this is done by photoelasticimetry.

A. Lagarde (ed.),
IUTAM Symposium on Advanced Optical Methods and Applications in Solid Mechanics, 49–56.

We recall that for a plane polariscope and a two-dimensional analysis of a beam, which can be mechanically sliced after stress freezing, allows us to visualize two fringe patterns. The directions of principal stresses are obtained from isoclinic fringes, their difference is given by isochromatic fringes. In this paper, we used an another experimental solution, developed in our laboratory. This technique is a non-destructive method of optical slicing giving the classical photoelastic fringes [Plouzennec, N., et al. 1998] [Dupré, J.C., et al. 1997] [Dupré, J.C., et al. 1996].

Many studies have been undertaken to separate the stresses, their orientations and to integrate the equilibrium equations [Dally, J.W., et al. 1991] in order to compare them with the simulated results. However these methods demand a high precision of measurement, a separation and an unwrapping of the isoclinic and isochromatic parameters. We present another solution avoiding most of these inconvenient. It consists in calculating the isoclinic and isochromatic fringes from a three-dimensional stress field obtained theoretically, for example by finite elements, and in comparing them with experimental results. Nevertheless we have to correctly determine the optical parameters due to the stress fields. The aim of this work is to study three approaches to a thick medium and to compare them with experimental results.

2 Optical approaches of a three dimensional medium

We calculate the photoelastic fringes arising from a plane polariscope in three ways.

2.1 TWO-DIMENSIONAL APPROACH

In this case, the difference between, and directions of, the stresses are constant along the thickness of the specimen.

The light intensity obtained in a plane polariscope is expressed by

$$I = I_0\left[1 - \sin^2 2\alpha \sin^2 \frac{\varphi}{2}\right] \qquad (1)$$

Here I_0 is the light intensity when the model is unloaded, α is the direction of one of the principal stresses. The birefringence φ is given by

$$\varphi = \frac{2\pi C}{\lambda}(\sigma_1 - \sigma_2)\, e \qquad (2)$$

Here e represents the slice thickness shown in figure 1, $(\sigma_1 - \sigma_2)$ is the difference between the principal stresses, C is the photoelastic constant and λ is the wavelength of the used light.

2.2 ABEN SCHEMATISATION

Aben's research (1966) allow us to obtain the mechanical parameters φ, α from a knowledge of the three physical parameters R, α^*, φ^* , provided that $(d\alpha/dz = \alpha_0)$, and $(\sigma' - \sigma'')$, the secondary principal stress difference, constant along the thickness of the specimen. The beam is schematized by a birefringent plate (α^* and φ^*) followed or preceded by a rotator power R (figure 2). The values of R, α^*, φ^* and α, α_0, φ are linked by the following relations [Brillaud, J., et al. 1983] [Desailly, R., et al. 1984] :

$$\mathrm{tgR} = \frac{\mathrm{tg}\alpha_0 - \frac{\alpha_0}{X}\mathrm{tgX}}{1 + \frac{\alpha_0}{X}\mathrm{tg}\alpha_0\mathrm{tgX}}, \qquad \cos\varphi^* = 1 - \frac{\varphi^2}{2X^2}\sin^2 X$$

$$X = \frac{\sqrt{\varphi^2 + 4\alpha_0{}^2}}{2}, \qquad \alpha^* = \alpha - \frac{R}{2} + \frac{\alpha_0}{2} \tag{3}$$

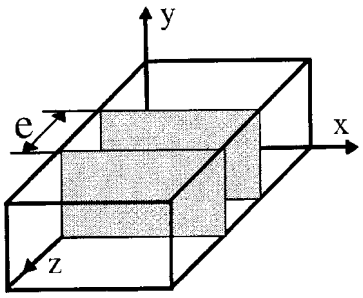

Figure 1 : The first approach

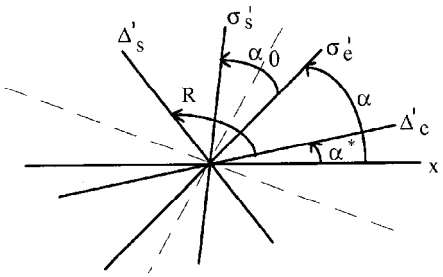

Figure 2 : Aben schematization

Figure 2, shows the optical parameters : (Δ'_e , Δ'_s), the characteristic directions of entrance and exit, and the mechanical parameters (σ'_e , σ'_s) in the principal secondary directions. The light intensity coming from the plane polariscope [Desailly, R., et al. 1984] is then

$$I = I_0\left[\cos^2 R - \sin 2\alpha^* \sin 2(\alpha^* + R)\sin^2 \varphi^*/2\right] \tag{4}$$

2.3 DISCRETE ANALYSIS INTO THIN SLICES

This technique consists in taking a thick beam and dividing it into n thin slices shown in figure 3. Every thin slice is characterized by α_i and φ_i constant along the thickness (as in the first approach) [Zenina, A., et al.19971 [Aben, H., et al. 1997].

An iterative process has been developed for the numerical calculation of the light components after crossing the first slice from a direction of given polarization (x_0, y_0). We use these new components (x_i , y_i) and repeat the calculation for the following beams, and soon until the last slice.

$$\begin{pmatrix} X_0 \\ Y_0 \end{pmatrix}_{(x_0,y_0)} \xrightarrow{R\alpha_1} \begin{pmatrix} X_0 \\ Y_0 \end{pmatrix}_{(x_1,y_1)} \xrightarrow{S\varphi_1} \begin{pmatrix} X_1 \\ Y_1 \end{pmatrix}_{(x_1,y_1)} \xrightarrow{R\alpha_2} \ldots \quad (5)$$

$$\ldots\ldots \xrightarrow{S\varphi_{n-1}} \begin{pmatrix} X_{n-1} \\ Y_{n-1} \end{pmatrix}_{(x_{n-1},y_{n-1})} \xrightarrow{R\alpha_n} \begin{pmatrix} X_{n-1} \\ Y_{n-1} \end{pmatrix}_{(x_n,y_n)} \xrightarrow{S\varphi_n} \begin{pmatrix} X_n \\ Yn \end{pmatrix}_{(x_n,y_n)}$$

with :

$$R_{\alpha i} = \begin{bmatrix} \cos\alpha i & \sin\alpha i \\ -\sin\alpha i & \cos\alpha i \end{bmatrix} \quad S_{\varphi i} = \begin{bmatrix} 1 & 0 \\ 0 & (\cos\varphi i - j\sin\varphi i) \end{bmatrix} \quad (\text{for } i = 1, n)$$

The components of the light after the last slice are (x_n, y_n). After crossing the analyzer (angle β figure 3), the light intensity is

$$I = I_0\left[(\mathrm{Re}(x_n)\cos\beta + \mathrm{Re}(y_n)\sin\beta)^2 + (\mathrm{Im}(x_n)\cos\beta + \mathrm{Im}(y_n)\sin\beta)^2\right] \quad (6)$$

Re and Im denote real and imaginary part.

In order to obtain the same fringes using the formulations (4) or (6), numerical simulations have shown that the ratio between α_0 and the number of slice is 1/3.

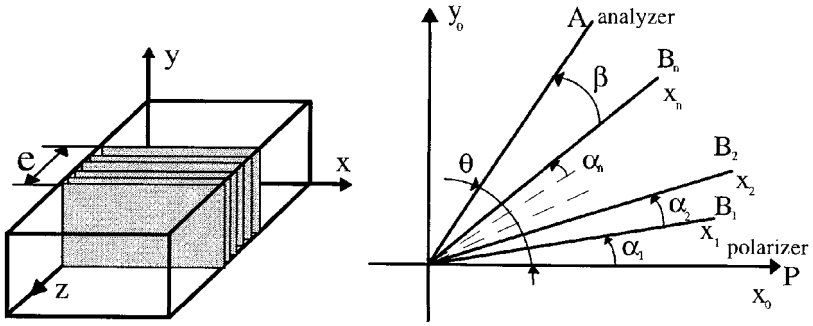

Figure 3 : Series of thin slices

2.4 COMPARISONS

We have numerically simulated the three approaches by varying φ from 0 to 10π horizontally and a from $-\pi/4$ to $\pi/4$ vertically and by applying different values of α_0. Figure 4 shows the series of images obtained.

The first image (figure 4A) corresponds to the first approach, the second one (figure 4B) to Aben's formulation, and the last (figure 4C) to the discrete calculation of a series of thin slices.

We note that the image obtained by the first approach, which cannot allow a variation of the stresses along the thickness, is different from the others. The second and the third images are obtained for a variation of the stress direction α_0 of 30 degree.

Furthermore Aben's formulation cannot be used for a variation of the stress difference along the thickness.

We note that numerical problems appear in Aben's scheme (paragraph 2.2); they are due to trigonometric calculation (equation 3), which is why this procedure is relatively complex.

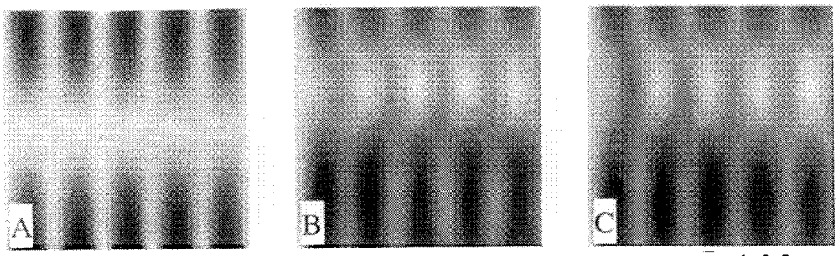

Approach 2.1 Approach 2.2 Approach 2.3

Figure 4 : Simulations for $\alpha_0 = 30°$

If we consider a variation of the stresses difference along the thickness of the specimen, we can apply only the third schematization (approach 2.3), We obtained the images shown in figure 5.

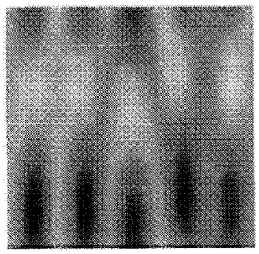

Approach 2.3

Figure 5 : Simulations for $\alpha_0 = 30°$ with a variation of the stress difference along the thickness

3 Application

3.1 EXAMPLE OF A TWO-DIMENSIONAL STUDY

The discrete calculation of a series of thin slices can be used from results obtained by the finite elements method. Figure 6 shows a plate of 10 mm of thickness submitted to combined torsion – bending; we have calculated the stress field with a corresponding mesh formed by 90x20x5 cells. The third approach gives more realistic images, and agrees with experimental images obtained by a plane polariscope.

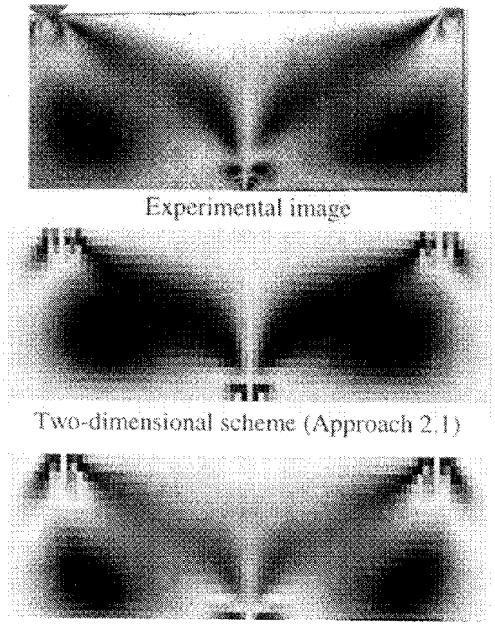

Figure 6 : Comparison for a combined torsion-bending test

3.2 EXAMPLE OF A THREE-DIMENSIONAL STUDY

If we study more complex problems, we must slice the specimens in several parts. The calculation of the fringes can be easily made by our approach (2-3) but for the experimental study we used a method developed in our laboratory. The photoelastic model is optically sliced by two plane laser beams. The analysis of the scattered light gives fringes equivalent to those obtained in a plane polariscope [Plouzennec, N., et al. 1998] [Dupré, J.C., et al. 1997] [Dupré, J.C., et al. 1996).

As we can modify the thickness of the slice from 0.5 mm to 10 mm, we used this technique in order to validate the various approaches.

Figure 7 shows simulated and experimental results for a torsion strain in a bar of square section. Using a theoretical expression of the stress field [Caignaert, G., et al. 1988] [Timoshenko, S., et al. 1961], we have simulated the different fringe patterns for the three schemes (formulas 1, 4 and 6).

The obtained images correspond to slices inclined at an angle of $\pi/4$ with respect to the axis of the model (figure 7). The experimental results show that the 2.3 and 2.2 designs are more faithful to reality than the first (2.1), especially for the disappearance of the isoclinic fringes. A difference appears between the two three-dimensional approaches because in this case we have an evolution of the stresses difference along the thickness; this condition is not included in Aben's theory.

In order to validate the boundary conditions, a difference of 10% of the rotation can be detected by comparing the figure 7 (approach (2.3)) and the figure 8.

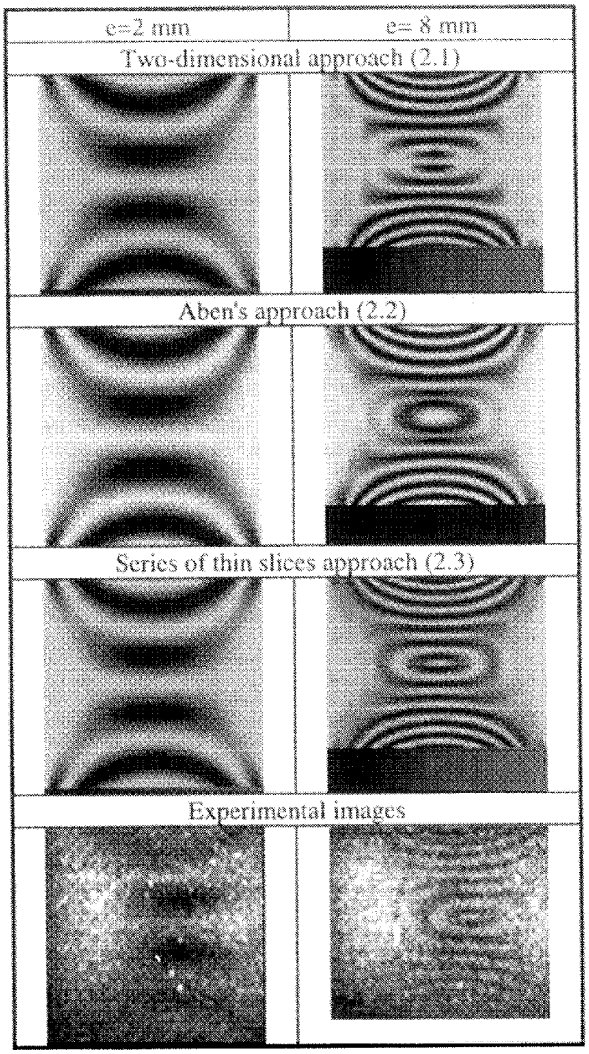

Figure 7 : Experimental and simulated fringes (imposed rotation 4°).

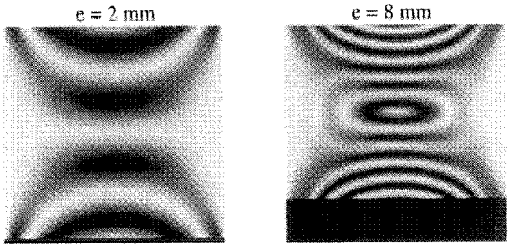

Figure 8 : Simulated fringes for a rotation of 3.6°.

4 Conclusion

Our purpose is to compare real photoelastic fringes with the fringe pattern calculated from a theoretical or numerical stress field. This process allows us to validate boundary conditions and the mesh of a three-dimensional mechanical problem. We present three approaches to a photoelastic medium. The results obtained by the discrete approach to the three-dimensional medium by a series of thin slices gives the best agreement with the experimental results.

The advantage of this method is its numerical simplicity, and that no hypothesis on α or φ is made at the level for a thick beam.We will use our process to compare simulated and experimental fringes. A difference between then can be due only to a bad mechanical design. This technique associated with the optical slicing method can be used for fast industrial investigation and validation for specimens realized by molding or stereolithography. The separation of the isoclinic and isochromatic parameters [Zénina, A., et al. 1998] and the calculation of the stress tensor is the next step of our work.

References

Aben, H., 1966, Optical phenomena in photoelastic models by the rotation of principal axes, *Experimental Mechanics,* vol. 6, n°1.

Aben, H., and Josepson, J., Oct. 1997, Strange interference blots in the interferometry of inhomogeneous birefringent objects, *Applied Optics,* vol. 36, n°28, pp. 7172-7179.

Brillaud, J., Desailly. R., and Lagarde, A., 1983, Paramètres optiques en photoélasticimétrie tridimensionnelle, *Revue Française de Mécanique,* n°1983-4.

Caignaert, G., and Henry, J.P., 1988, *Cours et exercices d'élasticité,* Dunod.

Dainty, J.C., 1975, Laser Speckle and related phenomena, Topics in Applied Physics, 9, Springer Verlag.

Dally, J.W., and Riley, F.W., 1991, *Experimental stress analysis,* McGraw-Hill, Inc.

Desailly, R., and Lagarde, A., 1984, Méthode de découpage optique de photoélasticimétrie tridimensionnelle, application, *Revue Française de Mécanique,* n°1984-1.

Dupré, J.C., Plouzennec, N., and Lagarde, A., 1996, Nouvelle méthode de découpage optique à champ complet en photoélasticimétrie tridimensionnelle utilisant des moyens numériques d'acquisition et d'analyse des champs de granularité en lumière diffusée, *C.R. Acad. Sci, Paris,* t, 323, Série II b, pp. 239-245.

Dupré, J.C., and Lagarde, A., Dec. 1997, Photoelastic analysis of a three-dimensional specimen by optical slicing and digital image processing, *Experimental Mechanics,* Vol. 37, No.4, pp. 393-397.

Plouzennec, N., Dupré, J.C., and Lagarde, A., Sept. 1998, Visualization of photoelastic fringes within three dimensional specimens using an optical slicing method, *Symposium I.U.T.A.M. « Advanced* Optical *Methods and Applications in Solid Mechanics »,* Poitiers, France.

Timoshenko, S., and Goodier, J.N., 1961, *Theory of elasticity,* Mc Graw-Hill, Inc, 2th edition.

Zénina, A., Dupré, J.C., and Lagarde, A., Sept. 1997, Découpage optique d'un milieu photoélastique épais pour l'étude des contraintes dans un milieu tridimensionnel, *13ème Congrés Français de Mécanique,* Poitiers, France, vol. 4, pp. 447-450.

Zénina, A., Dupré, J.C., and Lagarde, A., Sept. 1998, Plotting of isochromatics and isostatics patterns of slice optically isolated in a three dimensional photoelastic model, *Symposium I.U.T.A.M. « Advanced Optical Methods and Applications in Solid Mechanics »,* Poitiers, France.

AN APPROACH TO GENERAL 3-D STRESS ANALYSIS BY MULTIDIRECTIONAL SCATTERED LIGHT TECHNIQUE

Takahiro OI and Masahisa TAKASHI
Aoyama Gakuin University
6-16-1, Chitosedai, Setagaya-ku, Tokyo 157-8572, Japan
Phone: +81-3-5384-1193, Fax: +81-3-5384-6311
E-mail: ohi@shaqua.me.aoyama.ac.jp

Abstract

Scattered light photoelasticity provides a nondestructive analysis of stress components on a plane layer in the incident light path. For general three dimensional stress fields, however, the effect of birefringent axis rotation has to be taken into account, and hence the technique has been limited only in application to plane stress or symmetrical stress distributions.

In this study, the authors propose a method for determining not only the secondary principal stress difference, but also its direction, using multiple image data obtained by combination of the angles of incident polarization light and observation. As an example, a sphere under a pair of diametrical compressive forces is analysed to determine both the principal stress difference, and their directions in layers, with or without the rotation of the principal birefringent axis. The results show good agreement with theoretical analysis.

1. Introduction

Precise and accurate distribution of stress is necessary for optimum design of 3-D systems. There is still no reliable method for analysis of stress components inside a 3-D body under load.

Scattered light photoelasticity provide a nondestructive analysis of stress components for a plane layer in the incident light path. In general three dimensional stress fields, however, scattered photoelastic intensity superposes effects of birefringent axis rotation due to change in the direction of secondary principal stress along the light path. In addition, the intensity arises from the integration of optical effects along the light path. There is no convenient way to separate these effects ; the technique is limited to the analysis of stress models with some symmetry.

In this study, the authors propose a method for determining not only the secondary

A. Lagarde fed.),
IUTAM Symposium on Advanced Optical Methods and Applications in Solid Mechanics, 57–64,

principal stress difference, but also its direction, using multiple image data obtained by combining various angles of incident polarization light and observation. As an example, a sphere under a pair of diametrical compressive forces is analysed to determine the principal stress difference, and their directions in symmetrical and unsymmetrical layers ; the results are compared with theoretical results.

2. Intensity of Light Through a 3-D Model

Matrix calculation based on Stokes vector gives the relation between optical devices and intensity of scattered light. Fig.1 shows the arrangement of optical elements. The final Stokes vector S[1][2] observed by a camera in this optical setup is obtained as follows ;

$$S = M_{\psi+\frac{\pi}{2}} M(\theta) M_{\varphi}(\delta) S_0$$

$$S = \frac{1}{2}\begin{bmatrix} 1-a \\ a\cos 2\psi \\ a\sin 2\psi \\ 0 \end{bmatrix} \qquad (1)$$

with $a = \sin 2(\alpha-\varphi)\sin 2(\psi-\theta-\varphi)\cos\delta - \cos 2(\alpha-\varphi)\cos 2(\psi-\theta-\varphi)$

where, S_0 is the Stokes vectors of polarized incident light, $M_{\varphi}(\delta)$ the retarder of the specimen, $M(\theta)$ the rotator of the specimen, and $M_{\psi+\frac{\pi}{2}}$ the Stokes vector which shows the observational direction. Thus, the intensity of scattered light is expressed as

$$I = \frac{1}{2} k A^2 (1-a) \qquad (2)$$

here, I : Intensity of observed scattered light from the specimen,
k : Light scattering coefficient,
A^2 : Amplitude of monochromatic incident light,
α : Azimuth of the axis of incident light,
φ : Azimuth of the fast axis of the equivalent retarder,
ψ : Observational direction,
θ : Characteristic angle of the equivalent rotator,
δ : Retardation of the equivalent retarder

In this equation, $\theta + \varphi$ gives the secondary principal stress direction, and δ the secondary principal stress difference. In order to eliminate the other parameters, we choose various combinations of α and ψ. We denote the intensity for $\alpha = \alpha_1$ and $\psi = \psi_1$ by I_1, that for $\alpha = \alpha_2 = \alpha_1 + 45°$ and $\psi = \psi_2 = \psi_1 - 45°$ by I_2. Subtracting I_1 from

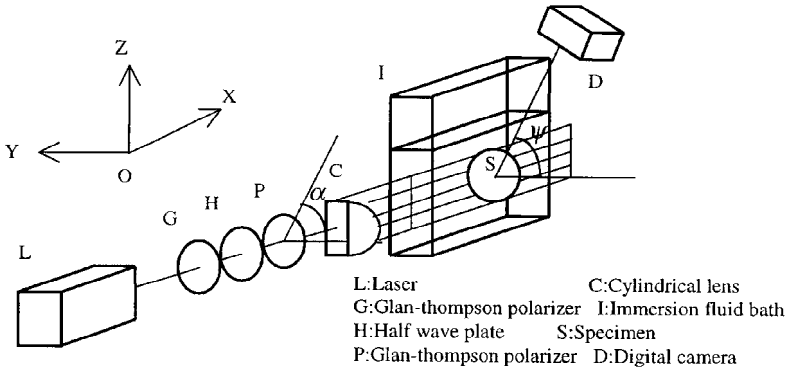

Fig. 1 Experimental set up

I_2 and denoting it by I_3 , we have

$$I_3 = I_2 - I_1 = \frac{1}{2}kA^2(1+\cos\delta)\cos 2(\alpha_1 - \psi_1 + \theta) \tag{3}$$

We repeat Eq.(3) for another combination of α and ψ : I_4 for of $\alpha_1 - \psi_1 = 0°$, and I_5 for $\alpha_1 - \psi_1 = 45°$. Then, θ and δ are obtained as follows :

$$\theta = -\frac{1}{2}\tan^{-1}\left(\frac{I_5}{I_4}\right) \tag{4}$$

$$\delta = 2\cos^{-1}\sqrt{\frac{\sqrt{I_4^2 + I_5^2}}{kA^2}} \tag{5}$$

Now return to Eq.(2). Let I_6 be the intensity for $\alpha = \alpha_6$ and $\psi = \psi_6$, and I_7 for $\alpha_7 = \alpha_6 + 45°$ and $\psi_7 = \psi_6 + 45°$. Their difference is I_8 :

$$I_8 = I_7 - I_6 = \frac{1}{2}kA^2(1-\cos\delta)\{\cos 2(\alpha_6 + \psi_6 - \theta - 2\varphi)\} \tag{6}$$

We use Eq.(6) for another set of combinations as follows. Let I_9 be the intensity for $\alpha_6 + \psi_6 = 90°$, and I_{10} be that for $\alpha_6 + \psi_6 = 180°$. We have,

$$\frac{I_{10}}{I_9} = \tan 2(-\theta - 2\varphi) \tag{7}$$

Then,

$$\therefore \varphi = \frac{1}{2}\left(-\theta - \frac{1}{2}\tan^{-1}\frac{I_{10}}{I_9}\right) = \frac{1}{4}\left(\tan^{-1}\frac{I_5}{I_4} - \tan^{-1}\frac{I_{10}}{I_9}\right) = \frac{1}{4}\tan^{-1}\left(\frac{I_5 I_9 - I_4 I_{10}}{I_4 I_9 + I_5 I_{10}}\right) \tag{8}$$

We note that these calculations require several image data sets for various combinations of α and ψ .

We note that these calculations require several image data sets for various combinations of α and ψ .

$$I_4 \Rightarrow \alpha_1 = 22.5°, \psi_1 = 22.5° \ , \ \alpha_2 = 67.5°, \psi_2 = -22.5°$$

$$I_5 \Rightarrow \alpha_1 = 67.5°, \psi_1 = 22.5° \ , \ \alpha_2 = 112.5°, \psi_2 = -22.5°$$

$$I_9 \Rightarrow \alpha_6 = 112.5°, \psi_6 = -22.5° \ , \ \alpha_7 = 157.5°, \psi_7 = 22.5°$$

$$I_{10} \Rightarrow \alpha_6 = 67.5°, \psi_6 = -22.5° \ , \ \alpha_7 = 112.5°, \psi_7 = 22.5°$$

Using six image data (two image data a overlaped.), the secondary principal stress direction is obtained as,

$$\therefore \theta + \varphi = -\frac{1}{2}\tan^{-1}\left(\frac{I_5}{I_4}\right) + \frac{1}{4}\tan^{-1}\left(\frac{I_5 I_9 - I_4 I_{10}}{I_4 I_9 + I_5 I_{10}}\right) \tag{9}$$

3. Experimental Procedures

3.1 Experimental Setup

Fig. 1 shows the experimental setup. A laser beam with small radius is polarized by a Glan-Thompson polarizer and then the angle of polarization is adjusted with a half wave plate. The light is polarized by a second Glan-Thompson polarizer (angle α) to confirm the angle of polarization, then expanded to a thin layer of light by a cylindrical lens. The beam is inserted into the specimen placed in an immersion bath filled with liquid of the same refraction index as the specimen. A scattered light photoelastic image is taken by a digital camera.

3.2 3-D Photoelastic Model

The 3-D photoelastic sphere model used in this study is made of Araldite B-CT200 epoxy-resin cured with a hardener HT903. After residual stresses were removed at high temperature, followed by a slow cooling process, the stress was frozen in the specimen under diametrical loads of 60N as shown in Fig.2.

3.3 Experimental and Analysis Procedures

To investigate symmetrical and more general stress distributions, a layer of incident light is inserted both on the meridian plane of the sphere and on a plane parallel to it as shown Fig.3(a). On the equatorial plane of the model and a plane parallel to it as shown Fig.3(b), the distribution of principal stress difference and directions are also investigated. Fringe patterns on these plane are taken we calculated by digital

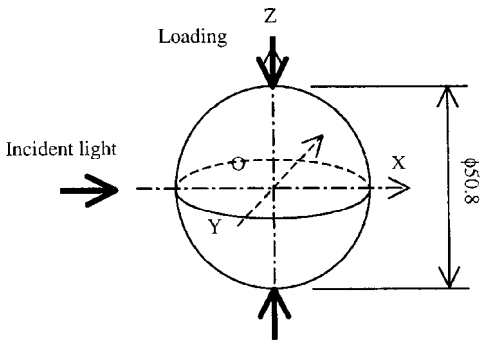

Fig2 Geometry of specimen and loading condition

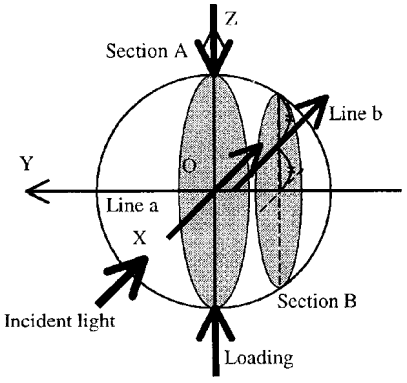

(a) the meridian plane and one parallel to it

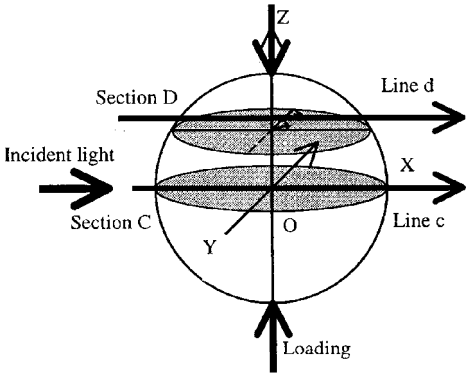

(b) the equator plane and one parallel to it

Fig.3 Analyzed region

4. Results and Discussion

Examples of scattered light image data are shown in Fig.4. Fig.5(a)~(d) show a comparison of experimental and theoretical results [3] ~ [6] for the secondary principal stress difference. The secondary principal stress directions are compared in Fig.6(a) ~(d). Let us discuss on the results of the secondary principal stress difference and direction separately.

1] On the secondary principal stress difference.

a) Experimental results show fairly good agreement with theoretical ones. However, some severe difficulties still remain, particularly around the portion of high stress concentration.

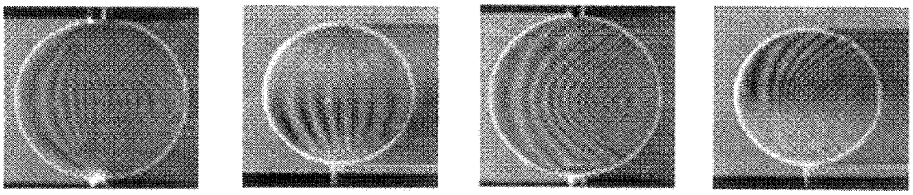

Section A (symmetrical plane) | Section B (unsymmetrical plane) | Section C (symmetrical plane) | Section D (unsymmetrical plane)

(a) $\alpha = 22.5°, \psi = 22.5°$

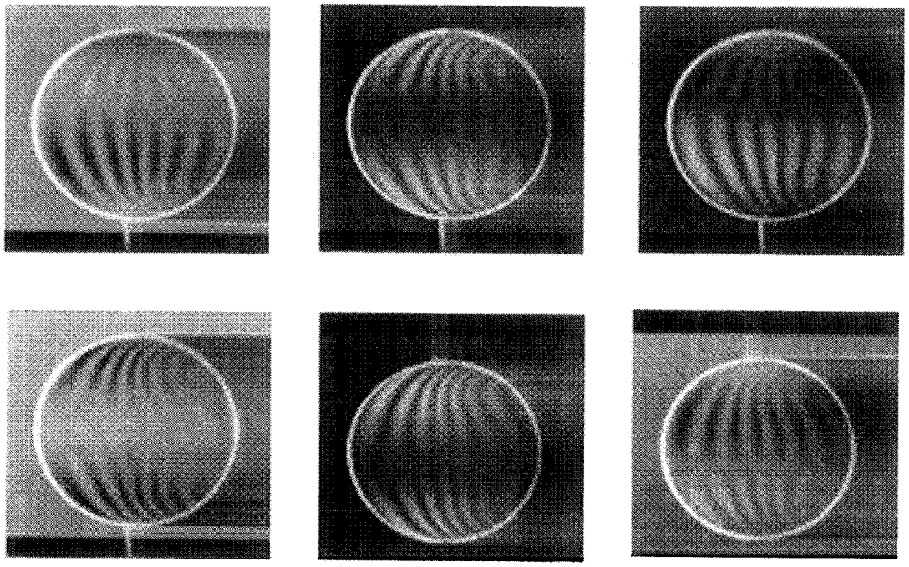

$\alpha = 22.5°, \psi = 157.5°$ | $\alpha = -22.5°, \psi = -67.5°$ | $\alpha = -22.5°, \psi = -112.5°$

(b) Section B

Fig.4 Examples of Image data

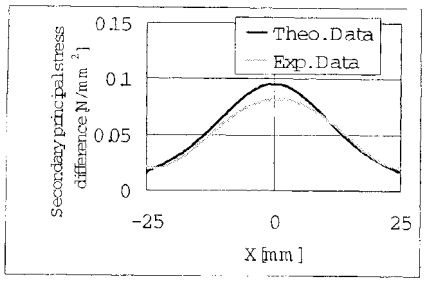

(a) Line a (symmetrical plane)

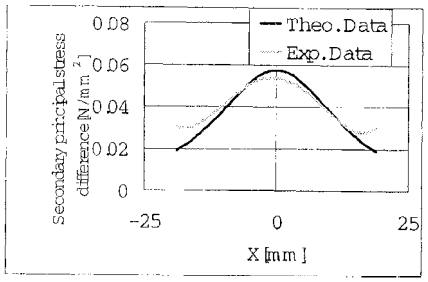

(b) Line b (unsymmetrical plane)

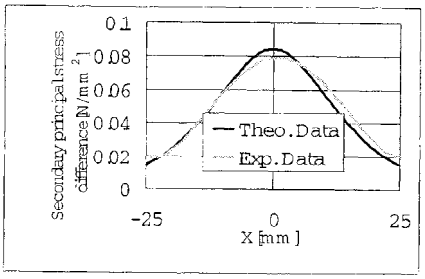

(c) Line a (symmetrical plane)

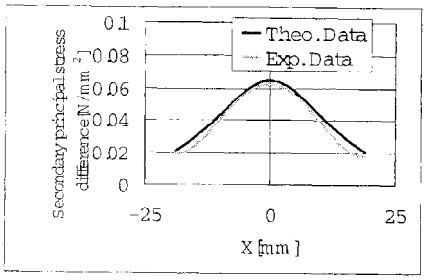

(d) Line b (unsymmetrical plane)

Fig.5 Secondary principal stress differnece

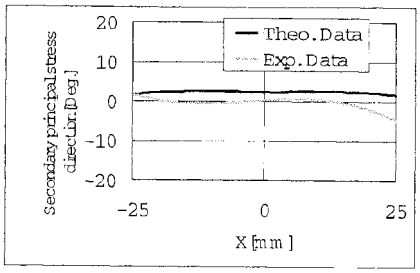

(a) Line a (symmetrical plane)

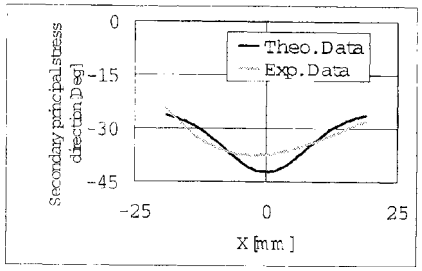

(b) Line b (unsymmetrical plane)

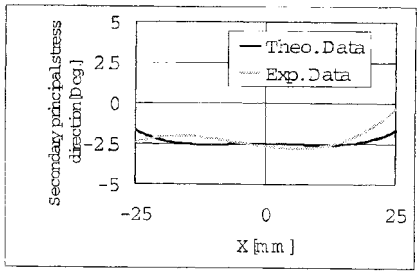

(c) Line a (symmetrical plane)

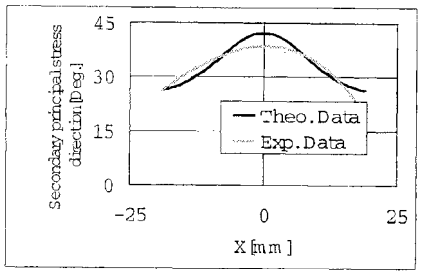

(d) Line b (unsymmetrical plane)

Fig.6 Secondary principal stress differnece

b) Around regions where the difference of secondary principal stress becomes large, considerable errors between theoretical and experimental data are observed. This comes from the fact that the density of fringe varies rapidly, the resolution of the camera is insufficient in this region ; a better camera is needed for such density of fringe order.

2]On the secondary principal stress direction.

c) The error between experimental and theoretical value of the secondary principal stress direction is larger than that for the secondary principal stress difference, because the influence of retardation by the equivalent retarder δ on the intensity of scattered light is larger than that expected by the theory.

d) Experimental values show some degree of agreement with the theoretical results on the symmetrical layer. On the other hand, the experimental results on the unsymmetrical layer show poor agreement with theoretical results and the errors are much larger than those on the symmetrical layer. We note that both the azimuth of the fast axis of the equivalent reterder and the characteristic angle of the equivalent rotator on symmetrical planes are obtained more easily and accurately than on unsymmetrical planes.

e) Since two solutions of the secondary principal stress direction obtained simultaneously in the calculation proposed, choice of proper solution from two is another problem in this method.

Similar levels of accuracy on the meridian and the equator plane of sphere model are obtained, thus it can be expected that we will be able to improve the technique to get accurate secondary principal stress distribution on every plane.

5. Concluding Remarks

The authors discussed a method for 3-D analysis of the direction and the difference of secondary principal stresses with a method based on the scattered light photoelastic technique. As an example, a sphere under a pair of diametrical compression is analysed. Good agreement was obtained with theory provided that the secondary principal stress difference and direction do not vary so much. The method shows promise for the development of general 3-D scattered light photoelastic stress technique.

References

[1] Theocaris, P.S. and Gdoutos, E.E. (1979) *Matrix Theory of Photoelasticity,* Springer Series in Optical Sciences, Berlin

[2] Azzam, R.M.A.A. and Bashara, N.M. (1977) *Ellipsometry and Polarized Light,* North-Holland Personal Library, Elsevier

[3]Sternberg, E. and Rosenthal, F. (1952) *J. Appl. Mech.,* 19-4, 413

[4]Weber, C. (1952) *Z. AMM,* 32-6, 186.

[5]Timoshenko, S.P. (1959) *Theory of Plates and Shells,* McGraw-Hill, 561

[6]Ulitko, A.F. (1968) *Prikladnaya Mekhanika,* 4-5,38

PLOTTING OF ISOCHROMATIC AND ISOSTATIC PATTERNS OF SLICE OPTICALLY ISOLATED IN A THREE DIMENSIONAL PHOTOELASTIC MODEL

A. ZENINA
LMS, Université de Poitiers, CNRS UMR 6610
SP2MI - Téléport 2 - BP 179, 86960 FUTUROSCOPE CEDEX, FRANCE

J.C. DUPRE
LMS, Université de Poitiers, CNRS UMR 6610
SP2MI - Téléport 2 - BP 179, 86960 FUTUROSCOPE CEDEX, FRANCE

A. LAGARDE
LMS, Université de Poitiers, CNRS UMR 6610
SP2MI - Téléport 2 - BP 179, 86960 FUTUROSCOPE CEDEX, FRANCE

Abstract

We present a non destructive experimental method which gives the isochromatics and isostatics patterns of slice optically isolated in a three dimensional photoelastic model. We used a non destructive method of optical slicing developed in our laboratory. In this method, the photoelastic model is optically sliced by two plane laser beams. The analysis of the scattered light gives fringes equivalent to those obtained in a plane polariscope (isochromatic and isoclinic fringes). In order to separate the isochromatic and the isoclinic fringes, we recorded several images for different polarization orientations, separated the isoclinic and isochromatic fringes using the Fourier transform, and plotted the isostatics pattern.

We show a test of a point loading on the top of a prismatic specimen and the possibilities of our method in an industrial case of a model realized by a stereolithography technique.

1. Introduction

Photoelasticity coupled with the stress frozen technique is still used by industrialists. Usually the three dimensional specimens are sliced by a mechanical process to obtain two dimensional models. The slices can be analyzed in a plane or a circular polariscope.

A. Lagarde (ed.),
IUTAM Symposium on Advanced Optical Methods and Applications in Solid Mechanics, 65–72.

We recall that for a plane polariscope, a two dimensional analysis of a beam allows us to visualize two fringe patterns. The direction of principal stresses is obtained from isoclinic fringes, their difference is given by isochromatic fringes.

Different two dimensional automated photoelastic fringe analysis has been recently investigated, there are techniques based on the use of a circular polariscope (Voloshin, A., et al. 1983) (Patterson, E.A., et al. 1991) or a plane polariscope (Dupré, J.C., et al. 1993) (Mueller, S.A., et al. 1993) (Morimoto, Y., et al. 1994). Other methods use two (Umezaki, E., et al. 1989) or three (Kihara, T., 1994) wavelengths. The mechanical slicing is a destructive procedure, can disturb the measurement and for different planes takes a lot of time. Furthermore it requires the molding of several models for a general study. Three dimensional methods have been developed (Srinath, L.S., et al. 1988) (Ezaki, K., et al. 1996) (Zénina, A., et al. 1997) (Zénina, A., et al. 1998).

In this paper an another experimental solution is proposed, we used a non-destructive method of optical slicing of three dimensional photoelastic model developed in our laboratory (Dupré, J.C., et al. 1997) (Plouzennec, N., et al. 1998). In this method we obtained a fringe pattern as in a light plane polariscope. We could not obtain a fringe pattern directly, corresponding to a circular polariscope, so we chose a procedure based on a Fourier transform (Morimoto, Y., et al. 1994) witch only used a plane polariscope configuration without modification of the angle between polarizer and analyzer.

To show the possibilities of this method, we present a test of a point loading on the top of a prismatic specimen, and an industrial model realized by stereolithography technique.

2. Principle of the optical slicing experimental method

The basic idea is to use the properties of polarization of the scattered light (Rayleigh's law). If one observes along the $\vec{z}$ vector, perpendicular to the direction of the propagated light beam $\vec{x}$, the scattered light is polarized rectilinearly along $\vec{z} \wedge \vec{x}$. The principle of the method is to isolate a slice of the photoelastic model between two parallel plane laser beams (figure 1) (Plouzennec, N., et al. 1998) (Dupré, J.C., et al. 1997) (Dupré, J.C., et al. 1996). In the direction perpendicular to the plane of the two illuminated sections, we observe a speckle pattern due to the interference of the light beams of each section. Their possibilities of interference depend on the birefringence of the isolated slice.

The correlation factor γ of the two speckle fields is given by

$$\gamma^2 = 1 - \sin^2 2\alpha \sin^2 \frac{\varphi}{2} \qquad (1)$$

Here, α is the angle of one of the principal stresses; the isochromatic parameter φ is expressed by

$$\varphi = \frac{2\pi Ce}{\lambda}(\sigma' - \sigma'') \qquad (2)$$

Here e is the thickness of the specimen, C presents the photoelastic constant, λ is the wavelength of the light used and $(\sigma' - \sigma'')$ is the secondary principal stress difference of the specimen.

Expression (1) is similar to the relationship for the light intensity obtained in a plane polariscope. Thus, the analysis of the scattered light gives fringes equivalent to those obtained in a plane polariscope (isochromatic and isoclinic fringes).

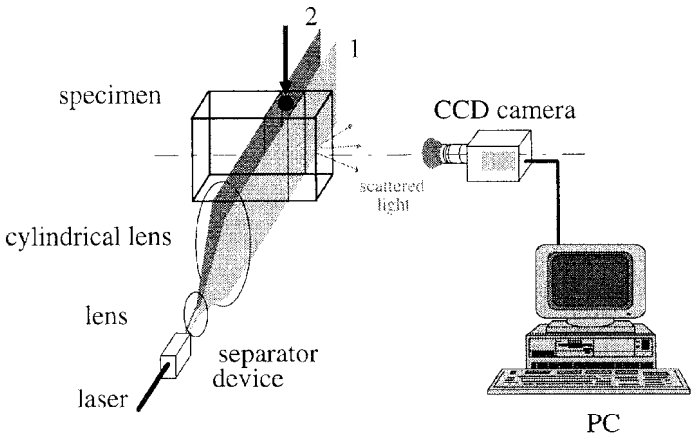

Figure 1 : Experimental set-up

3. Separation of isochromatic and isoclinic using Fourier transform

As we obtained fringes pattern from a plane polariscope, we chose a procedure based on the Fourier transform (Morimoto, Y., et al. 1994) which used only a plane polariscope configuration without variation of the angle between analyzer and polarizer.

3.1. PRINCIPLE

If we turn the polarizer and the analyzer direction through an angle θ, we find that expression (1) becomes

$$\gamma^2(\theta) = 1 - \sin^2 2(\alpha - \theta) \sin^2 \frac{\varphi}{2} \qquad (3)$$

$$\gamma^2(\theta) = [1 - \frac{A}{2}(1 - \cos 4(\alpha - \theta))] \qquad (4)$$

In each point of the image A, is constant ($A = \sin^2 \frac{\varphi}{2}$).

The signal (4) is a periodic function with a period $T = \frac{2\pi}{4} = \frac{\pi}{2}$, thus it is expressed in the Fourier series with respect to θ :

$$\gamma^2(\theta) = \sum_{n=-\infty}^{+\infty} C_n e^{jn\omega_0\theta} \qquad (5)$$

$$C_n = \frac{1}{T}\int_{-T/2}^{+T/2} \gamma^2(\theta) e^{-jn\omega_0\theta} d\theta \qquad (6)$$

with

$$\omega_0 = \frac{2\pi}{T} = \frac{2\pi}{\pi/2} = 4$$

The Fourier transform of equation (5) is :

$$\Gamma(\omega) = \int_{-\infty}^{+\infty} \gamma^2(\theta) e^{-j\omega\theta} d\theta$$

$$\Gamma(\omega) = \sum_{n=-\infty}^{+\infty} C_n \int_{-\infty}^{+\infty} e^{jn\omega_0\theta} e^{-j\omega\theta} d\theta$$

Using the flowing formulations (Brigham, O.E., 1974) :

$$\delta(\omega) = \int_{-\infty}^{+\infty} e^{j2\pi\omega\theta} d\theta$$

$$\delta(\omega - a) = \int_{-\infty}^{+\infty} e^{j2\pi(\omega-a)\theta} d\theta$$

We obtain

$$\Gamma(\omega) = \sum_{n=-\infty}^{+\infty} 2\pi C_n \delta(\omega - n\omega_0) \qquad (7)$$

Here δ is the Dirac delta function, ω is the frequency and j is the imaginary unit.

The signal (7) indicates the discrete frequency spectrum only for $\omega = n\omega_0$ ($n = \pm 0$, $n = \pm 1$, $n = \pm 2$, …).

n = 0 :

From equation (6), we obtain

$$2\pi C_0 = \frac{2\pi}{T}\int_{-T/2}^{+T/2} \gamma^2(\theta) d\theta$$

$$2\pi C_0 = 4\int_{-\pi/4}^{+\pi/4}[1-\frac{A}{2}(1-\cos 4(\alpha-\theta))]d\theta$$

$$2\pi C_0 = 2\pi - \pi A = 2\pi(1-\frac{A}{2}) \qquad (8)$$

Equation (8) indicates that the isoclinics are eliminated. The image of $2\pi C_0$ shows the isochromatic fringes in the whole field of the specimen.

n = +1 :

From equation (6), we obtain

$$2\pi C_{+1} = \frac{2\pi}{T}\int_{-T/2}^{+T/2}\gamma^2(\theta)e^{-j\omega_0\theta}d\theta$$

$$2\pi C_{+1} = 4\int_{-\pi/4}^{+\pi/4}[1-\frac{A}{2}(1-\cos 4(\alpha-\theta))]e^{-j\omega_0\theta}d\theta$$

By using : $\cos 4(\alpha-\theta) = \frac{1}{2}(e^{j4(\alpha-\theta)} + e^{-j4(\alpha-\theta)})$, we obtain

$$2\pi C_{+1} = 4\int_{-\pi/4}^{+\pi/4}e^{-j4\theta}d\theta - 2A\int_{-\pi/4}^{+\pi/4}e^{-j4\theta}d\theta + A[\int_{-\pi/4}^{+\pi/4}e^{-j4\alpha}d\theta + \int_{-\pi/4}^{+\pi/4}e^{j4(\alpha-2\theta)}d\theta]$$

$$2\pi C_{+1} = \frac{\pi}{2}Ae^{-j4\alpha} = \frac{\pi}{2}A[\cos 4\alpha - j\sin 4\alpha] \qquad (9)$$

Finally , we obtain the isoclinic parameter α by calculating the arctangent of the ratio of the imaginary and real parts of $2\pi C_{+1}$:

$$\alpha = \frac{1}{4}a\tan[\frac{-\Im m(2\pi C_{+1})}{\Re e(2\pi C_{+1})}] \qquad (10)$$

The method consist in recording several images for different orientations and in calculating the Fourier transform of the correlation factor of each pixel. The isoclinics and isochromatic fringes can be separated and the isostatics pattern can be plotted.

3.2. EXPERIMENTAL PROCEDURE

Experimentally we have to analyze images corresponding to different plane polariscope orientations. To circumvent refraction and reflection phenomena, the models are immersed in a tank of index liquid. The first solution is to turn the two laser beams, but this requires having a special tank shape, because the edge of the tank must be

perpendicular to the incident beams. The second solution is to turn the specimen through an angle between $-\pi/4$ to $\pi/4$. Then we record several images for different orientations of the model. Numerical rotation is applied for each image in order to obtain the correct position of the model, as we have turned the laser beams. This procedure is simpler but the area to all the images is a circle so we loose a part of the image.

By calculating the Fourier transform at each point of these images, we obtain the isochromatic pattern is obtained from the correlation factor data for the frequency $\omega = 0$. The Isoclinic image is obtained for $\omega = \pm \omega_0$ (figure.2).

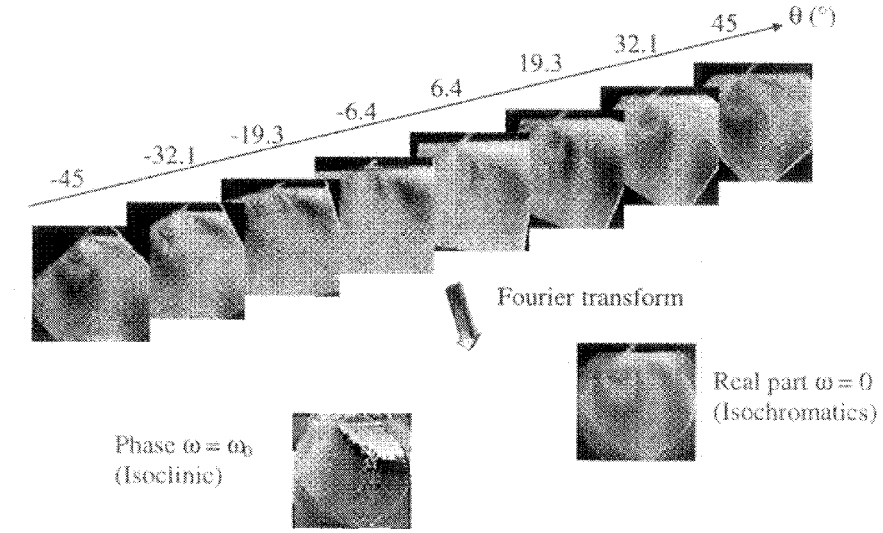

Figure 2 : Recorded images obtained by changing the angle of polarizer and analyzer and a part of the Fourier spectrum giving the isoclinic and the isochromatic parameters

4. Experimental results

Tje three dimensional photoelastic block model is made of an Araldite epoxy-resin. The model is loaded by a concentrated force (figure 1).

The model is placed in a tank of index liquid and illuminated perpendicularly to the observation direction. Several images are recorded for different polarization orientations i.e. for different rotations of the specimen in the interval $[-\pi/4 , \pi/4]$ by a CCD camera with 1024 grey levels of brightness. The minimal number of images recorded is eight (figure 2), but for the best contrast it is necessary to record sixteen images.

When the isoclinic α is determined for the whole field, the isostatics can be plotted to obtain a better visualization of the principal stress direction (figure 3).

Figure 4 shows an application in an industrial case of a model realized by stereolithography technique. We show a zoom in the particular zone for more details in the specimen.

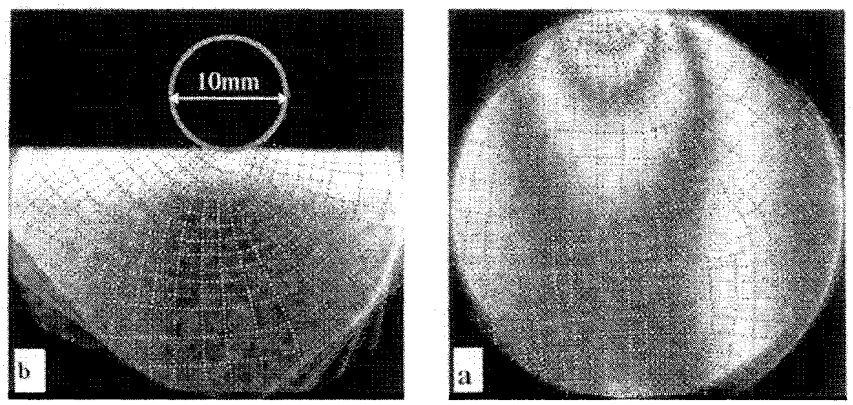

(slice : 1.5 mm) (slice : 4 mm)

Figure 3 : Isostatics and isachromatics patterns for two thicknesses of slice

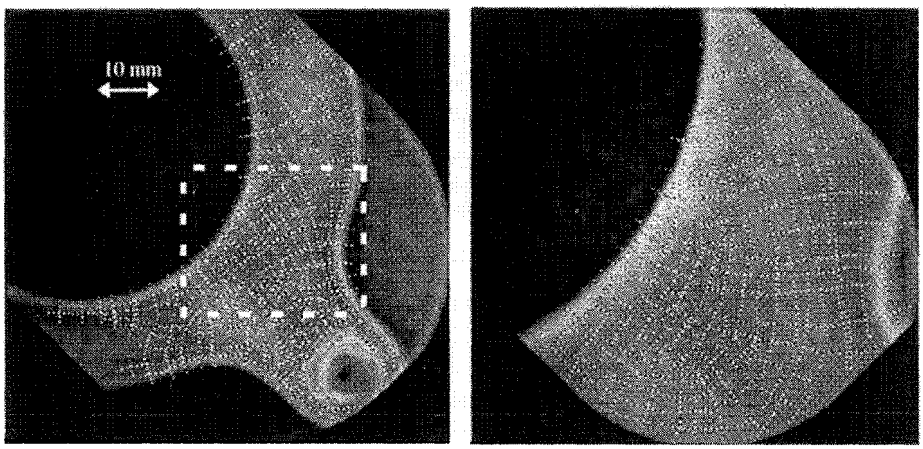

Figure 4 : Isostatics and isochromatic patterns for a model, provided by PSA, realized by stereolithography technique (slice : 2.5 mm).

5. Conclusion

We have developed a non destructive experimental technique for the study of the stress field in a three dimensional photoelastic specimen. This method allows us to separate the isochromatic and the isoclinic fringes and to plot the isostatics pattern.

This method is based on a simple experimental set up with few manipulations and requires only a short time.

The numerical procedure associated with the optical slicing method can be used, for fast industrial investigation of three dimensional specimens realized by molding or stereolithography.

6. Acknowledgments

We would like to thank PSA for its support to our work.

7. References

Brigham, O.E. (1974) *The fast Fourier transform,* Prentice-Hall Inc.

Dupré, J.C., Brémand, F., and Lagarde, A. (1993) Photoelastic data processing through digital image processing : isostatics and isochromatics reconstruction, *International conference on Photoelasticity* : *new instrumentation and data processing technique,* London.

Dupré, J.C., Plouzennec, N., and Lagarde, A. (1996) Nouvelle méthode de découpage optique à champ complet en photoélasticimétrie tridimensionnelle utilisant des moyens numériques d'acquisition et d'analyse des champs de granularité en lumière diffusée, *C.R. Acad. Sci,* Paris, t, 323, Série II b, pp. 239-245.

Dupré, J.C. and Lagarde, A. (Dec. 1997) Photoelastic analysis of a three dimensional specimen by optical slicing and digital image processing, *Experimental Mechanics,* Vol. 37., N° 4., pp. 393-397.

Ezaki, K., Ikeda, A., Mawatari, S., and Takashi, M. (1996) Comparison of transmitted and scattered light methods for 3-D photoelastic stress analysis, *Post Conference Proceeding of the 1996 VIII International Congress on Experimental Mechanics,* SEM, U.S.A, pp. 332-338.

Kihara, T. (1994) Automatic whole field measurement of principal stress directions using three wavelengths, *Recent advances in experimental mechanics,* J.F. Silva Gomes et al. Editors, pp. 95-99.

Morimoto, Y., Morimoto, Y. Jr., and Hayashi, T. (Sept./Oct. 1994) Separation of isochromatics and isoclinics using Fourier transform, *Experimental Techniques,* pp. 13-17.

Morimoto, Y. and Imamoto, Y. (1994) Error causes and error reduction in fringe pattern analysis by phase shifting method using Fourier transform, *Experimental Mechanics,* pp. 379-384.

Mueller, S.A. and Moslehy F.A. (Sept. 1993) An image analysis technique for constructing isostatics from isoclinics in photoelasticity, *International Symposium on Optical Tools for Manufacturing and Advanced Automation,* SPIE, Boston.

Patterson, E.A. and Wang Z.F. (May 1991) Towards full field automated photoelastic analysis of complex components, *Strain,* Vol. 27, n°2, pp. 49-56.

Plouzennec, N., Dupré, J.C., and Lagarde, A. (Sept. 1998) Visualization of photoelastic fringes within three dimensional specimens using an optical slicing method, *Symposium I.U.T.A.M. « Advanced Optical Methods and Applications in Solid Mechanics »,* Poitiers, France.

Srinath, L.S., Ramesh, K., and Ramamurti, V. (Mar. 1988) Determination of characteristic parameters in three dimensional photoelasticity, *Optical Engineering,* Vol. 27, N°3, pp. 225-230.

Umezaki, E., Tamaki, T., and Takahashi, S. (1989) Automated stress analysis of photoelastic experiment by use of image processing, *Experimental Techniques,* pp. 22-27.

Voloshin, A. and Burger C.P. (Sept. 1983) Half-fringe photoelasticity: a new approach to whole field stress analysis, *Experimental Mechanics,* pp. 304-313.

Zénina, A., Dupré, J.C., and Lagarde, A. (Sept. 1997) Découpage optique d'un milieu photoélastique épais pour l'étude des contraintes dans un milieu tridimensionnel, *13ème Congrès Français de Mécanique, Poitiers,* France, vol. 4, pp. 447-450.

Zénina, A., Dupré, J.C., and Lagarde, A. (Sept. 1998) Optical approaches of a photoelastic medium for theoretical and experimental study of the stresses in a three dimensional specimen, *Symposium I.U.T.A.M. « Advanced Optical Methods and Applications in Solid Mechanics »,* Poitiers, France.

A STUDY ON STRESS FREEZING METHOD BASED ON TIME AND TEMPERATURE DEPENDENT PHOTOVISCOELASTIC BEHAVIORS

S. SUGIMORI
Professor Kanazawa Technical College,
Hisayasu Kanazawa, 921-8601, Japan
Y. MIYANO
Professor, Materials System Research Laboratory,
Kanazawa Institute of Technology,
Yatsukaho Matto, 924-0838, Japan
T. KUNIO
Professor, Kanazawa Institute of Technology, Japan
Professor Emeritus, Keio University, Japan

1. Introduction

The stress freezing (SF) method has been widely known as a simple and useful photoelastic technique applicable to various kinds of experimental stress analysis problem, particularly for three-dimensional problems.

To achieve a reliable SF method, more careful attention should be paid to the temperature conditions of SF cycle, because thermoviscoelastic effects during heating and cooling process leading to non-uniformity of the temperature distribution in the whole model are very serious, since the model made from polymeric materials has generally significant time and temperature dependent characteristic properties. Additionally, the strain sensitivity of the optical property of thermosetting resin used for SF model is considerably smaller in the rubbery state than in the glassy state. Therefore, SF model should be much more distorted compared to a general photoelastic model. Thus, SF method involves an experimental analysis error.

The thermosetting resin used in SF method is very soft but has high stress sensitivity at temperatures higher than the glass transition temperature. Below the glassy transition temperature, the polymeric resin is very hard and has low stress sensitivity. Not only the mechanical but also optical properties of resin near the glass transition temperature show a significant time and temperature dependence, this is the so-called photoviscoelastic behavior.

This paper intends to propose a new technique for finding the most suitable holding SF temperature and optimizing the freezing cycle based on the quantitative character of the linear-photoviscoelastic behavior [1-3] of the model material. Various functions, including the strain sensitivity mentioned above, will be redefined from the view point of the photoviscoelastic behavior of the material. Their availability will be verified theoretically, together with experimental results obtained from a 4-point bending test of an epoxy resin beam.

A. Lagarde (ed.),
IUTAM Symposium on Advanced Optical Methods and Applications in Solid Mechanics, 73–80.

2. Estimate Functions for the Stress Freezing Method

Figure 1(a) shows two kinds of ordinary temperature cycles appearing in the SF cycle, when both maximum temperatures T_h are higher than the glassy transition temperature T_g, and T_c is the room temperature. Figure 1(b) shows the principal stress difference σ_1-σ_2 produced in a model due to application of a constant load. Fig. 1(c) and (d) show changes in the principal strain difference ε_1-ε_2 and the birefringence n. The principal stress difference at any point in the model, which was caused by applied loading, disappears on removal of this applied load. However, both principal strain difference ε_1-ε_2 and fringe order n per unit path of light still show time dependent variations during loading as seen in Fig. 1(c) and (d). Therefore, even after finishing one cycle of SF procedure and removing a constant applied loading, not only the frozen birefringence n_f but also the frozen principal strain difference are left in the model. This is the basic concept of the Stress Freezing method, in which the values n_f of frozen fringes are used to analyze stress or strain, as with fringe order in ordinary photoelasticity.

We consider the effect of SF temperature in two cases. The first case is shown by the thick lines in Fig. 1(a)-(d), in which the model used is loaded at a temperature T_h higher than the glass transition temperature T_g of the material, and then is cooled down very slowly to room temperature T_c lower than T_g . In this case, stress and strain fields at all points in the model respond to a given loading without any time lapse, so that magnitudes of both principal stress difference σ_1-σ_2 and strain difference ε_1-ε_2 are time independent. A similar situation oc-

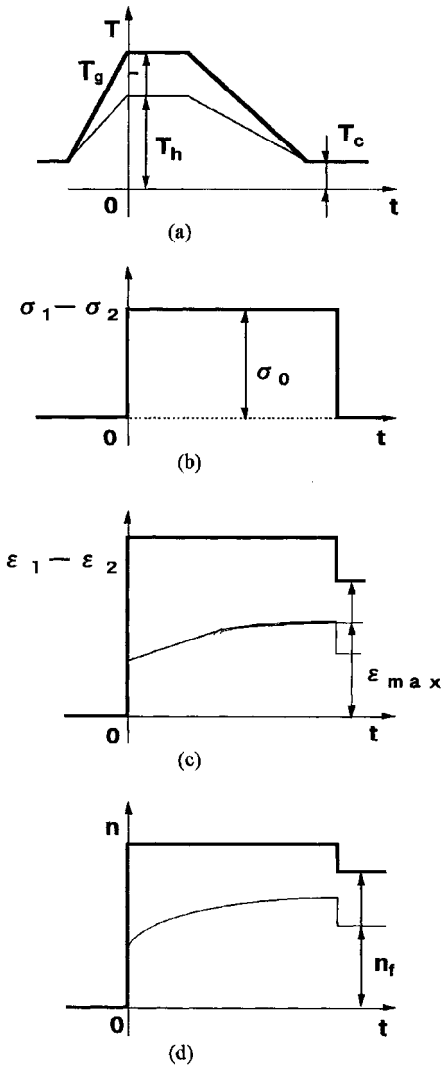

Fig. 1 Stress freezing procedure

curs for birefringence n produced in the model. Since the external loading for SF is removed from the model when SF procedure is complete, both the principal strain and birefringence may drop slightly after the load is removed as shown by the heavy lines in the Fig. 1(c) and (d). In the ordinary SF method, the principal stress difference σ_1-σ_2 by loading is experimentally analyzed by using the n_f.

In the second case shown as the thin lines in Fig. 1, the holding temperature T_h is in the so-called time and temperature dependent viscoelastic region. Both the principal strain difference ε_1-ε_2 and the birefringence n increase due to creep with time even during the constant loading interval. It is found that the ε_{max} as well as the frozen birefringence n_f drop slightly as the load is removed.

To improve the accuracy in the SF method, the model material used must have linear relations between stress, strain and birefringence throughout the loading and unloading. Also, the model must have a large ultimate strain in the viscoelastic region. Furthermore, the following three items are needed for improving the accuracy of SF method:

(1) The frozen birefringence produced should be as large as possible, within the limits of allowable distortion of model.

(2) The constant applied load σ_0 leading to the principal stress difference σ_1-σ_2 produced needs to be as large as possible under the condition (1).

(3) The frozen birefringence should be as large as possible to make the analysis easy and accurate.

These requisites cannot always be satisfied simultaneously. We must make a careful choice depending an experimental circumstance. To do this, we introduce three *estimation functions:*

$$k_1 = \frac{nf}{\varepsilon_{max}} \tag{1}$$

$$k_2 = \frac{\sigma_0}{\varepsilon_{max}} \tag{2}$$

$$k_3 = \frac{nf}{\sigma_0} \tag{3}$$

The first function k_1 is called as *Figure of Merit,* and has been widely used for three-dimensional stress analysis by SF method; k_2 and k_3 are new.

3. Theoretical Consideration of New Functions Based on Photoviscoelasticity

Assume that the model material exhibits a linear-photoviscoelatic behavior, is thermo-rheologically simple, and obeys the time-temperature superposition principle for both the optical and mechanical characteristics.

A three-dimensional model body made from linear- photoviscoelastic material is held for sufficiently long time without any constraint at a high holding temperature T_h at which the material shows viscoelastic behavior. At this period no stress, no strain and no birefringence exists. A load is applied to the body at time t=0, it is cooled down very slowly to the cooling temperature T_c, at which the material is in glassy state. Therefore, there is a uniform temperature distribution in the model during cooling process. The initial loading is kept constant throughout this cooling. The stress distribution due to a constant load will not change with time and also the directions of principal stress, principal strain and polarization of light coincide completely with each other at any point in the model, and do not change with time.

In this case, the fundamental equations between stress-strain-birefringence of the two-dimensional photoviscoelastic body, in which the temperature changes uniformly with time, can be expressed by the following hereditary integral equation by using the linear photoviscoelastic theory and the time-temperature superposition principle:

$$2\left[\varepsilon_1(x,t)-\varepsilon_2(x,t)\right]=\int_0^t Jc(t'-\tau',T_0)\frac{d}{d\tau}\left[\sigma_1(x,\tau)-\sigma_2(x,\tau)\right]d\tau \tag{4}$$

and

$$n(x,t)=\int_0^t Cc(t'-\tau',T_0)\frac{d}{d\tau}\left[\sigma_1(x,\tau)-\sigma_2(x,\tau)\right]d\tau \tag{5}$$

Here t' is reduced time calculated by the following relation

$$t'=\int_0^t \frac{du}{a_{T0}\left[T(x,u)\right]} \tag{6}$$

in which T_0 is the reference temperature, a_{T0} is the time-temperature shift factor with respect to T_0 and $J_c(t')$ and $C_c(t')$ are creep shear compliance and creep birefringence-stress coefficients, respectively. A transient uniform temperature T(t) and load W(x,t) are loaded in photoviscoelastic model used. The pulse shaped uniaxial stress σ_0 is applied to some point of the model as shown in Fig. 1(b). The axial strain ε and birefringence n are produced at this point. From equations (4), (5) and (6), the maximum strain ε_{max} and the frozen birefringence n_f in Fig. 1(c) and (d) are given by the equations.

$$\varepsilon_{max}=Dc(t',T_0)\sigma_0 \tag{7}$$

$$n_f=\left(Cc(t',T_0)-Cc(0,T_0)\right)\sigma_0 \tag{8}$$

where $D_c(t')$ is the creep compliance. Both $D_c(t')$ and $C_c(t')$ should be experimentally determined by mechanical and optical characterrzations.

The estimate functions k_1, k_2 and k_3 can be expressed from equations (1), (2) and (3) as follows,

$$k_1 = \frac{Cc(t', T_0) - Cc(0, T_0)}{Dc(t', T_0)} \tag{9}$$

$$k_2 = \frac{1}{Dc(t', T_0)} \tag{10}$$

$$k_3 = Cc(t', T_0) - Cc(0, T_0) \tag{11}$$

If two photoviscoelastic coefficients D_c and C_c are obtained before SF procedure, then theoretically we may find the most suitable temperature and loading conditions for SF method, by using three the estimate functions.

4. Theoretical and Experimental Verification

We used an epoxy resin beam with known photoviscoelastic coefficients. We applied a four-point bending test to the beam and optimized the SF method.

4.1. THEORETICAL VERIFICATION OF OPTIMIZING METHOD

The mechanical and optical properties of epoxy resin are tabulated in Table 1 and shown in Fig. 2 and 3. Figure 2 shows the master curves of creep compliance $D_c(t',T_0)$ and creep birefringence-strain coefficient $C_c(t'T_0)$ of the resin used. Figure 3 shows the time-temperature shift factor with respect to T_0 of these master curves.

This resin shows a glassy behavior in the region of short reduced time where both coefficients D_c and C_c keep low constant values, and is rubbery in the region of long reduced time, where these two coefficients keep high constant values. In the region of the intermediate reduced time, the epoxy shows viscoelastic behavior where both coefficients D_c and C_c increase significantly.

The three estimate functions k_1, k_2 and k_3 with respect to the reduced time t' can be theoretically calculated by using the photoviscoelastic coefficients of this resin and equations (9), (10) and (11). The theoretical values shown in Fig. 4, 5 and 6 were obtained from the master curves shown in Fig. 2.

First, k_1 has a peak value near $t'=10^4$ min, and remains constant value in long reduced time regions, as shown in Fig. 4. This means that the frozen birefringence n_f by the stress freezing from viscoelastic region is rather larger than that from rubbery

Table 1 Mechanical and optical properties

Item	Glassy	Rubbery
Young's modulus	1.31GPa	0.0124GPa
Poisson's ratio	0.35	0.5
Strain sensitivity	116×10^3fr / m	40.6×10^3 fr/ m
Coefficient of thermal expansion	61×10^{-6}°C^{-1}	166×10^{-6}°C^{-1}
Glass transition temperature	132°C	

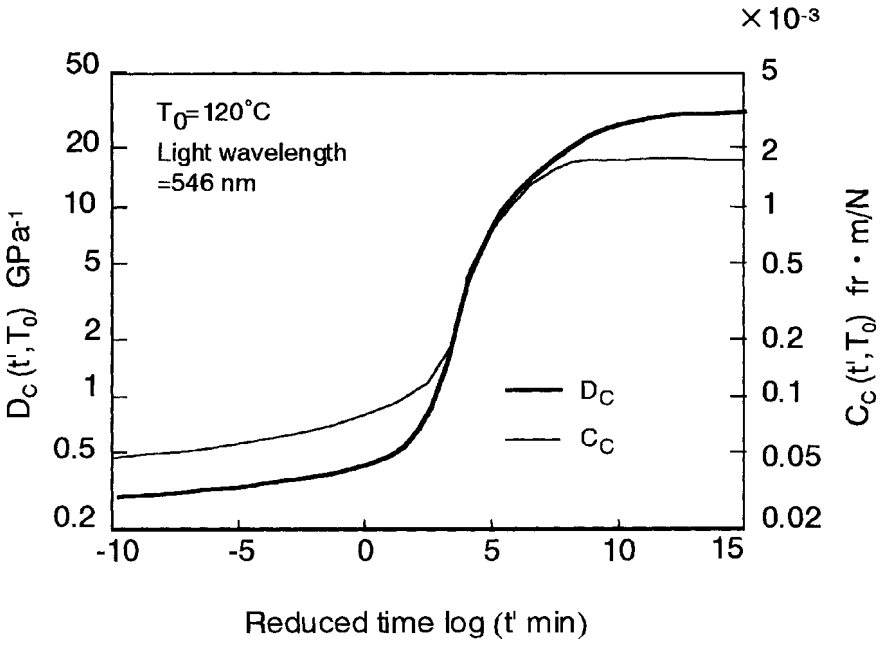

Fig.2 Master curves of photoviscoelastic coefficients

region, provided that the maximum frozen strain ε_{max} is fixed.

Secondly, k_2, the ratio of σ_ρ to ε_{max}, decreases as the reduced time t' increases, as shown in Fig. 5. This means that the large stress can be loaded, when the stress freezing is done during the short reduced time.

Finally, k_3, the ratio of n_f to σ_0, increases monotonically as t' increases, as shown in Fig. 6. This means that the large frozen birefringence can be obtained in the vicinity of rubbery state, provided that the stress σ_0 is fixed.

4.2. EXPERIMENTAL VERIFICATION OF OPTIMIZING METHOD

We applied the 4-point bending test to this epoxy resin. Gauge marks for measuring the deformation and strain were drawn on the surfaces of the specimen. As the glass transition temperature is 132 °C, five temperatures, 100 °C, 120 °C, 135 °C, 150 °C and 180 °C, were used as the holding tempera-

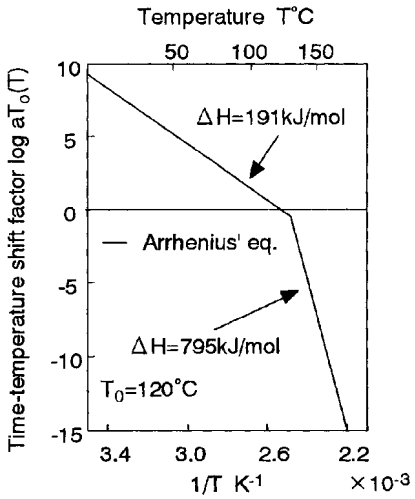

Fig.3 Time-temperature shift factor a_{T0} (T)

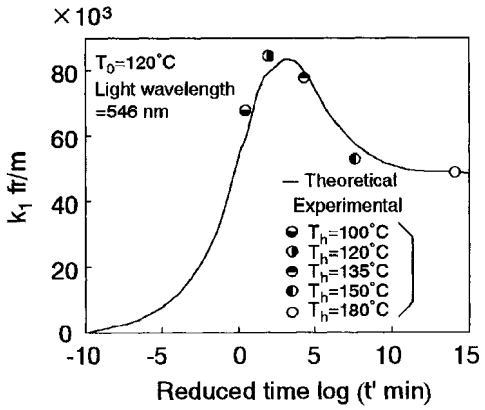

Fig.4 Estimate function k_1

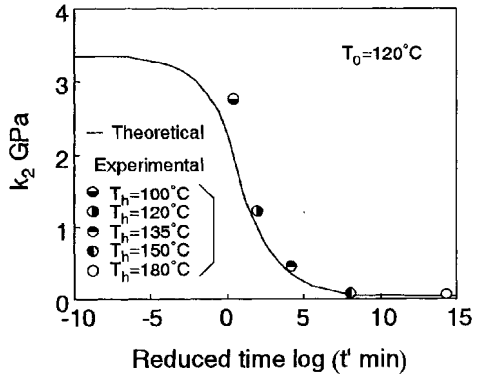

Fig.5 Estimate function k_2

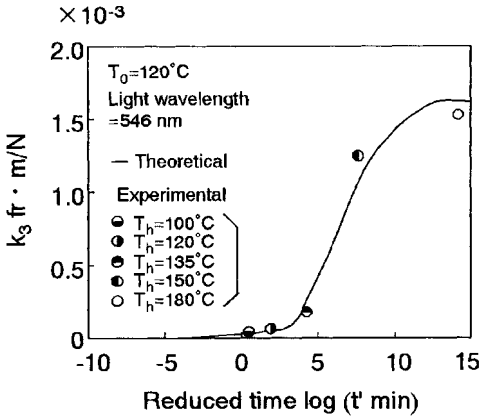

Fig.6 Estimate function k_3

ture T_h. The loads W at each T_h were determined using the master curve of creep compliance.

The specimen was held in the heating chamber for a sufficiently long time at each constant temperature T_h without loading, W was loaded on the specimen at time t=0 and was kept for 30 min, then the specimen was gradually cooled to room temperature T_c (=20 °C) at a cooling speed of approximately 0.5 °C/min. After cooling, the maximum strain ε_{max} was obtained by measuring gauge marks on the loaded specimen. The load was removed and the maximum frozen birefringence n_f at the edge of the specimen was obtained from the frozen fringe pattern recorded. Finally, experimental values of k_1, k_2 and k_3 were obtained by substituting these values into the equations (1) (2) and (3).

Figs. 4, 5 and 6 compare experimental and theoretical results; the agreement is good.

In an ordinary SF method, the SF procedure is arranged to keep k_3, the ratio of n_f and σ_0, as large as possible. But, in some cases, we need to hold k_1 or k_2 as large as possible. For example, during stress freezing from a high temperature at which the material is in a rubbery state, large frozen birefringence can be obtained, but e_{max} becomes considerably large. On the other hand, we have established that, if the strain limit is small, the SF from the temperature range at which the material is in a viscoelastic state leads to rather large frozen birefringence and larger frozen stress than the ordinary SF.

5. Conclusion

A new procedure for finding the most suitable holding SF temperature and optimizing the freezing cycle is proposed, based on the quantitative character of the linear-photoviscoelastic behavior of the model material. Three estimation functions are defined for practical SF method. Their availability was proved theoretically and experimentally.

References

1. Kunio, T. and Miyano, Y.(1968) Photoviscoelastic analysis by use of polyurethane rubber, *Applied Mechanics*(Proceeding of 12th International Congress of Applied Mechanics) 269-276.
2. Arenz, R. J., Ferguson, C. W. and Williams, M. L.(1967) The mechanical and optical characterization of a Solithane composition, *Experimental Mechanics* **7,** 183-188.
3. Sugimori, S., Miyano, Y. and Kunio, T.(1984) Photoviscoelastic analysis of thermal stress in a quenched epoxy beam, *Experimental Mechanics* **24**(2), 150-156.

THE ASSESSMENT OF THE T* FRACTURE PARAMETER DURING CREEP RELAXATION

C. WALKER, P. Mc KENZIE
Department of Mechanical Engineering
University of Strathclyde, Glasgow, Scotland

Abstract

While most fracture mechanics investigations are concerned with crack growth, there is a class of behaviour that occurs during creep relaxation where the plastic zone develops in a regime of reducing stress and near-zero crack growth. This behaviour has been measured in the aluminium alloy 7075 T6, using moiré interferometry at 190°C, and the experimental data have been used to investigate the T* integral fracture parameter as a function of time and creep deformation.

It was found that under time-dependant deformation conditions T* could be measured successfully. For a fuller investigation of T* as a function of the deformation a finite element model of the specimen was calibrated using experimental data.

Introduction

While the use of the J-integral has become widespread in fracture mechanics, progress has been slow towards a new parameter that will be valid for conditions where J is by definition outside its area of relevance. New fracture parameters such as the T* integral have been enunciated (1), and investigated by means of computational models, but the difficulties in carrying out valid experiments have meant that few studies have attempted to correlate theory, computation and experimental measurements (2, 3). It is only by such means that confidence may be established, and the new formalisms pass into routine use.

In a previous study the authors have shown how strain field data from a crack growth experiment may be analysed, to show that in reality J and T* are indeed equal in situations of modest crack growth as would be expected (3). The main conclusion from this work was a validated routine for assessing T* from the strain field components around the crack tip as visualised by moiré interferometry. The next phase in the investigation of T* is to evaluate it in a situation where either extensive plasticity or crack growth occur or where time dependent deformation takes place. This study is concerned with time-dependent deformation.

The particular situation it is one of stress relaxation where the specimen is held on a fixed grip configuration at a load sufficient to cause creep at the test temperature (190°C for the aluminium 7075 T6). In this experiment, the load steadily reduced as the

A. Lagarde (ed.),
IUTAM Symposium on Advanced Optical Methods and Applications in Solid Mechanics, 81–90.

specimen deformed. The crack in essence did not extend which meant that the data analysis was a simple matter compared to that for an extending crack.

T* Integral Fracture Parameter

The T* integral may be defined following the notation in Figure 1 as

$$T^* = \int_{\Gamma_\varepsilon} \left[W n_1 - T_i \, u_{i,1} \right] ds$$

T* may also be defined as a summation along the loading history of the incremental form ΔT^* viz.

$$\Delta T^* = \int_{\Gamma} \left[\Delta W \delta_{in} - (T_i + \Delta T_i) \Delta u_{i,l} - \Delta T_i - u_{i,l} \right] ds$$

The path Γ should be taken as small as possible but still contain (and avoid) the process zone, where intense microcracking will take place, and the strain field parameters will not be well defined

By suitable manipulation, one may derive

$$\Delta T^* = \int_{\Gamma} \left[\Delta W \delta_{1j} - (\sigma_{ij} + \Delta\sigma_{ij}) \Delta u_{i,1} - \Delta\sigma_{ij} \, u_{i,1} \right] n_j \, ds$$

$$- \int \int_{\nu - \nu_\varepsilon} \left\{ \Delta\varepsilon_{ij} \left(\sigma_{ij} + \frac{1}{2} \Delta\sigma_{ij} \right)_{,1} - \Delta\sigma_{ij} \left(\varepsilon_{ij} + \frac{1}{2} \Delta\varepsilon_{ij} \right)_{,1} \right\} dV$$

Where T* may now be calculated from the strain field parameters alone, with a knowledge of the constitutive relations for the material.

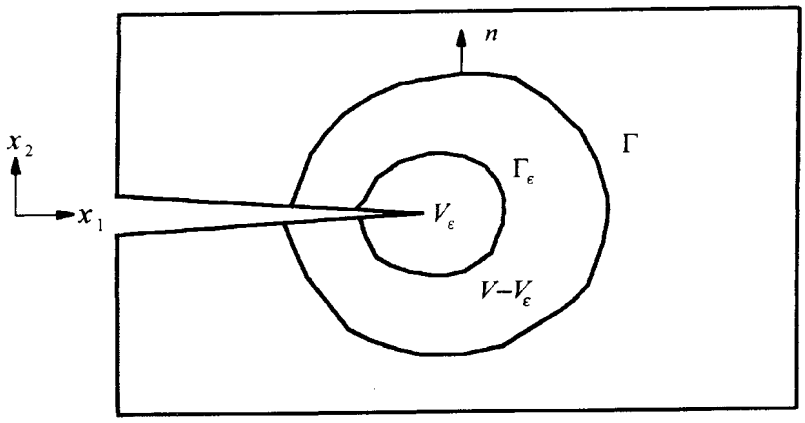

Figure 1. Integration contours for calculation of a path integral in a cracked body

n = outward normal

Γ = outer integration contour

Γ_ε = inner integration contour

V_ε = volume defined by Γ

$V - V_\varepsilon$ = volume defined by Γ_ε

x_2 , x_2 = coordinate system

Integration Path

In the summation of ΔT^* along the loading history, the path Γ stays stationery in relation to the cracked tip i.e. the Γ moves with the crack tip.

This implies that data needs to be recorded ahead of the crack tip for use eventually as the crack propagates. This is the one feature of the grating method that is highly attractive, as the whole crack-tip field is recorded as a unity. Given that no crack growth was intended in this study, a fixed contour could be used. (Dimensions are given in Figure 2).

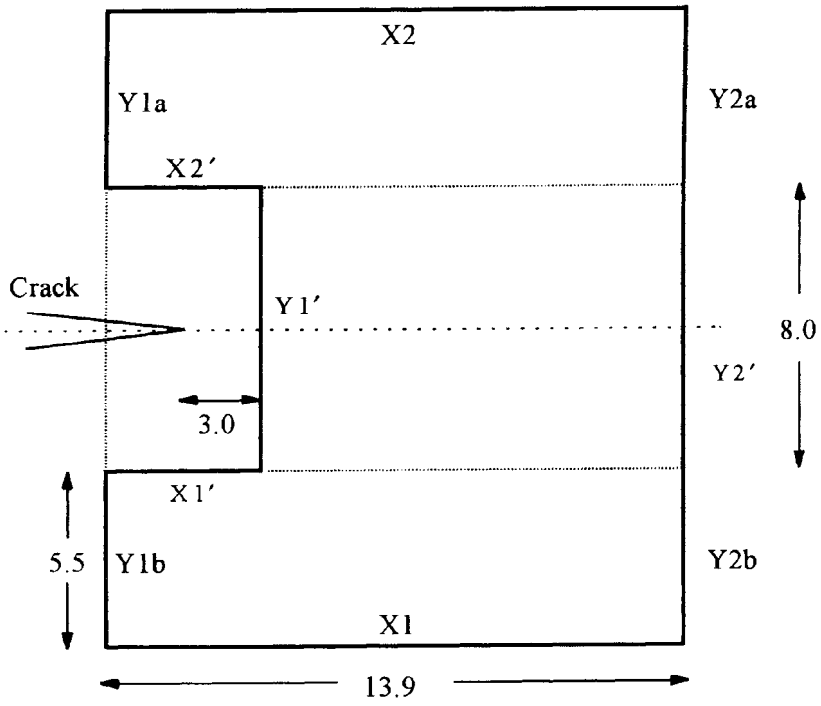

Figure 2. Path of integration (distances in mm)

Experimental Procedure

The specimen material was a high strength aluminium alloy (7075 T6), in the shape of a compact tension fracture specimen (Figure 3). The starter crack was fatigue precracked from a machined notch, although, in fact, due to the degree of creep deformation envisaged, this precaution was probably unnecessary. After precracking a 500line/mm

cross grating was cast on to the area around the crack tip. An epoxy resin was used although at 190°C, this was close to the upper operational limit for epoxy gratings. Perceptible degradation took place in the gratings over the period of the test (24 hours).

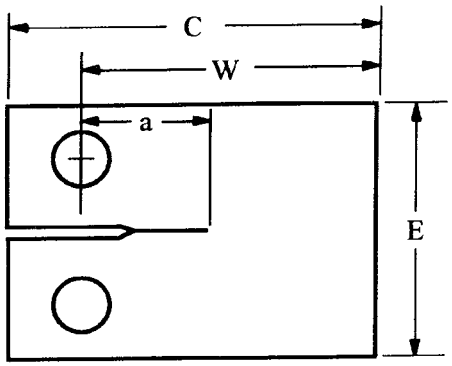

Specimen thickness = B

a = 15.6mm

W = 25.5mm

B = 12.7mm

C = 31.8mm

E = 30.5mm

Material - Al - alloy
7075 ~ T6

Figure 3. Specimen details

A servo hydraulic test frame applied the initial load of 12.5 kN and thereafter the displacement was held constant. An oven with a low-expansion glass window of optical quality maintained the temperature of the test. A shroud to minimise convection currents surrounded the windows. With this system, it was found that high quality interferograms could be recorded using a moire interferometer that has been previously described (4). This system is largely immune to ambient vibration; interferograms were recorded in three directions (0, 90, 45) so that a complete record of deformation was available for any point in the field for the times recorded (t= 0, 3, 8, 15, 23, 79, 283, 1318 minutes). (Sample interferograms are shown in Figure 3). Over the period of the tests, the load relaxed to 5.3kN – i.e. to less than 50 per cent of its original level.

Fringe Analysis

Each interferogram was overlain by the outline of the contour of integration. It will be seen that there is a region around the crack tip when no fringes are visible (Figure 4). While the basic cause of this is the intense deformation that causes the surface to dimple, fringes are actually formed in this region, but the surface rotation directs the diffracted light out of the system. For convenience, then, the inner contour was defined outside of this zone (Figure 2). Fringe analysis was then carried out using a graphics-

digitising tablet as input to an analysis programme (5). The volume integration was accomplished by decomposing the area between the contours into horizontal and vertical stripes (6). Only the bottom half of the area was digitised, in view of the symmetry about the crack. As a check to insure that the near-field path remained within the elastic regime, a test of the principal stresses was included in the T* evaluation using the von Mises criterion. No evidence of yielding was found for times up to 23 minutes.

Results

The calculated values for t=0 to t=23 minutes are shown in Table 2. Up to this point, the creep zone evolved close to the track tip. Beyond this time, the creep zone spread beyond the integration contour. It is possible to calculate T* in this regime, if the creep rates are known as a function of time at each position, and one is able to presume that the deformation is primarily creep. An interpolation of the creep rates from 79 to 1318 minutes showed unstable results. The fact remains that there are two simple situations – one where the creep zone is limited, and the other where creep is dominant throughout the specimen; in the transition between these two neither elastic not creep deformations are dominant, and the strain field cannot be easily measured experimentally. In order to decouple plasticity and creep, one could unload the specimen periodically, removing the elastic component (which is time-dependant due to the reducing load and the spreading creep field). Alternatively, the moire data could be used to validate an elastic – plastic finite-element model of the specimen. This option was adopted (7), and with the model, the spread of the creep zone (defined as a 0.1 per cent creep strain) from a small area around the crack at 15 minutes to a zone extending to the uncracked border by 203 minutes was analysed and predicted (Figure 5).

Conclusion

In a creep-relaxation experiment, it has been shown that T* may be measured solely from the strain field parameter so long as the creep strains are limited to a zone close to the crack tip. When the creep zone grows beyond the inner integration contour, and establishes dominance across a specimen, the elastic and plastics strains need to be decoupled. This may conveniently be accomplished with an elastic – plastic finite-element model of the specimen.

It should be noted that the results achievable with a combined approach are greater than with either of the techniques on its own, since the FE model gained its credibility from the comparison with the experimental data.

References:

1) Atluri, SN and Nagaki, M. An incremental path independent integral in inelastic and dynamic fracture mechanics. Engineering Fracture Mechanics, **20,** 1984, 209-244.

2) Atluri, SN et al. T*-Integral Analysis of Fracture Specimens, Proc ESDA 1996, Montpellier, **76,** 89-94. (ASME).
3) Walker, CA and MacKenzie PM. ECF11, Poitiers, France, 1996, pp1957-1964.
4) Macdonach, A et al. Experimental Techniques, **7,** (6), 20-24, June 1983.
5) MacKenzie, PM et al. Res Mechanica, **28,** 361-382, 1989.
6) Houssin, S. Experimental evaluation of the T* integral parameter under conditions of creep relaxation, MSc thesis, University of Strathclyde, Glasgow 1992.
7) Le Helloco, M. An evaluation of the T* integral under conditions of stress-relaxation. MSc thesis, University of Strathclyde, Glasgow 1992.

TABLE 1

Time	0	3	8	15	23
Y1b	5.90	1.90	-2.51	1.68	0.87
X1	17.26	0.81	-0.10	0.14	-0.42
Y2'	3.74	1.03	-0.41	0.64	0.05
Y2b	9.53	-0.18	-0.83	1.48	3.30
ΔT1	69.14	6.11	-7.39	7.40	7.52
ΔT2	-28.31	1.77	-9.12	-19.87	-18.76
ΔT*	97.45	4.34	1.73	27.28	26.29
T*	97.45	101.79	103.52	130.80	157.09

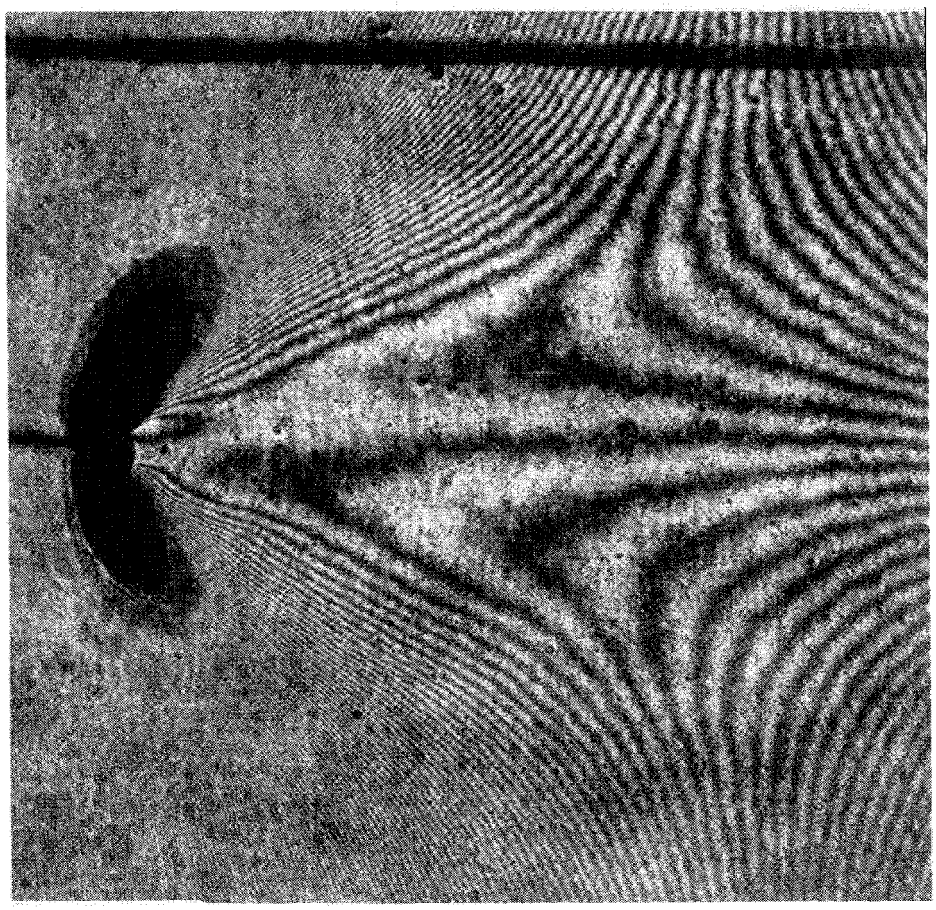

Figure 4a
Deformation Contours around the crack tip after 3minutes
(deformation contour interval – 1.05 micron, linear magnification 8.5x)

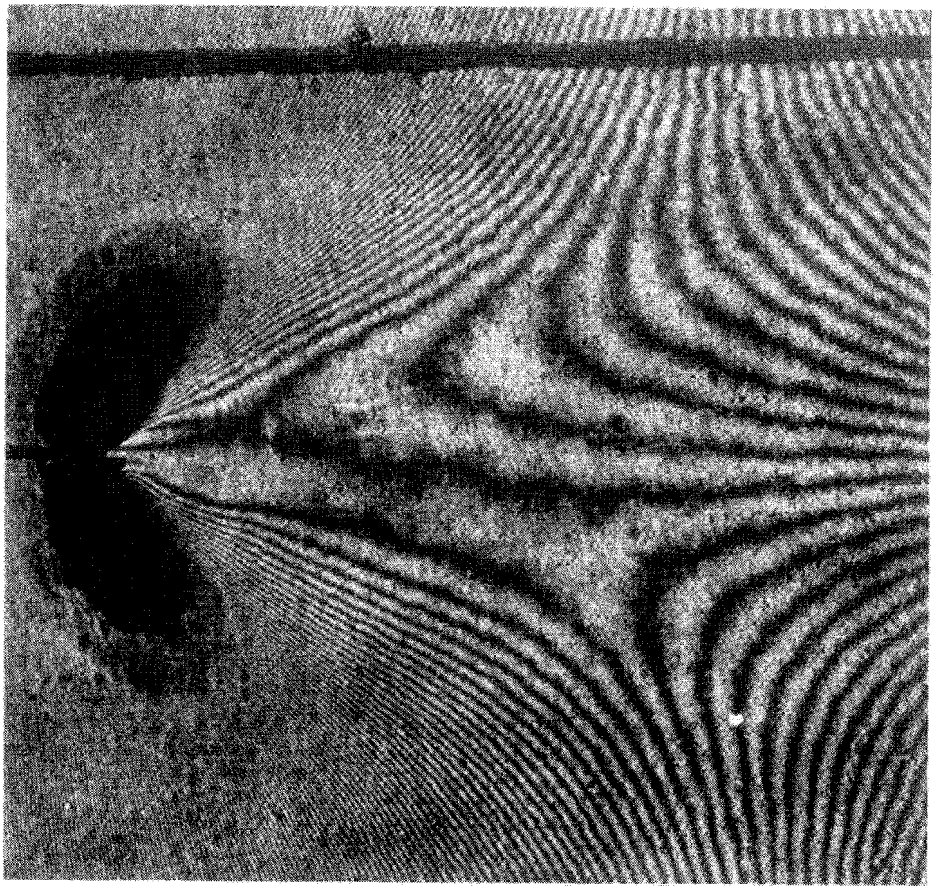

Figure 4b
Deformation Contours around the crack tip after 24 hours
(deformation contour interval – 1.05 micron, linear magnification 8.5x)

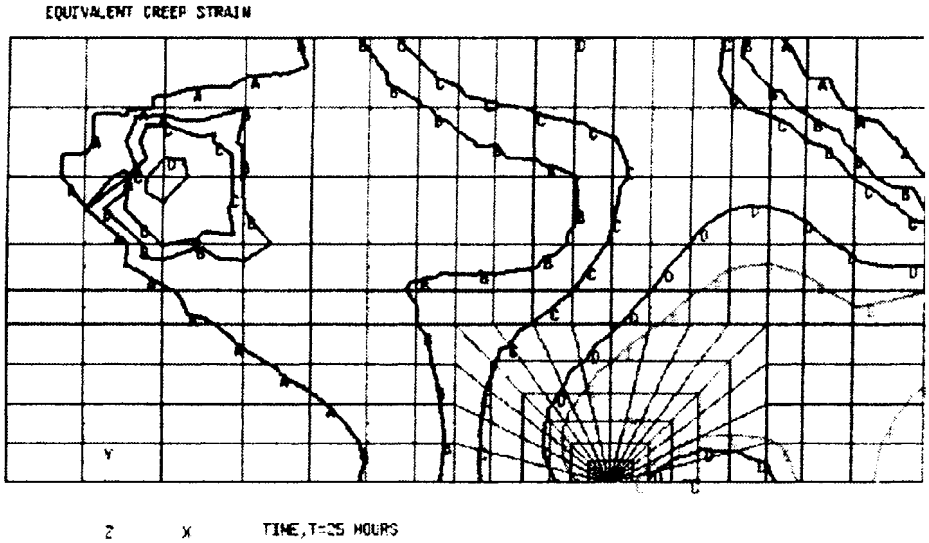

A = 0% creep strain

B = 0.005% creep strain

C = 0.01% creep strain

D = 0.05% creep strain

E = 0.1% creep strain

F = 0.5% creep strain

Fig.5

Predicted creep contours after 25h

TEMPERATURE INSENSITIVE MOIRÉ INTERFEROMETRY :

A QUANTITATIVE INVESTIGATION

J. Mc KELVIE, G. COLLIN
Department of Mechanical Engineering
University of Strathclyde, Glasgow, Scotland

ABSTRACT: Fringe patterns produced in an allegedly thermally-immune moire interferometry arrangement, through severely thermally disturbed air, have been analysed quantitatively. It is found that the spurious strains are generally less than 30 microstrain.

1. INTRODUCTION

Coherent-optical interferometric methods of strain measurement (holography, speckle and moire) have been usefully employed for almost thirty years now, but one of their limitations in common has been the effect of thermal non-uniformity in the medium through which the beams pass. The resulting disturbance of the phase of the light, and concomitantly of the pattern of the interference fringes, has generally meant that the methods have been employed only for investigations at ambient temperature; (but including, importantly, cases where the object has been heated and then cooled again, - a circumstance in which there is no thermal disturbance of the beams). An example of a moire interferogram is shown in Fig Ia, and the effect of disturbing one of the beams using the turbulent air ahead of a small blowtorch flame is shown in Fig I b.

A notable exception to this general avoidance of nonambient work has been the work of Kang et al. ([1] & [21). In that work, moiré interferometry was used for live investigations of specimens under load in ovens at temperatures up to 1100°C, with the light passing into and out of the oven through quartz windows, with no particular precautions being taken to obviate or quantify any thermal disturbance. The resulting interferograms published in that work are quite astonishingly good, considering the conditions, but in any such environment there must always be a measure of doubt as to the value of the information extracted. Even the absence of fringe movement is not a sufficient condition for confidence, since the existence of steady-state disturbance due to, for example, thermal gradients, cannot be discounted.

A more considered approach to the problem is that of Hyer et al. [3], in which the two illuminating beams of a moire interferometer are created very near to the specimen by using a suitable prism beam splitter in very close proximity, with single-beam illumination. Any

A. Lagarde (ed.),
IUTAM Symposium on Advanced Optical Methods and Applications in Solid Mechanics, 91–97.

phase disturbance of the single beam up to tile prism creates compensating disturbances in both incident beams. However, any thermal gradient that exists within the prism will cause phase disturbances that are not mutually compensating, although it is conceivable to monitor the extent of such gradients.

In McKelvie, [4], there was presented an optical arrangement for moire interferometry that is of its nature immune to thermal disturbance for the purpose of strain measurement (but, importantly not for more general displacement measurement). The efficacy was demonstrated purely qualitatively in that work by illustrating an interferogram undisturbed and then disturbed, where it could be seen that although there was major change of the fringe spacing in the direction parallel to the grating lines, the spacing perpendicular to them (which is the quantity of major interest) appeared to be hardly affected.

There was, however, no quantification of the disturbance, which is what this current work addresses.

2. THE EXTENT OF THE PROBLEM

A simple experiment was carried out to determine how serious the general problem might be. A raw He-Ne laser beam was set to pass through a small tube furnace held at 1100°C. The position of the spot at a distance of 1 metre was monitored on a screen. In steady conditions the spot moved approximately Imm, with a little obvious perturbance. In a typical moire interferometer (1200 lines/mm) such an angle of deflection of 0.06 degrees would correspond to a spurious strain of 900 microstrain,, or 2500 microstrain for the 600 lines/mm grating used by Kang. However, when a fan was used to blow air past the exit of the furnace tube, the deflection changed rapidly and erratically, and more severely, up to 4mm, corresponding to spurious strains of some 3,600 microstrain and 10,000 microstrain- respectively for the two grating frequencies.

By comparison, using a grazing incidence angle of 88.5°(and the appropriate grating frequency of 1580 1/mm), the corresponding spurious strains are 28microstrain and 112 microstrain for the 0.06° and 0.24° deviations, respectively.

In the context of typical engineering strains encountered at these temperatures, such error, as an outside limit, is very acceptable.

3 THE OPTICAL ARRANGEMENT

For the sake of completeness, the generic optical arrangement for moire interferometry is shown in Fig2.

There is some degree of immunity to thermal disturbance, imparted by virtue of the fact that two emerging diffracted rays that are brought together in the plane of the image pass through essentially the same intervening space, (because their angle of divergence is very

small). Their phases will be altered to the same degree therefore, so that there results a very substantial immunity to thermal disturbance in that space between specimen and camera, as is easily demonstrated. The difficulty arises in the two illuminating beams, whose phases will be altered the one quite independently from the other. These effects are indicated schematically by the actions of the prisms in Fig 2.

The essence of the solution is in arranging that the angles of incidence of the illuminating beams be close to 90' (i.e. grazing incidence). An analysis explaining the immunity is presented in McKelvie, 1997.

Fig.3 shows the particular layout for the experimental work. Because no grating was to hand that corresponded to grazing incidence together with normal emergence for the He-Ne laser wavelength, the emergent beams actually diverged, as indicated, but were brought to interference using a beam recombiner. The thermal disturbance was introduced in one of the input beams by means of the blow-torch as used in generating Fig lb. A video recording was taken, and three frames are illustrated as Figs 4a, 4b, 4c. What appears to be the worst case, Fig 4c, was chosen for detailed comparison with the undisturbed original "zero" condition, shown in Fig 1a.

19

4. THE FRINGE ANALYSIS

The fringes were manually digitised by estimating the y positions of their centres along vertical lines spaced at 20mm intervals (the prints being 240mm long) in the x direction. The fringe values, N, at these positions were entered into a Stanford Graphics package, and 6th order polynomials $N=f(y)$ were fitted to the data. Values of fringe order N on a matrix

x = 0 to 240 (20mm intervals)
y=0 to 180 (10mm intervals)

were calculated. Contours of the constant N are shown as Fig5, corresponding to Fig I a. The agreement is seen to be generally good, but for the purpose of determining strains, fitting with a two-dimensional polynomial was found to be not sufficiently accurate. Instead, the values on individual columns (y=constant) were fitted with 4th order polynomials, N=f(x), from which the derivative was calculated. For the "deformed" case, (Fig 4c), it was not possible to fit N--f(x) for the whole y- range from 0 to 180 due to a particularly powerful disturbance that can be seen running across the field, approximately half way up. Instead, the curve-fitting was done up to y=100mm, and then separately from y=100mm upwards (with a small overlap region). The fringe contour interval was 1/3OOOmm, (grating frequency 1500 lines/mm). Knowing that, and the magnification

(from frames in which the blow-torch appeared), the connection between the derivative - in the space of the print and in the space of the grating is known.

Since strain is the derivative of the fringe spacing, it was straightforward to generate estimates of the x-strains for each interferogram, and thus their differences, by differentiation of the fitted polynomials.

The resulting “errors” - that is the apparent strain field introduced by the very violent thermal disturbance - are plotted as Fig 6. It can be seen that generally the error rarely exceeds 30microstrain except near edges, where the value may rise to over 60microstrain-. (‘The highest error recorded was 137 microstrain -, occurring in the extreme left-hand bottom corner, where, in fact, there is no information at all in the undisturbed field).

At edges of course,- and especially at corners - the curve-fitting algorithms would be rather more prone to error than elsewhere.

5.POSSIBLE APPLICATION IN OTHER COHERENT SYSTEMS

There are systems, in holographic and speckle interferometry that are sensitive essentially to in-plane displacements, using two conjugate collimated illuminating beams - as in moire interferometry. Grazing incidence will endow the same degree of immunity on the incident beams in these systems as for the moire system, but the emergent beams present a different problem. That is because the interference that produces the displacement fringes arises not only between two beams, but, in effect, four, - the two in the first exposure and the two in the second - so that any change in the relative phases across the space in the interval between the exposures will cause distortion of the fringes. Any application must therefore employ rapid double-exposure, so that the thermal distribution has no time to alter, - but such circumstances would also obviate the need for grazing incidence anyway.

6. CONCLUSION

It has been demonstrated quantitatively that the use of grazing incidence in the illuminating beams renders moire interferometry immune within typical engineering acceptability, to the effects of even quite violent thermal disturbance of the surrounding space. The stratagem would not be of benefit in the analogous systems using holographic or speckle interferometry.

REFERENCES

1 Kang, B.S.-J., Zhang, G.Z., Jenkins, M.G., Ferber,M, & Ifju, P. 1993. Development of Moire Interferometery for In-situ Material Surface Deformation. Measurement at High Temperature. Proc. *SEM Conf. on Experimental Mechanics,* Dearborn, MI, 964-976

2. Kang, B.S.-J., Zhang, G.Z., Manohar, E., & Liu, P., 1994. Creep Crack Growth of Inconel 718 Superalloy at Elevated Temperature Using Moire Interferometry Proc. *SEM Spring Conf. on Experimental Mechanics,* Baltimore, MD, 904-912.

3, Hyer, W.M., Herakovitch, C.T., & Post, D. 1982,Thermal Expansion of Graphite Epoxy. *Advances in Aerospace Structures and Materials,* ASME 1982.

4 McKelvie,J, 1997. Thermal-insensitive Moire Interferometry, *Opt. Lett., 22,* 1, 55-58.

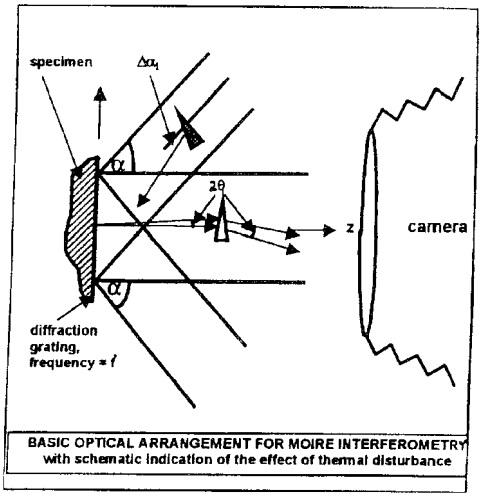

Fig.2

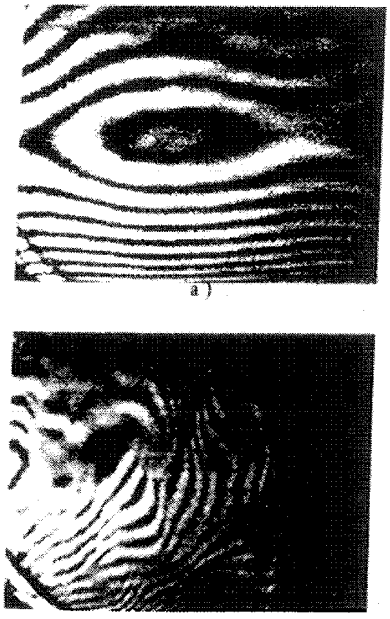

Fig. 1

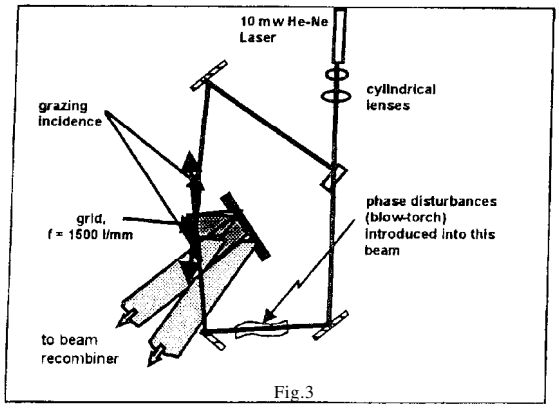

Fig.3

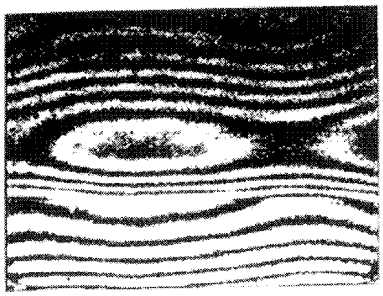

a)

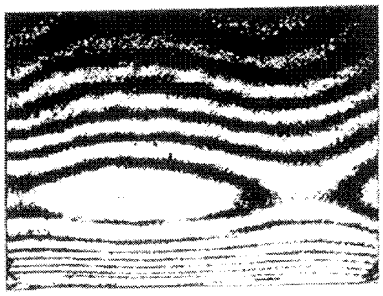

b)

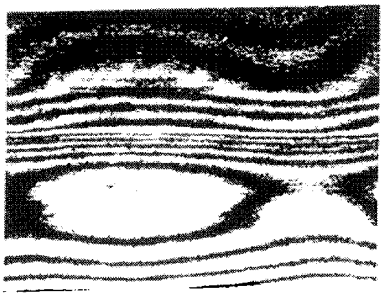

c)

Fig. 4

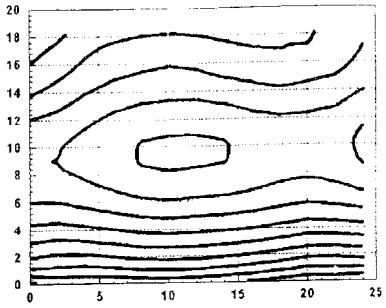

Fig. 5

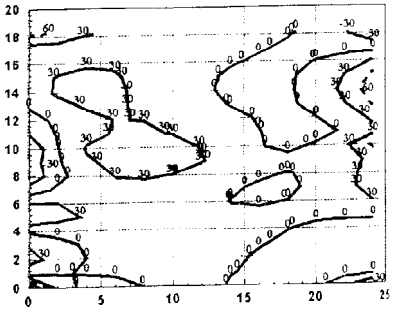

Fig. 6

This Page Intentionally Left Blank

THEORY OF MOIRÉ FRINGE FORMATION WITH AN ELECTRON BEAM[1]

D. T. READ
National Institute of Standards and Technology
Boulder, Colorado 80303, USA

J.W. DALLY
University of Maryland
College Park, MD 20742, USA

Abstract

When a specimen surface carrying a high-frequency line grating is examined under a scanning electron microscope (SEM), moire fringes are observed at several different magnifications. The fringes are characterized by their spatial frequency, orientation, and contrast. These features depend on the spatial frequency mismatch between the specimen grating and the raster scan lines, the diameter of the electron beam, and the detailed topography of the lines on the specimen.

A mathematical model of e-beam moire is developed that depicts the spatial dependence of the SEM image brightness as a product of the local intensity of the scanning beam and the local scattering function from the specimen grating. Equations are derived that show the spatial frequency of the moire fringes as functions of the microscope settings and the spatial frequency of the specimen grating. The model also describes the contrast of several different types of moire fringes observed at different magnifications. The different types of fringe patterns are divided into categories including: natural fringes, fringes of multiplication, and fringes of division.

1. Introduction

When a specimen surface that carries a regular array of lines is examined under a scanning electron microscope (SEM), moire fringes can be observed at several different magnifications. Some confusion can arise in the interpretation of the different fringe patterns, because the spatial frequency of the moire fringes changes with mismatch, rotation, a multiplication phenomena, and a division phenomena. In this paper, we first demonstrate these different fringe patterns and then explain their formation based on a Fourier series representation.

---

[1] Contribution of the U. S. National Institute of Standards; not subject to copyright in the U. S.

A. Lagarde (ed.),
IUTAM Symposium on Advanced Optical Methods and Applications in Solid Mechanics, 99–108.

Optical moire fringes, either geometric or interferometric, are widely employed in experimental mechanics. The classical treatments of geometric moire by Parks[1], Durelli and Parks[2], and Theocaris[3], and the descriptions of interferometric moire by Post [4], Graham [5], and McKelvie [6] are most helpful in interpreting fringe pattern formation in e-beam moire. However, certain features of the phenomenon of electron beam moire were not anticipated in these classic treatments of optical moire. These features occur because no actual reference grating exists in electron beam moire. Instead, the electron beam raster scan replaces the reference grating.

The e-beam raster scan is similar in may respects to the video raster scan employed by Morimoto [7] in forming moire fringes using low frequency specimen gratings. Kishimoto [8] recognized the similarity between the video and SEM raster scans and was the first to report the use of e-beam moire fringes for experimental mechanics. However, neither Morimoto nor Kishimoto discussed the many fringe patterns that may be observed when scanning lines are employed as the reference grating. With the controls available on a typical SEM, it is possible to vary the e-beam diameter, the pitch of the raster scan, and the angle between the scan lines and the grating lines. All affect the fringe pattern.

We develop a mathematical model of e-beam moire fringe formation that allows us to reproduce and extend certain results previously derived for optical moire. The model is based on two postulates used in treatments of optical moiré [5]:

1. The spatial dependence of both the pattern of the scan lines and the specimen grating can be described using Fourier series.
2. The SEM image can be represented numerically as a set of intensity values given by the product of the scattering power of the specimen grating and the intensity of the scanning lines. The spatially extended interaction of the e-beam with the near-surface region of the specimen, due to back-scattered and secondary electrons, is incorporated as a contribution to the width of the scanning lines.

Based on these postulates, a model is derived that concisely describes natural moire fringes, fringes of multiplication and fringes of division. Experimental examples are demonstrated. The model is well-suited to determine the fringe contrast and the fringe shape as functions of the raster scan pitch, the scan line width and specimen grating parameters.

2. Observation of Specimen Gratings and e-Beam Moiré Fringes

Several high-frequency gratings (2.5 to 10 line/μm) were written on a brass specimen using the methods described in [9]. A macroscopic view of the small areas written with different frequencies and different e-beam exposures is presented in Figure 1. A line grating with a frequency f_g = 5 line/μm at 55,000X is presented in Figure 2. Depending on the effectiveness of the process used to fabricate such lines, they may appear in the SEM display as high-contrast stripes of black and white, as shown in Figure 2, or as low

contrast stripes represented by intensity modulations in a gray field. Local imperfections in the specimen surface and in the grating produce irregularities in the brightness of the image. Additional imperfections are generated by the imaging process even though the SEM image is recorded at a slow scan rate.

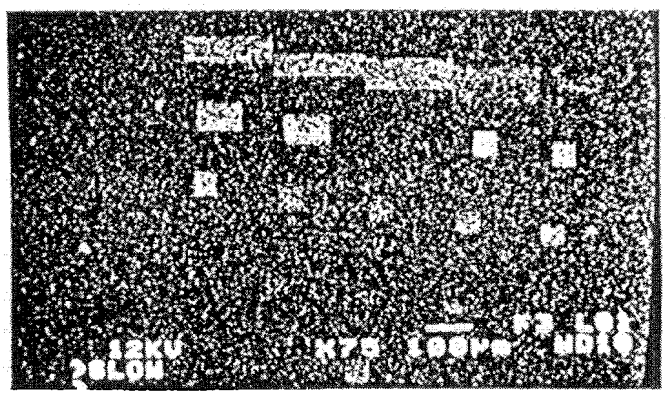

Figure 1 Several line gratings written with different frequencies and exposures on a brass specimen,

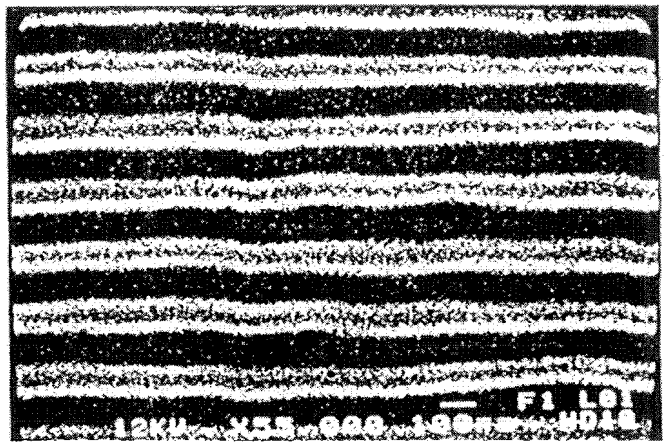

Figure 2 SEM image of a line grating with p_g = 220 nm at a magnification of 55,000X

When a grating with f_g = 5 line/μm is observed, moire fringes appear at several different magnifications from 300 to 3000 X. Typical moire patterns are illustrated in Figs. 3 to 5. We have divided these fringe patterns into three categories based on the relative sizes of the spatial frequency of the specimen grating and the raster scan. Moire fringes of division, where $f_g > f_b$, are presented in Figure 3. Natural moire fringes, where $f_g \cong f_b$, are shown in Figure 4. Moiré fringes of multiplication, first observed optically by Post [8], are also generated with e-beam moire when $f_b > f_g$. Multiplication by a factor of

three is depicted in Figure 5.

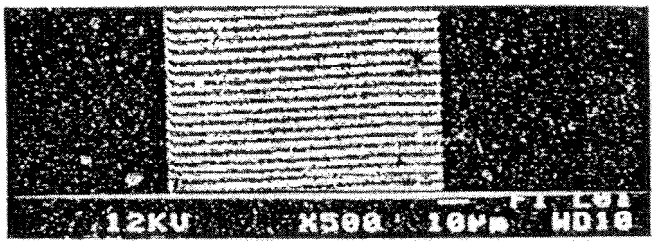

Figure 3 Moiré fringes of division on with p_g = 2000 nm at a magnification o f 500.

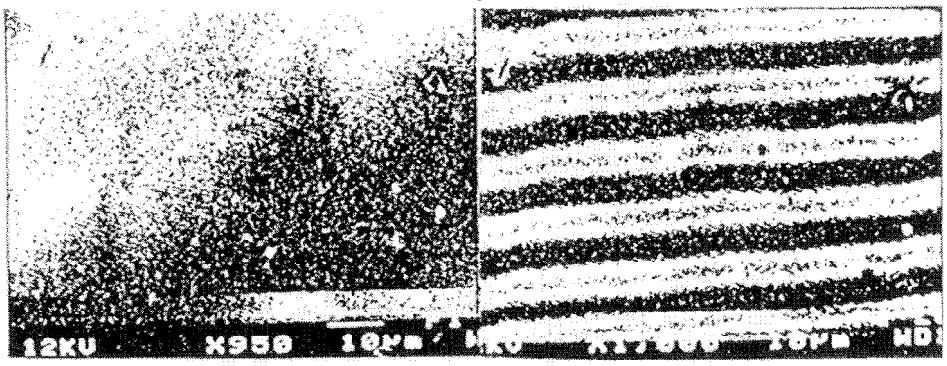

Figure 4 Natural moiré fringes with p_g = 200 nm at magnifications of 950 and 1000

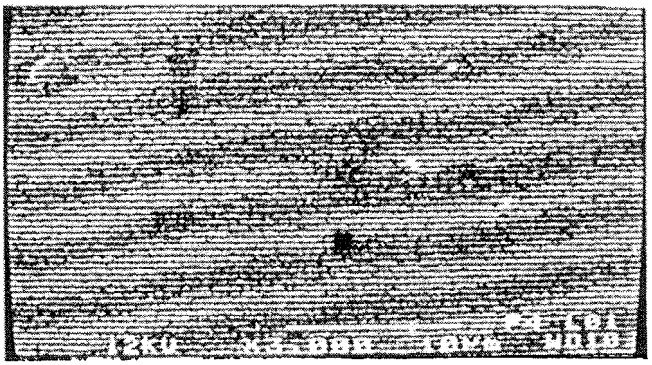

Figure 5 Moiré fringes of multiplication with p_g = 200 nm at a magnification of 3000.

3. Theory of e-Beam Moiré Fringe Formation

We introduce a theory to describe the formation of the several different types of moiré fringes observed in a SEM. The theory is similar to that used to describe the formation of fringes in optical geometric moiré. Fourier series representations describe the SEM raster scan, the specimen line grating, and the moiré fringes. The results are interpreted to

explain the occurrence of fringes classified as natural, multiplied, and divided.

3.1 THE SEM RASTER SCAN SYSTEM

The image observed in a SEM is produced by scanning the specimen grating with an e-beam raster scan. We locate a point in this image by its coordinates (x, y). The e-beam is scanned continuously across the imaged field in the x direction. The e-beam scan lines are equally spaced, with pitch p_b in the y direction. The magnified image, viewed on the CRT display, has a nominal size of 90 mm in the y direction which is related to the size of a common photomicrograph. In a SEM the raster pattern is always aligned with the viewing screen and the camera frame, so the x-axis is horizontal and the y-axis is vertical in all SEM images.

The specimen carries an array of lines extending in the ± x direction, spaced equally with pitch p_g in the y-direction. The reciprocal of p_g is f_g, the spatial frequency. The e-beam and specimen coordinates may be rotated with respect to one another by a control on the SEM

The number of scan lines used to form the image can be set at various values. Typical nominal settings are 500, 1000, or 2000 scans to produce an image. The images in Figs. 3 to 5 were made with 500 lines. Possible magnification values range from 10 to 300,000. Because of the design of most SEMs, only discrete values of the magnification are available. As a consequence, it is usually not possible to achieve a null-field moire fringe pattern.

The pitch of the electron beam raster scan lines, p_b, depends on the magnification, *M,* the nominal image size, *S,* and the number of raster scans R forming the image:

$$p_b = S / M R \tag{1}$$

For example, with 500 lines per image, a nominal image height of 90 mm, and a magnification of 1900, the scan pitch p_b is 95 nm.

The effective width of the electron beam scan lines depends on the actual e-beam diameter and the interaction of the beam with the specimen surface. Beam diameters of 5 to 20 nm are reported in the literature and in the specifications for a typical SEM. Attainment of very small beam diameters (10 nm) requires very low beam currents, a well-aligned microscope, a small aperture and extremely sharp focussing. The interaction zone diameter depends on the specimen material and the electron beam energy (accelerating voltage). We believe a value of 15 to 30 nm is typical for the effective width of the raster scan lines used in this study.

The specimen gratings are formed by etching thin slits in a polymeric film about 100 nm thick. The frequencies obtained vary from 2.5 to 10 line/μm. The lines (slits) appear as dark stripes in the image and the flats between the slits appear as light stripes. In our densest gratings, the width of the slits and the flats is approximately equal. A y-direction trace of the image intensity shows a profile with gradual, rather than abrupt, changes in the image intensity. It appears that our gratings are between “phase grating” and an “amplitude grating” according to the usage of these terms in optical moire.

3.2 FOURIER REPRESENTATIONS OF THE GRATING AND SCANNING LINES

We follow the approach introduced by Sciamarella [8] for optical moire, and assume the local intensity of the image proportional to the product of the local scattering power of the specimen grating and the local intensity of the e-beam scan line. The scattering function G(y) for the specimen grating is represented by a Fourier series:

$$G(y) = \frac{g_0}{2} + \sum_{n=1}^{\infty} g_n \cos\,(2\pi n f_g\, y) \tag{2}$$

where the g_n are Fourier coefficients and f_g is the spatial frequency of the grating lines. After deformation, the specimen grating frequency f_g can vary with position over the specimen. However, in this treatment we simplify the analysis by considering only deformation fields that produce constant strain over the local region of interest. The frequency f_g represents the current value at the time of image formation, which is usually different from the original value.

The intensity of the e-beam scan lines B(y) is also represented by a Fourier series:

$$B(y) = \frac{b_o}{2} + \sum_{m=1}^{\infty} b_m \cos\,(2\pi\, mf_b\, y) \tag{3}$$

where the b_m are Fourier coefficients and f_b is the spatial frequency of the raster lines.

The moire pattern M(y) is represented as the product of the raster function and the grating function:

$$M(y) = B(y)\, G(y) \tag{4}$$

Substituting Eqs. (2) and (3) into Eq. (4) and arranging the products of the cosine terms into sum and difference cosine functions gives a relation of the form:

$$M(y) = C + F(y) + S(y) + D(y) \tag{5}$$

where C = $g_0 b_0/4$ is a constant. The functions:

$$F(y) = (b_0/2)\Sigma g_n \cos(2\pi n f_g y) + (g_0/2)\Sigma b_m \cos(2\pi m f_b y)$$
$$S(y) = \Sigma\Sigma(g_n b_m/2)\cos 2\pi(nf_g + mf_b)y$$

exhibit a frequency that is too high to be observed. The difference function:

$$D(y) = \Sigma\Sigma(g_n b_m/2)\cos 2\pi(nf_g - mf_b)y$$

is the term in the double series expansion that produces the image observed and identified as the moire fringe pattern. We simplify Eq. (5) to give:

$$M(y) = C_1 + \sum_{m=1}^{\infty} \sum_{n=1}^{\infty} g_n b_m \cos \left[2\pi \left(n f_g - m f_b \right) y \right] \qquad (6)$$

where $C_1 = C + F(y) + S(y)$ is the intensity of the background.

The result is similar to that obtained in optical moiré. When the magnification yields moiré fringes, the grating lines cannot be clearly imaged. The coefficients g_n in the specimen grating function G(y) decrease rapidly with n because of the topography of the grating. The coefficients b_m of the scanning beam raster function B(y) do not decay as rapidly with increasing order m of the expansion.

3.3 NATURAL MOIRÉ FRINGES

The simplest condition for fringe formation in optical moire is the near-match condition when $f_g \cong f_b$. In e-beam moiré, we refer to fringes formed under this near-match condition as natural fringes. Because only discrete values of magnification are available on our SEM, it was not possible to achieve a perfect null field, where $f_g = f_b$ and the pitch of the moiré fringes p_m becomes infinite.

The frequency f_m of the moire fringe function M(y) is determined by considering the first term in Eq. (6) (n = m = 1) for the near match condition.

$$f_m = f_g - f_b \qquad (7)$$

In Eq. (7), negative values of the moiré fringe frequency are allowed, because moiré fringes are formed both for $f_g > f_b$ and for $f_g < f_b$.

Consider small uniform longitudinal strains along the y direction, relative to the ideal initial condition where $f_g = f_b$ and $\theta = 0$. Equation 7 implies that the tensile strain ε is given by

$$\varepsilon = - \frac{f_m}{(f_b + f_m)} \qquad (8)$$

The periodic form of Eqs. (2) to (6) permits us to adopt a vast body of previous developments to interpret e-beam moiré fringes. Some familiar wave phenomena have analogs in SEM images of line gratings. For example, it is clear from Eq. (7) that the moire fringes are analogous to the beat frequency due to two pure sound tones of slightly different frequencies.

The contrast of the natural moiré fringes is determined primarily by the amplitude term $g_1 b_1 /2$ although higher order terms also affect the contrast. Higher order harmonics of the fringe frequency occur for $m = n = 2, 3, \ldots$etc. These harmonics distort the pure

sinusoid of the fundamental and degrade the contrast of the image. Other higher order terms occur when n ≠ m and produce signals with a very high frequency which can be disregarded except for their detrimental effect on contrast.

3.4 FRINGES OF MULTIPLICATION

Post [11] showed that fringe multiplication occurred in optical moire when, the spatial frequency of the reference grating was a near multiple of the spatial frequency of the specimen grating. The same fringe multiplication occurs in e-beam moire. We express the spatial frequency of the scan lines, following the notation introduced by Post [11] as:

(9)

where β is a positive integer and λ is a small fraction. Substituting Eq. (9) into Eq. (7) shows that the spatial frequency of the moire fringes is:

$$f_m = [n - m\beta(1 - \lambda)]\, f_g = [(n - \beta m) - m\lambda\beta]\, f_g \tag{10}$$

Moire fringes may be observed when $n = \beta m$; then f_m becomes:

$$f_m = -m\,\lambda\,\beta\,f_g \tag{11}$$

The amplitude of the moire fringe terms in Eq. (6) is given by $g_n b_m/2$. Since β is typically an integer from 2 to 5, n = βm is always greater than one. Maximum contrast requires m = 1; hence, fringes of multiplication occur when we match the fundamental frequency of e-beam raster scan with the second, third, etc. harmonics of the grating function. Difficulties in obtaining high contrast in attempts to employ fringe multiplication are due to the use of decreasing Fourier amplitudes of higher harmonics of the grating function. To illustrate this important result, let β = 2 and consider a specimen grating that is represented by a symmetric square wave (a grating with bar width equal to space width). Since $g_2 = 0$, the coefficient of the second harmonic for a square wave, contrast vanishes and these fringes of multiplication cannot be observed.

These results show the importance of the grating scattering function for the contrast of fringes of multiplication. A grating with narrow lines and wide spaces exhibits stronger even harmonics than a balanced grating with equally wide lines and spaces. However, for all shapes, except the periodic delta function, the general rule is that the coefficients g_n decrease rapidly with increasing order of the harmonic.

3.5 FRINGES OF DIVISION

Moire fringes of division also occur when the specimen grating frequency is a multiple of the scan line frequency. Fringes of division are commonly observed at low magnification settings on the SEM, when p_b is larger than p_g. The formation of the fringes of division and their contrast is evident from Eq. (6). Consider an observation in the SEM with a

frequency relation given by

$$f_b = (1 + \Lambda) f_g / \beta \tag{12}$$

The frequency of the resulting moiré fringe pattern is obtained from Eq. (6) as:

$$f_m = [(n - m/\beta) - m\Lambda/\beta] f_g \tag{13}$$

The moire pattern can be observed when $n = m/\beta$ and Eq. (13) reduces to:

$$f_m = -m\Lambda f_g / \beta \tag{14}$$

Since β is an integer typically from 2 to 5, $m = \beta n$ is always greater than one. This fact shows that moire fringes of division are formed by combining the fundamental frequency component of the specimen grating with higher harmonics of the e-beam raster pattern. The e-beam scan lines that are produced at low magnification have relatively high coefficients b_n for n as large as 10.

4. Conclusions

The formation of e-beam moire fringes in a SEM can be described with a model based on a Fourier series representation of the specimen grating line function G(y) and the raster scan line function B(y). The moire function M(y) is the product of these two functions. The model describes the variation in the spatial frequency fm of the moire fringes with the magnification used in producing the image. It also provides a means for estimating the contrast of different moiré fringe patterns that are observed in the SEM. The spatial frequency fm can be used to measure the spatial frequency fg of the specimen grating to determine displacements.

The sensitivity and resolution of measurements made with e-beam moire are limited by the frequency of the specimen grating. Fringes of multiplication offer enhanced displacement sensitivity per fringe, but require that the specimen grating be fabricated with a slit-ridge ratio that produces substantial higher order Fourier components. Fringes of division are observed as easily as natural moire fringes because the raster scan lines at low magnifications exhibit significant Fourier coefficients for the higher order terms in the expansion. Fringes of division are useful because they permit a larger field of observation.

REFERENCES

1. Parks, Vincent J., “Geometric Moiré,” in Handbook on Experimental Mechanics, edited by Albert S. Kobayashi, Prentice-Hall, Englewood Cliffs, New Jersey, 1987, pp. 282-313.
2. Durelli, A. J. and Parks, V., Moiré Analysis of Strain, Prentice-Hall, Englewood Cliffs, New Jersey, 1970.

3. Theocaris, P. S., Moire Fringes in Strain Analysis, Pergamon Press, Elmsford, N.Y., 1969.
4. Post, Daniel, "Moiré Interferometry," in [1].
5. Graham, S. M., "Sensitivity and Resolution Limitations of Various Moire Methods," Optics and Lasers in Engineering 12, 119-133, 1990.
6. McKelvie, J., "On the Limits to the Information Obtainable from a Moire Fringe Pattern," in Proceedings of the 1986 SEM Spring Conference on Experimental Mechanics, SEM, 1986.
7. Morimoto, Y. and Hayashi, T. "Deformation Measurement During Powder Compaction by a Scanning Moire Method," Experimental Mechanics, Vol. 24, pp. 112–116, 1984.
8. Kishimoto, S. Egashira, M. and Shina, N., "Measurements of Grain Boundary Sliding and Observation of Microgrids for High Temperature Use," Journal of Society for Materials Science Japan, Vol. 40, No. 452, pp. 637-641, 1991 (in Japanese).
9. Dally, J. W. and Read, D. T., "Electron Beam Moire," Experimental Mechanics, 33, 270-277, 1993.
10. Sciamaralla, C. A., "Basic Optical Law in the Interpretation of Moire Patterns Applied to the Analysis of Strains--Part I," Experimental Mechanics 5, 154-160, 1965.
11. Post, D., "Sharpening and Multiplication of Moire Fringes," Experimental Mechanics 28, 329-335, 1988.
12. Read, D. T. and Dally, J. W., "Theory of Electron Beam Moire," Journal of Research NIST, 101, 47-61, 1996.

A GEOMETRICAL INTERPRETATION OF THE TENSORIAL CHARACTERISATIONS OF FINITE STRAINS

P. ROUGÉE
LMT-Cachan (E.N.S. de Cachan / C.N.R.S. / Univ. Paris 6)
61, Avenue du Président Wilson, 94235 Cachan Cedex, France

Abstract. In classical Lagrangian approaches, e.g. in order to state the constitutive laws, a strain measure (or a metric tensor) is used in an attempt to model, whether intrinsically or relative to a reference state, the current state of stretching at the considered point (the local "metric state"). We will show that, in this manner, a kind of partial linearisation is being performed, thereby leading to an approximate theory: the curved space of all possible local metric states is approximated by one of its linear (or flat) charts. The quality of the approximation is then a function of this chart's reliability. Some particular charts, associated with more or less classical strain parameters, are studied herein. The chart associated with the logarithmic strain measure would appear as the most satisfactory.

Notations and terminology. Let A and B be two linear spaces.

- Lin(A;B): the linear space of linear maps of A into B, Lin (A): = Lin (A;A)
- A*: = Lin(A;R), the dual space of A, with duality denoted $<,>_A$, or <,>, A** = A
- $f^* \varepsilon$ Lin(B*;A*): transpose of $f \varepsilon$ Lin(A;B) : $< f^* v,u >_A = <v,fu >_B$
- Lin(A;A*) is canonicaly isomorphic to $A^* \otimes A^*$, the space of covariant tensors of rank 2 on A (we write: $\mathrm{Lin}(A;A^*) \overset{i}{=} A^* \otimes A^*$).
- $\Gamma(A)$: = LinS(A;A*), the space of symmetrical elements of Lin(A;A*) ($f^* = f$)
- $\Gamma^+(A) = \mathrm{Lin}\overset{+}{S}(A;A^*)$: the space of elements of $\Gamma(A)$ defined positive

If A and B are Euclidean spaces (scalar products denoted $\overset{A}{\cdot}$ and $\overset{B}{\cdot}$):

- $f^T \varepsilon$ Lin(B;A): the adjunct of $f \varepsilon$ Lin(A;B): $F^T v \overset{A}{\cdot} u = v \overset{B}{\cdot} Fu$

1. Introduction

The kinematic analysis of continuous media in generale supposes small or finite strains in finite displacement theory (F.D.) (and no small strains in small displacement theory (S.D.)). This analysis presents specific geometrical non-linearities. The scalars, vectors and tensors used classically are themselves of a linear nature : they vary in open subsets of different linear spaces, thus in *flat* spaces. The non-linearities are then introduced by means of non-linear relations connecting these *linear variables.* Such relations are the manifestation of underlying geometrical facts which once known, or recognized, help the overall understanding. Our objective herein is to explain this geometry and, in order to accomplish this, to reevaluate some practices and concepts.

1.1 AN ILLUSTRATION

Let us consider the set of non-linear (and dependent) relations:

$$x^2 + y^2 + z^2 = R^2 \ , \quad x = R\cos\theta\cos\psi, \quad y = R\cos\theta\sin\psi \ , \quad z = R\sin\theta$$

A. Lagarde (ed.),
IUTAM Symposium on Advanced Optical Methods and Applications in Solid Mechanics, 109–122,

connecting five scalar (linear) variables, x, y, z, θ and ψ. These relations are high lighted by taking into account the sphere S of radius R centred at the origin, as described by the point M with coordinates (x, y, z) in the flat space R^3. Note that M going over S is a non-linear variable. For example, S is the Earth's surface and M is an intercontinental jet whose latitude and longitude are θ and ψ. In this case, we initially have the sphere in mind, and the equations are simply the analytical translation of this initial geometrical understanding. What we are proposing for F.D. is the inverse approach, which consists of discovering the geometrical meaning of a known non-linear formalism, and from this improving its understanding.

Some straightforward remarks concerning this example will help specify our terminology and approach. First of all, any point of the Earth's surface may be characterised by its latitude and longitude. The variable (θ,ψ) over a domain of the flat space R^2 is a flat representation of M over S. Such a representation is obviously misleading: a point on the Earth's surface may be *characterised* by its latitude and longitude, however an appropriate *model* is obtained by a point on a sphere. In the *characterisation,* by means of the linear variable $(\theta,\psi) \in R^2$, the flat geometry of R^2 does not convey a physical meaning (all of the physical meaning is provided in the relations). In the *model,* by means of the non-linear variable $M \in S$, all of the physical meaning is provided in the sphere. In the following discussion, it will be important to carefully distinguish between *characterisation* and *modelling*.

Such a flat representation of the Earth's surface is the precise purpose of the *cartography.* It is well-known that the main drawback of charts pertains to their being non-isometric representations. The projections used in their production display various qualities and have been chosen in recognition of the problem to be treated. For example, the map underlying the use of (θ,ψ) is that obtained by developing the meridians on the generating straight lines of the cylinder circumscribed by the Earth along the equator. This map is isometric for the meridians and thus perfect for exclusively North-South world tours.

A flat approximation of the Earth's surface proves to be perfectly reasonable when restricted to the vicinity of a point. The sphere may then be approximated by its tangent plane at this point, and the notion of a (free) vector allows composing, or indeed comparing, certain displacements not starting from the same point. Thus, two sprinters may compete in two parallel lanes, which is not possible for two jets taking off one from Paris and the other from New York; there is generally no parallelogram on a curved surface.

1.2 MATERIAL MODEL AND PLACEMENT

The medium is studied in a space frame E (possibly identified to R^3 after the choice of a coordinate frame) with an associated linear space E. In S.D., the small displacement of the medium is neglected: it is used solely to define the small strain tensor ε_L, the symmetrical part of its gradient. This is not true in L.D. In this case, two different positions are introduced: the current one, Ω, which varies, and another Ω_0 used as the reference, which does not vary and is presumed to be known. The motion is then described by the map which, at each time t and for any $X \in \Omega_0$, provides the current position $x = p(t,X) \in \Omega$ of the point of the medium lying at X in the reference position. Let u be the vector displacement from X to x ($u = x-X$). For local considerations, the transformation p from the reference position to the current position appears only by its gradient at time t:

$$F = \frac{dx}{dX} = 1_E + \frac{du}{dX} \in \mathrm{Lin}(E_0;E) \qquad (1)$$

This gradient F is a linear map of $E_0 = E$ (denoted E_0 because it is considered as tangent to Ω_0 at the point X), into E, the tangent to Ω at the point x. It yields the position dx = FdX at the point x of the small material segment which has the position dX at point X in the reference position. This is the local transformation of the (small) material segments. The transformation of the other (small) material local elements, associated with other kinds of tensors, is performed by other operators which, being defined on the basis of F, we denote $\overset{*}{F}$. As an example, the covectors (elements of E*, modeling *slices* - between two parallel planes - as vectors model segments) are transformed by $F^{-*} = (F^*)^{-1}$.

The points $x \in \Omega$ and $X \in \Omega_0$ and the local elements $dx \in E$ and $dX \in E_0$, are strictly spatial elements. However, both reasoning and calculus always concern the material elements for which they are either the current or the reference position. The *Eulerian approach* consists of working with the medium by considering it in its current position, thus with x and dx (or their components x^α and dx^α which are the *Eulerian variables*). The *Lagrangian approach* consists of working with the medium by considering it in its reference position, thus with X and dX (or with *Lagrangian variables* X^i and dX^i).

The reference position may be seen as a time-independent representation of the medium. Beyond being a simple particular position, Ω_0, E_0,..., X, dX, .., become then the first elements of a time-independent model of the medium itself : the *material model.* From this new point of view, the maps p(t,.) and F (F, F^{-*},...) appear as being the *placements* in space of both the medium and its local elements, and they serve to perform the change from a *material* or Lagrangian approach thought as being performed on the material model itself and not on the reference position, to a *spatial* or Eulerian one, in the spatial model. For this, these maps (and the inverse maps) are no more named transformations in this paper, but *transfers.*

Nonetheless, in order to obtain the real material model, it is necessary to overlook what in Ω_0 and E_0 depends on the reference position being used. Thus, E_0, which models (small) material segments emanating from a point, is a Euclidian linear space, i.e. a linear space T_0, the *underlying* linear space, provided with a scalar product $\langle\!\langle \cdot , \cdot \rangle\!\rangle_0$: $E_0 = (T_0, \langle\!\langle \cdot , \cdot \rangle\!\rangle_0)$. If three material segments dX, dX', dX", satisfy the equation dX = dX'+dX" in the reference position used, they also satisfy it in all other positions (both continuity and differentiability hypotheses). Yet $\langle\!\langle dX, dX' \rangle\!\rangle_0$ depends on the reference position (stretching hypothesis). Thus, in $E_0 = (T_0, \langle\!\langle \cdot , \cdot \rangle\!\rangle_0)$, only T_0 is relevant to the constant material model, and $\langle\!\langle \cdot , \cdot \rangle\!\rangle_0$ is simply one particular value of the variable metric state of the medium.

A final remark: from an experimental point of view, in two dimensions, the small elements of a grid engraved on the medium serve to define at each point a time-independent basis in T_0, which is convected by the medium.

1.3 STRAIN: AN INITIAL APPROACH

We can now consider the main objective of the kinematic analysis of a continuous medium: the description and evolution of its *local state of strain.* The stretching (or strain rate) tensor D, the symmetrical part of the gradient of the velocity field V,

$$D = \left(\frac{dV}{dx}\right)_S = \tfrac{1}{2}\left(\frac{dV}{dx} + \frac{dV}{dx}^T\right) \in \mathrm{Lin}_S(E), \qquad (2)$$

models the speed of evolution of this local state of strain. Its quality in this respect is undisputed. A considerable use is make of this model in Fluid Mechanics. The associated stress variable is also undisputed; it is the Cauchy stress tensor $\sigma \in Lin_S(E)$ or even the Kirchhoff stress tensor σ/ρ (where ρ is the mass density), which leads to the following expression for the specific internal power P:

$$P = D : \sigma/\rho \equiv Tr\,(D\,\sigma/\rho) \tag{3}$$

The only disadvantage of these tools is that they are Eulerian tools: as such, they do not relate to the medium in a direct manner (e.g., the eigen axes of D indicate a set of three material axes which, as a first order relative to dt, are orthogonal at both times t and t+dt; however, these material axes do not get indicated directly by their dX in the material model T_0, but rather by their current position dx = FdX in the spatial frame E). The *transferred* into T_0 of these tools, by the inverse placement F^{-1}, the tensors

$$D_0 = \overset{*}{F}\ D \equiv F^{-1}DF \in Lin_S(T_0),\quad \sigma_0/\rho_0 = \overset{*}{F}\ \sigma/\rho \equiv J/\rho_0\, F^{-1}\sigma F \in Lin_S(T_0) \tag{4}$$

such that $$P = D_0 : \sigma_0/\rho_0 \equiv Tr\,(D_0\sigma_0/\rho_0)\,, \qquad (J = \rho_0/\rho)$$

are better adjusted Lagrangian, or material, tools. Indeed, both D and D_0, as well as σ/ρ and σ_0/ρ_0 display the same eigen values, and eigen vectors which are homologous by F, and those of D_0 and σ_0/ρ_0 are defined in the material model.

In the field of Solid Mechanics, the strain rate alone does not suffice: it is necessary to know the state of the strain itself. The scalar product dx.dx', with dx = FdX and dx' = FdX', of any two (small) material fibres dX and dX', is used to characterise this state locally. It is classically introduced by the Cauchy-Green tensor $C \in Lin_S(E_0)$ (we prefer C/2), or by the Green-Lagrange strain tensor $\varepsilon \in Lin_S(E_0)$, by setting:

$$dx.dx' = FdX.FdX' = CdX \cdot dX' = (1_{E_0} + 2\varepsilon)dX \cdot dX',$$

$$C = F^TF\ , \qquad \varepsilon = \frac{1}{2}(C - 1_{E_0}) = \frac{1}{2}\left(\frac{du}{dX} + \frac{du}{dX}^T + \frac{du}{dX}^T \frac{du}{dX}\right) \tag{5}$$

Indeed, by acting in the material model, both C/2 and ε express the current scalar product of any two material fibres, and thus describe the current state of the length and angle of these fibres, i.e. the local *metric state* of the medium. Nevertheless, this is carried out by means of relation (5) which makes use of the scalar product in the reference position. Moreover, both C and ε themselves depend on this position. In fact, they characterise the current metric state not directly, but rather by means of the current state of strain relative to the chosen reference position. Their eigen vectors are the material principal axes of this strain (the set of three material axes which are orthogonal in the two positions). The eigen values of C are the squares $C_i = \lambda_i^2$ of the relative extensions $\lambda = l/l_0$ of the material segments in these directions. In addition, ε vanishes when F is an isometry ($F^T = F^{-1}$) and in S.D., the last term in (5-2) may be neglected and ε then becomes equivalent to ε_L.

1.4 THE PROBLEMS

The Green-Lagrange strain tensor ε (or C, or even C/2), a linear variable spanning the flat space $Lin_S(T_0)$ of dimension 6, *characterises* (more or less directly) the current metric state of the medium, *while not actually modelling it.* It is through considering the strain

rate that we can prove this important remark. In physics, the variable which serves to model the velocity of a evolution of a phenomenon is necessarily the time derivative of the variable which models this phenomenon. The tensors ε and C/2 have the same time derivative. In order for them to model the state of strain, this derivative must not exactly be D, but rather its transferred D_0 in the material model (the *material strain rate*) or, at least, a tensor displaying the same characteristics.

In S.D., this condition is indeed satisfied. To the first order F is equal to 1_E and as a result we have

$$D \cong D_0 \cong \dot{\varepsilon}_L \cong \dot{C}/2 \qquad \text{(as well as } \rho \cong \rho_0 \text{ and } \sigma \cong \sigma_0\text{)}$$

We are within a linearised context. This state-oriented approach by means of the difference with respect to a reference state does not cause any particular problem. This situation corresponds exactly to when, in the (flat) spatial frame E, we substitute the vector r = (x - O)$\in$E for a point x, O being an arbitrary origin. In particular, the velocity, the time derivative of x, is then also equal to the time derivative of r.

In L.D., and with ε or C/2, this condition is not satisfied. Indeed, their common time derivative is not equal to the material strain rate :

$$\dot{C}/2 = \dot{\varepsilon} = F^T D F = C D_0 \neq D_0 \qquad (6)$$

Moreover, this derivative does not exhibit the qualities of the undisputed Eulerian strain rate D: its eigen elements do not provide information about the strain rate. For example, when D is spherical, the principal axes of $\dot{\varepsilon}$ are the principal axes of *strain.* Lastly, the associated stress variable, which is the Piola-Kirchhoff stress tensor K defined by

$$K = JF^{-1}\sigma F^{-T} \qquad \text{(such that: } P = \dot{\varepsilon} : K/\rho_0\text{)} \qquad (7)$$

presents the same drawbacks. For example, when the stress is a hydrostatic pressure, the principal axes of K are indeed the principal axes of the *strain*!

In Sections **2** and **3,** some documented attempts to model the current metric state, or the strain from the reference state, using other linear variables, are described. These attempts implicitly suppose that the space of all potential *a priori* local metric states is a flat space. They all fail, and *this finding strongly suggests that this space is in fact not flat.* The situation corresponds exactly to the fact that the velocity of a point on the Earth's surface is not equal to the velocity of its representation in a flat chart, even after taking into account the scale effect. In Section **4,** we propose a model using a *non-linear* variable, thus spanning a curved space, which appears to be entirely satisfactory. The previous linear characterisations then appear as being flat charts of this curved space, whose level of reliability will be studied in Section **6.**

2. The strain measures

It is well-known that the polar decomposition F = RU, with $U = C^{1/2} \in \mathrm{Lin}_S(E_0)$ and R being a rotation of E_0 = E into E, decomposes the local placement F in an initial transformation U in E_0, which produces all of the strain in the material model and which is followed by the isometric map R into the spatial frame E. The tensor U, and also $\varepsilon_1 = (U - 1_E)$ which vanishes in the case of no strain, which are functions of C, are new linear variables characterising the current metric state.

The eigen vectors of U and ε_1 are the same as those of C and ε. They define the material principal axes of strain. Let (b_{01}, b_{02}, b_{03}) be an orthogonal basis of E_0 built with such common eigen vectors (the material segments b_{0i} are orthogonal both in the reference position and in the current position). Let b_0^{-1} denote the linear map which, for any element of E_0, associates its matrix-column of components in this basis, and let $[[a_i]]$ be the diagonal matrix whose coefficients are the a_i (i = 1, 2, 3). We then have:

$$C = b_0[[C_i]]b_0^{-1} = b_0[[\lambda_i^2]]b_0^{-1} \quad \text{and} \quad U = b_0[[\lambda_i]]b_0^{-1} \tag{8}$$

Many other linear variables have been proposed in order to characterise the current metric state via the strain from the reference position to the current one. They may be written:

$$\varepsilon_f = b_0[[f(\lambda_i)]]b_0^{-1} \quad \text{(denoted } f(U)) \tag{9}$$

where f is an increasing map of R into R that satisfies the following conditions:

$$f(1) = 0 \text{ and } f'(1) = 1 \tag{10}$$

which make ε_f equivalent to ε_L in S.D. The ε_n defined in Seth (1964) and Hill (1968, 1978) for any relative integer n by:

$$\varepsilon_n = b_0[[(\lambda_i^n - 1)/n]]b_0^{-1} = (U^n - 1_E)/n \quad \text{for } n \neq 0$$

$$\varepsilon_0 = b_0[[\text{Log}\lambda_i]]b_0^{-1} = \text{Log}U = 1/2\ \text{Log}C \tag{11}$$

are a subfamily of ε_f, with for f the following f_n :

$$f_n(x) = (x^n-1)/n\ , \qquad f_0(x) = \text{Lim}_{n\to 0}\,(x^n-1)/n = \text{Log}\ x \tag{12}$$

Let us highlight within this subfamily, for n = 1 and n = 2, the preceding ε_1 and Green-Lagrange tensor ε, for n = -2 the following Almansi-Lagrange tensor

$$\varepsilon_{-2} = (1_E - U^{-2})/2 = (1_E - C^{-1})/2, \tag{13}$$

and for n = 0, at the centre of the subfamily, Hencky's logarithmic strain measure ε_0 .

Since the strains are not small, these variables are not equivalent. For example, in a homogeneous expansion around a point O, we have:

$$(x - O) = \lambda(X - O),\ F = \lambda 1_E \text{ and } \varepsilon_n = k_n\, 1_E \text{ with } k_n = (\lambda^n - 1)/n,$$

and the following table provides the values of k_n for some values of n and λ.

λ	0	1/2	1	2	∞
k_4	-1/4	-0,23	0	3,75	∞
k_2	-1/2	-0,37	0	1,5	∞
k_0	$-\infty$	-1,43	0	1,43	∞
k_{-2}	$-\infty$	-1,5	0	0,37	1/2
k_{-4}	$-\infty$	-3,75	0	0,23	1,4

With respect to the Green-Lagrange tensor in (6) and (7), for each ε_f, there is a specific transfer Φ of D onto its time derivative, along with a conjugate stress tensor K_f/ρ_0 obtained from σ/ρ by means of another transfer, transposed in some way from the previous one:

$$\dot{\varepsilon}_f = \Phi D \ , \quad K_f/\rho_0 = \Phi^T \sigma/\rho \ , \quad P = \dot{\varepsilon}_f : K_f/\rho_0 \tag{14}$$

where Φ and Φ^T are linear maps that depend on both F and f. For example, for ε_{-2}:

$$\dot{\varepsilon}_{-2} = F^{-1} D F^{-T} \ , \quad K_{-2} = J F^T \sigma F \quad \text{(such that } P = \dot{\varepsilon}_{-2} : K_{-2}/\rho_0) \tag{15}$$

and we can remark that relative to (6) and (7), there is an exchange of the transfers Φ and Φ^T. In the general case, the calculus of these transfers is more difficult. For ε_0, which appears as being a very interesting case, see Hoger (1986) for example.

Each linear variable ε_f characterises the current local metric state (via the strain from the reference state). But any of them may be retained to model this state, because any of the transfers Φ is in order to generate the required consistency between $\dot{\varepsilon}_f$ and D. In fact, ε_f and K_f/ρ_0 present exactly the same drawbacks as do ε and K/ρ_0. This is an implicitly well-known fact, and the linear variables ε_f are simply called strain *measures* and not strain tensors. If the Green-Lagrange tensor ε is currently used in practice, this is probably due to the fact that both its expression as a function of the displacement (5) and the associated transfers (6) and (7) are quite easy to obtain. However, the logarithmic strain measure, whose qualities will appear in the following has become more widely used (Peric, 1992).

3. The metric tensors

3.1. THE COVARIANT METRIC TENSOR

In a Euclidean space E = (T,.), the scalar product may be written

$$u.v = \langle gu,v \rangle \ (= g_{ij} u^i v^j), \qquad g \in \Gamma^+(T) \equiv \mathrm{Lin}^+_S(T;T^*) \ , \tag{16}$$

where g, a covariant positive symmetrical tensor of rank 2 on the subjacent linear space T, is the metric tensor associated with the scalar product. In a basis $b = (b_i)$, its components g_{ij} are the scalar products $b_i.b_j$. Their matrix is the Gram matrix of b. We can write E = (T,g), as well as E = (T,.) but E and T are often designated by the same symbol.

By setting E = (T,g) and $E_0 = (T_0,g_0)$ (with g_0 équal to g but not acting at the same point), (5) can then be developed in the following relations:

$$dx.dx' = \langle gFdX,FdX' \rangle = \langle F^* gFdX,dX' \rangle = CdX \cdot dX' = \langle g_0 CdX,dX' \rangle \tag{17}$$

The initial result of this is that the current scalar product of any two material fibres dX and dX' can be characterised in the material model by the following metric tensor:

$$\gamma = F^* g F \in \Gamma^+(T_0) \equiv \mathrm{Lin}^+_S(T_0;T_0^*) \tag{18}$$

In the same manner as g_0, γ is defined on T_0, yet remains different from g_0. We thus distinguish two Euclidean spaces having T_0 as underlying linear space: E_0, which models the material fibres at the considered point in their metric state of reference, and (T_0, γ), which models these fibres in their current metric state. It should be noted that γ is transfered from

g in the material model ($\gamma = \overset{*}{F}\, g$). As a result, F is an isometry of (T_0 ,γ) on E. Obviously, when the medium is in the reference position ($F = 1_E$), γ is then equal to g_0 (= g). Furthermore, in two dimensions, γ is experimentally available by the grid method; its components in the basis of T_0 built with the grid elements $b_{0\,i}$ at the considered point, are the scalar products $\gamma_{ij} = b_i.b_j$ of the current positions $b_i = Fb_{0\,i}$ of these $b_{0\,i}$.

Secondly, equation (17) results in the following relations which show that C is a kind of *quotient* of the metric tensors for the metric states in both the current and reference positions, as well as that, with a factor 1/2, the Green and Almansi tensors are their relative differences with repect to the state of reference and the current state respectively:

$$C = g_0^{-1}\gamma, \qquad (\varepsilon_2 =)\ \varepsilon = g_0^{-1}(\gamma/2 - g_0/2), \quad \varepsilon_{-2} = \gamma^{-1}(\gamma/2 - g_0/2) \tag{19}$$

Note that if the basis $b_{0\,i}$ used in T_0 is orthonormal in the reference position, then the matrix of g_0 is the unity matrix, and C and γ have the same matrix of components.

The variable $\gamma \in \Gamma^+(T_0)$, or rather $\gamma/2$, does not depend on the reference position. It *characterises* the current metric state itself, and not this state's "difference" with respect to the reference state. This constitutes an improvement relative to the strain measures. However, due to linearly dependence on C, the intended purpose is no longer to model this state. In particular, the time derivative

$$\dot{\gamma}/2 = F^*gDF \tag{20}$$

does not exhibit the required properties. Belonging to $\Gamma(T_0)$, this derivative does not possess eigen elements. As opposed to D or D_0, it is unable to yield the principal elements of the strain rate.

3.2 THE CONTRAVARIANT METRIC TENSOR

If $\gamma \in \mathrm{Lin}_S^+(T_0;T_0^*)$ characterises the current metric state, then its inverse

$$\gamma^{-1} \in \mathrm{Lin}_S^+(T_0^*;T_0) = \mathrm{Lin}_S^+(T_0^*;T_0^{**}) = \Gamma^+(T_0^*),$$

obviously a function of γ, also characterises this state. This tensor γ^{-1} is a contravariant tensor of rank 2. The matrix of its components γ^{ij} is the inverse of the matrix of the γ_{ij}. Its meaning is clear: when T_0 is rendered Euclidian by the metric tensor γ, its dual space T_0^* is also rendered Euclidian, by means of a metric tensor which is γ^{-1}.

The space T_0 models the material *segments* generated from the considered point X. More precisely, the segment that $u \in T_0$ models is the set of points Y defined by:

$$Y\text{-}X = \lambda u, \quad \lambda \in (0,1), \tag{21}$$

and the scalar product in T_0, defined by γ, provides information on both the current length 1 and the current relative angles θ of these segments, or material fibres :

$$u \,.\, u = \langle \gamma u, u \rangle = l^2, \qquad u \,.\, u' = \langle \gamma u, u' \rangle = ll'\cos\theta \tag{22}$$

The dual space T_0^* also has a geometrical meaning, which is as strong as the one for T_0, but generally goes unrecognized. An element $v \in T_0^*$ can be considered as modelling the *slice* (between two parallel planes) constituted by the set of points Y satisfying:

$$\langle v, Y\text{-}X \rangle \in (0,1) \tag{23}$$

and the scalar product in T_0^*, defined by γ^{-1}, provides informtion on the current thinness m (the inverse $m = e^{-1}$ of the thickness e) and the current relative angles ϕ (of the dihedrons) of these slices:

$$v \cdot v = \langle v, \gamma^{-1} v \rangle = m^2, \quad v \cdot v' = \langle v, \gamma^{-1} v' \rangle = mm' \cos\phi \qquad (24)$$

These two dual aspects are complementary and equally justified. A material parallelepipedic elementary volume element may be considered not only as being built up on three material segments, thereby constituting a basis of T_0, but also as being the intersection of the three material slices defined by its faces, thereby constituting the dual basis in T_0^*. Also, (18) may be written:

$$\varepsilon = [(-\gamma^{-1}/2) - (-g_0^{-1}/2)](\gamma^{-1})^{-1}, \qquad \varepsilon_{-2} = [(-\gamma^{-1}/2) - (-g_0^{-1}/2)](g_0^{-1})^{-1}, \quad (25)$$

which shows that the Green and Almansi tensors are also the two relative variations of the variable $-\gamma^{-1}/2$ between the reference state and the current state.

The linear variable $-\gamma^{-1}/2$ thus appears as being the rival of $\gamma/2$ in the characterisation of the current metric state. However, it is as incapable of modelling this state as was $\gamma/2$. Indeed, the relation between its time derivative and D is as poor as was (20) for $\gamma/2$:

$$\frac{d}{dt}(-\gamma^{-1}/2) = F^{-1} D g F^{-*} \qquad (26)$$

3.3 THE ASSOCIATED STRESS TENSORS

The spaces $\Gamma(T_0)$ and $\Gamma(T_0^*)$, in which the linear variables $\gamma/2$ and $-\gamma^{-1}/2$ are defined, are not Euclidian. The specific internal power therefore cannot be expressed as an internal scalar product in these spaces. The associated stress tensors will thus not belong to the same space as was those for the strain measures. They are defined by a duality scalar product and hence belong to the dual spaces, i.e. to $\Gamma(T_0^*)$ and $\Gamma(T_0)$ respectively:

$$P = D : \sigma/\rho = \langle \dot{\gamma}/2, \underline{\theta} \rangle = \mathrm{Tr}(\dot{\gamma}\underline{\theta})/2, \qquad \underline{\theta} = F^{-1}\sigma/\rho g^{-1} F^{-*} \in \Gamma(T_0^*) \stackrel{i}{=} (\Gamma(T_0))^*$$

$$P = \langle \frac{d}{dt}(-\gamma^{-1}/2), \bar{\theta} \rangle = \mathrm{Tr}[\frac{d}{dt}(-\gamma^{-1})\bar{\theta}]/2, \qquad \bar{\theta} = F^* g \sigma/\rho F \in \Gamma(T_0) \stackrel{i}{=} (\Gamma(T_0^*))^* \quad (27)$$

4. The manifold of the metrics

This very symmetrical rivalry between $\gamma/2$ and $-\gamma^{-1}/2$ is resolved by the synthesis expressed in the following statement. The results combined into this statement have been very succinctly justified herein. For more details, see Rougée (1991, 1992, 1997).

Theorem:

1 - *The couple* $\mathbf{m} = (\gamma/2, -\gamma^{-1}/2) \in \Gamma(T_0) \times \Gamma(T_0^*)$ *of the two rival linear variables* $\gamma/2$ *and* $-\gamma^{-1}/2$ *may be used to characterise the current local metric state. This* **m** *is a non-linear variable. Its definition set*

$$\mathbf{M} = \{(\gamma/2, -\gamma^{-1}/2), \gamma \in \Gamma^+(T_0)\} \subset \Gamma(T_0) \times \Gamma(T_0^*) \qquad (28)$$

is a sub-manifold of dimension 6 *of the* 12*-dimensioned linear space* $\Gamma(T_0) \times \Gamma(T_0^*)$.

This is obvious: **m** is a reversible function of γ. Note that the "coordinates"

$\bar{m} = \gamma/2$ and $\underline{m} = -\gamma^{-1}/2$

of **m** in the Cartesian product $\Gamma(T_0) \times \Gamma(T_0^*)$ satisfy the following equation which shows that **M** may be seen as a kind of hyperbolic branch (see Figure 1)

$$4\,\bar{m}\,\underline{m} = -1_E \qquad (29)$$

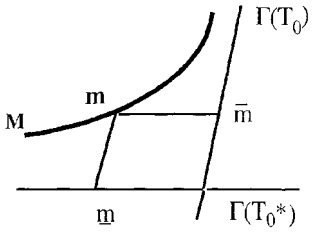

Figure 1

2 - *During a strain process, the time derivative of* **m** *is the symmetric second-order Euclidian tensor on* (T_0,γ) *defined by* D_0, *written* $\mathbf{D}_0$, *which is transfered by* F *on the symmetric second-order Euclidian tensor* **D** *defined by* D.

$$\dot{\mathbf{m}} = \mathbf{D}_0 \quad (\Leftrightarrow \quad \overset{*}{F}\,\dot{\mathbf{m}} = \mathbf{D}) \qquad (30)$$

It is well known that, in a Euclidian linear space, E = (T,g), g is an isometry of E on the Euclidian dual linear space $E^* = (T^*,g^{-1})$ and that this isometry allows identifying E* with E (in Euclidian geometry, vectors are used but not covectors). A second order Euclidian tensor such as D is then totally identified with the $D \in Lin(E)$ which serves to define it, and the notion of a Euclidian tensor does not have to be made clear (only its various components, exhibiting different kinds of variance, sometimes get mentioned). In mathematics, such identifications between isomorphic spaces are commonplace and absolutely necessary. Nonetheless, the isomorphism used has to be intrinsic, or at least constant! *Such however is not true for the Euclidian space* (T_0,γ) *and its dual space*: γ *is a variable.* It is thus necessary to forego the identification, both for (T_0,γ) and for E, and a precise definition of Euclidian tensors then becomes necessary.

This was carried out in Rougée (1997). According to this definition, a first order Euclidian tensor on E = (T,g) is an element of T*xT, which is composed of a covector and a vector homologous by g. The space **E** of the first order Euclidian tensors is thus the graph of the isometries g and g^{-1} between the two Euclidian spaces E and E* (see Figure 2). It is a new Euclidian linear space, which is isometric to the previous E and E* by the canonical projections of T*xT on T and T*. The three spaces E, E* and **E** are identified when T and T* are identified by g. In extending this definition to higher orders, the Euclidian tensor **A** of rank 2 defined by $A \in Lin(E) = E \otimes E^*$ is the couple of the covariant and contravariant tensors of rank 2 associated with A (components $A_{\alpha\beta}$ and $A^{\alpha\beta}$):

$$\mathbf{A} = (gA,\, Ag^{-1}) \in Lin(T;T^*) \times Lin(T^*;T) \doteq (T^* \otimes T^*) \times (T \otimes T)$$

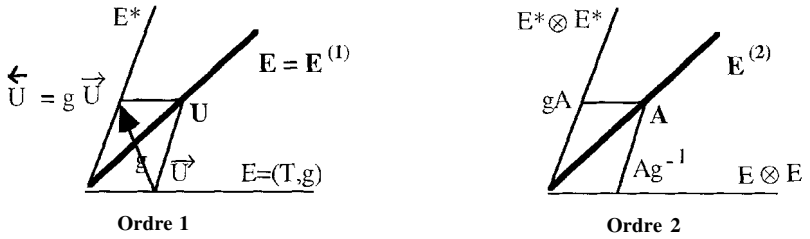

Ordre 1 **Ordre 2**

Figure 2 : Euclidian tensors

With this definition, (30-2) appears as being exactly the couple of equations (20) and (26), and thus (30) is satisfied. Equations (20) and (26) are not independent: one is the

result of the other. To take them both as the outcome in (30-2) is the equivalent of taking into account both T and T*.

3 - *The variable* $\mathbf{m} \in \mathbf{M}$ *models (and not simply characterises) the local metric state. Its definition set* **M** *is the manifold of all the potential a* priori *local metric states (when there is no internal liaison).*

The reason herein is that with F being an isometry of (T_0, γ) on E, the relation (30-2) between **D** and $\dot{\mathbf{m}}$ presents (at long last!) all of the required qualities. In fact, **D** and $\dot{\mathbf{m}}$ have the same eigen values and have eigen elements homologous by F.

4 - *The linear space* T**m**, *tangent in* **m** *to* **M**, *is the space of symmetrical second-order Euclidian tensors (s. 2-o. E. t.) on the Euclidian space* (T_0, γ).

This is a result of point **2.** The underlying linear space T_0, the space of material fibres, is constant. Yet, the Euclidian space (T_0, γ) varies with γ. The space T**m** thus varies with **m,** as it does for the "plane" tangent to a curved "surface".

Such a space of second order Euclidian tensor on a Eucidian space constitutes a Euclidian space. The scalar product of two second order Euclidian tensors **A** and **B,** defined by two linear maps A and B, is:

$$\mathbf{A}:\mathbf{B} = \mathrm{Tr}(AB^T) = A^i{}_j B_i{}^j = A_{ij}B^{ij} = A^{ij}B_{ij}$$

The tangent spaces T**m** are thus Euclidian, and the manifold **M** is Riemannian. The length of a curve written on **M** may thus be defined. Measured in this fashion, the length of a strain path is equal to the classical cumulative strain

$$\int_{t'}^{t''} (\dot{\mathbf{m}} : \dot{\mathbf{m}})^{1/2} dt = \int_{t'}^{t''} (\mathbf{D} : \mathbf{D})^{1/2} dt = \int_{t'}^{t''} (\mathrm{Tr}D^2)^{1/2} dt$$

Moreover, the specific internal power may be written with a scalar product in T**m:**

$$P = D : \sigma/\rho = \dot{\mathbf{m}} : \theta, \quad \theta \in T\mathbf{m} \tag{31}$$

The material stress tensor θ thereby introduced is the symmetric second order Euclidian tensor transferred by F^{-1} of the symmetric second order Euclidian tensor defined by σ/ρ. It is exactly the couple of the covariant tensor θ and the contravariant tensor $\underline{\theta}$ of (27):

$$\theta = (\theta, \underline{\theta}) \in \mathrm{Lin}(T_0;T_0^*) \times \mathrm{Lin}(T_0^*;T_0) \doteq (T_0^* \otimes T_0^*) \times (T_0 \otimes T_0) \tag{32}$$

5. Cartography of M

The various characterisations of the local metric state by means of the linear variables $\mathbf{x} \in \mathbf{X}$ indexed in Sections **2** and **3** are flat representations of **M.** They are global charts obtained through various projections $\Pi_x : \mathbf{m} \to \mathbf{x}$. We have deliberately mentioned that these linear variables are only various *characterisations* of the metric state. However, in practice, when one of these variables is used, it is commonly considered as *being,* i.e. as modelling, this metric state, or rather its variation from the reference state. In particular, in the Lagrangian statement of non-linear constitutive laws, the time derivative and associated stress variable are considered as being the strain rate and the stress, respectively. These Lagrangian **x-**theories thus appear as being approximate theories founded on the approximation of the manifold **M** by its charts **X**. We are thus herein confronted with the issue of the reliability of these charts.

The two characterisations presented in Section **3** (using $\bar{m} = \gamma/2$ and $\underline{m} = -\gamma^{-1}/2$) are obtained by straightforward mappings: they are the two projections of the "hyperbolic branch" **M** on its two "asymptotes" which are the spaces $\Gamma(T_0)$ and $\Gamma(T_0^*)$ of the symmetrical covariant and contravariant second order tensors on T_0. Let us reiterate at this juncture that these spaces are not Euclidian and that this implies that the stress variables have to be sought in dual spaces. Furthermore, let us add that this also implies that, in these approximations, it is impossible to define a scalar strain rate or the length of a strain path.

Let us now consider the characterisations using the strain measures $\varepsilon_f \in \mathrm{Lin}_S(E_0)$ of Section 2. Let $\mathbf{m}_0 = (g_0/2, -g_0^{-1}/2)$ be the metric state in the reference position. Each ε_f defines an s. 2-o. E. t. on $E_0 = (T_0, g_0^{-1})$, denoted by ε_f, which is an element of the linear space $T\mathbf{m}_0$ tangent to **M** at point $\mathbf{m}_0$. Let us now intoduce, within the space $T\mathbf{m}_0$ tangent to **M** in $\mathbf{m}_0$ (flat sub manifold of $\Gamma(T_0)x\Gamma(T_0^*)$ whose $T\mathbf{m}_0$ is only the asociated linear space) the point $\mathbf{m}_f$ defined by:

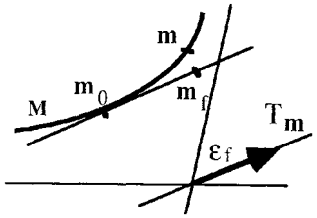

Figure 3

$$\mathbf{m}_f = \mathbf{m}_0 + \varepsilon_f$$

The chart used when characterising the metric state by a strain measure ε_f *may then be seen as being the chart obtained by the projection* Π_f *of* **M** *on the tangent space* $T\mathbf{m}_0$, *which projects* **m** *on* $\mathbf{m}_f$ (see Figure 3). The following results provide information on some of these projections Π_f (Π_n is the projection associated with ε_n).

Theorem:

1- *The projections* Π_2 *and* Π_{-2}, *relative to* $\varepsilon = \varepsilon_2$ *and* ε_{-2} *(Green and Almansi tensors, respectively) are parallel to the "asymptotes" of the "hyperbola"* **M** *(see Figure 4)*

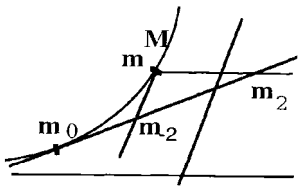

Figure 4

It is easy to see that these charts are unreliable.

2- *The projection* $\Pi_\perp$ *associated with the average* $\varepsilon_\perp = 1/2(\varepsilon_2 + \varepsilon_{-2})$*of both the Green and Almansi tensors, is the orthogonal projection on* $\mathbf{Tm}_0$.

The space $\Gamma(T_0)x\Gamma(T_0^*)$ is not Euclidian. This orthogonality is a local orthogonality in $\mathbf{m}_0$. This $\varepsilon_\perp$ is not used in practice; however, it would be tempting in the case of a relatively limited strain.

3- *For a small strain from the reference state (but possibly large displacements), the segment* $(\mathbf{m} - \mathbf{m}_f)$ *is infinitely small of a first order relative to* $(\mathbf{m} - \mathbf{m}_0)$, *and* $(\Pi_\perp \mathbf{m} - \mathbf{m}_f)$ *is infinitely small of a third order when* $f''(1) = -1$.

The first property is an outcome of conditions (10) assigned to f in order to make ε_f equivalent to ε_L in the case of S.D. Among, the measures ε_n, only Hencky's logarithmic measure $\varepsilon_0 = \mathrm{Log}U$ satisfies the condition $f''(1) = -1$. This ε_0 may thus also be used for relatively limited strain. This is especially true, in as much as the following points will show that ε_0 is still satisfactory for large strains.

4- *The projection* Π_0, *associated with the logarithmic measure* ε_0, *is obtained by developing each geodesic curve of* **M** *containing* $\mathbf{m}_0$ *on its tangent at* $\mathbf{m}_0$.

In $\mathbf{m}_0$, we can thus point out m by ε_0 in exactly the same manner as, by being in Poitiers, we can explain that Peking is at a distance of six thousand kilometres in a *horizontal* direction which we can indicate.

The geodesic curves of **M** containing $\mathbf{m}_0$ are generated by starting from the reference position whose metric state is $\mathbf{m}_0$, and holding the material principal axes of strain constant and the relative lengthening λ_i in these directions proportional.

The projection Π_0 is quite satisfactory. In particular, if the manifold **M** were flat, it would be an isometry, i.e. a perfectly reliable chart (such is not the case for $\Pi_\perp$: imagine that **M** is a cylinder in three dimensions). The manifold **M** is obviously not flat, yet it does display many flat sub-manifolds containing $\mathbf{m}_0$, for which the chart is thus perfect:

> **5 -** *For any basis* B *of* T_0, *let us denote by* $\mathbf{M}_B$ *the set of metric states* $\mathbf{m} \in \mathbf{M}$ *for which* B *is orthogonal. These* $\mathbf{M}_B$ *are flat, three-dimensional submanifolds of* **M**. *The* $\mathbf{M}_B$ *associated with a basis* B *orthogonal in the reference position contains* $\mathbf{m}_0$, *and* Π_0 *is an isometry, thus a perfect chart, for any of them.*

This serves to reinforce the favorable opinion provided for Π_0 and therefore for the choice of the logarithmic strain measure as an approximated linear model of the local metric state.

6. Conclusion

The approach stated in the abstract has been carried out; however the subject has not necessarily been thoroughly covered. Variables other than strain measures have been introduced in order to describe the metric (or strain) state. Nonetheless these have always proved to be ineffective linear variables.

The drawbacks of the strain measures are the result of the poor transfer between their derivative and D; hence, an effort has been undertaken to start from D and to provide a better transfer, thereby taking as a (linear) strain variable

$$x = \int_{t_0}^{t} \mathbf{r}^{-1}\mathbf{D}\mathbf{r}\,dt \qquad \Leftrightarrow \qquad (\dot{x} = \mathbf{r}^{-1}\mathbf{D}\mathbf{r}, \quad x_{t=0} = 0)$$

where r is a rotation that models the mean rotation of the medium, for example the rotation R of F = RU or the rotation Q obtained by integrating the spin, i.e. the skew symmetrical part of the gradient of the velocity field (Ladeveze, 1980) (Dogui, 1987) (Boucard et al, 1997). In (Xiao et al, 1997), after expressing the results in their Lagrangian form, a rotation r was identified such that x accepts the integrated form: $x = QR^{-1}\varepsilon_0 RQ^{-1}$

Unfortunately, the variables obtained in this manner are not state variables. They depend on the path followed between the starting state and the final state: they are cumulative strain tensors (Gilormini et al, 1993). This therefore differs from the approximation of the curved space **M** by a six-dimentionned flat space It is simply an approximation of the considered strain path on **M** by means of an anlogous path in a six dimensioned flat space. The geometrical interpretation of the projection of the first path on the second one can be found in Rougée (1997).

In conclusion, the issue in question is thus still strongly open to dispute. Please, refer for example to Lehmann (1991), Reinhardt (1996), etc., as well as to Haupt et al. (1989) in which the transfer has been taken as an almost autonomous parameter. Our opinion is that its understanding is not possible if, as is the case in the literature, only linear variables and

Euclidian geometry are being considered. To reach such an understanding, it is necessary to confront in a resolute manner, as we have herein, the non-linearity with non-linear variables and the loss of constant metric (thereby Euclidian) properties for a continuous medium by appropriate non-Euclidian tools, with the first of these being the dual space of a linear space.

Références.

Boucard P. A., Ladevèze P., Poss M., Rougée P., 1997, A non incremental approach for large displacement problems, *Computers and structures* **64** N° 1-4, 499-508

Dogui A. , Sidoroff F., 1987, Large strain formulation of anisotropic elasto-plasticity formetal forming, In "Computational methods for predicting material processing defects" *Predeleanu M. Ed., Elsevier Science, Amsterdam*

Gilormini P., Roudier P., Rougée P., 1993, Les déformations cumulées tensorielles, *C.R. Acad. Sci Paris,* **316**, Série II, 1499-1504 et 1659-1666.

Gurtin M.E., Spear K., 1983, On the relationbship between the logarithmic strain rate and the stretching tensor, *Int. J. Solids Structures,* **19**, n° 5, 437-444

Haupf P., Tsakmakis Ch., 1989, On the application of dual variable in continuum mechanics, *Continuum Mech. and Thermodyn.,* **I**, 165-196

Hill R., 1968, On constitutive inequalities for simple materials, *J. Mech. Phys. Solids,* **16**, I, 229-242, II, 315-322

Hill R., 1978, Aspects of invariance in solid mechanics, Advances in Applied Mechanics, Yih Ed, Academic Press N.Y., **18**, l-75

Hoger A., 1986, The material derivative of logarithmic strain, *Int. J. Solids Structures,* **22**, n° 9, 1019-1032

Ladevèze P., 1980, Sur la théorie de la plasticité en grandes déformations, Rapport LMT Cachan n° 9

Lehmann Th., Guo Z.H., Liang H., 1991, The conjugacy between Cauchy stress and logarithm of the left stretch tensor, *Eur. J. A/Solids,* 10, 395-404

Peric D., Owen D.R.J., 1992, A model for finite strain elasto-plasticity based on logarithmic strains: Computational issues, *Computer Meth. in Ap. Mech.and Eng.,* **94**, 35-61

Rougée P., 1991, A new Lagrangian intrinsic approach to large deformations in continuous media. *Eur. J. Mech., A/Solids, Vol.* **10**, 15 - 39.

Rougée P., 1992, Kinematics of finite deformations, *Arch. Mech.,* **44-1**, 117-132

Rougée P., 1997, Mécanique des grandes transformations, Mathematiques et Application 25, Springer Verlag

Seth B.R., 1964, Generalised strain measure with application to physical problems, in Second Order Effects in Elasticity, Plasticity and Fluid Dynamics, Reiner M. and Abir D. Eds, Macmillam N.Y., 162-171

Xiao H., Bruhns O.T., Meyers A., 1997, Hypo-Elasticity Model based upon the Logarithmic Stress Rate, *Journal of Elasticity,* **47**, 51-68

SHAPE, SURFACE AND DEFORMATION MEASUREMENT: SCOPE AND TRENDS

H.J. TIZIANI
University of Stuttgart
Institute of Technical Optics
Pfaffenwaldring 9
70569 Stuttgart
Germany

1. Introduction

Different techniques can be used for optical three-dimensional measurements. Time-of-flight and phase measurement techniques are well known and developed, up to the point of distance measurements with resolutions in the order of 1 mm respectively 0,1 mm. For close-range measurements the principle of triangulation and related techniques like light sectioning and projected fringe methods can be used. They are applied rather frequently in industry together with the automated fringe analysis. Moiré techniques and projected fringe methods lead to surface shape-, deformation-, or vibration-measurements.

Image plane locating systems such as the confocal principle and white-light interferometry have now reached a very high technical standard. They can be used to study biological objects as well as to measure the topography of engineering surfaces.

Laser interferometry is one of the most commonly used techniques for high-resolution measurements in metrology. A stabilized HeNe laser offers a light source with an absolute wavelength stability of better than 10^{-7}. However, the accuracy for length measurement is mainly limited by atmospheric conditions or vibrations. Diode lasers are increasingly used in metrology, even though frequency stability can still be a problem especially for high precision interferometry applications. Two and multiple wavelengths interferometry leads to an extension of the unambiguity range as well as to the application of interferometry to optically rougher surfaces. However, interferometry is frequently too sensitive to be applied on technical surfaces.

Holograpic and speckle techniques are used for deformation and shape analysis. More recently, digital holography becomes interesting with the development of high resolution detector arrays.

A. Lagarde (ed.),
IUTAM Symposium on Advanced Optical Methods and Applications in Solid Mechanics, 123–136.

The basic idea for wavelength varying interferometry is to record a sequence of phase maps in time, forming a three-dimensional phase distribution. The phase at each pixel is then unwrapped along the time axis. Because the unwrapping path does not cross object discontinuities, 2π phase errors do not propagate across the image as with conventional spatial unwrapping approaches. The method leads to a simple and robust technique for deformation analysis.

2. Fringe projection for 3D-shape measurement of technical objects

A number of techniques have been developed for micro- and macrotopography measurements. The choice of an appropriate technique depends on the application, required sensitivity and resolution. Moiré and projected fringe techniques are not as sensitive as interferometric and holographic techniques but are less susceptible to environmental disturbances [1,2].

Projected fringe techniques as an extension of triangulation for out-of-plane topography measurements are well established. Projected fringe patterns can be formed by different methods such as projecting either a grating-like structure or an interference pattern onto the object. Height variations or object deformations lead to a modification of the projected fringes, which in turn are compared with the original or synthetically generated patterns. The image processing for the fringe analysis is well known. Phase shifting techniques are frequently used. Typical contour-line separations can vary between micrometers and millimeters.

For fringe projection, grating like structures can be generated by means of electrically adressed liquid crystal cells or digital micro mirrors. The fringe spacing can be adjusted in a wide range. In an interferometric setup, the fringe spacing is adjusted by varying the angle of the interfering waves. This is important for extending the unambiguity range as well as for absolute measurements of optically rough surfaces. Gratings with different periods are needed to extend the unambiguity range. A fine grating structure is required for high resolution and a coarse for extending the unambiguity range. Speckles can limit the resolution of the technique. Coded grating like structures can be used.

The methods are established for different technical and biological applications [1,2]. A new approach for exact object positioning of non-cooperative objects is based on correlation analysis of fringe patterns projected onto 3D objects [2].

A very promising approach for fast examination of shape and shape deviation is the use of object-adapted fringes together with Moiré techniques.

2.1 FRINGE PROJECTION FOR MEASURING SHAPE AND MICROSTRUCTURE OF CYLINDRICAL OBJECTS

The measurement of the structure of a cylinder is an important task in industry. Fringe projection is used in a special set-up for measuring A1-Si surfaces of a motor liner for instance. The basic principle is shown in Fig. 1 where a grating like structure is illuminated via an optical fiber by a light-source. A microscopic system is projecting the grating onto the cylinder surface. For convenience, two illumination directions are used. The grating-structure is deformed by the object. The detector signal from the CCD camera chip is analysed using phase-shifting by a motor-driven grating.

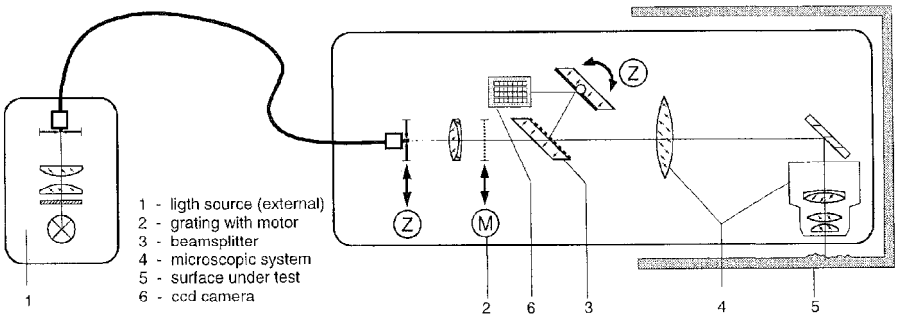

Figure 1: Optical layout of a cylinder-topograph

Fig. 1 shows the topography of a honed surface of a motor-liner. The mean roughness is 0.7 µm.

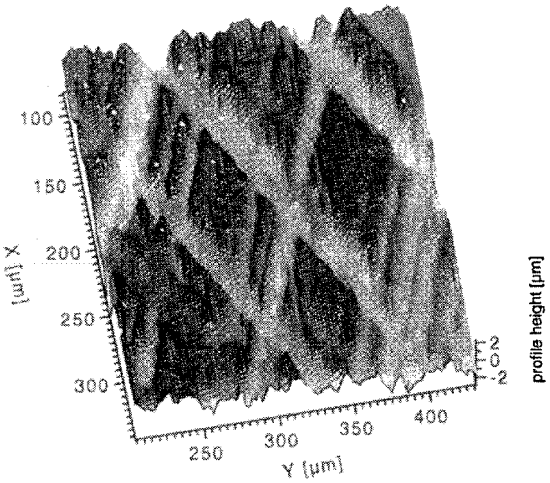

Figure 2: 3D-detail of a honed surface.

2.2. SHAPE ADAPTED FRINGE PATTERN

For fast shape analysis, shape-compensating fringes can be projected (Fig. 3). From the shape data of a master object, given by CAD data or from the measurement of a reference object, a distorted fringe pattern ist computed and transferred to a two-dimensional spatial light modulator (SLM) or micromirror system. After the projection of the shape adapted fringes onto the test-object, straight equidistant fringes are obtained on the detector, a CCD chip [2].

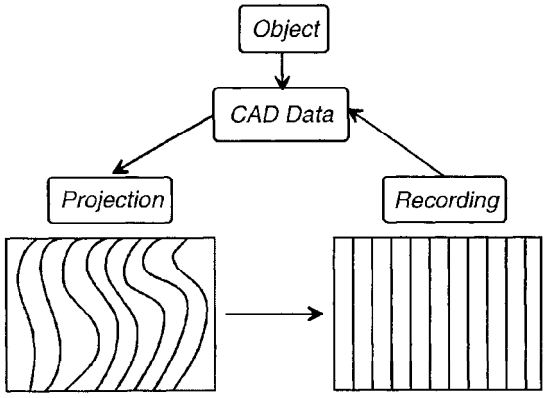

Figure 3: Shape-adapted fringes for 3D measurements.

In our experiments we used an electrically addressed liquid crystal display (LCD) as well as a digital micromirror device (DMD). The setup includes object illumination, object positioning, object detection, and process control (Fig. 3 and Fig. 4).

For a perfect object shape, straight and equidistant fringes should be observed and can be compared with a reference grating or the CCD camera chip array in the detector plane. Shape deviations, defects, or a wrong object position result in distorted fringes. The shape deviation can be seen as a Moire fringe pattern leading to a fast shape or defect analysis. The Moire pattern obtained is a direct measure of the shape deviation. No further digital image processing is required. With this scheme, real time shape control is possible.

Furthermore, with a grey scale SLM the local object brightness can be compensated, which is important for shape and position detection.

For shape measurements and comparison used for defect analysis the well-known phase shifting methods can be applied. In our setup, instead of shifting a grating-like mask, the actual sinusoidal pattern is written into the matrix SLM. No moving parts are required. For absolute shape deviation measurements referring to a synthetic master object the quality of calibration is essential. There are different methods for calibration of imaging systems (calibration marks, a sequence of vertical and horizontal lines or edges).

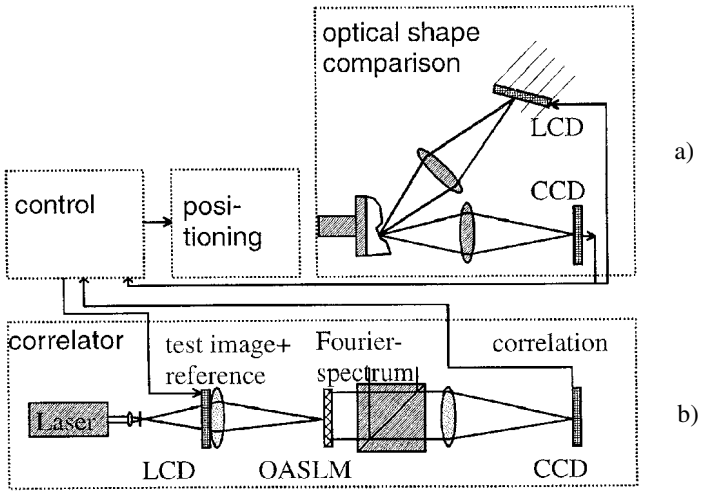

Figure 4: Setup for shape-adapted fringe pattern evaluation (a) and position detection (b).

In addition to the visual interpretation of the Moire fringes, quantitative fringe analysis can be performed. Fourier analysis of the shifted fringe pattern can be used to calculate the shape deviation.

Fig. 5 shows an object adapted fringe mask (left) and an image of the mask when projected onto a convex shaped turbine wing. Straight lines are observed.

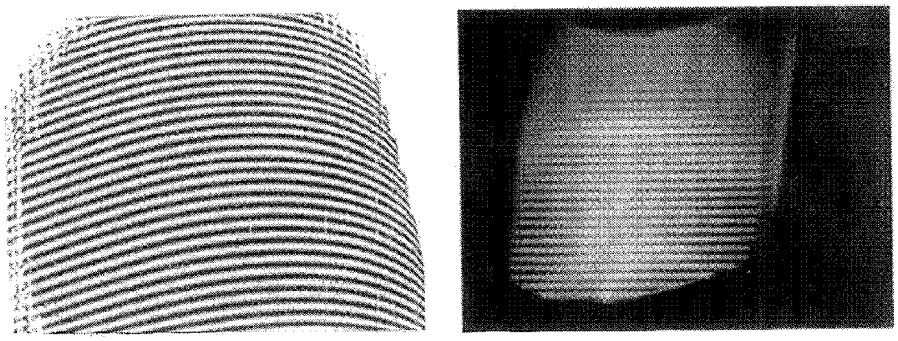

Figure 5: An object adapted fringe mask (left) results in straight lines when projected onto a convex shaped turbine blade (right).

3 Object positioning by optical correlation

For automated two-dimensional object positioning, nonlinear joint transform correlators are good candidates. They are rather immune against noise and localized errors and offer sub-pixel accuracy. Fast implementation is possible by digital electronics or by optical means. Therefore we combine correlation with fringe projection in order to achieve improvement in positioning of noncooperative objects. The joint Fourier transform principle is used (Fig. 4b): The expected fringe pattern is recorded together with the actual test pattern on an electrically addressed liquid crystal. Their joint Fourier transformation is stored in an optically addressed liquid crystal from where the cross-correlation peaks are obtained by a further Fourier-transform and hence the information on the object position, which in turn will be corrected.

Simple local and easy implementable nonlinearities were used. For our optical correlations is was sufficient to use an appropriate camera shutter speed in combination with the nonlinear responses of the LCDs and the CCDs.

For fringe projection in combination with correlation, it turned out to be advantageous to use two images with fringes shifted by half of a period in the second image. The resulting images are subtracted from each other and histogram equalized (simple normalisation works nearly equally well) [2].

4. Shape measurement by interferometry and speckle techniques using wavelength scanning

Interferometric techniques have a high resolution, but have only a small range of unambiguity, and are usually limited to polished surfaces. To measure on rough surfaces, it is possible to increase the range of unambiguity by oblique incidence interferometry which uses a longer effective wavelength or by multiple wavelength interferometry [3-6].

Wavelength-shift interferometry for absolute profilometry [4-6] is an interferometric technique that works on rough as well as on smooth surfaces. It can lead both to high resolution measurements and to a large absolute measuring range.

In an unequal two beam interference arrangement the phase φ of the interference signal at a point is proportional to the optical path difference between the corresponding points on the object and on the reference plane.

The phase change as a function of the wavelength change, $\Delta\lambda$ is

$$\Delta\varphi\,(x,y) = -2\pi\, L(x,y)\,\frac{\Delta\lambda}{\lambda^2} \tag{1}$$

A set-up for the wavelength-shift interferometry for absolute profilometry can be based on a standard Michelson interferometer (Fig. 6). The reference mirror is placed in one arm, the specimen in the other. The object is imaged on a CCD (charge-coupled device) camera chip through a telecentric system whose aperture is used to control the speckle size for optically rough surfaces. We used a high-speed digital-camera with a resolution of 128 x 128 pixels, at frame rates of up to 830 frames per second. During measurement, the image data are transferred to the PC that at the same time controls the wavelength tuning of the light source. As conventional laser diode wavelength tuning without mode hops, by current or temperature modulation, is limited to small ranges (0.1nm), we built a diode laser with external cavity. This laser achieved a mode hop free wavelength tuning range of over 25 nm in one second.

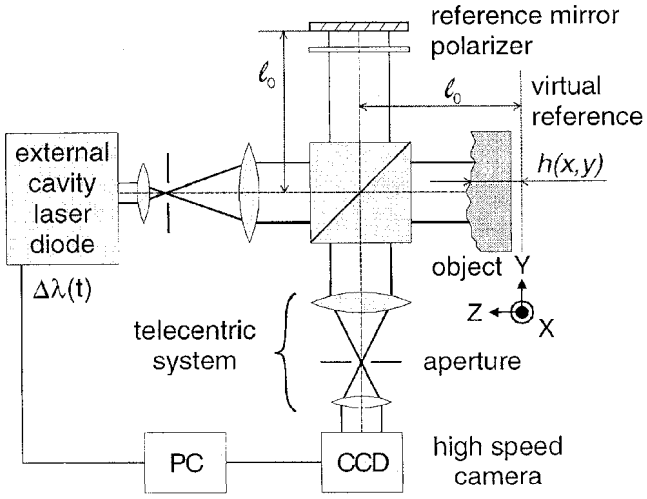

Figure 6: Setup for wavelength-shift interferometry for absolute profilometry

The total phase change of the interference signal for a given wavelength tuning range is proportional to the absolute optical path difference at that point between the object and reference path. To get the path difference of this point, we have to somehow count the periods of the signal (fringe counting) or measure its frequency. The latter requires a constant dv/dt (or a constant $d\lambda/dt$ with $\Delta\lambda << \lambda$), i.e. a linear variation of the laser frequency. To get the frequency of the pixel signal it is convenient to compute the fast Fourier transform of the signal and look for the largest peak in the frequency.

Takeda and Yamamoto [6] have discussed and used a technique called 'Fourier-transform speckle profilometry' (FTSP) for wavelength-shift speckle interferometry. This technique is based on the Fourier transform method Takeda *et al.* introduced earlier for spatial-carrier fringe-pattern analysis. It works by pixel-wise Fourier transforming the data, zeroing everything but a band around the peak frequence, and transforming back

into the time domain, thereby effectively performing as a band-pass filter. The phase of the complex result of the reverse Fourier transform is the phase of the filtered fringe signal, which is unwrapped. The total phase difference between start and end of the measurement is proportional to the optical path difference and therefore also to the physical height of the object at that pixel, provided the exact wavelength tuning range is known. Otherwise, it is possible to use a reference point of known height.

The method works equally well for mirror like structures where higher resolution is obtained as by optically rough surface where the depth resolution is limited by the optical roughness of the surface under test.

Fig. 7 shows the results of a measurement of an aluminium cube with a milled surface with steps of 0.4 mm and 0.8 mm. The bias on the top is 10°. The cube itself was tilted by 5°. It should be remembered that for optically rough surfaces, the phase variation of speckles is considered.

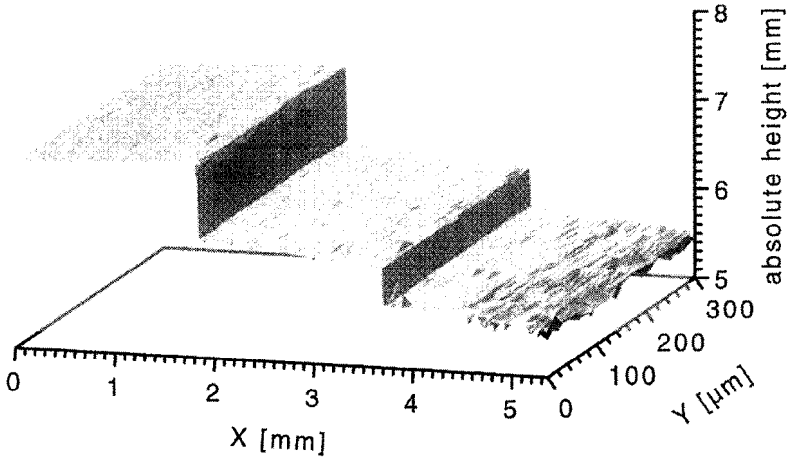

Figure 7: Milled steps of 0.4 mm and 0.8 mm.

5. Temporal shape evaluation for measuring large object deformation

In temporal speckle pattern interferometry (TSPI) whole field object deformation can be extracted. Speckle pattern variation is recorded in a sequence as the object is being deformed. Observing a point in the object over time provides the temporal evolution related to its movement. By analysing the signals, large object deformations ranging from a few micrometers to a few hundreds of micrometers can be measured. The range of deformation measurement depends on the instrumentation and the correlation between the speckle patterns. Various methods such as fringe counting and Fourier transforma-

tion techniques can be used to determine the number of cycles of modulation through which the object deformation can be extracted. For the Fourier transformation method that is used mainly, as in the previous section the signal is first transformed, and afterwards one side of the spectrum is filtered with a bandpass filter. The filtered spectrum is then inverse transformed to obtain the phase fluctuation that is then unwrapped to obtain the total phase at a given point. Furthermore the Fouriertransform technique can be combined with a wavelength shift for measuring absolute step height and object shapes.

The schematics of the temporal Fourier-transform speckle interferometric method (TSPI) is shown in Fig. 8.

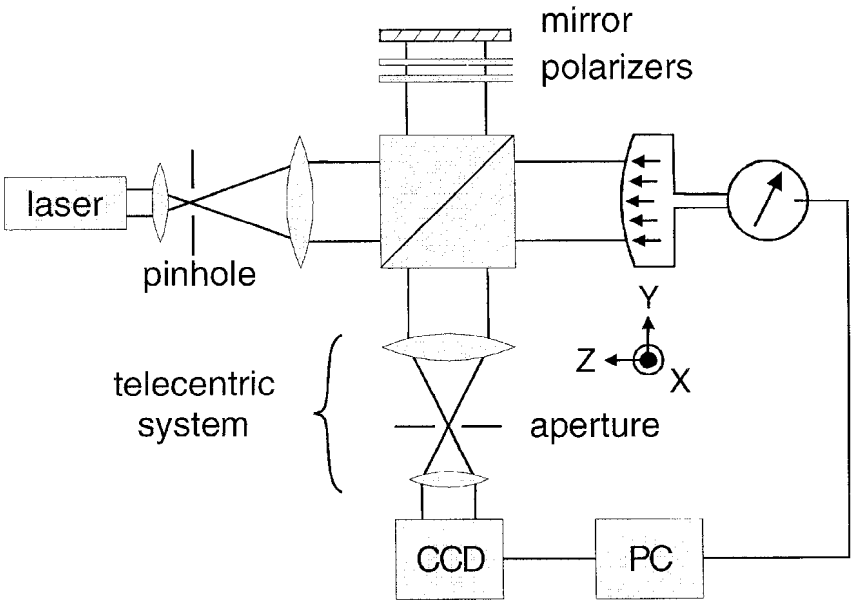

Figure 8: Schematic of the experimental arrangement of the temporal Fourier-transform speckle interferometric method.

The configuration is similar to that of a Michelson interferometer, except that one of the mirrors is replaced by the diffuse test-object. The reference arm and the object arm are set to have an arbitrary unequal path length from the beam splitter. A telecentric system is used to focus the object onto the sensor, a high-speed CCD camera. In addition, the telecentric system ensures that the propagation axis of the beam from the mirror and the object is colinear. It is very well known that the angle between the object and the reference beam should be such that the fringes modulating the individual speckles are resolved by the CCD camera [8]. At the plane of the sensor, the object and the reference beam interfere, forming a complex interference pattern. The intensity at an image point of the object at the sensor plane can be expressed as

$$I(x,y,t) = I_o(x,y)\left\{1 + V\cos\left[\Phi_0(x,y) + \frac{4\pi Z(x,y,t)}{\lambda}\right]\right\} \quad (2)$$

where $I_O(x,y)$ is the bias intensity of the speckle pattern, V is the visibility of the speckle modulation, $\Phi_O(x,y)$ is the initial phase that can be random, and Z(x,y,t) is the object deformation. The sensitivity of the speckle interferometric system in our arrangement lies along the Z direction. For the object deformation $\Delta Z(x,y,t)$ at (x,y), the median temporal frequency of the signal observed at a given point of the object is

$$f_{med}(x,y) = \frac{2\,\Delta Z(x,y,t)}{\lambda t} \quad (3)$$

This shows that the median temporal frequency of the signal observed at different points depends on the local deformation. A series of frames of the speckle pattern is recorded, where each frame records the speckles and their intensity at a certain instant of time. For each pixel its variation over time is observed providing the pixel history. Determining the difference in the temporal frequency at various points on the object leads to the object deformation. Alternatively, the Fourier transform of each pixel history can be taken. The accuracy of the Fourier-transform analysis increases with increasing temporal frequency. The upper limit of the modulation frequency is set by the Nyquist criterion and is given by half the total number of frames.

Eventually, the phase is unwrapped and thereby a threedimensional (3-D) map of the time-dependent phase of the object deformation is generated. From the 3-D data, the beginning and the end phase of the object deformation can be obtained. The final phase can be expressed as

$$\Phi(x,y) = \Phi_0(x,y) + \frac{4\pi\Delta Z(x,y)}{\lambda} \quad (4)$$

where $\Phi_0(x,y)$ is the initial phase, that is usually a constant and can be disregarded. Essentially the instantaneous angular frequency or the linear velocity generated during deformation of the object point is determined. From these extrapolations the 3-D plot of the object deformation is extracted.

Fig. 9 shows as an example a result of a deformation measurement of a 1,5-mm-thick rubber from a tube pressure loaded at the center. The air pressure was uniformly increased by a piston arrangement where the compression was controlled by a linear translation stage. The rubber diaphragm was deformed about 70 μm at the center. A ridge, being harder than the other regions, has deformed less than its surrounding. A contour plot of the deformation in Fig. 9 shows the deviations of the lines around the region of the defect. The smallest object deformation that can be measured is limited by the signal analysis method which in our case is a few cycles of modulation. Using fringe counting, deformations leading to half a cycle of modulation in the total number of frames can be measured.

Temporal modulation of speckles can also be used for shape analysis. The temporal modulation of one speckle caused by in-plane or out-of-plane motion is observed over

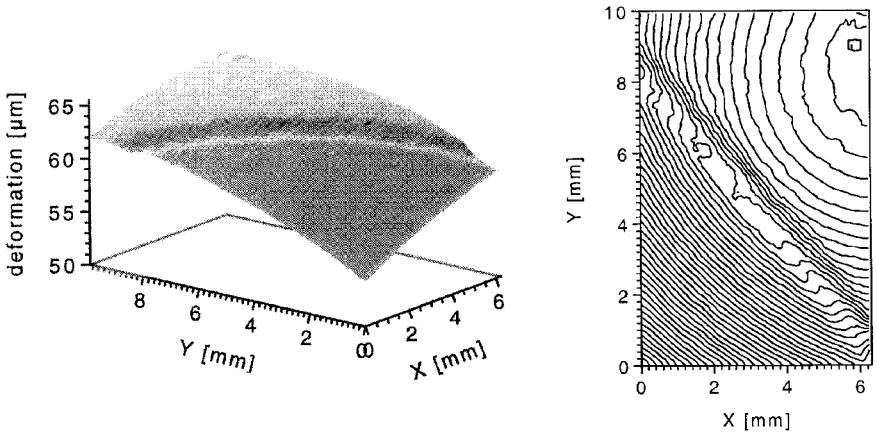

a) b)

Figure 9: a). The results with a rubber diaphragm uniformly pressure loaded upto 70 µm at the center. b) Contour plot of the slices showing the deviation of the lines around the defect.

an extended period of time. Thus observation of all the speckles provides the temporal variation over the whole object during the time of movement. These temporal speckle patterns are then analysed by the Fourier-transform method to extract the absolute height of the object or its shape. Unlike the dual-beam illumination ESPI system for shape measurement, this technique can be used on objects whose shapes change slowly or sharply. Height variations ranging from few hundreds micrometers to few tens of millimeters can be determined [9].

6. Digital holography for shape measurement

Holographic interferometry, speckle techniques, or digital holography can be applied for 3D-topometry by using double exposure technique, where after the first exposure the direction of the incident illumination onto the object or the refractive index of the medium surrounding the object or the wavelength are changed. In digital holography the holograms are recorded on a CCD chip. The reconstruction is virtual i.e. by means of computer techniques. No physical reconstruction occurs.

6.1 TWO-WAVELENGTH CONTOURING

The two wavelengths can be introduced by changing the wavelength of a diode laser by changing the temperature or injection current [11]. For contour measurement of moving objects, the double pulse technique is appropriate. The same technique can be used for contouring and deformation measurements.

For the wavelength change between the two exposures, the two holograms are recorded at different wavelengths λ_1 and λ_2. The interference of the two reconstructed wavefronts leads to an effective wavelength [10,11]

$$\Lambda_{12} = \frac{\lambda_1 \lambda_2}{|\lambda_1 - \lambda_2|} \tag{5}$$

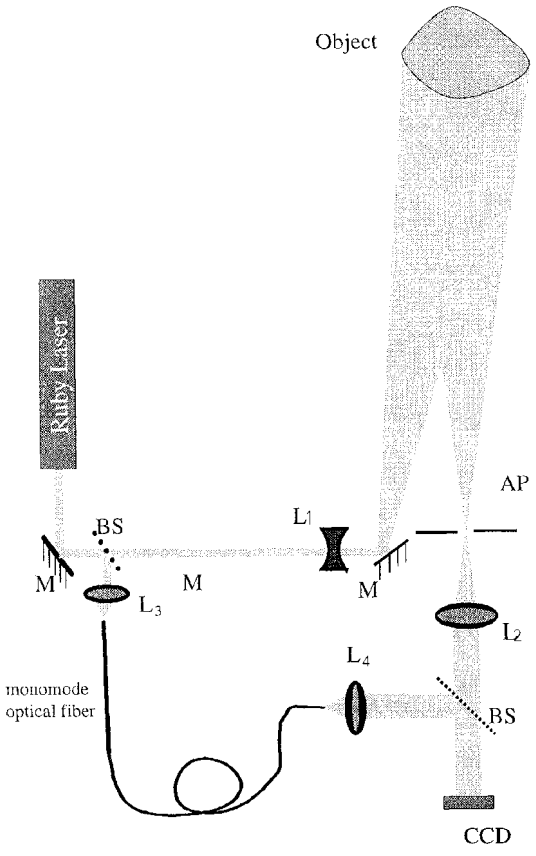

Figure 10: Set-up for object contouring with two wavelengths.

The fringes obtained with a normal incidence and a normal view represent an object contour with contour intervals of

$$\Delta h = \frac{\Lambda_{12}}{2} \tag{6}$$

The spectral output of a ruby laser for holographic use is determined by a combination of the fluorescence emission of the ruby rod, the resonance of the optical cavity (resonator), and the mode selection of the output and the intra cavity etalon. By changing the temperature of the etalons it is possible to change the emission wavelength of the laser [10]. Changing the cavity length by a piezo leads again to a wavelength change. Object and reference waves are superimposed on a CCD chip. After the double pulse, by changing the wavelength between the two pulses, the analysis takes place on the computer only. Fig. 10 shows the experimental set-up and Fig. 11 shows the contour measurement of a cognac glass, where the wavelength of the ruby laser was changed by $\Delta\lambda$=0.338A between the two exposures, the contour interval was thus 7.1 mm.

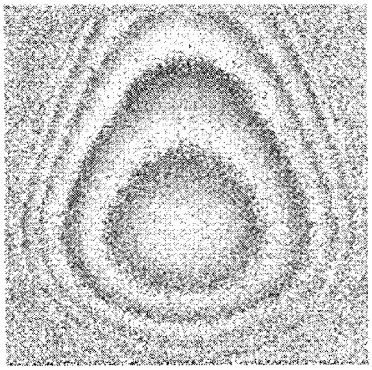

Figure 11. Contour measurement of a Cognac glass phase map using a ruby laser. The wavelength change was $\Delta\lambda$=0.338A, corresponding to a contour interval of 7.1 mm.

I acknowledge the financial support by the DFG (German Research Foundation) and BMBF (German Ministry for Education and Research) as well as the contributions of P. Haible, C. Joenathan, M. Schönleber, T. Haist, S. Franz, G. Pedrini and M. Totzeck.

References

[1] H.J. Tiziani, "Optical metrology of engineering surfacesscope and trends," in *Optical Measurement Techniques and Applications,* P.K. Rastogi, ed. (Artech House, Boston, 1997).

[2] H.J. Tiziani, M. Schönleber, T. Haist, "Adaptive Micro- and Macro 3D-Measurements" in *Optical 3D-measuring techniques IV* (Wichmann Verlag 1997).

[3] Joenathan, B. Franze, H.J. Tiziani, "Oblique incidence and observation electronic speckle pattern interferometry," Appl. Opt. 33, 7311 (1994).

[4] H.J. Tiziani, B. Franze, P. Haible, "Wavelength-shift speckle interferometry for absolute profilometry using a mode-hop free external cavity diode laser," J. Mod. Opt. 44 1485-1496 (1997).

[5] S. Kuwamura, I. Yamaguchi, "Wavelength scanning profilometry for real-time surface shape measurements, Pll. Opt. 36, 4473-4482 (1997).

[6] M. Takeda and H. Yamamoto, "Fourier-transform speckle profilometry: three-dimensional shape measurements of diffuse objects with large height steps and / or spatially isolated surfaces", Appl. Opt. 33, 7829-7837 (1994).

[7] C. Joenathan, B. Franze, P. Haible, and H. J. Tiziani, "Speckle interferometry with temporal phase evaluation for measuring large object deformation," Appl.Opt. 37, 2608-2614 [1998].

[8] Erf, *Speckle Metrology* (Academic, New York, 1978).

[9] C. Jonathan, B. Franze, P. Haible, H.J. Tiziani, "Shape measurement by use of temporal Fourier ttransformation in dual-beam illumination speckle interferometry", Appl. Opt. 37, 3385-3390 (1998).

[10] Zou, G. Pedrini und H.J. Tiziani, "Two-wavelength contouring with a pulsed ruby laser by empolying TV-holography," J. Mod. Optics 4, 639-646 (1996).

[11] Zou, G. Pedrini und H. Tiziani, "Surface contouring in video frame by changing the wavelength of a diode laser" Opt. Eng. 35, 1074-1079 (1996).

[12] G.Pedrini, H.J. Tiziani, "Double pulse-electronic speckle interferometry for vibration analysis", Appl. Opt. 33, 7857-7863 (1994).

OPTICAL MEASUREMENT OF STRAIN ON THIN-FILM POLYSILICON TENSILE SPECIMENS

WILLIAM N. SHARPE, JR.
Department of Mechanical Engineering
Johns Hopkins University
Baltimore, Maryland 21218-2686

Abstract

Techniques and procedures are described for measuring strain on thin polysilicon films by laser interferometry. Tiny gold lines serve as the gage markers, and strains have been measured on films as thin as 1.5 micron. Biaxial strains can also be measured to determine Poisson's ratio along with Young's modulus.

1. Introduction

Polysilicon is the most widely used material in microelectromechanical systems (MEMS) where it makes up the structural element of microdevices such as accelerometers and pressure transducers. It is by nature thin because it is simply polycrystalline silicon that is vapor-deposited. Structural polysilicon is nominally 2 microns thick, although it is possible to make films 10 microns thick.

The forces and displacements necessary to test a thin tensile specimen are small; however, this is actually not a serious problem. Preparation and handling of a specimen is challenging, but procedures have been developed for releasing cantilever beams, resonant structures, membranes, and tensile specimens by etching away underlying supporting layers. Many of the common polysilicon test structures are configured in such a manner that friction is not a problem. One issue that is not so easily addressed is direct and accurate strain measurement on a specimen — as opposed to inferring the strain from displacements. This paper presents an interferometric method for measuring axial and lateral strain directly on polysilicon tensile specimens.

The Interferometric Strain/Displacement Gage (ISDG) is a short gage length strain measurement technique developed by the author, students, and colleagues over the years. The concept originated in 1966 and the first published research [1] used a laser impinging on two closely spaced grooves ruled on polished aluminum specimens. The resulting interference fringe patterns were monitored by cameras and the films were read manually to translate the fringe movement into strain. As the technique developed, Vickers microhardness indentations replaced the grooves, and linear diode arrays and microcomputers enabled real-time strain measurement. Various applications of the ISDG are described in [2,3], and a NASA report [4] is a detailed 'handbook'.

A. Lagarde (ed.),
IUTAM Symposium on Advanced Optical Methods and Applications in Solid Mechanics, 137–144.

This noncontacting optical method can measure strains on thin films provided suitable reflective gage markers can be applied. Thin and narrow metal reflective strips can be easily deposited in suitable patterns on polysilicon as part of the manufacturing process. The next section discusses the principles of the ISDG and its application to polysilicon. Two shapes of tensile specimens have been tested — 3.5 μm thick by 600 μm wide and 1.5 μm thick by 20 μm wide — and those test procedures are described. Typical results from both kinds of specimens are presented in the next two sections, and the paper closes with some remarks.

2. ISDG Principles

The principle of the ISDG is illustrated in Figure 1.

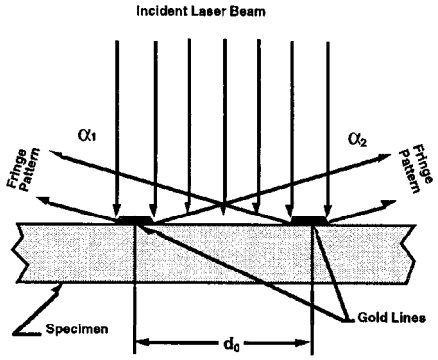

Figure 1. Schematic of the ISDG. The gold lines, which run perpendicular to the paper, are 1/2 micron thick and 20 microns wide.

The incident laser beam is reflected from the edges of the gold lines; more accurately, it is diffracted because of the small size of the lines. The reflected light rays travel different path lengths and therefore generate interference fringe patterns. As the gold lines (which are gage markers) move relative to each other, the fringes move and their motion can be translated into strain.

The governing equation relating strain, ε, to fringe motions Δm_1 and Δm_2 is:

$$\varepsilon = \frac{\lambda}{2d_0}\left(\frac{\Delta m_1}{\sin \alpha_1} + \frac{\Delta m_2}{\sin \alpha_2}\right) \tag{1}$$

where λ is the wavelength of the laser, d_0 is the gage length between the two gold lines, and α_1 and α_2 are the angles between the incident laser beams and the central portions of the fringe patterns. Ideally, α_1 and α_2 would be equal, but there is always some difference in the placement of the diode arrays. The fringe motions Δm_1 and Δm_2 are not equal because of rigid body motion as the specimen is strained. Averaging the two fringe motions as done in Equation (1) eliminates the effect of rigid-body motion in the direction of strain. More details on both the optical principles and the experimental setup are available in [4].

Figure 2 is a SEM photograph of two sets of gold lines deposited on a 3.5 μm thick by 600 μm wide polysilicon tensile specimen to enable biaxial strain measurement, Figure 3 is a SEM photograph of the edge of a gold line and shows the rounded edge from which the light rays are diffracted.

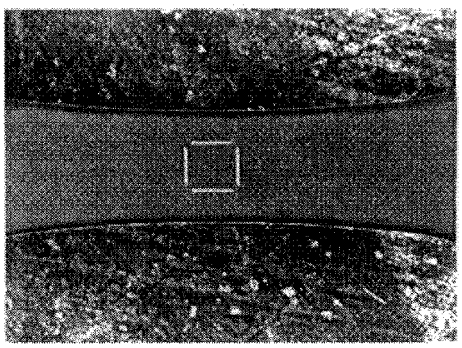

Figure 2. Four gold lines deposited on a polysilicon tensile specimen. The line spacing is 250 μm.

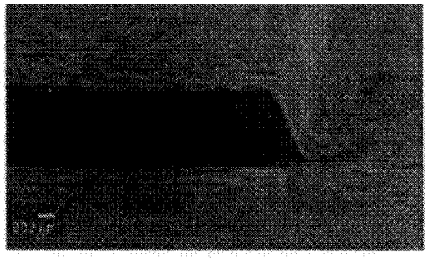

Figure 3. SEM photograph of the edge of a gold line.

The ISDG is based on the movement of interference fringes, not the diffraction pattern. Figure 4 is a plot of the fringe intensity for a typical interference pattern. The diffraction envelope is drawn in as a dashed line. The fringes move within this diffraction envelope as the specimen is strained.

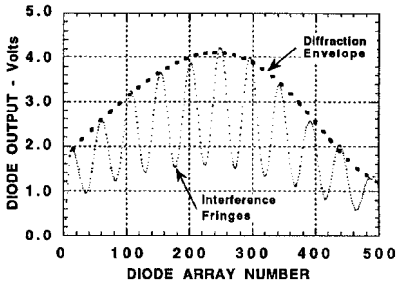

Figure 4. Fringe pattern intensity recorded by a linear diode array.

3. ISDG Measurement System

A tensile test setup consists of grips for the specimen, a method for pulling it, a load cell, and a means of measuring strain. The emphasis in this paper is on the latter. Figure 5 is a schematic of the system for testing the larger specimens, which are 3.5 μm thick, 600 μm wide, and 4 mm long in the test section [5].

The polysilicon specimen is mounted across an opening in a one-centimeter die which is glued into the grips. The side support strips of the die are then cut with a diamond saw to free the specimen. The linear air bearing effectively eliminates friction in the load train, and the piezoelectric translator pulls the specimen under computer control.

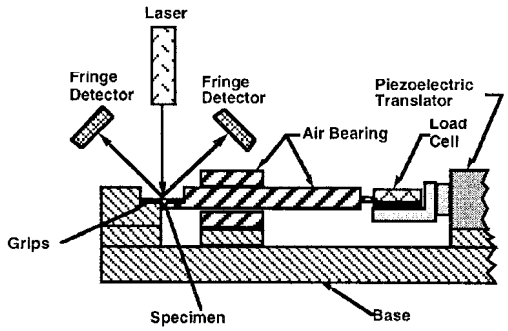

Figure 5. Schematic of the test system for biaxial tests. Two additional fringe detectors (not shown) are included for lateral strain [5].

The fringe detectors of Figure 5 are linear diode arrays with 512 diodes - each with an aperture of 13 μm by 2.5 mm - packaged in a 16-pin chip; the total size of the array is 2.5 mm by 12.6 mm. The arrays are inserted in circuit boards containing amplifying circuitry and mounted in plastic mini-boxes attached to translation stages which are mounted on adjustable rods. This provides the two degrees-of-freedom necessary to position the diode array in the center of the fringe pattern. Each diode array is accessed by a motherboard which samples each diode in turn and provides an output signal from 0 to 5 volts. Figure 4 is a plot of the output of one diode array (only 500 of the 512 outputs are plotted). The diode arrays are connected to a microcomputer that tracks the motions of the fringes and computes the strain. A test is thus run in real time — taking data points at approximately 10 per second.

In a typical setup, the spacing between minimum (or maximum) intensity is approximately 80 diodes on the array. If one identifies a local minimum by simply taking the lowest value, then the smallest resolvable fringe movement is 1/80. Since the two fringe patterns are averaged in Equation (1), the minimum strain resolution occurs when one minimum moves one diode position. The geometry of the setup is such that the relative displacement for both fringes moving from one peak to the next is approximately one μm. The strain resolution is therefore approximately 1/2 x 1/80 x 1/200 = 31 microstrain if a 200 μm gage length is used. This resolution can be increased by a factor of 100 by fitting a curve to data points surrounding a minimum and interpolating between the diode locations. A resolution of 0.3 microstrain is not really meaningful; it is estimated that the resolution is approximately 5 microstrain. The relative uncertainty is estimated as ± 3% with most of that coming from uncertainty in measurement of the angles α_1 and α_2.

Figure 6 is a schematic of the specimen and the test setup for smaller polysilicon specimens [6]. Eighteen of these specimens are deposited on a one-centimeter square die; each is fixed at one end and has a large free end that is gripped by electrostatic forces. This arrangement allows one to test smaller specimens; the smallest one on the die is 1.5 μm thick, 2 μm wide, and 20 μm long. Gold lines, if they were deposited on the smallest specimens, would not reflect enough to generate usable fringe patterns. The smallest specimen on which strain can be measured directly with gold lines is 20 μm wide.

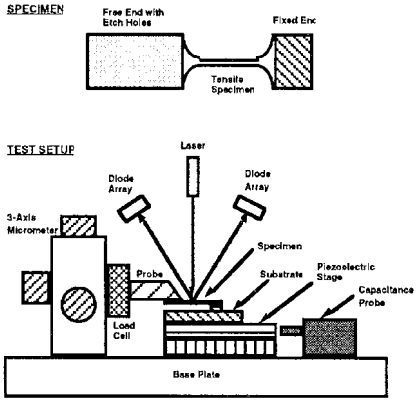

Figure 6. Schematic of the test setup for small tensile specimens [6].

The small tensile specimens remain mounted on the die. The 3-axis micrometer is used to move the probe into position over the large free end of a single specimen. The probe, which is insulated with a 600 nm layer of silicon nitride, is placed approximately 10 μm above the specimen's free end and a potential on the order of 100 volts is applied. this grips the free end electrostatically with enough force to pull the specimen to failure. The pulling action occurs through a piezoelectric stage (different than the one in Figure 5) under computer control. The capacitance probe in Figure 6 monitors the displacement of the specimen's fixed end and enables the computation of Young's modulus from the force-displacement record and the stiffness of the load cell.

4. Biaxial Strain Test Results

Figure 7 is a plot of stress versus axial and lateral strains for a polysilicon specimen such as the one shown in Figure 2 and tested in the system of Figure 5. All 353 data points are plotted there without any smoothing or other post-processing. Note that the initial strain of Figure 7 is not actually zero because a small tension must be applied initially to straighten the specimen.

The material is very linear and brittle, but of high strength. The Young's modulus, E, of 169 GPa agrees almost exactly with the 168 GPa predicted from randomly oriented silicon grains. This is probably fortuitous because the thin-film silicon has a columnar, not random, grain structure. The Poisson's ratio of 0.22 is the first measured for this material and agrees in general with values for silicate glasses.

Figure 8 is a plot of the fringe motions of channels 1 and 2, which measure the axial strain recorded in Figure 7. Again, the actual data points are plotted and the very linear response indicates that there was no unusual rigid-body motion.

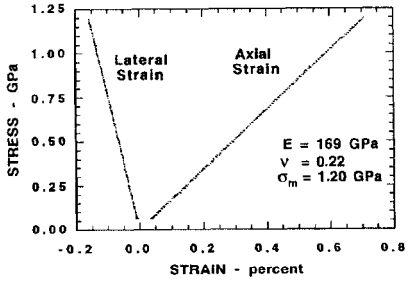

Figure 7. Typical axial and lateral strains for a wide polysilicon specimen.

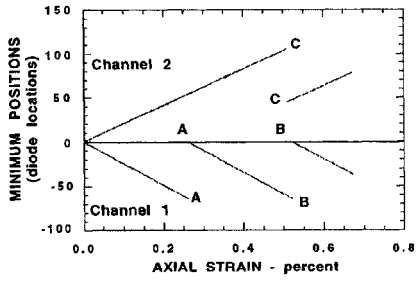

Figure 8. Fringe motions due to axial strain for the test of Figure 7.

The initial minimum position is subtracted from the minimum position at a particular strain, which is why the plot in Figure 8 starts at zero. The minimum positions are not integers corresponding to the 512 diodes in the array, but are determined by fitting a parabola to values from neighboring diode locations and using the minimum of this fitted curve. This calculation is performed for each data point. The fringe monitoring program tracks a single fringe along with one neighbor on each side. The relative fringe motion, Δm is computed by dividing the movement of the central minimum by the average spacing between it and the two adjacent minimums. When the minimums being tracked approach the edge of the diode array, the program switches to an adjacent minimum further from the edge. This explains the jumps at A, B, and C in Figure 8.

Table 1 presents a summary of the results of biaxial tests of specimens from five different production runs at MCNC under their MUMPs program [5]. The mean ± one standard deviation are listed.

Table 1. Mechanical property data for polysilicon [5].

MUMPs	Young's Modulus (GPa)	Poisson's Ratio	Tensile Strength (GPa)
6	163 ± 4.78	-	1.23 ± .200
8	173 ± 6.94	-	1.27 ± .107
10	173 ± 2.00	-	1.14 ± .155
11	168 ± 7.15	0.22 ± .015	1.19 ± .155
12	168 ± 1.59	0.22 ± .003	1.17 ± .100
All Data	**169 ± 6.15**	**0.22 ± .011**	**1.20 ± .150**

One sees that there is little variation in the mechanical properties among the specimens fabricated at different times. Further, the relatively low coefficient of variations (standard deviation / mean) of 3.6%, 5%, and 12.5% indicate that both the manufacturing process and the test method are quite consistent.

5. Electrostatic Results

Figure 9 is a stress-strain plot for a polysilicon specimen gripped electrostatically in the system of Figure 6; the test section is 1.5 μm thick, 20 μm wide, and 500 μm long. Axial strain is measured with the ISDG.

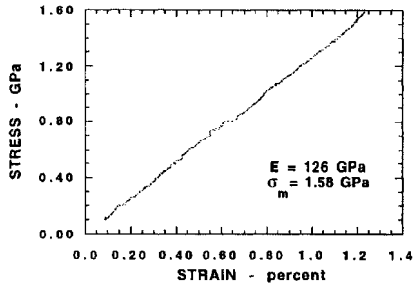

Figure 9. Stress-strain curve for a specimen 1.5 μm thick and 20 μm wide.

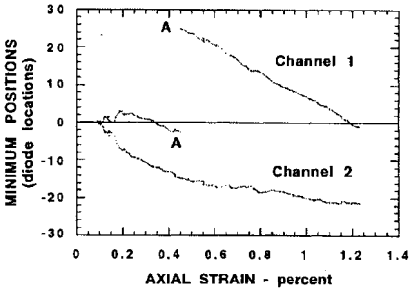

Figure 10. Fringe motions for the axial strain of Figure 9.

The Young's modulus for this specimen was measured to be 126 GPa, but the value extracted from the force-displacement record (taken simultaneously) was 153 GPa for the very same specimen. There is considerably more scatter in the results for these smaller specimens. The lower measured modulus for these smaller specimens is a matter of continuing investigation.

Figure 10 is a plot of the fringe motions associated with the strain data of Figure 9. These fringe movements are not so smooth and linear as in Figure 8 for the larger specimen. There is more rigid-body and perhaps twisting motion as the specimen is strained; this contributes to the nonlinear movement of both fringe patterns. Again, there is a shift of one fringe spacing on Channel 1 as the tracked fringe moves too near the edge of the diode array. The fact that both fringes move in a negative direction has little meaning; the sign of motion depends on the arrangement of the diode arrays. The proper sign for strain computation is included in the ISDG program. It is perhaps remarkable that the strain record of Figure 9 looks almost as good as the one of Figure 7 even though the specimen is much smaller and the fringe motion is much rougher.

A series of load-unload tests were conducted on a slightly larger tensile specimen than the one whose results are shown in Figure 9. The specimen was 3.5 μm thick, 50 μm wide, and 500 μm long in the test section. Stress-strain curves from those 16 tests are shown in Figure 11.

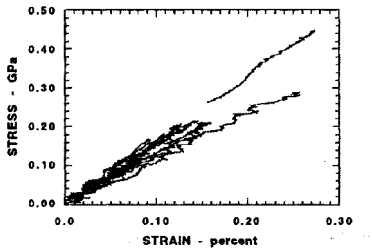

Figure 11. Stress-strain records of 10 loading tests and 6 unloading tests on the same polysilicon specimen.

Most of the tests were conducted at low stresses, and all were shifted along the strain axis after a straight line was fitted to the data. The scatter appearing in Figure 11 is large, but this is a very small specimen. The average Young's modulus is 151 GPa and the standard deviation is 16.3 GPa. The coefficient of variation is 11% which is quite a bit higher than the less than one would expect from similar measurements on large metal specimens. There was no significant difference between the average loading value (150 GPa) and the unloading value (151 GPa).

6. Concluding Remarks

It is important to measure strain directly on specimens, rather than inferring it from overall displacements or deflections. The techniques and procedures presented here have proved very effective in the study of the thin-film polysilicon that is widely used in MEMS. Such methods are clearly applicable to the mechanical property measurements of other thin, small, or fragile materials.

Acknowledgments

This research was supported by the National Science Foundation and the Air Force Office of Scientific Research. The significant contributions of students and colleagues to this work over the past four years is greatly appreciated.

References

1. Sharpe, W. N., Jr., "The Interferometric Strain Gage," *Experimental Mechanics,* Vol. 8, pp. 164-170 (April 1968).
2. Sharpe, W. N., Jr., "Applications of the Interferometric Strain/Displacement Gage," *Optical Engineering,* Vol. .21, pp. 483-488 (1982).
3. Sharpe, W. N., Jr. "Crack Tip Opening Displacement Measurement Techniques," Experimental Techniques in Fracture, Society for Experimental Mechanics, Inc. Bethel, CT, Chapter 7, pp. 219-252, (1993).
4. Sharpe, W. N., Jr., "An Interferometric Strain/Displacement Measurement System", NASA Technical Memorandum 101638, (1989).
5. Sharpe, W. N., Jr., Yuan, B., Edwards, R. L., and Vaidyanathan, R., "Measurements of Young's modulus, Poisson's ratio, and Tensile Strength of Polysilicon", *Proceedings of the Tenth IEEE International Workshop on Microelectromechanical Systems,* Nagoya, Japan pp. 424-429 (1997).
6. Sharpe, W. N., Jr., Turner, K., and Edwards, R. L., "Polysilicon Tensile Testing with Electrostatic Gripping", presented at *Microelectromechanical Structures for Materials Research - Symposium N,* Materials Research Society and accepted for publication in the proceedings (April, 1998).

RESIDUAL STRESS MEASUREMENT WITH OPTICAL STRAIN ROSETTES

KEYU LI
Department of Mechanical Engineering
Oakland University
Rochester, MI 48309

1. Abstract

Optical strain gages were developed in 1960s and have many advantages over resistance strain gages. For instance, they are noncontacting, have extremely short gage lengths, and can be used to measure large strains. The interferometric strain rosettes are extended from the interferometric strain gages and have recently been developed to measure residual stresses. The technique is quantitative and is expected to be an accurate method of residual stress measurement. The method can potentially resolve many challenging problems which may not be tackled by any other means.

2. Introduction

Residual stresses exist in a solid body free from external forces and constraints. They are frequently induced during fabrication operations, such as casting, rolling, welding, stamping and forging. Traditional methods employed for determining residual stresses include hole-drilling, in which the strains relieved by the hole are measured with a resistance strain rosette (Kobayashi, 1993). However, the method has several drawbacks such as being destructive to test objects, attachment requirement to a surface area, and high costs incurred for mounting a rosette, installing a milling guide and gathering data. Nondestructive methods such as X-ray diffraction, ultrasonic and magnetic methods are all highly sensitive to microstructure properties such as texture, working hardening and grain size (Lu et al, 1995). The methods remain semi-quantitative and are only useful for comparative measurements. Recently there has been considerable interest in using optical methods such as moiré, holographic and speckle interferometric methods in measurements of residual stresses (McDonach et al, 1983, Nicoletto, 1991, Dai et al, 1996, Wang and Chiang, 1997, Perry et al, 1997, Nelson et al, 1994, Hung et al, 1996, Antonov, 1983, Goncalves et al, 1996). Some of the limitations of conventional methods can be overcome by using optical methods which are noncontacting and don't require center-hole drilling. However, application of the moiré method can be time consuming and is limited to flat objects (Post et al, 1994). The holographic interferometry method requires strict vibration isolation (Vest, 1976) and thus is not well suited for industrial

A. Lagarde (ed.),
IUTAM Symposium on Advanced Optical Methods and Applications in Solid Mechanics, 145–152.

settings. Most full-field optical methods require either flat surfaces or rather strict vibration isolation.

In contrast to the full-field optical methods, optical strain gages were developed to measure strain components on one location of a material surface. Grating diffraction strain gage was developed to measure dynamic strains (Bell, 1956; Valle, Cottron and Largarde, 1996), and the diffiactographic strain gage was based on laser diffraction from the gap between two blades attached to a specimen surface (Pryor and North, 1971). The interferometric strain/displacement gage technique (ISDG) was based on interference of laser reflected from two grooves (Sharpe, 1968). The interferometric strain rosette technique (ISR) (Li, 1995) was recently extended from the ISDG. Compared with resistance strain rosettes (Dally and Riley, 1991), the ISR is quantitative in nature and has high accuracy for measurements of three strain components. In addition, the ISR possesses a few advantages over resistance strain rosettes. For instance, the ISR has been developed to measure out-of-plane displacement derivatives (Li, 1996) and has a high frequency response to measure vibrations (Li, 1997a). Both the ISDG and ISR have extremely short gage lengths on the order of 100 micrometers so that localized strains can be measured. In fact, the ISDG has been used to measure displacements and strains in miniature specimens (LaVan and Sharpe, 1997).

3. Principle of Residual Stress Measurement by ISR

An ISR consists of three micro-indentations and may have the configurations of delta and rectangular rosettes. Fig. 1 shows a typical 60° ISR which has a delta configuration. Fig. 2 shows a typical 45° ISR which has a rectangular configuration. Three in-plane strains in the separating directions of the indentations can be measured. For instance, a 60° ISR can measure normal strains in the directions of 0, 60 and 120 degrees. A 45° rosette can measure normal strains in the directions correlation with 0, 90, and 135 degrees.

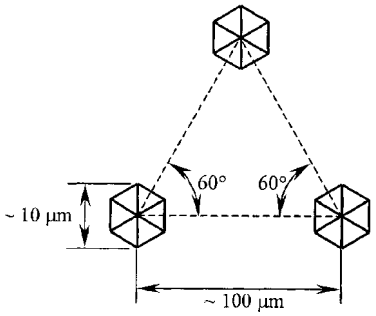

Fig. 1 The schematic diagram of a 60° ISR

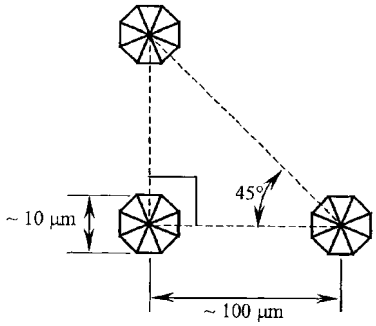

Fig. 2 The schematic diagram of a 45° ISR

The ISR may be used in conjunction with the hole-drilling method or ring-core method to measure residual stresses. Three micro indentations of an ISR are depressed on the

surface of an evaluated object. When a micro-hole or a ring core is drilled near an ISR, the residual stresses at the location of an ISR are released. The released stresses cause strains between the three indentations. The relieved strains are measured by the ISR and are used to calculate residual stresses.

3.1 RING-CORE METHOD

The basis for ring-core method is to completely remove a ring of the material around an ISR. When a ring-core is cut around a 60° ISR, the measured strains are in the directions of 0, 60 and 120 degrees, namely, ε_0 ε_{60} and ε_{120}. Then the three strain components ε_x ε_y and γ_{xy} are calculated by using strain transformation equations as follows:

$$\begin{aligned} \varepsilon_x &= \varepsilon_0 \\ \varepsilon_y &= \varepsilon_{60} + \varepsilon_{120} - \varepsilon_0 \\ \gamma_{xy} &= (\varepsilon_{60} - \varepsilon_{120})/\sin 60 \end{aligned} \tag{1}$$

Similarly, the strain components can be calculated from the measurements of a 45° ISR by using strain transformation equations. The relieved residual stresses can be calculated by using Hooke's law.

$$\begin{aligned} \sigma_y &= E(\nu\varepsilon_x + \varepsilon_y)/(1-\nu^2) \\ \sigma_x &= E(\varepsilon_x + \nu\varepsilon_y)/(1-\nu^2) \\ \tau_{xy} &= G\,\gamma_{xy} \end{aligned} \tag{2}$$

where E is Young's modulus, ν is Poisson's ratio, σ_y and σ_x are normal stresses, and τ_{xy} is shear stress.

It is assumed that the residual stresses at the location of the ISR are completed relieved. The amount of relieved stresses approximately equals to the amount of real residual stresses. Since the size of the ISR is tiny, the inner diameter of the ring-core can be made very small that the measurement is highly localized. The cutting process should be more convenient than that used with a resistance strain rosette.

3.2 HOLE-DRILLING METHOD

A hole can be drilled to relieve residual stresses. In a thin-thickness specimen, a through hole is drilled. The residual stresses are determined by employing Kirsh's equations for an infinite plate subjected to a biaxial stress state (Li, 1997b). In a thick component, a blind hole is drilled (Li et al, 1997). When the residual stress distribution versus depth is of concern, an incremental hole drilling process is employed (Tjhung et al, 1998). For incremental hole-drilling, residual stresses are calculated from the measured strains by employing either calibrated coefficients or finite element methods.

The method of material removal may also be done using other techniques. For example, chemical etching technique may be used to remove layers of materials to study the distribution of the residual stresses with depth. The chemical environment should not interfere with the ISR in contrast to the case of a resistance strain rosette.

4. Two-step Measurement Program and Evaluation Tests

A movable ISR system was constructed. It contains an 8-mw He-Ne laser and six photodiode sensors. The direction and distance between sensors are adjustable. The system is vertical and may be set up in front of any machine for testing purposes. Traditionally, the ISR system is was used for real-time measurements. When the specimen is loaded, the ISR records the strain increment for each step of loading. The total strain value is an accumulation of the increments in real time.

When the ISR is used to measure residual stress, a two-step measurement procedure must be developed for taking two sets of data separately. An IBM computer is programmed to record the two measurements and calculate the strain incurred between the two steps of measurements.

To evaluate the measurement procedure and the computer program, various tensile/compressive tests are conducted on a bar specimen. The dimensions of the specimen are: thickness =3.175mm, width=51.2 mm, Length =300mm. The material properties of the specimen are recorded in TABLE 1.

TABLE 1: Material properties of aluminum 6061

E	G	v	σ_y	σ_u
70 GPa	26 GPa	0.33	270MPa	310MPa

The ISR movable system is set up at a distance of 44 cm from the specimen. The gage length of the ISR is 250 micrometers. The first group of tests are the so called “zero-shift” tests. When the applied load is zero, two-step measurements are taken within a few minutes. Theoretically, there is zero strain in the specimen and the program should output zero readings. But in real experiments, nonzero strains were recorded. The strain components in x-y coordinates along the transverse and axial directions of the bar are calculated by using equation (1) and shown in TABLE 2. The maximum shift of strain readings between the two steps of measurements is about 7 microstrains. The maximum difference for the stresses calculated from the strains is 0.7 MPa. These nonzero results may be due to the sensitivity of the electrical-optical system to its environment.

TABLE 2: Two step measurements of strain and stress by the ISR at zero load

Test #	Axial strain, $\varepsilon_y(\mu\varepsilon)$	Transverse strain, $\varepsilon_x(\mu\varepsilon)$	Shear strain, $\gamma\ (\mu\varepsilon)$	Axial stress, σ_y(MPa)	Transverse stress, σ_x(MPa)	Shear stress, τ (MPa)
Test 1	–1.66	–0.31	3.56	–0.14	–0.68	0.09
Test 2	4.08	1.47	–5.38	0.28	0.097	–0.15
Test 3	4.28	–0.1	–0.52	0.33	0.10	–0.013
Test 4	–0.33	–1.34	1.56	–0.11	–0.06	0.04
Test 5	4.28	–0.10	–0.52	0.33	0.10	–0.013
Test 6	1.2	0.34	1.17	0.10	0.057	–0.03
Test 7	2.42	1.51	1.61	0.23	0.18	0.04
Test 8	–0.66	–2.76	–6.25	–0.23	–0.12	–0.16
max value	5	3	7	0.4	0.7	0.2

The second group of tests apply loads to the bar. Two-step measurements are conducted before and after a load is applied. The stress and strain between zero and the applied load can be calculated from the theory of uniaxial loading. The measured strains by the ISR agree well with the results of the calculation and resistance strain gages in TABLE 3 and Figure 3. The maximum relative difference of the axial strain is 6% between the ISR data and the calculated strains.

TABLE 3: The comparison of the results of the ISR measurements with that of the calculation and the resistance strain gage measurements.

Test #	σ_y (MPa) Theory	Axial strains , ε_y ($\mu\varepsilon$)				Transverse strains, ε_x ($\mu\varepsilon$)		
		Theory	ISR	Strain Gage	Difference between ISR & Theory	Theory	ISR	Difference between ISR & Theory
1	27.64	394.85	385.00	394	–9.85	–130.30	–133.93	–3.63
2	27.37	390.94	383.11	409	–7.83	–129.01	–143.53	–14.52
3	–13.96	–199.43	–201.93	–213	–2.50	65.81	81.88	16.07
4	–16.42	–234.57	–250.52	–249	–15.95	77.41	100.20	22.79
5	–24.90	–355.76	–358.09	–376	–2.33	117.40	126.07	8.67
6	–27.37	–390.94	–381.83	–408	9.11	129.01	137.31	8.30
7	–35.30	–504.32	–524.00	–529	–19.68	166.42	208.04	41.62
8	–41.05	–586.41	–566.77	–592	19.64	193.52	200.49	6.97
9	–42.69	–609.87	–583.35	–611	26.52	201.26	219.15	17.89

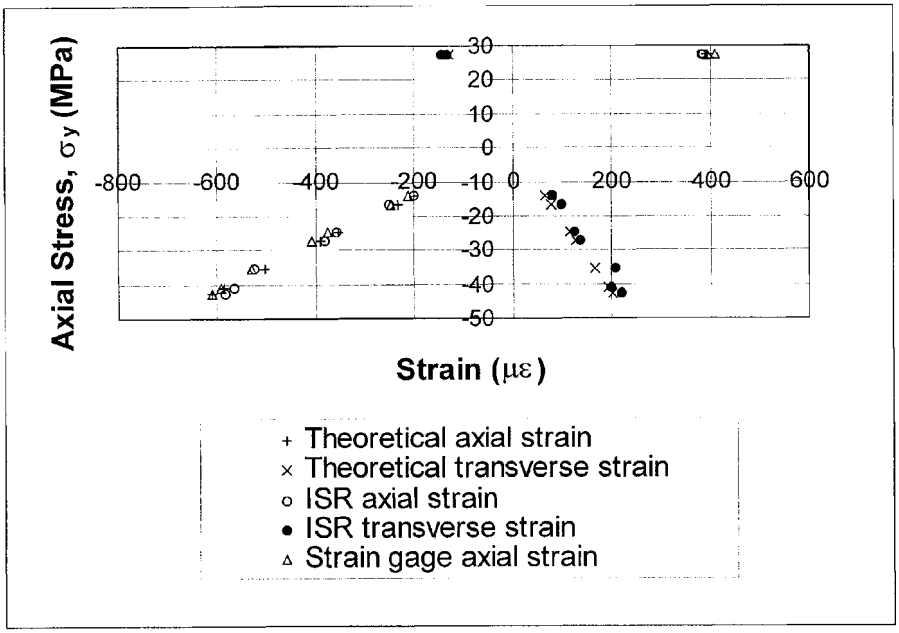

Figure 3. The plots of the ISR data, the resistance strain gage data and the calculated stress-strain.

5. Experiments of Residual Stress Measurements by Ring-core and Hole-drilling

Once the two-step measurement procedure is established and evaluated, the ISR method may be used to measure real residual stresses in manufactured components. For example, the aluminum 6061 bar specimen used in the above uniaxial tests contains residual stresses induced during its rolling process. The bar specimen after a heat-treatment is taken as the test sample of the ISR experiment by using the ring-core method. A cutter is specially made and hardened. The inner diameter of the cutter is 2.0 mm and the outer diameter is 4.5 mm. First, a 60° ISR of 250 micrometer gage length was indented on the surface of the bar specimen. Secondly, the ISR system was set up in the same way as the previous uniaxial tests. Then the first step of the measurement is done. A milling guide (model RS-200, Measurement Group, Inc.) was positioned, and a milling rod with a universal joint connected with a hand-drill was used to cut a ring around the ISR. Precaution must be taken to avoid any disturbance to the ISR system. The second step of measurement process was done by measuring the strains relieved during the ring-core cutting. The results are listed in TABLE 4. Strain components in x-y coordinates along the transverse and axial directions of the bar are calculated by using equation (1). The ring has an inner diameter of 2.0 mm and outer diameter of 5.0 mm. The depth of the cutting is about 2 mm, which is supposedly enough to relieve the residual stresses completely. The original residual stresses should take the opposite signs of the stress calculated by using equation (2). In fact, the ring-core cutting relieves positive residual stresses to get negative strains in the center of the remaining materials. The residual stresses are recorded in TABLE 4.

TABLE 4: Measurement of residual stresses in the aluminum bar and titanium block by using the ISR and ring-core cutting method.

Test #	Strains (με)						Residual stress (MPa)		
	ISR strains			Strain components					
	ε_{60}	ε_{0}	ε_{120}	ε_{xx}	ε_{yy}	γ_{xy}	σ_{xx}	σ_{yy}	τ_{xy}
1	–659.4	– 569.0	–508.3	–569.0	–588.8	–174.5	94.2	95.9	7.2
2	112.8	155.6	175.3	155.6	140.3	–72	–21.7	–20.6	3.0

The second ring-core cutting experiment was performed on a surface shot-peened titanium block. The material properties of TA6V are: E=110 GPa and v=0.3. Since the material was extremely hard, drilling was too difficult to cut more than 0.1 mm in depth. The inner diameter of the ring-core is 2 mm, and the outer diameter is 4.5 mm. The strains measured by ISR, the calculated strain components, and the calculated residual stresses are recorded in the second row of TABLE 4. Since the depth of the drilling is very shallow, only a small portion of the residual stresses is relieved. The measurement values should be much smaller than the real values of residual stresses. The measurement results show that the residual stresses on the surface are compressive, as found by using a resistance strain rosette reported in a previous paper (Li et al, 1997).

The hole drilling method is under development for residual stress measurements by the ISR. The size of the hole, and the distance between the center of the hole and the ISR influence the measurement sensitivity. There is no requirement for a center hole

drilling. We have applied the ISR to various manufactured samples including aluminum tubes (Li, 1996), and surface-shot peened titanium alloy blocks (Li et al, 1997). We are currently applying the method to measure residual stresses in welds (Tjhung et al, 1998). The ISR results have shown favorable agreement with the results of resistance strain rosettes. In addition, we are investigating the ISR technique for analyzing and validating analytical models of simulating casting and quenching processes (Li et al, 1998). The study aims to optimize the design of the process parameters. As residual stresses are minimized, distortion during the machining of the materials will be eliminated or reduced.

6. Conclusions

Following our previous efforts on developing the interferometric strain rosette technique (ISR), we have extended the method into measurement and evaluation of residual stresses. The measurement system has been reconstructed as a movable structure. A two-step measurement procedure and software have been established. The accuracy of the two-step measurement has been evaluated by the uniaxial tests. The maximum zero shift was found to be 7 microstrains, and the difference between the theoretical and measurement results is less than 6%. Ring-core and hole-drilling methods are under development for use with the ISR technique. The feasibility of the two methods has been verified. The applicability is being studied and evaluated on various manufactured samples. The ISR has the potential to be developed as an accurate method of residual stress evaluation. The deployment of the method will enable resolution of many challenging problems in mechanics and industry.

7. Acknowledgment

The author would like to thank Mr. Forrest Wright, a machine specialist, for the design of the ring-core cutter, and Mr. Xi Zhang, a visiting scholar, for the design of the adjustable arms to support the six photodiode sensors of the ISR system. She acknowledges the laboratory assistance received from Ms. Ming Yu and Mr. Liangdao Xia, who were master graduate students. Mr. Tana Tjhung, a research assistant, drew the figures. Financial support for this work and the presentation is provided by the Civil & Mechanical Systems Div. of NFS (Grant CMS-9503621 and Career award CMS-9734533) and Alcoa Foundation's Science Support.

8. Reference

Antonov, A. A. (1983), Inspecting the level of residual stresses in welded joints by laser interferometry, Weld Prod., 30, 29-31.

Bell, J. F. (1956) Determination of dynamic plastic strain through the use of diffraction grating, Journal of Applied Physics, **27,** 1109-1113.

Dally, J.W., and Rilley, W. F. (1991) *Experimental Stress Analysis,* McGraw-Hill, Inc.

Dai, F., Shi, L., Huang, L., Tang, X. (1996) Residual thermal strain measurements inside Pb/Sn solder joints, Abstract Proceedings of VIII International Congress on Experimental Mechanics, pp. 33-34.

Kobayashi, A. S. (1993) *Handbook on Experimental Mechanics,* Prentice-Hall Inc., pp. 785-829.

Goncalves, Jr., Kanda, C., Boettger, J., (1996) Residual stress measurement using a radial interferometer - a preliminary analysis, Abstract Proceedings of VIII International Congress on Experimental Mechanics, pp. 27-28.

Hung, Y.Y., Long, K.W., Wang, J.Q., and Hovanesian (1996) Automated measurement of residual stresses by phase-shift shearography, Abstract Proceedings of VIII International Congress on Experimental Mechanics, pp. 122-123.

Joh, D., Byun, K. Y., & Ha, J. (1993), Thermal residual stresses in thick graphite/epoxy composite laminates - uniaxial approach, Experimental Mechanics, **33,** 276-80.

LaVan, D. A., and Sharpe, W. N., Jr. (1997) Strain measurement on miniature tension specimen, Abstract Proceedings of the SEM Spring Conference on Experimental Mechanics, June 2-4, Bellevue, WA, pp.116-117.

Li, K. (1995) Interferometric 45° and 60° strain rosettes, Journal of Applied Optics, **34,** 6376-6379.

Li, K. (1996) Out-of-plane displacement derivative measurements using interferometric strain/slope gage, Journal of Applied Mechanics, **63,** 1033-1038.

Li, K. (1997a) Interferometric strain/slope rosette for static and dynamic measurements, Experimental Mechanics, **37,** 111-118.

Li, K. (1997b) Application of interferometric strain rosette to residual stress measurements, Journal of Optics and Lasers in Engineering, Special Issue on Optical Methods for Residual strain Measurement, **27,** 125-136

Li, K., Xia, L, and Lu, J. (1997) Residual stress measurements on a surface peened block by resistance and interferometric strain rosettes, Abstract Proceedings of SEM Spring Conference, Bellevue, WA, June 2-6, pp. 259-260.

Li, K., Tjhung, T., Li, N., Pien, J. (1998) Numerical simulation and experimental evaluation of residual stresses in casting and quenched components, Abstract Proceedings of SEM Spring Conference, Houston, TX, 416-418.

Lu, J. (1995) editorial boards: James, M., Lu, J., and Roy, G., *Handbook on Techniques of Measurement of Residual Stresses,* Society of Experimental Mechanics, Inc..

McDonach, A., McKelvie, A., MacKenzie, P., & Walker, C. A. (1983) Improved moire interferometry and applications in fracture mechanics, residual stress and damaged composites, Experimental Mechanics, **7,** 20-24.

Nelson, D., Fuchs, E., Makino, A., and Williams, D. (1994) Residual stress determination by single-axis holographic interferometry and hole drilling - part II: experiments, Experimental Mechanics, March 1994, 79-88.

Nicoletto, G., (1991) Moiré interferometry determination of residual stresses in presence of gradients, Experimental Mechanics, **31,** 252-236.

Perry K.E., Jr, Epstein, J.S., and Clark D.E. (1997) Phase shift moire studies of processing-induced residual strains in nickel 200 spot welds, Journal of Optics and Lasers in Engineering, Special Issue on Optical Methods for Residual strain Measurement, **27,** 125-136

Pryor, T.R., and North, W. P.T. (1971) The diffiactographic strain gage, Experimental Mechanics, **11,** 565-568.

Post, D., Han, B., and Ifju, P. (1994) *High Sensitivity Moiré,* Springer Verlag.

Sharpe, W. N., Jr. (1968) The interferometric strain gage, Experimental Mechanics, **8,** 164-170.

Tjhung, T., Li, K., Barber, G., Hassan, A. (1998) Measurement of unequal biaxial residual stresses in the vicinity of welds by the interferometric strain rosette technique, Abstract Proceedings of SEM Spring Conference, Houston, TX, pp. 228-231.

Valle, V., Cottron, M., and Lagarde, A. (1996) Grating diffraction for local strain determination under dynamic loading, PD-Vol. **76,** ESDA, Volume 4, ASME 1996, The Third Biennal Conference, Montpellier France, July 1-4.

Vest, M. L. (1976) *Holographic interferometry,* Johns Wiley & Sons, Inc.

Wang, Y.Y., and Chiang, F. P. (1997) Experimental study of three-dimensional residual stresses in rails by moire interferometry and dissecting methods, Journal of Optics and Lasers in Engineering, Special Issue on Optical Methods for Residual strain Measurement, **27,** 89-100.

HIGH SPEED LOCAL STRAIN DETERMINATION FROM GRATING DIFFRACTION

V. VALLE
LMS, Université de Poitiers, CNRS UMR 6610
SP2MI - Téléport 2 - BP 179, 86960 FUTUROSCOPE CEDEX, FRANCE

M. COTTRON
LMS, Université de Poitiers, CNRS UMR 6610
SP2MI - Téléport 2 - BP 179, 86960 FUTUROSCOPE CEDEX, FRANCE

A. LAGARDE
LMS, Université de Poitiers, CNRS UMR 6610
SP2MI - Téléport 2 - BP 179, 86960 FUTUROSCOPE CEDEX, FRANCE

Abstract

The spectral analysis of grating allows, for static loading, the direct measurement of local strains at the surface of a body. This grating analysis is achieved by two ways (optical diffraction phenomenon or numerical Fourier transform) in order to determine at each step of load pitches and orientations of crossed grating. Our purpose is to extend this strain measurement method to investigate dynamic problems. The grating interrogation is performed using optical diffraction of a laser beam with an oblique incidence. In order to separate the diffracted beams during the dynamic event, we associate with each strain state a specific angle of the incident laser beam. This procedure allows to record 23 strain states at a maximum frequency equal to 1 MHz. The diffracted spots can be stored by two ways (film and CCD camera) and their analysis gives a strain sensitivity of 2.10^{-4}.

1. Introduction

The measurement of mechanical quantities without contact, without destruction of the specimen or in hostile environment can be achieved by optical investigations. The grid method [1], one of these, allows one to determine the magnitude and the orientation of the principal strain as well as the rigid body rotation [2]. This is achieved by the comparison between the geometry of a deformed crossed grating (pitch and orientation

A. Lagarde (ed.),
IUTAM Symposium on Advanced Optical Methods and Applications in Solid Mechanics, 153–160.

of each direction of grating) with the geometry of the same grating in the initial state. The analysis of the grating is obtained for static investigations by an optical Fourier transform or a numerical one [3][4]. This method is performed for the measurement of small and large strains with a sensitivity comparable to the one obtained by strain gauge [5].

Investigations of dynamic problems from grating analysis have been performed [6] few decades ago. The easy use of laser and the recent development of numerical tools like the CCD camera allows the construction, of accurate and simple experimental devices. This new method is based on an interrogation of a crossed grating from diffraction phenomena under oblique incidence.

2. recording and analysis device

2.1. OBLIQUE DIFFRACTION PHENOMENON

By associating with each strain state a specific angle of the incident laser beam, we can separate the diffracted beams during the dynamic event. We have so to take account of the diffraction phenomenon in oblique incidence [7]. Figure 1 shows the oblique diffraction phenomenon for an uni-directional grating of pitch p analysed on reflection by a laser beam.

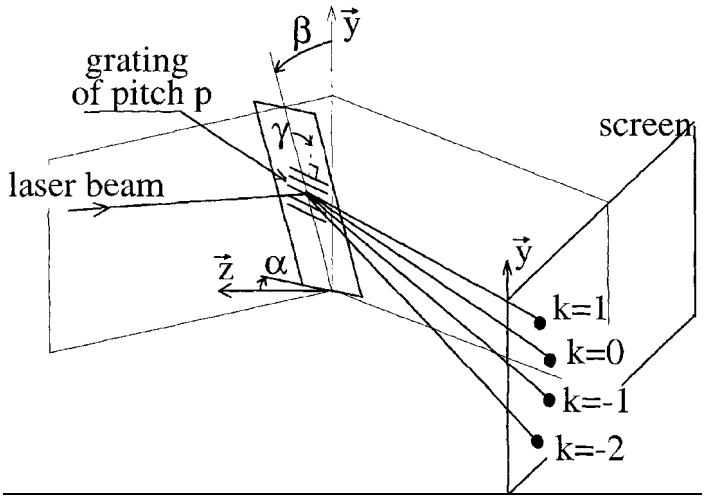

Figure 1 : Oblique diffraction of a laser beam from an uni-directional grating

Figure 2 shows the geometrical distribution of the diffracted spots (experimentally realised with an oblique incidence of α=30°) given by a crossed grating.

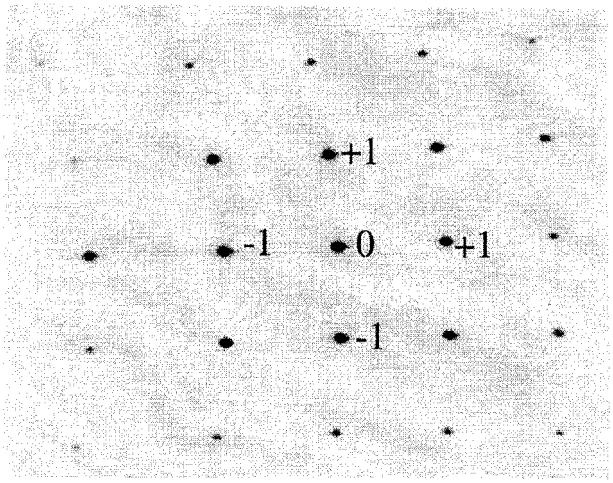

Figure 2 : Photography realised from the diffraction in oblique incidence of a laser beam through a crossed grating

The recording and the localisation of +1, 0 and -1 orders of diffraction give not only the 4 geometrical characteristics of the crossed grating, but also the 2 angular positions and the 3 components of the position of the measurement base. The comparison of these 9 parameters with the quantities in the initial state gives the strain tensor, the rigid body rotation and the rigid body displacement [8].

2.2. RECORDING DEVICE

The variation of the orientation of the incident laser beam is experimentally achieved by the use of acousto-optics deflectors [9][10] (Figure 3 and Figure 4). These elements allow the recording of 23 sequential measurements during the dynamic event at a maximum frequency near 1 MHz.

An acousto-optic shutter controls exposure time equal to 30 ns and an optical element constituted of 48 mirrors permits the movement of each beam in the direction of the measurement base.

A study of the optical efficiency of this experimental device shows that the use of a recording film of 400 ASA sensitivity or a direct recording on CCD camera with a 250 mW laser power gives a minimum exposure time equal to 0.1 μs. This value, ten percent of the maximum frame rate, is sufficient to provide instantaneous measurements.

Under these conditions, the developed device can be applied for strain measurement during a dynamic loading of a minimal duration equal to 23 μs.

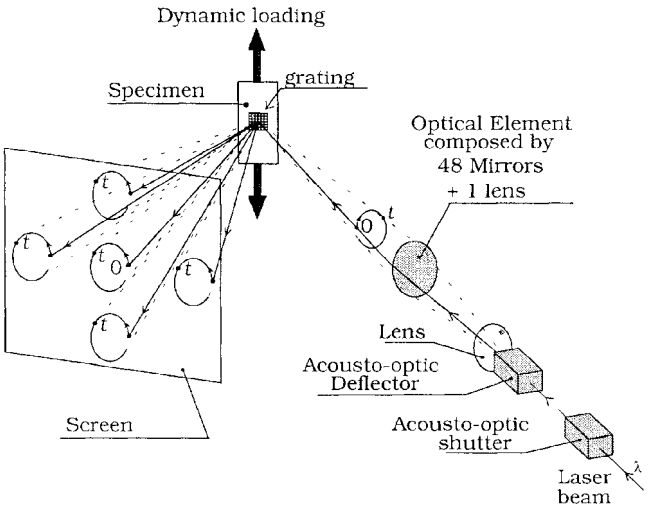

Figure 3 : Schema of the optical recording device

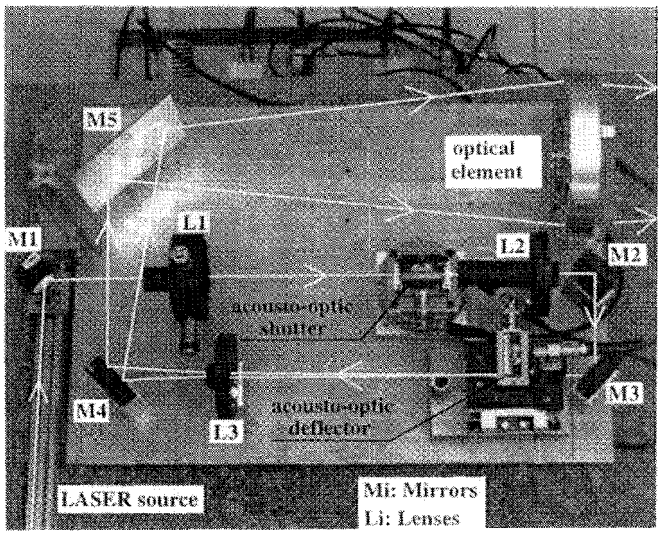

Figure 4 : Photography of the optical recording device

The small dimension of this recording device, about 300x500x200 mm^3, allows the use of this technique on most experimental or industrial sites.

2.3. STORAGE ON PHOTOGRAPHIC FILM

For a photographic storage of the diffraction picture we replace the screen of the Figure 3 by a 9x12 cm photographic film (400 ASA). An adapted analysis device has been

developed to determine the position of the 115 spots (5 orders of diffraction x 23 states of loading) recorded on the photographic film. This device consists of a XY displacement table (Figure 5) with 10 µm sensitivity for moving the film, and a CCD camera for the acquisition of the spots.

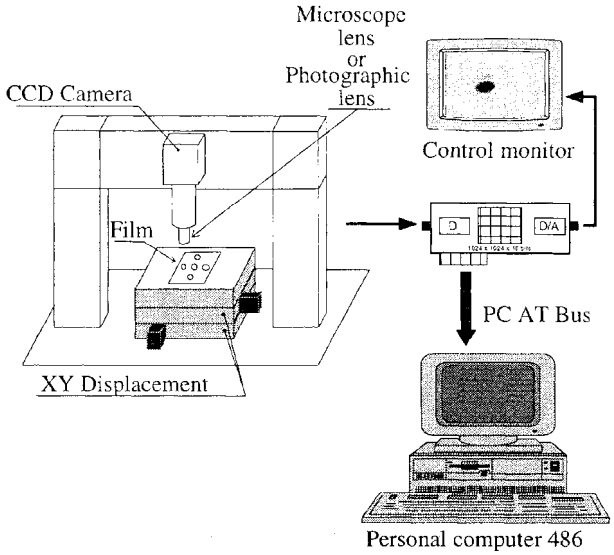

Figure 5 : Experimental device for photographic film analysis

First we create a XY file containing the position of the spots obtained by a global analysis of the film. This analysis is achieved by mounting a photographic lens on the CCD camera. Then, we use the XY file to move the film with a motorised displacement table; The-diffraction picture is then analysed spot by spot mounting a microscope lens on the CCD camera. In this way, we virtually multiply the number of pixels of the CCD camera (1024x1024 pixels to 8000x8000 pixels with 10 µm resolution of the XY displacement). After 10 minutes of photographic film analysis, we obtain a strain sensitivity of approximately 2.10^{-4}.

The maximum strain rate depends. on the strain sensitivity and on the minimum exposure time;it is obtained by- dividing the strain sensitivity by the exposure time. For example, a dynamic event analysed with a sensitivity of 2.10^{-4} and an exposure time of 0.1 µs is sufficient for a maximum strain rate of 2000 s^{-1}. We can analyse a higher strain rate of 20000 s^{-1} if the strain sensitivity is equal to 2.10^{-3}.

2.4. DIRECT STORAGE ON CCD CAMERA

For a CCD storage of the diffraction picture we replace the screen of the Figure 3 by a CCD camera with 1024x1024 pixels on 10 bits. The storage of the diffracted spots is obtained by synchronisation of the CCD camera acquisition with the dynamic loading.

This device is simpler, but the pitch of the CCD grid (larger than the film grain) induces a smaller strain sensitivity. In our case the strain sensitivity reaches to 10^{-3} .

The optical efficiency of this experimental device gives the same performances as the first (20 μs of minimum loading time with 0.1 μs of exposure time and 250 mW of laser power). The maximum strain rate is equal to 10000 s^{-1} .

3. Tests

For all the experimental investigations, the diameter of the measurement base is about 1 mm. The crossed grating is realised by a replication technique [11] and the density is 200 lines per millimetre. The tests are realised with a CCD camera with 1024x1024 pixels for the direct technique and a 400 ASA film of 9x12 cm for the photographic one. On our figures, we compare the optically measured strain with that obtained by a classical extensometry using a strain gauge.

3.1. PHOTOGRAPHIC RECORDING

We give (Figure 6) a compression test using the impact of a mass on the mobile grip supporting the specimen. The storage of the optical data is realised on a photographic film. For this impact of 600 μs duration, we chose the frame rate equal to 35 kHz and an exposure time of 2.8 μs.

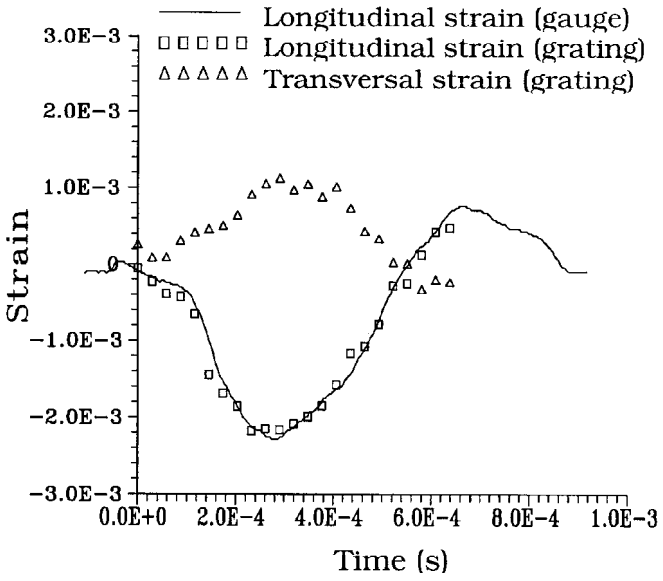

Figure 6 : Dynamic compression test with photographic acquisition

3.2. CCD CAMERA RECORDING

Figure 7 shows a compression test performing with a Hopkinson bar loading. We have adjusted the framing rate to 1 MHz according to the duration of the loading (20 μs). In this test, the exposure time is 10% of the framing rate (0.1 μs).

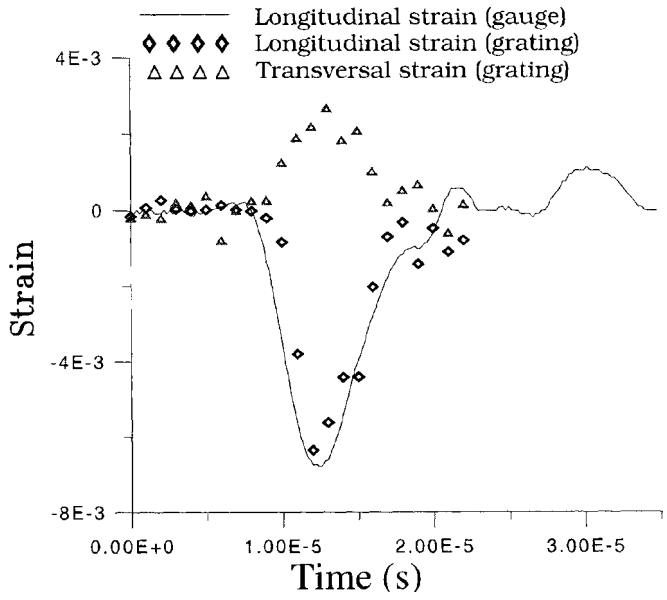

Figure 7 : Dynamic compression test with CCD acquisition.

These two dynamic tests give a good idea of the performance of this method. The agreement between longitudinal strains optically determined and classically measured demonstrates the efficiency of the method.

4. Conclusion

This measurement method performed by an interrogation of the grating using the optical diffraction with an oblique incidence allows one to determine not only the strain tensor given by the optical diffraction in normal incidence, but also the six rigid motions of a measurement base of 1 mm.

The use of acousto-optic components allows one to separate the information easily during a dynamic or a static loading [12], and to record 23 states of the specimen at up to 1,000,000 frames per second.

The recording of the diffraction image can be achieved in two ways : the acquisition on a photographic film analysed by a specific device composed of a digital image processing using a CCD camera, or the direct acquisition on a CCD camera. These two procedures accomodate different strain sensitivities and maximum strain rates.

The direct determination of strains without any contact is well adapted to the analysis of impact loadings with the measurement directly obtained from the specimen, to the study of behaviour laws in static and dynamic loading, or to the control of structures in vibratory regimes.

References

1. Sevenhuijsen, P.J. 1989. Grid method : a new future. *Proceeding of SEM Spring Conference.*

2. Brémand, F. and A. Lagarde (1988) Analyse spectrale bidimensionnelle d'un réseau de traits croisés. Application à la mesure des grandes et petites déformations. *C.R. Académic des Sciences.* t 307. serie II 683-688.

3. Brémand, F., J.C. Dupré and A. Lagarde (1992) Non-contact and non disturbing local strain measurement methods. I - Principle. *European Journal of Mechanics. A/Solids.* Vol.11 **3**:349-366.

4. Cardenas-Garcia, J.F. and M.S. Wu (1989) Further development of the video optical diffractometer for strain measurement. *Proceeding of the SEM Spring Conference.*

5. Dupré, J.C., M. Cottron and A. Lagarde (1994) Phase shifting technique for local measurements of small strains by grid method. *Proceedings 10th International Conference on Experimental Mechnics.*

6. Bell, J. F. (1956) Determination of dynamic. plastic strain through the use of diffraction gratings. *Journal of Applied Physics.* Vol.27 **10** 1109-1113.

7. Valle, V., M. Cottron and A. Lagarde (1995) Utilisation du phénomène de diffraction sous incidence oblique d'un faisceau laser par un réseau croisé pour la mesure locale en statique et dynamique des deformations et des mouvements de solide. *Mechanics Research Communications.* Vol 22. **2** 103-107.

8. Valle, V., M. Cottron and A. Lagarde (1994) A new optical method for dynamic strain measurement. Proceeding *10th International Conference on Experimental Mechanics* :549-553.

9. Brillouin, L. (1921). *Ann. de Phys.* **17** 103.

10. Debye, P. and F.W. Sears (1932) *Proc. Nat. Acad. Sci., Washington* **18** 409.

11. Post, D. (1982) Developments in moire interferometry. *Optical Engineering,* **21** :458-467.

12. Valle, V., M. Cottron & A. Lagarde (1996) Grating diffraction for local strain determination under dynamic loading. *ESDA* 96. **4** 69-74.

HIGH SPEED MEASUREMENT OF DISCONTINUOUS SURFACE PROFILES

J.M. HUNTLEY, C.R. COGGRAVE
Loughborough University
Department of Mechanical Engineering
Loughborough, LE11 3TU, UK

Abstract. The measurement of surface profile by projecting phase-stepped fringe patterns at an angle to the observation direction is well known. Ambiguous range data results, however, when the object has discontinuities in its profile. The ambiguities can be prevented by projecting fringes of varying spatial frequency. In this paper we describe an approach which combines high accuracy and reliability. The spatial frequency is reduced exponentially from the maximum value. The sequence of phase values at a given pixel is then unwrapped independently of the other image pixels, and all the intermediate phase values contribute in a least squares sense to the final range estimate for the pixel. The algorithm has been implemented on a pipeline image processing system. The fringe patterns are projected at 30 frames s^{-1} using a high resolution data projector. Images are acquired and analysed in real time, at the same framing rate. A total acquisition and processing time of 0.75 s has been achieved for a maximum spatial frequency of 16 fringes across the field of view.

1. Introduction

Projected fringes have been used over many years for measuring surface profiles [1-3]. The fringes are usually created by imaging a fixed or programmable mask, having a sinusoidal density profile, onto the object. Interference patterns from a coherent light source can also be used, resulting in an extended depth of field, but with more speckle noise and greater sensitivity to environmental disturbance. If the projection direction is different from the observation direction, the phase distribution of the measured fringe pattern includes information on the surface height profile of the object.

The fringe phase distribution is normally calculated from the images either by Fourier transformation or by phase-stepping of the fringe patterns. Both methods result in phase maps which are wrapped onto the range $-\pi$ to $+\pi$. When the object surface is continuous, the phase map can be unwrapped (i.e. the 2π phase discontinuities removed) by a spatial comparison of neighbouring pixels. When the object has surface discontinuties, however, this process will fail and it then becomes necessary to project

A. Lagarde (ed.),
IUTAM Symposium on Advanced Optical Methods and Applications in Solid Mechanics, 161–168,

fringe patterns of varying spatial frequency [4-8]. The resulting sequence of phase values at each pixel can be unwrapped over time ("temporal phase unwrapping") to give an absolute phase value independent of the other pixels in the image.

In this paper we describe an optimised version of this approach in which the fringe spatial frequency is reduced from a maximum value down to zero by an exponentially growing decrement[9,10]. Intermediate phase values are included in a least squares sense to reduce the random errors in the calculated range values. The so-called "reversed exponential" algorithm has been implemented on a pipeline image processor with the aim of calculating range data at rates in excess of 10^5 coordinates s^{-1}. The system hardware and preliminary results are described in section 3.

2. Temporal phase unwrapping: reversed exponential method

Figure 1 shows the standard set up used for shape measurement by projected fringes. The projector fills a region of space with a three-dimensional sinusoidal intensity distribution. The fringe normals are assumed to lie in the plane of the page. To apply the "forward exponential" temporal unwrapping method, the fringe spatial frequency is increased exponentially over time. Initially (t = 1), a single fringe is projected, so that the fringe phase ranges from $-\pi$ on one side to $+\pi$ on the other side of the field of view. For subsequent measurements (t = 2,4,8…s) the number of fringes is set equal to t so that the phase range increases to ($-t\pi$, $t\pi$). For each t value, a number (typically 4) of phase-stepped images, $I(k,t)$ (where k = 1,2,3,4 for the four frame algorithm), is acquired. The situation depicted in Figure 1 corresponds to the case t = 2.

The phase change $\Delta\Phi_w(i, j)$ occurring at a given pixel due to a change in fringe frequency from t= i to t= j is calculated from the two sets of intensity values using the formula:

$$\Delta\Phi(i,j) = \Phi(i) - \Phi(j) \tag{1}$$

where

$$\Phi(t) = \tan^{-1}\left[\frac{\Delta I_{42}(t)}{\Delta I_{13}(t)}\right] \tag{2}$$

and

$$\Delta I_{kl}(t) = I(k,t) - I(l,t). \tag{3}$$

The phase values calculated by Eqn, (2) lie in the range ($-\pi$, π) and therefore the incremental phase changes calculated by Eqn. (1) lie in the range (-2π, 2π). It is convenient to rewrap these back into the range ($-\pi$, π) using the unwrapping operator $U\{\Phi_1, \Phi_2\}$:

$$\Delta\Phi_w(i,j) = U\{\Delta\Phi(i,j), 0\} \tag{4}$$

where

$$U\{\Phi_1, \Phi_2\} = \Phi_1 - 2\pi\mathrm{NINT}\left[\frac{\Phi_1 - \Phi_2}{2\pi}\right] \tag{5}$$

and NINT[…] denotes rounding to the nearest integer. The subscript *w* denotes a wrapped phase value (i.e., one lying in the range $(-\pi, \pi)$), and subscript *u* will be used to denote an unwrapped phase value (i.e., adjusted by addition of the correct integral multiple of 2π).

The sequence of measured phase values, for a pixel receiving light from a scattering point on plane P of Figure 1, is illustrated in Figure 2(a). $\Delta\Phi_w(1, 0)$ and $\Delta\Phi_w(2, 1)$ are both equal to the corresponding unwrapped phase changes, because in each case the number of projected fringes is increased by just one, and they can therefore be added to give $\Delta\Phi_u(2, 0)$. $\Delta\Phi_w(4, 2)$ will in general contain phase wraps, but can be unwrapped by noting that $\Delta\Phi_u(4, 2)$ should be equal to $\Delta\Phi_u(2, 0)$. The sum $\Delta\Phi_u(4, 2)$ and $\Delta\Phi_u(2, 0)$ then results in $\Delta\Phi_u(4, 0)$. This process can be repeated with an exponentially growing sequence of fringe densities. The final unwrapped phase value, Ψ, then defines the plane on which the scattering point lies.

The accuracy of the range value can, however, be improved by least squares fitting a line to the phase values. The gradient ω, rather than the unwrapped value Ψ, is used to define the plane on which the scattering point lies. The problem with the forward exponential sequence is that most of the phase values lie at the low-*t* end of the Φ-*t* graph. Low *t* values do not provide reliable estimates of the gradient, and so do not contribute significantly to the least-squares fit. However, the algorithm can be modified by starting at the maximum fringe density ($t = s$), and reducing the number of fringes by 1,2,4,8…*s*/2. This ensures that the measured phase values are now clustered at the high-*t* end of the Φ-*t* graph. The least-squares estimator for ω is given by[9,10]

$$\hat{\omega} = \frac{s\Phi_u(s) + \sum_{v=0}^{\log_2 s - 1} (s - 2^v)\Phi_u(s - 2^v)}{s^2 + \sum_{v=0}^{\log_2 s - 1} (s - 2^v)^2} \tag{6}$$

and the standard deviation of the range value is reduced by a factor of approximately $\sqrt{\log_2 s}$, compared with that from the basic temporal unwrapping algorithm.

3. Real-time implentation of reversed exponential algorithm

A commercial pipeline processing system has been used to implement the reversed exponential algorithm in real-time. The Datacube MaxTD system consists of two

MaxVideo250 image processing boards with the addition of one Advanced Processor module.

During the initialisation period a lookup table (LUT) is created which contains the projected fringe pattern data. Each row of the LUT can be expanded at run-time using the pipeline hardware to create a complete projection image as illustrated in Figure 3. Hence, a reversed exponential sequence of phase stepped images starting with 16 fringes (ie. t=16, 15, 14, 12, 8) requires a LUT with 20 rows of pixel data. In this way projected images are generated at a rate of 30 frames s^{-1} and projected onto the test object using a Proxima DLP SVGA projector.

A digital CCD camera (EEV16) is sychronised to the projector and acquires the intensity maps into virtual surface image memories (VSIM) on the MaxVideo boards. Multi-buffering of the dual-ported memories is employed to allow the data to be processed during the acquisition period. Hence, at any given time during the experiment four operations occur in parallel: (i) generation of the fringe pattern image; (ii) transfer of the fringe pattern image to the projector; (iii) acquisition of the intensity map from the camera; and (iv) processing the acquired data.

Implementing the processing algorithm using pipeline processing hardware dictates that the arithmetic is performed using fixed point arithmetic. Furthermore the intermediate results that are stored on VSIMs must have 8 or 16 bit resolution to make efficient use of available resources so some rounding of results is inevitable. The propagation of these errors has been minimised by scaling all intermediate values such that the full dynamic range of the register stores are utilised.

The processing algorithm can be divided into four sections as illustrated in Figure 4, each of which can be performed in one frame period. Hence, the updated phase gradient estimate (ω) is computed every four frame periods which corresponds to the time taken for one acquisition cycle. The first step computes a 16 bit wrapped phase value (Φ_w) from the acquired 8 bit intensity maps (I(1,t)..I(4,t)) according to equation (2). The intermediate results (ΔI_{42} and ΔI_{13}) are rounded to 8 bits and used as inputs to a 16 bit x 16 bit LUT which performs the atan2() function. The second step derives the change in wrapped phase ($\Delta\Phi_w$) according to equation (1) and generates the unwrapped phase using a running sum of unwrapped phase value ($\Sigma\Phi_u$). Step 3 then adds the new unwrapped phase value to the running total. Step 4 updates the running phase gradient estimate ω with a weighted sum of the unwrapped phase value.

The final stage is the calculation of a surface height value from each ω value. This is done using pre-determined values of calibration constants following the procedure described in [6].

4. Results

Figures 5 and 6 show results obtained from a test object containing surface steps. Figure 5 is the wrapped phase map from the highest fringe density (16 fringes across the field of view). From this map alone it is impossible to determine the relative heights of the surface steps. In addition, holes and shadowed regions would cause difficulties for most spatial unwrapping algorithms. A reversed exponential sequence with a maximum

of 16 fringes was used to illuminate the sample. A projection and acquisition rate of 30 frames s^{-1} was employed, with the resulting (512x508) depth matrix available in 0.75 s. This is shown as a surface plot in Figure 6. Despite the problem areas the profile is reconstructed correctly in the regions where valid data is available. Shadowed regions are detected automatically by thresholding a modulation map so as to create a binary mask. The mask is generated at run time and can be toggled on or off as required by the user.

5. Conclusions

When measuring surface profile by the method of phase-shifted projected fringes, the use of fringes of varying pitch combined with temporal phase unwrapping allows unique range data to be calculated at each camera pixel. The optimal approach described in the paper involves decreasing the number of fringes exponentially to zero from the maximum value, s. This method combines a superior unwrapping reliability, a reduction in data acquisition and processing time by a factor $(\log_2 s)/s$ and a decrease in measurement error of $\sqrt{\log_2 s}$, compared with the basic temporal unwrapping method (in which the number of fringes increases linearly from 1 to s). It is the most appropriate of the methods in situations where the emphasis is on achieving a high measurement speed with reasonable accuracy.

A shape measurement system has been built based on this algorithm in which fringe patterns are projected, and images acquired at 30 frames s^{-1}. The images are analysed in real time on a pipeline processor. The entire process of projecting the patterns, acquiring the images, calculating and unwrapping the phase maps, generating the valid-data mask, performing the least squares fitting along the time axis, and converting the data to height values takes under 0.8 s for ca. 250,000 coordinates. Depth measurement accuracies of ca. 1 part in 1500 have been achieved to date with the current fringe density of 16 across the field of view. Such a system is likely to find application in areas such as high speed quality control and robot vision systems.

6. Acknowledgments

This work was supported by the Royal Society and by the Engineering and Physical Sciences Research Council under research grant GR/K67274.

7. References

1. Brooks R E and Heflinger L O *Appl. Opt.* **8** (1969) 935-939.
2. Indebetouw G *Appl. Opt.* **17** (1978) 2930-2933.
3. Srinivasan V, Liu H C and Halioua M *Appl. Opt.* **23** (1984) 3105-3108.
4. Zhao H, Chen W and Tan Y *Appl. Opt.* **33** (1994) 4497 - 4500.
5. Saldner H O and Huntley J M *Appl. Opt.* **36** (1997) 2770 - 2775.

6. Saldner H O and Huntley J M *Opt. Eng.* **36** (1997) 610-615.
7. Nadebom W, Andrä P and Osten W *Opt. Lasers Eng.* **24** (1996) 245-260.
8. Xie X, Atkinson J T, Lalor M J and Burton D *Opt. Lasers Eng.* **27** (1997) 247-257.
9. Huntley J M and Saldner H O *J. Opt. Soc. Am. A* **14** (1997) 3188-3196.
10. Huntley J M and Saldner H O *Proc. SPIE* **3100** (1997) 185-192.
11. Huntley J M and Saldner H O *Appl. Opt.* **32** (1993) 3047-3052.
12. Creath K in *Interferogram Analysis* D. W. Robinson and G. T. Reid, eds. (Bristol: Institute of Physics) 1993.
13. Huntley J M and Saldner H O *Meas. Sci. Technol.* **8** (1997) 986-992.

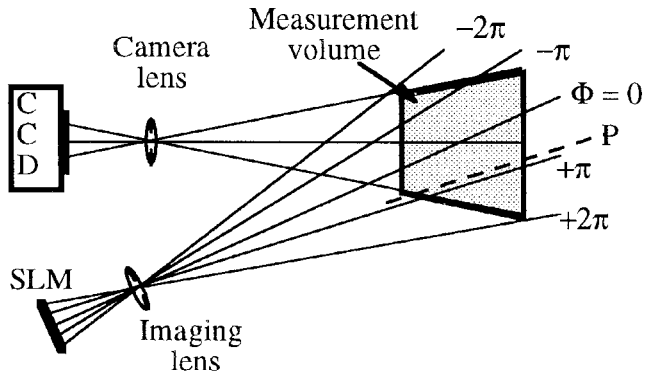

Figure 1. Set-up used to measure the surface shape of an object within the measurement volume. The dashed line is the cross-section through plane P referred to in the text.

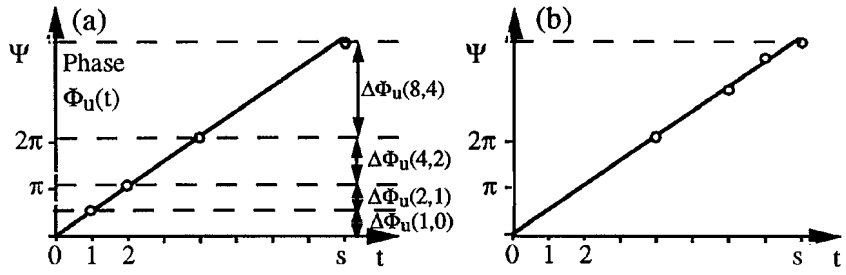

Figure 2. Time-varying unwrapped phase for a given pixel: forward and reversed exponential methods (a) and (b), respectively.

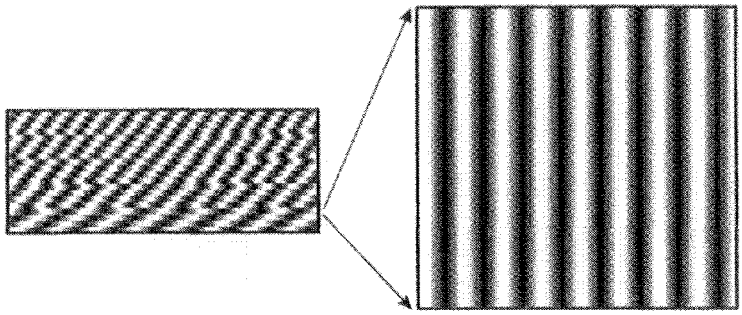

Figure 3. Pipeline processing hardware generates each fringe pattern image from one row of the LUT.

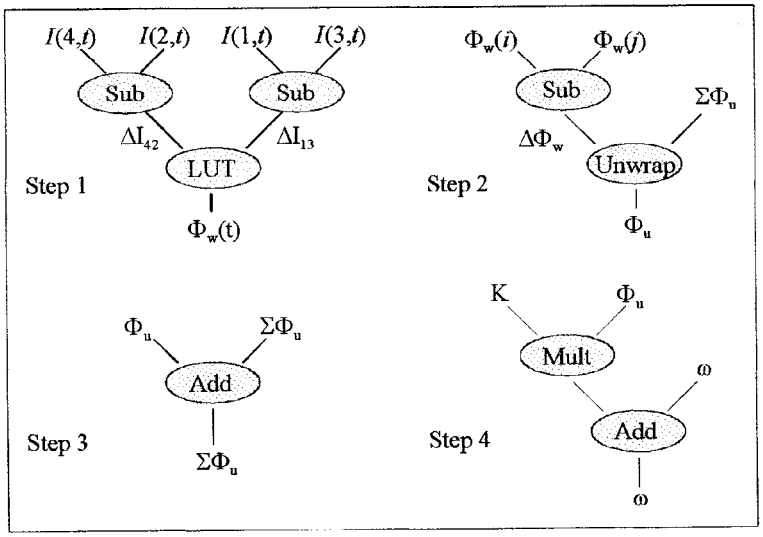

Figure 4. Pipeline image processing operations for the four steps referred to in section 3.

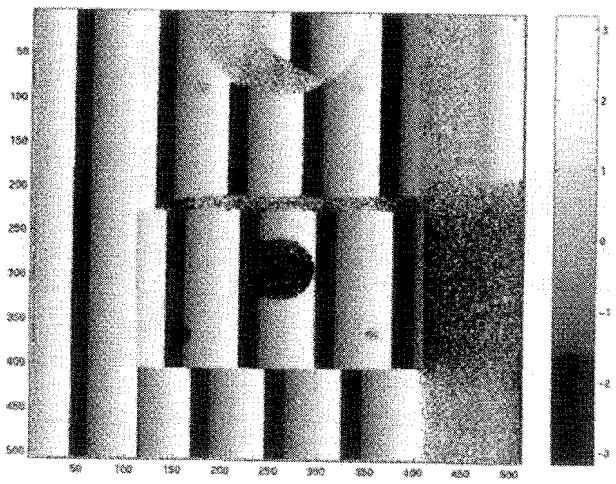

Figure 5. Wrapped phase map for a plate with surface steps. Black and white represent phase values of $-\pi$ and $+\pi$, respectively.

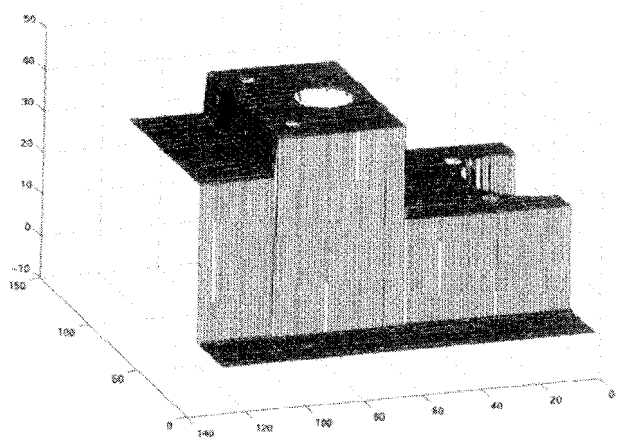

Figure 6. Surface profile for the plate shown in Figure 5 as measured by the high speed system described in this paper. Units for the axes are mm.

TRANSIENT STRESS ANALYSIS UNDER LOW VELOCITY IMPACT BY WHITE LIGHT PHOTOVISCOELASTIC TECHNIQUE

S. YONEYAMA AND M. TAKASHI
Aoyama Gakuin University
6-16-1 Chitosedai, Setagaya, Tokyo 157-8572, Japan

Abstract. This paper discusses a new method for determining fringe order and the principal direction of birefringence from a single image in practical photoviscoelastic analysis. Using an elliptically polarized white light and color image processing, fringe pattern at each instant is analyzed from three monochromatic images obtained with a single shot. It will be emphasized that no repetition of experiment under the same condition nor multiple images acquisition is necessary, which is usually adopted in the current techniques. An example problem in the case of a plate subjected to low velocity impact is successfully analyzed by use of the method proposed, then the time variation of stress around the point of impact is traced taking the constitutive equations of photoviscoelasticity into account.

1. Introduction

From the viewpoint of experimental analysis of time-dependent stress and strain in a viscoelastic material, photoviscoelastic technique [1–4] is a very useful tool. In the currently available fringe analysis techniques such as phase-shifting methods with a monochromatic light [5,6], multiple images are inevitably required to determine both fringe order and the principal direction of birefringence. Namely, multiple measurements are required assuming the same stress and strain state involving their history could arise under repeated experiments. Thus, the current techniques cannot be applied to the problems in which the good repeatability of experiment is not expected. In order to analyze stresses in a viscoelastic body, it is required to determine both of fringe order and the principal direction of birefringence from an image data obtained with a single shot at each instant.

The objective of this study is to develop a method, using photoviscoelastic technique, for studying time-variant stress distributions. In the previous

A. Lagarde (ed.),
IUTAM Symposium on Advanced Optical Methods and Applications in Solid Mechanics, 169–176.

paper, the authors [7] have proposed a photoelastic method for determining both fringe order and the principal direction of birefringence from a single color image using an elliptically polarized white light. Applying the method proposed to sequential color photoviscoelastic image data, time-dependent fringe order and the principal direction of birefringence distributions at each instant can be determined, and the following time-dependent stress and strain analysis can be performed using the constitutive equations of photoviscoelasticity. In this paper, the theory of the proposed fringe analysis method is described briefly. Then, the successful application of the method to a photoviscoelastic analysis is demonstrated in the case of a plate subjected to low velocity impact.

2. Optical Constitutive Equations of Photoviscoelasticity

In two-dimensional linearly photoviscoelastic analysis, the time-dependent differences of principal stresses $\sigma_1(t) - \sigma_2(t)$ and strains $\varepsilon_1(t) - \varepsilon_2(t)$ as well as the angle $\beta(t)$ of the principal stress direction and the angle $\gamma(t)$ of the principal strain direction can be calculated by measuring isochromatic fringe order per unit thickness of a specimen $n(t) = N(t)/h$ (where h is the thickness of the specimen) and the principal direction of birefringence $\alpha(t)$ which change with time t. The 2-D photoviscoelastic constitutive relations are expressed by the following equations [2–4].

$$\{\sigma_1(t) - \sigma_2(t)\}\cos 2\beta(t) = C_{\sigma r}^{-1}(t)n(0)\cos 2\alpha(0) + \int_0^t C_{\sigma r}^{-1}(t-\tau)\frac{dn(\tau)\cos 2\alpha(t)}{d\tau}d\tau \quad (1)$$

$$\{\sigma_1(t) - \sigma_2(t)\}\sin 2\beta(t) = C_{\sigma r}^{-1}(t)n(0)\sin 2\alpha(0) + \int_0^t C_{\sigma r}^{-1}(t-\tau)\frac{dn(\tau)\sin 2\alpha(t)}{d\tau}d\tau \quad (2)$$

$$\{\varepsilon_1(t) - \varepsilon_2(t)\}\cos 2\gamma(t) = C_{\varepsilon c}^{-1}(t)n(0)\cos 2\alpha(0) + \int_0^t C_{\varepsilon c}^{-1}(t-\tau)\frac{dn(\tau)\cos 2\alpha(t)}{d\tau}d\tau \quad (3)$$

$$\{\varepsilon_1(t) - \varepsilon_2(t)\}\sin 2\gamma(t) = C_{\varepsilon c}^{-1}(t)n(0)\sin 2\alpha(0) + \int_0^t C_{\varepsilon c}^{-1}(t-\tau)\frac{dn(\tau)\sin 2\alpha(t)}{d\tau}d\tau \quad (4)$$

where $C_{\sigma r}^{-1}(t)$ denotes the inverse relaxation stress-birefringence coefficient and $C_{\varepsilon c}^{-1}(t)$ is the inverse creep strain-birefringence coefficient, which are material properties and must be measured and determined beforehand.

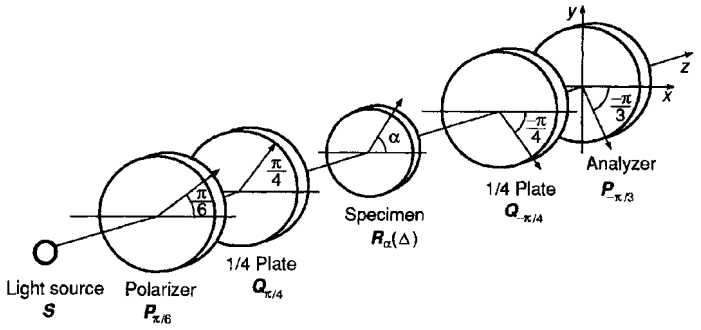

Figure 1. Arrangement of the optical elements.

3. Fringe Analysis Using Elliptically Polarized White Light

3.1. FRINGE ORDER DETERMINATION

When a color CCD camera is used to record fringe pattern with white light, a digitized color image data consists of three monochromatic images corresponding to the three primary colors, i.e., red, green and blue, and each of three monochromatic images has its own intensity level and distribution. The brightness distribution of the photoviscoelastic image through a polariscope arranged as shown in Figure 1 is expressed as [7]

$$I_i = \frac{1}{16}\frac{1}{\lambda_{i2}-\lambda_{i1}}\int_{\lambda_{i1}}^{\lambda_{i2}} I_0 F_i \sin^2\frac{\delta\pi}{\lambda}\left(9+\cos 2\varepsilon+5\cos 4\alpha + \cos 2\varepsilon\cos 4\alpha + 4\sqrt{3}\sin\varepsilon\sin 4\alpha\right)\mathrm{d}\lambda \qquad (i=r,g,b) \tag{5}$$

where I_0 $(= I_0(\lambda))$ expresses the spectral distribution of the light used, $i = r, g, b$ denotes red, green and blue colors, λ_{i1} and λ_{i2} are the lower and upper limits of the spectrum of the filters in the camera, F_i $(=F_i(\lambda))$, the spectral responses of the red, green and blue filters, δ, retardation, α, the principal direction of birefringence, ε, the quarter-wave plate error [8], respectively.

By comparing the light intensity values at each data point with the corresponding values in a calibration table which connects fringe order with the light intensity values, fringe order can be determined in a good accuracy. Different from the data-base-search method proposed by Ajovalasit et al. [9], to eliminate the effect of the principal direction of birefringence α of the image data, the gray levels have to be normalized before comparing these values from the model and the calibration table in the proposed method. Fringe order can be determined by means of an error function E_j as

$$E_j = \left(\frac{R_j}{X_j}-\frac{R_m}{X_m}\right)^2+\left(\frac{G_j}{X_j}-\frac{G_m}{X_m}\right)^2+\left(\frac{B_j}{X_j}-\frac{B_m}{X_m}\right)^2 \tag{6}$$

where R_m, G_m and B_m are the digitized values of light intensities I_r, I_g and I_b, i.e., the gray levels of a image data at each point, and R_j, G_j and B_j are also digitized in the calibration table, respectively. X_m and X_j are the sum of the intensity levels, i.e.,

$$X_m = R_m + G_m + B_m, \quad X_j = R_j + G_j + B_j \tag{7}$$

Fringe order at a point can be determined by searching index j which minimize the error function E_j. If the variation of the fringe order in the calibration beam is linear and the first pixel of the calibration table could be zero fringe order, the fringe order N_j corresponding to the pixel index j is expressed as [9]

$$N_j = N_m \frac{j}{j_m} \tag{8}$$

where N_m is the maximum fringe order in the calibration table and j_m is the number of the values stored in the calibration table.

3.2. PRINCIPAL DIRECTION OF BIREFRINGENCE DETERMINATION

If the retardation error ε could be treated as a constant for each color, Equation (5) can be rewritten as

$$I_i = Y_i \cdot Z_i \tag{9}$$

where

$$Y_i = 9 + \cos 2\varepsilon_i + 5\cos 4\alpha + \cos 2\varepsilon_i \cos 4\alpha + 4\sqrt{3}\sin \varepsilon_i \sin 4\alpha \tag{10}$$

$$Z_i = \frac{1}{16}\frac{1}{\lambda_2 - \lambda_1}\int_{\lambda_{i1}}^{\lambda_{i2}} I_0 F_i \sin^2 \frac{\delta\pi}{\lambda} d\lambda \qquad (i = r, g, b) \tag{11}$$

Here, ε_i represents the retardation errors of the quarter-wave plates at the center wavelengths of the spectrums captured by each sensor in the color camera. In the following, Equation (9) is adopted for the calculation of the principal direction of birefringence.

The value of Equation (11) can be obtained from the digitized intensity values in the calibration table if the calibration test is performed with the polarization angle 0 rad. Thus, using the light intensity values in the calibration table, the following equation is derived [7].

$$X_m - Y_r \cdot \frac{8}{7 + \cos \varepsilon_r} \cdot R_t - Y_g \cdot \frac{8}{7 + \cos \varepsilon_g} \cdot G_t - Y_b \cdot \frac{8}{7 + \cos \varepsilon_b} \cdot B_t = 0 \tag{12}$$

where R_t, G_t and B_t are the gray levels stored in the calibration table, i.e., they are corresponding to Equation (11). Equation (12) is a non-linear equation with respect to the principal direction of birefringence α. The value of α can be obtained by solving Equation (12), numerically.

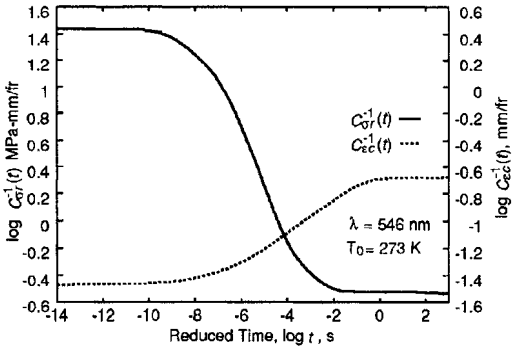

Figure 2. Master curves of $C_{\sigma r}^{-1}(t)$ and $C_{\varepsilon c}^{-1}(t)$ of the material.

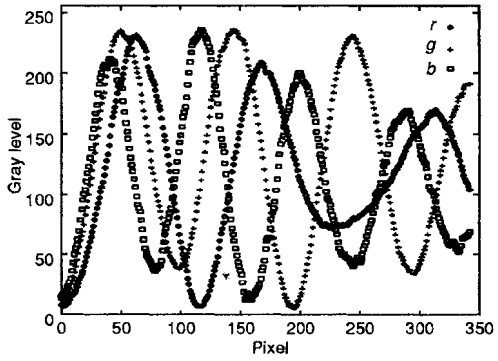

Figure 3. Calibration table (Gray level distributions of the calibration beam).

4. Material Properties and Experimental Procedure

The material used in this study is a polyurethane rubber [2]. This material is linearly viscoelastic, thermorheologically simple and birefringent, and exhibits excellent light transmission properties. Its glass transition temperature was measured as T_g = 223 K. Figure 2 shows the photoviscoelastic characteristics of the material, i.e., the master curves of the inverse relaxation stress-birefringence coefficient $C_{\sigma r}^{-1}(t)$ and the inverse creep strain-birefringence coefficient $C_{\varepsilon c}^{-1}(t)$. Details of the experimental procedure for determining photoviscoelastic coefficients are given in Ref [1].

The calibration test to make up the calibration table linking the digitized light intensity levels with fringe order was performed using a beam specimen made of the same material (polyurethane rubber). A beam specimen, 40 mm height, 140 mm width and 10 mm thickness, was subjected to a tension-bending load. The color fringe pattern around the center of

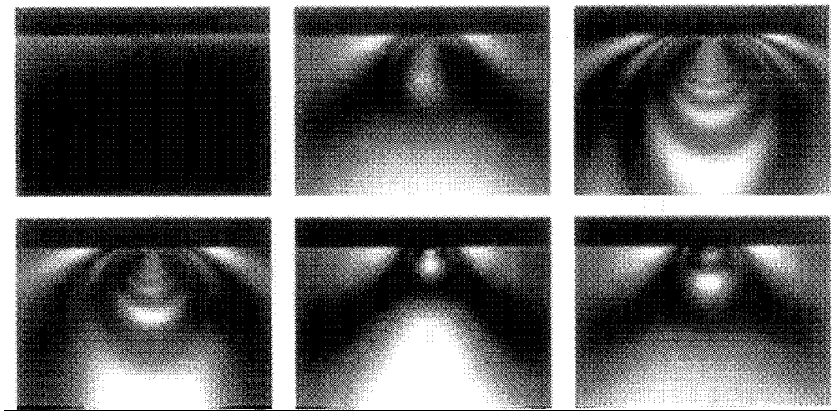

Figure 4. Series of 6 consecutive photoviscoelastic fringe patterns; camera speed—1000 frames per sec (Note that these are color images).

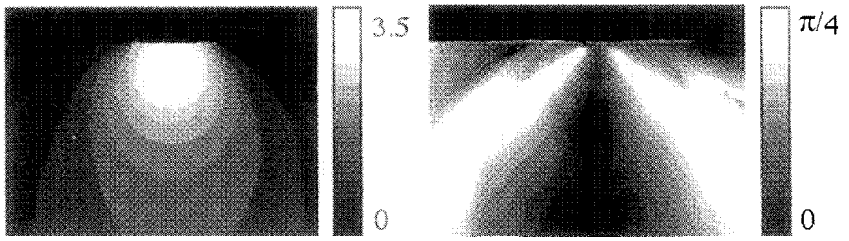

Figure 5. An example set of the distributions of fringe order and the principal direction of birefringence.

the beam was acquired and the light intensity levels at each pixel along the transverse section of the calibration beam were stored in an ascending order array with fringe order for the wavelength 546 nm as the calibration table, as shown in Figure 3.

A plate specimen made of polyurethane rubber, 150 mm width, 50 mm height and 10 mm thickness, was subjected to low velocity impact of 1.64 kg disk type weight falling from a height of 10 mm. The photoviscoelastic fringe patterns were recorded by a color video camera operated at a speed of 1000 frames per sec. The constant temperature T = 237 K was carefully maintained during the whole experiment within ±0.5 K. At this temperature the material shows a remarkably viscoelastic behavior.

5. Results and Discussion

Figure 4 shows the first 6 frames of the photoviscoelastic fringe pattern. Note that the color images are expressed by gray levels, here. The attenua-

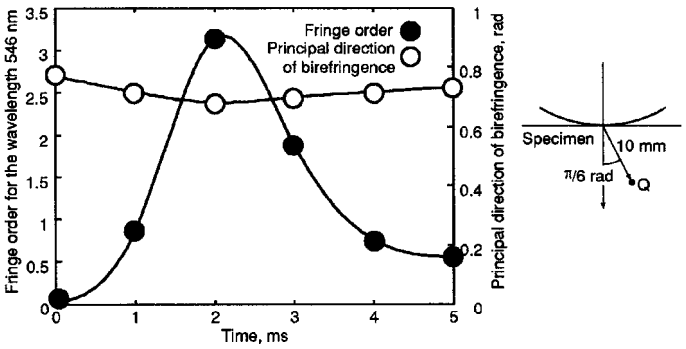

Figure 6. Time variations of the fringe order and the principal direction of birefringence.

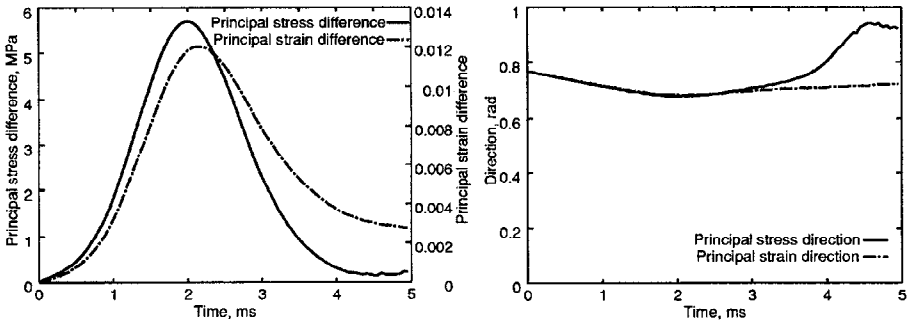

Figure 7. Time variations of the differences of principal stresses and strains, and their directions

tion of fringes due to the ellipticity of the light used is obviously seen. The fringe patterns look significantly different from static ones [10] or Hertz elastic contact [11] where maximum fringes appear inside a specimen. The distributions of the fringe order and the principal direction of birefringence at each instant were determined by the method proposed. Figure 5 shows an example set of the distributions of the fringe order and the principal direction of birefringence. Here, the values are expressed in 10 steps contour maps. Figure 6 shows the time variations of the fringe order and the principal direction of birefringence at an example point Q shown in this figure. The principal direction of birefringence varies with time reflecting the nonproportional loading condition. The time variations of the differences of the principal stresses and strains as well as their directions were calculated using the optical constitutive equations of photoviscoelasticity as shown in Figure 7. Reflecting the viscoelastic properties of the material, not only $\sigma_1(t) - \sigma_2(t)$ and $\varepsilon_1(t) - \varepsilon_2(t)$ but $\beta(t)$ and $\gamma(t)$ show different

time variations each other.

6. Concluding Remarks

This study discussed a new method for determining fringe order and the principal direction of birefringence from a single image using an elliptically polarized white light and color image processing for practical photoviscoelastic analysis. Using the method proposed, the time variation of fringe order and the principal direction of birefringence in a plate subjected to low velocity impact were determined without the repetition of experiment. Also, the time variations of the differences of the principal stresses and strains as well as their directions were evaluated using the optical constitutive equations of photoviscoelasticity.

It is pointed out that time-varying problems in which good repeatability of experiments is not expected can be analyzed by the method proposed.

Acknowledgment

This work was partly supported by the Center for Science and Engineering Research Institute, Aoyama Gakuin University.

References

1. Williams, M.L. and Arenz, R.J.: The engineering analysis of linear photoviscoelastic materials, *Exp. Mech.* **4** (1964), 249–262.
2. Kunio, T. and Miyano, Y.: Photoviscoelastic analysis by use of polyurethane rubber, in *Applied Mechanics (Proc. 12th Int. Cong. Appl. Mech.),* H. Hetenyi and W. Vincenti (eds), Springer-Verlag, Berlin (1969), 269–276.
3. Gotoh, J., Horie, H., Misawa, A. and Takashi, M.: Photoviscoelastic method for time-dependent stress and strain analysis under non-proportional loading, in *Proc. SEM Spring Conf. Exp. Mech.,* Grand Rapids (1995), 234–241.
4. Yoneyama, S., Ayame, D., Gotoh, J. and Takashi, M.: Photoviscoelastic stress and strain analysis around a surface groove under rolling contact load, *JSME Int. J., Ser. A* **40** (1997), 44–50.
5. Patterson, E.A. and Wang, Z.F.: Towards full field automated photoelastic analysis of complex components, *Strain* **27** (1991), 49–56.
6. Mawatari, S., Takashi, M., Toyoda, Y. and Kunio, T.: A single valued representative function for determination of principal stress direction in photoelastic analysis, in *Proc. 9th Int. Conf. Exp. Mech.,* Copenhagen (1990), 2069–2078.
7. Yoneyama, S. and Takashi, M.: A new method for photoelastic fringe analysis from a single image using elliptically polarized white light, *Submitted for Publication in Optics and Lasers in Engineering.*
8. Redner, A.S.: Photoelastic measurements by means of computer-assisted spectral-content analysis, *Exp. Mech.* **25** (1985),. 148–153.
9. Ajovalasit, A., Barone, S. and Perucci, G.: Towards RGB photoelasticity: full-field automated photoelasticity in white light, *Exp. Mech.* **35** (1995), 193–200.
10. Yoneyama, S., Gotoh, J. and Takashi, M.: Tricolor photoviscoelastic technique and its application to moving contact, *Accepted for Publication in Exp. Mech.*
11. Johnson, K.L.: *Contact Mechanics,* Cambridge University Press, Cambridge, 1985.

SPECKLE INTERFEROMETRY

F. P. CHIANG, F. JIN, Q. WANG AND N. ZHU
Dept. of Mechanical Engineering
Lab. for Experimental Mechanics Research
State University of New York at Stony Brook
NY 11794-2300, USA

Abstract

Before the milestone work of Leedertz in 1970 coherent speckles generated from a laser illuminated object are considered noise to be eliminated or minimized. Leedertz shows that coherent speckles are actually information carriers. Since then the speckle technique has found many applications to fields of mechanics, metrology, nondestructive evaluation and material sciences. Speckles need not be coherent. Artificially created so-called white light speckles can also be used as information carriers. In this paper we present two recent developments of speckle technique with applications to micromechanics problems using SIEM (Speckle Interferometry with Electron Microscopy), to nondestructive evaluation of crevice corrosion and composite disbond and vibration of large structures using TADS (Time-Average Digital Specklegraphy).

1. Introduction

Ever since the first paper by Leedertz (1970), speckles are no longer considered noise but information carrier. Over the past quarter century, various speckle techniques have been developed for mechanics, metrology and material studies. In this paper we present two major developments of the speckle technique as applied to micromechanics, nondestructive evaluation and vibration analysis of large structures.

2. Micromechanics Studies Using Nanospeckles

It is well known that in general the metrological information carried by a speckle pattern cannot be smaller than the size of speckles. Using optical instruments and visible light, the smallest speckle that can be generated and recorded cannot be smaller than one half of the wavelength of the radiation used. To increase the spatial resolution Chiang (1982) proposed the use of nanospeckles generated by either physical or chemical vapor deposition process and use electron microscopes to record them. Through the development of computer aided speckle interferometry technique (CASI) (Chen and

A. Lagarde (ed.),
IUTAM Symposium on Advanced Optical Methods and Applications in Solid Mechanics, 177–190.

Chiang, 1993; Chen et al., 1993) a new micromechanics measurement technique called SIEM (Speckle Interferometry with Electron Microscopy) has been developed (Chiang, Wang & Lehman, F., 1996). In the following we shall describe some recent applications of the nanomechanics technique.

2.1. DISTRIBUTION OF MECHANICAL PROPERTY ACROSS HEAT AFFECTED ZONE OF HSLA80 WELDMENT (WANG & CHIANG, 1998)

Fusion welding is of great importance in the fabrication of engineering structures. Since a welded joint is often the weakest linkage, the integrity of metallic structures such as ship or marine platform may hinge upon the integrity of its structural welds. The performance of a weldment is determined by the microstructure-property relationship. Typically, the metallurgy of a fusion welded joint can be roughly divided into two major regions, the fusion zone(FZ) and heat affected zone (HAZ). Due to the complexity of weld microstructure, the characterization of mechanical properties of a weldment, especially the HAZ, still remains as one of the most important areas of welding research. A method for determining the distribution of mechanical property across HAZ by SIEM is described as below.

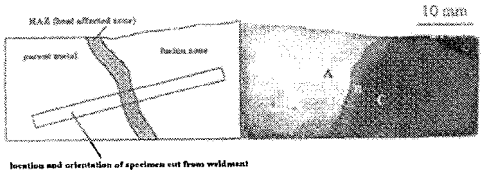

Fig. 1 Weldment macrostructure.

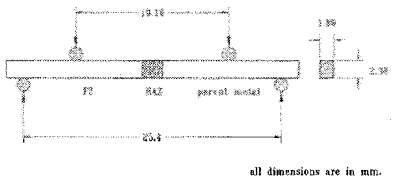

Fig.2 Specimen geometry

The tested material was a fusion welded plate of high strength low alloy steel HSLA-80. The weldment macrostructure is shown in Fig.1 . The thickness of HAZ is in the range of 1.4 to about 2.0 mm. A small coupon specimen was cut along the direction perpendicular to the heat affected zone. Its dimension and the load of four point bending are schematically shown in Fig.2. The middle part of the beam containing HAZ was subjected to pure bending. A nanospeckle pattern was deposited on the surface of the beam and the SIEM technique was used to map the displacement field under different loading. Typical patterns of u and v displacement contours are shown in Fig.3.

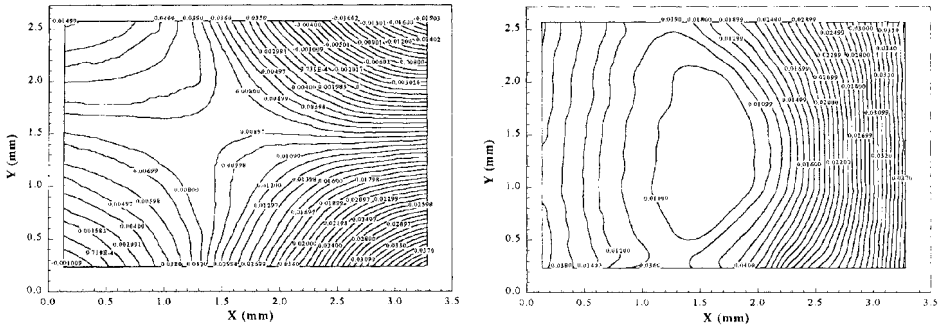

Fig.3 u-(right) and v-displacement (left) fields of HAZ under *M=2.32 (N,m)*

Experimental results indicate that the beam material may be considered as being transversely isotropic and elastic-perfectly plastic, as schematically shown in Fig.4. From displacement fields calculated by SIEM and the corresponding strain fields, it was determined that the assumption of plane-remained-plane assumption was a valid assumption for the beam. Thus, by using a model of a beam under elastic-plastic bending we were able to calculate the variation of yield strength σ_y and Young's modulus E as shown in Figs 5&6, respectively.

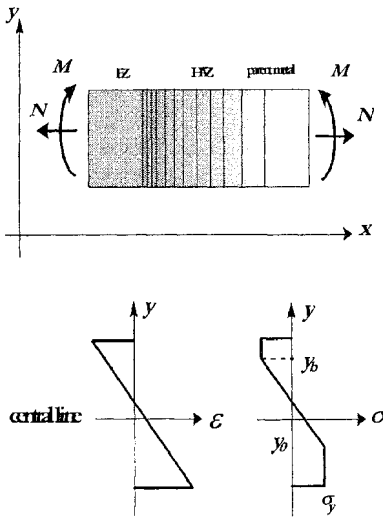

Fig.4.Elastic-plastic bending.

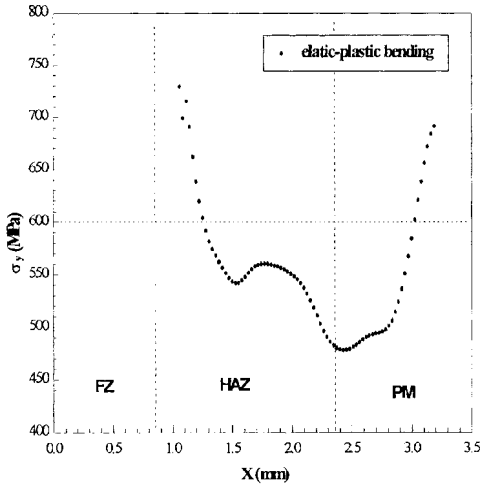

Fig.5 Distribution of yield strength σ_y across HAZ

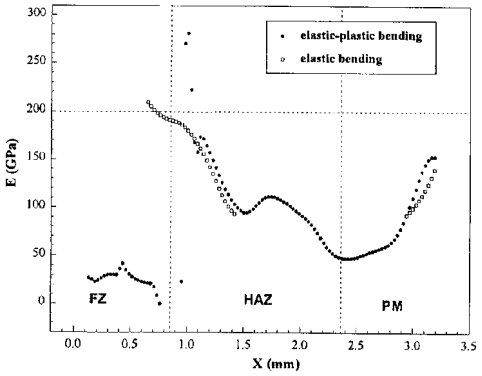

Fig.6 Distribution of E across HAZ.

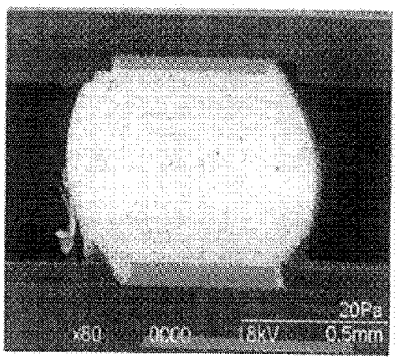

Fig.7 Cross section of a NSMD solder ball

2.2. LOCAL THERMAL DEFORMATION FIELD OF A SOLDER JOINT (WANG, GUO, CHANG & CHIANG, 1998)

A major reliability concern in microelectronics industry is the failure of solder interconnects in surface mount devices. The failure is usually caused by the thermal strain due to the mismatch of coefficients of thermal expansion of the solder joint assembly. Therefore, an accurate assessment of stress and strain distribution in package structures is essential to product design. Currently, the scale of local joint structures is continuously being reduced to achieve a higher integration of package. Direct measurement of mechanical behavior at a dimension smaller than that of a solder ball presents a challenge to experimentalists. Hybrid method has been suggested to estimate the strain concentration for individual solder ball with boundary conditions obtained from measurements using moire or microscopic moire interferometry.(Han and Guo, 1995) With SIEM the detailed strain distribution within a solder joint can be resolved.

Strip specimens with thickness between 1.0mm and 2.0mm were cut from a solder joint assembly by using a slow speed diamond blade. Their cross section surfaces were carefully polished and then deposited with speckle particles by vacuum evaporation. Fig.7 shows the cross section of a solder ball in NSMD (non solder mask defined) attachment with deposited speckles. Thermal loading was applied by a pyrolytic graphite heating element inside SEM. Fig.8 shows the u- and v-displacement contour plots obtained from the thermal loading ΔT=96°C. The difference between neighboring contour lines is around 0.3 to 0.5μm. From these contour patterns, it is clear that the largest shear deformation concentrates at the upper-right corner of the solder ball. The calculated distributions of shear strain E_{xy} and principal strain E_1 also show that bond lines between solder ball and circuit board are places of potential failures. It is also noted

that for the particular joint tested, an unfilled gap exists between the solder ball and circuit board. This manufacturing defect is the primary stress raiser which induces the strain concentration. Furthermore, large local shear exits at interfaces.

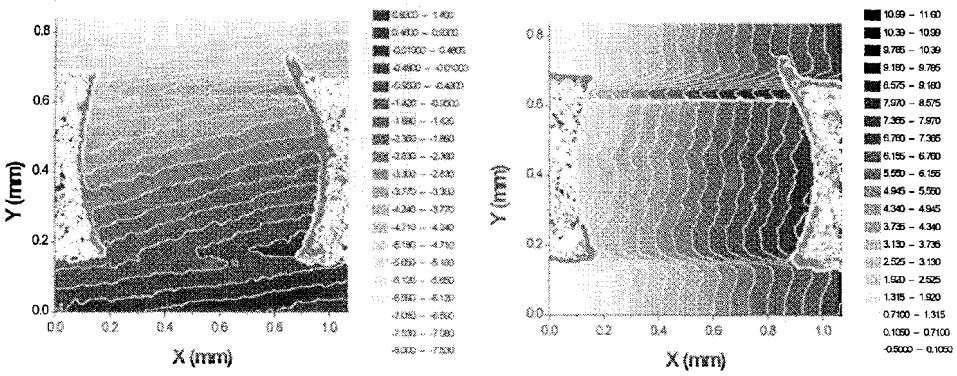

Fig.8. u-(left) and v-displacement(right) field under the ΔT=96°C.

2.3. KINKING MECHANISM IN FIBROUS COMPOSITE (WANG, CHIANG, MORAN AND SHIH, 1996)

A major concern in the design and application of fibrous composite material is that its uniaxial compressive strength of fibrous composite material is often less than 60 percent of its tensile strength. Kinking or microbuckling is primarily a compressive failure mode. Compressive failure is an unstable phenomenon, which appears in an instantaneous and catastrophic manner at macroscopic scale. However, at microscopic scale there exists a stage of kink band development starting from material imperfection. During past three decades, most research works were based on post-mortem examination (Rosen, 1965, Argon, 1972, Budiansky, 1983, Budiansky and Fleck, 1993, etc.) Little attention has been paid to the kinematics of kinking.

In this study, an special testing procedure was introduced to control the initiation and propagation of in-plane kink band. The experimental system and a kink band are shown in Fig.9. The composite material is ICI Fiberite APC-2 which consists of unidirectional IM7 graphite fiber and Victrex PEEK matrix. The u- and v-displacement fields around kink band tip were mapped by SIEM, as shown in Fig. 10. It is found that the v-displacement field is similar to that of a mode-I crack and u-field more close to a mode-II crack. Kink band tip field is of mix-mode characteristic and shear is its dominant deformation mode. Kinking is often accompanied by fiber delamination and the SIEM calculated displacement curves indicate where the delamination would take place as shown in Fig. 10.

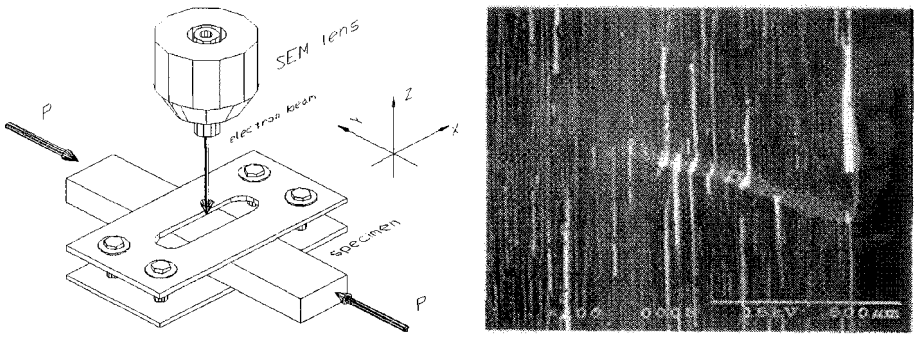

Fig.9 Compression test and in-plane kink band during transverse propagation.

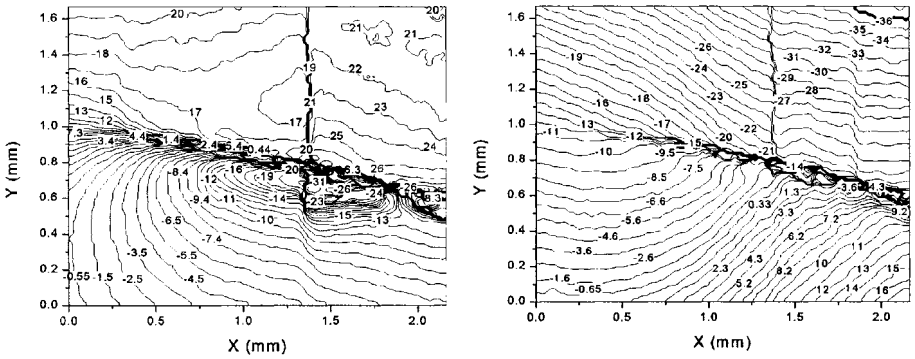

Fig. 10 u-(left) and v-displacement(right) fields during the propagation of kink band.

2.4. PLASTIC DEFORMATION AT FATIGUE CRACK TIP (WANG, DU AND CHIANG, 1997)

High cycle fatigue is an extremely important issue in aircraft industry, especially in the jet engine community. Under high loading frequencies, fatigue life becomes very short and failure is generally characterized by coalescence of small cracks. Material defects of the size in the order of hundreds micrometers are potential crack initiation sites. It is of great concern as to how small defects would grow to reach the critical dimension and how do regions of associated microstructural damage evolve. The behavior of a small crack is very different from that of a large crack. The theory of linear elastic fracture mechanics can not provide an accurate description of the local stress and deformation fields ahead of a crack tip (Ritchie, 1996). To understand the micromechanics at fatigue crack tips, SIEM is employed to investigate the evolution of plastic zone at a crack tip during cyclic loading.

The material tested was AISI-SAE 1035 carbon steel. After being fatigued for certain number of cycles, load was released and irreversible displacement fields (plastic field) at

the crack tip were examined by SIEM. Fig. 11 shows displacement contours at the crack tip. In all cases studied, plastic deformation always concentrates in one or two narrow branched zones ahead of the crack tip. Crack extends itself by nucleating microcracks in plastic bands, which results in a locally zigzag crack path. This reveals the important shielding mechanism, crack-wake bridging. Crack advances in mixed mode when subject to normal loading at the far field. The material flow at crack tip is visualized by the displacement vector plot, as shown in Fig.12. It shows that shear is the dominant deformation mode for crack advance.

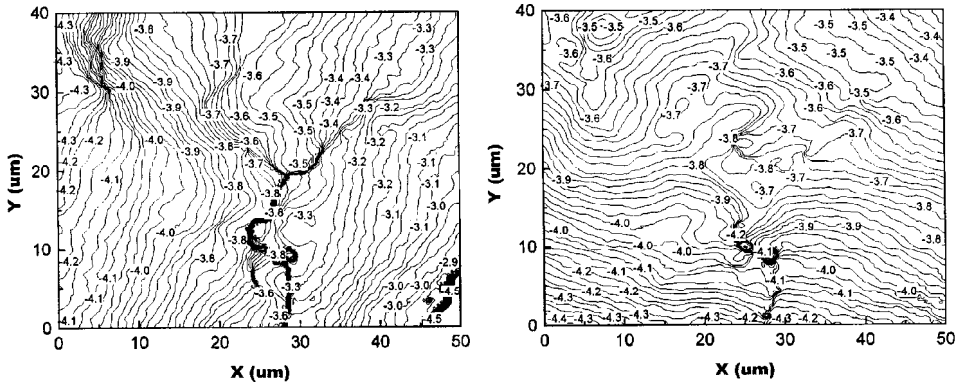

Fig. 11 u-(left) and v-displacement(right) contour after 2,000 cycles

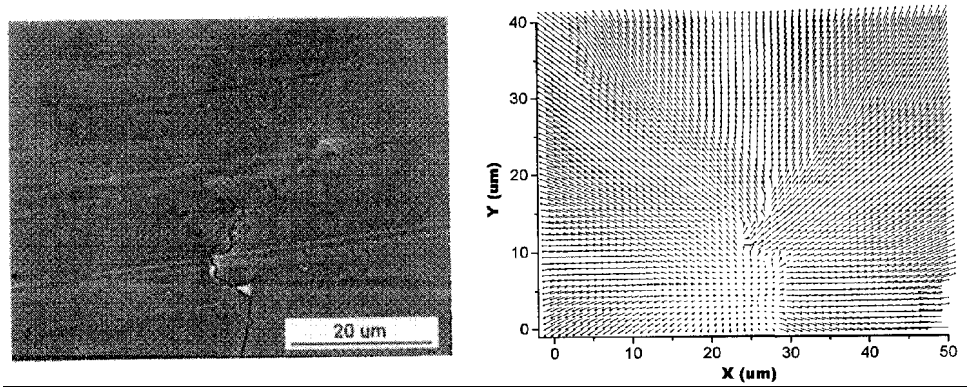

Fig. 12 Local crack path and the displacement vector plot after 2,000 cycle fatigue

3. Nondestructive Evaluation Using Laser Speckle

One of the laser speckle technique that was invented by Chiang & Juang (1976) some twenty years ago has rarely been exploited beyond the original work. In this section we shall present some results applying this technique to nondestructive evaluation of crevice corrosion, disbond of sandwiched composite plates, and vibration of large structures. The basic principle of this technique is schematically shown in Fig.3.1. As depicted, laser speckles form in the space in front of an optically rough object surface. These speckles move when the object surface is displaced or tilted (in much the same way as a mirror tilts a light beam). If the recording camera is focused on a plane a certain distance away from the object surface, one can record the speckle movement due to deformation induced tilt alone, provided of course that the object has limited rigid body movement. Indeed it can be shown (Chiang & Juang 1976) that when certain conditions are met the object's surface slope change Φ can be related to the speckle displacement $\mathbf{d}(x,y)$ and the defocused distance D as

$$\Phi(x,y) = \frac{\mathbf{d}(x,y)}{2D}$$

It is this speckle movement due to tilt that we have exploited for the following applications.

3.1 DETECTION OF CREVICE CORROSION AND COMPOSITE DISBOND VIA TIME-AVERAGE DIGITAL SPECKLEGRAPHY (TADS) (JIN & CHIANG, 1996)

The schematics of the TADS system is shown in Fig.3.1. It consists of a high resolution CCD (charge-coupled device) camera, a workstation computer for image acquisition and processing, a laser and a set of single mode fiber optics components for illumination. The CCD camera has a resolution of 2029×2048 pixels with pixel size being 9x9 microns. The fiber optic devices for light outlet are mounted on the CCD camera, rendering it a portable illuminating/imaging device. The entire optical head can be mounted on a tripod. The compact design makes the system convenient for field test.

The schematic of a crevice corrosion specimen is shown in Fig.3.2. It was a double-layer aluminum alloy structure with a thick back plate (3.175 mm) and a thin front plate (1.143 mm) bonded together by bolts simulating an aircraft fuselage structure. In between the plates there existed a crevice corrosion cavity wherein the interior central portion of the front plate had been thinned. The cavity was unnoticeable from the outside. When disassembled, it has the appearance as shown in Fig. 3.3(a).

The coherent light source was a 40 mw He-Ne laser with a wavelength of 633nm. The CCD camera was set to focus on a plane a small distance away from the surface. A hot air gun (a commercial hair dryer of 500/100w output) was used to blow the top surface of

the specimen assembly for a couple of seconds (at 500 w output). Right after the thermal loading was stopped, a series of images (3 -- 8 frames) were recorded and results averaged. The intensity-averaged images contain a variety of information concerning the displacement of the surface and can be immediately displayed on a monitor. A typical time-average speckle pattern is shown in Fig.3.3(b). The anomalies on the speckle patterns reveal the existence of weakened region. Further image processing can substantially enhance the visibility of the defect. Fig.3.3(c) shows the same speckle pattern processed by a contrast-based segmentation algorithm, and Fig.3.3(d) by a binarization algorithm. It is seen that both algorithms work well in distinguishing the weakened region of the specimen.

TADS can be used to detect other defects as well. An example is the delamination defect in structures. Fig.3.4 shows the application of TADS to the detection of composite disbond of a honeycomb plate with metal face plates commonly used in aircraft construction. It had a narrow blade shaped delamination on one side of the plate. The TADS technique was employed to detect its existence and the result is as shown. Fig.3.4(b) depicts the resulting speckle pattern after a small thermal loading without image enhancement and Fig.3.4(c) with image enhancement. It is seen that the delamination area is distinctly revealed.

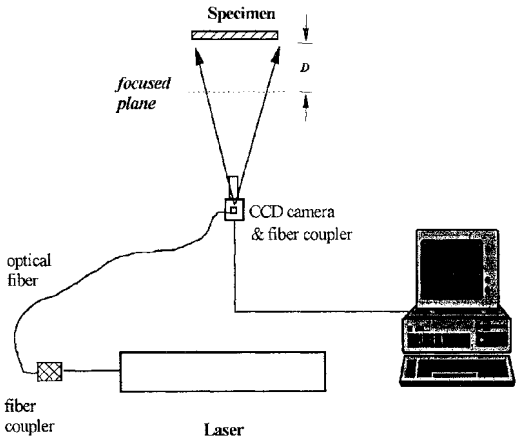

Fig.3.1 System setup of TADS

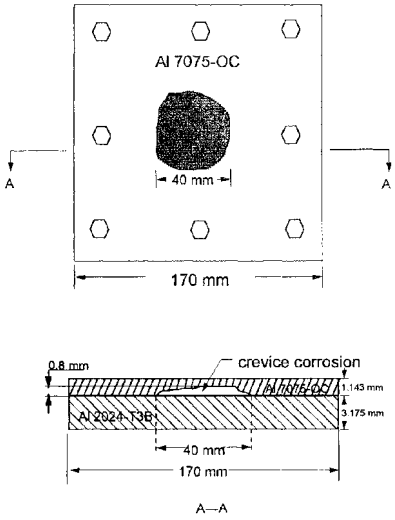

Fig.3.2 The schematic of a crevice corrosion specimen

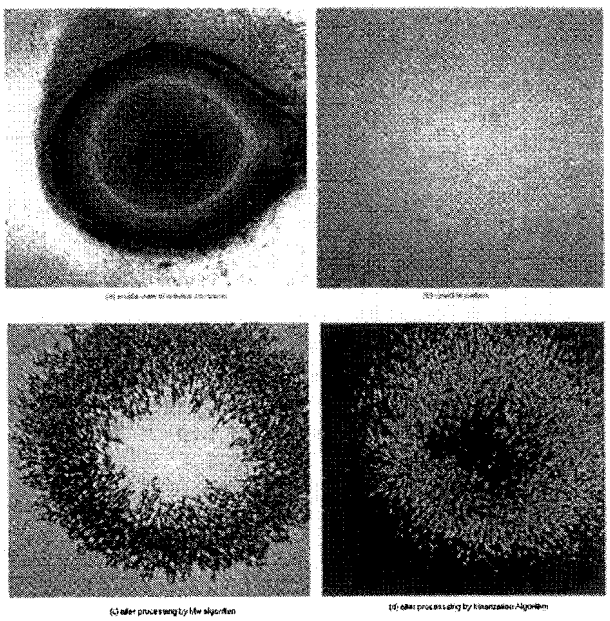

Fig.3.3 Crevice corrosion and TADS patterns

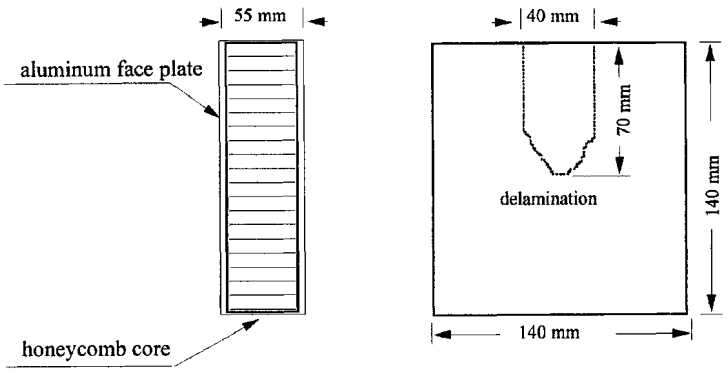

Fig. 3.4 (a) Honeycomb structure plate with delamination

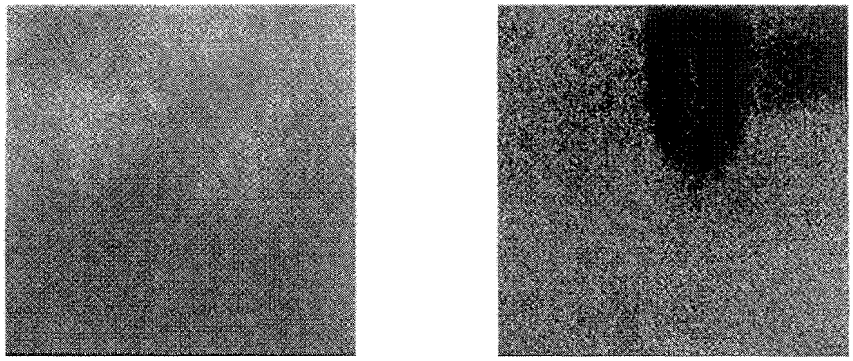

(b) (c)

Fig. 3.4 (b) Resulting TADS pattern (c) enhanced pattern

3.2 VIBRATION ANALYSIS OF LARGE STRUCTURES WITH LASER SPECKLES

The most elegant optical technique for studying vibration is arguably the method of holography. The sharpness and detailed information that can be obtained from a time average hologram is remarkable. However, recording a hologram requires a vibration isolated environment unless a short duration pulsed laser is used. And a powerful pulsed laser (e.g. ruby) is both expansive and difficult to operate (in TEM_{00} mode). A time average specklegram, however, is quite a different matter. It does not require stringent vibration isolation and with the help of retroreflective paint it can be applied to large structures using a low power cw laser (e.g. 30 mw He-Ne laser).

The first example of application is to the study of a bulkhead reinforced thin cylinder made of steel. It has a diameter of 0.53m, thickness of 2.54mm and length of 1.2m. Fig. 3.5 shows a typical time average speckle fringe pattern of the cylinder. The fringe profile is of the form of zero-th order Bessel function and the bright fringes representing anti-nodal lines where the slope is zero. The thick bright fringe in the center is where the bulkhead is located. Another application is to a 6.68m cylinder of the same diameter and thickness. Fig.3.6a shows a typical vibration pattern obtained by the time average speckle technique. Only a portion (about 1.5m) of the 6.68m tall cylinder was viewed because the testing room was not large enough to allow the camera to record the entire length of the cyliner. The cylinder was simply free standing on laboratory floor and vibration was induced by a piezoelectric transducer. In both cases the cylinder was painted with retro-reflective paint and the laser used was a 30mw He-Ne gas laser.

By using a CCD camera time average specklegram can also be used to reveal vibration modes via digital image processing techniques. However, because of the low resolution of the CCD camera (as compared to photographic films) detailed information between

the anti-nodal fringes are not obtainable. But it is quite fast (almost real time) and portable, thus making it convenient for field application. An example is shown in Fig.3.7 where a vibration mode of a truss (2.3m × 6.1m) is revealed by this technique. The test was performed in a shipyard where many other manufacturing activities were going on simultaneously. More detail of these applications can be found in Zhu(1998).

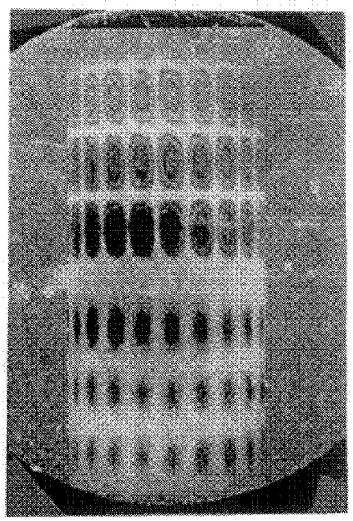

Fig.3.5 Typical speckle fringe pattern of a 1.2m cylinder under vibration

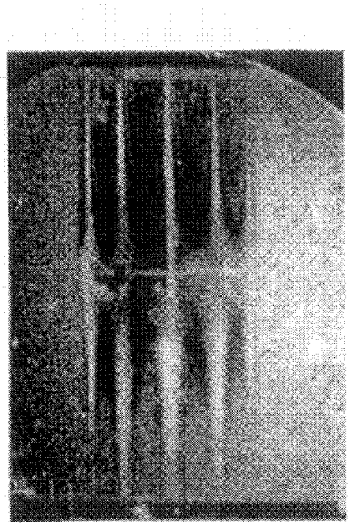

Fig.3.6 Speckle fringe pattern of a portion (1.5m) of a cylinder (6.68m) vibrating at 324 Hz

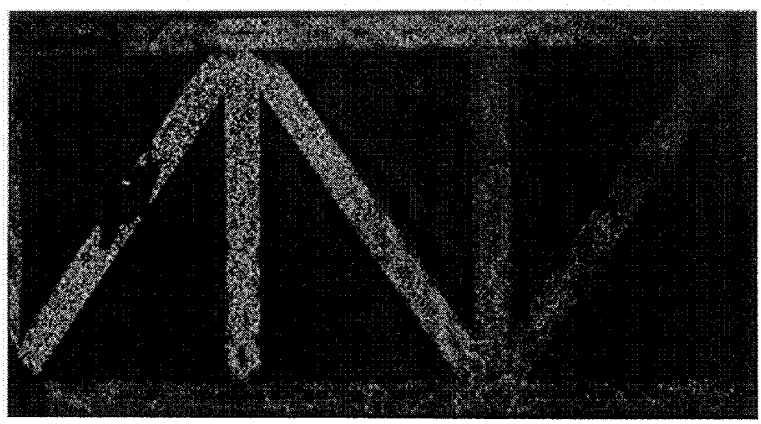

Fig.3.7 Speckle fringe pattern of a steel truss (2.3m × 6.1m) vibrating at 754Hz

4. Conclusion & Discussion

The application of speckle technique to various mechanics, metrology and material problem are only limited by imagination. In this paper we only presented two of the recent major developments; namely a micromechanics technique called SIEM, and a NDE technique called TADS. The examples we cited are limited due to the limitation of paper length. We are currently exploring application of the speckle technique to other fields.

5. Acknowledgment

The work presented here has been supported over the years by many agencies including The National Science Foundation, The Office of Naval Research, The Air Force Office of Scientific Research, and The Army Research Office. We would like to acknowledge our gratefulness to the granting agencies and the encouragement of the program directors.

6. References

Argon, A. S., 1972, "Fracture of composites," In *Treatise of Materials Science and Technology* (Edited by H. Herman), Vol. 1, pp79-114, Academic Press, New York.

Budiansky, B., 1983, "Micromechanics," *Computers and Structures.* Vol. 16, pp3-12

Budiansky, B. and Fleck, N. A., 1993, "Compressive failure of fiber composites," *J. Mech. Phys. Solids,* Vol.41, pp183-211

Chen, D. J. and Chiang, F. P., 1993, "Computer-Aided Speckle Interferometry Using Spectral Amplitude Fringes," Applied Optics, 32(2), 225-236.

Chen, D. J., Chiang, F. P., Tan Y. S. and Don, H. S., 1993, "Digital Speckle Displacement Measurement Using a Complex Spectrum Method," Applied Optics, 32(11), 1839-1849.

Chiang, F. P. and Juang, R. M. , 1976, "Vibration analysis of plate and shell by laser speckle interferometry", OPTICA ACTA, 23(12), 997-1009.

Chiang, F. P., 1982, "Speckle Method with Electron Microscope," SEM Spring Meeting, HI, May 23-28.

Chiang, F. P., 1985, "Random (speckle) patterns for displacement and strain measurement: some recent advances", Optical Engineering 24(6), 936-943.

Chiang, F. P., Wang W., and Lehman, F., 1997, "New Development in Full Field Stain Measurements Using Speckles," Nontraditional Methods of Sensing Stress, Strain, and Damage in Materials and Structures, ASTM STP 1318, 156-169.

Chubb, J. P., Morad, T. A., Hockenhull, B. S. and Bristow, J. W., 1995, "The Effect of Exfoliation Corrosion on the Fracture and Fatigue Behavior of 7178-T6 Aluminum," *International Journal of Fatigue,* Vol. 17, No. 1, pp.49-54.

Guo, Y. and Li, L., 1996, "Application of Hybrid Method for Local Thermal Strain Determinations in PBGA Solder Joints", *SEM Experimental/Numerical Mechanics in Electronic Packaging,* Vol.II,

Han, B and Guo, Y., 1995, "Thermal Deformation Analysis of Various Electronic Packaging Products by Moire and Microscopic Moire Interferomtry", *J. Electronic Packaging,* Vol. 117, pp 185-191.

Jin, F. and Chiang, F.P. (1996) "Time-Average Digital Specklegraphy (TADS) for NDE of Crevice Corrosion and Composite Debond", Proc. Of SEM VIII International Congress on Experimental Mechanics, 236-237.

Jones, R. and Wykes, C., 1990, Holography and Speckle Interferometry, p. 165. Cambridge University Press, Cambridge.

Leendertz, J.A., 1970, "Interferometric displacement measurements on scattering surfaces utilizing speckle effect," J. Phs. E 3, 214.
Li, D. W. and Chiang, F. P., 1986, "Laws of Laser Speckle Movement", Optical Engineering, 25(5), 667-670.
Li, D. W. and Chiang, F. P., 1986, J. Opt. Soc. Am. A 3: 1023-31.
Osintsev, A. V., Ostrovskii, Yu. I., Shchepinov, V. P. and Yakvlev., V. V., 1988,"Determination of a contact surface by the method of speckle photography", Sov. Phys. Tech. Phys., 33, pp. 847-849.
Ritchie, R. O., 1996, "Small Cracks and High-Cycle Fatigue", *Proceedings of the ASME Aerospace Division,* AD-Vol.52, pp321-333
Rosen, B. W., 1965, "Mechanics of composite strengthening," In *Fiber Composite Materials,* Am. Soc. Metals Seminar, pp37-75
Wang, Q. and Chiang, F. P., 1998, "Characterization of Mechanical Property Gradient of HSLA80 Weldment", The 13th National Congress of Applied Mechanics, Florida, 1998
Streckenrider, J. S. & Wagner, J. W., 1995,Optics and Lasers in Engineering 22: 3-15.
Wang, Q., Chiang, F. P, Moran, P. M. and Shih, C., 1996, "Deformation Field at the Tip of a Propagating Kink Band under Compression in Graphite/PEEK Composite", *ASME 1996 Winter Annual Meeting,* Atlanta, Georgia, November 17-22.
Wang, Q., Du, M. and Chiang, F. P., 1997, "Micromechanics Study of Plastic Zone at Crack-tip in Steel under Cyclic Load", *Proceedings of 1997 International Mechanical Engineering Congress,* Dallas, Texas, November 16-27.
Wang, Q., Guo, Y., Chang, S. and Chiang, F. P., 1997, "Measurement of Local Thermal Deformation in a Solder Joint Using Speckle Interferometry with Electron Microscopy", *SEM Numerical/Experimental Mechanics in Electronic Packaging, Volume I.*
Zhu, N., 1998 ,"Study of the Vibration of Bulkhead-Stiffened Cylindrical Shells by Laser-based Methods", Ph.D. Dissertation, State University of New York at Stony Brook.

USE OF SPECKLE INTERFEROMETRY UNDER EXTREME THERMAL CONDITIONS

P. ASWENDT
Fraunhofer Institute IWU, Reichenhainer Str. 88, D-09126 Chemnitz, Germany

Abstract. The range of application of a non-contacting optical technique, speckle pattern interferometry, has been extended to high temperature and thermal shock testing. Extreme thermal conditions cause disturbances that have been studied systematically. Based upon these pre-tests, two prototype systems were developed. They proved well-suited for measuring fields of strain data up to 1500°C and to monitor strain development during rapid heating or cooling. Various examples illustrate the new possibilities in materials testing.

1. Introduction

During the last decade speckle interferometry has been established as a measuring technique for a variety of applications mostly at room temperature. With increasing temperature a number of disturbing influences occurs making successful measurements very complicated. However, there is a demand for non-contacting characterization of advanced materials in the temperature range from 1000°C to 1500°C. Conventional techniques like extensometers and strain gauges do not completely satisfy the requirements with respect to operating temperature, chemical compatibility and the number of measuring points, for example. Encouraged by former attempts /1-5/ it was promising to qualify speckle interferometry as a reliable tool in optical strain gauging at elevated temperatures.
In this paper a set of actions are explained to overcome the difficulties for interferometric measurement under extreme conditions. The work started with a systematic study of disturbing influences and their suppression. Various solutions are presented concerning both speckle recording as well as speckle processing. Finally, the performance of the interferometric systems is demonstrated at two different extremes:

- testing of ceramic composites (CMC) at 1500°C and
- thermal shock testing of superalloys with heating rates up to 200 K/sec.

A. Lagarde (ed.),
IUTAM Symposium on Advanced Optical Methods and Applications in Solid Mechanics, 191–198.

2. Suppression of disturbances

The speckle pattern is the carrier of the measuring signal. Therefore, a high contrast, stable and well-correlated speckle field has to be maintained during the measuring time. However, under extreme conditions one has to cope with various disturbances, which may decrease the signal to noise ratio. The most significant influences for both extremes are listed in Table 1. They do not apply in parallel and have varying weight depending upon the kind of heating, the material under investigation, and the environmental conditions.

TABLE 1. Influence parameters for speckle metrology at high temperatures

Problem			Solution	
disturbing influence	speckle contrast	speckle correlation	modified recording	modified processing
thermal emmission	↘		interference filter and high power laser	
heating radiation	↘	↘	interference filter	offset compensation
instability of microstructure		↘		
current of air	↘		vacuum or laminar flow	
heating rate	↘	↘	short exposure time	separation of image fields
rigid body motion		↘	PZT shift compensation	

The convection problem is relaxed to some degree if using a dual illumination interferometer for in-plane sensitivity [6-8]. At higher temperatures, however, it may be necessary to introduce vacuum conditions or a forced laminar flow. Rigid body motion is a general issue in interferometric testing. For example, motions associated with speckle pattern translations can be compensated by properly shifting the CCD sensor. The most important influence parameters for high temperatures are discussed in more detail below.

2.1. THERMAL EMISSION

If temperature approaches 1200°C or more, the spectral density of thermal emission in the area of laser light (500 - 800 nm) grows rapidly. Narrow band filters are used to reduce the influence of this background radiation. Intensity histograms of laser illuminated, hot specimens were recorded to check the efficiency of interference filters at diffe-

rent wavelengths of light. The underlying idea is based upon the fact, that a fully developed speckle pattern obeyes a negative exponential distribution of grey levels. Such a perfect histogram can be actually observed at room temperature. Increasing temperature lowers the speckle contrast necessary to measure; the number of black spots is reduced and the histogram changes. To give a visual impression, Fig. 2 compares the CCD output at 700°C and 1300°C, respectively. The contrast is reduced considerably, while speckle correlation is kept.

T=700°C T=1300°C

Figure 2. Speckle patterns at $\lambda = 488$ nm and $\Delta\lambda = 7$ nm

The histograms describe this behaviour quite good, the results obtained from experiments with various wavelengths of laser light are given in Fig. 3. It becomes obvious that well speckle contrast is maintained up to 1300°C and 1500°C depending upon the wavelength of laser light. Best performance has been obtained by using the Nd:YAG-laser and one interference filter with 0.93 nm bandwidth and a center wavelength of 532.03 nm.

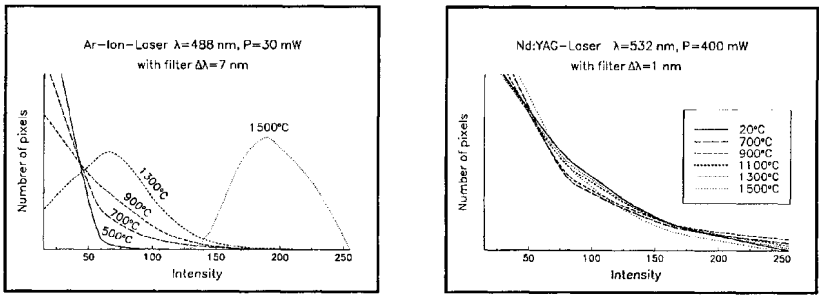

Figure 3. Influence of thermal radiation on the speckle contrast

2.2. INSTABILITY OF MICROSTRUCTURE

The surface of superalloys does not pose any problems with respect to microstructural changes up to 1100°C. In contrast, ceramic composites (CMC) which are tested above 1200°C have a very complex surface structure with the consequence of high tendency to instabilities. To study the conservation of speckle structure the hot CMC surfaces have been analysed. The correlation coefficient between

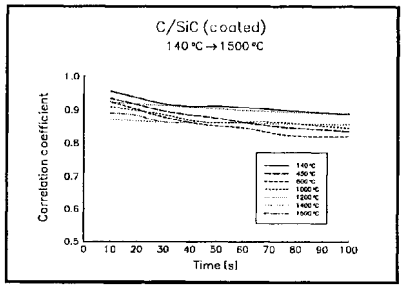

Figure 4. Correlation coefficient vs. time and temperature

an initial speckle field $I(t_0)$ and consecutive recordings I(t) has been measured during 100 seconds for different materials cycled between 100°C and 1500°C. The experiments with carbon fibre-reinforced silicon carbide (C/SiC) prove that surface microstructure is stable enough over an interval that is sufficient for interferometric measurements, Fig.4.

2.3. HEATING RATE

If the temperature changes rapidly, speckle contrast and speckle correlation are affected. The introduction of very short exposure times < 1ms by using electronic shutter cameras is one way to perform successful measurements. However, short time recording has to be combined with a modified processing scheme if an interlaced camera is used. Odd and even image lines are recorded with a pause of 20 ms. As the object state changes during this interval different fringe patterns may result for odd and even field, respectively. Fig. 5 gives an example. No fringes are visible in the usually processed TV frame but they actually appear if both fields are separated. During the experiment the patterns are recorded and stored each 40 ms. Afterwards two patterns can be combined yielding fringes for any given time interval.

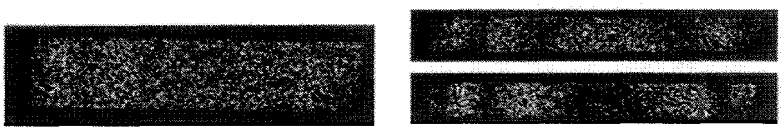

Figure 5. Separation of odd and even image fields

3. Measurements at 1500°C temperature

To verify the capability of speckle interferometry for strain measurement up to 1500°C ceramic specimens have been investigated under different loading conditions. All the means described in chapter 2 have been taken into account to obtain displacement and strain fields.

3.1. TESTING FACILITY

Fig. 6 illustrates the hardware solution specially designed for this purpose. An UTS 20 testing machine is fitted with a modified MAYTEC furnace. The water cooled device realizes temperatures up to 1600°C with an accuracy of ± 3 K in 1 mbar vacuum or air, respectively. Compressive or bending load is applied by means of ceramic fixtures. An arrangement of five windows made of quartz glass provides optical access to a 30×30×30 mm^3 volume of the 1 dm^3 chamber. A parallel beam of laser light (λ =532nm), 20 mm in

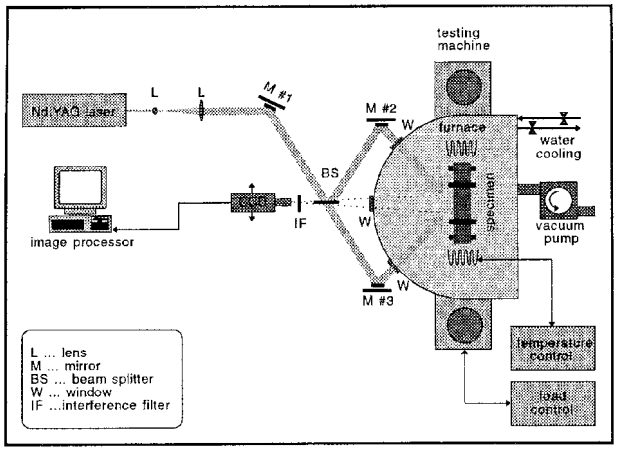

Figure 6. Testing facility for T=l500°C

diameter, is splitted with a 50:50 ratio, each of the two waves passes a furnace window; they illuminate the specimen symmetrically providing in-plane sensitivity. There exists a rigid connection between the optical elements (beamsplitter, mirror #2 and #3), the furnace, and the testing machine to guarantee interferometric stability. A third window allows to collect the laser light reflected from the specimen and an interference filter in front of the camera lens blocks out the thermal radiation. The dual illumination of the sample can be realized in horizontal (x) and vertical (y) direction.

3.2. RESULTS

The test facility with the interferometric system proved well suited for measurements under extreme temperatures and combined thermal and mechanical load. 4-point-bending tests have been successfully performed with C/SiC specimens, 4×3×50 [mm] in size. Using the x-sensitivity, a field of displacement and strain values has been determined by an interactive quantitative evaluation of the fringes shown in Fig. 7.

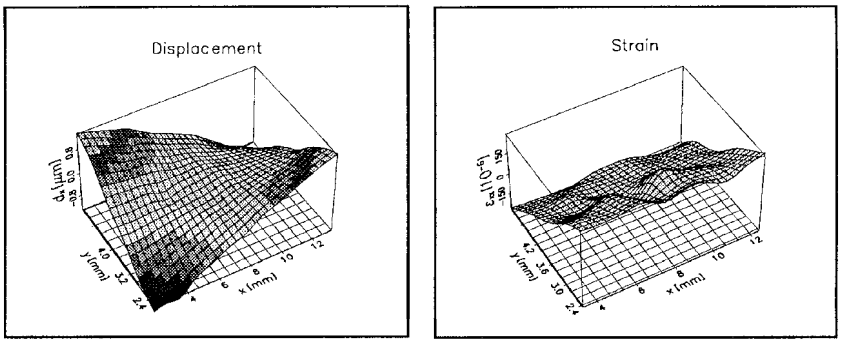

Figure 7. C/SiC specimen under h-point bending load at T=l500 °C

The test facility in Fig. 6 can be modified in such a way that the interferometer detects displacement in y-direction. To this end both illuminating beams have to be turned by 90°, using the vertically arranged windows in the furnace. This set-up is suited to derive bending lines $d_y(x)$ from the fringe patterns directly. As the theoretical relation is well-known, the measuring data can be compared with the least squares fit. The experimental bending line is evaluated from one fringe pattern. The graph shows the good correspondance between theory and experiment for a C/SiC specimen at 1200°C.

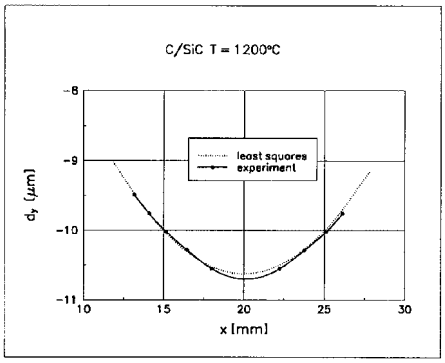

Figure 8. Comparison of theoretical and experimental bending line

4. Measurements at 200 K/s heating rate

In the second case the maximum temperature does not exceed 1100°C but fast heating and cooling represent another challenge for metrology. Superalloy specimen are subjected to thermal shock by induction heating and subsequent rapid air cooling. Experiments were carried out at MTU Munich GmbH to prove the feasibility of interferometric testing under such conditions.

4.1 TESTING FACILITY

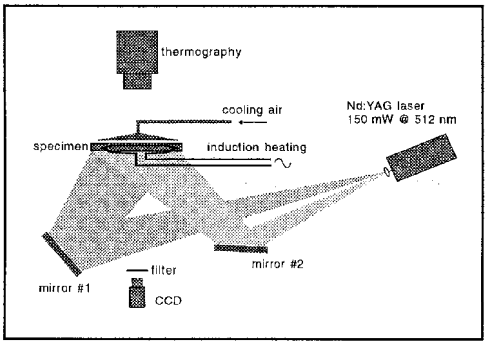

Figure 9. DSPI interferometer for thermal shock testing

A thermal shock testing stand at MTU was additionally equipped with a DSPI interferometer. The layout is shown in Fig. 9. The superalloy specimen has a size of 60×30×5 [mm] and it takes about 45 seconds to reach the maximum temperature. The maximum temperatures as well as the highest temporal temperature gradients are found at the top where the induction heating is coupled into the metallic specimen and where the cooling air flows in. The modified DSPI scheme described in 2.3. was used to record the process during a period of respective 7

seconds. Interest is focused on the beginning of heating and cooling cycles when the highest strain rates occur.

4.2. RESULTS

Experimental work started with investigations during the heating period. The interferometer was carefully designed in such a way that the inevitable convection does not seriously disturb the measurements during induction heating. So, after digital recording of a series of 200 speckle patterns, fringes of good quality could be constructed by offline correlation choosing a convenient time difference. Interactive determination of fringe spacing directly yields strain values, e.g. along a vertical line in the centre of the specimen. The diagram in Fig. 10 (left) gives an impression, how the strain distribution changes with the heating time. It is worth mentioning that compression occurs at the bottom of the specimen in an early stage of heating.

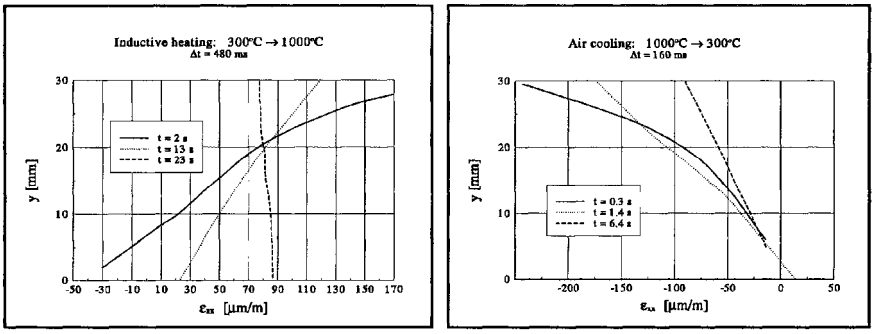

Figure 10. Strain along a vertical line obtained from DSPI fringe patterns

When a maximum of 1000°C is reached, both temperature and strain are quite even distributed across the specimen. At this moment, a powerful air current is automatically switched on to cause rapid cooling of the hot superalloy. Now, the question arises wether or not speckle interferometry will work during this cooling period. Pretests were carried out showing that clear and stable fringe patterns are obtained as long as the air is flowing. So, it can be concluded that the turbulences in the air current do not prevent the recording of stable speckle patterns. Again, the quality of the correlation fringes allows interactive quantitative evaluation and corresponding results for the vertical line are given in Fig. 10 (right). A time difference of 160 ms is used for the strain curves in this case and the first interval suited for evaluation started only 0.32 s after switching on the cooling air. Applying a modified DSPI scheme to thermal shock experiments both, heating and cooling section of a load cycle for superalloy testing, have been successfully investigated and quantitative strain distributions could be obtained providing far more information than a single strain gauge.

5. Conclusion

After a systematic study of influence parameters for speckle pattern interferometry under extreme thermal conditions, modified recording and processing schemes have been successfully applied in two cases. The first one concerns materials testing at elevated temperatures. It has been shown, that strain fields as well as bending lines can be obtained from fibre reinforced ceramic 4-point-bending specimens at 1500°C and the experimental results are in good agreement with theoretical expections.
The second investigation has proved that speckle pattern interferometry is also operating under thermal shock conditions for temperatures up to 1000°C and maximum heating/cooling rates of 200 K/s. Quantitative strain distributions could be measured during inductive heating but also in the cooling cycle when a strong air current flows over the specimen.

6. References

[1] K.A. Stetson, The use of heterodyne speckle photogrammetry to measure high-temperature strain distributions, *Proc. SPIE,* **370** (1983), 46-55.

[2] C.T. Lant and J.P. Barrenger, Progress in High Teperature Speckle-Shift Strain Measurement System, *Proc. SEM Fall Conference on Hologram Interferometry and Speckle Metrology,* Baltimore, (1990), 203-209.

[3] J.T. Malmo, O.J. Lokberg and G.A. Slettemoen, Interferometric testing at very high temperatures by TV holography (ESPI), Experimental Mechanics, **28** (1988), 315-321.

[4] P. Aswendt, R. Höfling and W. Totzauer, Digital speckle pattern interferometry applied to thermal strain measurements of metal-ceramic compounds, *Optics and Laser Techn.,* **22** (1990), 278-282.

[5] P. Aswendt and R. Höfling, Speckle interferometry for analysing anisotropic thermal expansion - application to specimens and components, *COMPOSITES* **24** (1993), 611-617.

[6] P. Aswendt and R. Höfling, Interferometrische Dehnungsmessung - Aufbau und Anwendung eines DSPI-Meβsystems, in: W. Waidelich (ed.), *Laser in der Technik* , Springer-Verlag, Berlin, 1994, pp. 172-175.

[7] P. Aswendt, Nachweis der Matrixplastizität von faserverstärktem Aluminium bei thermischer Beanspruchung, *Fortschrittberichte VDI,* Reihe 5, Nr. 436, VDI Verlag, Düsseldorf, 1996

[8] P. Aswendt, R. Höfling, Steps towards the use of DSPI for high temperature strain measurement, Proc. SPIE, **2782** (1996), 152-159.

SPECKLE INTERFEROMETRY IMPROVEMENTS FOR APPLICATIONS IN CIVIL ENGINEERING

P. JACQUOT, M. LEHMANN, X. COLONNA DE LEGA & M. FACCHINI
Stress Analysis Laboratory, IMAC, Swiss Federal Institute of Technology, CH-1015 Lausanne

Abstract

In civil engineering, a significant part of the experimentation should be performed on real, full-scale structures, either in situ or in ad-hoc testing halls. Under these conditions, micro-deformation measurements using interferometric methods are certainly not an easy task and could even appear meaningless.
The general orientation of this paper is, however, to present recent improvements towards the possibility of using speckle interferometry for micro-displacement analyses of large surfaces outside the laboratory. Two main categories of arguments are considered. First, the results of an in-depth statistical analysis of speckle interferometry, showing in which way it is judicious to optimise the interferometric signals, are summarised. Then, the advantages of a dynamic phase-shifting technique, involving the recording of sequences of time-varying speckle interferograms, and the resources of wavelet analysis, are emphasised.

1. Introduction

Remote inspection of large structures and related measurements have been recurrently suggested as constituting one of the major areas of application for interferometric imaging, since the emergence of the holographic and speckle techniques 35 years ago. In this respect, some well known landmarks are Gregory (1979), Løkberg and Malmo (1987), Gülker et al. (1990), Steinbichler et al. (1990), Trolinger et al. (1991) and Maji et al. (1997). A special group of interest for in situ applications is also to be found in the fields of artwork diagnostic, preservation and conservation of cultural heritage, see Paoletti and Spagnolo (1996), Lucia et al. (1997) and Boone et al. (1997). Though impressive success has sometimes been achieved, these types of measurements remain singularly laborious to carry out. Admittedly, the required equipment is too expensive, cumbersome to transport and the operation of the systems necessitates highly specialized teams. For instance, the pulsed laser of 10 J class, often referred to in these tests, gives in itself a concrete idea of their degree of difficulty. It is nevertheless the case that in situ interferometric measurements of large structures deserve a strong interest. In an attempt to improve the situation, two thesis works have been initiated in our group, (Colonna de Lega, 1997 and Lehmann, 1998). Holographic techniques were

A. Lagarde (ed.),
IUTAM Symposium on Advanced Optical Methods and Applications in Solid Mechanics, 199–212.

discarded ab initio from the possible domain of investigation, insofar as holography involves critical high spatial frequency recordings and owing to the poor photosensitivity of the corresponding materials. This option was taken being well aware that the possible coming out of new photorefractive crystals could call the above choice into question at any time. Speckle photography techniques were discarded too, though their medium range and simultaneous sensitivity to both in-plane displacement components are attractive factors for civil and environmental engineering applications. However, it appeared that speckle photography could be a useful tool only in the presence of real time recording materials exhibiting spatial frequency in excess of 1000 mm^{-1}. This range is, by far, not yet achievable by CCD imagers. Here again, the hypothetical appearance of high density electronic imaging devices would lead to reconsider this second choice.

Finally, speckle interferometry, (SI), was selected as the most promising method. Two domains of investigation, where improvements seemed possible and worthwhile, were privileged, corresponding respectively to the above mentioned thesis works: i) the statistical study of well chosen random variables, pertinent to SI recordings and still unexplored; ii) the search for new methods of processing time-evolving interference patterns, without stringent restriction on their rate of temporal change. In both cases, the research efforts have brought interesting outcomes and led to actually propose operative solutions for using SI in large scale measurements. Section 2 regroups the results gained from the statistical analyses in order to prepare the most appropriate recording conditions for acquiring as much as possible of a reliable information and to optimise the quality of SI signals. Section 3 deals with the question of processing this temporally changing information and shows that the combination of dynamic phase-shifting and wavelet analysis solves quite efficiently the problem. In both sections, an experimental example serves to briefly illustrate the practical scope of the theoretical results.

2. Statistical Analysis for the Optimisation of SI Signals

2.1. RANDOM VARIABLES OF INTEREST IN SI

SI methods consist basically in recording a two-wave interference pattern, of respective complex amplitude A_S and A_A, possessing the following general characteristics: A_S is a speckle wave, diffused in reflection or transmission by a coherently illuminated rough surface, and considered, often but not necessarily, in the in-focus image plane of the surface. The observation system has a finite aperture strongly influencing the statistical properties of this "object" speckle wave. A_A has many degrees of freedom: it can be a smooth or a speckle wave, produced in the latter case by the same or by another surface. A_A should simply be coherently added to A_S. A_S and A_A are uncorrelated random variables. The classical two-beam interference formula represents adequately the resulting intensity, I:

$$I = I_S + I_A + 2\sqrt{I_S I_A}\cos\tilde{\varphi}\,, \tag{1}$$

with:

$$I_{S,A} = \left|A_{S,A}\right|^2, \tag{2}$$

I_S and I_A being the respective intensities of the two waves and $\tilde{\varphi}$ their phase difference. The arguments of the functions, defining the position of the observation point, are omitted for simplicity. In the hypotheses of the well known Gaussian model, (Goodman, 1975), it is easily shown that the phase $\tilde{\varphi}$ of the interference signal is a random variable equiprobably distributed on a 2π interval, irrespective of the exact nature of A_A. It follows that $\tilde{\varphi}$ is not adapted to specify the quality of the signal, since its effect is only to multiply by a quantity taken arbitrarily in the interval [-1,+1] the modulation term $I_M = 2\sqrt{(I_S I_A)}$. This latter term and the background term $I_B = I_S + I_A$ are, on the contrary, the relevant parameters for characterising the signal in a given point, since they determine the maximum, the minimum and the average of all possible realisations of the signal in this point - just what is strictly needed to know for a proper recording of the signal. A more convenient form of Eq. 1 then reads:

$$I = I_B + I_M \cos\tilde{\varphi}\,, \tag{3}$$

I_B and I_M being, at least provisionally, the two new random variables of interest, as defined above.

However, Eq. 3 describes an aerial intensity distribution in a point, while the actual information will be available from a recorded distribution, always involving some spatial integration of the signal. Therefore, the pertinent random variables are integrated forms of I_B and I_M, where the integration is possibly performed over areas containing several speckle grains with strongly varying intensities. At this point, it should be remembered that it has been customary believed for a long time in the necessity to resolve the speckle grains of both contributing fields as a mandatory condition for a successful application of SI. At the same time, in practice, the integration effect due to the recording, especially with CCD imagers, was generally greatly underestimated. A very important parameter to deal with this problem is the number of speckle correlation cells per pixel, *m*, defined by Goodman (1975) as :

$$m = \frac{(lL)^2}{4\int_0^l\int_0^L (l-x)(L-y)\left|\mu_S(x,y)\right|^2 dxdy}\,, \tag{4}$$

where l and L are the pixel dimensions and μ_s is the normalised autocorrelation of the amplitude of the considered speckle field(s). Table 1 makes explicit the correspondence between the parameter *m* and the *f*-number of an usual observation system.

f-number	1.2	1.7	2	2.8	4	5.6	8	11	16	22	32	100
m	113	59	43	23	13	7.1	4.0	2.6	1.70	1.35	1.16	1.01

Table 1. Correspondence between the number of correlation cells per pixel, *m,* and the *f*-number of the observation system. These values stand for a standard pixel of 6.3 x 8.3 µm² , at 532 nm and an observation system considered to be focused at infinity.

It is indeed really difficult to record a fully resolved speckle field, since even with apertures as small as *f*/ 16, producing large speckle grains, there are still roughly 2 correlation cells in a standard 6 x 8 µm² pixel, (Lehmann, 1997). Hence, most of the

recordings thought to strictly obey the resolved regime ($m = 1$) belonged indeed already to a regime of weak spatial integration. That SI can work even in a strong integration regime, involving for instance 100 correlation cells, is easily understood if the summation of the elementary random signals of Eq. 3 is performed. Each contribution i exhibits a background, a modulation and a phase term I_{Bi}, I_{Mi} and $\tilde{\varphi}_i$ of its own; the important point is that all the contributions of a same integration cell change their phase by the same amount, φ. The resultant signal I_+ then changes its phase by φ too and, therefore, the analytical representation of integrated SI is formally the same as for resolved SI (Eq. 3):

$$I_+ = I_{BR} + I_{MR}\cos(\varphi + \tilde{\varphi}_R) \tag{6}$$

I_{BR} , I_{MR} and $\tilde{\varphi}_R$ are respectively the sum of the background components, the sum of the modulation terms and the resulting phase in the complex plane. I_{BR} , I_{MR} and $\tilde{\varphi}_R$ are the three sought random variables of the pixel interferogram which fully characterise the statistical behaviour of SI signals in any regime of integration.

2.2. STATISTICS OF THE RANDOM VARIABLES OF INTEREST

These statistics are given by Lehmann (1996). Their computation is quite involved and the complete derivation is outside the scope of this paper. When both interfering fields are speckle fields having the same mean intensity <*I*>, the joint probability density, $p^{(S)}$ of the background I_{BR} and the modulation I_{MR} obeys :

$$p^{(S)}_{I_{BR}I_{MR}}(I_{BR}, I_{MR}) = \left(\frac{m}{\langle I\rangle}\right)^{2m} \frac{I_{MR}\left(I_{BR}^2 - I_{MR}^2\right)^{m-\frac{3}{2}}}{\Gamma(2m-1)} \exp\left(-\frac{mI_{BR}}{\langle I\rangle}\right), \quad (m \geq 1;\ 0 \leq I_{MR} < I_{BR}) \tag{7}$$

In the case of a smooth field added to a speckle field, the joint probability, $p^{(A)}$ becomes :

$$p^{(A)}_{I_{BR}I_{MR}}(I_{BR}, I_{MR}) = \left(\frac{m}{\langle I\rangle}\right)^{m} \frac{I_{MR}\left(I_{BR} - I_A - \frac{I_{MR}^2}{4I_A}\right)^{m-2}}{2I_A\Gamma(m-1)} \exp\left(-\frac{m(I_{BR} - I_A)}{\langle I\rangle}\right), \quad (m \geq 1;\ \frac{I_{MR}^2}{4I_A} < I_{BR} - I_A) \tag{8}$$

m being, as above, the number of correlation cells per pixel and I_A the intensity of the smooth field. Again the resulting phase $\tilde{\varphi}_R$ is uniformly distributed in a 2π interval. An example of the two joint probability densities $p^{(S)}$ and $p^{(A)}$ is plotted in Fig. 1 for m = 7.1.
Both statistics have been experimentally verified, (Lehmann, 1997), showing a good agreement between theory and experiments.
These two densities summarise the whole set of first order statistical properties available on any SI method, whether the interference takes place between two speckle or a speckle and a smooth wave and whether the observation resolves or not the speckles. They represent nearly all of what it is useful to know about SI signals.

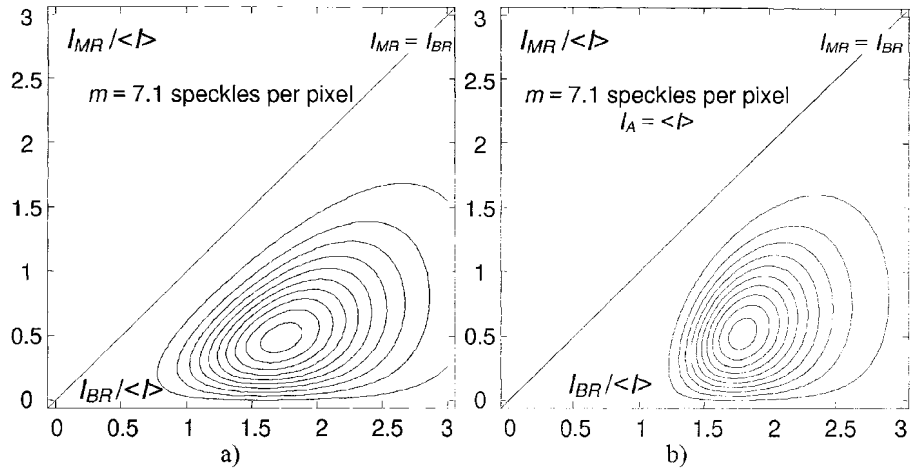

Figure 1. For m = 7.1, joint probability density of the background I_{BR} and the modulation I_{MR} , a) for two speckle waves and b) for a speckle and a smooth wave. Contour lines are between 5% and 95%, with an equidistance of 10% of the distribution maximum.

2.3. MAIN PRACTICAL CONSEQUENCE

The knowledge of the statistics of the background and modulation terms in all generality has a far reaching significance. First, it confirms on theoretical grounds that SI works in the unresolved case. Then, for a given power of the laser and a given object area and reflectivity, it allows the selection of the optimal value of the parameter m, leading to the highest probability for the modulation and the background terms. To this value corresponds the optimal aperture of the observation system. Furthermore, it can be seen that SI is still practicable at quite high m values, since, for example, at m = 20 in a two speckle waves arrangement, every second pixel exhibits a modulation exceeding 0.4 times the mean intensity $<I>$. Translated into f-numbers, this means that apertures of $f/2$ or even higher are possible, thereby opening the practice of SI to the domain of large surfaces. Another way to reach the same conclusion is to compute the mean pixel modulation from the above probability densities. For large values of m, the following result is obtained :

$$\langle I_{MR} \rangle = \sqrt{\frac{\pi}{m}} \langle I \rangle \quad \text{or} \quad \langle I_{MR} \rangle = \sqrt{\frac{\pi I_A \langle I \rangle}{m}} \ , \tag{9}$$

for two speckle or a speckle and a smooth wave, respectively. On an average, the modulation drops as the square root of the number of integrated correlation cells. As the lens aperture is increased, the modulation loss caused by an increased m is counteracted by the increased object intensity $<I>$: in the case of two object speckle waves, there is even a net gain in the mean modulation with increasing lens aperture, as long as there is no saturation.

The principal result of having revisited the statistical properties of SI methods is to allow for an optimal choice of the aperture of the observation system – a result particularly useful in the study of large objects, where the energy of the source is one of the limiting factors.

2.4. OTHER CONSEQUENCES

Using large apertures in SI applied to extended surfaces offers another advantage : it reduces the detrimental effects of pupil plane decorrelation. Large surfaces can only be observed at some distance. At these distances, minute rotations of the specimen, in the range of 100 μrad or more, are enough to create an overall displacement of the speckle wave in front of the pupil of the same order as the size of pupil, if this latter is strongly stopped down, e.g. at $f/22$ or less. This would lead to create two uncorrelated states of the object wave in the image plane, making meaningless the comparison between the successive interference patterns coding the object evolution. At least one order of magnitude can be gained in the tolerance to pupil plane decorrelation by using the observation system at its full aperture.

Moreover, the sensitivity to lateral image plane decorrelation does not increase for large lens apertures. The integration of many correlation cells in a single pixel simply produces a new measured random intensity distribution. Measurements can be performed as long as the lateral superposition of the successive interference states is better than the pixel width. In the particular case of very small speckles, a lateral displacement even larger than this correlation cell size does not lead to decorrelation, as long as most of the speckles remain within the same pixel. The condition of a lateral displacement smaller than the pixel size is quite easily satisfied for large objects: for pixels of 10 μm and magnifications of 1/100 or lower, rigid body displacements of the order of 1 mm can be tolerated between consecutive states.

Large apertures, however, impose stringent longitudinal correlation conditions since the longitudinal speckle correlation cell size decreases : for an $f/1$ system nearly focused at infinity, the longitudinal speckle displacement in the image plane must remain smaller than 4 μm. Fortunately, the usual magnifications for the observation of large objects are of the order of 1/100. Translated into the object space, 4 μm then amounts to an upper limit of 40 mm for the object out-of plane rigid body displacement between the two compared states, far in excess of the common conditions of measurements. Hence, recording large surfaces at large apertures in SI not only allows one to cope with the finite energy of the laser sources, but also helps to avoid decorrelation.

Although bearing no relationship to the above theoretical considerations, two additional favourable circumstances encountered in the application of SI methods to civil engineering problems are worth to be mentioned here. First, there is most often no inconvenience on the heavy structures to fix a light optical component like a corner cube, which will redirect the auxiliary wave to the CCD camera in the case of an arrangement with a speckle and a smooth wave. In this common path scheme, the effects of air turbulence and too large out-of-plane motion of the object are strongly attenuated. In the second place, it can even be conceived that the whole optical head is attached to the structures in well chosen points. The weight of specially designed heads, fed with optical fibers, can be of the order of 1 kg, including the CCD camera, the observation lens and the beam splitting and combining components. Compared to the tens of tons to which these

structures are often subjected, the perturbation associated with the fixation of the optical set up to the structure is negligibly small. The benefit expected from such a layout is to avoid the effects of vibration and gross object motions.

2.5. EXAMPLE

A plaster wall, slightly rotated in its own plane, will serve to illustrate the possibilities of SI outside the laboratory, in the standard environment of a testing hall, taking into account the above theoretical results. The in-plane sensitive SI arrangement is designed for producing one fringe only every 60 μm of vertical displacement. The wall is 4 x 2.8 m^2 and is observed by a 16 mm camera lens fitted to a standard CCD camera. The power of the cw Nd:YVO_4 laser is set at 800 mW. The key factor responsible for the successful completion of this test was to choose an $f/1.4$ aperture for the lens, not only for an efficient light collection, but also for reducing the effects of pupil plane decorrelation.
Fig. 2 shows the wall and a wrapped phase map obtained by a standard phase-shifting technique, corresponding to a raising of 0.28 mm of the lower right comer of the wall.

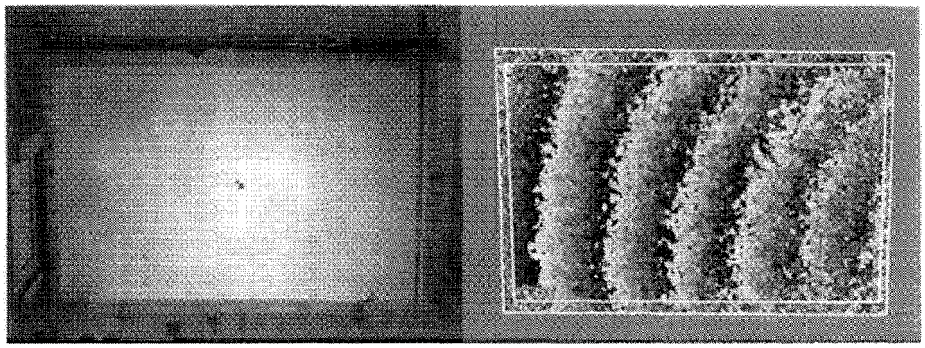

a) b)

Figure 2. Result of an in-plane SI measurement with a 60 μm per fringe sensitivity. a) 4 x 2.8 m^2 plaster wall subjected to an in-plane rotation around its lower left corner ; the right bottom corner is lifted by 0.28 mm; b) the resulting phase map obtained by phase-shifting, (Lehmann, 1998).

It is interesting to note that the de-sensitised setup used is quite immune to ambient vibrations and turbulence. Thus it is possible to acquire several phase-shifted images and to calculate phase maps. Further experimental verifications confirmed that the noise observed in b) is essentially caused by pupil plane decorrelation and not by the acquisition system or insufficient pixel modulation. We finally mention that the systematic use of interference filters allows us to carry out measurements in the presence of ambient daylight.

3. Processing Schemes for Time evolving SI Signals

3.1. DYNAMIC PHASE-SHIFTING

The processing of interferograms is widely performed by phase-shifting techniques. n versions of the same interferogram are prepared, differing from each other by a fixed

phase increment. Phase increments are realized by a number of means, most often by changing step by step the optical path length of one interferometer arm with a piezo element. Analytical solutions for the phase of the interferogram are obtained as soon as three images are recorded. Many algorithms have been studied (Creath, 1988). Recently, the technique, formerly restricted to quasi-static analyses, has been extended to dynamic situations, thanks to the concepts of dynamic phase-shifting (Colonna de Lega, 1996 a). Phase-shifting is thus a more interesting solution than heterodyne or pure image processing procedures.

Dynamic phase-shifting consists in incrementing the phase through two processes simultaneously: i) a natural incrementation due to the object evolution; ii) an external staircase incrementation, with equispaced steps over a 2π: interval. The external incrementation furnishes a solution to two serious difficulties: the determination of the sign of the unknown phase and the recoverability of this unknown phase in areas of nearly zero phase change. Obviously, without external incrementation, it would be impossible to find out the sign of the phase, since the natural phase increments are themselves unknown. It would also be impossible to retrieve the phase of the interferogram where only minute phase changes took place, since all algorithms fail to reconstruct a cosine function from too closely distributed samples in a small portion of its period. The only assumption made regarding the natural incrementation is that the object phase behaves locally as a linear function of time. "Locally" refers to the time interval taken to acquire the *n* images needed by the specific algorithm in use. Fulfilling this assumption hence comes to select an observation system of fast enough acquisition rate in comparison with the velocity of the studied phenomenon. According to the sampling theorem, the total phase increment between two consecutive acquisitions, in any point of the interferogram, should not exceed π, for an adequate reconstruction of the signal. On this premise, a suitable choice for the external phase increment is $\pi/2$ between each acquisition, while the tolerable natural phase step lies within $[-\pi/2, \pi/2]$. Moreover, relying on the fair results achieved in classical static situations, a modified 5-image algorithms may be adopted, as offering a valuable trade-off between the duration of acquisition of groups of five interferograms and the accuracy of the computed phase. After thorough simulations, including robustness against different types of noise, the following inversion formula, giving the phase φ of the interferogram at the third acquisition, was retained among many other solutions, (Colonna de Lega, 1997):

$$\varphi = tg^{-1}\left[\frac{2(I_2 - I_4)}{2I_3 - I_1 - I_5}\sin\Delta\varphi\right] \quad ; \quad \Delta\varphi = \cos^{-1}\left[\frac{I_5 - I_1}{2(I_4 - I_2)}\right] , \qquad (10)$$

I_1 to I_5 being the five acquired temporal samples. For any sequence of five consecutive interferograms, Eq. 10 provides a spatial numerical solution for the phase distribution of the mid interferogram or, more simply, the phase map at mid time of the sequence. In SI, such phase maps are of course, according to Eq. 6, meaningless random distributions. Subtraction of correlated phase maps, corresponding to sequences centred at different instants will leave however only the deterministic phase change φ characteristic of the object deformation between these two instants.

Besides these spatial solutions, temporal solutions can be envisaged as well.

3.2. WAVELET PROCESSING

Temporal solutions are more attractive than spatial solutions in many respects. The phase unwrapping process consisting in removing the 2π jumps of the phase is easier to perform along the time axis. Also easier is the determination of the absolute displacement undergone by the object at any time, opening the possibility to make a movie of the deformation. The basic principles of dynamic phase-shifting lend themselves to temporal analyses by wavelet transform, (Colonna de Lega, 1996 b). A typical 1D temporal signal is built from the digitised grey levels of an isolated single pixel, sampled at the frame rate of the acquisition system during the full recording sequence. Between any couple of consecutive frames, an external $\pi/2$ phase step is recurrently applied. A "naturally" stationary pixel would thus exhibit a constant frequency modulation.

Each time that both temporal and spectral characteristics of a signal need to be simultaneously analysed, wavelet processing becomes the right tool and supersedes Fourier transform methods. Here, the interest is to know both the temporal frequency change of the pixel signal and the time at which the change occurred. By their peculiar windowing properties, fitting at best the time-frequency content of the signal, wavelets are ideally suited to the task.

In (Colonna de Lega, 1997), the temporal interferometric signals, $s(t)$, are analysed by a Morlet wavelet transform, $S(a,b)$, expressed by:

$$S(a,b)=\frac{1}{a}\int_{-\infty}^{+\infty} s(t)\exp\left(-\frac{(t-b)^2}{2a^2}\right)\exp\left(-i\frac{\omega_0}{a}(t-b)\right)dt\,. \tag{11}$$

Fig. 3 may help to understand the meaning of this transform.

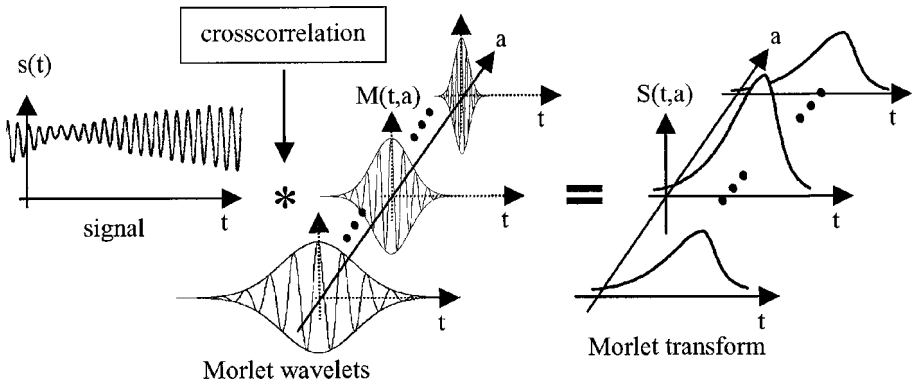

Figure 3. Schematic representation of the real part of the Morlet transform as a crosscorrelation function between the signal and parametric Morlet wavelets.

Clearly, Eq. 11 can be contracted into a shorter formula:

$$S(a,b)=\frac{1}{a}\int_{-\infty}^{+\infty} s(t)\,\overline{M}\left(\frac{t-b}{a}\right)dt \qquad (12)$$

where $^-$ denotes complex conjugation and the generic function, *M(t),* acting as a parametric windowing function, is the Morlet wavelet defined by the product of two exponentials:

$$M(t)=\exp\left(-\frac{t^2}{2}\right)\exp(i\omega_0 t) \qquad (13)$$

The transform *S(a,b)* is a 2D complex signal, function of the two variables *a* and *b*. From the definition of the Morlet transform, Eq. 11, the variable *b* is clearly a time variable, describing the time translation of the window function *M(t).* The variable *a* determines the width of the analysis window (real Gaussian exponential) and, at the same time, the frequency ω_0/a of the analysing signal (complex oscillating exponential), by dilation of a " mother " frequency ω_0. Thus, the variation of *a* allows to scan a full range of temporal frequencies of interest and *a* represents the frequency axis of the transform. For a given mother frequency, the double role played by *a* insures a constant number of oscillations of the analysing signal within the varying width of the window, as depicted in Fig. 3. Moreover, the contracted definition, Eq. 12, indicates that the Morlet transform is basically a set of crosscorrelation functions between the signal and the various wavelets functions: denoting by the symbol * the usual crosscorrelation integral, any profile $S_\alpha(b)$ cut for a particular value α of *a* can be computed using the following relations:

$$\overline{M}\left(\frac{t-b}{\alpha}\right)=\exp\left(-\frac{(t-b)^2}{2\alpha^2}\right)\exp\left(-i\frac{\omega_0}{\alpha}(t-b)\right)=\overline{M}_\alpha(t-b) \qquad (14)$$

$$S_\alpha(b)=S(\alpha,b)=\frac{1}{\alpha}\int_{-\infty}^{+\infty} s(t)\,\overline{M}_\alpha(t-b)dt=\frac{1}{\alpha}s(b)*M_\alpha(b) \qquad (15)$$

The statement in term of correlation function provides the intuitive understanding that the transform will reach its maximum value in the region of the *(a,b)* space where the signal and the wavelet are locally the most similar, thereby offering a definite knowledge of the signal in this region. This property will be exploited more mathematically herein after.

Fig. 4 shows another possible representation of the complete modulus and phase of the Morlet transform of an actual 1D SI signal.

At this point, several options are open. For instance, by analogy with Fourier transform methods, improved versions of the 1D interferometric signal can be reconstructed by inverse wavelet transform, using a restricted domain or after some sort of filtering of the direct transform. The reconstructed signals are improved in the sense that noise in definite bandwidths can be eliminated and modulation depth can be increased, but now, compared to Fourier methods, with the added advantage of specific and differentiated effects along the time axis. These signals are then amenable to classical 1D signal processing schemes.

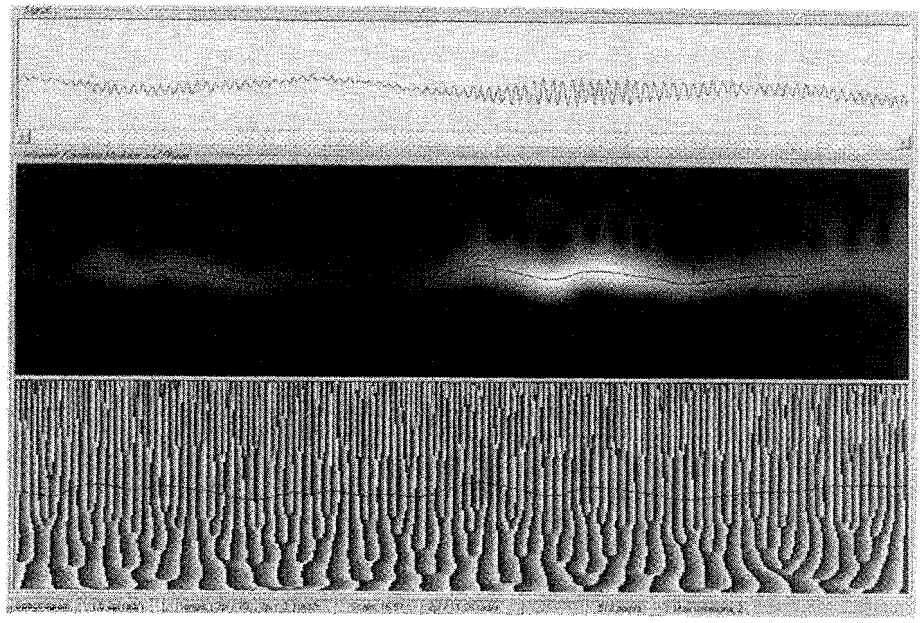

Figure 4. Morlet wavelet transform of a SI signal shown on top ; middle and bottom maps are the grey level representation of the modulus and the phase of the transform. The horizontal time axis represents 512 measurement points; the signal modulation occupies less than 20 of the 256 available levels; the vertical frequency axis range from $1.5/\pi$ to $10/\pi$. In this particular example, no external phase steps were introduced.

A simpler and more straightforward approach consists in utilising directly the phase properties of the Morlet transform, (Colonna de Lega, 1997). A signal of constant amplitude and frequency and its transform have the same phase in a frequency domain of the transform close to the signal frequency. The modulus of the transform is maximun when the analysing frequency equals the signal frequency ($\omega_0 /a=\omega_{\text{signal}}$). This condition defines the so-called *ridge* of the transform, clearly visible as the black lines in Fig. 4, middle and bottom. These two properties still hold for signals of slowly varying amplitude and frequency, to an accuracy which can be evaluated from the rate of change of these signals. In other words, along the ridge, the phase of the transform is a worthy approximation of the phase of the signal. In dynamic phase-shifting, the constant frequency signal corresponds to the external and linear phase incrementation, while the varying component comes from the natural phase incrementation caused by the object evolution. In practice, the computation of the ridge-phase of the transform and hence of the phase of the signal is quite easy and fast.

An iterative routine is adopted. At an arbitrary instant b_i, or step (i), the calculation loop starts with a guess ω_{e0} of the signal frequency equal to the ridge-frequency ω_{Ri-1} found at the previous step (i-l). At this frequency, the phase of the transform is calculated in a couple of equispaced points of the time axis, on both side of b_i, allowing to compute in turn the phase gradient of the transform on this time interval. This local gradient is nothing else but a new estimate of the ridge-frequency ω_{e1} . By construction, this

estimate can only be better or as good as the previous one, ω_{eo}. The evaluation is then repeated iteratively using ω_{e1} as the new analysis frequency and so on until the algorithm converges. Convergence is reached when the difference between two successive values $| \omega_{ej} - \omega_{ej-1} |$ is smaller than a predetermined small constant. The final estimate ω_{ej} becomes the ridge frequency ω_{Ri} at instant b_i. The phase of the signal is the phase of the transform at (b_i,ω_{Ri}). Less than 3 iterations generally suffice. Intuitively, this rapid convergence comes from the fact that the equality between transform and signal phases extends over a finite frequency range framing the ridge. In the phase diagram of the bottom of Fig. 4, as in all transform phase maps, the phase is predominantly constant along relatively long vertical segments. The frequency guess at the first step is arbitrary , but usually taken equal to the external carrier frequency. Fig 5 represents the phase of the signal shown and analysed in Fig. 4, after phase unwrapping, obtained by the algorithm just described above.

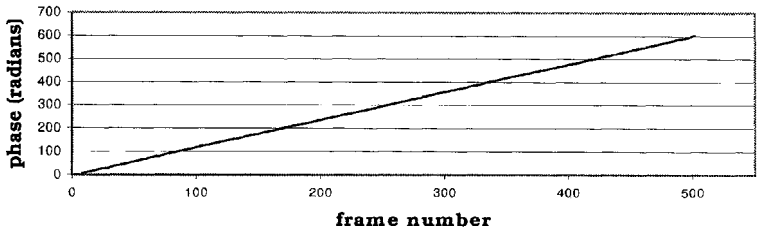

Figure 5. Phase of the signal presented in Fig. 4 and obtained from the phase of the transform along the ridge.

The practical scope of this wavelet analysis is illustrated below through a civil engineering application.

3.3. EXAMPLE

This example compares the results obtained by a direct application of the dynamic phase-shifting algorithm and of the wavelet-based analysis.

The experiment was conducted on a concrete beam (100 x 15 x 15 cm) subjected to three-point bending (Fig. 6a). The loading was applied with a standard testing machine and the surrounding conditions were really far from those that could be met in an optical laboratory. The acquisition of the in-plane horizontal displacement was performed with a full-field digital camera at 40 Hz with a feed-back loop PZT producing the reference $\pi/2$ steps. The object was subjected to a large vertical displacement producing an important speckle decorrelation. A series of 512 images was acquired.

As a first step, the image is processed with the dynamic phase-shifting algorithm, but due to the decorrelation, the phase difference between the beginning and the end of the sequence gives fringes that are barely visible. A better result can be however obtained in this case since the vertical image plane translation of the speckle field is of the order of one pixel. If the phase map obtained at the beginning of the sequence is translated one pixel vertically before being subtracted to the final phase image, the resulting fringe

pattern (Fig. 6b) is really of nice quality and the unwrapped image (Fig. 6c) can be easily generated.

The wavelet processing has been then applied to the same image sequence. At first, the phase evolution of the pixels located along the black horizontal line AB in Fig. 6c is calculated according to the above presented procedure. Indeed the shown diagram of Fig. 7a results from a weighted combination of the signals of neighbouring pixels. This graphic depicts the horizontal displacement evolution (u) and the microcrack opening can be evaluated with a precision down to a fraction of micron. In a second step, Fig. 7b, the wavelet calculation is applied to recover the u displacement in all pixels belonging to the area delimited with the black rectangle in Fig. 6c.

It is important to emphasise that an accurate absolute measurement is obtained with the wavelet processing, despite of a large decorrelation introduced during the experiment, without any need of manual recorrelation. This speaks well for the robustness of the technique in adverse conditions.

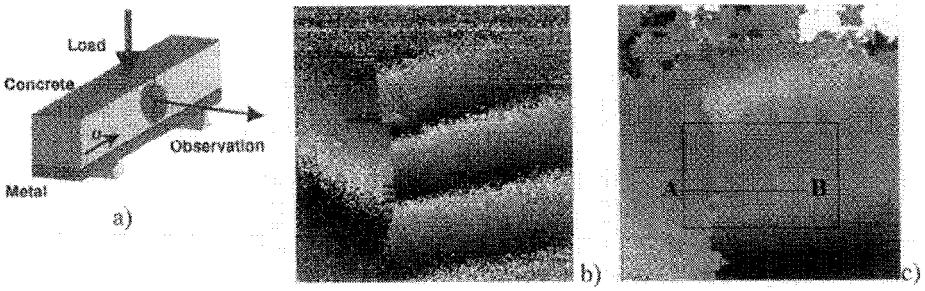

Figure 6. a) Loading scheme; b) Wrapped phase obtained with the dynamic phase-shifting algorithm; c) Unwrapped phase.

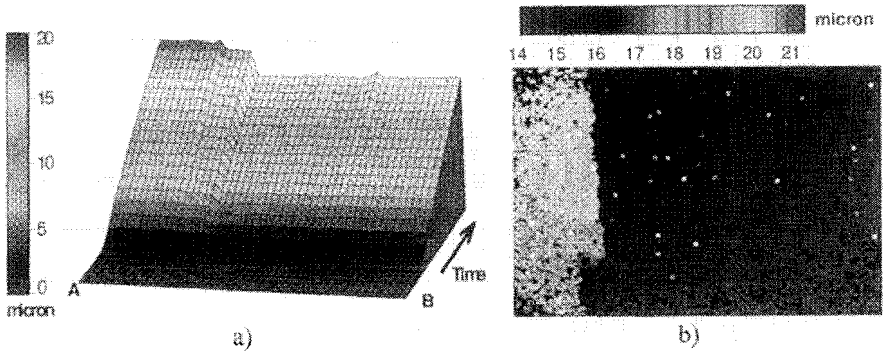

Figure 7. Wavelet processing: a) Displacement along line AB of Fig. 6c as function of time. b) Displacement during the acquired sequence in the rectangle area of Fig. 6c, (Colonna de Lega, 1997).

4. Conclusion

The successful involvement of SI in civil and environmental engineering measurements of large objects forces to resort to the ultimate capabilities of these methods. From a methodological point of view, this means that efforts for improving and optimising the performances of the various SI techniques should be attempted in all directions: a better understanding of the fine mechanisms governing the significance of the acquired information, the search for more powerful methods for processing this information and the development of a specific technology coping with the demands of the theory and tailored to the user's requirements. This paper has drawn attention on two theoretical investigations related to two of these research axes: an in-depth statistical study of the relevant random variables of SI; the presentation of a new processing scheme based on wavelet analysis. These investigations led to define a more efficient way to use SI techniques. Encouraging results have indeed been obtained, two of which being evoked in the paper. The difficult conditions prevailing in these experiments incite to believe that a standard application of the techniques would have otherwise failed.

5. References

Boone, P. M., Markov, V. B., Burykin, N. M. and Ovsyannikov, V. V. (1997), "Coherent-optical localization and assessment of importance of damage and defects of cultural heritage", *NDT & E Int.,* 30, 61-67.

Colonna de Lega, X. and Jacquot, P. (1996 a), "Deformation measurement with object-induced dynamic phase-shifting", *Appl. Opt.,* 35, 5115-5121.

Colonna de Lega, X. (1996 b), "Continuous deformation measurement using dynamic phase-shifting and wavelet transforms", *Appl. Opt. Div. Conf. Proceedings, Reading,* IOP Publishing Ltd, 261-267.

Colonna de Lega, X. (1997), "Processing of non-stationary interference patterns: adapted phase-shifting algorithms and wavelet analysis. Application to dynamic deformation measurements by holographic and speckle interferometry", *Thesis dissertation n° 1666,* EPFL.

Creath, IS. (1988), "Phase-measurement interferometry techniques", *Progress in optics XXVI,* Elsevier Science Publishers R.V., chap. 5, 350-393.

Goodman, J. W. (1975), "Statistical properties of laser speckle patterns", Laser speckle and related phenomena, Springer Verlag, chap. 2, 9-75.

Gregory, D. A. (1979), "Laser speckle photography and the sub-micron measurement of surface deformations on engineering structures", *NDT Int.,* 4, 61-70.

Gülker, G., Hinsch, IS., Hölscher, C., Kramer, A. and Neunaber, H. (1990), "Electronic speckle pattern interferometry system for in situ deformation monitoring on buildings", *Opt. Eng.,* 29, 816-820.

Lehmann, M. (1996), "Phase-shifting speckle interferometry with unresolved speckles: A theoretical investigation", *Opt. Comm.,* 128, 325-340.

Lehmann, M. (1997), "Measurements optimization in speckle interferometry: the influence of the imaging lens aperture", *Opt. Eng.,* 36, 1162-1168.

Lehmann, M. (1998), "Statistical theory of two-wave speckle interferometry and its application to the optimization of deformation measurements", *Thesis dissertation n° 1797,* EPFL.

Løkberg, O. J. and Malmo, J.T. (1988), "Long-distance electronic speckle pattern interferometry", *Opt. Eng.,* 27, 150-l56.

Lucia, A. C., Zanetta, P. M. and Facchini, M. (1997), "Electronic speckle pattern interferometry applied to the study and conservation of paintings", *Opt. and Lasers in Eng.,* 26, 221-233.

Maji, A. K., Satpathi, D. and Zawaydeh, S. (1997), "Assessment of electronic shearography for structural inspection", *Experimental Mechanics,* 37, 197-204.

Paoletti, D. and Spagnolo, G.S. (1996), "Interferometric methods for artwork diagnostics", *Progress in Optics XXXV,* North-Holland Publishing Company, 197-255.

Steinbichler, H., Engelsberger, J., Sixt, W., Sun, J. and Franz, Th. (1990), "Application of computer-aided evaluation for holography and similar techniques", *Opt. and Lasers in Eng.,* 13, 39-50.

Trolinger, J. D., Weber, D. C., Pardoen, G. C., Gunnarson G. T. and Fagan, W.F. (1991), "Application of long-range holography in earthquake engineering", *Opt. Eng.,* 30, 1315-1319.

PANORAMIC INTERFEROMETRY

Leonid A. BORYNYAK and Eugene A. KRASNOPEVTSEV
Novosibirsk State Pedagogical University
Vilyuskaya 28, Novosibirsk, 630126, Russia

1. Introduction

To investigate a deformed state of axisymmetrical objects with diameter < 0.1 m a new class of measuring instruments – panoramic interferometers is proposed. This class includes: panoramic holographic and speckle interferometers, panoramic holographic tomographs. The first two of them are intended for measuring components of the displacements vector of diffusely scattered emission surface points of cylindrical objects with the uniform sensitivity for all points. The range of the measured displacements is 10^{-7} – 10^{-5} m. The third one is intended for investigation of an optical transparent objects and in particular, for analysis of the deformed state of a thick-wall cylindrical shells and for determination a stress-strain state of a whole object. The main element of panoramic interferometers is a conic mirror principal coaxial with the object. It is intended for illumination and observation of the object with definite visual angles. A photographic plate is fixed near the larger cone base. The measuring process consists of three stages: a) generation of a two-exposure hologram of an object; b) obtaining of a set of interferograms, which allows one to identify the deformation character on the basis of a fringe pattern; and c) quantitative analysis of interferograms and calculation of projection fields of displacements or stresses. Panoramic holographic interferometers have proved to be rather useful to estimate the deformed state of various industrial constructions.

2. Panoramic holographic interferometer

As distinct from the traditional methods of investigating surface deformations, the panoramic interferometry allows to determine the displacements for all points of a cylindrical surface with equal measurement sensitivity. To obtain a panoramic hologram of cylindrical surface of an object B , we use a conical mirror M with an apex angle θ (Fig. la). A coherent collimated beam passes at first through a photoplate F, then it is reflected from the mirror and illuminates all points of coaxially positioned object B at an equal angle. Being diffusely scattered by the object surface, the radiation falls onto the photoplate F. Then the surface points are moved, and the second exposure of the photoplate is taken. A two-exposure hologram of the object surface in counterbeams is obtained. It is possible to use a real-time technique. When a two-exposure hologram is illuminated by a copy of the reference beam, two virtual images of the studied surface appear. As a result of their interference on the background of visible object surface, we

A. Lagarde (ed.),
IUTAM Symposium on Advanced Optical Methods and Applications in Solid Mechanics, 213–226.

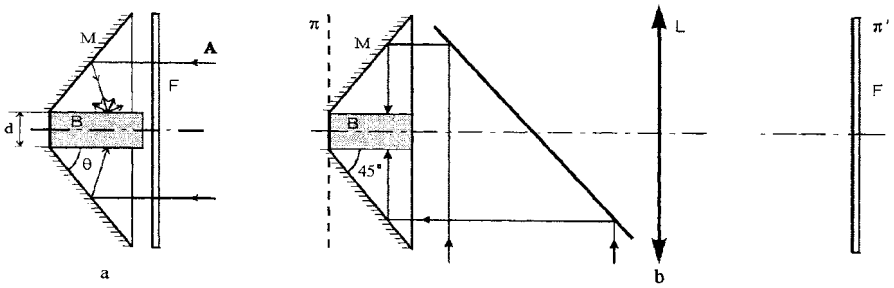

Figure I. Panoramic holographic (a) and speckle (b) interferometers.

observe a system of interference fringes whose position depends on the observation angle α (Fig.2). The photoplate in Fig. la is placed near the object; therefore, the angular aperture is large, and the angle α can be varied within rather wide range to obtain interferograms corresponding to identification of various projections of the

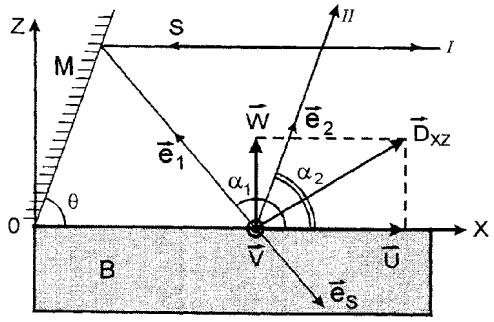

Figure 2. The W, U and V components of the displacement vector D, the unit illumination vector e_s , *the unit observation vectors* e_1 and e_2 for beams 1 and 11.

displacement vector. The interferogram observation angle should be the same for all points of the studied surface to obtain an equal measurement sensitivity for the points. Various configurations of obtaining interferograms consistent with this demand are presented in Fig.3. Figure 3a shows configurations of observation beams 1 parallel to the optic axis, for which the condition $\alpha_1 = 2\theta$ is valid. Figure 3b,c shows variants of using conical circular mirrors C for revealing observation beams *11* (see Fig.2) [1]. The configuration in Fig.3b shows the interferogram with an observation angle $\alpha \le \theta$, while the configuration in Fig.3c allows for simultaneous obtaining of two interferograms with angles $\alpha_1 = 2\theta$ and $\alpha_2 \le \theta$.

The relationship between the absolute order of the interference fringe m and a value of the displacement vector $\mathbf{D}(\mathbf{W},\mathbf{U},\mathbf{V})$ is established on the basis of a geometric model [2]. For $|D| << l$, where l is the reference scale of an object, the interference condition is

$$(\mathbf{e}_k - \mathbf{e}_s)\,\mathbf{D} = \mathbf{m}_k \lambda\,, \quad k = 1,2, \tag{1}$$

where $\mathbf{e}_s$ and $\mathbf{e}_k$ are the unit vectors of illumination and observation for beams *1* and *11*.

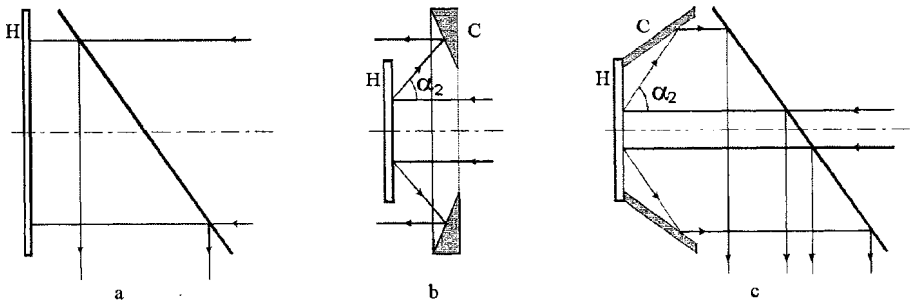

Figure 3. Configurations of observation of two-exposure hologram H: (a) identification of beams 1, (b) identification of beams 11, (c) identification of beams 1 and 11.

Equation (1) can be expressed in terms of parameters shown in Fig.2, and we obtain the displacement vector components

$$W = \lambda f(\alpha,\theta)\,[-(m_1/2)(\cos\alpha + \cos 2\theta) + m_2\cos 2\theta], \quad (2)$$
$$U = \lambda f(\alpha,\theta)\,[(m_1/2)(\sin\alpha + \sin 2\theta) - m_2\sin 2\theta],$$

here $f(\alpha,\theta) = (\sin\alpha\cos 2\theta - \cos\alpha\sin 2\theta)^{-1}$; m_1, m_2 are the orders of interference fringes at the same point for observation beams *1* and *11,* respectively; $\alpha \le \theta$ is the visibility condition for the entire surface.. For $\theta = 45°$ we obtain from (2) that

$$W = \lambda m_1/2, \quad (3)$$
$$U = (\lambda/\cos\alpha)\,[(-m_1/2)(1 + \sin\alpha) + m_2],$$

with a being the observation angle in the XZ-plane in Fig.2.

Analysis of methodical errors showed [1,3] that their value is mainly related to counting the order of interference fringes and has the minimum value at $\theta = 45°$ if $\alpha = 45°$. In this case $(\Delta U|/|\Delta W| = 5.3$; hence, the presented holographic interferometer yields a better accuracy of measuring the component W than U.

The examined interferometer is modified by changing the position and the shape of an exposed hologram. A glass cylindrical tube is mounted coaxially with the conical mirror with an angle $\theta = 45°$ and the object. The internal diameter of the tube is slightly larger than the object diameter. The external surface of the tube is covered by high resolved emulsion doped with tanning substance (formaldehyde). After two exposures the emulsion is developed and transferred in water onto a flat glass plate. Interferograms of the examined surface sweep are obtained by photographing of this hologram in parallel beams of different directions. If bending the hologram then a wave field of each point of the object surface is changed. These changes are equal for a short distance points. So a fringe pattern is not changed. This method allows for obtaining a hologram with the maximum aperture and, thus, ensures a high accuracy of measuring not only the components W and U following from the equation (3) but also the component V following from

$$V = (\lambda/\cos\delta)\,[(-m_1/2)(1 + \sin\delta) + m_3], \quad (4)$$

with δ being the observation angle in the YZ-plane (Fig.2).

3. Panoramic speckle interferometer

To obtain a panoramic two-exposure focused specklogram of the surface of a cylindrical object B (Fig.1b), we use a conical mirror M with an apex angle of 45° [1,3], which generates a circular band, which is the image of the examined surface in the plane π. The plane π is mapped by the lens L to a specklogram plane π' here the photoplate F is located. The focused specklogram registers the components U and V of the displacement vector. Their local values can be determined by exposing the specklogram to a laser beam. Pairs of identical points of two images generate an interferogram in the form of Young's fringes with a period P, which are observed within the diffraction cone. The direction of these fringes is orthogonal to the point displacement direction on the specklogram Thus, we obtain

$$U = (\lambda/\beta)\,(L/P)\sin\gamma, \qquad V = (\lambda/\beta)\,(L/P)\cos\gamma, \tag{5}$$

where β is the magnification of the speckle interferometer lens in Fig.1b, L is the distance between the specklogram and speckle interferogram, γ is the angle between the fringes direction and the plane passing through the optic axis of the specklogram and the examined point.

To find the degree of homogeneity of the overall deformation and measure the displacement field parameters, one can use a configuration shown in Fig.4. Illuminating the two-exposure specklogram S, a plane coherent wave is diffracted on a speckle structure. A panoramic image of the examined surface located in the plane S and a system of interference fringes P are observed within the diffraction cone. The screen D eliminates the direct light transmission by interrupting the image of the end face of the object. The diffracted beams from identical points of two images generate an interference pattern in the plane P located at a distance $L_x \sim F_1 / 2$ from the lens K, where F_1 is the focal distance of the lens K.

An equation for interference fringes is obtained on the basis of the geometric model.

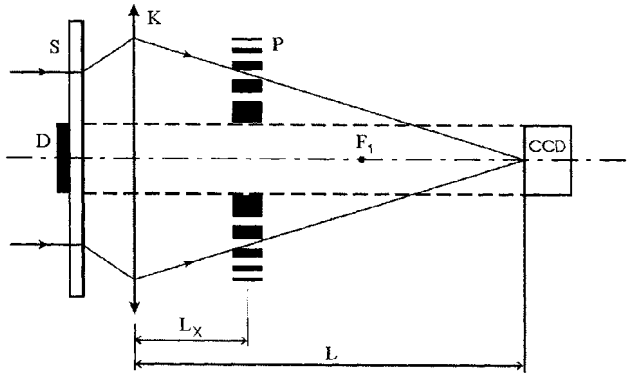

Figure 4.Configuration for obtaining a speckle interferogram: S - specklogram, K - lens, P - system of interference fringes.

The displacement V in the first order is small, and for the displacement U we obtain

$$U = \lambda\eta(m/r), \tag{6}$$

where $\eta^{-1} = \beta^2(1/F_1 - 1/L)$, β is the magnification of the focusing system in the configuration shown in Fig. 1b, r is the distance from the optic axis to the image of the examined point on the specklogram, m is the order of the interference fringe passing through this point. The error of this method is mainly due to inaccuracy of counting the order of interference fringes. The estimated range of measured displacements is $U^{min} \sim \lambda/2$, $U^{max} \sim 200l$. An empirical estimate of the maximum measured displacements shows that for a panoramic speckle interferometer is higher by an order of magnitude than for a panoramic holographic interferometer.

4. Panoramic tomograph for studying optically transparent objects

Classical tomography yields information about the scalar function values at points of an object cross-section in the form of low-frequency component of the overall image. The latter is composed of a set of exposures of the object in several directions, whose lines cross each other at points of the examined cross-section. The overall image for objects, slowly changing in space, is in reasonable agreement with the real distribution [4], if discrete experimental data are approximated with a special selected functions. Subsequent increase of reconstructions precision is achieved on the basis of Radon transform. For an object illuminated before and after the internal action, the interferogram registers the change of the optical path length $\delta\Delta_K(x,y,\varphi)$ for a light beam passing through the point (x,y) on the object, which belongs to a plane oriented at an angle φ to some arbitrarily chosen direction; K is the translucence aspect. As first degree of approximation let us confine to filtering-free reconstruction, then the change in the low-frequency component of the refractive index at the point (x,y,φ) is determined by the formula

$$\delta n^{(J)}(x,y,\varphi) = (1/N)\sum_K \delta\Delta_K(x,y,\varphi)/L_K, \tag{7}$$

where L_K is the beam path length through the object, N is the number of translucence aspects. The summation is taken over all translucence aspects.

A multiple-aspect exposure can be conducted by using conical mirrors. Figure 5 shows a compact (D = 3d) optical configuration of a panoramic three-aspect tomograph on the basis of the conical mirror C with an angle of 60°. Beams 1–3 lying in the plane of the figure pass through the point P of an optically transparent object B of the size of about d. The mirror C returns the beams, and the photoplate F is exposed in counterbeams to form a two-exposure hologram. An interferogram is obtained in beams normal to the hologram. Interference fringes on the section m—n yield information about the refractive index changes in the object cross-section by the plane coincident with the plane of the figure. This section is composed of three parts representing the interference of beams 1-3, respectively. Introducing coordinates z_1, z_2, z_3, for these parts, we can find their relationship with the coordinates x,y of the point P for the linear case, when the working space is filled by immersion oil:

$$z_1 = x(\sqrt{3})/2 - y/2, \quad z_2 = y, \quad z_3 = x(\sqrt{3})/2 + y/2 \tag{8}$$

From equation (7) we obtain

$$\delta n^{(l)}(x,y) = (\lambda/6) \sum_K (m_K/L_K), \qquad (9)$$

where K = 1,2,3; m_K is the order of interference fringe on the interferogram at the point Z_K, L_K is the object length along the beam related to the aspect K.

Assuming $m_K^{min} \sim 1/4$ in the measurements, we obtain from (9) the threshold value $(\delta n)^{min} \sim \lambda/(8d)$.

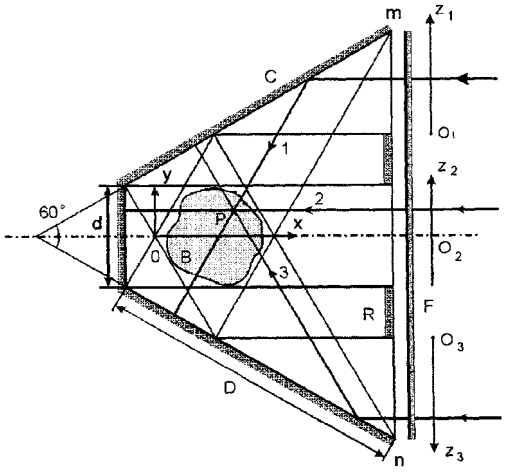

Figure 5. Panoramic three-aspect tomograph: C – conical mirror, B – object, P – point of the object, R – circular diaphragm, F – photoplate, and 1 – 3 – translucence beams.

If a set of experimental projections $P_e(z,\alpha_m)$ is known, where α is the observation angle, and it is condition $P(z,-\alpha) = P(z,\alpha)$, then the projection function $P(z,\alpha)$ may be approximated by the form

$$P(z,\alpha) = \sum_{m=0}^{M} a_m(z) \cos m\alpha . \qquad (10)$$

From the conditions $P(z,\alpha_m) = P_e(z,\alpha_m)$, we obtain for M = 2:

$$\begin{aligned} a_0(z) &= [(\gamma_1\delta_2-\gamma_2\delta_1) P_e(z,\alpha_0) + (\gamma_2\delta_0-\gamma_0\delta_2) P_e(z,\alpha_1) + (\gamma_0\delta_1-\gamma_1\delta_0) P_e(z,\alpha_2)]/\Delta, \\ a_1(z) &= [(\delta_1-\delta_2) P_e(z,\alpha_0) + (\delta_2-\delta_0) P_e(z,\alpha_1) + (\delta_0-\delta_1) P_e(z,\alpha_2)]/\Delta, \\ a_2(z) &= [(\gamma_2-\gamma_1) P_e(z,\alpha_0) + (\gamma_0-\gamma_2) P_e(z,\alpha_1) + (\gamma_1-\gamma_0) P_e(z,\alpha_2)]/\Delta, \end{aligned} \qquad (11)$$

where $\Delta = \gamma_0(\delta_1-\delta_2) + \gamma_1(\delta_2-\delta_0) + \gamma_2(\delta_0-\delta_1)$, $\gamma_m \equiv \cos\alpha_m$, $\delta_m \equiv \cos 2\alpha_m$.

The function F(x,y) in the plane φ may be restored by the Radon transform of its projections $P(z,\alpha)$. From the Radon transform in polar coordinates we obtain the approximation [5], if only three experimental projections are known

$$F(r,\theta) = \frac{1}{2\pi} \mathrm{Re}\left[\sum_{m=0}^{2} i^m \cos m\theta \int_0^{\infty} d\omega\ \omega\ A_m(\omega)\ J_m(\omega r) \right], \qquad (12)$$

where $A_m(\omega) = \int_{-\infty}^{+\infty} a_m(z) \cdot \exp(-i\omega z) \cdot dz$, $J_m(\omega r)$ - Bessel functions.

Figure 6 shows a panoramic five-aspect tomograph whose construction is based on three circular conical mirrors. A circular phase diffraction grid Z, which has only the first-order diffraction, deflects light beams 2 and 4 at an angle of 36°. Five beams of equal width directed at an angle of 36° to each other pass two times through the object. The photoplate F forms a two-exposure hologram in counterbeams. Each of the five sections of the hologram shows the initial and final states of the object, which are considered at a proper angle.

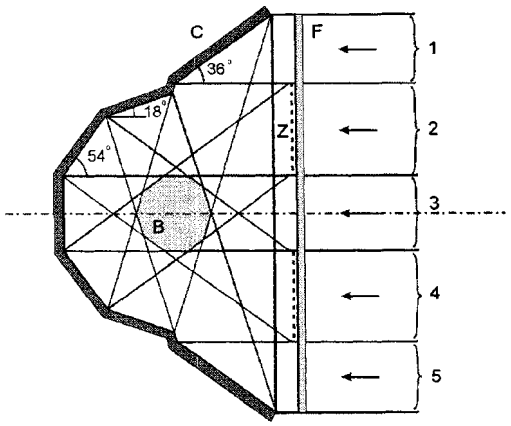

Figure 6. Panoramic five-aspect tomograph: C-mirror composed of conical elements, B- object location, Z-circular phase grid deflecting beams 2 and 4, F-photoplate.

5. Panoramic tomograph for studying cylindrical shells

Cylindrical shells made of optically transparent material with weak anisotropy can be studied by using a holographic tomograph shown in Fig.7. The illuminating beams A are plane-polarized in the plane of incidence or perpendicular to it. Being reflected on the conical mirror C at an angle $\theta = 60°$, they pass through the examined object B and are scattered by the coaxial cylindrical motionless surface S. Many beams coming at various directions pass through the examined point P with the coordinates x,y,φ and arrive at the photoplate F forming a two-exposure hologram. Photographing this hologram in beams 1 – 3, we obtain the corresponding interferograms. Since the object B is optically transparent, on the background of the surface S we see a system of interference fringes whose position depends on the direction of translucence beams and on their polarization. The positions of the fringes are fixed by placing the coordinate grid (z,φ) onto the surface S.

A modification of the aforementioned configuration is a panoramic holographic tomograph with the maximum aperture. A cylindrical glass tube is placed coaxially to

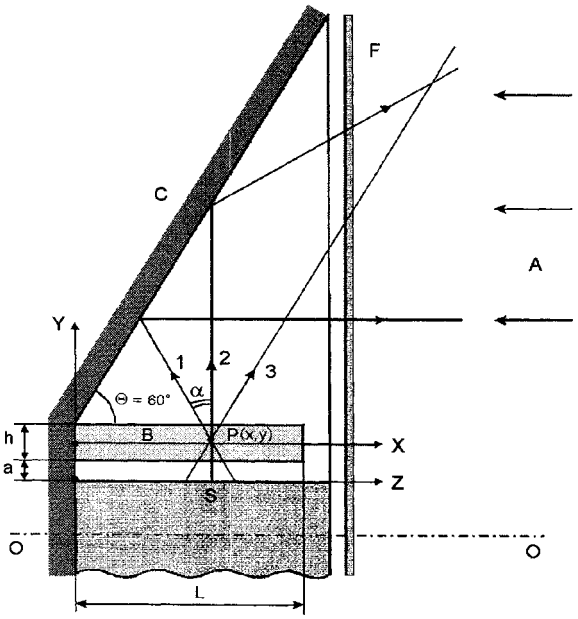

Figure 7. Panoramic tomograph for studying cylindrical shells: C – conic mirror, B – object, P – point of the object, S – light-scattering cylindrical surface, A – illuminating beams.

the conical mirror with an angle $\theta = 45°$ and the examined shell, near the latter. Its external surface is covered by photoemulsion which is transferred onto a flat glass surface after two exposures. The resultant hologram is illuminated along the normal by a coherent collimated beam. The interferogram recording is produced by means of a CCD camera with an observation angle placed in a plane perpendicular to the hologram. After determination of the fringe orders we have a two-dimensional database. The observation angle changes in diapason from $-\pi/2$ to $+\pi/2$ and we have a three-dimensional database. On this basis it is possible to reconstruct the change of refractive index in all object points by the Radon transform.

The axisymmetric polarization of the illuminating beam A, necessary for operation of the tomograph, can be obtained by the optical configuration shown in Fig.8. A plane-polarized beam 1 of a He-Ne laser goes through a quarter-wave plate P; the resultant beam 2 with circular polarization is directed to an expander E; leaving the expander, the diverging bunch of beams passes through a polaroid film F rolled into a cylindrical tube and located coaxially with the optical axis OO of the expander. One polaroid film lets through oscillations lying in the plane passing through this beam and the optic axis of the expander. Azimuthal oscillations are allowed by another polaroid. After that, a collecting lens L generates the collimated beam A. The refraction of beams by this lens followed by reflection from the mirror (see Fig.7) does not alter the axisymmetric polarization.

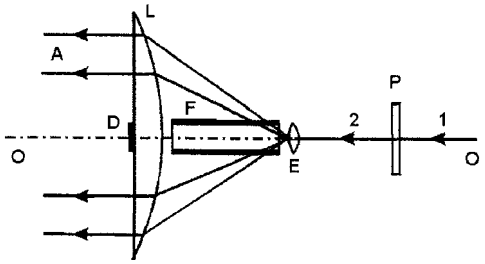

Figure 8. Creation of the axisymmetric polarization beam A. F- polaroid film, P- quarter-wave plate, l-plane-polarized beam, D- diaphragm.

The change of the optical path length $\delta\Delta(z,\alpha)$ in the point z of the surface S in Fig.7 is determined by the change of the $\delta\tilde{\Delta}(z,\alpha)$, which is fixed on the interferogram

$$\delta\Delta(z,\alpha) = \delta\tilde{\Delta}(z,\alpha) - \frac{1}{2}\cdot\delta\tilde{\Delta}(z,\alpha_s) \tag{13}$$

where α, is the angle of the illuminating beam. The change of the optical path length through the immersed object is determined by changing the refractive index $\delta n(x,y)$. For the quantities x, y, z in Fig.7 the Radon transform is

$$\delta\Delta(z,\alpha) = \int dl\cdot\delta n(x,y) = \frac{1}{\cos\alpha}\int_{-\infty}^{\infty} dy\cdot\delta n[z - y\cdot tg\alpha - T(\alpha), y] = \tag{14}$$

$$= \int_{-\infty}^{\infty}\int_{-\infty}^{\infty} dx\cdot dy\cdot\delta n(x,y)\cdot\delta\{[z - x - T(\alpha)]\cdot\cos\alpha - y\cdot\sin\alpha\}$$

where $T(\alpha) = (h/2 + a)\cdot tg\alpha$; $-\pi/2 < \alpha < \pi/2$; $\delta n(x,y) = 0$, if $x < 0$, $x > L$, $|y| > h/2$. The Fourier transform of $\delta\Delta(z,\alpha)$ is

$$\delta\hat{\Delta}(\omega,\alpha) = \int_{-\infty}^{\infty} dz\cdot\delta\Delta(z,\alpha)\cdot\exp(-i\omega z) = \tag{15}$$

$$= \frac{1}{\cos\alpha}\iint dx\cdot dy\cdot\delta n(x,y)\cdot\exp\{-i\omega[x + y\cdot tg\alpha + T(\alpha)]\} = \frac{\exp[-i\omega T(\alpha)]}{\cos\alpha}\cdot\delta\hat{n}(\omega_x,\omega_y),$$

where $\omega_x = \omega$, $\omega_y = \omega\cdot tg\alpha$. Taking into account that $d\omega_x\cdot d\omega_y = \frac{d\alpha\cdot|\omega|\cdot d\omega}{\cos^2\alpha}$, the two-dimensional inverted Fourier transform of $\delta\hat{n}$ gives δn as

$$\delta n(x,y) = \frac{1}{4\pi^2}\iint\frac{d\alpha}{\cos\alpha}\cdot d\omega\,|\omega|\,\delta\hat{\Delta}(\omega,\alpha)\cdot\exp(i\omega\zeta) =$$

$$= \frac{1}{4\pi^2}\int_{-\pi/2}^{\pi/2}\frac{d\alpha}{\cos\alpha}\int_{-\infty}^{+\infty} d\omega\cdot|\omega|\int_{-\infty}^{\infty} dz\cdot\delta\Delta(z,\alpha)\cdot\exp[-i\omega(z-\zeta)], \tag{16}$$

where $\zeta = x + y \cdot tg\alpha + T(\alpha)$. Thus the change of refractive index in the point P(x,y) (Fig.7) is reconstructed by the transform

$$\delta n(x,y) = \frac{1}{\pi}\int_{-\pi/2}^{\pi/2}\frac{d\alpha}{\cos\alpha}\cdot\int_{-\infty}^{\infty}dz\cdot\delta\Delta(z,\alpha)\cdot h(z-\zeta), \tag{17}$$

where $h(z-\zeta) = \frac{1}{4\pi}\int_{-\infty}^{\infty}d\omega\cdot|\omega|\cdot\exp[-i\omega(z-\zeta)]$ is the deblurring function.

If $\delta\hat{\Delta}(\omega, \alpha = 0)$ is small for $|\omega| > A$ then $\delta\hat{\Delta}(\omega,\alpha)$ is small for $|\omega| > A(\alpha)$, where $A(\alpha) = A\cdot\cos\alpha$. In this case the deblurring function may be approximated [6] according to (16) by the form

$$h(z,\alpha) = \frac{1}{4\pi}\int_{-A(\alpha)}^{A(\alpha)}d\omega\cdot|\omega|\cdot\exp(-i\omega z) = \frac{A^2(\alpha)}{4\pi}\left\{2\frac{\sin[zA(\alpha])}{zA(\alpha)} - \frac{\sin^2[zA(\alpha)/2]}{[zA(\alpha)/2]^2}\right\} \tag{18}$$

Let s be the ray spacing distance between parallel rays in each view and N be the number of rays. If $h(z,\alpha)$ is known only for equidistant points $z_m = \frac{m\cdot s}{\cos\alpha}$ and $A = \frac{\pi}{s}$ then the deblurring function may be approximated by a δ-function series

$$h(z,\alpha) = \frac{s}{\cos\alpha}\sum_{m=-N}^{N}h(z_m,\alpha)\cdot\delta(z-z_m) \tag{19}$$

From (18) we obtain: $h(0,\alpha) = \frac{\pi\cdot\cos^2\alpha}{4s^2}$ for m = 0, $h(z_m,\alpha) = -\frac{\cos^2\alpha}{\pi s^2 m^2}$ if m is odd, $h(z_m,\alpha) = 0$ if m is even. From (19) it follows

$$h(z-\zeta,\alpha) = \frac{\pi\cos\alpha}{4s}\left\{\delta(z-\zeta) - \frac{4}{\pi^2}\sum_{\substack{m=1\\(odd)}}^{N}\frac{1}{m^2}\left[\delta\left(z-\zeta-\frac{ms}{\cos\alpha}\right)+\delta\left(z-\zeta+\frac{ms}{\cos\alpha}\right)\right]\right\} \tag{20}$$

then the approximate form of the equation (17) is

$$\delta n_a(x,y) = \frac{1}{4s}\left\{\int_{-\pi/2}^{\pi/2}d\alpha\cdot\delta\Delta(\zeta,\alpha) - \frac{4}{\pi^2}\sum_{\substack{m=1\\(odd)}}^{N}\frac{1}{m^2}\int_{-\pi/2}^{\pi/2}d\alpha\cdot\left[\delta\Delta\left(\zeta+\frac{ms}{\cos\alpha},\alpha\right)+\right.\right.$$

$$\left.\left.+\delta\Delta\left(\zeta-\frac{ms}{\cos\alpha},\alpha\right)\right]\right\} \tag{21}$$

where s is the interval of discretization, $\zeta = x + y\cdot tg\alpha + T(\alpha)$.

For the point function

$$\delta n(x,y) = l^2\ \delta(x\text{-}x_o)\ \delta(y\text{-}y_o) \tag{22}$$

we obtain from (14) the projection

$$\delta\Delta(z,\alpha) = \frac{l^2}{\cos\alpha}\cdot\delta(z-\zeta_0)\,, \tag{23}$$

where $\zeta_0 = x_0 + y_0 \cdot \mathrm{tg}\alpha + T(\alpha)$. From (17) the precision reconstruction is

$$\delta n(x,y) = \frac{l^2}{4\pi^2}\int_{-\pi/2}^{\pi/2}\frac{d\alpha}{\cos^2\alpha}\cdot\int_{-\infty}^{\infty}d\omega\cdot|\omega|\cdot\exp[i\omega(\zeta-\zeta_0)] = \tag{24}$$

$$= \frac{l^2}{4\pi^2}\int_{-\infty}^{\infty}d\omega\cdot|\omega|\cdot\exp[i\omega(x-x_0)]\cdot\int_{-\infty}^{\infty}du\cdot\exp[i\omega(y-y_0)u]$$

Since $\int_{-\infty}^{\infty}du\cdot\exp[i\omega(y-y_0)u] = \frac{2\pi}{|\omega|}\cdot\delta(y-y_0)$, we have from (24) the function (22).

For the point function (22) we obtain $\delta\Delta\left(\zeta+\frac{ms}{\cos\alpha}\right) =$

$= l^2\ \delta[(x\text{-}x_o)\cos\alpha + (y\text{-}y_o)\sin\alpha + ms] = l^2\cdot(r^2 - m^2 s^2)^{-1/2}\cdot\delta(\alpha-\alpha_o)$, where $r^2 = (x-x_o)^2 + (y-y_o)^2$. From (21) we have the approximate reconstruction

$$\delta n_a(r) = \frac{l^2}{4s}\left[\frac{1}{r} - \frac{8}{\pi^2}\sum_{\substack{m=1\\(odd)}}^{N} m^{-2}(r^2 - m^2 s^2)^{-1/2}\right], \tag{25}$$

where $r > ms$. For $r^2 >> m^2 s^2$ the restored point function is the rapid decreasing function $\delta n_a(r) \sim r^{-3}$. This means that the reconstruction with the aid of the approximation (21) gives a acceptable accuracy.

6. Experiment

Panoramic interferometers were used for qualitative and quantitative studies of the deformed state of industrial units. Some examples are presented below.

6.1. INFLUENCE OF SPRINGS PLACED IN THE SHELL

A spring lock was compressed in a cylindrical shell, made of zirconium, with internal diameter of 8 mm and wall thickness of 0.5 mm. The spring had a variable radius. The

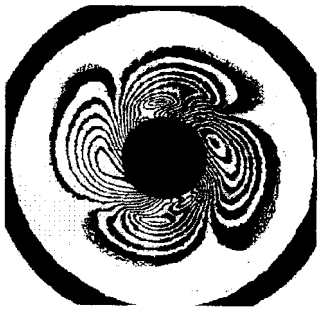

Figure 9. An interferogram of the surface of a cylindrical lock with compressed spring.

diameter of the wide cylindrical section was equal to the internal diameter of the shell. Using a panoramic holographic interferometer with an angle $\theta = 45°$ we studied the flexure of the shell walls due to spring compression. The resultant interferogram with $\alpha = 90°$ is presented in Fig.9. The fringe pattern shows that the spring action upon the shell walls in each circular cross-section is nonuniform, its force is concentrated at four points. Studying the flexure of the shell walls under a cyclic load of the spring lock allowed us to conclude that the spring rotates with respect to the shell walls. The carried out study allowed for refining the calculation model and working out certain requirements to production practice.

6.2. STUDY OF WELDED SHELLS

A panoramic holographic interferometer was used to study thin cylindrical shells loaded by internal pressure. A zirconium fuel element with an internal diameter of 8 mm and a wall thickness of 0.5 mm was studied. A metal bottom was welded to the shell edge. The bottom was made in two variants. The shells that were made by using the first and second techniques were fixed by a collet clamp of the interferometer whose conical mirror had an angle $\theta = 45°$. Fig. 10a shows a typical interferogram with an angle

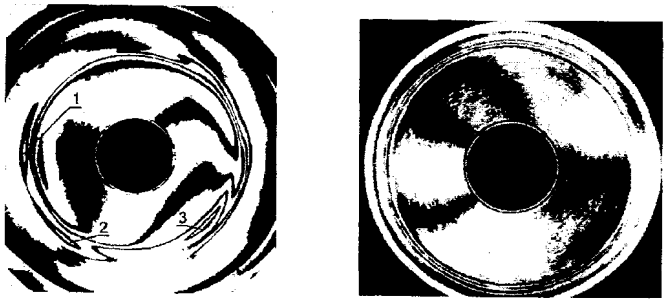

a b

Figure 10. Interferograms of shell surfaces made by using the first (a) and second (b) techniques, 1 – 3 are zones of anomalous flexure.

$\alpha = 90°$ of the weld made according to the first technique for the case of an internal pressure of 40 atm. There are local interference fringes on sections 1 – 3, which points to the presence of zones of anomalous flexure of the shell surface. Fig.10b shows a typical interferogram of the deformed state of a shell whose weld was made in accordance with the second technique. The performed analysis allowed us to conclude that the weld made by using the second technique leads to smaller nonuniformities of the deformed state than a weld made by using the first technique.

6.3. STUDY OF CYLINDRICAL SHELL WITH ORIFICES

The shell was made of acrylic plastic, its diameter was 27 mm, the wall thickness was 1 mm. Two symmetrical circular orifices of 6 mm in diameter were made in the side wall of the shell. One of the shell bottoms was rigidly fixed in the panoramic interferometer with $\theta = 45°$, the other was covered by a steel lid which experienced an axial compression force of 50 N. The resultant panoramic interferogram with an angle $\alpha = 90°$ is shown in Fig. 11a. It bears information about the shell surface flexure. Fig. 11b shows a developed interferogram of the same shell subjected to a 100 N axial compression force. It was obtained using a panoramic holographic interferometer with the maximum aperture. The value of the observation angle α is 90°.

a b

Figure 11. Panoramic (a) and developed (b) interferograms of the surface of a cylindrical shell.

6.4. OTHER ILLUSTRATIONS

The shell with the diameter of 27 mm and the wall thickness of 1 mm was made of acrylic plastic. The axial compression was created by 50 N value. In Fig.12a the panoramic interferogram for beams 11 with an angle $\alpha = 45°$ is represented. The hologram was obtained by means of the interferometer with $\theta = 45°$. Fig. 12b represents two simultaneously obtained interferograms for beams 1 with $\alpha = 120°$ and for beams 11 with $\alpha = 45°$. In this case the hologram was obtained by means of the interferometer with $\theta = 60°$. The same shell with axial compression of 400 N was studied by the panoramic speckle interferometer. The panoramic speckle interferogram is represented in Fig. 12c.

For shells the magnitudes of the surface points displacements were obtained by using a panoramic holographic interferometer in diapason of $(0.3 – 10)\ 10^{-6}$ m, and by using a

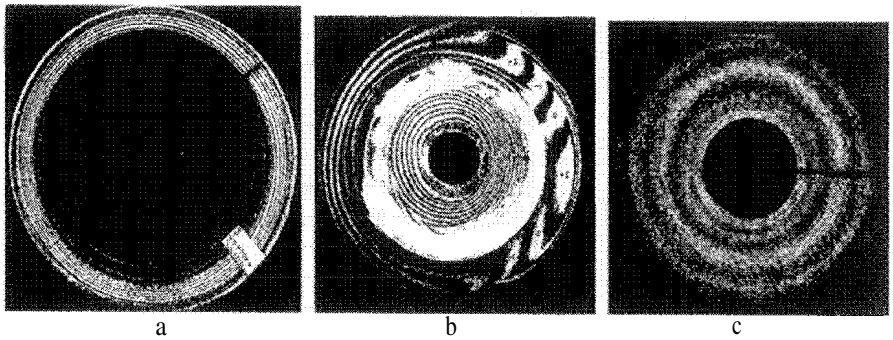

a b c

Figure 12. Panoramic interferograms of a cylindrical shell for beams 11 (a), for beams 1 and 11 (b), and speckle interferogram (c).

panoramic speckle interferometer in diapason of (10 – 100) 10^{-6} m. Relative measurement errors are ~ 5 %. The conducted experimental studies verified that reliable results are obtained using the methods of panoramic interferometry and that the considered devices can be used in industry.

7. Conclusions

The fundamentals and operation principles of panoramic interferometers are presented. This is a new class of measurement instruments designed to study the strain state of axisymmetric objects less than 0.1 m in diameter. Three directions are presented in this class: holographic interferometry, speckle interferometry, and holographic tomography. The first direction has been developed theoretically and experimentally, and effectively used in industry, the second direction has been verified in laboratory conditions, the third one is in theoretically and experimentally elaboration. High-sensitive panoramic interferometry is free of a number of principal metrological and technical constraints inherent in the traditional methods of experimental mechanics. Panoramic interferometers are simple and compact, they save labor efforts by taking several aspects of an object on one hologram. On the basis of one hologram, the instruments allow to obtain the displacement vector components of all points of the deformed surface with equal sensitivity.

8. References

1. Borynyak, L.A., Krasnopevtsev, E.A. and Loginov, A.V. (1996) Panoramic interferometers for investigating deformations of the axisymmetric objects, *Proceedings SPIE* **2791**, 136-138.
2. Vest, Ch.M. (1979) *Holographic interferometry*, John Wiley & Sons, New York.
3. Borynyak, L.A. and Krasnopevtsev, E.A. (1998) Panoramic interferometers for investigating deformations of the axisymmetric objects, *Proceedings SPIE* **3486**, 27-30.
4. Levin, G.G. and Vishnyakov, G.N. (1988) *Optical Tomography* (in Russian). Radio i Svyaz', Moscow.
5. Logan, B.F. (1975) The uncertainty principle in reconstructing functions from projections, *Duke mathematical journal* **42**, 661-706.
6. Lewitt, Robert M. (1983) Reconstruction Algorithms. Transform Methods, *Proceedings of the IEEE* **71**, 390-408.

DEFORMATION MEASUREMENT AND ANALYSIS ON RELATED CURVED SURFACES BY HOLOGRAPHY

W. SCHUMANN

CH 8032 Zürich
Switzerland

Abstract

The technique with two holograms is investigated in case of large deformations of an opaque body. The recovering of invisible fringes by a modification and the strain determination are briefly outlined. Two conditions from the first derivative of the optical path difference should ensure locally a spacing and a contrast of the fringes. The three linear forms from this derivative are analysed with the polar decomposition of the deformation, some affine connections and the transverse ray aberration. The correlation for the fringe visibility, Frenet's relations of curvature, changes of geodesic curvature and the integrability are involved. The second derivative of the path difference contains three quadratic forms with the derivatives of the dilatation, the curvature changes of the object surface and the virtual deformation of the images besides a term with the fringe vector. A duality from the aberration permits the elimination of a bilinear form.

1. Introduction

The basic linear equation of *holographic Interferometry* to investigate the deformation of an opaque body by the technique of recording on two holograms reads

$$D = \mathbf{u}\cdot(\mathbf{k}-\mathbf{h}) - \mathbf{t}\cdot(\mathbf{k}-\mathbf{c}) + \mathbf{t'}_r\cdot(\mathbf{k}-\mathbf{c'}_r)\ . \tag{1}$$

D means here the optical path difference; it is equal to the fringe order v times the wavelength λ. Further, $\mathbf{u}$ denotes the displacement vector from the point P of the undeformed object surface to the point P' of the deformed surface. We use small bold letters for vectors; capital bold letters mark later linear transformations (tensors). The difference $\mathbf{k} - \mathbf{h} = \mathbf{g}$ is the sensitivity vector, where $\mathbf{k}$ and $\mathbf{h}$ are unit vectors of the reflected ray PR and the incident ray SP. The vectors $\mathbf{t}$, $\mathbf{t'}_r$ denote shifts, at the

A. Lagarde (ed.),
IUTAM Symposium on Advanced Optical Methods and Applications in Solid Mechanics, 227–234.

reconstruction, of the hologram points $\hat{\Pi}$, $\hat{H}'_r$ on PR, whereas **c,** $\mathbf{c}'_r$ are unit vectors on $Q\hat{H}$, $Q'\hat{H}'_r$. Eq.(1) holds only for small displacements. In case of a large deformation we start with the exact expression $D = (\lambda / 2\pi)(\tilde{\varphi} - \tilde{\varphi}') - (\tilde{L} - \tilde{L}')$ of the path difference, where $\tilde{L}$, $\tilde{L}'$ are the distances from the image points $\tilde{P}$, $\tilde{P}'$ to a point $\tilde{K}$ of fringe localisation (figure 1). The phases $\tilde{\varphi}$, $\tilde{\varphi}'$ at $\tilde{P}$, $\tilde{P}'$ relate the interference to the diffraction

$$\tilde{\varphi} = \frac{2\pi}{\lambda}\left(L_T + L_S + p - q - q_T - \tilde{p} + \tilde{q} + \tilde{q}_T\right) + \pi + \tilde{\psi} , \qquad \tilde{\varphi}' = \ldots , \tag{2}$$

with the phase $\tilde{\psi}$ at $\tilde{T}$, distances L_T, L_S, p, q, q_T, $\tilde{p}$, $\tilde{q}$, $\tilde{q}_T$,.... Therefore we get

$$D = L_S - L'_S - \left(\tilde{L} + \tilde{p}\right) + \left(\tilde{L}' + \tilde{p}'\right) + p - q - p' + q' + \tilde{q} - \tilde{q}' + L_T - L'_T + \tilde{q}_T - \tilde{q}'_T . \tag{3}$$

Several authors [1 - 5] have investigated the problems which arise: 1. recovering of invisible fringes, 2. elimination of the influence of the rotation and 3. analysis of the modified fringes to determine the strains. Two conditions from the first derivative of the path difference should ensure, with the overlapping of the areas covered by the aperture, a spacing and a contrast of the fringes. As these conditions are fullfilled only locally, fringes appear in a small vicinity (figure 2). To render the optical path difference quasi stationary in a larger domain, one should investigate the second derivative, which will be analysed here. It reveals also peculiar properties as a by-product.

2. First derivative of the path difference. Fringe and visibility vectors

The differential of the path difference (3) is $dD = dL_S - dL'_S - d(\tilde{L} + \tilde{p}) + \ldots + d\tilde{q} - d\tilde{q}'$, where we have $dL_S = d\mathrm{r} \cdot N\nabla L_S = d\mathbf{r} \cdot \nabla_n L_S = d\mathbf{r} \cdot \mathrm{Nh}$, implying the normal projector $\mathbf{N} = \mathbf{I} - \mathbf{n} \otimes \mathbf{n}$. Generally we use the rules $\mathbf{v}(\mathbf{a} \otimes \mathbf{b}) = (\mathbf{v} \cdot \mathbf{a})\mathbf{b}$, $(\mathbf{a} \otimes \mathbf{b})\mathbf{w} = \mathbf{a}(\mathbf{b} \cdot \mathbf{w})$ for any dyadic product. The operator $\nabla_n = N\nabla = \mathbf{a}^\alpha(\partial/\partial\theta^\alpha)$ (sum from 1 to 2) appears as a formal projection of ∇, the index recalling the normal **n** (or **n**'…). It can also be expressed by curvilinear coordinates θ^α and base vectors $\mathbf{a}^\alpha$ on the surface. In summary we get

$$\begin{aligned} dD = {} & d\mathbf{r}\mathbf{N} \cdot \mathbf{h} - d\mathbf{r}'\mathbf{N}' \cdot \mathbf{h}' - \left(d\hat{\mathbf{r}}\hat{\mathbf{N}} - d\tilde{\rho}\tilde{\mathbf{K}}_{\tilde{\rho}}\right) \cdot \tilde{\mathbf{k}} + \left(d\hat{\mathbf{r}}'\hat{\mathbf{N}}' - d\tilde{\rho}\tilde{\mathbf{K}}_{\tilde{\rho}}\right) \cdot \tilde{\mathbf{k}}' \\ & + \left(d\hat{\mathbf{r}}\hat{\mathbf{N}} - d\mathbf{r}\mathbf{N}\right) \cdot \mathbf{k} - d\hat{\mathbf{r}}\hat{\mathbf{N}} \cdot \mathbf{c} - \left(d\hat{\mathbf{r}}'\hat{\mathbf{N}}' - d\mathbf{r}'\mathbf{N}'\right) \cdot \mathbf{k}' + d\hat{\mathbf{r}}'\hat{\mathbf{N}}' \cdot \mathbf{c}' + d\hat{\mathbf{r}}\hat{\mathbf{N}} \cdot \tilde{\mathbf{c}} - d\hat{\mathbf{r}}'\hat{\mathbf{N}}' \cdot \tilde{\mathbf{c}}' . \end{aligned} \tag{4}$$

The object- and hologram-deformations are $\mathbf{N}'\,d\mathbf{r}' = \mathrm{FN}d\mathbf{r}$, $\hat{\mathbf{N}}d\hat{\mathbf{r}} = \hat{\mathbf{F}}\hat{\mathbf{N}}d\hat{\mathbf{r}}$,… at the surfaces, so that only the semi-projections **FN**,… of the deformation gradients **F**,… intervene. The polar decomposition reads $\mathbf{F} = \mathbf{QU}$, with the symmetric dilatation **U** (defined by the Cauchy-Green tensor $\mathbf{F}^T\mathbf{F} = \mathbf{UU}$) and the orthogonal rotation tensor **Q** of the volume element. At the surface element the polar decomposition is with the in-

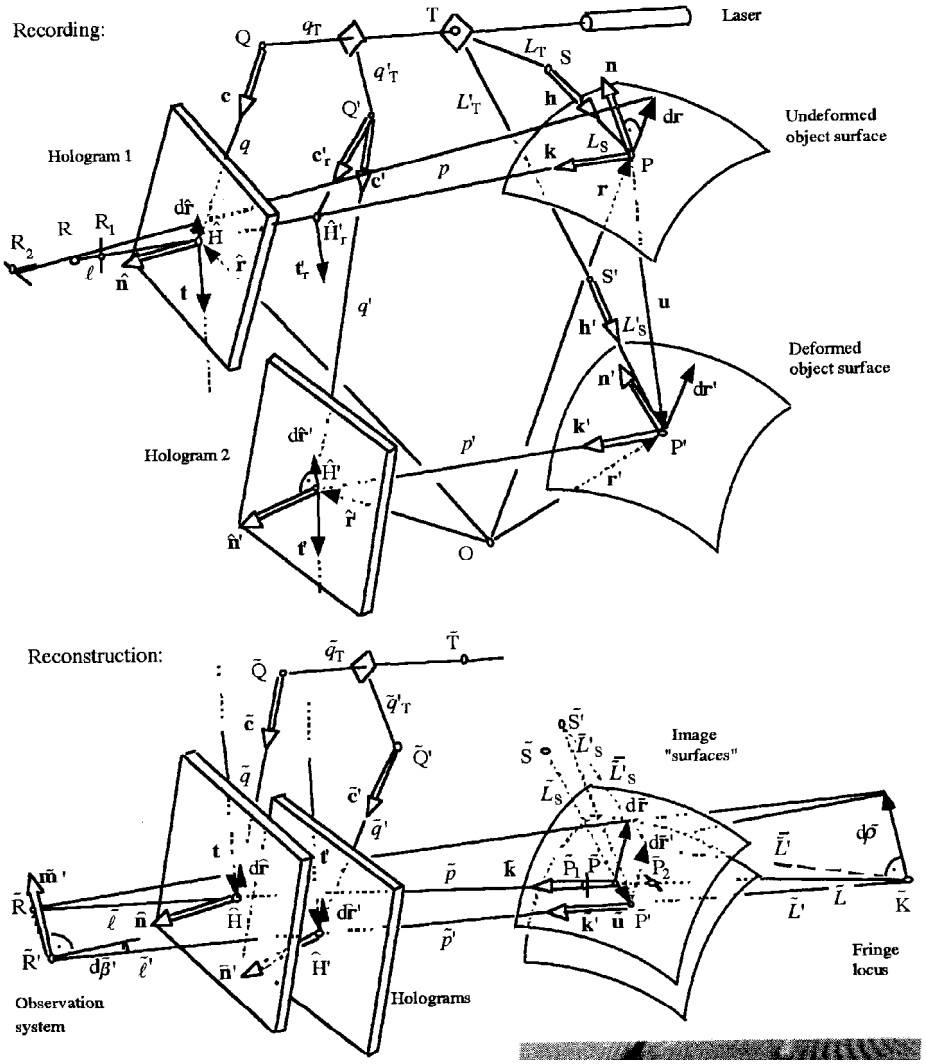

Figure 1: Recording on separate holograms in case of a large deformation of an opaque body. Reconstruction with a modification and quasi overlapping of the image surfaces.

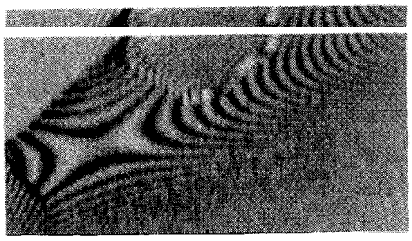

Figure 2: Recovery of local fringes in case of a moderate deformation (courtesy of Dr.D.Cuche).

plane dilatation $\mathbf{V}$ ($\mathbf{NF}^T\mathbf{FN} = \mathbf{VV}$) and the surface rotation tensor $\mathbf{Q}_n$ ($\mathbf{Q}_n\,\mathbf{n} = \mathbf{n}'$)

$$\mathbf{FN} = \mathbf{Q}_n\,\mathbf{V}. \tag{5}$$

Note also the additive decomposition for small strain γ, small inclination ω and small pivot rotation Ω. Then $\mathbf{Q}_n \cong \mathbf{I} - \boldsymbol{\omega} \otimes \mathbf{n} + \mathbf{n} \otimes \boldsymbol{\omega} - \Omega\mathbf{E}$, $\mathbf{V} \cong \mathbf{N} + \boldsymbol{\gamma}$, $\mathbf{FN} = \mathbf{N} + \boldsymbol{\gamma} - \Omega\mathbf{E} + \mathbf{n} \otimes \boldsymbol{\omega}$, where the 2D skewsymmetric permutation tensor $\mathbf{E}$ rotates any surface vector by –90° ($\mathbf{EE} = -\mathbf{N}$). We use also the derivatives of $\mathbf{n}$ and $\mathbf{N}$

$$\nabla_n \otimes \mathbf{n} = -\mathbf{B}\,, \quad \nabla_n \otimes \mathbf{N} = \mathbf{B} \otimes \mathbf{n} + \mathbf{B} \otimes \mathbf{n}]^T . \tag{6}$$

The in-plane tensor $\mathfrak{B} = B_{\alpha\beta}\mathbf{a}^\alpha \otimes \mathbf{a}^\beta$ describes the (exterior) curvature of the surface. Eqs.(6) correspond to Frenet's relations $\mathrm{d}\mathbf{n}/\mathrm{d}s = -\mathbf{a}/R$, $\mathrm{d}\mathbf{a}/\mathrm{d}s = \mathbf{n}/R$ of a plane curve with intrinsic base a, n. The open bracket $]^T$ in eq.(6b) indicates here a transposition of the 2[d] and the 3[d] factor, thus $\mathbf{B} \otimes \mathbf{n}]^T = B_{\alpha\beta}\mathbf{a}^\alpha \otimes \mathbf{n} \otimes \mathbf{a}^\beta$. If a vector $\mathbf{u} = \mathbf{v} + w\,\mathbf{n}$ has the interior part $\mathbf{v} = \mathbf{N}\mathbf{u}$, we have $\nabla_n \otimes \mathbf{u} = (\nabla_n \otimes \mathbf{v})\mathbf{N} - \mathbf{B}w + (\nabla_n w + \mathbf{B}\mathbf{v}) \otimes \mathbf{n}$. Eq.(4) becomes now with the multiplicative polar decomposition (5)

$$\begin{aligned} \mathrm{d}D = {} & \mathrm{d}\mathbf{r} \cdot \mathbf{N}\left[\mathbf{V}\mathbf{Q}_n^T(\mathbf{k}' - \mathbf{h}') - (\mathbf{k} - \mathbf{h})\right] + \mathrm{d}\tilde{\rho} \cdot \tilde{\mathbf{K}}_{\tilde{\rho}}\left(\tilde{\mathbf{k}} - \tilde{\mathbf{k}}'\right) \\ & - \mathrm{d}\hat{\mathbf{r}} \cdot \hat{\mathbf{N}}\left[\hat{\mathbf{V}}\hat{\mathbf{Q}}_{\hat{n}}^T\left(\tilde{\mathbf{k}} - \tilde{\mathbf{c}}\right) - (\mathbf{k} - \mathbf{c})\right] + \mathrm{d}\hat{\mathbf{r}}' \cdot \hat{\mathbf{N}}'\left[\hat{\mathbf{V}}'\,\hat{\mathbf{Q}}_{\hat{n}'}^T\left(\tilde{\mathbf{k}}' - \tilde{\mathbf{c}}'\right) - (\mathbf{k}' - \mathbf{c}')\right] . \end{aligned} \tag{7}$$

The differentiation of $\mathbf{Q}_n^T\mathbf{Q}_n = \mathbf{I}$ gives $\mathrm{d}\mathbf{Q}_n^T\mathbf{Q}_n + \mathbf{Q}_n^T\mathrm{d}\mathbf{Q}_n = 0$. Thus, $\mathrm{d}\mathbf{Q}_n = \mathbf{Q}_n\, d\boldsymbol{\Psi}^T$, where $d\boldsymbol{\Psi}^T = -d\boldsymbol{\Psi}$ is skew-symmetric, but in space this is not the differential of a tensor. However, at the surface we may locally write a differential of a small rotation $d\boldsymbol{\Psi} = \mathrm{d}(\boldsymbol{\omega} \otimes \mathbf{n} - \mathbf{n} \otimes \boldsymbol{\omega} + \Omega\mathbf{E})$. We obtain then ($\omega$ is a surface vector)

$$\begin{aligned} \mathrm{d}\mathbf{Q}_n = \mathbf{Q}_n\big(\mathrm{d}\mathbf{r}\{ & -(\nabla_n \otimes \boldsymbol{\omega} - \mathbf{B}\mathbf{E}\,\Omega)\mathbf{N} \otimes \mathbf{n} + \\ & + (\nabla_n \otimes \boldsymbol{\omega} - \mathbf{B}\mathbf{E}\,\Omega)\mathbf{N} \otimes \mathbf{n}]^T - (\nabla_n \Omega + \mathbf{B}\mathbf{E}\,\boldsymbol{\omega}) \otimes \mathbf{E}\}\big) . \end{aligned} \tag{8}$$

The equation of a geodesic curve with the arc s on a surface is $\mathbf{N}\mathrm{d}^2\mathbf{r}/\mathrm{d}s^2 = 0$, because the osculating plane contains the normal $\mathbf{n}$ by definition. After a deformation we get $\mathbf{N}'\,\mathrm{d}^2\mathbf{r}'(s) = \mathbf{N}'\,\mathrm{d}(\mathrm{d}\mathbf{r}') = \mathbf{N}'\left[\mathrm{d}(\mathbf{FN})\mathrm{d}\mathbf{r} + \mathbf{FN}\mathrm{d}^2\mathbf{r}\right] = \mathbf{N}'\left(\mathrm{d}\mathbf{Q}_n\mathbf{V} + \mathbf{Q}_n\mathrm{d}\mathbf{V}\right)\mathrm{d}\mathbf{r}$. The derivative of the dilatation is $\nabla_n \otimes \mathbf{V} = (\nabla_n \otimes \mathbf{V})\mathbf{N}|\mathbf{N} + \mathbf{B}\mathbf{V} \otimes \mathbf{n} + \mathbf{B}\mathbf{V} \otimes \mathbf{n}]^T$ (the sign $|\mathbf{N}$ marks a projection of the middle factor). The interior part $(\nabla_n \otimes \mathbf{V})\mathbf{N}|\mathbf{N}$ has the components $V_{\beta\gamma;\alpha} = V_{\beta\gamma,\alpha} - \Gamma^\lambda{}_{\beta\alpha}V_{\lambda\gamma} - \Gamma^\lambda{}_{\gamma\alpha}V_{\beta\lambda}$ (A). With eq.(8) and $\mathbf{N}'\mathbf{Q}_n\mathbf{n} = \mathbf{N}'\mathbf{n}' = 0$ we obtain

$$\mathbf{N}'\,\mathrm{d}^2\mathbf{r}'(s) = \mathbf{Q}_n\{\mathrm{d}\mathbf{r}[(\nabla_n \otimes \mathbf{V})\mathbf{N}|\mathbf{N} - (\nabla_n \Omega + \mathbf{B}\mathbf{E}\,\boldsymbol{\omega}) \otimes \mathbf{E}\mathbf{V}]\mathrm{d}\mathbf{r}\} . \tag{9}$$

To eliminate the rotation increment, we apply Gauss'theorem for the deformation on a domain A with closed boundary ∂A. In the dislocation theory one uses Burger's vector $\mathbf{b}'_n = \lim_{A\to 0}\frac{1}{A}\oint_{\partial A}\mathrm{d}\mathbf{r}\mathbf{F}^T = \lim_{A\to 0}\frac{1}{A}\iint_A \nabla_n\left(\mathbf{E}\mathbf{F}^T\right)\mathrm{d}A = \nabla_n\left(\mathbf{E}\mathbf{F}^T\right)$. Without dislocations, $\partial A'$

is also closed and $\nabla_n(\mathbf{E}\mathbf{F}^T) = 0$ is a necessary and sufficient condition of integrability, so that $\mathbf{N}\mathbf{F}^T = \mathbf{N} + \nabla_n \otimes \mathbf{u}$. Using eqs.(5, 8) the interior part reads then

$$\nabla_n(\mathbf{E}\mathbf{V}\mathbf{E})\mathbf{V}^{(-1)}\mathbf{E} + \nabla_n\Omega + \mathbf{B}\mathbf{E}\omega = 0\,. \tag{10}$$

$\mathbf{V}^{(-1)}$ plays the role of a 2D „inverse", defined by $\mathbf{V}^{(-1)}\,\mathbf{V} = \mathbf{N}$. The pair $\mathbf{E}(\ldots)\mathbf{E}$ is an involution, used in shells. We eliminate the rotation from (9) and (10) and get

$$\mathbf{N}'\,\mathrm{d}^2\mathbf{r}'\,(s) = \mathbf{N}'\,\mathbf{Q}_n\{\mathrm{d}\mathbf{r}\mathbf{D}_{\mathrm{V}}\,\mathrm{d}\mathbf{r}\}\,,\quad \mathbf{D}_{\mathrm{V}} = (\nabla_n \otimes \mathbf{V})\mathbf{N}\big|\mathbf{N} + \nabla_n(\mathbf{E}\mathbf{V}\mathbf{E})\mathbf{V}^{(-1)}\mathbf{E} \otimes \mathbf{E}\mathbf{V}\,. \tag{11,12}$$

We return to eq.(7). The direction to $<\tilde{\mathrm{P}}>$ is with $\theta_{\mathrm{P}} = (2\pi/\lambda)\big[(\tilde{p} - \tilde{q}) - (p - q)\big]$ defined by $\mathrm{d}\theta_{\mathrm{P}} = 0$ or also by $\mathrm{d}\theta_{\tilde{\mathrm{R}}} = 0$, where $\theta_{\tilde{\mathrm{R}}} = (2\pi/\lambda)\Big[(\ell + q) - (\tilde{\ell} + \tilde{q})\Big]$. Both conditions lead to

$$\hat{\mathbf{N}}\Big[\hat{\mathbf{V}}\hat{\mathbf{Q}}_{\hat{n}}^T(\tilde{\mathbf{k}} - \tilde{\mathbf{c}}) - (\mathbf{k} - \mathbf{c})\Big] = 0\,. \tag{13}$$

For other rays we have $\mathrm{d}\bar{\theta}_{\tilde{\mathrm{R}}} = \mathrm{d}\theta_{\tilde{\mathrm{R}}} + \mathrm{d}^2\theta_{\tilde{\mathrm{R}}}/2 + \ldots$, thus also $\mathrm{d}^2(\ell + q - \tilde{\ell} - \tilde{q}) = 0$ with $\mathrm{d}^2 q = \mathrm{d}(\mathrm{d}\hat{\mathbf{r}}\hat{\mathbf{N}}\cdot\mathbf{c}) = \mathrm{d}^2\hat{\mathbf{r}}\hat{\mathbf{N}}\cdot\mathbf{c} + \mathrm{d}\hat{\mathbf{r}}\mathrm{d}\hat{\mathbf{N}}\cdot\mathbf{c} + \mathrm{d}\hat{\mathbf{r}}\hat{\mathbf{N}}\cdot\mathrm{d}\mathbf{c}$ and $\mathrm{d}\hat{\mathbf{r}}\mathrm{d}\hat{\mathbf{N}}\cdot\mathbf{c} = (\mathrm{d}\hat{\mathbf{r}}\cdot\hat{\mathbf{B}}\mathrm{d}\hat{\mathbf{r}})(\hat{\mathbf{n}}\cdot\mathbf{c})$ (if the hologram is curved). Further $\mathrm{d}\mathbf{c} = (1/q)\mathbf{C}\hat{\mathbf{N}}\mathrm{d}\hat{\mathbf{r}}$, where $\mathbf{C} = \mathbf{I} - \mathbf{c}\otimes\mathbf{c}$. We get then

$$\mathrm{d}^2 q = \left(\hat{\mathbf{N}}\mathrm{d}^2\hat{\mathbf{r}}\right)\cdot\mathbf{c} + \mathrm{d}\hat{\mathbf{r}}\cdot\hat{\mathbf{B}}_{\mathrm{C}}\mathrm{d}\hat{\mathbf{r}}\,,\quad \mathrm{d}^2\tilde{q} = \left(\hat{\mathbf{N}}\mathrm{d}^2\hat{\mathbf{r}}\right)\cdot\tilde{\mathbf{c}} + \mathrm{d}\hat{\mathbf{r}}\cdot\hat{\mathbf{B}}_{\tilde{\mathrm{C}}}\mathrm{d}\hat{\mathbf{r}}\,,\quad \ldots\,, \tag{14}$$

$$\hat{\mathbf{B}}_{\mathrm{C}} = \hat{\mathbf{B}}(\hat{\mathbf{n}}\cdot\mathbf{c}) + \frac{1}{q}\hat{\mathbf{N}}\mathbf{C}\hat{\mathbf{N}}\,,\qquad \hat{\mathbf{B}}_{\tilde{\mathrm{C}}} = \hat{\mathbf{B}}(\hat{\mathbf{n}}\cdot\tilde{\mathbf{c}}) + \frac{1}{\tilde{q}}\hat{\mathbf{N}}\tilde{\mathbf{C}}\hat{\mathbf{N}}\,. \tag{15}$$

For a general curve on the hologram we have $\hat{\mathbf{N}}\mathrm{d}^2\hat{\mathbf{r}} = \hat{\mathbf{N}}\mathrm{d}(\mathrm{d}\hat{\mathbf{r}}) = \hat{\mathbf{N}}\Big[\mathrm{d}(\hat{\mathbf{F}}\hat{\mathbf{N}})\mathrm{d}\hat{\mathbf{r}} + \hat{\mathbf{F}}\hat{\mathbf{N}}\mathrm{d}^2\hat{\mathbf{r}}\Big]$. Here we can introduce the analogue of eq.(11) in the first geodesic term, which gives

$$\hat{\mathbf{N}}\mathrm{d}^2\hat{\mathbf{r}} = \hat{\mathbf{Q}}_{\hat{n}}\hat{\mathbf{V}}\hat{\mathbf{N}}\mathrm{d}^2\hat{\mathbf{r}} - \hat{\mathbf{V}}^{(-1)}\left(\mathrm{d}\hat{\mathbf{r}}\hat{\mathbf{D}}_{\hat{\mathrm{V}}}\mathrm{d}\hat{\mathbf{r}}\right)\,. \tag{16}$$

We use in addition the affine connections $\mathrm{d}\hat{\mathbf{r}} = -\tilde{\ell}\hat{\mathbf{M}}^T\mathrm{d}\tilde{\mathbf{k}}$, $\mathrm{d}\hat{\mathbf{r}} = -\ell\hat{\mathbf{M}}^T\mathrm{d}\mathbf{k}$, where $\hat{\mathbf{M}} = \mathbf{I} - (\hat{\mathbf{n}}\otimes\tilde{\mathbf{k}})/(\hat{\mathbf{n}}\cdot\tilde{\mathbf{k}})$, $\hat{\mathbf{M}} = \mathbf{I} - (\hat{\mathbf{n}}\otimes\mathbf{k})/(\hat{\mathbf{n}}\cdot\mathbf{k})$ are oblique projectors. Note that $\mathrm{d}^2\ell = -(\hat{\mathbf{N}}\mathrm{d}^2\hat{\mathbf{r}})\cdot\mathbf{k} - (\mathrm{d}\hat{\mathbf{r}}\cdot\hat{\mathbf{B}}\mathrm{d}\hat{\mathbf{r}})(\hat{\mathbf{n}}\cdot\mathbf{k}) - \mathrm{d}\hat{\mathbf{r}}\hat{\mathbf{N}}\cdot\mathrm{d}\bar{\mathbf{k}}$ does not lead to a normal projector for $\mathrm{d}\bar{\mathbf{k}}$, because intersecting rays at $\tilde{\mathrm{R}}$ correspond to skewed rays forming an astigmatic interval <R>. If we resolve $\mathrm{d}^2\theta_{\tilde{\mathrm{R}}} = 0$ for $\mathrm{d}\hat{\mathbf{r}}\hat{\mathbf{N}}\cdot\mathrm{d}\bar{\mathbf{k}}$ the terms with $\hat{\mathbf{N}}\mathrm{d}^2\hat{\mathbf{r}}$ cancel because of eq.(13). The isolation of a factor dk gives $\mathrm{d}\bar{\mathbf{k}} = l\mathbf{T}\mathrm{d}\mathbf{k}$, where the tensor

$$\mathbf{T} = -\hat{\mathbf{M}}\Big\{\hat{\mathbf{B}}_{\mathrm{C}} - \hat{\mathbf{B}}(\hat{\mathbf{n}}\cdot\mathbf{k}) - \hat{\mathbf{V}}\hat{\mathbf{Q}}_{\hat{n}}^T\Big[\hat{\mathbf{B}}_{\tilde{\mathrm{C}}} - \hat{\mathbf{B}}\Big(\hat{\mathbf{n}}\cdot\tilde{\mathbf{k}}\Big) + \hat{\mathbf{D}}_{\hat{\mathrm{V}}}\hat{\mathbf{V}}^{(-1)}\Big(\tilde{\mathbf{k}} - \tilde{\mathbf{c}}\Big) + \frac{1}{\tilde{\ell}}\tilde{\mathbf{K}}\Big]\hat{\mathbf{Q}}_{\hat{n}}\hat{\mathbf{V}}\Big\}\hat{\mathbf{M}}^T \tag{17}$$

describes the curvature of the converging wavefront in $\hat{\mathrm{H}}$. The inverses of the distances l_1, l_2 to the focal lines are its eigenvalues. The equation of transverse ray aberration is $\mathbf{K}d\mathbf{r} = \mathbf{K}d\hat{\mathbf{r}} - p\,d\overline{\mathbf{k}} = -\ell(d\mathbf{k} + p\mathbf{T}d\mathbf{k})$. If we combine the affine connections with eq. (5), we find the bridge $\ell\,d\mathbf{k} = \tilde{\ell}\mathbf{K}\hat{\mathbf{V}}^{(-1)}\hat{\mathbf{Q}}_{\hat{n}}^{T}\hat{\mathbf{M}}^{T}d\tilde{\mathbf{k}} = \tilde{\ell}\mathbf{K}\hat{\mathbf{Q}}_{\tilde{n}}\hat{\mathbf{V}}\hat{\mathbf{M}}^{T}d\tilde{\mathbf{k}}$, which leads to

$$\mathbf{K}d\mathbf{r} = -(\tilde{\ell}+\tilde{p})d\tilde{\mathbf{k}}\tilde{\mathbf{G}}_{\tilde{\mathrm{R}}}^{T} = \tilde{\mathbf{G}}_{\tilde{\mathrm{R}}}(\tilde{\mathbf{K}}d\tilde{\mathbf{r}}) , \qquad \tilde{\mathbf{G}}_{\tilde{\mathrm{R}}} = \frac{\tilde{\ell}p}{\tilde{\ell}+\tilde{p}}\left(\mathbf{T} + \frac{1}{p}\mathbf{K}\right)\hat{\mathbf{V}}^{(-1)}\hat{\mathbf{Q}}_{\hat{n}}^{T}\hat{\mathbf{M}}^{T} . \quad (18,19)$$

We assume now a sufficient overlapping of corresponding areas covered by the aperture on both images; the superposition vector $\tilde{\mathbf{f}}_S = \tilde{\mathbf{K}}\tilde{\mathbf{u}} \cong -\tilde{L}'(\tilde{\mathbf{k}} - \tilde{\mathbf{k}}')$ must be small compared to the diameter of these areas, which should not differ much apparently, otherwise the correlation is not possible. We use also $\tilde{\mathbf{K}}'\,d\tilde{\rho} = -(\tilde{\ell}' + \tilde{p}' + \tilde{L}')d\tilde{\mathbf{k}}'$, dr' = $\mathbf{M}'^{T}(\mathbf{K}'\mathbf{dr}')$ with $\mathbf{M}' = \mathbf{I} - (\mathbf{n}' \otimes \mathbf{k}')/(\mathbf{n}'\cdot\mathbf{k}')$ and we apply eqs.(13,18,19), written in primes. If we express $d\tilde{\mathbf{k}}' = -\tilde{\mathbf{m}}'\,d\tilde{\beta}'$ by a lateral unit vector and an angular increment, we can write eq.(7) in the form $dD_{\tilde{\mathrm{R}}'} / d\tilde{\beta}' = \tilde{\mathbf{m}}' \cdot \tilde{\mathbf{f}}'_{\tilde{\mathrm{R}}'}$, which implies the Stetson fringe vector

$$\tilde{\mathbf{f}}'_{\tilde{\mathrm{R}}'} = \left(\tilde{\ell}' + \tilde{p}'\right)\tilde{\mathbf{G}}'^{T}_{\tilde{\mathrm{R}}'}\mathbf{M}'\left[(\mathbf{k}' - \mathbf{h}') - \mathbf{Q}_n\mathbf{V}^{(-1)}(\mathbf{k} - \mathbf{h})\right] - \frac{\tilde{\ell}' + \tilde{p}' + \tilde{L}'}{\tilde{L}'}\tilde{\mathbf{K}}'\tilde{\mathbf{f}}_S . \quad (20)$$

It is normal to the fringes and its inverse value gives the fringe spacing. If $\tilde{\mathrm{K}}$ is the fixed point, we exchange $\tilde{\ell}' + \tilde{p}'$ by $-\tilde{L}'$ in (20). We obtain then the visibility vector

$$\tilde{\mathbf{f}}'_{\tilde{\mathrm{K}}} = \tilde{L}'\tilde{\mathbf{G}}'^{T}_{\tilde{\mathrm{K}}}\mathbf{M}'\left[(\mathbf{k}' - \mathbf{h}') - \mathbf{Q}_n\mathbf{V}^{(-1)}(\mathbf{k} - \mathbf{h})\right] , \quad (21)$$

situated between the homologous rays. The fringe is contrasted there, if this vector, divided by the image distance, is small compared to the ratio of λ and aperture diameter.

3. Second derivative of the optical path difference, fringe curvature

The second differential of eq.(3) is $\mathrm{d}^2D = \mathrm{d}^2L_{\mathrm{S}} - \mathrm{d}^2L'_{\mathrm{S}} - \mathrm{d}^2\left(\tilde{L} + \tilde{p}\right) + \ldots + \mathrm{d}^2\tilde{q} - \mathrm{d}^2\tilde{q}'$. We use the relations $(\tilde{L} + \tilde{p} + \tilde{\ell})\left|d\tilde{\mathbf{k}}\right| \cong (\tilde{L}' + \tilde{p}' + \tilde{\ell}')\left|d\tilde{\mathbf{k}}'\right|$, $\mathrm{d}^2L_{\mathrm{S}} = (\mathbf{N}\mathrm{d}^2\mathbf{r})\cdot\mathbf{h} + \mathbf{dr}\cdot\mathbf{B}_{\mathrm{H}}\mathbf{dr}$, … and the reverse eq.(16). We get then with eqs.(13,18) provisionally

$$\mathrm{d}^2D_{\tilde{\mathrm{R}}'} = \left(\mathbf{N}'\,\mathrm{d}^2\mathbf{r}'\right)\cdot\mathbf{M}'\left[(\mathbf{k}' - \mathbf{h}') - \mathbf{Q}_n\mathbf{V}^{(-1)}(\mathbf{k} - \mathbf{h})\right] - \frac{1}{\tilde{L}'}\left(\tilde{\mathbf{K}}'\,\mathrm{d}^2\tilde{\rho}\right)\cdot\tilde{\mathbf{f}}_S - \frac{2}{p}d\hat{\mathbf{r}}\cdot\mathbf{K}d\mathbf{r} + \ldots$$
$$- p'^2\tilde{\ell}'^2\left(\tilde{\ell}' + \tilde{p}'\right)^2 d\tilde{\mathbf{k}}'\cdot\tilde{\mathbf{G}}'^{T}_{\tilde{\mathrm{R}}'}\left(\mathbf{T}'_{\mathrm{F}} + \frac{1}{p'}\mathbf{K}'\right)\tilde{\mathbf{G}}'_{\tilde{\mathrm{R}}'}\,d\tilde{\mathbf{k}}' + \tilde{\ell}^2 d\tilde{\mathbf{k}}\cdot\left(\tilde{\mathbf{T}} + \frac{1}{\tilde{\ell}}\tilde{\mathbf{K}}\right)d\tilde{\mathbf{k}} - \ldots , \quad (22)$$

$$\mathbf{T'}_{\mathrm{F}} = \mathbf{M'}\Big\{\mathbf{B'}_{\mathrm{H'}} - \mathbf{B'}(\mathbf{n'}\cdot\mathbf{k'}) - \mathbf{V'}\,\mathbf{Q'}_{n'}^{T}\Big[\mathbf{B}_{\mathrm{H}} - \mathbf{B}(\mathbf{n}\cdot\mathbf{k}) + \mathbf{D}_{\mathrm{V}}\mathbf{V}^{(-1)}(\mathbf{k}-\mathbf{h}) + \frac{1}{p}\mathbf{K}\Big]\mathbf{Q'}_{n'}\,\mathbf{V'}\Big\}\mathbf{M'}^{T}$$

$$\tilde{\mathbf{T}} = \hat{\mathbf{M}}\Big\{\hat{\mathbf{B}}_{\tilde{\mathrm{C}}} - \hat{\mathbf{B}}\big(\hat{\mathbf{n}}\cdot\tilde{\mathbf{k}}\big) - \hat{\mathbf{V}}\hat{\mathbf{Q}}_{\tilde{n}}^{T}\Big[\hat{\mathbf{B}}_{\mathrm{C}} - \hat{\mathbf{B}}\big(\hat{\mathbf{n}}\cdot\mathbf{k}\big) + \hat{\mathbf{D}}_{\hat{\mathrm{V}}}\hat{\mathbf{V}}^{(-1)}(\mathbf{k}-\mathbf{c}) - \frac{1}{p}\mathbf{K}\Big]\hat{\mathbf{Q}}_{\tilde{n}}\hat{\mathbf{V}}\Big\}\hat{\mathbf{M}}^{T}. \quad (23)$$

The tensor $\tilde{\mathbf{T}}$ determines the astigmatic interval $<\tilde{\mathrm{P}}>$ and is similar as $\mathbf{T}$ in eq.(17). This indicates the duality expressed by $\hat{\mathbf{M}}\hat{\mathbf{V}}\hat{\mathbf{Q}}_{\hat{n}}^{T}\big[\tilde{\mathbf{T}} + \tilde{\mathbf{K}}/\tilde{\ell}\big] = [\mathbf{T} + \mathbf{K}/p]\hat{\mathbf{Q}}_{\tilde{n}}\hat{\mathbf{V}}\hat{\mathbf{M}}^{T}$. If we combine this relation with eqs.(18,19), we obtain $2\mathrm{d}\hat{\mathbf{r}}\cdot\mathbf{K}\mathrm{d}\mathbf{r} = 2p\tilde{\ell}^{2}\mathrm{d}\tilde{\mathbf{k}}\cdot(\tilde{\mathbf{T}} + \tilde{\mathbf{K}}/\tilde{\ell})\mathrm{d}\tilde{\mathbf{k}}$. Eq.(22) can now be simplified and the final result becomes with eqs.(20,21)

$$\frac{\mathrm{d}^{2}D_{\tilde{\mathrm{R}}'}}{\mathrm{d}\tilde{\beta}'^{2}} = \frac{\tilde{\mathbf{f}}'_{\tilde{\mathrm{R}}'}\cdot\big(\tilde{\mathbf{K}}'\,\mathrm{d}^{2}\tilde{\rho}\big)}{(\tilde{L}' + \tilde{p} + \tilde{\ell})\mathrm{d}\tilde{\beta}'^{2}} + \frac{\tilde{\mathbf{f}}'_{\tilde{\mathrm{K}}}\cdot\tilde{\mathbf{G}}'^{(-1)}_{\tilde{\mathrm{K}}}\big[\mathbf{N}'\,\mathrm{d}^{2}\mathbf{r}'\big]_{G}}{\tilde{L}'\,\mathrm{d}\tilde{\beta}'^{2}} - \quad (24)$$

$$-\big(\tilde{\ell} + \tilde{p}\big)^{2}\tilde{\mathbf{m}}'\cdot\tilde{\mathbf{G}}'^{T}_{\tilde{\mathrm{R}}'}\Big(\mathbf{T}'_{\mathrm{F}} + \frac{1}{p'}\mathbf{K}'\Big)\tilde{\mathbf{G}}'_{\tilde{\mathrm{R}}'}\,\tilde{\mathbf{m}}' - \tilde{\ell}^{2}\tilde{\mathbf{m}}\cdot\Big(\tilde{\mathbf{T}} + \frac{1}{\tilde{\ell}}\tilde{\mathbf{K}}\Big)\tilde{\mathbf{m}} + \tilde{\ell}'^{2}\,\tilde{\mathbf{m}}'\cdot\Big(\tilde{\mathbf{T}}' + \frac{1}{\tilde{\ell}'}\tilde{\mathbf{K}}'\Big)\tilde{\mathbf{m}}'.$$

The second term is negligible on the ridge of a fringe with a very good contrast. Then eq.(24) relates the fringe vector times the curvature to the three quadratic forms. Let us add, that we have with $\mathbf{dr'}\cdot\nabla_{n'} = \mathbf{dr}\cdot\nabla_{n} = \mathbf{dr'}\cdot\mathbf{Q}_{n}\mathbf{V}^{(-1)}\nabla_{n}$, the integrability and eq.(8)

$$\mathbf{B'} = -\nabla_{n'}\otimes\mathbf{n'} = -\mathbf{Q}_{n}\mathbf{V}^{(-1)}\nabla_{n}\otimes\big(\mathbf{Q}_{n}\mathbf{n}\big) = \mathbf{Q}_{n}\mathbf{V}^{(-1)}\big(\mathbf{B} - \boldsymbol{\kappa}_{c}\big)\mathbf{V}^{(-1)}\mathbf{Q}_{n}^{T}. \quad (25)$$

The term $\boldsymbol{\kappa}_{c} = \mathbf{B} - (1/2)\Big\{\big[(\nabla_{n}\otimes\boldsymbol{\omega})\mathbf{N} - \mathbf{BE}\boldsymbol{\Omega} + \mathbf{B}\big]\mathbf{V} + \mathbf{V}\big[\mathbf{B} + \mathbf{EB}\,\boldsymbol{\Omega} + \mathbf{N}(\nabla_{n}\otimes\boldsymbol{\omega})^{T}\big]\Big\}$ describes the *curvature change*. For a small isometric deformation it turns into the reduced curvature of Koiter-Sanders from the shell theory. In conclusion we remark, that the three linear forms in eq.(7) and the three quadratic forms of eq.(24) replace somehow the three scalar products with displacement vectors of eq.(1).

Appendix: On the meaning of curvature changes

This section is only indirectly related to the subject. We illustrate (by a short extension) the meaning of the curvature changes eqs.(25) and (16), which are here expressed by the polar decomposition (5) and the curvature eq.(6). For $\mathbf{B} \equiv 0$ eq.(25) describes the curvature $\mathbf{B'}$ of a surface $\mathcal{A}^{2} \subset \mathcal{R}^{3}$ by a virtual deformation of a plane. This can be generalized to $\mathcal{A}^{n-1} \subset \mathcal{R}^{n}$, with an interpretation of the interior Ricci tensor $\mathbf{R}$ and an embedding. We recall the components $R_{\alpha\beta} = \Gamma^{\lambda}_{\alpha\lambda,\beta} - \Gamma^{\lambda}_{\alpha\beta,\lambda} + \Gamma^{\mu}_{\alpha\lambda}\Gamma^{\lambda}_{\mu\beta} - \Gamma^{\mu}_{\alpha\beta}\Gamma^{\lambda}_{\mu\lambda}$ with Christoffel symbols $\Gamma^{\lambda}_{\alpha\beta} = a^{\lambda\mu}\big(a_{\mu\alpha,\beta} + a_{\mu\beta,\alpha} - a_{\alpha\beta,\mu}\big)/2$ and interprete $\mathrm{a}_{\alpha\beta}$ as components of the projector $\mathbf{N'} = \mathbf{I} - \mathbf{n'}\otimes\mathbf{n'} = a_{\alpha\beta}\mathbf{a}^{\alpha}\otimes\mathbf{a}^{\beta} = \mathbf{a}^{\alpha}\otimes\mathbf{a}_{\alpha}$ We write $\mathbf{N'}\big[\mathbf{N'}\big[\nabla_{n'}\otimes\big(\nabla_{n'}\otimes\mathbf{N'}\big) - \nabla_{n'}\otimes\big(\nabla_{n'}\otimes\mathbf{N'}\big)^{T}\big]\mathbf{N'}\big[\mathbf{N'} = \boldsymbol{R}^{T} = \mathbf{B'}\otimes\mathbf{B'} - \mathbf{B'}\otimes\mathbf{B'}\big]^{T}$, according

to eq.(6). The sign $]]^T$ marks a transposition of the 2nd and the 4th factor. In fact, the Riemann-Christoffel tensor $\boldsymbol{R}$ (with components $R^{\lambda}{}_{\alpha\beta\gamma}$) appears in this relation, see f.i. [6], eq.(1.13.39). The Ricci tensor becomes by contraction $\mathbf{R} = \mathbf{B'B'} - \mathbf{B'}\,(\mathbf{B'\cdot N'})$, where $\mathbf{B'\cdot N'} = \mathbf{trB'}$ is the trace of $\mathbf{B'}$. On a surface we have $\mathbf{R} = -K\mathbf{N'}$ with the Gauss' curvature K. As a simple example of the use of eqs.(25) for $\mathbf{R}$ we outline an interpretation by a „deformation" of the Schwarzschild-solution for the central field of gravitation. $d\sigma'^2 = -(1-2M/r)c^2dt^2 + (1-2M/r)^{-1}dr^2 + r^2d\theta^2 + r^2\sin^2\theta d\varphi^2$ (see [7], p.607), where $2M$ is the Schwarzschild radius. With $\sqrt{2M/r} = \sin\psi$ we have $a_{00} = -\cos^2\psi$, $a_{11} = \cos^{-2}\psi$, $a_{22} = r^2$, $a_{33} = r^2\sin^2\theta$ and a relatively long calculation shows, that the 4D-Ricci tensor vanishes in accordance with the field equations. However, the 3D-Ricci tensor $\mathbf{R}$ of the space part has the non-vanishing components $R_{11} = \tan^2\psi/r^2$, $R_{22} = -\sin^2\psi/2$, $R_{33} = R_{22}\sin^2\theta$. Alternatively we start with $\mathbf{r'} = r\mathbf{k} + w(r)\mathbf{n}$, where $\mathbf{k}(\theta,\varphi)$ is the radial unit vector and n the unit normal of $\mathcal{R}^3$. With $\nabla_n \otimes \mathbf{k} = \overline{\mathbf{K}}/r$, $\overline{\mathbf{K}} = \mathbf{N} - \mathbf{k}\otimes\mathbf{k}$, we have $d\mathbf{r'} = d\mathbf{r}\left[\mathbf{k}\otimes(\mathbf{k} + w_{,r}\mathbf{n}) + \overline{\mathbf{K}}\right] = d\mathbf{r}\mathbf{N}\mathbf{F}^T$ and $ds'^2 = d\mathbf{r}\cdot\mathbf{N}\mathbf{F}^T\mathbf{F}\mathbf{N}d\mathbf{r} = d\mathbf{r}\cdot\left[(1+w_{,r}^2)\mathbf{k}\otimes\mathbf{k} + \overline{\mathbf{K}}\right]d\mathbf{r}$, thus $\mathbf{V}^{(-1)} = \mathbf{k}\otimes\mathbf{k}/\sqrt{1+w_{,r}^2} + \overline{\mathbf{K}}$ $= \mathbf{k}\otimes\mathbf{k}\cos\psi + \overline{\mathbf{K}}$. The polar decomposition eq.(5) gives with $\mathbf{k'} = \mathbf{k}\cos\psi + \mathbf{n}\sin\psi$ $\mathbf{Q}_n\mathbf{N} = \mathbf{F}\mathbf{N}\mathbf{V}^{(-1)} = \mathbf{k'}\otimes\mathbf{k} + \overline{\mathbf{K}}$, $\nabla_n \otimes \mathbf{Q}_n\mathbf{n} = \mathbf{k}\otimes\mathbf{k'}\tan\psi/2r - \overline{\mathbf{K}}\sin\psi/r$. Thus eq.(25) leads to $\mathbf{B'} = \frac{\sin\psi}{r}\left(\overline{\mathbf{K}} - \frac{1}{2}\mathbf{k'}\otimes\mathbf{k'}\right)$, $\mathbf{B'}\cdot\mathbf{N'} = \frac{3\sin\psi}{2r}$, $\mathbf{R} = \frac{\sin^2\psi}{r^2}\left(\mathbf{k'}\otimes\mathbf{k'} - \frac{1}{2}\overline{\mathbf{K}}\right)$, or $R_1^1 = \sin^2\psi/r^2 = R_{11}a^{11}$, $R_2^2 = -\sin^2\psi/2r^2 = R_3^3$, q.e.d.. Finally two equations of type (16) would show a curious relation between the images of 4D-null-geodesics (light rays) and the images of 3D-geodesics of the vase-like surface $w(r)$ ([7], p.837).

References

1. Fagan, W.F., Beeck, M.A. and Kreitlow, H. (1981) The holographic vibration analysis of rotating objects using a reflect. image derotator. *Opt. Lasers Eng.,* 2, 21-32.
2. Stimpfling, A. and Smigielski, P. (1985) New method for compens. and measuring any motion of 3-dim. objects in hologr. Interferometry, *Opt. Eng.* 24 (5), 821-823.
3. Cuche, D. (1989) Large deformation analysis by holographic Interferometry. *Proc. 2d International. Conference on holographic Systems, Comp. and Applications,* Bath (UK).
4. Khedre, O.M. and Stupnicki, J. (1990) Large deflect.of shells measured by use immersion method of hologr. Interf., *Proc. 9th Int. Conf. on Exp. Mech.,* Copenhagen, 1897.
5. Tatasciore, Ph. (1989) Récupération des franges en interférométrie holographique appliquée aux grandes déformations des corps opaques. Thesis 8917, ETH, Zürich.
6. Green, A.E. and Zerna, W. (1968) *Theoretical Elasticity.* 2nd ed. Clarendon Press, Oxford, 34-36.
7. Misner, C.W., Thorne, K.S. and Wheeler, J.A. (1972) *Gravitation.* W.H. Freeman & Company, New York, 607, 837.

INTERFERENCE OF FRACTURE SURFACES OBSERVED BY MEANS OF OPTICAL METHODS FOR THE CRACKS SUBJECTED TO SHEAR AND COMPRESSION

M.SZPAKOWSKA, P.PYRZANOWSKI, J.STUPNICKI
Institute of Aeronautics and Applied Mechanics
Warsaw University of Technology
ul. Nowowiejska 24, 00-665 Warszawa, Poland

1. INTRODUCTION

There are many works to be found in the literature on fracture mechanics, in which numerical simulations of the stress state at a tip of fatigue crack under cyclic loads are presented. The authors usually describe mechanisms of crack opening, that provides a basis for the amplitudes of variation of the Stress Intensity Factors (SIFs) to be determined. The fact that the rough crack surfaces interfere is of crucial importance in the cases when a crack tip propagates due to shear, i.e. in II and III modes of crack propagation under conditions of simultaneous crack closing. We deal with such a situation when considering the crack propagation in a surface layer subjected to a contact load. These problems appear e.g. in bearing race, toothed flanks, or rail-wheel contact and were discussed in [1-10]. The authors presented numerical procedures allowing for the accurate description of a stress state at a tip of a crack, in which complex geometry of the object was taken into account, as well as high gradients of residual stresses occurring in a surface layer, together with normal and tangential loads. However, the contact flexibility of crack edges was neglected while their tangential interaction was represented in terms of the Amontons friction law.

In these works neither a complicated geometrical structure of the real crack faces was taken into account nor the fact that tangential loads might be transmitted through the surface aspherities interaction rather than due to friction.

Further development in this field requires a more accurate description of the process of crack faces interference as well as demands the wear of crack surfaces due to cyclic loads and microslips to be included into the model. The experimental investigations are therefore necessary into the crack surfaces interaction under normal and tangential loads.

The work presents the methods and results of the investigation into interference and microslips of crack faces under simultaneous normal and tangential loads, which was carried out by means of the Electronic Speckle Pattern Interferometry (ESPI) and Grating Holographic Interferometry (GHI).

A. Lagarde (ed.),
IUTAM Symposium on Advanced Optical Methods and Applications in Solid Mechanics, 235–246.

2. THE OBJECT EXAMINED

The experiments were performed on samples of the shape shown in Figure 1, made of the 900A steel. The samples had undergone the fatigue process performed on the INSTRON machine with the following three loading cycles applied: R = 0, - 0.5, -1.0 ($R = \sigma_{min} / \sigma_{max}$) for a crack of the length a a ≈ 12 mm to be produced. The samples pre-treated in this way were then subjected to the compressive force P acting in the direction which made an angle of $\alpha = 30 \div 90^0$ with the tangent to the crack surface. The loading force within the range of P = 0 ÷ 15000N was generated by the loading frame, in which the actuator was driven by a manual pump to avoid any vibrations.

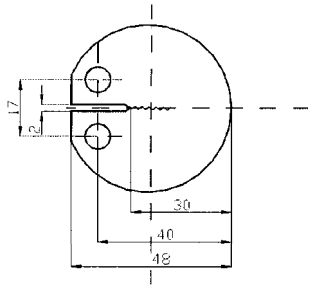

Figure 1. The samples made of 900A steel, after the fatigue process

3. THE EXPERIMENTAL METHODS APPLIED

Two optical methods, i.e., the Electronic Speckle Pattern Interferometry (ESPI) [11] and Grating Holographic Interferometry (GHI) [12] were used for examination of the displacement.

3.1. ESPI METHOD

The speckle interferometer had two orthogonal branches. Fig.2 shows the zx branch of interferometer. The argon laser beam of light ($\lambda = 514.5$ nm) was pre-split into four beams, which illuminated the object in the planes zx and zy symmetrically about the z-axis, i.e. the observation direction. The laser beams travelling in the plane zx, which made the angle $\theta = 30^o$ with the normal were used for determination of the displacements u along the x-axis, while the beams travelling in the zy plane, which made the angle $\theta = 45^o$ with the normal and were used for determination of the displacement v along the y-axis.

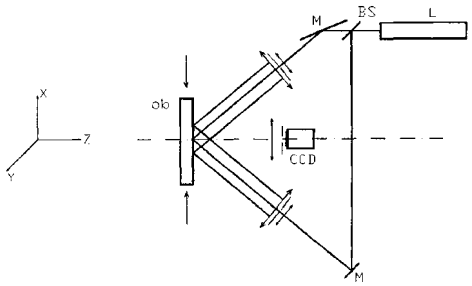

Figure 2. The Scheme of Electronic Speckle Pattern Interferometry set-up, ob – the sample, CCD –the camera CCD, BS- beam splitter, M–mirror, L –laser.

The monochromatic camera CCD of 512x480 pixels was used for registration of the light intensity distribution.

The method consists in registration of the light intensity distributions before and after the object displacement, respectively. Then the respective intensities are subtracted and the module of the obtained difference is determined. As a result, we have the following formula for the light intensity distribution

$$I = |I_1 - I_2| = \left|4\sqrt{I_0 I_r}\sin(\Delta\phi + \psi)\sin 2\Delta\phi\right| \tag{1}$$

where:

I_1,I_2 - light intensities before and after the object displacement, respectively,

$4\sqrt{I_0 I_r}$ - amplitude of the image intensity modulation,

$\sin(\Delta\phi + \psi)$ - random factor, which does not contain any information, a source of noise,

$\sin\Delta\phi$ - factor responsible for generation of the fringe pattern

where $\Delta\phi$ stands for the phase difference being sought.

At the same time the geometrical configuration of the speckle interferometer used makes the following equation true:

$$I = I_B + I_M \cos\left(\frac{4\pi}{\lambda} u \sin\theta\right) \tag{2}$$

similarly, for the second pair of beams:

$$I = I_B + I_M \cos\left(\frac{4\pi}{\lambda} v \sin\theta\right) \tag{3}$$

where I_B, I_M stand for the background intensity and intensity modulation, respectively, u, v represent the displacement in the direction coincident with the sensitivity vector, θ stands for the angle the illumination makes with the observation direction, λ denotes the wave length.

In the present tests a series of ineterferograms have been registered for the step-wise growing loads.

A chosen fringe close to the support of the specimen was assigned with the zero number while the subsequent fringes got the respective subsequent fringe orders, which has enabled the displacement of any point on the sample surface to be

determined. Using formulas (2) and (3) the displacement components u and v directed along the x and y axes were determined for the points lying on the sample surface along the normal to the crack surface. These components were then recalculated to obtain the displacement components δ_n and δ_t normal and tangential to the crack, respectively.

3.2. GRATING HOLOGRAPHIC INTERFEOMETRY

Figure 3 shows the optical arrangement for registration of the holograms superimposed with the use of diffraction gratings. A flat surface of the examined object is covered with the crossed line diffraction grating, while a holographic plate without an antihalation backing is mounted directly in front of the object with the emulsion-covered side facing the grating. The collimated He-Ne laser beam illuminates the object. A part of the light illuminating the holographic plate passes through it and illuminates the object surface with the grating put on it. The part of the beam diffracted by the grating illuminates the emulsion of the holographic plate once again and interferes with the illuminating beam. The double exposure hologram for two subsequent levels of loading provides the information about the wave fronts variation during the process of the object displacement. In the process of reconstruction, like in registration, the collimated laser beam illuminates the hologram. The wave fronts diffracted on the grating, which has arosen in the holographic plate, create at least four images of the object located in the planes perpendicular to the diffraction grating. The images are angularly separated from each other and can be observed from the directions making angles $\pm\theta$ with the normal to the holographic plate. The angle θ depends on the grating frequency f and the light wavelength λ applied to the reconstruction, i.e.

$$\theta = \arcsin \lambda \cdot f \tag{4}$$

Figure 4 shows a scheme of the hologram reconstruction system. Each of the images contains the interference lines depending on the object surface displacement. These images might be observed on the screen or recorded using a camera. The fringe pattern analysis requires the displacement vector components together with the sensitivity vectors to be considered.

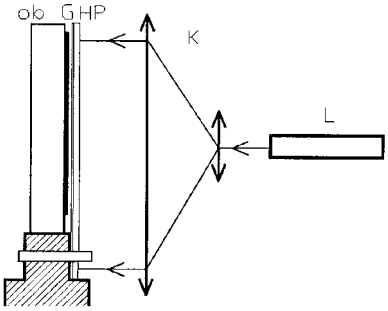

Figure 3. The optical arrangement for registration of the holograms superimposed with the use of diffraction gratings, ob – sample, G – grating, HP – holographic plate, K – collimator, L – laser.

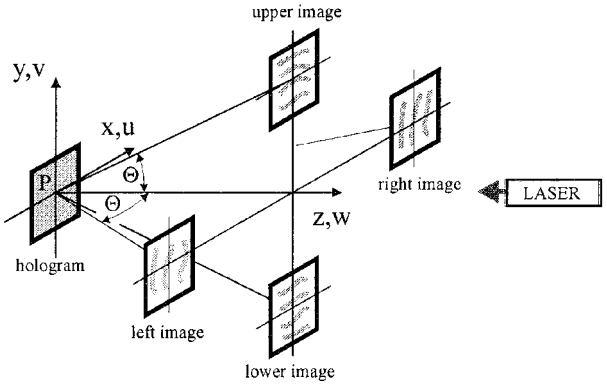

Figure 4. Scheme of the hologram reconstruction system.

Upon assuming the co-ordinate system, in which the z-axis is normal to the object surface, while the axes *x* and *y* coincide with the grating lines, one can consider separately the displacement components in zx and zy planes, respectively. The fringe order N_{1x} at a given point results from the displacements u and w. For the interferogram observed in the plane xz at the angle θ relative to the normal we have:

$$N_{1x} = \frac{1}{\lambda}\left[w(1+\cos\theta)+u\sin\theta\right] \tag{5}$$

Similarly, for the interferogram observed at the angle – θ for the same point of object surface we can write

$$N_{2x} = \frac{1}{\lambda}\left[w(1+\cos\theta)-u\sin\theta\right] \tag{6}$$

For the second pair of interferograms observed in the plane zy at the angles θ and –θ we have:

$$N_{1y} = \frac{1}{\lambda}\left[w(1+\cos\theta)+v\sin\theta\right] \tag{7}$$

$$N_{2y} = \frac{1}{\lambda}\left[w(1+\cos\theta)-v\sin\theta\right] \tag{8}$$

After adding and subtracting equations (5) and (6) the displacement components can be determined as follows:

$$w = \frac{\lambda}{2(1+\cos\theta)}\left(N_{1x}+N_{2x}\right) \tag{9}$$

$$u = \frac{\lambda}{2\sin\theta}\left(N_{1x}-N_{2x}\right) \tag{10}$$

Similarly from equations (7) and (8) we have

$$w = \frac{\lambda}{2(1+\cos\theta)}\left(N_{1y}+N_{2y}\right) \tag{11}$$

$$v = \frac{\lambda}{2\sin\theta}\left(N_{1y}-N_{2y}\right) \tag{12}$$

For the integral fringe order number N to be determined there should exist in the examined area some points not undergoing displacement, i.e. the zero fringe order has to cross the area. This condition is very difficult to satisfy. However, the structure of formulas (5) - (8) enables one to determine, instead of the integral fringe order at a given point, only its relative number to the fringe order at the point we assume as the reference one. However, for the sign of the fringe order to be determined some additional information about the object displacement is needed.
The results coming from formulas (9) and (11), for the out-of-plane displacement determined from the iterferograms reconstructed in the planes zx and zy should be the same, which might be helpful in verification of the fringe order number.

4. RESULTS

The ESPI method was applied to examination of the sample, shown in Fig.1 subjected to loads acting at the angles $\alpha = 90^0$, 45^0, and 30^0 with the tangent to the crack surface. Fig. 5 a and b shows the two fringe patterns obtained at the tenth steps of analysis for the force P acting at the angle $\alpha = 30^0$. The displacement components u and v for the points lying on the sample surface were determined from formulas (2) and (3) and then recalculated to obtain the components normal δ_n and tangential δ_t to the fracture surface, respectively. The ratio between the tangential and normal components corresponding to the angle $\alpha = 30^0$ reads

$$P_t/P_n \cong 1.7.$$

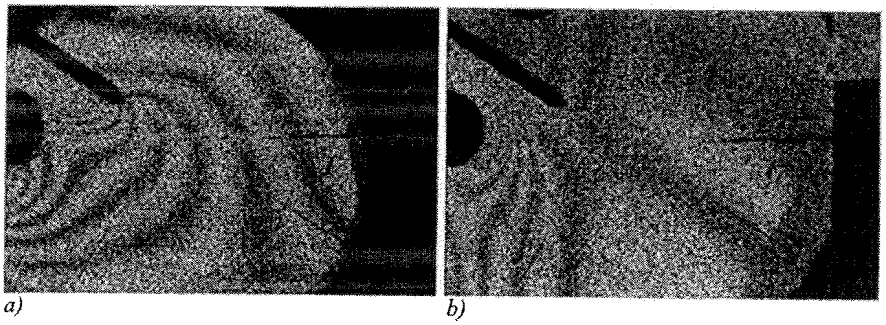

Figure 5. The fringe patterns obtained by means of the Electronic Speckle Pattern Interferometry method a) lines of equal u displacement, b) lines of equal v displacement.

The results were obtained for two cross-sections made at distances of 9 mm and 7 mm from the crack tip. In these cases any component of the displacement has had no discontinuity, it means that even the initial loading by means of the force P_0 = 300N has already closed the crack forcing at the same time the asperities matching and eliminating slips on the surface, as well.
The distributions of δ_n and δ_t for the points of the cross-section made at a distance of 9 mm from the crack tip along the sample diameter normal to the fracture are presented in Figure 6 a and b. The diagrams show the total displacements after

subsequent steps of analysis within the range of force from P_0 = 325N to P_{max} = 14560 N.

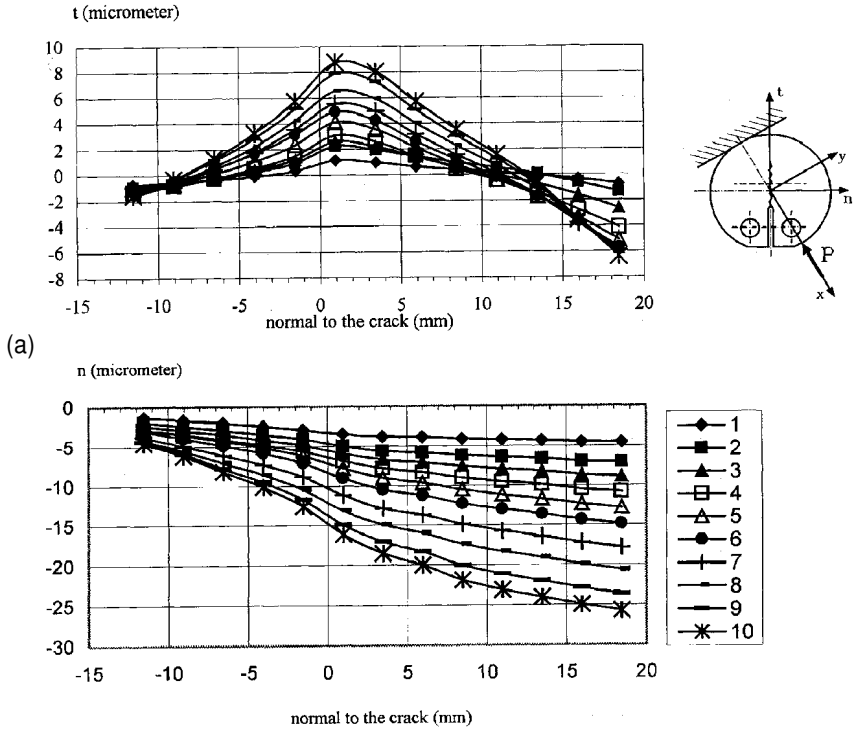

Figure 6. The distribution of displacement obtained by means ESPI method for cross-section made at a distance of 9.2mm from the crack tip, a) tangential component b) normal component.

The method of Holographic Grating Iterferometry was applied to examination of the samples shown in Figure1 subjected to the forces acting at the angles $\alpha = 90^0$ and 30^0. The force P was increased in a step-wise way and at each level of the loading the holograms were registered. The first exposure of the holographic plate at the step (i) was performed under the load corresponding to that for the second exposure at the previous step (i-1).

Figure 7 a, b and c, d show the four fringe patterns lying in the planes zx and zy, which have been reconstructed from one hologram following the schematic diagram presented in Figure 4 The sample was loaded at the angle $\alpha = 90^0$ and the first exposure was made for the force P = 300 N, while the second one for P = 7800 N.

Due to a direct registration of images by means of CCD camera at the angle $\theta = \pm 38^0$, some distortion of the images has arosen, being then eliminated numerically.

The two components of displacement u, v, which for $\alpha = 90^0$ denote the normal and tangential ones to the crack faces, while w is the out-of-plane component, have been determined on the assumption that the zero order fringe runs across the intersection of the sample axis and the left-hand edge of the examined area of the sample. The fringe order sign fulfills the experiment conditions i.e., compression of the sample.

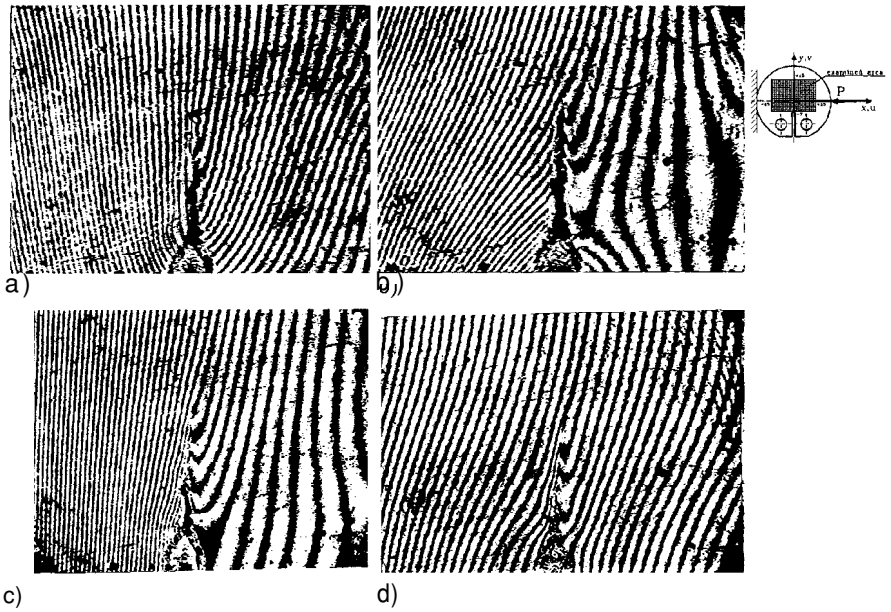

Figure 7. The four fringe patterns represent the displacement obtained in grating holographic method in planes a, b) zx and c, d) zy, for the sample loaded at the angle $\alpha = 90^0$.

Figure 8 shows the diagrams of the components determined along the sample axis. It should be emphasised that the component u normal to the fracture reveals discontinuity and the out of plane component has a significant value.
Although this component is neglected in the ESPI approach, due to the nature of the loading (compression of the sample) it could not have been avoided in our experiments.

Figure 9 a, b, b, d show the four fringe patterns lying in the planes of zx and zy, obtained for the load acting at the angle $\alpha = 30°$. The first exposure was made for the force P = 300 N while the second one for the P = 7800 N.
Figure 10 a, b show the diagrams of the u and v components of displacement along the five cross-sections of the sample.

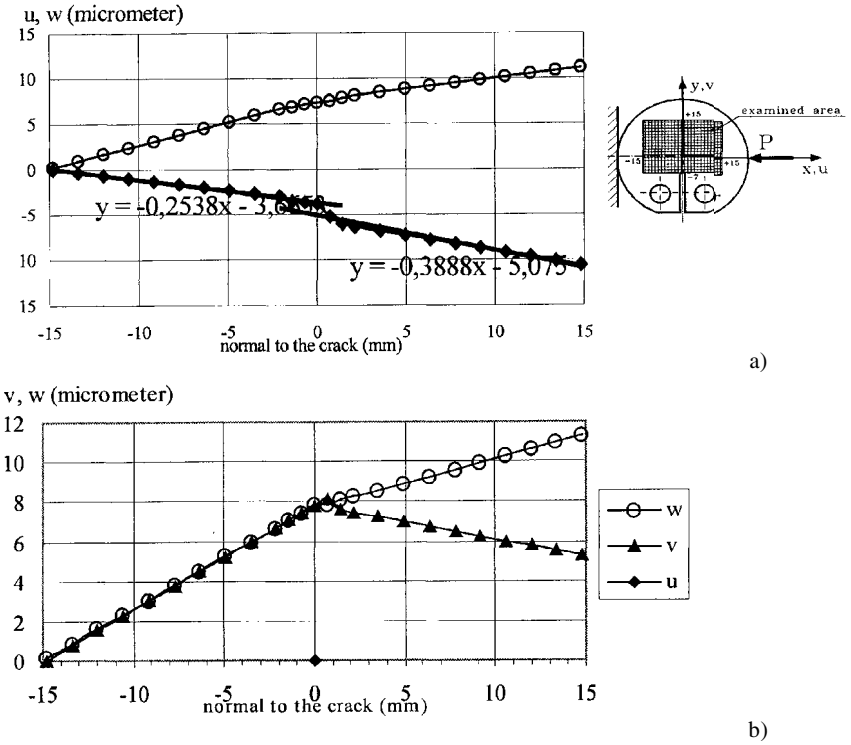

Figure 8. The distribution of displacement obtained by means of the Grating Holographic Interferometry for the cross-section made at a distance 7.2 mm from the crack tip a) the u, w components and b) v, w components

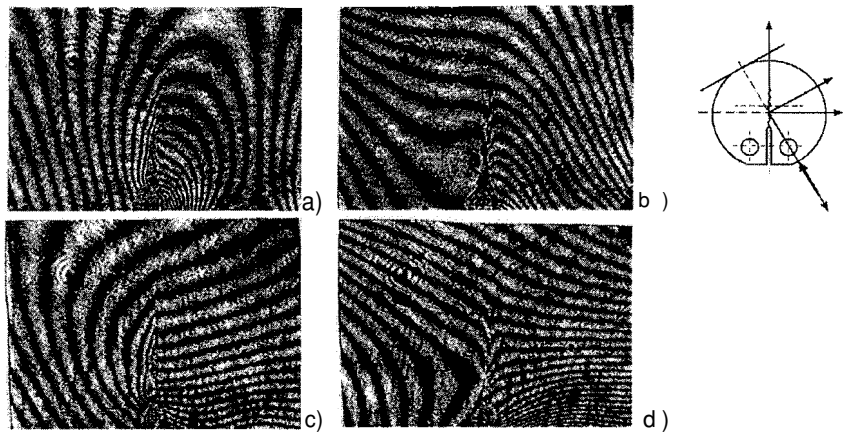

Figure 9. The four fringe patterns represent the displacement obtained from the grating holographic method in planes a, b) zx c, d) zy respectirely, for the sample loaded at the angle $\alpha = 30^0$

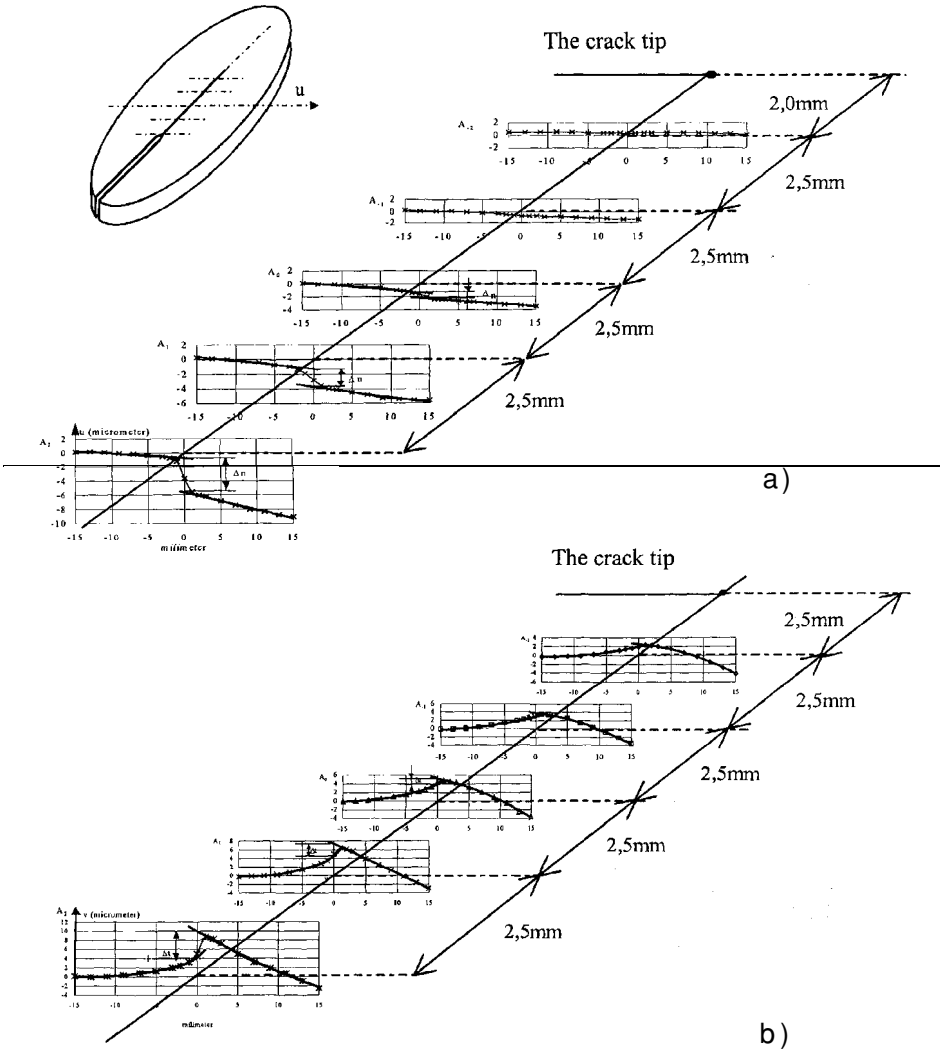

Figure 10. The results obtained by the use of GHI method for the cross-sections made at the distances 2 mm, 4.5mm, 7 mm, 9.5 mm, 12 mm respectirely from the crack tip a) normal displacement, b) tangential displacement

It should be emphasised that the components u and v reveal discontinuity for the three cross-sections far from the crack tip. Two cross-sections running across the crack at distances 2 and 4.5 mm from the crack tip reveal no disconuities. If the tangential component of displacement in the vinicity of the crack tip has a neglible value the Stress Intensity Factor K_{II} is equal to zero.

5. CONCLUSIONS

As concerns the examined problems:

1. The evidence has been found that the rough surfaces occurring due to propagation of the fatigue crack, which have not been damaged by micro slips create a kind of "shape joint", which when subjected to the compressive stresses normal to the crack faces may transmit high tangential loads, magnitudes of which exceed those resulting from the friction laws.
2. In the vicinity of crack faces, far from the crack tip, the strain concentrations were observed which resulted from local interactions between asperities of the faces.
3. The experiment has to be extended to cover the cases when the crack faces have been smoothed due to wear under condition of micro slips.

As concerns the experimental methods:

1. The results coming from the ESPI and GHI methods are in a good agreement.
2. The **ESPI** method is very convenient.
   - 2a. The object surface needs no special treatment and acquisition and storing of specklegrams in computer memory at subsequent stages of loading poses no difficulties.
   - 2b. In the course of analysis one can combine the loading stages optionally for a clear and contrast fringe pattern to be obtained.
   - 2c. The full field result of the fringe pattern provides immediately the information about displacement components, which allows for detection of discontinuities of displacements in the neighbourhood of cracks or at the strain concentration areas.
   - 2d. The two in plane components of the displacements u and v at subsequent stages of load growth can be determined almost straightforward.
   - 2e. By summing up the displacements registered at subsequent steps one can examine relatively high displacements. Moreover, registration of displacements at many steps facilitates observation of non-linear processes of deformation.
3. The **GHI** method has an advantage consisting in the fact that there is no need for concidering the displacement of the whole object as the holographic plate is mounted close to the examined part of the object surface. Moreover, this method is much less sensitive to vibrations of the object.
   - 3a. The fringe patterns obtained by means of the GHI method are very clear and four images are reconstructed from a single hologram. Discontinuities caused by the displacements due to the crack are visible at once.
   - 3b. The procedure of GHI requires some preparation of the object surface, i.e. the diffraction grating should be superimposed on it, which limits the applications to flat surfaces of the objects.
   - 3c. At each steps of the load growth a new holographic plate should be mounted on the object. Additionally the wet process of the hologram developing and fixation is needed combined with drying which delays the process of hologram analysis.

3d. Once the holographic plate are formed they can be analysed on separate stands yielding fringe patterns of good quality.

3e. The signs of the fringe orders for each interferogram have to be determined basing on some additional information about the object displacement

REFERENCES

1. Wójcik R. (1981). The analysis of strain and stress state near the crack tip in contact of deformable bodies. *Ph.D. Thesis* (in polish), Warsaw University of Technology.
2. Sih G.C., Tzou D.Y. (1984) Three-dimensional transverse fatigue crack growth in rail head. *Theor. Appl. Fracture Mech.* 103, pp. 103-115.
3. Hearle A.D., Johnson K.L. (1985). Mode II stress intensities for a crack parallel to the surface of an elastic half-space subjected to a moving point load. *J. Mech. Phys. Solids* 33, pp. 61-81.
4. Clayton P., Hill D.N. (1986). Rolling contact fatigue of rail steel. *Proc. of the Second International Symposium on Contact and Wear of Rail/Wheel System.* Kingston, Rhode Island, July, pp. 361-378.
5. Bower (1988). The influence of crack face friction and trapped fluid on surface initiated rolling contact fatigue cracks. *ASME, Journal of Tribology* 110, 704-711.
6. Olzak M., Stupnicki J., Wójcik R.(1991). Investigation of crack propagation during contact by finite element method. *Wear* 146, 229-240.
7. Stupnicki J., Olzak M., Wójcik R. (1991). Numerical analysis of surface crack propagation in rail-wheel contact zone. *Rail Quality and Maintenance for Modern Railway Operation.* Kluwer Academic, The Netherlands, pp. 385-395.
8. Bogdañski S., Olzak M., Stupnicki J.(1996). The effect of face friction and tractive force on propagation of 3D 'squat' type of rolling contact fatigue crack. *Proc. 2nd conf. on contact mech. and wear of rail/wheel syst.* Budapest 29-31 July 1996, 164-173.
9. Bogdañski S., Olzak M., Stupnicki J.: (1998). Numerical modelling of a 3D Rail RCF 'squat' type crack under operating load. Submitted and accepted: *Fatigue and Fracture of Engineering Materials and Structures.,* 1998, 21, pp. 923-935.
10. Olzak M., Stupnicki J. (1998). Effect of model of crack faces interaction on the value and the plot of Stress Intensity Factors (in polish). *Proc. of the XVII Symp. on Fatigue and Fracture,* Bydgoszcz Pieczysko, 1998.
11. Olszak A.: Integrated fiber digital speckle pattern interferometer with frequency modulated laser diode and its application. *Edit. WUT,* Warsaw 1997 p.21-35
12. Meirong Pu, P.J. Gielisser, Wei Xu. Grating holographic interferometry for three dimensional displacement measurements. *Proc. of Spring Conference on Experimental Mechanics,* June 7-9 1993, Dearborn, Michigan, pp.55-64.

SHEAROGRAPHY IN EXPERIMENTAL MECHANICS AND NONDESTRUCTIVE TESTING

Y.Y. HUNG
Department of Mechanical Engineering
Oakland University
Rochester, Michigan 48309, USA

Abstract

This paper reviews shearography and its applications in experimental mechanics and nondestructive testing. Shearography is an interferometric method for measuring surface displacement derivatives. Unlike holography, it does not require special vibration isolation; hence it can be employed in field/factory environments. The technique has already received wide industrial acceptance for nondestructive testing. Other applications include strain measurement, material characterization, residual stress evaluation, vibration studies and 3D shape measurement.

1. Introduction

Shearography is an interferometric technique developed to overcome several limitations of holography. Contrary to holography which measures surface displacements, shearography measures derivatives of surface displacements, thus eliminating the need to numerically differentiating displacement data to yield strains. More significantly, it eliminates the reference beam of holography, leading to the advantages of simplified optical setup, reduced coherence length requirement of laser, and not requiring special vibration isolation. Shearography is practical, therefore it has already received wide industrial acceptance for nondestructive testing. Currenlty the rubber industry is routinely using shearography for evaluating tires and the aerospace industry has adopted the technique for nondestructive testing of composite structures. Other applications of shearography include measurement of strains, material properties, residual stresses, 3-D shapes, as well as vibration studies.

There are three versions of shearography employing different recording media: photographic emulsion[1], thermoplastic[2] and video[3]. Video shearography is a computerized process which is superior to the other two versions. It uses video sensors (such as CCD) as recording medium and digital image processing technology to acquire the results thus eliminating the consumable materials used by the photographic and thermoplastic versions. Furthermore, the computerization of shearography allows the automation of fringe analysis. This paper reviews computerized shearography and its applications.

2. Video shearography

2.1. DESCRIPTION OF THE TECHNIQUE

A typical set-up of video shearography is illustrated in Fig. 1 The object to be studied is illuminated with a point source of coherent light and it is imaged by a video image-shearing camera. The shearing device used a birefringent crystal which splits one object point into two in the image plane. A pair of laterally sheared images is received by the image sensor and thus the technique is named as shearography. The key to the video recording in shearography is the birefringent crystal serving as a shearing device. As illustated in Fig. 2, the shearing crystal brings two non-parallel beams scattered from two

A. Lagarde (ed.),
IUTAM Symposium on Advanced Optical Methods and Applications in Solid Mechanics, 247–261.

different points on the object surface to become colinear or nearly co-linear. Note that the spatial frequency of the interference pattern produced by the two beams is proportional to sine the half-angle between the interference beams. In this case the angle is nearly zero, therefore the spatial frequency is so low that it is resolvable by video image sensors such as a CCD. Since the two sheared wavefronts transmitted by the two axes of the birefringent crystal are orthogonally polarized, a polarizer oriented at 45° to the crystal's axes is needed to make the two wavefronts to interfere. Because the object surface is rough, the interference produces a random interference pattern known as a speckle pattern. In the process, the two speckle patterns of the test object (before and after deformation) are sequentially digitized into a micro-computer via a frame grabber. The difference of the two speckle patterns computed by the computer produces a fringe pattern depicting the displacement derivative with respective to the direction of shearing. A frame grabber with on-board processing capability allows the fringe pattern to be produced in real-time (i.e. video rate).

Fig. 3(a) shows a fringe pattern depicting the derivative of deflection with respect to x-direction of a rectangular plate clamped along its boundaries and subjected to uniform pressure, and Fig.3(b) shows the y derivative of the plate deflection.

2.2. FRINGE FORMATION

A shearographic speckle pattern of an object may be mathematically represented as:

$$I = a + b\cos(\beta) \tag{1}$$

where : **I** is the intensity distribution of the speckle pattern, **a** - the dc intensity, **b** - the modulation of the interference fringes, and β is a random phase angle. After the object is deformed, this speckle pattern is slightly changed to **I'** which is mathematically represented as:

$$I' = a + b\cos(\beta + \Delta) \tag{2}$$

where A is a phase change due to surface deformation. The difference of the two speckle patterns before and after deformation yields:

$$I_d = b(\cos(\beta + \Delta) - \cos(\beta)) \tag{3}$$

where $\mathbf{I}_d$, the intensity distribution of the difference, shows a fringe pattern. Dark fringe lines corresponds to $\Delta = 2n\pi$; n is the fringe order. Traditional fringe analysis requires identification of fringe orders. The computerized shearography allows Δ, the phase change due to deformation , to be automatically determined using a phase determination technique described below.

2.3. PHASE DETERMINATION TECHNIQUE

Phase shift technique is used to determine the fringe phase distribution A of the fringe pattern. Generally speaking, there are a total of four unknowns at each point in the speckle patterns of Eq(1) and Eq(2), namely, **a** - the dc intensity, **b** - the modulation of the interference fringes, β the random phase angle, and the fringe phase Δ. A minimum of

four equations are required to solve for the four unknowns. However, the only information we want is Δ.

The ability to determine the phase distribution in a shearographic fringe pattern relies on a phase shift technique which adds a uniform phase change to the speckle pattern. With the setup of Fig. 1, the phase shift can be performed by simply translating the shearing crystal in a direction perpendicular to line of sight. Within a small phase shift range of zero to 2π, the amount of the phase shift is proportional to the translation of the shearing crystal. The proportionality is determined by a calibration procedure, and the translation is precisely controlled by a micro-translation stage.

Here, a four-frame algorithm is used to determine the fringe phase. By sequentially digitizing four speckle patterns with phase shift of 0, $\pi/2$, π and $3\pi/2$ before deformation yields:

$$\begin{aligned} \mathbf{I}_1 &= \mathbf{a} + \mathbf{b}\cos(\boldsymbol{\beta}) \\ \mathbf{I}_2 &= \mathbf{a} + \mathbf{b}\cos(\boldsymbol{\beta} + \pi/2) \\ \mathbf{I}_3 &= \mathbf{a} + \mathbf{b}\cos(\boldsymbol{\beta} + \pi) \\ \mathbf{I}_4 &= \mathbf{a} + \mathbf{b}\cos(\boldsymbol{\beta} + 3\pi/2) \end{aligned} \tag{4}$$

Using Eq.4, the random phase β is determined by:

$$\boldsymbol{\beta} = \arctan\left((\mathbf{I}_2 - \mathbf{I}_4) / (\mathbf{I}_3 - \mathbf{I}_1)\right) \tag{5}$$

Likewise, four speckle patterns are digitized after deformation.

$$\begin{aligned} \mathbf{I'}_1 &= \mathbf{a} + \mathbf{b}\cos(\boldsymbol{\beta} + \Delta) \\ \mathbf{I'}_2 &= \mathbf{a} + \mathbf{b}\cos(\boldsymbol{\beta} + \Delta + \pi/2) \\ \mathbf{I'}_3 &= \mathbf{a} + \mathbf{b}\cos(\boldsymbol{\beta} + \Delta + \pi) \\ \mathbf{I'}_4 &= \mathbf{a} + \mathbf{b}\cos(\boldsymbol{\beta} + \Delta + 3\pi/2) \end{aligned} \tag{6}$$

which gives:

(7)

Eq(5) and Eq(7) allows Δ to be computed. The computed phase is, however, wrapped into the range of $-\pi$ and π. A phase unwrapping algorithm such as that proposed by Macy[4] can be used to unwrap the phase. Since the fringe patterns of digital shearography are generally noisy which will be a problem in the phase unwrapping process. The iteration noise suppression algorithm[5] is found to be very effective for suppressing speckle noises. Other phase determination algorithms can also be used. A summary of the various phase determination algorithms can be found in reference(6).

Fig.4 shows 3-D plots of the phase distribution in fringe patterns of Fig. 3 determined by the phase determination technique.

2.4. FRINGE INTERPRETATION

The phase Δ is induced by the relative optical path length change between the light scattered from two neighboring points, P(x,y,z) and P(x+ δx, y, z) on the object surface. In this case the shearing direction is assumed parallel to the x-axis, and the amount of

shearing is δx. It can be shown that Δ is related to the relative displacement (δu, δv, δw) of two neighboring points separated by:

$$\Delta = \frac{2\pi}{\lambda}(A\delta u + B\delta v + C\delta w) \tag{8}$$

where (u,v,w) and (u+ δu, v+ δv, w+ δw) are the displacement vectors of P(x,y,z) and P(x+ δx,y,z), respectively; λ is the wavelength of light; A,B, and C are sensitivity factors related to the position of the illumination point $S(x_S,y_S,z_S)$ and the camera position $O(x_0,y_0,z_0)$ by:

$$A = \left(\frac{x-x_0}{R_0} = +\frac{x-x_s}{R_s}\right)$$

$$B = \left(\frac{y-y_0}{R_0} + \frac{y-y_s}{R_s}\right) \tag{9}$$

$$C = \left(\frac{z-z_0}{R_0} + \frac{z-z_s}{R_s}\right)$$

where: $R^2 = x_0^2 + y_0^2 + z_0^2$ and $R_s^2 = x_s^2 + y_s^2 + z_s^2$ Note that z(x,y) describes the object surface. Hence on the surface, z is not an independent variable. Eq.(8) may be rewritten in the following form:

$$\Delta = \frac{2\pi}{\lambda}\left(A\frac{\delta u}{\delta x} + B\frac{\delta v}{\delta x} + C\frac{\delta w}{\delta x}\right)\cdot\delta x \tag{10}$$

If the amount of shearing, δx, is small, the relative displacement approximates the derivatives of displacements with respect to x. The direction of shearing may be altered by rotating the shearing prism about the optical axis. Should the shearing direction be parallel to the y direction, the derivatives in Eq.(10) becomes the displacement derivatives with respect to y. It is possible to employ a multiple image-shearing camera[7] to record the displacement derivatives with respect to both x and y simultaneously.

Eq.(10) shows that the technique measures a combination of the derivatives of three displacement components. Therefore in general, three measurements with different sensitivity factors are required to allow the separation of the three displacement derivatives. One may choose a particular optical setup such that Both A and B are approximately zero. In this case the technique measures only the derivatives of w-component. However, it is not possible to make C vanishes for the determination of u- and v- derivatives independent of w-derivative.

3. In-plane strain measurement

Strains are functions of the derivatives of in-plane displacement components. For measurement of the derivative of in-plane displacement, a dual-illumination scheme[8] shown in Fig. 5 is used. The object to be measured is alternately illuminated by two

colliminated laser beams inclined at equal angle to the z-axis. The orientation of the beams depends on the strain component to be measured. For measurement of strain component parallel to the x-direction, two beams should be incident symmetrically with respect to the yz-plane as shown in the figure. The phase changes due to object deformation for the right illumination beam and the left illumination are different. For colluminated beam illumination, ΔR, the phase change due to right illumination, may be approximated by:

$$\Delta R = 2\pi/\lambda \; ((\, 1+ \cos \phi \,)(\partial w/\partial x) + \sin \phi(\partial u/\partial x))(\delta x) \qquad (11)$$

where λ is the wavelength of laser, and δx is the amount of shearing which is equivalent to the gage length.

For the left illumination beam, the phase change ΔL is given by:

$$\Delta L = 2\pi/\lambda \; (\, (\, 1 + \cos \phi)(\partial w/\partial x) - \sin \phi(\partial u/\partial x) \,) \; (\delta x) \qquad (12)$$

In the measurement, the object is illuminated with one beam at a time. Each of the phases ΔR and ΔL in the speckle patterns is determined by the phase determination technique described above. Subtrating Eq(12) from Eq(11) yields:

$$\Delta R - \Delta L = (2\pi/\lambda)\; 2\sin \phi \; (\partial u/\partial x)\; \delta x \qquad (13)$$

Hence, the in-plane strain in the x-direction is determined. Should the illuminations be rotated 90° about the z-axis and the shearing direction be parallel to y, $\partial u/\partial x$ in Eq(13) is replaced by $(\partial v/\partial y)$. Indeed, the derivatives of any in-plane displacement component can be measured by adjusting the orientation of the illumination system. With three different illumination orientations, the measurement system is equivalent to a full-field strain rosette.

The derivatives of out-of-plane displacement may also be determined by computing the sum of $(\Delta R + \Delta L)$ which yields:

$$\Delta R + \Delta L = (2\pi/\lambda)2(\; 1+ \cos \phi \,)(\partial w/\partial x)\;\; \delta x \qquad (14)$$

Fig. 6(a) shows a fringe pattern reconstructed from the phase difference $(\Delta R - \Delta L)$ depicting $\partial u/\partial x$, the horizontal strain component, of a cantilever beam fixed on the left and subjected to a point load at the free end (right). Fig. 6(b) is the predicted theoretical fringe pattern. The comparison shows a good agreement.

4. Residual stress measurement

The hole-drilling strain gaging technique is commonly employed to determine residual stresses in materials. In the process, the strain released by the hole is measured with a special strain gage rosette. Shearography may be used to replace the special strain gage rosette, and the residual stresses are accordingly determined. This eliminates the need to mount the special strain gage rosette and the critical alignment requirement of the drilled hole with respect to the positions of each gage in the rosette.

Here, a method for rapid detection of residual stresses is suggested[9] . Instead of drilling a hole, a micro-indentation method can be used to relieve residual stresses in materials, and shearography is used to measure the deformation produced by the indentation. The deformation of the indentation for the material having residual stresses will be considerably different from that without resdiual stresses. For the measurement, a

shearographic scheme with relatively large shearing illustrated in Fig.7 is employed. In this case, the technique basically compares the deformation of two different regions on the object surface. In essence, one region acts as a reference for the other as shown in in figure. The fringe pattern produced thus depicts the relative displacement between the two regions. Since the deformation due to stress relief by a micro-indentation is very localized, the other region is hardly affected and thus it serves as a reference beam. Thus the technique measures the absolute displacements around the neighborhood of the indentation. In the setup, only the out-of-plane displacement is measured.

In the presence of residual stresses, the indentation also causes a stress release. Fig.8(a) shows a fringe pattern due to an indendation but without residual stresses whereas Fig.8(b) shows a fringe pattern due to indentation and relief of residual stresses. Note that without residual stresses, the fringe pattern is more or less axisymmetrical. The presence of residual stresses will cause the fringe pattern to be deviated from the axisymmetrical form. The principal stress directions are indicated by the two axes of symmetry; the residual stress magnitude is related to the degree of deviation from axisymmetry. Since the mechanics of stresses relief is very difficult, the measurement with this method is only semi quantitative. The technique, however, provides a fast means of detecting residual stresses. It can be used in a field/production environment. Besides, the micro-indentation can be some small that the technique may be considered as non-destructive.

5. Measurement of vibration and time-dependent deformation

Traditionally, three techniques of shearography were used for vibration measurement. These are: the time-averaged technique, the stroboscopic technique and the double-pulsed technique. The first two techniques are only applicable to measurement of the mode shapes of steady state vibrating structures. In the case of double-pulsed shearography, the surface displacement gradient of a transiently vibrating structure at only two discrete times can be compared.

High speed shearography allows time-dependent deformation in an object to be studied by continuously digitizing the speckle images of a deforming object using a high speed digital image acquisition system. The image acquisition system used in the experiment is a Kodah EktaPro Model 4540 High Speed Motion Analyzer, which has a maximum frame rate of 40,500 frames/sec. After recording, the images are downloaded to a video tape and can be played back at the normal video rate of 30 frames per second. A fringe pattern can be produced by computing the difference of any two speckle images. These images are then digitized by a microcomputer such as a 486-computer through a frame grabber. The displacement versus time for any point of interest can be extracted by plotting the phase change of the speckle pattern at the point versus time from the computer memory. The total phase change can be obtained by integrating the phase curve. Fig.9 shows the phase variation versus time of a point on an object vibrating at 600 Hz acquired at a speed of 4,500 frames per second. In essence, the technique is equivalent to many massless and noncontact deformation sensors for measuring dynamic deformation. For example, a typical image digitization of 256x256 is equivalent to 65,536 sensors. Moreover, the technique does not influcence the real behavior of the structure under study.

6. Nondestructive evaluation

6.1. FLAW DETECTION

Shearography permits full-field observation of surface deformation in a test object. Since a flaw in an object usually induces strain anomalies, shearography reveals flaws by identifying the flaw-induced strain anomalies which are translated into anomolies in the fringe pattern. Although shearography measures surface strains, both surface and internal flaws can be detected. This is because the internal flaws unless very remote from the surface also affect the surface deformation.

Shearography has already received industrial acceptance for nondestructive inspection. An earlier report of the NDT applications can be founded in Ref.(10). Shearography is particularly effective in revealing delaminations in composite structures, including tires. It is also suitable for inspecting pressure vessels. Recently a new application for rapid evaluation of hermetic seal of microelectronic packages[11] is developed which employs high speed shearography.

6.2. SHEAROGRAPHY VERSUS ULTRASONIC

Fig. 10 is a comparison of the result of digital shearography and that obtained by a C-scan ultrasonic technique on a composite sample. The edge pullout and a delamination are detected by both techniques. However, digital shearography revealed the flaws in a fraction of a second, whereas the ultrasonic technique required point-by-point scanning of the part and it also needed the fluid coupling of the transducer to the object surface. One limitation of shearography is the need to impose stresses (or additional stresses) on test object.

6.3. METHOD OF TESTING

Flaw revealment by shearography is based on the comparison of two states of deformaton in the test object. Development of nondestructive testing procedures employing shearography essentially becomes the development of a practical means of stressing which can reveal flaws. Ideally, it is desirable to impose stresses similar to the stress state found in service. If components under testing are loaded in a stress mode similar to the actual one experienced in service, shearography can be used to reveal critical flaws only (i.e. flaws that create strain concentrations and thus reduce the strength of the component). Cosmetic flaws can be ignored and false rejects can be avoided. Examples of cosmetic flaws include those located in low stress regions which will not jeopardize the strength of the structures. In this regard shearography has an advantage over ultrasonic techniques. Ultrasonic techniques detect flaws by identifying inhomogeneities in the materials and provide no direct infomation about the criticality of the flaws. However, exact duplication and applicaton of actual loading may be difficulty or impractical in the testing. Therefore, for each nondestructive inspection application, development of a practical means of stressing is required. One precaution in stressing the test object is the prevention of rigid body motion. Excess rigid body motion would cause decorrelation of the speckles in the two images (deformed and undeformed) resulting in degradation of fringe quality. Excessive rigid body translation, however, can be negated by the technique report in Ref(12).

Several methods of stressing which normally do not produce intoleratble rigid body motion are: pressure stressing, vacuum stressing, thermal stressing, acoustical stressing and vibrational excitation. Microwave which excite water molecules is ideal as a stressing means for detecting moisture in plastics and non-metal composites. The stressing techniques reported in reference(13) for holographic nondestructive testing are generally applicable to shearography.

7. Conclusion

Shearography has been proven to be a practical approach for nondestructive testing. The recent development of the computerized version has greatly facilitated and economized the employment of shearography for industrial applications. Shearography is rapidly gaining acceptance by industry for nondestructive testing. However, other measurement application, requires further development before they can be transferred to industry. Shearography is still relatively young and its full capability awaits further exploration.

8. Acknowledgment

The research reported in this articles was sponsored by a National Science Foundation grant (CMS9601778). The author would like to thank Dr. Oscar Dillon of NSF for the support.

9. References

1. Hung Y.Y., Shearography : A new optical method for strain measurement and nondestructive testing, *Optical Engineering*, pp. 391-395, May-June, 1982

2. Hung Y.Y. and Hovanesian J.D., Fast detection of residual stresses in an industrial environment by thermoplastic-based shearography, *Proceedings of the 1990 SEM Spring Conference on Experimental Mechanics*, pp. 769-775, Albuquerques, New Mexico, June 4-6, 1990

3. Hung Y.Y., Apparatus and Method for electronic analysis of test object, US Patent 4,887,899 (1989)

4. Macy W.W., Two dimensional fringe analysis, *Appl. Optics*, 22, pp.3898, 1983

5. Jie Gu, Hung Y.Y. and Fang Chen, Iteration algorithm for computer aided speckle interferometry, *Appl. Optics*, Vo1.33, N°23, 1994

6. Creath K., Phase measurement techniques for nondestructive testing, *Preceedings of SEM Conference on Hologram Interferometry and Speckle Metrology*, pp. 474-478, Baltimore, Maryland, November 5-8, 1990

7. Hung Y.Y. and Durelli A.J., Simultaneous measurement of three displacement derivatives using a multiple image shearing interferometric camera, *J. of Strain Analysis*, Vol. 14, N° 3, pp. 81-88, 1979

8. Hung Y.Y. and Wang J.Q., Dual-beam phase shift shearography for measurement of in-plane strains, *Optics and Lasers in Engineering*, Vol. 24, N° 5-6, pp. 403-413, May/June, 1996

9. Hung Y.Y. and Long K.W., Industrial residual stress measurement by large shear computerized shearography, *Proceedings of 1997 International Conference on Advanced Technology in Experimental Mechanics*, pp. 405-410, Wakayama, Japan, July 25-26, 1997

10. Hung Y.Y., Shearography : a novel and practical approach for nondestructive testing, *J. of nondestructive testing*, Vol.8, N°2, pp.55-67, June, 1989

11. Hung Y.Y. and Shi D., Rapid evaluation of hermetic seals of microelectronic packages using digital shearography, *Proceedings for the 1995 SEM Spring Conference*, pp. 692-697, Grand Rapid, Michigan, June, 1995

12. Hung Y.Y. and Wang J.Q., Technique for compensating excessive rigid body motion in NDT of large structure using shearography, *Optics and Lasers in Engineering*, Vol.26, pp. 249-258, 1997

13. Kershe L.A., Laminate structure inspection, *Holographic Nondestructive Testing,* edited by R.K.Erf, Academic Press (1974)

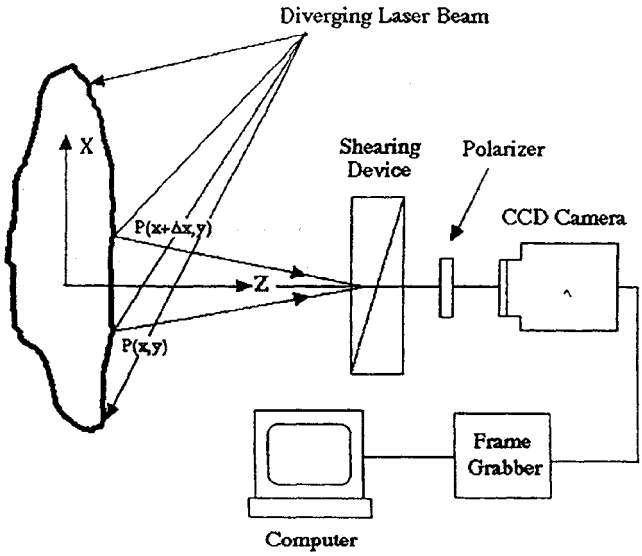

Fig. 1 Schematic diagram of video shearography

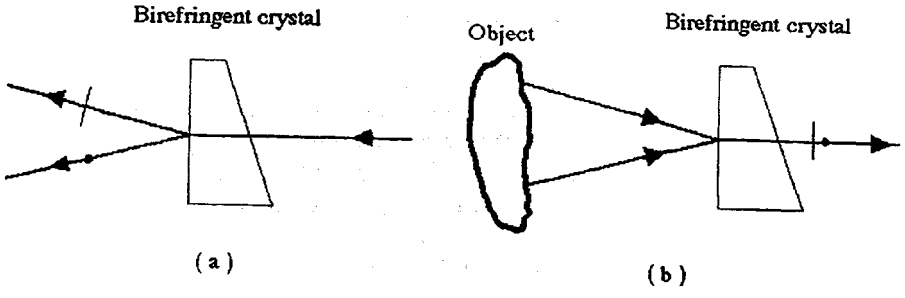

Fig. 2 Illustration of the birefringent crystal serving as shearing device. (a) One ray is split into two and orthogonally polarized. (b) Conversely, two nonplarallel rays scattered from two neighboring points on the object are combined and become collinear.

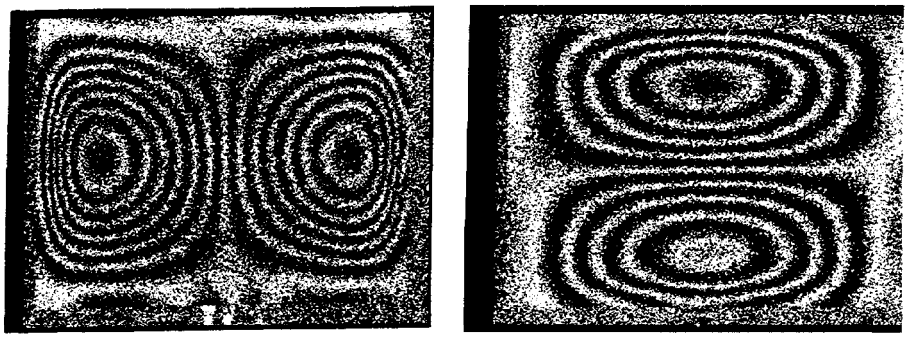

(a) (b)

Fig. 3 Fringe patterns depicting the deformation of a rectangular plate clamped alongs its boundaries and subjected to uniform pressure: (a) Derivative of deflection with respect to x. (b) Derivative of deflection with respect to y.

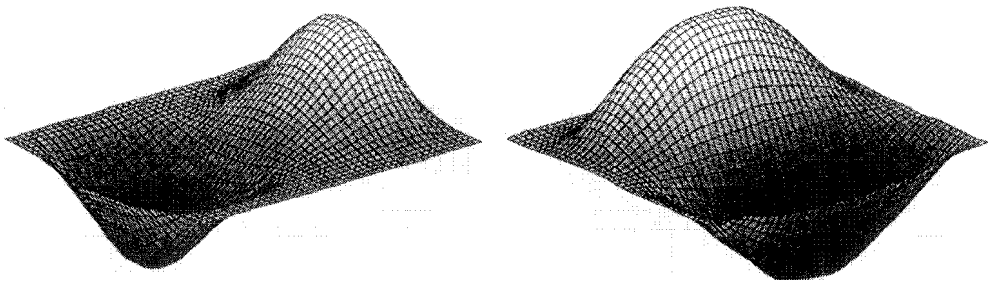

(a) (b)

Fig. 4 Three-dimensional plot of the phase distribution determined by the phase shift algorithm, depicting (a) derivative of deflection with respect to x, (b) derivative of deflection with respect to y, of the plate deformation of Fig.3.

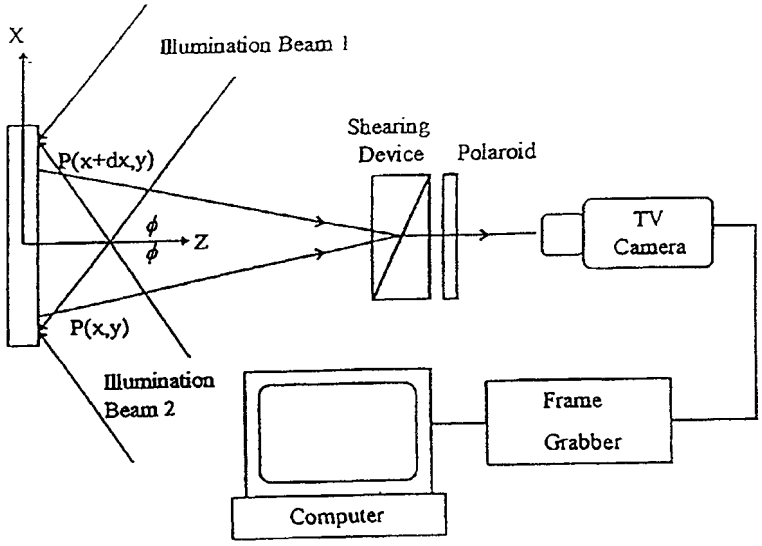

Fig. 5 Dual-beam illumination scheme for in-plane strain measurement.

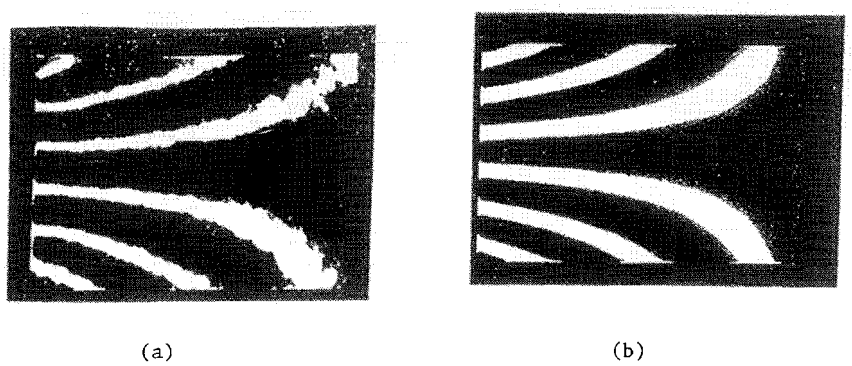

(a) (b)

Fig. 6 Computer-reconstructed fringe patterns depicting the horizontal in-plane strain component of the cantilever plate: (a) result of the dual beam shearography, (b) theoretical result.

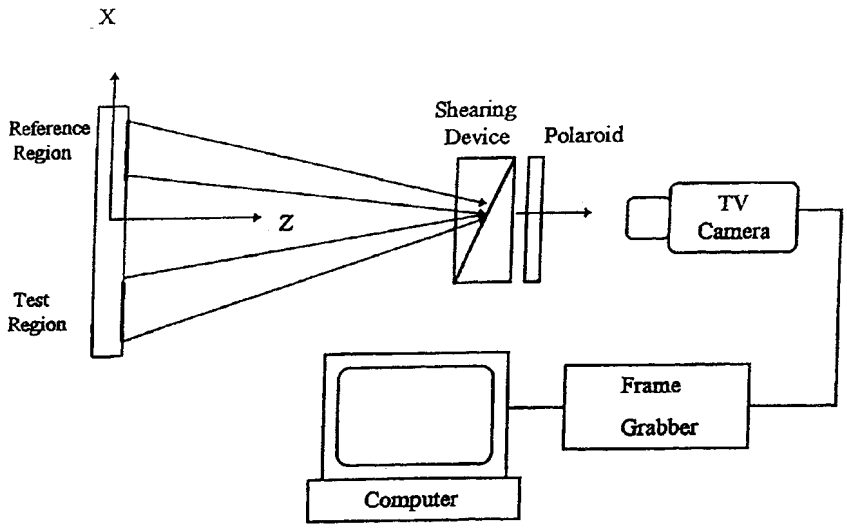

Fig. 7 Schematic diagram of the large shear shearography for residual stress measurement.

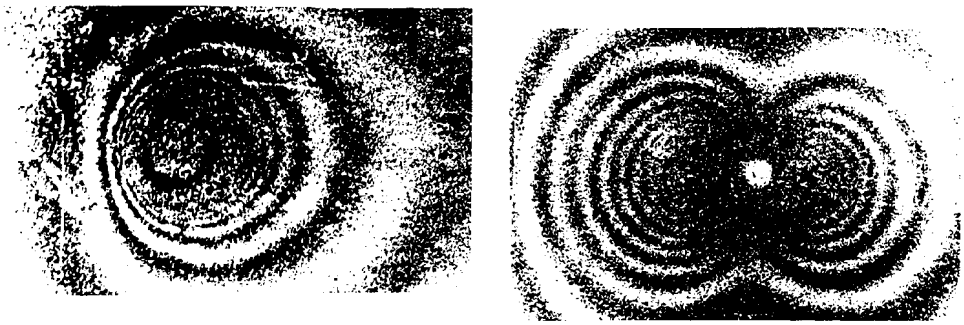

Fig. 8 Fringe patterns due to surface indentation: (a) without residual stresses, (b) with residual stresses.

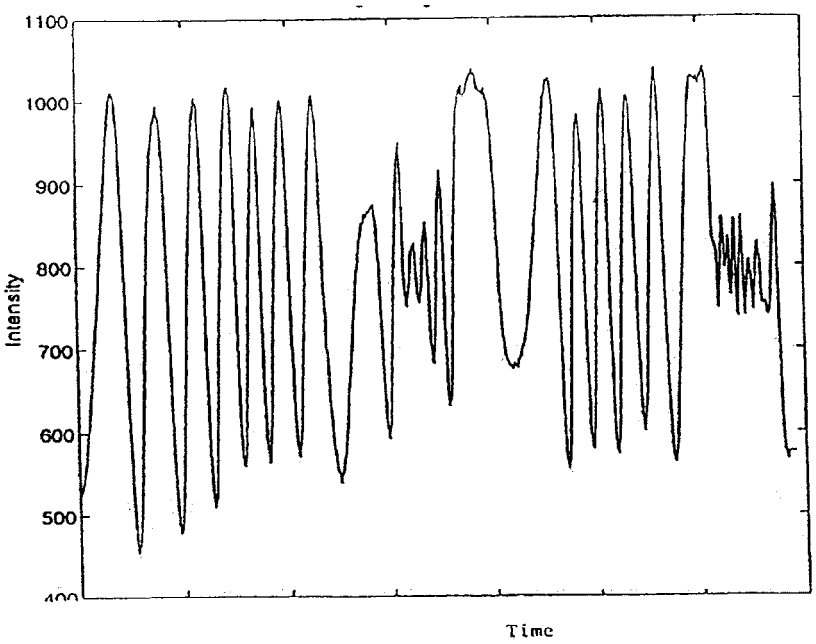

Fig. 9 Pixel intensity versus time at a point of a plate vibrating at 600 Hz, acquired at a speed of 4,500 frames per second with high speed shearography.

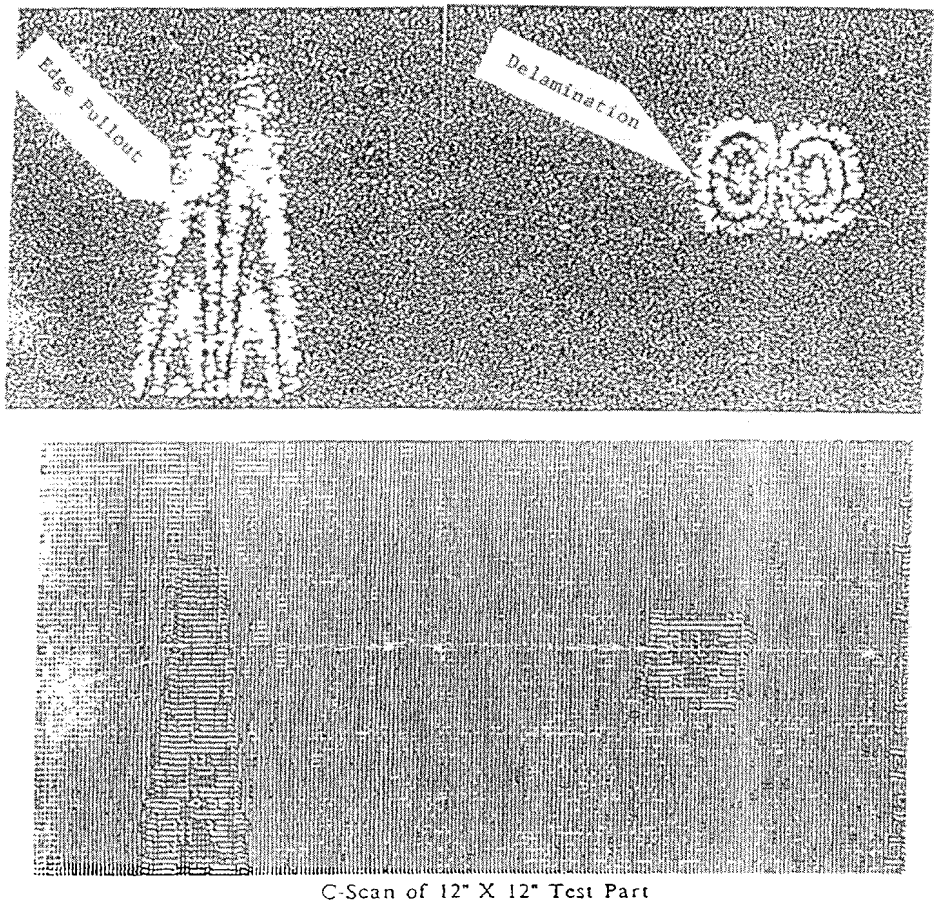

Fig. 10 Comparison of shearography with C-scan ultrasound. An edge pullout and a delamination in a graphite composite panel are revealed by both techniques. Time requried: one second for shearography and 10 minutes for ultrasound. Moreover, fluid coupling is needed in the ultrasonic testing.

This Page Intentionally Left Blank

VIBRATION ANALYSIS BY MEANS OF DIGITAL SPECKLE PATTERN SHEARING INTERFEROMETRY (DIGITAL SHEAROGRAPHY)

W. STEINCHEN, L.X. YANG, G. KUPFER, P. MÄCKEL, F. VÖSSING

University of Kassel, Dept. of Mechanical Engineering
Laboratory of Photoelasticity, Holography and Shearography
(Lab SHS)
D - 34109 Kassel, Germany

Abstract

Digital speckle pattern shearing interferometry is described as a robust measuring method due to its simple optical setup and the insensitivity against ambient disturbances. It has been used in industry for nondestructive testing and strain measuring. This paper explores the possibilities for vibration analysis using digital speckle pattern shearing interferometry. The measuring device performing both time-average and stroboscopic methods is described. The time average digital speckle pattern shearing interferometry in conjunction with the stroboscopic technique is suited well for both qualitative and quantitative vibration analysis. The determination of the dynamic deformation and the strain fields from the phase map of shearogram is demonstrated, and some preliminary results are shown.

Keywords: digital speckle pattern shearing interferometry, vibration analysis, nondestructive testing, time-average, stroboscopic technique.

1. Introduction

Using stroboscopic illumination, digital speckle pattern shearing interferometry, also called digital shearography or TV-shearography, has been used for vibration measurement of objects subjected to harmonic excitation [1]. In this technique the out-of-plane deformation gradient $\partial w/\partial x$ can be measured directly. However, the dynamic deformation or the strain field themselves are more interesting than the deformation gradient in the field of vibration analysis. To obtain these information, not only the phase map of the shearogram, but also the determination of the zero-order fringe positions is required. But the zero-order fringe position cannot be determined by the stroboscopic illumination method.

A. Lagarde (ed.),
IUTAM Symposium on Advanced Optical Methods and Applications in Solid Mechanics, 263–274.

This paper describes the time average digital speckle pattern shearing interferometry in conjunction with the stroboscopic illumination technique for vibration measurement. The measuring device performing both the time average and the stroboscopic method is described. In the state of real time observation the test object is illuminated by a continuous laser beam. By using the real time subtraction with the refreshing reference frame the resonant frequencies of the vibrating object are determined simply and rapidly. The fringe pattern obtained in this state is a time average digital shearogram. Thus the zero-order fringe position, i.e. the positions where $\partial w/\partial x = 0$, can be determined easily. If the further evaluation of the shearogram in a certain resonant frequency is required, i.e. the amplitudes and the mode, an accurate phase map can be obtained by applying the stroboscopic illumination. The selection of the continuous (in case of time-average method) or stroboscopic illumination is caused by adjusting a controller and performed simply by the developed program ***Shearwin****. Not only the deformation derivatives but also the dynamic deformation or the strain field of the vibrating object by integrating or differentiating the phase map of the shearogram can be thus determined. It is suited well for both qualitative and quantitative vibration analysis.

2. Measuring principle

Figure 1 shows the experimental setup of digital speckle pattern shearing interferometry using continuous or stroboscopic illumination method. The test object is illuminated by an expanded laser beam. The light reflected from the object surface is focused on the image plane of an image shearing CCD - camera in which a Michelson interferometer is implemented in front of its lens. By turning the mirror 1 in one of the two illumination arms of the interferometer for a very small angle, a pair of sheared images of the object are generated on the image plane of the CCD camera. The two sheared wavefronts interfere with each other producing a speckle interferogram, i.e. the so called "specklegram".

When measuring, the CCD-camera records first a specklegram and stores it in one frame, i.e. the reference frame. After the object is stressed, the second specklegram is registered by the CCD-camera again and stored in another frame. Digital subtraction between the two recorded specklegrams generates the so called digital shearogram which depicts deformation gradients directly rather than the deformation itself like holography [2]. A commercially available image processing board (IM-640 from Matrox Company) allows to subtract the arriving specklegram from the reference specklegram at video rate. Thus a digital shearogram is observed in real time (at video rate) [3].

To acquire the stroboscopic illumination, an acousto-optic modulator (AOM) is thus built into the measuring device. *Fig. 2* shows the principle of the acousto-optic modulator. An acoustic beam, propagating through a crystal in the Bragg cell, produces periodic variations in the refractive index of the material forming a phase grating which moves through the crystal at the sound velocity of the material. When the laser beam passes through the Bragg cell under the Bragg angle of incidence θ_B ,

* The program ***Shearwin*** can be ordered by Lab SHS

the diffracted laser beam induced by the phase grating is characterized mainly in the first order of diffraction. By using a trigger system and a driver, a stroboscopic laser beam is generated in the direction of the 1st order of diffraction. A controller is here required to synchronize the frequencies between the stroboscopic pulses and the object vibrations and to control the position and the width of the pulses (*cf.* Fig. 3). The position of the pulses can be frozen-in at any point in the 360° period. The pulse width of the laser beam should be usually as narrow as possible if the power of the laser is high enough, so that the specklegram can be frozen-in at one point and each instantaneous vibration can be measured.

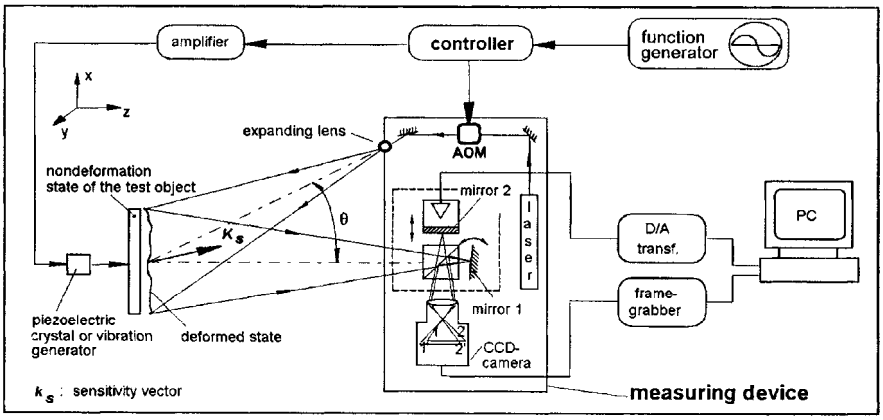

Fig. 1 : Experimental setup of digital speckle pattern shearing interferometry using continuous or stroboscopic illumination method.

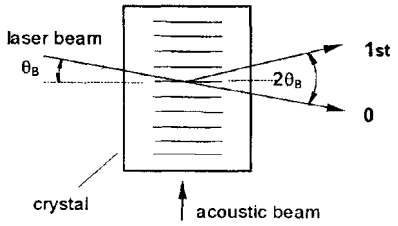

Fig. 2: Principle of the acousto-optic modulator

In order to obtain the continuous illuminating beam, this controller has been designed for generating not only a short pulse-width, but a long pulse-width too. By adjusting the pulse-width until 360°, the stroboscopic illuminating beam becomes the continuous illuminating beam. Therefore, the time average technique can be applied using this measuring device without any change in the optical setup. The selection of

the continuous illumination or the stroboscopic illumination is performed simply by the developed program ***Shearwin.***

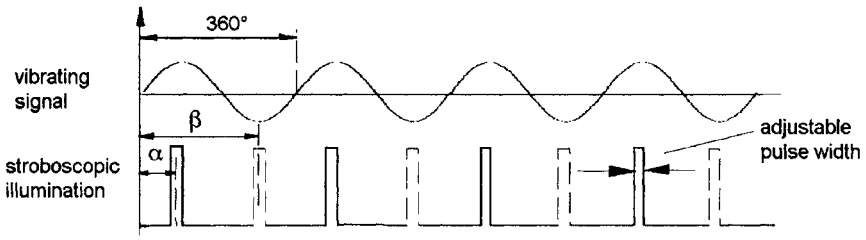

Fig.3: Stroboscopic illumination by AOM synchronized with the vibrating signal of the test object by the controller

Theoretically, a continuous illuminating beam can also be generated by adjusting the pulse-width to 0°. In this situation the stroboscopic illuminating beam in the direction of the 1st order of diffraction disappears and a continuous illuminating beam appears in the direction of the zero order diffraction. However, the illuminating direction in this way is changed and the additional expanding lens, mirrors etc. are required to expand the laser beam. So this method is not adopted in the experimental setup.

The time average and the stroboscopic technique are by far the most usual techniques for measuring the object vibrations by harmonic excitation; each of them has its merits. Of course, each has shortcomings as well. The experimental arrangement and the control system shown in *Fig. 1* combine the time average method with the stroboscopic method. This measuring device incorporates the merits of each technique and overcomes the shortcomings for each of them. Thus it is suited well for the vibration analysis.

3. Real time observation using continuous illuminating beam

In general, vibrations, especially in the cases of resonant frequencies occurring, in machines and structures are undesirable because of the increased stresses and the energy losses which accompany them. They should be eliminated or reduced as much as possible by an appropriated design. Therefore, the first task of vibration analysis is to determine the resonant frequencies of the object. In order to find out the natural frequencies simply and rapidly, the technique of real time observation is usually required. In this stage of the real time observation, the test object is illuminated by a continuous laser beam. The observed fringe pattern is thus a time average shearogram. The fringe pattern is not as sharp like this using the stroboscopic illumination.

However, it is sufficient to find out the resonant frequencies and to determine the position of the zero-order fringe. In the conventional technique for the real time observation using a continuous illumination beam, the current frames are subtracted at video rate from the original reference frame which is usually acquired at the stationary state. The fringe pattern obtained by the real time subtraction is modulated by a system of fringes described by the term $[1-J_0(\Omega)]$, where J_0 is the zero-order Bessel function of the first kind [4]. The contrast of the real time visible fringe pattern is obviously low.

A new approach for the real time observation with refreshing reference frame has been used in the stroboscopic illumination digital speckle pattern shearing interferometry so that a fringe pattern which is insensitive against ambient disturbances such as thermal air waves or lower frequency vibrations can be obtained [1]. This technique can be introduced into the time average digital speckle pattern shearing interferometry too and it can be put into practice easily without any change in the optical setup. The new method is a three-step process [5]: If the current frame is the Nth frame, the reference frame is the (N-1)th frame rather than the frame acquired at the stationary state. First, an image is recorded in the (N-1)th frame. If the object is vibrating in the steady state with the frequency f much higher than the video frame rate, the specklegram recorded in the (N-1)th frame is a time-average correlogram due to the continuous illumination and it can be represented by:

$$I_{(N-1)}(x,y)_{ave} = 2I_0 [1 + \gamma \cos \phi (x,y) \ J_0(\Omega)], \qquad (1)$$

where I_0 represents the average intensity of the two sheared light waves, γ the modulation of the interference term and $\phi(x,y)$ the random relative phase angle between the two sheared images. Ω is equal to $[\delta x \ (4\pi/\lambda) \ (\partial w/\partial x)]$ and δx is the shearing amount in the x-direction. Due to the high level of the self interference term, the fringe contrast of the time average correlogram is very low and the fringes are barely visible. If the Nth current frame is now subtracted directly from the (N-1)th frame without introducing a phase shift between the two frames, no fringe can be observed either, because the algebraic expressions for $I_{(N-1)}(x,y)_{ave}$ and $I_N(x,y)_{ave}$ are exactly identical. Therefore, a 180° phase shift after the (N-1)th frame is introduced in the second step (the phase shift can be chosen at any value, it is 180° in this experimental setup). This phase shift can be introducd by a piezoelectric transducer (PZT) actuated mirror 2 in one of the two illumination arms of the Michelson interferometer (*cf. Fig. 1*) and controlled by the software ***Shearwin*** developed by University of Kassel. Then in a second step, the Nth frame is taken. Now the image recorded in the Nth frame becomes:

$$I_N(x,y)_{ave} = 2I_0 \{1 + \gamma \cos [\phi (x,y) + 180°] \ J_0(\Omega) \}. \qquad (2)$$

The Nth current frame is then subtracted digitally from the (N-1)th frame. Obviously, the self interference term in Eq. (1) or (2) is eliminated and a visible fringe pattern can thus be observed:

$$I_S = I_{(N-1)}(x,y)_{ave} - I_N(x,y)_{ave} = 4\, I_0\, \gamma \cos \phi\,(x,y)\;\; J_0\,(\Omega). \qquad (3)$$

Repeating the three step process, a fringe pattern modulated exactly by $J_0\ (\Omega)$ rather than by $[1- J_0\ (\Omega)]$ can be observed in real time. The contrast of the fringes will be higher than that from the term $[1 - J_0\ (\Omega)]$. Furthermore, the low frequency ambient disturbances caused by thermal air currents and low frequency vibrations are greatly suppressed due to the great reduction of the time between the acquisition of the current and the reference frame.

Passing the range from low until very high frequencies, the real time fringe patterns corresponding to resonant frequencies respectively are observed. Each resonant frequency can be thus determined. The dynamic excitation can be performed by a piezoelectric crystal. The exciting frequency generated by the piezoelectric crystal can reach until and above 10 MHz. However, it is limited by the amplifier of the piezoelectric crystal. In general, it is no problem to excite the object with the frequency between 0 and 50 kHz.

A dynamic investigation of a vibrating circular aluminum plate by using this technique was performed. This plate was clamped all around and was excited sinusoidally by a piezoelectric crystal on the back side. Each resonant frequency as well as the corresponding time average digital shearogram can be determined. *Fig. 4* shows the time average digital shearograms corresponding to the frequencies of 1270 Hz, 4300 Hz and 4860 Hz (from left to right). By searching for the brightest fringes, the position of the zero-order fringe can be determined. It should be noted that the positions of the zero-order fringe are not the position of the nodal lines of the vibrating object in the time average shearogram. The shearogram depicts the amplitude gradients $\partial w/\partial x$. The zero-order fringe shows the positions where the amplitude gradients $\partial w/\partial x$ are zero, i.e. the position of $\partial w/\partial x = 0$. In other words, the brightest fringes indicate the position of the maximal or minimal amplitude of the vibrating object. In contrast, the brightest fringes of the time average hologram indicate the position of the zero amplitude, i.e. the nodal lines of the vibrating object. From the zero-order fringe of the shearogram which depict the position of the maximal or minimal amplitude of the vibrating object, the vibrating form can be imagined. Therefore, the qualitative "modal analysis" can be performed by this method [6]. Moreover, this technique can be also applied for nondestructive testing to detect the defects on the surface and in the subsurface of the object [7].

4. Quantitative analysis using stroboscopic illumination

If the further evaluation of the shearogram of an interesting resonant frequency is required, an accurate phase map can be obtained by applying the stroboscopic illumination. Giving an instruction in the program ***Shearwin***, the stroboscopic illumination is performed.

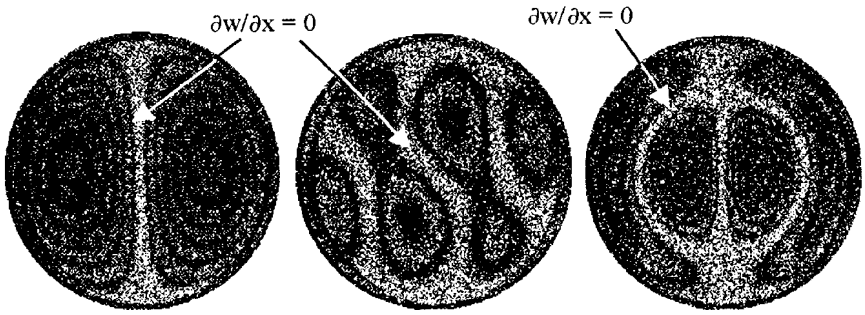

Fig. 4: Time average digital shearograms which depict the deformation gradients ∂w/∂x (i.e. x-shearing direction) for a thin circular aluminium plate (Ø=150mm, t=3mm) clamped all around using harmonic excitation showing the frequencies 1270, 4300 and 4860 Hz (from left to right).

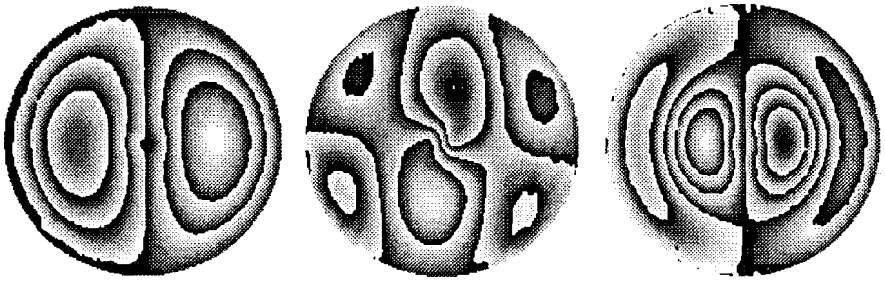

Fig. 5 shows the phase maps of shearograms recorded by the stroboscopic illumination method for the same plate shown in Fig. 4 for the same exciting method and same frequencies of 1270 Hz, 4300 Hz and 4860 Hz (from left to right)

4.1. DETERMINATION OF THE DYNAMIC DEFORMATION GRADIENT FIELD

Real time observation by using the continuous illumination is suited well to find out the resonant frequencies of the vibrating object and to determine the zero-order fringe from the recorded shearogram. For the quantitative analysis, the phase map of shearogram is required. The phase shift technique has been applied to obtain the phase map of an interferogram. However, it is required to record three or four interferograms for the same state of the deformation. Obviously, this technique is not suited to apply for the time average shearography. With the introduction of the stroboscopic illumination, the interferogram (speckle pattern) can be frozen-in at any point of the periodic illumination in the shape of short stroboscopic pulses synchronized with the frequency of the vibrating object respectively. Each instantaneous vibration in the interesting resonant frequency can thus be measured by

adjusting the trigger position. Moreover, the phase shift technique can be applied for this illumination so that an accurate phase map of the shearogram can be obtained.

First, the trigger position is adjusted to a fixed phase α. The intensities corresponding to each pulse illumination are added by the CCD-camera resulting an interferogram (speckle pattern). It is obvious that the interferogram is frozen-in at a certain state of deformation. Thus, four interferograms corresponding to phase shifts of 0, $\pi/2$, π and $3\pi/2$ in the stage of same deformation state can be recorded. The D/A board provides the voltage steps necessary for the PZT driven mirror 2 (*cf. Fig. 1*) to create these four different phase shifts. The phase distribution ϕ_α of the interferogram corresponding to the state of deformation with respect to the fixed phase α can be calculated from the four recorded intensity distributions as following:

$$\phi_\alpha = \arctan [(I_4 - I_2)/(I_1 - I_3)] \qquad (4)$$

Second, adjusting the trigger position to the different phase β (*cf. Fig. 3*), four more frames of the intensity data are taken while shifting the phase for the same amount as for the first set of data. The phase distribution ϕ_β of the interferogram corresponding to the state of β can also be calculated such as ϕ_α . Once these data are taken, the phase map of shearogram depicting the change of the phase distribution between two speckle interferograms can be obtained simply by subtracting ϕ_β from ϕ_α . The phase map of shearogram describes quantitatively the relative amplitude gradient field $\partial w/\partial x$ between vibrating phase angles α and β.

Fig. 5 shows the phase maps of shearograms recorded by the stroboscopic illumination method for the same plate shown in *Fig. 4* for the same excited frequencies of 1270 Hz, 4300 Hz and 4860 Hz (from left to right) ready for quantitative evaluation.

From the Eq (4) the relative phase distributions ϕ_α and ϕ_β can be determined only within the limits of 2π, thus, the phase map obtained by subtracting ϕ_β from ϕ_α is a fringe pattern of phase modulo 2π. An unwrapped phase distribution can be determined by a phase unwrapping algorithm [8]. From the unwrapping phase map of shearogram, the continuous distribution of the amplitude gradient field $\partial w/\partial x$ is determined. Therefore, the quantitative evaluation and representation of 3D-plot for the shearogram becomes possible.

Fig. 6 shows the evaluation of the phase map of the shearogram with the exciting frequency f = 4860 Hz, which is displayed in *Fig. 4* (right). The unwrapped phase map of the shearogram and its 3D-plot are shown in *Fig. 6b* and *Fig. 6c*, respectively.

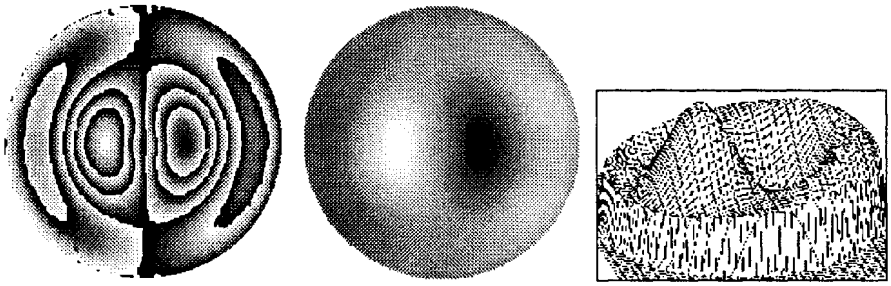

Fig. 6: (a) The phase maps of the shearogram shown in *Fig. 4* (right) for the circular plate excited by the natural frequency 4860 Hz, (b) the unwrapped phase map and
(c) the 3D plot depicting the amplitude derivative field $\partial w/\partial x$.

4.2 DETERMINATION OF THE VIBRATING MODE AND STRAIN FIELDS

In the field of vibration analysis the vibrating mode or strain field itself rather than the amplitude gradient field is more interesting. In order to obtain the vibrating mode, i.e. the dynamic deformation field w, the unwrapped phase map of the shearogram, which depicts directly $\partial w/\partial x$, should be integrated. However, the unwrapped phase map of the shearogram depicts only a relative distribution of $\partial w/\partial x$ relative to a reference position. If the vibrating mode, i.e. the dynamic deformation field w, should be obtained by integrating $\partial w/\partial x$, the distribution for the absolute magnitude of $\partial w/\partial x$ should be determined. In order to know exactly the distribution of the absolute magnitude $\partial w/\partial x$, the zero-order fringe position, i.e. the positions of $\partial w/\partial x = 0$, should be determined.

In general, the zero-order fringe cannot be determined from the phase map. However, this problem is solved easily in the developed experimental setup, because the zero-order fringe has been observed form the time average digital shearogram in the state of real time observation. After the distribution of the absolute magnitude $\partial w/\partial x$ has been determined, the vibrating mode can be obtained by the developmental program ***Shearwin*** using an integration algorithm. *Fig. 7* shows a new phase map depicting the vibrating mode, i.e. the deformation field (w), of the circular plate shown in Fig. 6 with the resonant frequency f = 4860 Hz obtained by integrating the unwrapped phase map of the shearogram shown in *Fig 6b*; its 3D-plot represents clearly the vibration shape (right).

For the thin plates the normal strains ε_{xx} and ε_{yy} and the shear strain ε_{xy} are related to the second derivatives of the out-of-plane deformation (w). Thus the fringe patterns representing full-field flexural and shear strains in plates can be obtained by differentiating the phase map of $\partial w/\partial x$ in x-direction obtaining $\varepsilon_{xx} \sim \partial^2 w/\partial x^2$, in y - direction getting $\gamma_{xy} \sim \partial^2 w/\partial x \partial y$. When the phase map of $\partial w/\partial y$ is differentiated in y-direction, the normal strain $\varepsilon_{yy} \sim \partial^2 w/\partial y^2$ can also be determined.

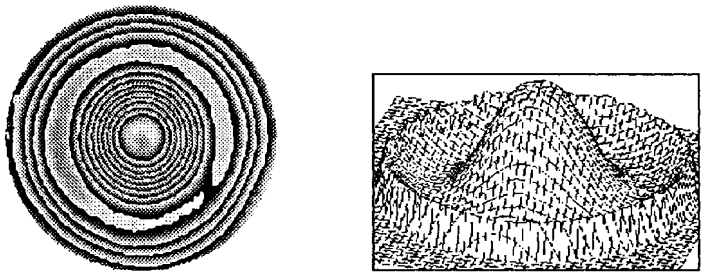

Fig. 7: Fringe pattern depicting the vibrating mode (distribution of w) of the plate shown in Fig 6 under the resonant frequency 4860 Hz, obtained by integrating the unwrapped phase map shown in Fig 6b (left) and the 3D plot, i.e. the vibrating shape (right).

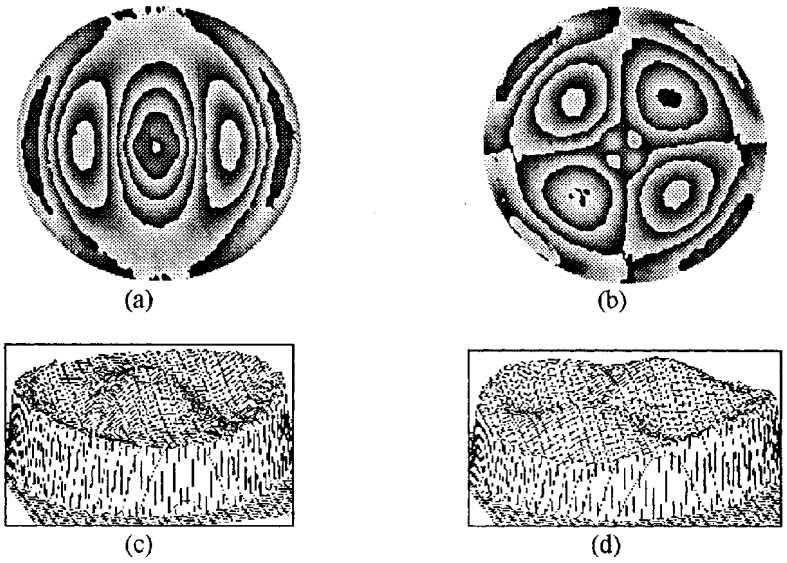

Fig. 8. (a) - (b) Fringe patterns, depicting flexural normal strain field ε_{xx} and shear strain ε_{xy}, respectively, of plate shown in Fig. 6 under the resonant frequency 4860 Hz, obtained by differentiating method, (c) - (d) their corresponding 3D plots.

Similarly, the normal strains ε_{xx} and ε_{yy} and the shear strain γ_{xy} in plates can also be determined by the program ***Shearwin*** using a differentiation algorithm. The detailed reports on the integrating and differentiating the phase map of the shearogram can be found in Ref. [9]. *Fig. 8a and 8b* show the fringe patterns of the same plate as Fig. 6 under the resonant frequency 4860 Hz, which depict flexural normal strain field ε_{xx} and shear strain ε_{xy}, respectively. They are obtained by differentiating method. *Fig. 8c and 8d* show their corresponding 3D plots.

5. Conclusions

Digital speckle pattern shearing interferometry, also called digital shearography, provides an alternative to TV-holography for vibration analysis. It provides a wider measuring range compared as the TV-holography. In general, TV-holography has a smaller controllable range sensitivity, so the larger amplitude (usually larger than 15 μm) cannot be measured. However, digital shearography can measure relatively large amplitude, e.g. larger than 100 μm. The measuring range can usually be controlled by adjusting the shearing amount [10]. The measuring accurate is dependent on the shearing amount too. The detail discussion on the measuring accurate can be found in Ref. [9].

The greatly reduced path-length imbalance as compared with the typical holographic configurations makes it possible to illuminate the test object using simple laser diodes indeed without temperature stabilization. Therefor, this technique is suited well for industrial on-line measuring and testing.

The developed method presented in this paper enables time average and stroboscopic techniques to be performed by one measuring device without any change in the experimental setup. Not only the accurate phase map but also the zero-order fringe of the shearogram can be determined. Both qualitative and quantitative vibration analysis can be performed. The dynamic deformation derivative field as well as the dynamic deformation and strain fields of the vibrating object can be determined by this measuring device in conjunction with the developed program ***Shearwin***. It is expected that a wide range of applications by this technique will be seen in the near future.

6. Acknowledgement

This investigation was supported by DFG, Deutsche Forschungsgemeinschaft, Bonn, FRG, under Ste 248/15-1/2, which is gratefully acknowledged.

7. References

1. T.C. Chatters, B.F. Pouet and S. Krishnaswamy, *Additive-subtractive Phase-modulated Shearography with Synchronized Acoustic Stressing*, Experimental Mechanics, June 1995, pp. 159-165.
2. Y.Y. Hung, Shearography: *A new optical Method for Strain Measurement and Nondestructive Testing*, Optical Engineering, 21 (1982), pp 391 - 395.
3. W. Steinchen, L.X. Yang, G. Kupfer and M. Schuth, *Shearography - Zerstörungsfreie TV-Materialprüfung*, Material Prüfung -- Materials Testing, Vol. 37, No.6, 1995, pp. 224 - 226.
4. C. M. Vest, *Holographic Interferometry*, John Wiley & Sons, Inc. (1979).

5. W. Steinchen, L.X. Yang, G. Kupfer, *Schwingungsmessung mittels Digital Shearografie*, **tm** - Technisches Messen, 64 (1997), Juni, 1997.
6. W. Steinchen, L.X. Yang, M. Schuth and G. Kupfer, *Analyse von TV - Shearogramm für eine schwingungs-erregte dünne Kreisplatte,* Materialwissenschaft u. Werkstofftechnik, 26 (1995), pp 217 - 222.
7. W. Steinchen, L.X. Yang, G. Kupfer, *Digital shearography for nondestructive testing and vibration analysis*, Experimental Techniques, 1997, (in press).
8. D. W. Robinson, G. T. Reid, *Interferogram Analysis - Digital Fringe Pattern Measurement Technique*, Institute of Physics Publishing, 1993.
9. L.X. Yang, *Grundlagen und Anwendungen der Phasenschiebe-Shearografie zur zerstörungsfreien Werkstoffprüffung, Dehnungsmessung und Schwingungsanalyse*, Ph. D Thesis, Fortschritt-Bereichte, Reihe 8, Nr. 682, VDI Verlag, Düsseldorf, 1998
10. M. Schuth, *Aufbau ung Anwendung der Shearografie als praxisgerechtes, optisches Prüf- und Meβverfahren zur Dehnungsanalyse, Qualitätssicherung und Bauteiloptimierung*, Ph.D Thesis, Fortschritt-Berichte VDI Nr. 539, 1996

STUDY OF SUB-INTERFACIAL QUASI-STATIC CRACK PROPAGATION USING SHEARING INTERFEROMETRY

HANSUK LEE and SRIDHAR KRISHNASWAMY
Department of Mechanical Engineering
Northwestern University
Evanston, IL 60208-3020, USA

Abstract

Cracks on the interface between two materials have been extensively studied in view of their applications to failure processes in composite materials [1-3]. In this work, we look at the case of cracks that are *off* but close to an interface. Some early studies have indicated that under certain circumstances such sub-interfacial cracks tend to grow along a path that is parallel to the interface at a characteristic distance from the interface depending on the loading and material properties of the two materials. In this study, we optically map crack-tip stress fields for cracks that start off the interface, and track them as they subsequently propagate off the interface. The optical technique that was developed in our laboratory and which is used in this study will be explained. This shearing interferometer is used in conjunction with a 1000 frame/sec video camera. The resulting fringe patterns are evaluated to obtain information about the stress-state during initiation and propagation. The conditions for crack propagation parallel to the interface are explained. The experimental results are compared with crack trajectories predicted by finite element simulations.

1. Shearing Interferometry Part of PSI and Fringe Pattern Analysis

The optical layout and the schematic of the shearing interferometric mode of a polariscope/shearing interferometer (PSI) device [1] are shown in figures 1 and 2.

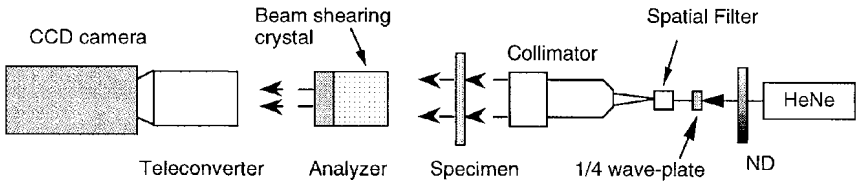

Figure 1. Optical layout of the shearing interferometric system

A 5mW HeNe laser is used as the coherent light source. A quarter waveplate is used to circularly polarize the beam. A set of micro-objective lenses, spatial filter and beam collimator is used to obtain a clean and collimated plane wave. The beam then passes

A. Lagarde (ed.),
IUTAM Symposium on Advanced Optical Methods and Applications in Solid Mechanics, 275–282.

through the transparent PMMA specimen under test. The transmitted beam is then sheared by a specially designed prism as shown in figure 2. The specially cut prism is made of birefringent calcite and generates two orthogonally polarized parallel and laterally-shifted copies of the input beam (see figure 2). These two beams are made to interfere by use of an analyzer. The stressed specimen causes stress-induced phase-shifts in the optical beam, resulting in fringe patterns that can be related to the stress-state.

For optically isotropic materials such as PMMA, the stress-induced phase retardation is independent of polarization, and the total phase retardation Φ_{sp} at any point due to transmission through the specimen is related to the stresses at that point through [2]

$$\Phi_{sp}(x,y) = \frac{2\pi hc}{\lambda}\{\sigma_1 + \sigma_2\} \tag{1}$$

where h is specimen thickness, λ is wavelength of the laser beam, c is a stress optic constant of the optically isotropic PMMA material and σ_1 and σ_2 are in-plane principal stresses.

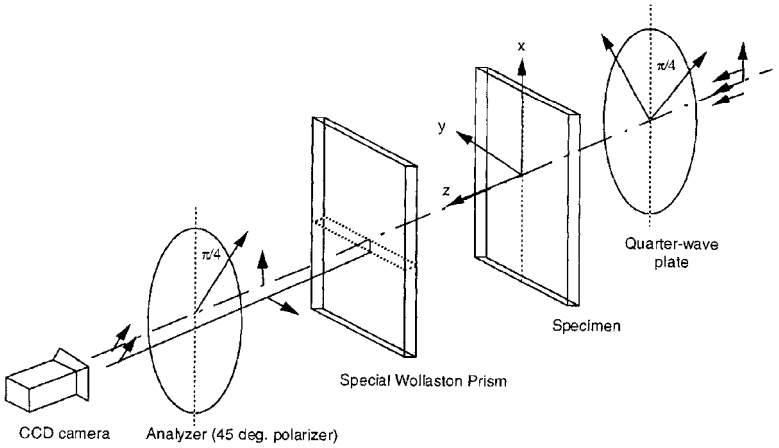

Figure 2. Schematic of the shearing interferometer

As discussed in Ref. [1], the fringe relation for bright fringes is given by:

$$\frac{ch}{\lambda} \bullet \Delta X \bullet \frac{\partial(\sigma_1 + \sigma_2)}{\partial X} = m, \tag{2}$$

where m is the fringe order, and shearing by amount ΔX is in the global X coordinates as shown in figure 3. A similar relation is obtained for shearing in other directions. These relations are similar to the fringe relations obtained using the coherent gradient sensor (CGS) developed by Tippur, Krishnaswamy and Rosakis [2] for fracture studies in optically isotropic materials

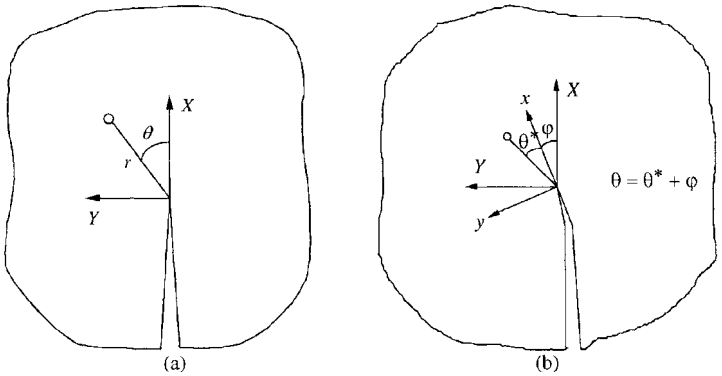

Figure 3. Global and local coordinate systems for a propagating crack

The in-plane stress components for a crack in a homogeneous media is asymptotically given by [4] :

$$\sigma_{ij}(r,\theta) = \sum_{n=0}^{\infty} \frac{r^{(n-1)/2}}{\sqrt{2\pi}} \left\{ \mathrm{Re}(k_n)\tilde{\sigma}_{ijn}^{\ I}(\theta) + \mathrm{Im}(k_n)\tilde{\sigma}_{ijn}^{\ II}(\theta) \right\}, \tag{3}$$

where r and θ are spatial coordinates shown in figure 3(a), k_n are complex amplitudes of which $k_0 = \mathbf{K} = K_I + iK_{II}$ is the complex stress-intensity factor, and $\tilde{\sigma}_{ijn}^{I}(\theta)$ and $\tilde{\sigma}_{ijn}^{II}(\theta)$ are dimensionless functions that are completely known [4].
The sum of in-plane stresses is therefore given by:

$$\sigma_1 + \sigma_2 = \sum_{n=0}^{\infty} \frac{2r^{(n-1)/2}}{\sqrt{2\pi}} \left\{ \mathrm{Re}(k_n)\cos\left(\frac{n-1}{2}\theta\right) + \mathrm{Im}(k_n)\sin\left(\frac{n-1}{2}\theta\right) \right\} \tag{4}$$

By using equations. (1), (2) and (4), the fringe relations with the derivative fields of in-plane stresses sum can be given by:

$$\frac{\partial(\sigma_1+\sigma_2)}{\partial X} = \sum_{n=0}^{\infty} (n-1)\frac{r^{(n-3)/2}}{\sqrt{2\pi}} \left\{ \mathrm{Re}(k_n)\cos\left(\frac{n-3}{2}\theta\right) + \mathrm{Im}(k_n)\sin\left(\frac{n-3}{2}\theta\right) \right\} = \frac{m\lambda}{ch\Delta X} \tag{5}$$

$$\frac{\partial(\sigma_1+\sigma_2)}{\partial Y} = \sum_{n=0}^{\infty} (n-1)\frac{r^{(n-3)/2}}{\sqrt{2\pi}} \left\{ -\mathrm{Re}(k_n)\sin\left(\frac{n-3}{2}\theta\right) + \mathrm{Im}(k_n)\cos\left(\frac{n-3}{2}\theta\right) \right\} = \frac{n\lambda}{ch\Delta Y} \tag{6}$$

The real and imaginary components K_I and K_{II} of the complex stress intensity factor $\mathbf{K} = K_I + i\,K_{II}$ represent crack opening mode and in-plane sliding mode respectively at the initial crack position. However these representations are only available for the cracks which are parallel to the *X*-direction or *Y*-direction. To extract mode I and mode II components of complex stress intensity factors in the interferometric fringes of curved crack path, a local (variable) coordinate system may be used. As shown in figure 3(b),

the global coordinates X and Y are parallel and perpendicular to the initial crack line and local coordinates x and y are those of newly generated crack front line.
In the optical system, the shearing direction is controlled by rotation of the prism. Since the prism is fixed in a certain direction, generally in the X-direction, we cannot get x-derivative stress fields directly. Hence the x-derivative in-plane stress field is given by

$$\frac{\partial(\sigma_1+\sigma_2)}{\partial x} = \frac{\partial(\sigma_1+\sigma_2)}{\partial X}\frac{\partial X}{\partial x} + \frac{\partial(\sigma_1+\sigma_2)}{\partial Y}\frac{\partial Y}{\partial x}$$
$$= \sum_{n=0}^{\infty}(n-1)\frac{r^{(n-3)/2}}{\sqrt{2\pi}}\left\{\mathrm{Re}\left(k_n^*\right)\cos\left(\frac{n-3}{2}\theta^*\right) + \mathrm{Im}\left(k_n^*\right)\sin\left(\frac{n-3}{2}\theta^*\right)\right\} \quad (7)$$

where

$$\mathrm{Re}\left(k_n^*\right) = \cos\left(\frac{n-1}{2}\varphi\right)\bullet\mathrm{Re}\left(k_n\right) + \sin\left(\frac{n-1}{2}\varphi\right)\bullet\mathrm{Im}\left(k_n\right) \quad (8)$$

and

$$\mathrm{Im}\left(k_n^*\right) = -\sin\left(\frac{n-1}{2}\varphi\right)\bullet\mathrm{Re}\left(k_n\right) + \cos\left(\frac{n-1}{2}\varphi\right)\bullet\mathrm{Im}\left(k_n\right) \quad (9)$$

where φ is the kink angle, θ^* is the angular coordinate of the newly generated crack front, $k_0^* = K_I + iK_{II}$, and K_I and K_{II} represent mode I and mode II of the propagating crack, respectively. Thus the components of the complex stress intensity factor $\mathbf{K} = k_0$ of the new coordinate x and y can be extracted by $\varphi/2$ rotation of those of global coordinates. And the higher order components of the series expansion stress field have analogous relation with the zero-th order **K**. The complex stress intensity factor **K** is extracted by an over-deterministic scheme and decomposed to mode I and II values as the crack propagates.

2. Experiments And Results

2.1 CRACK PROPAGATION IN HOMOGENEOUS PMMA SPECIMENS

In this work the stress states near quasi-statically propagating crack-tip in homogeneous PMMA is investigated by use of the shearing interferometer. We used 3-point bending specimen as shown in figure 4(a). For the homogeneous PMMA specimen, load point at the top of the specimen is shifted from the center of PMMA to obtain mixed mode crack propagation. As shown in figure 4(b), experimental crack path has a kink angle from the initial crack line caused by the non-symmetric load; hence the crack trajectory is curved. The sequence of fringe patterns obtained was used to extract the stress intensity factor **K** using equations (5) and (7).]. The speed of the crack was quite slow (< 1 mm /sec) during the initial propagation of the crack, thus we can assume quasi-static conditions. The kink angle of the propagating crack depends on mode mixity [6]. As the crack initiated, |**K**| increases in the early stages (around 0-2 mm growth) and becomes a constant while the propagation is quasi-static. Fluctuations of the stress intensity factors in the 4-15 mm increment area occurred and were associated with a

rough crack propagation as indicated post-mortem by crack surface features. The phase angle defined by $\phi = \tan^{-1}(K_{II}/K_I)$, is around -2° ~ 2°. This means that the shear mode in the propagating direction around the crack-tip is near zero; ie. $K_{II}=0$ criterion is applicable. The experimental crack path also closely matched that of a numerical simulation by FRANC [5] using the maximum strain energy release rate (ERR-criterion).

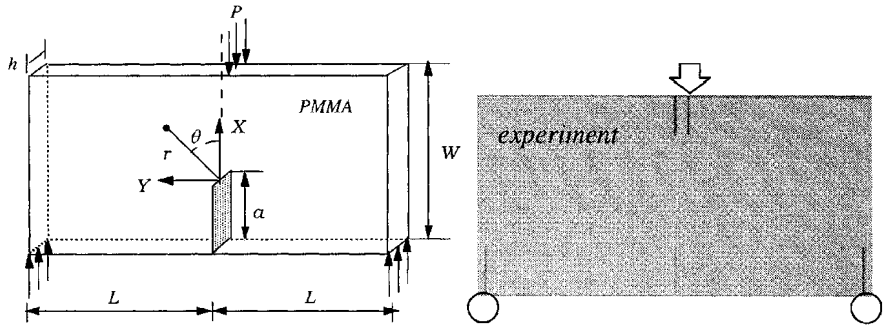

(a) homogeneous PMMA specimen (b) experimental crack propagation trajectory

Figure 4. Geometry of PMMA specimen used in the test
(L=150 mm, h=9.1 mm, W=150 mm and a=30 mm)

The consistency of these paths indicate that the quasi-static crack propagation of homogeneous PMMA can be considered by linear elastic fracture method macroscopically, and the two criteria yield the same results. The magnitude of the stress intensity factor through the slow crack propagation has a constant value around 1.1 $M \bullet Pa\sqrt{m}$. And these results are quite consistent in other loading conditions. In homogeneous media, such as homogeneous PMMA, the crack propagates under condition of zero mode II criteria which is essentially the same as maximum strain energy release rate (ERR) [6] for linear elastic materials. And this indicates that crack propagation in homogenous PMMA under mixed mode conditions is governed by zero mode II conditions or ERR-criterion.

3.2 SUB-INTERFACIAL CRACK PROPAGATION IN BIMATERIAL SPECIMENS

The sub-interfacial crack propagation in aluminum / PMMA bimaterial under 3-point bending specimens (shown in figure 5(a)) was investigated. In this loading configuration which is symmetric with respect to the specimen (not material) geometry, the crack propagates initially outward from the bimaterial interface and then begins to propagate parallel to the specimen. This phenomena arises from the fact that the mismatch parameter [3] for this particular combination of materials is $\varepsilon = 0.098$ (note that for a homogeneous material $\varepsilon = 0$). Figure 5 (b) shows a superposed photograph of the fractured specimen and simulated crack path; and these two paths are well matched. Figure 6 shows a sequence of shearing interferometric images as the crack initiates and propagates. A 1000 frame/sec video recorder was used to image the crack propagation. Due to the opacity of the aluminum material, only the results for PMMA part were

available. If the non-transparent specimen was also of interest, a reflectometric technique may be utilized but with additional complication to the optical system [1-2].

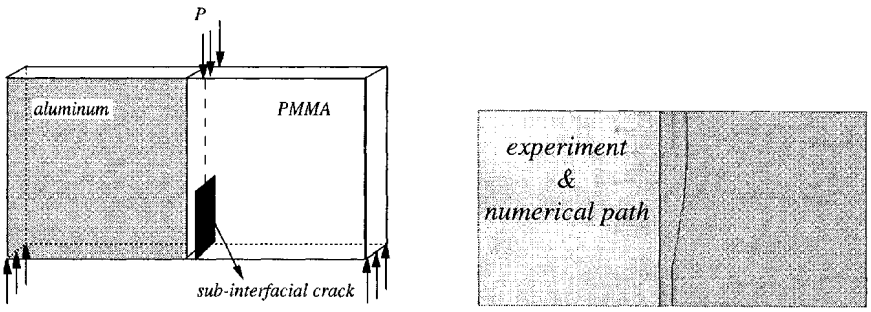

(a) geometry of subinterface crack (b) experimental & numerical paths superposition

Figure 5. Subinterface crack in aluminum/PMMA bimaterial specimen I

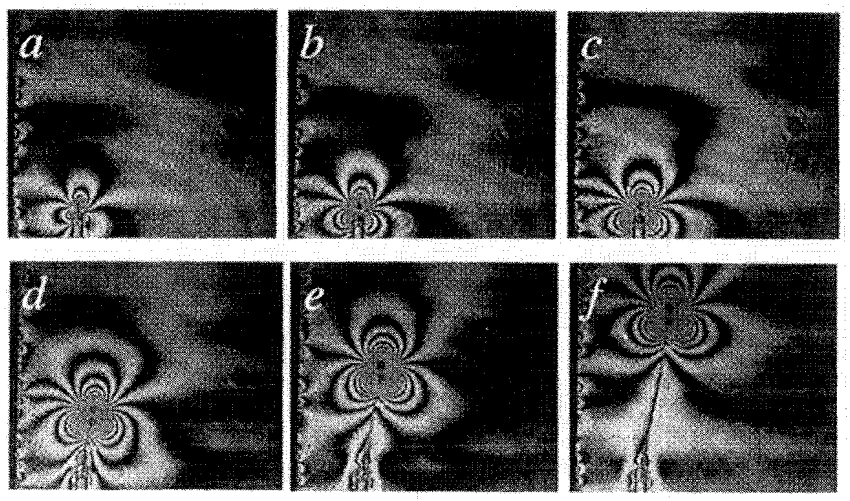

Figure 6. Shearing interferometric fringes in aluminum/PMMA bimaterial specimen I

For the subinterface crack, even though the structure is a bimaterial system, the crack is located entirely inside of the PMMA. Thus we can use the stress for those of homogeneous media asymptotically in the near tip region. We tested similar aluminum/PMMA bimaterial specimens but under different load conditions. The specimens II, III and IV in figure 7 were tested with different ratios of L_2/L_1 to generate various mode mixities. FRANC was used to simulate these cases using the ERR criterion. It is noted that crack path discrepancies arise especially in cases where the subinterface cracks propagate toward but still stay off the interface. Figure 7 shows this discrepancy clearly. Through the analysis of shearing interferometric fringes, it is found that the fracture toughness was different from the homogeneous case, and also when the sub-interface crack propagates *away* from the interface. In cases of specimen I and II, crack propagation paths are well matched with the simulation, and stress intensity factors are the same as that of homogeneous PMMA. However in the cases of

specimen III and IV, the experimental results show that crack trajectories are toward the interface and results in a larger increment of the fracture toughness. From the observation of the crack surfaces of fractured specimens, specimen III and IV have much rougher features. And these features cause contact of crack surfaces and non-negligible friction. Thus more energy is necessary to make new crack fronts. As seen in figure 8, the crack trajectories are as follows: cracks initiate, move in a curved line and finally grow parallel to the interface. In figure 8(a), d and d* indicate initial and final (when crack grows parallel) distances from the interface under the various L_2/L_1 ratios. The discrepancies between experiments and numerical simulations are shown in figure 8(b). For the outward and parallel propagation of cracks , that is $d^*/d > 1$ ($L_2/L_1 > 0.55$), numerical calculation is in good agreement with experiment. However, when that is $d^*/d < 1$ ($L_2/L_1 < 0.55$), ie the crack propagates toward the interface, the mechanisms of crack propagations are not governed well anymore by zero mode II (or ERR).

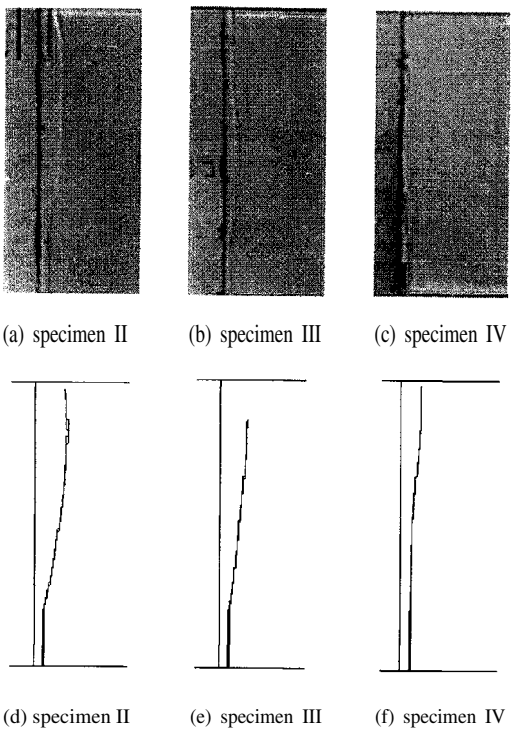

(a) specimen II (b) specimen III (c) specimen IV

(d) specimen II (e) specimen III (f) specimen IV

Figure 7. Crack propagation trajectories for different loading conditions : (a) &(d), (b) & (e) and (c) & (f) are from experiments and numerical simulation respectively

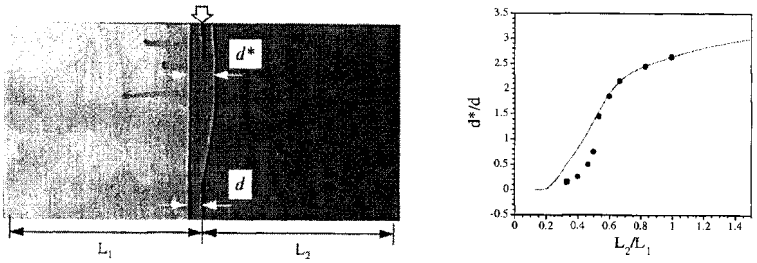

(a) (b)

Figure 8. Characteristic distance d*/d under different load conditions : (a) L_1 is fixed (= 150 mm), d = 10 mm, (b) line -> numerical simulations, dots -> experimental measurements

3. Conclusions

A shearing interferometer was utilized to map the stress fields around quasi-statically propagating cracks in homogenous PMMA and subinterfacial cracks in aluminum/PMMA bimaterial systems. In homogeneous PMMA, crack propagation is well described by zero mode II criterion (or ERR-criterion). Experimental crack trajectories are matched well with numerically simulated ones. However, this zero mode II criterion does not appear to be a robust tool for the estimation of crack paths in complex structures such as aluminum/PMMA bimaterial specimens. In this study when the subinterface cracks that are initially located near the interface propagate toward the material interface, it appears that other effects such as crack surface friction need to be taken into account.

References

1. Lee, H. and Krishnaswamy, S., A compact polariscope / shearing-interferometer for mapping stress fields in bimaterial system, *Exp. Mech.*, 36 (1996) 404-411.
2. Tippur, H. V., Krishnaswamy, S. and Rosakis, A. J., Optical mapping of crack tip deformations using the methods of transmission and reflection coherent gradient sensing : a study of crack tip K-dominance, *International Journal of Fracture.*, 52 (1991) 91-117.
3. Hutchinson, J.W., Mear, M.E. and Rice, J.R., Crack Paralleling an Interface Between Dissimilar Materials, *Journal of Applied Mechanics*, 54 (1987) 828-832.
4. Deng, X., General Crack-Tip Fields for Stationary and Steadily Growing Interface Cracks in Anisotropic Bimaterials. *Journal of Applied Mechanics*, 60 (1993) 183-189.
5. Ingraffea , T., FRANC2D, Cornell University Fracture Group
6. Hussain, M. A., Pu, S. L. and Underwood, J., Strain Energy Release Rate for a Crack Under Combined Mode I and Mode II, *Fracture Analysis*, ASTM STP 560 (1974) 2-28.

SOME STUDIES OF THERMOMECHANICAL BEHAVIOUR OF SOLID MATERIALS BY INFRARED THERMOGRAPHY

O. MAISONNEUVE and A. CHRYSOCHOOS
LMGC, UMR 5508 CNRS-UMII, Place E. Bataillon 34095 Montpellier Cedex 05, France.

1. Introduction

The purpose of this paper is to show, through two examples, the scientific interest of infrared techniques in order to study the mechanical, but in fact, the thermomechanical behaviour of materials and, more generally, to investigate their thermodynamic behaviour.

We will consider first, the case of energy balances during elastoplastic deformation processes of metallic alloys, and second, the case of energy analysis of pseudoelastic behaviour of shape memory alloys (SMAs). In both examples, the same thermodynamic framework was used. This framework, used to interpret the experiments, is the classical thermodynamics of irreversible processes of continuous media.

The state of a particle is described in suitable form by a set of $n + 1$ state variables : $\alpha_0 = T$, the absolute temperature, $\alpha_1 = \varepsilon$ the linearised strain tensor, and $n - 1$ internal variables $\alpha_2, \alpha_3, \ldots, \alpha_n$. For example, some of α_i are plastic strain tensor or phase proportions. If we introduce the specific Helmholtz free energy ψ, s being the specific entropy, the second principle leads to the Clausius-Duhem inequality :

$$D = \sigma : \dot{\varepsilon} - \rho \frac{\partial \psi}{\partial \alpha_j} . \dot{\alpha}_j - \frac{q}{T} . \mathrm{grad} T \geq 0 \tag{1}$$

where σ is the Cauchy stress tensor, ρ is the mass density, q the heat influx vector, D being the dissipation.

The property $D \equiv 0$ defines a reversible thermodynamic process. Usually, the dissipation is divided into two parts : the intrinsic dissipation $D_1 = \sigma : \dot{\varepsilon} - \rho \psi_{,\alpha_j} . \dot{\alpha}_j$ and thermal dissipation $D_2 = -q/T \,.\mathrm{grad} T$. Then the local heat conduction equation can be written as :

$$\rho C_\alpha \dot{T} - k \Delta T = D_1 + \rho T \frac{\partial^2 \psi}{\partial T \partial \alpha_j} . \dot{\alpha}_j + r \tag{2}$$

A. Lagarde (ed.),
IUTAM Symposium on Advanced Optical Methods and Applications in Solid Mechanics, 283–296.

where C_α is the specific heat at α_j constant, $j \in \{1, 2, .., n\}$, k is the isotropic conduction coefficient, $\rho T \psi_{T\alpha_j} . \dot{\alpha}_j$ the thermomechanical coupling term, r the external heat supply.

With our experimental conditions, the external heat supply remaining a constant, the heat conduction equation can be simplified as:

$$\rho C_\alpha \dot{\theta} - k \Delta\theta = D_1 + \rho T \frac{\partial^2 \psi}{\partial T \partial \alpha_j} . \dot{\alpha}_j = w'_{ch} , \tag{3}$$

where $\theta = T - T_0$; T_0 is the equilibrium temperature field, while w'_{ch} denotes the volume heat source.

For energy balance associated to a small deformation process, it is necessary to consider the following energy terms :

$W_{ext} = \int_0^t \int_{D(\tau)} \sigma : \dot{\varepsilon} \, dx d\tau$, the deformation work, , $W_e = \int_0^t \int_{D(\tau)} \rho T \psi_{,\varepsilon} . \dot{\varepsilon} \, dx d\tau$, the elastic work, $W_a = W_{ext} - W_e$, the anelastic work, $W_{ch} = \int_0^t \int_{D(\tau)} w'_{ch} \, dx d\tau$ the evolved heat , $W_d = \int_0^t \int_{D(\tau)} D_1 \, dx d\tau$, the dissipated work converted into heat, $W_s = W_a - W_d$, the stored energy due to strain hardening, $W_{thm} = \int_0^t \int_{D(\tau)} \rho T \psi_{,T\alpha_j} . \dot{\alpha}_j \, dx d\tau$ the heat associated to thermomechanical couplings, $W_{is} = \int_0^t \int_{D(\tau)} \rho T \psi_{,T\varepsilon} . \dot{\varepsilon} \, dx d\tau$, the heat due to thermoelastic effects, $L(t) = \int_0^t \int_{D(\tau)} \rho T \psi_{,T\beta_k} . \dot{\beta}_k \, dx d\tau$ the latent heat, the β_ks being the state variables associated to the phases proportions.

In this context, the constitutive equations can be derived from the Helmholtz free energy and from a dissipation potential $\varphi : (\dot{\varepsilon}, \dot{\alpha}_j) \to \varphi(\dot{\varepsilon}, \dot{\alpha}_j)$:

$$s = -\frac{\partial \psi}{\partial T} , \ \sigma^r = \rho \frac{\partial \psi}{\partial \varepsilon} , \ X_j = -\rho \frac{\partial \psi}{\partial \alpha_j} , \ \sigma^{ir} = \frac{\partial \phi}{\partial \dot{\varepsilon}} , \ X_j = \frac{\partial \phi}{\partial \dot{\alpha}_j} \tag{4}$$

the stress tensor being split into a reversible part σ^r and the irreversible part σ^{ir}. Often ψ is written as the sum of two terms : a thermoelastic part and a complementary part depending on the chosen internal state variables. If there is no intrinsic dissipation,

ϕ is chosen identically equal to zero. It is interesting to take into account thermal effects : they are macroscopic manifestations of some important evolution of the microstructure and represent precious data to perform energy balances useful to choose the specific free energy form and the one of the dissipation potential.

2. Energy balance during an elastoplastic deformation process of metallic alloys

Metallic alloys like stainless steels (A316L), carbon steels (XC 38), or aluminium alloys (AU4G) were considered. The physical phenomena taken into account are the thermoelastic effects, the plastic dissipation phenomena, the energy storage due to strain hardening.

As it is well known, the thermoelastic effects were first studied by Lord Kelvin. The plastic dissipation and the stored energy phenomena were studied by many authors, often metallurgists, as it appears in [1]. These mechanisms are qualitatively well identified, like in the case of the wire which warms when it is alternatively twisted. But, as shown in *figure 1* extracted from [1], it is very difficult to obtain reliable results for stored energy. During many years, the 10 percent, obtained by G. I. Taylor and H. Quinney in [2] for the stored energy ratio W_s/W_a , was the reference. It is possible to see in [3] some references about the interesting works of R.O. Williams, H.D. Bui, D. Rönnpagel, H. Neuhäuser, C. Schwink, E. Krempl, *etc.,* on stored energy and dissipation phenomena associated with plastic deformation. In general, experiments were realised by means of calorimetric techniques, often using annealing processing. They were delicate or even «acrobatic» what explains the spread of results shown in *figure 1.*

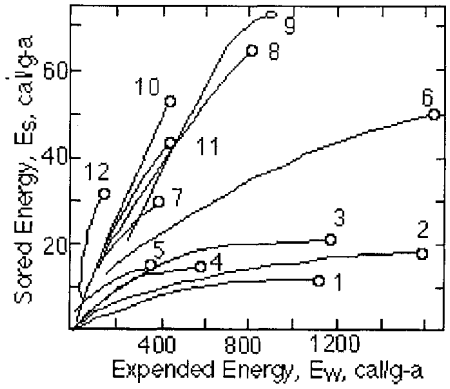

Figure 1: After [1]. Stored energy as a function of expended energy, reported by various investigators.

In a first time, we began also our dissipation measurements by determining indirectly the stored energy by using micro-calorimetric techniques [4-6]. The home-made micro-

calorimeter was directly placed on the testing machine, the sample passing through the cell of the thermopile. The possibility of taking into account the thermal losses gave more reliable results than the ones obtained by a simple calorimetric measurements performed after the loading. Nevertheless, the experimental procedure to get energy balances was time consuming and sensitive. In particular, it was only possible to realise global energy balance. So it quickly appeared preferable of using infrared techniques which allowed instantaneous and local energy balance in the sample gauge part. The *figure 2* shows the basic sketch of the experimental arrangement. An original characteristic of this experimental set-up is the simultaneous recording of thermal and mechanical data : surface temperature, load applied to the sample, and elongation of its gauge part. This set-up consists of a computerised uniaxial testing machine **(1, 2)** and an infrared thermography device **(4, 5, 6).** This latter is made of an infrared camera **(4),** a display unit **(5)** and a home-made numerizer **(6)** allowing storage and processing of the thermal images in a second microcomputer **(7).** Moreover, the numerizer allows recording at the beginning of each line of a thermal image, by the means of **(3),** the corresponding load and elongation signals and four other electric signals like the thermal level and thermal range characterising the state of the camera.

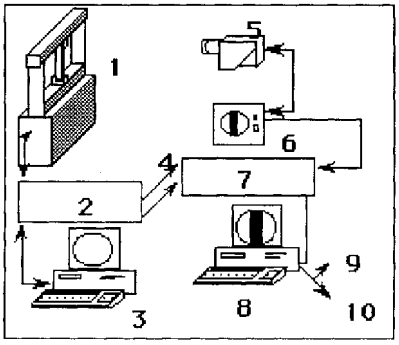

Figure 2 : Experimental set-up

The camera (Agema 880) is an infrared scanning system, with a single short wave detector InSb ([2-5.6] μm), liquid nitrogen cooled. The thermosignal, in Isothermal Unity proportional to the thermal radiation, is digitised and then converted into temperature in Celsius degree (°C) after a calibration operation.

Before our investigations, infrared techniques had been already used in relation with the dissipation energy measurement : the dissipation at the crack tip was studied by Nayroles and R. Bouc, R. Blanc and E. Giacometti, H. D. Bui , A. Erhlacher and Q .S. Nguyen, or the detection of the characteristic threshold of sheared sand in vibration was investigated by M. P. Luong (see references in [3]). But in all these works, the loading was periodic, what is an easier situation than quasistatic loading for the thermal image processing.

It seems that the first study where infrared techniques was used for quasistatic evolution of alloys, has been the one of C. Saix and P. Jouanna [7-9] in the prospect of civil engineering works supervision. From our collaboration with them on the plasticity effects [10], it appeared fortuitously that the fraction of stored energy was much more important than the 10 traditional percent, in particular at the beginning of work hardening. It was the start point of our investigations using two independent experimental techniques : micro-calorimetry and then infrared thermography. One of the main difficulties was the calibration particularly delicate of this kind of device. The calibration of the video signal was done with a special warming target equipped with thermocouples. The temperature variations were obtained by difference using a thermal reference image. The heat losses were assumed to be correctly described by linear laws of the temperature, then it was possible to simplify the heat equation (3) as follows :

$$\rho C_{\alpha}\left(\frac{\partial\theta}{\partial t}+\frac{\theta}{\tau_{\text{th}}}\right)-k\,\Delta\theta = w'_{\text{ch}}\,, \tag{5}$$

where τ_{th} is a time constant characterising the lateral heat losses. Then the volume heat source w'_{ch} may be determined by an inverse resolution of this partial derivative equation. Hypothesis of linear heat losses is justified for homogeneous tests and by the smallness of the temperature variations. The intuitive passage from thermal data to heat sources distribution is generally not obvious. The *figure 3* illustrates this passage in a general case and shows the consistency of the data processing.

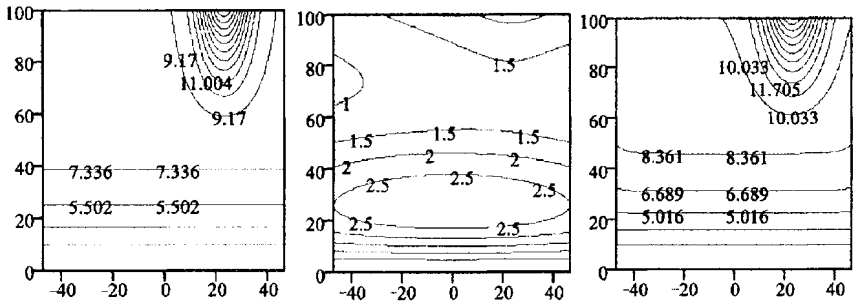

Figure 3 : Validity check of the data processing. (left) Analytic distribution of heat sources (°C.s^{-1}) at one given instant ; (middle), the corresponding temperature contour plots (°C) computed using spectral methods (direct problem) ; (right) reconstructed distribution of heat sources (°C.s^{-1}) using the thermal data processing (inverse problem). The X and Y axes are numbered in pixels.

Some experimental results obtained with a stainless steel A316 during a tensile test are given in *figures 4* and *5*. The *figure 4* shows the classical mechanical response when an homogeneous mechanical test is assumed, while in the *figure 5* the corresponding energy balance is plotted. The importance of the stored energy can be seen during the strain hardening.

Moreover, one can deduce from the energy balance that the stored energy ratio (W_s/W_a) decreases progressively. These results are of some interest : it is also possible to show that several elastoplastic models are not able to predict such energy evolution when they are only identified on the basis of mechanical tests [4-6], [1]- 12]. This led us to take into account the energy balance form in new modelling.

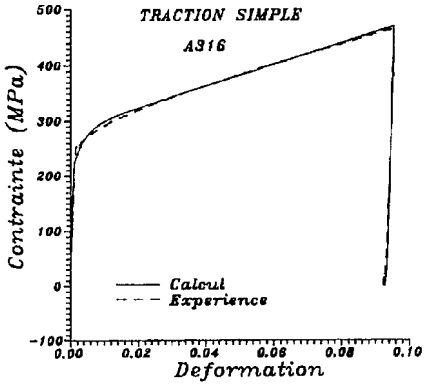

Figure 4 : Tensile test on stainless steel. Contrainte means stress, déformation means strain. [19]

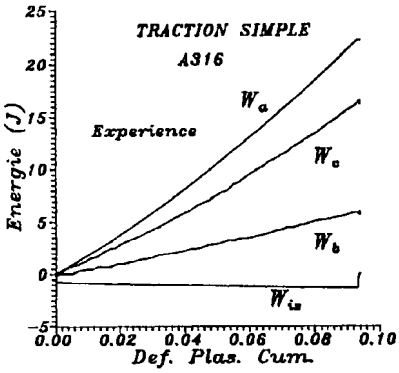

Figure 5 : Experimental energy balance corresponding to the mechanical test of *figure 4.* After [19], W_c stands for the dissipated energy while W_b is the stored energy.

When more complex loading was considered, other observations could be made. In *figure 6* for an aluminium alloy AU4G, there is a quasi perfect agreement between mechanical experiments and the modelling. In practice, it is generally not too difficult to propound quasi perfect mechanical constitutive equations for loading-unloading tests. But in *figure 8,* we can see that such a modelling is not at all appropriate to predict the evolution of stored energy W_s and the dissipated energy W_d.

Moreover, a release of stored energy during «elastic returns» can be observed by the mean of infrared techniques. This phenomena cannot be predicted within the classical framework of time-independent elastoplasticity. In principle, inside the elastic domain, the hardening state is fixed, so that no dissipation or no release of stored energy can occur.

A same kind of remark must be done in the case of cyclic test presented in *figure 7.* We can observe, once again, a quasi-perfect agreement between mechanical experimental results and the predictions of the model. However, a release of the stored energy is experimentally detected during an upholding of the load at the end of the test. The classical framework of rate independent elastoplasticity cannot predict an evolution of W_s during a load upholding.

We refer the reader to the references [19,20] for other experimental results about complex loading and to [21, 22] for a presentation of the corresponding constitutive

laws taking into account the evolution of stored energy : in these papers, the thermodynamic forces are no longer the hardening parameters but are function of these latter. The agreement between the predictions of the enhanced models and the experimental observations made in the energy plan was considered satisfactory.

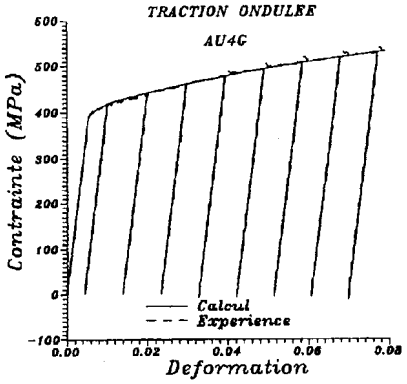

Figure 6 : Pulsating test on aluminium alloy. The experimental and predicted by a theoretical model data [19,20] are quasi indistinguishable.

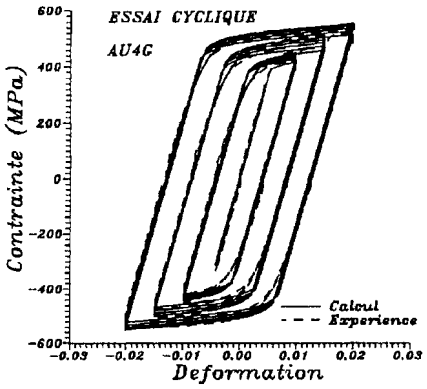

Figure 7 : Cyclic test on aluminium alloy. With the same model as previously [19,20], the experimental and predicted data are once again in a good agreement.

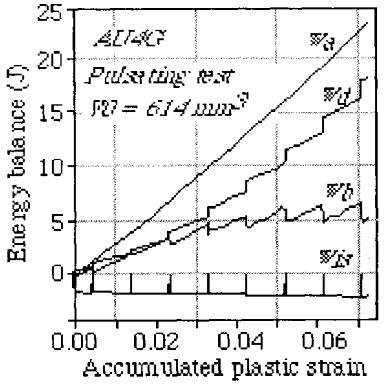

Figure 8 : Energy balance for an aluminium alloy during a tensile test (*figure 6*). Release of stored energy « elastic » returns can be experimentally observed. This phenomenon cannot be predicted within the classical framework of elastoplasticity.

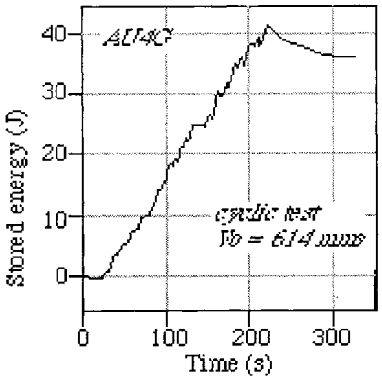

Figure 9 : Release of stored energy during un upholding of the load is experimentally observed after a cyclic test (*figure 7*). Once again, the classical framework of the time rate independence elastoplasticity cannot predict such an evolution.

3. Thermomechanical approach of martensite phase transition during pseudo-elastic transformation of SMAs

Another interesting example of the infrared techniques' use to study the thermomechanical behaviour of solid materials is that of SMAs. These alloys are characterised by a strongly non linear but reversible mechanical behaviour. Hysteretic stress-strain curves are classically obtained for tests performed at a constant room temperature. It is now well-known that this hysteresis is due to an austenite-martensite stress induced phase transition.

Many experimental or theoretical works have been realised about SMAs among which it is convenient to mention those of M. Berveiller and E. Patoor, C. Lexcellent and B. Raniecki, I. Muller, P.F. Gobin, G. Guenin, M. Morin, M. Fremond, C. Licht, R. Peyroux, M. Favier, J. Ortin and Planes, J. Van-Humbeck, J.M. Ball and R.D. James, O. Bruno, D. Rios-Jara, S. Pagano *et a,* C. Berriet. Most of references about these works may be found in [13]. In the present paper, we indicate how it is possible to characterise, from a thermodynamic point of view, the stress-induced phase transition process, at a constant room temperature, by mean of infrared techniques described in section 2 [13-22]. In fact, it is possible to answer two decisive questions. For quasi-static loading, can the phase change be considered as an isothermal process or not ? What is the magnitude of the dissipative phenomena being able to accompany the phase change ? These answers are fundamental to explain the origins of the hysteresis loops and to identify a behavioural model energetically consistent.

The thermodynamic framework is the same as in sections 1 and 2, but the state variables α_j for $j \geq 2$ are now the volume proportions of n martensite variants. In the case of zero stress, if the temperature T of material is greater or equal to A_f (austenite finish), then $\alpha_j = 0$ and only the austenite phase exists. If T is less than or equal to M_f (martensite finish), then we have $\sum_{j=2}^{n} \alpha_j = 1$ and the martensite phase solely exists. Now, if $M_f < T < A_f$, then $0 < \alpha_j < 1$ with $\sum_{j=2}^{n} \alpha_j < 1$, and there is a coexistence of martensite and austenite phases. The heat equation is the same as in section 1 and 2 but the term $\rho T \psi_{,T\alpha} . \dot{\alpha}$ represents now the thermomechanical coupling term due to the phase change, *i.e.,* the latent heat rate.

From an experimental point of view, as shown in section 2, it is difficult to measure weak temperature variations and to pass from temperature data to the distribution of heat sources. Experiments were performed on thin and flat samples of Cu-Zn-Al polycrystalline alloys. The percentage in weight are 70.17% of copper, 25,63% of zinc and 3.66% aluminium. In *table 1,* are gathered the thermo-physical characteristics of such a material. The samples are annealed at 850 °C during ten minutes and the oil-quenched during one hour. Before testing, a thin coat of black paint was applied on the surface of the sample to improve its emissivity.

TABLE 1 : Thermo-physical parameters of a Cu-Zn-AL SMA.

ρ (kg. m^{-3})	C_α (J. kg^{-1}. K^{-1})	λ_{th} (K^{-1})	L (J)	A_s (°C)	M_s (°C)
7700	393	18.10^{-6}	6000	7	15
E (Mpa)	v	k (W.m^{-1}. K^{-1})	τ_{th} (s)	A_f	M_f
$2.5.10^4$	0.33	80	60	19.5	6

Two kinds of experiments were performed :

- load-unload paths with increasing strain amplitude
- load-unload cycles with constant strain amplitude.

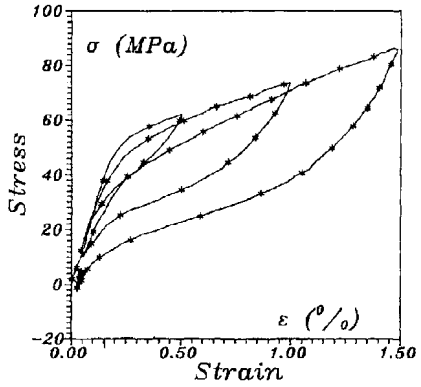

Figure 10 : Hystersis loop increasing

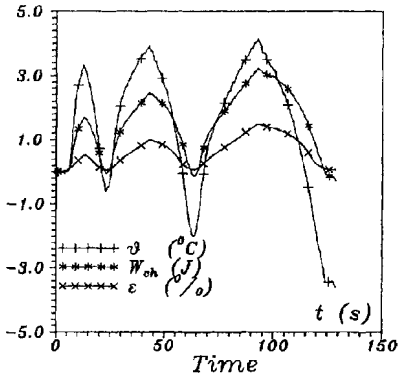

Figure 11 : themal and energy responses associated with *figure 10.*

The mechanical loading was strain-controlled during the load and load-controlled during unloading to avoid buckling phenomena. The *figure 10* gives the stress-strain curves during load-unload paths with increasing amplitude of strain. Let us remark that the hysteresis loops overlap and that the strain vanishes at the end of each loop at zero stress. In correspondence with the *figure 10,* the *figure 11* shows the evolution of the strain, of the temperature in the middle of the gauge part of the sample, and of the heat due to the transformation. The amplitude of the temperature variation reaches up to 7 °C what is important when compared to the difference $A_f - M_f = 13.5$ °C . One other important characteristic is that the amount of the evolved heat approximately vanishes at the end of each loop. The same kind of results were found with the second type of experiments, see *figures 12* and *13.* The loops stabilised after a slight cyclic softening ; and as often in plasticity a shakedown was realised.

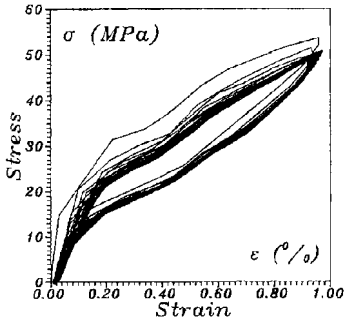

figure 12 : thermomechanical shakedown of SMA after a slight cyclic softening.

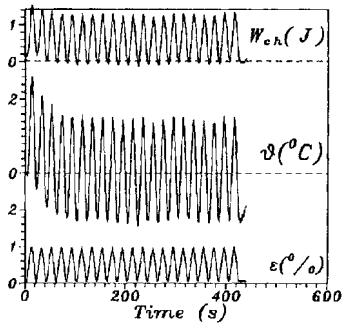

figure 13 : thermal and energy responses associated with *figure 12*. Note that the loop of hysteresis is stabilised as soon as the thermal response becomes symmetric and periodic.

However, from a thermodynamic viewpoint, this shakedown must be related to the temperature variations that become periodic and symmetric. This is the manifestation of a strong thermomechanical coupling. Note also that the amounts of heat return approximately to zero at the end of each hysteresis loops.
The main observations for these two cases are : first, the temperature variations during the tests are not negligible in comparison with the transition domain « width » ($A_f - M_f$); second, the heat globally exchanged between the sample and the surroundings approximately vanishes at the end of a hysteresis cycle. It appeared that the stress induced phase change could not be regarded any more as an isothermal thermodynamic process insofar as the temperature variations induced by the phase change strongly modify the kinetics of the transformation.

What consequence can we deduce from such results ? Can we conclude that the transformation is non dissipative ? Is it possible to associate a thermodynamic cycle of duration C to each hysteresis loop, so that we get

$$A_h = \int_C w'_{ch}\, d\tau \,, \tag{6}$$

and if it is, can we deduce that the intrinsic dissipation D_1 is equal to zero ?
Observing the hysteresis loop, we can admit that the strain at the end of the loop is approximately equal to the initial strain. At zero stress, the temperature is greater than A_f , the state is afresh austenitic. In accordance with what was supposed higher, we shall admit that the internal state variables take again their initial value. Two cases may occur :

- the final temperature equals the initial one as for instance it is the case for the second experiments after some load-unload cycles and $\varepsilon_{final} = \varepsilon_{initial}$, $\alpha_{j_{final}} = \alpha_{j_{initial}}$, the hysteresis loop is then a thermodynamic cycle ;

- the final temperature is different from the initial one : it, is then possible to virtually close the cycle by adding a fictitious therrnoelastic transformation.

This transformation passes from T_{final} to T_{initial} at zero stress. The energy cost of such a transformation can be expressed as a function of the temperature difference $T_{\text{final}} - T_{\text{inital}}$ as soon as an isotropic and linear thermoelastic behaviour is supposed :

$$\left[W_{\text{ch}}\right]_{\text{F}}^{\text{I}} = -V_0\left(\lambda_{\text{th}}{}^2\, T_0\, E(T_{\text{initial}} - T_{\text{final}})\right) \tag{7}$$

where V_0 is the gauge volume of the sample, λ_{th} is the linear thermal expansion coefficient and E is the Young's modulus.

For a temperature difference less than 2°C, the energy cost is around 2.10^{-3} Joules for a strain amplitude less than 10^{-4}. This order of magnitude is undetectable by our instruments. We then admit the extension of this experimental result to a thermodynamic cycle. In such conditions, we can show that the intrinsic dissipation is identically equal to zero. For all thermodynamic cycle of duration C, the entropy being a state function, we have :

$$\int_{\text{C}} \rho\, \dot{s}\, \mathrm{d}t = \int_{\text{C}} \rho\, C_\alpha\, \frac{\dot{T}}{T}\mathrm{d}t - \int_{\text{C}} \rho \frac{\partial^2 \psi}{\partial T \partial \alpha_{\text{j}}}.\dot{\alpha}_{\text{j}}\mathrm{d}t = 0 \tag{8}$$

The specific heat C_α being constant as the mass density , the corresponding integral vanishes for a thermodynamic cycle, so that we get :

$$\int_{\text{C}} \rho \frac{\partial^2 \psi}{\partial T \partial \alpha_{\text{j}}}.\dot{\alpha}_{\text{j}}\mathrm{d}t = 0 \tag{9}$$

Finally, a linearised version of the heat conduction equation, with $\theta/T_0 < 2.10^{-2}$

$$\int_{\text{C}} \rho\, C_\alpha \left(\dot{\theta} + \frac{\theta}{\tau_{\text{th}}}\right)\mathrm{d}t \;\; = \int_{\text{C}} D_{\text{I}}\mathrm{d}t + \int_{\text{C}} \rho\,(1 + \frac{\theta}{T_0}) \frac{\partial^2 \psi}{\partial T \partial \alpha_{\text{j}}}.\dot{\alpha}_{\text{j}}\,\mathrm{d}t \tag{10}$$

leads, with the positivity of D_1, to $D_1 \equiv 0$. In practice, this result indicates that the intrinsic dissipation remains very small in comparison with the latent heat rate. To examine, the relative importance of the dissipated energy, let us consider the ratio :

$$R_{\text{T}} = \frac{\int_{\text{HLD}} w'_{\text{ch}}(t)\,\mathrm{d}t}{\int_{\text{HLD}} \left|w'_{\text{ch}}(t)\right|\mathrm{d}t} \tag{12}$$

where HLD represents the hysteresis loop duration. The numerator stands for the heat balance associated with the hysteresis loop and the denominator the accumulated heat as in plasticity the accumulated plastic strain.

The more the dissipation is preponderant, the more R_{T} is to 1. Conversely, the closer R_{T} is to 0, the more the dissipation is negligible compared with the heat evolved by thermomechanical couplings.

Besides, to characterise the mechanical importance of the hysteresis loop, it is useful to consider the ratio R_{M} :

$$R_M = \frac{\int_{HLD} \sigma : \dot{\varepsilon}\, dt}{\int_{LOD} \sigma : \dot{\varepsilon}\, dt} \qquad (13)$$

where LOD is the loading duration. The numerator represents the work associated with the hysteresis loop. The denominator is the mechanical work used to deform the sample. If R_M equals zero there is no hysteresis loop.

The *table 2* gives the evolution of R_T and R_M during the tests with increasing strain amplitude.

TABLE 2 : Evolution of R_T and R_M indicators for increasing strain amplitudes.

ε_{max}	$V_0 \int_{HLD} \lvert w'_{ch}(t) \rvert dt.10^{-3}$	R_T	$V_0 \int_{HLD} \sigma : \dot{\varepsilon}\, dt.10^{-3}$	R_M
0.5	3585	0.021	6	0.18
1	5173	0.027	27	0. 3
1.5	8010	0.05	55	0.43

We can observe that R_T is less than 0.03. The hysteresis energy is around 10^{-2} Joules, what is very small opposite to the latent heat that is greater than 1 Joule. If the hysteresis loop is small from an energy point of view, it is not negligible in the case of a purely mechanical description. In fact, R_M is greater than 0.15 and it reaches up to 0.43.

Other experimental results, have some interest as the influence of the strain rate, (*figures 14* and *15*). For compression tests, at a constant room temperature T_0, we observe a stress hardening due the simple temperature variations induced by the phase change : because of the heat diffusion, the maximal temperature amplitude increases with the strain rate, while the evolved heat level remains constant. This could not have been the case if the stress increase had been related to viscous effects.

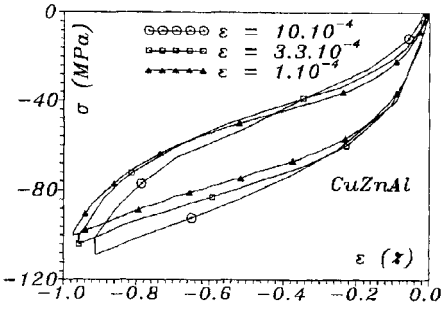

Figure 14 : Influence of the strain rate on the stress-strain curves.

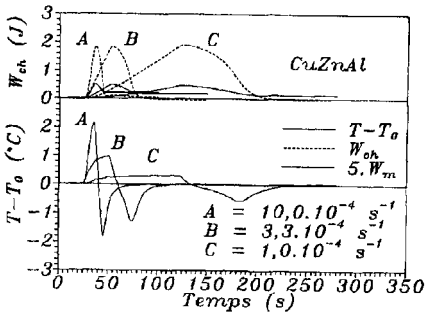

Figure 15 : Thermal and energy responses associated with *figure 14.*

The *figures 16* and *17* show for two very close temperatures the influence of T_0 : a slight and systematic asymmetry was observed between the hysteresis obtained in compression and that obtained in tension. All happens as if the phase change starts later and develops more intensively in compression than in tension.

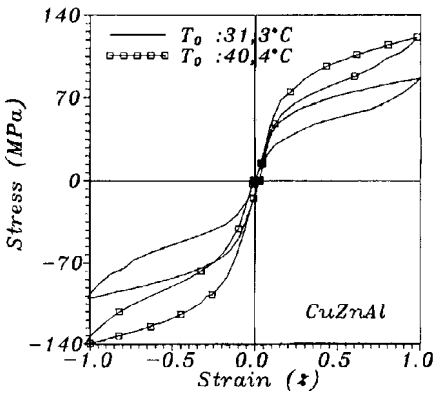

Figure 16 : Cyclic tests at different T_0.

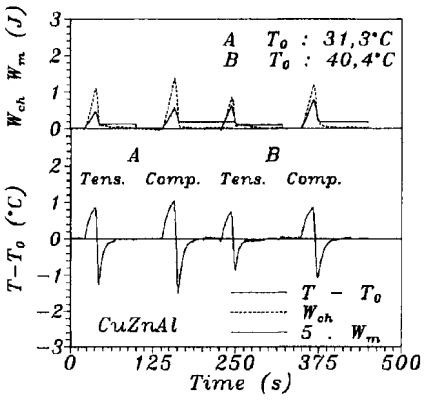

Figure 17 : Thermal and energy responses associated with *figure 17.*

4. Concluding comments

The infrared techniques, in constant progress, at every moment make it possible to know the distribution of the temperatures of surface of a sample with a good precision. From these thermal data, it is also possible to locally derive the heat sources intensity and the energy balance useful to identify the models. More than a simple non destructive method, the infrared thermography is, when coupled with data processing and with numerical inverse methods, a powerful investigation mean for studying the thermoelastic effects, the dissipation phenomena, the energy storages, the phase changes, the strain localisations due to damage, *etc.*

In conclusion, the fields to be approached by the infra-red imaging represent in fact a considerable realm of investigation. The thermomechanical behaviour of materials under mechanical and thermal loading is still too often treated by identifying the temperature of material with that of the thermal regulation. When its role is not reduced to that of parameter, the temperature is often described as *variable of control.* We are persuaded that these approximations undoubtedly hide important phenomena which could be highlighted by following a true thermomechanical approach of the solid materials' behaviour.

5. References

1. BEVER, M.B., HOLT, D.L., TITCHENER, A.L.: *The stored energy of cold work,* Progress in materials science n° 17, Pergamon Press, 1975.
2. TAYLOR, G.I. , QUINNEY, H.: *The latent energy remaining in a metal after cold working* , Proc. Roy. Sot., London, 1934.
3. CHRYSOCHOOS, A. : *Dissipation et blocage d'énergie lors d'un écrouissage en traction simple,* state thesis, Montpellier University, 1987.
4. CHRYSOCHOOS, A. : *Contribution à l'étude de la dissipation intrinsèque des matériaux élastoplastiques en grandes deformations* , D.I. thesis of Montpellier University, 1987.
5. CHRYSOCHOOS, A., MAISONNEUVE O. *: Bilan énergetique en élastoplasticité grandes deformations,* C. R. Acad. Sci. Paris, t.300, Série II, n° 20,985990, 1983.
6. CHRYSOCHOOS, A.: *Bilan énergétique en élastoplasticité grandes déformations,* J. Met. Théo. Et Appl. Vol. 4 n°5, pp.589-614, 1985.
7. SAIX,.C. : *Plasticité expérimentale par thermographie de surface,* D.I. thesis of Montpellier University, 1978.
8. SAIX, C., JOUANNA, P. : *Dissipation plastique et thermographie de surface. Premiers résultats expérimentaux,* Matériaux et Constructions, 12, 1979.
9. SAIX, C., JOUANNA, P. : Analyse de la dissipation plastique dans des pièces métalliques, J. de Met. Appl., Vol. 5, n°1, 1981.
10. CHRYSOCHOOS, A. : *Phénomènes de blocage d'énergie lors de transformations plastiques,* DEA. Montpellier University, 198 1.
11. CHRYSOCHOOS, A. , MAISONNEUVE, O., MARTIN, G. *: Dissipative and non dissipative phenomena during an elastoplastic deformation process,* Trans 9th Int. Conf. SMIRT, vol. L, pp. 357-366, Balkema Ed., 1987.
12. CHRYSOCHOOS, A., MAISONNEUVE, O., MARTIN, G, CAUMON, H., CHEZEAUX, J.C. *: Plastic and dissipated work and stored energy,* Nucl. Eng. And Des., vol.1 14, pp 323-33, 1989.
13. LÖBEL, M : *Caractérisation thermomécanique d'alliages à mémoire de forme de type NiTi et CuZnAL ; domaine de transition et cinétique de changement de phase,* Thesis of Montpellier University, 1995.
14. CHRYSOCHOOS, A., PHAM, H., MAISONNEUVE, O.: *Une analyse expérimentale du comportement thermomécnaique d'un alliage à mémoire de forme de type CuZnAL,* C. R. Acad. Sci. Paris, t.3 16, Série II, pp.1031-1036, 1993.
15. CHRYSOCHOOS, A., PHAM, H., MAISONNEUVE, O.: *An experimental analysis of thermomechanical behaviour of CuZnAZ SMA,* SMIRT 12, Ed. K. KUSSMAUL, Elsevier Sci. Pub., vol.L, pp.35-46, 1993.
16. PHAM, H. : *Analyse thermomkcanique du comportement d'un alliage à mémoire de forme de type CuZnAlL,* Thesis of Montpellier University, 1994.
17. CHRYSOCHOOS, A., PHAM, H., MAISONNEUVE, O. : *Energy balance of thermoelastic martensite transformation under stress,* Nuclear Engineering and Design, 162, pp. 1- 12, 1996
18. CHRYSOCHOOS, A, LÖBEL, M. : *A thermomechanical approach of martensite phase transition during pseudoelastic transformation of shape memory alloys,* 8th Int. Symp. CMDS, Ed. K.Z. MARKOV, World Scientific Pub., pp. 21-29, 1996.
19. BELMAHJOUB, F. : *Comportement thermomécanique de matériaux métalliques sous divers chargements uniaxes,* Thesis of Montpellier University.
20. CHRYSOCHOOS, A., .BELMAHJOUB, F. : *Thermographic Analysis of Thermo-mechanical Couplings,* Archives of Mechanics, 44, pp.55-68, 1992
21. MALAL, N.E. : *Modélisation et simulation numérique du cornportement thermomécanique d'alliages métalliques,* Thesis of Montpellier University, 1992.
22. SOOS, E. : *A new theory of the stored energy in elasto-plasticity and the torsion test,* Eur. J. Mech. A/Solids, 16, n0 3, 467-500: 1997.

INFRARED THERMOGRAPHY OF THERMOMECHANICAL COUPLINGS IN SOLIDS

M.P. LUONG[1-2], D. PARGANIN[2] & J. LOIZEAU[2]
[1] *CNRS-MS Ecole Polytechnipe 91128 Palaiseau France*
[2] *INSEP 11 Avenue du Tremblay 75012 Paris France*
Email: luong@lms.polytechniqzre.fr

Abstract

The present paper aims to illustrate three advantages of infrared thermography as a non-destructive, real-time and non-contact technique to mechanically characterise solid materials. It permits observation of the macrostructural aspects of. thermoplasticity describing damage and failure processes in diverse and various engineering materials and their components subjected to monotonous, cyclic or vibratory loading. It usefully suggests the definition of a *threshold of acceptable damage* TAD for materials related to sport equipment such as leather shoe, leather-like composites or sail synthetics. Particularly in case of metallic products or automotive components subjected to fatigue loading, this newly proposed method could evaluate in a non-destructive manner the *fatigue limit* FL in a very short time compared to traditional fatigue testing techniques that are much more time-consuming and excessively expensive. In addition owing to the thermomechanical coupling, infrared thermography readily describes the damage location, the dissipative regime and the evolution of structural failure.

1. Introduction

The thermal effect due to thermomechanical coupling at the tip of a moving crack has been investigated [4] within the framework of thermodynamics, taking into account stress and strain singularities. Internal energy dissipation was recognised by well-known scientists [1015-16-25-26-28]. Carrying out experiments on the cyclic twisting of cylindrical bars, Dillon [7] identified the work done to the system by plastic deformation as the major contribution to the heat effect, and proposed an internal dissipation rate D. Well-developed empirical theories of plastic deformation in metal allowed engineers successfully to predict the behaviour of a variety of structures and machine elements loaded beyond the elastic limit for purposes of design.

This paper emphasises the application of infrared thermography to detect the macrostructural aspects of thermoplasticity describing the occurrence of damage in engineering materials under monotonous loading and metallic products subject to fatigue testing.

A. Lagarde (ed.),
IUTAM Symposium on Advanced Optical Methods and Applications in Solid Mechanics, 297-304.

2. Heat production mechanism

Damage theories rely on assumed discontinuous phenomena at the microscopic scale [5]. Kachanov [13] introduced a continuous variable D, related to the scalar density of defects. Taking into account the most fundamental aspects of inelastic deformation and neglecting the details at the microstructural level, Mroz [24] suggested phenomenological constitutive models for engineering applications. On the basis of micro- and macro-scale relationships, Dang-van [6] proposed a multiaxial fatigue criterion with a realistic physical interpretation of fatigue phenomena. During a polycyclic fatigue test, the stress at the macroscopic scale remains elastic. However, at the microscopic scale, the metal is neither isotropic nor homogeneous; it is constituted of randomly oriented crystals. This induces local fluctuations of the microscopic stress and defines the macroscopic stress. Thus the local microscopic stress can locally exceed the yield strength in certain unfavourably oriented grains, whereas the macroscopic stress remains elastic. If the cyclic plastic response of the grain is not an elastic shakedown, then some microcracks will be nucleated. They could coalesce to form a crack of detectable size. Since fatigue is generally caused by cyclic plastic strain, the plastic strain energy plays a very significant role in the damage process [9-12-22-23]. The significance of such an energy approach is in its ability to unify microscopic and macroscopic testing data. Therefore, the idea of relating fatigue to the intrinsic dissipation detected by infrared thermography seems to be highly relevant. Metal fatigue of aircraft components was detected very early in the history of powered flight [19], and it was also of major importance in determining the durability of ground vehicles. The failure mode was identified early by railway engineers. Even very low failure rates can produce an appreciable number of failures [20]. Fatigue phenomena, leading for example to the failure of diesel engines [11], were poorly understood until recently because they occur unexpectedly at relatively low stress levels. Some progress has been made recently in design methods [2].

Despite this wealth of methods developed by engineers over the years, the principal question that remains unanswered is this: what is the physical phenomenon called fatigue damage? The ASTM STP 811 meeting in 1982 on fatigue mechanisms (advances in quantitative measurement of physical damage) concluded that fatigue damage can be defined as either: i) a chemical-physical process whereby irreversible degradation of a specific property results from the application of cyclic stress and strain, or ii) a physical separation of the material (cracks, cavitation, etc.). Understanding fatigue damage requires making a clear distinction between the physical damage, the process of damage, and the *manifestation of damage*. Various heat production mechanisms have been proposed by various authors and are now discussed. According to Moore and Kommers [21], the temperature test was suggested and to some extent used by C.E. Stromeyer of Manchester in England as early as 1913. However, their search for some short-time test to predict fatigue resistance, based on the use of thermocouples, was not conclusive since they could not identify a critical temperature with the endurance limit of steel specimens subjected to cyclic loading.

This paper proposes using differential infrared thermography to quantitatively evaluate the *evolution of temperature* generated by the specimen under reversed stresses applied for a few minutes or less. Infrared thermography has been successfully used as an experimental method to detect the plastic deformation of a steel plate under monotonic

loading [3], or as a laboratory technique for investigating damage, fatigue, and failure mechanisms occurring in engineering materials [17-18]. Plastic deformation is not homogeneous and the stress acting on a plastic inhomogeneity embedded in an elastic surrounding is a function of its plastic strain, diminishing with increasing strain. Due to the thermomechanical coupling, the generated plastic dissipation is readily detected by infrared thermography.

3. Thermomechanical coupling in solids

The development of the thermo-elastic-plasticity equations [l-7-10-14] leads to the following coupled thermomechanical equation:

$$\rho C_v \dot{T} = r_0 + K\nabla^2 T - \left(\beta : \overset{(4)}{\underset{\sim}{D}} : \dot{E}^e \right) T + S : \dot{E}^I$$

where β denotes the coefficient of the thermal expansion matrix, r_0 the heat supply, E^e the elastic strain tensor, E^I the inelastic strain tensor, C_v the specific heat at constant deformation, $\overset{(4)}{\underset{\sim}{D}}$ the fourth-order elasticity tensor, e the specific internal energy, K the thermal conductivity, and finally T the absolute temperature.

This equation shows the potential applications of the infrared scanning technique in diverse engineering domains: detection of fluid leakage, non-destructive testing using thermal conduction phenomena, elastic stress measurements, and localisation of dissipative phenomena. Thus the detected temperature change, resulting from four quite different phenomena, must be correctly discriminated by particular test conditions and/or specific data reduction. This is the main difficulty when interpreting the thermal images obtained from experiments under the usual conditions.

The last term on the right-hand side of the thermomechanical equation defines the energy dissipation due to plasticity and/or viscosity. The work done by plastic deformation per unit volume can be evaluated by integrating the material stress-strain curve. Infrared thermography readily detects the internal dissipation term, which constitutes a significant part of the non-linear coupled thermomechanical analysis. The proposed thermographic technique is mainly concerned with the differences in temperature (or thermal gradients) that exist in the material rather than with the absolute values of temperature. It conveniently detects the *dissipation evolution* of the material under loading. The reported work considers intrinsic dissipation as a highly accurate indicator of damage manifestation. It highlights the advantages of the infrared thermographic technique, used for the detection and the discrimination of physical phenomena involved in this non-linear coupled thermomechanical effect.

4. Infrared thermographic technique

Infrared thermography is a convenient technique for producing heat pictures from the invisible radiant energy emitted from stationary or moving objects at any distance and

without surface contact or any perturbation of the actual surface temperature of the objects viewed. A scanning camera, analogous to a television camera, uses an infrared detector in a sophisticated electronics system. It detects radiated energy and converts it into a detailed real-time thermal picture in a video system either in colour or monochromatically. Response times are shorter than one microsecond. Temperature differences in the heat patterns are discernible instantly and are represented by several hues. The quantity of energy W emitted as infrared radiation, is a function of the temperature and emissivity of the specimen. The higher the temperature, the greater the emitted energy. Differences of radiated energy correspond to differences of temperature. The AGA 782 SW infrared scanner unit in use comprises the following:

(a) a set of infrared lenses which focuses the electromagnetic energy radiating from the object being scanned, into the vertical prism;
(b) an electro-optical mechanism which discriminates the field of view into 10^4 pixels by means of two rotating vertical (180 rpm) and horizontal (18,000 rpm) prisms with a scanning rate of 25 fields per second;
(c) a set of relay optics containing a selectable aperture unit and a filter cassette unit which focuses the output from the horizontal prism onto a single-element point detector located in the wall of a Dewar chamber;
(d) a photovoltaic SW short-wave infrared detector composed of Indium Antimonide InSb which produces an electronic signal output varying in proportion to the radiation from the object within the spectral response 3.5 μm to 5.6 μm;
(e) a liquid nitrogen Dewar that maintains the InSb detector at a very low temperature of -196 °C, allowing a very short response time of about one microsecond; and
(f) an electronic control with preamplifier that produces a video signal on the display screen.

The received radiation has a non-linear relation with the object temperature, can be affected by atmosphere damping, and includes reflected radiation from the object's surrounding. In consequence, calibration and correction procedures have to be applied. Knowing the temperature of the reference, we can calculate the view-field temperature with a sensitivity of 0.1 °C at 20 °C. This infrared device is used to scan specimens in the following two test programs.

5. Threshold of acceptable damage

On August 22, 1851, the yacht *America* raced a fleet of English cutters and schooners around the Isle of Wight. According to the legend, *America* easily prevailed. *America's* sails were unusual [8]. Through innovative technology, engineers have continually found ways to make stronger, lighter sails. The resistance of the fabric to stretching is especially crucial, as is its breaking strength. Also, yield strength, or the load beyond which the material is permanently elongated, is relevant, because even if they do not break, sails can be ruined by deformation. There is thus a need to detect damage using a very sensitive and non-invasive technique [27].

Before 1924 the whole sport footwear (upper and sole) was made in leather, thanks to its ability to absorb the sweating that is 6 to 8 times higher during a sport activity than as usual. Today leather is still well present in the sport footwears. Annually France produces 320 000 pairs for tennis, basket, training and footing, 200 000 pairs with staples and toes, 930 000 pairs for touring, 24 000 pairs for riding, and 180 000 pairs for dancing. Leather is a product made by stabilising through tanning the proteins of animal skins that are by-products of the meat industry. While about five-sixths of all the leather produced is used by the shoe industry, special uses of leather fill many real industrial needs. Through its many uses of boots, shoes, clothing, straps, harness or handbags, wallets, billfolds, leather novelties, etc., leather has become a most essential commodity of man. Softness, damage and strength behaviour is an important consideration in connection with designs or regulations. An other concern is to produce leather of uniform good quality, for example, which is acceptable to the shoe manufacturer and the wearer of the shoes. Balls for football games were made in leather. Since World Cup 1986 in Mexico, synthetic composites substituted leather. However they are mechanically considered as leather-like materials. A specimen of soccer ball envelope was tested under uniaxial tension test. *Figure 1* shows the load-displacement curve of this leather-like specimen. The Agema SW-782 infrared scanner, incorporating a high-temperature filter and equipped with a real time system Discon (Digital Infrared System for Coloration) converting thermal images into a ten-colour isotherm display, was used to record the bulk of the heat emission data. That device displays a ten-colour calibrated surface-temperature picture of the specimen. Infrared thermography readily detects intrinsic dissipation announcing the occurrence of damage, preceding the failure of leather-like specimen. *Figure 2* presents the evolution of intrinsic dissipation when loading increases up to failure and thus defines a *threshold of acceptable dissipation or damage* (TAD), separating low and high regimes of dissipation or damage occurrence.

The process of tailoring leather-like products involves the transformation of a two-dimensional structure (planar sheet fabric) into a three-dimensional form. It necessitates the formation of extreme curvatures by sewing or fusing and pressing. The joining of different pieces of leather components is achieved by sewing with sewing threads. There are many problems associated with the performance of sewing threads during the sewing process that can reach very high speeds. During the stitching process, thread is subjected to complex kinematic and dynamic conditions. Tensile and bending stresses, that take place at very high speeds, localised heating that may cause reduction of strength of thermoplastic sewing threads by as much as 60 %. In addition the mechanics of the thread structure and their properties in the seams after sewing include seam strength. Stretch and pucker are also extremely important. Current design procedures for leather-like seams are based upon simplified assumptions of connection behaviour. The increased use of diverse types of seams by sewing and/or glueing suggests that a more thorough understanding of the behaviour of seams would be beneficial for upgrading design procedures. As infrared thermographic scanning offers new information on leather-like connection behaviour, refinement of design procedures can be made as needed and new, more effective, and specialised seam configurations can be contemplated. *Figure 3* presents a tension test on a soccer envelope seam. A threshold of acceptable dissipation or damage TAD for the seam appears on *Figure 4*. This experimental result shows that the process of leather-like seam could be optimised in order to meet a higher value for its TAD limit.

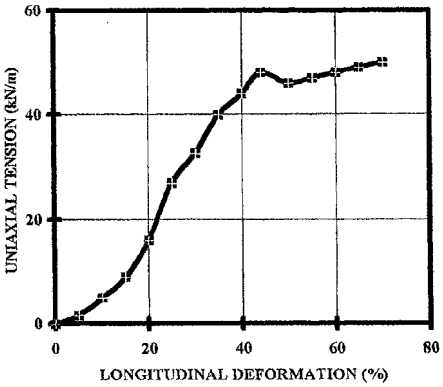

Figure 1. Tension-deformation of a specimen of football envelope.

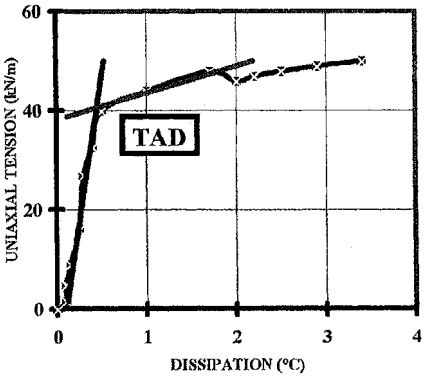

Figure 2. Corresponding tension-dissipation curve for the same specimen. The two straight lines define a *threshold of acceptable damage* (TAD). This means that the material fails if this load is exceeded.

Figure 3. Tension testing on a soccer envelope seam.

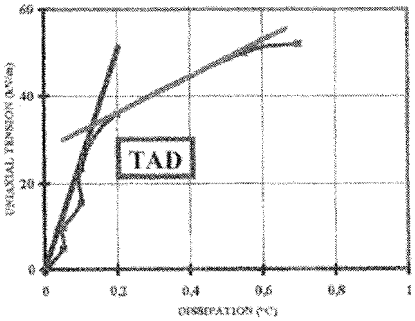

Figure 4. Tension-dissipation curve for a football envelope seam The two straight lines define a *threshold of acceptable damage* (TAD). This means that the envelope seam fails if this load is exceeded.

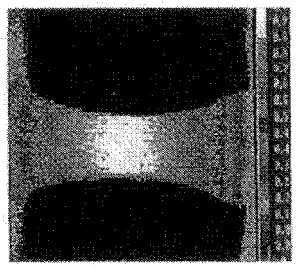

Figure 5. intrinsic dissipation of the specimen under 390 MPa after 6,000 load cycles (Temperature scale is given in °C).

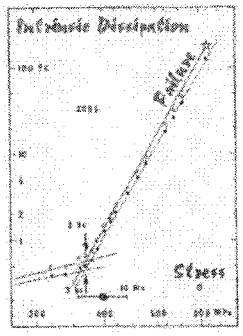

Figure 6. Graphical determination of fatigue limit (FL) of XC55 steel specimen.

6. Evaluation of fatigue strength

The material for the rotating bending tests was XC55 steel, quite extensively used in automobile construction. To minimise scatter, the 6.74 mm diameter specimens have been prepared from a single melt. The number of load cycles was 10^7, corresponding to automobile fatigue damage. Cyclic fatigue tests were performed on a 4-point loading rotating bending Schenck machine, running at approximately 100 Hz. A total of 18 specimens was step-tested according to the Staircase or Up-and-Down method. This procedure means that each specimen was run for 10^7 cycles at 370 MPa for example, whereupon the stress was raised in 10 MPa steps in the absence of failure, and lowered otherwise. Using standard methods of statistical analysis, we estimated the fatigue limit to be 399 MPa with a standard deviation of 41 MPa.

A series of five rotating bending tests has been scanned by the infrared system at different stress levels that were chosen in accordance with the step-by-step procedures for using statistical methods in usual fatigue testing. All specimens were coated with matte spray paint to maximise their emissivity. The paint coating raises the surface emissivity to a uniformly high level. In addition, it allows examination of the surface which is undertaken at oblique angles, without degradation of sensitivity. The recommended paint coating also reduces surface reflections and ensures uniformity of response across the specimen. With a loading frequency of 100 Hz and after stabilisation of the temperature rise, the load duration chosen was 30 seconds and 60 seconds corresponding to 3,000 load cycles and 6,000 load cycles respectively.

Computer-aided thermography software TIC 8000 allowed data reduction of thermal images that shows heat generation after 6,000 load cycles at 390 MPa (*Figure 5*). These thermal images provided quantitative values of the intrinsic dissipation of a steel specimen in rotating bending caused by 3,000 and 6,000 load cycles. The same procedure has been applied for each load step. The manifestation of the fatigue damage mechanism is revealed by a break in the intrinsic dissipation regime of the loaded specimen. Experimental results are summarised in *Figure 6* which shows how fatigue limit is determined using a graphical procedure. The threshold of critical thermal dissipation is roughly the same for the 3,000 and 6,000 cycle curves. It corresponds to the value deduced from standard procedure. The star point at co-ordinates (600 MPa, 180 °C) represents the last load step at which failure occurred.

These experiments showed that infrared thermography can provide the fatigue limit of XC55 steel within a few hours instead of the several months required when using the standard staircase method.

7. Concluding remarks

This work has demonstrated that material dissipativity is a highly sensitive and accurate manifestation of damage, owing to the thermomechanical coupling. Infrared thermography provides a non-destructive, real-time and no contact technique to observe the physical processes of degradation and to detect the occurrence of intrinsic dissipation. It readily evaluates the threshold of acceptable damage under monotonous loading and the fatigue limit in cases of fatigue testing.

8. References

1. Allen, D.H., R.T. : A prediction of heat generation in a therrnoviscoplastic uniaxial bar, *Int J. Solids & Structures,* **21,** 4 (1985), 325-342.
2. Ballard, P., Dang-van, K., Deperrois, A. and Papadopoulos, Y.V. : High cycle fatigue and a finite element analysis, *Fatigue Fract. Engng Mater. Struct.,* **18,** 3 (1995), 397-411.
3. Bui, H.D., Ehrlacher, A. et Nguyen, Q. S.: Etude experimentale de la dissipation dans la propagation de la fissure par thermographie infrarouge, *C.R. Acad. Sci.,* **293,** II (198 1), 10 15- 10 17.
4. Bui, H.D., Ehrlacher, A. et Nguyen, Q.S. : Thennomechanical coupling in fracture mechanics, *Thermomechanical Coupling in Solids,* H.D.Bui and Q.S.Nguyen ed., Elsevier Sci. Pub., IUTAM (1987), 327-341.
5. Bui, H.D. and Stolz, C.: Damage theories for brittle and ductile materials, *Fracture of Non-Metallic Materials,* ed. Herrmann & Larsson (1987), 33-46.
6. Dang-van, K.: Sur la resistance à la fatigue des métaux, *Sc. et Techn. Armement, Mémorial Artillerie Française,* 3e fascicule (1973), 647-722.
7. Dillon, O. W. Jr. : Coupled thermoplasticity, *J, Mech. Phys. Solids,* **11** (1963), 2 l-23.
8. Doyle, B.P,: Strong fabrics for fast sails, *Scientific American,* July (1997), 46-53.
9. Ellyin, F. and Kujawski, D.: Plastic strain energy in fatigue failure, *Trans. ASME,* **106,** November (1984), 342-347.
10. Farren, W.S. and Taylor, G.I.: The heat developed during plastic extension of metals, *Proc. Roy. Soc.,* **A,** 107 (1925), 422-451.
11. Habib, K. and Husain, A.: Failure analysis of a broken diesel engine, *Fatigue,* Butterworth-Heinemann Ltd, 16 July (1994), 357-359.
12. Irwin, G.R. : Fracture, *Encyclopedia of Physics,* **II,** Springer-Verlag, Heidelberg, (1965), 7.
13. Kachanov, L.M.: Time of rupture process under creep conditions, *Izv. Akad. Nauk. S.S.R.Otd. Tekh. Nauk.,* **8** (1958), 26-31.
14. Kratochvil, J. and Dillon, O. W. Jr. : Thermodynamics of elastic-plastic materials as a theory with internal state variables, *J. Appl. Phys.,* **40** (1969), 3207-32 18.
15. Lee, E.H.: Elastic plastic deformations at finite strains, *J. Appl. Mech.,* **36** (1969): l-6.
16. Lehman, Th. : Coupling phenomena in thermoplasticity, *SMiRT5 Berlin,* Paper L 1/1 (1979).
17. Luong, M.P.: Detection par thermographie infrarouge du seuil caractéristique d'un sable cisaillé en vibrations, *C.R. Acad. Sci.,* **295,** II (1982), 87-90.
18. Luong, M.P.: Infrared thermovision of damage processes in concrete and rock, *Engineering Fracture Mechanics,* **35,** l-2-3 (1990), 127-135.
19. Mann, J. Y .: Aircraft fatigue with particular emphasis on Australian operations and research, *Proc. 12th ICAF Symp. May 1983 Toulouse,* ed. R. Labourdette & D. Deviller, Paper 1 .0 (1983).
20. McLester, R.: Railway component fatigue testing, *Full-scale Fatigue Testing of Components and Structures,* ed. K.J. Marsh, Butterworths (1988), 59-76.
21. Moore, H.F. and Kommers, J.B.: Fatigue of metals under repeated stress, *Chemical and Metallurgical Engineering,* **25,** December (1921), 1141- 1144.
22. Morrow, J.D.: Cyclic plastic strain energy and fatigue of metals, *Internal Friction Damping and Cyclic Plasticity,* ASTM STP **378,** July (1965), 45-84.
23. Mroz, Z. : Hardening and degradation rules for metals under monotonic and cyclic loading, *J. Engng Mater. Techn., ASME,* **105,** April (1983), 113-l 19.
24. Mroz, Z.: Phenomenological constitutive models for metals, *Modelling small deformations of polycrystals,* Elsevier (1986), 293-344.
25. Mroz, Z. and Raniecki, B.: On the uniqueness problem in coupled thermoplasticity, *Int. J. Eng. Sci.,* **14** (1976), 211-221.
26. Nied H.A. and Batterman, S.C. : On the thermal feedback reduction of latent energy in the heat conduction equation, *Mater. Sci. Eng.,* **9** (1976), 243 -245.
27. Parganin, D., Luong, M.P. and Loizeau, J. : Infrared scanning of damage in sail material, *Proc. 2nd* Int. *Conference on The Engineering of Sport,* Sheffield (1998), UK.
28. Raniecki, B. and Sawczuk, A.: Thermal effects in plasticity, *Z. Angew Math Mech.,* 55, 333-341, 363-373.

AUTOMATED PHOTOELASTICITY APPLIED WITH THERMOELASTICITY TO REAL COMPONENTS

S. BARONE*, Z. F. WANG and E.A. PATTERSON
Department of Mechanical Engineering
University of Sheffield, Mappin Street, Sheffield S1 3JD, UK

**Dipartimento di Costruzioni Meccaniche e Nucleari*
Universitci di Pisa, Pisa, ITALY

Abstract

A complete definition of stresses requires an evaluation of the magnitude and directions of the components of stress related to a co-ordinate system. The combination of thermoelasticity and photoelasticity offers the potential to achieve this objective since photoelasticity provides the direction of principal stresses and difference in magnitude, whilst thermoelasticity yields the sum of the magnitude. Recent experiments have shown that simultaneous measurements can be made. The demands of simultaneous measurement for a full-field of view imply that all the photoelastic information must be captured quickly. A hybrid technique based on spectral contents analysis and phase-stepping has been developed. The methodology and instrumentation for combining the automated photoelasticity with thermoelasticity has been developed In conclusion, it is shown that the complete state of stress over an area of the surface of the component can be evaluated without any prior knowledge of the stress state.

1. Introduction

Thermoelastic stress analysis [Stanley and Chan, 1985] is an experimental tool for non-contacting stress measurements of cyclically loaded components. The technique is based on infrared detection of the small changes in temperature that accompany changes in stress. For isotropic materials, the change in temperature at a point is proportional to the change in the sum of the principal stresses at that point provided adiabatic conditions prevail. On the other hand photoelasticity provides full-field information on the principal stress differences and directions. The advent of automated photoelastic systems [Ajovalasit et al, 1998] has allowed experimentalists to speed up the rate of analysis and to perform more complex investigations. Photoelastic analysis provides the principal stress difference but, like the thermoelastic stress analysis, no information is provided on the individual principal stresses. Such information is frequently required in analysis or design and it is important to develop techniques for determining individual stress values, i.e. stress separation.

A. Lagarde (ed.),
IUTAM Symposium on Advanced Optical Methods and Applications in Solid Mechanics, 305–312.

A variety of separation techniques have been developed for thermoelasticity by Huang et al (1990a & b) amongst others, and for photoelasticity [Haake & Patterson, 1992]. Commonly, individual values for the principal stresses cannot be obtained directly from the experimental data without employing numerical methods or using supplementary information such as compatibility and/or equilibrium conditions, or progressing from a known stress state such as a boundary. Consequently, it would be useful to be able to determine the principal stress components directly from experimental data without reference to prior knowledge of the stress distribution.

Barone and Patterson (1996) have proposed the combined use of thermoelasticity and reflection photoelasticity for the separation of the stress components. This approach does not require any knowledge of boundary conditions and no integration or differencing procedure is applied. Audenino and Calderale (1996) applied a similar technique to the analysis of an automotive front suspension link to obtain individual stresses and relative directions at specific points. However reflection photoelasticity requires the application of a birefringent coating on the structure to be analysed, whereas thermoelasticity requires a surface of uniform emissitivity which is usually achieved by applying a matt black paint to the surface. As consequence of the need for two different coatings, Barone and Patterson (1996) applied the two techniques to opposite faces of a plate, so that the analysis was limited to bidimensional problems. Whilst the method developed by Audenino and Calderale (1996) required either two independent suspension links or one link with one of the coatings being removed to allow subsequent application of the other coating.

In a more recent study Barone and Patterson (1998) have shown that polycarbonate, typically used in reflection photoelasticity, can be used as a strain witness in thermoelastcity. This has led to the development of a new hybrid experimental technique based on the integration of thermoelastic and photoelastic stress analyses.

2. Thermoelastic Stress Analysis

Thermoelastic stress analysis is based on the thermodynamic relationship between the change in stress in a component under elastic loading and the corresponding temperature change. When the small surface temperature change is measured using an infrared detector, then for a linear, homogeneous, elastic component under adiabatic conditions:

$$\Delta(\sigma_1 + \sigma_2) = A_{th}\, S \tag{1}$$

where S is the thermoelastic signal (uncalibrated signal units (U)) and A_{th} is the calibration factor ($Nm^{-2}U^{-1}$) and is given by the following equation:

$$A_{th} = \frac{DGR}{Te\,2048\,K} \tag{2}$$

where D is the temperature responsivity of the infrared detector (Kelvin V^{-1}), G is the sensitivity setting (v), R is the surface temperature correction factor and e is the surface emissivity. The infrared detector used in this work is a SPATE (Stress Pattern Analysis

by Thermal Emission) system consisting of a computer-controlled scanning radiometer which measures the small temperature changes produced on the surface of a component subjected to cyclic loading.

Thermoelastic stress analysis requires a black coating to be applied on the component so as to provide a surface of uniform emissivity, and to convert the component into a "black body" thus maximising the emitted infrared signal. The usual high-emissivity coatings recommended are black paints with emissivity values around 0.92. Most of the viable coatings typically have a relatively low thermoelastic effect when compared to metallic substrates. Therefore the coating tends to act as an insulating layer, and the thermoelastic response shows a progressive attenuation with increasing frequency and thickness of the coating. However, MacKenzie (1989) reported a recovery of the signal seen in the region beyond about 50 Hz at thickness above 70 microns. This effect is to be attributed to the thermoelastic effect of the coating itself and constructive or destructive interference due to the main effect coming from the substrate.

When the specimen is loaded, the displacements at the specimen-coating interface are transmitted to the coating to produce a strain field through the thickness of the coating. If the coating is thin relative to the thickness of the specimen, the strains developed at the surface of the specimen are transmitted without significant alteration to the coating. Moreover it is reasonable to assume that the stresses normal to the surface both of the coating and the specimen vanish. Thus the sum of the principal stresses acting on the surface of the specimen is linearly related to the sum of the principal stresses acting in the coating by the following relation:

$$\Delta\left(\sigma_1^s + \sigma_2^s\right) = \frac{E^s\left(1-\nu^c\right)}{E^c\left(1-\nu^s\right)} A_{th}^c \; S^c \qquad (3)$$

where E and v are the modulus of elasticity, and the Poisson's ratio respectively, A_{th}^c is the thermoelastic factor of the coating and the superscripts s and c refer to the structure and coating respectively. Equation (3) indicates that the coating could be employed as strain witness to give the sum of the principal stresses in the specimen provided that the signal S^c is related to the thermoelastic response of the coating. Hence the use of coatings in the strain witness role requires materials with high thermoelastic effect and also with adequate infrared opacity in order to have a good emissivity. Barone and Patterson (1998) have shown the effectiveness of polycarbonate in fulfilling this role.

3. Automated Photoelastic Stress Analysis

The phase-stepping concept has been described as changing the absolute phase of the reference wave in equal steps and measuring the local light intensity after each step. This change in phase is achieved in practice by rotation of the output optical elements of the polariscope, i.e. the analyser and output quarter-wave plate. In this study an instrument developed by Patterson and Wang (1998) was employed. The new polariscope, known as PSIOS (Phase Stepped Images Observed Simultaneously), allows

four phase stepped images, $i_1 \cdots i_4$ to be observed and captured simultaneously. The instrument consists of a focal lens through which the light is received from the photoelastic component, then collimated and subsequently split into two twice using cube beam splitters to generate four beams of nominally equal intensity. The four beams are collected by identical focal lenses and are incident onto four identical CCD cameras. Appropriately orientated quarter-wave plates and polarisers are placed in the path of each of the beams so that the phase-stepped images are generated. The polarising effect of the beam splitters is accounted for in processing the data. The output from the four cameras can be fed to a multiplex device which will combine them into a single picture that can be read by a digitiser, thus permitting simultaneous capture of the four phase-stepped images. These maps of intensity were used in well-established phase-stepping procedures to evaluate the isoclinic parameter and the relative retardation at individual points in the field of view without reference to neighbouring points.

The isochromatic fringe order, N is obtained as a fractional value from the phase-stepping method. The phase map can be calibrated by the operator or alternatively an automated approach can be employed. It has been shown by Ji and Patterson (1998) that, whilst the use of broadband light introduces errors in the results of phase-stepping, these errors are acceptable if the bandwidth is limited to approximately 100 nm. Hence, it is viable to use the three colours from an RGB camera to generate three sets of results by phase-stepping. By considering the output from the RGB camera as a spectrum that is a characteristic of the fringe order viewed, it is possible to automatically calibrate the phase-map for fringe orders upto three. A continuous map of the isochromatic parameter can be obtained by stacking the periods of the data and taking account of the first derivative of the data with respect to its spatial position.

In reflection photoelasticity, the relationship between the isochromatic fringe order N and the principal stresses σ_1 and σ_2 in the surface of the component can be written as [Zandman et al, 1977]:

$$\sigma_1^s - \sigma_2^s = \frac{E^s}{E^c}\frac{1+\nu^c}{1+\nu^s} A_{ph} N \tag{4}$$

where as before the subscripts s and c refer to the component surface and reflective coating respectively, and A_{ph} is a constant defined as:

$$A_{ph} = \frac{f_c}{2h_c} \tag{5}$$

where h_c and f_c are the thickness and material fringe constant of the photoelastic coating respectively.

4. Simultaneous Thermo- and Photo-elastic Stress Analyses

The experimental approach proposed in this paper is based upon acquiring and processing the data corresponding to thermoelastic signals, isochromatics and isoclinics to completely define the stress field in an engineering structure. The thermoelastic information and the isochromatic and isoclinic data were obtained from the same

surface of a component coated with a commercially available birefringent coating, using a SPATE 8000 system and the new automated reflection polariscope. The configuration of the experimental set-up is shown in Figure 1. An optical low-pass filter (*hot mirror*) which transmits light in the visible while simultaneously reflects light in the infrared spectrum, was placed in front of the specimen. This low-pass filter should generally be used in collimated light at normal incidence. Figure 1 shows that the angles of incidence depend on the distance between the filter and the measurement devices, i.e., SPATE scan unit and CCD cameras. Angles other than those corresponding to normal incidence can produce a shift of the cut-off wavelength, however, no appreciable variation of the characteristics of the edge filter were observed.

The number of the measurement points in the area to be analysed is controlled by the operator both for the thermoelastic and the photoelastic analysis. The working-distance between the SPATE scan unit and the surface of the specimen determines the spatial stress detail, whilst the resolution is chosen by the operator. In the photoelastic set-up the number of measurement points (pixels) is controlled by the choice of lens. The experimental data are stored in the form of two arrays of values corresponding to the fringe order N (i.e., $N_{p,q}$ for p x q data points) and the thermoelastic signal S (i.e., $S_{m,n}$ for m x n data points). Generally the number of measurement points in the analysed area are not the same because of the different resolutions of the two systems. The bigger array is then reduced to the same format as the smaller array by computer processing and, considering equations (3) and (4), the individual principal stresses were then achieved respectively as:

$$\left(\sigma_1^s\right)_{j,k} = \frac{1}{2}\frac{E^s}{E^c}\frac{1-\upsilon^c}{1-\upsilon^s}\left(A_{ph}N_{j,k} + A_{th}S_{j,k}\right) \tag{6}$$

$$\left(\sigma_2^s\right)_{j,k} = \frac{1}{2}\frac{E^s}{E^c}\frac{1-\upsilon^c}{1-\upsilon^s}\left(A_{ph}N_{j,k} - A_{th}S_{j,k}\right) \tag{7}$$

Equations (6) and (7) enable the individual stresses to be evaluated directly using the thermoelastic infrared signal S and the photoelastic fringe order N at each point j,k.

5. Experimental results

The evaluation of the individual stresses by using thermoelastic and photoelastic data was validated by the application of the procedure to an aluminium plate of width 120 mm and thickness 6 mm with a central hole of radius 10 mm. A thin (1 mm thick) photoelastic coating (type PS-1D, Measurement Group Inc.) was bonded onto the plate of the surface of the plate in its central section. The tests were carried out in a servo-controlled hydraulic test machine applying a sinusoidal cyclic load at a frequency of 10 Hz to achieve adiabatic conditions. The load was tensile over the whole cyclic range and the far-field nominal stress was σ_0=27.7 N/mm^2.

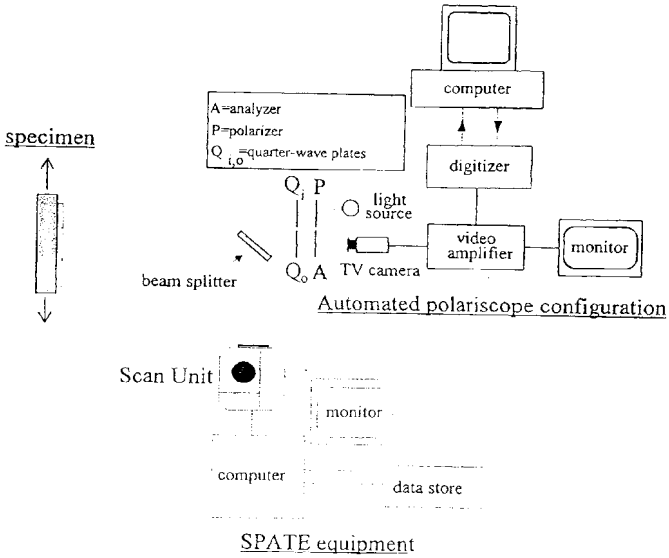

Figure 1. Schematic diagram of the experimental set-up

The SPATE data were obtained by scanning a rectangular array selected on the coating bonded on to the component. The calibration factor A_{th} was evaluated by a uniaxial resistance gage bonded on to a uniformly stressed area of the coating. The strain gauge readings were converted to stress using values for the Young's modulus and Poisson's ratio of the coating of 2.5 GPa and 0.38 respectively. The SPATE 8000 head was placed in front of the beam splitter and the total working-distance was 500 mm. This working-distance allowed the measurement of a spatial stress detail of 0.5 mm and the resolution was chosen so as to define a spacing between each measurement point of 0.76 mm which resulted in 55x48 measurement spots. The isochromatic and isoclinic data were acquired from the same area of the component using the PSIOS system. The number of measurement points (pixels) was 255×225

Figure 2 shows the contour maps of the sum and the difference of the principal stresses obtained by the thermoelastic and the photoelastic analysis for a rectangular patch in one ligament of the plate, centred on the axis of symmetry perpendicular to the direction of loading and with one edge passing through the hole. All the data presented in the figures that relates to stresses are normalised with respect to the nominal, applied stress σ_0. Figure 2 also shows the individual principal stresses as obtained by equations (6) and (7) respectively.

The experimental results were compared with those obtained from the theory for an axially loaded strip of infinite width with a central circular hole [Savin, 1961] as shown in figure 3. In general the agreement between the experiment and theory is good. No

smoothing of the measured data was performed. The average differences were 0.05 and 0.026 and the standard deviations 0.032 and 0.02 for maximum and minimum principal stress, respectively.

6. Discussion and Conclusions

Clearly the combined technique, other than the compliance of the double experiment, inherits the restrictions of both techniques such as the need for a coating. Errors are evident in the thermoelastic data at the edge of the specimens. These errors arise due to the movement of the edge during cyclic loading causing the detector to average data from the specimen and the adjacent free space. It is difficult experimentally to avoid this boundary effect. However, the principal stresses at the edges could be evaluated either by post-processing the thermoelastic data or by using only the photoelastic data on free edges. The data produced using reflection photoelasticity are influenced by the diffuse nature of the reflected light field due to the irregular reflectivity of the bonding agent, the non-uniformity of light source, and defects in the coating and bond. The scatter in the distributions of principal stresses is no greater than found in the thermo- and photo-elastic data, and the comparisons with theoretical data showed good correlation.

7. References

Ajovalasit, A., Barone, S ., Petrucci, G., (1998), A review of automated methods for the collection and analysis of photoelastic data, *Journal of Strain Analysis,* 33(2).

Audenino, A.L., Calderale, P.M., (1996) Combined Thermoelastic and Photoelastic Stress Analysis of an Automotive Front Suspension Link, *International Journal of Materials and Product Technology,* 11(5/6), 345-356.

Barone, S., Patterson, E.A.(1996) Full Field Separation of Principal Stresses by Combined Thermo- and Photo-elasticity, *Experimental Mechanics,* 36(4), 318-324.

Barone, S., Patterson, E.A., (1998) Polymer Coatings as a Strain Witness in Thermo- and Photo- Elasticity, *Journal of Strain Analysis,* in press.

Haake, S . J., Patterson, E. A., (1992) The Determination of Principal Stresses from Photoelastic Data, *Strain,* 153-158.

Huang, Y.M., Rowlands, R.E., Lesniak, J.R. (1990) Simultaneous Stress Separation, Smoothing of Measured Thermoelastic Isopachic Information and Enhanced Boundary Data, *Experimental Mechanics,* 30 (4), 398-404.

Ji, W., Patterson, E.A., (1998), Simulation of errors in automated photoelasticity, *Experimental Mechanics,* 38(2).

MacKenzie, A. K., (1989) Effects of Surface Coatings on Infrared Measurements of Thermoelastic Responses, *Proc. Int. Conf on Stress and Vibration: Recent Developments in Industrial Measurement and Analysis,* ed. P. Stanley, SPIE, vol. 1084, 59-71, London.

Patterson, E.A., Wang, Z.F., (1998) Simultaneous Observation of Phase-Stepped Images for Automated Photoelasticity, *Journal of Strain Analysis,* 33 (1)) 1-16

Savin, G. N., (1961) *Stress Concentration around Holes,* Pergamon Press, New York, London.

Stanley, P., Chan, W.K., (1985) Quantitative Stress Analysis by means of the Thermoelastic Effect, *Journal of Strain Analysis,* 20 (3), 129-137.

Zandman, F., Redner, S., Dally, J. W., (1977) *Photoelastic Coatings,* SESA Monograph No.3, published by the Iowa State University Press.

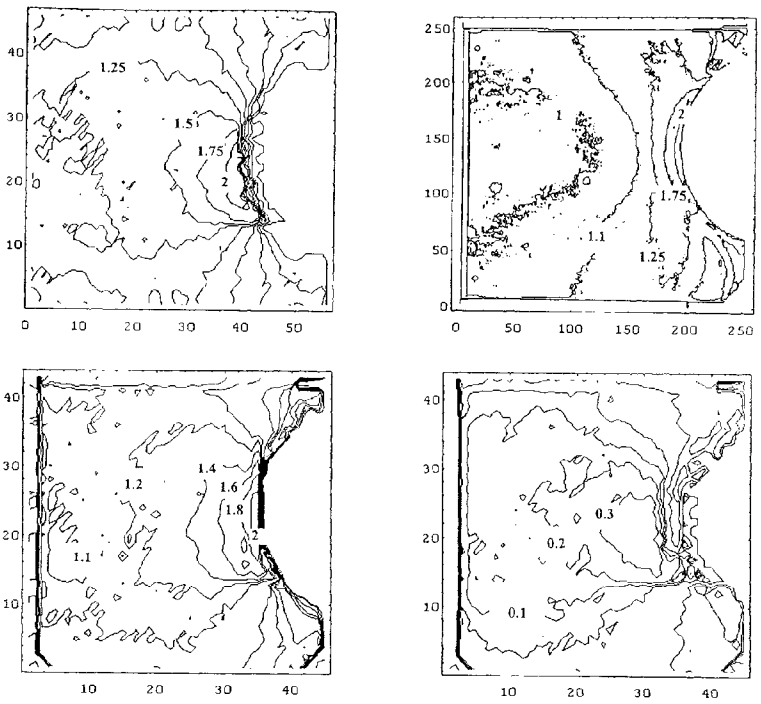

Figure 2. Contour maps of the sum of *(top, left),* the difference in (top, right), the maximum (bottom, left) and the minimum (bottom, right) principal stresses normalised with respect to the nominal stress.

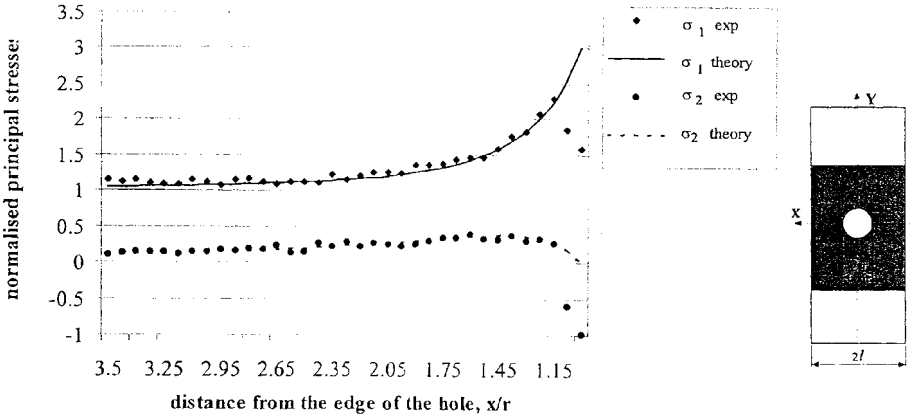

Figure 3. Separated normalised principal stresses along the axis of symmetry normal to the loading on the plate together with the theoretical solutions due to Savin (1961).

EXPERIMENTAL ANALYSIS OF LOCALIZATION MECHANISMS IN MILD STEELS BY INFRARED AND SPECKLE IMAGE PROCESSING

A. CHRYSOCHOOS (*), H. LOUCHE (*), J.-M. MURACCIOLE (*), M. NÉMOZ-GAILLARD (**), J.-L. SAUREL (*), B. WATTRISSE (**)
(*) Equipe Thermomécanique, LMGC UMR 5508 CNRS-UMII, Place E. Bataillon 34095 Montpellier Cédex 05.
(**) Laboratoire de Mécanique et Métrologie, Ecole des Mines d Alès, 6 Avenue de Clavièrs, 30319 Alès Cedex.

Abstract - The linked evolution of heat source distributions and strain rate fields was determined on the surface of steel samples during monotone tensile tests using infrared thermography and speckle techniques. We first showed that one or more narrow and dissipative bands, characterized by high strain rates, propagate along the gauge part of the sample during the plastic plateau that precedes strain hardening. We then describe the early and progressive concentration of strong dissipation zones during the strain hardening phase, which prefigures the localized necking of the sample.

1. Introduction

When a structure is mechanically loaded, its deformation passes more or less suddenly from a diffuse mode characterized by regular strain fields to localized modes defined by zones where the strains develop and concentrate. The research fields related to localization phenomena are very active. Many authors have worked and still work today on the experimental, theoretical and numerical aspects of such deformation mechanisms. In the bibliography references, just a small part of the very large diversity of scientific approaches proposed in the literature is mentioned. In the particular case of the plastic or viscoplastic materials, the studies have tried to take account of the large variety of loading and have naturally focused on the kinematic aspects of the localization. Let us mention for instance the works of Consider-e [1], Hill [2], Mandel, [3], Hart [4], Rice [5], and more recently Benallal [6] and Fressengeas [7]. When the material behaviour is time-independent, the localization phenomenon is to appear as soon as a bifurcated solution to the linearized problem exist. This bifurcation can then be physically translated by a spatial discontinuity of the strain rate field. If the behaviour is time-dependent, a perturbation analysis of the linearized problem is often proposed. In such a case, the localization is related to an instability ; the perturbation

A. Lagarde (ed.),
IUTAM Symposium on Advanced Optical Methods and Applications in Solid Mechanics, 313-320.

amplitude does not diminish but on the contrary increases. Other works as those done by Estrin [8], Neuhauser [9], Zaizer [10], describe the microstructural origins of localization phenomena that sometimes occur under the form of Lüders or PLC bands. Sometimes authors like Ferron [11], Marchand, [12], give an account of the thermal effects accompanying some localization processes. In this paper, the aim is to show that the experimental improvements made in the field of infrared thermography and speckle image processing allow the dissipative and kinematic manifestations related to localization to be observed. The dissipation is deduced from the thermal data via a numerical inversion of the heat equation while the strain rate field is more classically derived from the displacement fields obtained by intercorrelation of speckle image.

After having given a brief reminder of the thermomechanical context, the experimental arrangements and the respective data processing are succinctly introduced. Results then exhibit the prominent dissipative and kinematic features associated with the Lüders band propagation and put forward the early and progressive emergence of the local necking during quasi-static tensile tests on steel samples.

2. Heat evolved during plastic hardening

The thermomechanical framework used here, is the Generalized Standard Materials formalism [13]. The thermodynamic state of a material volume element is defined by a set of variables. In the case of elastoplastic material, the following set of state variables is generally chosen : the absolute temperature $\alpha_0 = T$, a large strain tensor $\alpha_1 = \varepsilon$, and n-1 internal variables $\{\alpha_i\}_{i=2,..,n}$, characterizing the hardening state of the material. The chosen thermodynamic potential is then the Helmholtz free energy ψ. The mass density, the Cauchy stress tensor and the Eulerian strain rate tensor are denoted by ρ, σ, and D, respectively. For finite transformations, the strain rate tensor is no longer the time derivative of the strain tensor.

The relative smallness of the thermal dilatability of steels allows to suggest that the heat source due to the thermoelastic couplings becomes rapidly negligible when compared with the intrinsic dissipation d_1 developed during the elastoplastic transformation

$$\rho T \psi''_{T,\varepsilon} : \dot{\varepsilon} << d_1 = \sigma : D - \rho \psi'_{\alpha_i} . \dot{\alpha}_i \; ; \; i = 1,..,n \tag{1}$$

In addition, we can reasonably admit that the small temperature variations induced by the deformation process have no influence on the hardening state. As a consequence, the heat sources related to the coupling terms between temperature and the hardening variables can also be neglected :

$$\rho T \psi''_{T,\alpha_i} \dot{\alpha}_i \approx 0 \; ; \; i = 2,..,n \tag{2}$$

If C_α denotes the specific heat at $\{\alpha_i\}$ i = 1,.., n constant and if the isotropic conduction coefficient k is supposed to be constant, the heat equation can then be averaged throughout the sample depth and written as [14] :

$$\rho C_\alpha \left(\dot{\theta} + \frac{\theta}{\tau_{th}} \right) - k \, \Delta\theta = d_1 \tag{3}$$

where $\theta = T - T_0$ represents the temperature variation depthwise averaged with respect to the equilibrium temperature T_0. The constant τ_{th} symbolizes the heat losses perpendicularly to the plane of the sample and the heat conduction in the plane is taken into account by the two-dimensional Laplacian operator.

3. Experimental Arrangement and Image Processing

Both experimental set-up use 100 kN tension-compression testing machines. The lens axes of the cameras are kept fixed regarding the frame of the testing machine and perpendicular to the sample surface. Quasi-static monotone tensile tests have been performed on standard. thin and flat samples (2.5mm × 12.5mm × 50 mm). The experiments are displacement-controlled and the room temperature is kept constant (300 K). Several shades of steel, frequently used in metal forming, were chosen,. They are named S355MC, HR55, DD14 and have been given by the steel industry Sollac.

3.1. INFRARED IMAGE PROCESSING

The dissipation is determined by evaluating the left hand member of equation (3) and by using the digitized temperature charts recorded by the infrared camera. The thermal information being discrete and noisy, the differential operator is estimated by law-pass convolutive filtering and discrete Fourier transform. To avoid high spatial frequencies due to the non-periodicty of images and to reduce the boundary effects, strongly amplified here by the Laplacian operator, a C_2 periodic extension of the data is first performed. The thermal noise is well modeled by a white noise characterized by a Gaussian probability distribution and a uniform power spectrum. Note that this last feature implies that the filtering method, whatever it is, is unable to eliminate completely the parasitic frequencies.

A calibration of the method in conditions close to the experimental situation is then inevitable. The validity check of the data processing is realized as follows : starting from a given heat source distribution, the corresponding temperature charts are calculated using spectral methods with realistic boundary conditions. The influence of noise on the data processing is then tested. The heat sources derived from the noisy thermal data are compared to the given initial ones.

More information on the data processing and its performances can be found in [15] and soon in [16]. The data processing check shows that the calculation error on the source determination grows rapidly with the thermal noise level. This unstable nature of the temperature-source passage (inverse problem) comes from the regularizing effects of the diffusion phenomena (direct problem). To limit noise effects, the cut-off frequencies of the numerical filters may be reduced ; in return, one observes as it does a diminution of the sources intensity and a sprawl of zones where the heat sources concentrate.

3.2. SPECKLE IMAGE PROCESSING

The fundamental influence of experimental results on the theoretical views led us to develop, in parallel, another and independent experimental approach using speckle images and correlation techniques to get two-dimensional fields of kinematic variables (displacement, strain rate, …). Pictures are registered via a CCD camera. A better contrast can be achieved, if necessary, by speckling with paint the investigated surface. This later is "virtually" meshed in the reference configuration. Each point of the grid $M(x_0, y_0)$, representing a material particle, is defined at each time t, by the distribution of the light intensity f(x, y, t) in a chosen M's neighbourhood, say V. For two times t_1 and t_2 (*i.e.* two images I_1 and I_2), corresponding to a small strain increment, the displacement components (χ, ξ) are given by maximising the intercorrelation function :

$$P(M,\chi,\xi,t_1,t_2)=\frac{\iint_V f(x,y,t_1)\,f(x-\chi,y-\xi,t_2)\,dx\,dy}{\sqrt{\iint_V f^2(x,y,t_1)\,dx\,dy.\iint_V f^2(x,y,t_2)\,dx\,dy}} \tag{4}$$

Step by step the displacement data can be used to construct the paths of the material points and to upgrade the mesh. To get strain and strain rate evolution, the noisy displacement data have to be filtered before time and space differentiation. The filtering uses a Savitsky-Golay method based on a local least square approximation of the displacement field. The differentiation is then applied to the approximation function to obtain the different Lagrangian or Eulerian strain tensors. To preserve the boundary data and to reduce boundary effects, a C_1 continuity extension is made.

To check the image processing, the algorithms of intercorrelation and of differentiation are tested on several analytic examples and on computer-generated speckle images. The direct intercorrelation calculation shows a one pixel periodic and systematic error. Its amplitude depends on the speckle's properties and it can be efficiently reduced by superimposing a random displacement and a filtering. The differential operators are estimated with these noisy displacement data and compared to the analytic results. More information on the method and its performances are available in [17].

4. Experimental Results

The passage from dissipation to dissipated energy is possible while the displacement fields of the transformation are known as it is the case in the framework of small perturbations (negligible displacement) or homogeneous tension tests (uniform strain fields). In order not to prejudge the homogeneity of the sample response, we would rather present the time evolution of the dissipation distribution. The kinematic observations, using the speckle method, have supported this prudent attitude.

To get a first and simple insight of the thermomechanical behaviour of the three steel shades, profiles of dissipation and of strain rate, captured along the longitudinal sample axis, have been gathered in a one-dimensional space-time chart. To further simplify the figure interpretation, contour plots have been chosen to quickly visualize

level curves. The normalized evolution of the load is also plotted to enable the reader to see a correspondence between the global response of the sample and the local measurements. The maximal amplitude of load is systematically told in the figure legends.

When a plastic plateau exists, a first mode of localization is observed between the bounds *A* and *B*. In such cases, one (*figure 1*) or more (*Figure 2*) dissipative and strain rate « waves » propagate at a constant velocity along the gauge part of the sample. Both energetic and kinematic effects have naturally been associated with Lüders band propagation. The angle between the loading axis and the band front during its movement is around 70°. The waves break when strain hardening starts.

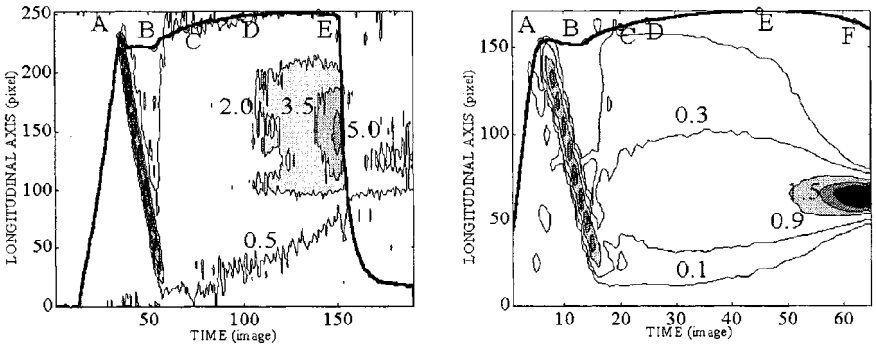

Figure 1 : S355MC steel ; lengthwise profiles of the intrinsic dissipation (left) and of the longitudinal component of the Green-Lagrange strain tensor rate (right). The dissipation unit is W .cm^{-3} ; the strain rate unit is 10^{-2} s^{-1}. The maximum load is about F_{max} = 16.2 kN.

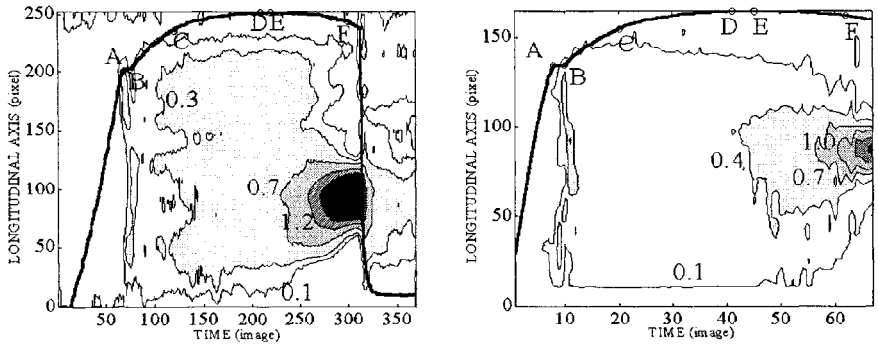

Figure 2 : HR55 steel ; lengthwise profiles of the intrinsic dissipation (left) and of the longitudinal component of the Green-Lagrange strain rate tensor (right). F_{max} = 24.5 kN

At the beginning of the strain hardening (stage *B-D*), the dissipation field remains approximately uniform, then, stronger dissipation zones with high strain rate appear and concentrate progressively until the maximum of load is reached (stage *D-E*). During the strain softening (stage *E-F*), the dissipative and kinematic effects of localization

explode. In the particular case of S355MC steel, the dissipation chart corresponding to each step previously mentioned is drawn in *figure 5*. Remember that infrared and speckle tests are for the moment separately performed. As a consequence, energetic and kinematic results are not obtained with the same sample. The loci where necking takes place may naturally be different from one sample to another.

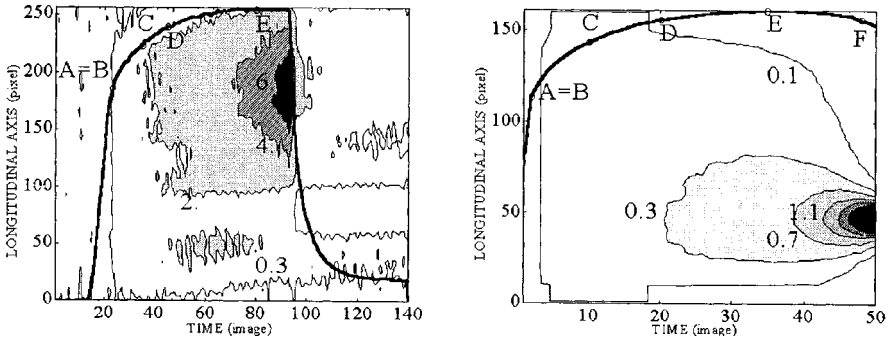

Figure 3 : DD14 steel ; lengthwise profile evolution of the intrinsic dissipation (left) and of the longitudinal component of the Green-Lagrange strain rate tensor (right). F_{max} = 13.5 kN

Note that the DD14 load-elongation curve does not present a plastic plateau (*figure 3*) ; as mentioned above, no band effect has been observed. The kinematic and dissipative phenomena related to band propagation are illustrated in detail in *figure 4* for S355MC steel by plotting several lengthwise profiles between points *A* and *B*.

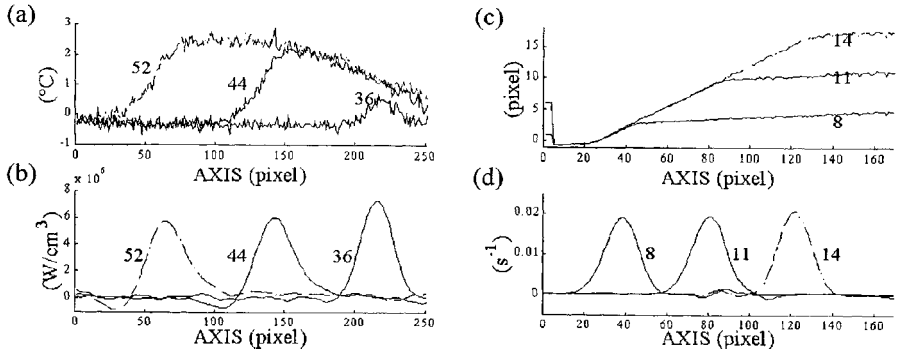

Figure 4 : S355MC Steel ; Thermomechanical manifestations associated with a Lüders band propagation : (a) temperature, (b) intrinsic dissipation, (c) longitudinal displacement, (d) longitudinal component profiles of the Lagrangian strain rate. Profiles n°36, 44 and 52 have been selected for the infrared approach and profiles n° 8, 11 and 14 for the speckle one.

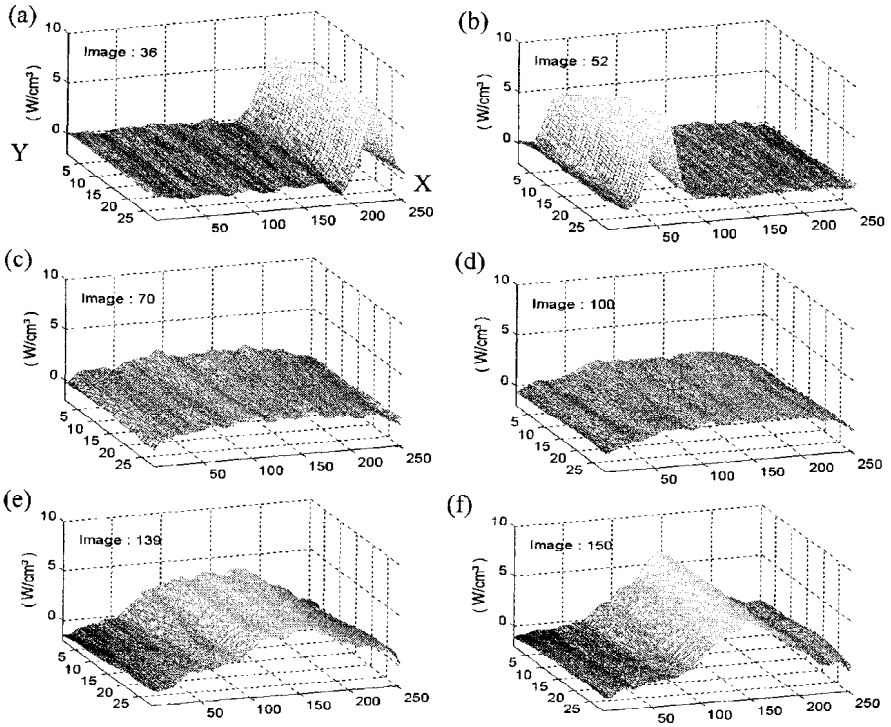

Figure 5 : Dissipation charts in the case of the S355MC steel. The X and Y axes are lengthwise and widthwise taken, respectively. Charts a) and b) evidence the band propagation. Charts c) to f) illustrate the progressive concentration of strong dissipation zones

5. Discussion

This paper aimed to show that thermography and speckle techniques could be combined to good effect. The present performances of both image processing allow the local thermomechanical effects of localization mechanisms to be observe. Sudden and violent manifestations occurring during the plastic plateau have been related to Lüders band propagation, whereas early and progressive features arising during the strain hardening have been interpreted as heraldic signs of the local necking. An important information given by such experimental analyses seems to be the precocity of the heterogeneity development in the macroscopic fields of thermomechanical variables. The gauge part of the sample must be considered as a structure and no longer as an elementary material volume uniformly strained and stressed. This unpalatable fact is currently difficult to reconcile with the theoretical views since classical formalisms are based on the subtle knowledge of the constitutive equations of the material. These equations are in effect identified on the basis of a range of tests, such as the classical tensile test, for which the existence of homogeneous strain and stress fields is very often implicitly assumed. For

the moment, only the pioneering Considère criterion will be briefly evoked here [1] because it concerns the whole specimen. This criterion claims that the necking starts in tension as soon as the maximal load supported by the sample is reached. To make the classical Considère construction the uniaxial « true » stress is defined as the load divided by the instantaneous sample section which is deduced from the initial section assuming isovolumic and homogeneous transformation. This last assertion is obviously not in agreement with the results shown here. The localization develops during the hardening of the structure and sometimes just after the yield load.

Acknowledgements : *The authors are indebted to the Research Center of Sollac-Fos for provinding steel samples.*

6. References

1. Considère, A., (1885) : *L 'emploi du fer et de l'acier dans les constructions,* Ann. Ponts Chaussèes, vol 9, p. 574-595.
2. Hill, R ., (1958) : *A general theory of uniqueness and stability in elastic-plastic solids,* J. Mech. Phys. Solids, 6, pp. 236-249.
3. Mandel, J., (1964) : *Condition de stabilitè et postulat de Drücker,* Rhèologie et Mècanique des sols, Kravtchenko et Syries (Ed.), IUTAM Symposium, Grenoble.
4. Hart, E.W., (1967) : *Theory of tensile test,* Acta metall., vol.15, pp.351-355.
5. Rice, J.R., (1976) : *The localisation ojplastic deformation,* J. of Theoretical and Applied Mechanics, W. T. Koiter (Ed), North Holland, Amsterdam.
6. Benallal., A., (1992) : *On localization phenomena in thermo-elasto-plasticity* ; Arch. Mech., 44, 1, pp.1 5-29, Warsawa.
7. Fressengeas, C., Molinari, A., (1985) : Inertia and thermal effects on the localization of plastic flow, Acata metall., vo1.33,pp.387-396.
8. Estrin,Y., Kubin, L.P., (1988) : *Plastic instabilities : Classijication and Physical Mechanisms,* Res Mechanica, 23, pp. 197-221.
9. Neuhäuer, H., (1993) : *Collective micro-shear processes and plastic instabilities in crystaline and amorphous structures,* Int. J. of Plast., vol 9,pp. 421-435.
10. Zaiser, M., Hähner, P.,(1997) : *Oscillatory modes of plastic deformation : theoretical concepts,* Phys. Stat. Sol. (b), Review Article, vol.199, pp. 267-330.
11. Ferron, G., (1981) : *Influence of heating generation and conduction on plastic stability under uniaxial tension* , Mat. Sci. Engng., 49, pp. 241-248.
12. Marchand, A., Duffy, J., (1988) : *An experimental study of the formation process of adiabatic shear bands in a structural steel,* J. Mech. Phys. Solids, Vol 36, n°3, pp. 251-283.
13. Halphen, B., Nguyen, Q.S.,(1975) : *Sur les matéiaux standard generalisés,* J.de Méc., vol. 14, n°l, pp.39-6.
14. Chrysochoos, A., (1995) *Analyse du comportement des materiaux par thermographie infiarouge,* Actes du Colloque National Photomécanique 95, Eyrolles Ed, pp.203-211.
15. Louche, H., Chrysochoos, A. : (1998) *Analyse thermodynamique de la localisation de la deformation dans des aciers par thermographie infiarouge,* Actes du Colloque National, Photomécanique 98, Eyrolles Ed, pp.207-2 15
16. Chrysochoos, A. and Louche, H., : *Infrared analysis of dissipative effects accompanying strain localization in steels,* in prep. for Int. J. of Eng. Sci.
17. Wattrisse, B., Némoz-Gaillard, M., Muracciole, J.-M., Chrysochoos, A. : (1998) *Etude cinématique des phénomenès de localisation dans un acier par intercorrélation d'images.,* Actes du Colloque National, Photomécanique 98, Eyrolles Ed, pp. 21-28.

HIBRID STRESS ANALYSIS BY CONSTRUCTION OF APPROXIMATE ANALYTICAL SOLUTION

M. TAKASHI, S. MAWATARI
Aoyama Gakuin University
6-16-1 Chitosedai, Setagaya, Tokyo 157-8572, Japan

1. Introduction

Methods for elastic stress/strain analysis are broadly classified into the well known three categories, namely theoretical, experimental and computational analyses. Although some merits and demerits surely exist in all cases, there still exist some difficulties for each method in the categories to accomplish analysis by itself in closed form involving error estimation under general mechanical conditions. The authors have investigated for long time on a new hybrid method which reconstitutes together not only basic concepts but also various techniques involved in the three categories, in order to improve the accuracy and preciseness of 2-D and 3-D elastic stress/strain analysis. The fundamental concepts of the method have been already proposed in the previous paper [1]. In this paper, the authors discuss a method for the determination of unknown coefficients involved in the discretized representative function of analytical solution in Somigliana type.

2. Formal Solution of Displacement

2.1. STRUCTURAL EQUATION OF DISPLACEMENT

It is well known that there are several types of formulation for the structural equation of elastic stress/strain analysis. In this paper, for convenience, the authors adopt the Navier equation in a closed bounded domain $G \in R^n$ ($n =$ 2or 3) having the piecewisely smooth boundary ∂G. The equation about displacement u is expressed as;

$$\Phi u(x) = \mu \Delta u(x) + (\lambda + \mu)\,\mathrm{grad}\ \mathrm{div}\, u(x) = -f(x) \qquad (x \in G) \tag{2.1}$$

where λ and μ are Lamé's constants, $f(x)$ is body force on G.

A. Lagarde (ed.),
IUTAM Symposium on Advanced Optical Methods and Applications in Solid Mechanics, 321-332.

2.2. DISTRIBUTION EXPRESSION OF DISPLACEMENT

Let $\Gamma(x)$ be an elementary solution of Eq. (2.1). One of the distribution solutions of Eq. (2.1) is expressed as;

$$u(x) = -\int_G \Gamma(x-y)\Phi u(y)dy + \int_{\partial G}\left\{\Gamma(x-y)\frac{du(y)}{dn} - \left\{\frac{d\Gamma(x-y)}{dn_y}\right\}^t u(y)\right\}ds \quad (2.1)$$

where, in case of $n = 2$,

$$\Gamma(x) = \frac{1}{8\pi\mu(1-\nu)}\begin{bmatrix} R_\nu + \dfrac{\partial r}{\partial x_1}\cdot\dfrac{\partial r}{\partial x_1} & \dfrac{\partial r}{\partial x_1}\cdot\dfrac{\partial r}{\partial x_2} \\ \dfrac{\partial r}{\partial x_2}\cdot\dfrac{\partial r}{\partial x_1} & R_\nu + \dfrac{\partial r}{\partial x_2}\cdot\dfrac{\partial r}{\partial x_2} \end{bmatrix}$$

$$\text{where} \quad r \equiv \sqrt{x_1^2 + x_2^2}, \quad R_\nu \equiv (3-4\nu)\log\frac{1}{r}$$

and in case of $n = 3$,

$$\Gamma(x) = \frac{1}{16\pi\mu(1-\nu)r}\begin{bmatrix} (3-4\nu)+\left(\dfrac{\partial r}{\partial x_1}\right)^2 & \dfrac{\partial r}{\partial x_1}\cdot\dfrac{\partial r}{\partial x_2} & \dfrac{\partial r}{\partial x_1}\cdot\dfrac{\partial r}{\partial x_3} \\ \dfrac{\partial r}{\partial x_2}\cdot\dfrac{\partial r}{\partial x_1} & (3-4\nu)+\left(\dfrac{\partial r}{\partial x_2}\right)^2 & \dfrac{\partial r}{\partial x_2}\cdot\dfrac{\partial r}{\partial x_3} \\ \dfrac{\partial r}{\partial x_3}\cdot\dfrac{\partial r}{\partial x_1} & \dfrac{\partial r}{\partial x_3}\cdot\dfrac{\partial r}{\partial x_2} & (3-4\nu)+\left(\dfrac{\partial r}{\partial x_3}\right)^2 \end{bmatrix}$$

$$\text{where} \quad r \equiv \sqrt{x_1^2 + x_2^2 + x_3^2}$$

3. Equivalent Transformation of Boundary Condition

Unknown function $u(y)$ on ∂G in Eq. (2.2) has to be determined as to fit with boundary conditions.

3.1. PROBLEMS IN BOUNDARY CONDITIONS

Boundary condition is usually expressed with Dirichret, Nuemann, Robin condition or

their combination. Furthermore, since the original domain deforms under load, Euler or Lagrangian coordinate system has to be selected in order to discriminate the state before and after deformation, in a strict sense. However, since the shape of boundary after deformation and transformation formulae from one state to another is not known in advance, a certain consideration is necessary to handle boundary conditions.

3.2. UTILIZATION OF EXPERIMENTAL DATA

In order to avoid the difficulties mentioned above, the authors have proposed to utilize reliable experimental data in actual situation. Here, we pay attention to some data of firinge order of isochromatics in photoelasticity.

3.3. THEOREM OF RELATIVE FRINGE ORDER

The determination of fringe order of isochromatics is somewhat delicate in general. When we look at two different fringes, however, the difference of orders between them could be found easily, then the concept of relative fringe order comes up.

Let a domain D be a part of an isochromatics image pattern. Retardation δ is connected with principal stress difference as

$$\delta = \frac{2\pi c}{\lambda} d(\sigma_1 - \sigma_2) \tag{3.1}$$

where λ is the wave length of incident light, c: photoelastic constant and d: specimen thickness. The brightness intensity of isochromatics in the dark field, I, is expressed as;

$$I = a^2 \sin^2\left(\frac{\delta}{2}\right) \tag{3.2}$$

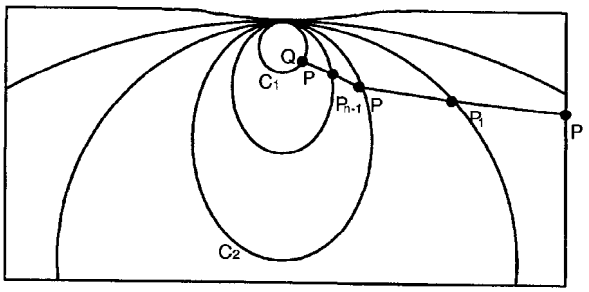

Figure 1. Schematic diagram of explanation for relative fringe order

Here, let us call a point at which $\delta = m\pi$ (m: integer) as a fringe point. In Fig.1, curves C_i except a curve $[P,P_1,...,P_n]$ and boundary lines show isochromatics schematically. On point $P \in D$, we denote the values of I and δ as $I(P)$ and $\delta(p)$, respectively. Taking another fringe point $Q \in D$, let us consider a continuous curve $C \subset D$ which is connecting points P and Q;

$$C : t \to C(t) \in D \quad (0 \le t \le 1), \quad C(0) = P \text{ and } C(1) = Q . \tag{3.3}$$

The point P is called as a regular point, when the following two conditions are satisfied. 1) δ varies from P to Q on curve C monotonically, and 2) between P and Q, there exist at least one fringe point excluding themselves. Then, the point Q and the curve C are named as a fringe point and a curve subordinating to the regular point P.

Let P be the regular point and Q the subordinating point. A point array $\{P_k\}^n{}_{k-1}$ is called as a fringe point resolution of the regular point P, when we can recognize the following facts such as; i) $P_k = C(t_k)$ $(0 = t_0 < t_1 \cdots < t_n = 1)$, $(1 \le k \le n-1)$ is all fringe points, and ii) there is no fringe point in an open interval (t_{k-1}, t_k). In this context, the following relation is obtained;

$$\frac{1}{2}\left|\delta(P) - \delta(Q)\right| = \frac{1}{2}(n-1)\pi + \alpha \tag{3.4}$$

where

$$\alpha = \mathrm{Sin}^{-1}\left[\left\{\left|\frac{I(P) - I(P_1)}{I(P_{n-1}) - I(P_n)}\right|\right\}^{\frac{1}{2}}\right]. \tag{3.5}$$

When P lies on a fringe point, the value of α comes to $\pi/2$. We call here the right hand side in Eq. (3.4) the relative fringe order. Relative fringe order is equivalent to boundary condition within the domain governed by corresponding structural equation, namely an equivalent transformation of boundary condition. Thus, we can treat hereafter the relative fringe order as an alternative of boundary condition.

4. Discretization of Representative Function in Terms of Stress Components

4.1. THE FORM OF REPRESENTATION OF STRESS COMPONENTS

From Eq. (2.2) and the stress-displacement relation, we have;

$$\sigma_{ij}(x) = \int_{\partial G} D_{ij}^{T}(y,x)\zeta(y)ds_y \qquad (x \in G) \tag{4.1}$$

where $\xi(y)$ is an unknown function on ∂G and a vector D_{ij} is expressed as follows;

$$\begin{aligned} D_{ij} &= \left[D_{1ij}, D_{2ij}\right]^T \qquad \text{for } n = 2 \\ D_{ij} &= \left[D_{1ij}, D_{2ij}, D_{3ij}\right]^T \quad \text{for } n = 3 \end{aligned} \tag{4.2}$$

and

$$D_{kij} = \frac{1}{4\alpha\pi(1-\nu)} \cdot \frac{1}{r^{\alpha}}\left[(1-2\nu)\left\{\delta_{ki}r_{,j} + \delta_{kj}r_{,i} - \delta_{ij}r_{,k}\right\} + \beta r_{,i}r_{,j}r_{,k}\right] \tag{4.3}$$

for n=2, k=1, 2; p = 1 ; b =2
for n=3, k=1, 2, 3; p= 2 ; b=3

Also, the function ξ is called a density function. Attention should be paid to the following items. That is, (1) the integration in Eq. (4.1) is defined on every point in the original domain *G,* and (2) the integration in Eq. (4.1) involves the first kind discontinuity at $x_0 \in \partial G$ where $\xi(x_0) \neq 0$, and is continuous on any other points. Namely, we can denote as;

$$\hat{\sigma}_{ij}(x_0) - \breve{\sigma}_{ij}(x_0) = 2\pi\zeta(x_0) \tag{4.4-1}$$

$$\sigma_{ij}(x_0) = \frac{1}{2}\left\{\hat{\sigma}_{ij}(x_0) + \breve{\sigma}_{ij}(x_0)\right\} \quad \text{(finitely determined)} \tag{4.4-2}$$

where $\hat{\sigma}_{ij}(x_0) = \lim_{x \to x_0} \hat{\sigma}_{ij}(x)$ in G, $\breve{\sigma}_{ij}(x_0) = \lim_{x \to x_0} \breve{\sigma}_{ij}(x)$ in $R^n - G$.

4.2. DISCRETIZATION

Utilizing photoelastic data, we can reconstruct the deformed boundary shape of specimen under load. Now, let us confine our discussion into the case of 2-dimension for convenience, hereafter. In a domain, $\partial G = \{(y_1(t), y_2(t)): t \in [0, L]\}$, let us put as;

$$\zeta(x) = \begin{bmatrix} w_1(x) \\ w_2(x) \end{bmatrix}. \tag{4.5}$$

Then, the unknown function ξ(x) is approximated by use of spline function as follows;

$$\tilde{\zeta}(y(t)) = \begin{bmatrix} \sum_{i=1}^{m} w_{1i} N_i(t) \\ \sum_{i=1}^{m} w_{2i} N_i(t) \end{bmatrix}, \quad y(t) \in \partial G, \quad \mathrm{Supp}(N_i(t)) = [t_i, t_{i+4}] \tag{4.6}$$

Here, we have an approximation of Eq. (4.1) as;

$$\begin{aligned} \sigma_{ij}(x) &= \sum_{l=1}^{m} w_{1l} \left\{ \int_{t_l}^{t_{l+4}} D_{1ij}(y(t), x) N_l(t) g_1 dt \right\} \\ &\quad + \sum_{l=1}^{m} w_{2l} \left\{ \int_{t_l}^{t_{l+4}} D_{2ij}(y(t), x) N_l(t) g_1 dt \right\} \\ &= \sum_{l=1}^{2m} \upsilon_l V_{lij}(x) \end{aligned} \tag{4.7}$$

where

$$\begin{cases} \upsilon_l = w_{1l}, \quad V_{lij}(x) = \int_{t_l}^{t_{l+4}} D_{1ij}(y(t), x) N_l(t) g_1 dt \\ \upsilon_{l+m} = w_{2l}, \quad V_{(l+m)ij}(x) = \int_{t_l}^{t_{l+4}} D_{2ij}(y(t), x) N_l(t) g_1 dt \end{cases} \tag{4.8}$$
$$(l = 1, 2, \cdots, m)$$

$$g_1 = g_1(t) = \left\{ \left(\frac{dx_1}{dt} \right)^2 + \left(\frac{dx_2}{dt} \right)^2 \right\}^{\frac{1}{2}} \tag{4.9}$$

5. Formulation of Density Function Determination Problem into mathematical Programming

5.1. SAMPLE POINT EXTRACTION BASED ON EQUIVALENT BOUNDARY CONDITION

To determine unknown coefficient υ_l Eq. (4.7), we select several fringes of which relative fringe order are known, and extract sample points on them appropriately as same as the number of unknown coefficient.

Now, recalling the relation between principal stresses and other stress components, we can obtain the following expression from Eq. (4.7),

$$(\sigma_1 - \sigma_2)^2 = (\sigma_{11} - \sigma_{22})^2 + 4\sigma_{12}$$
$$= \left[\sum_{l=1}^{2m} \upsilon_l \{V_{l11}(x) - V_{l22}(x)\}\right]^2 + 4\left[\sum_{l=1}^{2m} \upsilon_l V_{l12}(x)\right]^2 \quad (5.1)$$
$$= \sum_{k=1}^{2m}\sum_{l=1}^{2m} \upsilon_k \upsilon_l \left[\{V_{k11}(x) - V_{k22}(x)\}\{V_{l11}(x) - V_{l22}(x)\} + 4V_{k12}(x)V_{l12}(x)\right]$$

When putting,

$$(x) = \sum_{k=1}^{2m}\sum_{l=1}^{2m} \upsilon_k \upsilon_l \left[\{V_{k11}(x) - V_{k22}(x)\}\{V_{l11}(x) - V_{l22}(x)\} + 4V_{k12}(x)V_{l12}(x)\right], \quad (5.2)$$

we can evaluate the followings.

$$F(\upsilon, q_j) \equiv F_\upsilon(q_j) - (\upsilon_{2m+1} + z_j)^2 \quad (5.3)$$

$$H(\upsilon) \equiv \sum_{j=1}^{2m} \left\{F_\upsilon(q_j) - (\upsilon_{2m+1} + z_j)^2\right\}^2 . \quad (5.4)$$

5.2. MATHEMATICAL PROGRAMMING FOR DETERMINATION OF DENSITY FUNCTION

The problem of determination of unknown coefficient υ_l as that relative fringe order on sample points calculated by Eq. (5.2) fits to experimental data, is formulated into the following optimization problem as;

$$\begin{aligned} &\min H(\upsilon) \\ &\text{s.t.} \quad \upsilon \in R^{2m+1} \end{aligned} \quad (5.5)$$

6. Solution for Problems of Nonlinear Mathematical Programming

6.1. PROBLEMS IN NONLINEAR MATHEMATICAL PROGRAMMING

Since Eq. (5.5) is a type of nonlinear mathematical programming problems of degree four, local solution could be found by usual techniques such as Newton method or steepest decent method. However, there exist severe difficulties as follows [2].

1) Selection of Initial Value for Global Optimum Solution
Eq. (5.4) has, in general, multiple local optimum solutions. The solution obtained by

starting from an arbitrary initial value is one of those local solutions. To find a global or true optimum solution, a suitable initial value has to be selected adequately. However, it is usually difficult to be attained.

2) Speed of Convergence

In cases that an optimum solution exists at the top/bottom of locally convex/concave surface, a step-by-step solution along the surface converges rapidly. However, since there often exist some ill points in a domain related to nonlinear optimization problem, the behavior of function value in the neighborhood of a local solution is so complicated that the value and the speed of convergence in step-by-step procedure are not known in advance.

6.2. IMPROVEMENT OF PROCEDURE TO SOLUTION

In order to overcome the difficulties and improve the solution, the authors developed a method of "Depth-First Homotopy."

1) Homotopy Method

Taking μ-smooth functions $F_k(\upsilon)$ $(k = 1,2,\cdots,\mu)$, we consider a μ-dimensional vector function $F(\upsilon)$ of which components are given by $F_k(\upsilon)$. Homotopy method is explain as follows. To solve the μ-dimensional nonlinear equation $F(\upsilon) = 0$, settling an arbitrary point υ in the domain, the following equation in a domain $(x,t) \in R^{\mu} \times [0,1]$,

$$\Lambda(v,t) = F(v) + (t-1)F(\bar{v}) = 0 \tag{6.1}$$

is translated into the following equation, by use of the implicit function theorem.

$$\begin{bmatrix} \frac{dv_1}{dt} \\ \frac{dv_2}{dt} \\ \vdots \\ \frac{dv_\mu}{dt} \end{bmatrix} = -J_F(v)^{-1} \begin{bmatrix} F_1(\bar{v}) \\ F_2(\bar{v}) \\ \vdots \\ F_\mu(\bar{v}) \end{bmatrix} \qquad (v = \bar{v} \text{ when } t = 0) \tag{6.2}$$

Taking the Jacobian as follows;

$$J_F(\upsilon) = \begin{bmatrix} \dfrac{\partial F_1}{\partial \upsilon_1} & \dfrac{\partial F_1}{\partial \upsilon_2} & \cdots & \dfrac{\partial F_1}{\partial \upsilon_\mu} \\ \dfrac{\partial F_2}{\partial \upsilon_1} & \cdots & \cdots & \cdots \\ \cdots & \cdots & \cdots & \cdots \\ \dfrac{\partial F_\mu}{\partial \upsilon_1} & \dfrac{\partial F_\mu}{\partial \upsilon_2} & \cdots & \dfrac{\partial F_\mu}{\partial \upsilon_\mu} \end{bmatrix}$$

In the numerical solutions of Eq. (6.2), the solution for $t = 1$ is one of solutions we look for.

2) Depth -First Optimization

For a real value function $\Phi(\upsilon)$ with μ-variables defined in a domain $D \subset R^\mu$, the following algorithm is called as "Depth-First Optimization."

[1] Let us take as E=D.

i) Divide E into m-pieces of subdomain, E_1 , $\cdots$, E_m, with a certain procedure.

ii) From each subdomain, extract a sample point P_1 , $\cdots$, P_m .

iii) On each sample point, find the minimum value of $\Phi(\upsilon)$. Here let us denote the point of minimum $\Phi(\upsilon)$ as P_k and the subdomain as E_k.

[2] Repeat the above procedure, considering the subdomain E_k as a new domain E.

[3] Taking a certain stopping rule into account, [1] and [2] procedures are repeated.

3) Depth-First Homotopy Method

For the variables involved in Eq.(5.4), the variable υ_{2m+1} holds different characteristics from other variables. Taking the fact into account, we construct an algorithm called "Depth -First Homotopy Method." To apply the Homotopy method to experimental data, a point x_0 in Eq.(6.1) is selected arbitrarily and the initial value of α is settled as zero, namely $\alpha = 0$.

[1] For a given initial integer L, let us search the variable V_μ within a finite closed interval of $\left[\alpha - 9\text{x}10^L , \alpha + 9\text{x}10^L\right]$.

[2] Substituting the values $\alpha - 9 \text{ x } 10^L, \alpha - 8 \text{ x } 10^L, \ldots, \alpha + 8 \text{ x } 10^L$, $\alpha + 9 \text{ x } 10^L$ into V_μ , other variables remained are solved by Homotopy method.

[3] When the point at which the error $H(\upsilon)$ in Eq.(5.4) comes to minimum is obtained as $\alpha + k \times 10^L$, we denote the solution by Homotopy method as υ .

[4] Then, after decreasing the value of L by 1 and setting new values of a and υ as to be $\alpha + k \times 10^L$ and υ , repeat the procedures from [l] to [3].

[5] According to a certain stopping rule, the same procedure is repeated within a designated times.

4) Discussion from Viewpoint of Mechanical Engineering

The solution obtained by the method of Depth -First Homotopy proposed in this paper is a local solution approved within a certain accuracy. On the other hand, since the variable V_μ corresponds to the value of principal stress difference in the domain under consideration, it is expected that the value would not oscillate so steeply. Taking these into account, the solution obtained by the method proposed could be expected to be very close to the true optimum solution.

7. Example Application

Now, let us apply the method and algorithm to a photoelastic data in contact problem. The experimental conditions and the results obtained are shown as follows.

1) Experimental conditions

Fig.2 shows a schematic diagram of a rectangular plate specimen loaded by a concentrated contact force of 50 kN at the top surface. The bottom of the specimen is rested on a rigid bed. Dot marks on the boundary curve show the selected knots for the construction of basic spline function $N_i(t)$ in Eq.(4.6). Two isochromatics are selected for sample points of relative fringe order.

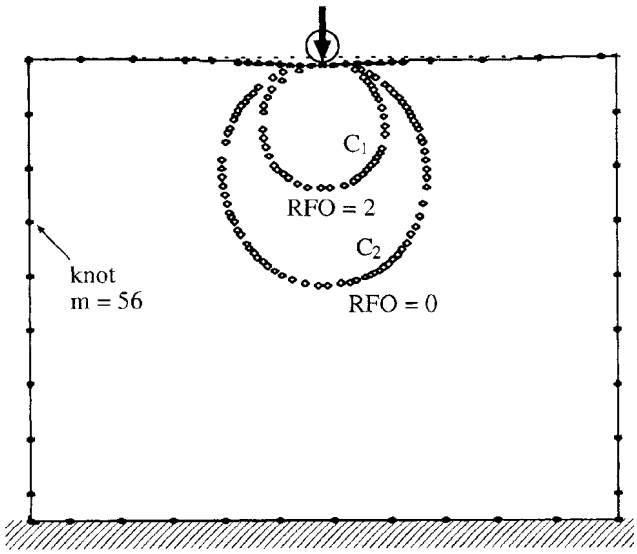

Figure 2. Schematic diagram of specimen and sample data selected.

2) Results obtained

Fig.3 shows the whole field distribution of photoelastic fringe obtained by the method proposed. Particularly around the contact point, fringes are successfully reconstructed. Not only aorund the contact region but on the free boundary and the bottom region, we can see fairly good reconstruction of fringe distribution in comparison with the original experimental data.

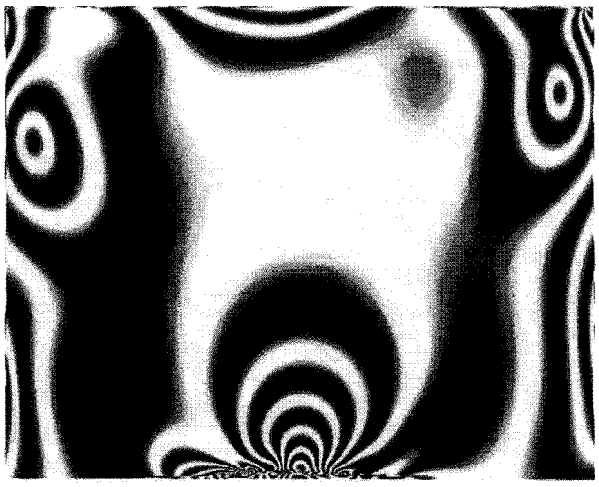

Figure 3. The whole field fringe pattern reconstructed by the method proposed.

8. Concluding Remarks

In this paper, the authors discussed on the determination of unknown coefficients involved in a representative function taking an example of the formulation of Navier equation. The method mentioned here is available if the distribution (hyperfunction) solution of displacement in linear elasticity is obtainable. Even in cases that it is difficult to obtain some formal solution, if a certain basic function that has similar characteristics with structural equations under consideration such as multi-harmonic nature, the procedures proposed will be applicable except the techniques in Chapter 2 and 4. Furthermore, the method mentioned is a part in the series of Hybrid Method for Stress Analysis that can include error estimation. From the viewpoint of the global system of the hybrid method, it is important to develop and complete the techniques and to increase examples of application.

References

1. Takashi, M., Mawatari, S. and Omori, Y.: An Approach to Hybrid Method for Elastic Analysis Using Photoelastic Image Data, *Post Conference Proceedings of VIII International Congress on Experimental Mechanics,* Nashville, (1996) l-7.
2. Host, R., Pardalos, P. M. and Thoai, N. V.: *Introduction to Global Optimization,* Kluwer Academic Press, Netherlands, 1995.

HYBRIDIZING OPTICAL METHODS WITH ANALYTICAL AND COMPUTATIONAL TECHNIQUES FOR STRESS ANALYSIS

R. E. ROWLANDS
Mechanical Engineering
University of Wisconsin
Madison, WI 53706 USA

1. Abstract

Contemporary needs involve effective, accurate and expedient nondestructive methods of stress analysis. Individual experimental, numerical or theoretical techniques are often less than ideal. Shortcomings of specific approaches include difficulties in obtaining stresses theoretically in finite shapes or for other than isotropic material, reliable numerical results when loading or geometry are not adequately known, and dependable measured data at geometric discontinuities where most serious stresses frequently occur. The typical need for many small elements when evaluating stress concentrations by conventional FEM increases computer storage demands and run times. This paper demonstrates synergizing experimental and numerical methods with theoretical concepts to stress analyze components fabricated from isotropic or orthotropic composite materials. Although thermoelastic data are emphasized, applications to moire, isochromatics, isopachics, holography and finite elements are discussed.

2. Analytical Background

The classical analytical method of stress analyzing a component such as that in the lower portion of Figure 1 typically involves satisfying equilibrium and compatibility, subject to the boundary conditions. In terms of the Airy Stress Function F, for orthotropy one obtains the following compatibility equation [1]:

$$a_{22}\frac{\partial^4 F}{\partial x^4} - 2a_{26}\frac{\partial^4 F}{\partial x^3 \partial y} + (2a_{12} + a_{66})\frac{\partial^4 F}{\partial x^2 \partial y^2} - 2a_{16}\frac{\partial^4 F}{\partial x \partial y^3} + a_{11}\frac{\partial^4 F}{\partial y^4} = 0, \qquad (1)$$

where a_{ij} are compliances. The plane problem of classical elastic theory is now reduced to determining F throughout the component such that Equation (1) and the boundary conditions are satisfied. Considering F must be a real function of variables x and y, it can be expressed as follows:

A. Lagarde (ed.),
IUTAM Symposium on Advanced Optical Methods and Applications in Solid Mechanics, 333-340.

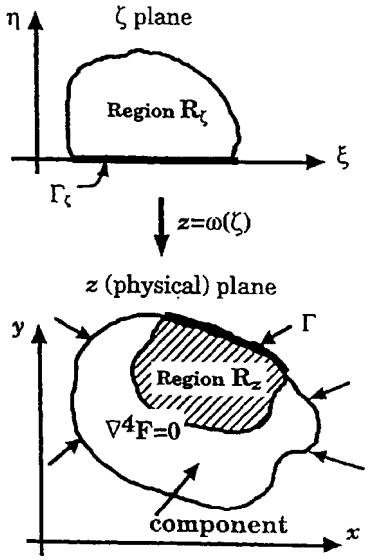

Figure 1. Loaded component.

• In the case of different complex roots μ_1 and μ_2 :

$$F = 2\,\mathrm{Re}\left[F_1(z_1) + F_2(z_2)\right] \tag{2}$$

• In the case of pairwise equal complex roots μ_1 and μ_2:

$$F = 2\,\mathrm{Re}\left[F_1(z_1) + \bar{z}_1 F_1(z1)\right], \tag{3}$$

where $z_j = x + \mu_j y$, μ_j are complex material properties whose values are obtained from the characteristic equation associated with Equation (l), and $j = 1,2$. For isotropy, $z_1 = z = x + iy$, $z_1 = z$. One can sometimes construct a representative stress function for a specific problem. On the other hand, many plane problems of elasticity can be solved by representing the stress function in terms of a truncated series, satisfying boundary conditions along only the edge adjacent to the region of interest, and combining the resulting equations with measured data.

For isotropy, $E_{11} = E_{22} = E$, $\nu_{12} = \nu_{21} = \nu$, $G = E/2(1+\nu)$, $a_{11} = a_{22} = 1/E$, $a_{12} = -\nu/E$, $a_{66} = 1/G$, $a_{16} = a_{26} = 0$, $\mu_1 = \mu_2 = i$ and the individual stresses can be written in terms of two analytical functions, i.e. [1, 2],

$$\begin{aligned}
\sigma_x &= \mathrm{Re}\left\{2\phi'(z) - \left[\bar{z}\phi''(z) + \psi'(z)\right]\right\} \\
\sigma_y &= \mathrm{Re}\left\{2\phi'(z) + \left[\bar{z}\phi''(z) + \psi'(z)\right]\right\} \\
\tau_{xy} &= \mathrm{Im}\left[\bar{z}\phi''(z) + \psi'(z)\right]
\end{aligned} \tag{4}$$

where the stress function of Equation (1) is

$$F = \mathrm{Re}\left[\int^z \psi(z)dz + \bar{z}\phi(z)\right], \tag{5}$$

$\psi(z) = \chi'(z)$ and primes denote differentiation. The compatibility relationship of Equation (1) becomes

$$\nabla^4 F = \nabla^2(\sigma_x + \sigma_y) = \nabla^2(S) = 0. \tag{6}$$

Stresses of Equation (4) satisfy equilibrium and associated strains satisfy compatibility. One can therefore solve plane problems analytically by ensuring that the stresses associated with the stress functions ϕ and ψ satisfy the boundary conditions. However, analytic solutions are generally only possible for problems having simple geometries. As an aid in analyzing plane problems having complicated shapes, conformal mapping techniques can be used to transform the complicated geometry of the physical plane into a simpler shape in a different plane, Figure 1. Moreover, at least for a region adjacent to a traction-free boundary, the individual stress functions ϕ and ψ can be related to each other through the concept of analytic continuation.

Assume the function

$$z = \omega(\zeta) \tag{7}$$

maps the region R_ζ of the $\zeta(= \xi + i\eta)$ -plane into region R_z of the physical z-plane, Figure 1. Stress functions $\phi(z) = \phi[\omega(\zeta)] \equiv \phi(\zeta)$ and $\psi(z) = \psi[\omega(\zeta)] \equiv \psi(\zeta)$ of Equations (4) and (5) are analytic functions of ζ. Analyticity of the mapping function $\omega(\zeta)$ guarantees that equilibrium and compatibility equations are satisfied inside region R_z. For isotropy, combining Equations (4) through (7) gives

$$\begin{aligned}
\sigma_x &= \mathrm{Re}\left\{2\frac{\phi'(\zeta)}{\omega'(\zeta)} - \left[\overline{\omega(\zeta)}\left(\frac{\phi''(\zeta)}{\omega'(\zeta)^2} - \frac{\omega''(\zeta)}{\omega'(\zeta)^3}\phi'(\zeta)\right) + \frac{\psi'(\zeta)}{\omega'(\zeta)}\right]\right\} \\
\sigma_y &= \mathrm{Re}\left\{2\frac{\phi'(\zeta)}{\omega'(\zeta)} + \left[\overline{\omega(\zeta)}\left(\frac{\phi''(\zeta)}{\omega'(\zeta)^2} - \frac{\omega''(\zeta)}{\omega'(\zeta)^3}\phi'(\zeta)\right) + \frac{\psi'(\zeta)}{\omega'(\zeta)}\right]\right\} \\
\tau_{xy} &= \mathrm{Im}\left\{\overline{\omega(\zeta)}\left[\frac{\phi''(\zeta)}{\omega'(\zeta)^2} - \frac{\omega''(\zeta)}{\omega'(\zeta)^3}\phi'(\zeta)\right] + \frac{\psi'(\zeta)}{\omega'(\zeta)}\right\}.
\end{aligned} \tag{8}$$

For orthotropy, expressions for the stresses corresponding to Equations (8) can be written as

$$\begin{aligned}
\sigma_x &= 2\,\mathrm{Re}\left\{\mu_1^2\frac{\Phi'(\zeta_1)}{\omega_1'(\zeta_1)} + \mu_2^2\frac{\Psi'(\zeta_2)}{\omega_2'(\zeta_2)}\right\} \\
\sigma_y &= 2\,\mathrm{Re}\left\{\frac{\Phi'(\zeta_1)}{\omega_1'(\zeta_1)} + \frac{\Psi'(\zeta_2)}{\omega_2'(\zeta_2)}\right\}
\end{aligned} \tag{9}$$

$$\tau_{xy} = -2\,\mathrm{Re}\left\{\mu_1 \frac{\Phi'(\zeta_1)}{\omega_1'(\zeta_1)} + \mu_2 \frac{\Psi'(\zeta_2)}{\omega_2'(\zeta_2)}\right\}.$$

where

$$\Phi(z_1) = \frac{dF_1(z_1)}{dz_1} = \Phi[\omega_1(\zeta_1)] \equiv \Phi(\zeta_1) \text{ and } \Psi(z_2) = \frac{dF_2(z_2)}{dz_2} = \Psi[\omega_2(\zeta_2)] \equiv \Psi(\zeta_2). \quad (10)$$

The functions $\Phi(z_1)$ and $\psi(z_2)$ are analytic in the complex z_1- and z_2-planes, respectively, where $z_1 = x + \mu_1 y$ and $z_2 = x + \mu_2 y$. Substituting $z_j = x + \mu_j y$ into Equation (7) yields the following induced mapping function in terms of $\zeta_j (= \xi + \mu_j \eta)$:

$$z_j = \omega_j(\zeta_j), \quad j = 1,2. \quad (11)$$

Stress functions Φ and Ψ are now analytic functions of ζ_1 and ζ_2, respectively.

The classical stress analysis boundary-value problem entails satisfying equilibrium and compatibility throughout the entire engineering component (say bottom portion of Figure 1), subject to the boundary conditions. However, one can collect measured information in only the region of interest, say R_z of Figure 1, and then using relevant analytical and/or numerical tools, plus boundary information on the adjacent edge, Γ, evaluate the individual stresses throughout R_z. The region R_z might well involve a stress concentration. In some cases, because the measured data are unreliable on the edge Γ, experimental information is collected only away from the edge, although the final individual stresses are evaluated throughout the entire region R_z, including along the edge, Γ, of R_z. It may then only be necessary to map the edge Γ and its adjacent region R_z into the ζ plane, Figure 1.

For a region R_z adjacent to a circular fillet or notch of radius R, the conformal transformation

$$z = \omega(\zeta) = i\,\mathrm{Re}^{-i\zeta} + z_c \quad (12)$$

maps the region R_z of the ζ-plane into the physical region R_z of the z-plane, Figures 1 and 2, where z_c is the center of the discontinuity [1, 2]. The circular boundary Γ in the physical z-plane is conformally mapped onto Γ_ζ, a section of the real axis ($\eta = 0$ surface) of the ζ-plane. For orthotropy, one has the following induced mapping functions:

$$z_j = \omega_j(\zeta_j) = \frac{iR}{2}\left[(1 - i\mu_j)e^{-i\zeta_j} - (1 + i\mu_j)e^{i\zeta_j}\right], \quad j = 1,2. \quad (13)$$

The relationship between the two relevant stress functions of Equations (9) is

$$\Psi(\zeta_2) = B\overline{\Phi(\bar{\zeta}_2)} + C\Phi(\zeta_2), \quad (14)$$

where

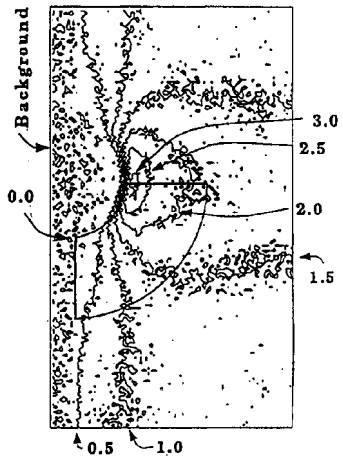

Figure 2. Thermoelastically measured S* in vertically-loaded symmetrically notched (radius R) composite strip.

$$B = \frac{\bar{\mu}_2 - \bar{\mu}_1}{\mu_2 - \bar{\mu}_2} \text{ and } C = \frac{\bar{\mu}_2 - \mu_1}{\mu_2 - \bar{\mu}_2}. \tag{15}$$

Traction-free conditions on the boundary of the physical z-plane are enforced by these relations which reduce the two stress functions into a single stress function, i.e., Φ for anisotropy. This is accomplished by introducing the conformal mapping function $\omega(\zeta)$ which maps the traction-free physical boundary onto say the real axis ($\eta = 0$ surface) of the ζ-plane.

The representation of the stress function Φ in the ζ_1 -plane can be approximated by a truncated power series,

$$\Phi(\zeta_1) = \sum_{j=0}^{N} \left\{ A_j (\zeta_1 - \zeta_0)^j \right\}. \tag{16}$$

Location ζ_0 is some point on the boundary Γ_ζ ($\eta = 0$ surface). From Equations (9), (14), (15) and (16), for orthotropy,

$$\begin{aligned}
\sigma_x &= 2 \sum_{j=1}^{N} \mathrm{Re} \left\{ \left[\frac{j\mu_1^2}{\omega_1'(\zeta_1)} (\zeta_1 - \zeta_0)^{j-1} + \frac{j\mu_2^2 C}{\omega_2'(\zeta_2)} (\zeta_2 - \zeta_0)^{j-1} \right] A_j \right. \\
&\quad \left. + \left[\frac{j\mu_2^2 B}{\omega_2'(\zeta_2)} (\zeta_2 - \zeta_0)^{j-1} \right] \bar{A}_j \right\} \\
\sigma_y &= 2 \sum_{j=1}^{N} \mathrm{Re} \left\{ \left[\frac{j}{\omega_1'(\zeta_1)} (\zeta_1 - \zeta_0)^{j-1} + \frac{jC}{\omega_2'(\zeta_2)} (\zeta_2 - \zeta_0)^{j-1} \right] A_j \right. \\
&\quad \left. + \left[\frac{jB}{\omega_2'(\zeta_2)} (\zeta_2 - \zeta_0)^{j-1} \right] \bar{A}_j \right\}
\end{aligned} \tag{17}$$

$$\tau_{xy} = -2\sum_{j=1}^{N} \mathrm{Re}\left\{\left[\frac{j\mu_1}{\omega_1'(\zeta_1)}(\zeta_1-\zeta_0)^{j-1} + \frac{j\mu_2 C}{\omega_2'(\zeta_2)}(\zeta_2-\zeta_0)^{j-1}\right]A_j + \left[\frac{j\mu_2 B}{\omega_2'(\zeta_2)}(\zeta_2-\zeta_0)^{j-1}\right]\bar{A}_j\right\}. \tag{17}$$

By using conformal mapping and continuation techniques, Equations (17) imply that the stresses satisfy traction-free conditions in the adjacent portion of the entire boundary. However, unlike a classical boundary-value problem where one would typically evaluate the unknown coefficients, A_j, by satisfying the boundary conditions around the entire shape, one can use some combination of the measured stresses of Equations (17) from the interior of the region R_z of interest to determine these unknown coefficients. Additional known boundary conditions can also be imposed at discrete locations.

An example of employing some combination of the stresses of Equations (17) is to choose the x-axis of an orthotropic composite material parallel to its strong, stiff direction (i.e., l-direction) such that thermoelastic data S^* can then be expressed as

$$\begin{aligned} S^* &= K_1\sigma_x + K_2\sigma_y \\ &= 2\sum \mathrm{Re}\left\{\left[\frac{j(K_1\mu_1^2+K_2)}{\omega_1'(\zeta_1)}(\zeta_1-\zeta_0)^{j-1} + \frac{j(K_1\mu_2^2+K_2)C}{\omega_2'(\zeta_2)}(\zeta_2-\zeta_0)^{j-1}\right]A_j \right. \\ &\quad \left. + \left[\frac{j(K_1\mu_2^2+K_2)B}{\omega_2'(\zeta_2)}(\zeta_2-\zeta_0)^{j-1}\right]\bar{A}_j\right\} \end{aligned} \tag{18}$$

The A_j coefficients can now be evaluated from thermoelastically measured input values of S^* and Equations (18). Thermal mechanical coefficients K_1 and K_2 of Equation (18) are normally determined experimentally.

3. Results

Figure 2 shows thermoelastic data throughout an edge section of a vertically-loaded strain-gaged composite ($E_{11}/E_{22} = 2.4$) strip containing symmetrical side notches of radius $R = 6.35$ mm. These measured values of S^* were used with Equation (18) to evaluate the A_j coefficients and hence the stress functions of Equations (14) and (16), from which individual stresses along and adjacent to the notch boundary were obtained from Equations (17). The resulting strain between the side notches is compared in Figure 3 with those from strain gages and FEM. In this case 141 measured interior values of S^* were used between 1.2 R and 2.5 R, together with $\sigma_x, = \tau_{xy} = 0$ imposed at 13 locations along the traction-free vertical straight edge below the notch and $\tau_{xy} = 0$ at 20 positions along the vertical and horizontal lines of symmetry to evaluate the 26 unknown coefficients of Equation (16).

Displayed results use measured thermoelastic data. We have also found this general hybrid approach to be advantageous for determining stresses from holographically

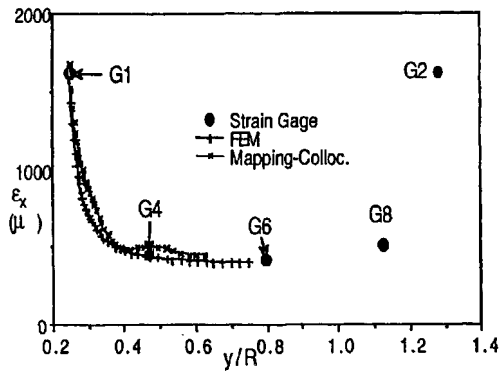

Figure 3. Longitudinal strains between the side notches in the tensile composite strip of Fig. 2 as obtained from strain gages (G), FEM and thermoelasticity.

measured isopachics, pure isochromatics (without the need of isopachics or isoclinics) and moiré [1-9]. Moreover, synergizing such analytical and numerical concept tools enables one to determine accurate stresses at reentry corners using essentially classical FEM but with only a few, very coarse elements [10]. Applications include stress analysis of isotropic and orthotropic structural and machine elements, wood engineering and fracture mechanics. Reference 11 describes a new, nondestructive hybrid experimental-theoretical-numerical method for stress analyzing 3-D components from thermoelastic plus photoelastic surface information.

4. Sumary, Conclusions and Discussion

Whereas individual experimental, theoretical or numerical methods of stress analysis are often lacking, synergizing aspects of the specific approaches can be very advantageous. Space permits emphasizing here only the benefits of combining theoretical and numerical concepts with measured thermoelastic data, but the references contain applications to moiré, isochromatics, holography and finite elements.

5. Acknowledgement

Ford Motor Co., USDA and NSF funded aspects of the research reported here. I also wish to thank Lynda Litzkow of the ME Department, Univ. of Wisconsin, for preparing this manuscript.

6. References

1. Lin, S. T. and Rowlands, R. E. (1995), Thermoelastic Stress Analysis of Orthotropic Composites, *Experimental Mechanics,* 35(3), 257-265.
2. Huang, Y. M., Rowlands, R. E. and Lesniak, J. R. (1990), Simultaneous Stress Separation, Smoothing of Measured Thermoelastic Information, and Enhanced Boundary Data, *Experimental Mechanics,* 30(4), 398-403.
3. Lin, S. T., Miles, J. P. and Rowlands, R. E. (1997), Image Enhancement and Stress Separation of Thermoelastically Measured Data under Random Loading, *Experimental Mechanics,* 37(3),225-231.
4. Rauch, B. J. and Rowlands, R. E. (1997), Filtering Thermoelastically Measured Isopachic Data, *Experimental Mechanics,* 37(4),387-392.
5. Matthys, D. R., Wolfe, R.W., Lin, C. H. and Rowlands, R. E., Thermoelastic Analysis of Metal-Plate Connected Wood Trusses, in preparation.
6. Lin, C. H. (1994), A New Digital Isopachic Contouring Technique for Stress Analyzing Composite Materials, Ph.D. thesis, Univ. of Wisconsin.
7. Hawong, J. S., Lin, C. H. Lin, S. T., Rhee, 3. and Rowlands, R. E. (1995), A Hybrid Method to Determine Individual Stresses in Orthotropic Composites using only Measured Isopachic Data, *Jour. Composite Materials,* 29(18), 2366-2387.
8. Lin, S. T. and Rowlands, R. E., Hybrid Stress Analysis, to appear in *Optics and Laser Engineering.*
9. Rhee, J. and Rowlands, R. E. (1996), Hybrid Moire-Numerical Stress Analysis around Cutouts in Loaded Composites, *Experimental Mechanics,* 36(4) 379-387.
10. Lin, S. T., Lin, C. H. and Rowlands, R. E., Reliable Edge Stresses at Geometric Discontinuities using Large Conventional Finite Elements, accepted for publication in *Jour. Finite Elements in Analysis and Design.*
11. Gao, X. L. (1998), On 2-and 3-D Stress Analyses of Loaded Solids, Ph.D. thesis, Univ. of Wisconsin.

HYBRID STRESS ANALYSIS WITH INTEGRATED PHOTOELASTICITY

H.ABEN AND L.AINOLA

Institute of Cybernetics,
Tallinn Technical University, 21 Akadeemia tee,
EE0026 Tallinn, Estonia

Abstract. In the case of weak birefringence integrated photoelasticity allows for the determination of the distribution of the normal stress in any section of a 3-D specimen. In the case of axial symmetry distribution of the shear stress can also be determined. The question arises how to determine the other stress components. This problem of hybrid mechanics is especially complicated by investigating residual stresses in glass since residual stresses are caused by incompatibility of residual deformations. Due to that, direct application of the compatibility equations is not possible. In this paper formulas are derived for the complete determination of residual stresses in glass in the axisymmetric case and in the case of plane deformation. Examples of complete residual stress analysis are given.

1. The Case of Weak Birefringence

In integrated photoelasticity [1] the specimen is placed in an immersion bath and a beam of polarised light is passed through the specimen (Fig.1). Transformation of the polarisation of light in the specimen is measured on many rays. In certain cases this integrated optical information enables one to determine distribution of some components of the stress tensor.

In the general case, due to the rotation of the principal stress directions on the light rays, optical phenomena are complicated and so are the algorithms for the interpretation of the measurement data. Howewer, if birefringence is weak, photoelastic measurements with a 3-D specimen can be carried out similarly to the 2-D case [2, 3]. That is, on every ray it is possible to measure the parameter of the isoclinic φ and optical retardation Δ. The latter are related to the components of the stress tensor on the ray by simple integral relationships

A. Lagarde (ed.),
IUTAM Symposium on Advanced Optical Methods and Applications in Solid Mechanics, 341–348.

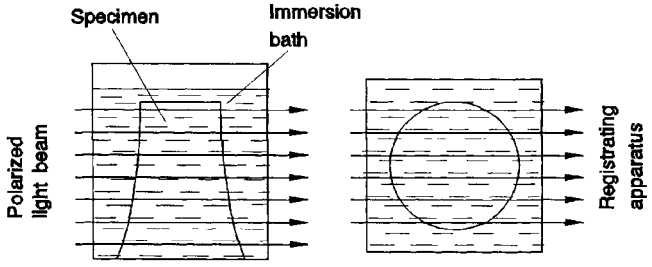

Figure 1. Experimental setup in integrated photoelasticity,

$$\Delta \cos 2\varphi = C \int (\sigma_z - \sigma_x) dy = V_1, \tag{1.1}$$

$$\Delta \sin 2\varphi = 2C \int \tau_{zx} dy = V_2. \tag{1.2}$$

Here C is the photoelastic constant and σ_x, σ_z and τ_{zx} are components of the stress tensor in the plane zx which is perpendicular to the wave normal y.

Using numerical experiments it has been shown [2] that in the case of axial symmetry relationships (1.1) and (1.2) are valid if Δ is less than $3\lambda/4$ (λ denotes wavelength), and rotation of the principal directions is not strong. In the general case Eqs. (1.1) and (1.2) can be used if $\Delta < \lambda/3$.

2. Axisymmetric Stress Distribution

2.1. STRESSES DUE TO EXTERNAL LOADS

In the case of axisymmetric stress distribution, Eqs. (1.1) and (1.2) permit determination of the distributions of the axial stress σ_z and shear stress τ_{rz}. The other stress components, σ_r and α_θ, can be determined using the equilibrium equation

$$\frac{\partial \sigma_r}{\partial r} + \frac{\sigma_r - \sigma_\theta}{r} + \frac{\partial \tau_{rz}}{\partial z} = 0, \tag{2.1}$$

and the compatibility equation

$$\frac{\partial \epsilon_\theta}{\partial r} - \frac{\epsilon_r - \epsilon_\theta}{r} = 0, \tag{2.2}$$

where ε_r and ε_θ are components of the deformation tensor in cylindrical coordinates. Introducing into Eq. (2.2) the Hooke's law

$$\epsilon_r = \frac{1}{E}[\sigma_r - \mu(\sigma_\theta + \sigma_z)] + \alpha T, \tag{2.3}$$

$$\epsilon_\theta = \frac{1}{E}[\sigma_\theta - \mu(\sigma_z + \sigma_r)] + \alpha T, \tag{2.4}$$

$$\epsilon_z = \frac{1}{E}[\sigma_z - \mu(\sigma_r + \sigma_\theta)] + \alpha T, \tag{2.5}$$

we obtain, taking T =const:

$$\frac{\partial}{\partial r}[\sigma_\theta - \mu(\sigma_r + \sigma_z)] - (1+\mu)\frac{\sigma_r - \sigma_\theta}{r} = 0. \tag{2.6}$$

Here E is the elasticity modulus, μ is the Poisson coefficient, α is the thermal expansion coefficient and T is temperature. The algorithm for determining σ_r and σ_θ from Eqs. (2.1) and (2.6) has ben elaborated by Doyle and Danyluk [4, 5].

2.2. THE CASE OF RESIDUAL STRESSES

In the case of residual stresses in glass, in Eqs. (2.3) to (2.5) the term αT must be included. Since residual stresses in glass have thermal origin, they can be considered as being caused by a fictitious temperature field [6, 7]. Unfortunately, this temperature field is not known. Therefore, the compatibility equation cannot be used when investigating residual stresses in glass and one has to look for other analytical relationships between the stress components.

Thermal stresses in an axisymmetric body can be expressed as [8].

$$\sigma_r = 2G\left(\frac{\partial^2 F}{\partial r^2} - \Delta F\right) + \frac{2G}{1-2\mu}\frac{\partial}{\partial z}\left(\mu\Delta L - \frac{\partial^2 L}{\partial r^2}\right), \tag{2.7}$$

$$\sigma_\theta = 2G\left(\frac{1}{r}\frac{\partial F}{\partial r} - \Delta F\right) + \frac{2G}{1-2\mu}\frac{\partial}{\partial z}\left(\mu\Delta L - \frac{1}{r}\frac{\partial L}{\partial r}\right), \tag{2.8}$$

$$\sigma_z = 2G\left(\frac{\partial^2 F}{\partial z^2} - \Delta F\right) + \frac{2G}{1-2\mu}\frac{\partial}{\partial z}\left[(2-\mu)\Delta L - \frac{\partial^2 L}{\partial z^2}\right], \tag{2.9}$$

$$\tau_{rz} = 2G\frac{\partial^2 F}{\partial r \partial z} + \frac{2G}{1-2\mu}\frac{\partial}{\partial r}\left[(1-\mu)\Delta L - \frac{\partial^2 L}{\partial z^2}\right], \tag{2.10}$$

where F is stress function and L Love's displacement function,

$$\Delta F = \frac{1+\mu}{1-\mu}\alpha T, \quad \Delta\Delta L = 0, \quad G = \frac{E}{2(1+\mu)}, \quad \Delta = \frac{\partial^2}{\partial r^2} + \frac{1}{r}\frac{\partial}{\partial r} + \frac{\partial^2}{\partial z^2}. \tag{2.11}$$

Let us assume that a long cylinder or tube is manufactured by solidifying it in an axisymmetric temperature field without gradient in the axial direction. In this case the thermal (and residual) stresses are the same in all cross sections of the cylinder, except the parts near the ends of the latter. Now from Eqs. (2.7) to (2.9) follows the classical sum rule

$$\sigma_r + \sigma_\theta = \sigma_z. \tag{2.12}$$

The classical sum rule (2.12) was in a somewhat different way first derived by O'Rourke [9].

Using the equilibrium equation (2.1) and the classical sum rule (2.12), all the residual stress components can be determined. This method has been widely used for residual stress measurement in glass cylinders, and in axisymmetric fibers and fiber preforms [10, 11].

In the general case, in axisymmetric glass articles stress gradient in axial direction cannot be ignored. Let us try to derive from Eqs. (2.7) to (2.10) a relationship between stress components for that case.

If stress gradient in axial direction is present but smooth, we may write

$$\frac{\partial^2 F}{\partial z^2} = \frac{\partial^2 L}{\partial z^2} = 0. \tag{2.13}$$

Now from Eqs. (2.7) to (2.10) follows

$$\sigma_r + \sigma_\theta = \sigma_z + \frac{2G}{1-2\mu}\frac{\partial}{\partial z}[3(\mu-1)\Delta L]. \tag{2.14}$$

Differentiating (2.10) relative to z and integrating along r reveals

$$\int_0^r \frac{\partial \tau_{rz}}{\partial z} dr = \frac{2G}{1-2\mu}\frac{\partial}{\partial z}[(1-\mu)\Delta L] + C(z), \tag{2.15}$$

where $C(z)$ is the integration constant.

From (2.14) and (2.15) follows

$$\sigma_r + \sigma_\theta = \sigma_z - 3\int_0^r \frac{\partial \tau_{rz}}{\partial z} dr + C(z). \tag{2.16}$$

The last relationship is named the generalized sum rule. It is valid when stress gradient in the axial direction is present, with certain restrictions (2.13) upon the functions F and L, Actually, Eq. (2.16) is first approximation of the generalized sum rule. By handling Eqs. (2.7) to (2.10) asymptotically, higher approximations of the generalized sum rule can be obtained.

As a practical example, residual stress distribution in a section of an axisymmetric article of optical glass is shown in Fig. 2.

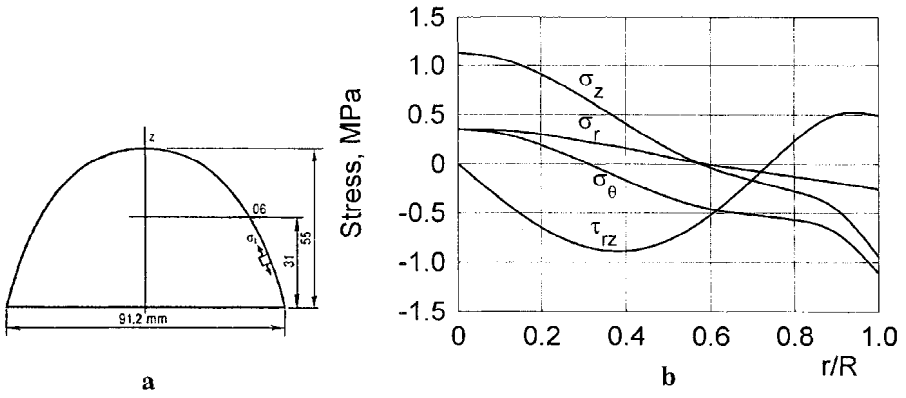

Figure 2. Geometry of the axisymmetric article of optical glass (a), and distribution of residual stresses in section 06 (b).

3. Specimens of Arbitrary Shape

In the case of articles of arbitrary shape, measurement of the integrals (1.1) and (1.2) should be carried out scanning two parallel cross sections, Δz apart from each other, under different angles Θ (Fig. 3). From the equilibrium condition of the segment ABC one obtains

$$\int_A^C \sigma_z dy' = \frac{1}{2C\Delta z}\left[\int_l^B V_2' dx' - \int_l^B V_2 dx'\right] - \frac{V_1}{C}. \tag{3.1}$$

Here V_2' denotes the value of V_2 for the auxiliary section.

Formula (3.1) enables one to calculate the line integral of σ_z for any light ray. From tomography it is known that if one can measure line integrals of a certain field along many rays then the field can be reconstructed using the Radon inversion [13]. In this respect we are actually dealing with optical tomography of the stress field which has been considered in papers [14, 15].

Unfortunately, in the general case of a 3-D article axial stress σ_z is the only stress component which can be determined directly from the measurements.

4. The Case of Plane Deformation

In cylindrical coordinates an algorithm for complete stress determination has been considered by Puro and Kell [16] who have used their method for

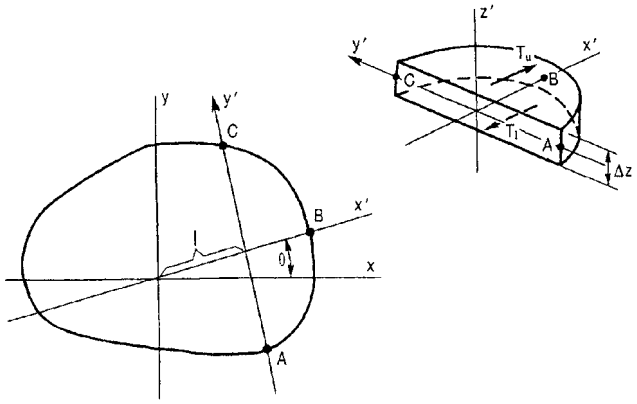

Figure 3. Illustration to the investigation of the general 3-D state of stress.

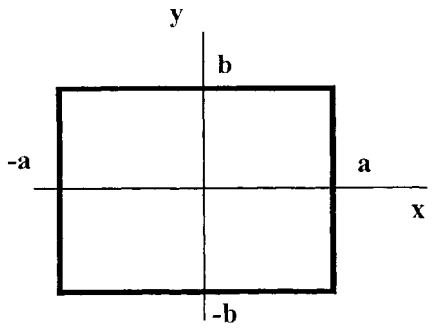

Figure 4. Considering plane deformation in rectangular coordinates.

stress measurement in an optical fiber preform of complicated cross section. Let us consider the same problem in rectangular coordinates (Fig. 4).

Our aim will be to express the stress function φ through the axial stress σ_z which we can determine directly from the measurement data.

Let us express the stress function $\varphi(x,y)$ in the form

$$\varphi(x,y) = \sum_{i,k=0}^{m} \alpha_{ik}\varphi_{ik}(x,y), \tag{4.1}$$

where

$$\varphi_{ik}(x,y) = (x^2 - a^2)^2(y^2 - b^2)^2 x^{2i} y^{2k}. \tag{4.2}$$

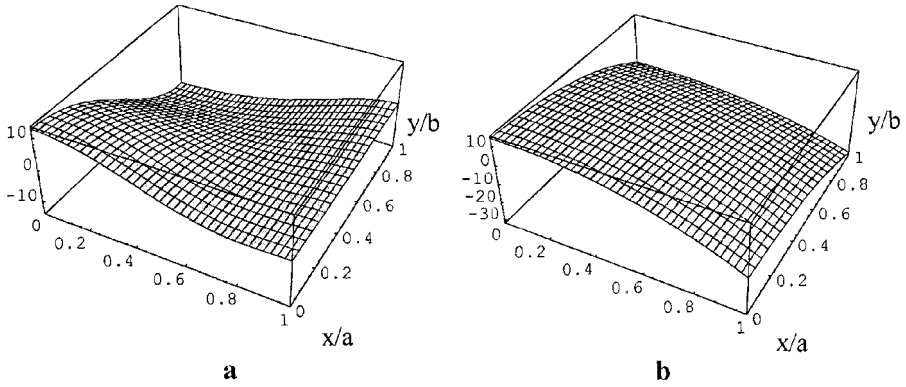

Figure 5. Distribution of the normal stresses σ_x (a) and σ_z (b) in a quadrant of the glass prism.

It can be shown that the coefficients $\propto_{ik}$ can be determined if distribution of σ_z is known. Knowing the stress function, the normal stresses σ_x: and σ_y are determined as

$$\sigma_x = \sum_{i,k=0}^{m} \alpha_{ik} \frac{\partial^2 \varphi_{ik}}{\partial y^2}, \quad \sigma_y = \sum_{i,k=0}^{m} \alpha_{ik} \frac{\partial^2 \varphi_{ik}}{\partial x^2}. \tag{4.3}$$

The method described above has been used for complete determination of the residual stresses in a glass prism of quadratic cross section 40 × 40 mm. Axial stress distribution was determined with an automatic polariscope passing the light through the cross section of the prism in 60 directions (step 3 deg). For every direction of observation optical retardation was recorded at 140 points. Since in the middle of the prism stress gradient in axial direction can be ignored, we have practically the case of plane deformation.

The stress function was approximated in normalized coordinates as

$$\varphi(x, y) = (x^2 - 1)^2 (y^2 - 1)^2 [\alpha_{00} + \alpha_{10}(x^2 + y^2) + \alpha_{11} x^2 y^2]. \tag{4.4}$$

Distribution of the normal stresses σ_z and σ_x is shown in Fig. 5. Macrostatic equilibrium conditions for σ_x and σ_z are well observed.

5. Conclusion

It has been shown that after distribution of the normal stress σ_z has been measured experimentally with integrated photoelasticity, axisymmetric thermal stresses (or axisymmetric residual stresses in glass) and stress

distribution in the case of plane deformation can be completely determined using relationships derived from the equations of the theory of elasticity.

6. Acknowledgement

The support by the Estonian Science Foundation (grant No. 2248) is greatly appreciated.

References

1. Aben, H.: *Integrated Photoelasticity,* McGraw-Hill, New York *et al.,* 1979.
2. Aben, H.K., Josepson, J.I., and Kell, K-J.E.: The case of weak birefringence in integrated photoelasticity. *Optics and Lasers in Eng,* **11** (1989),145-X7.
3. Aben, H., Josepson, J., and Puro, A.: Cases of weak and strong birefringence in integrated photoelasticity. In M.Kh.Akhmetzjanov, S.I.Gerasimov, and K.L.Komarov (eds.), *Photomechanics' 95.* Proc. SPIE, vol. 2791, 1996, pp. 2-7.
4. Doyle, J.F., and Danyluk, H.T.: Integrated photoelasticity for axisymmetric problems. *Exp. Mech.* **1 8** (1978), 215-220.
5. Doyle. J.F.: Closed-form inversion of the axisymmetric integrated photoelasticity equations. *J.Appl.Mech.* **47** (1980), 431-433.
6. Bartenev, G.M.: *The Structure and Mechanical Properties of Inorganic Glasses.* Wolters-Nordhoff Publ., Groningen, 1970.
7. Gardon, R.: Thermal tempering of glass. In D.R.Uhlmann, and N.J.Kreidl (eds.), *Elasticity and Strenght of Glass. Glass: Science and Technology. 5.* Academic Press, New York, 1980, pp. 196-217.
8. Melan, E., and Parkus, H.: *Wärmespunnungen infolge stationärer Temperuturjelder.* Springer-Verlag, Wien. 1953.
9. O'Rourke, R.C.: Three-dimensional photoelasticity. *J. Appl. Phys.* **22** (1951), 872-878.
10. Aben, H., and Guillemet, C.: *Photoelasticity of Glass. Springer-Verlag,* Berlin *et al.,* 1993.
11. Urbanczyk, W., and Pietraskiewicz, K.: Measurement of stress anisotropy in fiber preform: modification of the dynamic spatial filtering technique. *Appl. Opt.* **2 7** (1988), 4117-4122.
12. Timoshenko, S., and Goodier, J.N.: *Theory of Elasticity,* McGraw-Hill, New York et al., 1951.
13. Herman, G.T.: *Image Reconstruction from Projections.* Academic Press, New York, 1980.
14. Aben, H.: Tomographie optique des champs de contraintes. *Rev. Française de Méchunique,* No 1 (1989), 121-130.
15. Aben, H.K., Idnurm, S. J., Josepson, J.I., Kell, K.-J.E., and Puro, A.: Optical tomography of the stress tensor field. In G.Levin (ed.), *Analytical Methods for Optical Tomography,* Proc. SPIE, vol. 1843, 1992, pp. 220-229.
16. Puro, A.E., and Kell, K.-J.E.: Complet determination of stress in fiber preforms of arbitrary cross section. *J. Lightwave Technol.* **10** (1992), 1010-1014.

DIGITAL IMAGE PROCESSING BY PHASE SHIFTING METHOD USING FOURIER TRANSFORM

Y. MORIMOTO and M. FUJIGAKI
Department of Opto-Mechatronics, Faculty of Systems Engineering
Wakayama University
Sakaedani, Wakayama 640-8510, JAPAN

Abstract

Phase analysis methods provide accurate results of fringe pattern analysis. A phase shifting method using Fourier transform uses many images obtained by changing the phases of fringe patterns. The phase at each pixel point is analyzed by calculating the argument using Fourier transform of the phase shifted brightness at the pixel point. It is applied to the analysis of fringe patterns obtained by a Twyman-Green interferometer and photoelastic fringe patterns obtained by a linear polariscope. Furthermore it is extended to a phase shifting method using correlation with rectangular functions to measure a 3-D shape by a grating projection method.

1. Introduction

Small displacement, stress and optical shape of specimens are able to be measured by using optical interferometry such as moire interferometry, Twyman-Green interferometry, Fizeau interferometry and photoelasticity. The shape of a 3-D object is also measured by grating projection methods. The displacement and the shape are measured by analyzing the images of fringe patterns. The analysis of fringe patterns by hand requires great skill. It is, furthermore, tedious and it consumes much labor and much time because of an enormous amount of two-dimensional data. The images are recently analyzed by a computer using digital image processing technique to perform automated, high speed and accurate analysis [1-3]. In the early stage of fringe pattern analysis using computers, the analysis methods were similar to the method by hand. It required skillful technique to obtain the positions of the center lines of fringe lines and to determine fringe orders.

To analyze interference fringes accurately, phase-measurement techniques [4-19] becomes popular. A fringe pattern obtained by optical interferometry usually has a cosinusoidal brightness distribution. If the phase information of the cosinusoidal brightness is analyzed at each pixel point on the image, the displacement at each point of the whole interference field is obtained accurately.

A. Lagarde (ed.),
IUTAM Symposium on Advanced Optical Methods and Applications in Solid Mechanics, 349–362.

There are some methods for the phase analysis. The first is the phase stepping method (PSM) [5-6] using a few images obtained by changing the phase shift amount. The second is the Fourier transform moire and grid methods (FTP, FTM or FTMGM) [7-12] using one image. The third is the phase shifting method using extraction of characteristic (PSM/EC) [13-14] using many images obtained by changing the phase shift amount. The method obtains the phase distribution by detecting the maximum brightness on each pixel point of the fringe images while the phase of the images shifts through 2π. As the fourth, the authors developed a method using wavelet transform to analyze phase information from one image [16]. The authors also proposed a method using Gabor transform [17].

In the PSM, the accuracy is not good in case that the image input equipment has nonlinearity or the images have noise and phase shift error. In the FTMGM, the results include some errors at the both edges of the image if the image has a discontinuity at the both edges of the image. The PSMZEC does not require any complicated processing which the PSM and the FTMGM require. It resists the nonlinearity of the image input equipment. But this method is more sensitive to noise such as random noise and phase shift error than the Fourier transform methods. Though the wavelet transform method gives accurate strain distributions, it requires too much time to calculate. The Gabor transform method can be applied to wider frequency region than the FTMGM.

Bruning et. al. [4] proposed a phase analysis method using several images obtained by changing the phase shift amount. The authors applied this method to the measurement of beam deflection [14]. The authors also applied it to the photoelastic fringe pattern analysis to separate the isochromatics and the isoclinics from the images obtained by a plane polariscope [15]. The authors call this method the phase shifting method using Fourier transform (PSMZFT). These methods are useful to obtain a wrapped phase distribution using a 3-D image. Huntley et al. [18] introduced a phase unwrapping method using a 3-D image.

Furthermore the authors extend it to a phase shifting method using correlation to measure 3-D shapes by a grating projection method.

In this paper the phase shifting method using Fourier transform applied to Twyman-Green interferometer and a plane polariscope are introduced, and also the phase shifting method using correlation of the rectangular brightness of a projected grating and two rectangular functions to analyze 3-D shapes are explained [19].

2. Phase shifting method using Fourier transform applied to Twyman-Green interferometer [14]

2.1 THEORY OF PHASE SHIFTING METHOD USING FOURIER TRANSFORM

Let us show the theory of the phase shifting method using Fourier transform, PSM/FT. A fringe pattern obtained by interferometry such as Twyman-Green interferometry, moire interferometry and holographic interferometry has a cosinusoidal brightness distribution.

The fringe pattern is usually produced by the interference between two beams i.e. an object beam and a reference one. If the optical path of one of the beams is moved a little in

the direction normal to the optical path, the phase of the fringe at every point is shifted by a constant value. The brightness distribution $f(x, y)$, when the phase shifting is performed, is expressed as follows:

$$f(x,y)=a(x,y)\cdot\cos\{\phi(x,y)-\alpha\}+b(x,y) \tag{1}$$

where $a(x, y)$ is the amplitude of the brightness, $b(x, y)$ is the average brightness, $\phi(x, y)$ is the phase value which we have to analyze at any point (x, y) on the original fringe pattern, and α is the amount of the phase shift of the optical path. When the interferometer has an object beam and a reference beam, the phase shifting is usually performed by moving a mirror with a piezoelectric transducer (PZT) or by tilting a glass plate in the reference beam. The phase is shifted little by little until the amount of the phase shift α covers from 0 to 2π, and every 2-D (x, y) image is recorded. A 3-D (x, y, α) image consists of the sequentially phase shifted 2-D (x, y) images. Figure 1 (a) shows an example of a 3-D image when the number of the 2-D images is six. Figure l(b) shows the brightness distributions along an x-directional line of the 3-D image. In the same pixel point on the x-y plane of this 3-D image, the α-directional brightness distribution is one cycle of a cosinusoidal form. An example is shown as a thick line in the figure.

In the method PSM/FT, the brightness distribution $f(x, y)$ expressed in Eq. (1) is regarded as a function of α. The α-directional brightness distribution $f(\alpha)$ is expressed in the Fourier series with respect to α, because it is a periodic function with a period $T=2\pi$. That is

$$f(\alpha)=\sum_{n=-\infty}^{\infty} c_n\cdot\exp(jn\omega_0\alpha) \tag{2}$$

where

$$c_n=\frac{1}{T}\int_{-\frac{T}{2}}^{\frac{T}{2}} f(\alpha)\cdot\exp(-jn\omega_0\alpha)\,d\alpha \tag{3}$$

j is the imaginary unit and $\omega_0(=1)$ is the fundamental frequency.

The α-directional Fourier transform of Eq. (2) is

$$F(\omega)=\int_{-\infty}^{\infty} f(\alpha)\cdot\exp(-j\omega\alpha)\,d\omega=\sum_{n=-\infty}^{\infty} c_n\int_{-\infty}^{\infty}\exp(jn\omega_0\alpha)\cdot\exp\{-j\alpha\,(n\omega_0-n\omega)\}\,d\alpha$$

$$=\sum_{n=-\infty}^{\infty} 2\pi\cdot c_n\cdot\delta(\omega-n\omega_0) \tag{4}$$

where ω is frequency and δ is the Dirac delta function. If the phase shifting is performed perfectly and the 3-D image data have no noise, the frequency spectrum expressed in Eq. (4) appears only at the frequency $\omega = -1, 0, 1$. By substituting Eqs. (1) and (3) into Eq. (4) when $\omega = 1$ and $n= 1$, $F(\omega_0)$ is obtained.

$$F(\omega_0)=\frac{2\pi}{T}\delta(0)\int_{-\frac{T}{2}}^{\frac{T}{2}} f(\alpha)\cdot exp(-j\omega_0\alpha)d\alpha = \delta(0)\int_{-\pi}^{\pi}\{a\cdot cos(\phi-\alpha)+b\}\cdot\exp(-j\alpha)d\alpha$$
$$=\pi\cdot a\cdot\delta(0)\cdot\exp(-j\phi) \tag{5}$$

This means that the phase value ϕ is obtained by calculating the argument, i.e., the arctangent of the ratio of the imaginary part to the real part of $F(\omega_0)$:

$$\phi = -\tan^{-1}\left[\frac{\mathrm{Im}\{F(\omega_0)\}}{\mathrm{Re}\{F(\omega_0)\}}\right] \tag{6}$$

Like this, the phase distribution $\phi(x, y)$ is obtained. The displacement or the shape of the specimen is calculated from the phase distribution.

In this method, because only the harmonic with frequency 1 is extracted, phase shifting error and the other experimental noise which appears at other frequency components are eliminated.

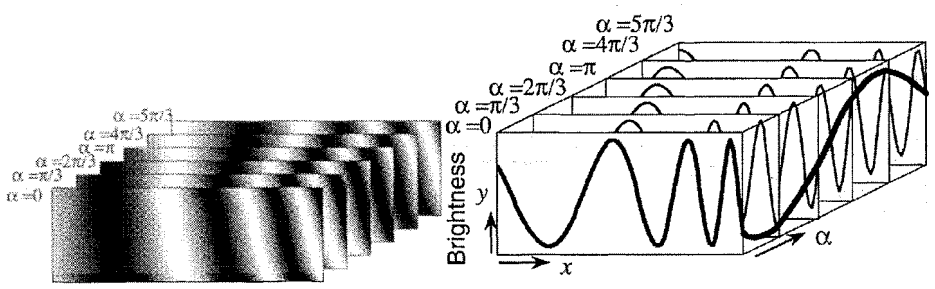

(a) Phase shifted fringe pattern (b) Brightness distribution along a line

Figure 1. x-directional brightness distributions of phase shifted fringe patterns of 3-D image

2.2 EXPERIMENT FOR CANTILEVER BEAM

2.2.1 *Experimental procedure*

Figure 2 shows an application of the PSMZFT to the measurement of the out-of-plane displacement distribution of a cantilever beam using a Twyman-Green interferometer. Figure 3 shows the specimen and the measured area of this experiment. The specimen is a glass plate and it has an initial deformation. One end of the plate is fixed on a thick steel plate with a plastic glue and it is deformed at one line near the other end shown as the dashed line in Fig. 3. The displacement value at the loading point is 2μm.

In this study, the phase shifting in the interferometer is performed by moving the reference mirror with a PZT control stage. The resolution of the stage movement is fine in the order of a few nanometer, the stage is moved along the optical path, as shown in the plain arrow line in Fig. 2. A reference mirror is moved little by little, and all the images are recorded in an image grabber system through a CCD camera. The phase at each pixel

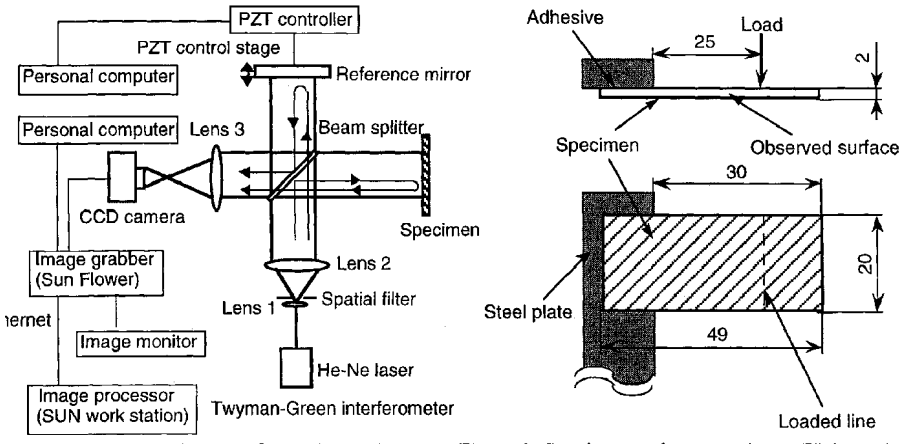

Figure 2. Schematic diagram of experimental system *Figure 3.* Specimen and measured area (Unit mm)

point of the interference image is analyzed as mentioned in the previous section. In order to calculate displacement, the sequential phase shifted images before and after deformation are recorded respectively. The difference $\Delta\phi$ of the phases at each pixel point between images before and after deformation is analyzed. The displacement is calculated from the following equation.

$$u=\frac{\lambda}{4\pi}\Delta\phi \tag{7}$$

where u is the displacement and λ is the wavelength of the laser. In this experiment, a He-Ne laser is used as the light source, the wavelength λ is 633 nm.

2.2.2 *Experimental results*

Fig. 4 shows some parts of the sequential phase shifted fringe patterns before and after deformation respectively. The fringe images before deformation represent the initial deformation of the specimen and the optical system. The amount of one step of the phase shift is $\pi/15$. The 3-D image consists of 30 phase shifted 2-D images. Figure 4 shows

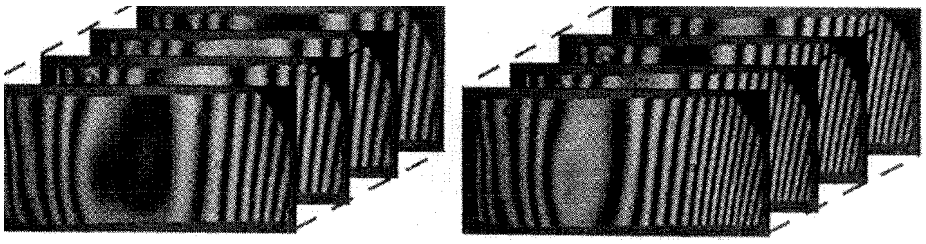

(a) Before deformation (b) After deformation

Figure 4. Phase shifted fringe patterns of 3-D image;

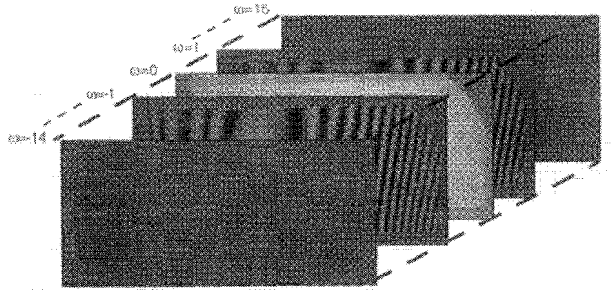

Figure 5. Fouriere spectrum (After deformation)

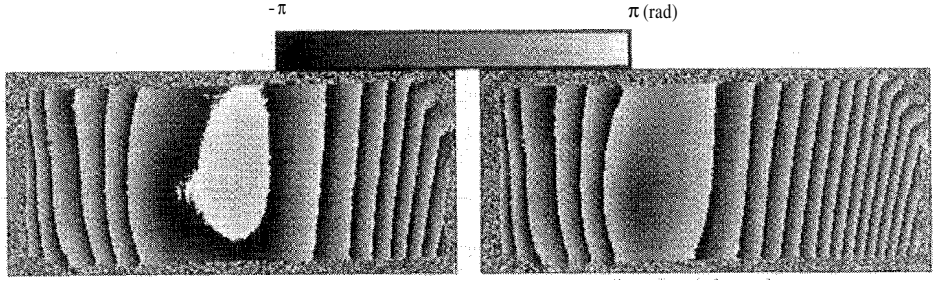

(a) Before deformation (b) After deformation

Figure 6. Wrapped phase distribution

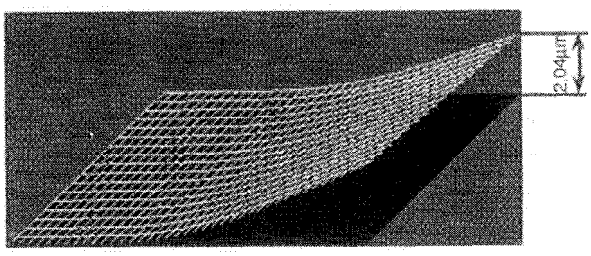

Figure 7. Displacement distribution obtained by the PSMIFT (3-D plot)

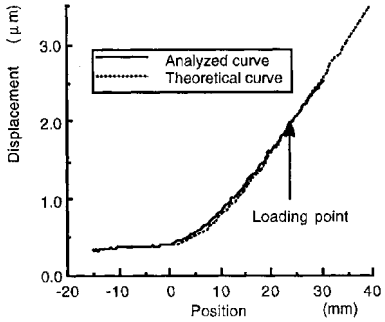

Figure 8. Displacement curve along x-directional center line

only 4 2-D images to understand easily in visualization. After performing the α-directional Fourier transform on the 3-D image using the mixed radix FFT as used in our previous method [11, 12], the Fourier spectrum for the data after deformation are obtained as shown in Fig. 5. This figure shows only 5 2-D images although there are 30 2-D images. The brightness corresponds to the real part of the frequency at the pixel point. The brightness is low in the images except the frequency 1, 0 and -1. They are showing the error components. By extracting the frequency with 1 and calculating the argument at every point, the wrapped phase distribution is obtained as shown in Fig. 6. After connecting the wrapped phase distributionsare smoothly by adding $\pm 2\pi$ at the discontiunity, the unwrapped phase distributions are obtained. The displacement distribution is calculated from the difference of the phase between before and after deformation. the result is shown in Fig. 7. Figure 8 shows the displcement curve along the *x*-directional center line. The theoretical curve is shown in Fig. 8 for comparison.

3. Phase Shifting method using Fourier transform applied to plane polariscope [15] polariscrope [15]

In photoelasticity, the image obtained in the field of a plane polariscope consists of isochromatics and isoclinics. In analysis of stress, though it is necessary to separate the isochromatics and the isoclinics, it is difficult. The most popular method is to use the isochromatic fringe image captured in the field of a circular polariscope [20]. The isoclinics are not obtained by a circular polariscope. the positions of the isoclinics obtained by a plane polariscope are not so accurate because of the wide width of the isoclinics lines and the accuracy of quarter wave plates. The authors [13] developed a software of 3-D image processing, and applied it to the analysis of the 3-D (x, y, θ) image data consisted with the spatial coordinates (x, y) and the angle θ of the crossed polaroids.

In this section, the phase shifting method using Fourier transform applied to the separation of the isochromatics and the isoclinics is shown.

3.1 THEORY OF SEPARATION OF ISOCHROMATICS AND ISOCLINICS

The light intensity obtained in a dark-field plane polariscope, shown in Fig. 9, is expressed by

$$i(\theta) = a^2 \sin^2\{2(\phi - \theta)\} \cdot \sin^2(m\pi) \tag{8}$$

$$= \frac{a^2}{2}\{1 - \cos 4(\phi - \theta)\} \cdot \sin^2(m\pi) \tag{9}$$

where a is the amplitude of the incident polarized light, ϕ is the angle of the principal stress and θ is the angle of the analyzer and m is the isochromatic fringe order. The fringe order m is expressed as follows:

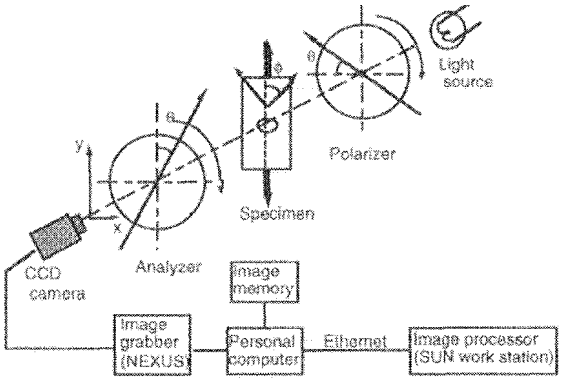

Figure 9. Schematics of polariscope and image processor

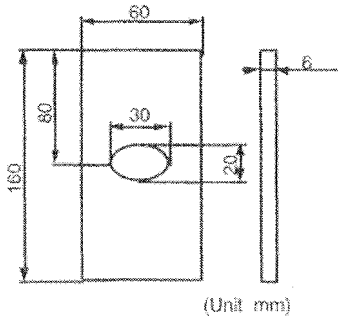

Figure 10. Specimen

$$m = (C/\lambda)d(\sigma_1 - \sigma_2)$$

where C is the photoelastic constant, d is the thickness of the specimen, λ is the walvelength and $(\sigma_1 - \sigma_2)$ is the principal stress difference of the specimen.

Equation (8) is expressed in the Fourier series with respect to θ, because it is a period function with a period $T=\pi/2$. That is

$$i(\theta) = \sum_{n=-\infty}^{\infty} c_n \exp(jn\omega_0\theta) \tag{11}$$

where

$$c_n = \frac{1}{T}\int_{-\frac{T}{2}}^{\frac{T}{2}} i(\theta)\cdot\exp(-jn\omega_0\theta)\,d\theta \tag{12}$$

and

$$\omega_0 = \frac{2\pi}{T} = \frac{2\pi}{\pi/2} = 4 \tag{13}$$

The Fourier transform of Eq. (11) is

$$I(\omega) = \int_{-\infty}^{\infty} i(\theta)\cdot\exp(-j\omega\theta)\,d\theta = \sum_{n=-\infty}^{\infty} c_n \int_{-\infty}^{\infty} \exp(jn\omega_0\theta)\cdot\exp(-j\omega\theta)\,d\theta$$

$$= \sum_{n=-\infty}^{\infty} 2\pi\cdot c_n\,\delta(\omega - n\omega_0) \tag{14}$$

where j is the imaginary unit, ω is frequency and δ is the Dirac delta function.

Equation (14) indicates the discrete frequency spectrum which appears only on the frequency components $n\omega_0$ (n=0, ±1, ±2…). By extracting the delta functions $27\pi\cdot c_0\,\delta(0)$ and substituting Eq. (9) and Eq. (12) into Eq. (14) when n=0, $2\pi c_0$ (n=0) is

obtained

$$2\pi c_0 = \frac{2\pi}{T}\int_{-\frac{T}{2}}^{\frac{T}{2}} i(\theta)\mathrm{d}\theta = 4\int_{-\frac{\pi}{4}}^{\frac{\pi}{4}} \frac{a^2}{2}\{1 - \cos 4(\phi - \theta)\}\cdot \sin^2(m\pi)\mathrm{d}\theta$$

$$= 2a^2\sin^2(m\pi)\int_{-\frac{\pi}{4}}^{\frac{\pi}{4}}\{1 - \cos 4(\phi - \theta)\}\mathrm{d}\theta = \pi a^2\sin^2(m\pi) \tag{15}$$

$2\pi c_0 = \pi a^2 \sin^2(m\pi)$ is obtained from the amplitude at $\omega=0$ of the Fourier spectrum of the θ directional brightness distribution. Equation (15) indicates that the isoclinics are eliminated. That is, the image of $2\pi c_0$ shows the isochromatics in the whole field of the specimen.

In the same way, from Eq. (9), Eq. (12) and Eq. (14) where n=-1, can be written as

$$2\pi c_{-1} = \frac{2\pi}{T}\int_{-\frac{T}{2}}^{\frac{T}{2}} i(\theta)\cdot\exp(\mathrm{j}\omega_0\theta)\mathrm{d}\theta$$

$$= 4\int_{-\frac{\pi}{4}}^{\frac{\pi}{4}} \frac{a^2}{2}\{1 - \cos 4(\phi - \theta)\}\cdot \sin^2(m\pi)\cdot\exp(\mathrm{j}4\theta)\mathrm{d}\theta$$

$$= 2a^2\sin^2(m\pi)\left[\int_{-\frac{\pi}{4}}^{\frac{\pi}{4}} \exp(\mathrm{j}4\theta)\mathrm{d}\theta - \frac{1}{2}\int_{-\frac{\pi}{4}}^{\frac{\pi}{4}}\left[\exp\{\mathrm{j}4(\phi - \theta)\} + \exp\{-\mathrm{j}4(\phi - \theta)\}\right]\cdot\exp(\mathrm{j}4\theta)\mathrm{d}\theta\right]$$

$$= -a^2\sin^2(m\pi)\left[\int_{-\frac{\pi}{4}}^{\frac{\pi}{4}} \exp(\mathrm{j}4\phi)\mathrm{d}\theta + \int_{-\frac{\pi}{4}}^{\frac{\pi}{4}} \exp\{-\mathrm{j}4(\phi - 2\theta)\}\mathrm{d}\theta\right]$$

$$= -\frac{\pi}{2}a^2\sin^2(m\pi)\cdot\exp(\mathrm{j}4\phi) \tag{16}$$

The argument 4ϕ is obtained by calculating the arctangent of the ratio of the imaginary and real parts of $2\pi c_{-1}$:

$$4\phi = \tan^{-1}\left\{\frac{\mathrm{Im}(2\pi c_{-1})}{\mathrm{Re}(2\pi c_{-1})}\right\} \tag{17}$$

Equation (17) indicates that one fourth of the argument is equal to the direction of principal stress.

In this method, by calculating the Fourier transform of the sequential images captured by the rotating the angle θ of the crossed polaroids, the isochromatic image is

obtained from only the intensity data of the frequency where $\omega = 0$. The direction of principal stress on each point is computed from only the argument where $\omega = -\omega_0$. The other frequency components, in other words, experimental noise is completely eliminated.

3.2 EXPERIMENT FOR PLATE WITH ELLIPTIC HOLE

The photoelastic experiment system with the crossed plane polariscope is shown in Fig. 9. Figure 10 shows the specimen made of epoxy resin. The rectangular plate has an elliptic hole at the center. The constant tensile load along the y axis yielding on the specimen is 6.5 N. The Polaroids are rotated in the crossed position when the angle θ is from -45° to 44°

Ninety sequential 2-D images recorded at every 1° angle of θ from -45° to 44° with a CCD camera are stored into a hard disk. One mm corresponds to 1.98 pixels. The ninety 2-D images are treated as a 3-D image as shown in Fig. 11. The size of the 3-D image is 128 (width) × 120 (height) × 90 (depth) pixels. The 3-D image data are directly processed using the 3-D image processing program including Fourier transform programmed by the authors.

The mixed radix fast Fourier transform (MRFFT) in the θ direction yields the 3-D image data, i.e. the Fourier spectrum as shown in Fig. 12. In this figure, the 2-D image at $\omega = 0$ shows the isochromatics. Figure 13 is the isochromatics.

By calculating the arctangents of the ratios of the imaginary parts and the real parts of the data in the frequency at $\omega = -\omega_0$, the directions of principal stresses are determined in the whole field of the specimen as shown in Fig. 14.

This method is insensitive of high frequency noise, because the high frequency components are eliminated using Fourier filter. The positions and angles may have finer resolution than those in the conventional method, because the data obtained using Fourier transform is naturally smooth.

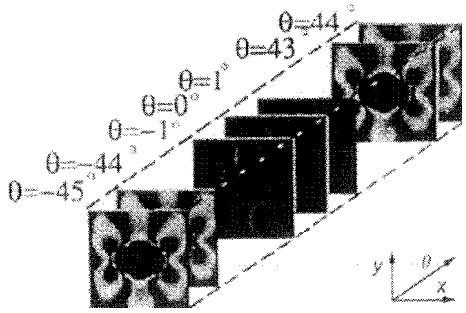

Figure 11. Three-dimensional image data

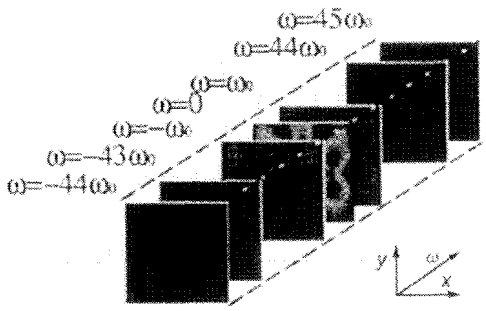

Figure 12. θ directional frequency spectrum of image data of Fig. 11

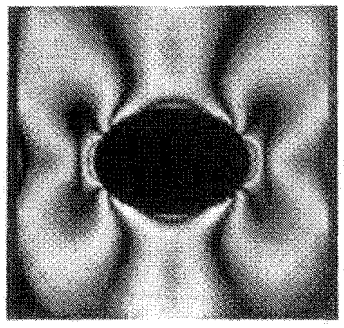

Figure 13. Isochromatics obtained by PSM/FT

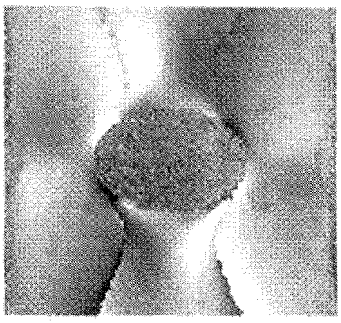

Figure 14. Distribution of principal stress direction

4. Phase shifting method using correlation with rectangular function applied to 3-D shape measurement [19]

In this section, we propose a new phase shifting method to analyze phase distribution using the correlation between the brightness of the projected grating and a rectangular function. Figure 15 shows the brightness distributions of the projected grating at a pixel point while the projected phases are shifted. Figures 15(a) and (b) show examples when the initial phases of the grating projected at the points are 0 and ϕ, respectively. The distribution is a rectangular function with a period 2π. The upper and lower brightness intensities are mainly depending on the reflection ratio of the object. After normalizing the brightness, the normalized brightness is multiplied by two weight functions f_0 and f_1 shown in Fig. 16 (a) and (b), respectively. Figure 16(a) is a rectangular weight with phase 0. Figure 10(b) is a rectangular weight with phase $\pi/2$. The products are integrated from $\alpha=0$ to $\alpha=2\pi$, respectively.

Figure 17(a) shows the relationship between the initial phase ϕ and the integration values S. From the two integration values S_0 and S_1 obtained by two weight functions f_0 and f_1, respectively, the phase ϕ is determined as wrapped phase ϕ' uniquely from the following conditions.

$$
\begin{aligned}
&\text{A: } \phi' = -S_1/4 && \text{when } S_0 > S_1 \text{ and } |S_0| > |S_1| \\
&\text{B: } \phi' = -S_0/4 + \pi/2 && \text{when } S_0 > S_1 \text{ and } |S_0| < |S_1| \\
&\text{C: } \phi' = -S_0/4 + \pi/2 && \text{when } S_0 = S_1 \text{ and } S_0 < 0 \\
&\text{D: } \phi' = S_1/4 - \pi && \text{when } S_0 < S_1,\ S_1 >= 0 \text{ and } |S_0| > |S_1| \quad (18) \\
&\text{E: } \phi' = S_1/4 + \pi && \text{when } S_0 > S_1,\ S_1 < 0 \text{ and } |S_0| > |S_1| \\
&\text{F: } \phi' = -S_0/4 - \pi/2 && \text{when } S_0 < S_1 \text{ and } |S_0| < |S_1| \\
&\text{G: } \phi' = -S_0/4 - \pi/2 && \text{when } S_0 = S_1 \text{ and } S_0 > 0
\end{aligned}
$$

The results are shown in Fig. 17(b).

Since this algorithm is very simple, it is easy to perform high-speed processing. Since the grating brightness function is rectangular, the non-linearity of input devices does not affect the results.

This method is applied to shape measurement of a rubber ball and a metal spoon.

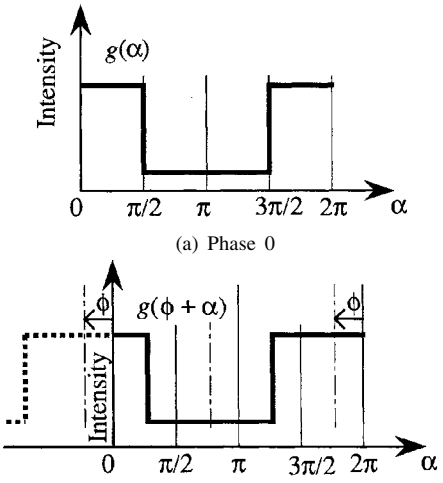

(a) Phase 0

(b) Phase ϕ

Figure 15. Brightness distribution of projected grating obtained by shifting phase

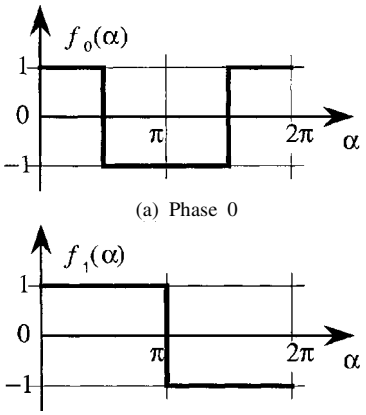

(a) Phase 0

(b) Phase $\pi/2$

Figure 16. Weight distributions of filters

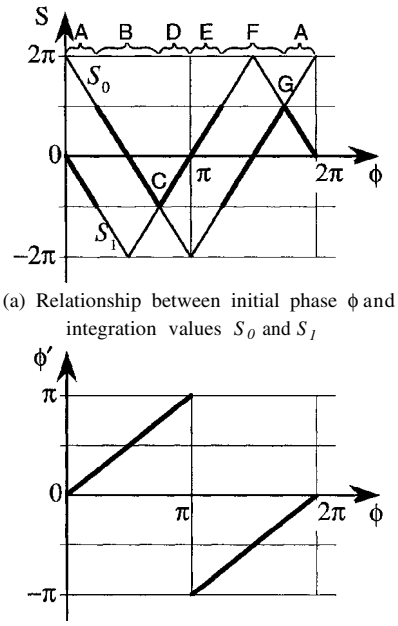

(a) Relationship between initial phase ϕ and integration values S_0 and S_1

(b) Calculated wrapped phase

Figure 17. Relationships between initial phase ϕ and integration values and calculated phase

The projected grating is shifted by $2\pi/32$, and the 32 products are calculated and added. All the images are used for this analysis. As we use only a conventional personal computer, in this paper, the processing time is a few second. It is, however, possible to make a real-time hardware for this method.

Figure 18(a) shows one of the 32 images. The resultant phase distribution is shown in Fig. 18(b). This method is useful even if the material of an object is metal because the use of a grating with rectangular brightness can detect the brightness change.

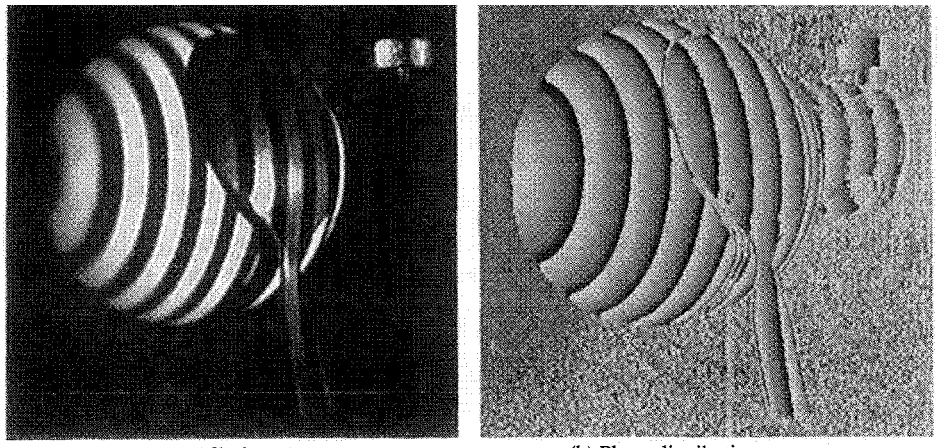

(a) Projected grating (b) Phase distribution

Figure 18. Phase distribution of rubber ball and metal spoon obtained by phase shifting method using correlation with rectangular

5. CONCLUSIONS

The phase shifting method using Fourier transform (PSWT) has been introduced to analyze the phase distribution of interference fringes. In this method many sequentially phase shifted fringe patterns are required, however, the effect of noise and phase shifting error of the patterns are eliminated by performing the a-directional Fourier transform and extracting the harmonic with frequency 0, 1 or -1. This method is more insensitive to noise than the other methods and error does not appear at the both edges of the image unlike the results obtained by the conventional 2-D Fourier transform method (FTMGM). If accurate phase shifting is performed, the phase is analyzed from only a few phase shifted fringe images. The PSM/FT has been applied to measurement of the displacement distribution of a cantilever beam using Twyman-Green Interferometer.

The PSM/FT has been applied to the separation of the isochromatics and the isoclinics obtained in the plane polariscope. The isochromatics and the isoclinics are separated almost automatically from the 3-D image data obtained by rotating the crossed polaroids.

Full automated analysis is possible and this method is useful for not only optical interferometric fringe analysis but also the other fringe pattern analysis such as shape measurement by the grating projection method.

The authors have also proposed the real-time phase shifting method using correlation with two rectangular functions. By using this method, the 3-D shapes of a ball and a spoon have been analyzed.

This study is supported by Research Project (Project No. 09555033), the Grant-in-aid for Scientific Research of the Ministry of Education, Science and Culture.

6. REFERENCES

1. Sirkis, J. S. Chen, Y., Singh, H. and Cheng, A. Y.: Computerized optical fringe pattern analysis in photomechanics: a review, *Opt. Eng.,* **31** -2, (1992), 304-3 14.
2. Kujawinska, M.: Automatic fringe pattern analysis in optical methods of testing, *Warsaw Univ. Technol. Sci. Rep.,* **138,** (1990), 1-80.
3. Morimoto, Y.: Chap. 21 Digital image processing, in Kobayashi, A. S. (Ed), *Handbookon Experimental Mechanics, Second Revised Ed.,* , Soc. for Exp. Mech., (1993), 969-1030.
4. Brunning, J.H., Herriott, D. R., Gallagher, J.E., Rosenfeld, D. P., White, A.D. and Brangaccio, D.J.: Digital wave front measuring interferometer for testing optical surface and lenses, *Appl. Opt.,* **13,** (1974), 2693-2703.
5. Hariharan, P. Oreb B. F. and Brown, N.: A digital phase-measurement system for real-time holographic interferometry, *Optics Communications,* **41,** (1982), 393-396.
6. Creath, K.: Phase measurement interferometry techniques, *Prog. Opt.,* **26,** (1988), 350-393.
7. Sciammarella, C. A. and Sturgeon, D. L.: Digital-filtering techniques applied to the interpolation of moire-fringes data, *Experimental Mechanics,* **7** - 11, (1967), 468-475.
8. Takeda, M. Ina, H. and Kobayashi, S.: Fourier transform method of fringe pattern analysis for computer-based topography and interferometry, *J. Opt. Soc. Am.,* **72**- 1, (1982), 156- 160.
9. Macy, W. W. Jr.: Two-dimensional fringe-pattern analysis, *Appl. Opt.,* **22**-23, (1983), 3898-3901.
10. Bone, D. J., Bachor, H. A. and sandeman, R. J.: Fringe-pattern analysis using a 2-D Fourier transform, *Appl. Opt.,* **25**-10, (1986), 1653-1660.
11. Morimoto Y., Seguchi , Y. and Higashi, T.: Application of moire analysis of strain by Fourier transform, *Optical Engineering,* **27,** (1988), 650-656.
12. Morimoto Y., Seguchi , Y. and Higashi, T.: Two-dimensional moire method and grid method using Fourier transform, *Experimental Mechanics,* **29,** (1989), 399-404.
13. Morimoto, Y., Morimoto, Y. Jr. and Hayashi, T.: Separation of isochromatics and isoclinics using 3-D image processing, *Proc. Japan Soc. for Photoelasticity (in Japanese),* **13**-1, (1993), 23-28.
14. Morimoto Y. and Fujisawa, M. : Fringe-pattern analysis by phase-shifting method using extraction of characteristic, *Experimental Mechanics,* **20**-4, (1996), 25-29.
15. Morimoto, Y., Morimoto, Y. Jr. and Hayashi, T. : Separation of isochromatics and isoclinics using Fourier transform", *Experimental Technique,* 17-5, (1994), 13- 16.
16. Morimoto, Y. and Imamoto, Y.: Application of Wavelet Transform to Displacement and Strain Measurement by Grid Method, *Proc. of 1995 SEM Spring Conf on Exp. Mech.,* (1995), 898-903.
17. Morimoto, Y., Inoue, H. and Fujigaki, M.: Application of Gabor Transform to 3-D Shape Analysis Using Grating Pattern Projection Method, *Int. Symp. on Adv. Tech. in Exp. Mech., JSME-MMD,* (1995), 67-72.
18. Huntley, J. M. and Saldner, H. : Temporal phase-unwrapping algorithm for automated interferogram analysis, *Appl. Opt.,* **32** -17, (1993), 3047-3052.
19. Morimoto, Y. and Fujigaki, M.: Real-time phase-distribution analysis of fringe patterns, *Int. Conf on Applied Optical Metrology, in Balatonfured, Hungary, SPIE,* submitted, 1998
20. Burger, C.P., "Chap. 5 Photoelasticity," in Kobayashi, A. S. (Ed), *Handbookon Experimental Mechanics, Second Revised Ed.,* , Soc. for Exp. Mech., (1993), 165-266

DIGITAL IMAGE COMPARATOR FOR EXPERIMENTAL ANALYSIS OF DEFORMATIONS

L. BERKA[1], J. KLIMA[2], M. DRUCKMÜLLER[3], M. SOVA[4]
1 Faculty of Civil Engineering, Czech Technical University
Thakurova 7, 166 29 Prague, Czech Republic
2 Tescan Ltd, Brno
3 Faculty of Mechanical Engineering, TU Brno
4 SOVAX, Prague

Abstract. Optical methods of deformation measurements represent one of the oldest and the most widespread area of experimental mechanics. The optic methods of strain measurements are generally-interferometry, stereo image analysis and digital image analysis. The above-mentioned optical methods are of particular importance for deformation analysis in microstructures and microobjects, where they are the only possible experimental tools. The basis of the stereoscopic technique of deformation measurements is the taking of pair stereoscopic photographs of objects, using the time base principle, i.e. photographs of objects before and after the deformation under the entirely same conditions are taken. The further step in stereoimage method of the strain analysis is the stereocomparation of the pair of images. Up to now we have used for it the analog apparatus ZEISS-Stecometr. The paper which is presented describe a digital system of reading and comparation of the pairs of stereoimages.

1. Introduction

Optical methods of deformation measurements represent one of the oldest and the most widespread area of experimental mechanics. The furthest and the most frequently used principle of optical methods is interference [1], and almost a hundred years old history has the stereoscopic principle [2]. Newer are photomethods applying image analysis to calculate coordinates of identification points fields [3].

The above-mentioned optical methods are of particular importance for deformations analyses in microstructures and microobjects, where they are the only possible experimental tool. Evolution of optical methods of deformations measurements in the field of experimental micromechanics commences at the end of 1980s. In the field of interferometry there are contributions of Sciammarella [4], and Michel and Kuhnert [5]. Stereoscopic method was employed by Davidson [6], and Berka and Růžek [7]. Image analysis of microidentification point structures was worked-in-progress by Allais [8] and Fischer [9].

At present, the best sophisticated and the most frequently used method in this area is the interferation micro-moire' technique of D. Post [10]. In our country, Vaclavík and

A. Lagarde (ed.),
IUTAM Symposium on Advanced Optical Methods and Applications in Solid Mechanics, 363-370.

Minster [11] are working with this technique. Advantage of it is the fill-surface scan of deformations field and the high accuracy, reached by using grids pairs with the density of 1200 lines/mm, positioned both in the interferometer and also in the measured object. Development of the technique was influenced also by the rapid evolution of image analysis and digital technique, enabling measurement in the real time.

Evolution of the stereoscopic method of deformation analysis is connected with the overall development for evaluation of pairs stereoscopic photographs. This results from the fact that taking photographs and their analysis does not take place simultaneously. With regards to specific conditions of taking ground photographs by using special cameras, the evaluation systems are equipped with the high resolution scanners that markedly enhance purchase and operating expenses of these systems, and thus they become hard available. Users of stereoscopic measurement technique, who can work with digital image recording, gained by CCD camera or scanning electron microscope, therefore try to create on-line system enabling record, processing and comparation of images obtained by the time base method (Fig. 1). The system described in the following contribution is a digital image of the hitherto used analog system for recording and evaluation of stereoscopic photographs pairs, that was referred to on the previous conferences EAN [12].

2. The deformation analysis by the stereoimage technique

The basis of stereoscopic technique of deformation measurements is the taking of stereoscopic objects photographs pairs, using the time base principle, i.e. photographs of objects before and after the deformation under the entirely same conditions. To fulfil this requirement, it is necessary not only for the image-taking apparatus, a microscope in our case, but also for the CCD camera to ensure, by their external (sample and apparatus position) and also internal (magnification stability, orientation) a reproducibility of photographs with accuracy attributed on the deformation measurement accuracy. This can be different according to the nature of solved problem (elastic or plastic deformation). According to it, it is also necessary to choose an appropriate method.
Taking into consideration deformation measurements in the vicinity of the agreed plasticity limit of steel, having a size of 0.2 % with accuracy 10 %, i.e. value of $\Delta\varepsilon =$ 0.02 %, the requirement follows on the accuracy of the couple of stereoscopic photographs evaluation of undeformed specimen, obtained by the time base method. It means that after the first image processing, the specimen is undertaken to all necessary measurement operations, and then the second image is performed. Found values of fictive deformations represent faults of measurements that must be lower than the required value of 10% of plasticity limit. Deviations may result from:
-- differences in the position and microscopic identity of sample surface in its taking out and reloading into the vacuum microscope chamber
-- differences in the resetting of microscope electronic regime during exchange or the switching the device off.

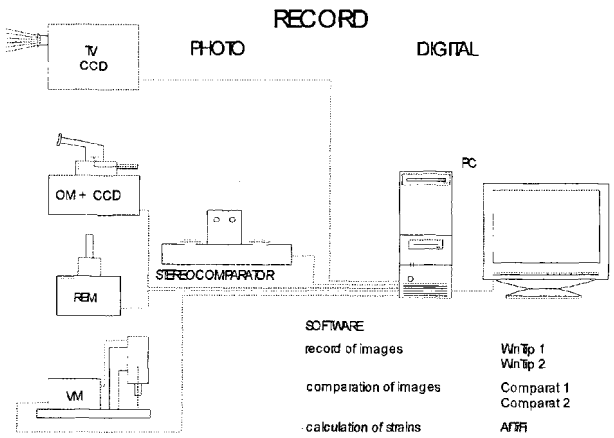

Figure 1. The schematic drawing of the measuring systém

To minimize these deviations, it is necessary, regardless the type of a microscope, to choose such a method that will limit changes in the setting of device parameters, used in the first photographs processing, at maximum. This is the question of keeping the working distance and set magnification, whose deviations are equal to a relative error in their deformations measurements. Errors in the measured deformation can be caused also by overfocusing and higher differences in the brightness and contrast setting, which change dimensions of microobject image and thus conditions of the photographic comparison.

Further group of errors is connected with the quality of image recording, both photographic and digital. In case of the stereocomparation, besides identity of microsurface images, it is also internal resolution of stereocomparator $\Delta 1$, which at device ZEISS Stecometr is 2 μm. The necessary precision in the deformation measurement equal to $\Delta\varepsilon = 0.0002$ is reached at the photographic distance of compared points $\underline{1}$ equal to $\Delta 1/\Delta\varepsilon = 2/0.0002 = 1.10$ μm. At the smaller points distance, the error is bigger than presumed 10%.

At digital system of evaluation of a stereoscopic pair of photographs, the accuracy of a points position is measured mainly by the resolution at which the image is taken.

3. The reading and image processing - system TESCAN

TESCAN has developed a device for digitization, preprocessing and recording of electron microscopic image. Hardware of the device is composed of personal computer, digital generator of scan signal and acquisition device of video signal, positioned on the special developed card in the ISA computer bus and converters units D/A and A/D

in the separate box, where there are the circuits for an option of input analog signal, signal filters, power supplies and auxiliary circuits.

Signal for electron beam sweeping in the microscope tube is generated in the computer in the digital form. According to the generation principle, it is necessary to resolve fast and slow raster scanning. In the fast raster scanning mode - called “fast” in the program - the step signal is generated mainly by hardware tools - everything is subordinate to reaching the maximum speed of raster scanning. Sweeping is not synchronized with the power supply. This mode serves to the rapid scanning of specimen and to the microscope setting.

Generated sweeping signal is then, in the D/A converters units, transformed from the digital form onto the analog signal, and in the output circuit, it is possible to set its polarity, amplitude and ss level suitable for an appropriate type of microscope (between -10 and + 10V). The basic setting of system magnification is carried out here in order that the operating field of system may be concordant with the original field of electron microscope.

Analog video signal generated and strengthened in the microscope is brought via input switching circuits into an A/D converter. Even four signal from different detectors from the microscope is possible to transfer into the input circuits, and one of them to choose for display by means of the program. In the A/D converter, the analog video signal is converted onto the digital form simultaneously with the filtration - all higher frequencies that are not necessary for real image signal transmission are reduced, and thus the image noise is reduced. Digital video signal is then via special interface, located on the same card in the computer as a generator of sweeping, brought into the computer video memory and - as far as an operator commands by means of the control program - the image is set also on the chosen memory medium.

The entire process of sweeping and image acquisition is controlled by the program that operates in the Window 95 environment and uses the standard image format BMP. The program includes also procedures for image preprocessing - brightness and contrast manipulation, image focusing and noise reducing. Program offers ample possibilities in the software calibration field of image magnification on the basis of known objects and measuring of formations in the image.

The big attention in the program creation has been also payed to the comfortable and users-friendly storage system, which enables quick scanning, copying and opening of stored images by means of “album” of their miniatures, sorting according to the data in the head stored with each image etc. Program enables to make images with the resolution of 256x256 up to 4096x4096 of image elements (pixels).

The researchers payed an extraordinary attention to the problem of necessary resolution (i.e. fineness of the raster step) and its fitting with the other requirements on the system. These requirements are rather controversial. As mentioned above,

improvement of the signal/noise ratio is possible to reach by the duration of electron beam in each pixel, while in order to reach the higher resolution of optical microscope system, it is necessary to operate with “thinner” and unfortunately less intensive electron beam. Increasing of requirement on the duration in each pixel and simultaneously increasing of numbers of pixels in the given image leads to the disproportionate prolongation of time for one image - above the level, which is usually guaranteed by producers for stability of their devices and after all above the time acceptable for an operator. Thus, the probability is increased that during the long time of photo performing , a random failure of power supply or a shake etc. may happen, which is displayed by the image error. For example, in the size magnification of units of thousands and image division onto the 4096×4096 pixels, which is a requirement for microdeformation measurement with the above mentioned accuracy, at the microscopes with thermoemission electron gun is the time necessary for one pixel about 200 μs, which at 4096×4096 pixels represents the time of image processing 60 minutes. During this time, defocusing of image may happen as well as its shifting by device drift or a change of brightness. When solving this problem, the procedure has been developed, which enables in the lower resolution raster regime (as a basic raster regime we consider resolution 512×512 pixels) to choose a window of the chosen size (using the multiple of two), to place this window on the chosen object decisive for microdeformations evaluations, and then to scan the image in this window with the very fine raster scanning, which corresponds to 4096 image elements on the row throughout the whole image. Thus, scanned chosen parts of image are screened on the display with the full resolution, and can be used for evaluation of microdeformations by digital comparator.

In conclusion, it is necessary to add that the proposed system requires the best quality computer hardware. The necessity is the high quality resolution monitor and a graphic card with the memory 4 MB, fixed disc with the high capacity, or further tools for recording of digitized images sets.

4. The digital comparation of stereoimages - system COMPARAT

To evaluate a stereoscopic pair of raster electron microscope images, the software system has been developed. The system enables an operation with images up to maximum dimension of 2048x2048 pixels. Both compared images are displayed simultaneously on the computer display in complementary colours. The high sensitivity of the human eye on the change of colour tone, which is near to neutral gray, is utilized. Changes in images are shown as garish colour changes. A user marks in an interactive way a certain amount of points corresponding each other in the both images. Thus, the relative shifts in these points are determined. The absolute shifts are possible to determine only after the precise matching of both compared images. Three following methods are possible to employ.

1) The precise matching of compared images is guaranteed by the technical solution of experiment. In this case, relative shifts are considered as absolute ones. In practice, it is very difficult to find such a technical solution.

2) During images scanning, it is guaranteed that both images have the same scale, i.e. magnification of the raster electron microscope is in both images identical. In this case, such a translation and rotation of the second of the images pair is searched in order that the sum of deviation quadrates in the users tagged points was minimal. Practically it is carried out in such a way that both images are placed into the complex numbers plane and linear transformation

$$w = a.z. + b$$

is searched, where a, b are complex constants and abs (a) = 1 is valid. After the linear transformation with required attributes has been found, the second of the images is transformed. Shifts between marked point in the first image and transformed second image are considered to be absolute.

3) This method is used then, when it is not possible to guarantee that compared images have the same scale. In this case, such a translation, rotation and homotetie (a scale change) is searched in order that the sum of deviation quadrates in the points marked by the user may be minimal. Analogously with the item 2), the linear transformation is searched in the complex plane with the difference that abs (a) need not to equal to 1. It is possible to employ this method only if we accept an assumption that the size of surfaces has not been changed by deformation. After the linear transformation with required attributes has been found, the second of the images is transformed. Shifts between marked points in the first image and transformed second image are considered to be absolute.

After the absolute shifts have been found, the conform scan, determined by the absolute shifts in the set points is searched. This display is then employed for shifts matrix generation in the sufficiently dense grid of points. For images of 2048x2048 pixels, the grid with the step of 64 pixels is applied. This matrix of shifts is an output of the comparator. The system has also a possibility of graphic output in which the shifts vectors are plotted in the nodal points of a grid. To reach the maximum possible accuracy of printing on all possible types of printers, the system TEX has been chosen. The comparator generates automatically the source set for TEX, and therefore it is sufficient to translate this set using some of the TEX version (quite sufficient is the version Plain TEX) and print out. When employing laser printers 300 dpi or some better, the printing accuracy is comparable or better than an error caused by discretization of the image processed by the comparator.

5. Objects of microstrain analysis*

The deformations caused by machining were analysed. The machine technologies give many exemples about the influence of machining conditions on the resulting properties of produced parts. The next figure shows the deformation of the plate due to the

grinding (Fig. 2) and its analysis was carried out according the technique and by the equipments describes in the paper.

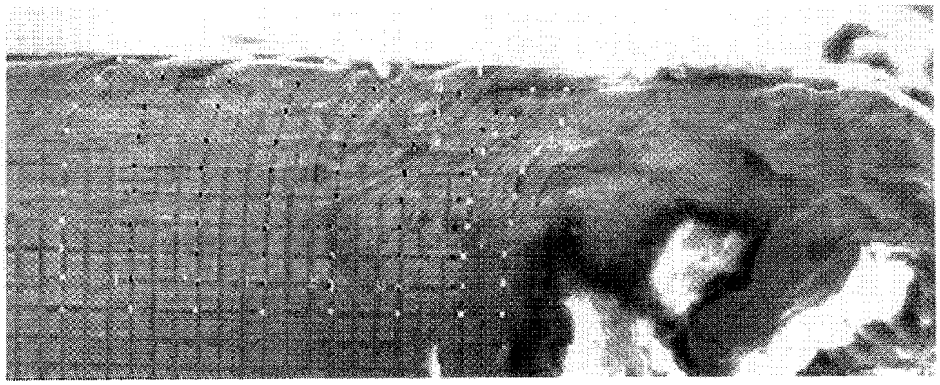

Figure 2. The plate edge after grinding, 400 x magnification. The mechanically cut grid with the step of 10 μm can be seen on the lef t hand side.

The microscopic pictures of analyzed area are recorded by using of the WinTip software, before and after grinding. The software Comparat is then used for interactive comparation of both images. The relative displacements of individual points in the x , y directions of the area are then determined , (Fig. 3). The obtained data are processed further by the program for strain analysis. The dispalcement values in the ninepoint matrix are processed by the affine transformation and the deformation gradients are calculated from them. The finite strains in x , y directions are then determined , (Fig. 4).

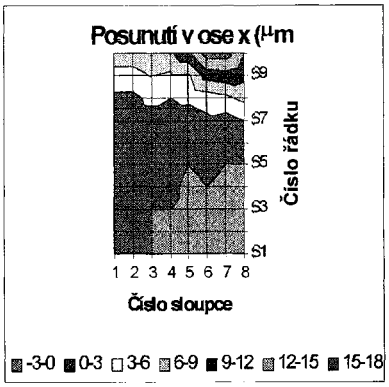

Figure 3. The displacements between the compared points in the x - direction after grinding.

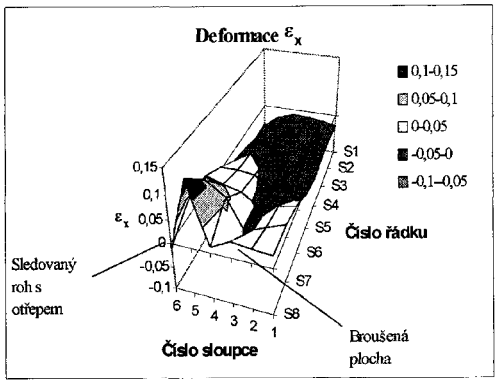

Figure 4. The strains between the compared points in the x - direction after grinding.

* P. Hoftian, PhD Thesis, CTU Prague, Fat. of Mech. Eng., 1998

6. References

[1] Born, M., Wolf, E., Principles of Optics, 4th ed., Pergamon Press, N. Y., London (1970)
[2] Pantoflíček J., Technický obzor (Technical Survey, Prague), 21 (1913)
[3] Hendryks, M. A. N., Identification of the Mechanical Behavior of Solid Materials. PhD. Thesis, TU Eidhoven (1991)
[4] Sciammarella, CA., Bhat, G., An electro-optical system to measure strains. Proc. of 9th Int. Conf. on Experimental Mechanics, TU Denmark, Copenhagen, 5(1990), 1924- 1933.
[5] Kühnert, R., Michel, B., Moire' techniques by means of scanning electron microscopy. Phys. State Solids (a) 89(1985), 163-165.
[6] Davidson, D.L., The observation and measurement of displacements and strain by stereoimaging. Scanning Electron Microscopy 2(1979), 79-86.
[7] Berka, L.; Rüzek, M.: Analysis of microdeformations in a structure of polycrystals. J. Mater.Sci. 19, 5(1984), 1486-1495.
[8] Alais, L., Bomert, M., Bretheau, T., Caldemaison, D., Experimental characterization of the local strain field in a heterogeneous elastoplastic material. Acta metall.mater. 42(1994) 3865-3880
[9] Crostack, H.-A., Fischer, G., Deformation measurement at microstructural level by means of object grating method within SEM. Proceedings of the 15th Riso International Symposium on Materials Science, 1994,275-280
[10] Post , D., Moire Interferometry for Composites. Manual on Experimental Methods for Mechanical Testing of Composites, Pendleton, R. L. - Tuttle, M. E. Eds., SEM, (1989)
[11] Vaclavik, M., Minster, D., Replikace mřížek pro moirovou interferometrii uzitím interfere&m fotografické matrice. Jemná mechanika a optika, 41, 1(1996)
[12] Berka L., Sova M., Experimental Methods of Strain Measurements in Microstructures, Sbomik EAN 1994,32. konference o experimentální analýze napětí.

Acknowledgment

Support of the Grant Agency of the Czech Republic (Project No. 106/95/0596, 106/98/0476) is gratefully acknowledged.

PRECISE AND ROBUST PHASE MEASUREMENT ALGORITHMS

M. F. KÜCHEL
Fachhochschule Aalen
Heinrich-Rieger-Strasse 22/l
D-73430 Aalen
email: mkuech@zws.JJ&aalen. de

1. Abstract

Explicit analytical expressions for families of 3-point, 4-point, 5-point, and 6-point (m-point) phase-measurement formulas are presented, which are exactly valid for 1, 2, 3, 4, (m-2) different values of the phase-steps, applied in the sequence of intensity-measurements. These values are the "design phase-steps", which can be chosen in accordance with the actual necessity. These formulas are equally suited for the temporal as well as for the spatial case. In the spatial case, the formulas can be used as components to design very compact two dimensional convolution kernels, which lead to high spatial resolution and minimized sensitivity to higher-order miscalibration errors.
We also present formulas with m points, which have (m-2) design phase-steps located symmetrical with respect to $\pi/2$. These formulas give the lowest errors over the largest range.
Finally we present formulas which are insensitive to linear phase-shifter calibration errors and at the same time to nonlinearity of the intensity measurements or non-cosine fringe profiles.
The basic theory to derive these formulas and to design two dimensional convolution kernels was established by the author in 1986 and applied during the production of the ESO-NTT primary from 1986 to 1987 within the Carl Zeiss company [1]. It was patented by Carl Zeiss [2], was called the "Direct Measuring Interferometry" (DMI) method, and implemented in the Laser-Interferometer DIRECT 100, which has real-time wavefront measuring and evaluating capability on a set of 480×480 measurement points [3]. The features of this method have been presented in different papers [4,5,6], the theory behind some of the formulas is given in greater detail in [7].

2. Introduction

It is the purpose of this paper to present phase algorithms, which are robust and precise at the same time: now, before telling how, I want to say, why and give an idea for the benefits!
Measurements are taken in real world conditions, that means, they are prone to harmful influences in many respects. As one cannot expect measurement results with mathe-

A. Lagarde (ed.),
IUTAM Symposium on Advanced Optical Methods and Applications in Solid Mechanics, 371-384.

matical precision, it makes sense to search for procedures, which give the most precise result in a given situation. So it was the goal, to find methods and the appropriate formulas which are intrinsically “good conditioned’, that means, if the error function is plotted against any of the error influences, one should encounter a nearly horizontal tangent around the working point. When you are lucky enough to establish such a procedure, then - may be after some calibrations -, you will end up with a stable, robust and precise method!

In order to explain what I mean with good condition, I want to give an example from the field of optics. Suppose you have to design a lens which is intended to be used with a diode laser on the axis only. At first glance one would guess, that it would not be necessary to correct the lens for more than the working wavelength and not for any field angle. But correcting it for a second wavelength will generate a horizontal tangent for the dependence of the focal length from small changes of the wavelength emitted and field correction will generate a horizontal tangent for the aberration coeffcients plotted against the field angle. This will ensure, that no difficulties will be encountered during alignment. I would say, a corrected lens is a “better conditioned creature” than a single (aspherical) lens corrected for spherical aberration and for one wavelength only.

Phase shifting is the most common technique for fringe evaluation in interferometry, fringe projection, moire techniques and other fields, where „ftiges“ are involved. Two principles have established themselves and are widely used:

- the temporal phase shift techniques have a high resolution in space but suffer from the fact, that several very precise phase steps have to be realized in the (time) sequence of measurements, a demand which is difficult to fulfill in production environment;
- the spatial phase shift technique, where the acquisition of only one fringe-measurement is necessary but where the spatial resolution might be not optimal.[1]

In both cases it is difficult to precisely control the values of the phase steps. Especially for the second case, where the intrinsically given phase variations from one camera pixel to the next are used as the phase steps, there is a systematic deviation of the actual phase step from the nominal value by principle. So, one has to deal with a phase step error (linear or higher order, as described later) , which varies across the fringe map and would lead to severe measurement artifacts (reported by others, see for example [9]), unless an algorithm is applied, which is highly tolerant for phase step deviations.

Another source of errors with both, the temporal phase shift technique as well as the spatial phase shift technique, is the nonlinearity of the device, which measures the fringe intensity (normally a CCD-camera). For instance, when the signal is clipped due to saturation, the intensity values transferred to the computer might not be well described by a function $a + b\cos(\phi)$. The same applies in the case of the fringe projection techniques, if a Ronchi ruling is used for projection.

[1] Our aim was therefore to develop a spatial phase shift technique, which is intrinsically robust against vibrations and has a uniform high spatial resolution, which is not the case with the Fourier-method [8].

3. Phase-shifting formulas with m points, which are valid for m-2 values of the phase-step

3.1 THEORY

The theory of deriving the following phase-shifting formulas is given in greater detail in [7]; the following outline is rather briefly.
In two-beam interferometry, we end up with an equation, given below in different forms:

$$I(\phi+\delta) = B\cos(\phi+\delta) + A \tag{1a}$$

$$I(\phi+\delta) = \cos\delta \cdot B\cos\phi - \sin\delta \cdot B\sin\phi + A = \cos\delta \cdot N - \sin\delta \cdot Z + A \tag{Ib}$$

$$I(\phi+\delta) = \mathrm{Re}\{B\exp(i\phi)\cdot\exp(i\delta)\} + A = \mathrm{Re}\{\mathcal{B}\cdot\exp(i\delta)\} + A \tag{Ic}$$

In (la) A is the mean intensity, B is the modulation of the fringes[2], ϕ is the phase to be measured and δ is the additional phase, which is added to the fringe map for phase shifting purposes. Whereas A, B and ϕ depend on the spatial coordinates x,y of the camera, δ is constant over the whole interferogram and is changed in steps in order to generate additional equations. For (lb) the cos-term is expanded and the products $B\cos\phi$ and $B\sin\phi$ are substituted by N and Z respectively. For (1c) $B\cos(\phi+\delta)$ is substituted by the real part of the complex expression $B\exp(i\phi)\cdot\exp(i\delta)$. We interpret $B\exp(i\phi)$ to be a vector B in the complex plane, which has the two components iZ and N in a Cartesian coordinate system and the magnitude B and phase ϕ in a polar coordinate system:

$$\mathcal{B} = \begin{pmatrix} N \\ iZ \end{pmatrix} = Be^{i\phi} \;\rightarrow\; \phi = \arg(\mathcal{B}) = \arctan\frac{Z}{N} = \arctan\frac{B\sin\phi}{B\cos\phi};\quad B = \sqrt{Z^2+N^2} \tag{2}$$

For phase-shifting, three intensity measurements I_1, I_2, I_3 are taken at each pixel of the CCD-camera., with the extra phase-values of δ_1, δ_2, δ_3 applied to the interferogram:

$$\begin{aligned} I_1 &= B\cos(\phi+\delta_1) + A = \cos\delta_1 \cdot N - \sin\delta_1 \cdot Z + A \\ I_2 &= B\cos(\phi+\delta_2) + A = \cos\delta_2 \cdot N - \sin\delta_2 \cdot Z + A \\ I_3 &= B\cos(\phi+\delta_3) + A = \cos\delta_3 \cdot N - \sin\delta_3 \cdot Z + A \end{aligned} \tag{3a}$$

$$\begin{pmatrix} \cos\delta_1 & -\sin\delta_1 & 1 \\ \cos\delta_2 & -\sin\delta_2 & 1 \\ \cos\delta_3 & -\sin\delta_3 & 1 \end{pmatrix} \begin{pmatrix} N \\ Z \\ A \end{pmatrix} = \begin{pmatrix} I_1 \\ I_2 \\ I_3 \end{pmatrix} \tag{3b}$$

Provided that the determinant

$$DET_{123} = \sin(\delta_2-\delta_3) + \sin(\delta_3-\delta_1) + \sin(\delta_1-\delta_2) \tag{4}$$

of this linear system of equations is not zero, we get the solutions for N, Z and A:

$$N = I_1\frac{[\sin\delta_3 - \sin\delta_2]}{DET_{123}} + I_2\frac{[\sin\delta_1 - \sin\delta_3]}{DET_{123}} + I_3\frac{[\sin\delta_2 - \sin\delta_1]}{DET_{123}} \tag{5a}$$

$$Z = I_1\frac{[\cos\delta_3 - \cos\delta_2]}{DET_{123}} + I_2\frac{[\cos\delta_1 - \cos\delta_3]}{DET_{123}} + I_3\frac{[\cos\delta_2 - \cos\delta_1]}{DET_{123}} \tag{5b}$$

---

[2] The quantity $C=B/A$ is the „contrast“ according to the definition of Michelson; in some of the literature C is called the „modulation“.

$$A = I_1 \frac{\sin(\delta_2 - \delta_3)}{DET_{123}} + I_2 \frac{\sin(\delta_3 - \delta_1)}{DET_{123}} + I_3 \frac{\sin(\delta_1 - \delta_2)}{DET_{123}} \qquad (5c)$$

For us, the equations (5a) end (5b) are the most interesting. Both vector-components, *N* and *Z*, which establish the vector *B* in the complex plane, are built up as a weighted sum of the three intensity measurements. It is important to notice, that the equations (5) are mathematical identities, provided that the phase constants δ_k and the intensity measurements I_k are known with infinite precision. In this case, the computed quantities DET_{123}, *N, Z, A* are exact; the same is true for the derived quantities *B* and ϕ. If under real world conditions, the phase-values δ_k deviate from the values which we suppose they would have, but instead have the values δ_k*, then the equations will not deliver the correct results for DET_{123}, *N, Z, A, B* and ϕ. Instead the more or less faulty values DET_{123}*, *N*, Z*, A*, B** and ϕ* are derived. So errors occur due to wrong values for the additional phase δ_k, especially the phase-error $\Delta\phi = \phi^* - \phi$.

Until here, there was nothing really new! Now we will introduce the new and most important idea (see also [2]): the only thing actually said about the values for δ_1, δ_2, δ_3 is, that the determinant DET_{123} should not be zero. If we would use another set δ_2, δ_3, δ_4, for the additional phase-values for instance, we should end up with essentially the same vector *B*! So if we use in total *m* different values for the additional phase δ_k, performing *m* intensity measurements and collect them into *(m–2)* packages, each package containing three successive measurements, we will be able to compute *(m–2)* vectors B_1 to $B_{(m-2)}$, which all shall point in the same direction and all shall have equal magnitude. So, we are free to build a new "super-vector" *B*, as a **weighted vector-sum** of those vectors, using the weighting-factors $\propto_1$ to $\propto_{(m-2)}$

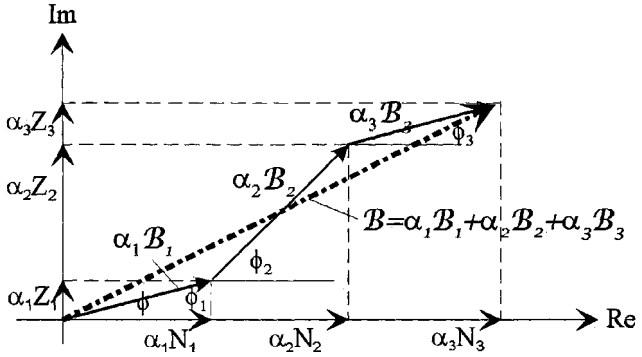

Figure 1: Example of the construction of a 5-point formula: three vectors B_1 B_2 B_3 added with weighting factors $\propto_1 = 0.25, \propto_2 = 0.5, \propto_3 = 0.25$, to set up the new vector *B*, shown for a case, where the phase-steps $\Delta\delta$ deviate considerably from their nominal value

$$\mathcal{B} = \alpha_1\mathcal{B}_1 + \alpha_2\mathcal{B}_2 + \ldots + \alpha_{(m-2)}\mathcal{B}_{(m-2)} = \alpha_1\begin{pmatrix} N_1 \\ iZ_1 \end{pmatrix} + \alpha_2\begin{pmatrix} N_2 \\ iZ_2 \end{pmatrix} + \ldots + \alpha_{(m-2)}\begin{pmatrix} N_{(m-2)} \\ iZ_{(m-2)} \end{pmatrix} \qquad (6)$$

We will show, that this new vector B will not only act as the individual components, but can have new characteristics concerning the phase-values δ_k, for which the mathematical correct value for ϕ results. Like an achromatic lens has the same focal length for more than one wavelength, the new vector B can have the correct argument ϕ for more than one set of phase-values δ_k or phase-steps $\delta=\delta_k-\delta_{(k-1)}$. Tailoring of the features of B is done by calculating and applying the appropriate weighting factors α_1 to $\alpha_{(m-2)}$ to the vectors B_k. We will show, that B can either be given ultimate robustness against false phase-steps with reasonable errors $\Delta\phi$ in between the design phase steps, or can be made to create very small errors $\Delta\phi$ over a smaller range for δ.
For reasons of simplicity, we will restrict ourselves to equal phase-steps (linear phase-shift miscalibration). The basic phase-step, from which all the vectors B_k are originally calculated, is named δ. Additional phase-steps, for which only the super-vector (the weighted sum of the vectors B_k) has the correct argument ϕ are named $\beta_1, \beta_2, \ldots, \beta_{(m-3)}$.

3.2 THE GENERAL 3-POINT FORMULA

We suppose, three measurements are taken with the phase-values increasing by δ in each measurement, and having a zero additional phase for the central measurement (this is an important assumption!): $\delta_1=-\delta$; $\delta_2=0$; $\delta_3=\delta$.

$$I_1 = B\cos(\phi-\delta)+A \qquad (7a)$$

$$I_2 = B\cos(\phi)+A \qquad (7b)$$

$$I_3 = B\cos(\phi+\delta)+A \qquad (7c)$$

Then the general 3-point formula (which is only exact for the phase step value δ) is immediately derived from (5a) and (5b):

$$N = -\sin\delta\cdot I_1 + 2\sin\delta\cdot I_2 - \sin\delta\cdot I_3 \qquad (8a)$$

$$Z = (1-\cos\delta)\cdot I_1 + 0\cdot I_2 - (1-\cos\delta)\cdot I_3 \qquad (8b)$$

According to (8), Z and N are derived by a convolution of the intensity measurements I_1 to I_3 by one kernel for the numerator and one kernel for the denominator. In the following we will associate with the components of those kernels the symbols $z_1, z_2, \ldots, z_m$ and $n_1, n_2, \ldots, n_m$ for a m-point formula. The general form for the computation of ϕ is then:

$$\tan\phi = \frac{z_1 I_1 + z_2 I_2 + \ldots + z_m I_m}{n_1 I_1 + n_2 I_2 + \ldots + n_m I_m} \qquad (9)$$

Rather than to compute absolute values for B, it is sufficient in most cases, that a quantity proportional to B is achieved. Then it is possible to cancel out common factors in the denominator and the numerator of (9), in order to simplify the kernels further. We will do so for the rest of the paper. Then we can present the general form for the 3-point formula as:

$$z_1 = +\sin\left(\frac{\delta}{2}\right) \qquad z_2 = 0 \qquad z_3 = -\sin\left(\frac{\delta}{2}\right) \qquad (10a)$$

$$n_1 = -\cos\left(\frac{\delta}{2}\right) \qquad n_2 = +2\cos\left(\frac{\delta}{2}\right) \qquad n_3 = -\cos\left(\frac{\delta}{2}\right) \qquad (10b)$$

3.3 GENERAL 4-POINT FORMULAS

Due to the limited space, we will give only the results, without any derivation. With our theory, it is possible to derive 4-point formulas, which work exactly for two different values of the phase steps. We have computed two different general 4-point formulas with this feature; the first one has its design phase-steps at $\pi/2$ and δ, the second one has its design phase-steps at δ and $(\pi-\delta)$. Given are the convolution kernels for Z and N:

$$Z:\ \sin\left(\frac{\delta}{2}\right)-\cos\left(\frac{\delta}{2}\right)\quad \sin\left(\frac{\delta}{2}\right)+3\cos\left(\frac{\delta}{2}\right)\quad -\sin\left(\frac{\delta}{2}\right)-3\cos\left(\frac{\delta}{2}\right)\quad -\sin\left(\frac{\delta}{2}\right)+\cos\left(\frac{\delta}{2}\right)$$

$$N:\ -\sin\left(\frac{\delta}{2}\right)-\cos\left(\frac{\delta}{2}\right)\quad \sin\left(\frac{\delta}{2}\right)+\cos\left(\frac{\delta}{2}\right)\quad \sin\left(\frac{\delta}{2}\right)+\cos\left(\frac{\delta}{2}\right)\quad -\sin\left(\frac{\delta}{2}\right)-\cos\left(\frac{\delta}{2}\right) \tag{11}$$

Z:	0	$2\sin\delta$	$-2\sin\delta$	0	(12)
N:	-1	1	1	- 1	

3.4 GENERAL 5-POINT FORMULAS

In the case of 5-point formulas we present here 3 types, which are different with respect to the location, symmetry and multitude of the design phase-steps. It is possible to have 3 zero–positions in the error function at maximum, but that is not guaranteed in any case.

The following formula (13) is the most simple one, and is related to formula (12) for 4-points. It has a fixed design phase-step at $\pi/2$ and an other, which can be chosen, at β_1, where zero-positions of the error function are located. Then due to the symmetry of the formula, an additional zero position at $\beta_2 = \pi - \beta_1$ is generated.

Z:	-1	$+2(1+\sin\beta_1)$	0	$-2(1+\sin\beta_1)$	+1	(13)
N:	-1	$-2\sin\beta_1$	$+2(1+2\sin\beta_1)$	$-2\sin\beta_1$	-1	

In the next formula (14) the design phase steps are δ and β_1, which can be chosen ad lib. and where zero-positions for the error function are generated! Provided $2\delta+\beta_1<2\pi$, then there exists another zero-position of the error function at $\beta_2 = 2\pi - 2\delta - \beta_1$.

$$\begin{aligned}
z_1 &= -z_5 = \cos\delta\sin\beta_1 + (1-\cos\beta_1)\sin\delta - \sin\beta_1\\
z_2 &= -z_4 = -2(2(1-\cos\beta_1)\sin\delta + \sin\beta_1\cos\beta_1)\cos\delta + 2\cos\beta_1((1-\cos\beta_1)\sin\delta + \sin\beta_1)\\
z_3 &= 0\\
n_1 &= n_5 = (1-\cos\beta_1)(1+\cos\delta) - \sin\delta\sin\beta_1\\
n_2 &= n_4 = 2((\cos\beta_1)^2 + 2\sin\delta\sin\beta_1 - 1)\cos\delta + 2(1-\cos\beta_1)\sin\beta_1\sin\delta - 2(1-(\cos\beta_1)^2)\\
n_3 &= 2(\cos\beta_1 - 4\sin\delta\sin\beta_1 + 1 - 2(\cos\beta_1)^2)\cos\delta + 2(2\cos\beta_1 - 1)(\sin\beta_1\sin\delta - \cos\beta_1) + 2
\end{aligned} \tag{14}$$

The third formula has only one design phase-step δ, but the error function has a double zero position there. Provided that $\delta < 2\pi/3$, a third zero position is at $\beta_1 < 2\pi - 3\delta$.

$$
\begin{aligned}
z_1 &= -z_5 = -(1-\cos\delta)\\
z_2 &= -z_4 = 4(\cos\delta)^3 - 6(\cos\delta)^2 - 2\cos\delta + 4\\
z_3 &= 0\\
n_1 &= n_5 = -\sin\delta\\
n_2 &= n_4 = -2\sin\delta(1-\cos\delta - 2(\cos\delta)^2)\\
n_3 &= 2\sin\delta(3-2\cos\delta - 4(\cos\delta)^2)
\end{aligned}
\tag{15}
$$

3.5 GENERAL 6-POINT FORMULAS

We present here only one 6-point formula, which has the two design phase-steps δ and β_1, where zero positions are located. Then the formula generates two more zero-positions for the phase-steps $\beta_2 = \pi - \delta$ and $\beta_3 = 2\pi - 2\delta - \beta_1$. Since the formula is lengthy, we have used abbreviations. Care should be taken when the 4 zero-positions are selected: the formula is not valid for any two-fold zero-position!

$$
\begin{aligned}
z_1 &= -z_6 = -(c1d - c3d)(c3b\cdot s1d - c1b\cdot s1d - s1b\cdot c3d + s1b\cdot c1d)\\
z_2 &= -z_4 = (c1d - c5d)(c3b\cdot s1d - c1b\cdot s1d - s1b\cdot c3d + s1b\cdot c1d)\\
z_3 &= -z_4 = c5b\cdot s3d\cdot c3d - s1d\cdot c1b\cdot c5d + s5b\cdot c1d^2 + s3b\cdot c1d\cdot c3d + c5b\cdot s1d\cdot c1d\\
&\quad + s3b\cdot c5d\cdot c1d + s1d\cdot c3b\cdot c5d + s1d\cdot c1b\cdot c3d + c1b\cdot s3d\cdot c1d + s5d\cdot c3d + s5b\cdot c3d^2\\
&\quad - s3b\cdot c5d\cdot c3d - c1b\cdot s3d\cdot c3d - 2\cdot s5b\cdot c1d\cdot c3d + c3b\cdot s5d\cdot c1d - c5b\cdot s1d\cdot c3d\\
&\quad - c5b\cdot s3d\cdot c1d - c3b\cdot s5d\cdot c3d - c1b\cdot s5d\cdot c1d - s3b\cdot c1d^2 - c3b\cdot s1d\cdot c1d\\
n_1 &= n_6 = s1b\cdot c1d\cdot s1d - c3b\cdot s1d\cdot s3d - c1b + c1b\cdot c1d^2 + s1b\cdot c3d\cdot s3d + c3b\\
&\quad - c3b\cdot c1d^2 - s1b\cdot c3d\cdot s1d - s1b\cdot c1d\cdot s3d + c1b\cdot s1d\cdot s3d\\
n_2 &= n_5 = c1b - s5b\cdot c1d\cdot s1d - c5b + s1b\cdot c1d\cdot s5d + c5b\cdot c1d + s1b\cdot c5d\cdot s1d\\
&\quad - s3b\cdot c5d\cdot s1d - s1b\cdot c1d\cdot s1d - c1b\cdot s1d\cdot s3d - s1b\cdot c3d\cdot s5d + s5b\cdot c3d\cdot s1d\\
&\quad + s3b\cdot c1d\cdot s1d - c1b\cdot c1d^2 + c5b\cdot s3d\cdot s1d\\
n_3 &= n_4 = c3b\cdot s1d\cdot s3d + s5b\cdot c1d\cdot s1d - c5b\cdot c1d^2 - s1b\cdot c3d\cdot s3d - c3b - s1b\cdot c1d\cdot s5d\\
&\quad + s1b\cdot c3d\cdot s1d - s1b\cdot c5d\cdot s1d + s3b\cdot c5d\cdot s1d + s1b\cdot c1d\cdot s3d\\
&\quad + c5b + s1b\cdot c3d\cdot s5d - s5b\cdot c3d\cdot s1d - s3b\cdot c1d\cdot s1d + c3b\cdot c1d^2 - c5b\cdot s3d\cdot s1d
\end{aligned}
\tag{16}
$$

$$
\begin{aligned}
&c1d = \cos(\tfrac{1}{2}\delta); \quad c3d = \cos(\tfrac{3}{2}\delta); \quad c5d = \cos(\tfrac{5}{2}\delta);\\
&s1d = \sin(\tfrac{1}{2}\delta); \quad s3d = \sin(\tfrac{3}{2}\delta); \quad s5d = \sin(\tfrac{5}{2}\delta);\\
&c1b = \cos(\tfrac{1}{2}\beta_1); \quad c3b = \cos(\tfrac{3}{2}\beta_1); \quad c5b = \cos(\tfrac{5}{2}\beta_1);\\
&s1b = \sin(\tfrac{1}{2}\beta_1); \quad s3b = \sin(\tfrac{3}{2}\beta_1); \quad s5b = \sin(\tfrac{5}{2}\beta_1);
\end{aligned}
\tag{17}
$$

3.6 m-POINT FORMULAS WITH A (m-2)-FOLD ZERO AT π/2

As a special case of the formulas presented so far, one can compute m-point formulas with a (m-2)-fold zero at π/2 by a very simple rule: in this case, the weighting-factors $\alpha_1, \alpha_2, ..., \alpha_{(m-2)}$ are simply the binomial coefficients. Another alternative for computing the final values of the kernels is by a very simple recursion, which we can not present here due to the limitation of space. In the following table, the coefficients for the convolution kernels are given until to a 16-point formula. Every first row shows the kernel for the numerator, every second the kernel for the denominator.

3	1	0	-1													
	-1	2	-1													
4	0	2	-2	0												
	-1	1	1	-1												
5	-1	4	0	-4	1											
	-1	-2	6	-2	-1											
6	-1	1	6	-6	-1	1										
	0	-4	4	4	-4	0										
7	-1	-4	15	0	-15	4	1									
	1	-6	-5	20	-5	-6	1									
8	0	-6	6	20	-20	-6	6	0								
	1	-1	-15	15	15	-15	-1	1								
9	1	-8	-14	56	0	-56	14	8	-1							
	1	6	-28	-14	70	-14	-28	6	1							
10	1	-1	-28	28	70	-70	-28	28	1	-1						
	0	8	-8	-56	56	56	-56	-8	8	0						
11	1	8	-45	-48	210	0	-210	48	45	-8	-1					
	-1	10	27	-120	-42	252	-42	-120	27	10	-1					
12	0	10	-10	-120	120	252	-252	-120	120	10	-10	0				
	-1	1	45	-45	-210	210	210	-210	-45	45	1	-1				
13	-1	12	44	-220	-165	792	0	-792	165	220	-44	-12	1			
	-1	-10	66	110	-495	-132	924	-132	-495	110	66	-10	-1			
14	-1	1	66	-66	-495	495	924	-924	-495	495	66	-66	-1	1		
	0	-12	12	220	-220	-792	792	792	-792	-220	220	12	-12	0		
15	-1	-12	91	208	-1.001	-572	3.003	0	-3.003	572	1.001	-208	-91	12	1	
	1	-14	-65	364	429	-2.002	-429	3.432	-429	-2.002	429	364	-65	-14	1	
16	0	-14	14	364	-364	-2.002	2.002	3.432	-3.432	-2.002	2.002	364	-364	-14	14	0
	1	-1	-91	91	1.001	-1.001	-3.003	3.003	3.003	-3.003	-1.001	1.001	91	-91	-1	1

TABLE 1. Convolution kernels for m-point formulas with a (m-2) fold zero of the error function at π/2.

3.7 SYMMETRICAL m-POINT FORMULAS WITH DISTRIBUTED ZERO-POSITIONS

The following formulas are extremely useful, since they produce the smallest errors over the largest region. They are constructed as a superposition of the formulas shown in Table 1. When for instance a new 9-point formula has to be designed, the convolution kernels for the numerator and the convolution kernels for the denominator are established by a weighted sum of the kernels from the 3-point, 5-point, 7-point and 9-point formulas of table 1. Depending on the weighting factors chosen, the new formula will have its zero-positions at different locations. But it is also possible to compute the necessary weighting factors which produce exactly the desired zero-positions. This procedure is best done numerically. I have written a program which delivers the final formula, when I type in the desired number of points and locations of the zero-positions (e.g. the design-phase-steps). As there is a nearly infinite multitude of different formulas, which can be computed, I will only give some examples to demonstrate the superior quality of these new kernels. Since the 9 coefficients have odd and even symmetry, we only give the first 5 of them.

9-point formula with an oscillating error function; useful range $30° < \theta < 150°$:
design phase-steps: 31°, 41°, 61°, 90°, 119°, 139°, 149°
P/V error smaller than $1.2\ 10^{-4}$ fringe-numbers[3] over the range $30° < \theta < 150°$
Z: 1 –6.091 433 622 –7.448 639 941 31.535 820 411 0
N: 1 4.091 433 622 –17.631 507 185 –6.455 673 284 37.991 493 694

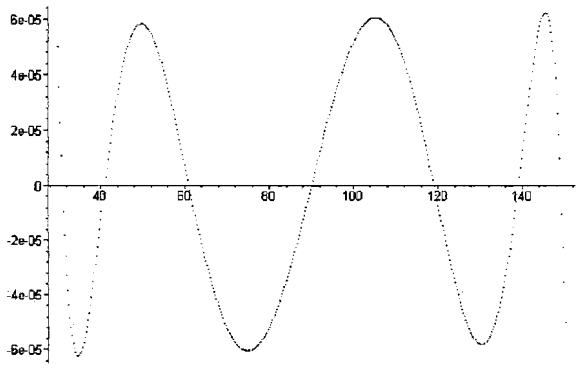

Figure 2: Error function for the 9-point formula given above. The oscillating character is seen clearly, also the location of the design phase-steps, which are the zero-positions of the error function. The units of the abscissa are degrees, the units of the ordinate are fringe-fractions.

9-point formula with an oscillating error function; useful range $50° < \theta < 130°$:
design phase-steps: 51°, 58.4°, 72°, 90°, 108°, 121.6°, 129°
P/V error smaller than $4\ 10^{-6}$ fringe-numbers over the range $50° < \theta < 130°$
Z: 1 –7.159 858 824 –10.844 265 315 44.204 264 421 0,
N: 1 5.159 858 824 –23.163 982 962 –10.196 016 144 54.400 280 564

9-point formula with an oscillating error function; useful range $67.2° < \theta < 112.8°$:
design phase-steps: 67,7°, 72°, 80°, 90°, 100°, 108°, 112.3°
P/V error smaller than $7\ 10^{-8}$ fringe-numbers over the range $67.2° < \theta < 112.8°$
Z: 1 –7.722 147 975 –12.910 753 065 51.920 419 395 0
N: 1 5.722 147 975 –26.355 049 016 –12.654 617 314 64.575 036 709

8-point formula with an oscillating error function; useful range $71° < \theta < 109°$:
design phase-steps: 72°, 80°, 90°, 90°, 100°, 108°
P/V error smaller than $4.4\ 10^{-7}$ fringe-numbers over the range $71° < \theta < 109°$
Z: 0 –5.871 728 539 5.871 728 539 19.236 319 724
N: 1 –1 –14.489 888 400 14.489 888 400

[3] one fringe-period is equivalent to 2π or 360° respectively; in interferometry one fringe-period equals 1 λ

4. Phase-shifting formulas which are insensitive to a nonlinear characteristic curve of the camera and at the same time to fringes, which deviate from the cos-profile.

The formulas given so far can compensate linear "phase-shifter" calibration errors to an extent, which is far beyond measurement precision. This feature is absolutely necessary, when the formulas are used for the purpose of extracting the phase from a map of high density fringes (the DMI technique) and high precision is wanted. We have also used the DMI kernels for extracting the phase out of fringe maps, which have been photocopied or published in papers and had been "hard-clipped", that means, they contain only black and white. The technique still works amazingly good, but it is clear, that you will end up with high frequency artifacts. In this case, the fringe intensity is no longer well described by equation (1a), so the formulas cannot give error free results. The same applies in any case, where the fringe intensity deviates from (1a), as in fringe projection technique, when a Ronchi ruling is projected or in the case of a nonlinear characteristic function for the device, with which the intensity is measured.

In all these cases, the resulting intensity pattern can be described to any level of precision by a function, containing higher harmonics of the phase-function ϕ. Making this function the new starting point for the phase-shifting formulas, the problem is solved totally!

$$\begin{aligned} I &= A + B_1\cos(\phi_1+\delta) + B_2\cos\big(2\cdot(\phi_1+\alpha_2+\delta)\big) \\ &\quad + B_3\cos\big(3\cdot(\phi_1+\alpha_3+\delta)\big) + B_4\cos\big(4\cdot(\phi_1+\alpha_4+\delta)\big) + \ldots \\ &= A - \sin(\delta)\cdot Z_1 + \cos(\delta)\cdot N_1 - \sin(2\delta)\cdot Z_2 + \cos(2\delta)\cdot N_2 \\ &\quad - \sin(3\delta)\cdot Z_3 + \cos(3\delta)\cdot N_3 - \sin(4\delta)\cdot Z_4 + \cos(4\delta)\cdot N_4 - \ldots \end{aligned} \tag{18}$$

$$\phi_1 = \arctan\left(\frac{Z_1}{N_1}\right); \qquad \phi_2 = \phi_1+\alpha_2 = \arctan\left(\frac{Z_2}{N_2}\right)$$
$$\phi_3 = \phi_1+\alpha_3 = \arctan\left(\frac{Z_3}{N_3}\right); \qquad \phi_4 = \phi_1+\alpha_4 = \arctan\left(\frac{Z_4}{N_4}\right) \tag{19}$$

$$\begin{pmatrix} 1 & -\sin(\delta_1) & \cos(\delta_1) & -\sin(2\delta_1) & \cos(2\delta_1) & -\sin(3\delta_1) & \cos(3\delta_1) & -\sin(4\delta_1) & \cos(4\delta_1) \\ 1 & -\sin(\delta_2) & \cos(\delta_2) & -\sin(2\delta_2) & \cos(2\delta_2) & -\sin(3\delta_2) & \cos(3\delta_2) & -\sin(4\delta_2) & \cos(4\delta_2) \\ 1 & -\sin(\delta_3) & \cos(\delta_3) & -\sin(2\delta_3) & \cos(2\delta_3) & -\sin(3\delta_3) & \cos(3\delta_3) & -\sin(4\delta_3) & \cos(4\delta_3) \\ 1 & -\sin(\delta_4) & \cos(\delta_4) & -\sin(2\delta_4) & \cos(2\delta_4) & -\sin(3\delta_4) & \cos(3\delta_4) & -\sin(4\delta_4) & \cos(4\delta_4) \\ 1 & -\sin(\delta_5) & \cos(\delta_5) & -\sin(2\delta_5) & \cos(2\delta_5) & -\sin(3\delta_5) & \cos(3\delta_5) & -\sin(4\delta_5) & \cos(4\delta_5) \\ 1 & -\sin(\delta_6) & \cos(\delta_6) & -\sin(2\delta_6) & \cos(2\delta_6) & -\sin(3\delta_6) & \cos(3\delta_6) & -\sin(4\delta_6) & \cos(4\delta_6) \\ 1 & -\sin(\delta_7) & \cos(\delta_7) & -\sin(2\delta_7) & \cos(2\delta_7) & -\sin(3\delta_7) & \cos(3\delta_7) & -\sin(4\delta_7) & \cos(4\delta_7) \\ 1 & -\sin(\delta_8) & \cos(\delta_8) & -\sin(2\delta_8) & \cos(2\delta_8) & -\sin(3\delta_8) & \cos(3\delta_8) & -\sin(4\delta_8) & \cos(4\delta_8) \\ 1 & -\sin(\delta_9) & \cos(\delta_9) & -\sin(2\delta_9) & \cos(2\delta_9) & -\sin(3\delta_9) & \cos(3\delta_9) & -\sin(4\delta_9) & \cos(4\delta_9) \end{pmatrix} \cdot \begin{pmatrix} A \\ Z_1 \\ N_1 \\ Z_2 \\ N_2 \\ Z_3 \\ N_3 \\ Z_4 \\ N_4 \end{pmatrix} = \begin{pmatrix} I_1 \\ I_2 \\ I_3 \\ I_4 \\ I_5 \\ I_6 \\ I_7 \\ I_8 \\ I_9 \end{pmatrix} \tag{20}$$

If the series expansion (18) for the fringe intensity is truncated after the fourth harmonic, as given in the example of equation (20), one can see, that at least 9 intensity measurements are necessary to solve the resulting linear system of equations. Normally one is only interested in the quantities Z_1 and N_1, from which the phase ϕ can be com-

puted, but nevertheless it is necessary that the rank of the matrix is 9. In order to end up with robust formulas, the magnitude of the determinant of the matrix in (20) should be as big as possible. This is the case, if the phase-steps are properly chosen, for instance in our case of 9 intensity measurements phase-steps of $\delta = 2\pi/9$ equally to (40°) would be a good value to be considered. But you can compute the magnitude of the determinant as a function of δ and chose the phase-steps with regard to that.

Solving eq. (20) for Z_l and N_l in a general (analytical) manner gives the general phase-shifting formula for the case of harmonics up to the 4^{th} order; this is then the basis to compute the vector B_1 as described in section 3.1. If one applies two additional phase-shifts, e.g. in total $m=11$ measurements in our case, it is possible to compute another vector B_2, which can be added up with the first one in such a way, that the resultant vector B will have a zero position of its error function at a second phase-step value, e.g. the formula works with two different design phase-steps. In general, you need $m=2w+2r-1$ intensity measurements to construct a formula which is exact for r different design phase-steps and take into consideration an intensity profile up to the w^{th} harmonic of the phase ϕ.
I have written another program, that computes the kernels for the numerator Z and the denominator N, after typing in the design phase-steps and the harmonics to be taken into account. There might be situations, where you know that the fringe profiles are symmetric, and therefore do not want that the odd-harmonics (3, 5,…) are considered. In this case, you can compute smaller kernels, reducing the effort.

Before I give explicit examples, I want to point out an important special case. This is to consider only the second harmonic, which will cover the biggest part of detector nonlinearity, see for example [10]. In this case, it is not necessary to establish a new theory, but simply construct a new odd-point kernel out of an even-point and an odd-point kernel, by interlacing the two kernels. If both known kernels have the same design phase-steps (the odd kernel will have one in addition, but this doesn't care), then the new kernel will have the same design phase steps, but divided by two! I will give an example to make things clearer.

If you superimpose the last two kernels given in section 3.7, you end up with the following (9+8)-point=17-point kernels (due to symmetry only the first 9 coefficients!):

17-point formula with an oscillating error function; useful range $35.5° < \theta < 54.5°$:
design phase-steps: 36°, 40°, 45°, 50°, 54°
P/V error smaller than $8\ 10^{-8}$ fringe-numbers for α=0.1: range $35.5° < \theta < 54.5°$
Z: 1 0α –7.722 147 975 –5.871 728 539α –12.910 753 065
5.871 728 539α 51.920 419 395 19.236 319 724α 0
N: 1 1α 5.722 147 975 - 1α –26.355 049 016
-14.489 888 400α –12.654 617 314 14.489 888 400α 64.575 036 709
This formula will work for any value of α, for instance for α=0.1, but can be optimized, by applying to α an optimal value. A total set of error-functions can be computed with different values for α (having zero-positions as stated) and then the optimal one chosen.

A very interesting new 9-point phase-step function is gained, if you combine equations (12) and (13) to new kernels:

$$\begin{array}{ccccccccc} -1 & 0\alpha & +2(1+\sin 2\beta_1) & +2\alpha\sin 2\delta & 0 & -2\alpha\sin 2\delta & -2(1+\sin 2\beta_1) & 0\alpha & +1 \\ -1 & -1\alpha & -2\sin 2\beta_1 & +1\alpha & +2(1+2\sin 2\beta_1) & +1\alpha & -2\sin 2\beta_1 & -1\alpha & -1 \end{array} \tag{21}$$

$\pi/4$ is here the naturally given design phase-step. Therefore $\delta = \beta_1 = \pi/4$ will give very good results, but also $\delta = \beta_1 = 2\pi/9$ equal 40° could be considered for example. In this case there will be a second zero-position of the error function located 50°, due to the symmetry of the formula with respect to 45°. Again, the factor α is another degree of freedom in this formula, which can be used for optimization.

Now going back to the general case: as an example of the result of my program, I will now give a 17-point formula, which takes into account all higher harmonics till the 4^{th} and at the same time has 5 design phase-steps 36°, 40°, 45°, 50°, 54°, the same values as in the example above! These are not totally optimal distributed, but for reasons of comparison I chose them. Fig. 3 shows the error-function for the first harmonic ϕ.

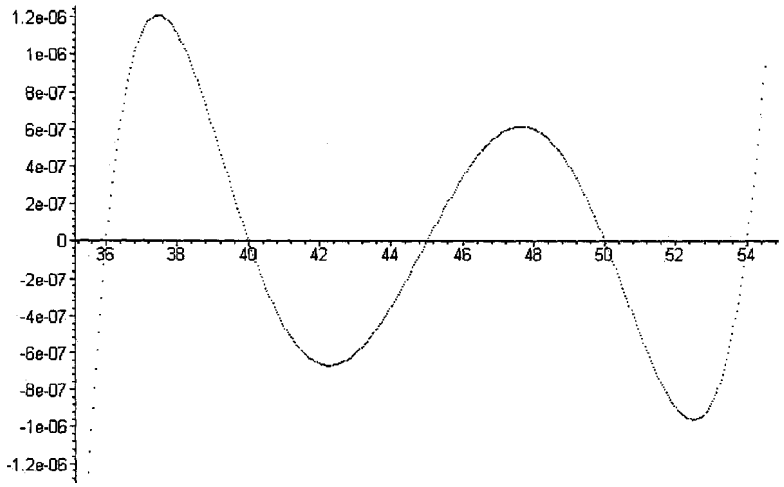

Figure 3: Error function for the 17-point formula given below. The units of the abscissa are degrees, the units of the ordinate are fringe-fractions.

The coefficients for the kernels are:

Z: 1. .277 370 –4.482 025 1.060 792 –14.159 974
11.724 757 10.599 099 10.941 335 0

N: .226 979 1.209 593 3.281 505 –.540 325 –7.540 562
–10.123 640 –3.281 505 9.454 373 14.627 167

5. Miscellaneous

There are some things left, which are important in constructing robust procedures, which I can not consider in detail, but rather would mention it here.

Due to limited space, I can not describe, how to construct two-dimensional convolution kernels, which are based on the new formulas. What I want to do is to give some hints with respect to phase shifting in time as well as in space.

It is very useful to study the error function $\Delta\phi = \Delta\phi(\phi,\theta)$ of the formulas as a function of the two variables ϕ and θ, where ϕ is the phase to be measured and θ is the phase-step value actual applied. As was already pointed out by Schwider et al, this is a periodic function in ϕ. The extreme values of this function are normally found around $\pi/4 \pm n \cdot \pi/2$. Our sketches of the error functions are traces computed for values $\phi = \pi/4$. Due to the periodic character of the error function with a main period of 2ϕ, one can cancel out residual phase-errors by accumulating phase-results from measurements with a randomly distributed starting phase. Alternatively one can accumulate phase-results and applying a continuously changing starting phase, as is done in the interferometer DIRECT 100 with a measurement frequency of 25 Hz.

My new idea is, to add **an odd** number *p=(2n+1)* of measurements (*n=1 or 2 or 3* all would work perfectly), and changing the starting phase in steps by $\psi = n \cdot 2\pi/p$. This is a much better procedure than the "Averaging 3&3" technique, which is reported frequently and was first introduced by Schwider et al [11] and by Koliopoulos [12]. The reason is, that the error function contains mainly terms with an even symmetry with ϕ, which are cancelled out completely by this procedure.

The next point to be considered are higher order phase-calibration errors. I have not dealt with that problem analytically till now, but numerical simulations proved me, that the zero-positions of the error-functions of my formulas are shifted a little bit away from the design phase-steps, when I apply a higher order calibration error to the phase-steps. Therefore one can conclude, that the robustness of the formulas prevent them for going obsolete, and that higher orders can be taken into account by the design of the formulas, if their values are known a priori.

The last point concerns the number of fringes, which one introduces in an interferogram. It is clear, that with higher numbers of fringes, the test set-up is less "common path" and therefore more prone to errors, which are not cancelled out to the same degree, as when the fringes are nulled. This is for the optical side; now we want to consider the phase-measurement side: assuming that you have a phase-measurement error due to any reason, this error by principle will be located between 0 and 2π. In other words, only fringe fractions are subject to errors, not the integer fringe numbers (it is impossible, that 2π is not one period!). Therefore the more fringes you introduce, the higher is the spatial frequency of the errors. These errors are filtered out very easily by any low-pass filtering procedure, as for instance applying a Zernike fit to the phase-

map. Since the most pronounced remaining errors have a period of π which equals half a fringe period, they are nearly completely washed out by averaging 2x2 pixels, if the carrier frequency is chosen to have 4 pixels at one fringe period ($\rightarrow$ phase-shift of 90°). With the DMI method, a reproducibility of better than 0.05nm r.m.s. is reached by averaging during one minute, but without any averaging in space!

6. References

/1/ Küchel,M., W.Wiedmann: "In-process metrology for large astronomical mirrors". Invited Paper in *Advanced Optical Manufacturing and Testing,* San Diego, California, 9-11 July (1990), Proc. SPIE Vol. 1333, pp. 280-294.

/2/ Küchel, Michael (Erfinder), Firma Carl Zeiss (Patentinhaber); Europäische Patentschrift: "Verfahren und Vorrichtung zur Messung eines phasenmodulierten Signals". Pat.Nr. 0 455 218 B1 . Anmeldetag: 30.4.1991, Priorität 02.05.90 DE 4014019. Küchel, Michael (Inventor), Carl-Zeiss-Stiftung (Assignee); United States Patent: "Method and Apparatus for Phase Evaluation of Pattern Images used in Optical Measurement". Pat.Nr. 5,361,312. Date of Patent: Nov. 1, 1994.

/3/ Küchel,M.: "The new Zeiss interferometer". Special Paper in C.P.Grover (ed.) *Optical Testing and Metrology III: Recent Advances in Industrial Optical Inspection,* San Diego, California, 9-11 July (1990). Proc. SPIE Vol. 1332, pp. 655-663.

/4/ Freischlad,K., M.Küchel, K.H.Schuster, U.Wegmann, W.Kaiser: "Real-time wavefront measurement with lambda/10 fringe spacing for the optical shop". in C.P.Grover (ed.) *Optical Testing and Metrology III: Recent Advances in Industrial Optical Inspection,* Proc. SPIE Vol. 1332, (1991), pp. 18-24.

/5/ Küchel,M.F.: "Advances in interferometric wavefront-measuring technology through the Direct Measuring Interferometry method". in Baker (ed.) *Commercial Applications of Precision Manufacturing at the Sub-Micron Level,* Proc. SPIE 1573, London, United Kingdom, 19-21 Nov. (1991), pp.159-162.

/6/ Küchel,M.F: "Advanced Interferometry at Carl Zeiss", Invited Paper in *International Symposium on Optical Fabrication, Testing, and Surface Evaluation,* Tokyo, Japan 10-12 June, (1992), Proc. SPIE Vol. 1720, pp. 452-455.

/7/ Küchel,M.F.: Some Progress in Phase Measurement Techniques", in W. Jüptner and W. Osten (eds.), *Fringe '97, Automatic Processing of Fringe Patterns,* Bremen, Germany, Sept. 15-17, 1997, Akademie Verlag, Berlin pp. 27-44.

/8/ Takeda,M., H.Ina, S.Kobayashi: „Fourier-transform method of fringe-pattern analysis for computer-based topography and interferometry. J. Opt. Soc. Am. 72 (1982) 156-160.

/9/ Pirga,M., M. Kujawinska: "Errors in two-directional spatial-carrier phase shifting method" , in M. Kujawinska, R.Pryputniewicz, M.Takeda (eds.), *Interferometry VII: Techniques and Analysis,* 11-12 July 1995, San Diego, SPIE Proceedings Vol. 2544, pp. 112-121.

/10/ Creath,K. : "Phase-Measurement Interferometry Techniques", E. Wolf (ed.) in *Progress in Optics XXVI,* Elsevier Science Publishers B.V., 1988, pp. 351-393.

/11/ Schwider,J., R.Burow, K.-E.Elßner, J.Grzanna, R.Spolaczyk and K.Merkel: „Digital wave-front measuring interferometry: some systematic error sources". Appl. Opt., 22 (1983) 3421-3432.

/12/ Koliopoulos,Ch.L.: „Interferometric Optical Phase Measurement Techniques". Ph.D. Thesis, U. Arizona (1981).

Holographic photorefractive images storage for applied metrology by interferometry

Ph. C. LEMAIRE, M. P. GEORGES
Centre Spatial de Liège, Université de Liège
Parc Scientifique du Sart Tilman, Avenue du Pré Aily
B-4031 ANGLEUR (LIEGE)
tel : 32-4-3676668, fax : 32-4-3675613, mail : mgeorges@ulg.ac.be

Abstract

We present a holographic camera based on a photorefractive crystal. The historical interest of this recording support is first discussed for its application in holographic interferometry. Afterwards, based on our experiences, a prototype instrument is described and attention is paid on the accuracy and interpretation of the measurements (from the interference pattern to the object displacement). Some applications are presented and show the versatility of the instrument as well as the high quality of the results. Future prospects are then discussed.

1. Introduction

1.1. HOLOGRAPHIC INTERFEROMETRY BASICS

Holographic Interferometry (HI) is a powerful whole-field optical method permitting the contactless displacements measurement in the micrometric to submicrometric ranges [1,2,3]. It is employed in numerous applications such as strain/stress analysis, flow/damage detection, resonance modes visualization and measurement, monitoring of crystal/protein growth, velocity fields and convection processes observation in fluids, among others [3,4]

HI consists in producing the interference between two (or more) wavefronts (WF), at least one of which being recorded as a hologram in a photosensitive plate. The recording step requires the superimposition of the object beam having travelled via the studied object and of a reference beam taken from the same light source (figure 1). At the readout step the hologram is illuminated by the same reference beam that has served for the recording. One

A. Lagarde (ed.),
IUTAM Symposium on Advanced Optical Methods and Applications in Solid Mechanics, 385–399.

generally distinguishes several procedures. In real-time HI only one hologram is recorded. At the readout step, the object is still illuminated and one observes the interference pattern (interferogram) resulting from the superimposition of the WF diffracted by the hologram and the one coming directly from the object (transmitted through the hologram). Each variation is then observed directly (*live fringes*). The double-exposure HI requires the recording of two holograms in the same plate. A further readout step shows the superimposition of both stored WF (*frozen fringes*). A third technique exists for the case of vibrating objects : the time-average HI. The hologram is recorded during the vibration of the object and over a time longer than the vibration period.

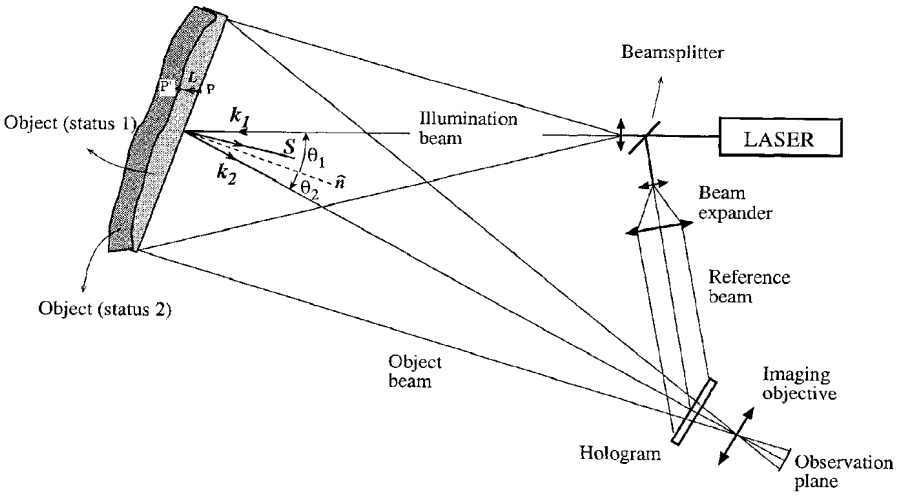

Figure 1.

In real-time and double-exposure, the interference pattern in the observation plane is of the type

$$I(x,y) = I_{average}(x,y)\left[1 + m(x,y)\cos\left(\phi(x,y)\right)\right] \qquad (1)$$

where $I_{average}$ is the average intensity of the interferogram, m is the contrast and ø is the phase difference between both WF. In time-average HI, it can be shown that the fringes have the profile of the Bessel function J_0^2 with maximum of the latter at the vibration node. In the case of opaque objects that reflect the light diffusively, the quantity ø is related to the displacement vector $\boldsymbol{L}$ of each object point by

$$\phi = \boldsymbol{S} \,.\, \boldsymbol{L} = M\, 2\pi \qquad (M \text{ integer}) \qquad (2)$$

where $\boldsymbol{S}$ is the sensitivity-vector defined as the bissector of the illumination and observation vectors (resp. $\boldsymbol{k}_1$ and $\boldsymbol{k}_2$. Equation (2) indicates that bright fringes appear when the phase

difference is a multiple integer of 2π. We will see later how to calculate the displacement $\boldsymbol{L}$ from a measurement of ϕ .

1.2. THE PHOTOREFRACTIVE CRYSTALS FOR HOLOGRAPHIC RECORDING

A crucial element of HI is the photosensitive medium used for the hologram recording. The interesting figures of merit are principally the energetic sensitivity (that gives the response time) and the diffraction efficiency defined as the ratio between the diffracted intensity and the reference/readout intensity (giving the quantity of light that can be used to recover the holographic image). Other features are important for the applicability of HI : the self-processing and the erasability/reusability of the medium.

The classical media used for the hologram recording are the silver halides and the thermoplastics [5]. Both have a high sensitivity (so they require few luminous intensity for a fast recording) and generally exhibit high diffraction efficiency (of a few % to tens of %) which is largely cumfortable to observe with CCD cameras. Nevertheless, silver halides require chemical processing in a remote location (dark room) and repositioning before the readout step, what limits their use. Thermoplastics require electric charging and heating before recording and cooling down after. They can in principle be reused (plates) but a limited number of times (about 100) due to their deterioration by dusts (rolls can be used to avoid this problem). Nevertheless thermoplastic systems are cumbersome and the hologram is available after tens of seconds. With both materials, at the readout step, the ratio of the beams (object/reference) has to be changed in order to equalize the intensities of both WF and to maximise the interferogram contrast. This decreases the userfriendliness of the recording media.

Another class of recording materials for HI is the one of the photorefractive crystals (PRCs) [6]. In these crystals charge migration appears, under the photoconduction effect, between illuminated and dark zones that result from the interference between the object and the reference beams. After trapping in crystal defects of the non illuminated zones, a local space charge field is created and modulates the refractive index through the linear electro-optic effect, yielding a phase hologram. This process is dynamic and reversible and can take place under thermal diffusion (diffusive regime) and/or and external electric field (drift regime). Particularly, the PRCs belonging to the sillenite family, $Bi_{12}SiO_{20}$ (BSO), $Bi_{12}GeO_{20}$(BGO) and $Bi_{12}TiO_{20}$ (BTO), have been studied for applications in HI because they are among the most photosensitive. One generally distinguishes two particular configurations with these crystals which exhibit interesting properties that can be used advantageously in HI. The first one is the anisotropy of diffraction, or polarization transfer, that can be observed when no electric field is applied to the crystal (diffusive regime). Before entering the crystal, the polarizations are linearized and, if the angle is correctly chosen, the polarization of the transmitted object wavefront is perpendicular to the diffracted. They can interfere after a second polarizer and the contrast of the interference can be maximised. The second interesting possibility is the coupling effect between beams inside the crystal. It can be shown that all or a large part of the energy can be transfered under some conditions from the reference beam into the diffracted beam. This can be interesting to amplify weak object

beams. The major part of works in HI with PRCs are based on one of these configurations.

Pioneering experiments have been carried out by the group of Huignard. They proposed the double-exposure with BSO at 514 nm for observing phase variations in transparent objects [7]. Later they showed the use of energy transfer applied to vibration visualization by the time-average method [8]. In 1985, Kamshilin and Petrov propose for the first time the use of the anisotropy of diffraction applied to the time-average method with a BSO at 514 nm and a BTO at 633 nm [9]. This configuration has been successfully used later by Troth and Dainty who showed high quality interferograms with double-exposure and time-averaged methods with BSO at 514 nm [10]. In all these examples, the diffuse objects are relatively small (a few cm^2). The largest object studied by holography using PRCs in these early works was a 20×20 cm^2 plate under vibration and with the time-average method as shown by the group of Huignard [11]. They used an external field applied to the crystal to increase the diffraction efficiency and, although the diffraction anisotropy is not insured, a certain degree of polarization separation is present and can serve to obtain good quality interferograms.

Recently, some groups have focussed their works on the development of instruments for applications in industrial or medical fields. They all aim to perform quantitative measurements on opaque objects. The group of von Bally has developed a holographic camera that records sequence of double-exposure [12,13]. It is based on a BTO crystal at 514 nm. Each double exposed hologram is readout and the interferogram is processed by the Fourier transform filtering technique [12] or by phase-shifting [13] considering the double-reference technique (we will discuss these techniques in a further section). With the double-exposure method, they need very short recording times, i.e. high intensities on the crystal. As a consequence, very small objects are examined but this technique is suitable for medical applications. The group of G. Roosen proposed the use of the energy transfer with a special polarization separation technique for obtaining simultaneously two phase-shifted images of the same object displacement [14]. They can so perform quantitative phase measurement of high accuracy based on a single shot. Their holographic camera is breadbaorded and has been successfully used in cw at 514 nm and was furtherly used in pulsed illumination with a ruby laser (694 nm) [15]. In the last case, the wavelength is badly adapted to the sensitivity range of the sillenite crystal. For that reason, a BGO doped copper crystal has been especially developed for increasing the response at these wavelengths. Though the response is weak in these conditions, the quality of the results is acceptable. This is the first use of pulsed illumination with a PRC on an industrial example (turbine blade under vibration).

2. Development of a holographic camera

2.1. CHOICE OF THE METHOD

We have developed a breadboarded holographic camera with the following aims [16,17]. The instrument must be transportable, as compact as possible, observe displacements on large objects (typically 50×50 cm^2), easy to use (the fewest manipulations at the level of the optics), the results must be obtained rapidly and easy to interpret (good quality of images

and computer-aided pattern evaluation). Also the range of applications covered must be as large as possible and the instrument must be sufficiently versatile in its adaptation to the different kind of measurements. Following these considerations, a method was first chosen and a thorough study has been carried out to optimise the set-up. It has to be noted that only continuous lasers were first considered in this development. We will analyse further the possibility of pulsed illumination with this system.

The method used is the real-time HI (RTHI) associated with the crystal configuration exhibiting anisotropy of diffraction. The choice of the latter is justified by the fact that it appears when no electric field is applied to the crystal. It can be shown in these conditions that the diffraction efficiency is maximised at large angles between reference and object beams. This permits to use short focal lengths optics close to the crystal without being disturbed by the reference beam. As a consequence, large objects placed close to the holographic head can be observed. Also, short focal lengths render the optical system very compact, what is also an advantage. At last, anisotropy of diffraction leads to very high contrast of the interferograms. In this configuration, once the necessary polarizers are correctly orientated, there is no further adjustment needed, what copes with the “ease of use” condition. The choice of the RTHI technique is justified by the fact that it is *a priori* open to more applications than other techniques (double-exposure (2EHI) and time-averaging (TAHI)). Indeed, static, dynamic and vibratory displacements can be examined in RTHI. 2EHI can be used also in all cases but is more complicated in the case of the dynamic (continuously evolving) displacements because sequences of double exposed holograms must be related one to another, what necessitates multiplexing procedures. Also, phase quantification techniques are more complicated to introduce with 2EHI. TAHI is only applicable with vibrating objects so basically it is too much limited. Also, phase quantification technique are generally addressed to sinusoidal fringe patterns, what is not the case in TAHI (bessel fringe profiles).

2.2. WORKING PRINCIPLE

The basic scheme of our instrument is shown in figure 2. The whole instrument is included in a casing, including the laser (YAG diode pumped solid state, P=500 mW, λ=532 nm). The light from the laser source is separated by a variable beamsplitter (VBS) into two parts : the reference beam (RB) and the object beam (OB). The OB illuminates the object via a microscope objective (MO). The RB is spatially filtered (SF) and collimated by a lens (L1) before entering the crystal (PRC). With the chosen method, both beams are always incident upon the crystal. Once recorded within a certain response time, the reconstructed image of the object is observed by self-diffraction of the hologram by mean of a CCD camera and objective lens after the crystal. Any variation of the object beam is then directly visualised and if the object is in a new stable status, the first hologram is erased and a new hologram is recorded. Of course, the interferogram disappears during this process and a frame grabber is necessary to record the image. The response time is inversely proportional to the total intensity impinging the PRC and it is mainly given by the reference beam intensity (the object beam intensity is weak when diffuse objects are considered). With the crystal of

BGO doped copper and a reference beam intensity of 2 mW/cm², the response time of the hologram recording (or erasure) is about 8 seconds. This intensity value is a good compromise: if it is higher, the noise by diffusion becomes higher and can degrade the quality of the interferograms. The object areas observed are typically 55 × 37 cm² with object placed at 1 meter. All operations are managed by a computer : holographic operations (shutters SH openings/closing), PZT actuation for phase-shifting (to be explained later), switch for any object stimulation unit (SU) and image acquisition and post-processing.

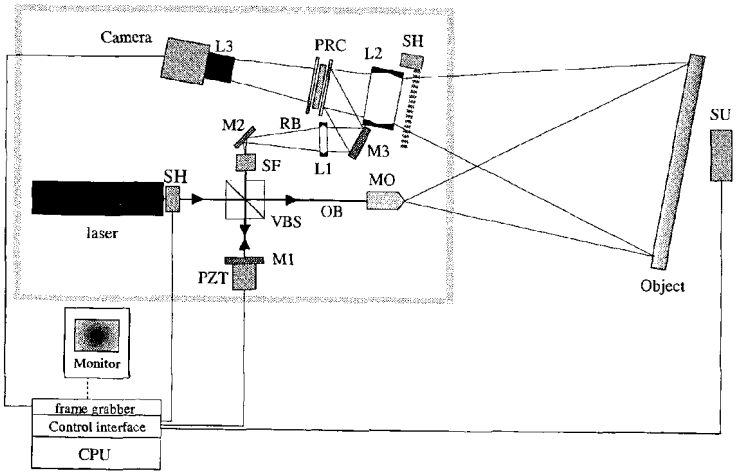

Figure 2.

This prototype has been built after an optimization study [16] of which results are summarized hereafter.

2.3. OPTIMIZATION OF THE TRANSPORTABLE HOLOGRAPHIC CAMERA

2.3.1. *Study of the optical set-up*

The scope of this study is to optimise the ratio of observed area to illumination power. For that purpose, A first solution is to set the object as close as possible to the optical head. This implies to use large crystals : the largest that can be obtained with good optical quality have windows of typically 3×3 cm². Two optical systems were studied with such crystals and their performances compared. The only constraint was that they have to observe the same object area and that the luminous intensity coming from the object at the level of the crystal is the same for both systems. The first system uses a single objective lens after the crystal, with a short (16 mm) focal length (f.1.) and the object is set at 1.3 m from the optical head. The second system uses 2 objective lens : a first one (frontal objective, 50 mm f.1.) images the object at the level of the crystal and the second one (relay objective, 26 mm

f.1.) images the intermediate image onto the CCD. In this case, the object is closer to the optical head : 1 meter.

On this basis, both systems achieve the same field of view (55x37 cm²) but the second system requires only 340 mW to illuminate the object while the first one requires 2 W. Afterwards, their respective response (diffracted, transmitted and diffusion intensities) were measured and the interferometric quality was deduced (average intensity and contrast of interferograms). It is found that the interferogram quality is slightly smaller with the second system, principally due to the fact that the diffusion noise is higher in that case. Nevertheless it has a negligible influence on the final results (quantified phase calculated after phase-shifting). For the final prototype, the second system is then selected because it requires less than 400 mW to achieve typical surfaces of 50×50 cm² and also because the distance of the object is smaller.

2.3.2. *Study of the crystal*

It was interesting to compare the performances of crystals of the sillenite family that can be grown in large sizes, typically 3×3 cm² : BSO, BGO and BGO doped copper (BGO:Cu) samples (although showing interesting responses, the BTO cannot be grown in such dimensions). The response times and diffraction signals were measured for these 3 species. It was found that the BGO:Cu is the one diffracting the most, while BSO has the shorter response times. A BGO:Cu was then selected mainly because it has the best level of diffraction and response homogeneity.

2.4. INTERPRETATION OF THE INTERFEROGRAMS

An important point of this kind of instrument is the way to interpret the fringe pattern in terms of displacement/deformation of the object studied. Two consecutive steps must be considered. First, the analysis of the fringe pattern (1) that gives a continuous mapping of the phase difference ϕ across the surface of the object. Second, the calculation of the displacement in each point of the object on the basis of the phase map (equation (2)).

2.4.1. Phase quantification

Several phase quantification techniques exist [18]. A first class is the phase-shifting methods. They consists of introducing a known phase constant in the cosine of (1) in addition to the phase difference ϕ to be determined. They can be introduced temporally (temporal phase-shifting, TPS) at the holographic readout step by shifting an optical element of one of the beam (e.g. the reference beam) by mean of a piezo translator (see figure 2). Several interferograms with the same object displacement (same ϕ) are acquired sequentially with a given phase steps between each other. The phase ϕ is then calculated with formulas similar to what is used in synchronous detection. This technique is known for giving the best accuracy. The drawback is that the object cannot undergo any displacement during the phase-shifting acquisition (typically 1 sec.). Figure 3 shows the kind of results obtainable with TPS. Figure 3(a) is one of the phase-shifted interferograms

(intensity pattern), (b) is the corresponding phase map modulo 2π (displayed in grey level, 0 rad = black, 2π = white) after phase calculation. A continuous phase map (c) can be derived from (b) by suppressing the 2π phase jumps (phase unwrapping process).

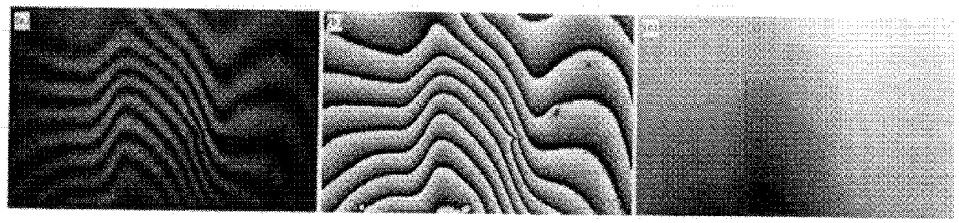

Figure 3.

When fast events are considered, TPS is not applicable so one has to apply alternative techniques. A first one, the simultaneous phase-shifting (SPS), consists of observing the same scene with several channels simultaneously, each of them visualising an image that is phase shifted with respect to the other ones (by considering polarization separation techniques). A second alternative, the Fourier transform (FT) technique, requires only one interferogram for the phase calculation, so it is well adapted to fast events. Before the readout step, a spatial carrier phase $\phi_c = 2\pi x f_x$ is introduced in the cosine of (1), giving a high number of rectilinear fringes parallel to direction x. The interferogram is then Fourier transformed and the information of the phase ϕ is present in the sidelobes that are located at a distance f_x from the Fourier space origin. This lobe is filtered from the remaining and the result is Fourier transformed inversely to obtain the phase ϕ (result similar to figure 3(b)).

We have studied the possibility of introducing TPS and FT techniques in our instrument. The main idea was to analyse the problems arising from the particularities of the PRCs. Also, the possibility of SPS has been analysed by the group of G. Roosen.

Temporal phase-shifting. With PRCs, during the readout of the hologram, the interferogram disappears due to the hologram erasure. This has a consequence on the error on the calculated phase ϕ. It is obvious that this error will depend on the erasure time and the time needed to acquire the sequence of phase-shifted interferograms. In practice, the PRC response time that is set in our instrument is typically 8 to 10 sec and the phase-shifting total time (for 4 interferograms) is 600 msec. In this case, the error is negligible compared to other error sources that are usual to this technique. These other errors have been studied [16,19] and it is found that the prominent limitations to the accuracy are the environmental perturbations (vibrations, air turbulences). An accuracy of $\lambda/40$ RMS is found on the object displacement, say 13 nm for a wavelength λ=514 nm.

Spatial phase-shifting. As described in section 1.2, The group G. Roosen has used this technique with continuous and short pulse illuminations [15]. It is a based on a 2-channels system with a relative $\pi/2$ phase-shift and preliminary acquisition of an average intensity

image. The accuracy of their instrument was certified at 514 nm on a 20×20 cm² object and the error found is λ/31 RMS. It was found to be λ/15 RMS at 694 nm (ruby laser), which is lower (though acceptable in NDT) due to the higher noise and lower level of response of the crystal at that wavelength.

Fourier transform. Generally, the carrier fringes are introduced in the interferogram by producing a tilt in the reference beam before the readout. This is not possible with thick holograms such as those recorded in PRCs, due to the known angular selectivity property. To overcome this we have shown that carrier fringes can be introduced by translating laterally the microscope objective illuminating the object. The errors level is mainly depending on the filtering process and has been analysed previously by numerous authors [18].

2.4.2. *Calculation of the displacement*

This final step, that links the observed phase variation deduced from the interferogram to the determination of the object displacement, involves different kinds of problems and must be carefully carried out if one wants to benefit of the high resolution level of HI. First, as mentioned before, the measurement is the projection of the displacement onto the sensitivity-vector (equation (2)). As a result, totally different displacements can give the same interferogram. If one does not know a *priori* the object movement, 3 measurements have to be performed with different directions of the sensitivity-vector. The displacement of each object point is then computable in any coordinates set by solving a linear equations system. There exist several ways to vary the sensitivity vector (e.g. by considering several illumination sources or camera heads). On this point of view, the use of a photorefractive sensor gives no difficulty in its principle with regards to other systems. We will have the opportunity to illustrate this problem later. Secondly, even if the displacement is predictable, the sensitivity-vector field inhomogeneity (in direction and magnitude) over the object surface cannot be neglected is some cases. This is particularly true when the observation distance, the object dimension and/or the distance between illumination and observation points are of the same magnitude. Such conditions are common in HI measurements and also with our instrument, simply because it is necessary for the compactness and minimises the illumination power. This effect is depicted by the example of figure 4 where an aluminium plate (20 × 16 cm², not represented at scale) undergoes a rotation around a vertical axis. The latter lies in the center of the object plane. Consequently for small and relevant angles, the movement is essentially out-of-plane and the fringes pattern would consist in straight and equally spaced fringes. We measure the rotation angle by computing on a line the slope of the continuous phase map data coming from this interferogram. Moreover, this process performed on different lines gives us the possibility to refine the measurement with a large statistical basis. However, the short distance from the camera (≈ 40 cm) induces significative variations of the sensitivity-vector in direction and magnitude (up to 10%). Therefore we can observe distortions from the straightness in the edges of the pattern. Angle of rotation directly deduced from this interferogram shows

deviations around 5% from the one obtained with a control interferometer (HP 5529 calibrator). After correction of the sensitivity-vector non-uniformity, the correlation with the HP interferometer data is perfect (within its error range) and the dispersion line-to-line is less than 0.4% (< 0.1 arcsec over a range of ± 30 arcsec).

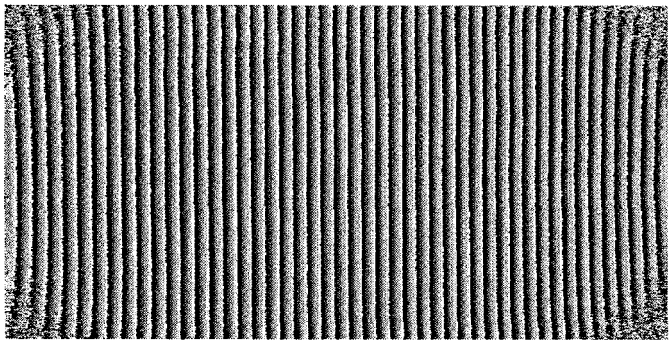

Figure 4.

3. Applications

One can distinguish 3 classes of displacements that can be studied : static, dynamic (non vibratory), and vibratory.

3.1. STATIC DISPLACEMENTS

A static displacement is when the object is in a new stable position or is permanently deformed after a given stimulus. This is the simplest case that can be found. All phase quantification techniques can be applied in this case. An interesting particular applications of this type is found in the search of damages and defects of composite structures (here used in the aeronautical industry). The following results were obtained in the framework of the project EUCLID-CEPA3-RTP3.1. The procedure consists in first recording the hologram of the sample at the rest, afterwards it is heated a few seconds by IR lamp. The heating is then switched off and the object is under thermal relaxation. After a certain time (tens of seconds), the object is in a sufficiently stable deformation status and the hologram can be readout. A typical interferogram observed is shown in figure 3 (a) and the TPS can be applied, to obtain the phase map (figure 3 (b), (c)). The defects and damages are found as local variations of the global residual deformation. To enhance the visibility of the defects, one can use post-processing techniques, such as the differentiation of the continuous phase map. The corresponding result of figure 3 (c) is shown in figure 5 (a). Figures 5 (b) and (c) are other examples.

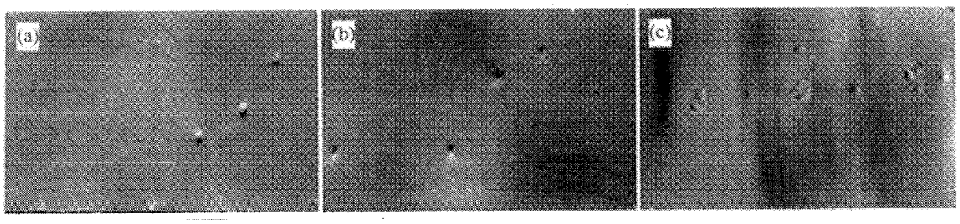

Figure 5.

Another example of static displacement is thermal deformation analysis in order to evaluate a finite element model (FEM) and correlate it to the temperature distribution prediction. The sample is here a honeycomb (core and skin both in aluminium). One of the goal of these measurements is also to determine the influence of the presence of inserts. The thermal stimulation is applied by a sheet electric resistance strapped on the back side of the panel which is clamped on the table by thermally insulated holder. Fig. 6 shows 2 examples of typical interferograms acquired after thermal stabilisation (≈ 1 hour after hologram of object at rest recording). Typical temperature increases are around 3 to 4 °C from ambient. The heater is centred on the honeycomb (25 × 25 cm²) and the observe area is about 15 × 19 cm² (located 7 cm above the holder). A strong but local perturbation is clearly induced by the insert (fig. 6 (b)) in comparison with the case without inserts (fig. 6 (a)). On the methodological point-of-view, more instructive is the comparison of out-of-plane displacement predicted by the FEM (fig. 7 (a)) to the measurement (fig. 7 (b)) that is essentially out-of-plane sensitive. Qualitatively, both shapes appear to be in excellent agreement. However quantitatively the agreement is less good and a more advanced analysis (contribution of the in-plane displacement projected onto the sensitivity-vector) increases this discrepancy. After complementary investigations the basic problem appears to come from the holder. The latter, due to its insulating character and the fact that thermal stabilisation is waited before measurement, is thermally unstable and moves significantly. This superimposition of displacements induces a complicated situation that can only be described by using a 3 sensitivity-vectors set (e.g. 3 viewing directions) and knowing a reference fixed point (e.g. on the holder).

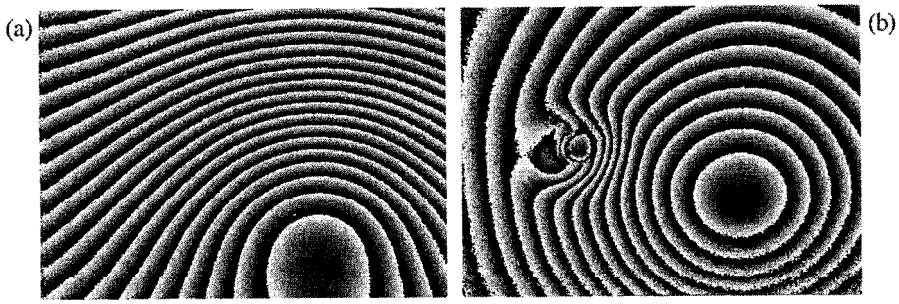

Figure 6.

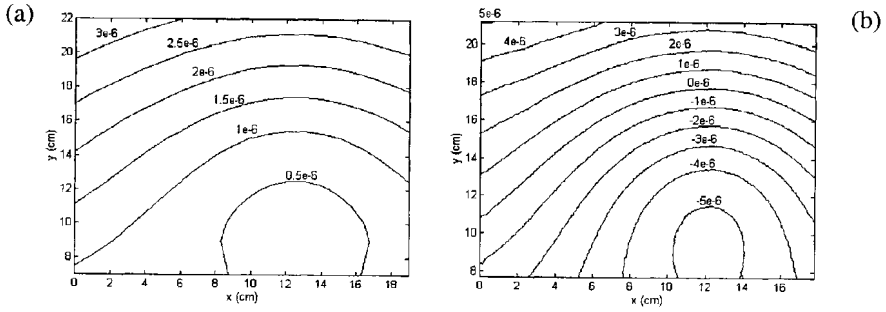

Figure 7.

3.2. DYNAMIC DISPLACEMENTS

A hologram of the object at the rest is recorded. When the object undergoes a continuous displacement, one can observe a sequence of interferograms at different further instants. The problem is that the hologram is erasing at the readout, so the successive readouts must be limited to the time necessary to the image acquisition. When the displacements are too fast to analyze with the TPS technique, a single interferogram analysis technique has to be used, in this case the FT [20]. Figure 8 shows a sequence of 3D plots of the deformation of a wooden panel under heating. The time delay between each image is 1 minute. This application is also an example of the rather good ability of sillenite crystals to store information at medium terms (when kept in darkness). Indeed, storage times up to 1 day can easily be reached.

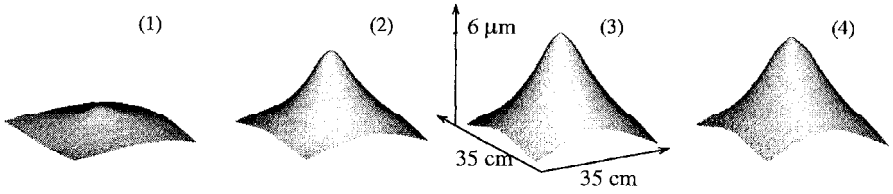

Figure 8.

3.3. VIBRATORY DISPLACEMENTS

The example shown below is an adpatation of our instrument which combines the real-time HI method and the stroboscopic illumination readout. It allows to visualise stationary vibration modes of objects stimulated by sinusoidal excitation. In a first step, an hologram of the object is recorded at the rest. In a second step (readout), a stroboscopic shutter (at the laser output) is synchronised to the vibration and is open at the maximum of modal displacement, when all object points are in a quasi-stationary position. The real-time

method (live fringes) allows an interactive and rapid detection of the resonance frequencies. The sinusoidal shape of the fringes optimises the contrast over the entire image and authorises the use of classical phase quantification techniques. The counterpart is the loss of light due to the duty cycle of the stroboscopic illumination that has to be low (10-20 %) to obtain good fringes contrast. This technique was certified in regard to the particularities of the PRC [21]. Figure 9 shows two examples of turbine blade modes excited by a piezoelectric transducer.

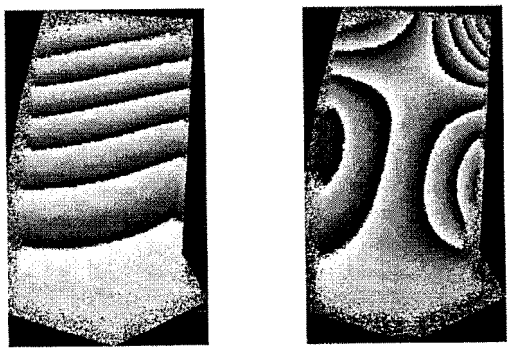

(432 Hz) (2.97 kHz)

Figure 9

4. Conclusion and future prospects

These examples show that, if HI is a high resolution investigation method, it absolutely implies to dispose of an instrument which is dynamic, with a high repetition rate and easy to use and to configure to the specific problem. Photorefractive systems naturally bring these properties and provide in the same time high spatial resolution with low noise interferometric images. We have shown that the apparent disadvantages of the PRCs (relative weak sensitivity, low diffraction efficiencies and erasure at the readout) do not cause significant problems or can be solved by the present evolution of peripheral systems (lasers, cameras, image acquisition HW/SW). In addition, crystals with large sizes and a good optical quality can be obtained now. Consequently, user-friendly systems can be built in order to start metrological works that can be more dedicated to the comparison between measurements and modelling (FEM).

In terms of the system itself, several developments are still needed in order to render the device more flexible and enlarge its field of applications. The improvement of the holographic head compactness is presently under investigation, mainly by considering the use of optical fibers. It offers the main principle advantage to make easier the interfacing with a large fixed laser and to limit the optical head to some basic components (camera, crystal and imaging objectives). It is well known that the main drawback of high resolution methods such HI is the influence of the environmental perturbations (air turbulences, vibrations). This problem must be solved by shortening appropriately the hologram

recording time, the readout time and also the delay between both steps. For this purpose, pulsed lasers are generally useful. In regards of appropriate wavelengths for PRCs, the YAG Q-switched are good candidates. This choice is all the more relevant that these lasers are presently mature for applications in HI (high energies with excellent beam quality) and in good evolution for industrial use (in terms of robustness, compactness and decrease of power consumption). We are investigating the best optical scheme and the laser characteristics which can constitute the basis for an industrial system.

Acknowledgements

This work is supported by the General Direction of Technologies, Research and Energy of the Ministry of the Walloon Region of Belgium. The authors would like to thank Drs. G. Roosen and G. Pauliat at the Institut d'Optique Théorique et Appliquée of Orsay (France) for their helpful discussions and open collaboration.

References

1. Rastogi, PK. , Ed.: *Holographic Interferometry : Principles and Methods,* Springer Series in Optical Sciences **68,** Springer-Verlag, Berlin, 1994
2. Kreis, T.: *Holographic Interferometry : Principles and Methods,* Akademie Verlag Series in Optical Metrology **1,** Akademie Verlag, Berlin, 1996
3. Vest, C.M.: *Holographic Interferometry,* John Wiley & Sons, New York, 1979
4. Smigielski, P.: *Holographie industrielle,* Teknea, Toulouse, 1994
5. Hariharan, P.: *Optical holography : Principles, techniques and methods,* Cambridge Studies in Modern Optics **2,** Cambridge Universtiy Press, Cambridge, 1986
6. Günter, P., Huignard J-P., eds.: *Photorefractive materials and their applications I, Fundamental phenomena,* Topics in Applied Physics **61,** Springer Verlag, Berlin, 1988
7. Huignard, J-P., Herriau, J-P., Real-time double exposure interferometry with $Bi_{12}SiO_{20}$ crystals in transverse electrooptic configuration, *Appl. Opt.* **16** (1977), 1807- 1809
8. Huignard, J-P., Marrakchi, A., Two-wave mixing and energy transfer in $Bi_{12}SiO_{20}$ crystals : application to image amplification and vibration analysis, *Opt. Lett.* **6** (198l), 622-624
9. Kamshilin, A.A., Petrov, M.P., Continuous reconstruction of holographic interferograms through anisotropic diffraction in photorefractive crystals, *Opt. Comm.* **53** (1985), 23-26
10. Troth, R., Dainty, J.C., Holographic interferometry using anisotropic self-diffraction in $Bi_{12}SiO_{20}$, *Opt. Lett.* **16** (1991), 53-55
11. Herriau, J-P., Huignard, J-P., Apostolidis, A.G., Mallick, S., Polarization properties in two wave mixing with moving grating in photorefractive BSO crystals. Application to dynamic interferometry, *Opt. Comm.* **56** (1985), 141-144

12. Dirksen, D., von Bally, G., Holographic double exposure interferometry in near real time with photorefractive crystals, *J. Opt. Soc. Am.* B **11** (1994), 1858-1863
13. Dirksen, D., Matthes, F., Riehemann, S., von Bally, G., Phase shifting holographic double exposure interferometry with fast photorefractive crystals, *Opt. Comm.* **134** (1997), 310-316
14. Labrunie, L., Pauliat, G., Roosen, G., Launay, J-C., Simultaneous acquisition of $\pi/2$ phase-stepped interferograms with a photorefractive $Bi_{12}GeO_{20}$ crystal : application to real-time double-pulse holography, *Opt. Lett.* **20** (1995), 1652- 1654
15. Labrunie, L., Pauliat, G., Launay, J-C., Leidenbach, S., Roosen, G., Real-time double exposure holographic phase shifting interferometer using a photorefractive crystal, *Opt. Comm.* **140** (1997), 119-127
16. Georges, M.P.: *Etude, développement et applications à l'interférométrie d'une caméra holographique dynamique basée sur des cristaux photoréfractifs du type sillénite,* Thèse de doctorat de l'Université de Liège, 1998
17. Georges M.P. , Lemaire, Ph.C., Real-time holographic interferometry with sillenite crystals : a breadboard system for industrial applications II. Optimization, Proc. of JSAP/OSA Topical Meeting on *Photorefractive Materials, Effects and Devices,* Chiba, Japan (1997), 637-640
18. Robinson, D.W., Reid, G.T., Eds.: *Interferogram Analysis : Digital Fringe Pattern Measurement Techniques,* Institute of Physics, London, 1993.
19. Georges, M.P., Lemaire, Ph.C., Phase-shifting real-time holographic interferometry that uses bismuth silicon oxide crystals, *Appl. Opt.* **34** (1995), 7497-7506
20. Georges, M.P., Lemaire, Ph.C., Holographic interferometry using photorefractive crystal : recent advances and applications, Proc. SPIE **2782** on *Optical Inspection and Micromeasurements I,* Besançon, France (1996), 476-485
21. Georges, M.P., Lemaire, Ph.C., Real-time stroboscopic holographic interferometry using sillenite crystals for the quantitative analysis of vibrations, *Optics Comm.* **145** (1998), 249-257

This Page Intentionally Left Blank

NEW GENERATION OF OPTICAL ULTRASONIC SENSORS ADAPTED TO INDUSTRIAL CONSTRAINTS

PHILIPPE DELAYE, GÉRALD ROOSEN
Laboratoire Charles Fabry de l'Institut d'Optique, Unité de Recherche Associée au Centre National de la Recherche Scientifique, Bat. 503, Centre Scientifique d'Orsay, B.P. 147, 91403 Orsay Cedex, France.

In the field of non destructive testing the ultrasonic techniques are widely used for thickness measurements, flaw detection or material characterization [1]. Ultrasonic vibrations are usually generated and detected with piezoelectric transducers, coupled to the tested part by a direct contact or through a water bath or a water jet. This contact, as well as the presence of a coupling liquid, have a negative impact for their use in a lot of industrial applications, particularly for on line control, for the characterization of parts at high temperature or for the inspection of advanced materials. This explains the interest of optical techniques for the detection of ultrasound [2,3] which, despite the fact that they are less sensitive than piezoelectric sensor, have the great advantage of being non contact and of having a large frequency bandwidth. Optical systems developed until now are based on the coherent detection of phase modulation, imprinted on the beam by the vibrating surface, that uses the exact superposition of the wave issued from the target with a plane reference wave. These devices thus only operate with a plane wave signal beam. This requires either to polish the tested surface (what is generally not possible in industrial environment) or to filter the beam (what leads to a strong loss in light power, and subsequently a strong reduction of the detection performances). As a consequence, although largely used in laboratories, laser ultrasonic systems see their spread in industry greatly slowed down by these constraints.

The use of dynamic holographic materials as, for example, photorefractive crystals, relaxes these constraints and allows to realize an interferometer with a large field of view and thus with a large light gathering power. Different systems were proposed and two of them, which have led to industrial developments, will be presented below. They are the photorefractive beam combiner, that is an homodyne detection set-up in which a reference wavefront adapted to the signal beam is reconstructed holographically, and the adaptive photodetector, based on an effect close to the photorefractive effect, the non steady state photoelectromotive force, in which the phase modulation is electronically detected directly on the photorefractive crystal.

1. The Photorefractive Beam Combiner

The first system we will describe is the photorefractive beam combiner that uses two-wave mixing [4-7]. This is the first photorefractive system developed for phase demodulation. This is the system we more particularly studied, as we see it as the most promising among the different systems described in this paper.

A. Lagarde (ed.),
IUTAM Symposium on Advanced Optical Methods and Applications in Solid Mechanics, 401 – 408.

The photorefractive crystal is used as a dynamic holographic medium in which an hologram of the wavefront of the signal beam is written by interference with the pump beam (Fig. 1). This pump beam then reads the hologram that diffracts, in the direction of the transmitted signal beam, a local oscillator that has exactly the same wavefront structure than the transmitted phase modulated signal beam. The signal and its local oscillator are then sent on a detector to demodulate the phase modulation in an homodyne detection scheme. The scheme is then identical to a classical reference beam homodyne detection scheme with the main difference that the local oscillator now perfectly matches the signal beam whatever its structure and without any active stabilization required.

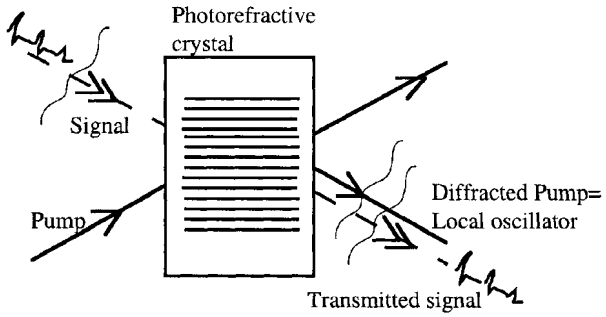

Figure 1 : Schematic diagram of the photorefractive beam combiner

The recorded index grating adapts itself to low frequency variations of the signal beam while it is transparent to the high frequency phase modulation to be detected, leading to a high pass frequency response of the device. The cut-off frequency of the device is proportional to the inverse response time of the photorefractive effect (governed by the pump beam irradiance), whereas the high frequency cut-off is only limited by the detector used and its electronics.

This ability to detect phase modulations on large étendue speckle beams and to be insensitive to slow variations of both the spatial and the temporal structure of the incident signal beam makes this photoerfractive beam combiner very attractive for the detection of ultrasonic signals in industrial environment.

The system presented can be easily described theoretically [8,9]. We take the simplest configuration of a photorefractive crystal in which s-polarized beams write an index grating, characterized by a photorefractive gain in amplitude $\gamma = \gamma' + i\,\gamma''$ (the real part represents the gain related to the index grating component that is $\pi/2$ phase-shifted versus the illumination grating and the imaginary part the unshifted component). The diffracted beam is also s-polarized. This geometry is the so-called "beam coupling geometry" of photorefractive crystals. In the high frequency domain (phase modulation frequency higher than the frequency cut-off of the device) the amplitude of the signal beam $E_d(x,t)$ at the exit of the crystal (of thickness d) is [8] :

$$E_d(d,t) = e^{-\frac{\alpha d}{2}} E_d(0,0)\left[\left(e^{\gamma d} - 1\right) + e^{i\varphi(t)}\right] \qquad (1)$$

The first term of the expression is the diffracted beam amplitude, whereas the second term is the transmitted beam amplitude. From this expression, in the limit of low amplitude phase shift ($\varphi(t) \ll \pi/2$), we have for the intensity incident on the detector :

$$I_d(d,t) = e^{-\alpha d} I_d(0,0)\left[e^{2\gamma' d} + 2e^{\gamma' d}\sin(\gamma'' d)\varphi(t)\right] \quad (2)$$

From this expression and in the limit where the photon noise of the beam on the detector is the limiting noise, we have for the phase measurement a signal to noise ratio :

$$SNR = \sqrt{\frac{2\eta I_d(0,0)}{h\nu\,\Delta f}}\, e^{-\alpha d/2} \sin(\gamma'' d)\frac{4\pi\delta}{\lambda} \quad (3)$$

where η is the quantum efficiency of the detector, $h\nu$ is the photon energy and λ its wavelength, δ is the RMS displacement that creates the phase modulation, Δf is the measurement bandwidth and $I_d(0,0)$ is the signal beam intensity incident on the photorefractive crystal.

We then calculate a normalized detection limit (corresponding to a signal to noise ratio of 1 and normalized to a bandwidth of 1Hz and an incident power of 1W) :

$$\delta_{lim} = \frac{\lambda}{4\pi}\sqrt{\frac{h\nu}{2\eta}}\,\frac{e^{+\alpha d/2}}{\sin(\gamma'' d)} \quad (4)$$

In the limit of zero absorption and optimum gain ($\gamma'd=\pi/2$) we obtain the classical homodyne detection limit $\delta_{lim}^{classic} = \frac{\lambda}{4\pi}\sqrt{\frac{h\nu}{2\eta}}$. This absolute limit can only be reached asymptotically as zero absorption can not be obtained in photorefractive crystals (the photorefractive effect is based on the absorption of photons that creates carriers).

The two parameters that govern the sensitivity of the photorefractive beam combiner are the absorption that has to be reduced and the imaginary part of the photorefractive gain in amplitude γ". For CdTe crystals, successful effort was achieved by the growth laboratory [10], to eliminate all the causes of losses that were not purely photorefractive (inclusions, precipitates,…). For the gain, the aim is to obtain a value of parameter $\sin(\gamma' d)$ the closest as possible to 1. In usual photorefractive crystals, the only way to have a non zero value of γ" is to be in the drift regime, i.e. to apply an external electric field to the crystal. We have shown that for a sufficiently small grating wave vector, and a moderate value of the electric field (far from the trap limited regime), we have [11] :

$$\gamma'' = \frac{\pi n_0^3 r_{eff}}{\lambda\cos\theta} E_0 \quad (5)$$

where n_0 is the refractive index, r_{eff} effective electrooptic coefficient, θ the is half angle between the beams inside the crystal. In this expression E_0 is the amplitude of the applied electric field.

This dependence of the photorefractive gain with the applied electric field allows us to control the efficiency of the photorefractive combiner, and to obtain values of the gain such that $\sin(\gamma'' d)=1$. This high value of the gain combined with a low absorption of the crystal such as $\alpha d < 1.5$), leads to a device having a detection limit of $5\times10^{-8}\ nm\sqrt{W/Hz}$ that is only two times above the ideal detection limit of an homodyne detection working with plane waves. This sensitivity corresponds to the detection of vibrations having an amplitude of the order of 50pm at 1.06μm with a

returned power of 100µW and a detection bandwidth of 100MHz. These values are obtained in a set-up in which the signal beam is carried by large core multimode fiber (corresponding to an étendue of 0.1mm^2 .sr).

Regarding the frequency response we measure the expected high frequency behaviour of this device [11]. The cut-off frequency is of some tens of Hz for a pump power of 22mW.cm^{-2}. This would lead to a cut-off frequency of the order of 1kHz for a pump power of 1W.cm^{-2}. Such a value is enough to eliminate most of the vibrations that can be encountered in the industry. Higher values of this cut-off frequency (greater than 10kHz) were even obtained using a high power long pulse (50µs) laser [9]. In such conditions of measurement, Doppler frequency shifts as high as 1MHz (and displacement velocity around 1m.s^{-1}) could be tolerated [9] indicating the possibility of using such a system for a control on parts moving on-line. At high frequency we are just limited by the detector and its electronics, signals up to 350MHz were obtained with this kind of set-up [12].

Different laboratory prototypes of the device were developped (Fig. 2) and the system is now commercially available [13].

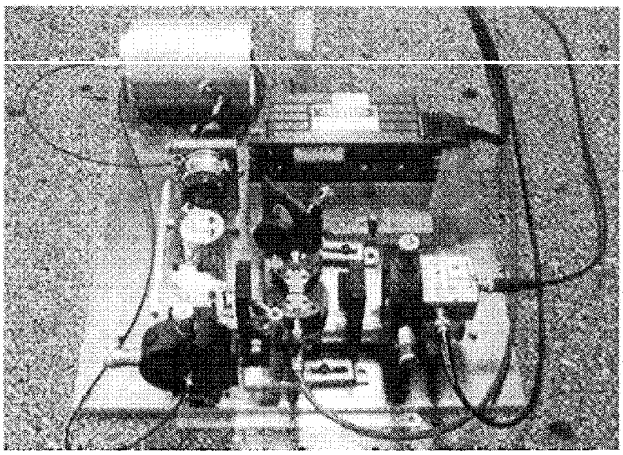

Figure 2 : Photograph of a laboratory prototype developed at the Laboratoire Cherles Fabry de l'Institut d'Optique

2. Adaptive Photodetector

The adaptive photodetector is the simplest of the techniques using photorefractive materials for the detection of ultrasound. It just requires that the phase modulated speckled beam is sent on a photorefractive crystal with another coherent beam. The ultrasonic signal is just given by a measurement of the current that runs through the crystal. The working principle of this adaptive detector based on the non steady state photo electromotive force (photo-emf) [14, 15] is the following. The two incident beams write in the material a space charge field grating through the

photorefractive effect (Fig.3). It also creates in the material a photoconductivity grating and under steady state conditions, without electric field applied to the crystal, no current runs through the crystal. If now a high frequency phase modulation is applied to one of the interfering beams (such as the phase modulation signal induced by the ultrasonic vibration) the illumination grating, and thus the photoconductivity grating shifts with a displacement that reproduces the phase modulation, whereas the space charge field grating does not react (Fig.3). We have thus a photoconductivity grating that moves in a fixed space charge field grating, what induces a non steady state current (or a non steady state photo electromotive force) that reproduces the temporal structure of the rapid displacement. A simple measurement of this current allows to go back to the phase modulation then to the ultrasonic signal.

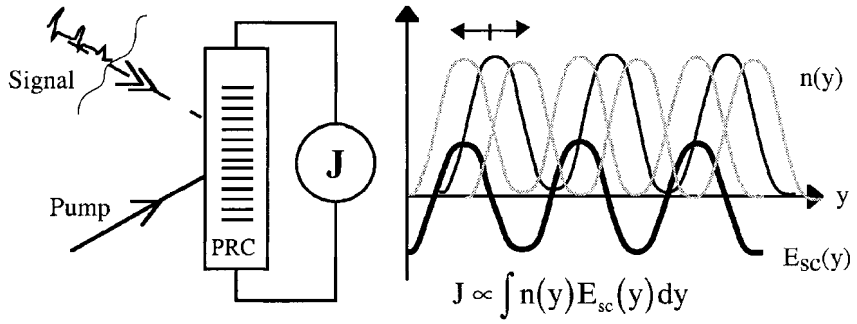

Figure 3 : Schematic diagram of the adaptive photodetector. At right is shown a scheme of the working principle of photo-emf : the bold line represents the space charge field Esc(y) ; the dark line represents the carrier concentration n(y) (i.e. photoconductivity) at equilibrium giving a null current ; the gray line represents the moving carrier concentration n(y) in the presence of a phase modulation giving a transient current.

We see that the operating principle is very simple as it reduces to the measurement of an electronic signal. But the system has other properties that enhance its interest for the detection of ultrasonic signals. First the grating written in the sample can be generalized to an hologram : the hologram of the speckled structure of the signal beam. Second, if the structure of the signal beam changes slowly (compared to the response time of the space charge field grating), the space charge field grating will follow the displacement of the illumination and the system will always remain in steady state, i.e. without any current circulating. So the photo-emf detector, will adapt both to the spatial and the temporal structure of the incident signal beam and will work with slowly varying speckled beams making it very attractive for the detection of ultrasonic signals in industrial environment.

Going further we now make some remarks about the practical realization of this adaptive photodetector. We mentioned in the above description the use of a photorefractive material. The reason is that most of the studies on photo-emf effect were performed in photorefractive materials (GaAs, $Bi_{12}Si0_{20}$). But there is no need of a pure photorefractive material, as its electrooptic properties are not used. What is only needed is a photoconductor with a high dark resistivity. In addition, a transparent material is not even required. A possible limitation is that the adaptive photodetector has an high cut-off frequency that is inversely proportional to the carrier recombination time. Also, the amplitude of the photo-emf depends on the grating period with a maximum that

occurs for grating spacings of the order of the diffusion length of carriers, typically of the order of a few micrometer in semiconductors. The noise characteristics of the system were described in Ref. [15], the sensitivity of the adaptive photodetector to the detection of small phase shifts is at best within a factor of $4\sqrt{2}$ of that of a coherent detector working with plane waves [16].

The implementation of a ultrasonic vibration sensor using this adaptive photodetector was performed with a GaAs crystal illuminated with green (frequency doubled Nd:YAG laser λ=532nm) or red light (He-Ne laser λ=633nm) [17-19]. In such a system, the laser beam is split to form first a signal beam that is sent on the sample under test, and second the pump beam, with which the signal beam that returns from the sample will interfere on the crystal. The current is measured at the electrodes that sandwiched the crystal.

If we now look at the performances (all the data are taken from Ref. [18]) of the ultrasonic detection system based on the adaptive detector, we have first to consider the sensitivity to surface displacement. This sensitivity is reduced compared to a coherent detection system by a factor $4\sqrt{2}$. Experimentally, the sensitivity was measured with an Argon laser (λ=514.5nm) at a value of 3.9×10^{-6} $\mathrm{nm}\sqrt{\mathrm{W/Hz}}$ which is about one order of magnitude larger than the theoretical value. The frequency bandwidth was around 30MHz limited by the electronic circuitry after the crystal (recently a higher bandwidth of 80MHz has been reported, due to a better electronic [20]). In the system the angle between the two beams was limited to 1.5° by the value of the diffusion length in the crystal. This low value of the angle limits the étendue of the system to a value of $5 \times 10^{3}\,\mathrm{mm}^2.\mathrm{sr}$ (taking into account the surface of the detector) and thus reduces its light gathering power. Regarding the low frequency cut-off and the adaptivity of the system to low frequency vibrations it was estimated to 10kHz. This low frequency cut-off also characterizes the ability of the system to measure on samples moving perpendicularly to the line of sight. This photo-emf sensor is able to make measurement on plates moving at speed up to $2\mathrm{m.s}^{-1}$ with only a small reduction of the ultrasonic signal.

We can make some comments about these performances. First the sensitivity is rather low, even if one considers the maximum theoretical value. This will be the most important limitation of this kind of device especially if we compare it with concurrent techniques as the photorefractive beam combiner. The frequency response is adequate. The low frequency vibrations that perturb the measurements are well eliminated (cut-off around 10kHz) and the frequency bandwidth is good (of the order of 80MHz). This frequency response makes the system very efficient for measurements on moving parts, case that is encountered in industry. Nevertheless the system can be limited at very high frequency (>l00MHz) by the presence of a high frequency cut-off linked to carrier recombination time. The étendue of the system is rather poor due to the small angle between the two beams for an optimum signal. The system is very simple to implement and compact (a system comprizing the crystal and its amplifier electronics is announced in a TO-8 photodiode package). An ultrasound detection system based on this adaptive photodetector is commercially available [21].

3. Conclusion

We have described two different systems based on the photorefractive effect and used for the detection of ultrasounds on rough surfaces. Both systems have their advantages and drawbacks. Regarding their performances for the detection of ultrasonic signals, the best system is the photorefractive beam combiner that reaches the sensitivity obtained with plane waves by the heterodyne detection system. For the adaptive photodetector, the sensitivity is inherently smaller by a factor $4\sqrt{2}$ (with even lower experimental values), a factor that is important if one reminds that all optical systems have a reduced sensitivity compared to piezoelectric devices, due to photon noise. Note that the development of systems that can amplify the phase modulation will enable to overpass this limitation. Such components based on photorefractive rings [22] have been successfully implemented [23]. However their operating conditions are still too critical for industrial systems.

Regarding the response time of the systems, the adaptive photodetector and the photorefractive beam combiner are equivalent, with perhaps a little advantage to the adaptive photodetector, that is slightly more rapid at equivalent incident power. These performances are sufficient to give the system a certain insensitivity to a Doppler shift eventually present on the beam (until some $m.s^{-1}$ of speed for the target).

The étendue of the adaptive photodetector is smaller but should be improvable by an optimization of the crystal used as detector. The actual étendue is generally limited by the multimode fibers that are used to carry the beams.

The last point of comparison is qualitative only; this is the ease of use, the simplicity, and versatility of the device. An universal device, that will be optimum in all conditions that can be encountered in industry certainly does not exist. But a system that can cover most of the applications with perhaps slightly changes in its architecture is certainly feasible. To realize such a system, the photorefractive beam combiner is certainly the best, as it has several variants which satisfy various demands (differential response, possibility to work with depolarized beams, …). Less simple than the adaptive photodetector that can be implemented as an electronic circuit, it is still very simple to implement and operate.

These photorefractive sensors bring new perspectives for the spread of laser ultrasonics in industry, allowing for the development of systems that can work on rough surfaces with a sensitivity at least equivalent to other optical systems. The adaptivity of these photorefractive devices to low frequency vibrations gives systems that are insensitive to external perturbations that can be found in an industrial environment.

4. References

1. *Nondestruetive Testing Handbook, , Ultrasonic Testing* ,vol. 7, 2nd ed., edited by A. S. Birks, R. E. Green, Jr. and P. McIntire (American Society For Nondestructive Testing, 1991).
2. J.-P. Monchalin and J. Wagner, "Optical Generation and Detection of Ultrasound", in Other Ultrasonic Techniques (section 10), *Nondestructive Testing Handbook, , Ultrasonic Testing* , **7,** 2nd ed., **op. cit.,** see section 10 , part 1, 1991.
3. C. B. Scruby, and L. E. Drain, *Laser-Ultrasonics: Techniques and applications* (Adam Hilger, Bristol, UK, 1990).
4. R. K. Ing and J.-P. Monchalin , "Broadband Optical Detection of Ultrasound by Two-Wave Mixing in a Photorefractive Crystal", Appl.Phys.Lett. **59,** 3233-3235 (1991).

5. CT. Field, F.M. Davidson, "Photorefractive two-wave mixing in the presence of high-speed optical phase modulation" Appl. Opt. **32,** 5285-5298 (1993).
6. A. Blouin and J.-P. Monchalin, "Detection of ultrasonic motion of a scattering surface by two-wave mixing in a photorefractive GaAs crystal", Appl. Phys. Lett. **65,** 932-934 (1994).
7. L.A. de Montmorillon, I. Biaggio, Ph. Delaye, J.C. Launay, G. Roosen, "Eye safe large field of view homodyne detection using a photorefractive CdTe:V crystal". Opt. Commun. **129,** 293-300 (1996).
8. Ph. Delaye, L.A. de Montmorillon, G. Roosen, "Transmission of time modulated optical signals through an absorbing photorefractive crystal" Opt. Commun. **118,** 154- 164 (1995).
9. Ph. Delaye, A. Blouin, D. Drolet, L.A. de Montmorillon, G. Roosen, J.P. Monchalin "Detection of ultrasonic motion of a scattering surface by photorefractive InP:Fe under an applied DC field' J. Opt Soc. Am. B **14.** 1723-1734 (1997).
10. Grown in the group of J.C. Launay at Action Aquitaine de Recherche en Apesanteur (3AR), B.P. 11, 33165 Saint Médard en Jalles Cedex, France.
11. L.A. de Montmorillon, Ph. Delaye, J.C. Launay, G. Roosen, "Novel theoretical aspects on photorefractive ultrasonic detection and implementation of a sensor with an optimum sensitivity". J. Appl. Phys. **82,** 5913-5922 (1997).
12. Ph. Delaye, A. Blouin, L.A. de Montmorillon, I, Biaggio, D. Drolet, J.P. Monchalin, G. Roosen, "Detection of ultrasonic vibrations on rough surfaces through the photorefractive effect" Proc. SPIE **2782,** 464-475 (1996).
13. PHIRST : PHotorefractive Interferometer Receiver SysTem. UltraOptec inc. 27, rue de Lauzon, Boucherville (Québec) J4B 1E7 Canada.
14. M.P. Petrov, I.A. Sokolov, S.I. Stepanov, G.S. Trofimov, "Non-steady-state photo-electromotive-force induced by dynamic gratings in partially compensated photoconductors", J. Appl. Phys. **68,** 2216-2225 (1990).
15. S.I. Stepanov, "Sensitivity of non-steady-state photoelectromotive force-based adaptive photodetectors and characterization techniques", Appl. Opt. **33,** 915-920 (1994).
16. N. Korneev, P. Rodriguez, B. Sanchez,S. Stepanov, "Non-steady-state photoelectromotive force-based GaAs adaptive photodetectors at 632.8nm", Optik **102,** 21-23 (1996).
17. S.I. Stepanov, I.A. Sokolov, G.S. Trofimov,V.I. Vlad, D. Popa, I. Apostol, "Measuring vibration amplitudes in the picometer range using moving light gratings in photoconductive GaAs:Cr", Opt. Lett. **15,** 1239-1241 (1990).
18. D.M. Pepper, P.V. Mitchell, G. J. Dunning, S. W. McCahon, M.B. Klein, T.R. O' Meara, "Double-pumped conjugators and photo-induced EMF sensors : Two novel, high bandwidth, auto compensating, laser based ultrasound detectors", Mat. Sci. Forum, **210-213,** 425-432 (1996).
19. D.M. Pepper, G.J. Dunning, P.V. Mitchell, S.W. McCahon, M.B. Klein, T.R. O'Meara, "Materials inspection and process control using compensated laser ultrasound evaluation (CLUE) : Demonstration of a low cost laser-ultrasonic sensor", Proc. SPIE **2703,** 91-102 (1996).
20. G.J. Dunning, M.P. Chiao, D.M. Pepper, P.V. Mitchell, "Optimizing the photo-induced-emf response for broadband remote sensing", CLEO 98, paper CF17, 533-534 (1998).
21. PIE-830. Lasson Technologies, 1331, Avenida de Cortez, Pacific Palissades CA 90272, USA.
22. L. Jimenez, J. Sanchez-Mondragon, S.Stepanov, "Enhancement of phase modulation detection sensitivity in ring photorefractive configurations" J. Mod. Opt. **42,** 1965-1969 (1995).
23. Ph. Delaye, L. Frey, A. Mugnier, G. Roosen, "Experimental investigation of a photorefractive ring phase modulation amplifier", Opt. Cormmun. **139,** 148-156 (1997).

ADAPTIVE HOLOGRAPHIC INTERFEROMETRY USING PHOTOREFRACTIVE RECORDING MEDIA FOR FULL-FIELD OPTICAL MAPPING OF STRESS AND DEFORMATION FIELDS

B. POUET, H. TUOVINEN, and S. KRISHNASWAMY
Department of Mechanical Engineering
Northwestern University
Evanston, IL 60208-3020, USA

Abstract: Holographic interferometry can be used to measure the stress-field in optically transparent phase objects, as well as to measure the deformation of diffusively scattering opaque objects. The high spatial resolution of holographic interferometry is desirable in situations where the deformation gradients are so high that the resulting high fringe density requires a high-resolution imaging system. However, classical holography has not always been the technique of choice in experimental stress analysis due to the rather cumbersome processing associated with either photographic or thermoplastic recording media. In this paper, we present two adaptive holographic interferometers that use photorefractive BSO crystals as the dynamic reusable recording medium. The first scheme is for deformation measurement on a diffusively reflective opaque aluminum specimen, and the second scheme is a dual-reference beam system for measurement of stress-induced changes in refractive index of a transparent phase object. Both schemes have been implemented in conjunction with phase stepping in order to provide phase maps rather than just fringe patterns. Applications to modal analysis of vibrating plates, and experimental fracture mechanics are demonstrated.

1 Introduction

In photorefractive crystals (PRCs) under non-uniform illumination, electrons/holes that are trapped in impurities can be photo-excited into the conduction band. These electrons/holes migrate toward areas of dark illumination, where they get trapped again. A non-uniform space-charge field is thus created, leading to spatial modulation of the refractive index via the electro-optic effect. Thus, PRCs can be used to store phase holograms. Since the first observation of the photorefractive effect in $LiNBO_3$ [1], many photorefractive materials with different physical properties have been investigated. In order for PRCs to be widely use as dynamic holographic recording media, they must be able to perform fast recording with moderate laser power and still provide good contrast holographic fringes. The serious difficulty that arises when one uses PRCs for holographic interferometry of diffusely reflecting object is the limited amount of object light that can be collected into the crystal. The sillenite family ($Bi_{12}SiO_{20}$, $Bi_{12}TiO_{20}$, $Bi_{12}GeO_{20}$) exhibits the highest sensitivity among presently known PRCs. Using the

A. Lagarde (ed.),
IUTAM Symposium on Advanced Optical Methods and Applications in Solid Mechanics, 409–414.

high-sensitivity of BSO in conjunction with its efficient polarization separation of the recorded and reconstructed waves when using the anisotropic self-diffraction effect, high quality dynamic holographic interferograms can be obtained [2-4].

In this paper we show that BSO crystals can be used to develop quasi-real-time holographic interferometers. It was found that the slow time response of BTO crystals makes them less suitable for quasi-real time setups such as those described in this paper. In the first part, we demonstrate phase shifting interferometry of vibrating diffusely scattering opaque specimens. For this, a sequence of at least three double pulse interferograms are recorded with different phase shifts of the reference beam. Because of the high quality of the interferometric image, no post digital processing, such as low-pass filtering, is needed before phase unwrapping. In a second experiment, the phase map of a phase object under transient load is obtained through quasi-heterodyne holographic interferometry [5]. In this case, two holograms corresponding to a deformed and the undeformed state are recorded with two separate reference beams. The read-out of the hologram is then done simultaneously with both reference beams. By introducing phase shifts between the two reference beams during the read-out, the phase maps can be obtained.

2 Experimental Results

2.1 – ADAPTIVE HETERODYNE INTERFEROMETRY FOR DEFORMATION ANALYSIS

The experimental setup used to study the vibration modes of continuously vibrating specimens is shown Fig. 1. An acousto-optic modulator is used to pulse the light from an Argon laser according to the extrema of the acoustic vibrational displacement, allowing continuous recording of a double-pulse hologram. In this way, the intensity recorded on the camera upon readout of the hologram exhibits fringes with a cosine dependence on the deformation. In our experiment a duty cycle of 22% is able to give reasonable cosine fringes, while still providing sufficient intensity. A sequence of three interferograms is obtained. An optical phase shift is introduced by means of the electro-optic modulator in the reference beam during the recording process between the time of the maximum and minimum acoustic deformation.

The first hologram of the sequence has no phase shift between the maximum and minimum deformation:

$$I_1=\beta I_o(1+\cos 2M) \qquad (1)$$

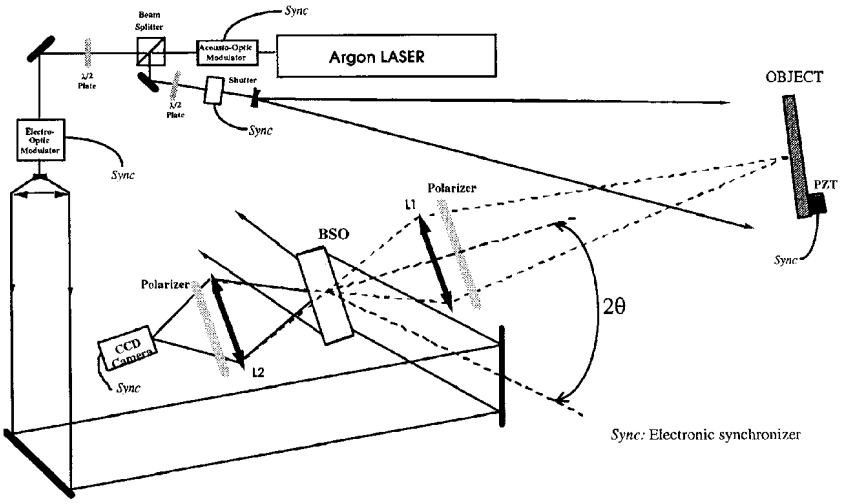

Figure 1: Dynamic holographic interferometer setup in reflection.

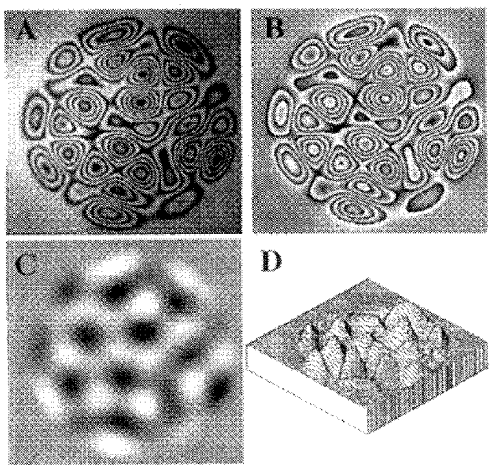

Figure 2: Visualization using DHI of a clamped circular plate vibrating at 69 kHz. A) Holographic interferogram with no phase shift, B) wrapped phase map, C) unwrapped phase map, D) 3D view of the unwrapped phase map.

In the second hologram of the sequence a phase shift of $-\pi/2$ and $+\pi/2$ is introduced at the minimum and maximum deformation, respectively, such that the fringe function obtained is:

$$I_2=\beta I_o(1-\cos 2M) \qquad (2)$$

In the third hologram, a phase shift of 0 and $+\pi/2$ is introduced at the minimum and maximum deformation, respectively, such that the fringe function obtained is:

$$I_3=\beta I_o(1+\sin 2M) \tag{3}$$

The deformation signal of interest M which is directly proportional to the out of plane displacement can then be extracted via:

$$\tan 2M=[2I_3-(I_1+I_2)]/(I_2-I_1) \tag{4}$$

The 2π phase jumps in the phase map can be removed by a phase unwrapping procedure. Using such a procedure, we can see that an indetermination arises if locally the information term goes down to zero, corresponding to a dead pixel. Before using the phase unwrapping procedure one must first ensure that there are no dead pixels. This is usually done using low-pass filtering of the image. The number of pixels which are invalid for phase calculation due to speckle noise can thus be greatly decreased and this ensures that the phase extraction procedure works satisfactorily. The main drawback of using a low-pass filtering procedure is its limitation of the fringe resolution. With DHI a large aperture imaging system can be used, leading to a speckle size much smaller than the pixel size of the ccd camera and thus leading to only few (if any) dead pixels, and so low-pass filtering is usually not needed. This is clearly a great advantage of using DHI compared to speckle interferometry such as ESPI. In the case of ESPI it is not possible to record interferograms without dead pixels and low-pass filtering is mandatory. An example of phase unwrapping of DHI images is shown Fig. 2. It corresponds to a complex vibration mode of a circular membrane excited at 69 kHz. Sharp and dense fringes are resolved and no low-pass filtering was needed before the phase extraction procedure was applied. The separate lobes of vibration are clearly visible.

2.2 – ADAPTIVE HETERODYNE INTERFEROMETRY FOR STRESS ANALYSIS

For the study of transient non-recurring events, only one double exposure hologram can be recorded; therefore quasi-heterodyne interferometry is used to extract the phase information [5]. Here, independent access to the two recorded wavefronts is necessary in order to subsequently control their relative phase. This implies independent recording of each wavefront by using different reference beams. The optical arrangements for dual-reference-beam holographic interferometry of a phase object is sketched in Fig. 3. The first object state O_1 is recorded by reference R_1 and the second object state O_2 by reference R_2 in the same crystal. During the read-out of the hologram, the interferogram is analyzed at least three times, and the relative phase between R1 and R2 is changed each time using a piezo-electric mirror. The local intensities I_k are then given by:

$$I_k(x)=a(x)(1+m(x)\cos[M(x)+\varphi_k]) \tag{5}$$

which correspond for k=1,2,3 to a system of three equations with three unknown values: the mean intensity a(x), the fringe contrast m(x), and the phase term M(x) which

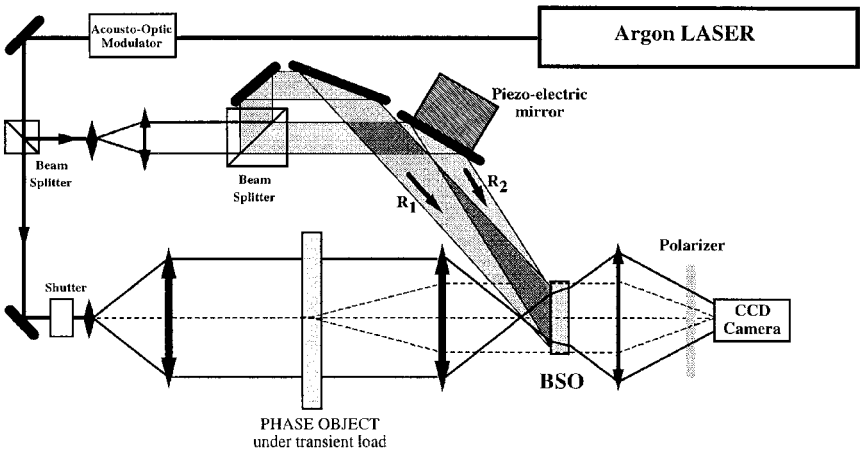

Figure 3:Two-reference-beam dynamic holographic interferometer setup.

is related to the stress in the object. By using $\varphi_k=0$, π, and $\pi/2$, the set of equations is similar to Eq. 1,2, and 3, and we can use Eq.4 to calculate the phase term M.

Figure 4 shows an example result of the stress state near a crack in a PMMA plate containing a pre-cut crack. The specimen was placed in a load frame for testing in a three-point bend configuration. A double-pulse hologram was recorded as the load was increased. The first recorded hologram starts to be erased during the recording of the second hologram. In order to obtain a near-unity fringe contrast, the intensity and width of the second pulse are adjusted such that the exponential erasure of the first hologram and the exponential increase of the second hologram lead to two holograms with the same net diffraction efficiency. We must also take into account the time decay of the diffraction efficiency during the read-out process. In this case, a(x) will not be the same for the three phase shifted images. Fortunately, by using low intensity reference beams for the read-out, the mean intensity a(x) can be assumed to be constant for the read-out of the three phase shifted images. It is thus possible to use such a system to study the phase maps generated by non-recurring events.

3 Conclusion

We have shown that adaptive photorefractive interferometers can be used for real-time as well as quasi-heterodyne holographic interferometry. Applications to modal and stress analyses have been presented. The techniques can be used in conjunction with phase-stepping methods to provide quantitative information about object displacements or stresses.

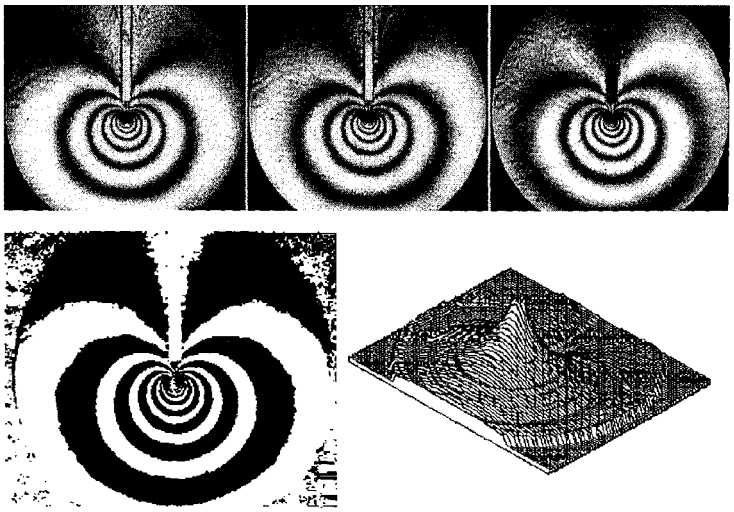

Figure 4: Stress state in a three-point bend loaded PMMA plate with pre-cut crack. Top row: sequence of three phase-shifted images. Bottom left: phase-wrapped image. Bottom right: 3D image of unwrapped phase.

References

1. A. Ashkin, G. D Boyd, J. M. Dziedzik, R. G. Smith, A. A. Ballman, J. j. Levinstein, and K. Nassau, "Optically induced refractive index inhomogeneities in LiNbO3 and LiTaO3," Appl. Phys. Lett. **9,** 72 (1966).

2. M. P. Petrov, S. V. Miridonov, S. I. Stepanov, and V. V. Kulikov, "Light diffraction and nonlinear image processing in electro-optic BSO," Opt. Commun. **31** (1), 301-304 (1979).

3. R. C. Troth and J. C. Dainty, "Holographic interferometry using anisotropic self-diffraction in BSO," Optics Lett. **16** (1), 53-55 (1991).

4. B. Pouet and S. Krishnaswamy, "Dynamic holographic interferometry by photorefractive crystals for quantitative deformation measurements," Appl. Optics. **35** (5), 787-794 (1996).

5. R. Dändliker and R. Thalmann, "Heterodyne and quasi-heterodyne holographic interferometry," Opt. Eng. **24** (5), 824 - 831 (1985).

6. A. Marrakchi, J. P. Huignard, and P.Günter, "Diffraction efficiency and energy transfer in two-wave mixing experiment with BSO crystals," Appl. Phys. **24,** 131-138 (1981).

7. Pochi Yeh, "Introduction to photorefractive nonlinear optics," Wiley series in pure and applied optics (1993).

8. K. Walsh, A. K. Powell, C. State, and T. J. Hall, "Techniques for the enhancement of space-charge fields in photorefractive materials," J. Opt. Soc. Am. B **7** (3), 288-303 (1990).

ITERATIVE ALGORITHMS : AN ALTERNATIVE TO HOLOGRAPHY

A. DESFARGES-BERTHELEMOT, B. COLOMBEAU, C. FROEHLY,
V. KERMENE, M. VAMPOUILLE
Institut de Recherche en Communications Optiques et Microondes
UMR CNRS/ Univ. Limoges n°6615,
123, av. A. Thomas – 87060 Limoges cedex (France)
tel/facsimile : 33(0) 5 55 45 74 16

Abstract: standard holographic techniques will be compared to less-known referenceless wavefront recording and reconstruction techniques based on numerical or analogical iterative diffraction procedures. The relevance of such alternatives to holography in photomechanics will be shortly discussed.

1. Introduction

Most of the holographic tools are well-known and of wide use in the photomechanics community. Their main applications are : displacement and vibration measurement by holographic interferometry ; recording of fast 3D transients with the help of pulsed laser illumination ; fluid dynamics studies (3D velocity distributions) by multiple-exposure pulsed holography…

Unfortunately, a lot of practical constraints often reduces the effectiveness of holography : for instance, the high thermo-mechanical stability requirements of interferometric devices, that are hardly compatible with industrial environment ; the lack of sensitivity of the holographic photodetectors (photographic, photopolymers, photorefractive and other materials), due to their very high spatial resolution ($> 10^6 mm^{-2}$); the restricted spectral sensitivity of the holographic photodetectors available today : only UV and visible wavelengths, in spite of the large potential interest of IR holography ; and, last but not least, lack of compatibility with the new generations of opto-electronic photodetector arrays, due to the presently low pixel number of these devices (e.g. 10^6), to be compared with the huge storage capacity of conventional holograms : therefore holography is still far from compatibility with the very rich -and fastly growing- techniques of real-time digital image processing, automatic fringe pattern assessment and metrology…

Although they are still used in a few very specialized scientific fields (astronomic observation, design of laser resonators, non-linear « optical phase conjugation » …), other non-holographic techniques may also be applied today to the recording and reconstruction of coherent optical wavefronts, with

- the following advantages on conventional holography : no need for interferometric set up ; compatibility with any photodetector (as well point-like scanning detectors as 1D or 2D arrays) and therefore with digital image processing and high sensitivity real-time operation over a very broad spectral range (UV to IR)
- the following main limitation : applicability restricted to coherent beams of reduced angular aperture and cross-section, the maximum number of sampling points of the beam (at the FOURIER analysis sense) being much smaller than the number of

A. Lagarde (ed.),
IUTAM Symposium on Advanced Optical Methods and Applications in Solid Mechanics, 415–428.

the photodetector pixels, for the beam reconstruction to be accurate.

All these techniques are grounded on the same general idea, that a complex (i.e.coherent) monochromatic field distribution may be fully specified by the knowledge of its energy distribution in a few well-prescribed cross-sections of the beam : the unknown phase distribution may be recovered from numerical computations (usually iterative algorithms) or analogic processes (usually iterative diffractive transformations).

A short survey of holographic and non-holographic tools for optical wavefront reconstruction will now be presented, organised in three sections (i) flash-back on holography (spatial, temporal) (ii) non-holographic optical wavefront recording and reconstruction (3D wavefront storage, phase retrieval techniques), (iii) relevance of referenceless wavefront reconstruction for Solid Mechanics.

2. Basic holographic procedures

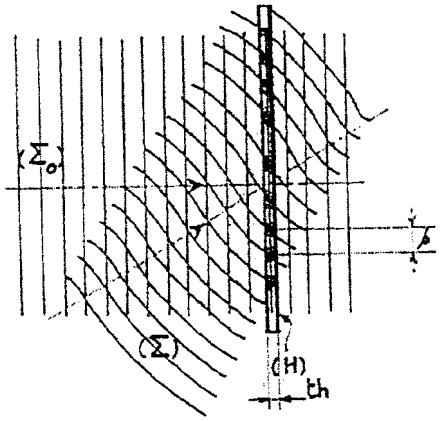

Fig. 1.1 – Photographic recording (H) of the interference of an arbitrary wave (Σ) with a reference wave (Σ_0)

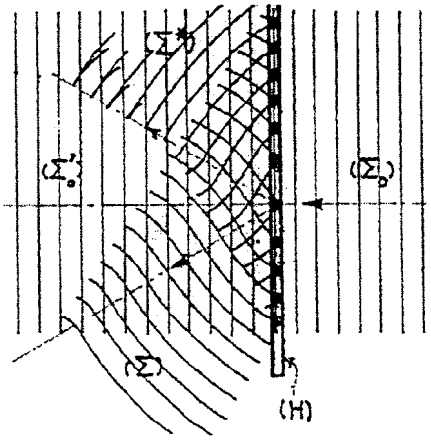

Fig. 1.2. – Reconstruction of (Σ), (Σ^*) and (Σ_0) by diffraction of (Σ_0) through (H), with reversed propagation direction

Remark: when the thickness th of the photosensitive layer (H) gets much larger than the interference spacing ϕ - usually a few micrometers - then (Σ^*) and (Σ'_0) get vanishing : a « thick hologram » (also said « BRAGG hologram* ») may convert (Σ_0) into (Σ) with high energy yield.

Figures 1.1 and 1.2 depict the recording and reconstruction steps of conventional holography in monochromatic radiation ; the reference beam (Σ_0) was here taken as a plane beam, what reconstructs two mutually complex conjugated beams (Σ) and (Σ^*) on figure 1.2. If the reference beam were of spherical or other geometrical shape, then (Σ^*) would be replaced by more complex wave surfaces, whereas (Σ) would keep its rigorous strigmatism.

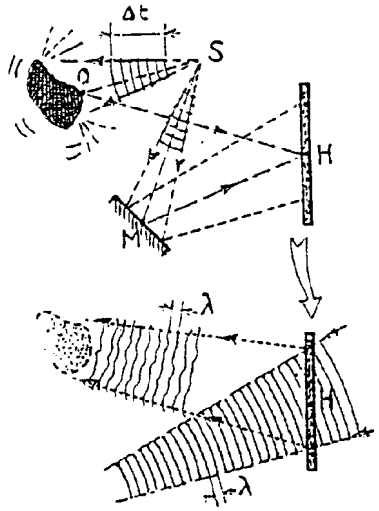

Interferometric requirements :

* stability (better than $\lambda/4$)
* SO + OH ≈ SM + MH
* $\lambda / \Delta\lambda$ > holographic fringe number

Fig. 2.1. – Coherent imaging – and interferometric analysis – of one transient state « frozen » by pulsed holographic recording

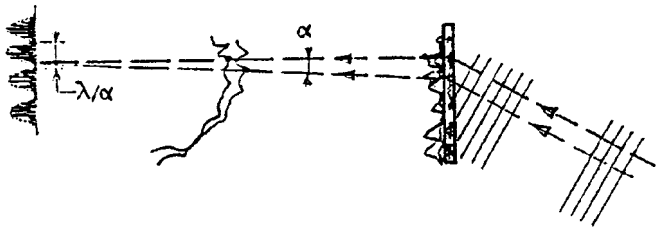

Fig. 2.2 – Metrology of transverse micro-displacements : double or multiple-exposure interferometry by « freezing » two – or more – successive states on the same hologram and then by reconstructing their interference fringes

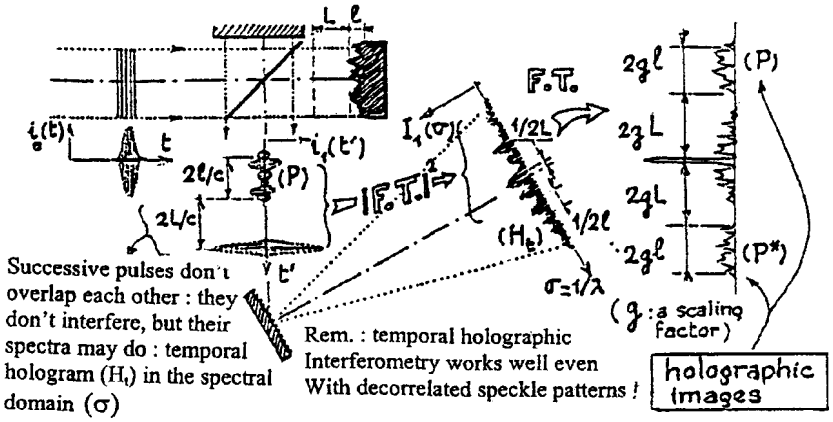

Fig. 2.3. – Metrology of longitudinal micro-structures and micro-displacements by « Temporal FOURIER Holography » and holographic interferometry of frequency spectra

Figures 2-1, 2-2, 2-3 illustrate three important applications of holography, the less-known « temporal holography » being concerned on figure 2-3 and shown in its early application to absolute thickness measurements on figure 3 ; « F.T. » (figure 2-3) means « FOURIER Transformation », performed either numerically or analogically by FRAUNHOFER diffraction of a monochromatic laser beam through the spectrogram (H_t) (the « temporal hologram »). It may be noted that « temporal holography » has got today an increasing importance in « femtosecond FOURIER optics », that is for FOURIER optical processing of femtosecond laser pulses, and was generally renamed « femtosecond spectral interferometry » by the north-american literature.

Space(x)-time(v) holographic recording of a thickness distribution Figure 3
(Optics Lab., Besançon, 1973)

Space-time holographic set-up
(O, microscope objective ;
Sp spectroscope ; F spectroscope slit)

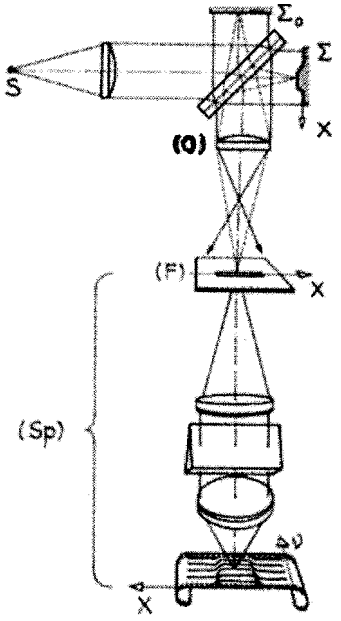

Space-time hologram =
a «channelled spectrum »

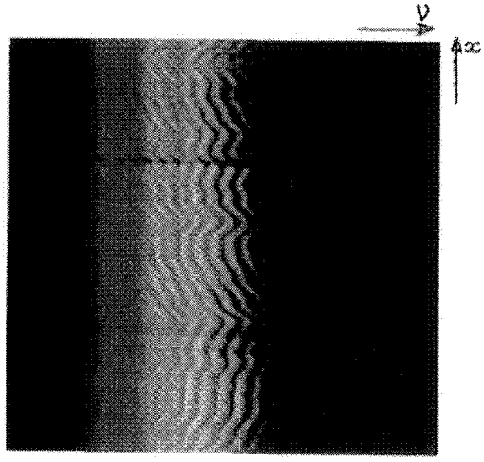

3. Referenceless wavefront storage and reconstruction

Whereas the whole coherent optics international community explored the new areas opened to the holographic tools, other completely original approaches to optical wavefront storage and reconstruction were suggested very early (1970 ≈ 1972) quasi-simultaneously and independently, by Yu. DENISYUK, by R.W. GERCHBERG and W.O. SAXTON, by H. KOGELNIK and C.V. SHANK, by V. RAGULSKII and B. YA

ZEL DOVITCH in various fields of optics : Yu. DENISYUK (figure 4) felt that the three-dimensional speckle pattern scattered from a spatially coherent source should behave like a referenceless hologram after its recording inside a photosensitive volume.

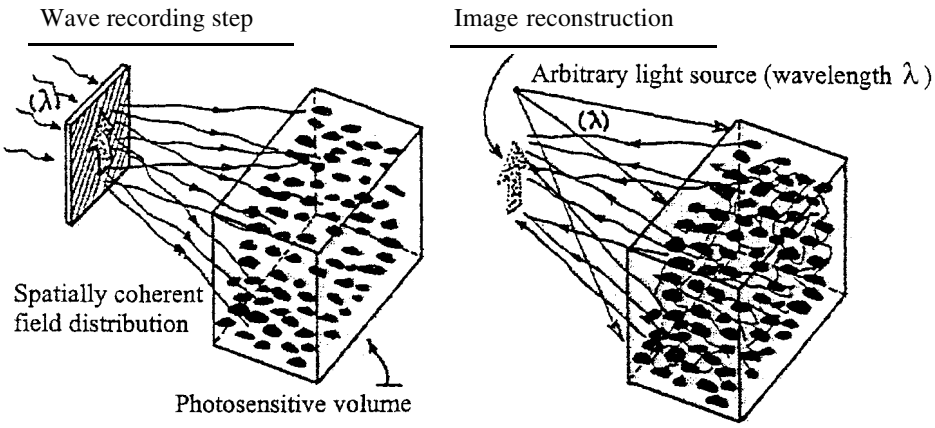

. Not yet observed with photosensitive (e.g. photographic) materials – i.e. absorption distributions –

. But striking similar experiments with 3D gain distributions : « Distributed Feedback » wave synsthesis …

Fig. 4 – Yu. Denisyuk's proposition of referenceless wavefront storage and reconstruction

No direct experimental proof of this bright intuition was given, but indirect confirmations came from laser designers and from nonlinear optics at the same time (figure 4) : H. KOGELNIK and C.V. SHANK's « distributed feedback » lasers generated a collimated and monochromatic laser beam at wavelength $\lambda/2na$ from a spatially periodic gain distribution, of periodicity a, « written » inside a semi-conductor material of refractive index n. V. RAGULSKII and B. YA ZEL'DOVITCH fortuitiously observed that the intense illumination of transparent optically nonlinear dielectrics by speckle patterns gave rise to intense coherent backscattered light at a slightly downshifted frequency (« BRILLOUIN-MANDEL'STAM shift ») with amplitude and phase distributions being exact replicas of the incident speckle fields.

These experiments may be viewed like striking confirmations of the general idea that three-dimensional distributions of scattering centres may generate well-definite coherent wavefronts : for such a generation to be effective, the scattering sources should only exhibit optical «.gain » (should amplify light) at a prescribed wavelength λ, in the place of absorption.

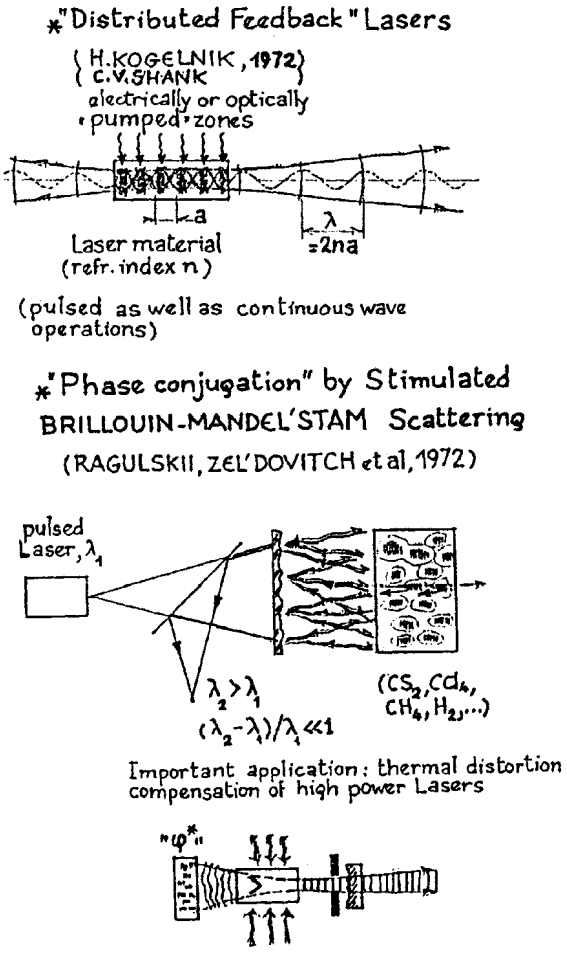

Remark concerning referenceless wavefront generation

- no wave shape storage (not applicable to « double/multiple exposure interferometry »)
- requirements for
  . 3D amplifying media
  . powerful lasers ($< 10^6$ w.cm^{-2}) in case of « phase conjugation »

Fig. 5 – Coherent wavefront generation by 3D distributions of GAIN (in the place of ABSORPTION)

The basic reason why wavefront reconstruction may be automatically achieved by three-dimensional gain distributions, without the need of any holographic reference beam, may be understood from figure 6 : any monochromatic coherent beam, in the frame of the scalar paraxial approximation, consists of a particular energy distribution confined inside a conical volume. Schematically this volume may be divided into two regions : the « far field » (FRAUNHOFER diffraction pattern), where the energy

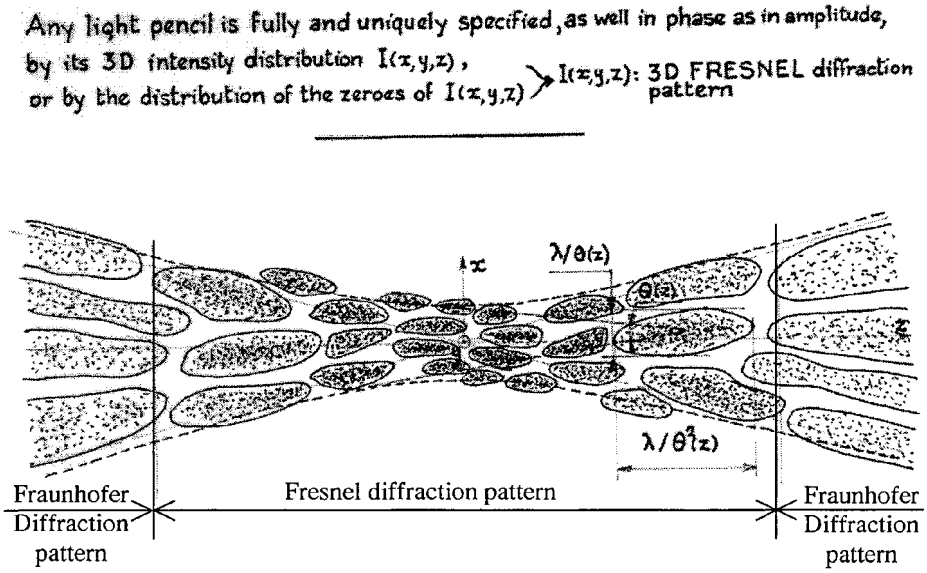

Fig. 6 – The three-dimensional diffraction pattern of a spatially multimode light beam

distribution over any cross-section of the beam keeps an invariant shape, a scaling factor proportional to z being omitted ; and the « FRESNEL diffraction volume », where various energy distributions may be observed in various cross-sections. An important feature of the FRESNEL diffraction volume is that its three-dimensional energy distribution specifies the beam in an unique way : indeed it is a complex, multiple beam interference pattern, the structure of which is ruled by the amplitude and phase relationship connecting enery part of the beam field to every other one … It may be said as « a three-dimensional self-interferogram » of the monochromatic coherent beam : two beams exhibiting the same FRESNEL diffraction volume are identical to each other, a scaling energy factor being omitted. The larger is the number of energy maximums (or minimums) inside that volume, the greater is the beam complexity, quantitatively characterized by the number of its SHANNON samples, also said « number of transverse modes », or « number of its FOURIER components », equal to the ratio of the beam « étendue » to the square of the wavelength.

R.W. GERSCHBERG and W.O. SAXTON showed even in 1972 that the knowledge of the whole energy distribution I(x,y,z) inside the FRESNEL volume will be not required for determining the beam amplitude and phase unambiguously : full phase retrieval was

demontrated with the knowledge of energy distributions $I_1(x,y)$ and $I_2(\xi,\eta)$ in only two mutually confocal cross-sections of the beam.

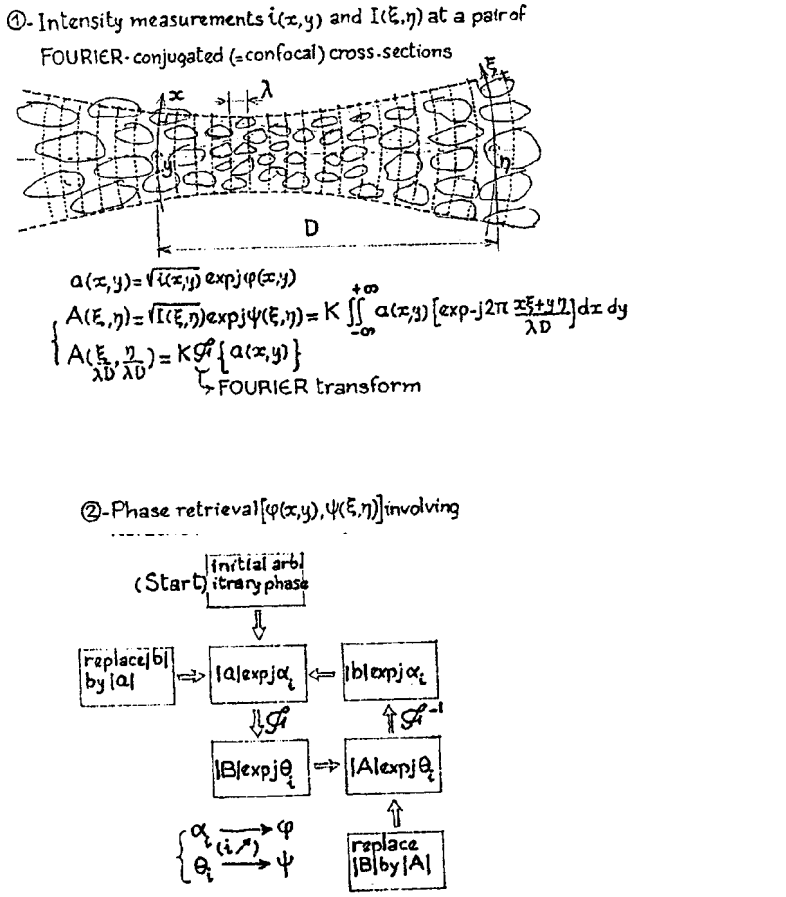

Fig. 7 : the GERCHBERG and SAXTON's phase retrieval algorithm and applications to coherent optical fields evaluation

The iterative FOURIER transform phase retrieval procedure is explained on figure 7, that also presents the beautiful application, successfully performed by C. and F. RODDIER in 1991, of such numerical algorithms to the measurement of HUBBLE space telescope's aberrations : from observations of a star image with various amounts of defocusing (figure 8) these authors found that the wavefront distortion had its origin in shape deviations of the primary mirror, and they measured these distortions with subwavelength accuracy. This extraordinary « referenceless wavefront reconstruction », that allowed HUBBLE's further correction, was apparently the first application of these non-interferometric techniques to high performance surface metrology, although similar algorithms were soon of wide use for two decades in astronomical imaging by aperture synthesis.

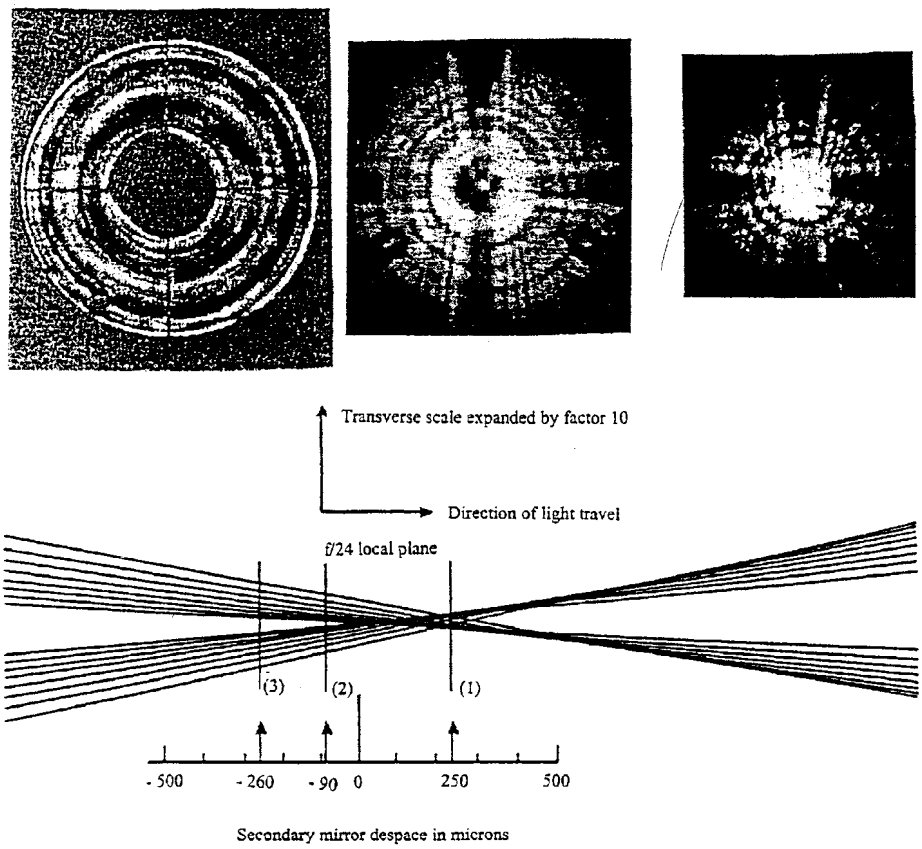

Fig. 8 – Reconstruction of the Hubble space telescope wavefront distortion from stellar images taken at various focus positions. May 1991 (JPL final report)

Iterative FOURIER transforms may also be performed very easily and quickly by light itself : its iterative diffraction along many round-trips between the two mirrors M_1

and M_2 of a « FOURIER-transform resonator », that is a confocal or a telescopic resonator filtered by appropriate stops (binary filters # 1 and # 2, figure 9), was shown able to convert any initial optical noisy seed into a stable, monochromatic coherent beam ; the complex amplitude of that beam will be fully specified by the geometrical structure of the two binary filters. Traveling light should be regenerated at each round-trip by transmission through an amplifying component (G) : such a resonator equipped with filters and gain is nothing but a laser -a « FOURIER transform Laser »- source of a variety of coherent beam shapes. It behaves like a hologram, as it generates well-controlled amplitude and phase distributions by transmission of light through transparencies (the binary filters), but it works as well with (figure 10) as without (figure 11) reference beam : figure 10 demonstrates the referenceless laser emission of a beam exhibing a square shape in one of its cross-sections and, consequently, a $(\text{sinc})^2$ shape in the FOURIER-conjugate other cross-section ; this laser is built today by the « BM Industries » factory (Evry, France) ; figure 11 demonstrates the laser generation of a more complex image by iterative diffractions through photographic filters, one of them being a conventional FOURIER hologram of this image.

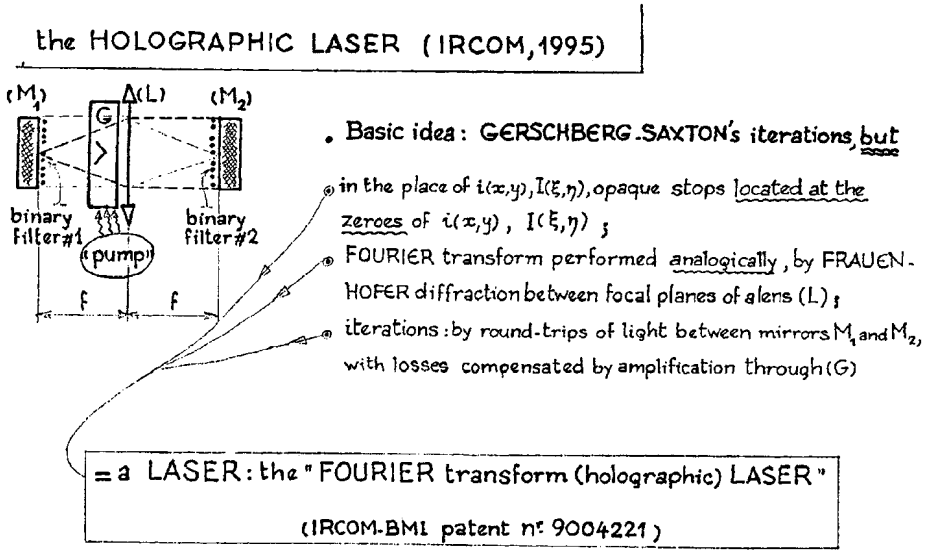

Fig. 9 – Principles of a "holographic laser"

a « FOURIER transform Laser »

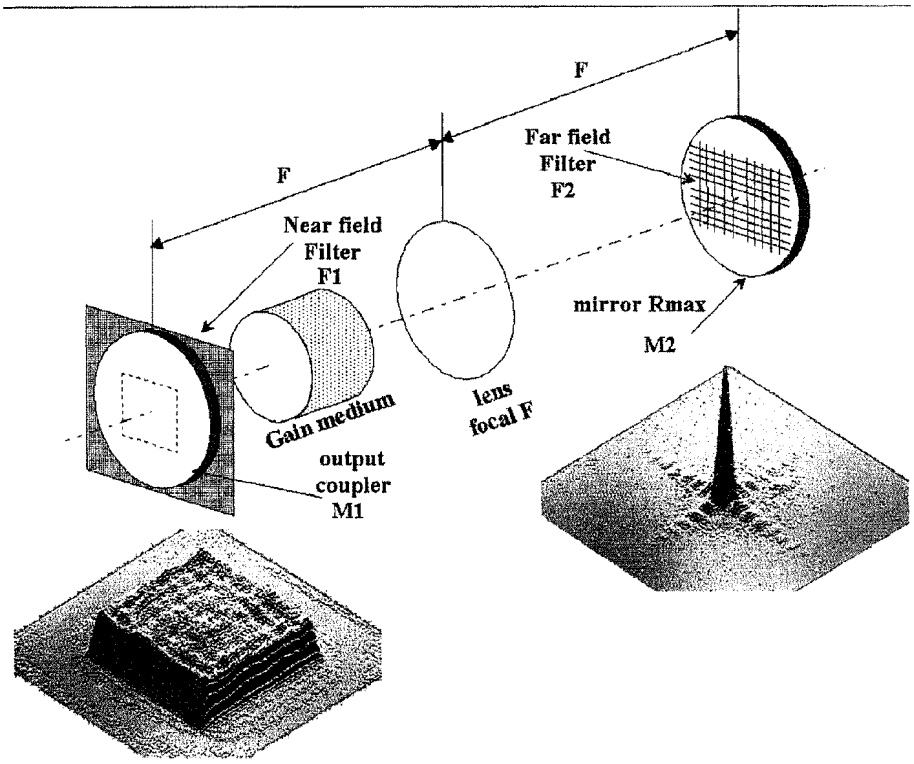

Fig. 10 : Generation of a « square-shaped » coherent beam by a Fourier-Transform laser resonator including two Fourier conjugated spatial frequency filters

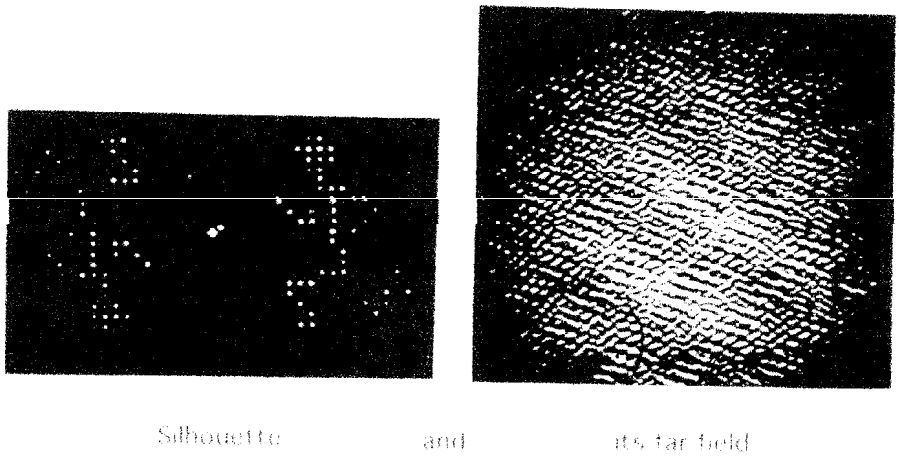

Silhouette and its far field

Fig. 11 : Generation of a coherent picture by the « holographic laser »

Figure 12 is a pictorial summary of the respective advantages and drawbacks of referenceless as holographic wavefront storage and reconstruction considered from the point of view of their present or potential applications to photomechanics, the main superiority of the iterative procedure lying probably in their compatibility with opto-electronic photodetector arrays and digital image processing techniques.

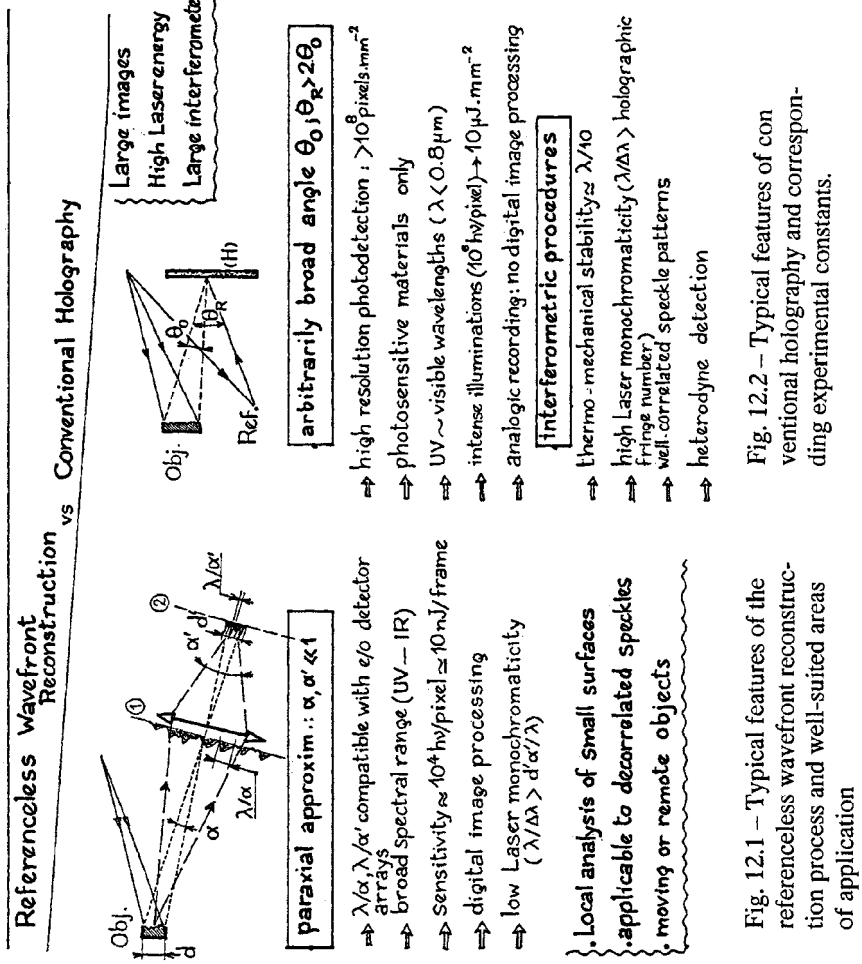

Fig. 12.1 – Typical features of the referenceless wavefront reconstruction process and well-suited areas of application

Fig. 12.2 – Typical features of conventional holography and corresponding experimental constants.

Conclusion

Various types of holographic techniques were recalled, including the less-known "temporal holography", with their main areas of application in Solid Mechanics ; emphasis was put on the specific features, advantages and limitations of these interferometric processes : holography and holographic interferometry are still today clearly unsurpassable tools of coherent Optics for three-dimensional image storage, sub-micrometric metrology of large scenes or mechanical structures, "freezing" of fast moving objects … More generally, for high accuracy displacement and distortion analysis of volumes, up to cubic meter sized. But also the cost of such performances may be considered as rather high : very stringent interferometric requirements (sub-wavelength thermo-mechanical stability of interferometric set-up, powerful and monochromatic laser radiation) ; sub-micrometric resolution-usually larger than 3.10^3 mm^{-1} – two-dimensional photodetectors, being usually photographic or photorefractive materials of low sensitivity working in the visible spectral range only ; and the very restrictive condition that no speckle pattern decorrelation will reduce or blur the interference fringe contrast, what implies displacement and deformation amplitudes to be practically limited to a few tens of micrometers. From these discussions resulted the conclusion, that holographic wavefront reconstruction could not be applied to many situations, where the knowledge of optical field structures would nevertheless be of great interest, for instance : diffraction metrology of remote objects ; wavefront reconstruction outside the spectral sensitivity domain of holographic materials ; large deformation measurements ; real-time detection of coherent, time-dependent patterns ; and micrometric observations of bodies under environmental conditions where interferometric techniques cannot be involved, what frequently arises on industrial sites.

Some of these problems were seen solvable thanks to "referenceless wavefront reconstruction", whose basic idea, today not widespread through the Photomechanics Community, is that any coherent wavefield may be fully specified, both in its amplitude and phase, by the knowledge of an appropriate set of its energy distribution samples. The main advantage of these unconventional coherent Optics methods with respect to holographic wavefront reconstruction was found in the simplicity of non-interferometric set-up, the compatibility with illumination by a variety of laser sources and with the use of opto-electronic detector arrays, allowing real-time digital image processing. The accuracy of the reconstructed wavefronts is then proportional to the detector pixel number. This number is today in the order of 10^6, whereas the capacity of holographic plates is about 10^7 pixels per square millimeter, the area of a hologram being usually as large as 10^4, or even $10^6 mm^{-2}$: up to now referenceless iterative field processing techniques may be considered assuitable for real-time observation of rather small-sized moving surfaces or volumes, under continuous as well as pulsed laser illumination, the laser working like a coherent stroboscope in this latter case. This is nevertheless quite a provisional conclusion promised to get obsolete when the continuing progress of microelectronic devices will let photodetector arrays compete with "analogic" photosensitive materials, not only by their sensitivity, spectral and temporal responses but also by their increasing pixel density : then, thanks to the increasing power of Fourier-transform computers, iterative referenceless reconstruction of optical wavefronts could perhaps take the place of conventional holography in most of its scientific or technical applications.

Bibliography

Holography
J.W. GOODMAN ; Introduction to FOURIER Optics (Mc Graw Hill, N.Y. 1968)

Temporal FOURIER Holography
C. FROEHLY, B. COLOMBEAU, M. VAMPOUILLE : Shaping and Analysis of Picosecond Light Pulses ; Progress in Optics, vol. XX, E. WOLF Ed., North Holland Publ., chap. II, § 4.3.5, (1983).

C. FROEHLY, B. COLOMBEAU, M. VAMPOUILLE ; Diffraction, dispersion and space-time FOURIER Optics ; Perspectives in Optoelectronics, S.S. JHA Ed., World scientific publ., chap. 16, § 2-3-4, p. 928-929, (1995).

Referenceless wavefront reconstruction
Yu. DENISYUK, "Holography and its Prospects", Zhurnal Prikladnoi Specktroscopii 33, p. 397 (1980).

B. Ya. ZEL'DOVITCH, V.I. POPOVICHEV, V.V. RAGULSKII, F.S. FAIZULLOV : On the relationship between wavefronts of reflected and exciting light in stimulated Brillouin scattering ; Pis'ma Zh. Eksp. Teor. Fiz. 15, 160 (1972) [English transl. : JETP Letters 15, 109 (1972)].

O. Yu NOZACH, V.I. POPOVICHEV, V.V. RAGULSKII, F.Z. FAIZULLOV : Compensation of phase distortions in a gain medium by a "Brillouin mirror", Pis'ma Zh. Eksp. Teor. Fiz. 16, 617 (1972) [English transl : JETP Letters, 16, 435 (1972)].

H. KOGELNIK, C.V. SHANK : Appl. Phys. Lett. 18, 152, (1971),
J. Appl. Phys. 43, 2347, (1972).

R.W. GERCHBERG, W.O. SAXTON : A practical algorithm for the determination of phase from image and diffraction plane pictures ; Optik, 35, 237 (1972).

C. RODDIER, F. RODDIER : Reconstruction of the Hubble Space Telescope wavefront distortions from stellar images taken at various focus positions : JLP contract n° 958893, final report, (may 1991).

C. RODDIER, F. RODDIER : A combined approach to HST wavefront distortion analysis, Applied Optics, "Space Optics" special issue, (1992).

Holographic Laser
B. COLOMBEAU, M. VAMPOUILLE, V. KERMENE, A. DESFARGES, C. FROEHLY : Spatial shaping of coherent waves inside a confocal laser. Pure Appl. Opt. 3, 757-773 (1994).

A. DESFARGES, V. KERMENE, B. COLOMBEAU, M. VAMPOUILLE, C. FROEHLY : Wavefront reconstruction with a FOURIER hologram in a phase-conjugating mirror oscillator ; Opt. Lett. 20, 19, 1940 (1995).

COHERENT IMAGES AMPLIFIED BY NON LINEAR OPTIC WAVES MIXING

E. LANTZ, F. DEVAUX, G. LE TOLGUENEC, E. GUIOT, M. MÜLLER
Laboratoire d'optique P.M. Duffieux, U.M.R. 6603 CNRS
Université de Franche-Comté, 25030 Besançon Cedex, France

Abstract

Image parametric amplification and its applications are summarized. The link between resolution and phase matching is first presented. We report then applications to ultrafast imaging, imaging through diffusing media, correction of distortions by phase-conjugation and fluorescence life-time measurements. Last, degenerate schemes are proved to permit polychromatic amplification as well as phase-sensitive amplification.

1. Introduction.

Since its early stages, nonlinear Optics has been applied to image processing to obtain infrared to visible parametric up-conversion[1], amplification in photorefractive materials[2] or visualization of ultrafast phenomena with Kerr gates[3]. More recently, the power increase of current picosecond lasers has permitted high gain parametric amplification in only one pass through a birefringent crystal. Hence, parametric amplification of images has become possible, provided that phase-matching could be fulfilled. This paper aims to give a summary of the different schemes that have been proposed, the underlying theory and the possible applications.

Section 2 describes specific phase-matching conditions that have to be fulfilled for the amplification of a monochromatic image. Section 3 is devoted to the use of parametric image amplification as an ultrafast optical gate. Such a scheme can be applied to imaging through diffusing media. Results obtained in this very promising way are summarized. Section 4 reports the elimination of distorsions by phase-conjugation. In section 5, the amplification of a polychromatic image is addressed. Such a large bandwidth amplification is useful to amplify fluorescence signals, as described in section 6. Finally, phase sensitive amplification, that allows noiseless amplification, is reported in section 7.

2. Phase matching in image parametric amplification

2.1 Amplification of an image

The object is a (possibly complex) transparency illuminated by a monochromatic plane

A. Lagarde (ed.),
IUTAM Symposium on Advanced Optical Methods and Applications in Solid Mechanics, 429–436.

wave. The scattered light forming the signal can be considered as a superposition of plane waves, each plane wave being associated by the laws of Fourier Optics to a spatial frequency of the object. The pump beam, as well collimated and monochromatic as possible is superimposed with the signal in a nonlinear birefringent crystal. The formation of an amplified image can be obtained in (at least) three different ways :

a) no imaging system is used and the image is formed with the idler wave, that is phase-conjugate of the signal wave [4-7] : see section 4

b) the crystal is placed in the Fourier plane of the imaging system [8-10] . The range of amplified spatial frequencies is then determined in this plane by the transverse cross-section of either the crystal or the pump beam (the latter situation occurs if the diameter of the pump beam is not large enough to ensure uniform illumination of the crystal). On the other hand, the field of view is determined by the angular acceptance that can be derived from the phase-matching conditions.

c) The crystal is placed in a first image plane and a second image is formed on the detector [11-15] . The field of view is determined by the lateral sizes of the crystal (or of the pump beam), while the amplified spatial frequencies are determined by the phase-matching conditions.

The basic experimental set-up used in ref 11 and 12 is sketched in fig.1

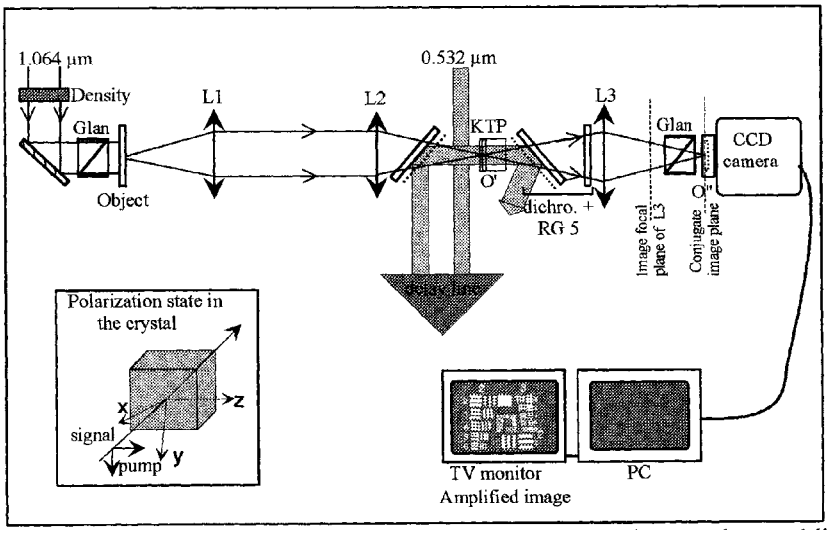

figure 1: Experimental set-up used in refs. 11 and 12. The infrared and green pulses are delivered by a partially frequency-doubled Nd:YAG laser. The horizontally polarized infared beam illuminates a transparency (the object) which is imaged by a telescopic system at the input face of a 5 mm long KTP crystal of 4x4 mm cross-section. The frequency-doubled light is used as the pump beam. This pulse is synchronised with the infrared pulse by means of a delay line and then illuminates the crystal. A dichroïc mirror and a chromatic filter eliminate the pump beam after crossing the crystal.

2.2 Phase matching and resolution

The amplification of a wide range of spatial frequencies is obtained if phase-matching occurs for a wide range of directions of the signal wave, the pump direction being fixed with respect to the principal crystal axes. A natural way to obtain such a range is using a "non critical" one-beam phase-matching scheme. In its usual sense, non critical phase-matching is obtained when the derivative of the phase-mismatch vector vanishes with respect to a rotation of the crystal. The concept of "one beam non critical phase matching", introduced by Dou et al [16], means that the phase-mismatch derivative vanishes with respect to a rotation of two of the three interacting beams, the third one (the pump in our case) keeping a fixed direction with respect to the crystal axes. We have shown [17] that, in a type I crystal, parametric amplification is one-beam non critical for the signal wavelength as well as for the signal direction near a collinear degenerate configuration (see section 4).

For a 20 mm long Type II KTP crystal, the angular range where the efficiency of phase-matching remains greater than 50 % is 14mrad in both X and Y directions. This phase-matching range corresponds to a resolution of about 90 μm in the crystal, for the 1,064 μm wavelength of a Nd : Yag laser. While the field of view and the resolution on the object depend on the magnification of the optical system, the resolution on the crystal remains constant. Even placing the crystal in the Fourier plane does not change this resolution, that is in this latter case inversely proportional to the field of view. Hence, the number of resolved points in an amplified image is constant for a given crystal and a given wavelength, whatever the particular arrangement of the imaging system. With a 7 x 7 x 20 mm³ KTP crystal, 80 x 80 points have been resolved, with a gain of 40 dB.

A simple rotation of the crystal yields a transition from amplification of the low spatial frequencies to amplification of higher spatial frequencies [18]. In this configuration, phase matching acts as a coherent spatial filter, permitting basic image processing operations, like edges reinforcement [12] (fig.2).

Fig. 2 : Amplified images of a four number corresponding respectively to low pass (left) and a band pass (right) configuration of phase-matching. (After ref. 12)

3) Ultrafast photography and application to imaging through diffusing media.

In a type 2 crystal, like KTP, the signal and the idler are cross-polarized. Hence, it is possible to separate the idler from the signal with a polarizer even if both waves have the same wavelength. Since the idler is generated only during the interaction with the pump pulse, parametric image amplification acts as an ultrafast shutter that permits imaging with a picosecond exposure time.

As a first application, we obtained photographs of light pulses propagating on a diffusing screen[13].

The most promising application of ultrafast imaging is detection of an object hidden by a diffusing medium. Imaging through biological tissues has been widely investigated during the last years. After the traversal of a diffusing medium, the light issued from a short pulse that illuminated an hidden objet can be divided in three parts[19] :

- a very small part has not been diffused. This light, called ballistic, conserves coherence properties of the pulse and arrives at first,
- the light that arrives just after has experienced a small number of diffusions, merely in the forward direction. Hence, these so-called “snake photons” are no more coherent but can carry to some extent a spatial information about the hidden object,
- last, the strongly diffused light, that represents the great major part of the transmitted pulse energy, carries no useful information and must be rejected.

To detect the ballistic light, the so called “Optical coherent tomography”[20] has become a standard technique that showed impressive results. This low coherence interferometric method uses coherence properties of the ballistic image. Hence, though high quality images were obtained through one millimeter of biological tissue, extension to much thicker tissues is not possible, since the ballistic image completely disappears. On the other hand, imaging with snake photons should be possible in this case with a much lower resolution. Time gating appears as the efficient technique to select these photons.

The principle of detection of the ballistic light by image parametric amplification was demonstrated in two first experiments[10,14]. In both cases, 40 ps to 50 ps pulses at 1,06µ m where used, resulting in a severe degradation of the signal to noise ratio due to an insufficient temporal separation between the ballistic and the diffused light. However, the resolution seemed unaffected by the diffusing medium. Recently, we have fitted the experimental signal to noise ratio with a theoretical model that takes in account the temporal positions of the pump, ballistic and diffused pulses[15] , for different thicknesses of the diffusing medium composed of latex beads. Because of the good agreement with the experiment, we can conclude that conditions where a ballistic image can be formed are well understood.

Mammography applications necessitate obtaining images through several centimeter thick tissues. For such a thickness, the ballistic light has disappeared and snake photons must be used. In a first attempt, we have obtained images through 9 mm

of ham with a resolution of 3 mm[7]. In the next future, we will characterize the obtainable resolution with respect to the thickness of the tissues.

4) Imaging by phase-conjugation

At the degeneracy, the forward propagating idler is phase-conjugate with the signal, provided that the pump is a plane wave without distortion. Hence, we recorded[7] without any imaging system images formed by the idler in the conjugate plane, symmetrically located with respect to the crystal. The main interest of such a method is the restoration of an image after the traversal of an aberrant, though deterministic, medium. This restoration has been experimentally obtained by placing a mirror after the crystal to obtain a back-propagating wave that traverses a second time the aberrant medium. At he exit, the wave is aberration-free. We will present at the symposium very recent results obtained with a diffusing plate as aberrant medium.

5) Amplification of a polychromatic image

Amplification of a polychromatic image could lead, for example, to time-resolved studies of fluorescence phenomena (see next paragraph). To obtain such an amplification, phase-matching must be simultaneously satisfied over the widest area of both spatial and temporal frequencies. We have theoretically shown[17] that, in a type I crystal, parametric amplification is one beam non-critical for the signal wavelength as well as for the signal direction around a collinear degenerate configuration. It means that a variation of the refractive index for the signal wave, due to a shift of either its wavelength or its direction of propagation, is compensated by an opposite variation with the same amplitude of the index for the idler wave, provided that these variations are small enough to locally describe the index as a linear function of both the wavelength and the propagation angle. Hence, it is possible to amplify the signal for a large cone of wavevectors centered on the pump direction, with a large wavelength bandwidth centered on twice the pump wavelength (fig.3). The resulting wave forms a polychromatic image whose the mean propagation direction is collinear with the pump direction and corresponds to the zero spatial frequency.

Such a polychromatic image amplification has been experimentally demonstrated[22]. The polychromatic source was a continuum of wavelengths between 1064 and 1138 nm obtained through a Raman cell. This source illuminated the object and the image was formed in a LBO crystal. In order to verify that the image was correctly amplified for each wavelength of the theoretically expected 140 nm range (the wavelengths between 994 and 1064 nm being obtained with the idler), the amplified image was filtered with an interference filter whose bandpass is 5 nm. The filtered wavelength was tuned by rotation of the filter. At each wavelength, we verified that the obtained spatial resolution was in agreement with the theory.

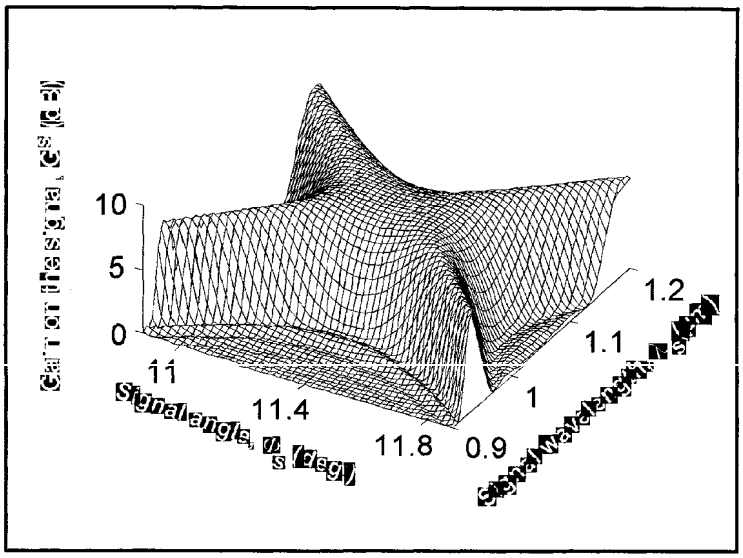

Fig. 3 : Effective gain on the signal Gs (in dB) , versus the signal wavelength and the signal direction in a 15 mm long LBO crystal. The angular width (FWHM) of the plateau is 8 mrad, while the wavelength bandwidth is 140 nm. The direction of the pump beam with respect to the crystal axes is fixed and corresponds to collinear degenerate phase matching. (After ref. 22)

6) Amplification of fluorescence signals

Fluorescence lifetime imaging is a powerful technique[23] , used to characterize biological samples. Images were recently obtained in the picosecond range with gated intensified cameras[24]. However, electronic limits the time resolution to one hundred picoseconds. By varying the delay between the excitation and the amplification, we have recently measured the decline time of a dye and we hope to extend in the next future these results to an imaging configuration. Results will be presented at the symposium. The time resolution of such a method is given by the duration of the pump pulse, inasmuch as this duration is greater than 1 ps. For shorter durations, walk-off effects and the non-monochromaticity of the pump pulse lead to reduction in the amplification efficiency. On the other hand , the fluorescence signal is amplified through all his spectral bandwidth, thank to the polychromatic nature of the amplification.

7) Phase-sensitive amplification

In a type I crystal at the degeneracy, the signal and the idler waves have the same polarization and the same wavelength. Hence, the image is formed by the coherent superposition of both waves. Two situations can occur :

- The incident signal plane wave is not collinear with the pump wave. In this

configuration, the mean direction of the idler wave, corresponding to the zero spatial frequency, is different from the mean direction of the signal wave. In the Fourier plane, spectra of the idler and of the signal are distinct. On the other hand, the idler and the signal add coherently in the image plane and form interference fringes that modulate the image. The position of these fringes depends on the relative phase of the three waves . Hence, the image amplification is phase-sensitive.

- If the incident signal wave is collinear with the pump wave, the signal and the idler can no more be distinguished, in the Fourier plane as well in the image plane. There is no more fringes but the global intensity in the amplified image is strongly dependent on the relative phase between the pump and the signal at the input of the crystal. In our experiments, this phase randomly varied from one laser shot to another, since the optical paths were not stabilized .

It was theoretically shown that these phase sensitive properties can be used to squeeze the noise[25] in optical images or to noiselessly amplify these images[26] (i.e. amplify without modification of the signal to noise ratio). These results can be thought of as the spatial domain counterpart of the phase-sensitive amplifiers in the time domain[27]. These properties were demonstrated to permit the amplification of a time-modulated quantum noise limited optical signal with an added noise level smaller than the 3-dB minimum characterizing a phase insensitive amplifier[28].

8. Conclusion.

Image parametric amplification appears as a promising technique to observe fast reproducible phenomena with a good resolution in two spatial and one temporal dimension.

References.

[1] J. E. Midwinter, "Image conversion from 1.6 µm to the visible in Lithium Niobate" Appl. Phys. Letters **12** (1968) 68-70.

[2] Y. Fainman, E. Klancnik and Sing H. Lee, "Optimal coherent image amplification by two-wave coupling in photorefractive $BaTiO_3$ ", Optical Engineering, **25**(1986) 228-234.

[3] M. A. Duguay and A. T. Mattick, "Ultrahigh speed photography of picosecond light pulses and echoes", Applied Optics **10** (1971) 2162-2170.

[4] P. V. Avizonis, F.A. Hopf, W.D. Bomberger, S. F. Jacobs, A. Tomita, M. H. Womack, "Optical phase conjugation in a lithium formate crystal", Appl. Phys. Letters **31** (1977) 435-437

[5] L. Lefort and A. Barthélémy, "Revisiting optical phase conjugation by difference-frequency generation", Optics Letters **21** (1996) 848-850

[6] F. Devaux, G. Le Tolguenec, E.Lantz, "Phase conjugate imaging by type II parametric amplification", Optics communications **147** (1998) 309-312.

[7] G. Le Tolguenec, F. Devaux, E. Lantz, "Imaging through thick biological tissues by parametric image amplification and phase conjugation", Journ. of Optics **28** (1997) 214-217

[8] D. Guthals and D. Sox, "Quantum limited optical parametric image amplification", Proceedings of International Conference on Lasers' 89, D. G. Harris and T. M. Shay Ed., (STS, Mclean,Va, 1990) 808-815.

[9] S. S. Ma, D. M. Guthals,B. F. Campbell and P H. Hu, "Three-dimensional anisotropic physical optics modeling of three wave mixing" , SPIE proceedings of conference "Laser resonators and coherent

optics : modeling, technology and applications", Jan. 1993, Los Angeles, USA. Vol 1868, 135-142.
[10] G. W. Faris, M. Banks, "Upconverting timegate for imaging through highly scattering media", Opt. Lett. 19 (1994) 1813-1815.
[11] F. Devaux, E. Lantz, A. Lacourt, D. Gindre, H. Maillotte, P. A. Doreau and T. Laurent, "Picosecond parametric amplification of a monochromatic image",
Nonlinear Optics **11** (1995) 25-37.
[12] F. Devaux and E. Lantz, "Transfer function of spatial frequencies in parametric image amplification : experimental analysis and application to picosecond spatial filtering",
Opt.Comm.**114** (1995), 295-300.
[13] F. Devaux and E. Lantz, "Ultrahigh-speed imaging by parametric amplification",
Opt. Comm. **118** (1995), 25-27.
[14] F. Devaux , E. Lantz, H. Maillotte, "Imaging through scattering media by parametric image amplification", Journal of Nonlinear Optical Physics and Materials **5** (1996),413 -417
[15] G. Le Tolguenec, E. Lantz , F. Devaux, "Imaging through scattering media by parametric amplification of images : study of the resolution and signal to noise ratio", Applied Optics **36** (1997) 8292-8297
[16] S. X. Dou, D. Josse and J. Zyss", Noncritical properties of noncollinear phase-matched second-harmonic and sum-frequency generation in 3-methyl-4-nitropyridine- 1-oxide",
J. Opt. Soc. Am. B **8** (1991) 1732-1739.
[17] E. Lantz, L. Han, A. Lacourt and J. Zyss, "Simultaneous angle and wavelength one-beam noncritical phase-matching in optical parametric amplification",
Optics Communications **97** (1993) 245-249.
[18] P. A. Laferriere, C. J. Wetterer, L. P. Schelonka and M. A. Kramer, " Spatial-frequency selection using down conversion optical parametric amplification",
J. Appl. Phys. **65** (1989) 3347-3350.
[19] B.C. Wilson, S.L. Jacques, "Optical reflectance and Transmittance of Tissues : Principles and Applications", IEEE Journ. of Quantum Electronics **26** (1990) 2186-2199.
[20] G. J. Tearney, B. E. Bouma, S. A. Boppart, B. Golubovic, E. A. Swanson, J. G. Fujimoto, "High Speed Optical Coherence Tomography", in Advances in Optical Imaging and Photon Migration 1996 technical digest, OSA, Washington DC, USA (1996) 217-219.
[21]G. J. Whitman and D.B. Kopans, "Mammography", in Advances in Optical Imaging and Photon Migration 1996 technical digest, OSA, Washington DC, USA (1996) 2-4.
[22] F. Devaux and E. Lantz, "Parametric amplification of a polychromatic image",
J. Opt. Soc. Am. B **12** *(1995)*, pp. 2245-2252.
[23] X.F. Wang and B.Herman Ed., "Fluorescence Imaging Spectroscopy and Microscopy", John Wiley & Sons Inc, New York (1996)
[24]K; Dowling, M. J. Dayel, M. J. Lever, P.M. W. French, J.D. Hares and A.K.L. Dymoke-Bradshaw,"Fluorescence lifetime imaging with picosecond resolution for biomedical applications", Opt. Letters **23** (1998) 810-812
[25] M. I. Kolobov and I. V. Sokolov, " Squeezed states of light and noise-free optical images", Phys. Lett. A. **140** (1989) 101-104.
[26] M. I. Kolobov and L. A. Lugiato, " Noiseless amplification of optical images",
Phys. Rev. A **52** (1995) 4930-4940
[27]C. M. Caves, " Quantum limits on noise in linear amplifiers",
Phys. Rev. D **26** (1982) 1817-1839.
[28] J. A. Levenson, I. Abram and T. Rivera, " Reduction of quantum noise in optical parametric amplification, J. Opt. Soc. Am. B **10** (1993) 2233-2238.

DETECTION OF FLAWS IN MATERIALS BY LASER-ULTRASONICS

J.-P.MONOCHALIN, C. NÉRON, M. CHOQUET, A. BLOUIN
B. REID, D. LÉVESQUE
Industrial Materials Institute, National Research Council of Canada
7.5 de Mortagne Blvd, Boucherville, Québec, J4B 6Y4, Canada

P. BOUCHARD, C. PADIOLEAU, R. HÉON
UltraOptec Inc. 27 de Lauzon St, Boucherville, Québec, J4B 1E7, Canada

Abstract

Laser-ultrasonics is a novel technology that uses lasers for the generation and detection of ultrasound and presents many advantages compared to conventional piezoelectric-based ultrasonics. In this presentation, the developments performed in this area at the Industrial Materials Institute of the National Research Council of Canada will be reviewed. Laser-ultrasonics has been used to detect flaws in a variety polymer-matrix composite materials and has been commercialized for this application. The detection of small flaws, in particular in metallic materials, by laser-ultrasonics has been addressed by using a numerical reconstruction algorithm based on the Synthetic Aperture Focusing Technique.

Keywords : laser-ultrasonic, laser-ultrasound, polymer composites, ultrasonics, ultrasonic nondestructive testing, Synthetic Aperture, Synthetic Aperture Focusing Technique, SAFT.

Introduction

Ultrasonic techniques are widely used for detecting flaws in materials [1]. The ultrasonic waves are usually generated and detected by piezoelectric transducers and coupled to the inspected part either by direct contact or through a water bath or a water jet. Although widespread and generally cost effective, these conventional ultrasonic techniques are of limited use in the case of parts at elevated temperature and of complex geometries. The first limitation follows from the need of a coupling medium (often water) or of contact between the transducer and the inspected part, whereas the second one is associated to the need of proper orientation of the transducer with respect to the surface (for pulse-echo mode measurements). Angular tolerance is about a few degrees or much less if the amplitude of the ultrasonic echoes has to be precisely monitored. Consequently, the inspection of curved or contoured parts requires a

A. Lagarde (ed.),
IUTAM Symposium on Advanced Optical Methods and Applications in Solid Mechanics, 437–450.

surface contour following device, which will be very complex and difficult to implement, especially in the case of acute discontinuities of the surface.

These limitations are eliminated by laser-ultrasonics that uses lasers for the generation and detection of ultrasound [2,3]. In laser-ultrasonics, transduction of ultrasound is performed at a distance, which in practice can range from centimeters to meters and therefore, eliminates the difficulties encountered by conventional ultrasonics for probing parts at elevated temperature. In laser-ultrasonics, the source of ultrasound is located at the surface of the material and detection of ultrasonic motion is performed off the same surface, which eliminates, as it will be explained below, the normalcy requirement of conventional ultrasonics.

We are reporting here the application of laser-ultrasonics to the detection of flaws in polymer-matrix composite materials and to the detection of much smaller flaws in a variety of materials, particularly in metals.

Principle of generation

The two applications reported here rely on different modes of generation. For polymer-matrix composite materials, the flaws of interest are essentially delaminations between layers or disbonds and are parallel to the surface. In this case a laser, such as the CO_2 TEA laser, which gives distributed absorption below the surface (10 to 100 μm typically) is used. Light penetration, which gives a buried acoustic source, conjugated with a sufficiently large spot size (typically 5mm or more in diameter) produces the emission of a longitudinal wave normal to the surface. This occurs independently of the shape of the surface and of the orientation of the laser beam. Unless very high power densities are used, the absorption of laser energy being distributed below the surface, generation is performed without any damage to the material.

For the other application, based on data processing with the Synthetic Aperture Focusing Technique (SAFT), a highly diverging ultrasonic wave is needed. In this case a small generation spot is used producing by diffraction the divergence needed. An ablation regime is also used and, according to the application, ranges from slight ablation and surface removal of contaminants (dirt, oil) to stronger ablation leaving a distinct crater on the surface. This regime produces much stronger emission than the thermoelastic non-invasive regime and gives also a broad emission lobe for the longitudinal wave centered along the normal to the surface instead of sharper lobes directed at an angle.

Principle of detection

The ultrasonic waves, after reflection or scattering by flaws inside the material or the back wall of the part, cause a small surface motion (typically in the range of one tenth of a nanometer to a few nanometers). The technique uses a laser different from the

laser used for generation to illuminate the area on the part where this motion occurs. The pulse duration of this laser should be sufficiently long to capture all the echoes of interest, which means for most practical applications a pulse duration of at least 10 μs. The use of a continuous laser is not a proper choice, since in this case, most of the light energy is obviously not used. The low power, which can in practice be obtained from a continuous laser compared to a pulsed laser, results also into a much lower sensitivity. We have developed a high power long pulse laser (typically 50 μs) based on Nd-YAG technology which is described below.

The ultrasonic surface motion produces a small phase shift or frequency shift (Doppler effect) in the scattered light, which is detected by an interferometric system. Note that, by opposition to most laboratory applications of laser-ultrasonics reported in the literature, the surface in the case of industrial use is usually rough and leads to a scattered beam with a random distribution of intensity and phase, known as speckle. Essentially, three approaches can be considered for detection: passive reference beam interferometry (called also optical heterodyning), time-delay interferometry (called also velocity interferometry) [4] and adaptive reference beam interferometry [5] (we are only considering the detection of normal or out-of-plane motion, not the detection of in-plane motion, which can also be detected by optical interferometry [6]). These approaches are explained below and their principles are sketched in Figure 1 a, b, c.

As shown in Figure 1a, in the case of passive reference beam interferometry [4], the surface of the inspected part acts as a mirror of the interferometer (represented here as a Michelson interferometer, but other two-wave interferometers such as the Mach-Zehnder can be used as well). The wave scattered by the surface that is affected by speckle interferes with the reference wave as shown in the insert diagram of Fig. la. Since the phase distribution across the scattered beam is random, the small phase shift produced by ultrasound is nearly averaged out, except if the phase distribution has been made sufficiently uniform by focusing onto the surface. Even in this case the final result can be very variable since the intensity of the collected speckle spot interfering with the reference beam is extremely variable. Therefore this technique presents many difficulties for application in industry. Note also that focusing could damage materials that are strongly absorbing (such as many polymer-matrix materials). Introducing an optical fiber link for additional flexibility causes also several difficulties (critical alignment, limitation of the transmitted power), since the fiber has to be single mode in order to preserve phase coherency. The reference beam technique has however a broad detection bandwidth essentially limited by the detector bandwidth. Note however that the technique can be improved by cleaning the wave scattered by the surface from its speckles by optical phase conjugation in a photorefractive crystal, using either a double passage on the surface [7] or the Double Phase Conjugation Mirror scheme [8]. The improvement is however limited, either by the increased attenuation caused by the double passage on the surface or the slow response time of the Double Phase Conjugation Mirror.

The principle of time-delay interferometry [4], which is a better scheme for detection in an industrial environment, is shown schematically in Figure lb. In this

technique the scattered light is frequency or phase demodulated by an optical filter, as shown schematically by the insert of Figure 1b. This optical filter is in practice realized by an interferometer giving time delay between the interfering waves. Note that in this case, the probed surface is not part of the interferometer as such. Although two-wave interferometers such the Michelson (represented in Figure 1b) or the Mach-Zehnder can be used, they would be very bulky for efficient detection of frequencies in the 1-15 MHz range, most appropriate to our applications because of the long path delay required. A multiple-wave interferometer, i.e. a Fabry-Perot, is then preferable and is used in the systems we have developed. In the technique of time-delay interferometry, when the interferometer used has a sufficiently large étendue or throughput (field-widened Michelson or Mach-Zehnder or Fabry-Perot of the confocal type [9]), adaptation of the delayed wave front(s) to the undelayed one(s) is automatically realized. This technique then effectively uses many speckles for detection and focusing onto the surface is not required. The collected light can also be coupled through a large core multi-mode fiber for additional flexibility. A drawback that follows from the principle of optical filtering is a non-flat detection bandwidth. This is however not a severe limitation, since the interferometer can be designed to give sensitivity in the frequency range of interest by adjusting the time delay or varying the reflectivity of the mirrors (in the case of the confocal Fabry-Perot). One should also remember that conventional ultrasonic inspection uses essentially bandwidth-limited devices for emission and detection. The systems we have developed use typically 50 cm or one meter long confocal Fabry-Perot with an optical bandwidth of typically 5 to 10 MHz. Detected light is coupled to the interferometer by a large core multi-mode fiber having an étendue slightly less the confocal Fabry-Perot. It should also be noted that a very broad bandwidth extending towards high frequencies is obtained when the confocal Fabry-Perot is used in reflection [10]. In this case the interferometer behaves likes a two-wave interferometer in which the wave scattered off the surface and reflected by the front mirror interferes with a reference wave without sidebands leaked by the cavity.

However time-delay interferometry or the confocal Fabry-Perot scheme cannot provide a flat response towards low ultrasonics frequencies (below 1 or 2 MHz). The combination of broad frequency response only limited by the detector and speckle insensitive detection is obtained by adaptive reference interferometry, the principle of which is sketched in Figure 1c. A photorefractive crystal is used as an adaptive mixer between the signal wave scattered off the surface and a reference wave diffracted by the hologram produced inside the crystal. In order to have holograms which follow the change of the speckle caused by vibrations and sample motion, as well as the risetime of the detection laser pulse, semiconductors crystal have to be used (GaAs, InP, CdTe). Recent developments pursued in association with the Institut d'Optique Théorique et Appliquée/CNRS (Orsay, France) and Laboratoire d'Action Aquitaine en Apesenteur (Bordeaux, France) have shown that this approach has an excellent sensitivity, exceeding the one obtained with the confocal Fabry-Perot used in transmission and approaching the ultimate sensitivity that can be obtained by interferometry [11].

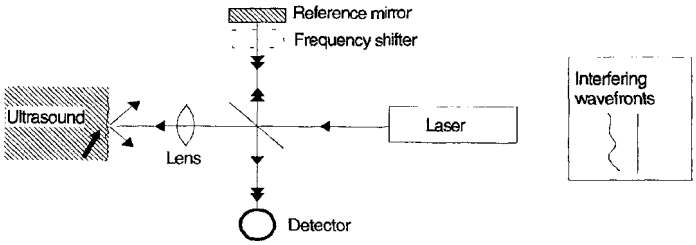

a. Reference beam interferometry

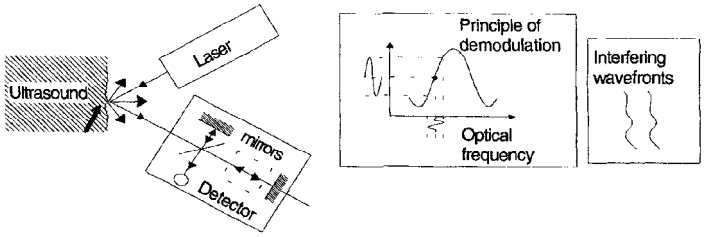

b. Time-delay interferometry

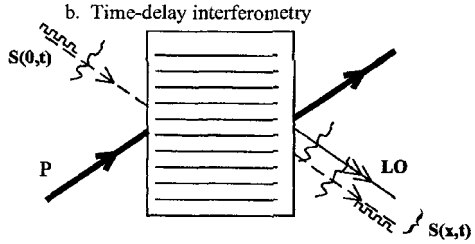

c. Two-wave mixing in a photorefractive crystal

Figure 1. Schematic of the three possible interferometric detection techniques:

a. Reference beam interferometry: in some interferometric schemes the reference wave is frequency offset by a RF frequency (heterodyne interferometers). The ultrasonic signal then appears as a phase modulation at the offset frequency. The insert schematically represents the two interfering wavefronts, when focusing is not optimized.

b. Time-delay interferometry: the principle is illustrated here with a Michelson interferometer (which has been field-widened, as indicated by the dashed line box in the long interferometer arm), but a multiple-wave interferometer such as the confocal Fabry-Perot is often preferable. The two inserts represent the principle of demodulation and, schematically, the two interfering wavefronts which, in this case match in good approximation.

c. Adaptive reference interferometry (two-wave mixing): the transmitted signal wave scattered off the surface S is mixed with an adapted reference wave originating from the diffraction by the hologram of the pump wave P derived from the laser. The interfering wavefronts and the signal modulation are shown schematically.

Detection of flaws in polymer-matrix composite materials

We first describe the system that has been developed and then present the numerous results obtained with it.

DESCRIPTION OF THE SYSTEM DEVELOPED

The laser-ultrasonic system developed is made of two units, a detection unit and a generation unit, linked by optical fibers and is sketched in Figure 2 [3,12-13]. The generation unit comprises a TEA CO_2 laser for ultrasound generation, optics for coupling colinearly the generation and detection laser beams and large size optics for collecting the scattered light from the surface of the inspected part. In addition, a two-axis mirror scanner, the same size as the collection optics, is used for scanning across the part. The generation spot is typically 5 mm.

The generation unit is linked by optical fibers to the detection unit comprising the detection laser and the demodulating interferometer, which is a confocal Fabry-Perot used in transmission. One fiber is used to transmit light from the detection laser, while the other one is used to bring scattered light to the interferometer. Both fibers are approximately 15 meters long and shielded. The detection laser is based on Nd-YAG technology, provides long pulses (~ 50 μs long) at the repetition rate of 100 Hz, is highly stable in frequency and has high peak power (~ 2 kW). The confocal Fabry-Perot is one meter long and has an optical bandwidth of ~ 8 MHz. A PC computer controls the optical scanner and houses a sampling card for digital acquisition of the A-scans. Specially developed imaging software is then used to display C-scans and B-scans.

The system we have developed operates at a distance of ~ 1.5 m between the surface and the optical scanner and can scan from a fixed system position an area of ~ 1.8 m x 1.8 m or even larger depending upon the scattering properties of the surface.

Such a system is commercially available. In more recent developments, a system that allows the scanning of much larger surfaces was assembled by UltraOptec for the US Air Force. By mounting the generation unit at the end of the arm of a gantry robot, parts of the size of a wing can be inspected. This system includes also a distance-measuring device to determine at the same time during the scan the shape of the part. This system is associated to a 3-D imaging software that allows visualizing part shape and ultrasonic results at the same time (as shown in Figure 4 below).

Finally, note that the confocal Fabry-Perot used in the system described above could advantageously be replaced now by the recently developed adaptive photorefractive reference interferometer. With this novel detection scheme, we have demonstrated that deeply buried flaws are more easily detected, as expected from the increased sensitivity at low ultrasonic frequencies [14].

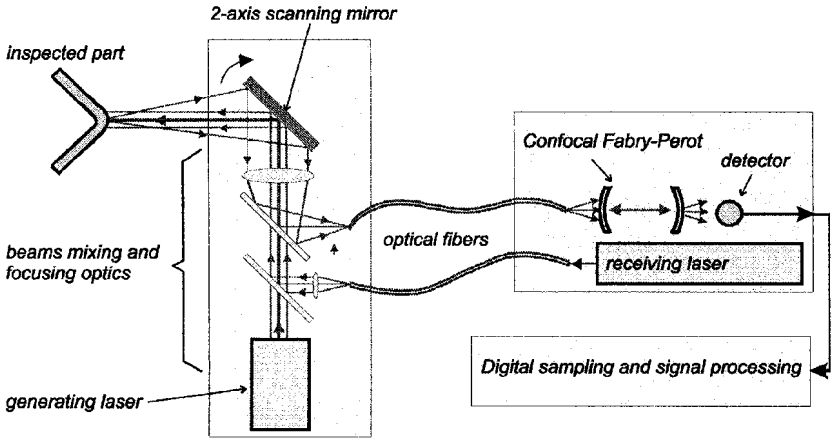

Figure 2: Schematic of the system developed for composite materials inspection

RESULTS OBTAINED ON COMPOSITE PARTS

The use of the system described above with the confocal Fabry-Perot receiver has been demonstrated on parts of more than one meter across and on a large variety of smaller parts with acute curvature [3,12-13]. These parts included laminates of various thicknesses (from a few plies to a thickness of more than one inch), made of various materials (graphite epoxy, kevlar epoxy, glass epoxy), with a bare surface or a painted surface. Specimens with slopes and comers and parts with U-shape, T-shape and sine wave cross sections were also tested. The technique was also demonstrated on various honeycomb structures. Defects such as porosity, disbonds, delaminations and impact damage can be detected.

As an example we show in Figure 3 the detection of the delaminations caused by an impact on a flat specimen. The specimen was impacted at 4 locations with various amounts of energy. Delaminations were produced at two locations as shown by laser ultrasonic inspection. As a second example, in a 3-D view, we show in Figure 4 the results of the inspection of a contoured specimen, which has a U-shape and has implanted flaws at various depths along two flat surfaces and along one corner. The various implanted flaws, including the ones implanted along the corner, are all clearly located. A thickness increase when going through the comer is also observed.

INSPECTION OF A CF-18 PLANE IN A MAINTENANCE HANGAR

These tests were performed at the Canadian maintenance facility for CF-18 fighters and conducted on a plane that had already been serviced and inspected according to the prescribed maintenance procedure (using in particular manual ultrasonic inspection) [12-13]. It was in a flying condition and fully loaded with fuel. It had not been the object of any particular preparation for laser ultrasonic inspection.

Various parts of the aircraft fuselage, wing and stabilizer were inspected. We are presenting here, as example, only one result obtained on the horizontal stabilizer, which is a complex composite structure with an aluminum honeycomb core (see Figure 5 below). The laser-ultrasonic inspection reveals the complex inner structure of this part. As should have been expected, since the plane had gone through complete inspection before our tests, we did not find any important flaw over the whole airframe, which would have required a repair. Only a small defect was found, of a size well below the critical size requiring corrective action.

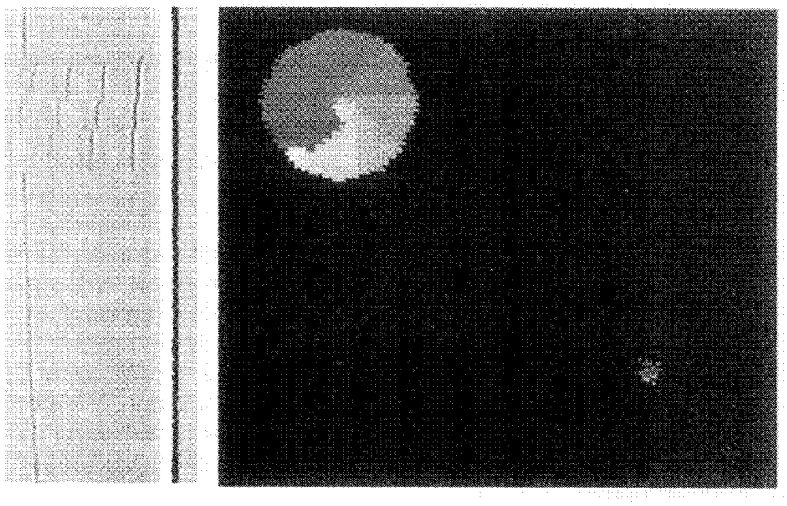

Figure 3: Laser-ultrasonic C-scan image of the damage produced by an impact on a graphite-epoxy laminate. Right: time-of-flight C-scan, left: B-scan though the severe impact.

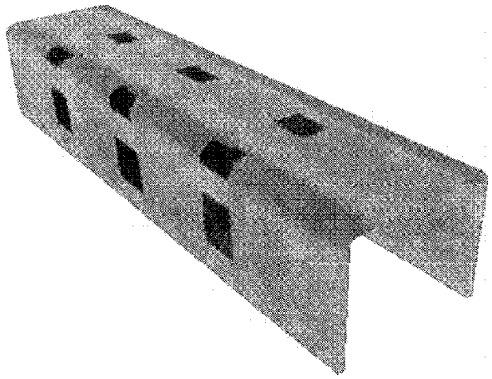

Figure 4: Laser ultrasonic time-of-flight C-scan of the comer part shown in 3-D.

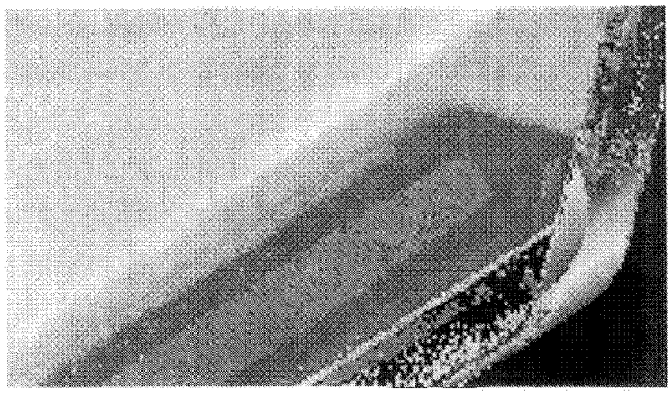

Figure 5: Laser-ultrasonic C-scan image of the edge of the horizontal stabilizer of a CF-18.

Detection of small defects by laser-ultrasonics and SAFT processing

The system described above uses broad laser spot illumination (typically 5 mm in diameter) and produces an ultrasonic beam with little divergence. Its resolution is essentially limited by the size of this spot, so it is inadequate for detecting small defects of size of 1mm and less. On the other hand, if the laser beam is focused onto a small spot, a strongly diverging wave is obtained, leading also to poor resolution for the detection of deep flaws. In conventional ultrasonics, the detection of small buried defects is achieved by focusing the acoustic field with lenses or curved transducers or using a computational technique that basically consists in performing the focusing numerically, the Synthetic Aperture Focusing Technique (SAFT). We are reporting below the use of SAFT coupled to laser-ultrasonics to detect small flaws [15].

PRINCIPLE OF SAFT

We assume that the generation and detection beams are focused at the same location onto the surface. By scanning the beams or moving the part fixed on an X-Y translation table with discrete and equal steps, a 2-D mesh at the surface of the specimen is obtained. As shown in figure 6, if a pointlike flaw is present at point C located at a depth z within the sample, this flaw re-radiates the acoustic field originating at point M_i. The acoustic signal $S(M_i,t)$ received at any point M_i in the measurement mesh exhibits a peak at time $t = 2d_i /v$, where v is the longitudinal acoustic velocity in the material and di the distance CM_i. Consequently, the summation

$$\Sigma(C) = \sum_{M_i \in \text{mesh}} S\left(M_i, t = \frac{2\,d_i}{v}\right) \qquad (1)$$

separates the points C where superpositions build up and flaws are present, from the points C where no coherent superposition occurs and the material is sound. Moreover,

the function $\Sigma(C)$ increases the signal-to-noise ratio for the detection of flaws by the factor $\sqrt{N}$, where N is the number of points M_i in the measurement mesh aperture (the synthetic aperture).

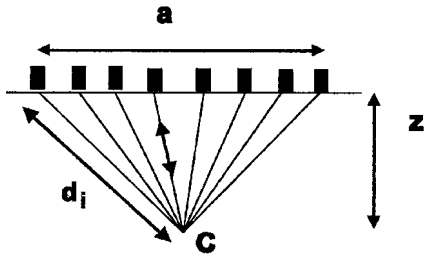

Figure 6. Principle of SAFT.

It can be shown that SAFT processing leads to improved lateral resolution while maintaining depth resolution. These resolutions are respectively:

$$\Delta x \approx v\Delta t\frac{z}{a} \quad , \quad \Delta z \approx \frac{v\Delta t}{2} \qquad (2)$$

where Δt is the ultrasonic pulse duration and a is the dimension of the synthetic aperture. In practice, the strength of ultrasonic wave emission and the detection sensitivity both decrease away from the normal to the surface, so that the total opening angle of the synthetic aperture is limited to roughly 60°, which means a ~ z.

This data processing approach, while straightforward in its principle and implementation, is not very efficient and is very computation intensive. For this purpose, we have developed a better approach performing data processing in the Fourier domain (F-SAFT). This approach benefits from the Fast Fourier Transform algorithm and leads to reduced processing time [16-17].

DESCRIPTION OF THE LASER-ULTRASONIC SETUP AND OF THE TEST SPECIMEN

The generation laser was a short pulse (≈ 5 ns) Q-switched Nd:YAG laser operating on its fourth harmonic and producing slight ablation at the sample surface. Detection used the long pulse Nd:YAG laser mentioned above and a confocal Fabry-Perot interferometer. The generation and detection lasers were focused onto the flat surface of the specimen at about the same location. For practical reasons, an X-Y translation table was used to move the tested parts instead of scanning the laser beams.

The test specimen was made from a 40 x 16 x 7 mm aluminum block. One of its surface was machined to obtain a non-planar back surface, as shown in figure 7. To simulate buried flaws, two flat-bottom holes of 1 and 0.5 mm in diameter and 1.5 mm deep were drilled from the back surface. The step size of the scan was 0.1 mm and the scanned area was about 25.4 x 10 mm. The generation and detection spot sizes were 0.1

mm and 0.3 mm respectively. For each node M_i of the measurement mesh, an A-scan was collected, digitized and stored in the computer memory.

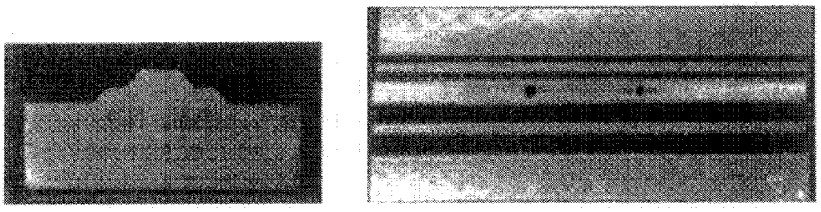

Figure 7: Pictures of the test specimen, left: side view, right: top view.

EXPERIMENTAL RESULTS OBTAINED ON THE ALUMINUM TEST SPECIMEN

An improvement to the raw data was first obtained by applying a high pass filter with a cut-off frequency of 4 MHz on the signals, to remove any offset and low frequency surface waves. The filtered data were then processed using the F-SAFT algorithm and figure 8 shows C-scans of both the filtered and F-SAFT processed data. Each C-scan was obtained by selecting the peak-to-peak value from each A-scan in a narrow gate at depths between 5.2 and 5.7 mm corresponding to the bottom of the holes. The profiles along a line crossing the holes on these C-scans are also shown. When compared to the filtered data, the F-SAFT processed data show strong improvements of the detectivity and of the lateral resolution of the flat-bottom holes. The temporal width of the ultrasonic pulse extracted from the backwall echo was $\Delta t = 90$ ns, which yields lateral and depth resolution estimates from equation (2) of $\Delta x \approx 0.6$ mm and $\Delta z \approx 0.3$ mm, in agreement with experimental observations.

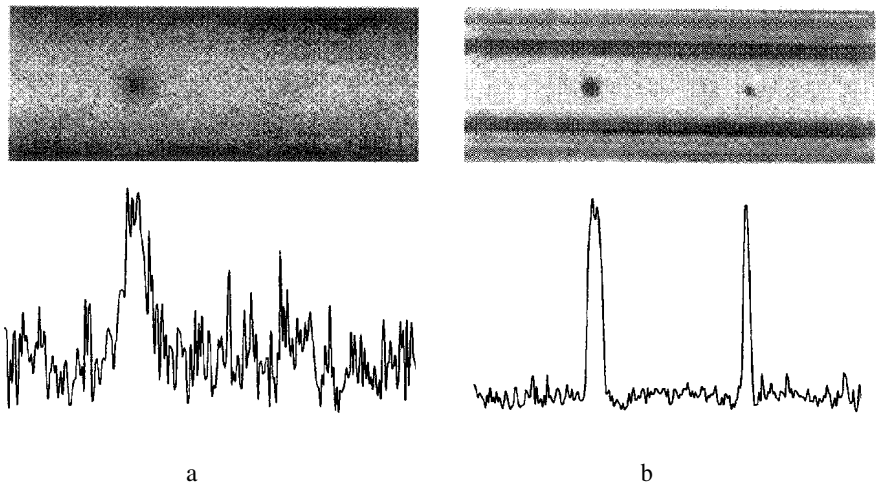

a b

Figure 8: C-scans and profiles of the (a) filtered and (b) F-SAFT data.

B-scans of the filtered and F-SAFT processed data are shown in figures 9a and 9b. These two images show that SAFT processing can also be used to resolve the contour of a non-planar back surface. In figures 9c and 9d, the B-scans are taken through the 0.5 mm diameter flat-bottom hole and both the contoured back surface and the flat-bottom holes are still resolved. With prior knowledge of the part shape, the laser-ultrasonics SAFT technique can also be applied to samples with contoured front surfaces. Quite clearly from these results, F-SAFT processing has brought a very significant improvement to defect detection and sizing and to the resolution of the backwall contour. It should be mentioned that the SAFT processing cannot be performed in real-time since it requires all data from the measurement mesh to operate. As an example, the F-SAFT processing time for this experiment was about 20 minutes on a PC Pentium Pro, 200 MHz under Windows NT for an initial data set of 255 x 101 A-scans of 301 data points ($\approx$ 7.7 x 10^6 data points) and for reconstruction at 151 depths.

Conclusion

We have developed new technology for detecting flaws in materials that allows ultrasonic inspection in cases where conventional ultrasonics had severe limitations or was not applicable at all. This technology has been applied to the detection of defects in polymer-matrix composite materials and it has been proven to be very effective, particular in the case of complex geometries. It is now commercially available.

We have then addressed the detection of defects smaller than the ones generally of interest in composite materials by coupling laser-ultrasonics and SAFT. We have demonstrated an improvement of lateral resolution and of the signal-to-noise ratio. With previous knowledge of the part shape the technique can be applied to parts with complex geometries.

Acknowledgements

The CF-18 inspection tests were sponsored by the Canadian Department of National Defense under contract no. W8477-2-AC30/01-BB. The impacted specimen was provided by the Institute for Aerospace Research of the National Research Council of Canada. The U-shape specimen was provided by the Department of National Defence of Canada.

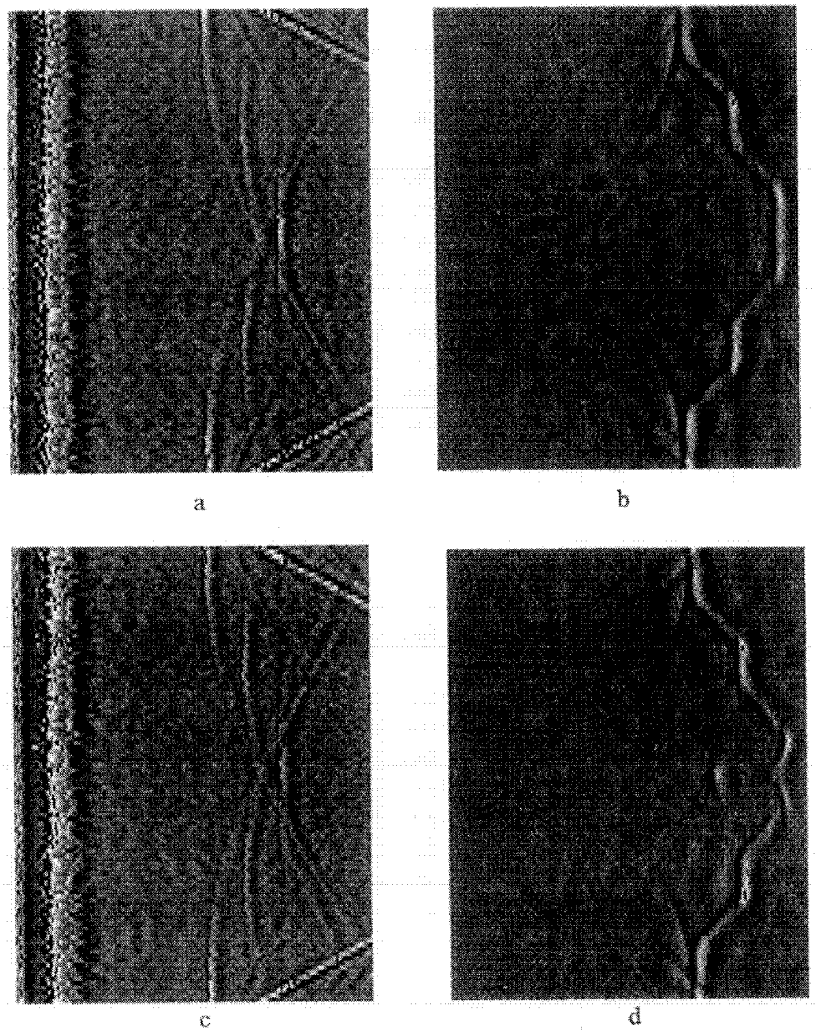

Figure 9: B-scans of filtered (a,c) and F-SAFT processed data (b,d) from the aluminum test specimen. The B-scans of figures 9c and 9d were taken through the 0.5-mm diameter flat-bottom hole.

References

1. J. Krautkrämer and E. Krautkrämer, *Ultrasonic Testing of Materials,* (Springer Verlag, New-York, 1983).
2. C. B. Scruby and L. E. Drain, *Laser-Ultrasonics: Techniques and Applications* (Adam Hilger, Bristol, UK, 1990)

3 J.-P. Monchalin, Progress towards the application of laser-ultrasonics in industry, *Review of Progress in Quantitative Nondestructive Evaluation,* edited by D. O. Thompson and D. E. Chimenti (Plenum Publishing Corporation, 1993), vol. 12, pp. 495-506.

4. J.-P. Monchalin, Optical detection of ultrasound, IEEE Trans. Sonics, Ultrasonics, Freq. Control, UFFC-33, pp. 485-499 (1986).

5. A. Blouin and J.-P. Monchalin, Detection of ultrasonic motion of a scattering surface by two-wave mixing in a photorefractive GaAs crystal, Appl. Phys. Lett., vol. 65, pp.932-934 (1994).

6. J.-P. Monchalin, J.-D. Aussel, R. Héon, C. K. Jen, A. Boudreault and R. Bernier, Measurements of In-Plane and Out-of-Plane Ultrasonic Displacements by Optical Heterodyne Interferometry, J. Nondestructive Evaluation, vol. 8, pp.121-133 (1989).

7. M. Paul, B. Betz and W. Arnold, Interferometric detection of ultrasound at rough surfaces using optical phase conjugation, Appl. Phys. Lett., vol. 50, pp. 1569-1571 (1987).

8. P. Delaye, A. Blouin, D. Drolet and J.-P. Monchalin, Heterodyne detection of ultrasound from rough surfaces using a double phase conjugate mirror, Appl. Phys. Lett., vol. 67, pp. 3251-3253 (1995).

9. J.-P. Monchalin and R. Héon, Laser ultrasonic generation and optical detection with a confocal Fabry-Perot interferometer, Materials Evaluation, vol. 44, pp. 1231-1237 (1986).

10. J.-P. Monchalin, R. Héon, P. Bouchard, C. Padioleau, Broadband optical detection of ultrasound by optical sideband stripping with a confocal Fabry-Perot, Appl. Phys. Lett., vol. 55, pp. 1612-1614 (1989).

11. P. Delaye, A. Blouin, L.-A. de Montmorillon, D. Drolet, J.-P. Monchalin, G. Roosen, Photorefractive detection of ultrasound, *SPIE conference* San Diego, July 1997, Proceedings SPIE vol. 3137, pp. 171-182 (1997).

12. J.-P..Monchalin, C. Néron, P..Bouchard, M. Choquet, R. Héon, C. Padioleau, Inspection of composite materials by laser-ultrasonics, Canadian Aeronautics and Space Journal, vol.43, no 1, pp.34-38 (1997).

13. J.-P. Monchalin, C. Néron, J. F. Bussière, P. Bouchard, C. Padioleau, R. Héon, M. Choquet, J.-D. Aussel, C. Carnois, P. Roy, G. Durou, J. A. Nilson, Laser-ultrasonics: from the laboratory to the shop floor, Advanced Performance Materials, vol. 5, pp.7-23 (1998).

14. A. Blouin, P. Delaye, D. Drolet, L.-A. de Montmorillon, J.-C. Launay, G..Roosen, J.-P. Monchalin, Optical detection of ultrasound using two-wave mixing in semiconductor photorefractive crystals and comparison with the Fabry-Perot, 8th International Symposium on Nondestructive Characterization of Materials, Boulder, Colorado, June 15-20, 1997, edited by R. E. Green Jr. and C.O. Ruud (Plenum Publishing Corporation, 1998), in press.

15. A. Blouin, D. Lévesque, C. Néron, F. Enguehard, D. Drolet and J.-P. Monchalin, "SAFT Data Processing Applied to Laser-Ultrasonic Inspection", *Review of Progress in Quantitative Nondestructive Evaluation,* edited by D. O. Thompson and D. E. Chimenti (Plenum Publishing Corpomtion,1998), vol 17, pp. 611-617.

16. K. Mayer, R. Marklein, K. J. Langenberg and T. Kreutter, Three-dimensional imaging system based on Fourier transform synthetic aperture focusing technique, Ultrasonics, vol. 28, p. 241 (1990).

17. L. J. Busse, "Three-dimensional imaging using a frequency-domain synthetic aperture focusing technique", IEEE Trans. Sonics, Ultrasonics, Freq. Control, UFFC- 39, p.174 (1992).

AN EXTENSION OF HOLOGRAPHIC MOIRÉ TO MICROMECHANICS

C.A. SCIAMMARELLA
F.M. SCIAMMARELLA
Illinois Institute of Technology
Dept. of Mechanical Materials and Aerospace Engineering
10 West 32nd St. El bldg. Chicago IL, 60616 U.S.A.

Abstract

The electronic Holographic Moiré is an ideal tool for micromechanics studies. It does not require a modification of the surface by the introduction of a reference grating. This is of particular advantage when dealing with materials such as solid propellant grains whose chemical nature and surface finish makes the application of a reference grating very difficult. Traditional electronic Holographic Moiré presents some difficult problems when large magnifications are needed and large rigid body motion takes place. This paper presents developments that solves these problems and extends the application of the technique to micromechanics.

1. Introduction

In [1] one of the authors presented a method to measure displacements and to obtain strains in the microscopic range by using electronic holography. This method can only be used in static problems. The method is based on repeated measurements of a specimen under the same conditions. This paper presents a different approach. A similar optical arrangement is utilized but the actual data processing method has been changed so that dynamic measurements can be performed.

2. Review of the Foundations of the Method

Recording holographic interference patterns via a CCD camera and the reconstruction of those patterns by electronic means are referred to in the literature as holographic TV, electronic holography, electronic speckle pattern interferometry. The patterns are recorded in the same way as in conventional lens holography with an almost in line reference beam. The fringe interpretation is the same as in conventional holographic interferometry. The basic equation of holographic interferometry is valid,

A. Lagarde (ed.),
IUTAM Symposium on Advanced Optical Methods and Applications in Solid Mechanics, 451–466,

$$\phi = \frac{2\pi}{\lambda}(\mathbf{d} \bullet \mathbf{s}) \tag{1}$$

where ϕ is the phase angle corresponding to a point in the region of analysis, l is the wavelength of the illuminating light, **d** is the displacement vector of the considered point and **S** is the sensitivity vector. In most of the currently utilized systems, the recovery of the displacement information is done by a method that is very similar to the method proposed initially by Leendertz [2] in speckle interferometry. This technique is based on the correlation of the speckle patterns corresponding to the initial or unloaded condition and the final or loaded condition. A complete description of this technique and examples of its application can be found in [3]. A computer version of this technique has been given in [4]. In [5] a different approach is presented. In [6] a procedure based on the precise relocation of a specimen by a control system, via fiduciary marks is presented.

2.1. HOLOGRAPHIC MICROSCOPY

The use of holography in microscopy has been the object of extensive studies. Holographic microscopy has also been applied to many different technical and scientific fields. The different applications shows the versatility of holography as a tool in microscopy, but at the same time they reveal the enormous difficulties there are to obtain optimum conditions. Most of the effort has been placed on eliminating the speckles to get adequate resolution. In the application that we are analyzing the information is encoded in the speckles, therefore we must preserve them. The resulting image will be of poor quality, thus the problem has to be approached in the following way. A white light image of the region of interest must be recorded to obtain the features of interest. The images to measure the displacements must be recorded with coherent light. Afterwards the displacement field must be related to the surface features. The speckle visibility must be optimized to obtain the displacement information with optimum signal to noise ratio. The speckle visibility depends on many variables and requires a complex statistical analysis. However, an elementary analysis can be employed to get an insight on the main variables controlling fringe visibility. The equation

$$I(r') = \left[\int_A k(r, r') A(r) e^{i\phi(r)} dA \right]^2 \tag{2}$$

expresses the intensity in the image plane of the recording lens system. In (2), r is the polar coordinate of a point in the object plane and r' is the coordinate of the same point in the image plane, the term $A(r)\, e^{i\phi(r)}$ represents the object field and k(r,r') represents the spread function of the imaging system. The spread function defines the area of the object that contributes to the image at a given point of the image. The other factor defines the amplitude and phase of the region of influence determined by the spread function. The amplitude variations depend on the changes in reflectivity and phase of the surface. In turn, these quantities depend on the statistical properties of the surface. The larger the changes of phase and reflectivity are in the area of influence of the point under observation, the greater are the changes of intensity in the image, causing speckles with more contrast.

2.1.1. *Basic Properties of the Microscope*
The basic properties of interest are:
a) Displacement resolution
b) Spatial resolution
d) Magnification
e) Depth of focus
The displacement resolution depends on the configuration of the optical system. We are interested in the in-plane displacements consequently the double illumination technique is used. Since we have two beams that act as reference beams to each other, no additional reference beam is necessary. Calling θ the angle of the beams with the normal to the surface that at the same time is the direction of observation we get,

$$\Delta d = \frac{\lambda}{2\sin\theta} \tag{3}$$

One important consideration in making microscopic measurements is the fact that since the region under observation is small, even if the strains are high, the displacements will also be small. We can see that the sensitivity is limited by θ and by the wavelength of the light. The spatial resolution Δs is related to the numerical aperture (NA) of the lens system through a relationship of the form,

$$\Delta s \propto NA^{-1} \tag{4}$$

The above equation indicates that to get the best resolution possible the NA must be increased. There is another requirement, depth of focus Δz,

$$\Delta z \propto NA^{-2} \tag{5}$$

This implies that if we increase the NA to get the best resolution possible we lose depth of focus. The transversal size of the speckle is given by,

$$\Delta p \propto NA^{-1} \tag{6}$$

and the longitudinal size Δl,

$$\Delta L \propto NA^{-2} \tag{7}$$

3. Techniques to Obtain Displacement Information

As shown in Fig. 1 we have a specimen that is illuminated coherently by four symmetrically oriented beams. The microscope focuses the surface of the specimen onto the CCD camera sensor. If we consider a region within the area of influence

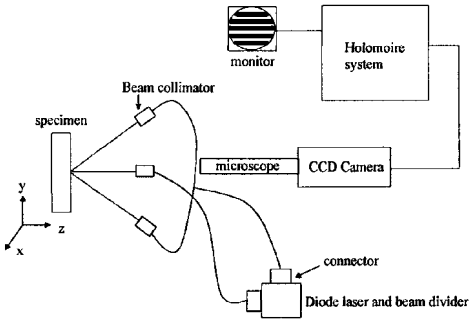

Figure 1. Set up

defined by equation (2), the total light amplitude reaching this region is made out of four components. We have four beams, two in the x-direction and two in the y-direction. $E_{1x}=E_{1x}\, e^{i\phi}{}_x$, $E'_{1x}=E_{1x}\, e^{-i\phi'}{}_x$ in the x-direction and $E_{2y}=E_{2y}\, e^{i\phi}{}_y$, $E'_{2y}=E_{2y}\, e^{-i\phi'}{}_y$ in the y-direction. In these equations the E's represent the amplitudes of the illumination beams, and the ϕ's represent the phases in the same region. If we assume that the two orthogonal systems of illumination are non coherent (direction of polarization orthogonal to each other), the intensity gathered in the region will be,

$$I_{1T}(x,y) = I_o + 2I_{1x}\cos\psi_x(x,y) + 2I_{2y}\cos\psi_y(x,y) \tag{8}$$

where $I_{1x}=(E_{1x})^2, I_{2y}=(E_{2y})^2$, $\psi_x(x,y) = \phi_x-\phi_x'$, $\psi_y(x,y) = \phi_y-\phi_y'$. Let us assume that a deformation has been applied to the specimen and that this deformation leaves the E's substantially unchanged and only causes phase changes. The second exposure results in an intensity distribution,

$$I_{2T}(x,y) = I_o + 2I_{1x}\cos\left[\psi_x(x,y)+\Delta\phi_x\right] + 2I_{2y}\cos\left[\psi_y(x,y)+\Delta\phi_y\right] \tag{9}$$

where,

$$\Delta\phi_x = 2\pi f_p u(x,y) \tag{10}$$

$$\Delta\phi_y = 2\pi f_p v(x,y) \tag{11}$$

In the above equations $f_p = 2\pi \sin\theta/\lambda$ and u, v are the components of displacement parallel to the x and y directions respectively. The intensities are converted into voltages, and without loss of generality can be considered proportional to the received intensities. A non-linear recording will produce [7] additional harmonics that can be removed by spatial filtering. By subtracting the signals to remove the background term we obtain,

$$\begin{aligned} V(x,y) = K\{&2I_{1x}\left[\cos\psi_x(x,y)-\cos\left[\psi_x(x,y)+\Delta\phi_x\right]\right] \\ &+2I_{2y}\left[\cos\psi_y(x,y)-\cos\left[\psi_y(x,y)+\Delta\phi_y\right]\right]\} \end{aligned} \tag{12}$$

Expanding the difference of the cosines, and taking the Fourier transform of (12), calling ξ and η the coordinates in the frequency space with the notations,

$$\bar{V}(\xi,\eta) = FT\left[V(x,y)\right] \tag{13}$$

$$A_x(\xi,\eta) = FT\left[\sin\left[\psi_x(x,y)+\frac{\Delta\phi_x}{2}\right]\right] \tag{14}$$

$$D_x(\xi,\eta) = FT\left[\sin\frac{\phi_x}{2}\right] \tag{15}$$

And similar definitions for $A_y(\xi,\eta)$ and $D_y(\xi,\eta)$ we get,

$$\bar{V}(\xi,\eta) = 4K\left\{I_{1x}\left[A_x(\xi,\eta)\otimes D_x(\xi,\eta)\right] + I_{2y}\left[A_y(\xi,\eta)\otimes D_y(\xi,\eta)\right]\right\} \quad (16)$$

where $\otimes$ indicates convolution. The quantities in brackets are the FT of random signals (speckles) convolved with a deterministic function that contains the displacement information. Our purpose is to separate the spectra of the functions that contain the displacement information from other spectral components. The approach presented here is to re-establish the correlation between the unloaded and the loaded images by a procedure that is a generalization of the optical technique described in [5].
With the notations,

$$F_{ix} = 2K_{1x}\cos\psi_x(x,y) \quad (17)$$

$$F_{dx} = 2KI_{1x}\cos\left[\psi_x(x,y) + \Delta\phi_x\right] \quad (18)$$

$$F_{iy} = 2KI_{2y}\cos\psi_y(x,y) \quad (19)$$

$$F_{dy} = 2KI_{2y}\cos\left[\psi_y(x,y) + \Delta\phi_y\right] \quad (20)$$

we can write equation (12) assuming that a displacement d_x is given to the loaded recording,

$$V(x,y) = F_{ix}\otimes\delta(x,y) - F_{dx}\otimes\delta(x+\Delta x,y) + F_{iy}\otimes\delta(x,y) - F_{dy}\otimes\delta(x+\Delta x,y) \quad (21)$$

If we take the FT (the FT is indicated by the bar quantities) of (21), and replace the subtraction by the addition with a phase change of π we obtain,

$$\bar{V}(\xi,\eta) = \bar{F}_{ix} + \bar{F}_{dx}e^{i\gamma} + \bar{F}_{iy} + \bar{F}_{dy}e^{i\gamma} \quad (22)$$

if we neglect the effect of the displacements caused by the deformations $\Delta x = d_x$ and the argument γ is,

$$\gamma = 2\pi d_x\,\xi + \pi \quad (23)$$

Then by squaring (22),

$$\left[\bar{V}(\xi,\eta)\right]^2 = H(\xi,\eta)\left[1 + C\cos\gamma\right] \quad (24)$$

where,

$$H = \left|\bar{F}_{ix} + \bar{F}_{iy}\right|^2 + \left|\bar{F}_{dx} + \bar{F}_{dy}\right|^2 \quad (25)$$

and

$$C = \frac{\left|\bar{F}_{ix} + \bar{F}_{iy}\right|\left|\bar{F}_{dx} + \bar{F}_{dy}\right|}{\left|\bar{F}_{ix} + \bar{F}_{iy}\right|^2 + \left|\bar{F}_{dx} + \bar{F}_{dy}\right|^2} \quad (26)$$

H (ξ,η) is a random function (speckle pattern) and C is a visibility term that provides the visibility of the fringes formed in the frequency space [8]. If we take the FT of (24),

$$\left|\overline{V(\xi,\eta)}\right|^2 = \overline{H(\xi,\eta)}\delta\,(0,0) + \left|\overline{CH(\xi,\eta)}\right|\,\delta\,(d_x,0) \tag{27}$$

To illustrate the formation of fringes in the frequency space the orthogonal patterns shown in Fig.2 were created. An initial image was recorded and then separately two recordings were made with shifts in the x and y directions. The FT's of the subtracted images were computed and then added bringing forth Fig. 2. If we take the FT of the pattern in Fig. 2 we get the spectrum of the fringes in the frequency space, Fig. 3. The

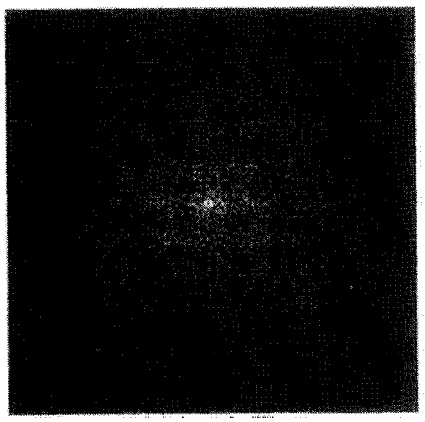

Figure 2. Fringes in FT space.

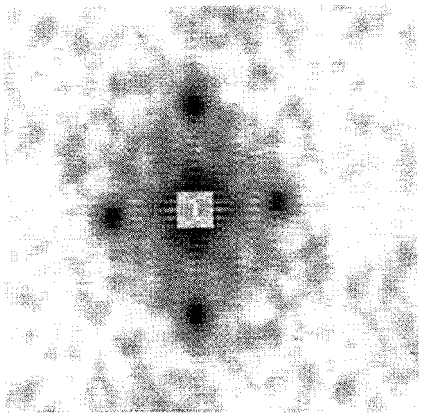

Figure 3. Spectrum of the fringes.

distances of the spectrum peaks in the x and y directions to the origin of coordinates provide the displacements d_x and d_y. If the image in Fig. 2 is filtered, we get Fig. 4 that displays the pattern of fringes without the background noise. Each time that the fringes have a minimum, for example in the x-direction,

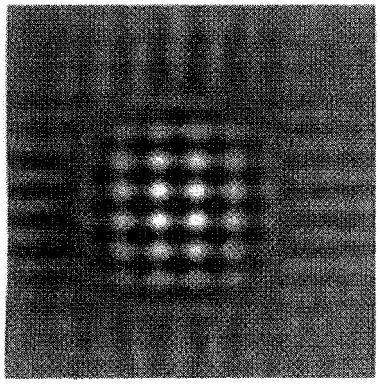

Figure 4. Filtered system of fringes.

$$\xi = \frac{2n-1}{2d_x} \tag{28}$$

the patterns in the initial and in the loaded conditions are re-correlated as it can be concluded from equation (22). When the following relationship is satisfied, Fig. 5,

$$f_0 = \xi_0 = \frac{1}{2d_x} \tag{29}$$

where f_o is the central frequency of the spectrum of the displacement fringes, the spectrum is located in its correct position. At any other minimum the fringe pattern will be shifted of a certain frequency shift $\Delta\xi$ with respect to the central frequency f_o as shown in Fig. 6. If we select a displacement such that the correlation occurs at the frequency ξ_1, then we filter the spectrum at this frequency we get,

$$V(x,y) = F_{ix} - F_{dx}e^{2\pi i\Delta_\xi x} \tag{30}$$

and

$$V(x,y) = 2KI_{1x}\left[\cos\psi_x(x,y) - \cos\left[\psi_x(x,y) + \Delta\phi_x + 2\pi\Delta_\xi x\right]\right] \tag{31}$$

Calling $\beta = \Delta\phi_x + 2\pi\,\Delta_\xi\,x$, after squaring we get the signal displayed in the monitor,

$$V^2(x,y) = 8K^2I_{1x}^2\sin^2\left[\psi_x(x,y) + \frac{\Delta\beta}{2}\right]\left[1 - \cos\beta\right] \tag{32}$$

If we integrate the speckle pattern in the x-direction and use the notation

$$I = 4K^2I_{1x}^2 \tag{33}$$

the signal has the form,

$$V^2(x,y) = I[1 - \cos\beta] \tag{34}$$

We have a pattern of fringes that contains the displacement information in the x-direction and have a visibility of one. The fringes will have minima at points where $\beta = 2n\pi$ and maxima every time that that $\beta = (2n+1)\,\pi$. These fringes contain a carrier frequency and to remove it one must know the central frequency of the spectrum of the fringes. If one has an estimate of the central frequency one can use two frequencies f_1

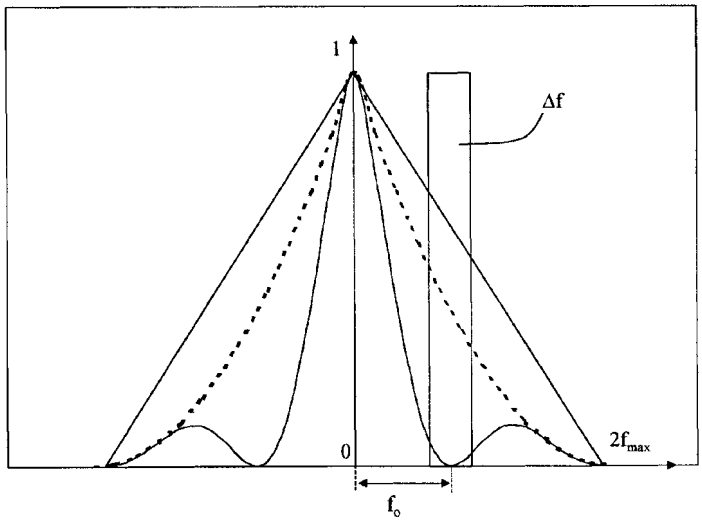

Figure 5. Filtering in the FT space.

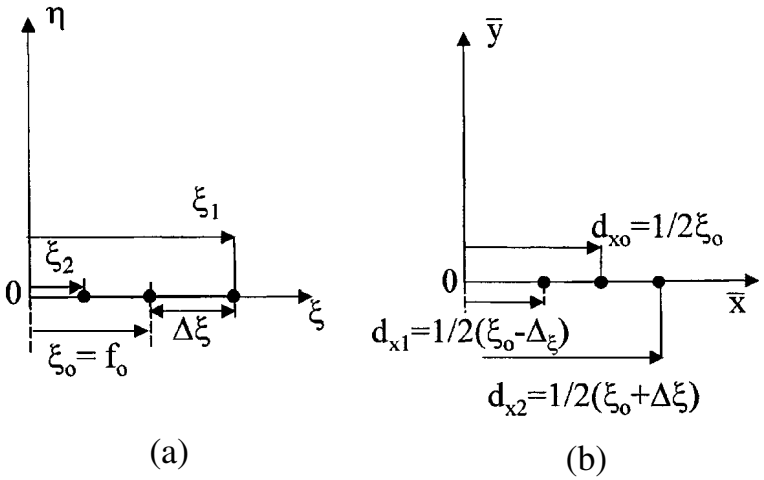

Figure 6. (a) Frequency space. Spectrum corresponding to the fringe in the physical space. (b) FT of the frequency space. Spectrum corresponding to the displacements in the physical space.

and f_2 above and below the central frequency and by successive steps reach f_o taking into consideration that the phase will remain stationary at f_o.

3.1. ALTERNATIVE TECHNIQUE TO RECOVER THE DISPLACEMENT INFORMATION

In the preceding sections, the spectrum of the displacement fringes was recovered by shifting the loaded image with respect to the unloaded of a given amount. An alternative technique for recovering displacement information can be used in the case when large magnifications are utilized and the individual speckles cover several pixels. This technique is carried out by means of fiduciary marks. These marks allow the two images to be re-positioned within one pixel, and thus the recovery of the displacement information can be achieved. The phases of the individual speckles in the unloaded and the loaded positions are determined [9]. The subtraction of these phases will yield,

$$[\psi_x(x+y)+\Delta\phi_x(x,y)]-\psi_x(x,y)=\Delta\phi_x(x,y) \tag{35}$$

The phase differences are encoded on a carrier,

$$V(x,y)=V_o\{1+\cos[2\pi f_{cx}x+\Delta\phi_x]\} \tag{36}$$

where f_{cx} is the carrier frequency in the x-direction. The spectrum of the displacement fringes is encoded in the fringes and can be recovered by filtering and removing the carrier.

4. Applications

Our example deals with strain measurements carried out on propellant grain tensile specimens. A system for testing tensile specimens was designed and built. The system consists of Fig. 1: a) a loading frame with micrometric motions in three orthogonal directions, b) an optical fiber interferometer, c) a microscope connected to an electronic system. The fiber optics interferometer consists of a solid state laser whose output goes to four fibers that produce four collimated beams to measure displacements in two orthogonal directions. The fibers are not polarization preserving fibers but light polarization was adjusted by bending the fibers and separately matching the polarization of the horizontal beams and of the vertical beams. The observation system uses a microscope and it is possible to perform measurements in the range of few hundreds of microns up to 3 mm, maximum size of the area illuminated by the fiber optics system. The basic characteristics of the illumination system are as follows: a) angle of illumination $\theta = 45°$, b) wavelength of laser $\lambda = 0.635$ μm, c) displacement sensitivity $\Delta d = 0.447$ μm. Fiduciary marks on the specimen surface were used to restore the position of the loaded image. Many measurements were carried out on these specimens. For this paper, we are going to concentrate on the micromechanics measurements.

Propellant grains are a mixture of a rubber matrix with crystalline particles embedded in it. A binder is added to the particles to insure the adherence of the particles to the matrix. The surface of the propellant is extremely rough and the numerical aperture of the lens (NA) in the measurements carried out in this work was limited by this circumstance. The large particles in the propellant are about 400 μm in size and of prismatic shape. Measurements were carried out at two different magnifications. In the first magnification the pixel size in the y-direction was $\Delta y = 1.83$ μm and in the second magnification applied $\Delta y = 0.834$ μm. The NA for the second group of measurements was NA = 0.0253. The speckle size was determined in three ways, directly by measurements in the image plane, by computation and by measuring the diameter of the halo in the frequency space. The three determinations yielded very close numbers around 15 μm for the pixel diameter. For this study, measurements were performed in a region of a tensile specimen where a particle was present. Since the particle has Young's modulus that is four orders of magnitude bigger than the rubber matrix, the particle can be considered as rigid. During the computation of the strains, the particle was considered as an internal boundary. Fig. 7a shows the strains in the axial directions for the image filtered at the central frequency determined by successive approximations, for the stress level in the tensile specimen of $\sigma = 78$ KPa. Fig. 7b shows the results of the same measurement by re-correlating the image using a displacement that satisfies equation (29). Fig. 8a shows the strains determined by introducing a displacement that moves the spectrum of the signal to the 12 harmonic. Fig. 8b shows the strains when the spectrum is displaced to the 16^{th} harmonic. In view of the difficulties involved in performing micromechanics measurements, the different patterns agree reasonably well. Fig. 9a shows the region around the particle for the stress level $\sigma = 39$ Kpa. The strains in this region were determined by re-correlating the spectra of the unloaded and the loaded recordings, obtained with the magnification yielding $\Delta y = 1.83$ μm. Fig. 9b shows the strains in the same region obtained with a different magnification ($\Delta y = 0.834$ μm). The two strain distributions agree well. To get the strain distribution shown in Fig. 9b the phases of the unloaded and the loaded images were computed, subtracted and then the phase difference was encoded in a carrier. The strains were obtained by differentiating the carrier [9] and removing the strain equivalent to the carrier frequency. In all the previous cases of fringe analysis the region of the gradients between the matrix and the particle are poorly resolved. It is not possible with the equipment at hand to have a broader view of a region and at the same time to obtain accurate spatial resolution if a steep gradient is present. The CCD camera has sensors at a given distance, so the frequency resolution in the frequency space depends on the size of the regions analyzed. To illustrate this point two regions of the particle-matrix boundary are analyzed. At the side of the particle the strain parallel to the particle (axial strain), must be zero at the surface of the particle and then it should build up to the value in the field. In Fig. 9 b the analyzed section is shown. Fig. 10 shows the first 50 μm of the boundary of the particle matrix. Fig. 11 shows the strains along the indicated cross-sections. At the end of the particle there is continuity of the stress and therefore the strain must jump to the prevailing value of the matrix, Fig. 9b shows the area that is analyzed. Fig. 12 shows the details of the region and Fig. 13 shows three cross sections.

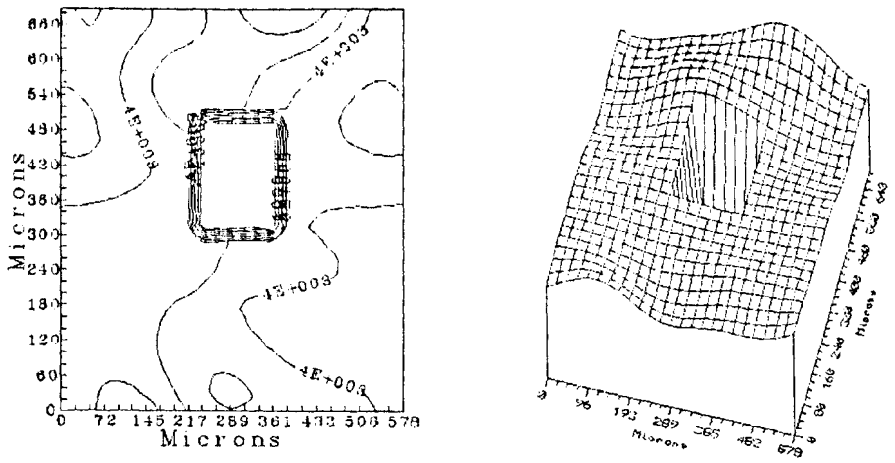

(a)

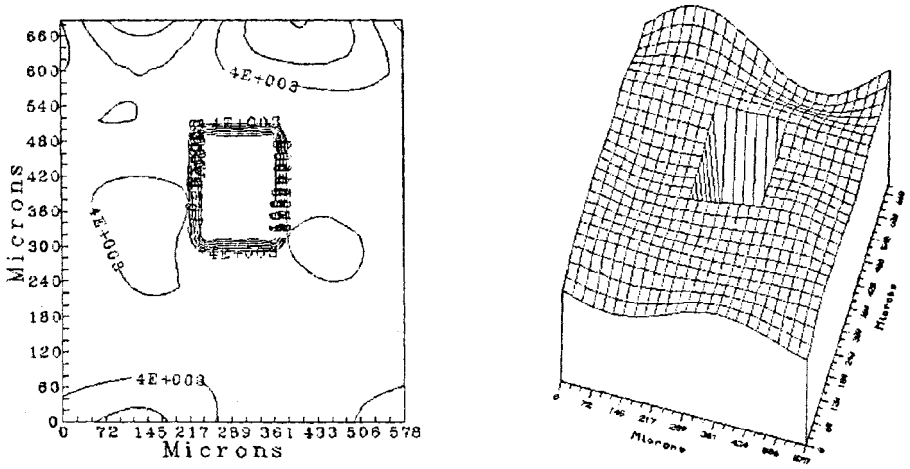

(b)

Figure 7. Strains in the y-direction (longitudinal direction)
in a region of a particle embedded in a rubber matrix.
(a) Filtered image at the frequency $f_o = 8$ harmonic.
(b) Filtered image (shifted 30 pixels) $f_{o1} = 8$ harmonic.

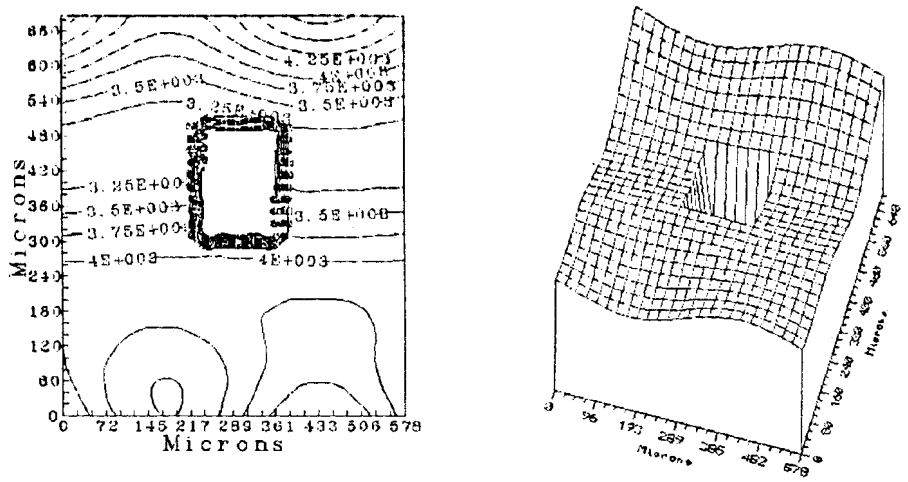

(a)

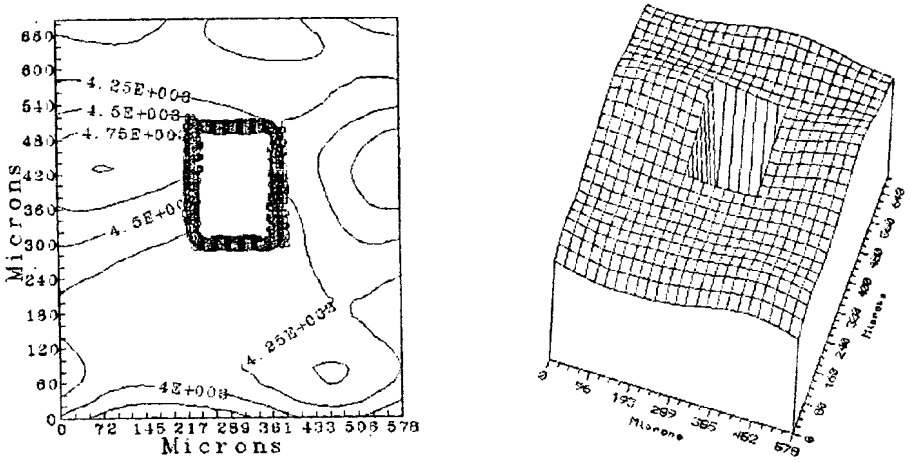

(b)

Figure 8. (a) Filtered image (shifted 20 pixels) $f_2 = 12$ harmonic and removing the carrier fringe with (4^{th} harmonic) to obtain $f_o = 8$ harmonic.
(b) Filtered image (shifted 15 pixels) $f_3 = 16$ harmonic and removing the carrier fringe with (8^{th} harmonic) to obtain $f_o = 8$ harmonic.

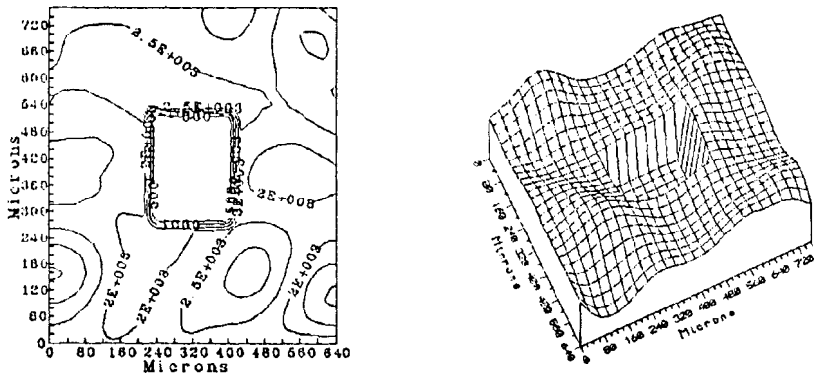

(a)

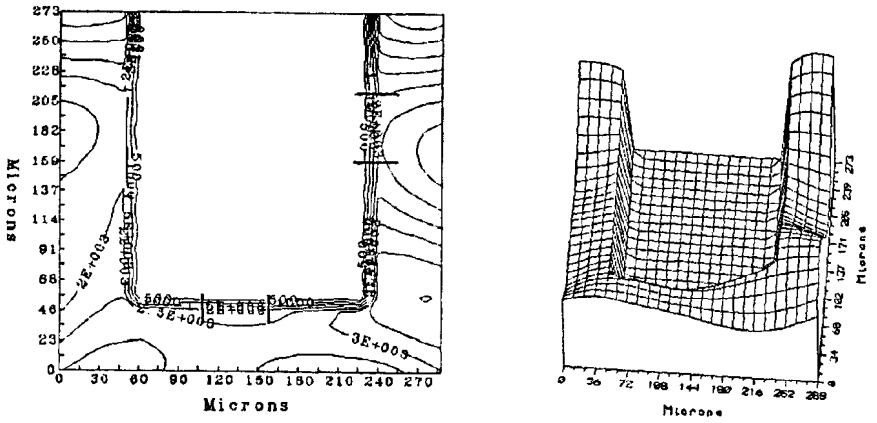

(b)

Figure 9. Strains in the y direction σ_y = 39 kPa
a) Obtained by recorrelation and filtering Δy = 1.83 μm.
b) Obtained by speckle phase subtraction and filtering Δy=0.847μm.

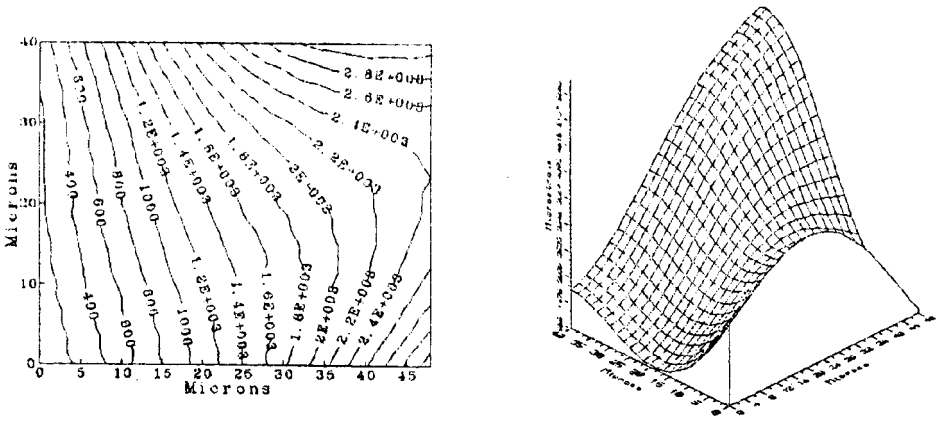

Figure 10. Strains at the right boundary of the particle region shown in Fig. 9b.

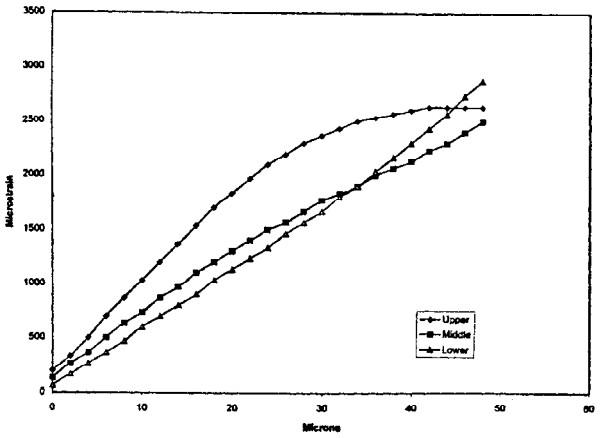

Figure 11. Cross sections of the strain distributions shown in Fig. 10.

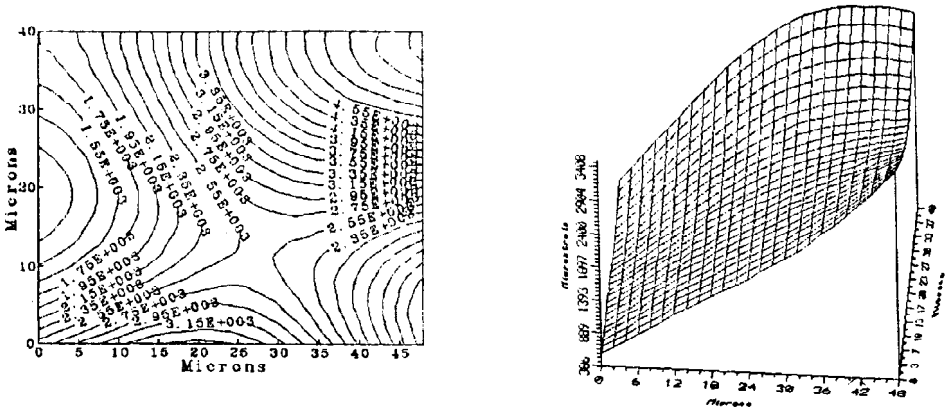

Figure 12. Strains at the lower boundary of the particle section shown in Fig. 9b.

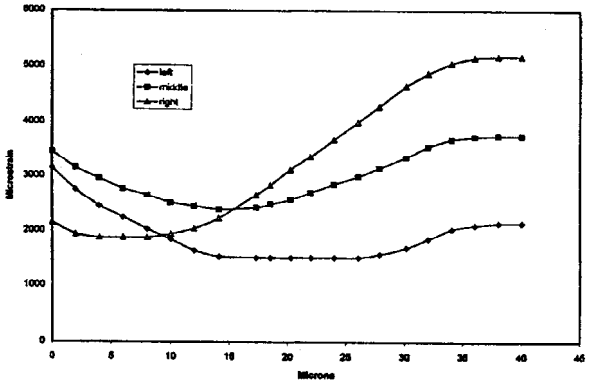

Figure 13. Cross sections of the strains shown in Fig. 12.

5. Discussion and Conclusions

The presence of large speckles in the field has a significant impact on the data processing particularly if the speckles have low modulation or if there are sudden changes of phase. These features introduce phase errors that are averaged by the filtering process. More work needs to be done to introduce standard procedures required to overcome the different problems that are encountered. In spite of all the obstacles that are posed by the characteristics of the propellants surface, valuable micromechanics information has been gathered and some of the obtained results are confirmed through data obtained by other means.

6. Acknowledgments

The application work presented in this paper has been supported by the United States Airforce. The authors would like to give special thanks to Dr. C.T. Liu of the Phillips Laboratory for his support.

7. References

1. Sciammarella, C.A., Bhat, G., Longinow, N., Zhao, M. (1989) A High Accuracy Micromechanics Displacement Measurement Optical Technique, in W.N. Sharpe, Jr. (editor), Micromechanics: Experimental Techniques, ASME, New York, pp. 121-132.
2. Leendertz, J.A. (1970) Interferometric Displacement Measurement on Scattering Surfaces Utilizing the Speckle Effect, *J. Phys. Series E: Scientific Instruments* **3,** 214-218.
3. Rastogi, P.K. (1979) Visualization et Measure des Déplacements Tangentiels, et de DéformationsAssociées, par Moiré Holographiques et Interférométrie Speckle, Doctoral Thesis France,L'Universite de Franche-Comte, Besancon, 49-51.
4. Ahmadshahi M.A., Krishnaswamy, S., Nemat-Naser, S. (1991) Dynamic Two-Beam Interferometry, in Fu Pen Chiang (editor), Proceedings of the Second International Conference in Photomechanics and Speckle, SPIE, Bellingham, Wa,**1554A,** 620-627.
5. Archbold, E., Burch, J.M., Ennos, A.E. (1970) Recording of in-plane Displacement by Double Exposure Speckle Photography, *Optica Acta,* **17**(12), 883-898.
6. Sciammarella, C.A., Bhat, G., Bayeux, P. (1993) A portable electro-optical interferometer, Proceedings of the Conference on Advanced Technology in Experimental Mechanics, The Japan Society of Mechanical Engineers, Tokyo, 155-160.
7. Sciammarella, C.A., Doddington, C.W. (1967) Effect of photographic-film nonlinearities on the Processing of moiré-fringe data, *Experimental Mechanics,* 7, 398-402.
8. Burch, J.M., Tokarski, M.J. (1968) Production of Multiple beam fringes from photographic scatters, *Optical Acta,* **15**(2), 102-111.
9. Sciammarella, C.A., Bhat, G. (1991) Computer assisted techniques to evaluate fringe patterns, in RysardJ. Pryputniewicz (editor), Laser Interferometry IV: Computer Aided Interferometry, SPIE, Bellingham, Wa, **1553,** 252-262.

STEREOLITHOGRAPHY AND MICRO-MECHANICS

Serge MONNERET, Serge CORBEL, Virginie LOUBERE
Département de Chimie Physique des Réactions
UMR 7630 CNRS-INPL
Ecole Nationale Supérieure des Industries Chimiques de Nancy
1 rue Grandville – BP 451 - 54001 Nancy Cedex
FRANCE

Abstract : Laser stereolithography deals with the manufacture of three-dimensional objects that are made by space-resolved laser-induced polymerization. In order to obtain three dimensional microobjects, we developed a new microstereolithography apparatus based on the use of a dynamic mask-generator which allows the manufacture of a complete layer by only one irradiation, the part being manufactured layer by layer. This process uses a broad-band visible light source, that leads to the elimination of speckle effects resulting from the conventional use of a laser beam. A lateral resolution of 2 μm * 2 μm has been demonstrated with this new process.

Introduction

Microtechnologies started a few centuries ago with the watch-making industry. The manufacturing of clock components has led to constant progress in the design of new mechanisms, as well as in the development of new technologies. Such a domination of mechanics as regards miniaturization and precision continued until the recent appearance of microelectronics, about 30 years ago : microelectronics technologies have been developed to improve miniaturization, in order to manufacture higher density integrated electronic components. This leads to a higher functional frequency due to shorter displacements of charge carriers inside the structures.

Nowadays, the same microfabrication processes are beginning to be applied to the manufacture of integrated mechanical systems on silicon chips. Such microsystems are called Micro Electro Mechanical systems (MEMs) and can lead to many applications such as micromotors, microsensors, microactuators, micropositioning systems [1-4]…

The main limitation of these processes is that they can be adapted only to manufacturing planar components presenting a maximal thickness of about 20 micrometers. Then, several recent processes have been developed to manufacture thick micro-parts. The most successful is the so-called LIGA process, based on deep-etch x-ray lithography and subsequent replication processes like electroforming and molding [5]. However, the use of a synchrotron source leads to limitations because of its expense and avaibility constraints. A new negative-tone near-UV resist (IBM SU-8) has been recently designed specifically for ultrathick, high-aspect-ratio MEMs-type

A. Lagarde (ed.),
IUTAM Symposium on Advanced Optical Methods and Applications in Solid Mechanics, 467–474.

applications, based on a low-cost LIGA-type process [6]. Because they are lithography-based, the main limitation of these LIGA-type processes is that complex shapes cannot be made easily, in particular ones with curved surfaces, or many layers.

This is why applying stereolithography (SL) to the field of micro-fabrication appears to be an attractive alternative process to the manufacture of real three-dimensional microobjects with complex shapes.

After recalling the principles of the SL technique, we briefly present previous research concerning applications of SL to microtechnics. Lastly, we describe a new apparatus of micro-SL, which is based on the use of a broad-band visible light source.

2. The Stereolithography technique

Stereolithography [7] is a process which has been performed to manufacture three-dimensional objects, mainly for rapid prototyping applications.

The basic principle is a space-resolved light-induced polymerization, consisting of a liquid/solid phototransformation. Current machines work by laying down a thin layer of resin and shining the proper wavelength of light on it in a pattern that describes the two-dimensional shape of a single cross section of the object to be built. Once a single cross section is built in this way, a new layer of resin is applied and the process is repeated. Then thin layers made of solidified photopolymer are stacked from bottom to top to create complicated three dimensional shapes, leading to true 3D microparts obtained quickly and with no assembly. Finally, a scraper is also used to ensure a homogeneous thickness of the new liquid resin layer, each time the process is repeated.

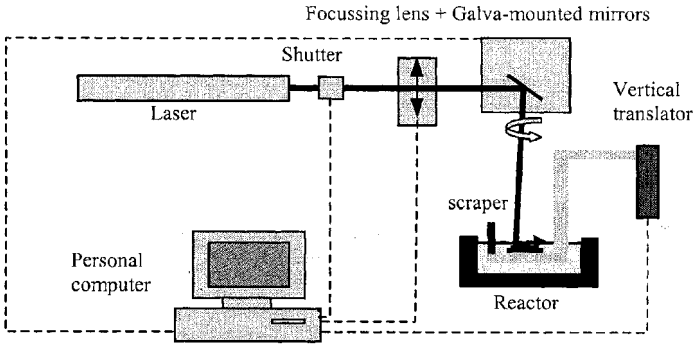

Figure 1. The conventional SL process

Once the object to be built is designed (generally using Computer Aided Design processes), it is then numerically sliced to define the different cross sections of the object to be manufactured. Then, the numerical data defining each of the sections are sequentially sent to the machine, in order to built them.

Two principal kinds of SL processes can be distinguished up to now, depending on the way is built the cross section . The first, which can be considered as conventional, is based on the vectorial tracing of each layer of the object by moving a focused laser beam over the surface of the resin (Fig. 1). Galva-mounted mirrors are then used, and the light is shut off by a mechanical shutter during jumps of the laser beam between different polymerized segments, or when a new layer of liquid monomer is made. A dynamic focusing lens is used to ensure the laser beam is exactly focused on the resin surface, at any place on it.

The second kind of process allows one to build a complete layer by only one irradiation, by imaging its pattern directly with a masked lamp. But this needs to define a mask each time the pattern is changed, and to use a laser beam with much stronger intensity.

When compared to the conventional machining techniques, SL has the advantages that it needs neither molds nor tools, and the parts can have almost any shape. It is used principally in the rapid prototyping field; the manufacturing industries which are already using this technology include automotive, aerospace, and medical industries. The manufactured objects have a typical volume of about a few dm^3 with a spatial resolution of 100 μm.

3. Extension to micro-Stereolithography

To improve the accuracy obtained by the SL technique for manufacturing three dimensional microobjects, several processes have been studied [8,9]. In order not to introduce moving elements which can lead to a loss of resolution, no galva-mounted mirrors nor dynamic focusing lens to deflect and focus the light beam are used. The focus point of the light beam then remains fixed on the surface of the resin, while an x-y positioning stage moves the resin reactor in which the object is made. But the reactor must be translated very slowly to ensure the required stability of the surface of the liquid resin during the polymerization step. The main limitation of this process is that it takes longer to manufacture a layer, compared to the use of galva-mounted mirrors.

This is why a new process of micro-stereolithography (μ-SL) technique has been developed in our laboratory [10], which allows us to manufacture a complete layer by only one irradiation, the three-dimensional microobject being still manufactured layer by layer. As already shown in Ref. [10], this type of μ-SL process presents a number of advantages, which will be briefly described now.

First, the limitation to only one moving operating element leads to a good stability during the curing step. Moreover, the light flux density on the surface of the resin is low compared to that is used with vectorial processes which are based on very fast displacements of a strongly focussed laser beam on the surface of the resin. As a consequence, thermal-induced problems can be considered as negligible. Finally, the process has the potential of being much faster than classical vectorial processes, since the irradiation of an entire layer is enacted simultaneously.

The major disadvantage of this process is that the liquid crystal matrix allows poor transmission for ultraviolet (UV) light. So, it is necessary to use a light source emitting in the visible spectrum and consequently to use a photochemical mixture which is photosensitive to these wavelengths [11].

An initial apparatus has been constructed using a coherent and visible light source (Ar+ laser emitting at 515 nm). It used a liquid crystal display (LCD) as a dynamic mask generator [10].

Complex objects have then been obtained with a resolution of 5 μm in the three directions of space [11]. Prototypes of microactuators having a distributed elasticity and made of multiple imbedded springs have also been realized. As an example, Fig. 2 shows such a microactuator which was moved by using shape memory alloy (SMA) wires in the clamping areas [12].

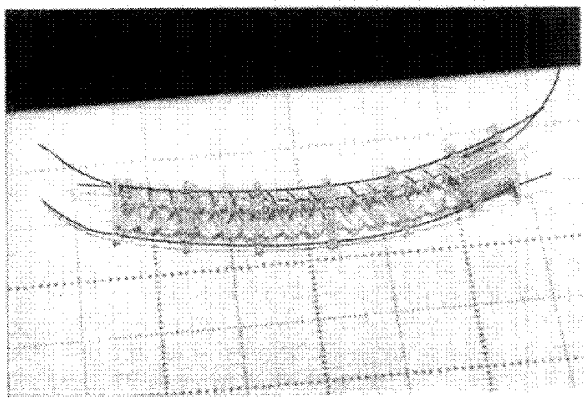

Figure 2. Photograph of a distributed elasticity microactuator after SMA wire assembly [12]

4. Micro-Stereolithography using a dynamic mask generator and a non coherent light source

We are now developing a new μSL apparatus still based on the use of a dynamic mask generator, but using a non-coherent broad-band halogenic light source. There are in fact several tradeoffs between using a masked enlarged laser beam versus a masked lamp to cure the layers of photopolymer resin :

- A laser is potentially more energy efficient, since a lamp generates much useless light outside the range of frequencies to which any particular resin is photosensitive.
- There is some evidence that monochromatic light, as generated by a laser, yields more uniform-in-depth curing for thicker layers, but the gaussian intensity

distribution of such a laser beam leads to non uniform curing in the covered mask area.

- The coherence of a laser beam leads to a strong local inhomogeneity of the projected image, due to speckle effects.
- The broad spectrum of a lamp means that it can be used with many different resins, whereas a laser must be used with resins specifically tuned to its frequency.
- The use of a lamp strongly decreases the production cost of the microparts.

Thus, it may be attractive to conceive a new μ-SL machine from a broad-band visible light source.

4.1. EXPERIMENTAL SETUP

The experimental setup of the process is given in figure 3. The beam is issued from a conventional halogenure light source (dataprojector-based). After its propagation through the computer-controlled liquid crystal display (L.C.D) which contains the pattern of the layer, the beam is then reduced and focused on the surface of the photocurable resin. As in Ref. [10], a LCD is then used as a dynamic mask generator. By connecting a computer to this device, we can set every pixel either to its transparent or to its opaque state by changing the orientation of molecules composing it. The contrast ratio of about 1:100 of the LCD is sufficient to use it also as a shutter (all the pixels are then in their dark state).

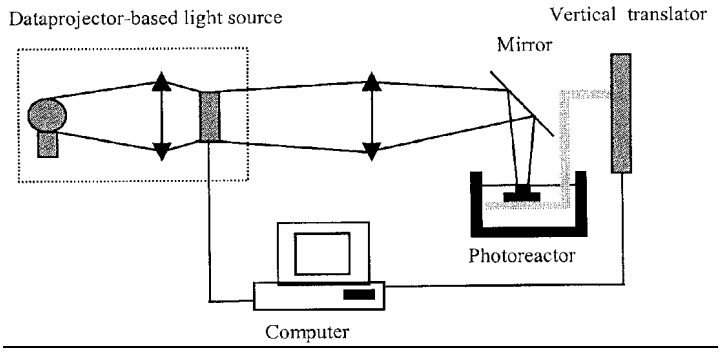

Figure 3. μSL device using a mask-generator display and a non-coherent light source

Contrary to the conventional SL process, no scraper can be used to add a layer of reactive medium on the surface of the part being manufactured because such a device could damage the microobjects during their manufacture. So, the time to obtain each new horizontal fresh layer of resin depends mainly on its rheological properties. As a result, only low viscosity photocurable resins can be used.

4.2. SPATIAL RESOLUTION

4.2.1. *Longitudinal resolution measurement*

As in Ref. [11], longitudinal resolution has been evaluated by measuring the depth of a single layer polymerized beam, manufactured under real operating conditions of the apparatus. We note that the cured depth has to be a little greater than the actual thickness of the layers that form the object, in order to allow a partial overlapping of the layers so that they can be joined together.

The polymerized beam has been inserted in a simple object with a « U » shape (see Fig. 4). Such an object can be manipulated without fear of breaking the polymerized beam.

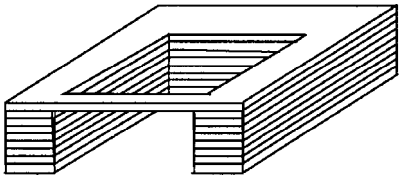

Figure 4. Supported beam to measure the longitudinal resolution

The experimental results are presented on Fig. 5. They give the evolution of the cured depth *versus* the irradiation time, showing clearly that the cured depth increases with irradiation time.

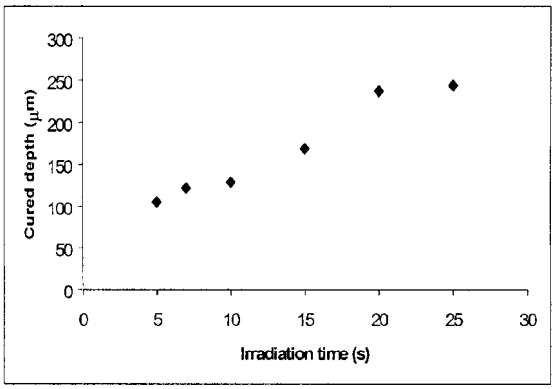

Figure 5. Cured depth versus the irradiation time

We have chosen to work with polymerized depths which are large enough to be manipulated without breaking. In fact, during the last step, there are strong strains on

the beam due to the effect of capillarity-type forces between the surface of the liquid resin and the object. However, during the normal manufacturing of multilayer 3D objects, the thickness of each layer can be as low as 5 µm because the object is never removed from the resin during the process.

The experimental results seem to be correct even if the washing operations, using solvents, needed before the measurement of the beam depth can damage it or cause deformations. However, the damage that can be caused by washing operations is strongly reduced when manufacturing complex objects. This is due to the overlapping of the layers, which gives a better mechanical quality to the part.

4.2.2. *Transversal resolution measurements*

In order to make transverse resolution measurements, we used an optical microscope that allows us to obtain the size of pixels that are contained in the image. For instance, the minimal obtained size of pixels is 2 µm x 2 µm. Fig. 6 gives an image of a single layer object and a detail of this object, showing the transverse resolution and the reliability of the process.

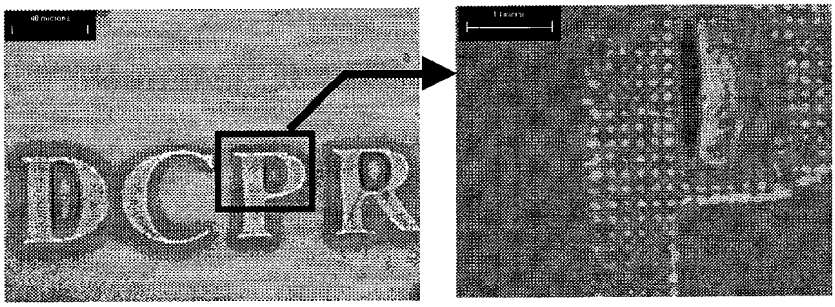

Figure 6. Example of a single layer object manufactured by the new process ; images obtained by an optical microscope.

5. Conclusion

We have proposed a new apparatus using a mask-generator display and a broad-band visible light source. It seems to be a very interesting process allowing one to manufacture small 3D micro-objects with complex shapes.

Currently, we are beginning to produce various small 3D objects made of many layers. The insertion of shape memory alloy wires in particular 3D polymer structures will allow the manufacture of new types of microactuators for micro-robotic applications.

References

1 . Mandle, J., Lefort, O., and Migeon, A. : A new macromachined silicon high-accuracy pressure sensor, *Sensors and Actuators A* 46-47, (1995), 129-132.

2 . Müllenborn, Dirac, Petersen, and Bouwstra : Fast three-dimensional laser micromachining of silicon for microsystems, *Sensors and Actuators A* **52,** (1996), 121-125.

3 . Moore, Daniel, and Walker : Nano and micro technology applications of focused ion beam processing, *Microelectronics Journal* **28,** (1997), 465-473.

4 . Kussul, E., Rachkovskij, D., Baidyk, T., and Talayev, S. : Micromechanical engineering : a basis for the low-cost manufacturing of mechanical microdevices using microequipment, *J. Micromech. Microeng.* **6,** (1996), 410-425.

5 . Lehr, H., Ehrfeld, W., Schmidt, M., Kallenbach, E., and Thuan, H. : Application of the LIGA technique for the development of microstructures based on electromagnetic principles, *J. Micromech. Microeng.* **2,** (1992), 229-233.

6 . Despont, M., Lorenz, H., Fahrni, N., Brugger, J., Renaud, P., and Vettiger, P. : High-aspect ratio, ultrathick, negative-tone near-UV photoresist for MEMs applications, IEEE (1997), 518-522.

7 . André, J.C., Corbel, S. (1994) *Stéréolithographie Laser,* Polytechnia Ed. Paris France.

8 . Ikuta, K., Hirowatari, K., and Ogata, T., Three dimensional micro integrated fluid system fabricated by stereolithography, *Proc. IEEE MEMS'93, (Fort Lauderdale, FL, Feb)* 42-47.

9 . Nakamoto, T., Yamaguchi, K., Abraha, P., and Mishima, K.: Manufacturing of three-dimensional micro-parts by UV laser induced polymerization, *J. Micromech. Microeng.* **6,** (1996), 240-253.

10. Bertsch, A., Zissi, S., Jézéquel, J.Y., Corbel, S., and André, J.C. : Microstereolithography using a liquid crystal display as dynamic mask-generator, *Microsystem Technologies* **3,** (1997), 42-47.

11. Bertsch, A., Jézéquel, J.Y., and André, J.C.: Study of the spatial resolution of a new 3D microfabrication process : the microstereophotolithography using a dynamic mask-generator technique, *Journal of Photochemistry and Photobiology A* **107** (1997), 275-281.

12. Bertsch, A., Zissi, S., Calin, M., Ballandras, S., Bourjault, A., Hauden, D., and André, J.C. : Conception and realization of miniaturized actuators fabricated by microstereophotolithography and actuated by shape memory alloys, *Proc. 3rd France-Japan Congress on Mechatronics, Besançon, vol 2* (October 1996), 631-634.

INTERFERENCE DISPLACEMENT MEASUREMENT OF SEMICONDUCTOR PRESSURE SENSOR

TOMASZ PANCEWICZ
Warsaw University of Technology
Institute of Aeronautics & Applied Mechanics
ul. Nowowiejska 24, 00-665 Warszawa, Poland

Abstract

The paper deals with the deflection measurement of membrane of the semiconductor pressure sensor under load. Optical interferometry was applied to measure deflection. On the base of obtained deformation the state of stress in the membrane is determined. Description of the experimental set-up, results and the analysis of measurement accuracy are presented.

1. Introduction

Semiconductor pressure and acceleration sensors are micromechanical structures (like: shells and beams) created in silicon plate. The operation principle of such devices is based on transformation of mechanical quantity into electrical signal. In the case of piezoresistive sensors applied load creates the state of stress in mechanical structure and causes the change of electrical resistance of resistors.

Designing of sensors demands creation of the model which enables determination of mechanical and electrical values. Nowadays modelling of structures of micro-mechanical sensors is based on finite elements method. Until now there was a lack of independent measurement of sensor deflection under applied load [1, 2]. Verification of computer modelling was possible mostly by comparison between a sensor output signal and a computer simulation. The main goal of this paper is to present application of optical interferometry for deflection measurement of the sensor. That experimental result is an independent information which allows to verify sensor model. On the base of measurement the state of stress in the sensor structure is determined.

1.1. INVESTIGATED SENSOR

In the paper investigations of piezoresistive pressure sensor Z100 (produced by the Institute of Electron Technology in Warsaw, measuring range 0-100kPa) shown in figure 1 are presented [3]. A silicon square membrane, which dimensions are 1000μm x 1000μm with the nominal thickness 15μm is the measuring element of the sensor.

A. Lagarde (ed.),
IUTAM Symposium on Advanced Optical Methods and Applications in Solid Mechanics, 475–481.

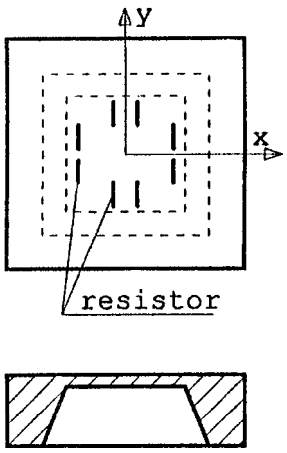

Fig. 1 Pressure sensor

Membrane deflection corresponding to the pressure range is included in the range 0-4μm. Eight resistors are diffused on the surface of the membrane.

2. Experimental set-up

An accurate measurement of membrane deflection is a very specific task, because of micro-size of the object and small values of deflection. Application of mechanical method is connected with the danger of destruction of sensor. Moreover determination of the measuring point on the surface of membrane is a difficult problem. Relative error of mechanical measurement is another question which should be answered, when the experimental method is selected.

Specific features of the measurement task caused, that optical interferometry was selected. Mentioned above problems disappear in optical experiment, because:

- full field measurement information is obtained,
- non-contact measurement is used,
- deflection sensitivity is in the range of fraction of the wave length λ,
- investigated area can be optically magnified.

The optical set-up is presented in figure 2. Measurements were carried out in special pressure chamber, where the sensor was simultaneously impact by pressure and was illuminated by monochromatic light. The interference image was observed in the magnifying optical system.

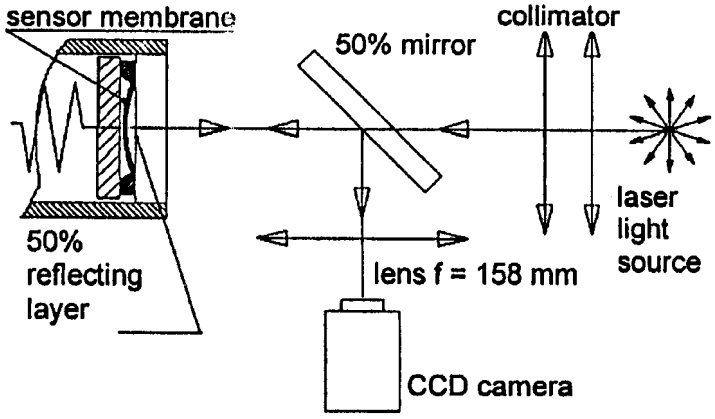

Fig. 2 Measurement set-up

Optically flat transparent quartz glass is one of the walls of the chamber. On the surface of that quartz glass from the inside of the chamber a semi-transparent layer was sprinkled. The sensor is placed in the chamber by use of elastic rubber element, which ensures parallel position of the sensor and the reference plane.

Monochromatic illuminating wave incidence perpendicularly to the transparent wall of the chamber. On the reference plane (on the semi-transparent layer) the illuminating wave is splited into object and reference wave. The object wave illuminates the sensor and reflects from the surface of the membrane. The reference wave reflects directly from the reference plane. The optical path difference between object and reference waves is equal to the double distance between sensor membrane and the reference plane. The interference image which appears as a result of interference between object and reference waves is magnified in the optical set-up. The distance between the lens and sensor was a little bit bigger then the focal length of applied lens. Real, magnified, reversed image is registered by CCD camera. The figure 3 a, b shows interference images obtained for pressure sensor for increasing pressure.

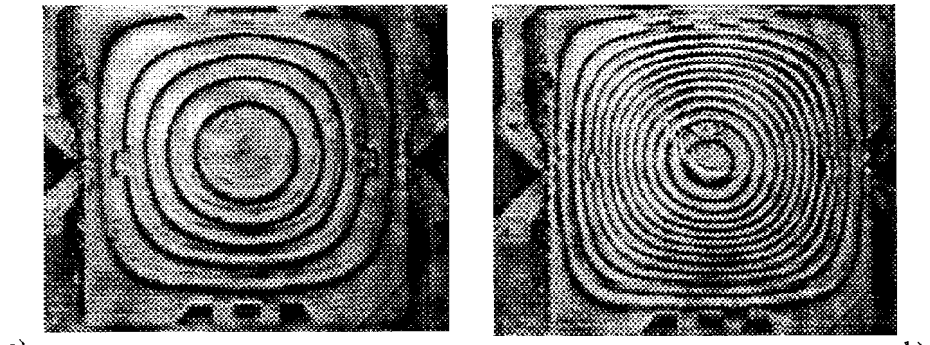

a) b)

Fig. 3 Interference pattern of sensor: a) pressure 0.04MPa, b) pressure 0.1 MPa

3. Deflection of the membrane

Investigated sensor was illuminated by Argon laser which wave length is λ=0,514μm. The accuracy of deflection measurement in a single point (assuming that dark and light fringes are taken into consideration) is $\lambda/4$=0.1285μm. The pressure was measured by manometer with accuracy $0.4 \cdot 10^{-3}$ MPa. Results of deflection in the centre of membrane in pressure range 0-0.1MPa are presented in figure 4. The thickness of membrane of investigated sensor was δ=15±0.2 mm.

3.1. THE CHARACTERISTIC DEFLECTION-PRESSURE OF SENSOR

Line characteristic deflection-pressure in the centre of membrane is presented in figure 4. Following equation describes the characteristic:

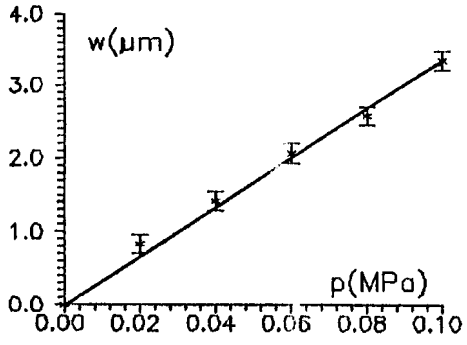

Fig. 4 The characteristic deflection-pressure of sensor

$$w_0 = b_0 \cdot p = 33.5p, \qquad (1)$$

where p-pressure in [MPa], and w-deflection in [μm]. The 95% confidence interval of the direction coefficient of the characteristic is:

$$b_0 = b_0 \pm t \cdot s(b_0) = 33.5 \pm 2.571\text{-}0.654, \qquad (2)$$

were $s(b_0)$-standard deviation of direction coefficient, t=2.571-number which probability of occurrence on the base of t-student distribution with five degree of freedom is equal 0.05. Hence $b_0 \in \langle 31.82, 35.18 \rangle$, therefore error of deflection calculated from equation (1) is $\Delta w_0 = \pm 1.68 \cdot p$. That confirms assumption concerning accuracy of deflection measurement in a single point.

3.2. THE DEFLECTION LINE OF MEMBRANE

The deflection line of the membrane under pressure 0.1 MPa in the section along X-axis of the co-ordinate system (compare fig. 1) is shown in figure 5. Measuring points shown in the picture are intersection points of dark interference fringes with X-axis. Deflection line was approximated by use of polynomial of fourth degree (solid line):

$$w(x) = a_0 + a_2 x^2 + a_4 x^4 = -3.3 + 22.6x^2 - 37.4x^4 , \qquad (3)$$

where x is given in [mm] and w in [μm]. The accuracy of fringe localisation on the plane XY was determined as $\Delta x = \pm 2.5$μm. For comparison the deflection line of a square plate which load and dimensions are equal to the investigated membrane is shown in the figure (dashed line). In calculations carried out according to the classical theory of thin plates [4] it was assumed: built-in edge, Young modulus $E = 1.69 \cdot 10^5$ MPa, Poisson ratio $\nu = 0.064$.

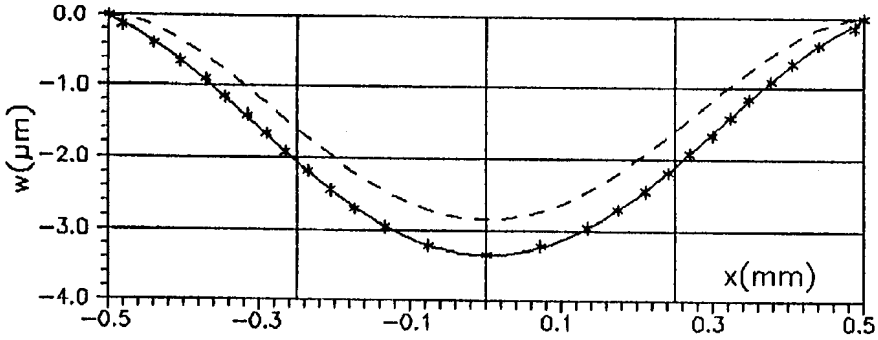

Fig. 5 The deflection line of membrane along X-axis; experimental (solid line), theoretical (dashed line)

It can be noticed, that measured deflection is higher than calculated. A significance difference exists near the edge of the plate. In the real membrane support conditions are not pure simple-supported neither build-in conditions.

4. The state of stress in the membrane

Calculation of the state of stress in the membrane is very important task in the case of piezoresistive devices, because it allows for determination of the change of resistance of resistors. Accordingly to solutions of theory of elasticity expenditures of bending moments in the plate can by calculated from equation (4, 5), if the deflection function w(x,y) is known:

$$m_x = -D(\partial^2 w/\partial^2 x + \nu \cdot \partial^2 w/\partial^2 y), \quad (4)$$

$$m_y = -D(\partial^2 w/\partial^2 y + \nu \cdot \partial^2 w/\partial^2 x), \quad (5)$$

where $D=E\delta^3/12(1-\nu^2)$ - bending stiffens of the plate, δ-thickness of the plate. In the previous section the polynomial approximation of the deflection line along X-axis of the co-ordinate system was determined. Fourth degree polynomial approximation was selected because, that function describes deformation of the circular plate with build-in edge. Because of the symmetry of load and structure obtained polynomial can be used for determination of the expenditures of bending moments and maximal stress in the centre of membrane. Obtained value of stress in the centre of membrane has a great significance for comparison with results calculated from computer models of sensor. For designing purposes however much more important are stress values near the edge of the membrane, because in that region resistors are placed.

The stress functions $\sigma_x(x)$, $\sigma_y(x)$ along the X-axis were determined according to the following steps:

- in twelve sections perpendicular to X-axis the deflection functions $w(x_i, y)$ were determined,
- in twelve intersection points of X-axis and section lines chosen in previous step expenditures of bending moments $m_x(x_i)$, $m_y(x_i)$ were calculated according to formulas (4, 5),
- stress functions were approximated based on values $m_x(x_i)$, $m_y(x_i)$ determined in previous step.

Figure 6 shows stress functions $\sigma_x(x)$, $\sigma_y(x)$ along the X-axis. For both stress functions 95% confidence intervals are determined. Boundary values of these functions are approximating polynomials calculated for maximal and minimal value of polynomial coefficients. The relative error of polynomial coefficients were evaluated for 5% for a_2 and 15% for a_4. It can be seen, that confidence intervals are being wilder with increase of co-ordinate *x*. That is caused because of growing significance for result of factor a_4. Larger error of that coefficient resulted from lower number of fringes in that region. Distance between fringes is the feature of investigated phenomenon and can't be easily changed.

The value of stress in the centre of membrane is calculated on the base of coefficient a_2, which is determined with smaller error. Therefore the confidence interval is narrower.

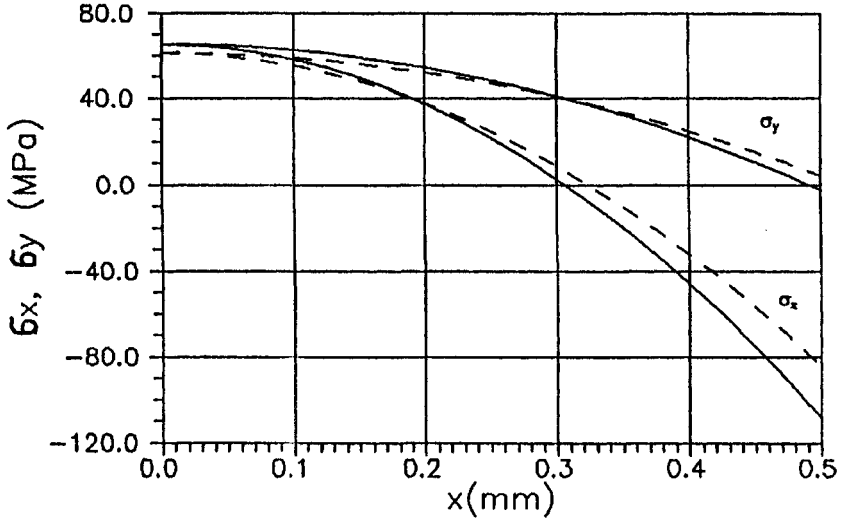

Fig. 6 Confidence intervals of stress functions $\sigma_x(x)$, $\sigma_y(x)$ along X-axis

Stress distribution $\sigma_x(x)$ obtained in the above described way was compared with stress function which was calculated from simplified formula (4). Simplified calculation was carried out under the assumption, that the term $v \cdot \partial^2 w / \partial^2 y$ can be neglected due to the small value of coefficient v=0.064. The differences between these two functions are smaller than 1%.

5. Conclusions

Presented investigations prove, that optical measurement is a powerful method in investigations of sensors. Presented images allow to visualise the shape of sensor under load. Big accuracy of deflection measurement is the feature of the method. For example disturbances in the direction of interference fringes can be noticed in bonding areas, where there is microscopic change of thickness of membrane.

Because of high accuracy of deflection measurement verification of FEM models should be performed on the stage of displacement calculations [5].

It should be noticed, that no contact between the sensor and measuring device is needed for the measurement. If the interference image is registered automatically automatization of result evaluation is possible.

Obtained results of membrane deflection can be used for verification of computer models of sensors. They can be also applied for verification of the assumed values of material constants like Young modulus and Poisson ratio.

The accuracy of determination of functions σ_x (x), σ_y (x) depends very strongly on the accuracy of deflection measurement. Relative error of determined stress values near the edge was estimated for 20%. Relative error of stress values in the centre of the membrane is evaluated for 5%. Though the accuracy of stress determination in the centre of membrane is very good, that result has lower significance because in these areas there are no resistors and the influence of boundary conditions is smaller. However that value can be used for verification of material constants of sensor and FEM models.

6. Acknowledgements

I highly acknowledge Prof. Ryszard Jachowicz from Institute of Electronic Fundamentals at Warsaw University of Technology for inspiration of these research and valuable discussions during investigations. I also thank to Mr. Pawel Kowalski from the Institute of Electron Technology in Warsaw for preparation of sensors for investigations.

The work was financed by Polish Committee of Scientific Research under the project PBZ 2705.

7. References

1. Azgin Z., Gniazdowski Z., Jachowicz R.: Temperature effects in micromechanical sensors concerning interactions housing-sensor, *Proc. of VI Conference Scientific Electron Technology ELTE'97,* Krynica Poland, May 1997 (in polish).
2. Gniazdowski Z., Kowalski P.: Practical approach to extraction of piezoresistance coefficient, *Sensors & Actuators: A Physical,* Vol. 68/1-3, 1998.
3. Gniazdowski Z.: Finite element modelling in microsystems technology, *MST News Poland,* No 2(6), July 1997.
4. Timoshenko S., Woinowsky-Krieger S. *Theory of Plates and Shells,* McGraw Hill, New York 1959.
5. Pancewicz T., Jachowicz R., Gniazdowski Z., Azgin Z., Kowalski P.: A new empirical method for modelling results verification for semiconductor pressure sensor, *Proc. of EUROSENSORS XII* University of Southampton 13-16 Sept. 1998.

This Page Intentionally Left Blank

MOIRÉ INTERFEROMETRY ANALYSIS OF FRACTURE

ALBERT S. KOBAYASHI
University of Washington
Department of Mechanical Engineering
Box 352600
Seattle, Washington 98195-2600

Abstract

Moiré interferometry with a low density grating was used to evaluate the suitability of the T^*_ε integral and CTOA as ductile fracture parameters for characterizing low cycle fatigue and dynamic crack growth in thin aluminum fracture specimens. Phase shifting Moiré interferometry with a high density grating was also used to determine the energy dissipation mechanism in brittle alumina ceramics.

1. Introduction

Prior to the dominant usage of finite element (FE) analysis, two- and three-dimensional photoelasticity were commonly used to determine a stress intensity factor (SIF) in a laboratory setting. While two-dimensional photoelasticity has, for all practical purpose, being replaced by FE analysis, three dimensional photoelasticity is still in use today [1]. Other popular optical techniques of the time include interferometry [2] and caustics [3,4] with the whole field version of the latter being referred to as the coherent gradient sensor [3]. As research in LEFM evolved beyond the mere compilation of SIF's for different boundary value problems, real structural materials had to be used in place of photoelastic material in order to model their fracture responses. Thus optical techniques, such as caustics and Moiré techniques came into use for studying the dynamic fracture, elastic-plastic fracture and time-dependent fracture responses of steel, aluminum, ceramics and concrete, etc. One of the earlier application of geometric Moiré in experimental fracture mechanics is a dynamic ductile fracture study [5, 6] using a single frame, ultra-high speed photography. In this study, the transient strain fields in fracturing magnesium, 7075-T6 and 7178-T6 aluminum alloy, center notch

A. Lagarde (ed.),
IUTAM Symposium on Advanced Optical Methods and Applications in Solid Mechanics, 483–496.

specimens were shown to vary with a strain singularity between 0.4 - 0.6 while the corresponding static strain had a strain singularity of about 0.6 - 0.8. These results suggested that a propagating ductile crack can be modeled, as a first approximation, by dynamic LEFM and thus justified the earlier and extensive LEFM approach to dynamic fracture. This pseudo-elastic response was associated with a relatively high crack velocity of 10 to 20 percent of the Rayleigh wave velocity generated by an overdriven crack at a blunt starter notch. In contrast, most dynamic ductile fracture phenomena are associated with lower crack velocities of 5 to 10 percent of the Rayleigh wave velocity. Reference [7] provides an up to date summary of some of the recent usage of geometric Moiré in elastic-plastic fracture mechanics (EPFM).

The lack of strain sensitivity in the earlier Moiré analysis was removed by the introduction of Moiré interferometry in the late 70's [8]. The specialized optical setups used and selected results obtained since that time are summarized in [9]. In the following, some results obtained by the author and his colleagues using Moiré interferometry over the past ten years are presented.

2. Moiré Interferometry

As mentioned previously, many of the popular Moiré interferometry setups are described in [9] and further theoretical and experimental details can be found in [10]. In this paper, only the low-spatial-frequency, steep grating that was developed for elastic-plastic analysis of the crack tip region in ductile material, and a phase-shifting Moiré interferometry of high sensitivity for fracture process zone analysis of structural ceramics are discussed.

2.1. LOW-SPATIAL-FREQUENCY STEEP GRATING

The low-spatial-steep grating consists of an ultra-thick, 5-10 μm thick, semi-transparent film which is etched with a deep grating on a mirrored surface of the specimen [11]. In order to enhance the diffraction efficiency of the grating, the specimen surface must be polished to a mirror grade. The film combines the function of a reference grating and a display layer. When the two coherent beams of A(x) and B(x) shown in Figure 1 intersect on the specimen surface, the diffraction beams, A(i+m, j) and B(i-m, j), interfere and are projected onto the recording surface. Unlike the standard Moiré interferometric fringes, this interference pattern can be observed clearly from any direction. For example, a grating of f=40 lines/mm in an argon laser field will project $i = j = (2m)^2 = (2{:}48)^2 = 9216$ visible diffracted beams in all directions. All but the minus or plus first order of the incident A(x) and B(x) beams, respectively are blocked by the steep grating. Good contrast of the displacement patterns is obtained even when the specimen surface is warped due to the large out-of-plane deformation of the crack tip plastic zone. For the low-spatial-frequency of 40 lines/mm used in this study, an incidence angle between the surface normal and the two coherent beams of 1.176° was

required. This shallow incident angle of the two coherent beams for a grating spatial frequency of 40 lines/mm required a special compact Moiré interferometer.

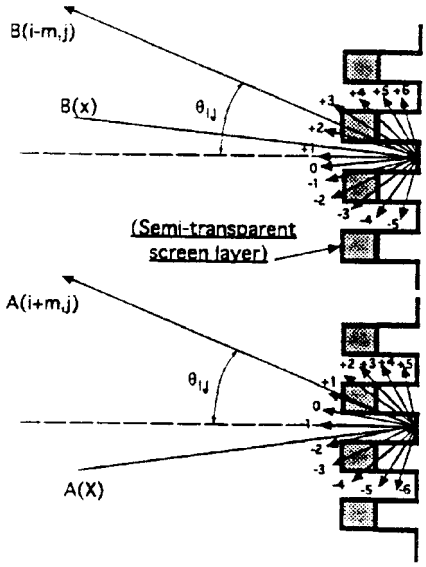

Figure 1. Diffraction angles of a steep grating.

2.2. PHASE SHIFTING MOIRÉ INTERFEROMETRY

The specimen grating for Moiré interferometry was affixed by the standard replica technique [10] where the master grating of 1200 lines/mm together with a highly reflective aluminum coating was transferred to a thin half-cured epoxy film coated on the fracture specimen. The specimen grating was then placed in a standard two-beam, phase-shifting Moiré interferometer, as shown in Figure 2, with an appropriate oblique incident illumination that yielded reflected diffraction of the order +/- 1 normal to the grating surface. In this study, only the v-displacement, which is perpendicular to the crack, was recorded. This optical setup effectively doubled the frequency of the specimen grating to 2400 line/mm. The two oblique beams also generated an interference fringe pattern, which becomes the reference grating, of 2400 lines/mm in front of the specimen grating. Phase shifting was accomplished by a piezoelectric transducer which translated one of the oblique beams and effectively shifted the spatial location of the Moiré reference grating. Four steps in the total PZT displacement generated shifts of 90°, 180°, 270° and 360° phase differences. When the specimen grating was distorted by the deformation in the specimen, the distorted diffraction of +/- 1 order interfered with the undistorted reference grating and generated the Moiré fringe

pattern in the space in front of the specimen. A CCD camera was focused on this Moire fringe pattern, which was recorded as a wrapped phase map, in space. A two dimension spatial unwrapping software provided the unwrapped phase distribution which is proportional to the displacement of interest. The estimated accuracy of the entire phase shifting Moire interferometry procedure is $\lambda/20$ or 0.03 μm.

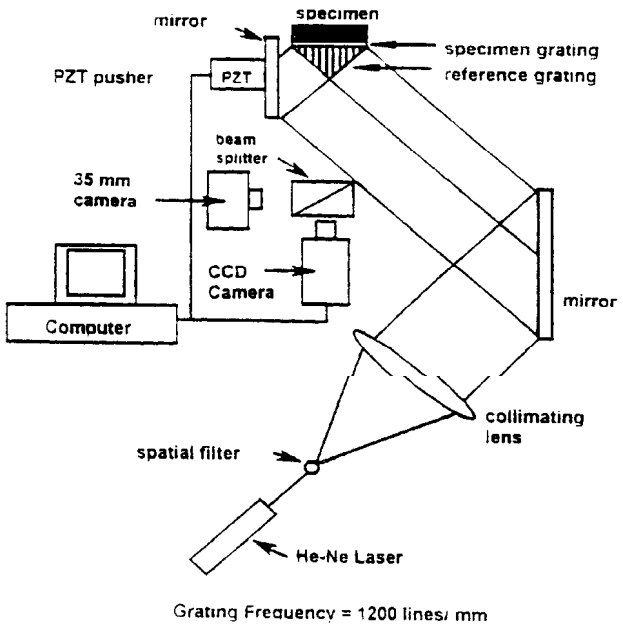

Figure 2. Phase stifting Moiré interferometry setup.

3. Ductile Fracture Parameters

3.1. T^*_ε INTEGRAL

For a stably growing crack, Brust et. al. [12] showed that the T^*_ε integral, which is based on the incremental theory of plasticity, reaches a steady state value during stable crack growth and could be an effective stable crack growth parameter. In this integral, the unloading effect is accounted by stretching the integration contour with the extending crack tip. For an integration contour close to the crack tip, T^*_ε represents the energy inflow to the wake as well as to the frontal crack tip region [13]. In contrast, the J integral represents the energy inflow to a closed contour that moves with the crack tip. Like the J, the T^*_ε is a path dependent integral in the presence of large scale

yielding and unloading. Thus it must be evaluated near the crack tip if it is to be considered a crack tip parameter. This near-field T^*_ε, is defined as

$$T^*_\varepsilon = \int_{\Gamma_\varepsilon} \left(W n_1 - t_i \frac{\partial u_i}{\partial x_1} \right) d\Gamma$$

where t_i are the surface tractions on the contour Γ_ε, W is the strain energy density and n_1 is the first component of the normal to the curve. Γ_ε is an arbitrary small contour immediately surrounding the crack tip and more importantly it elongates together with crack extension. T^*_ε, as defined by Equation (1), is identical in form to the J integral and therefore T^*_ε coincides with J where the deformation theory of plasticity prevails.

In terms of the incremental theory of plasticity, T^*_ε integral at the end of the Nth load steps is the sum of ΔT^*_ε which is the incremental change of T^*_ε over a load step. The current T^*_ε is thus dependent on the prior loading history, a property that is essential for elastic-plastic analysis under crack growth. Although such incremental analysis can be routinely conducted by finite element (FE) analysis, it is not practical in experimental analysis as the cumulative experimental errors per load step will eventually swamp the sought data. Fortunately Pyo et al [14] have shown, through numerical experiments, that the total T^*_ε integral computed directly by using the stresses and strains based on the incremental theory of plasticity, was for all practical purpose, equal to the summed ΔT^*_ε. Thus Equation (1) can be used for crack growth study without the cumbersome incremental procedure provided the states of stress and strain are based on the incremental theory of plasticity.

Another series of numerical experiments showed that the numerical integration process along the trailing contour behind the crack tip can be ignored if the contour is very close to the traction free crack, i.e. for a very small ε [13]. The magnitude of ε is governed by a characteristic dimension which assures that a plane stress state exists along the integration contour of Γ_ε. This distance, ε, is equated to the plate thickness after [15]. For a plane strain state, this characteristic distance could be several times the crack tip radius.

3.2. CTOA CRITERION.

The critical crack opening displacement (CTOA) criterion assumes that stable crack growth occurs when an angle made by a point on the upper surface of a crack surface, the crack tip, and a point on the lower surface reaches a critical angle. For convenience, a point 1 mm behind the crack tip has been used. Extensive experimental results from thin aluminum fracture specimens have shown that after an initial transient period, the CTOA remains constant throughout Mode I stable crack growth [16, 17]. Moreover, a two-dimension, elastic-plastic FE simulation of stable crack growth based on the CTOA

criterion correctly predicted the load-crack opening displacement (COD) relations and the Mode I crack extension histories of fracture specimens.

4. Low Cycle Fatigue

The objective of this study was to explore experimentally the feasibility of using T^*_ε as a cyclic crack growth criterion

4.1. EXPERIMENT ANALYSIS

The experimental procedure consisted of measuring the two orthogonal displacement fields surrounding a crack extending under low-cycle fatigue in an aluminum 2024-T3 central notched (CN) specimen. Moiré interferometry with a coarse cross diffraction grating of 40 lines/mm was used due to the presence of large scale yielding in the specimen. The stresses corresponding to the total strains were then computed using the equivalent stress-strain relation and the measured uniaxial stress-strain data of the 2024-T3 sheet. This use of the deformation theory of plasticity to compute stresses did not account for the unloading process, which occurred in the trailing wake of the extending crack. By restricting the integration contour very close to and along the extending crack, [13] showed that the contour integration trailing the crack tip can be neglected by virtue of the closeness of the integration path, Γ_ε, to the traction free crack surface. This partial contour integration, which was evaluated in the very vicinity of the moving crack tip not only simplifies the integration process but also eliminated the undesirable effects of the deformation theory of plasticity that was used to compute the stresses from the strains derived from the measured displacements.

4.2. NUMERICAL ANALYSIS

A finite element (FE) analysis based on the incremental theory of plasticity using the measured equivalent stress-strain relation was conducted for comparison purpose. Plane stress, FE model of a segment of the CN specimens was driven in its generation mode by the measured, time varying displacements and instantaneous crack length. The T^*_ε integral along the entire elongated contour surrounding the cyclically growing crack of the fracture specimens was computed. Since the FE analysis provided stresses which accounted for the unloading effect in the trailing wake of the extending crack tip, the entire contour with a domain integral [18] was used for the T^*_ε evaluation in order to mask the numerical errors in the FE data surrounding the crack tip. To recapitulate, the T^*_ε evaluation procedures for the Moire and FE studies differ in that the former used only the frontal segment of a near-field contour, Γ_ε, while the latter involved an equivalent domain integral over much of the crack length.

4.3. RESULTS

Figure 3 shows that the T^*_ε values, which was determined experimentally and by FE analyses, for $\varepsilon = 2.0$ mm are in good agreement with the exception of the unloaded T^*_ε values. This discrepancy is due to the use of deformation theory of plasticity in computing the T^*_ε integral at the unloading point. Despite the differences in the load versus loadline displacement curves for the three specimens, all three loading and reloading T^*_ε curves nearly coincide and suggests that crack growth under cyclic loading of thin aluminum fracture specimens could be characterized by a master T^*_ε versus crack extension curve for a given Γ_ε.

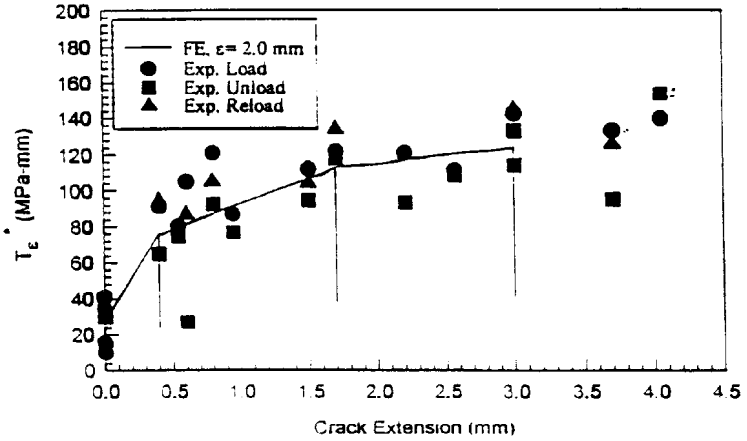

Figure 3. Experimental and FE T^*_ε for cyclically loaded 2024-T 3 CN specimens.

Figure 4 shows the experimental and FE CTOA variations with cyclic crack growth,

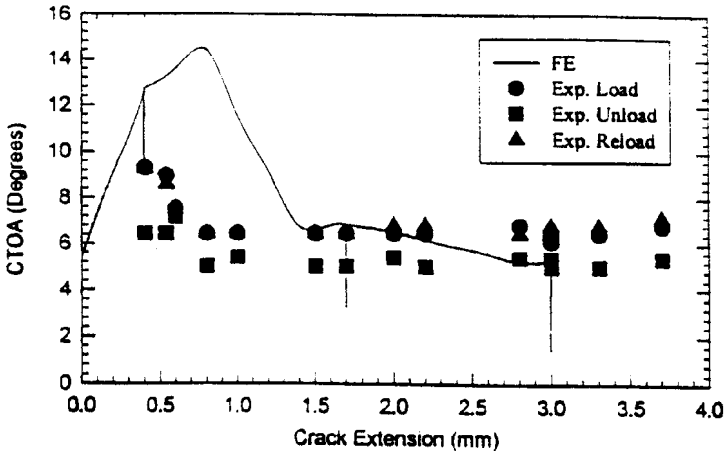

Figure 4. Experimental and FE CTOA for cyclically loaded 2024-T3 CN specimens.

The large differences in the experimental and FE generated CTOA at unloading showed that commercial FE code did not model the loading, unloading and reloading process. Likewise difference between the measured and FE determined T^*_ε at unloading, followed the results of Brust et. al. [12] thus suggesting a possible fundamental modeling error in the commercial computer code used in this study.

5.0 Dynamic Ductile Fracture

Dynamic Moiré interferometry was used in search of a dynamic fracture parameter that control rapid fracture of a somewhat ductile material.

5.1. EXPERIMENTAL ANALYSIS

Dynamic Moire interferometry was used to determine the transient displacement fields perpendicular and parallel to the running crack in 7075-T6 aluminum alloy, SEN specimen, 1.6 mm thick, that was either fatigue precracked or blunt notched for low and high crack velocity tests, respectively. Four frames of the Moiré fringe patterns corresponding to either the vertical or horizontal displacements were recorded by an IMACON 790 camera. This limited number of frames and the fixed framing rate, i.e., 100,000 frames per second, required multiple and separate u- and v-displacement recordings of identically loaded SEN specimens at different delay timings in order to capture the entire fracture event that lasted about 1.2 milliseconds. Despite all efforts to generate reproducible tests, no two dynamic fracture tests were identical and thus the final composite fracture event was constructed with due consideration of the load-time histories and the varying crack opening profiles of each fracture test. The compiled displacement records was then used to compute the T^*_ε integral according to the procedure described in Section 3.1.

5.2. RESULTS

Figure 5 shows typical dynamic Moire fringe patterns associated with the propagating crack. Crack velocities of about 35 m/s and 300 m/s were observed in the fatigue-precracked and blunt notched specimens, respectively. Figure 6 shows the variations of CTOA with crack extension. The data identified as the first series is from Lee et. al. [18] using fatigue precracked specimens and the second series refers to the data on the blunt notched specimens.

Figure 7 shows the T^*_ε versus crack velocity relations of 7075-T6 and 2024-T3 SEN specimens. The 2024-T3 results [19] are also shown for comparison. For the 7075-T6 specimens, T^*_ε increased with increasing crack velocity and eventually leveled off at a terminal velocity of about 300 m/s. In contrast, the crack velocity in the fatigued precracked 2024.T3 specimens did not reached a terminal velocity and arrested at a T^*_ε higher than its initiation value.

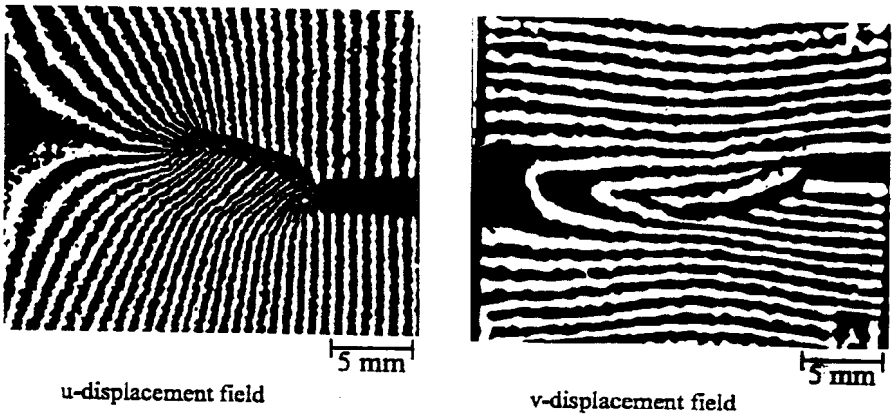

Figure 5. Dynamic Moiré pattern of a fracturing 7075-T6 SEN specimen.

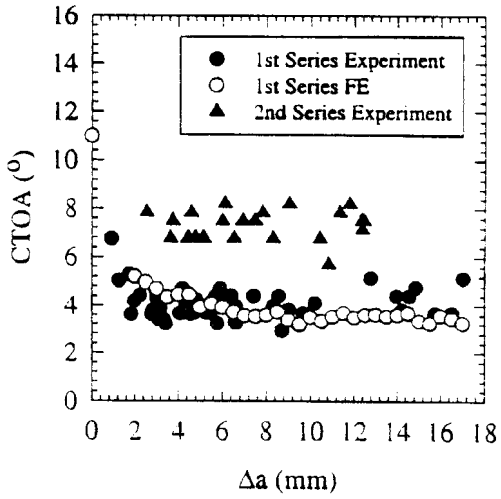

Figure 6. CTOA variations in a fracturing 7075-T6 SEN specimen.

The dynamic strain energy release rate, G_{ID}, with respect to crack velocity of 7075-T6, like other somewhat brittle materials, was expected to exhibit the characteristic gamma-shaped curve. To test this postulate, the crack tip opening displacement (CTOD) at a crack tip distance, r = 1 mm, was used to compute K_{ID}, and the strain energy release rate, G_{ID}, based on LEFM for the fatigue-precracked (fist series) and the machine-notched (second series) 7075-T6 SEN specimens. The same procedure was used to compute G_{ID} for the blunt-notched 7075-T6 SEN specimens of [6] and the characteristic gamma shaped G_{ID} versus crack velocity relation was obtained.

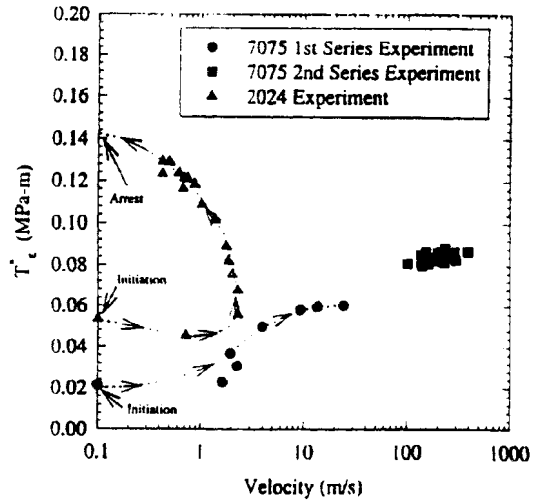

Figure 7. T^*_ε versus crack velocity relation of a fracturing 7075-T6 SEN specimen.

5.3. DISCUSSIONS

Both the T^*_ε and CTOA are being considered for stable crack growth criteria and likewise possibilities exist as dynamic ductile fracture criteria. CTOA, by definition, is a local crack tip parameter that exhibited a precipitous drop at the initial phase of rapid crack propagation in fatigue-precracked 2024-T3 and 7075-T6 SEN specimens. Dawicke et. al. [16] attributed this drop to the crack front tunneling prior to crack extension. However, the blunt, machine-notched 7075-T6 SEN specimens in this study did not exhibit the initial high CTOA. Thus the initial high value in CTOA in the fatigue-precracked SEN specimens is probably due to crack tip blunting prior to crack extension.

Both CTOA and T^*_ε remained constant despite the increasing crack velocity in the 7075-T6 SEN specimens and the decreasing crack velocity in the 2024-T3 specimens. CTOA in the 2024-T3 SEN specimens at crack arrest was lower than the CTOA's at the initiation of rapid crack propagation and during crack propagation. On the other hand, T^*_ε at crack arrest in the 2024-T3 SEN specimens was higher than its constant value during crack propagation as shown in Figure 7.

The distinct difference in the G_{ID} and T^*_ε responses at the terminal velocity, suggests that the traditional practice of characterizing dynamic fracture of somewhat ductile material through the G_{ID} versus crack velocity relation based on LEFM could be misleading. The LEFM approach results in a terminal velocity, which is insensitive to the driving force, G_{ID}, while the T^*_ε approach, based on elastic-plastic fracture

mechanics (EPFM), suggests that the terminal crack velocity is a consequence of the saturation of the dissipated plastic energy.

6. Process Zone of Polycrystalline Alumina

A hybrid experimental-numerical procedure was used to determine the crack closing stress (CCS) versus crack opening displacement (COD) relations of a high- and a medium-density polycrystalline alumina.

6.1. EXPERIMENTAL ANALYSIS

Wedge-loaded, double cantilever beam (WL-DCB) specimens were machined from high-density (AL23) and medium-density (AD90) commercial alumina. The grain sizes ranged from 5 to 45 μm with an average size of 18 μm for the former and an average grain size of 9 μm for the latter. A 50% side groove was machined to channel the stably growing crack that would otherwise curve away from it's intended straight path.

A 1200 lines/mm specimen grating was affixed by a replica technique on the ungrooved surface of the fracture specimen. The specimen grating was then placed in a two-beam, phase-shifting Moiré interferometer with an appropriate oblique incident illumination as described in Section 2.2.

The fracture specimen was loaded in a rigid displacement controlled loading fixture and the Moiré fringes at the peak load of each increment of increasing displacement loading and the stably growing crack were recorded. Load-line displacement was not recorded since the Moiré fringes provided an accurate displacement measurement at the contact point of the loading rod and specimen.

6.2. NUMERICAL ANALYSIS

A two-dimensional, linearly elastic, finite element (FE) model of the WL-DCB specimen was used in a propagation analysis with the applied wedge load, wedge-opening displacement, instantaneous crack length and the elastic properties as input conditions. The measured load at the time of recording of the Moiré fringe pattern, instead of the applied displacement, was used to reduce the sensitivity of the numerical analysis to the error in the load-line displacement measurement. The instantaneous crack tip location was determined from the Moiré data with an accuracy of 0.1 mm. The CCS versus COD relation and the modulus of elasticity were the two disposable parameters in this numerical analysis and the Poisson ratio was assumed to be 0.22. The latter variation in the modulus of elasticity was less than 6 percent of the manufacturer's quoted value and is within accepted tolerance.

6.3. RESULTS

A total of four specimens of each alumina, i.e., AL23 and AD90, were analyzed in this study. Moiré fringe patterns obtained from each test provided the crack opening profiles for the two microstructures for several crack lengths and loading. Using the inverse analysis described previously, the crack closing stress (CCS) versus the crack opening displacement (COD) relation, which provided the best fit between the calculated and measured COD profiles, was obtained through an iterative procedure. Figure 8 shows the CCS versus COD relation of AL-23 alumina. For comparison, the CCS versus

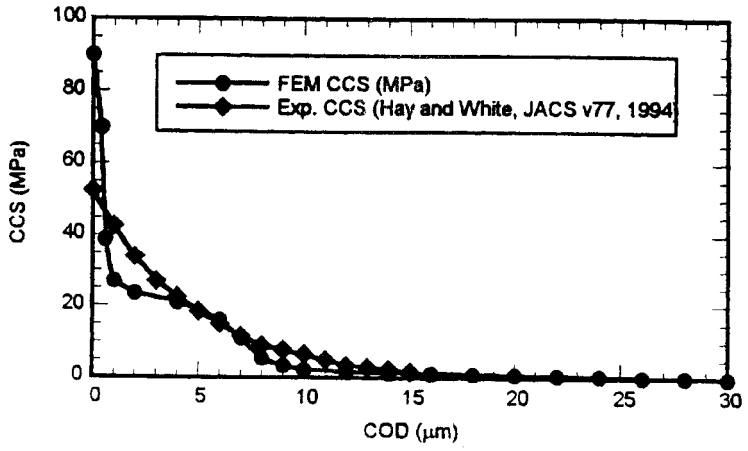

Figure 8. CCS versus COD relation for AL-23 alumina WL-DCB specimen.

COD relation, which was obtained by the post fracture tension (PFT) tests described in [20], is superimposed in Figure 8. The lower CCS near the crack tip, i.e., at a lower COD, is due to the averaging effect over a relatively large distance of 2 mm in the PFT specimen. The CCS versus COD relation of the AD90 specimen also compares well with that reported in [21]. This was expected, as the 11 μm average grain size of the alumina specimen of [21] was very close to the 9 μm grain size of AD90. The CCS versus COD relation of AD90, however, lacked the trailing tail in Figure 8 due to the lack of the broad grain size distribution of AL23. The smaller average grain of AD90 effectively reduced the bridging distance and hence the bridging force

The dissipated energy in the FPZ was computed by summing up the work done in the FPZ per incremental crack extension. The rate of energy dissipation is about 95 percent of the energy released which is the difference between the total work and the stored elastic energy. The result shows that the FPZ is the major energy dissipation mechanism in the brittle alumina.

6.4. SUMMARY

The crack closing stress versus crack opening displacement relations governing the fracture process zone, which trails a stably growing crack in the high-density alumina, WL-DCB specimens were quantified.

The fracture process zone trailing the crack tip was shown to be the major energy dissipation mechanism in alumina fracture specimen.

7. Conclusion

The effectiveness of Moiré interferometry for studying the fracture response of real structural material was demonstrated. New and controversial results in low cycle fatigue of thin 2024-T3 aluminum, dynamic fracture of 7075-T6 aluminum and fracture of AL23 and AD90 alumina were presented.

8. Acknowledgment

This paper summarizes the research conducted by J. H. Jackson, M. T. Kokaly, P. W. Lam, J. Lee, L. Ma, Y. Omori, D.K. Tran of the University of Washington, H. Okada, Kagoshima University and P. W. Tan of the FAA William Hughes Technical Center. This study is supported by FAA Research Grant 92-G-005, DOE Grants DE-FG06-94ER 14490, AFOSR Grant F49620-93-1-0210 and ONR Contract N0014-89-J-1276.

9. References

1. Smith. Charles W.: Measurements of three-dimensional effects in cracked body problems, in Jonathan S. Epstein (ed.), *Experimental Techniques in Fracture,* VCH Publishers, 1993, 253-289.

2. Liechti, Kenneth M.: On the use of classical interferometry techniques in fracture mechanics, ibid. loc. cit., 95-124.

3. Rosakis, Ares J.: Two optical techniques sensitive to gradients of optical path difference: the method of caustics and the coherent gradient sensor (CGS), ibid. loc. cit., 327-426.

4. Kalthoff, Joerg F.: Shadow optical method of caustics, in Albert S. Kobayashi (ed.), *Handbook on Experimental Mechanics,* VCH Publishers, 1993, 407-476.

5. Kobayashi, A. S., Harris, D. O. and Engstrom, W. L.: Transient analysis in a fracturing magnesium plate, *Experimental Mechanics,* 7, 10 (1967), 434-440.

6. Kobayashi, A. S. and Engstrom, W. L.: Transient analysis in fracturing aluminum plates, *Proc. 1967 JSME Semi-International Symposium,* 1997, 172-181.

7. Chiang, Fu-pen,: Moire and speckle method applied to elastic-plastic fracture mechanics, in Jonathan S. Epstein (ed.), *Experimental Techniques in Fracture,* VCH Publishers, 1993, 291-325.

8. Post, D.: Optical interference for deformation measurements - Classical holography and Moiré interferometry, in W.W. Stinchcomb (ed.), *Mechanics of Nondestructive Testing,* Plenum Press, 1980, 1-53.

9. Epstein, J.S. and Dadkhah, M.S.: Moiré interferometry in fracture research, in Jonathan S. Epstein (ed.), *Experimental Techniques in Fracture,* VCH Publishers, 1993, 427-140.

10. Post, D.: Moiré interferometry, in Albert S. Kobayashi (ed.), *Handbook on Experimental Mechanics,* VCH Publishers, 1993, 297-364.

11. Wang. F.X., May, G.G. and Kobayashi, A.S.: Low-spatial-frequency steep grating for use in Moiré interferometry, *Optical Engineering,* 33, 4 (1994), 1125-1131.

12. Brust, F.W., Nishioka, T., Atluri, S.N. and Nakagaki, M.: Further studies on elastic-plastic stable fracture utilizing the T*-integral, Engineering Fracture Mechanics, 22 (1985), 1079-1103..

13. Okada, H. and Atluri, S.N.: Further Study on the Near Tip Integral Parameter T^*_ε in Stable Crack Propagation in Thin Ductile Plate, *Proceedings of Aerospace Division, ASME,* AD-Vol. 52, J.C.I. Chang et. al. (eds.), 1997, 251-260.

14. Pyro, C.R., Okada, H. and Atluri, S.N.: An Elastic-Plastic Finite Element Alternating Method for Analyzing Wide Spread Fatigue Damage in Aircraft Structures, *Computational Mechanics,* 16 (1995), 62-68.

15. Narashimhan, R. and Rosakis, A.J.: Three-dimensional effects near a crack tip in a ductile three-point bend specimen: Part 1 - A numerical investigation, *ASME Journal of applied Mechanics,* 57 (1990), 607-617.

16. Dawicke, D.S., Newman, J.C. Jr., Sutton, M.A. and Amstutz, B.E.: Stable tearing behavior of a thin sheet material with multiple cracks, *Fracture Mechanics: 26th Volume,* ASTM STP 1256, W.G. Reuter, J.H. Underwood and J.C. Newman, Jr. (eds.), ASTM , 1995.

17. Dawicke, D.S., Plascik, R.S. and Newman, J.C. Jr.: Prediction of stable tearing and fracture of a 2000-series aluminum alloy plate using a CTOA criterion, *Fatigue and Fracture Mechanics; 27th Volume,* ASTM STP 1296, R.S. Plascik, J.C. Newman, Jr. and N.E. Dowling (eds.), ASTM, 1997, 90-104.

18. Nikishkov, G.P. and Atluri, S.N.: An equivalent domain integral method for computing crack-tip integral parameters in non-elastic, thermo-mechanical fracture, *Engineering Fracture Mechanics,* 26 (1987), 851-867.

19. Lee, J., Kokaly, M.T. and Kobayashi, A.S.: Dynamic ductile fracture of aluminum SEN specimens: An experimental-numerical analysis, *Advances in Fracture Research, ICF 9,* B.L.I. Karihaloo, Y.W. Mai, M.I. Ripley and R.O. Richie (eds.), Pergamon Press, 1997, 2965-2972,

20. Hay, J.C. and White, K.E.: Grain boundary phase and wake zone characterization in monolithic alumina, *J. of Amer. Ceramic Soc.,* 78 (1995), 1025-1032.

21. Roedel, J., Kelly, J.F. and Lawn, B.R.: In situ measurements of bridged crack interfaces in scanning electron microscope, *J. of Amer. Ceramic Soc.,* 73 (1990), 3313-3318.

THE STRESS FIELD AROUND TWO PARALLEL CRACKS IN A FINITE GEOMETRY: A HYBRID STUDY COMBINING HIGH-DENSITY GEOMETRIC MOIRE AND PHOTOELASTICITY WITH THE WESTERGAARD APPROACH AND LOCAL COLLOCATION METHODS

RAVINDER CHONA
Department of Mechanical Engineering
Texas A&M University, Mail Stop 3123
College Station, Texas 77843-3123, USA

Abstract

Finite geometry problems, in which two or more cracks are in close proximity so that their stress fields interact, are generally found to be substantially more challenging than problems involving single or isolated cracks. The present study how, combining optical techniques such as photoelasticity with high density geometric moire, a method of modelling single cracks with similar loadings and geometries, and an elasticity technique well-suited to problems with multiple boundaries, produces an overall solution for the stress field around multiple crack tips in finite geometries.

Introduction

The basic approach adopted here is to use the generalized Westergaard equations [1] to represent the stress field around each individual crack tip as if it were an isolated crack and then apply the Schwarz alternating method [2], or method of successive stress removal, to obtain the additional stress fields that must be superposed on the original (isolated) solutions to ensure that the boundary conditions on each of the crack faces are satisfied. The end result of this iterative approach provides the overall stress field for the. entire region surrounding both crack tips.

This overall stress field can then be utilized in a local collocation analysis procedure in an analogous manner to that currently followed for single crack problems [3,4]. Photoelastic isochromatic and high density geometric moire fringe patterns for the case of two parallel edge cracks in pure bending were the source for experimental data collection. Additional data was obtained from finite element models of similar geometries for which the calculated in-plane cartesian stress components were converted into isochromatic data and nodal displacement values were used directly.

A. Lagarde (ed.),
IUTAM Symposium on Advanced Optical Methods and Applications in Solid Mechanics, 497–504.

The objectives of the study can be summarized as being: (a) to utilize the combined Westergaard-Schwarz approach to obtain a full-field representation of the stress field surrounding two parallel edge cracks in a finite body; (b) to use this stress field representation to analyze the case of two parallel edge cracks under pure bending by performing local collocation analyses of experimental and finite-element-generated photoelastic and high-density geometric moire data; (c) to determine the influence of the presence of the other crack on the stress intensity factors for the multiple crack configuration; and (d) to establish guidelines for the separation distances at which the two cracks could be considered to behave as one crack or as two separate cracks which do not interact with one another. Obtaining converged solutions for the local collocation analyses was not always a trivial problem. However, in general, the combined Westergaard-Schwarz method gave satisfactory results for both the experimental and the finite-element-generated data.

The solutions for the experimental analyses were verified by comparing computer generated fringe plots [5] with the original fringe patterns. For the finite-element-generated data the verification was to compare the J-integral value calculated from the stress intensity factors for each crack tip with the J-integral value calculated directly from the finite element analysis.

Synopsis of Procedure and Results

The geometry of a four-point bend specimen with two parallel, interacting edge cracks is shown in Figure 1. In all cases, the length of the first crack, denoted a_1 in the figure, was kept constant at a value of $a_1/W = 0.50$. The length of the second crack, denoted a_2 in the figure, was then varied from $a_2/W = 0.25$ to $a_2/W = 0.625$, in steps of 0.125. This provided a range of values for the relative crack lengths, a_2/a_1 ranging from $a_2/a_1 = 0.5$ up to $a_2/a_1 = 1.25$, in steps of 0.25. The spacing between the two cracks, denoted c in the figure, was varied from a value of $c/a_1 = 0.50$ up to $c/a_1 = 1.00$, in steps of 0.25. In this manner, the interaction effects of the two crack tips could be examined as functions of both the relative crack size and the crack plane separation.

Finite-element models of the various geometrical combinations of a_2/a_1 and c/a_1 were generated using a standard pre-processor (PATRAN) and the nodal displacements and element stresses calculated using a commercially-available finite element code (ABAQUS). Eight-noded isoparametric elements were used throughout and no attempt was made to incorporate special crack-tip singularity-type elements. This choice was based on the desire to insulate the results from any kind of assumed singularity-dominance over a finite region since the size and shape of any singularity-dominated zone(s) would not be known *a priori* in a general application. Furthermore, it was desired to simulate the experimental data analysis conditions as closely as possible throughout and it would be necessary to exclude data from a finite region around the crack tip in any experimental arrangement because of a lack of generalized plane stress in the very near vicinity of the crack tip.

The experimental results were obtained using specimens machined from a PSM-1 polycarbonate sheet which was free of residual stresses. For the geometric moire experiments,

moire gratings with a grating frequency of 20 lines/mm (500 lines/inch) were photographically reproduced from a master grating and bonded to the specimens. Since both u-field and v-field information was desired, the specimen grating used was a bi-directional line grating, while the reference gratings employed were uni-directional line gratings of the same frequency. The test specimens were loaded in four-point bending using a displacement-controlled load frame placed within the optical arrangement of a standard, diffused-light polariscope for the photoelastic tests. The same light source was also utilised (without the polarizer-analyzer pairs) for the geometric moire experiments.

The resulting images were captured and stored using a CID camera and a commercially-available digital imaging system with 8-bit resolution. Figure 2 shows the changes observed in the u-field pattern as the relative crack size was increased from $a_2/a_1 = 0.50$ to $a_2/a_1 = 1.25$ for a fixed crack plane separation of $c/a_1 = 0.75$. Figure 3 shows the corresponding changes in the v-field pattern for the same relative crack sizes and crack plane separation.

Data points for analysis purposes were selected over pre-determined data gathering domains and stored in data files for later analysis by the local collocation programs that had been developed. The unknown coefficients of the series-type stress field representations employed were determined in a least-squares sense from these analyses. The quality of the solution was estimated quantitatively by examination of the average error between the computed and actual fringe orders over the data analysis region and by a visual comparison of the fringe pattern predicted by a solution set with the fringe pattern from which the data had been extracted.

An example of the quality of the comparison between predicted (computed) and actual photoelastic fringe patterns is shown in Figure 4 for the case of two cracks with a separation of $c/a_1 = 0.54$ and a relative crack length of $a_2/a_1 = 0.833$. A similar comparison is shown in Figure 5 for the case of a u-field corresponding to $c/a_1 = 1.0$ and $a_2/a_1 = 1.25$.

Figure 6 shows a comparison of the overall results for the case of two cracks with a crack plane separation of $c/a_1 = 0.75$, and relative crack length, a_2/a_1, varying from 0.50 to 1.25. The figure compares the J-integral value calculated directly (using a contour integral) from the finite element results with the J-value obtained from the stress intensity factors calculated at each crack tip using the local collocation analysis of the finite element data.

Conclusions

The Westergaard-Schwarz approach was found to be suitable for representing the stress and displacement fields over relatively large regions surrounding the tips of two parallel, interacting cracks in a finite geometry. The resulting model for the stress and displacement fields proved to be useful in interpreting the data for stresses and displacements obtained using the experimental techniques of photoelasticity and geometric moire and the method of finite elements.

The results showed that:

(a) as the length of one crack increases relative to the length of a second crack of fixed length, the interaction between the two crack-tip fields acts to lower the opening-mode stress intensity factor of the crack of fixed length;

(b) the opening mode stress intensity factors for the two cracks are not significantly affected by changes in the crack plane separation, at least over the separation range studied; and

(c) the interaction effect between the two crack-tip stress fields causes shear-mode stress intensity factors to develop in cases that would be under predominantly opening-mode loading in an isolated, single crack situation.

References

1. Sanford, RJ.: A Critical Re-examination of the Westergaard Method for Solving Opening-Mode Crack Problems, *Mechanics Research Commmications* **6** (1979), 289-294.

2. Ukadgaonker, V.G., and Naik, A.P.: Interaction Effect of Two Arbitrarily Oriented Cracks - Part I, *International Journal of Fracture,* **51** (1991), 219-230.

3. Sanford, R. J. : Application of the Least-Squares Method to Photoelastic Analysis, *Experimental Mechanics* **20** (1980), 192-197.

4. Chona, R: Extraction of Fracture Mechanics Parameters form Steady-State Dynamic Crack-Tip Fields, *Optics and Lasers in Engineering* **19** (1993), 171-199.

5. Sanford, R.J., Barker, D.B., and Chona, R.: Computer Generated Fringe Patterns in Speckle Analysis, *International Conference on Speckle* **SPIE 556** (1985).

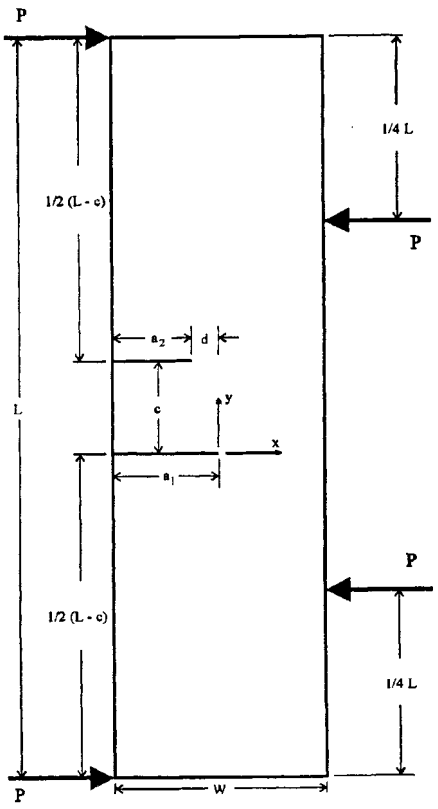

Figure 1 The geometry and loading of a four-point bend specimen with two parallel interacting edge cracks

a) EXP 2.1; a_2/a_1 =0.5; M=225 lb_f in

b) EXP 2.2; a_2/a_1=0.75; M=225 lb_f in

c) EXP 2.3; a_2/a_1=1.0; M=225 lb_f in

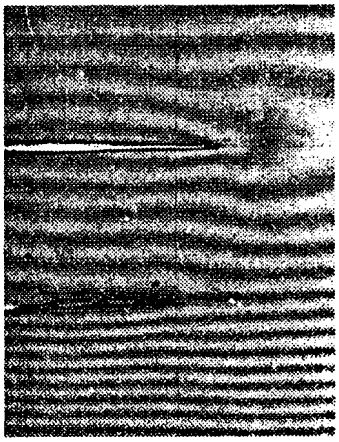

d) EXP 2.4; a_2/a_1=1.25; M-125 lb_f in

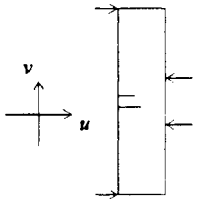

Figure 2 The changes in the u-field pattern observed as the relative crack size was increased from a_2/a_1 = 0.50 to a_2/a_1 = 1.25 for a fixed crack plane separation of c/a_1 = 0.75

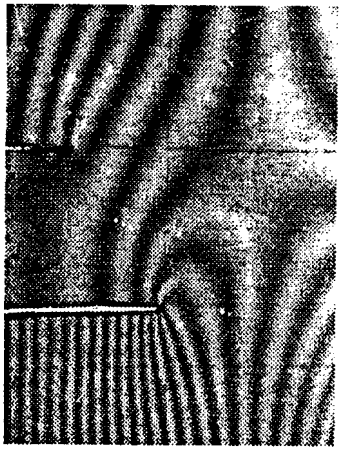

a) EXP 2.1; a_2/a_1=0.5; M-225 $1b_f$ in

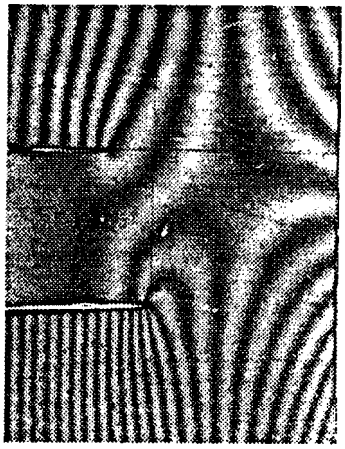

b) EXP 2.2; a_2/a_1=0.75; M=225 $1b_f$ in

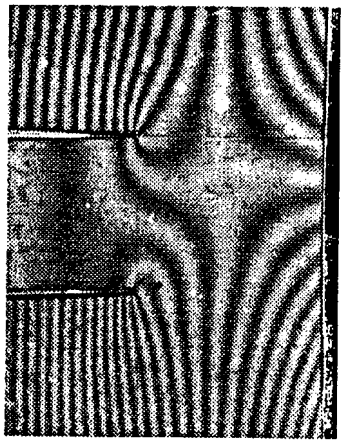

c) EXP 2.3; a_2/a_1=1.0; M-225 $1b_f$ in

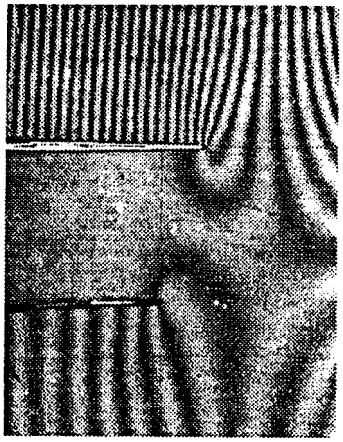

d) EXP 2.4; a_2/a_1=1.25; M-125 $1b_f$ in

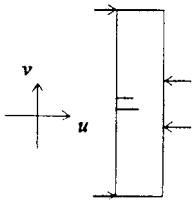

Figure 3 The changes in the v-field pattern observed as the relative crack size was increased from a_2/a_1 = 0.50 to a_2/a_1 = 1.25 for a fixed crack plane separation of c/a_1 = 0.75

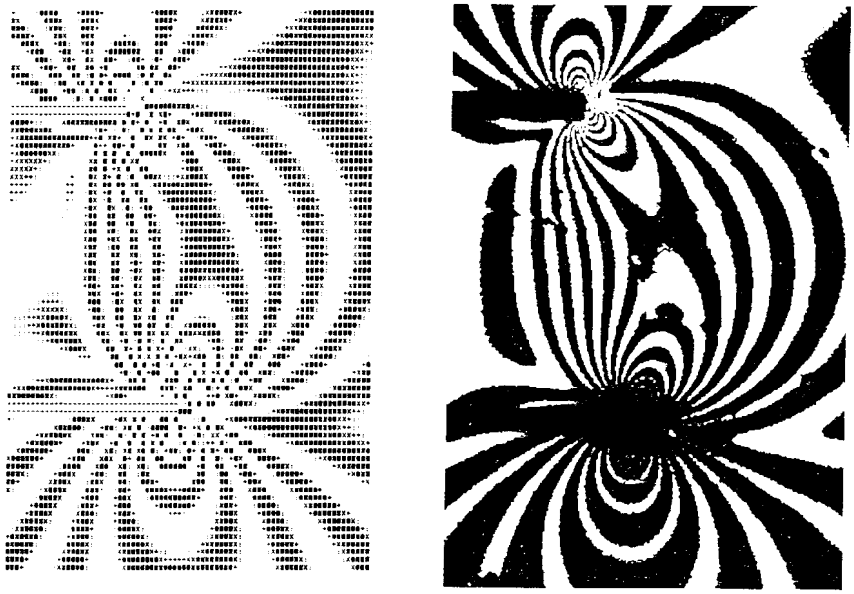

Figure 4 Reconstructed and experimentally recorded photoelastic fringe patterns corresponding to a relative crack size, $a_2/a_1 = 0.833$, for a crack plane separation, $c/a_1 = 0.54$

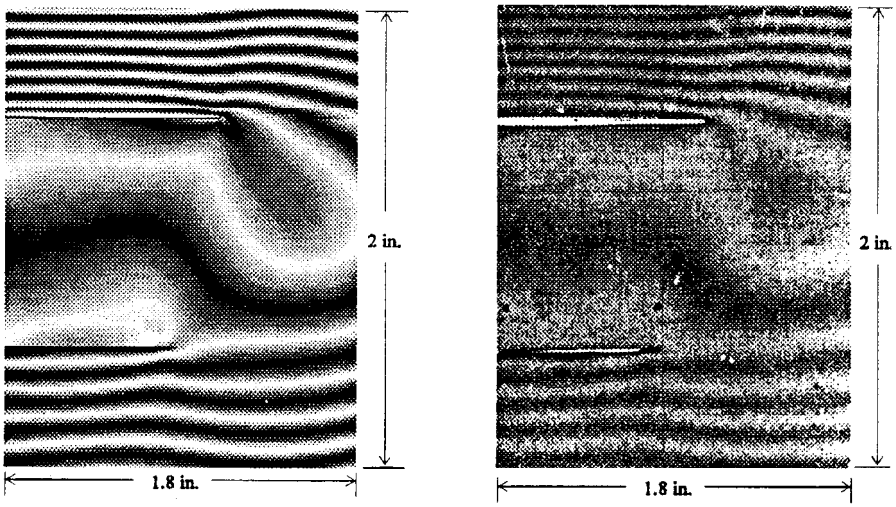

Figure 5 Reconstructed (computer-generated) and experimentally recorded u-field patterns corresponding to a relative crack size, $a_2/a_1 = 1.25$, for a crack plane separation, $c/a_1 = 1.0$

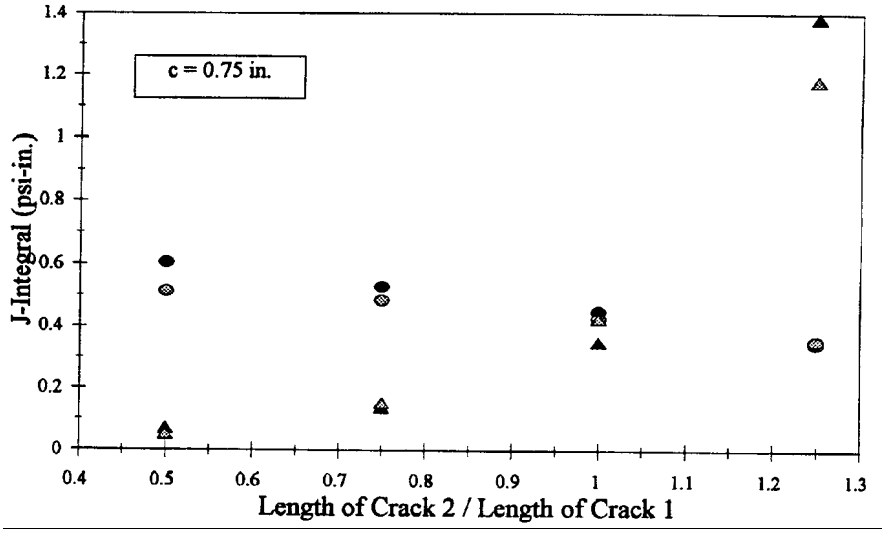

Figure 6 J-integral values calculated from finite element results using a contour integral and the stress intensity values at each crack tip calculated using the local collocation method; shown as a function of the relative crack size, a_2/a_1, for a crack plane separation, $c/a_1 = 0.75$

SOLUTION OF FRACTURE PROBLEMS BY NON-LINEAR PHOTOELASTIC METHODS UNDER LARGE ELASTIC AND PLASTIC STRAINS

MARAT AKHMETZYANOV, GALINA ALBAUT, VIKTOR BARYSHNIKOV
Novosibirsk State University of Architecture and Construction

Abstract

In this study the problems of fracture mechanics having geometrical and physical non-linearity were experimentally investigated by non-linear photoelastic methods. The strains changed in the range from -50% till +220% of relative lengthening. Changes in geometry and in thickness of the specimens were taken into consideration. Here, non-compressible birefringent polyurethane rubber was applied. Two schemes of polarizative-optical tests were used: 1) through translucence of rubber specimens; 2) photoelastic coating method for the study of large plastic strains in metals.

The main equations of the method evolved to verify experimental data are presented in this paper, and some elastic and plastic problems are studied as examples. Stress-strain state in rubber plates with cracks was determined the cracks taking ellipse or round forms under deformation. The inclined crack affect upon stress concentration coefficients k_σ and strain coefficients k_ε at its tip was studied. Applying the photoelastic coating method, the behaviour of concentration coefficients k_σ and k_ε was investigated in the specimens made of middle steel and having cuts of different outlines and in the weldment of mild steel under plastic deformation. Common laws were ferreted out with respect to the distribution of stress fields in the prefailure zone near cracks, also, the tendency of functions k_σ and k_ε to change under the increasing strains for different outlines' specimens made of different sorts of steel was showed up.

1. Introduction

Structural design for new rubber-like or composite materials is mathematically hampered especially in view of concentrators or cracks. The same kind of thing applies to metal structural elements working at the prefailure stage under large plastic strains. Some of the assumptions and hypotheses used in structural design must be experimentally tested and verified. The non-linear photoelastic method enables to solve similar problems through experiments.

A. Lagarde (ed.),
IUTAM Symposium on Advanced Optical Methods and Applications in Solid Mechanics, 505–512.

2. General Relationships

When investigating large plastic strains in rubber specimens, to measure stresses the true stress values were taken (σ_1 and σ_2 as the main components in the specimen's plane and σ_3 being equal to 0 along perpendicular); to measure strains in the specimen's plane the extents of lengthening λ_1 and λ_2 were exploited while λ_3 evaluated the strains in specimen's thickness. By the study of large plastic strains carried out by means of photoelastic coating method the lengthening extents were converted into logarithmic strains according to Hencky ($\varepsilon_i = \ln \lambda_i$, i=1,2,3). Below there is a set of relations to treat the experimental data for SKU-6 polyurethane specimens: (1) non-changeable volume condition; (2) differential equilibrium equation for a plane problem; (3) stress-strain connection equation exploiting Bartenev-Khazanovitch's elastic potential; (4) the general law of non-linear photoelasticity; (5) the corresponding optic-strain relationship.

$$\lambda_1\lambda_2\lambda_3 = 1 \; ; \tag{1}$$

$$\frac{\partial(\lambda_3\sigma_x)}{\partial x} + \frac{\partial(\lambda_3\tau_{xy})}{\partial y} = 0 \; ; \quad \frac{\partial(\lambda_3\sigma_y)}{\partial x} + \frac{\partial(\lambda_3\tau_{yx})}{\partial y} = 0 \; ; \tag{2}$$

$$\sigma_1 = A(\lambda_1 - \lambda_3) \; ; \quad \sigma_2 = A(\lambda_2 - \lambda_3) \; ; \tag{3}$$

$$\delta = C_\sigma \lambda_3 h_0 (\sigma_1 - \sigma_2) \; ; \tag{4}$$

$$\delta = C_\varepsilon \lambda_3 h_0 (\lambda_1 - \lambda_2) \; ; \tag{5}$$

when A is elastic constant, δ – optical path difference, C_σ and C_ε – stress and strain optical constants, h_0 – initial thickness [1].

Simple equations (3) are not universal, they approximate elastic properties of polyurethane SKU-6 quite well. Other kinds of rubber are advantageously characterised by relations (6) comprising 4 constants resulted from Moonley-Rivlin's theory of strains and the corresponding optic-strain relationship (7).

$$\begin{aligned} \sigma_1 &= 2(A_2 + B_2\lambda_2^2)(\lambda_1^2 - \lambda_3^2) + 4(A_4 + B_4\lambda_2^4)(\lambda_1^4 - \lambda_3^4) \; ; \\ \sigma_2 &= 2(A_2 + B_2\lambda_1^2)(\lambda_2^2 - \lambda_3^2) + 4(A_4 + B_4\lambda_1^4)(\lambda_2^4 - \lambda_3^4) \; ; \end{aligned} \tag{6}$$

$$\delta = C_\varepsilon h_0 \lambda_3 \left(2(A_2 + B_2\lambda_3^2)(\lambda_1^2 - \lambda_2^2) + 4(A_4 + B_4\lambda_3^4)(\lambda_1^4 - \lambda_2^4)\right) . \tag{7}$$

In this paper, the separation of stresses and strains is fulfilled by means of the method of numerical integration of equilibrium equations (2), with the subsequent use of the rest of the relations in the set (1)÷(5) [2].

There have been worked out some other separation methods: measuring cross strain method, method of coating cutting, tilted translucence method, etc.

This Page Intentionally Left Blank

This Page Intentionally Left Blank

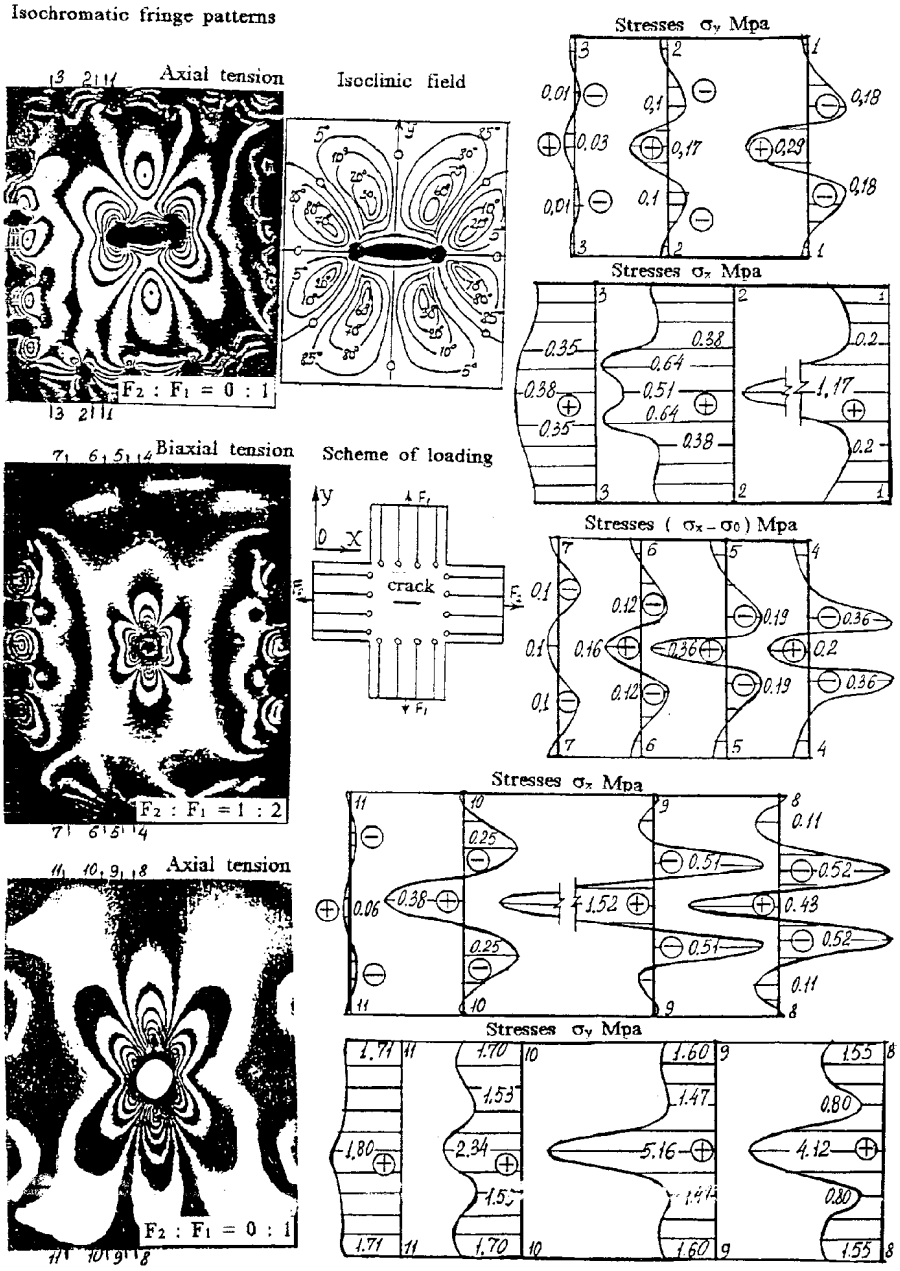

Figure 1. Stress determination in the rubber specimens with the crack

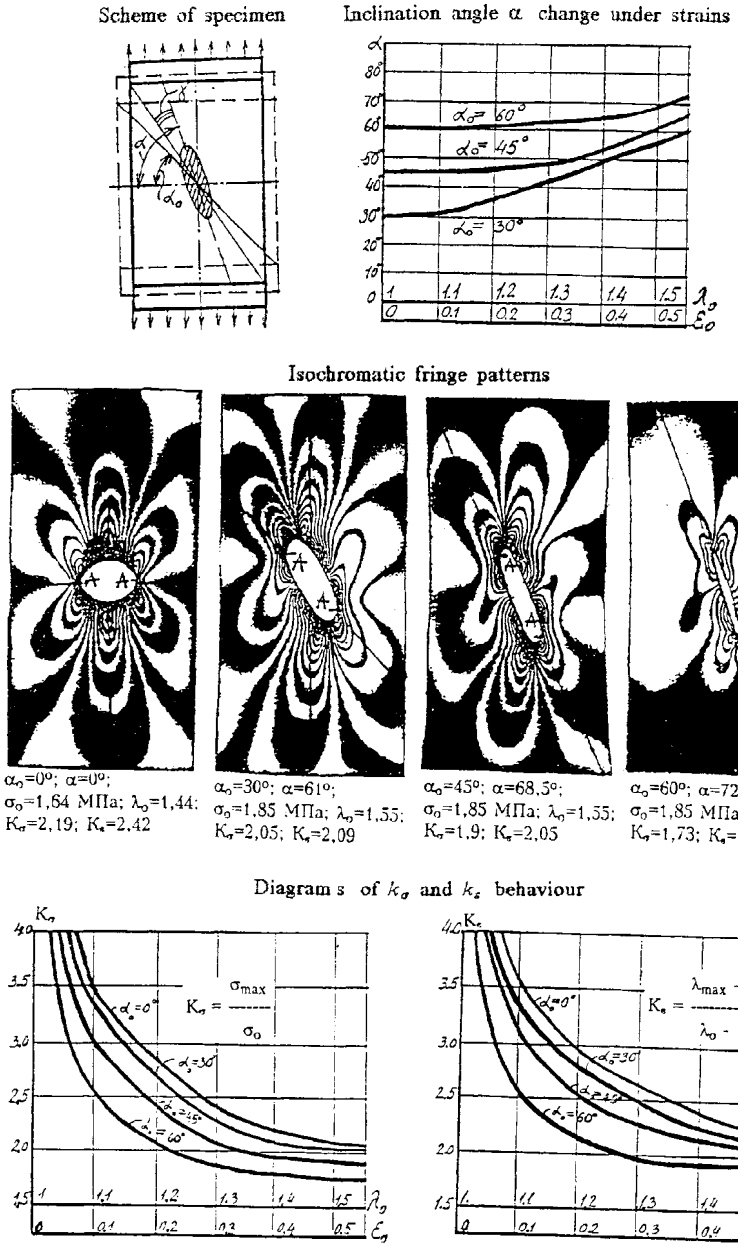

Figure 2. Inclined cracks affecting k_σ and k_ε behaviour under strains increase for rubber specimens

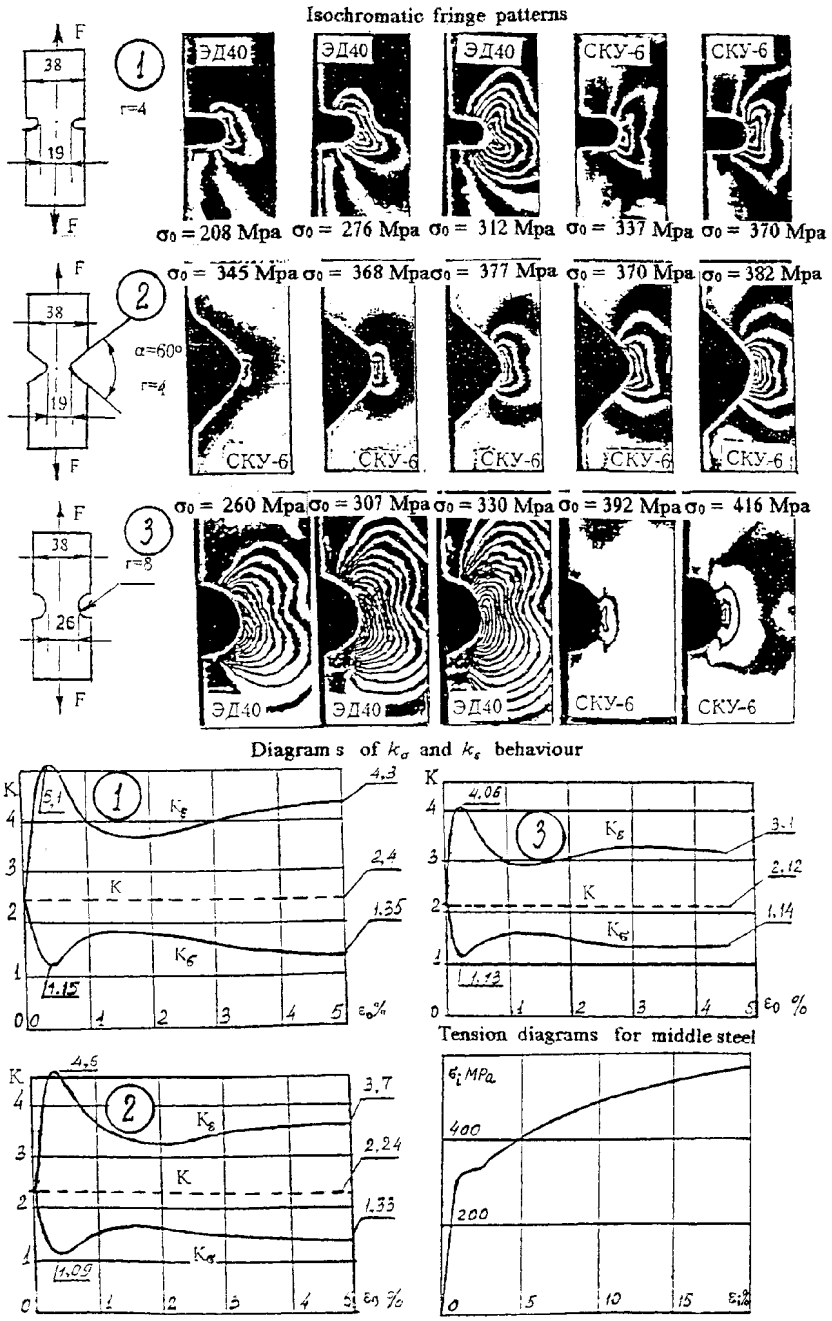

Figure 3. Study of k_σ and k_ε behaviour for developed plastic strains in the steel specimens with different cuts by photoelastic coating method

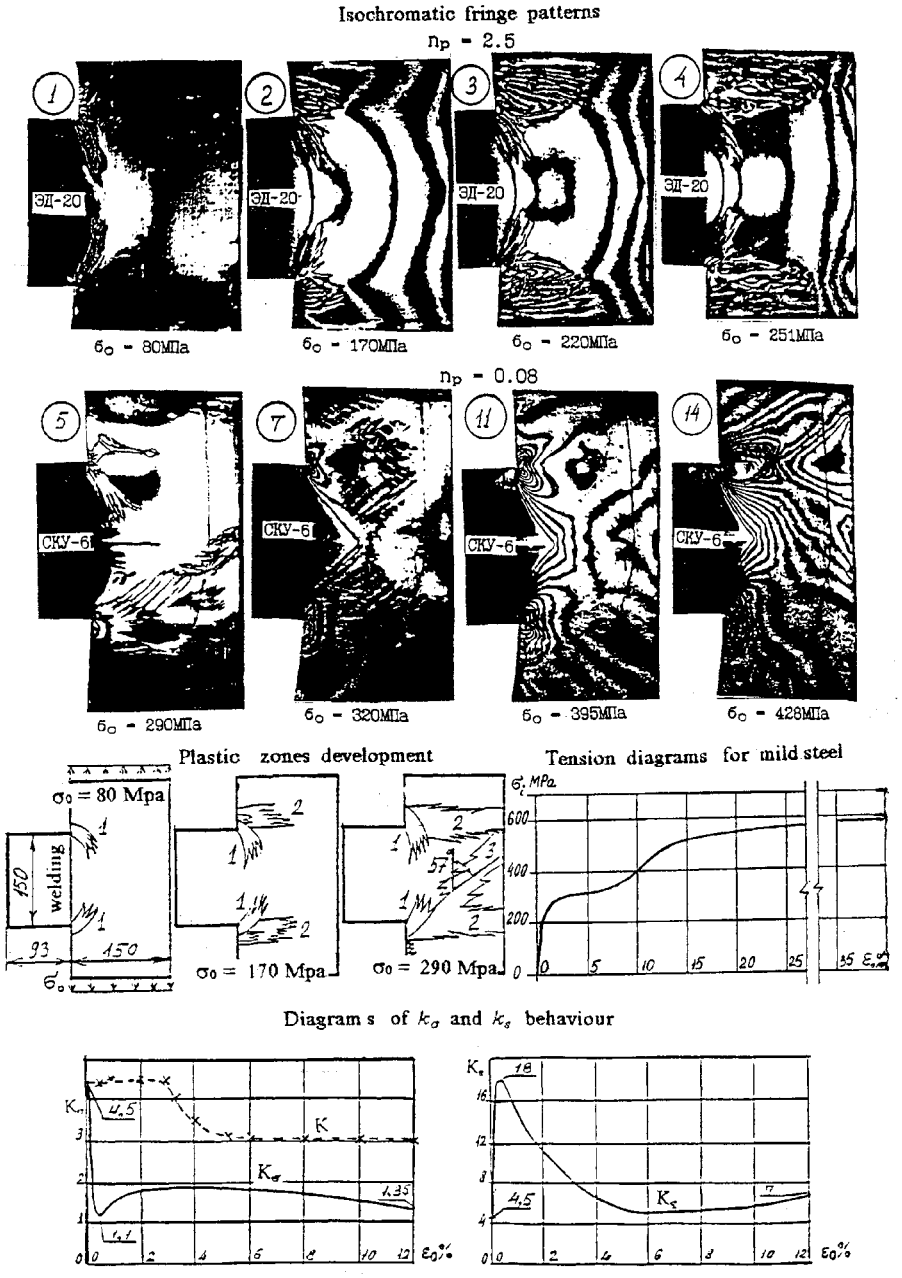

Figure 4. Study of k_σ and k_ε behaviour for developed plastic strains in the steel welded specimens under tension by phatoelastic coating method

APPLICATIONS OF OPTICAL METHODS OF STRESS ANALYSIS TO STUDY FRACTURE PHENOMENA

F. FERBER, K.P. HERRMANN, K. LINNENBROCK
Laboratorium fûr Technische Mechanick
Paderborn University, Pohlweg 47-49
D-33098 Paderborn, Germany

1. Introduction

An overview about the numerical simulation and experimental modelling of cracks arising in homogeneous and nonhomogeneous solids will be given. Shadow optical and photoelastic data were collected from digitally sharpened caustics and isochromatic fringe patterns by using a digital image analysis system. The geometry of the caustics is proportional to the stress field gradient and therefore the caustic contour can be taken as a quantity for experimental measurements.

The solutions of the corresponding mixed boundary value problems of the thermoelasticity were not only obtained by using the FE-method but also by applying the experimental method of photoelasticity as well as the shadow optical method of caustics.

A photoelastic analysis for cracked two-phase compounds has been performed by using the image analysis of isochromatic fringe loops. A combination of the so-called phase-stepping method, an automatic polariscope and the multiple point method results in an automatic method for the determination of stress intensity factors.

Based on the caustics equations measuring algorithms can be formulated in order to determine stress intensity factors from experimentally gained caustics. The numerical simulation of shadow spots and isochromatic fringe patterns, respectively, is based on the fundamental equations of optics. By applying a generated finite element mesh numerically simulated caustics at the tips of straight matrix and interface cracks, respectively, extending quasistatically in the matrix material or in the inclusion matrix interface of a circular composite unit cell were obtained.

In this research contribution, an overview about the experimental and numerical modelling of crack systems arising in thermomechanically loaded models of two-phase composite structures will be given [1-5].

A. Lagarde (ed.),
IUTAM Symposium on Advanced Optical Methods and Applications in Solid Mechanics, 513–520.

2. Photoelastic and Shadow Optical Crack Tip Analysis

A method for a determination of stress intensity factors from isochromatic fringe patterns by using numerous appropriate measuring points has been provided for the first time by Sanford & Dally [6]. By using the stress components near a crack tip as well as the basic equation of the photoelasticity the function g_k for a photoelastic data point k can be expressed as follows

$$g_k(K_I, K_{II}, a_3, ..., a_N) = \left(\frac{\sigma_{rr}(r_k, \varphi_k) - \sigma_{\varphi\varphi}(r_k, \varphi_k)}{2}\right)^2 + \tau_{r\varphi}^2(r_k, \varphi_k) - \left(\frac{Sn_k}{2d_{eff}}\right)^2 = 0 \tag{1}$$

After taking a Tailor's series expansion of g_k and retaining only the linear terms a system of algebraic equations can be obtained

$$g_{k_{i+1}} = g_{k_i} + \left(\frac{\partial g_k}{\partial K_I}\right)_i \Delta K_I + \left(\frac{\partial g_k}{\partial K_{II}}\right)_i \Delta K_{II} + \left(\frac{\partial g_k}{\partial a_3}\right)_i \Delta a_3 + ... + \left(\frac{\partial g_k}{\partial a_N}\right)_i \Delta a_N \tag{2}$$

where i refers to the ith iteration step. A standard Newton-Raphson procedure can be used to calculate the stress intensity factors K_I and K_{II} for a set of proper input data points. By utilizing digital-image-processing and computergraphics techniques, a set of menu-driven software has been developed for interactively implemented fringes processing [7]. The stress components in the vicinity of a crack tip under mixed-mode-loading are given as functions of the seven parameters K_I, K_{II} and the non-singular terms σ_{ox}, a_3, a_4, b_3, and b_4.

$$\begin{aligned}\sigma_{rr} = {} & \frac{K_I}{\sqrt{2\pi r}}\frac{1}{4}\left(5\cos\frac{\varphi}{2} - \cos\frac{3}{2}\varphi\right) + \frac{K_{II}}{\sqrt{2\pi r}}\frac{1}{4}\left(-5\sin\frac{\varphi}{2} + 3\sin\frac{3}{2}\varphi\right) \\ & + \sigma_{ox}\cos^2\varphi \\ & + a_3\sqrt{r}\frac{1}{4}\left(3\cos\frac{\varphi}{2} + \cos\frac{5}{2}\varphi\right) + a_4 r(\cos\varphi + 3\cos 3\varphi) \\ & - b_3\sqrt{r}\frac{1}{4}\cdot\left(9\sin\frac{\varphi}{2} + 15\sin\frac{5}{2}\varphi\right) - b_4 r2(\sin\varphi + \sin 3\varphi)\end{aligned} \tag{3a}$$

$$\begin{aligned}\sigma_{\varphi\varphi} = {} & \frac{K_I}{\sqrt{2\pi r}}\frac{1}{4}\left(3\cos\frac{\varphi}{2} + \cos\frac{3}{2}\varphi\right) - \frac{K_{II}}{\sqrt{2\pi r}}\frac{1}{4}\left(3\sin\frac{\varphi}{2} + 3\sin\frac{3}{2}\varphi\right) \\ & + \sigma_{ox}\sin^2\varphi \\ & + a_3\sqrt{r}\frac{1}{4}\left(5\cos\frac{\varphi}{2} - \cos\frac{5}{2}\varphi\right) + a_4 r3(\cos\varphi - \cos 3\varphi) \\ & - b_3\sqrt{r}\frac{1}{4}\left(15\sin\frac{\varphi}{2} - 15\sin\frac{5}{2}\varphi\right) + b_4 r3\left(\frac{5}{4}\sin\varphi - \frac{5}{12}\sin 3\varphi\right)\end{aligned} \tag{3b}$$

$$\begin{aligned}\tau_{r\varphi} = {} & \frac{K_I}{\sqrt{2\pi r}}\frac{1}{4}\left(\sin\frac{\varphi}{2} + \sin\frac{3}{2}\varphi\right) + \frac{K_{II}}{\sqrt{2\pi r}}\frac{1}{4}\left(\cos\frac{\varphi}{2} + 3\cos\frac{3}{2}\varphi\right) \\ & - \frac{1}{2}\sigma_{ox}\sin 2\varphi \\ & + a_3\sqrt{r}\frac{1}{4}\left(\sin\frac{\varphi}{2} - \sin\frac{5}{2}\varphi\right) + a_4 r(\sin\varphi - 3\sin 3\varphi) \\ & + b_3\sqrt{r}\frac{3}{4}\left(\cos\frac{\varphi}{2} - 5\cos\frac{5}{2}\varphi\right) + b_4 r2(\cos\varphi - \cos 3\varphi)\end{aligned} \tag{3c}$$

The principle and the experimental set-up of the phase-stepping method from Hecker and Morche [8] by using an automatic polariscope are shown in Figure 1. The determination of the principle stress directions and the isochromatic fringe order is possible by a mathematical combination from 10 images of different angle positions of the polariscope, namely: linear polariscope; α/β; 0/90; 30/120; 60/150; 45/135; 0/0 [°] and circular polariscope: α/β; 0/0; 60/60; 120/120; 0/45/; 0/-45 [°]. A combination of the phase-stepping method and the multiple point method results in an automatic method for the determination of stress intensity factors.

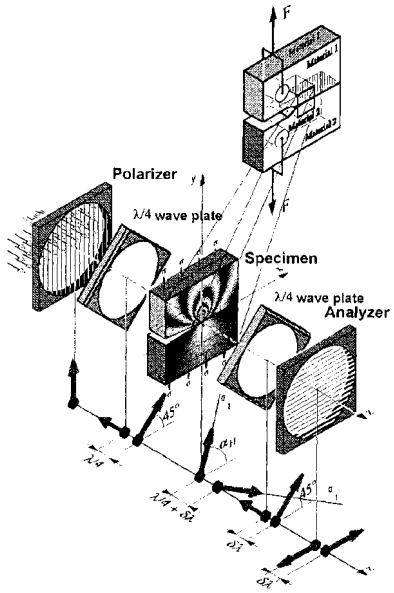

Figure 1. The principle and the experimental set-up of the phase-stepping method.

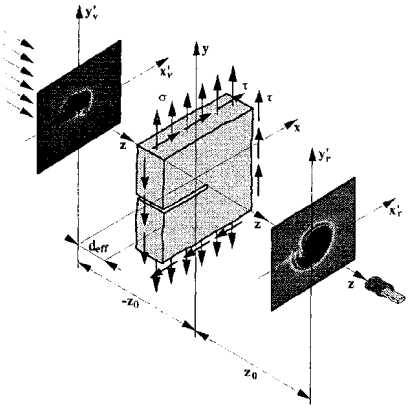

Figure 2. Experimental set-up for the shadow optical method of caustics.

The shadow optical method represents an important tool for the experimental determination of stress intensity factors at the tips of quasistatically extending and fast running cracks, respectively The physical principle underlying the method of shadow patterns is illustrated in Figure 2. A specimen containing a crack is illuminated with light generated by a point light source. In this case, a specimen of a transparent composite material is considered. The stress intensification in the region surrounding the crack tip leads to a reduction of both the thickness of the specimen and the refractive index of the material. As a consequence, in the transmission case, the light passing through the specimen is deflected outwards. On an image plane at any distance z_O behind the specimen, therefore, a dark shadow spot is formed. The spot is bounded by a bright light concentration, the caustic. The geometry of the caustic is proportional to the stress field gradient and therefore the caustic contour can be taken as a quantity for experimental measurements [9-13]. In the scope of an experimental failure analysis of brittle composites the method of caustics is applied to determine stress intensity factors or related quantities at crack tips situated in homogeneous components or at the interfaces of composites.

3. Material models of fibrous composites

3.1 MATERIAL MODEL OF A CRACKED MATRIX

Figure 3 shows a material model of a cracked matrix with an asymmetrically situated inclusion with respect to the crack under thermal load due to a cooling process.

Figure 4 shows experimentally obtained isochromatic fringe patterns and caustics for a straight crack near such an inclusion. Thereby the isochromatic fringes and caustics were obtained for a material combination of Araldite B and ceramics. The definition of a ring region in combination with different angle regions can also be used for the determination of the mixed-mode stress intensity factors K_I and K_{II} in relation to the selected crack tip areas.

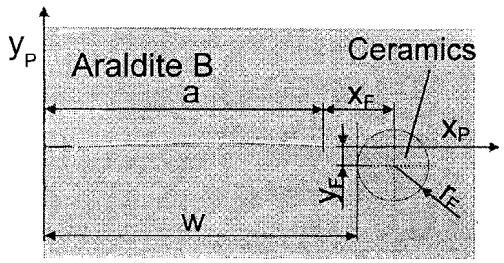

Figure 3. Model of a cracked matrix with an asymmetrically situated inclusion under thermal load (matrix: Araldite B; inclusion: Ceramics)
Specimen geometry: a=80 mm, x_F=25 mm, y_F=-14 mm, r_F=12.75 mm.

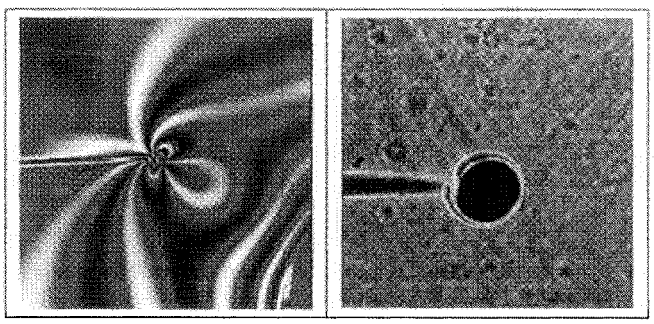

Figure 4. Experimentally obtained isochromatic fringe patterns and caustics

A typical result is given in Figure 5. It has been demonstrated, that the values of the mixed-mode stress intensity factors K_I, K_{II} and of the parameter σ_{ox} obtained experimentally by the method of photoelasticity show a very good coincidence with the corresponding numerical values determined by a finite element calculation.

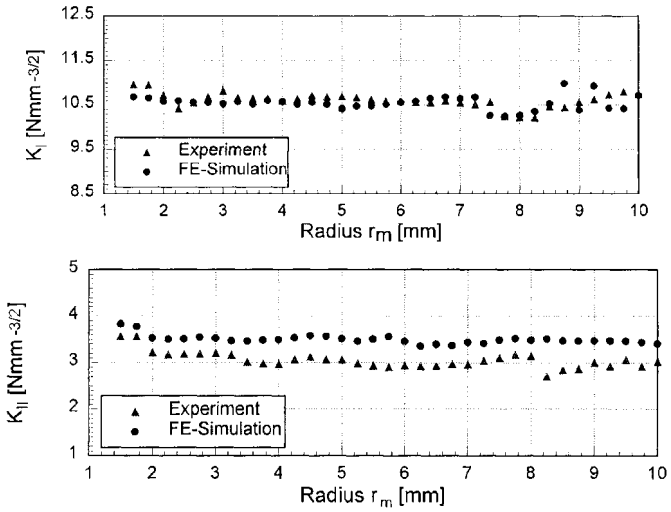

Figure 5. Stress intensity factors K_I, K_{II} in dependence on the crack tip distance r_m .

An accurate determination of the parameters from isochromatic fringe patterns is given within the range 2.5 mm < r_m< 7.5 mm of the radius r_m.

Figure 6 gives a comparison of stress intensity factors from experimentally obtained isochromatic fringe patterns and caustics, where a good agreement can be stated. Shown are typical results from specimens under different thermal loads.

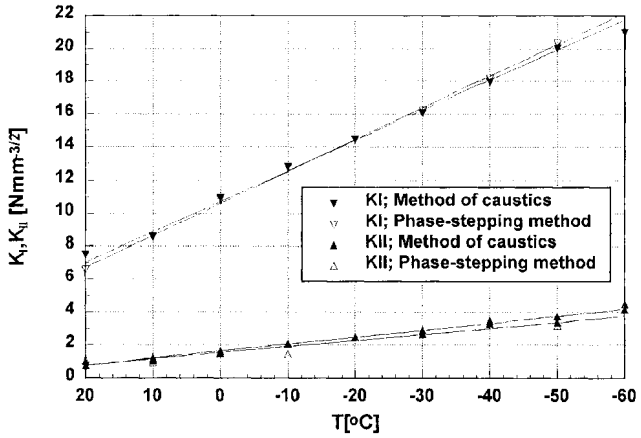

Figure 6. Stress intensity factors K_I, K_{II} in dependence on temperature (y_F=8mm; x_F=32mm).

Figure 7 gives a comparison of stress intensity factors from experimentally obtained isochromatic fringe patterns with a corresponding finite element calculation, where a good agreement can be stated. Shown are typical results from specimens under different thermal loads [14, 15].

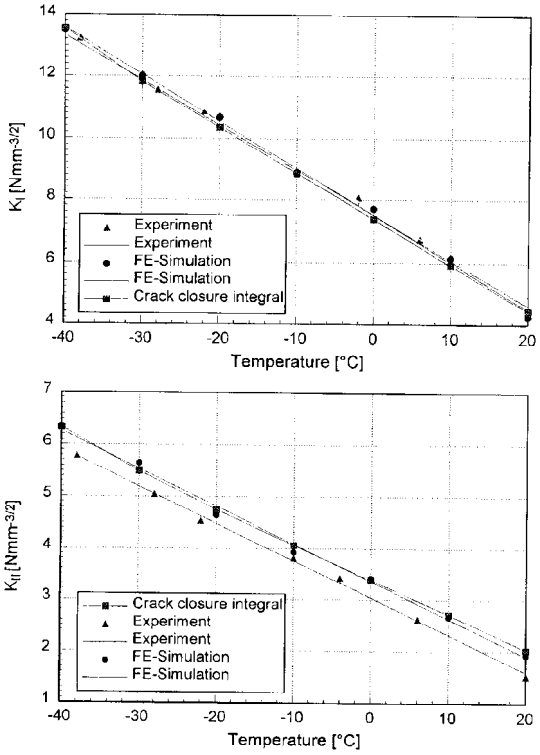

Figure 7. Stress intensity factors K_I, K_{II} in dependence on temperature.

3.2 BIMATERIAL MODEL

The experimental determination of stress intensity factors at the tip of a curvilinear thermal crack propagating in the matrix material, Araldite B, of a disk-like bimaterial model (cf. Figure 8 and 9) has been performed. Thereby a ring region can be used to calculate the stress intensity factors in dependence on the crack tip distance r_m.

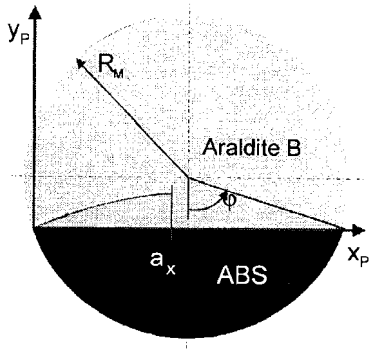

Figure 8. Model of a cracked disk-like bimaterial.

Figure 10 gives a comparison of the stress intensity factors K_I and K_{II} gained from experimentally obtained isochromatic fringe patterns by using the multiple point method of photoelasticity. In this case an accurate determination of the parameters σ_{ox}, a_3, a_4, b_3, and b_4 from isochromatic fringe patterns is given within the range 2mm< r_m <11mm of the radius r_m. This thermal loading process produces a pure mode-I loading, which can also be seen from the K_{II} -values.

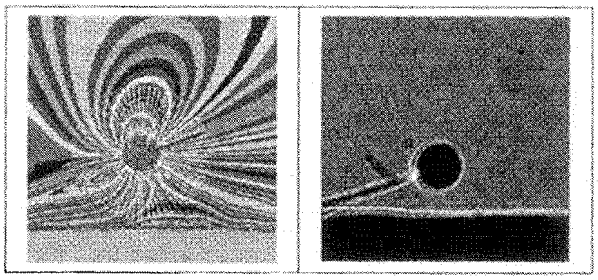

Figure 9. Experimentally obtained isochromatic fringe patterns and caustics

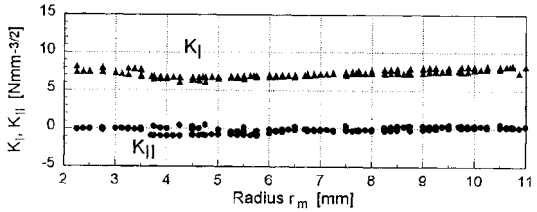

Figure 10. Comparison of stress intensity factors K_I and K_{II} gained from experimentally obtained isochromatic fringe patterns by using the multiple point method of photoelasticity.

Figure 11 gives a comparison of stress intensity factors from experimentally obtained isochromatic fringe patterns and caustics in dependence on projeced crack length a_x.

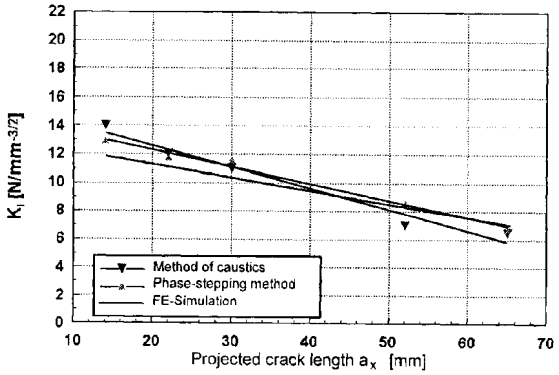

Figure 11. Stress intensity factors K_I and K_{II} gained from experimentally obtained isochromatic fringe patterns and caustics in dependence on projeced crack length a_x.

Conclusion

Shadow optical and photoelastic data were collected from digitally sharpened isochromatic fringe patterns and caustics by using a digital image analysis system. A photoelastic analysis for cracked two-phase compounds has been performed by using the image analysis of isochromatic fringe loops. A combination of the so-called phase-stepping method, an automatic polariscope and the multiple point method result in an automatic method for the determination of stress intensity factors. An overview about the experimental modelling of cracks arising in plane disk-like models of two-phase composite structures is given.

References

1 Ferber, F. (1986) Ph. D., Dissertation, Paderborn University

2 Ferber, F. and Herrmann, K.P. (1991) *Brittle Matrix Composites 3,* eds. A.M. Brandt and I.H. Marshall, Elsevier Applied Science Publishers, London/New York, 403-412

3 Dong, M. (1993) *Fortschritt Berichte,* VDI-Reihe 18, No 138

4 Noe, A. (1994) Ph. D., Dissertation, Paderborn University

5 Ferber, F. and Herrmann, K.P. (1994) *Brittle Matrix Composites 4,* eds. A.M. Brandt, V.C. Li and I.H. Marshall, IKE, Warschau/Woodhead Publ. Ltd., Cambridge, UK., 190-199

6 Sanford, R.J. and Dally, J.W. (1979) A general method for determining mixed-mode stress intensity factors from isochromatic fringe patterns. *Engineering Fracture Mechanics* **11,** pp. 621-633

7 Hinz, O. (1993) Ph. D., Dissertation, Paderborn University

8 Hecker, F.W. and Morche, B. (1986) *Computer-aided measurement of relative retardations in plane photo-elasticity.* In: Wieringa, H. (Ed.), Experimental Stress Analysis, 535-542, Martinus Nijhoff Publishers, Dordrecht, Boston, Lancaster

9 Manogg, P. (1964) Ph. D., Dissertation, Freiburg University

10 Kalthoff, J.F. (1985) *The Shadow Optical Method of Caustics.* In: A.S. Kobayashi (ed.), Handbook of Exp. Mech., 430-500. Englewood Cliffs, Prentice Hall

11 Theocaris, P.S. (1976) Partly unbonded interfaces between dissimilar materials under normal und shear loading. *Acta Mechanica,* **24,** pp. 99-115

12 Rossmanith, H.P. (1982) The method of caustics for static plane elasticity problems. *Journal of Elasticity,* **12,** pp. 193-200

13 Rossmanith, H.P. (1979) Determination of stress intensity factors by the dynamic method of caustics for optically isotropic materials. *Ingenieur- Archiv,* **48,** pp. 363-381

14 Ferber, F., Herrmann, K.P. and Linnenbrock, K. (1996) *Elementary failure analysis of composite models by using optical methods of stress analysis and modern digital image systems.* In: ESDA 1996, (Eds. A. Large and M. Raous) ASME, New York, Vol. 4, pp. 55-68

15 Ferber, F., Herrmann, K.P. and Linnenbrock, K. (1997) *Study of fracture phenomena in thermomechanically loaded composites by using optical methods of stress analysis and digital image systems.* In: Thermal Stresses '97 (Eds. R.B. Hetnarski, N. Noda and H. Ghoneim), Rochester Institut of Technology, pp. 523-526

ACTIVE CONTROL OF STRESS INTENSITY FACTOR K UNDER MIXED MODE STRESS IN THE SMA-FEC

A. SHIMAMOTO
Department of Mechanical Engineering, Saitama Institute of Technology, Okabe, Saitama, 369-0293, Japan e mail : shimamot@sit.ac.jp

Y. FURUYA
Department of Materials Processing, Tohoku University, Sendai, 980-8579, Japan

E.UMEZAKI
Department of Mechanical Engineering, Nippon Institute of Technology, Miyashiro, Saitama, 345-8501, Japan

Abstract

Shape memory TiNi fiber reinforced/epoxy matrix composite (SMA-FEC) is fabricated to demonstrate the suppression effect of crack tip stress concentration and the fracture toughness (K value) under mixed mode stresses in the composite. The test specimens have two types of angled notches to the transverse direction of the tensile type specimen. i.e. $\theta = 45°$, $90°$ with several crack lengths. The stress intensity at the notch tip is experimentally determined by photoelastic fringes. The decrease of the K value is attributed to the compressive stress field in the matrix which is induced when the prestrained the TiNi fibers contract to the initial length upon heating above the austenitic finish temperature of the TiNi fiber (T>Af). The dependencies of the K value on the prestrain value of TiNi fibers as well as on the compressive stress domain size between a crack tip and fiber are discussed.

1. Introduction

The active control of material degradation (i.e. damage accumulation, crack, delamination etc.) during the service time and the elongation of the failure life of the material components has become increasingly important in recent years owing to the increasing demands for improved safety design of various engineering devices and structures. Furthermore, the development of an artificial system for prevention of sudden failure of machinery and structures has also become a worthy and attractive research subject for the creation of a new design concept of intelligent/smart material systems and structures.

A. Lagarde (ed.),
IUTAM Symposium on Advanced Optical Methods and Applications in Solid Mechanics, 521–530.

As one of the works concerning active control of the strength and fracture of a material system, Rogers [1] proposed the active control method for retardation of fatigue crack propagation from a notch root by utilizing the contractions of an embedded SMA line type actuator. In his approach, the SMA actuator is heated by means of direct current joule heating, and then, the large compressive stresses in the matrix associated with the shrinkages of TiNi actuator act to reduce the mean stress level of cyclic loading. This enhances the crack closure phenomenon and the retardation of fatigue crack propagation. Rogers also attempted to explain an experimental result on the suppression of crack tip stresses in a precracked TiNi fiber/epoxy resin matrix composite specimen using a photoelastic fringe pattern. However, the change of stress intensity value K has not been clarified yet in detail as well as systematically.

Concerning this problem, the authors have recently attempted to improve the of mechanical strength as well as the active control of stress intensity value K_I under an uniaxial stress condition (i.e. mode 1) on the basis of basic experiments involving direct current joule heating of TiNi fibers embedded in a photoelastic epoxy matrix composite, $(TiNi)_f$/epoxy. [3] [4] [5] However, in general , mixed mode stresses work in machinery or structural component and result in the failure of the whole structure, therefore, in the present study, the suppression effect of crack tip stress concentration and the fracture toughness (K value) under mixed mode stresses in composite are studied. The test specimens have two types of angled notches in the transverse direction of the tensile type specimen. i.e. $\theta = 45°$, $90°$ with several crack lengths. The stress intensity at the notch tip is experimentally determined by photoelastic fringes. The decrease of the K value is attributed to the compressive stress field in the matrix which is induced when the prestrained TiNi fibers contract to the initial length upon heating above the austenitic finish temperature of TiNi fiber (T > Af). The dependencies of mixed-mode K values (K_I and K_{II}) on the prestrain value of TiNi fibers as well as on the compressive stress domain size between a crack tip and fiber are discussed systematically.

2. Design concept of shape memory composite

Thermoelastic shape memory effect (i.e. shape memory and recovery phenomenon) takes place during martensite (M) to austenite (A) phase transformation in SMA with increasing temperature. Therefore, the material functional properties of SMA change clearly depending on the change with the temperature [2] as summarized in Fig. It should be noted exhibits that SMA unique properties of a higher stiffness (2-3 times) and large recovery stress in the higher temperature region due to an inversely thermoelastic phase transformation in contrast to the weakening of those properties in general metals. As a consequence, SMA natively has the smart functions, i.e., (1) sensor (thermal), (2) actuator (shape memory deformation) and (3) memory and shape recovery (processor functions). These unique properties inherent to SMA can be utilized to strengthen the composite. The design concept for enhancing the mechanical properties of the SMA composite is schematically shown in Fig. 2. TiNi fibers are heat-treated to shape-memorize their initial length at higher temperatures (>Af), then quenched to room temperature (to almost martensite start temperature =Ms), subjected to tensile prestrain

eT (>0) and embedded in the matrix material to form a composite. The composite is then heated to the temperature (>Af) at which the TiNi fibers tend to shrink back to their initial length by the amount of prestrain eT, and then the matrix is subjected to compressive stress. It is this compressive stress in the matrix that contributes to the enhancement of the tensile properties of the composite and fracture toughness.

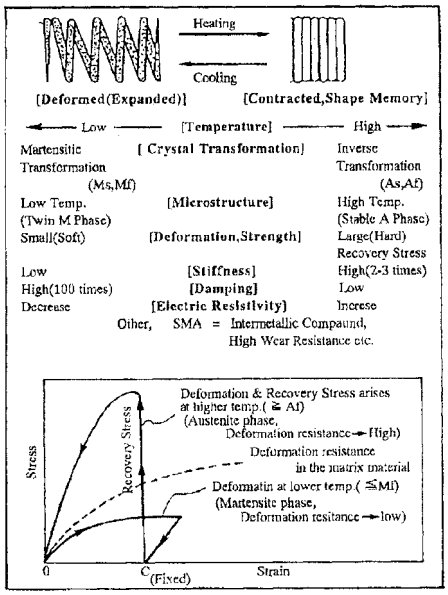

Figure 1 Material properties of shape memory alloy with increasing temperature

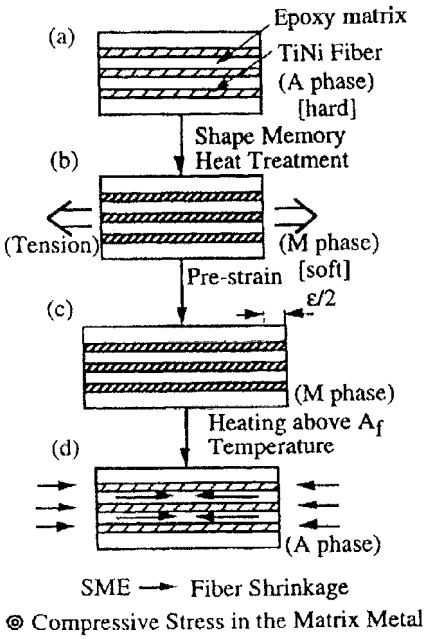

Figure. 2 Design concept of SMA smart composite.

3. Experiment

3.1 Test specimen

Experimental processing, mechanical testing of TiNi/epoxy composite is described. The shape memorized TiNi fibers (Ti-50.2at%Ni) of 0.4mm diameter supplied by Kantoc Ltd, Fujisawa, Japan are arranged a mold in which photoelastic epoxy and a specified amount of hardener were poured and then kept at 130°C for 2 hours for curing. The TiNi fibers were first annealed for 30min at 500°C,then quenched in icewater. Four transformation temperatures of TiNi fiber were determined: martensitic start Ms = 31°C,martensite finish Mf = 15°C, austenitic start As = 57°C, and austenitic finish Af = 63°C from the relationship between strain vs. temperature at a constant stress of 94MPa.

The photoelastic sensitivity constant of this epoxy resin matrix was α =0.116 mm/N. After curing, the as-molded composite was cooled to room temperature. During the process, TiNi fibers were kept in tension with four different prestrains of 0, 1, 3 and 5%. A center
notch which had different angle (θ) and length (a) in the care of each specimen was then cut into the as molded composite specimen using spark cutting and a thin knife edge. In the case of the specimen with angled crack, θ =90° (i.e. mode I)four different crack lengths, a=3.8, 5.0, 7.0 and 8.8mm were introduced, on the other hand, in the case of θ =45 (i.e. mode II), "three affeunt each length, a=7.5, 8.8 and 12.2mm were introduced' in mixed mode test specimens for changing the domain size (D) between a crack-tip and a fiber. The geometries of the composite specimens and precrack lengths are shown in Fig. 3.

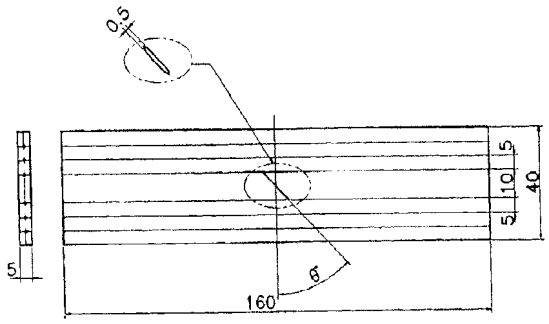

Angle (θ)	Length of crack (mm)
45°	7.5 8.8 12.2
90°	3.8 5.0 7.0 8.8

Figure 3 Geometry of TiNi/epoxy composite specimen with a center crack with θ

3.2 K-value determination

The composite specimens were loaded by a Tensilon/RTM-1T machine in which a constant temperature controllable furnace and photoelastic analysis apparatus were combined. A constant load of P=1078N was applied to the TiNi/epoxy specimen with an angled crack θ =90° , on the other hand, P=1274N at θ =45° for the controlled tensile test machine to form the third or fourth photoelastic fringe pattern. The changes of the number of fringe pattern lines developed around the notch tip was measured at different constant temperatures of 20, 30, 40, 50, 60, 70, 80, 90 and 100°C through the plane glass window fixed on the wall of the electric heating furnace. The photographs of the changes of fringe patterns around a crack tip with increasing temperature were continuously taken by a camera, and then, stress intensity factor K_I and K_{II} were

calculated from the following formula K_I of mode I (tensile type) by Irwin's method, and K_{II} of mixed-mode by Smith's method.

$$K_I = \frac{n\sqrt{2\pi r_m}}{\alpha t \sin\theta_m}\left[1+\left(\frac{2}{3\tan\theta_m}\right)^2\right]^{-0.5} \times \left[1+\frac{2\tan(3\theta_m/2)}{3\tan\theta_m}\right] \qquad \textit{Eqn (1)}$$

$$\left.\begin{aligned} K_I &= \frac{N_m(2\pi r_m)^{1/2}}{\alpha t\left\{\sin\theta_m + 2A\cos\theta_m + A^2\sin^2\theta_m\right\}^{1/2}} \\ K_{II} &= \frac{AN_m(2\pi r_m)^{1/2}}{\alpha t\left\{\sin\theta_m + 2A\cos\theta_m + A^2\sin^2\theta_m\right\}^{1/2}} \end{aligned}\right\} \qquad \textit{Eqn (2)}$$

where

$$A = \frac{K_{II}}{K_I} = \frac{2}{3}\left(\cot 2\theta \pm \sqrt{\cot^2\theta_m + \frac{3}{4}}\right)$$

n is the number of the fringe, t is the composite plate thickness, α is the epoxy photoelasticity sensitivity constant, r and θ_m are, respectively, the distance and angle in polar coordinates at point M, shown schematically in Fig. 4.

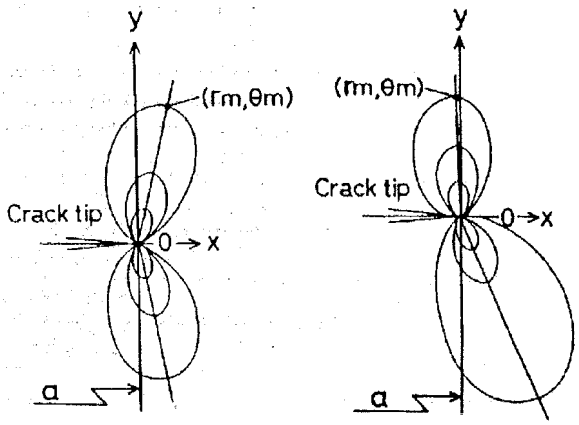

Figure 4 Photoelastic fringe pattern schematically developed aroud a crack (size: a) in the pole figure. (mode I and mixed mode II)

4. Results and discussion

The experimental results of the photoelastic fringe patterns are shown in Fig.5 for the TiNi/epoxy specimen with angled crack $\theta = 45°$ at P = 1274N in. Fig. 5(a), and angled crack $\theta = 90°$ at P = 1078N in Fig.5(b) respectively. It should be noted from Fig 5(a) and (b) that the photoelastic fringes decrease abruptly with the increasing temperature, especially, above Af(=63°C) temperature.

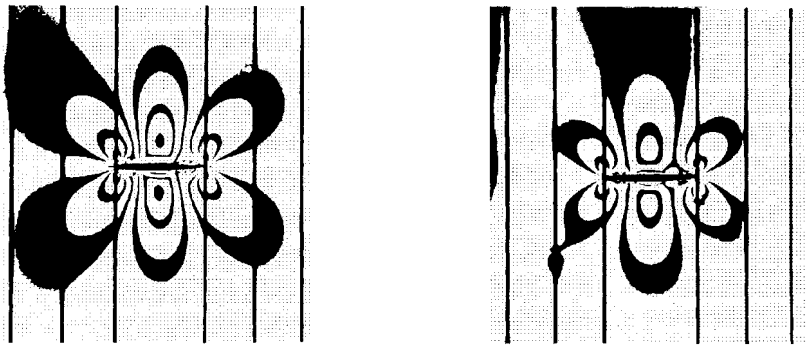

Prestrain ε t = 0%, ε t = 5%

(a) $\theta = 90°$

(b)

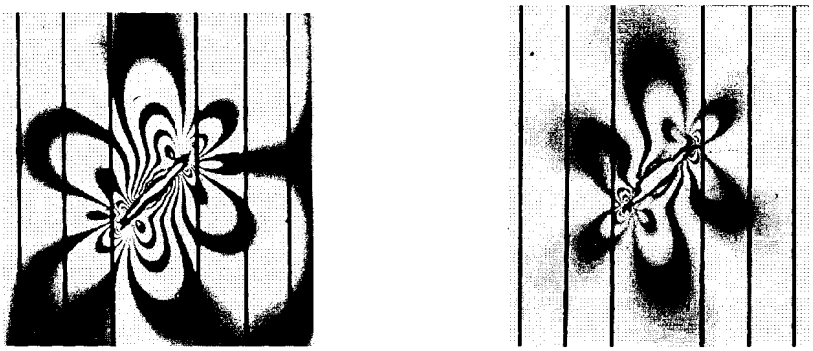

Prestrain ε t = 0%, ε t = 5%

(c) $\theta = 45°$

Figure 5 Photoelastic fringe pattern around a center crack in the TiNi/epoxy specimen

Considering the active control of the stress intensity at the crack tip, as an example, the dependencies of K_I value on environmental temperature (T) at the crack length of 8.8mm in the specimen with θ =90° are shown in Fig. 6.

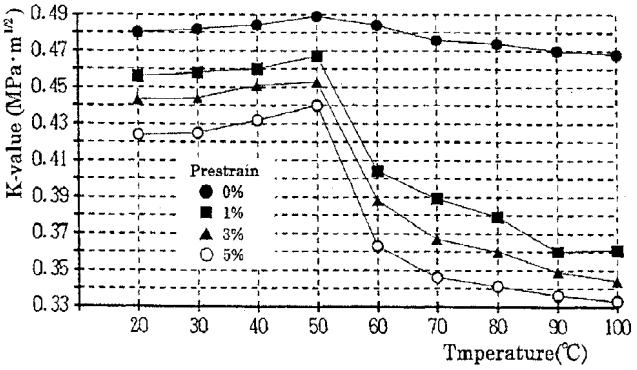

Figure 6 Stress intensity factor K_I-value as a functions of temperature under three different prestrains in the case of a specimen with crack length a=8.8mm and angle

The K_I value of the specimen with $\theta = 90°$ .prestrained TiNi fibers decreases clearly above 50~60°C, where the decreasing rate of the K_I value depends on the prestrain value. Although the initial absolute K value differs by inevitable effect induced by the initially introduced of residual stresses in the matrix during the fabrication process of the TiNi/epoxy composite. The decrease of the K value is scarcely recognized in the case of prestrain=0, but, the drop of K value increases as the pretensile strain of the TiNi fiber increases. These facts surely suggest that the shape memory effect of the embedded TiNi fibers can effectively reduce the stress concentration with increasing prestrain value.

The experimental result of the reduction in mode I stress intensity factor, K_I, at 80 °C(> Af) is plotted versus the prestrained values ε t= 0, 1, 3 and 5%, for several crack lengths in Fig. 7(a) and similarly shown for mode II, K_{II}, in Fig. 7(b) in the test specimen with angled crack of $\theta = 45°$ .The stress intensity factor ratio, K value ratio,
plotted along the Y axis indicates the normalized value of K which can be calculated from dividing the absolute K value in a certain prestrained specimen by the K value of a zero prestrained specimen. It should be noted that all the K values decrease with increase of the prestrain value, and these decrease rate(Δ K) becomes much more high depending on crack length(a). For instance, in the case of the specimen with a 5% prestrain and $\theta = 45°$ crack, the percentage of decrease in the case of shape memory effect are ΔK_I = 36%, ΔK_{II} = 21.4% at a = 7.5mm, ΔK_I = 45.4%, ΔK_{II} = 46% at a= 8.8mm, and ΔK_I = 48.7%, ΔK_{II} = 58.2% at a = 12.2mm. The same trend can be recognized in the case of single mode K_I in the specimen with angled crack $\theta = 90°$ as shown in Fig. 7(c), i.e., the decrease range, ΔK_I= 27.6% at a = 3.8mm, ΔKI = 29.5% at a = 5mm, ΔK_I = 30.7% at a= 7mm and ΔK_I = 82.8% at a = 8.8mm. These experimentally results with decreasing dependencies of K value (ΔK) on the crack length(a) suggest that the decrease of K seems to become most intense as the domain size between the crack tip

and fiber surface in front of a crack. The same trend of the dependence of the drop of the K value on the domain size was previously discussed by the authors using Eshelby's equivalent inclusion method. As for the relationship between the K ratio and prestrain value, the analytical model explains the same trend as the experimental results, i.e., K value decreases with an increase in prestrain, however, the predictions are apt to show larger values than those of the experiment.

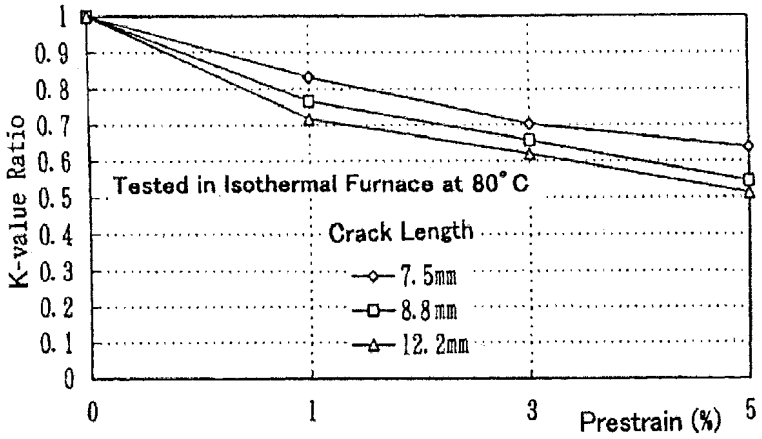

(a) mode K_I for $\theta = 45^\circ$

Figure 7(a) Normalized stress intensity factor K-value ratio vs. prestrain for different crack lengths

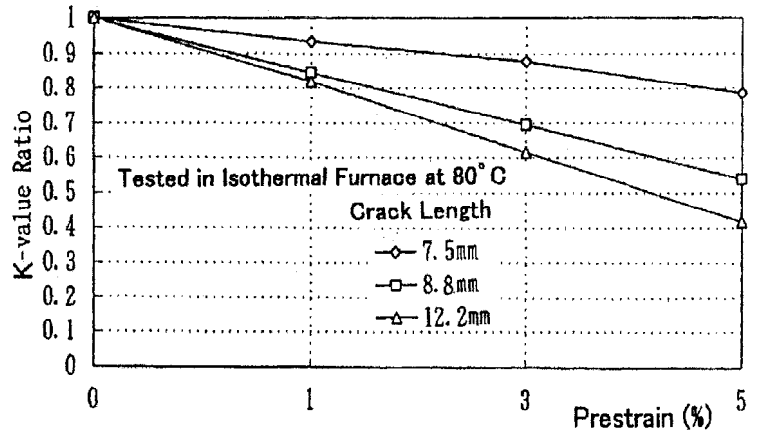

(b) mode K_{II} for $\theta = 45^\circ$

Figure 7(b) Normalized stress intensity factor K-value ratio vs. prestrain in different crack lengths:

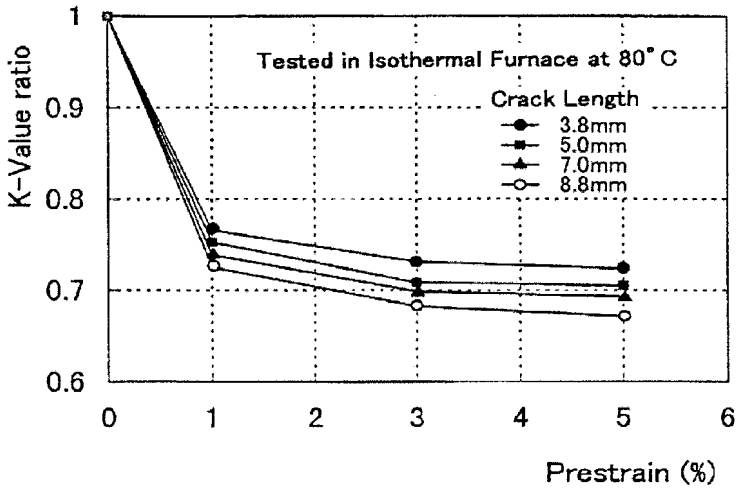

(c) mode K_I for $\theta = 90^\circ$

Figure 7(c) Normalized stress intensity factor K-value ratio vs. prestrain for different crack lengths

From the experimental evidence obtained in this study, our proposed "new material system for active failure prevention by using a SMA composite" is a promising concept for active control of material degradation (i.e. damage accumulation, crack formation, delamination etc.) in service time and for the elongation of failure life of the material components in the near future. Furthermore, the development of an artificial system for prevention of sudden failure of machinery and structures is also an important and attractive research subject for the creation of a new design concept of intelligent/smart material systems and structures.

4. Conclusion

Following the previous study on active suppression of crack tip stress concentration and the increase of fracture toughness (K value) using shape memory strengthening in a shape memory TiNi fiber reinforced /epoxy matrix composite (SMA-FEC), in the present paper, the control of crack-tip stress concentration and the fracture toughness (K value) under mixed mode stresses, K_I and K_{II} mode, are investigated. The test specimens have two types of anglednotches in the transverse direction of the tensile-type specimen. i.e. θ =45° ,90° with several crack lengths. The stress intensity at the notch tip is experimentally determined by photoelastic fringes. The decrease of the K_{II} value in the mixed mode was also experimentally confirmed similarly as in the case of the former mode I type (K_I) specimen when the prestrained TiNi fibers contract to the initial length upon heating above the austenitic finish temperature of the TiNi fiber (T > Af).

The dependencies of K value on the prestrain value of TiNi fibers and crack length (i.e., the compressive stress domain size between a cracktip and fiber) are recognized as previously predicted by the authors.

6. References

1. C.A.Rogers, C,Liang and S.Lee(1991) : Active damage control of hybrid material systems using induced strain actuator: Proc.AIAA/ASME /ASCE/AFS/ASC 32nd Structure, Structure Dynamics and Materials Conference (AIAA, Washington, 1991, Part II) 1190-1203
2. Y.Furuya, A. Sasaki and M.Taya, (1993) “Enhanced Mechanical Properties of TiNi Shape Memory Fiber/Al Matrix Composite”,Mater.Trans. JIM,Vol. 34(3), 224-227
3. A. Shimamoto and M.Taya (1997) “Reduction in KI by shape memory effect in a TiNi shape memory fiber reinforced epoxy matrix composite” J. JSME, 63-605-A(1997-1),26-31
4. A. Shimamoto, Y.Furuya and M.Taya (1997) : “Active control of crack-tip stress intensity by contraction of shape memory TiNi fibers embedded in epoxy matrix composite: Dependency of stress intensity factor on crack-tip domain size”,Proc.ICCM-11(Gold-coast,Australia,July,1997), Vol. 5,493-499.
5. S.Takahashi and S.Nagata(1986) : Science of machine(in Japanese), 38-1,82-86

HIGH RATE SHEAR INDUCED FAILURE IN SOLIDS

J.F. KALTHOFF
Experimental Mechanics
Ruhr- University Bochum
44780 Bochum, Germany

1. Introduction

The fracture mechanics methodology in principle applies to all three modes of loading: tension, in-plane shear, and out-of-plane shear, or to combinations of them. In practice, however, as regards standards for measuring material properties and/or applications to estimate the safety or failure probability of structures, tensile (mode-I) loading situations are mostly considered. In-plane shear (mode-II) loading is subject of fundamental analyses in most cases only [1,2]. Cracks or crack-like defects in impacted structures, on the other hand, are loaded by waves that are initiated by the impact event and to a large extent experience transient in-plane shear (mode-II) and mixed mode-II/mode-I loading situations. These types of loading, therefore, represent loading conditions of both practical relevance and dominating importance when high rate phenomena are of interest. This paper reports on the failure behaviour of different types of solids exposed to impact shear loading of different rates.

2. Dynamic High Rate Shear Loading of Cracks

2.1 LOADING TECHNIQUE

Waves initiated by an impact event in a solid are used to load existing cracks in the solid by almost pure in-plane shear (mode-II) conditions of loading. On this basis the author introduced the method of loading edge cracks by edge impact (LECEI) [3,4], its principle is shown in Fig. 1: A specimen with two parallel edge cracks or edge notches is considered. In the following text the term "crack" will be used in a general sense for a naturally sharp fatigue crack or a notch (saw cut) of finite bluntness at the notch tip. The specimen is impacted by a projectile having a diameter d equal to the distance h of the two cracks. The impinging projectile initiates a compressive wave in the middle part of the specimen, the rest of the specimen, in particular those parts on the other

A. Lagarde (ed.),
IUTAM Symposium on Advanced Optical Methods and Applications in Solid Mechanics, 531–546.

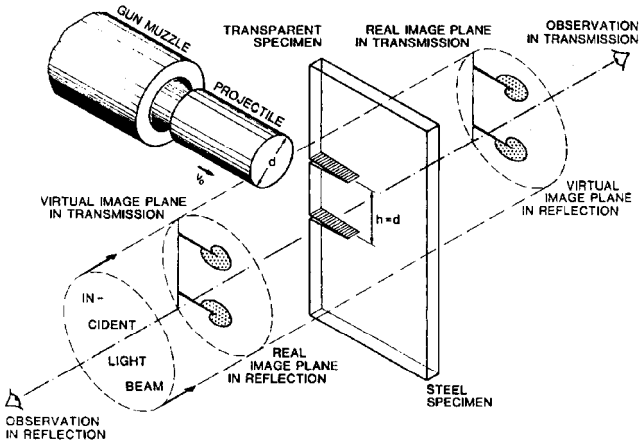

Figure 1. Principle of the technique of loading edge cracks by edge impact (LECEI) and shadow optical observation modes (schematically).

side of the crack, are stress free. The displacements associated with this stress wave field generate a mode-II loading situation at the crack tips. The sign of loading is different for the two cracks. The mode-II loading conditions will develop for the early time range of the impact event only, i.e. before waves that are reflected at the finite boundaries of the specimen will interfere with the crack tip again. This is also the range of interest for high rate failure investigations. The specimen is not held in a special loading fixture, it is loosely positioned on a table which is adjustable in order to allow for a correct alignment of the specimen perpendicular to the direction of the impinging projectile. The projectile is accelerated by an air gun with its muzzle directly in front of the specimen.

2.2 DETERMINATION OF STRESS INTENSIFICATION HISTORY BY CAUSTICS

The shadow optical method of caustics in combination with high speed photography is used to determine the resulting stress intensification history. The cracked specimen which may be transparent or opaque is illuminated by a collimated parallel light beam. Because of the stress concentrations at the tip of the crack, changes in the refractive index of the material and/or deformations of the surface of the specimens near the tip of the crack result. Because of these effects, the light rays are deflected from their original direction and thus form characteristic light intensity patterns in image planes at certain distances from the specimen plane. Looking in the direction of observation of the light intensity patterns these so called shadow planes or reference planes are real or virtual when located behind of (positive reference distance) or before (negative reference distance) the specimen (see Fig. 1). The caustic registration mode is considered positive/negative when the observation direction is identical/opposite to the

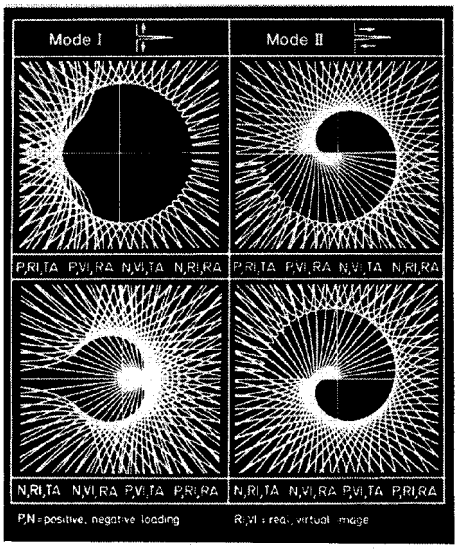

Figure 2. Shadow optical light intensity patterns and caustics.

direction of the illuminating light beam. Furthermore, tensile loading is considered positive and compressive loading negative (with the latter being applicable to notches only that allow for compressive stress concentration to be built up). Computer generated shadow optical light intensity patterns are shown in Fig. 2 for mode-I and mode-II cases of loading. For the patterns in the upper row of the figure the sign of the product of the signs of caustic registration mode, reference distance, and loading is negative and for the patterns in the lower row it is positive. Distinct shadow areas of darkness are obtained which are surrounded by areas of light concentration (high density of the bright lines in Fig. 2). The two areas are separated by sharply bounded curves, the caustics. For mixed mode-I/mode-II loading conditions the shape of the shadow patterns change continuously from the shape of the one to the other pure loading case. Size and shape of the shadow patterns are quantitatively correlated with the stress intensity factors. For pure mode-I or mode-II loading situations the size of the shadow patterns, e.g. the diameter of the caustic in a particular direction, determines the magnitude of the stress intensity factor K_I or K_{II}; for mixed mode loading conditions two size parameters of the caustics, e.g. the diameters of two branches of the caustic determine both stress intensity factors, K_I and K_{II}. The shadow patterns are experimentally recorded with regular cameras photographing the specimen in a controlled defocused manner. In the dynamic events under consideration high speed cameras are needed to register the shadowgraphs at successive times. A detailed description of the physical principles of the caustic method, quantitative evaluation formulas, and practical applications for determining stress intensity factors are given in [5].

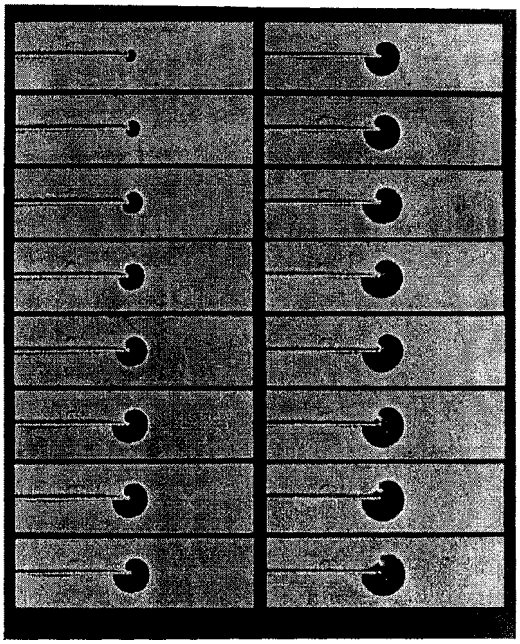

Figure 3. High speed series of shadow photographs of the stress intensification history at the lower notch in a typical LECEI-test (PMMA, picture interval time 2 μs).

The stress intensification history of edge impacted edge cracks has been monitored by means of the shadow optical method of caustics. Figure 3 shows a series of high speed shadowgraphs photographed with a specimen made from the transparent model material PMMA (Polymethylmethacrylat). The caustics were observed in a virtual shadow plane located ahead of the specimen (when looking in observation direction). Only the upper of the two cracks is shown, the picture interval time in this series of photographs is 2μs. A comparison of the observed caustics with the theoretically predicted curves (see Fig. 2) indeed indicates an almost undisturbed mode-II loading. A more detailed consideration reveals some influence of a superimposed mode-I loading for the very beginning of the impact event, which is due to lateral deformations associated with the compressive stress wave generated by the impact event. For later times, however, the mode-II loading is dominating and the superimposed mode-I loading becomes negligible. Deviations of the shadow pattern for pure mode-II loading in the last frames are indications that instability has taken place and that failure is developing.

Quantitative data have been determined with specimens made of the epoxy resin Araldite B and the high strength maraging steel X2 NiCoMo 18 9 5. These two materials are well suited for quantitative shadow optical investigations because of their

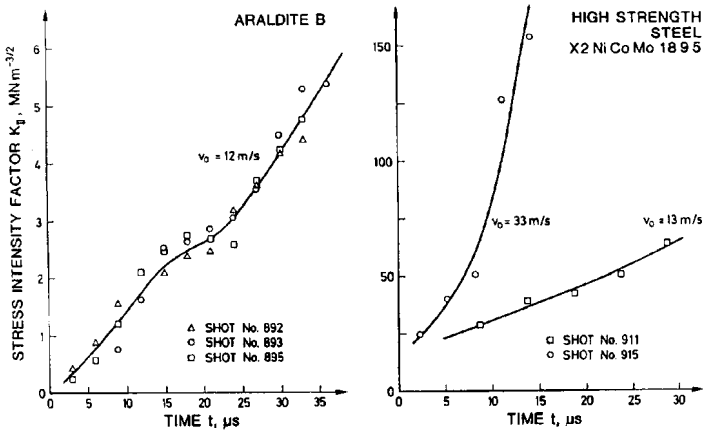

Figure 4. In-plane shear (mode-II) stress intensity factor histories observed in LECEI-tests.

well defined almost ideal linear-elastic behaviour. Results are shown in Fig. 4 for impact velocities of 12 m/s or 13 and 33 m/s respectively. The maximum crack tip stress intensification rates K_{II} are about 2 x 10^5 MN m$^{-3/2}$ s^{-1} for Araldite B and 2 x 10^7 MN m$^{-3/2}$s^{-1} for steel. These stress intensification rates are extremely high; they are of the same order or even higher than those obtained with Hopkinson's bars.

In summary, the technique of loading edge cracks by edge impact (LECEI) represents a rather simple experimental method to apply high rates of local shear (mode-II) loading using only modest impact velocities. The loading is of almost pure mode-II type. Extremely high loading rates are achievable that result in failure after very short loading times of a few microseconds only. The LECEI-technique in the meantime has been adopted by several researchers [6-9] for their investigations.

3. High Rate Shear Failure Behaviour of Materials

The technique of loading edge cracks by edge impact (LECEI) has been used to investigate the dynamic shear induced failure of three types of materials: an epoxy resin, a high strength steel, and an aluminum alloy. Specimens of about the same sizes were used throughout the investigations. The typical specimen dimensions were: height 150 to 200 mm, width 100 to 150 mm, thickness 9 to 20 mm. The length of the cracks was about half the width of the specimen; the two cracks were 50 mm apart corresponding to a projectile diameter of 50 mm. In several cases, however, instead of original LECEI-specimens with two cracks modified specimens with one crack only were used. The projectiles used in the tests were typically of the same type of material as the specimen to be investigated.

3.1. FAILURE CHARACTERISTICS OF STEEL

The high strength maraging steel X2 NiCoMo 18 9 5 has been used for these investigations [3,4]. This steel with its very high yield strength of about 2.1 GPa has not only been chosen because of suitability for shadow optical investigations (see Chapter 2.2), but also because of its suitability for a description by means of the concept of linear-elastic or small scale yielding fracture mechanics.

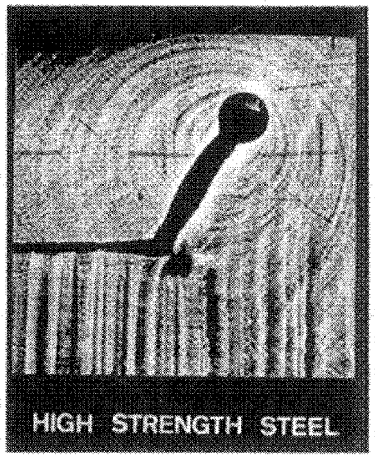

Figure 5. Shadow photograph of the failure phase a short time after instability in a low rate LECEI-experiment with steel.

In a first series of experiments specimens that did not contain sharp cracks but notches with a fixed bluntness at the tip were used. The notch tip radii were in the range from 0.75 to 0.85 mm. Tests were performed at increasing impact velocities. Very distinct differences in the failure behaviour were observed in low and high rate experiments. At low impact velocities, typically around 30 m/s, a behaviour as expected from usual fracture mechanics considerations is obtained, i.e. a tensile crack propagating at an angle of about 70° and a fracture surface with the typical indications of roughness and shear lips: Figure 5 shows a shadow optical picture photographed a few microseconds after instability in a low rate experiment. The obtained photograph shows an undisturbed tensile mode-I caustic at the tip of the initiated kinked crack. Furthermore, the photograph shows that the crack propagates in a direction of about 70° with respect to the ligament, i.e. a direction for which maximum tensile stresses result for the crack tip stress field. The observed crack propagation angle is further experimental evidence that indeed pure mode-II loading conditions prevailed at the starter notch, thus verifying the results of the shadow optical investigations on the LECEI-technique presented in the previous Chapter. In addition to the crack tip shadow spot, the shadowgraph also shows waves that emanate from the tip of the propagating crack.

These are Rayleigh waves causing deformations at the specimen surface that also produce a shadow optical effect. Similarly, the straight patterns observed in the lower part of the photograph visualize the compressive wave initiated by the impinging projectile. Figure 6 on its left side (low rate behaviour) gives further indications on the failure appearance. Figure 6a shows the direction of the failure path in a schematic representation. The crack propagates completely through the specimen separating the

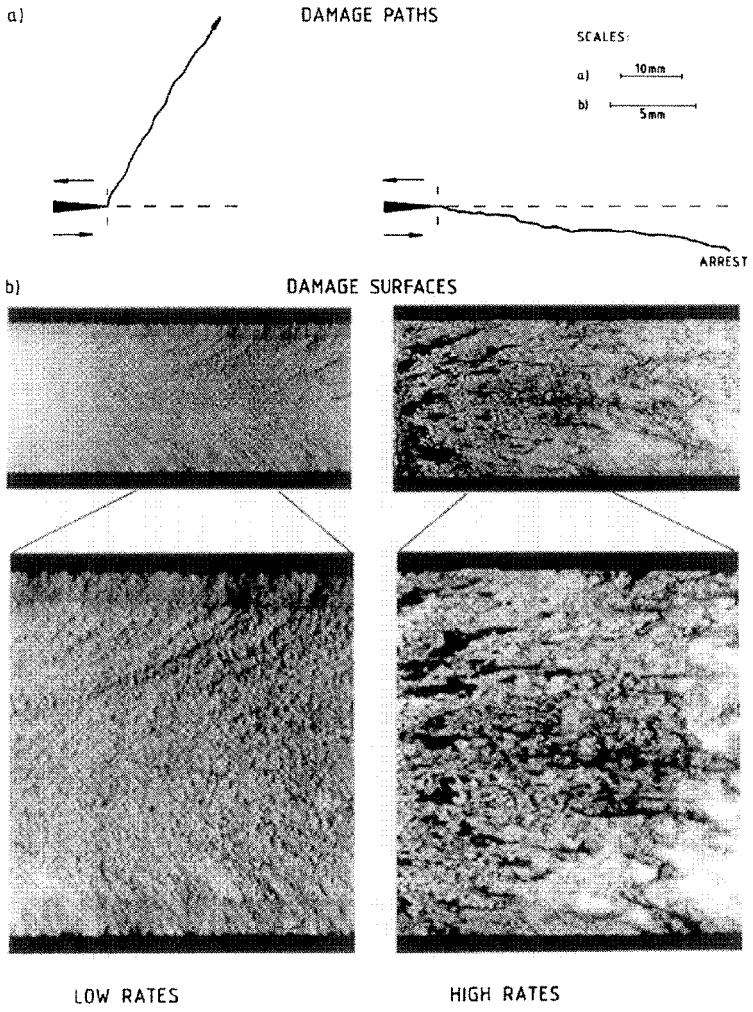

Figure 6. Failure behaviour observed in steel at low and high rates of mode-II loading, steel: X2 NiCoMo 18 9 5.

specimen into two halves. Photographs of the failure surface are given in Fig. 6b. These photographs show the typical characteristics of a usual fracture surface: roughness as it is usual for this steel and shear lips at the edges of the specimen.

Impact experiments performed at higher loading rates, typically around 70 m/s, result in a completely different failure behaviour. The results are presented on the right side of Fig. 6 (high rate behaviour). The failure path as well as the failure surface are shown in comparison to the equivalent results obtained at lower loading rates. The failure at high rates (Fig. 6a, right) develops in a direction that is almost identical to the direction of the initial starter notch, a 70° propagation angle is not observed anymore. Furthermore, the failure is arrested after a certain length, whereas complete failure of the specimen was observed in the low rate experiment. In addition, the appearance of the failure surface (Fig. 6b, right) is very different: Large smeared-over-regions that have a shiny, mirror-like appearance result, and, furthermore, there are no indications of any shear lips: The failure surface extends straight across the entire cross section of the specimen up to the very edge of the specimen. Obviously this failure at high loading rates does not represent a separation of material caused by a tensile crack, but a sliding of material due to the formation of an adiabatic shear band.

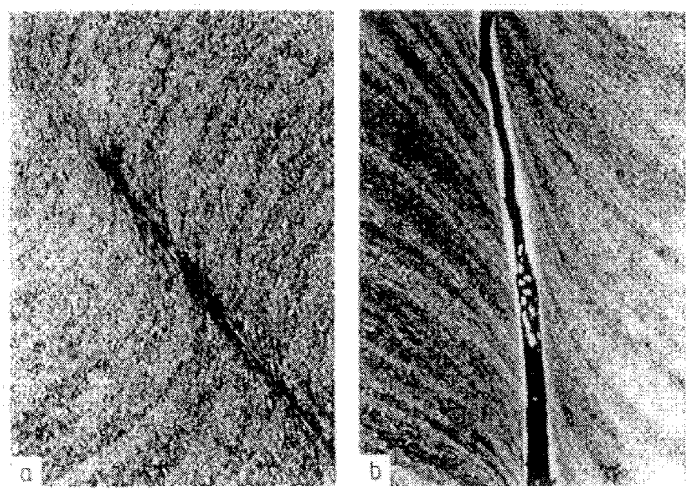

Figure 7. Micrographs of shear bands; a) deformed band, steel: X2 NiCoMo 18 9 5, b) transformed band, steel: 42 CrMo 4.

Metallographic micrographs of cuts through the specimen perpendicular to the failure surface are presented in Fig. 7 for the steel X2 NiCoMo 18 9 5 and also for the steel 42 CrMo 4, that was additionally investigated. Heavily sheared localized bands are visible. The shear band photographed with the steel X2 NiCoMo 18 9 5 shows a continuously increasing concentration of shear deformation towards the central region

of the shear zone. With the steel 42 CrMo 4 a wide edging band is visible indicating that a phase transformation has taken place with this material in the central region of the shear band. In particular the wide edging band is associated with a strong increase of hardness compared to the base material. The highly deformed (or also transformed) central zone of the shear band after having been formed obviously failed subsequently by a fracture process, as it is clearly indicated by Fig. 7b. Details of the formation of shear bands due to adiabatic conditions and softening processes that control this damage process shall not be discussed here (for details see e.g. [10,11]).

In addition to the reported LECEI-tests with notches of fixed notch tip radius, tests were performed with notches of other acuity. In these series of experiments, the notch tip radii were varied down to those of fatigue sharpened cracks. In particular interim notch tip bluntnesses corresponding to notch tip radii of about 0.3 mm were used. Data on the various test parameters applied and the observations made on the failure behaviour are summarized in Table 1. The observed damage paths are graphically shown in Fig. 8. The data show a dependence of the critical impact velocity for failure mode transition. The sharper the notch the lower the critical velocity: Whereas

TABLE 1. Test parameters and failure data of LECEI-tests with specimens of the steel X2 NiCoMo 18 9 5. (NOD = no damage, TFD = tensile fracture damage, SBD = shear band damage).

SHOT	B, mm	ρ, mm	v_0, m/s	DAMAGE MODE	a, mm	$v_0/\sqrt{\rho}$, $10^3\sqrt{m}$ / s
908	8.2	0.75	12.0	NOD		0.44
909	8.2	0.75	12.7	NOD	0	0.46
910	8.9	0.75	12.9	NOD	0	0.47
911	8.9	0.75	12.8	NOD	0	0.47
912	8.9	0.75	32.5	TFD	CF	1.19
913	9.3	0	19.8	SBD	4	1.42
914	9.3	0	31.9	SBD	30	2.29
915	8.4	0.25	32.5	SBD	17	2.06
916	7.9	0	31.7	SBD	26	2.27
918	9.4	0	32.0	SBD	20	2.29
919	8.6	0	30.3	SBD	20	2.17
920	8.8	0.35	32.4	SBD	12.5	1.73
921	8.5	0.35	50.7	SBD	37	2.71
955	18.8	0.85	39.3	SBD	0.5	1.35
955	18.8	0.85	39.3	TFD	CF	1.35
956	19.0	0.85	71.8	SBD	47	2.46
959	18.8	0.85	27.3	TFD	CF	0.94
960	19.0	0.30	29.8	SBD	5	1.72
961	19.0	0.30	38.2	SBD	31	2.21
962	19.4	0.35	22.4	TFD	CF	1.20
964	19.0	0	54.3	SBD	CF	3.89
965	19.0	0	32.1	SBD	31.5	2.30

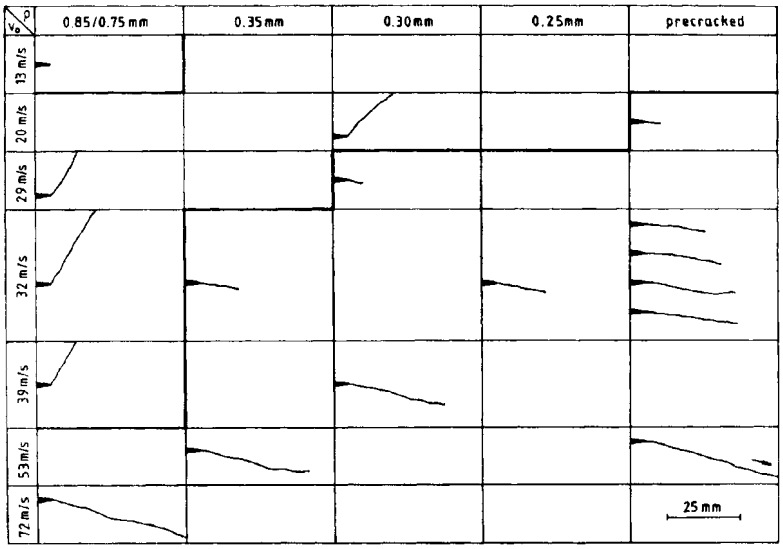

Figure 8. Damage paths observed in steel for different notch tip bluntnesses and impactor velocities.

failure mode transition takes place for $\rho = 0.8$ mm at a velocity between 39 m/s to 72 m/s, a value between 20 m/s and 29 m/s results for a notch tip radius of $\rho = 0.3$ mm, and a velocity of below 20 m/s results for precracked starter notches. In Fig. 8 only the beginning of the failure paths is shown. When failure occurs by tensile cracks, the cracks in all cases propagate completely through the specimen, dividing the specimen into two halves. On the other hand, when failure occurs by adiabatic shear bands, the failure is limited in length and comes to arrest in most of the cases (only in one experiment the shear band propagated completely through the specimen dividing it into two halves). The failure length is the larger the larger the impact velocity.

The data can also be looked at from a different point of view: For the same impact velocity failure mode transition between tensile cracks and adiabatic shear bands takes place when the notch tip acuity is varied: whereas failure by tensile cracks results for blunted notches, failure by adiabatic shear bands results for sharp notches. The higher the impact velocity, the more is the critical notch tip acuity for failure mode transition shifted to larger bluntnesses. If one extrapolates this behaviour, one would speculate that extremely high impact velocities would be needed with specimens which do not contain notches at all - which is indeed the case.

Since the strain at the tip of the notch increases with the acuity of the notch (i.e. with decreasing values of the notch tip radius), and, furthermore, since the rate at which this notch tip strain builds up increases with the impact velocity, it is evident that the

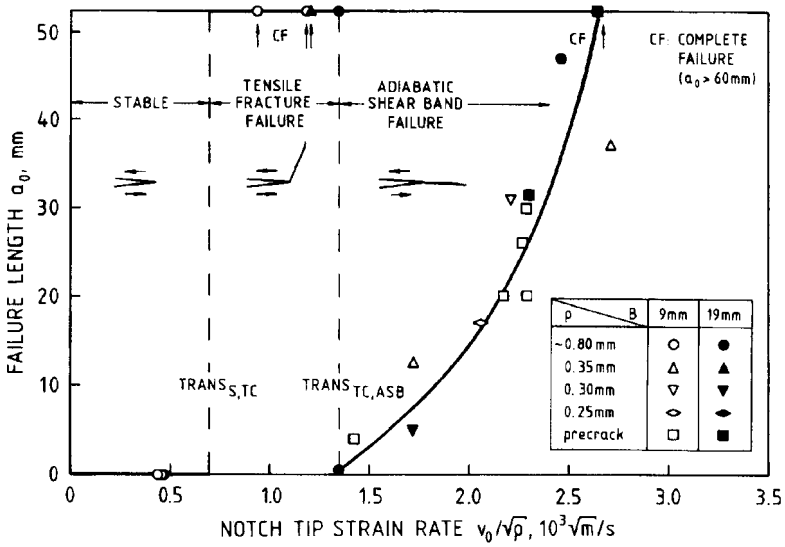

Figure 9. Modes of dynamic failure in steel for different rates of mode-II notch tip strain.

local strain rate at the tip of the notch is controlled by both parameters, the acuity and the impact velocity: The higher the acuity and the higher the impact velocity the higher the notch tip strain rate. Quantitatively the strain at the notch tip varies proportional to $1/\sqrt{\rho}$, where r is the notch tip radius. Furthermore, the rate at which the strain builds up, increases proportional to v_0, where v_0 is the impact velocity. Thus, the term $v_0/\sqrt{\rho}$ should be an appropriate quantitative measure of the notch tip strain rate. Values of the notch tip strain rate term $v_0/\sqrt{\rho}$ have been calculated and are given with the test parameters and failure observations of each experiment in Table 1. When fatigue sharpened starter notches were used an effective notch root radius of approximately the radius of the crack tip plastic zone (roughly 0.2 mm) was used. In Fig. 9 the observed failure is plotted as a function of the notch tip strain rate $v_0/\sqrt{\rho}$. The plot allows for a joint presentation of all the observed experimental findings in one diagram. In the diagram and the following text the subscripts S, TC, and ASB stand for "stable", "tensile crack", and "adiabatic shear band" respectively, and TRANS stands for "transition".

The following behaviour results:

- For notch tip strain rates $v_0/\sqrt{\rho} < \text{TRANS}_{S,TC}$ damage does not occur. The initial notches stay stable.
- In the interim regime of notch tip strain rates $\text{TRANS}_{S,TC} < v_0/\sqrt{\rho} < \text{TRANS}_{TC,ASB}$ failure occurs by tensile cracks that extend at an angle of about 70° with respect to the ligament, causing complete failure of the specimen. This failure behaviour is in accordance with fracture mechanics considerations.

- At notch tip strain rates $v_0 / \sqrt{\rho} = TRANS_{TC,ASB}$ failure mode transition takes place. For notch tip strain rates higher than $TR_{TC,ASB}$ failure occurs by localized shear bands. The adiabatic shear bands are limited in length and they extend in a direction which is almost identical with the direction of the original starter notch.

Despite of the very different test parameters utilized in the experiments (i.e. notch tip radii, impact velocities, specimen thicknesses) the failure mode transition from tensile cracks to adiabatic shear bands result for the same value of the notch tip strain rate and, furthermore, the observed lengths of the adiabatic shear bands follow the same curve, when the data are plotted as a function of the notch tip strain rate. This unique presentation of the results by means of the parameters ρ and v_0 in the suggested form as notch tip strain rate $v_0 / \sqrt{\rho}$ thus indicates that this term indeed represent the physical quantity that controls the processes. The unique presentation of all the data in one plot also shows: The damage length of shear band failure for notch tip strain rates $v_0 / \sqrt{\rho} > TRANS_{TC,ASB}$ is limited and considerably shorter than of tensile crack failure for notch tip strain rates $v_0 / \sqrt{\rho} < TRANS_{TC,ASB}$; i.e., although more energy is brought into the specimen to activate failure by adiabatic shear bands the resulting length of the generated damage is shorter than for tensile crack failure activated at lower energy levels. It is concluded, therefore, that adiabatic shear bands require and absorb more energy for propagation than tensile cracks.

3.2. FAILURE CHARACTERISTICS OF EPOXY RESIN

LECEI-tests as performed with steel have been carried out with specimens made of the epoxy resin Araldite B. The notch tip radii were varied from $\rho = 1.0$ mm to naturally sharp pre-cracks, the impact velocities were varied from the lowest velocity achievable with the gas gun, i.e. about 10 m/s, to higher values.

Low rate experiments were performed with impact velocities in the range of about 9 m/s to 18 m/s. For all notch tip radii failure occurred by tensile cracks propagation at about 70° with respect to the ligament. The specimens after the test were separated into two halves. Figure 10 shows a shadowgraph of the failure phase a short time after instability. The essentials of this figure are similar to those of Fig. 5 recorded with a steel specimen in a low rate experiment and shall not be repeated here. Thus, in all low rate experiments with epoxy resin the observations are of the same kind as found in the low rate steel experiments.

High rate impact experiments with impact velocities above 18 m/s have been performed with Araldite B specimens too, but, in all these cases the experiments failed: Damage occurred directly at the contact area between the projectile and the specimen; this damage practically destroyed the specimen. Thus, any information on the existence of an eventual failure mode transition to adiabatic shear bands could not be obtained because any eventually necessary higher loading rates could not be achieved.

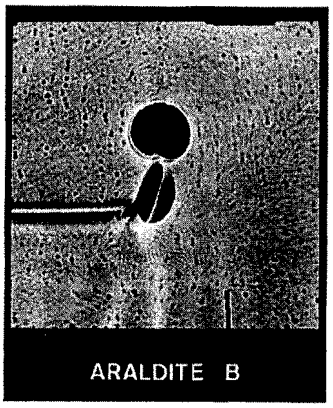

Figure 10. Shadow photograph of the failure phase a short time after instability in a LECEI-test with epoxy resin, Araldite B.

3.3. FAILURE CHARACTERISTICS OF ALUMINUM ALLOY

LECEI-tests similar as with steel have also been performed with the aluminum alloy A1 7075 [12]: Notches of relatively high acuity corresponding to an equivalent root radius of about 0.3 mm or fatigue sharpened cracks were used. Impact velocities up to about 70 m/s were applied. The regime of lower loading rates was extended down to even quasi-static loading conditions, i.e. loading times in the range of minutes. In these quasi-static tests the modified Arcan/Richard loading device [13,14] was used in combination with a universal tensile testing machine to load the specimen.

Typical high rate experiments, performed in the range of an impact velocity of 65 m/s result in failure of limited length that develops straight in the direction of the original starter notch. A failure surface is shown in Fig. 11b; it has a smeared over appearance, shear lips do not exist. Obviously, the findings are similar to those made with steels at high rates of loading, and it is speculated, therefore, that this failure is due to an adiabatic shear band process too.

In the low rate regime - even in the extreme case of quasi-static loading, that shall be considered for the moment - a behaviour is observed which is astonishable similar to the one observed at high rates. The failure is not arrested in this case, it develops completely through the specimen, but the failure extends straight in the direction of the original starter notch. Furthermore, the failure surface shown in Fig. 11a has a shiny, smeared over appearance which to a certain extent resembles that of the high rate experiment and shear lips do also not exist – similar as in the high rate experiments (compare with Fig. 11b). Failure by tensile cracks propagating at 70° with respect to the ligament showing the usual roughness of the failure surfaces and shear lips, as

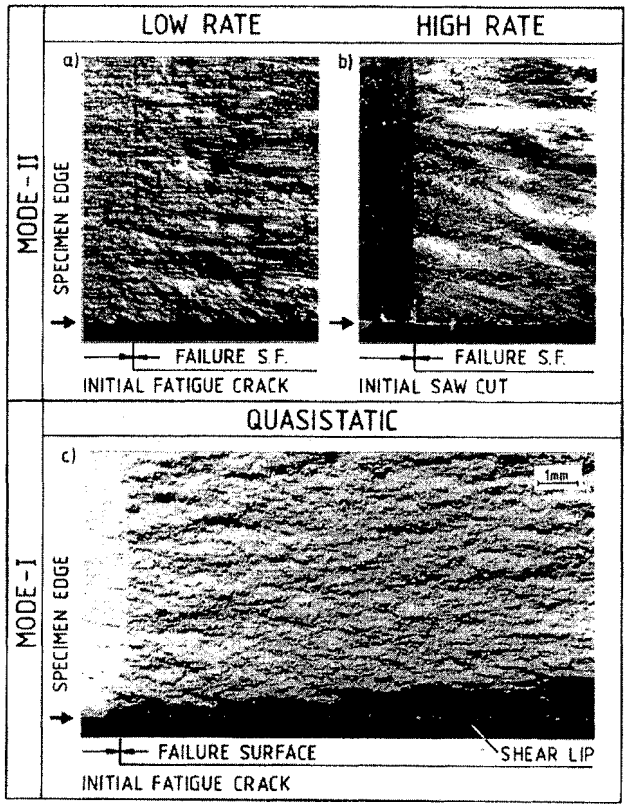

Figure 11. Failure surfaces in aluminum alloy (Al 7075) observed under mode-II loading of different rates: a) quasistatic loading with Arcan/Richard loading device, b) high rate loading with LECEI-test, $v_0 = 65$ m/s. In comparison c) failure surface observed under quasistatic mode-I conditions of loading. (SF = surface; same scale for all photographs).

expected from fracture mechanics considerations, are not observed. It is speculated therefore, that a shear band process controls failure in aluminum alloy also in the low rate or quasi-static regime, similar to adiabatic shear bands controlling failure in the high rate regime. For clarity it shall be mentioned that tensile cracks with the usual characteristic features of a fracture surface as mentioned above do exist for Al 7075, but such cracks are initiated when and only when mode-I loading conditions prevail. A fracture surface of such a tensile crack initiated under quasistatic mode-I loading is shown in Fig. 11c. Differences with respect to roughness of the failure surface and the existence of shear lips become evident by a comparison to the mode-II-initiated failure surfaces shown in Figs. 11a and b. Obviously under mode-II loading conditions such tensile crack failure processes extending in a non-straight direction as observed in steel

and in epoxy resin at low loading rates do not become activated in Al 7075 under any loading rate, even not under quasi-static conditions of loading. Straight failure propagation in aluminum alloy for mode-II loading conditions in quasistatic tests have also been reported by other investigators [15-17].

4. Summary

The principle of the technique of loading edge cracks by edge impact (LECEI) for generating high rates of crack tip shear (mode-II) loading is presented. The technique is used in conjunction with a gas gun for accelerating the impactor. The resulting shear (mode-II) stress intensification histories are monitored by means of the shadow optical method of caustics in combination with high speed photographic recording of the shadowgraphs. The LECEI-technique is used to study the high rate shear induced failure behaviour of three types of materials. The observations made for different levels of loading rates are summarized in Fig. 12. Epoxy resin (Araldite B) shows failure by tensile cracks up to the highest experimentally achievable loading rate. Steel (high strength maraging steel X2 NiCoMo 18 9 5) shows a failure mode transition: at low rates failure occurs by tensile cracks, at higher rates, above a certain limit velocity, failure by adiabatic shear bands is observed. Aluminum alloy (Al 7075) shows failure due to shear band processes in the high rate regime, but this failure mode is observed over the entire range of loading rates, even down to quasi-static conditions. Characteristics of the failure modes are presented. When transitions are observed in the failure process from tensile cracks to shear bands, the limit velocity for failure mode transition depends on the bluntness of the starter crack the failure is initiated from:

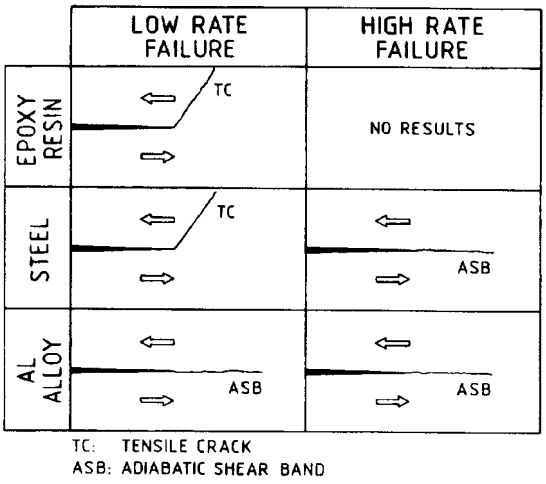

Figure 12. Modes of dynamic failure under mode-II conditions of loading observed with different materials for different loading rates.

The larger the bluntness of the starter crack the higher the critical limit velocity for failure mode transition. The data indicate that adiabatic shear bands require and absorb more energy for propagation than tensile cracks. Further work is needed and is on the way to specify the conditions that lead to shear induced failure by either tensile cracks or shear bands for different types of materials and different rates of loading.

6. References

1. ESIS 14, *Mixed Mode Fracture and Fatigue,* H-P. Rossmanith, H.A. Richard, Eds., European Structural Integrity Society, ESIS Publication 14, MEP (Inst. Mech. Engs.), London, 1993.
2. ASTM STP 1359, *Mixed-Mode Crack Behavior,* D.L. McDowell, K.J. Miller, Eds., American Society for Testing and Materials, West Conshohocken, PA, to appear.
3. J.F. Kalthoff, S. Winkler, Failure Mode Transition of High Rates of Shear Loading, Proc. Int. Conf. on *Impact Loading and Dynamic Behavior of Materials,* Eds. C.Y. Chiem, H.-D. Kunze, L.W. Meyer, Bremen, May 18-22, 1987, Deutsche Gesellschaft für Metallkunde, DGM-Verlag, Oberursel, 1988, 185-195.
4. J.F. Kalthoff, Transition in the Failure Behaviour of Dynamically Shear Loaded Cracks, Proc. *11th US National Congress of Applied Mechanics,* Ed. D.F. Chen, Tucson, Arizona, May 21-25, 1990 also *Appl. Mech. Rev.,* **43,** Part 2 (1990), 247-250.
5. J.F. Kalthoff, Shadow Optical Method of Caustics, Chapter 9 in *Handbook on Experimental Mechanics,* Ed. A.S. Kobayashi, Second Revised Edition, VCH Publishers, New York, 1993, 407-476.
6. J.J. Mason, A.J. Rosakis, G. Ravichandran, Full Field Measurements of the Dynamic Deformation Field Around a Growing Adiabatic Shear Band at the Tip of a Dynamically Loaded Crack or Notch, *J. Mech. Phys. Solids* **42** (1994), 1679 – 1697.
7. K. Ravi-Chandar, On the Failure Mode Transitions in Polycarbonate under Dynamic Mixed-Mode Loading, *Int. J. Solids Structures* **32** (1995), 925-938.
8. M. Zhou, G. Ravichandran, A.J. Rosakis, Dynamically Propagating Shear Bands in Impact Loaded Prenotched Plates, *J. Mech. Phys. Solids* **44** (1996), 981 and 1007.
9. R.C. Batra, N.Y. Nechitailo, Analysis of Fracture Modes in Impulsively Loaded Pre-Notched Steel Plates, *Int. J. Plasticity* **13** (1997), 291-308.
10. D.R. Curran, L. Seaman, D.A. Shockey, Dynamic Failure of Solids, *Physics Reports* **147** (1987), 253-388.
11. R. Dormeval, Adiabatic Shear Phenomena, Proc. Int. Conf. on *Impact Loading and Dynamic Behavior of Materials,* Eds. C.Y. Chiem, H.D. Kunze, L.W. Meyer, Bremen, May 18-22, 1987, Deutsche Gesellschaft für Metallkunde, DGM, 43-56.
12. J.F. Kalthoff, A. Bürgel, and W. Hiese, *Impact Failure Behaviour by Adiabatic Shear Bands,* Progress Reports to ONR Grant No. N 00014-89-J-1617, RUB EM 96/1, 97/2, Annual Year Report 1997.
13. L. Banks-Sills, M. Arcan, An Edge-Cracked Mode II Fracture Specimen, *Experimental Mechanics* **23** (1983), 257-261.
14. H.A. Richard, Eine Bruchmechanikprobe zur Bestimmung von K_{IIc}-Werten, *Schweiβen und Schneiden* **33** (1981), 606-608.
15. W. Hiese, J.F. Kalthoff, Determination of Valid Mode-II Fracture Toughnesses K_{IIc}, *Mixed-Mode Crack Behavior,* ASTM STP 1359, Atlanta, Georgia, May 6-7, 1998, D.L. McDowell, K.J. Miller, Eds., American Society for Testing and Materials, West Conshohocken, PA, paper accepted for publication.
16. H. Hallbäck, and F. Nilsson, Mixed-Mode I/II Fracture Behaviour of an Aluminium Alloy, *J. Mech. Phys. Solids* **42** (1994), 1345-1374.
17. R.A. Riddle, R.D. Streit, and I. Finnie, *The Failure of Aluminium Compact Shear Specimens Under Mixed-*Mode *Loading,* ASTM STP 945, American Society for Testing and Materials, Philadelphia, 1988, 118-133.
18. L. Banks-Sills, and D. Sherman, J_{II} Fracture Testing of a Plastically Deforming Material, *Int. Journal of Fracture* **50** (1991), 15-26.

DYNAMIC FAILURE INVESTIGATIONS IN POLYMERS

Z. ZHU AND K. RAVI-CHANDAR
Department of Mechanical Engineering
University of Houston
Houston. TX 77204-4792

1. Introduction

Photomechanics has played a significant role in investigations of dynamic fracture. Dynamic photoelasticity, the method of caustics, and the coherent gradient sensing methods have been used extensively to characterize the crack tip stress-state by many investigators, to numerous to list here. The main goal of the present manuscript is to demonstrate how dynamic photoelasticity is applied in the investigation of failure mode transition in polycarbonate. The asymmetrically loaded, edge-crack configuration is considered; the results of failure mode transition have been described in a previous publication (Ravi-Chandar, 1995). Upon impact loading, a dominant shear loading is generated near the crack tip; at small impact speeds a kinked opening mode crack is generated at an angle to the initial edge crack. However, at higher impact speeds, shear localization occurs along the initial crack line and the opening mode crack kink is not generated. The evolution of the crack tip stress field is the crucial factor in triggering this failure mode transition. We present some preliminary results aimed at evaluating the development of the crack tip stress field.

2. Experimental details

A single edge-notched specimen geometry shown in Figure 1 was used in evaluating the failure mode transitions in polycarbonate. The nominal plate thickness was 6.35 mm (¼ in), but the actual thickness was about 6 mm. A slit (300 μm wide 12.7 mm long) was machined in the specimen. A sharp crack was grown by fatigue from the slit by cyclic loading in a servohydraulic loading machine; by careful control of the load range and the cycling frequency, a fatigue crack with very little residual plastic deformation was obtained. Typically, the length of the fatigue crack was about 5 to 6 mm resulting in a final crack length of about 18 to 19 mm. A combined pressure and shear loading on the specimen is applied by impacting on one side of the crack using a projectile, moving with a speed V_p . The overall size of the specimen, usually $W = 100$ mm wide and $2H = 400$ mm tall, was determined so as to delay the arrival of the waves reflected from the far boundaries; thus for about the first 100 μs, the only loading on the specimen is due

A. Lagarde (ed.),
IUTAM Symposium on Advanced Optical Methods and Applications in Solid Mechanics, 547–554.

to the projectile impact; the length of the projectile was also tailored such that sustained loading occurs for 100 μs.

Impact loading is generated by launching a cylindrical polycarbonate projectile, (diameter 50 mm and length 100 mm), from a compressed air gun. Speeds in the range of 5 m/s to 100 m/s are possible, but in this series of experiments, we have used speeds of up to 40 m/s. Alignment of the projectile with the specimen is critical for appropriate interpretation of the experimental results. Proper alignment was ensured by placing the specimen very close to the exit of the barrel such that impact on the plate occurred just when the tail end of the projectile exited to barrel. Of course, this implies complications in projectile speed measurement system. In order to trigger the picture taking sequence of the high speed camera, a photodetector is used to sense the time of the projectile when it is 30 mm from the specimen; the picture taking is then initiated with a very precise delay so as to begin capturing pictures just prior to impact. Thus, combining the electronic trigger signal with the preset delay and the observation of the projectile in the high-speed photographs an accurate determination of the projectile speed is obtained. Once the projectile speed is known, a rough estimate of the particle speed in the specimen at the point of contact can be obtained by considering one dimensional wave propagation theory. Since both the specimen and the projectile are made of polycarbonate, the particle speed in the specimen, V_s can be written as

$$V_s = \frac{V_p}{1 + A_s / A_p}, \tag{1}$$

where A_s and A_p are cross sectional areas of the specimen and projectile respectively. For the particular projectile and specimen thickness used in this study, $V_s \sim 0.86 V_p$. The applied compressive stress is then approximately $\sigma \sim 0.86 \rho C_d V_p$, where ρ is the density of the specimen, and C_d is the dilatational wave speed. For polycarbonate, ρ = 1200 kg/m^3 and $C_d \sim$ 1750 m/s; thus as the impact speed varies in the range from 5 m/s to 50 m/s, the compressive stress at the impact face increases from 9 MPa to 90 MPa. However, the actual stress field is initially a biaxial compression and even at the highest projectile speed, plastic deformation was not observed either in the specimens or in the projectile.

The dynamic failure resulting from the impact loading on the specimens were recorded on film using a high-speed camera at a rate of 100,000 frames per second. The high-speed camera used was a continuous access rotating mirror camera. At a rate of 100,000 fps, the camera is capable of monitoring the evolution of the dynamic event for about 1.4 ms, although in most cases, only the first hundred microseconds are of interest. The rotating mirror places a limiting aperture in the optical system; as a result, a pseudoschlieren effect is observed in the high speed photographs and regions close to the crack tip (typically within about 3 to 5 mm, but larger in some cases) cannot be observed

Dynamic photoelasticity has been a standard technique for investigation of the crack tip stress field for a number of years. Here we present only a brief description in order to facilitate interpretation of the experimental results. The specimen is placed between two circular polarizers in a bright-field arrangement. The lines of constant light

intensity are contours of constant shear stress and are the isochromatics corresponding to the following expression

$$(\sigma_1 - \sigma_2) = \frac{f_\sigma}{h} N , \tag{2}$$

where N is the fringe number, h is the plate thickness (~6mm in the present experiments) and f_σ is the stress fringe value (7 kN/m for polycarbonate) and $\sigma_{1,2}$ are the principal stresses at any point; thus the shear stress level of a fringe of order N is 0.58 N MPa. The orientation of the principal planes is not determined in this arrangement; typically interpretation of the fringe pattern is accomplished by comparing the observed fringe pattern with a theoretically expected pattern. In the crack problem of interest here, such a theoretically expected pattern can be generated by using the calculated values of the stress intensity factors. Conversely, by fitting the crack tip asymptotic stress field, with many nonsingular terms, their amplitudes may be determined.

3. Experimental determination of the crack tip stress field

Figure 2 shows a selected sequence of high-speed photographs from a test corresponding to a specimen with a sharp fatigue crack tip impacted at a speed of 22.5 m/s. The crack line is oriented horizontally in the middle of each photograph with the crack tip itself located at the center of the picture; the crack tip is identified in frame 0. The grid lines on the specimen are 12.7 mm (½ in) apart. Note that the machined slot extends up to the first vertical grid line on the left and that the crack beyond this marker was introduced by fatigue. Impact of the projectile occurred on the lower part of the specimen and the projectile can be seen in the photographs. Impact usually occurs at some uncontrollable time between two frames; but the exact time of impact can be identified from the isochromatics observed. For instance, in the frame identified as 0 μs, no isochromatic fringes can be seen while in the frame identified as 10 μs, isochromatics are observed in the crack tip region indicating that the loading wave has already passed the crack tip region. By identifying the initial wave front and using the interframe timing, the precise impact time can be determined in each test. With increasing time, development of the isochromatic fringe pattern at the crack tip can be observed from the high-speed photographic sequence. A small dark region can be seen near the crack tip in all the pictures; this is caused by the pseudoschlieren effect discussed earlier; thus in these figures, a region of about 1 mm ahead of the crack tip cannot be observed. Fringe numbers can be identified easily since the top left boundary is traction free and the zeroth order fringe is always visible in this region.

The usual technique for quantitative interpretation of these isochromatic fringes is to extract parameters of an expansion of the crack tip stress field. Since this problem is one of a stationary crack with a time dependent loading, the crack tip stress field may be expressed as

$$\sigma_{\alpha\beta} = \frac{K_I(t)}{\sqrt{2\pi r}} f^I_{\alpha\beta}(\theta) + \frac{K_{II}(t)}{\sqrt{2\pi r}} f^{II}_{\alpha\beta}(\theta) + T(t)\delta_{\alpha 1}\delta_{\beta 1} + O(r^{1/2}) \tag{3}$$

where $K_I(t)$ and $K_{II}(t)$ are the mode I and II stress intensity factors and $T(t)$ is the first non-singular term, usually referred to as the T-stress. $f^{I}_{\alpha\beta}(\theta)$ and $f^{II}_{\alpha\beta}(\theta)$ are the known angular distributions of the singular crack tip stress field for the symmetric and antisymmetric parts respectively. Depending on the distance from the crack tip at which the isochromatic fringes are evaluated, more terms in the asymptotic expansion in Eq. (3) may be needed. For this asymmetric impact problem, the analysis of Lee and Freund (1990) indicates a negative mode I component implying interpenetration of the top and bottom crack faces; in fact, for the fatigue cracks used in the present experiments, one should have contact stresses along the fatigue crack tip, resulting in as yet unknown redistribution of the asymptotic stress field. It is possible to determine the theoretically expected isochromatic fringe patterns corresponding to the singular field by using Eqs. (2) and (3) and the evaluation of the dynamic stress intensity factors of Lee and Freund (1990). These isochromatic fringe patterns are shown in Figure 3 for the 20 and 30 μs after impact, noting that beyond this time, the calculated stress intensity factor variation is not applicable as discussed earlier. Comparing the fringe patterns in Figures 2 and 3, it can be concluded that a K-dominant field does not get established at these short times even at a distance of about 1 mm from the crack tip. While it might be possible to use many orders of terms in the expansion in Eq. (3) and obtain a best estimate of the stress intensity factors, we pursue an alternative approach.

In Figure 4, one frame corresponding to 40 ms after impact at 40 m/s is shown. Also shown in this figure is the variation of the maximum shear stress $(\sigma_1 - \sigma_2)/2$ along the line ahead of the crack. While acknowledging that the direction of this shear stress is not known, we can at least track its magnitude. Furthermore, from the nature of the loading, one could guess the direction of the shear stress both far away from the crack where the stress field is a biaxial compressive field and very close to the crack tip, where a mode II type loading should dominate. However, the most interesting observations from these results are the magnitude and gradient of the maximum shear stress. In Figure 5, the influence of the impact speed is shown. Clearly, as the impact speed is increased, the shear stresses in the crack tip region reach the yield stress of polycarbonate very quickly. As shown in Figure 6, the gradient of the shear stress normal to the crack line is significantly larger than the gradient along the crack line. This can be understood by considering the fact that the bottom half of the specimen has a large particle velocity parallel to the crack tip as a result of the impact loading while the top half can only be moved through a shearing along the crack line. In this large gradient field, the shear strain localizes along the line ahead of the crack tip into a shear band.

4. Conclusion

The use of dynamic photoelasticity in the examination of the crack tip stress field in the asymmetric impact loading configuration is discussed in this paper. The high-speed photographs indicate that a K-dominant field is not established over a length of even 1 mm in the short time scales of this experiment. The isochromatic fringe patterns indicate that the shear stress does reaches a high enough magnitude to cause yielding and shear localization.

References:

Lee, Y.J. and L.B. Freund, (1990). Fracture initiation due to asymmetric impact loading of an edge cracked plate, *Journal of Applied Mechanics,* **57,** pp. 104-111.

Ravi-Chandar, K., (1995). On the failure mode transitions in polycarbonate under dynamic mixed-mode loading, *International Journal of Solids and Structures,* **32,** 925-938.

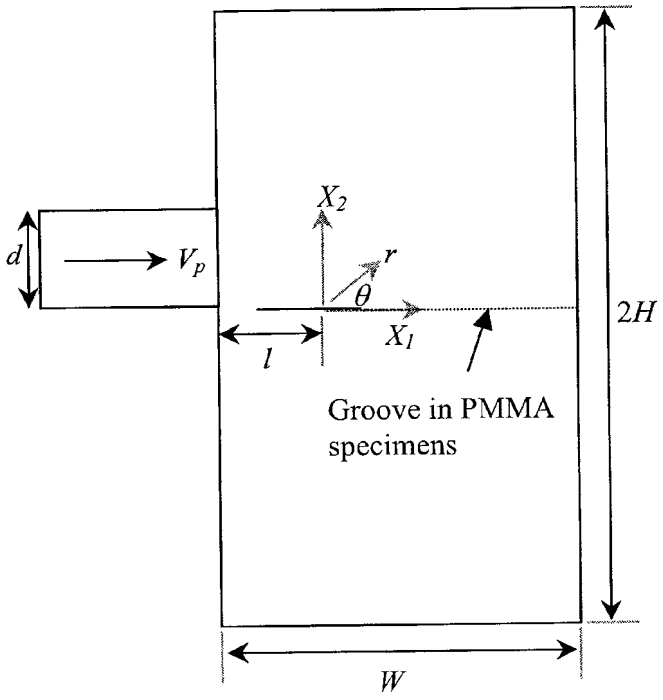

Figure 1. Geometry of the asymmetrically impacted edge-cracked specimen.

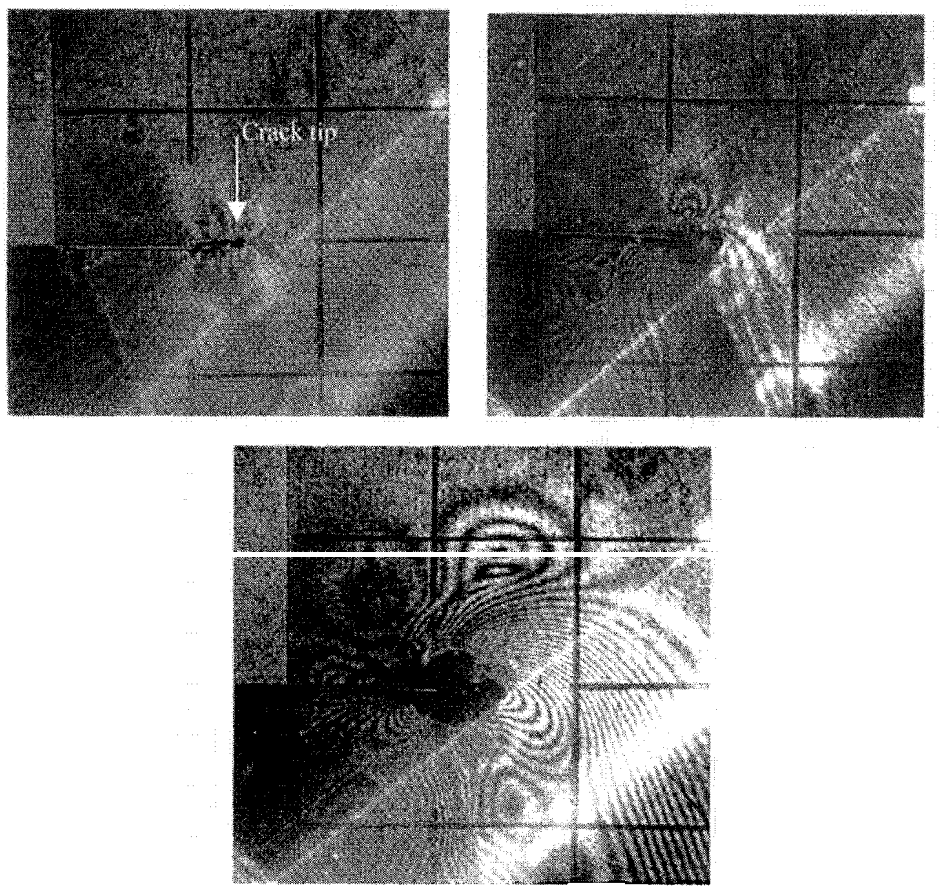

Figure 2. Selected sequence of high-speed photographs indicating the impact of the projectile and the development of the crack-tip stress field. (Polycarbonate, projectile speed V_p = 22.5 m/s); time between high-speed photographs: 10 μs.

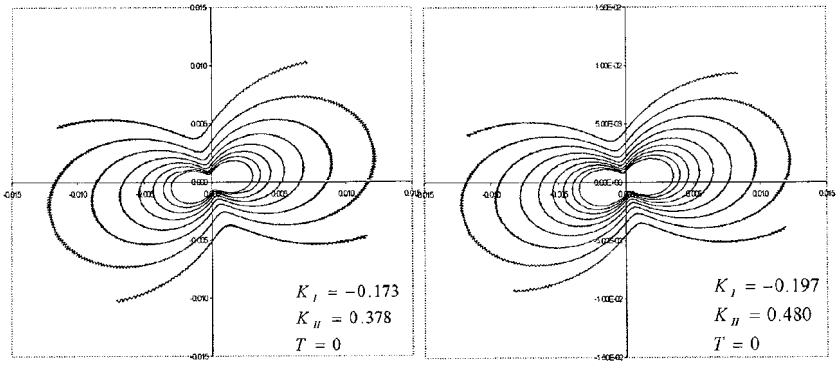

Figure 3. Isochromatic fringe patterns corresponding to a dominant K-field. The stress intensity factors used correspond to 20 μs after impact in (a) and 30 μs after impact in (b).

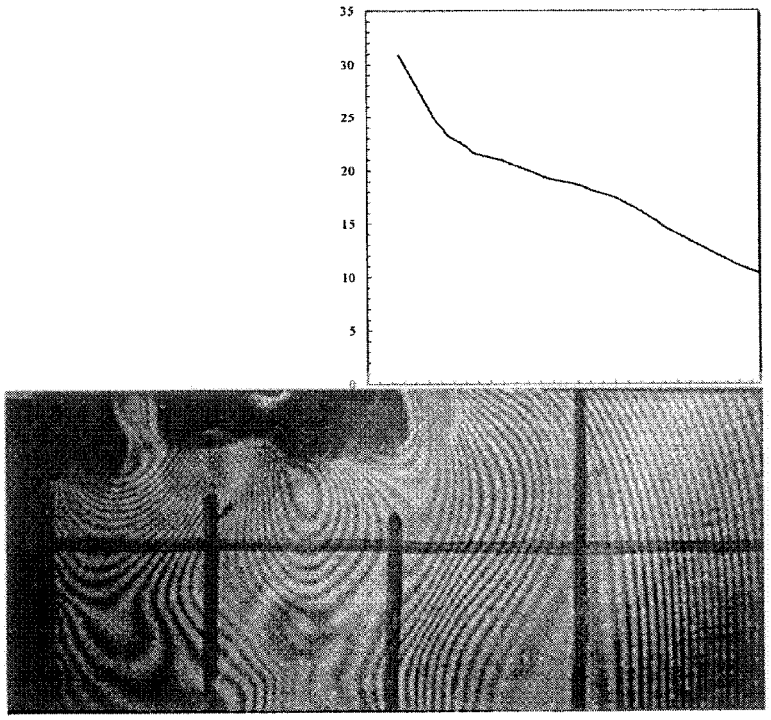

Figure 4. Selected high-speed photographs from impact at 40 m/s, 40 μs after impact. The maximum shear stress along the line ahead of the crack is also shown

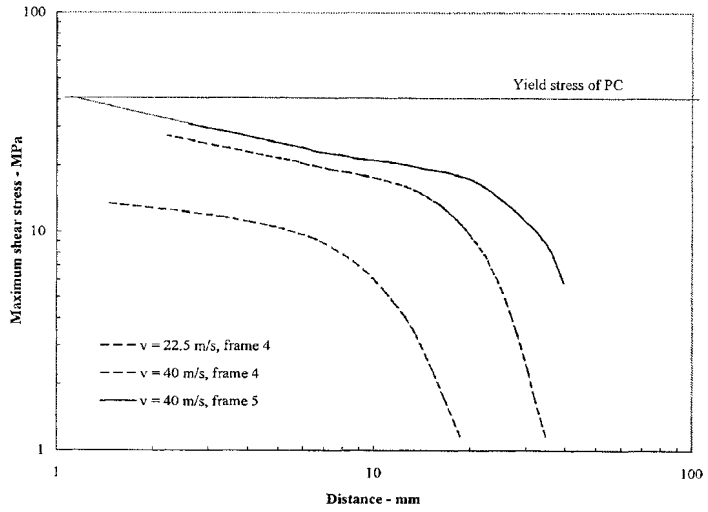

Figure 5. Variation of the maximum shear stress with distance from the crack tip. (V_p = 40 ms, t = 30 μs and V_p = 40 ms, t = 40 and 50 μs, all for θ = 0).

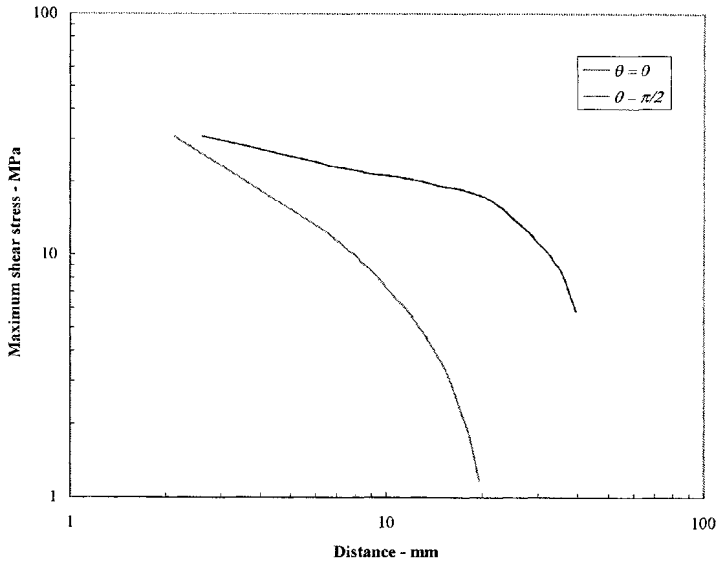

Figure 6. Variation of the maximum shear stress with distance from the crack tip. (V_p = 40 ms, t = 50 μs, for θ = 0 and π/2).

SUBSONIC AND INTERSONIC INTERFACIAL FRACTURE : DYNAMIC PHOTOELASTIC INVESTIGATION

A. SHUKLA, M. KAVATURU
Dynamic Photoelastics Laboratory
Department of Mechanical Engineering and Applied Mechanics
University of Rhode Island, Kingston, RI 02881

Abstract

A series of experiments was performed to investigate the phenomenon of dynamic interfacial fracture using the method of photoelasticity in combination with high-speed photography. Two different specimen geometries were utilized to understand interfacial fracture under both shear and opening mode dominated loading conditions. The experimental data was utilized to formulate a fracture criterion that establishes a generalized relationship between the dynamic energy release rate and the crack-tip velocity. The criterion is based on the premise that the vectorial crack-face displacement at a point behind the crack tip increases exponentially with the instantaneous crack-tip velocity.

Furthermore, in the intersonic regime, experiments were conducted to investigate the nature of crack propagation. The isochromatic fringe patterns were analyzed using recently developed stress field equations. A numerical technique based on Levenberg-Marquardt nonlinear least square scheme was utilized for the purpose of analysis. The results indicate that the crack growth in the intersonic regime is highly unstable. The experimental data fits well with the recently proposed intersonic interfacial fracture criterion.

1. Subsonic Regime

1.1. EXPLOSIVE LOADING EXPERIMENTS

The schematic of the bimaterial specimen used in this series of experiments is shown in figure 1. The bimaterial specimens consisted of a compliant PSM-1 half bonded directly to a stiff aluminum half. The interface was dynamically loaded by detonating two explosive charges containing 200 mg of lead azide explosive in the specimen as shown in figure 1. A stiff steel spacer was introduced between the side arms of the aluminum specimen and the explosive holder to further increase the loading rate. The detonation initiates a compressive wave in the side arms of the aluminum half of the bimaterial which reflects off the opposite free surface as a tensile wave. This tensile wave propagates down

A. Lagarde (ed.),
IUTAM Symposium on Advanced Optical Methods and Applications in Solid Mechanics, 555–562.

the aluminum half and develops a planar front before reaching the interface. The planar tensile wave loads the interface crack resulting in initiation, propagation and arrest, all in the same experiment.

1.2. IMPACT LOADING EXPERIMENTS

The schematic of the bimaterial specimen used to study the interfacial fracture under impact loading is shown in figure 2. The aluminum half of the bimaterial specimen was

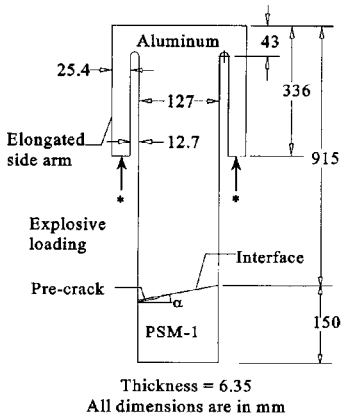

Figure 1. Schematic of the bimaterial specimen used to study the interface fracture under explosive loading.

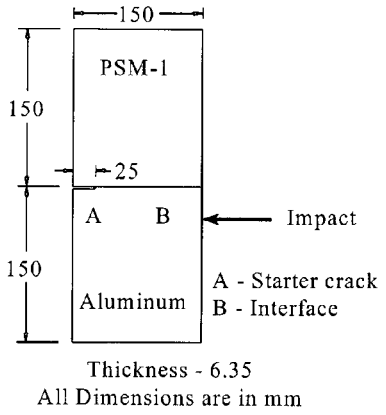

Figure 2. Schematic of the bimaterial used in the impact loading experiments.

subjected to impact by a projectile fired from a gas gun at low speeds on the order of 5 m/s. The impact sets up a compressive wave in aluminum half which traverses the width of the specimen and reflects off the free surface as a tensile wave. This tensile wave loads the interface crack, primarily in shear, resulting in crack initiation and subsequent propagation.

The entire event of dynamic fracture was observed by dynamic photoelasticity and the full field information in the PSM-1 half was recorded using a Cranz-Schardin type multiple spark high- speed camera, illustrated

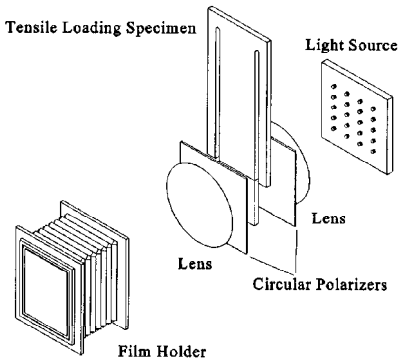

Figure 3. Schematic of the experimental set-up

in figure 3. A typical set of isochromatic fringe patterns obtained for the dynamic fracture of a PSM-1/aluminum bimaterial interface inclined at an angle of 10° is shown in the figure 4. Time $t = 0$ represents the time of incidence of the planar wave on the interface. The isochromatic fringe patterns obtained from the explosive and the impact loading experiments were analyzed to evaluate fracture parameters such as crack-tip velocity, the dynamic complex stress intensity factor, the dynamic energy release rate, and the instantaneous mixity. The crack-tip velocity history was obtained directly from the photographs from the knowledge of the crack-tip location as a function of time. The crack-tip velocity remained subsonic for the duration of the crack propagation in all these experiments. The histories of the dynamic complex stress intensity factor, the dynamic energy release rate, and the mixity were evaluated using the steady-state singular stress field equations developed by Yang *et al.* (1991).

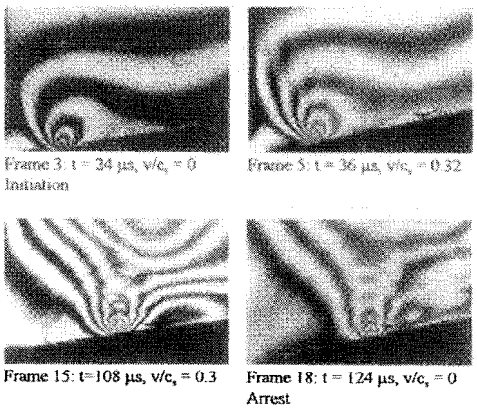

Figure 4. Isochromatic fringe patterns due to a crack propagating along a PSM-1/aluminum interface ($\alpha = 10°$) subjected to explosive loading (t is the post-incidence time).

1.3. RESULTS AND DISCUSSIONS

The history of crack-tip speed obtained in a typical explosive loading experiment involving the fracture of an interface inclined at an angle -10° is shown in figure 5. It can be seen from the figure that the complete process of crack initiation, propagation and arrest has been observed in the same experiment. The crack initiated a finite time, t_i = 26 μs, after the tensile wave reached the interface. After initiation, the crack accelerated at the rate of 1.5 x 10^6 g (g being the acceleration due to gravity) to a maximum velocity of

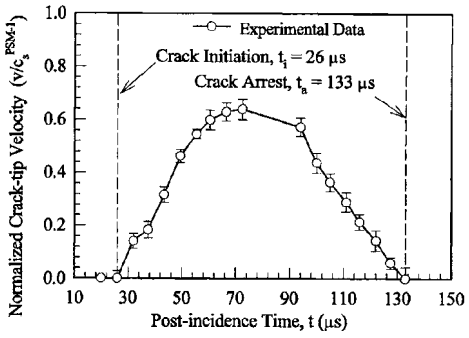

Figure 5. Crack-tip velocity history for a PSM-l/aluminum interface inclined at - 10^0

approximately 65% of the shear wave speed of the more compliant material. The crack decelerated after reaching the peak velocity and finally arrested. This phenomenon of *subsonic* crack propagation was observed in all the experiments involving fracture of inclined interfaces subjected to explosive loading. The steady-state singular stress field equations developed by Yang *et al.* (1991) were employed to evaluate the dynamic complex stress intensity factor, K^d (t).

The time histories of the energy release rate, G^d (t), and the mixity, ϕ(t), are shown in figures 6 and 7, respectively. In this typical experiment, the crack initiated at $G_i = 63$ J/m^2 and $\phi_i = 32°$ and the arrest occurred at $G_a = 49$ J/m^2 and $\phi_a = 24°$. It can be seen from figure 6 that the energy release rate increases monotonically to a peak value in 55 μs. During this time, the crack tip accelerated to achieve a speed of approximately 55% of shear wave speed of PSM-1 (c_s^{PSM-1}), as is evident from figure 5. Thus, it can be concluded that the energy release rate increased monotonically with the crack-tip velocity up to 55% of c_s^{PSM-1}. This increasing trend in the energy release rate with the crack-tip velocity suggests that the crack growth in this velocity range is stable ($dG^d/dv > 0$). The energy release rate after reaching a peak at 55 μs showed a decreasing trend up to about 90 μs. During this time period, 55 μs < t < 90 μs, the crack-tip velocity increased to approximately 65% of c_s^{PSM-1} as shown in figure 5. This decreasing trend in energy release rate with the crack-tip speed is typical of unstable crack growth behavior ($dG^d/dv < 0$). Finally, after 90 μs, the energy release rate dropped monotonically as the crack decelerated indicating stable crack growth ($dG^d/dv > 0$). This interesting phenomenon of transition from stable to unstable and back to stable crack growth was characteristic of all the experiments involving fracture of inclined interfaces in this loading

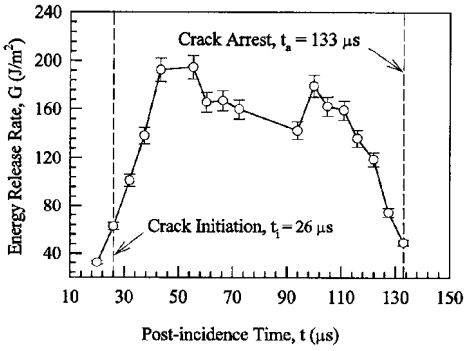

Figure 6. Time history of energy release rate for fracture of PSM-1/aluminum interface inclined at -10°

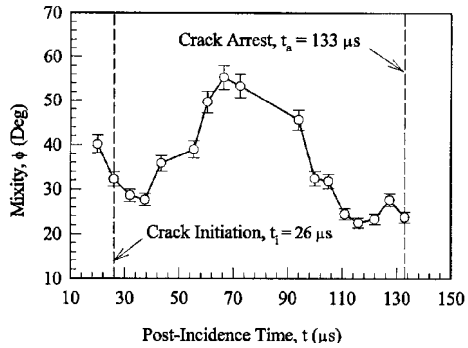

Figure 7. Time history of mixity for fracture of PSM-1/aluminum interface inclined -10°

configuration. On the other hand, the mixity, plotted in figure 6, increased continuously with crack-tip velocity after initiation and decreased as the crack tip decelerated.

A dynamic fracture criterion, namely, vectorial crack-face displacement criterion (VCD) was proposed by assuming that the vectorial crack-face displacement at a point a behind the crack tip increases exponentially with the crack-tip velocity:

$$\sqrt{\delta_2^2 + (\eta\,\delta_1)^2}\,\Big|_{r=a} = C_3 (v/c_s)^n, \tag{1}$$

where C_2 is a constant of proportionality, v is the instantaneous crack-tip velocity, c_s is shear wave speed of the compliant material and n is a parameter that depends on the bimaterial and on the cohesive properties of the bond. This assumption establishes a generalized relationship between the magnitude of complex stress intensity factor and the instantaneous crack-tip velocity given by

$$|K^d| = C_3 (v/c_s)^n \frac{\sqrt{1+4\epsilon^2}\cosh \pi\epsilon}{H_{22}} \sqrt{\frac{\pi}{2a}}, \tag{2}$$

A fit of the experimental data to the proposed criterion is shown in figure 7. In the figure, the solid line represent the criteria and the symbols denote the experimental data. The experimental data shows good agreement with the proposed criteria. For the case of crack propagation along PSM-1/aluminum bimaterial interface, the vectorial crack-face displacement at a point 2 mm behind the crack tip was observed to be proportional to $(v/c_s)^{0.15}$. Interestingly enough, the criterion predicts that the crack propagation turns unstable at crack-tip velocities of about 50% of the lower shear wave speed. Also, the criterion predicts that the energy release rate is finite in the limit of Rayleigh wave velocity of the compliant material.

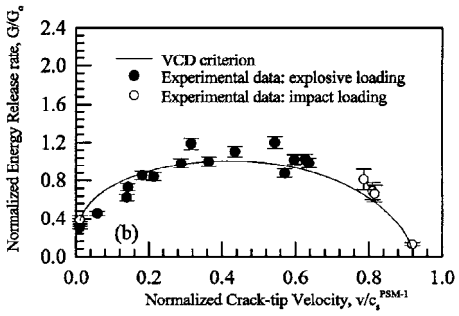

Figure 8. Fit of the proposed criterion with the experimental data

2. Intersonic Regime

In the intersonic regime, a series of experiments were performed to understand the nature of crack propagation using the method of dynamic photoelasticity. A non-linear least squares method based on the Levenberg-Marquardt scheme (More, 1977) was utilized to analyze the isochromatic fringe patterns obtained from experiments involving the fracture of Homalite-100/aluminum bimaterial specimens. The specimens were subjected to impact by a projectile fired from a gas gun which results in crack initiation and subsequent propagation. The entire fracture event was photographed using dynamic photoelasticity in combination with high-speed photography.

2.1. EXPERIMENTAL TECHNIQUE

A series of high velocity impact loading experiments were conducted on the impact loading specimen shown in figure 2. The specimen is subjected to impact by a projectile driven by a gas gun at velocities on the order of 25 m/s. The high velocity impact results in high crack-tip accelerations and velocities. The fracture event was photographed using dynamic photoelasticity in combination with high-speed photography. A sequence of isochromatic fringes obtained from an high velocity impact loading experiment is shown in Figure 9.

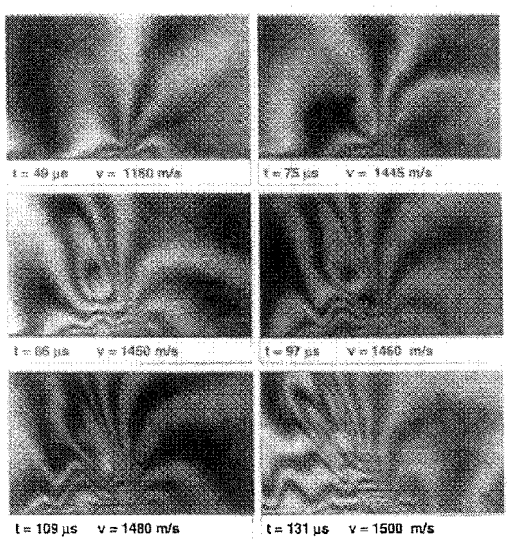

Figure 9. Typical isochromatic fringe patterns obtained for dynamic fracture along Homalite-100/aluminum interface subjected to impact loading

2.2. RESULTS AND DISCUSSION

The velocity of the interfacial crack tip was calculated from the knowledge of the crack-tip location history obtained from the photographs. The history of the crack-tip velocity for a typical impact loading experiment is as shown in Figure 10. As can be seen from the figure, the crack tip quickly accelerated to shear wave velocity of Homalite-100 soon after crack initiation. Thereafter, the crack tip continued to increase at a smaller rate to around 140% of the shear wave speed of Homalite-100. The figure also shows the history of velocities of the end of contact zone and the Rayleigh singularity. It can be seen from the figure that the Rayleigh singularity was traveling at the Rayleigh wave speed of

Homalite-100. Also, the trailing end of contact zone was observed to have the velocity as the interfacial crack tip.

The isochromatic fringe patterns surrounding the crack tip were analyzed using higher order stress field equations developed by Huang et al. (1997). A total of 40 data points were collected from the fringes ahead of the crack tip as well as the fringes inside the contact zone.

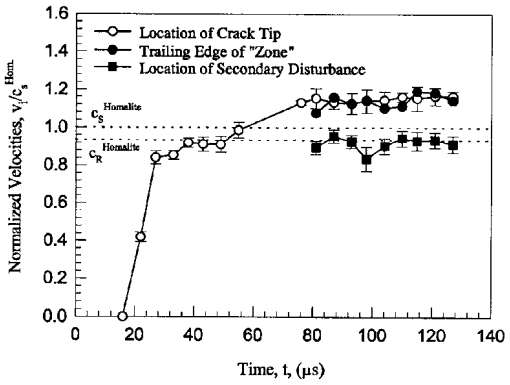

Figure 10. Histories of velocity of the crack tip, the end tailing end of contact zone and the Rayleigh wave Singularity

2.3. CRITICAL CRACK-FACE SLIDING DISPLACEMENT FAILURE CRITERION

Huang *et al.* (1997) proposed a criterion for intersonic crack growth along bimaterial interfaces. This criterion is based on the premise that the crack growth occurs in the presence of a constant critical sliding displacements (δ_c) evaluated at the end of the contact zone, i.e.,

$$u_1(\eta_1, = -l, \eta_2 = 0^-) = \delta \tag{3}$$

This was primarily motivated by the criterion proposed for subsonic interfacial crack growth by Lambros and Rosakis (1995).

This criterion establishes a relationship between the leading term of the stress series, B_o, and the crack-tip velocity, *v,* given by

$$B_0 = \frac{\delta_c l^{p+q-1}}{\beta(1-q, 1-p)\sin(q\pi)} \tag{4}$$

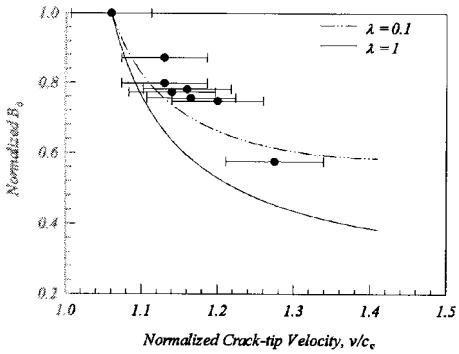

Figure 11. Fit of the experimental data with the critical crack face sliding criterion

where $\beta(x, y)$ is the β-function.

The data obtained from these high velocity impact experiments has been utilized to

verify this criterion. Equation (3) is plotted along with the experimental data in Figure 11. for two different values of λ, 0.1, and 1. The values of λ are so chosen since the values of λ obtained from the experiments fall within this range. The lines in Figure 11 represent the criterion and the symbols denote the experimental data. The critical sliding displacement, δ_c, was eliminated from equation (4) by normalizing with the corresponding value at $v = 1.05\ c_s$.

It is clear from the figure the data shows a reasonable agreement with the critical sliding displacement criterion. Additionally, B_0 and D reduce monotonically with the crack-tip velocity. This decreasing trend in the dissipation energy is characteristic of unstable crack propagation ($dD/dv < 0$).

3. Acknowledgment

The support of the National Science Foundation under grants CMS 9424114 and INT 9700670 is gratefully acknowledged.

4. References

Huang, Y., Wang, W., Liu, C., and Rosakis, A. J. (1997), "Intersonic Interfacial Crack Growth In a Bimaterial: An Investigation of Crack Face Contact," Submitted to *Journal of Mechanical and Physics of Solids.*

Lambros, J. and Rosakis, A. J. (1995), "Development of a Dynamic Decohesion Criterion for Subsonic Fracture of the Interface Between Two Dissimilar Materials," *Proceedings of the Royal Society (London),* Vol. A451, pp. 711-736.

Liechti, K. M. and Knauss, W. G. (1982), "Crack Propagation at Material Interfaces : II Experiments on Mode Interaction", *Experimental Mechanics,* **22,** 383-391.

Moré, J. J. (1977), "The Levenderg-Marqquardt Algorithm: Implementation and Analysis," *Numerical Analysis,* ed. G. A. Watson, Lecture Notes in Mathematics 630, Springer Verlag, pp. 105-116.

Yang, W., Suo, Z. and Shih, C.H. (1991), "Mechanics of Dynamic Debonding", *Proceedings of the Royal Society (London),* Vol. A433, pp. 679-697.

DYNAMIC BEHAVIOUR OF INTERFACIAL CRACK TIPS IN A WEDGE-SHAPED BIMATERIAL SPECIMEN UNDER IMPACT

J. FANG, C.Y. XIONG
Department of Mechanics &Engineering Science
Peking University, Beijing 100871, China

X.F. YAO
Department of Engineering Mechanics
Tsinghua University, Beijing 100084, China

Abstract

A specimen partially bonded by two wedge-shaped plates of dissimilar materials is impulsively loaded. Tip response of a crack along the interface is investigated to the action of stress wave with transmission and reflection. A hybrid technique of combining dynamic photoelasticity with dynamic caustics is used to analyze the wave propagation in media and the singular behavior of crack tips. Based on some characteristic dimensions of the caustic curves belonging to each medium, the complex stress intensity factors of the interfacial crack tips are computed, showing an oscillation history of the modulus with the passing of the compressive wave and the intersection of the reflected tensile pulse.

1. Introduction

Debonding of interface between two-phase material has been a typical failure in composite materials. Under impact loading, the interface of the multiphase materials may fracture rapidly due to the action of stress wave. Even in a homogeneous medium of elasticity, in fact, internal fracture may occur resulting from the focusing of the stress wave reflected from the boundaries of a solid body[1]. When a specimen of bimaterial is impulsively loaded, the tips of a crack lying along the interface may be initiated to cause a high speed debonding of the dissimilar media[2].

The optical method of caustics is a useful technique to study the singular behavior of crack tip with high stress gradients, as proved by plenty of work of Kalthoff[3], Theocaris[4], et al. For the interface crack in bimaterial, Theocaris[5] used the method to determine the complex stress intensity factors at tips under normal and shear loading.

A. Lagarde (ed.),
IUTAM Symposium on Advanced Optical Methods and Applications in Solid Mechanics, 563–570.

Herrman [6] extended the technique to dynamic case to evaluate the caustic patterns for arbitrary curvilinear interfacial cracks. When we investigate the response of interfacial crack tip to stress wave, however, the information provided by caustic shadows is often not enough to understand the dynamic behavior of multiphase media. The reason is that the optical caustics is a local effect of high stress gradient around crack tip, which can not offer a visual image of stress wave propagation in whole field.

A hybrid technique of combining dynamic caustics and dynamic photoelasticity has been proposed by the authors [7] , to study the fracture mechanism of crack in homogeneous material, that includes the interaction between the stress wave in a cantilever beam and the crack normal or inclined to the beam edge [8], the curving fracture of a crack in bent beam under impact [9] . In this paper, this optical method is applied to the response study of interfacial crack to stress wave focusing. Two kinds of patterns, the isochromatic fringes of photoelasticity and the optical shadows of caustics, are recorded at the same time instants but with separated films. With the help of the isochromatic patterns, the stress wave propagation in the whole field can be visualized through the movement of fringes in the bimaterial specimen, showing the transmitting and superimposing of the wave fringes. Meanwhile, the patterns of caustic shadows provide the local responses in the vicinity of crack tips to the wave action with mixed type of loading.

2. Impact Experiment and Dynamic Recording

2.1 SPECIMEN AND LOADING

The bimaterial specimen used in impact test is made of epoxy resin and polycarbonate, bonded together with a high speed adhesive. The shape of the specimen is a model easy to produce the focusing of stress wave, consisting of two wedge-shaped plates of angle α=22°, as illustrated in Figure 1. The mechanical properties of the materials are given in the Table 1, by showing the medium of epoxy resin as Phase 1 and that of polycarbonate as Phase 2, respectively.

A crack with length of 7mm is fabricated along the interface of the dissimilar materials, with its upper-tip U below the top edge AB of the specimen by a distance of l=(AB/2) sin2α. At the center position P of the top edge, an impulsive point load is acted by a bullet of gun, that produces a compressive stress wave propagating in the bimaterial specimen.

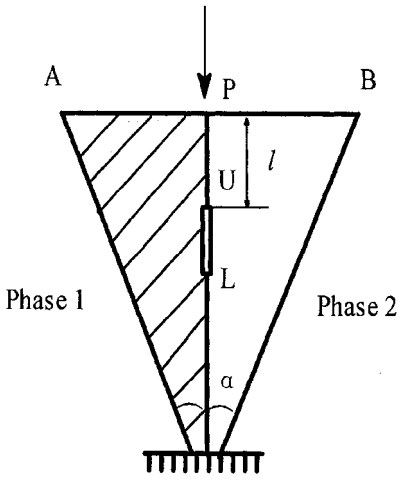

Figure 1, The specimen of bimaterial

TABLE 1 Mechanical properties of the materials

Material	Young's module (N/m^2)	Poisson's ratio	Thickness (mm)
Phase 1	E_1=4.7×10^9	v_1=0.38	t_1=6
Phase 2	E_2=2.6x10^9	v_1=0.35	t_2=5

2.2 HIGH-SPEED RECORDING SYSTEM

A modified Cranz-Schardin camera is used to record dynamic patterns of impact. The light source consists of 16 (4×4) spark gaps that are precharged with high voltage and then flash sequentially by discharge to produce strong point-like light sources.

The light beam is collimated by a field lens L_1 to illuminate the specimen B, as illustrated in Figure 2. The light becomes circularly polarized after passing through a polarizer P_1 and then a quarter wave plate Q_1. Another field lens L_2 focuses the light beam into an image lens l_i of small aperture, that corresponds to the i-th source flash of S_i. In a dark box, a partially reflecting mirror M_p separates the light beam into two parts. The reflected part is received by a set of films located on a plane I_c that is of a distance from the image plane I_0 of the specimen. The off-focusing of this recording plane enables the caustic shadow of crack tip to be recorded with an object distance of z_0 from the specimen. The light transmitting the mirror M_p, meanwhile, passes another quarter-wave plate Q_2, and then a polarizing analyzer P_2, to record the isochromatic patterns of moving fringes.

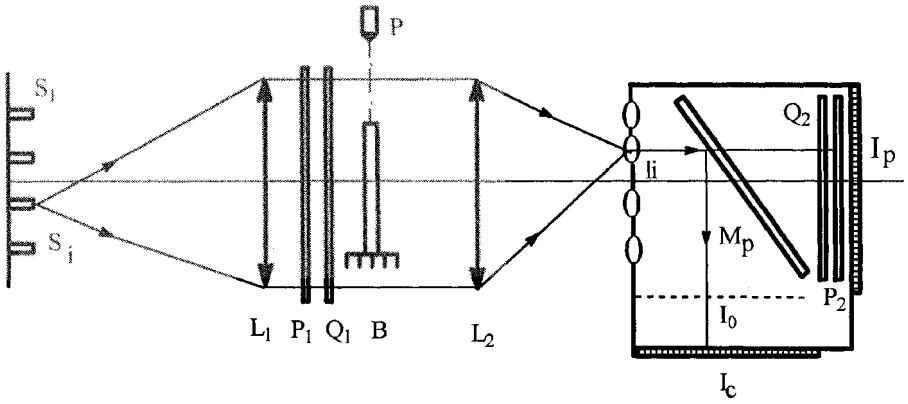

Figure 2, A schematic illustration of high speed recording system of the hybrid method

3.Results and Discussions

Figure 3 presents a series of photographs recorded by the camera system mentioned above. With different time sequence, the left column of patterns shows the isochromatic fringes of the specimen, and the right column gives the caustic shadows magnified around the crack tips, presenting the wave motion in whole field and the singular response of the interfacial crack, respectively.

3.1 DATA EVALUATION FROM PATTERNS

The isochromatic fringes result from the transparent specimen with optical property of stress-birefringence. The fringe number N is related to the difference of principal stresses given by

$$\sigma_1^{(i)} - \sigma_2^{(i)} = Nf_i / t_i \qquad (i=1,2) \tag{1}$$

where the index i means the i-th medium of bimaterial specimen, f_i the dynamic stress-fringe value calibrated by impact test, and t_i is the thickness of the plate as shown in Table 1.

The shadow pattern of caustics represents an optical mapping of the singularity at crack tip to the light distribution of caustic curve on a reference screen. When the bimaterial specimen is illuminated by collimated beams, as schematically illustrated by Figure 4, the light rays transmitting the near region of the crack tip are strongly deviated by the refractive index change of the materials and the thickness change of the specimen, due to the concentrated deformation around tips. Attaching a coordinate system of ξ-O-η to the specmen plane, with the axis ξ in coincidence with the interface of those two dissimilar materials, the shadow spot surrounded by bright caustic rim can be observed on the screen plane X-O'-Y. The caustic curve consists of points with complex variable $W_i = X_i + jY_i$, at which the deviated rays come from the position vector $\zeta_i = \xi_i + j\eta_i$ in the specimen plane, with a mapping equation of [10].

$$W_i = \zeta_i - C_i(\tfrac{1}{2} + j\beta)K_i\zeta_i^{-3/2-j\beta} \tag{2}$$

where C_i is a constant determined by the optical property of the material and the thickness of specimen, and also by the off-focusing distance z_0 of recording plane, K_j is the complex stress intensity factor of crack tip, with $K_1 = gK_2$, whereas g and β are constants.

An intial curve, surrounding the interfacial crack tip on the specimen plane to correspond to the caustic curve on the screen, satisfies the equation of

$$J = \partial(X,Y)/\partial(\xi,\eta) = 0 \tag{3}$$

Substituting the expression (2) into above equation and letting $\zeta_i = r_i e^{i\varphi_i}$, the radius r_j of the initial curve can be written as

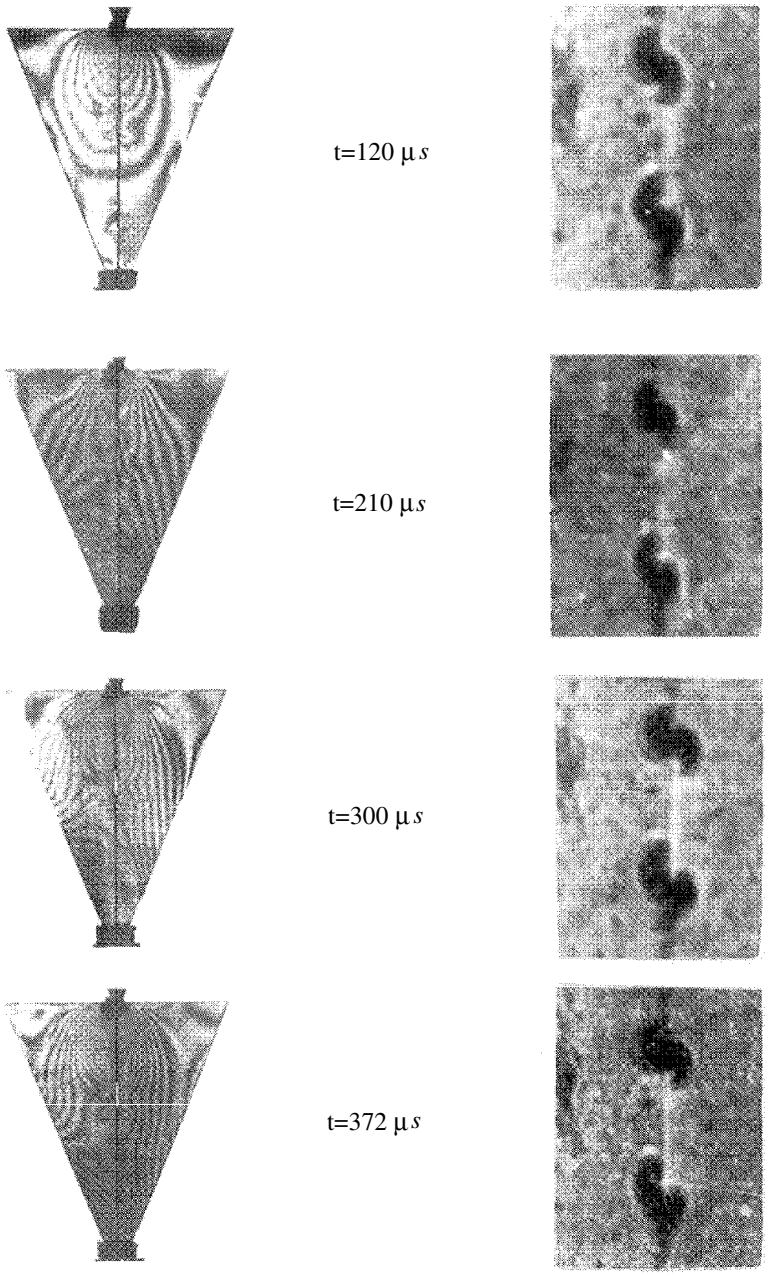

Figure 3, Dynamic patterns of isochromatic fringes and caustic shadows

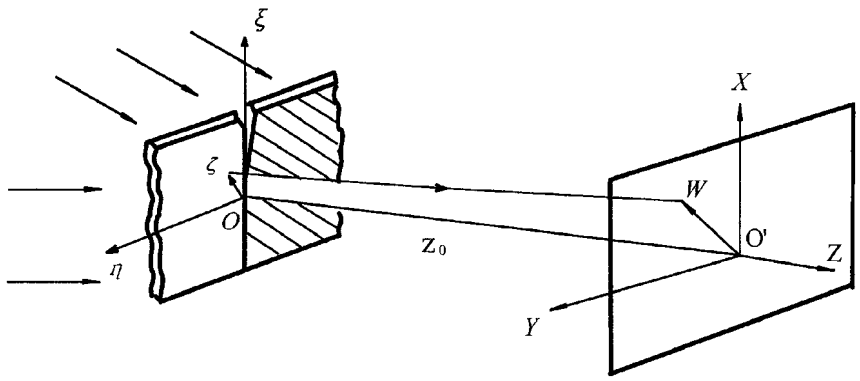

Figure 4, An illustration of caustic mapping for an interfacial crack in bimaterial,

$$r_i = H_i |K_i|^{5/2} \exp(\frac{2}{5}\beta\varphi_i) \tag{4}$$

where $H_i=|C_i(1/2+j\beta)(3/2+j\beta)|^{2/5}$. Therefore, the equation (2) of the caustic curves can be expressed as

$$\begin{aligned} W_i = {} & H_i |K_i|^{2/5} \exp(\tfrac{2}{5}\beta\phi_i) \exp(j\phi_j) + C_i(\tfrac{1}{2} - j\beta)|K_i| \left[H_i |K_i|^{2/5} \right]^{-\frac{3}{2}+j\beta} \\ & \exp(-\tfrac{3}{5}\beta\phi_i) \exp\left\{ j\left[-\theta_i + \beta \ln(H_i |K_i|^{2/5}) + \tfrac{2}{5}\beta^2\phi_i + \tfrac{3}{2}\phi_i \right] \right\} \end{aligned} \tag{5}$$

where θ_i is the argument of K_i.

By geometrical measurement of some characteristic dimensions of caustic curves, the evaluation of the stress intensity factors K_i can be convenient for the interfacial crack tips. The coordinates of the end-point of caustic branches, or $X^{(0)}{}_1$, $Y^{(0)}{}_1$, and $X^{(\pi)}{}_1$, $Y^{(\pi)}{}_1$, corresponding to $\phi=0$ and $\phi=\pi$ for the medium of epoxy resin, and $X^{(0)}{}_2$, $Y^{(0)}{}_2$, and $X^{(-\pi)}{}_2$, $Y^{(-\pi)}{}_2$, to $\phi=0$ and $\phi=-\pi$ for the medium of polycarbonate, respectively, are used to determine the distance d_i between the end-point of the caustics belonging to material *i*, from that the module $|K_i|$ and the argument θ_i can be solved by numerical computation.

3.2 DYNAMIC RESPONSE OF CRACK TIPS

Following a concentrated impact at the center position of the specimen top-edge, a compressive pulse radiates from there moving downwards; as shown by the isochromatic patterns of fringe rings in Figure 3. The stress wave propagates in the bimaterial specimen and the dynamic fringes soon reach the upper tip (Tip-U) of the interfacial crack and then the lower tip (Tip-L) by transmission. This action results in an

impulsive loading at the crack tips with stress concentration. The modulus of the dynamic stress intensity factors $|K_1|$ and $|K_2|$, determined by the caustic curves as described in the last section, show the tip response of the crack lying along the interface of those two dissimilar media, as given in Figure 5(a) and 5(b), respectively.

During the beginning period from the instant of t=116μs to t=206μs, the amount of K_i at the Tip-U varies between $3.5\times10^4 N/m^{3/2}$ and $6.5\times10^4 N/m^{3/2}$, and that of K_i at the Tip-L oscillates in a range of $4.2\times10^4 N/m^{3/2}$ to $10\times10^4 N/m^{3/2}$, respectively. The tendency of those variations is a decrease of K_i values, corresponding to the passing of the transmitting wave. The amount $|K_i|$ reaches the minimum at the instant of t=242μs, with $|K^U_1|=3.83\times10^4 N/m^{3/2}$, $|K^U_2|=3.2\times10^4 N/m^{3/2}$, and $|K^L_1|=4.7\times10^4 N/m^{3/2}$, $|K^L_2|=3.84\times10^4$ $N/m^{3/2}$, respectively, when the main part of the compressive pulse has run over the crack tips towards the lower base and the slop boundaries of the specimen, with fewer fringes around the interfacial crack.

The stress waves reflected from the slope sides of the wedge move back the interface of bimaterial and produce a tensile pulse intersecting on the crack, that makes the amount of $|K_i|$ increased rapidly due to a stress wave focusing. Since then, the form of isochromatic patterns has been changed from the fringe rings to those nearly parallel to the interface, as presented by the last part of the isochromatic fringe patterns in Figure 3. This kind of fringes become more and more and reach the highest density at the instant of t=296μs, with the arrival of the wave reflected from the wedge apex. Correspondingly, the module $|K_i|$ at Tip-L reaches the maximum value at first, with $|K^L_1|_{max}=14.6\times10^4 N/m^{3/2}$ and $|K^L_2|_{max}=12.1\times10^4 N/m^{3/2}$, respectively. And sequentially, with the movement of the reflected wave upwards, the amount of $|K_i|$ has the maximum of $|K^U_1|_{max}=8.8\times10^4 N/m^{3/2}$ and $|K^U_2|_{max}=7.4\times10^4 N/m^{3/2}$, respectively.

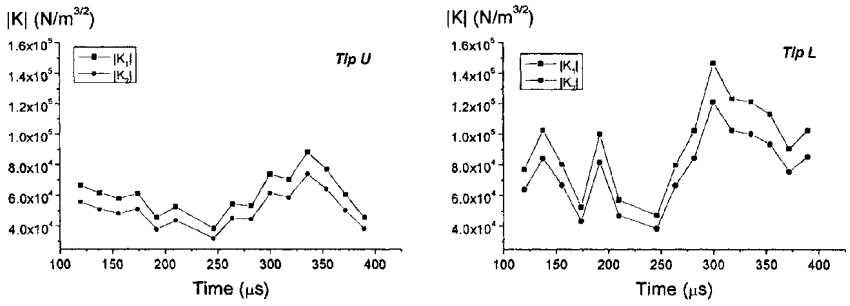

(a) (b)

Figure 5, The module of the complex stress intensity factors at the upper-(a) and lower- (b) tip

4. Conclusions

Under the action of impact load, a bimaterial specimen of wedge-shaped plate can be used to produce a tensile pulse in the interface of two dissimilar materials by stress wave focusing. In the dynamic history, the complex stress intensity factors K_i of crack tips show to be oscillated with the action of pulse wave. The amount $|K_i|$ in epoxy resin side is relatively higher than that in polycarbonate, but both of them reach their maximum values when the stress wave reflected from specimen boundaries by focusing at the crack tips.

The experimental results show that the hybrid method of combining dynamic photoelasticity and caustics is a useful technique to study the dynamic behavior of interfacial crack tips under impulsive loading. The isochromatic fringes give the stress wave transmission, reflection and focusing in the specimen of bimaterial. The caustic shadows present the responses of the crack tips to the wave action. The technique offers a visual way to interpret the dynamic stress history in the composite structure, and also a useful tool of quantitative analysis for the wave propagation in bimaterial and singularity evaluation of the interfacial crack tips.

Acknowledgements: The support of NNSF of China is greatly appreciated.

References

1. Gomes J.F.S. and Al-Hassani S.T.S. Internal fracture in spheres due to stress wave focusing. Int.J.Solids Structures, **13** (1977), 1007-1017
2. Liu C., Lambros J. and Rosakis A.J., Highly transient elastodynamic crack growth in a bimaterial interface, J. Mech. Phys. Solids, **41** (1993), 1887-1954.
3. Kalthoff J.F., On the measurement of dynamic fracture toughness-a review of recent work, International Journal of Fracture, **27** (1985), 277-298
4. Theocaris P.S. and Papandopolus G.A., Elastodynamic forms of caustics from running cracks under constant velocity, Engng. Frac. Mech., **13**(1980), 683-689.
5. Theocaris P.S. Partly unbonded interfaces between dissimilar material under normal and shear loading, Acta Mechania, **24**(1978), 99-115
6. Herrman K.P, Noe A. Analysis of dynamic mixed mode stress fields in bimaterials by the method of caustics. Theoretical and Applied Fracture Mechanics, **19**(1993), 49-59
7. Fang J, Qi, Jiang Z.D and Zhao Y.P., An experimental method to investigate the interaction between stress waves and cracks in polycarbonate, Recent advances in experimental mechanics, S. Gomes et al. (eds), Balkema, Rotterdam, 1994, 593-598.
8. Fang J, Qi J, Yao X.F, Zhao Y.P and Jiang ZD. The response and fracture of a crack in epoxy resin beam under the action of bending stress wave. DYMAT Journal, **2**(1995), 143-150.
9. Yao Xuefeng, Xiong Chunyang, Yang Zili and Fang Jing, Visualization of fracture behavior in crack curving, 4th Asian symposium on Visualization, Int. Academic Pub., 1996, 445-450.
10. Theocaris P.S, Stassinakis. Complex stress intensity factors at tips of cracks along interfaces of dissimilar media. Engineering Fracture Mechanics, **14**(1981), 363-372.

MEASUREMENT OF CRACK TIP OPENING DISPLACEMENT AND FULL-FIELD DEFORMATIONS DURING FRACTURE OF AEROSPACE MATERIALS USING 2D AND 3D IMAGE CORRELATION METHODS

PROF. MICHAEL A. SUTTON
PROF. STEPHEN R. MCNEILL
MR. JEFFREY D. HELM
MR. MICHAEL L. BOONE
Department of Mechanical Engineering
University of South Carolina
300 Main Street
Columbia, South Carolina 29208

1. Abstract

Two-dimensional and three-dimensional image correlation methods have been developed and used successfully to measure the surface displacement and strain fields during crack propagation in aerospace structures. Initial testing focused on obtaining experimental data for both the surface strain fields and the critical Crack Tip Opening Displacement (CTOD) in thin sheet 2024-T3 aluminum under predominantly tensile loads. This work was then expanded to include CTOD measurements under mixed mode loading, the study of crack closure effects, the study of buckling in large center-cracked specimens and the effect of multi-site damage on various aerospace materials.

In this work, a brief background for both the two-dimensional and the three-dimensional image correlation methods is provided. Results from two projects, one using 2-D image correlation for crack closure measurements during fatigue and another using 3-D image correlation to measure surface deformations in large cracked panels, are presented.

2. Background for 2-D Computer Vision

The basis of two-dimensional video image correlation (VIC2D) for the measurement of surface displacements is the matching of one point from the image of an object's surface before loading (the undeformed image) to a corresponding point in the image of the object's surface taken at a later time/loading (the deformed image), as noted in previous work [1-2]. Assuming a one-to-one correspondence between deformations in the image recorded by the camera and deformations of the surface of the object, an accurate, point-to-point mapping from the undeformed image to the deformed image will allow the displacement of the object's surface to be measured. Two main requirements must be met for the successful use of VIC2D. First, in order to provide features for the matching process, the surface of the object must have a pattern that produces varying intensities of diffusely

A. Lagarde (ed.),
IUTAM Symposium on Advanced Optical Methods and Applications in Solid Mechanics, 571–580.

reflected light. This pattern may be applied to the object or it may occur naturally. Secondly, the imaging camera must be positioned so its sensor plane is parallel to the surface of the planar object, as shown in Figure 1.

The 2-D image correlation process maps a small rectangular segment of the undeformed image onto the deformed image using a deformation model based on basic continuum mechanics. Because integer pixel locations in the undeformed image will most often be mapped to non-integer locations in the deformed image, the discrete gray level pattern of the deformed image is interpolated to obtain gray levels for non-integer locations. Once the deformation model is applied to a small segment of the undeformed image, the mismatch between the gray levels of the deformed subset and the recorded gray levels in the deformed image is quantified using a cross correlation error measure. The parameters of the deformation model, displacements and displacement gradients, are then modified using standard non-linear optimization techniques to obtain the optimal mapping from the undeformed image to the deformed image. This process is presented in greater detail in Reference [1].

It is noted that accurate measurement of surface deformations requires that the mapping from the undeformed image to the deformed image be as accurate as possible. Thus, it is important to "oversample" the intensity pattern, using several sensors to sample each feature of the intensity pattern. Through a combination of over-sampling, interpolation and at least 8 bit quantization of the gray levels, the continuous intensity pattern can be reconstructed with reasonable accuracy and the displacement field estimated with accuracy of +/- 0.02 pixels or better.

3. Background for 3-D Computer Vision

Three-dimensional image correlation overcomes many of the basic limitations of the two-dimensional system, which is limited to flat specimens that experience very little out-of-plane movement while under load. Three-dimensional image correlation has been used successfully to make shape and displacement measurements for both curved and flat panels that experienced significant out-of-plane movement and rotation during loading. In addition, because it uses features on the surface of the object rather than a projected pattern, it is capable of true, point-to-point surface displacement measurements. While the theoretical development for stereo imaging is well-documented [3-4], the main difficulty in making accurate three-dimensional measurements lies in the application of the underlying theory. In fact, it is only recently that computer vision based 3-D measurements have been successfully used in the field of experimental mechanics [3-4]. One of the early correlation type measurement systems was developed by Luo et al[3]. It used an image correlation algorithm that (a) matched square subsets in one image to square subsets in another and (b) used this data to triangulate and estimate the three-dimensional displacement field. The lack of perspective correction in the matching process of this system limited the range of camera orientations that could be used for accurate image evaluation. The projection/back-projection method developed recently by Helm et al [4], known as VIC3D, overcame these limitations and extended the capability of this measuring method to a greater range of problems.

The VIC3D system can be broken down into two main parts. The first is calibration of the camera system. The second is digital image correlation for determining surface

deformations. A schematic of a typical VIC3D measurement system is presented in Figure 2. Brief descriptions of both the calibration and measurement components are presented below; greater detail is given in Reference 4.

3.1 SYSTEM CALIBRATION

Calibration of a two-camera computer vision system determines the relative positions and operating characteristics of both cameras. The calibration system is based on a series of images of a grid with known line spacing. Each camera is calibrated to the grid individually but, because the positions of the cameras are both known relative to the same grid, their relative position is also known.

The camera and lens system is modeled as a pinhole device. To increase the accuracy of the model, it has been modified to correct for Seidel lens distortion. The imaging characteristics of a camera modeled in this manner can be described by five parameters. The pinhole distance (phd) is the perpendicular distance from the pinhole to the sensor plane of the camera. This parameter can be considered the magnification factor of the lens. The location of the center of the image (C_x, C_y) is defined as the point on the sensor whose normal passes through the pinhole. The lens distortion factor, κ, is a correction for Seidel lens distortion. The final parameter is the aspect ratio, λ, of the sensors. The aspect ratio is the ratio of the size of a pixel in the Y direction to its size in the X direction.

Six parameters X_o, Y_o, Z_o, and α, β, γ are required to describe the relationship between the camera and the coordinate system of the calibration grid. The parameters, X_o, Y_o and Z_o describe the position in space of the grid relative to the camera and α, β, γ describe the angular orientation of the grid relative to the camera. To calibrate a camera, an image of the grid is taken. The camera is then moved perpendicular to its sensor plane and a second image is taken. Using (a) the known spacing of the grid, (b) the known movement of the camera and (c) the location of the grid intersections, as extracted from the calibration images, a non-linear optimization can be used to find the parameters that best describe the position and operating characteristics of the camera. The process is then repeated, without moving the grid, for the second camera.

3.2 VIC3D MEASUREMENTS

Once calibration is completed, the VIC3D stereo vision system can be used to measure both the shape of an object's surface (profiling) and it's full field, three-dimensional surface displacement measurements. The measurement system uses a random pattern bonded to the surface to provide a unique set of features to map from one camera to the other. If the surface has a naturally occurring random pattern, it may be used for the measurement.

3.2.1 *Profile measurements*

The projection method used for profiling uses a pair of images of the surface of the object acquired simultaneously by camera one and camera two. Assuming that the surface of an object can be modeled as a series of small planar patches, a small square section of the image taken by camera one is mathematically projected onto a candidate plane in space. The candidate plane is described relative to camera one by two of the plane's direction angles (Θ, Φ) and the location of the intersection of the plane and the

optic axis for camera one, (Z_p). Because the operating characteristics of camera one are known, the gray levels of the subset can be projected onto the candidate plane, creating a virtual gray level pattern in space. The virtual gray level pattern is then projected into camera two, creating a second virtual gray level pattern at the sensor plane of the second camera. A cross-correlation error function between the recorded gray level pattern from camera two and the virtual gray level pattern projected onto the second camera's sensor is used to obtain the optimal values for the candidate plane variables. Once the system has been optimized, the three dimensional position of that point on the surface of the object can be calculated from the camera one parameters and the position of the candidate plane.

3.2.2 *Displacement measurement*

The displacement measurement system is used to locate points on the surface of the object as it deforms. This measurement requires a set of images taken before the object is loaded (undeformed images) and a second set taken after the load was applied to the specimen (deformed images). The first part of the displacement measurement system is the same as that of the profile measurement system. An initial candidate plane is chosen and a virtual gray level pattern in space is established. As with the profile system, the virtual pattern is projected back into camera two. At this point, the virtual gray level pattern is allowed to translate and rotate in a rigid-body manner to a second position in space. The displaced virtual gray level pattern is then projected back to the sensor planes in cameras one and two. As with the profile system, a cross-correlation error function is established between the virtual gray level patterns at the sensor planes of cameras one and two and the recorded gray level patterns from the deformed images recorded by those cameras. Three error functions are simultaneously optimized, establishing both the position and displacement of the subset on the surface of the object. By continuing the analysis on other portions of the undeformed camera one image, the profile and displacements of the surface of the object for the entire field of view shared by both cameras is measured.

4. Application of 2D Vision System

Crack closure is a well-documented phenomenon that has been shown to have a strong effect on fatigue crack growth behavior. As first discussed by Elbers[5,6], crack growth in metallic materials results in an increase in the load at which a crack is fully opened. Numerical analyses have shown that the effect observed by Elbers can be predicted by including the presence of the plastic wake, which would be present along the crack flanks, as the crack grows. This effect, known as plasticity-induced closure, induces a deviation from the Paris law that can be modeled by using a modified $\Delta K_{closure.}$ One method for determining when the effects of crack closure have been eliminated is to measure the crack opening displacement (COD) at positions behind the crack tip. When the slope of the load-COD curve shows a large reduction during the loading portion of the load cycle, the crack is assumed to be fully open and the crack tip region experiences the full effect of the applied load.

In this work, a small 0.80mm square region around a crack tip was imaged using a far-field microscope objective was used to obtain the desired level of magnification. The specimen surface was polished and filtered Xerox toner powder was applied to the surface to obtain a high contrast random pattern with spot sizes of ~ 20 μm. The surface was

illuminated by an on-axis light source, further enhancing the contrast of the pattern. During the fatigue process, VIC2D software was used to obtain the displacements for subsets on opposite sides of the crack line so COD could be calculated

To quantify the accuracy of the system at this high level of magnification prior to performing the fatigue test, a simple tension test was performed using a dog-bone specimen. By measuring the relative displacements along the direction of loading for two sets of three 91X91 pixel subsets in a 0.5mm by 0.30mm area that were separated by 0.16mm, the value for strain along the loading direction was determined. By comparison of the VIC2D results to multiple strain gage readings, the standard deviation in strain was determined to be 200$\mu\varepsilon$. Thus, an estimate for the displacement error in the method is approximately 30 nanometers or 0.05 pixels at the magnification used in this work.

Using the sample preparation process described above, images were acquired over a 0.8mm square region just behind the crack tip during fatigue loading of an 8009 aluminum alloy specimen. The specimen was machined into an extended compact tension geometry with a width of 38.1mm, a thickness of 2.3mm and an a/w ratio of 0.54. During the test, ΔK = 6.6 MPa $m^{1/2}$ and the R-ratio was held constant at 0.10 throughout the test. Figure 3 presents the measurement of crack opening displacement as a function of cyclic load at distances of 0.075mm and 0.224mm behind the current crack tip. As indicated in Figure 3, the measured COD curves at both locations behind the crack tip clearly show a sharp change in slope, corresponding to the elimination of crack surface contact at each position behind the crack tip[7,8]. Furthermore the data shows that the load at which crack surface contact was eliminated at the free surface of the specimen is a function of position behind the crack tip.

5. Application of 3-D Vision System

As the current fleet of commercial, military, and private aircraft continues to age, and with many aircraft exceeding their original design life, techniques are being developed to aid in the evaluation of aircraft structures and materials. As noted previously, two-dimensional digital image correlation has been used for many years to accurately measure the in-plane displacements of planar structures under a variety of loads. Because aircraft components and typical aerospace laboratory test specimens deform in a complex manner when loaded, surface measurement systems must be able to make accurate measurements in three-dimensional space. For example, for wide, thin panels fabricated from 2024-T3 aluminum and subjected to tensile loading, the presence of a flaw in the structure will cause the panel to buckle out-of-plane during crack growth. For this case, the VIC-3D system is required for accurate determination of the full-field, 3-D displacements during deformation

All tests were performed at NASA Langley Research Center in Hampton, Virginia[9]. The wide panel geometry for the 2024-T3-aluminum panel is shown in Figure 4. The panel was tested in a 1.3mN tension test frame. The area imaged on the aluminum sheet was approximately 500mm wide by 260mm tall and was located just below the center crack, extending from one edge of the sheet past the centerline of the specimen. All tests were performed under displacement control. Images were acquired every 8.9kN until crack growth occurred. After initial crack growth, images were acquired at intervals of approximately 4mm of crack growth until final fracture

The load-crack extension data is shown in Figure 5. As can be seen in the Fig. 5, crack growth began at 150kN and continued in a stable manner up through the

maximum load of 269kN until unstable crack growth fractured the panel at a load of 241kN.

Figure 6 presents contour plots for all three components of displacement for a load of 240.2kN, which was just before final fracture. Figure 7 presents the out-of-plane displacement for a horizontal line Y= -25mm, below the crack line for various load levels. As shown in Figure 7, the buckling of the panel continued to increase as the crack grew, reaching a maximum of 25mm just before failure. Furthermore, inspection of Figures 6 and 7 indicate that the edge of the panel appears to be flat during loading, with the centerline region showing increased buckling. This observation suggests that load transfer into the remaining ligaments during crack growth tends to flatten these areas.

6. Conclusions

Computer vision methods capable of determining either the in-plane deformation for planar objects undergoing in-plane loading (VIC2D) or the full, three-dimensional surface displacement field for curved or planar objects undergoing general loading conditions (VIC3D) have been developed. Application of the methods to a wide range of problems has shown that both methods are accurate and robust.

7. Acknowledgments

The authors wish to thank Dr. Charles E. Harris and Dr. James C. Newman, Jr. in the Mechanics and Materials Branch at NASA Langley Research Center for their faith in our measurement technology. Through their unwavering technical and financial assistance, the potential of the VIC3D method is now being realized.

8. References

[1] Sutton MA, Bruck HA, McNeil1 SR (1989) "Determination of Deformations Using Digital Correlation with the Newton-Raphson Method for Partial Differential Corrections," *Experimental Mechanics* **29** (3), 261-267.

[2] Chu TC, Ranson WF, Sutton MA, Peters WH (1985) "Applications of Digital Image Correlation Techniques to Experimental Mechanics," *Experimental Mechanics* **25** (3), 232-245.

[3] Luo PF, Chao YJ, Sutton MA (1993) "Computer Vision Methods for Surface Deformation Measurements in Fracture mechanics, *ASME-AMD Novel Experimental Methods in Fracture* **176,** 123-133.

[4] Helm JD, McNeil1 SR, Sutton MA (1996) "Improved 3-D Image Correlation for Surface Displacement Measurement," *Optical Engineering,* 35[7], 1911-1920.

[5] Elber W (1970) "Fatigue Crack Closure Under Cyclic Tension", *Engineering Fracture Mechanics* **2,** 37-45.

[6] Elber W (1971) "The Significance of Fatigue Crack Closure", *ASTM STP 486,* 230-242.

[7] Sutton MA, Zhao W, McNeil1 SR, Helm JD, Riddell W, Piascik RS (in press) Local crack closure measurements: Development of a measurement system using computer vision and a far-field microscope," *ASTM STP 1343,* Advances in Fatigue Crack Closure Measurements and Analysis **2.**

[8] Riddell W, Piascik RS, Sutton MA, Zhao W, McNeill SR, Helm JD (in press) Determining fatigue crack opening loads from near-crack-tip displacement

Measurements," *ASTM STP 1343,* Advances in Fatigue Crack Closure Measurements and Analysis **2.**

[9] Helm JD, Sutton MA, McNeill SR (1997) "Three-Dimensional Computer Vision Applications for Aircraft Fuselage Materials and Structures," 1st Joint DoD/FAA/NASA Conference on Aging Aircraft in Ogden, Utah.

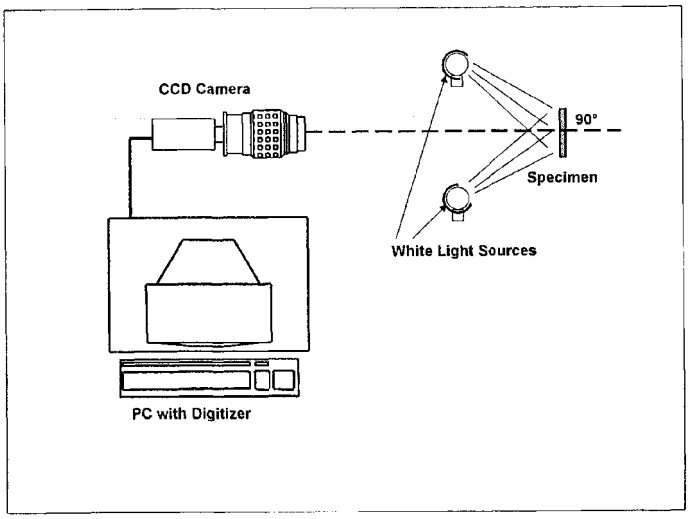

Figure 1. Typical VIC2D setup.

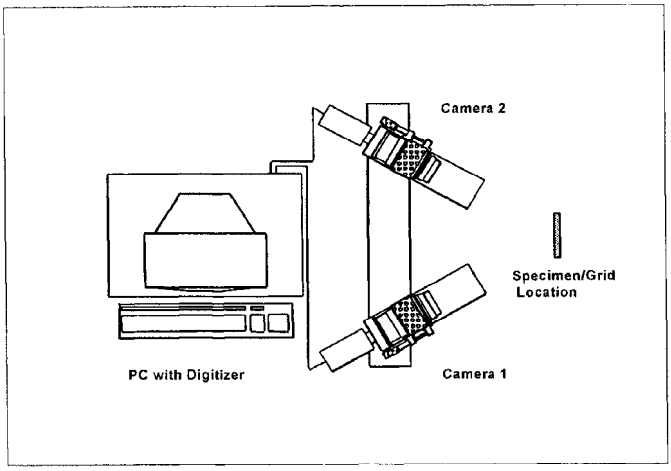

Figure 2. Typical VIC3D setup.

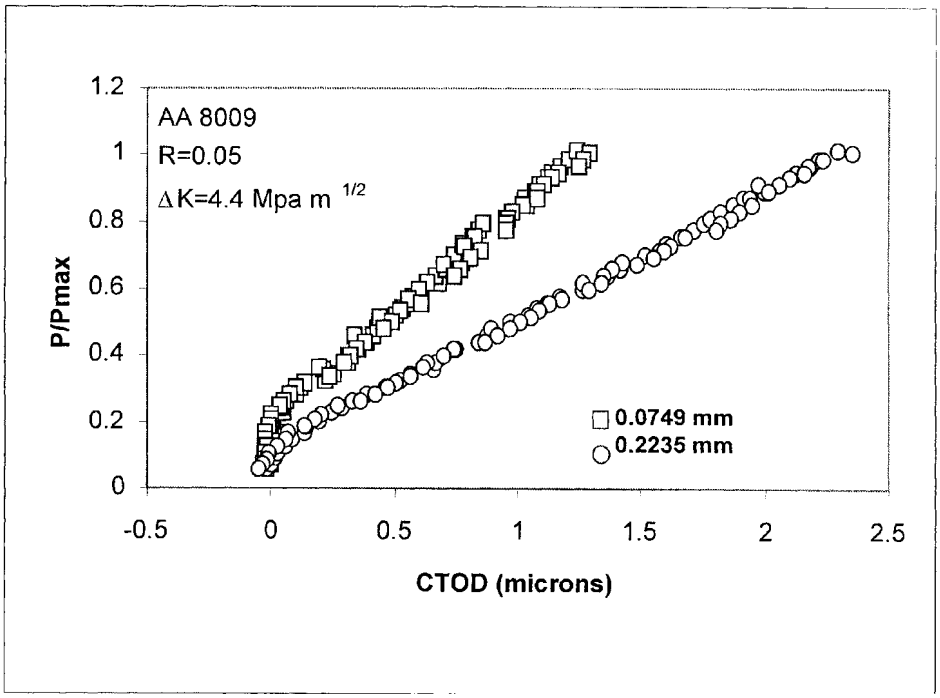

Figure 3. CTOD vs. Load for two distances behind the crack tip.

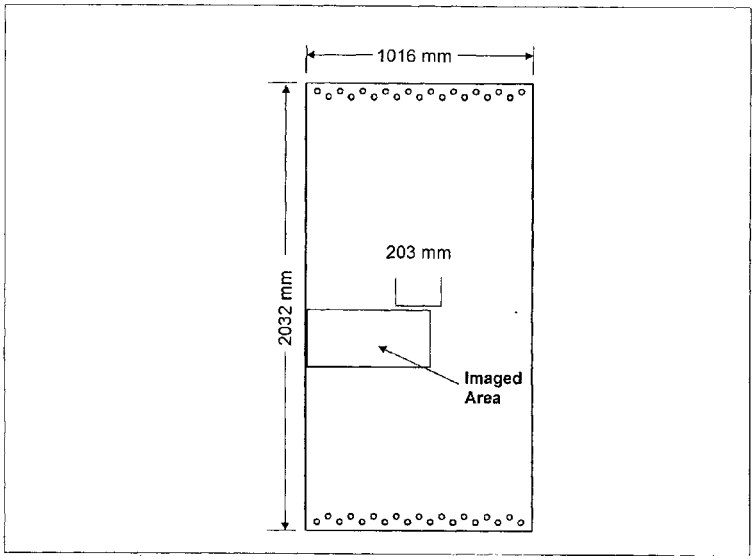

Figure 4. Wide panel geometry.

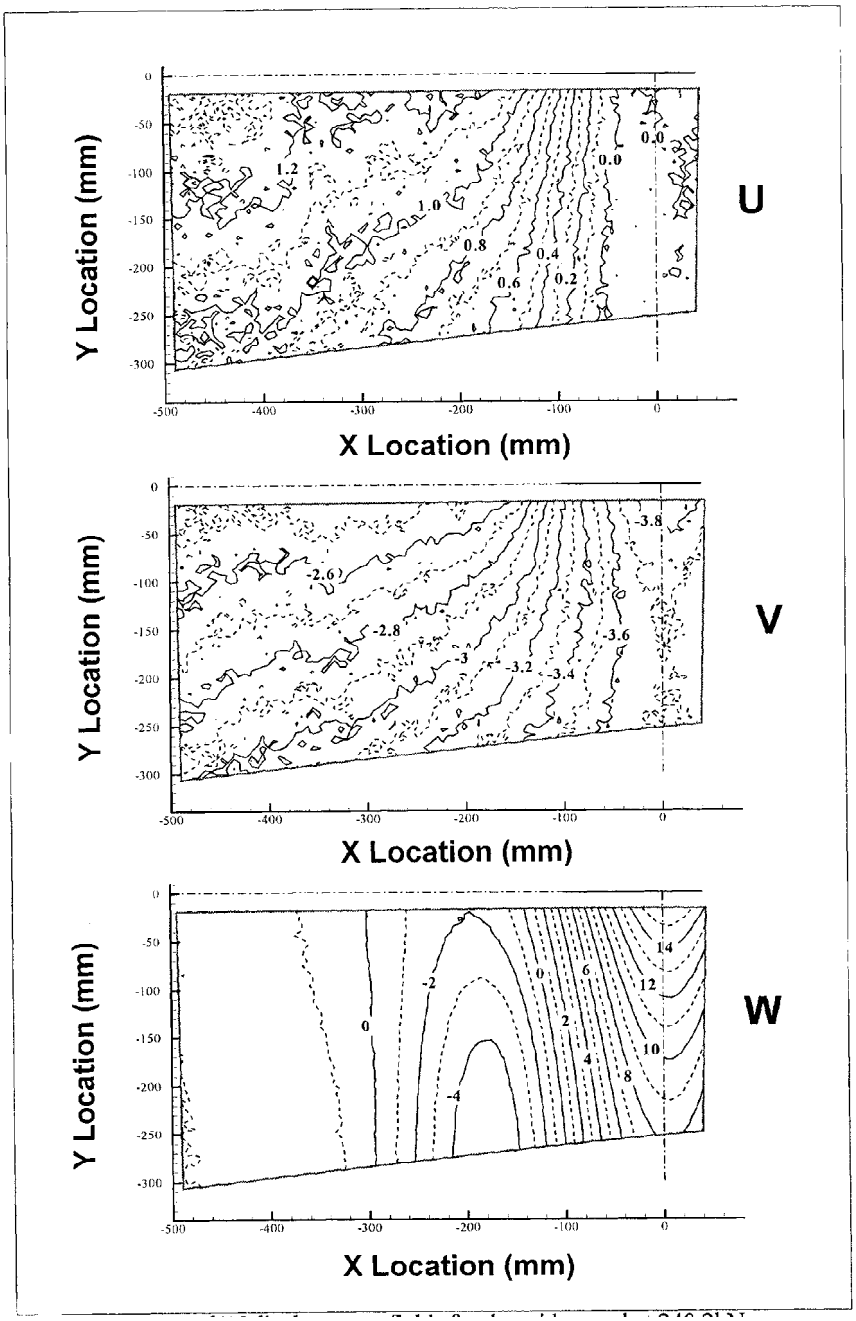

Figure 6. U, V and W displacement fields for the wide panel at 240.2kN

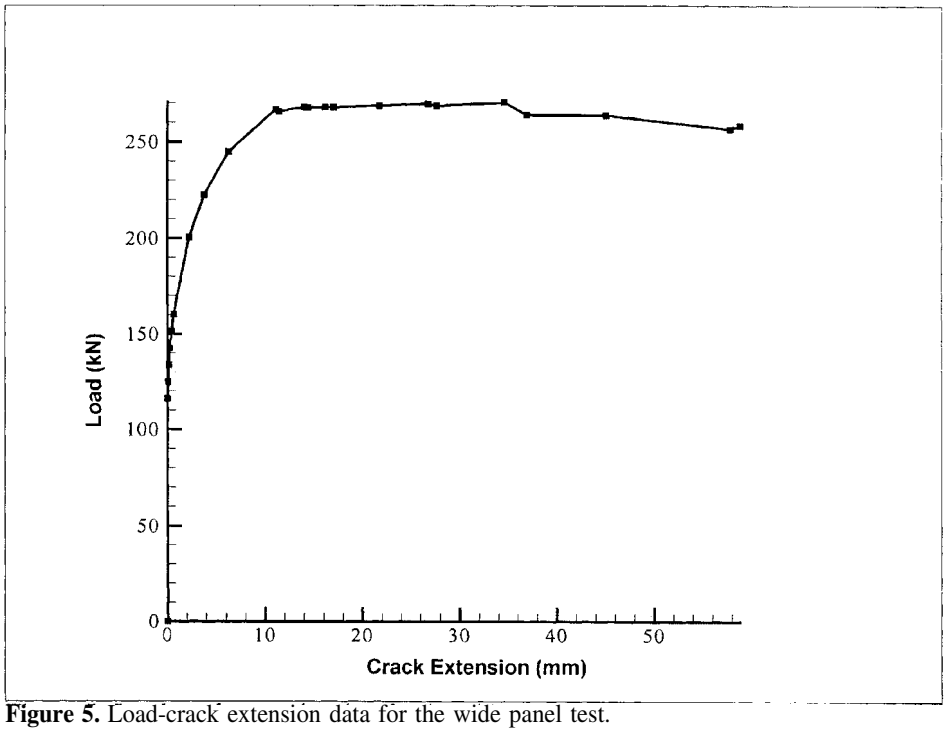

Figure 5. Load-crack extension data for the wide panel test.

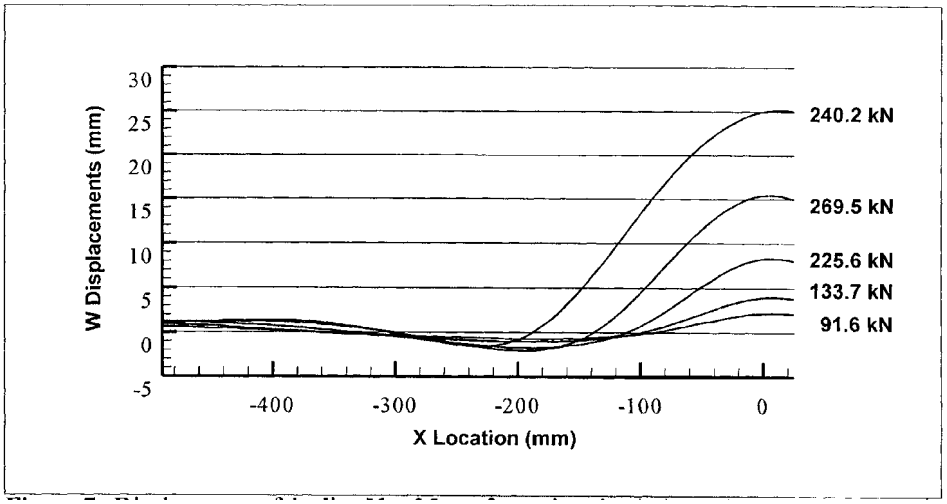

Figure 7. Displacement of the line Y= -25mm for various loads for wide panel test

COHERENT-OPTICAL STUDY OF CRACK PROPAGATION IN POLYMER PIPES AFTER IMPACT

P. BOONE, P. VAN SPEYBROECK, J. DEGRIECK, B. VERHEGGE
Department of Applied Mechanics, University Gent
Sint PIETERSNIEUWSTRAAT 41, B9000 Gent, Belgium

V. MARKOV
Institute for Applied Optics, Ukraïnian Academy of Siences
Kudryavskaya Street, Kiev, Ukraïne

1. Summary.

Several studies have been conducted that involved full scale investigation of rapid crack propagation (RCP) in polyethylene (PE) pipes. Greig & Ewing[1] showed that the critical pressure in a plastic pipe, which governs RCP, is very sensitive to temperature and that stringent controls on operating and proof test pressures are required for large diameter PE pipes.
Leevers[2] and Yayla[3] demonstrated with the S4 (Small Scale Steady State) test excellent correlation with the full scale test on smaller diameter pipes.
Vanspeybroeck [4] changed the S4 into the S5 (Small Scale Steady State Scum) test to avoid any decompression in the pipe sample and to simulate full scale testing. In this paper, we present some preliminary results of testing aided by holographic interferometry to determine stress fields associated with RCP.

Keywords : *holographic interferometry, destructive testing, crack propagation, polymers.*

2. Holographic investigation of stress fields associated with the different RCP testing methods.

In order to try to gain some insight into the stresses associated with running cracks in different test conditions, and in subsidiary order to get some information about crack oscillation and branching, a series of holographic experiments has been conducted (and are still in progress) on a number of different pipes using the experimental conditions described earlier.

A. Lagarde (ed.),
IUTAM Symposium on Advanced Optical Methods and Applications in Solid Mechanics, 581–586.

Due to the rapidity of the phenomena involved, double-pulsed holography was the only candidate for recording the interferograms. Methods based on phase shifting, with multiple reference and/or multiple "deformed" recording, are not applicable as the (large) specimen would distort somewhat (interferometrically speaking) between the successive exposures.

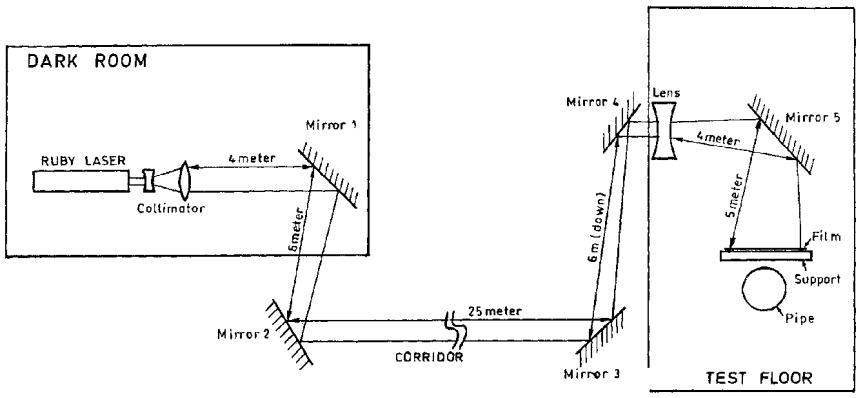

Fig.1. Schematic of set-up.

In a first stage and as a result of the relatively "explosive" nature of the tests, the idea of recording close range transmission types of holograms, requiring a relatively elaborate set-up quite near to the phenomena under study, was abandoned; heterodyne interrogation also had also to be dismissed.

We therefore relied on one of the simplest holographic recording schemes based on the Denisyuk set-up, combined with pointwise methods of interrogation for producing the raw displacement data.

Although those methods are quite cumbersome and may give rise to some uncertainties in describing the direction of the different displacement components, they have the advantage that they yield the orthogonal displacement components. As an example we show the sequence of operations for a relatively normal S4 test.

The set-up of the recording of the holograms (Fig.1) involves a double-pulsed ruby laser (typically a 2x1 Joule HLS2 System of Sumitomo, formerly Lumonics, itself formerly JK Lasers) at this moment Innolas used at about 50 m (linear) distance. Due to local circumstances, this optical distance had to be realized using four front surface mirrors, the last one resting on a ladder on top of the specimen. The recording medium was placed at about 15 mm distance from the top side of the tube on a thick (25 mm) perspex sheet, independently from the tube surface, in order to avoid phenomena due to shock waves or propagation of sound on air pressure differences.

A typical resulting fringe pattern is shown in Fig.2 for a test conducted on a 250 mm PE pipe, wall thickness 22 mm, laser triggered by a crack gauge located at 150 mm from the initiation point; the hologram centre was located at 150 mm "downstream" from the trigger wire. The interval between pulses was regulated to 3 μs, typically with a jitter of about 0,03 μs.

Out-of-plane displacements were derived directly from the photograph of the fringes and in- plane displacements from point-to-point fringe counting measurements. From these "exact" but pointwise measurements, displacement surfaces were derived using cubic-spline approximations; combining the results of derivatives of these surfaces one finally finds strain fields, and one can translate this to stress field using Hooke's equations. It has to be re-emphasized that these values are related to a 3 μs propagation of the crack, so they should be "convoluted" with the crack propagation phenomena to explain the stress behaviour at a point of the material.

On the other hand, one sees some kind of asymmetry in the displacement field as shown in Fig.2. Quite surprisingly (or perhaps not) the "hills" on the figure are related to the oscillating propagation mode of the crack after completion of the test.

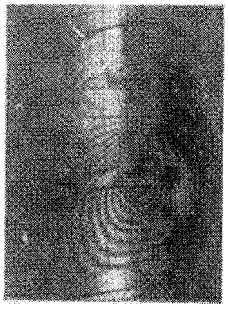

Fig.2. Reflection holographic fringe pattern.

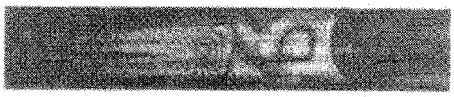

Fig.3. Transmission hologram of out-of-plane displacements.

In a second series of experiments, transmission type of holography was used from a relatively large distance (typically 2m), giving only information about out-of-plane displacements. A typical example of this is shown on Fig.3.

3. Propagation of displacements induced by impact.

Another interesting aspect which needs further clarification is the interaction of the stress field due to the running crack and displacement due to the vibrational modes introduced by the crack initiating instrument. It is indeed possible that the vibrations induce another stress field, and that the interaction between the two gives rise to typical sinusoidally oscillating crack propagation (that can also be observed in steel pipes, in ductile fractures of rubber hose pipes and even in some cracks propagating from the hull of ice-breaking ships in large Russian lakes). It is our feeling that the oscillating nature of these cracks is related to the varying biaxial stress field.

In order to try to gain some insight into the nature of displacement introduced in a large plastic pipe by a striking mass, a number of experiments were effected on a 6000-mm-long, 110-mm-diameter, 12-mm-thick HDPE tube simply supported on two concrete blocks 200mm wide and 4500mm apart. The impact was realized by a pendulum consisting of a 498N copper cylinder suspended by a 2300-mm-long nylon rope, impacting the tube at the middle of the span with different speeds, that could be altered by changing the starting height of the pendulum. The mechanical contact between striker and tube triggered the first laser pulse after impact; the second pulse was set at different intervals. Eventually, a delay line was installed to obtain greater retardation. An accelerometer gauge was installed 120mm from the impact point, along the same axial descriptix; each experiment was repeated three times to check the results.

As the reflection coefficient of PE is very low, the tube was painted with retroreflective paint (3M Scotchlite 831); the light from the laser was spread along the axial direction of the tube by introducing a (hand-) curved mirror in the illumination beam, essentially a normally polished stripe of yellow copper. This time, the set-up used was of the transmission type and the hologram recording site was very close to the curved mirror to optimize the efficiency. Some typical results of a series of more than 200 recordings are shown in Figure 4.

Fig.4. Displacements due to impact loading.

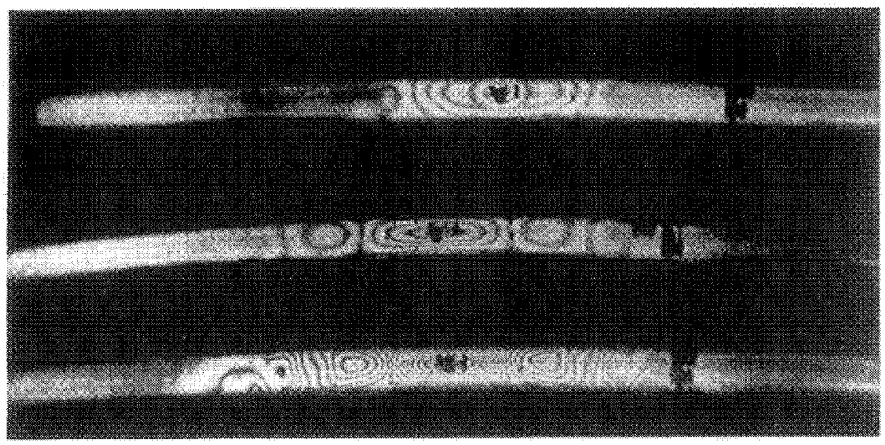

Pictorally, the results are quite rewarding; from a theoretical viewpoint, however, they are still not fully understood. In our opinion, there are a number of (probably interactive) non-linear parameters to be considered; the elasticity modulus E is a function of the impact speed and magnitude, the oscillation resonance frequency is a function of E, and the damping of the vibration is a function of the frequency.

We hope that a number of these topics will be investigated more extensively and covered in further reports on the subject.

4. Discussion and Conclusions.

Investigations on the displacement behaviour of plastics pipes subjected to rapid crack propagation and their interpretation have been presented. Some experimental details need optimization to yield results useful for common practice.Nevertheless, the holographic technique allows one to see phenomena that otherwise would have been unnoticed; on the other hand, some indications about displacement, stress and strain fields associated with RCP are gathered.

5. Acknowledgements.

The work reported here was supported by the Belgian National Foundation for Collective Fundamental Research through grants 2900878, 2001275 and 2004486; the first author also gratefully acknowledges the personal grant placed at his disposal by the National Science Foundation to study reflection hologram optimization.

6. References.

[1] Greig J.M. and Ewing L., "Fracture propagation in polyethylene gas pipe". Plastic pipe V, York, UK, September 1982.

[2] Leevers P.S. and Yayla P., "A new small scale test for rapid crack propagation". Proc. Eleventh Plastic Fuel Gas Pipe Symp., San Francisco, CA, October 1989.

[3] Yayla P., "Rapid crack propagation in polyethylene gas pipes". Ph.D. Thesis, University of London, Dept. of Mechanical Engineering, Imperial College of Science, Technology and Medicine, London, January 1991.

[4] Vanspeybroeck P., "Evaluation of test methods for determining rapid crack propagation propertiers of pressurized polyethylene gas pipes". Int. Conf. on Pipeline Reliability, Calgary, Alberta, Canada, June 1992.

STRESS FIELD MEASUREMENT AT BIFURCATION OF FAST PROPAGATING CRACKS BY HIGH-SPEED INTERFEROMETRY

S. SUZUKI, I. INAYAMA, N. ARAI and T. MIZUTA
Dept. Mechanical Engineering, Toyohashi University of Technology
Tempaku-cho, Toyohashi, 441-8580 Japan

Abstract

Interferometry with high-speed holographic microscopy is applied to investigate stress field near fast propagating crack tips at the instant of crack bifurcation. It is found that, at the instant of bifurcation, the stress field in the vicinity of fast propagating crack tips deviates from the singular stress field of the dynamic fracture mechanics. Such deviation is due to the existence of bifurcated crack tips.

1. Introduction

When brittle materials are broken by external force, fast propagating cracks often appear, whose speed of propagation is at several hundred m/sec or more. If the crack speed is high enough, a fast propagating crack bifurcates into two or more cracks.

Bifurcation is a characteristic feature of fast propagating cracks, accordingly, many researchers have tried to figure out the bifurcation mechanism [1]-[4]. However, the bifurcation mechanism has not been clearly understood yet, because many difficulties exist in experimental studies on dynamic fracture phenomena.

Recently, Suzuki developed high-speed holographic microscopy which can take three successive microscopic photographs of fast propagating cracks [5]-[8]. High-speed holographic microscopy has the spatial resolution of about 180 lines/mm, which is much higher than the other optical methods used for dynamic fracture research. High-speed holographic microscopy can therefore measure the stress field in the vicinity of fast propagating crack tips with very high accuracy.

The present study applies interferometry to measure stress field in the neighborhood of fast propagating crack tips. High-speed holographic microscopy is utilized to photograph the cracks, their bifurcation process and interference fringes with high spatial resolution. And it is found that, at the instant of bifurcation, the stress field in the vicinity of crack tips deviates from the singular stress field of the dynamic fracture mechanics. Such deviation occurs not only after bifurcation but just before bifurcation.

A. Lagarde (ed.),
IUTAM Symposium on Advanced Optical Methods and Applications in Solid Mechanics, 587–594.

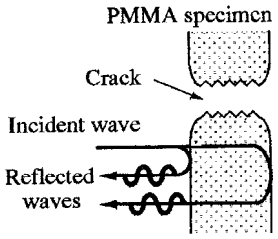

Fig. 1 Principle of Interferometry.

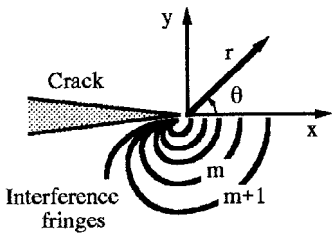

Fig.2 Crack, fringes and coordinates

2. Experimental Method

The present study uses transparent PMMA specimens with 3mm in thickness. A crack of the opening mode propagates rapidly in a specimen and bifurcates into two or more cracks in the observation area in the specimen.

2.1. INTERFEROMETRY

Figure 1 shows the principle of interferometry to measure stress field near crack tips. A crack propagates perpendicularly to the paper plane. An parallel light beam impinges upon specimen surfaces perpendicularly, and is reflected either by the front surface or by the back one of the specimen. The two reflected light waves interfere with each other and interference fringes appear around the crack tip. The interference fringes are contours of the thickness and refractive index of the specimen, consequently, they represent the contours of the sum of principal stresses.

The dynamic fracture mechanics says that there exists the singular stress field around fast propagating crack tips [9]. Using the formula for the singular stress field, one can obtain the following equation about $\partial m/\partial r$ as a function of r and θ,

$$\frac{\partial m}{\partial r} = A\, K_I(v) r^{-3/2} f(\theta, v) F(v) \qquad (1)$$

where m is the fringe order, r is the distance from the crack tip, θ is the angle measured from the crack propagation direction (Fig.2). And A is a constant, v is the crack speed, $K_I(v)$ is the dynamic stress intensity factor, $f(\theta,v)$ describes the circumferential variation of the stress field and F(v) expresses the dynamic effect. When you measure the crack speed v and $\partial m/\partial r$ at a certain position (r,θ) in the singular stress field, you can obtain the dynamic stress intensity factor $K_I(v)$ through the above equation.

Here it must be noticed that if $\partial m/\partial r$ is measured within the singular stress field of plane stress, the $\partial m/\partial r$ measurements always give the unique value of $K_I(v)$. But if the singular stress field does not exist around a crack tip, the $\partial m/\partial r$ measurements at different positions give different K values. Therefore, by measuring $\partial m/\partial r$ at some different positions, one can examine whether the singular field is developed or not.

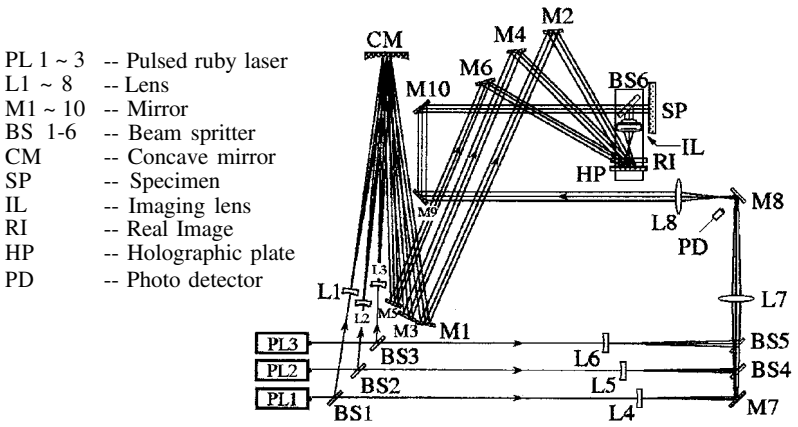

Fig.3 The optical system for high-speed holographic microscopy.

2.2. HIGH-SPEED HOLOGRAPHIC MICROSCOPY [5]-[8],[10]

Figure 3 shows the optical system for holographic recording of fast propagating cracks, in plan view [10]. A crack propagates in the specimen SP perpendicularly to the paper plane. When the crack is propagating in the observation area, the three pulsed ruby lasers oscillate successively in the order of PL1, PL2 and PL3. The three laser pulses record the crack as the first, the second and the third hologram, respectively. The frame interval is 1μ sec or more.

The light beam emitted from ruby laser PL1 is divided into two parts by beam splitter BS1. The reflected light beam from BS1 is diverged and collimated, and falls upon the holographic plate HP obliquely. This is the reference beam for the first hologram. The light beam transmitted through beam splitter BS1 is reflected by mirror M7, and passes through beam splitters BS4 and BS5. The light beam becomes a parallel light beam, passes through beam splitter BS6 and falls upon the specimen surfaces perpendicularly. The light beam is reflected either by the front surface or by the back one of the specimen, and makes interference fringes on the specimen. The reflected light from the specimen is reflected by beam splitter BS6, passes through imaging lens IL and impinges on the holographic plate perpendicularly; This is the object beam. The object beam is recorded as the first hologram.

The second and the third holograms are recorded similarly. The angles of incidence of the reference beams for the three holograms are different from one another, and the three holograms are superimposed on one holographic plate. That is the angle-multiplexing holography.

At reconstruction, each hologram reconstructs separately the crack image and interference fringes at the position where the specimen existed, at the recording. The reconstructed images are photographed through a conventional microscope.

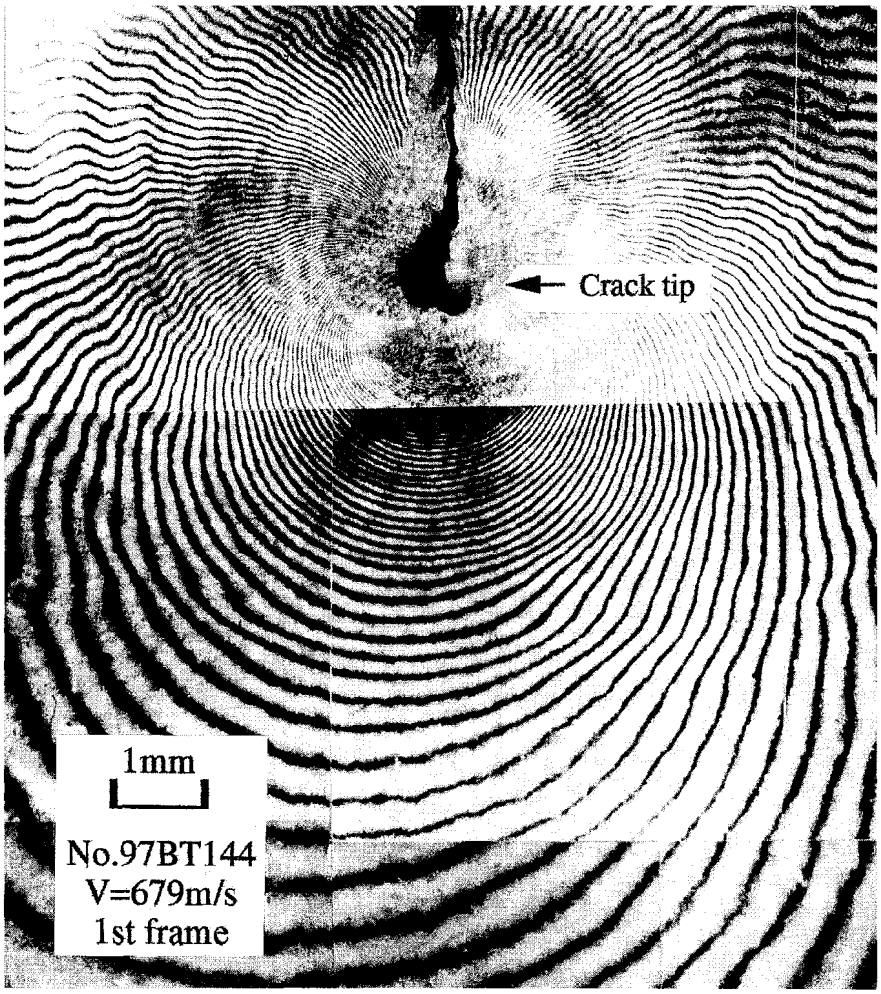

Fig4(a) A fast propagating crack at 3.1μsec before bifurcation. The first frame.

3. **Results and Discussions**

3.1. MICROSCOPIC PHOTOGRAPHS OF CRACK BIFURCATION

Figure 4(a), (b) and (c) show microscopic photographs of a crack at bifurcation. The crack is of the opening mode and was propagating in a PMMA plate specimen at a speed of 682m/sec. The frame interval was about 4.8μsec. The first frame in Fig.4(a) was photographed at 3.1μsec before the bifurcation. The second and the third frames in Fig.4(b) and (c) were taken at 1.8μsec and at 6.5μsec after the bifurcation, respectively.

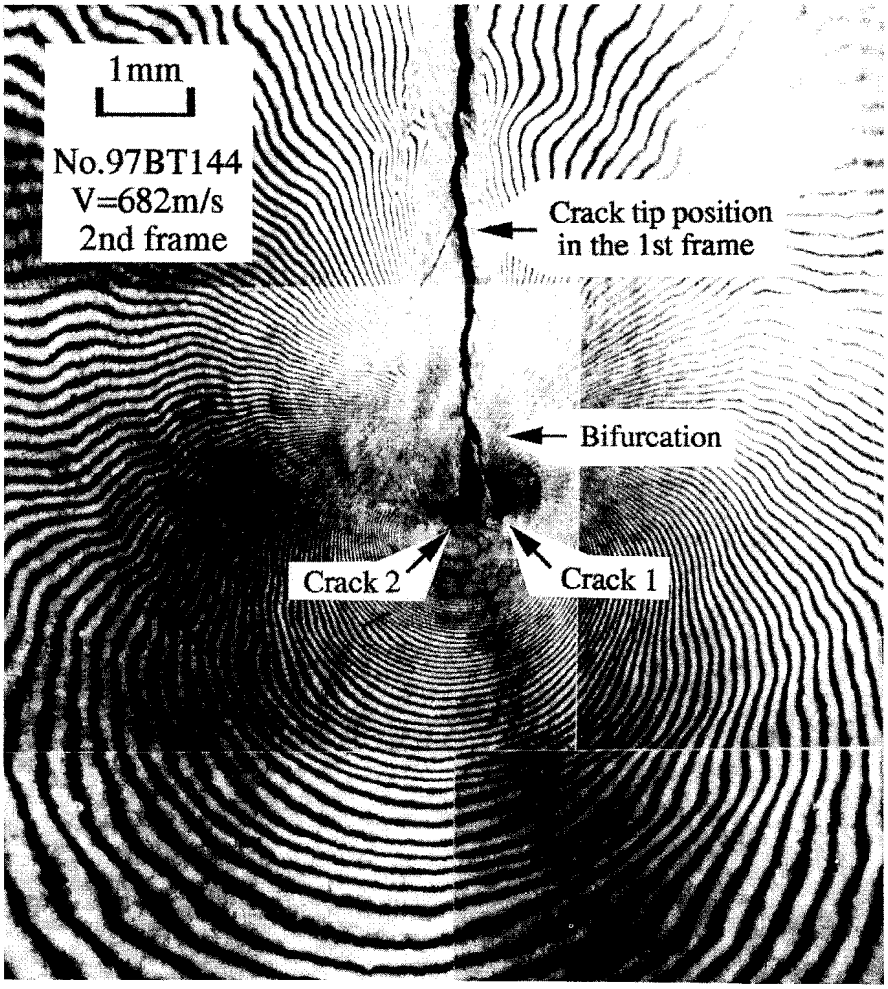

Fig.4(b) The fast propagating crack at 1.8μ sec after bifurcation. The second frame.

At first the crack bifurcated into two cracks, Crack 1 and Crack 2. Then Crack 2 bifurcated into Crack 3 and Crack 4. At the right of Crack 1 in the third frame, you can find a crack which has stopped propagating.

One can see many fine interference fringes around the crack tips. Stress field around the crack tips can be examined through the fringe analysis described in the previous section.

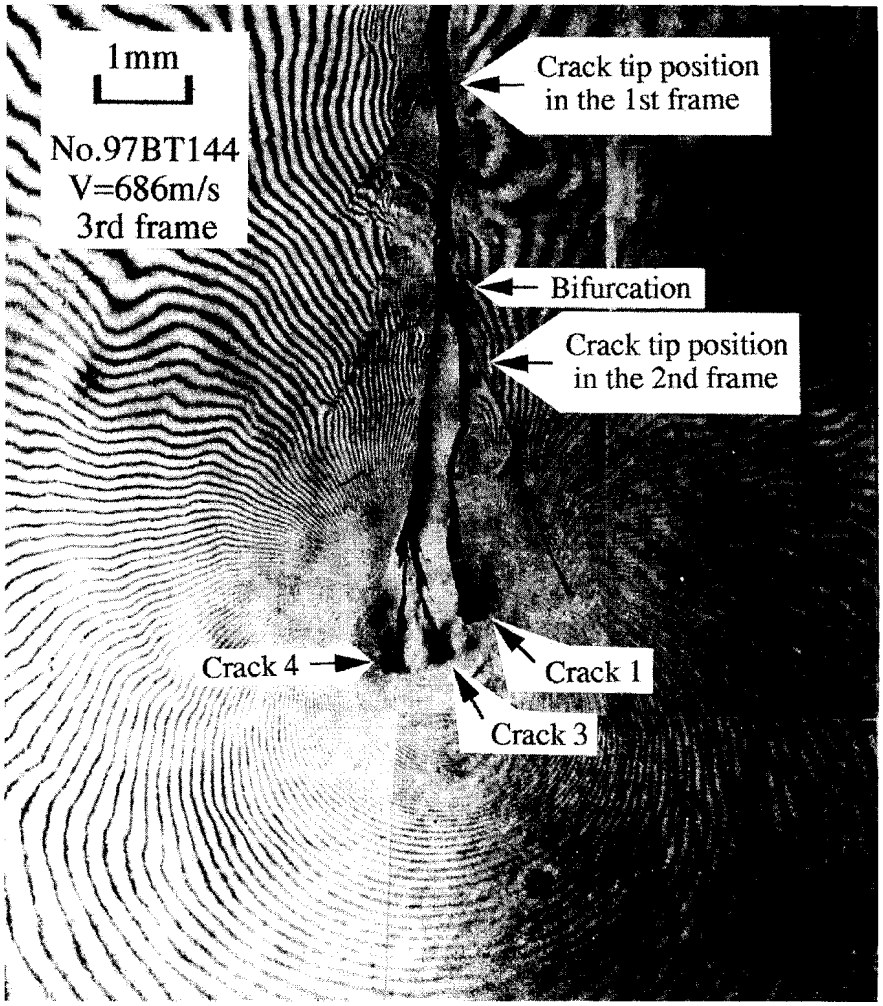

Fig.4(c) The fast propagating crack at 6.5μsec after bifurcation. The third frame.

3.2. NEAR-TIP STRESS FIELD AT BIFURCATION

Figure S(a), (b) and (c) show the results of fringe analysis of the photographs shown in Fig,4(a), (b) and (c), respectively. The horizontal axis indicates the distance r from a crack tip, and the vertical axis indicates the K value obtained from the $\partial m/\partial r$ measurement through Eq.(1). The $\partial m/\partial r$ measurement was carried out in the direction of $\theta=0°$, $\pm 72°$ and $\pm 90°$. As mentioned in the previous section, the K values must be constant if the measurement is carried out within the singular field of plane stress.

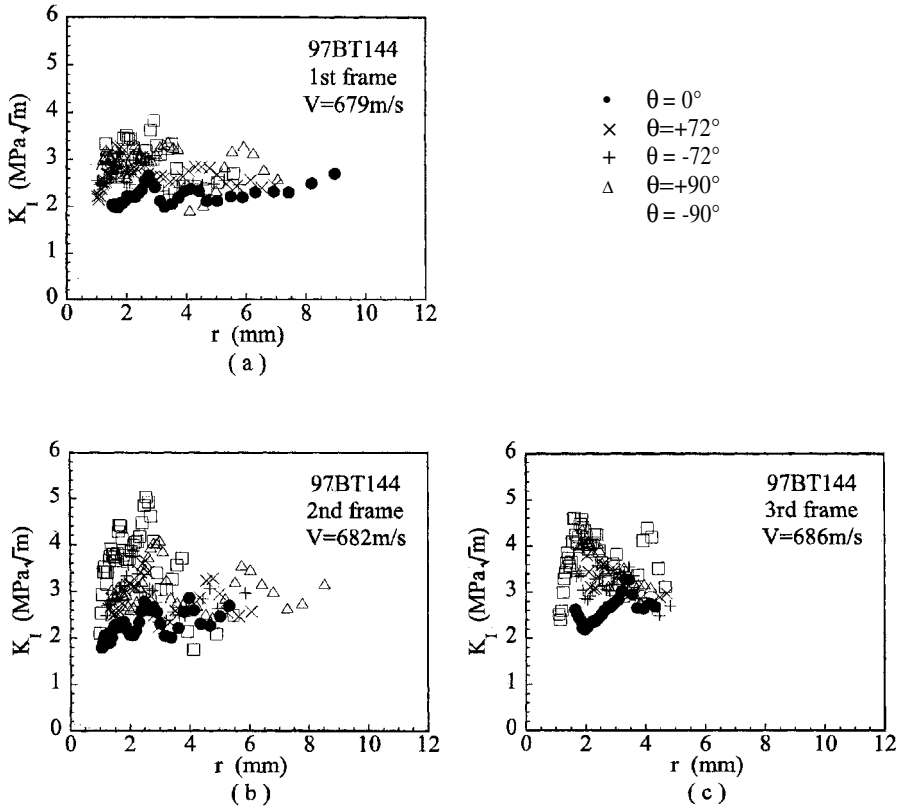

Fig.5 The dynamic stress intensity factor measured by interferometry. (a) At 3.1μ sec before bifurcation. (b), (c) At 1.8μsec and 6.5μsec after bifurcation.

3.2.1. *Near-Tip Field after Bifurcation*

Figure 5(b) and (c) show that, the K values in the direction of θ=±72° and ±90° are larger than those in the direction of θ=0 in the region of r, 1.5mm<r<4mm. This fact means that the K field does not exist in the region, 1.5mm<r<4mm. Figure S(b) and (c) show the results on the stress field after bifurcation, where there are two or more crack tips. The singular stress field of the dynamic fracture mechanics is for cracks whose tips are not bifurcated. The devision of the near-tip field from the singular stress field is caused by the bifurcated crack tips shown in Fig.4(b) and (c).

3.2.2. *Near-Tip Field before Bifurcation*

The most interesting thing in the measurement results is that the near-tip field deviates from the singular field in the region of r, 1.5mm<r<4mm, not only after bifurcation

but also before bifurcation (Fig.5(a)). This may be caused by microcracks and attempted branches which appear near a crack tip just before bifurcation.

Reflection type high-speed holographic microscopy can observe specimen surfaces only. Thus it can find microcracks and attempted branches on specimen surfaces, but cannot find those inside specimens. The deviation of the near-tip field from the singular field measured before bifurcation may be due to microcracks and attempted branches which were not photographed in Fig.4(a), but existed within the specimen. It has been reported that many attempted branches appear near crack tips just before bifurcation, and were photographed by high-speed holographic microscopy [10].

4. Conclusions

(1) Interferometry with the reflection type high-speed holographic microscopy can measure the stress field in the vicinity of crack tips at the instant of crack bifurcation.
(2) At bifurcation, the stress field in the vicinity of crack tips deviates from the singular field which exists near un-bifurcated crack tips. Such deviation occurs not only after bifurcation but also just before the bifurcation.
(3) The deviation just before bifurcation may be caused by microcracks and attempted branches which appear near crack tips just before bifurcation.

Acknowledgement
The present study was supported by Grant-in-Aid for Fundamental Scientific Research (09650097) of The Ministry of Education, Science and Culture. One of the authors, S.Suzuki, expresses his gratitude for the grant.

References

1. Yoffe,E.H.: The moving Griffith crack, *Phil. Mag*. **42** (1951), 739-750.
2. Baker,B.R.: Dynamic stresses created by a moving crack, *Trans. ASME, J.Appl.Mech*. **29** (1962), 449-458.
3. Ravi-Chandar,K. & Knauss,W.G.: An experimental investigation into dynamic fracture: **III**. On steady-state crack propagation and crack branching. *Int. J. Fracture*. **26** (1984), 141-154.
4. Ramuru,M. & Kobayashi,A.S.: Mechanism of crack curving and branching - a dynamic fracture analysis. *Int. J. Fracture*. **27** (1985), 187-201.
5. Suzuki,S. et al.: Optical measurement of stress waves and rapid crack propagation in the time domain of microseconds, in B.L.Karihaloo, Y-W.May, M.I.Ripley and R.O.Ritchie (eds.), Advances in Fracture Research, Proc. 9th Int. Conf. Fracture,Vol.6, Pergamon, (1997), 2925-2932.
6. Suzuki,S. et al.: High-speed holographic microscopy for fast propagating cracks in transparent materials, *Appl. Opt.* **36** (1997), 7224-7233.
7. Suzuki,S. et al.: Application of high-speed holographic microscopy to study on rapid crack propagation, in D.L.Paisley and A.M.Frank (eds.), *Proc. 22nd Int. Cong. High-Speed Photography and Photonics,* SPIE Vol.2869, (1997), 644-650.
8. Suzuki,S. et al.: Resolution of high-speed holographic microscopy for photographing fast propagating cracks. *Proc. Int. Conf. Advanced Technology in Exp. Mech:*, The Japan Society of Mechanical Engineers, Tokyo, (1997), 267-272.
9. Freund,L.B.: Dynamic fracture mechanics, Cambridge University Press, Cambridge, 1990.
10. Suzuki,S. et al.: Reflection type high-speed holographic microscopy to photograph crack bifurcation, *Proc. 11th Int. Conf. Experimental Mechanics,* Oxford, UK, August, Vol.1, Balkema (1998), 583-588.

OPTICAL INVESTIGATION OF A CONNECTING-ROD BIG END BEARING MODEL UNDER DYNAMIC LOADS

V. OPTASANU, D. BONNEAU
Laboratoire de Mécaniques des Solides, CNRS UMR 6610, SP2MI, Bd. 3, Téléport 2; BP 179, 86960 Futuroscope Cedex, France

Abstract
A new experimental device used for optical investigations of transient elastohydrodynamic behaviour of connecting-rod big end bearing models is presented. Photoelasticity method and digital image correlation method are used in order to visualise isochromatic fringe patterns and, respectively, displacement field. Validation of recording methods in dynamic regime are made. An isochromatic fringe pattern of the whole bearing is reconstructed using images taken for different regions of the model. An example of displacement visualisation of the interface cap/body of the bearing is presented

1. Introduction

Connecting-rod is a machine element the study of which is difficult due to its hard function conditions: high loads and velocities as well as dynamic loads. This is one of the reasons why there are few experimental studies. On the other hand, elastohydrodynamic numerical studies are well developed. There are many phenomena which make interpretation and modelisation very difficult. One of these phenomena arises because the body has two elements: connecting-rod cap, and body.

A set of experiments in real cases was carried out to measure lubricant film thickness, bearing and shaft. temperature (Bates et al., 1990) using methods other than optical. Numerical studies were done to simulate the elastohydrodynamic behaviour of connecting-rod big end bearings. Bonneau et al. (1995) published a finite element based algorithm for calculating the elastohydrodynamic (EHD) behaviour of the bearings, with application to the connecting-rod.

Photoelastic models of connecting rod big end bearings have been already used (Pierre-Eugène et al., 1982) for the study of the elastic behaviour of the bearings under static loads.

A new set of experiments based on optical methods is proposed here. In order to study the elastohydrodynamic behaviour of the connecting-rod big end bearing, models have been used. An experimental device has been realised. Materials with low Young modulus have been chosen to simulate the elastic behaviour of actual connecting-rod bearings. In order to respect the relative importance of the real phenomena, similarity

A. Lagarde (ed.),
IUTAM Symposium on Advanced Optical Methods and Applications in Solid Mechanics, 595–602.

conditions have been respected for the range of the applied loads and velocities, as well as for the geometric parameters of the model. A CCD progressive camera piloted by a PC provides the image acquisition and processing. The camera follows the movement of the connecting-rod, and takes images during the whole cycle at the same point of the connecting-rod.

Hydrodynamic pressure, generated by the rotation of the shaft, produces deformation of the housing. Studying this deformation, we can obtain information about the pressure field in the bearing. In the present study, bidimensional photoelasticity and digital image correlation methods have been used to visualise isochromatic fringe patterns and, respectively, deformations of the model. The interface between the connecting-rod cap and body is of particular interest.

Optical results are to be combined with temperature and lubricant film pressure data in order to complete the description of the phenomena produced in the model.

The present study provides various observations which may lead to a better understanding of EHD phenomena in connecting-rod bearings under dynamic loads.

2. Experimental Device

In order to investigate the EHD behaviour of a connecting-rod big end bearing, an experimental device has been realised at LMS (Laboratoire de Mécanique des Solides). This device faithfully models the kinematics of real connecting-rod - crank systems.

Figure 1 shows the scheme. An electric motor (1) running at various speeds between 0 and 1500 rpm rotates a crankshaft (3) through the intermediary of a speed reduction gearing (2). The rate of reduction of the gearing is 1/10, thus the crankshaft turns at various speed between 0 and 150 rpm. A photograph of the device is presented in figure 2.

A rigid master connecting-rod (4) is mounted on the crank. The big-end bearing of the connecting-rod is mounted on the crank-pin and the small end is attached to a “master piston” (6) which is able to slide on the two bars fixed to the support (see figure 2). It transforms the rotatory motion of the shaft into an alternating translatory one. The “piston” is pushed or pulled by the small end of the connecting-rod. This is the classic connecting-rod – crank motion.

The connecting-rod model (8) + (9) is mounted in parallel with the master connecting-rod. Its big end is supported by the crank-pin and its small end is attached to a sliding element, as seen in figure 3. This element plays the role of a real piston. We will call it “the small piston”. The only motion that it is able to complete is vertical.

During the motion, the inertia of the small piston is supported by the model which is deformed. For example, at the highest point the model is under tension by the inertia of the study piston which tends to follows the motion. At the lowest point the model is compressed by this inertia.

In order to simulate the combustion upward explosion in a real engine, a camshaft acts on the piston through the intermediary of a spring. Thus, at the maximal eccentricity of the cam we will have the maximal deformation of the spring and consequently the maximal force. This force acts on the model, which is deformed. The

maximal force applied to the model is given by the maximal deformation and the spring stiffness.

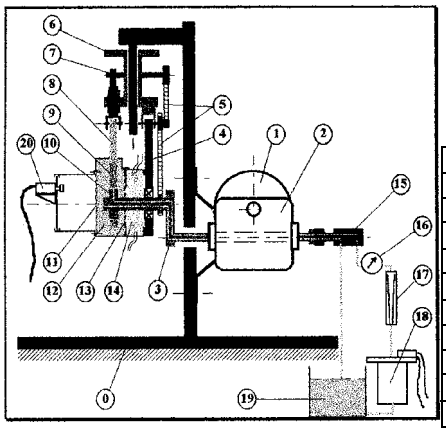

0.mian body	11. transparent sheet
1.electric motor	12. oil chamber
2.reduction gearing	13. translucent sheet
3. crank-shaft	14. halogens lamps room
4.master connecting rod	15. rotating oil distributor
5.notch belt	16. manometer
6."piston"	17. flowmeter
7. camshaft	18. oil pump
8.small end bearing	19. oil tank
9.connecting-rod model	20. CCD camera
10.crank-pin	

Figure 1. Functional scheme of the experimental device

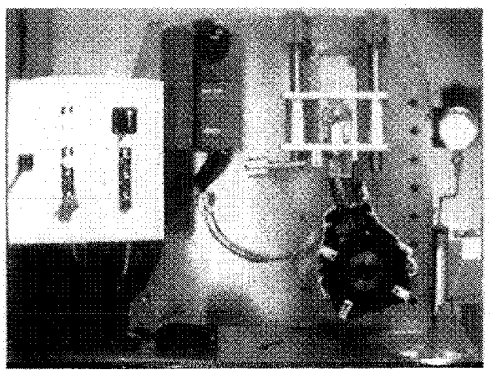

Figure 2. Photography of the experimental device. The vertical bars guide the sliding motion of the master piston.

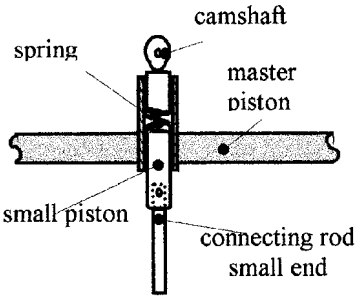

Figure 3. Scheme of the application system of the loads on the connecting rod model

The camshaft (7) is moved by the notch belts (5), which are mounted on four notch pulleys. The diameters of these pulleys are chosen to ensure that camshaft rotation speed is equal to half the crankshaft speed. Thus, the impulse given by the camshaft occurs once for every two rations of the crankshaft.

The connecting-rod model is immersed in oil. The oil chamber (12) is full of lubricant. The connecting-rod model enters the oil chamber through the upper side and an elastic seal closes the chamber and allows a relatively free motion of these elements.

The optical investigation of the model is realised by recording images during the cycle. The CCD camera (20) is placed in front of the oil chamber. The light is produced by four halogen lamps (a total of 200 W). Light passes successively through the translucent sheet (13) which separate the lights chamber (14) from the oil chamber, through the oil and the model and finally goes out through the transparent sheet (11). The light chamber is ventilated in order to evacuate the heat produced by the lamps.

Both supply and evacuation of the oil are realised via the shaft. The shaft has two ducts bored parallel to its axis. The oil admission into and evacuation from the turning shaft are carried out by a turning distributor. A manometer and a flowmeter are placed on the supply circuit. The oil supply of the bearing is completed via a hole placed in the crank-pin (10) communicating with the admission circuit of the shaft.

3. Image Acquisition and Process

A schema of the image acquisition chain is presented in figure 4. As above mentioned the camera follows the general motion of the model.

The equipment which is used for image acquisition contains :

- CCD progressive camera, 24 frames/s;
- Pulsar video card;
- incremental position transducer card (which provides the trigger);
- camera lens f12.5 or f35;
- Inspector32 software using Matrox Imaging Library.

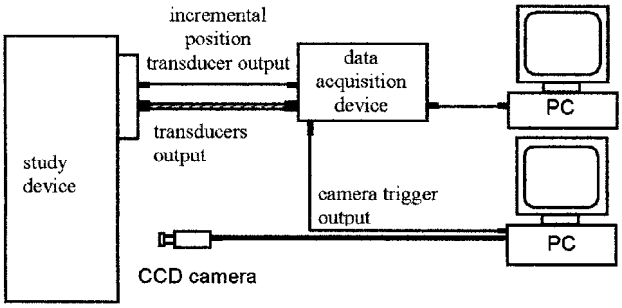

Figure 4. Measurement chain

3.1. IMAGE ACQUISITION PROCEDURE

Due to the important inertia of the machine elements during the motion, the camera cannot be placed far from the front of the oil chamber. Moreover, in order to investigate the local behaviour of the connecting-rod model, the camera must be close to the object. In this case the visualised field is small and one needs a multiple image acquisition and a reconstruction of the whole field if necessary.

The different positions of the camera in the acquisition process can be obtained by using a mobile camera support. This support allows three degrees of motion (two translations and a rotation).

Several parameters play an important role in the choice of the angular step. The camera field size depends on the camera lens focus and the distance between the camera and the object. A lens with a small focal length gives parallax errors. Particularly for the photoelasticity method, the parallax errors induced by the oblique rays on the corners and edges of the image oblige the operator to take small angular steps and to use only the central parts of images.

If rays pass obliquely through the model, the integrated thickness (the fringe order is function of the thickness) is modified. Thus, errors can be significant if concentrated stress is present in the visualised zone.

During measurements using the digital image correlation method, the parallax errors are less important, because the phenomena happen in a plane. Near the corners and edges, the measured displacement is sensibly reduced.

After they have been recorded, the field images at different positions have to be combined to give the whole field. In order to help the restoration procedure of the whole field, radial markers are painted on the model surface. They are used to merge the different images.

The image acquisition is started by a trigger. The electric signal for the trigger is emitted by an incremental position transducer which is mounted on the camshaft. Hence, the trigger signal is sent at a precise moment in the cycle, and the image is taken immediately.

Due to the relatively high rotational speed of the shaft, and yherefore, of the linear speed of the crank-pin surface versus the bearing surface, particular care must be taken concerning the exposure time. Good results are obtained with integration time of the camera around of 1^{-3} s. Particularly, the digital correlation method requires small exposure times because of the indispensable high resolution.

3.2. ISOCHROMATIC FRINGE PATTERN VISUALISATION USING PHOTOELASTICITY METHOD

The method selected for stress field visualisation is the two-dimensional transmission photoelasticity.

The polarizer and analyser are placed in order to obtain only the isochromatic fringe field.

The set consisting of polarizer + quarter wave plates + analyser + photoelastic model, is immersed in oil in order to avoid the interposition of elements which may disturb the isochromatic fringe visualisation.

A interferometric filter provides monochromatic light.

The photoelastic material used in this study is PSM4, a yellowish resin, with low Young's modulus and high photoelastic sensitivity. The mechanical and optical properties are presented in the appendix. The model is 19.2 mm thick and is obtained by pasting two 9.6 mm thick sheets together, using a resin with photoelastic and

mechanical properties close to the PSM4. The final shape is obtained by milling. Particular care must be taken during the milling because the material is very compliant.

A similar model was obtained by injection of a PVC transparent material, but it was abandoned because of its high viscoelasticity and its geometrical uncertainty. A picture of the upper part of the photoelastic big end bearing model is shown in figure 5.

The model is composed of two parts assembled using an adjustable tightening system.

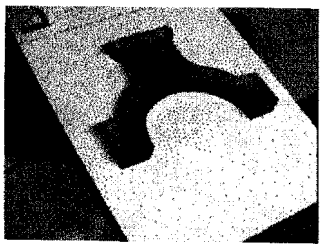

Figure 5. Photoelastic element of the big-end bearing model

3.3. DISPLACEMENT FIELD VISUALISATION USING DIGITAL IMAGES CORRELATION METHOD

In order to complete information about the mechanical behaviour of the model, a digital image correlation method is applied.

The method was developed by Sutton et al. (1983) and other authors, originally with coarse-fine methods which are prohibitively time consuming. Later, Bruck et al, (1989) introduced a method of correction based on the Newton-Raphson algorithm.

The principle of the image correlation method is to compare two images, undeformed and deformed, in order to obtain the displacements of the points on the model surface. The recorded image contains grey level written on 8 bits (0-255 values). Subsets are defined on the initial image and equivalent subsets matching as well as possible are sought on the deformed image. Hence a discrete displacement field is obtained.

The algorithm used here calculates the displacement by a correlation method based on FFT calculation. A reference subset is defined around a point in the undeformed image, where the displacement is to be found. The subset from the deformed image which best matches the reference subset from the undeformed image provides the maximum correlation product. Thus, we can obtain displacements.

In order to create a random pattern on the surface of the model, black paint was pulverised using a spray. The light traverses the model at the unpainted points, so bright and dark points are given by the random pattern of the pulverised paint. Such a sample is presented in figure 6. Bruck et al. (1989) specifies that the ideal dimension for the black speckle is about 3 or 4 pixels. The pattern we have chosen is rougher, about 6 or 7 pixels.

The exposure time for this method must be short, because the image must be as accurate as possible, for good results in the correlation

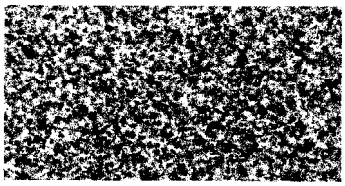

Figure 6. Random speckle pattern

4. Results

Series of images are recorded at different positions of the camera support. For each angular position, several images are taken at successive cycles in order to validate the repeatability of the recorded images. The images are taken at a rotation speed 150 rpm with a camera integration time 1^{-3} s.

For the photoelasticity method, a sequence of several images taken under the same conditions shows a very good repeatability, because variations do not induce significant visible variations in the isochromatic fringe pattern.

Series of images are taken for different camera support positions in order to cover the whole domain of the isochromatic field. Figure 7 presents a set of 4 images taken at 150 rpm of the crankshaft with an "explosion" force of 40 N. The camera is activated by the trigger at the "explosion" moment (i.e. the moment when the spring is most compressed by the camshaft). The angular step of the camera is 20°. The light intensity is reduced by the interferometric filter, so images need to be processed, because of the light insufficiency for this exposure time.

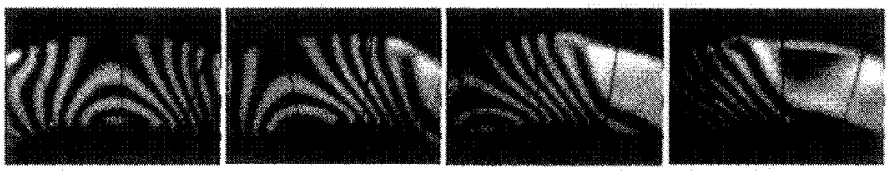

Figure 7. Set of 4 images taken with a angular step of 20°

Using the partial images of the isochromatic field we can reconstruct the whole isochromatic pattern. Such a reconstruction is presented in figure 8. We note that in the zones with concentrated stress, the parallax errors (which come from the integration on a different thickness) lead to relatively bad matching of the adjacent fields.

Applying the image correlation method to the successive images taken in the same functioning conditions we can evaluate the accuracy of the measurement process and of the entire experimental device. By calculating displacements between several deformed images taken under the same conditions we obtain errors lower than 1%. The errors are due to the low Young's modulus of the model which makes it very compliant, and to the large radial clearance of the bearing (1 mm). Consequently, there are significant rigid body displacements, which induce uncertainty due to the experimental device (vibrations, rotation speed not constant etc).

A very interesting visualisation is the interface cap - body of the connecting-rod bearing. Relative displacements between the two body have been recorded, as shown in figure 9.

Comparisons with numerical results obtained with FEM elastohydrodynamic algorithm are in progress.

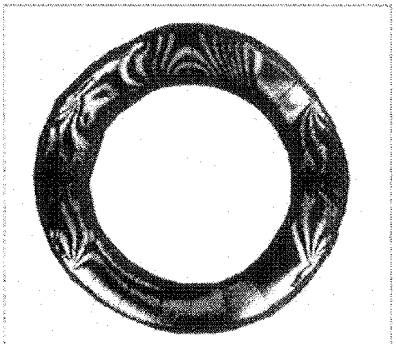

Figure 8. Whole isochromatic fringe pattern obtained by reconstruction.

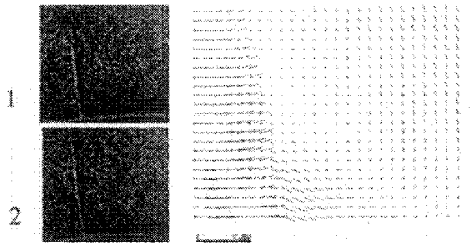

Figure 9. Undeformed (1), deformed (2) images and the associated displacement field (in pixels). Vectors magnification is 10.

References

Bates, T. W., Fantino, B., Launay, L., and Frêne, J., 1990 Oil Film Thickness in an Elastic Connecting-rod Bearing: Comparison Between Theory and Experiment, *STLE Tribology Transactions* **33,** 254-266

Bonneau, D., Guines, D., Frêne, J., and Toplosky, J., 1995 EHD Analysis, Including Structural Inertia Effects and Mass-Conserving Cavitation Model, *ASME Journal of Tribology* **117,** 540-547.

Bruck, H.A., McNeill, S.R., Sutton, M.A., Peters III W.H., 1989 Digital Image Correlation Using Newton-Raphson Method of Partial Differential Correction, *Experimental Mechanics* **29,** 261-267

Pierre-Eugene, J., Frêne, J., Fantino, B., Roussel, G., Du Parquet, J., 1982 Theory and experiments on elastic connecting-rod big end bearings under steady-state conditions, *9th Leeds-Lyon Symposium on Tribology,* 7-10 September, Leeds, England

Sutton, M.A., Wolters, W-J., Peters, V.H., Ranson, W.F., and McNeil, S.R., 1983 Determination of Displacements Using an Improved Digital Correlation Method, *Image Vision Computing* **1,** 133-139

Appendix

General configuration and constants:

rotation speed	0 – 150 rpm
motor electric power	4.5 kW
Maximum spring force	40 N
supply pressure	0.03 MPa
oil viscosity	0.01 Pa s
functioning temperature	20-40°C
Young's module for PSM4	4. MPa
photoelastic constant for PSM4	0.6-0.9 MPa/(fringe/mm)

APPLICATION OF INFRARED THERMOGRAPHY FOR CONTACT PROBLEMS

T. SAKAGAMI
Graduate School of Engineering, Osaka University
2-1 Yamadaoka, Suita, Osaka 565-0871 Japan

K. OGURA
Graduate School of Engineering Science, Osaka University
1-3 Machikaneyama, Toyonaka, Osaka 560-8531 Japan

S. KUBO
Graduate School of Engineering, Osaka University
2-1 Yamadaoka, Suita, Osaka 545-0871 Japan

T. N. FARRIS
School of Aeronautics and Astronautics, Purdue University
1282 Grissom Hall, West Lafayette IN 47907-1282 USA

1. Introduction

Investigation of tribological phenomena such as friction, wear and fretting fatigue is important in evaluating the reliability and safety of structures and mechanical components. In investigating these phenomena, though, it is often difficult to estimate physical parameters such as real contact area, friction coefficient, and contact stress distribution, because of the lack of robust experimental methods. Yet most tribological phenomena are usually accompanied with the generation of heat due to either friction-induced heat flux or plastic deformation at the contact surface. Small temperature changes arising from the thermoelastic effect are also associated with cyclic contact stress and strain fields. Thus measuring near-surface temperature fields offers an encouraging approach for characterizing the mechanics and physics of tribological phenomena. This paper will describe results from several experimental investigations of contact problems through the use of infrared thermography. First, a new technique using infrared thermography combined with infrared-transmitting materials is proposed for direct monitoring of the surface temperature of two contacting solids. This technique is applied to the frictional temperature measurement on the contact surface under dry sliding conditions, as well as the contact stress measurement based on thermoelasticity. Further a newly available infrared thermographic system is used to characterize the near-surface conditions associated with fretting contact.

A. Lagarde (ed.),
IUTAM Symposium on Advanced Optical Methods and Applications in Solid Mechanics, 603–610.

2. Tribological Measurement Using Infrared Transmitting Solid

Consider a contact problem, in which a ball is in contact with a disk, as illustrated in figure 1. When an infrared transmitting solid is employed as the disk material, the distribution of the infrared energy emitted from the contact surface can be measured by thermography since the infrared radiation generated at the contact surface passes through the infrared transmitting disk with a small amount of absorption and scatter. Therefore the temperature distribution on the contact surface of the ball can be visualized by thermography through the infrared transmitting disk. This enables us to continuously monitor tribological parameters, such as frictional temperature rise and the shape and size of the contact area, during the processes of friction and wear [1]. Further, the contact stress field can be measured directly using an infrared stress measurement system based on the thermoelastic effect [2].

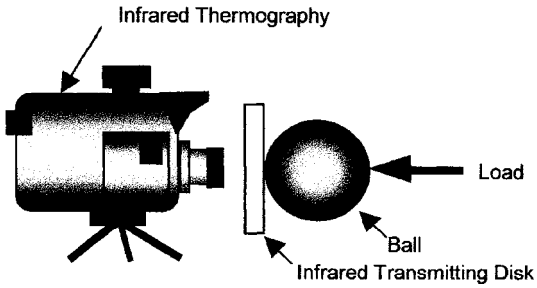

Figure 1. Thermographical measurement of contact surface using infrared transmitting materials.

2.1 MEASUREMENT OF DRY SLIDING CONTACT TEMPERATURE

Contact temperature distribution was measured under dry sliding contact using a pin-on-disk type testing system. A cylindrical pin with a spherical contact surface was brought into contact with the rotating disk and loaded. Then the temperature distribution on the contact surface was measured by infrared thermography. Figure 2 is an example of the thermal images, which shows steady state temperature distributions on the contact surface of the plastic pin sliding against an alumina ceramic disk, taken for several combinations of the sliding velocity and the load. The plastic pin was made by machining a PEEK (polyetheretherketone) rod. The curvature of the spherical contact surface, R, was 25mm. PTFE (polytetrafluoroethylene) was coated on the contact surface of the alumina disk to prevent the pin from excessive wear. Scanning infrared thermography with a magnification lens was employed in this experiment. The sliding direction is indicated by the arrow in the figure. ΔT_{max}, v, a and W are the maximum value of the frictional temperature rise, the sliding velocity, radius of contact area and the applied load, respectively. The circle in the figure shows the theoretical contact area, which is calculated by Hertz theory [3]. It is seen from figure 2 that a discrete temperature rise is observed in a restricted area with a maximum temperature rise at the center of the area. The area is circular in shape for low sliding velocity, but changes into elliptical for a higher sliding velocity. The length of the minor axis of the ellipsoidal high temperature area is in a good accordance with the diameter of the theoretical

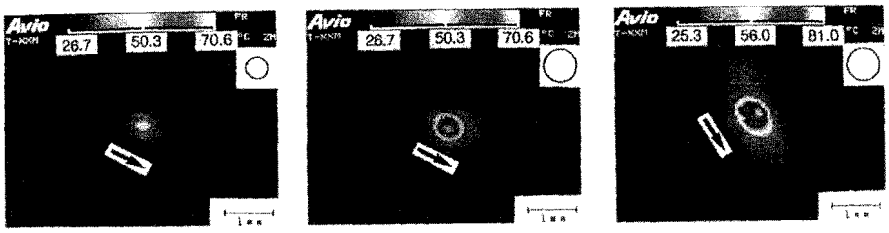

(a) W=2.94N, v=0.136m/s, $2a$=0.46mm, ΔT_{max}=11.1℃
(b) W=8.82N, v=0.136m/s, $2a$=0.68mm, ΔT_{max}=20.5℃
(c) W=8.82N, v=0.210m/s, $2a$=0.68mm, ΔT_{max}=29.0℃

Figure 2. Temperature images of contact surface measured by infrared thermography.

contact area, which is indicated by the circle in figure 2. It is found that the contact area is accurately analyzed from the thermal images.

The observed temperature distribution along the minor axis of the elliptical high temperature area normalized with the maximum temperature rise $\Delta T_{\max}$ was compared with the contact pressure distribution. The values of normalized temperature rise, $\Delta T/\Delta T_{\max}$, and normalized contact pressure, $p/p_{\max}$, are plotted along the normalized distance from the center of the contact surface, x/a, in figure 3, when the load and the sliding velocity were selected as W=5.88N and v=0.2m/s, respectively. The contact pressure p and the maximum contact pressure $p_{\max}$ were obtained from Hertz theory. It is found from the figure that the $\Delta T/\Delta T_{\max}$ versus x/a relation agrees quite well with the $p/p_{\max}$ versus x/a relation. This fact may indicate that the temperature distribution on the sliding contact surface is controlled mainly by the heat generation rate, which is in proportion to the product of the friction coefficient, the contact pressure and the sliding velocity.

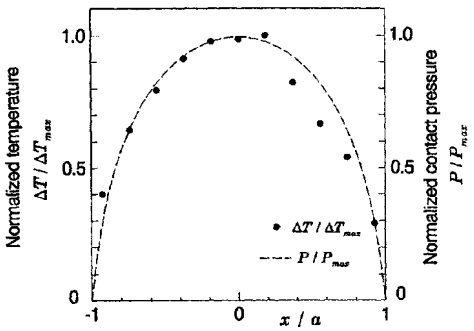

Figure 3. Distribution of normalized temperature and normalized contact pressure on contact surface.

2.2 CONTACT STRESS MEASUREMENT BASED ON THERMOELASTICITY

Consider a spherical contact under cyclic compressive load, in which an infrared transmitting lens with spherical convex surface is in contact with a plate sample as shown in figure 4. The thermoelastic temperature change (ΔT) due to the cyclic stress on the contact surface of the plate can be measured by differential thermography, since the infrared emission from the contact surface passes through the infrared transmitting lens. The range in sum of the principal stresses ($\Delta\sigma$) is determined by a relation of $\Delta\sigma = -k\Delta T$, where k is a thermoelastic constant. The load signal was monitored by a load cell and was employed as the reference signal for differential thermography. A spacer ring for magnification was mounted for the measurement of the stress distribution in a small area. The imaging area was 8.7mm square and the spatial resolution of the stress measurement was 70μm. Sapphire was chosen as the infrared transmitting lens, because

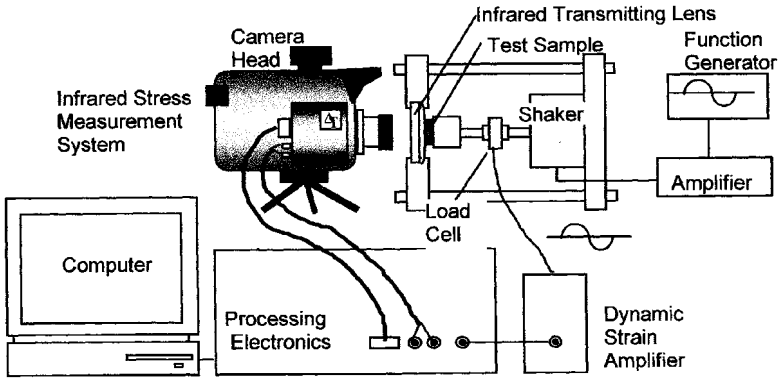

Figure 4. Schematic illustration of apparatus used for contact stress measurement.

it transmits infrared well in the 3-5μm range which is the sensible range for the InSb infrared sensor used in the thermography system.

Stresses caused by spherical Hertz contact were measured for several kinds of commercially available plastics. A flat plate sample (15mm × 15mm, 1.6mm in thickness) was mounted on the loading stage and was brought into contact with a sapphire convex lens that has a spherical contact surface with a radius of curvature of 150mm. Sand blasting was done on the contact surface of the plastic sample to prevent reflections and to obtain high emissivity. Cyclic compressive loads (45Hz) were applied in several combinations of mean and amplitude values. In this paper, polypropylene is selected as the flat plate sample and the analytical and experimental results obtained for three loading conditions are compased. Table 1 describes the loads and Hertz theory predictions for these cases.

Table 1. Loading conditions and ranges in sums of principal stresses by Hertz theory.

Exp. No	Applied load P (N)	a_{min} (mm)	a_{max} (mm)	$\Delta\sigma_{max}$ (MPa)	$\Delta\sigma_0$ (MPa)
A7-09	29.0± 11.8	1.17	1.56	14.1	5.4
A7-11	29.0 ± 19.9	0.95	1.65	18.6	9.7
A7-19	45.8± 11.7	1.47	1.75	12.9	3.8

Theoretical analysis for the contact area and contact stress distribution was done based on Hertz theory for spherical contact [2,3]. Distributions of $\Delta\sigma$ were calculated for the loading conditions shown in Table 1, and plotted in figure 5. a_{max} and a_{min} are the radius of the contact area at maximum and minimum compressive loads in the cycle, respectively. It is found that $\Delta\sigma$ shows an axisymmetric distribution, where $\Delta\sigma$ is increasing from its central value $\Delta\sigma_0$ up to the maximum value $\Delta\sigma_{max}$ at $r=a_{min}$, then $\Delta\sigma$ is decreasing to zero at $r=a_{max}$.

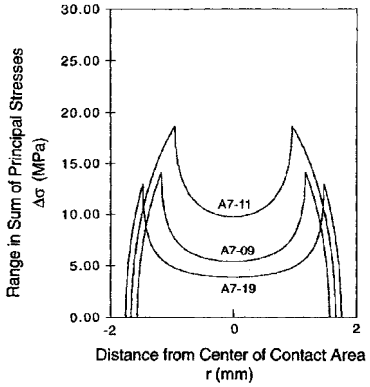

Figure 5. Distribution of range in sum of principal stresses by Hertz theory.

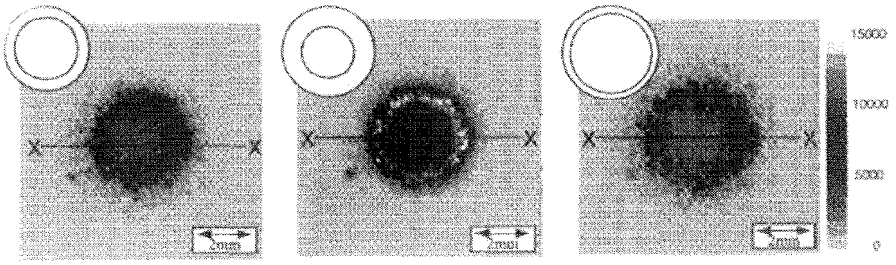

(a) A7-09 P=29.0±11.8 (N) *(b) A7-11 P=29.0±19.9 (N)* *(c) A7-19 P=45.8±11.7 (N)*

Figure 6. Images of contact stress distributions for Hertz contact between polypropylene sheet and sapphire convex lens obtained by infrared stress measurement system.

The contact stress distributions represented by the distribution of the intensity ΔV of infrared emission from the contact surface due to the thermoelastic effect are shown in figure 6. The circles indicate the maximum and minimum contact areas. Line profiles obtained along the lines x-x in figure 6 are plotted in figure 7. An excellent correspondence is found between the contact stress distributions measured by the infrared system and those obtained by Hertz theory. Δ V is increasing from the center of the contact area up to the maximum value at $r=a_{\min}$, then ΔV is decreasing to near zero at $r=a_{\max}$. Figures 5 and 7 show that a comparison for the magnitude of $\Delta\sigma$ can be made among different loading conditions. The asymmetric peaks in figure 7 are probably caused by inhomogeneous geometry of the surface in contact. Calibrations will be needed to obtain absolute values of contact stresses. The calibrations should involve reliable values of the thermal conduction from the plastic sample to the sapphire lens, the infrared transmittance in the sapphire lens, and the thermoelastic constant of the plastic sample.

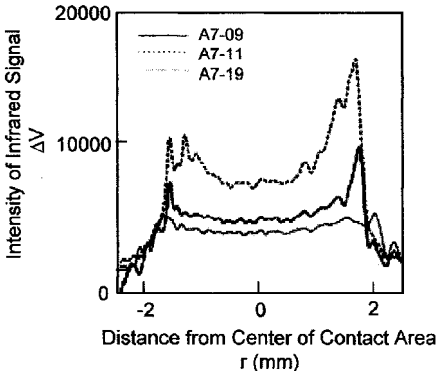

Figure 7. Distribution of intensity ΔV of infrared emission along lines X-X in figure 6.

3. Evaluation of Fretting Stresses through Full-Field Temperature Measurements

It is very important to analyze the mechanics of crack nucleation under the influence of fretting to secure the reliability and the safety of the any clamped components subjected to vibrations or oscillatory loading such as riveted lap joints and turbine blades. Mechanism of crack nucleation under fretting contact is thought to be associated with the near-surface tangential stress generated by the interfacial frictional traction and the applied bulk load. Computational evaluations [4] showed the presence of a tensile peak in the tangential stress at the trailing edge of contact, where most of the fretting fatigue cracks nucleate in the experiments. The focus of the present study is to obtain experimental results capturing the evolution of friction and characterizing the stress field under fretting conditions. A newly developed multi-element infrared camera was

employed to measure near-surface temperature distribution due to both frictional heating and thermoelastic effects under fretting condition [5].

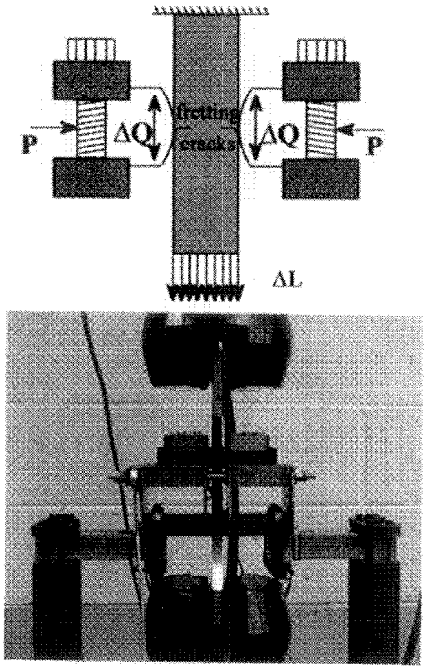

Figure 8. Schematic of fretting contact and photograph of fretting fatigue test fixture.

3.1 EXPERIMENTAL SETUP

A schematic of fretting contact and a photograph of the experimental setup are shown in figure 8. Temperature distribution was examined for 2024-T351 aluminum specimen and cylindrical pads. Cylindrical pads with the curvature radius R (R=178mm) were brought into contact to the specimen and applied normal load P (P=6.41kN). A cyclic bulk load with amplitude, ΔL (ΔL=16.1kN), fully-reversed in tension and compression, was applied to the specimen using a servo-hydraulic load frame. Then fretting contact between the specimen and pads was induced due to the oscillatory tangential load ΔQ.

The temperature distribution on the side surface of the specimen and pads were measured by the high speed and high resolution infrared thermography with an InSb focal plane array to convert thermal radiation into temperature values with a maximum sensitivity of 0.025 K. A thin coating of flat black paint was applied to the exposed surfaces of the pads and specimen to increase the emissivity of the metallic surfaces. Thin reference lines were etched mechanically on the exposed faces of both the pads and specimen to mark the centerline of contact. A 2024-T3 aluminum plate with an E-type thermocouples was used to obtain a calibration relation between infrared intensity and temperature. Temperature reading from the thermocouples was correlated with the infrared intensity value near by the thermocouple measured by thermography. A fretting experiment was conducted at a frequency of 2 Hz under fully-reversed loading conditions

3.2 EXPERIMENTAL RESULTS

Ten frames per cycle (20 Hz sampling rate) were captured for the first 150 cycles of the test, with subsequent images taken at cycles of 1000, 2000, 3000 and 4000. Infrared intensity data were converted to temperature data using the calibration relation and then filtered using a pixel-wise adaptive Wiener method.

Figures 9 and 10 show sequential temperature images taken at the 16th loading cycle and the 151st loading cycle, respectively, in the fretting experiment. The imaging area around the interface of the right pad and the specimen is indicated by the shaded area in figure 11. In figures 9 and 10, the top row of images shows temperature images during

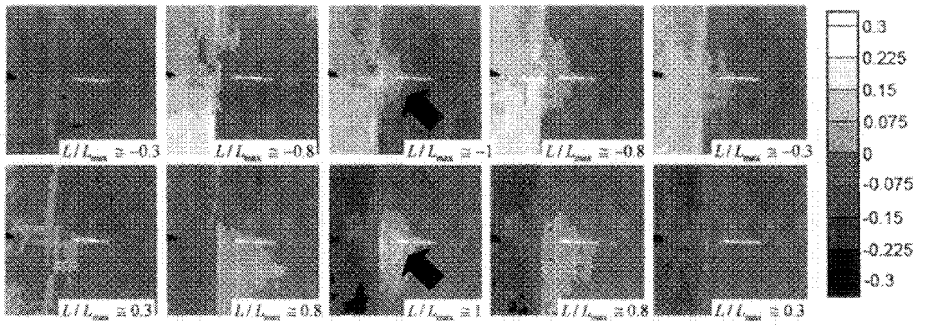

Figure 9. Sequence of thermal images near contact surface taken at the 16th loading cycle.

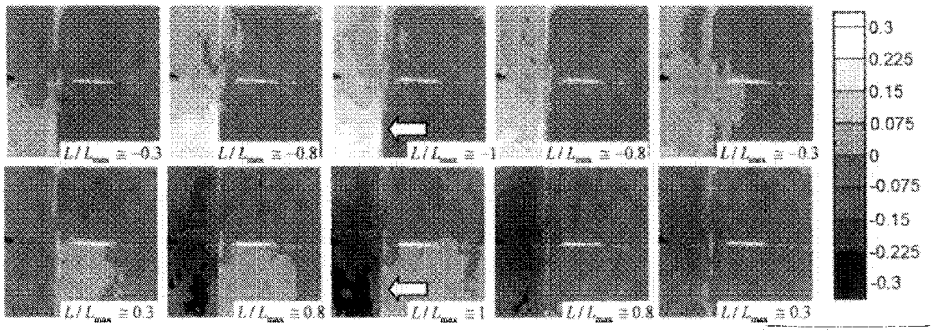

Figure 10. Sequence of thermal images near contact surface taken at the 151st loading cycle.

the compressive bulk loading in the loading cycle (L<0). Conversely, the lower row of images shows temperature images during the tensile bulk loading in the loading cycle (L>0). The gray scale bar indicates temperature changes from room temperature. The horizontal bright line on the pad, found in the temperature images, is caused by the mechanically etched mark indicating the nominal center of contact.

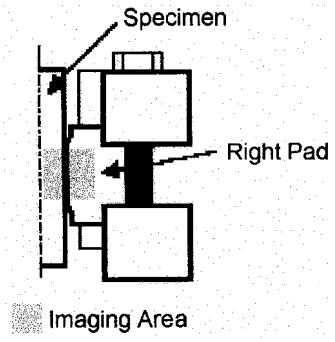

Figure 11. Schematic of imaging area by infrared thermography.

It is seen from figure 9 that the temperature distribution changes at the same frequency as that of the applied bulk load waveform on the specimen surface. This implies that the temperature change is caused by the thermoelastic effect induced by the cyclic bulk loading. The temperature distributions due to the thermoelasticity are nearly homogeneous in the entire specimen, and this indicates that the stress distribution in the specimen is also homogeneous at this stage. On the other hand, a localized near-surface heating spanning the width of the contact area is found in the pad. This heat generation can be observed twice in each loading cycle. This fact means this heat generation is caused by friction between the specimen and pad. It was found that in the beginning stage of fretting loading, gross sliding conditions due to the low frictional coefficient are dominant on the contact surface.

It is found from figure 10 that no frictional temperature rise due to the gross sliding can

be observed any more at the 151st loading cycle. This implies that the friction coefficient increased and partial slip conditions are dominant at this stage. It was also found that temperature distributions on the specimen was not homogeneous at this time. When tension is applied, lower temperature was observed near the lower trailing edge of contact in the specimen (indicated by arrow in figure 10). This means that higher tensile stress was generated at the lower trailing edge of contact. This indicates that contact tensile stress due to the partial slip condition was applied to the specimen in addition to the bulk tensile stress. Conversely, at compression, higher temperature was observed at the lower trailing edge of contact in the specimen (also indicated by arrow in figure 10). This means higher compressive stress was generated at the lower trailing edge of contact due to the contact compressive stress by the partial slip condition in addition to the bulk compressive stress.

Consequently, it was found that the maximum amplitude in cyclic temperature change, i.e., maximum amplitude in stress, was observed at the trailing edge of contact. This result agrees very well with the results from FEM computations [6] and also the fact that fretting fatigue cracks nucleate from the trailing edge of the contact.

4. Conclusions

Several experimental investigations of contact problems were made by the use of infrared thermography. A new experimental technique using infrared thermography combined with infrared transmitting materials was applied for continuous monitoring of the temperature distribution on the contact surface. Contact temperature measurement was examined for dry sliding contact of a plastic pin with an infrared transmitting disk. It was found that steady state contact surface temperature distribution was accurately monitored by thermography. Contact stress field was measured by an infrared stress measurement system based on the thermoelasticity through an infrared transmitting solid. It was found that the contact stress field was successfully visualized by the proposed method. Finally, a newly available infrared thermography system was used to characterize the near-surface conditions associated with fretting contact. It was found that both frictional temperature rise due to the interfacial global slip and the temperature fluctuation due to thermoelasticity can be measured to evaluate the nature of the contact stress field and the mechanics of partial slip fretting contacts.

5. References

1. Sakagami, T., Ogura, K. and Shoda, M.: Thermal sensing and imaging of the dry sliding contact surface using IR thermo-microscope, *SPIE Proceedings,* **2473** (1995), 263-272.

2. Sakagami, T., et al.: Visualization of contact stress distribution using infrared stress measurement system, *SPIE Proceedings,* **3056** (1997), 250-259.

3. Johnson, K. L.: *Contact Mechanics,* Cambridge University Press, 1985.

4. Szolwinski, M. P. and T. N. Farris.: Mechanics of fretting fatigue crack formation, *Wear* **198** (1996), 93-107.

5. Szolwinski, M.P., Harish, G., Farris, T. N. and Sakagami, T.: In-situ measurement of near-surface fretting contact temperatures in an aluminum alloy, *ASME Journal of Tribology,* (1998), In-Press.

6. McVeigh, P.A. and Farris, T. N.: Finite element analysis of fretting stresses, *ASME Journal of Tribology,* **119,** #4, (1997), 797-801.

APPLICATION OF GEOMETRIC MOIRÉ TO THE ANALYSIS OF LARGE DEFORMATION IN THREE-DIMENSIONAL MODELS

V. CICINELLI, C. PAPPALETTERE, W.M. SUN
Dipartimento di Progettazione e Produzione Industriale
Politecnico di Bari - Viale Japigia 182 - 70126 Bari (Italy)

L. SURACE
Dipartimento di Ingegneria Strutturale
Università della Calabria - 87036 Arcavacata di Rende, Cosenza (Italy)

Abstract

The application of geometric moiré in large deformation of 3-D models is discussed. Different aspects of the method, such as mismatch technique and mechanical differentiation, are taken into consideration for the measurement. An application of the method is given to the cushion disk of an artificial knee joint in whose axis-symmetric cross section a cross specimen grating of 0.5mm pitch was replicated. The analysis shows the applicability of the geometric moiré, together with its various approaches, in the large deformation measurement giving the whole field quantitative definition.

1. Introduction

1.1 GENERAL PROBLEM

The experimental techniques have made a great contribution to the analyses of mechanical behaviour of components and structures. In particular, the optical methods, such as holographic interferometry, moiré and speckle techniques etc., have played a very important role in both qualitative and quantitative determination of mechanical parameters [1]. However, most of them are limited to the application on the surface of models, while the analysis of the internal parts could be needed. Some techniques have been proposed by researchers to solve such problem, for instance, the white light speckle method where some form of inhomogeneity was formed within a cast block of model for interior strain measurement [2].

On the other hand the optical methods have been found their applications not only in traditional mechanical structures but also in a widespread fields (e.g. in biomechanics) where large deformation and non-linearity are present. Some of the optical techniques, such as grid analysis [3,4], have played a successful role in the measurements of large deformation.

A. Lagarde (ed.),
IUTAM Symposium on Advanced Optical Methods and Applications in Solid Mechanics, 611–618.

This research is aimed to apply geometric moiré in the analysis of an internal section of a model with large deformation to obtain directly whole field displacement measurement and strain field by means of mechanical differentiation.

1.2 APPLICATION TO KNEE JOINT

Arthroprosthesis design is based on the analogy existing between the human joint and the mechanical motion system. In general a knee joint is considered as mechanical contact structure in which mechanical actions are originated by muscles.

The first artificial joint was made by substituting a part of the knee with an inert material and the results obtained have lead to the utilisation of biocompatible materials. Then the total substitution of the human joint rather than some singular parts was preferred [5, 6, 7].

According to the mechanical kind of joints the prosthesis are classified (Fig. 1) in: 1) constrained prosthesis, where the motion is allowed only in one plane by a joint, 2) semi-constrained prosthesis, where the motion is allowed in two planes by a spherical joint between the femur and tibia, and 3) un-constrained prosthesis, where there is no connections between its components and any kind of motion is allowed. A good shape design must assure large stability to this last kind of knee prosthesis, which perfectly simulates the human motion of the knee.

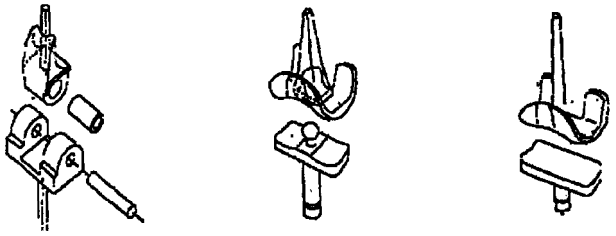

Fig. 1: Prosthesis classifications: constrained, semi-constrained and non-constrained prosthesis.

The artificial knee joint actually used (Fig. 2) is made of an inox steel structure inserted into the femur, a polyethylene disk and a tibial metal plate linked to the human tibia bone.

The characteristics of this prosthesis is the presence of the cushion part, the disk, actually made of UHMEPE. Here a disk made of a softer material, the polyurethane, is investigated.

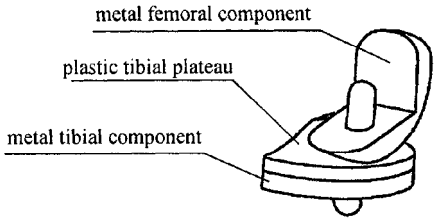

Fig. 2: Typical structure of an actual artificial knee joint.

2. In-plane geometric Moiré

2.1. GENERALS

In-plane moiré is typically carried out by gratings of equispaced, parallel lines [1]. One grating set is applied to a flat surface of the specimen, and a second set (reference grating) can be put in contact with the specimen grating or more conveniently recorded by an image processing system. The gratings can be x- or y- or cross oriented.

The strain can be determined by using four derivatives of the fringes:

$$\left.\begin{aligned}
\varepsilon_{xx} &= \sqrt{1 + 2p_0\frac{\partial N_x}{\partial x} + (p_0\frac{\partial N_x}{\partial x})^2 + (p_0\frac{\partial N_y}{\partial x})^2} - 1;\\
\varepsilon_{yy} &= \sqrt{1 + 2p_0\frac{\partial N_y}{\partial y} + (p_0\frac{\partial N_y}{\partial y})^2 + (p_0\frac{\partial N_x}{\partial y})^2} - 1;\\
\gamma_{xy} &= \arcsin\left[p_0\left(\frac{\partial N_x}{\partial y} + \frac{\partial N_y}{\partial x} + \frac{\partial N_x}{\partial x}\frac{\partial N_x}{\partial y} + \frac{\partial N_y}{\partial x}\frac{\partial N_y}{\partial y}\right)\Big/(1+\varepsilon_{xx})(1+\varepsilon_{xx})\right]
\end{aligned}\right\} \quad (1)$$

where respectively p_0 is the reference grating pitch, N_x and N_y are fringe orders of x and y displacements.

Despite the source of these equations, they are strictly geometric equalities and do not require elastic behaviour of the specimen; this allows a wide range of their applications. The superposition of specimen and reference gratings can be done by digital logical operations of grabbed images by an image processing system [8,9].

In relation to the subject of this paper, three aspects of in-plane geometric moire were considered here: (1) large deformation measurement; (2) mismatch method to increase (decrease) fringe numbers; (3) mechanical differentiation.

All these aspects were carried out using an image processing system.

2.1.1. *Large Deformation Measurements*

The sensitivity of the in-plane geometric moiré is equal to the reference grating pitch p_0. However, in the case of large deformation the applied grating pitch is relatively high and must be taken into consideration in strain calculation.

Between two fringes, spaced d, the average tension and compression strains may be calculated respectively by [10]:

$$\varepsilon_{tension} = +\frac{p_0}{d - p_0}, \qquad \varepsilon_{compression} = -\frac{p_0}{d + p_0} \quad (2)$$

2.1.2. *Mismatch Method for Non-uniform Deformation*

The choice of the grating pitches is always based on the strain range to be measured. For a 3-D model the specimen gratings are always replicated during its modelling, thus a change of grating pitches is not practicable. Moreover, in many cases where the non-linear and non-uniform strains are present, such as contact, material discontinuity and non-linear materials etc., a single pitch cannot satisfy the measurement of whole field.

In the case of large deformation, it is difficult to consider an application of very fine gratings since the large tension/compression deformation may destroy such fine gratings. Moreover, a fine grating may provide the fine measurement in one zone, but becomes

ineffective or over-effective in other zones.

The mismatch method, in providing different carrier fringes (tension or compression) to different measuring zones, is a very efficient way in the measurement of large and non-linear deformation.

The mismatch is carried out by taking some new reference gratings with the pitches different from that of original one. If the pitches of these new gratings are greater than that of original one, the number of fringes will be increased over the original fringes at the zone where the compression deformation goes on, while decreased the tension deformation. Inverse effect is present when the pitches of these new gratings are less than that of original one. In general, at least two new reference gratings are used, one with slightly greater pitch and one with slightly less pitch than that of the original one. If the deformation has a very large range, more reference gratings with different mismatch pitches may be taken to suit each strain level.

2.1.3. *Mechanical Differentiation*

The moiré method, as many other optical interferometry, provide directly the measurement of displacement field, while the structure is characterised by stress distribution. Nevertheless, the mechanical differentiation can give proportional strain distribution, proportional strain value and, in some cases, particular characteristics, for example contact area in contact problems, like in this study.

The mechanical differentiation is the superposition of two identical moiré patterns, one of which is shifted by increments Δx and Δy. In this way, the contour maps $\Delta N_x/\Delta_x$, $\Delta N_x/\Delta_y$, $\Delta N_y/\Delta_x$ and $\Delta N_y/\Delta_y$ can be obtained. To obtain strains, the basic displacement can be written in the form:

$$\Delta u_x = p_0 \Delta N_x, \qquad \Delta u_y = p_0 \Delta N_y \tag{3}$$

Then the strain can be defined as:

$$\varepsilon_{xx} = p_0 \frac{\Delta N_x}{\Delta x}, \qquad \varepsilon_{yy} = p_0 \frac{\Delta N_y}{\Delta y}, \qquad \gamma_{xy} = p_0 \left(\frac{\Delta N_x}{\Delta y} + \frac{\Delta N_y}{\Delta x}\right) \tag{4}$$

In practice, mechanical differentiation can be obtained by shifting directly two identical deformed grating images without generating ordinary moiré fringes. It should be noted that the above relationships are correctly applicable for small strain, i.e. the finite increment represent the true derivatives if the shifts Δx and Δy are small.

2.2. IMAGE PROCESSING

The specimen gratings need to be grabbed before and after loading. The software available to the purpose, IMAGEPRO by CORECO - USA provided the following image processing operators:

1. *horizontal and vertical edge filters,* to separate the crossed gratings respectively into vertical and horizontal lines for superposition of x and y displacement fields;
2. *contrast enhancement operators,* such as *stretching and equalising,* to obtain high contrast gratings and fringes (the image processing system also provides the binarization of images which gives images with only two grey levels);
3. *arithmetic and logical operators* to obtain the superposition of two grating patterns, for instance, to get average value of two images in each pixel;

4. *scaling operator* to generate mismatch reference gratings reducing or increasing the image scale;
5. image shifting for mechanical differentiation carried out by digitally positioning the gratings.

3. Preparation of the specimen analysed and the optic system applied

In order to evaluate the internal strains of the polyurethane tibial plateau, a 0.5mm pitch grid was engraved in a diametrical section of it. The elastomeric disk, 10mm thick with a diameter of 80mm, was made by sequential polymerisation of two half of it, casting the resin in a circular steel mould. The casting procedure was realised in a vacuum oven with controlled temperature (60°C). After the polymerisation of the first half of the cylinder a master grating was replicated onto the flat specimen section by a xerographic technique, which was adopted to produce a good quality cross grating. The master grating was drawn by a CAD system and printed on a film. After the replication of the grating, the specimen was cast into its complete form.

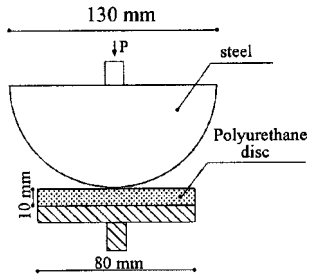

Fig. 3: Mechanical rig

Three specimens for each of three different ratios of the polyurethane resin to its hardener (1:1; 1:0.7; 1:0.5) were produced, plus another one, on whose section a 10 grid strain-gauges chain was bonded.

The mechanical load of 800 N was applied in 100 N steps by a steel sphere with a diameter of about 130mm, which simulated the femoral component (Fig. 3). The load was centrally applied on the diametrical plane of the sphere, then a three-dimensional axis-symmetric problem occurred.

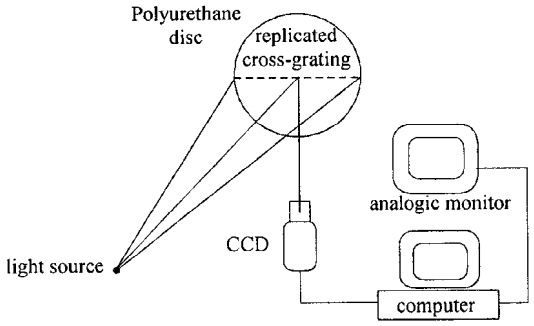

Fig. 4: In-plane moiré set-up

The optical set-up of in-plane geometrical moiré method is shown in Fig. 4. A white light was used. A laser light is not necessary for the illumination since it may produce unwanted speckles in the specimen surface. By recording and superposing the grating

patterns before and after loading, some digital imaging operations are carried out to obtain the x- and y-displacements and their corresponding strain distributions.

4. Results

The results obtained for the model with a ratio 1:1 of the polyurethane resin to the hardener are reported in the following.

Figs. 5 report for a load of 800 N the grating image as grabbed (Fig. 5a) and after it was transformed respectively by vertical (Fig. 5b) and horizontal (Fig. 5c) filtering provided by the image processing system.

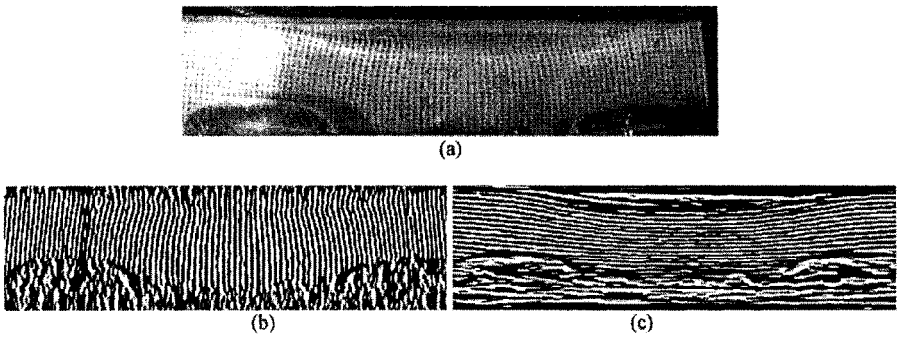

Fig. 5: Gratings imaging and processing at the loading of 800 N (a) original; (b) vertical filtering and (c) horizontal filtering.

The superposition of the deformed and non-deformed gratings were obtained for each loading step (100N). The horizontal, u_x, and vertical, u_y, displacement fringes under loading of 800 N are shown respectively in Figs. 6a and 6b.

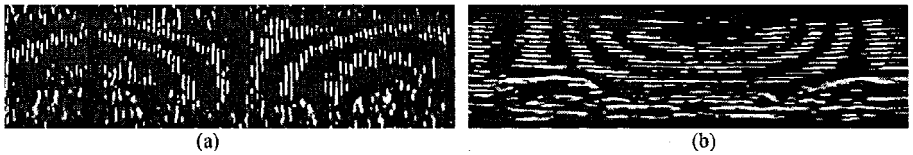

Fig. 6: Displacement fringes at the loading of 800 N: (a) u_x ; (b) u_y

Fig. 7: Mismatch fringes of u_x at the loading of 800 N

Close to the contact area, very few number of fringes were observed in the x displacement field due to its low deformation level. Then a mismatch reference grating with 15% reduction of the non-deformed grating (i.e., p_o'=0.425 mm) was superposed

onto the gratings to get more fringes. Fig. 7 gives the result of this operation in the case of a 800 N loading for another specimen.

Based on the above displacement measurement the strain distribution ε_{xx} and ε_{yy} along the different sections have been calculated as reported in Figs. 8, which shows that the strain ε_{xx} decreases going away from the contact centre, while the maximum strain ε_{yy} is located in the middle of the y section as stated in previous work.

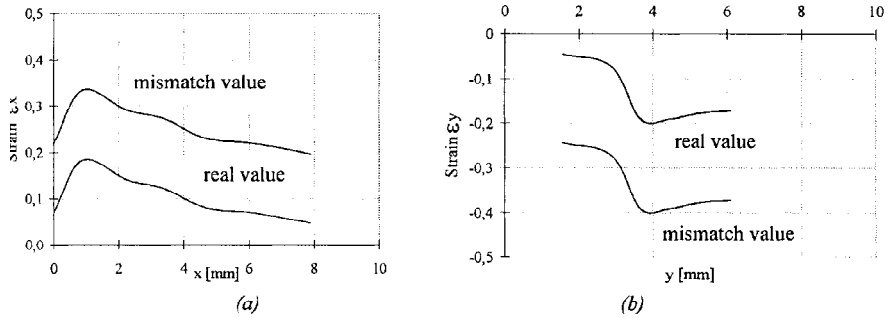

(a) *(b)*

Fig. 8: Strain distribution: (a) ε_{xx} (b) ε_{yy}

Maximum average strains and maximum vertical displacements are given in Figs. 9 for the loads applied. Their behaviours were confirmed by the numerical results obtained in other research works under study.

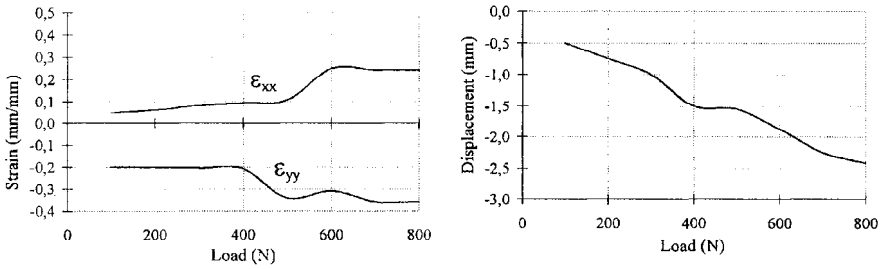

(a) *(b)*

Fig. 9: (a) maximum average strains; (b) maximum vertical displacements

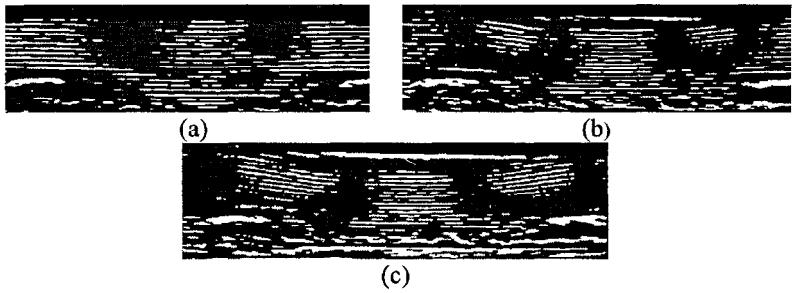

Fig. 10: Mechanical differentiation fringes of $\Delta N_y/\Delta x$ with Δx=3 mm
(a)100 N; (b)400 N; (c) 800 N.

The extension of the contact area is a very important factor in the present analysis. It may be measured directly by the image observation and more precisely, by mechanical differentiation to obtain the shear component. Figs. 10 show the mechanical differentiation fringes respectively for loads of 100 N, 400N and 800N. These fringes represent the $\Delta Ny/\Delta x$ component with shifting Δx=3 mm. The contact extension is given versus load increasing in Fig. 11.

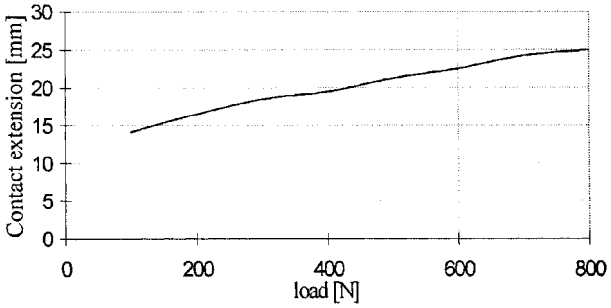

Fig. 11: Contact area extension.

5. Conclusions

Geometrical moiré technique was applied to the study of internal large strains of transparent models.

The results obtained for a biomechanical application showed the good feasibility of the technique.

Further researches are in progress on the refinement of the grating, automation of stress calculation and study of wear disk contact surface.

6. References

[1] A.S. Kobayashi, V.J. Parks: *Handbook on Experimental Mechanics,* Prentice-Hall Inc., 1987.
[2] A. Asundi, F.P. Chiang: Applications of the white light Speckle method to interior displacement measurement, *Journal of Strain Analysis,* Vol. 18, No. 1, 1983, 23-26.
[3] J. Dupré, F. Brémand, A. Lagarde: Numerical spectral analysis of a grid: Application to strain measurements, *Optics and Lasers in Engineering,* 18, 1993, 159-172.
[4] H. T. Goldrein, S.J.P. Palmer, J.M. Huntley: Automated fine grid technique for measurement of large-strain deformation maps, *Optics and Lasers in Engineering,* 23, 1995, 305-318.
[5] D.D. Auger, D. Dowson: Cushion form bearings for total knee joint replacement. Part 1: design, friction and lubrification. Proc.Instn. Mechan. Engrs, Part H, Journal of Engineering in Medicine, Vol.209, 1995.
[6] D.D. Auger, D. Dowson: Cushion form bearings for total knee joint replacement. Part 2: wear and durability. Proc.Instn. Mechan. Engrs, Part H, Journal of Engineering in Medicine, Vo1.209, 1995.
[7] E.G. Little, R. S. Olivito, L Surace: A numerical analysis of the contact problem of artificial knee joints, Proceedings of the International Conference on Material Engineering, Gallipoli, Italy, 1996.
[8] A. Asundi, K. H. Yung: Logical moiré and its application, *Experimental Mechanics,* 31(3), 1991.
[9] A. Asundi: Computer aided moiré methods, *Optics and Lasers in Engineering,* 18, 1993, 213-238.
[10] A. Bray, V. Vicentini: *Meccanica Sperimentale: misure ed analisi delle sollecitazioni,* Levrotto&Bella, Turin, 1975.

THE COMBINATION OF SPECKLE CORRELATION AND FRINGE PROJECTION FOR THE MEASUREMENT OF DYNAMIC 3-D DEFORMATIONS OF AIRBAG CAPS

HERBERT WEBER AND RALF LICHTENBERGER
Universität Karlsruhe
Institut für Mechanische Verfahrenstechnik und Mechanik
Bereich Angewandte Mechanik
D-76128 Karlsruhe

AND

THOMAS WOLF
Heidelberger Druckmaschinen AG
D-69019 Heidelberg

Abstract. Highly dynamic 3-D deformations of airbag caps in the time interval from the ignition of the airbag to the fracture of the covers have been studied optically. The large out-of-plane displacement compared to the in-plane displacements afforded that the measurement problem was solved by combining white light speckle correlation with fringe projection. In order to record the speckle patterns and the fringe patterns simultaneously by two high speed CCD cameras they had to be separated spectrally. The in-plane displacements yield from the speckle patterns by pattern recognition methods. The out-of-plane displacements can be calculated from the contour of the caps. They yield from the phase maps which are calculated from the fringe patterns. For each time instant only one image is available so that phase shifting procedures to evaluate the fringe patterns could not be applied. In this paper we present a method which is based on the simulation of a phase locked loop (PLL). This results in continuous phase maps without phase unwrapping.

1. Introduction

The inflation of an airbag causes fracture of the caps (Fig. 1) at certain predefined sites. The task of the engineers constructing the airbag systems is to optimize the process of deformation and subsequent fracture of the

A. Lagarde (ed.),
IUTAM Symposium on Advanced Optical Methods and Applications in Solid Mechanics, 619-626.

airbag caps. Usually this is done by FE calculations. The accuracy of the numerical simulations, however, strongly depends on the exact knowledge of the loading conditions, i.e. the local dependence of the pressure on time, and on the material behavior which is given by a set of rate and temperature dependent material parameters. Both the time sequence of the pressure as well as the material parameters are difficult to determine. Therefore the numerical results for the transient 3-D deformation of the airbag caps have to be compared with results of experiments in which the time dependent deformations are measured. As for a correct evaluation of the deformations many measurement points are needed in small time intervalls, only optical and fullframe measurement methods are suitable.

2. Experimental procedure

2.1. MEASURING METHODS

The out-of-plane deformations are expected to be large compared to the in-plane deformation. Besides this the deformation rate is high and the surface of the test object exhibits poor reflectivity. Therefore some of the well established 3-D measuring methods like electronic speckle pattern interferometry (ESPI) for instance cannot be applied. It turned out that the best way to solve the problem is to measure the in-plane deformations and out-of-plane deformations by separate methods [Wolf, 1996]. For the determination of the in-plane deformations a white light speckle correlation method seemed to be most suitable. This method yields the in-plane displacements. For the out-of-plane deformation fringe projection is used. With this method the contour of the airbag cap can be determined. From the contour map of the deformed cap and from an additional contour map of a reference state the out-of-plane displacement field can be calculated.

2.2. MEASURING SETUP

The setup for the measurement of all three components of the displacement vector field of the dynamically deformed air bag caps consists of a speckle correlation system with a white light source of 250 W and a CCD camera (camera 1) and of a fringe projection system with a fringe projector and an additional CCD camera (camera 2). The optical axis of the two systems lie in the same plane (Fig. 2). The cameras are high speed KODAK CCD cameras with frame rates of 4500 per second and an image size of 256x256 pixels. For synchroneous recording of the speckle pattern the cameras must be synchronized electronically. A spectral separation of the two systems is necessary, to supply the corresponding measurement information to each system. This is performed by application of spectral filters, respectively,

and by matching of the spectral sensitivity of the cameras to the frequency of the filters. For the speckle system blue filters are used and red ones for the fringe projection system.

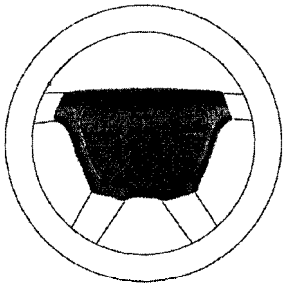

Figure 1. Steering wheel with airbag cap.

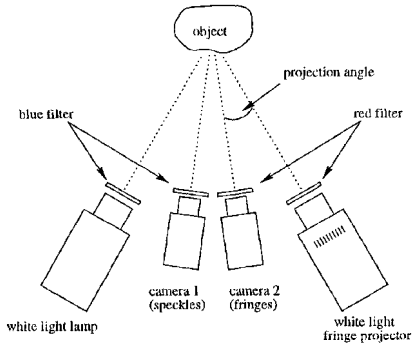

Figure 2. Measuring setup.

2.3. OBJECT SURFACE PREPARATION

In order to receive sufficiently high fringe modulation the reflectivity of the originally black surface of the caps is increased by a thin coating of white paint. The speckles, however, are artifically created by air brushing the surface of the airbag with red paint. Because the reflectivity of the red light from the fringe projector is the same for the white background of the speckle pattern and for the red speckles the speckles cannot be "seen" by the fringe camera. On the other hand the speckles appear black in the speckle camera because they do not reflect the blue light.

2.4. SPECKLE CORRELATION

The determination of an in-plane displacement vector field by speckle correlation is a problem of pattern recognition. The image of the surface is divided into correlation subsets of e.g. 32x32 pixels. The pattern of one subset in the undeformed state is then searched in the surface of the deformed state by direct digital cross correlation. In contrast to methods which are based on variational principles [Sutton et al, 1986] this method needs no interpolation of the discrete pixel data. Mathematical operations are restricted to multiplication of the discrete Fourier transforms of the subsets of the deformed and undeformed states and to a back transformation of their product. The maximum of the correlation function of a subset is identified as the correlation peak. It provides the position of the pattern in the deformed state.

If the grey level of the reference subset at pixel position m, n is given by $f(m, n)$ and the grey level of the deformed subset by $g(m, n)$ then the Fourier transform of f and g are

$$F(u,v) = \mathcal{F}\{f(m,n)\} \tag{1}$$

$$G(u,v) = \mathcal{F}\{g(m,n)\}\,. \tag{2}$$

The correlation function follows from

$$K_{gf}(m,n) = \mathcal{F}^{-1}[F(u,v) \cdot G^*(u,v)] \tag{3}$$

with G^* being the conjugate complex of the function G. In pattern recognition G^* is called a matched filter. It is known that for patterns which have nearly uniform distribution of amplitudes in the frequency space the relevant information is contained in the phase φ of the Fourier transform of the pattern. Therefore filters which primarily are sensitive to phase information seem to be of great benefit for solving pattern recognition problems. One of these filters is the phase-only filter (POF) [Hoerner and Gianino, 1984]. It is defined by

$$G^*_{POF}(u,v) = e^{-i\varphi(u,v)} = \frac{G^*(u,v)}{|G(u,v)|}. \tag{4}$$

With this filter the correlation function follows from

$$K_{POF}(m,n) = \mathcal{F}^{-1}\left\{\frac{G^*(u,v)}{|G(u,v)|} \cdot F(u,v)\right\}. \tag{5}$$

This filter we used sucessfully for the evaluation of speckle patterns [Gutmann, 1994]. Therefore we also applied it in this investigation.

2.5. FRINGE PROJECTION

The intensity distribution of a sinusoidal modulated fringe pattern recorded by the fringe camera is given by

$$I(m,n) = b(m,n) + a(m,n) \cdot sin\varphi(m,n) \tag{6}$$

as a function of the pixel position (m, n), containing the background intensity b and the fringe amplitude a. The phase difference $\Delta\varphi(m, n)$ between the phase value $\varphi_{obj}(m, n)$ of an object point and the corresponding phase value φ_{ref} at the same position m on a reference plane yields the height or contour $h(m, n)$ of the object by the relation

$$h(m,n) = s(m,n) \cdot \Delta\varphi(m,n) \tag{7}$$

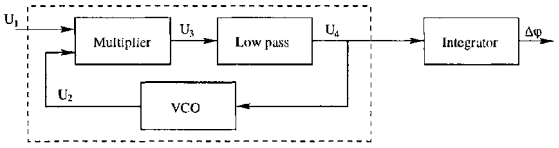

Figure 3. Block diagramm of the PLL.

with s being the scaling function which is determined by geometric calibration of the fringe projection system.

From the contour map of the deformed cap and from an additional contour map of a reference state the out-of-plane displacement field is calculated.

The most accurate method to determine the phase distributions is based on temporal phase shifting with subsequent phase unwrapping. In the highly dynamic measuring task under consideration, however only one fringe pattern for each time instant is available. Therefore the phase calculation must be performed by one-image techniques. Instead of using Fourier transform method [Takeda, 1982] which is recommended in literature we used a new method. It is based on a phase locked loop (PLL) [Rodriguez and Servin, 1993]. By this method the phase unwrapping process can be avoided completely. The only condition is that there are no discontinuities or steps in the contour of the object.

2.6. PHASE LOCKED LOOP AND ITS DIGITAL SIMULATION

Fig. 3 shows the block diagramm of the phase locked loop circuit for real time fringe evaluation. It consists of four main parts: Multiplier, voltage controlled oscillator (VCO), low pass filter and integrator. The signal $U_1(t)$ is generated by the fringe camera when scanning the fringe pattern with an intensity distribution given by eqn. (6). After cutting off the time independent part of the signal and normalising its amplitude to 1 U_1 reads as follows

$$U_1(t) = sin\,(\omega_0 \cdot t + \varphi_1(t))\,. \tag{8}$$

The signal $U_2(t)$ is chosen to be equivalent to the intensity distribution of the fringe pattern on the reference plane, i.e.

$$U_2(t) = cos\,(\omega_0 \cdot t + \varphi_2(t))\,. \tag{9}$$

U_1 and U_2 are multiplied in the multiplier and low pass filtered. For small phase differences $\Delta\varphi = \varphi_1 - \varphi_2$ this yields the signal

$$U_4(t) = \frac{1}{2}\Delta\varphi(t). \tag{10}$$

For each row which has to be scanned the process starts at the reference plane (locking period) so that $\varphi_1 \equiv \varphi_2$ or $\Delta\varphi = 0$. When the scanning process reaches the contour of the object φ_1 begins to differ from φ_2, i.e. $\Delta\varphi$ is no longer zero. During a small time interval dt a change $d(\Delta\varphi)$ of the phase difference is produced. This causes the control procedure of the PLL circuit to start by changing the frequency of the PLL circuit to start by changing the frequency of the signal U_2 in the VCO according to

$$\omega_{VCO}(t) = \omega_0 + 2\kappa \cdot U_4(t) = \omega_0 + \frac{d(\Delta\varphi)}{dt}. \tag{11}$$

in order to compensate $\delta(\Delta\varphi)$. In this equation κ is a feedback parameter which has to be properly selected [Wolf, 1996].

As we are interested in $\Delta\varphi(t)$ we have to integrate the output $U_4(t)$.

The contour of the airbag caps need not to be determined on-line. Therefore it is not necessary to use the analogue version of the PLL [Lichtenberger, 1998]. The electronic circuit can be simulated digitally [Rodriguez and Servin, 1993]. From eqn. (11) it follows that

$$\frac{d(\Delta\varphi)}{dt} = 2\kappa \cdot U_4(t). \tag{12}$$

Neglecting the low pass filter in the PLL circuit, $U_4(t)$ can be replaced by $U_3(t) = U_1(t) \cdot U_2(t)$. From eqn. (8) and (9) we receive the differential equation 13 aftre setting $\varphi_1(0) = 0$ and replacing t by x and $U_1(t)$ by $I(x)$ according to equation (6)

$$\frac{d(\Delta\varphi)}{dx} = 2\kappa \cdot I(x) \cdot cos(\omega_0 x + \Delta\varphi). \tag{13}$$

However, the constant backgound intensity b of I yields an offset in $\Delta\varphi$. Therefore instead of $I(x)$ the derivative $dI(x)/dx$ is used in eqn. (13). For numerical evaluation of (13) the differentials are replaced by finite differences with a step width $\Delta x = 1$. The equation for the calculation of the phase difference $\Delta\varphi$ at the pixel positions m,n then reads

$$\Delta\varphi(m+1,n) = \Delta\varphi(m,n) + \kappa \cdot [I(m+1,n) - I(m,n)] \cdot cos\,[\omega_0 m + \Delta\varphi(m,n)]\,. \tag{14}$$

The numerical integration procedure has the same effect as the low pass filter in the electronic circuit (Fig. 3).

3. Results

Fig. 4 shows an example for the 3-D deformation of an airbag cap which is gained by the combination of digital speckle correlation and fringe projection as described in the preceding chapters. The in-plane component of the

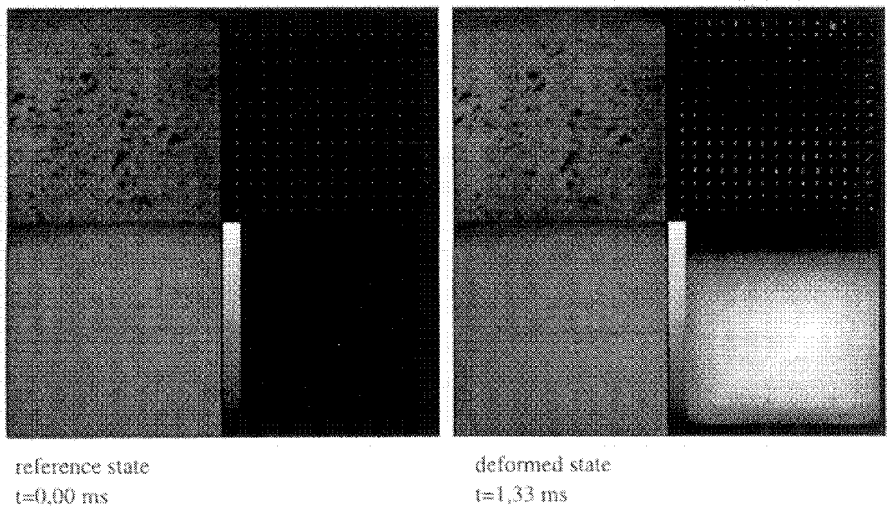

Figure 4. Reference state and deformed state. Shown on the left side are the speckle and fringe images and on the right side the in-plane vectors and grey level coded out-of-plane deformation.

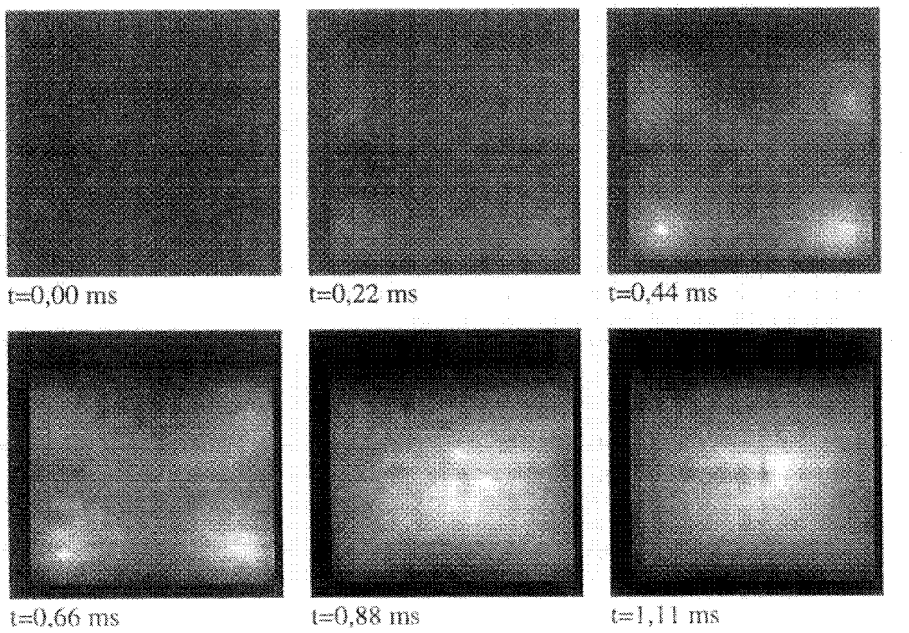

Figure 5. Time sequence of the grey level coded out-of-plane-displacement of an airbag cap.

deformation is much smaller than the out-of-plane component. The grey level coded out-of-plane component is scaled to the maximum value of 13,2 mm reached just before the fracture. Figure 5 shows a time series of the grey level coded out-of-plane displacement. Each image in Figure 5 is scaled to the minimum and maximum displacement values in the image. It can be seen that the deformation of the airbag cap starts in the four corners and not in the center of the cap.

4. Conclusion

Digital speckle coorelation and fringe projection can be combined to measure dynamic 3-D deformations in cases where the ranges of in-plane and out-of-plane displacements differ remarkably. This methods have been successfully applied to study the highly dynamic deformations of air bag caps after explosion of the bags. It was necessary to use a single-image procedure to determine the phase distributions of the fringe patterns from fringe projection. The digital simulation of a PLL circuit proved to be an alternative to Fourier transform methods because no phase unwrapping has to be performed. But not only the digital simulation of the PLL circuit can be used to get the phase information in contour measurement. The analogue realization of the circuit yields as well the possibility of realtime contour measurement by a simple and cheap electronic circuit. The grey level coded contour information can be observed at a monitor screen without using a computer.

References

Gutmann, B.: *Deformationsmessungen an Schaumstoffproben mit Methoden der digitalen Bildverarbeitung,* Diploma Thesis, Institut für Mechanische Verfahrenstechnik und Mechanik (AM), Universität Karlsruhe, 1994

Horner, J.L.; Gianino, P.D.: *Phase-only matched filtering,* Appl. Opt. 23, pp. 812-816, 1984

Lichtenberger, R.; Weber, H.: *Analogue phase evaluation of fringes for real time dynamic contour measurement,* Proc. of Photomecanique 98, GAMAC, 1998, pp. 165-170

Rodriguez, R.; Servin, M.: *Topographic Information Using a New Technique of Phase Measuring,* Proc. of Fringe 93, Akademie Verlag, Berlin 1993, pp. 223-229

Takeda; Ika; Kobayashi: *Fourier-Transform Method of Fringe Pattern Analysis for Computer Based Topography and Interferometry,* J.O.S.A., 1982

Wolf, T.: *Entwicklung eines optischen 3D-Verformungsanalyseverfahrens für geschäumte Polymere,* Ph.D. Thesis, Multimedia Verlag, Karlsruhe, 1996

ANALYSIS OF THE DEGRADATION MECHANISMS IN COMPOSITE MATERIALS THROUGH A CORRELATION TECHNIQUE IN WHITE LIGHT

Y. BERTHAUD

LMSGC, UMR 113 LCPC / CNRS
F-77420 Champs sur Marne, France

AND

S. CALLOCH, F. COLLIN, F. HILD AND Y. RICOTTI

LMT-Cachan, ENS de Cachan / CNRS / Université Paris 6
F-94235 Cachan, France

Abstract – The analyzed material is a vinylester matrix reinforced by randomly oriented continuous fibers. The degradation mechanisms are determined from tensile tests on coupons and SEM observations. Notched specimens and plates with central holes are then studied when loaded in remote uniaxial tension. Cross-shaped specimens are then studied. The evolution of the strain field is computed through a correlation technique in white light. In particular, the initiation location can be measured.

1. Introduction

The aim of this study is first to evaluate the effect of the fiber orientation of a composite material made by a Resin Transfer Molding (RTM) technique. Second, the notch sensitivity of this material is assessed for specimens loaded along one and two directions. The strain fields are evaluated by using a correlation technique. The initiation sites are determined by this technique coupled with a finite element computation.

2. Studied Material

The composite material is made of a vinylester matrix reinforced by continuous E glass fibers (see Fig. 1). The RTM process induces a random in-plane fiber bundle orientation (Fig. 2). The fiber volume fraction is equal to 30%.

A. Lagarde (ed.),
IUTAM Symposium on Advanced Optical Methods and Applications in Solid Mechanics, 627–634.

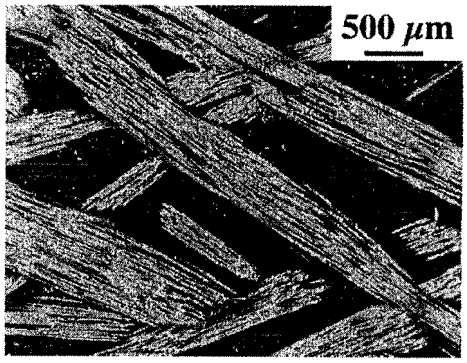

Figure 1. Surface of the composite.

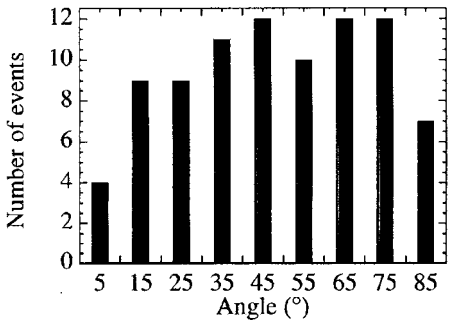

Figure 2. Angular distribution of fiber bundles in the material.

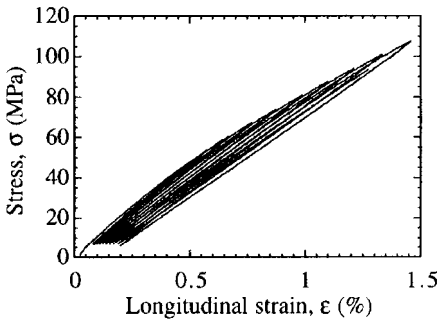

Figure 3. Stress/strain curve of a coupon specimen.

3. Uniaxial Loading

3.1. COUPONS

Tensile tests have been carried out on 25 × 3 × 150 mm^3 coupons (Fig. 3). To analyze the effect of fiber orientation, the coupons were cut in two perpendicular directions. There is no effect on the stress/strain response of the composite [1]. A microscopic analysis of the degradation mechanisms shows multiple matrix cracks (Fig. 4). Furthermore, single fiber pull-out has been observed. More importantly, fiber bundle pull-out is systematically present at the fracture surface (Fig. 5). The fiber bundle behaves like a fiber with a large cross-sectional area rather than the sum of single fibers of small diameters.

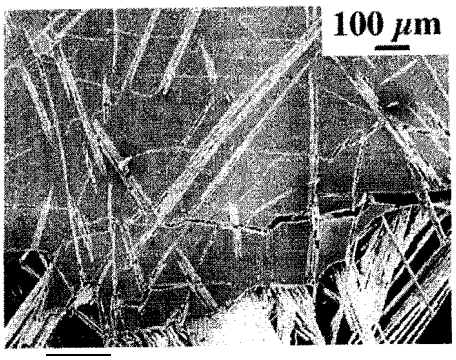

Figure 4. Cracking of the vinylester matrix.

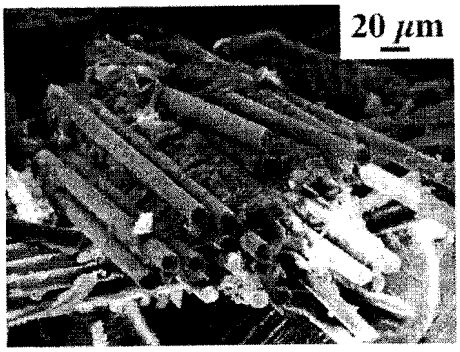

Figure 5. Fiber bundle failure and pull-out.

3.2. PLATES WITH NOTCHES OR HOLES

A series of experiments has been carried out on plates with holes (of radius R) and doubled edge-notched specimens (the total notch size is 2a). The total width L is identical to that of the coupons. Two ratios $2a/L$ and $2R/L$ have been considered: 1/2 and 1/4. These specimens are loaded in remote uniaxial tension. To compare the load levels of different configurations, the net section stress is computed. Figure 6 shows the net section stress vs. the strain measured in the vicinity of a notch by a 1 mm^2 strain gauge. The shape of the curve is comparable to that obtained with coupons (Fig. 3).

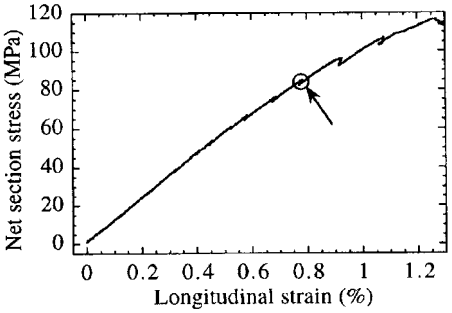

Figure 6. Tensile curve of a notched specimen ($2a/L$ = 0.25). The arrow shows the level corresponding to the strain measurements of Fig. 9.a.

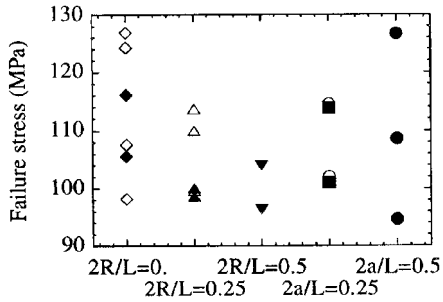

Figure 7. Net section stress at failure for different orientations (0°: filled symbols, 90°: open symbols) and different types of specimens.

Figure 7 shows the net section stress levels at failure for different specimens. One can see a scatter for all types of specimens. This scatter is

probably linked to the randomness of the bundle failure stress and orientation (Fig. 5). It is worth noting that the stress levels cannot be distinguished within each scatter. Furthermore, the effect of orientation is negligible. All these results tend to show that there is no influence of the presence of stress concentrators on the net section stress level at failure. Therefore the material is notch-insensitive in 'uniaxial' tension.

Figure 8 shows various shapes of the fracture surface. It can be noted that there is always a shear-type of failure (with an angle of 45° wrt. the loading direction). However sometimes a tensile-type of failure can be observed (perpendicular to the loading direction). In the following, the initiation sites will be determined by using the measured strain field through a correlation technique.

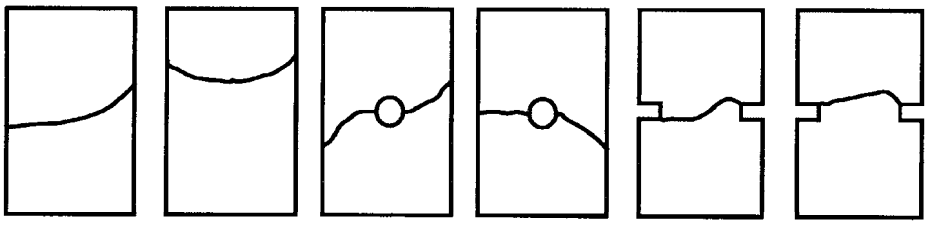

Figure 8. Examples of fracture surfaces.

3.3. CORRELATION TECHNIQUE

To locate the initiation site(s), the strain field is evaluated during the experiment. The specimen is polished and then coated by a random black and white pattern. By using a fixed CCD camera, pictures at different stages are recorded. The in-plane displacement map is computed by using a correlation technique between an initial picture (with no applied load) and a subsequent one (when the load is applied). This technique has been applied to different situations [2, 3, 4] even in the presence of finite strains [5].

The specimen is divided into a regular array of zones (cells), the size of which is equal to 32 × 32 pixel. The displacement vector is obtained by maximizing a correlation function between corresponding cells of the two pictures. This cross-correlation is computed in the Fourier space. A local parabolic interpolation about the peak allows a sub-pixel evaluation of its position. The second image is then shifted by the previous computed displacement to get the next value. An iterative scheme is used to get an auto-correlation function. With two or three iterations on 32 × 32 pixel cells, an accuracy of 3/100-th of pixel is obtained [6]. The main advantages

of this technique is its insensitivity to lightning variations and lack of focus. Its is well suited for small strain evaluations (of the order of 5% so that the hypothesis of solid displacement of the cells is fulfilled). To compute the strain field, the displacement map is prescribed on the same Finite Element (FE) mesh as the one used in the image analysis. This procedure allows a direct comparison between experiments and model predictions (usually obtained by non-linear FE analyses). The commercial FE code ABAQUS [7] has been used in the present study.

3.4. INITIATION SITE

The evolution of the strain field as a function of the load level is obtained by using the above-described method. In particular, the macrocrack initiation locus can be observed. In a double edge-notched specimen, the initiation mechanism is of shear nature (even though another tensile macrocrack is forming with some delay: Fig. 9.a). The two directions are also present on the fracture surface (Fig. 9.b). Figure 9.a shows that the longitudinal strains start to localize in a 45° direction. The corresponding levels are of the order of the failure strains given in Fig. 6. Therefore, this level will be referred to as initiation. In Fig. 6, the stress level at 'initiation' is shown: it occurs prior to reaching the peak level.

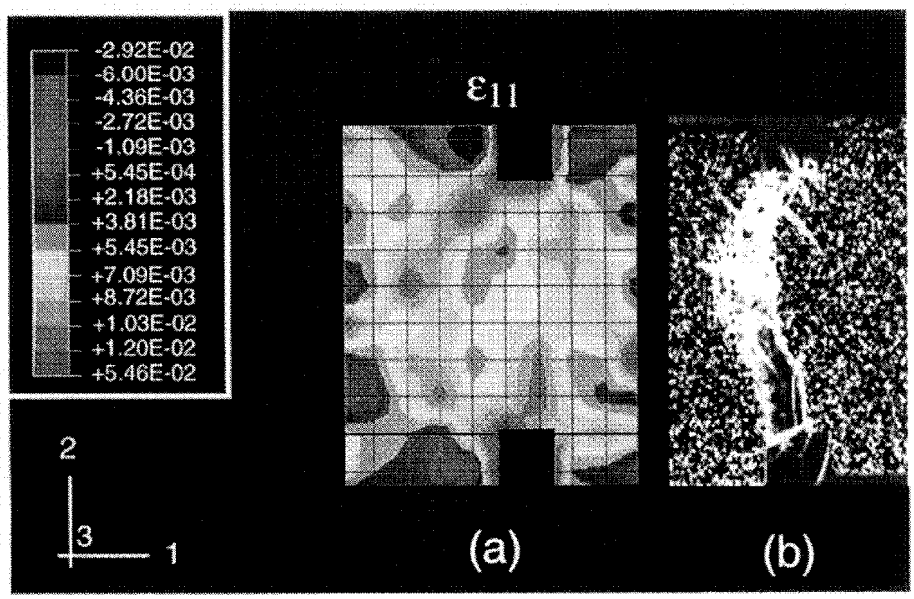

Figure 9. Strain field at 'initiation' (a), specimen surface after failure (b).

4. Biaxial Loading

4.1. SPECIMEN GEOMETRY AND EXPERIMENT

To investigate the effect of biaxial loading conditions, a cross-shaped specimen has been designed (Fig. 10). The ligament length is equal to 36.5 mm and the connecting radius is equal to 5 mm. This specimen is mounted in a triaxial testing machine ASTREE equipped with six servohydraulic actuators [8] (jointly developed by LMT-Cachan and Schenck AG, Darmstadt, Germany). To avoid the coupling between the different loading axes, the actuators are linked two by two along the three axes so that the central point of the specimen is motionless. The specimen fixed in the grips is shown in Fig. 11: four out of six servohydraulic actuators are used.

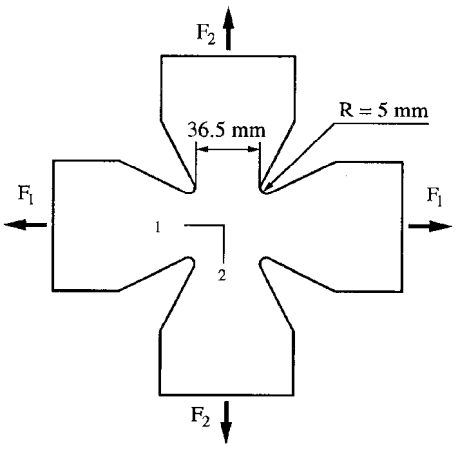

Figure 10. Specimen geometry.

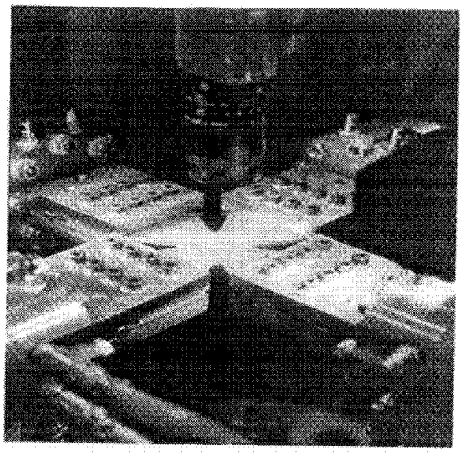

Figure 11. Specimen in the testing machine ASTREE.

4.2. TEST RESULTS

The testing machine allows non-proportional load histories: a squared loading cycle has been prescribed (Fig. 12). The effect of non-proportionality is a motion of the stress concentration zone along the connecting radius. The load level at failure (12 kN) corresponds to a net section stress of 101 MPa. This stress level is close to those observed previously (Fig. 7). This result seems to indicate that the notch-insensitivity is also observed for a non-proportional load history.

The broken specimen is shown in Fig. 13. The correlation technique is used to predict the initiation sites. To determine the location, it is assumed that a strain greater than 1.7% is likely to produce macrocracking (this

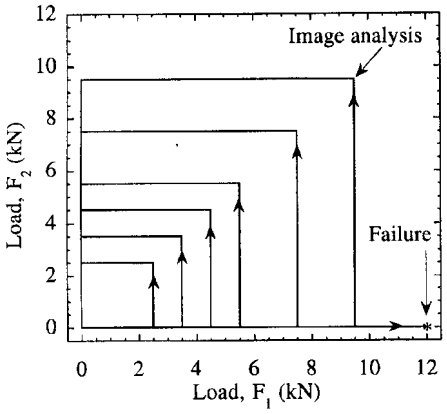

Figure 12. Load history.

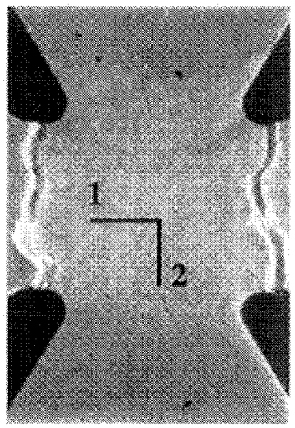

Figure 13. Failure surface.

strain level corresponds to the average failure strain of coupons). The force level for the present analysis is such that $F_1 = F_2 = 9.5$ kN. For this situation the strain field $\in_{11}$ and $\in_{22}$ is symmetrical about the first and second bisector. Any lack of symmetry is a probable indication of initiation. The longitudinal strains $\in_{11}$ and $\in_{22}$ determined from the displacement measurements are plotted in Fig. 14. It can be noticed that the strain levels are higher for the strains $\in_{11}$ than those of the strains $\in_{22}$. Furthermore, when the strains $\in_{11}$ are analyzed, one can see that the highest levels are almost identical on all stress concentration zones. This leads us to assume that initiation occurred independently on all sides along the l-direction for a load level of the order of 9.5 kN.

5. Summary

The results presented herein show that the overall composite behavior is isotropic. A scatter in failure stress has been observed for different specimen geometries and configurations. It is related to a bundle failure. A correlation technique in white light has been used to predict the initiation site(s). This method is applicable even in the presence of macrocracks. In all cases the initiation is predominantly of shear nature, even though tensile initiation may be present simultaneously. Lastly, in the experiments reported in this paper, it is shown that the composite material is notch insensitive when the net section stresses at failure are compared for notched specimens, plates with central holes and cross-shaped specimens. These experimental results will allow us to develop, identify and discriminate different mechanical models describing the behavior of these composites with a randomly

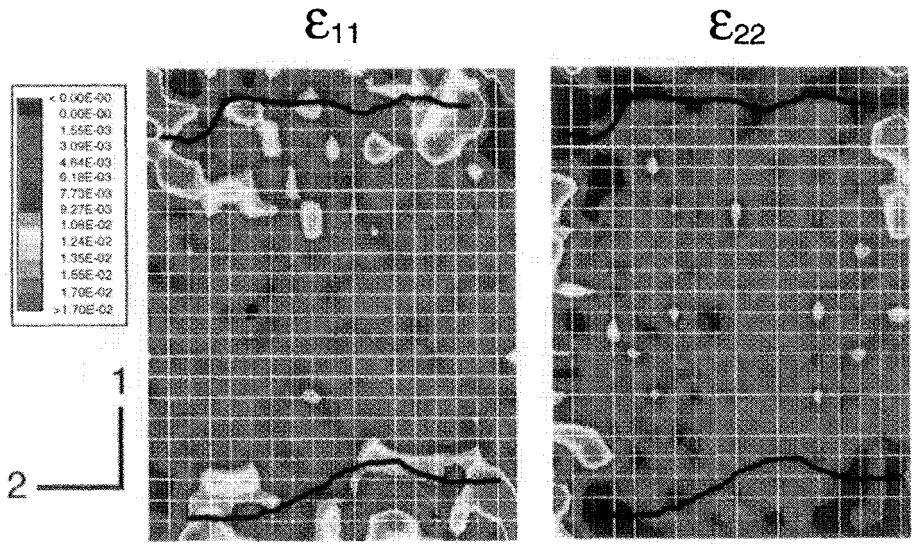

Figure 14. Longitudinal strain field $\in_{11}$ and $\in_{22}$ when $F_1 = F_2 = 9.5$ kN. The observed macrocracks are drawn in black.

oriented microstructure.

References

1. F. Collin, Y. Berthaud and F. Hild, in Y. Berthaud, M. Cottron, F. Morestin, P. Moucheront and M. Taroni (eds.), in Proceedings Photlomécanique 98, Marne-la-Vallée (France), GAMAC, (1998) 241.
2. M.A. Sutton, M.A., W.J. Wolters, W.H. Peters, W.F. Ranson and S.R. McNeill, Im. Vis. Comp. 1 [3] (1983) 133.
3. T. C. Chu, W. F. Ranson, M. A. Sutton and W. H. Petters, Exp. Mech. 3 [25] (1985) 232.
4. S. Choi and S. P. Shah, Exp. Mech. 3 [43] (1997) 307.
5. S. Mguil, F. Morestin and M. Brunet, in Y. Berthaud, M. Cottron, F. Morestin, P. Moucheront and M. Taroni (eds.), in Proceedings Photomécanique 98, Marne-la-Vallée (France), GAMAC, (1998) 361.
6. J. Thesing, Report, LMT-Cachan, 1996.
7. H. D. Hibbitt, B. I. Karlsson and P. Sorensen, Abaqus, User's MAnual, version 5.6, 1996.
8. S. Calloch and D. Marquis, Int. J. Plast. [accepted] (1998).

PROGRESS IN MECHANICS OF MATERIALS BY USING LASER SPECKLE METHOD

F. LAGATTU, J. BRILLAUD, M.C. LAFARIE-FRENOT
LMPM, UMR CNRS 6617, ENSMA, BP 109, 86960 Futuroscope

Abstract. The aim of this paper is to present some examples of the use of laser speckle method for the study of composite and polymer mechanical behaviour. A specific mechanical device has been designed in order to realise in-situ singly exposed speckle photographs. It is thus possible to obtain quite rapidly and easily « in-situ » displacement measurements, that is to say on the tensile testing machine, and with a good accuracy. This method has been applied to check and improve mechanical constitutive laws of structural composite materials. It has also been applied to validate new mechanical tests, for example shear tests, by verifying the uniformity of strain fields in the specimens. Moreover, this method allowed us to characterise strain fields around crack tips in polymers.

1. Introduction

Structural mechanical analysis and design need to know material constitutive laws. The mechanical behaviour of advanced materials such as long fibre polymer matrix composites is very complex. So, in order to propose realistic constitutive laws for such materials, deformation, damage and fracture mechanisms must be well understood. In this context, experimental measurements of stress and/or strain fields in various specimens of composite and polymer materials tested with numerous mechanical conditions are very useful. The aim of this paper is to present some examples of the use of laser speckle method for the study of composite and polymer mechanical behaviour.

To measure the stress and/or strain fields, numerous methods are available : photoelasticity, moiré, laser granularity, holography, thermography, microgrid, etc…The efficiency of one or another method depends on the measurement requirements. The goal of our study is to obtain quite rapidly and easily « in-situ » displacement measurements, that is to say on the tensile testing machine, and with a good accuracy. Thus, we have chosen to apply the laser speckle method [Bigaud et al., 1997 ; Barham et al.,1996].

A specific mechanical device has been designed in order to realise in-situ singly exposed speckle photographs [Brillaud et al., 1994]. This optical method is now used in our laboratory in various configurations, in order to :

- check and improve material mechanical constitutive laws,
- validate new mechanical tests and verify the uniformity of strain fields in the specimens,

A. Lagarde (ed.),
IUTAM Symposium on Advanced Optical Methods and Applications in Solid Mechanics, 635–642.

- characterise plasticity and damage phenomena in advanced materials.

2. Experimental set-up

The laser speckle method is based on the grainy, or « speckled » appearance of a surface illuminated with coherent light and observed through a lens (eyes, camera objective...). In order to obtain a good random diffuser for every tested material, specimen surface has been sprayed with a thin coat of matt white paint.

2.1. DEVICE FOR SPECKLE PHOTOGRAPHS

The aim was to obtain a displacement measurement accuracy of about one micrometer, although measurements would be done « in-situ », that is to say on the tensile testing machine.

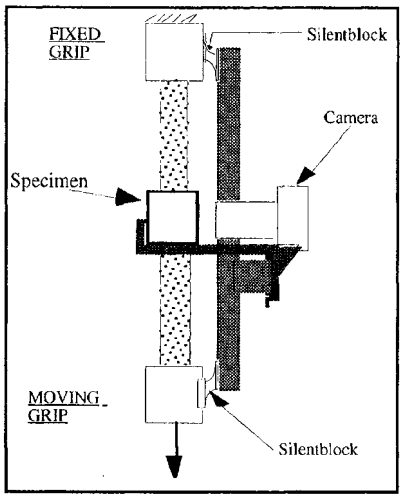

Figure 1 : Schematic representation of the mechanical device for in situ speckle pattern measurements.

In order to limit general displacement, a mechanical device was designed, using elastic properties of « silent blocks » (figure 1). The specimen was illuminated using a laser beam with a wavelength λ of 0,6328 μm. Photographs have been taken with a Nikon camera, on very sensitive holographic films. Optic parameters have been chosen in order to obtain a 1:1 magnification, with an aperture of 2,8. It leads to a very small depth of field : only 38 μm. In order to limit the out-of-plane displacement between specimen and negative at values smaller than 38 μm, the camera was placed on a low friction guide-way and a finger keeps contact with the studied zone (figure 1).

2.2. ANALYSIS OF PHOTOGRAPHS

The technique developed in our laboratory allows to take single exposures of the speckle pattern, at different steps of loading. An automatic analysis of negatives has been realised. Negatives (24mm*36mm) are placed in front of an objective of microscope combined with a CCD video camera. It is thus possible to record speckle images at every point on the negative. Micrometric motors automatically displace the negative according to a previously chosen set of points. In order to have a good correlation between the different speckle grain fields, pictures of 128pixels*128pixels are recorded, corresponding to a « point » of about 128 μm*128 μm.

At every point, the displacement vector resulting from the difference of loading between two negatives N_1 and N_2, is obtained by correlation of the two corresponding speckle images, using Fourier transform :

$$N_1(x) * N_2(x) = N_1(x) \otimes N_2(-x) = TF^{-1}\left[TF(N_1(x)).TF(N_2(-x))\right] \quad (1)$$

where TF designs Fourier transform.
Figure 2 presents an example of peak of correlation : the noise is suppressed by applying a threshold, and the displacement vector is determined as being the vector from the image centre to the peak centre.

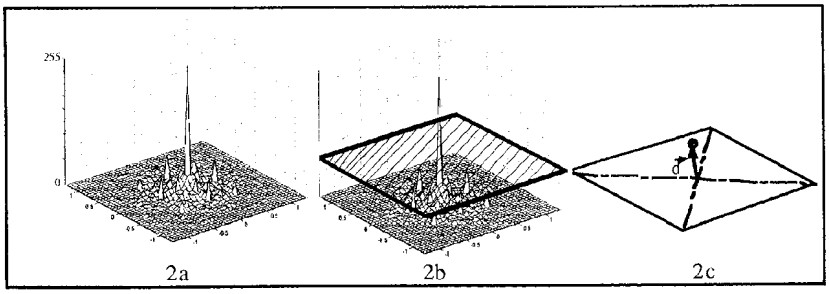

Figure 2 : Image of the peak of correlation (2a), application of threshold (2b), determination of displacement vector (2c).

When the complete displacement field is obtained, the rigid body displacement is suppressed to visualise the deformation of the material. Then, in order to calculate and visualise strain maps, displacements are derived using a finite element code : each point becomes a node of the finite element mesh, and the measured displacement vectors are imposed as the boundary conditions.

This optical method, based on an in-situ device for speckle photographs and an automatic analysis of singly exposed negatives, has been used for a better understanding of mechanics of materials. Some examples are presented below.

3. Behaviour of notched composite materials : theory and experiment

The APC-2 composite material is a continuous carbon-fibre-reinforced thermoplastic, mainly used in aeronautical and space equipment. For the assembly of complex structures, different parts are often connected with bolts or rivets. The understanding of notched specimens behaviour becomes therefore necessary for the design of such structures.

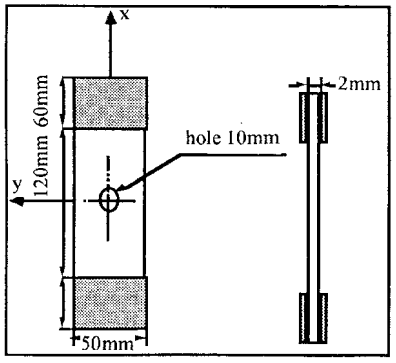

Figure 3 : Specimen geometry for tensile loading on notched specimen.

For this study, tensile tests have been performed on $[0_2/45/0_2/-45/90_2]_s$ APC-2 laminate specimens with a centre hole (figure 3). Tests have been realised at room temperature, with a constant crosshead displacement rate of 1mm/min [Touchard-Lagattu et al., 1996]. The laser speckle pattern technique has allowed us to measure in-plane displacements around the hole at different stages of the loading history.

First, this method was used in the elastic range. Measurements have been made around the hole for an applied load equal to about 10% of the specimen failure load. Measured displacements were smoothed and then derived in order to visualise the strain field around the hole. For example, the measured longitudinal strain ε_{xx} map is presented in figure 4b.

A theoretical elastic approach [Lekhnitskii, 1977] gives the strain field around the notch as a function of the hole radius and the elastic laminate constants. Using this approach, a calculation of the theoretical strain fields has been made (figure 4a), with the same finite element mesh than for the experimental strain determination. One can see on figure 4 that theoretical and experimental strain maps are in good agreement, pointing out that the elastic approach is available at this loading level.

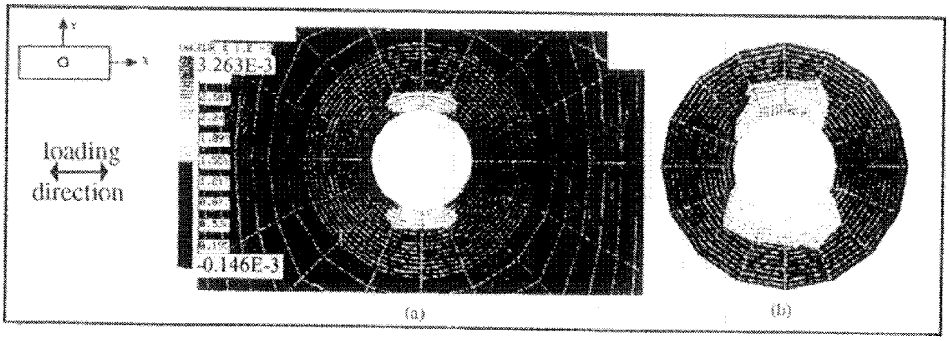

Figure 4 :Longitudinal elastic strain ε_{xx} around the hole in APC-2 $[0_2/45/0_2/-45/90_2]_s$ laminate subjected to a load of 8kN: (a) finite element calculation, (b) speckle measurements.

In order to measure the permanent strains which develop near the notch in the APC-2 material, two photographs of the unloaded specimen have been done: one before, and one after the application of a very high tensile load. Figure 5 shows, as an example, the residual shear strain γ_{xy} map, measured in the unloaded specimen after a loading up to 89% of the failure load. It is compared with the associated X-radiograph of the specimen. One can see in fig. 5 that permanent strain areas exist around the hole and

that they are particularly developed near the longitudinal splits which can be visualised on the x-ray picture. This observation shows the importance of taking into account the damage processes to describe the mechanical behaviour of these advanced composite materials.

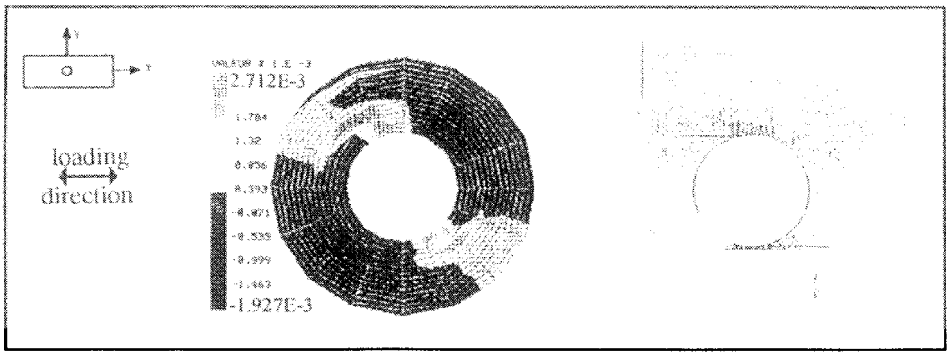

Figure 5 : Residual shear strain γ_{xy} measured by speckle method around the hole in APC-2 $[0_2/45/0_2/-45/90_2]_s$ laminate after loading to 89% of the ultimate load, and the associated X-radiograph.

4. Validation of two different shear tests of unidirectional long fibre composites

Failure mechanisms of composite materials are strongly related to their shear behaviour. In order to test long-fibre composite laminates under pure shear loading, many experimental tests have been proposed. For highly anisotropic materials, the difficulties are to obtain a pure shear loading, and to avoid the interaction of boundary conditions. In the two following examples, the laser speckle method has been used to validate original shear tests of unidirectional composite laminates.

In the first case, a parallelogram device has been developed in our laboratory [Fialeix and al., 1997] in order to study the in-plane shear behaviour of a carbon fibre/PEEK matrix $[0]_8$ laminate. Figure 6 shows the vectors of displacements measured at the centre of the specimen in a 8mm*8mm square area. One can see on figure 6 the uniformity of the observed pure shear zone and its relatively large size. The proposed experimental protocol for determining the constitutive shear laws of such a material has thus been validated.

The other shear test has been developed by Hassaïni and al., 1997. It enables the study of the six possible shear inter and intralaminar behaviours of an unidirectional composite by testing cubic specimens cut out from a same plate along the three orthotropic directions. For example, figure 7 presents the results obtained by speckle measurements with a glass/epoxy composite tested in shear in the (1,2) plane, the direction 1 corresponding to the fibre direction. These measurements have shown that, in a centre zone of about $3*3mm^2$ size, the shear strains are maximal and quasi-constant. As a result, this observation allows the use of strain gauges to measure maximal shear strains during a test.

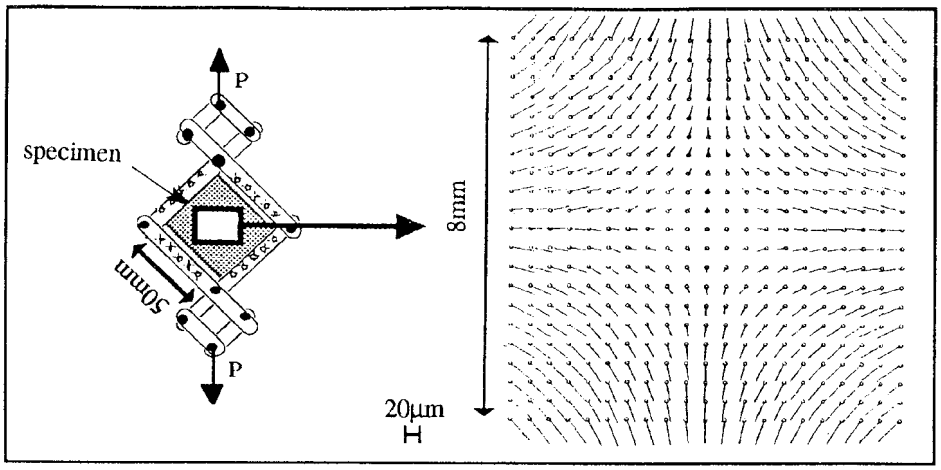

Figure. 6 : Displacements measured by laser speckle method on carbon/PEEK $[0]_8$ specimen subjected to a load of 1500N with parallelogram shear test.

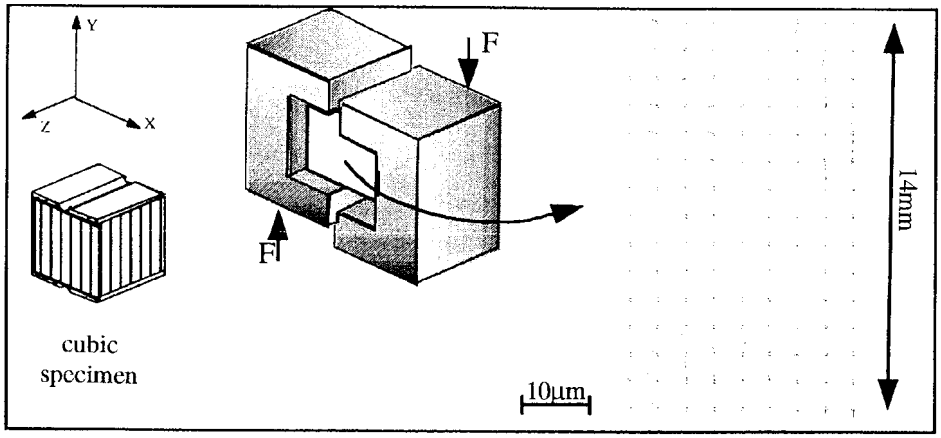

Figure 7 : Displacements measured by laser speckle method on glass/epoxy specimen subjected to a load of 3000N with « cube » test.

5. Localised strains around crack tip in polymers

Some polymers are now used as structural components. Such applications need predictive data concerning crack propagation mechanisms. Crack motion understanding and modelling goes through the knowledge of stress and strain kids at the crack tip [Kaminskii, 1996].

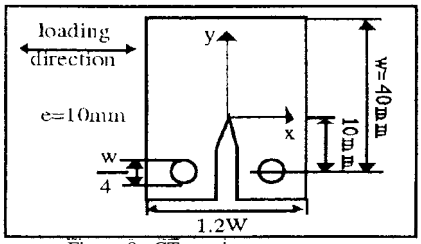

Figure 8 : CT specimen geometry.

This study deals with two amorphous thermoplastic polymers : the polymethyl methacrylate (PMMA) and the polycarbonate (PC). In our test conditions (room temperature and 0,1mm/min for the crosshead displacement rate), PMMA has an elastic and brittle behaviour, whereas PC shows an important ductility before fracture. Compact tension specimens have been tested, in order to characterise the pure mode I cracking behaviour (figure 8).

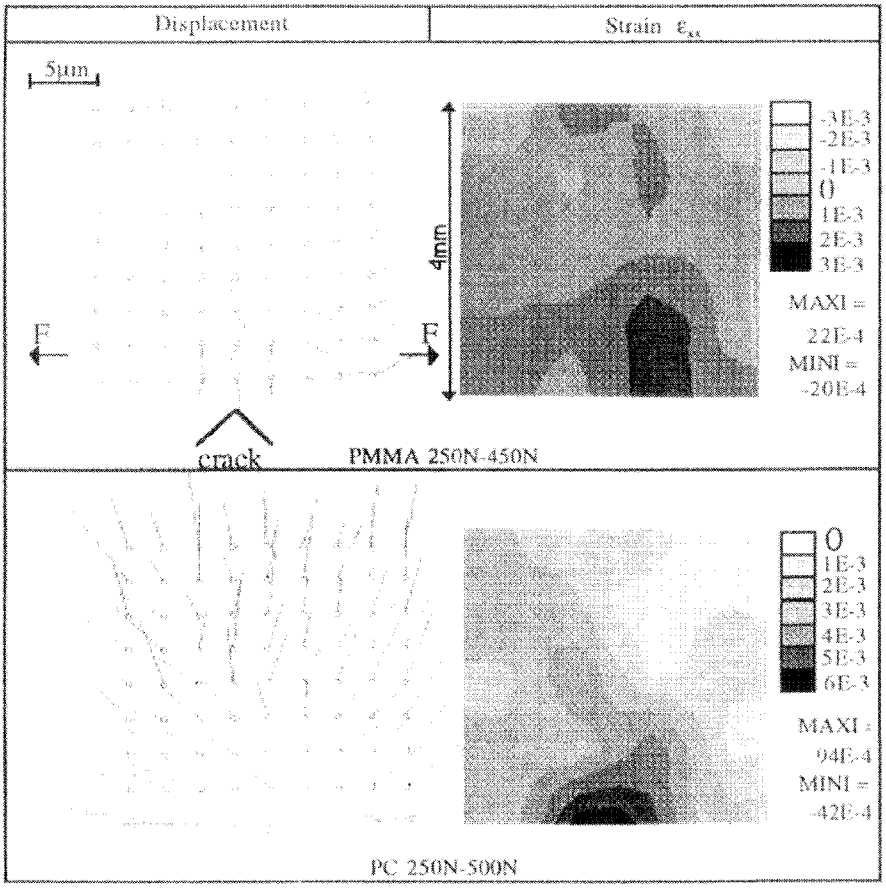

Figure 9 : Displacement and strain ε_{xx} maps obtained by speckle method at crack tip on PC and PMMA specimens.

Figure 9 shows for both materials the measured displacement vectors and ε_{xx} strain fields which develop near the notch tip in the elastic range. One can see on fig. 9 that the shapes of the strain maps are similar for the two materials : there is a zone with very high strain values near the crack tip, and, elsewhere, one can observe that the values decrease while the distance to the crack tip increases. We can also notice that the

displacement values measured on the PMMA specimen are very small (between 0,5µm and 3µ m), compared to those measured on the PC specimen (between 4µm and 10µm).

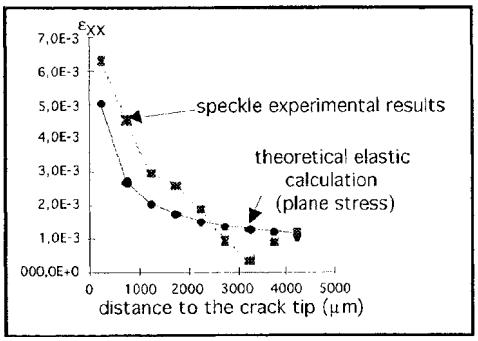

Figure 10 : Comparison between speckle experimental results and theoretical calculation at the crack front on PC specimen subjected to a load of 250N (500N-250N).

In figure 10, the experimental ε_{xx} strain values for PC specimen, and the theoretical elastic ones, are plotted against the distance from the crack tip. One can see on this figure there is a good correlation between theory and experiment. These results confirm the ability of the speckle method to measure displacements with a very good accuracy and a precise spatial resolution, even where strains are very localised. Work is in progress to characterise plastic and damage behaviour of such materials in front of a propagating crack.

6. Conclusion

Laser speckle method has been used for several studies concerning the mechanical behaviour of advanced materials. A specific mechanical device mounted on the testing machine has been realised and an automatic analysis of digitised speckle images has been developed. This technique has allowed us to obtain accurate measurements of in-plane displacements for several configurations of loading, specimens and materials.

References

Barham L., Baher C. and Conley E. ,1996, “Speckle-photography study of nuclear-waste vault deformations”. Experimental Mechanics ,42-48.

Bigaud M.D., Lagarde G., Hamelin P.,1997, “Laser granularity applied to local displacements analysis between two bonded bodies”. Euromech, Nevers (F).

Brillaud J., Lafarie-Frenot M. C. and Touchard F., 1994, "Experimental determination by laser speckle patterns of plastic strains near a hole in a thermoplastic composite laminate.". 10th Int. Conf. on Experimental Mechanics, Lisbon, Portugal, 343-348.

Fialeix G., Brillaud J., Lafarie-Frenot M. C., 1997, “Protocole experimental de caractérisation du comportement en cisaillement de matériaux composites et polymères par granularité laser“, Congrés Français de Mécanique, Futuroscope (France).

Hassaïni D., Vittecoq E., Degallaix G., 1997, "Monotonic inter- and intra-laminar shearing behaviour of an unidirectional glass-epoxy composite". 4th International Conference on deformation and fracture of composites, 24-26 mars 1997, Manchester, pp 515-524.

Kaminskii A. A., 1996, “Modeling quasistatic fracture at a crack tip in polymers and composites under long-term loading (Review)“. Int Appl Mech Engl Tr. International Applied Mechanics,32,7,493-517.

Lagattu F., Villain S., Lafarie-Frenot M. C., Brillaud J., 1998, “Caractérisation du comportement en fissuration de deux polymères amorphes : PMMA et PC.“, Colloque Photomécanique, Paris, France.

Lekhnitskii S.G., 1977, “Theory of elasticity of an anisotropic body“, Mir Publishers, Moscow.

Touchard-Lagattu F. and Lafarie-Frenot M. C., 1996, “Damage and inelastic deformation mechanisms in thermoset and thermoplastic notched laminates.“. Composites Science and technology,56,5,557-568.

DEVELOPMENT OF A STEREOSCOPIC OPTICAL STRAIN MEASUREMENT TECHNIQUE : APPLICATION OF MAIZE ROOTS

S. DENIS
LMS, Université de Poitiers, CNRS UMR 6610
SP2MI - Téléport 2 - BP 30179, 86962 FUTUROSCOPE CEDEX, FRANCE

F. BREMAND
LMS, Université de Poitiers, CNRS UMR 6610
SP2MI - Téléport 2 - BP 30179, 86962 FUTUROSCOPE CEDEX, FRANCE

Abstract

The main goal of this work concerns the experimental measurement of the rigidity modulus of a vegetal material in order to numerically simulate the mechanical behavior of a maize root system in soil. Due to the complexity of such material, non-contact and non-disturbing optical methods of strain measurement have a big advantage over classical extensometers. Among all these techniques, the tracking of two markers constitutes the best choice. Since a maize root is not rectilinear, a tension test introduces two important perturbations given by the transverse and the out-of plane displacements. To avoid these unwanted strains, we have used two CCD cameras allowing the determination of the spatial coordinates of the two markers. Then the longitudinal strain can be easily extracted. With stress evaluated from a special testing machine, the rigidity modulus for three genotypes of maize is finally shown.

1. Introduction

Beating down of maize by wind and storms is an accident that causes the destruction of the plants. Our common goal with the INRA (National Institute of Agronomic Research) is to evaluate the influence of each parameter governing the embedding of the root system in soil. Agronomists from INRA (Lusignan, France) are specially studying the biological observations (lignin rate…) and some geometrical aspects such as length, radius of roots… On our side, we are carrying out experimental analysis on the mechanical behavior root system for various maize genotypes. The correlation between both approaches will be made by Finite Element Method with a numerical evaluation of the mechanical behavior of each genotype [Denis, S. and Brémand, F. 1998]. In a first step, the soil is simulated by a stiffness depending on the humidity rate, and a linear

A. Lagarde (ed.),
IUTAM Symposium on Advanced Optical Methods and Applications in Solid Mechanics, 643–650.

constitutive law is assumed for this complex material. Furthermore we suppose that roots on any one inter-node have the same rigidity coefficient (Figure 1). In this paper, we present the experimental technique used for the evaluation of this parameter.

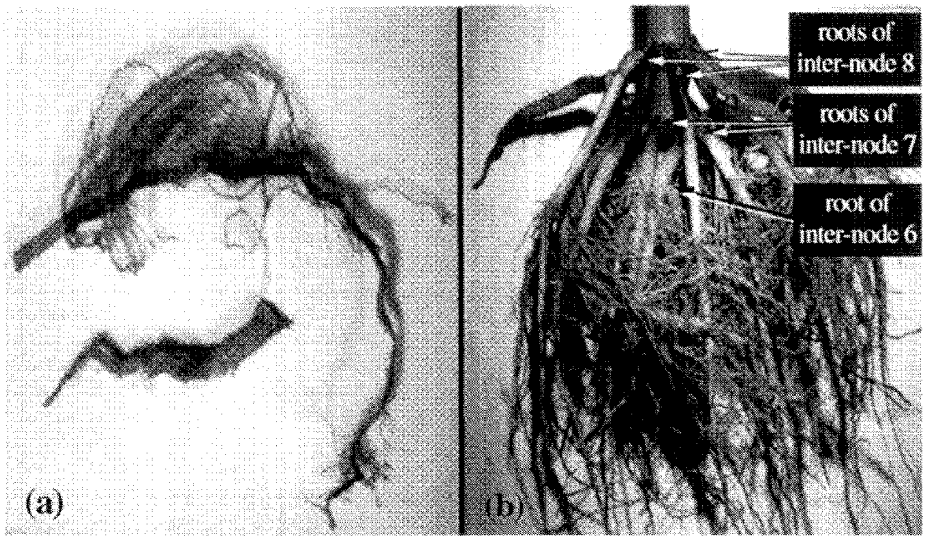

Figure 1 : (a) maize roots, (b) root system

A tensile test is performed on a 50 mm long specimen extracted from the more rectilinear part of the root. Since this complex material is non-homogeneous with a surface that can present some roughness or some important irregularities (Figure 1), classical extensometers as strain gauges are not suitable. The choice of optical methods of strain measurement appears very important because they perform non-contact and non-disturbing strain evaluation. Several methods are available such as optical diffraction of a laser beam by a grating marked on the surface [Brémand, F. and Lagarde, A., 1986], numerical spectral analysis by FFT [Dupré, J.C., et al. 1993]. But they require engraving of a grid on the surface, which is not possible with maize roots [Denis, S., 1996]. White light speckle by numerical correlation [Sutton, M. A., et al. 1986] can be used, but the natural speckle is not suitable. To obtain the longitudinal elongation only two points need to be identified. So two marks are drawn with black ink. With the help of an imaging system, the method consists in recording images of the specimen for each loading step [Brémand, F. et al. 1995]. Thus, the x and y coordinates are obtained by the calculation of the center of gravity of each mark.

During the tests, we noted different displacements. The longitudinal one is due to the tensile force, whereas the transverse and the out-of plane displacements come from the irregular geometry of maize roots [Denis, S. et al. 1998]. The latter induces variations in the enlargement ratio leading to unsuitable strains. To avoid these variations, a stereoscopic experimental set-up is used.

2. Stereoscopic method for strain evaluation

In order to quantify the transverse and the out-of plane displacements, two identical CCD cameras are used. They are located perpendicularly (Figure 2) in such a manner that the transverse displacements measured by one camera corresponds to the out-of plane displacements obtained by the other. The physical referential is determined as follows :

- X-axis is parallel to the line passing through the focal points I_1 (-L, L) and I_2(-L, -L) of the cameras,
- Y-axis is perpendicular to X-axis and it belongs to the plane defined by the optical axes of the cameras,
- Z-axis is vertical,
- the origin O is defined as the intersection of the two optical axis which are located at 45° relative to Y-axis.

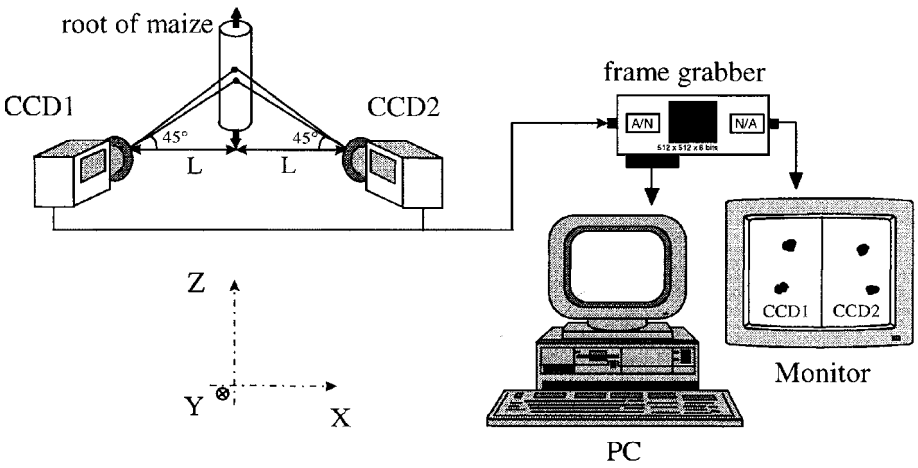

Figure 2 : Experimental apparatus using two CCD cameras

Each camera is adjusted such that the image of the point O corresponds to the center (x_0, z_0) of the camera (Figure 3). In our case, $x_0 = z_0 = 256$ pixels. The physical coordinates (x, y, z) of a point M are obtained by triangulation with the two corresponding points M_1 and M_2 (images of M respectively by CCD1 and CCD2). Let us call a_1 and b_1 the coordinates of M_1 and a_2 and b_2 the coordinates of M_2, these quantities are expressed in pixels and are obtained from the calculation of the gravity center by a classical interpolation [Brémand et al., 1992]. Since the two cameras have identical lenses with a focal length f, the same enlargement ratio G can be deduced for both cameras. The numerical technique consists in calculating in millimeters the two shifts δ_1 of M_1 and δ_2 of M_2 related to the center (x_0, z_0) of each image.

The x and y values of M should first be obtained from the x-component dx_1 of δ_1 and the x-component dx_2 of δ_2. Then the third coordinate z of M. (Figure 4) can be determined from the z-component dz_1 of δ_1 (or dz_2 of δ_2).

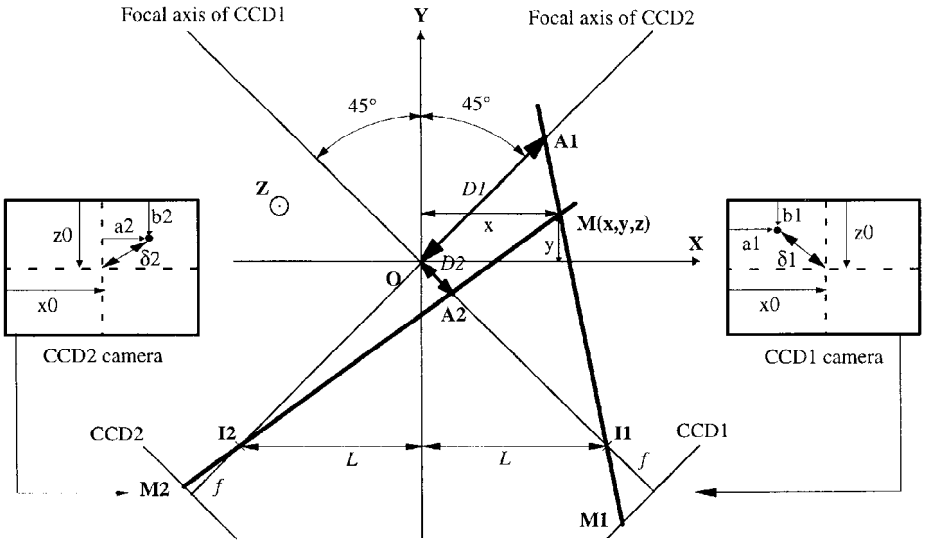

Figure 3 : Schematization of the experimental device

The two straight lines passing I_1 M, and I_2M intersect the optical axes at A_1 and A_2 respectively (Figure 3). The coordinates of these points are

$$A_1 = \left(\frac{D_1\sqrt{2}}{2}, \frac{D_1\sqrt{2}}{2}\right) \qquad A_2 = \left(\frac{D_2\sqrt{2}}{2}, -\frac{D_2\sqrt{2}}{2}\right) \tag{1}$$

where the distances D_1 and D_2 are

$$\frac{D_1}{dx_1} = \frac{D_2}{dx_2} = \frac{L\sqrt{2}}{f} \tag{2}$$

and the two shifts are

$$dx_1 = G\,(a_1 - x_0) \quad \text{and} \quad dx_2 = G\,(a_2 - x_0) \tag{3}$$

The x and y coordinates of M can be determined from the calculation of the intersection of the two straight lines A_1I_1 and A_2I_2 , hence

$$x = \frac{L * f * (dx_1 + dx_2)}{dx_1 * dx_2 + f^2} \tag{4}$$

$$y = \frac{L * f * (dx_1 + dx_2)(dx_1 + f) - 2 * dx_1 * L * (dx_1 * dx_2 + f^2)}{(dx_1 * dx_2 + f^2)(dx_1 - f)} \tag{5}$$

The last coordinate z is obtained from x and y. One camera, say CCD1, is sufficient to determine z (Figure 4).

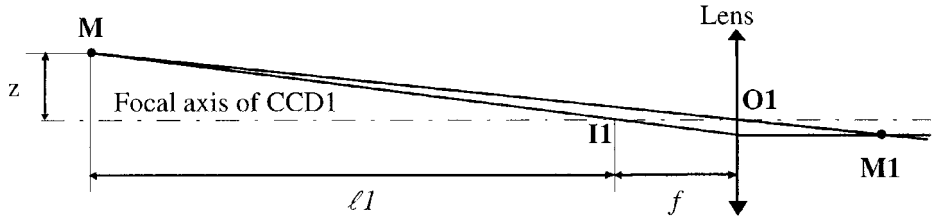

Figure 4 : Determination of the third coordinate z

So one can write

$$z = -dz_1 * \frac{\ell 1}{f} \tag{6}$$

where

$$\ell 1 = MI_1 = \sqrt{(x-L)^2 + (y+L)^2}$$
$$dz_1 = G\,(b_1 - z_0) \tag{7}$$

The three displacement-components (u_x , u_y, u_z), for one point, are obtained between a deformed state (index d) and the initial state (index o) by

$$u_x = x^d - x^o \quad , \quad u_y = y^d - y^o \quad , \quad u_z = z^d - z^o \tag{8}$$

Finally a classical differentiation, between the two markers, is used to get

$$\varepsilon_{zz} = \frac{1}{2}(2 * u_{z,z} + u_{x,z}^2 + u_{y,z}^2 + u_{z,z}^2) \tag{9}$$

Usually we consider that the error made in the location of one marker is a tenth of a pixel. For our experiments (with L = 370 mm and f = 50 mm), an accuracy around one hundredth of millimeter has been obtained for each coordinate. As the distance between the two points is around 5 mm, the strain accuracy is estimated to 10^{-3}, which is more than enough for our purpose.

3. Application

For the measurement of the rigidity modulus of each root, our colleagues from INRA have chosen three genotypes (5, 7 and 16) of maize with very different agronomic behaviors. For each variety inter-nodes 6, 7, 8 (when existing) have been studied (Figure 1). Roots have been selected with respect to some important geometrical conditions; First of all we must chose the part of the root close to the stem because it is the more rectilinear. Furthermore its length should be at least 50 mm and its cross-

section should be roughly constant. In fact, if the roots are too curved, we do not realize a pure tensile test but a combined tension-bending test that does not correctly provide the rigidity modulus.

3.1. EXPERIMENTAL APPARATUS

In order to perform these tests, a specially designed low charge-testing machine is used. Its stepper motor is controlled by a PC. The loading is made at imposed displacement speed (1 mm/min) and is recorded by an acquisition card at regular intervals, Δ_t = 2 s, chosen by the user (Figure 5). Stress σ is obtained by dividing the load by the cross-sectional area. A second PC is in charge of the image acquisition. It contains a frame grabber Matrox PIP 1024 (512*512 pixels, 8 bits). This card receives pictures from the two CCD cameras for the same time interval Δ_t = 2 s.

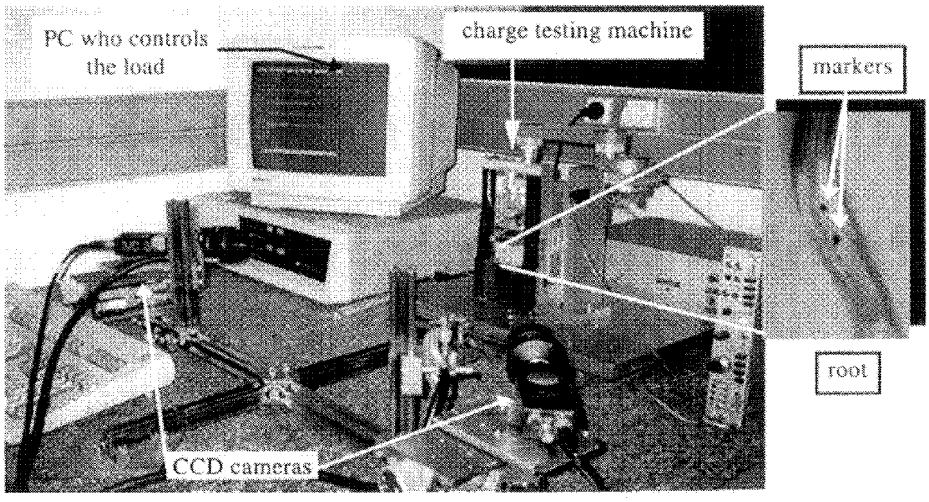

Figure 5 : View of testing machine

3.2. RESULTS

A hundred tests were performed. For each of them, we plotted the stress σ versus the longitudinal strain ε. We chose two representative tests which are presented in Figure 6. We also plotted the curves $\sigma = f(\varepsilon_{ccd1})$ and $\sigma = f(\varepsilon_{ccd2})$, where ε_{ccd1} and ε_{ccd2} are respectively the longitudinal strains obtained by CCD1 and CCD2. Due to the nature of maize roots (non-homogeneous...), experimental curves are not exactly linear. Figure 6 shows that, in some cases, the longitudinal strains obtained by one of the two cameras are irregular and negative. This is the result of out-plane displacements in which the specimen moves in the opposite direction from CCD camera. Note that the stereoscopic results are quite different from either of CCD1 or CCD2; it is a complex function of the two, not just the average. We also note that the stereoscopic curve is smoother than either of the CCD1 and CCD2 curves.

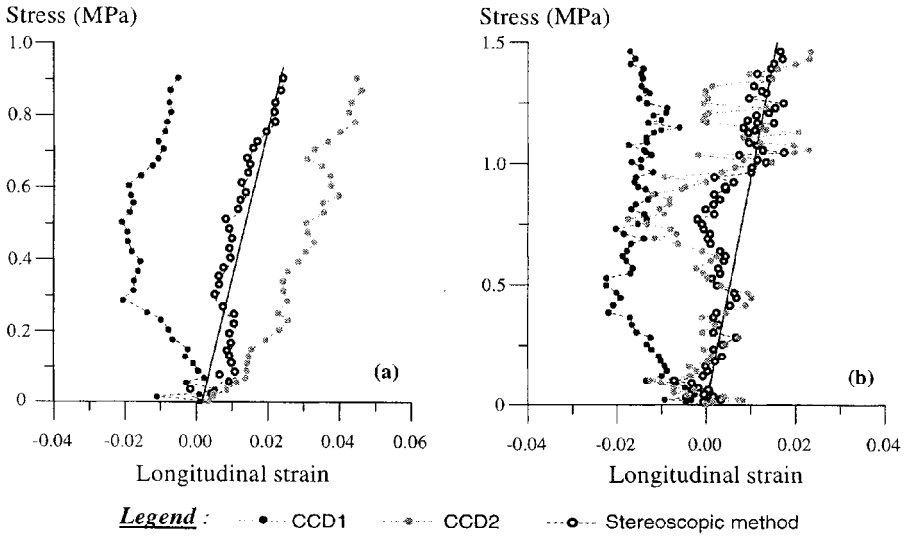

Figure 6 : two examples of experimental curves

To obtain the rigidity modulus for each curve $\sigma = f(\varepsilon)$, we carried out a least-squares straight line interpolation by minimizing the normal distance between experimental results and the fitting curve. The rigidity moduli, given by the slopes of these lines, are shown in Figure 7.

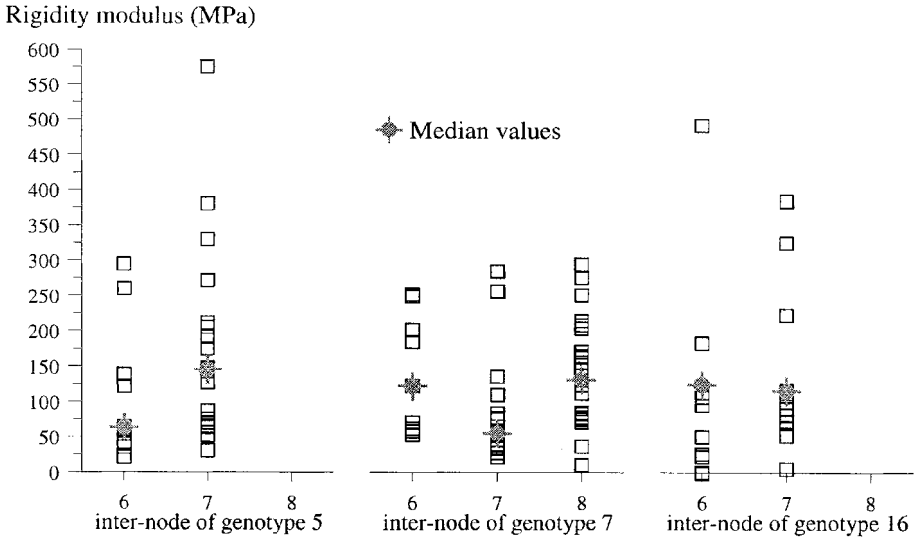

Figure 7 : rigidity modulus for each inter-node of each genotype

For each inter-node of each variety, we found a considerable spread in the values of the rigidity modulus due to the nature of material. In fact, biological and geometrical studies, realized in parallel by agronomists from INRA such as lignin rate or radius of roots, also show considerable spread in results. That is why the median of the rigidity modulus of each inter-node will be used in the numerical simulation of the mechanical behavior of a maize root system in soil.

4. Conclusion

The use of a non-contact and a non-disturbing optical method allows us to test vegetal materials. The study of the mechanical behavior of a maize root system requires the tracking of two markers associated with a stereoscopic method to determine the three spatial coordinates of the points for each loading step. We obtain coordinates with an accuracy around 10^{-2}mm and longitudinal strain accuracy is estimated to 10^{-3}.

The rigidity modulus so determined will be used in a finite element study of each genotype. This work is still in progress.

5. Acknowledgments

We acknowledge Region Poitou-Charentes for their financial support and Yannick HEBERT from INRA for his parallel research.

6. References

Brémand, F., Lagarde, A., 1986, A new method of optical strain measurement with applications, *Proceeding of the 1986 SEM Spring Conference on Experimental Mechanics,* pp 686-694.

Brémand, F., Dupré, J.C.,Lagarde,A., 1992, Non-contact and non-disturbing local strain measurement methods. Part. I : Principle, *European Journal of Mechanics.* vol : 11 A, n° 3, pp 349-366, 1992.

Brémand, F., Dupré, J.C., Lagarde, A., 1995, Mesure des déformations sans contact par analyse d'images, *Photomécanique 95,* Cachan, Eyrolles, pp 171-178.

Denis, S., 1996, Etude des propriétés mécaniques du système racinaire et de ses organes chez le maïs, DEA, Université de Poitiers.

Denis, S., Belkadi, S., Brémand, F., 1998, Mesure des déformations par stéréoscopie sur surface quelconque - Application aux racines de maïs, *Photomécanique 98,* Marne la Vallée, pp 73-80.

Denis, S., Brémand, F., Hébert, Y., 1998, An experimental study on the mechanical behaviour of maize root system: analysis of the soil/root bond and determination of rigidity modulus, *International Conference of the International Union of Forestry Research Organizations,* Bordeaux.

Dupré, J.C., Brémand, F., Lagarde, A., 1993, Numerical spectral analysis of a grid. Application to strain measurements, *Optics and Lasers in Engineering.* vol 18, n° 3, pp 159-172.

Sutton, M.A., Cheng, M., Peters, W.H., Chao, Y. J., Mc Neill, S.R., 1986, Application of optimized digital correlation method to planar deformations analysis, *Image and Vision Computing* vol. 4 n°3, pp 143-150.

MEASUREMENT OF RESIDUAL DEFORMATIONS INDUCED BY HIGH TEMPERATURE LOAD

N. CAVALLO*, F. MORESTIN**, J.F. JULLIEN*
INSA de Lyon, 20 avenue Albert Einstein, 69100 Villeurbanne
** URGC-Structures, ** LMSo*

Abstract : Validation of models introduced to simulate the thermo-mechanical consequences of phase transformations in the Heat Affected Zone (H.A.Z.) during welding is a difficult task because of the multiple effects that take place such as heat transfer and the convection of the melting zone. There is also a tridimensionnality induced by the geometry of the pieces to be welded and by the melting zone and displacement of the heat source.
This work treats the development of a specific device to validate thermo-mechanical models describing the H.A.Z.. All the "parasitic phenomena" that occur in reality do not take place under conditions for the wanted validation : there is no melting zone and the problem is axisymmetric. However, all thermo-mechanical consequences of phase transformations occur. Many measurement are taken to validate each step of the simulations : thermal, metallurgical and mechanical.
An original software for the strain field measurement has been developed to high temperature measurement. This software used the correlation principle and is limited nowadays to the plane surface measurement. This method is particularly well adapted to measure small deformations with high gradients. This new high temperature measurement method without contact can be another tool for validating numerical simulations of the Heat Affected Zone during welding.

1. Introduction

The prediction of residual stresses is a particularly difficult task in the case of welding, where structural transformations take place. In order to validate the models generally used to simulate the thermo-mechanical consequences of phase transformations (difference of volume of the phases and dilatation coefficients, transformation plasticity, hardening recovery and multiphased behaviour), a large program is investigated by Electricité de France and the Bureau de Contrôle des Chaudières Nucléaires on a carbon manganese steel (16MND5 in the AFNOR norm). This program is divided into two main parts as described by Cavallo [1 and 2]. The first one concerns the identification and validation of each model on specimens without thermal gradients. The second one concerns the validation on specimens with thermal gradients and structural effects.

A. Lagarde (ed.),
IUTAM Symposium on Advanced Optical Methods and Applications in Solid Mechanics, 651–657.

This paper only deals with the second part. A specific device has been developed and realised. It consists of applying an axisymmetric thermal load and in acquiring the maximum quantity of measurements used to validate numerical simulations. To avoid the problems induced by the melting zone an the tridimensionality due to the displacements of the heat source and specimen geometry which occur in reality, the analysis is limited to the Heat Affected Zone (H.A.Z.), which is the zone where structural transformations happen in a solid state, and the thermal load and the geometry are chosen to be axisymmetric. By keeping on the creation of H.A.Z. phenomena, even of the thermal cycles are slower that the welding ones, the model's validation taking into account phase transformations becomes easier.
To validate strain calculations, a new application of the correlation method has been developed. It permits to measure the plane strain load of the front side of the specimen which is submitted to a high temperature load.
In this paper, the device and the correlation method results are presented.

2. Experimental device

2.1. DISK SIZE DEFINITION

The thermal load is chosen to produce a totally martensitic transformation during the cooling process in the centre of the disk and through its thickness. Therefore, the maximum temperature must be higher than 850°C which is the temperature of the end of austenization for the considered steel, and every point of the disk which maximum temperature is higher than 750°C must have a minimum cooling rate of 10°C/s between 850°C and 390°C (temperature of the beginning of the martensitic transformation). Knowing that the thermal load is applying by a CO_2 laser which produces a flow assumed to be axisymmetric and have a defined form, numerical simulations are performed to estimate the thickness and the diameter of the disk and to produce measurable strains and stresses. Then, the disk is defined to be 5 millimetres thick and to have a diameter of 160 millimetres.

2.2. DISK ELABORATION

Dilatometry tests have shown that infernal stresses take place in the steel because of lamination, therefore the samples are taken to be larger than the defined geometry. They are submitted to a preliminary thermal cycle to relax internal stresses.
Disk are manufactured, rectified and polished to reduce the hardening of the disk sides as much as possible.

2.3. BOUNDARY CONDITIONS

The disk support is made of three alumina shafts which extremities are pointed to reduce the contact surface. The shafts are planed to be in contact with the parts of the disk which are assumed to stay cold. All the surfaces of the disk are supposed to be cooled by free convection and radiation.

2.4. MEASUREMENT METHODS

2.4.1. Temperature measurements

Temperature measurements are done on both faces of the disk.
On the side submitted to the thermal flow (front side), the temperature is measured by an infrared camera and pyrometers which permit measurements without contacting the disk. On the back side, thermocouples 78µm diameter type K are welded every two millimetres along a diameter.
The number and the positions of the thermocouples have been determined to allow the use of the inverse method as described in Blanc [3] to estimate the thermal load in the entire specimen. The measurements done of the front side of the disk which are less precise, are only made to verify the thermal load estimated.

2.4.2. Displacements measurements

Three displacement sensors LVDT type are equally distributed around the circumference (3x120°) to measure the specimen's diameter variation and verify the axisymmetric of the thermal load without preventing the free dilatation of the disk.
Seven other sensors type LVDT measure the axial displacement of the inferior side among a diameter every 5 millimeters.

2.4.3. "Post-mortem" measurements

Final shapes of the two sides are measured by LVDT sensors along four diameters. Residual stresses are measured at the Ecole Nationale Supérieure des Arts et Métiers (ENSAM France) by X-ray diffraction after the test and before the microstructure analyses. Finally, the disk is divided in two parts. It is polished and chemically attacked. Then, microstructure observations are made, completed by micro-hardness and hardness measurements.

2.4.4. Plane strain measurements on the front side by the correlation method

Correlation method. The correlation method of numerical images is used to estimate the plane displacement of a fuzzy motif "speckle type" deposed on the disk surface.
This method consists in taking pictures of the specimen before and after it is submitted to the thermal load, and estimating the displacement of each pixel of the picture between the two states using the *SIFASOFT 3.0 code* developed by the Laboratoire de Mécanique des Solides of INSA Lyon (see Mguil [4]). Knowing the displacements of the points of the surface, deformations can be estimate during interpolation.

Pattern definitions. The correlation method requires a special equipment and few precautions. The analysed picture must have been the most random aspect as possible : each pattern of the image must be different from each other. Usually, the speckle aspect is obtained by pulverisation of white and black painting. In our case, the pattern must be high temperature resistant, permit the absorption of the laser beam, and provide the lamination. The fuzzy pattern chose is composed of a first fine layer of graphite powder and a second one of bore nitrate.

Experimental apparatus. The pictures are obtained with a numeric camera Kodak Mega Plus (1024*1024 pixels). This high definition camera with square contiguous pixels is linked to an acquisition card Matrox PIIP1280 connected by a PC 486 DX50. The axial displacement is not taken into account by the use of a telecentric lens Melles Griot, Invaritar Pin 59LGL 428 model.

2.5. DISK POSITIONNING

A preliminary test is done on a A33 disk, 1.5 millimetre thick. In this test, differential thermocouples are welded on the back side of the disk. Those thermocouples directly measure the difference of temperature between each couple of points located symmetrically from the centre. Numerically controlled machine allowed in plane disk positioning in order to assure that the centre of the disk lies in the axis of the laser, providing this way an axisymmetric heating.

2.6. SCHEME OF THE DEVICE

The experimental device permits the application of an axisymmetric heating load on the front side of the disk. Temperature measurements are done to determine the thermal load in the whole specimen. Deformations are measured during the test on the back side of the specimen. The final deformations of two faces are measured as well as the in-plane deformations of the front side and the superficial residual stresses. Final microstructures are determined by microstructure analyses and hardness measurements.
A simplified scheme of the device is presented in Figure 1.

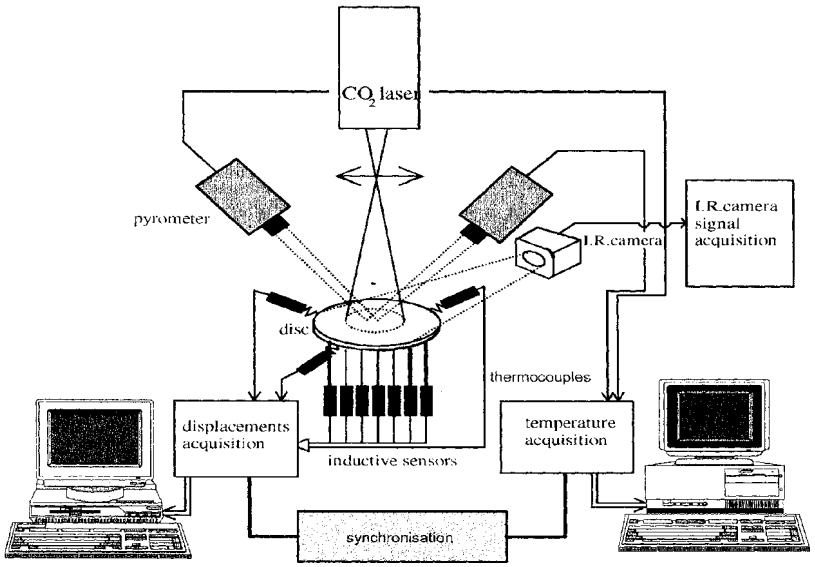

Figure 1 : Scheme of the device

3. Results

Only few results are presented here to discuss more about the correlation method results. The maximum temperature reached during the test is 950°C on the front side of the disk. Microstructure analyses and hardness measurements are taken to estimate the metallurgical phases in the different zones of the disk. A diagram of the different zones is presented in Figure 2. Three particularly zones are determined : a totally austenized one during the heating (1), a partially transformed (2) one and the non thermally affected one (3).
The displacements measured on the back side on the specimen present the same evolution in different proportions. To facilitate its analysis, only one curve is plotted and its evolution is compared to that of the temperature in Figure 3 for two points placed at 10 millimetres from the centre of the disk (which is a point of the H.A.Z.). The disk is heated by the front side. It is noticed that the phase transformations occurring during the cooling do not produce important displacements and therefore produce stresses.

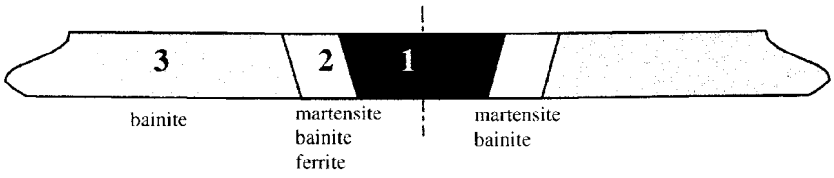

Figure 2 : Material zones

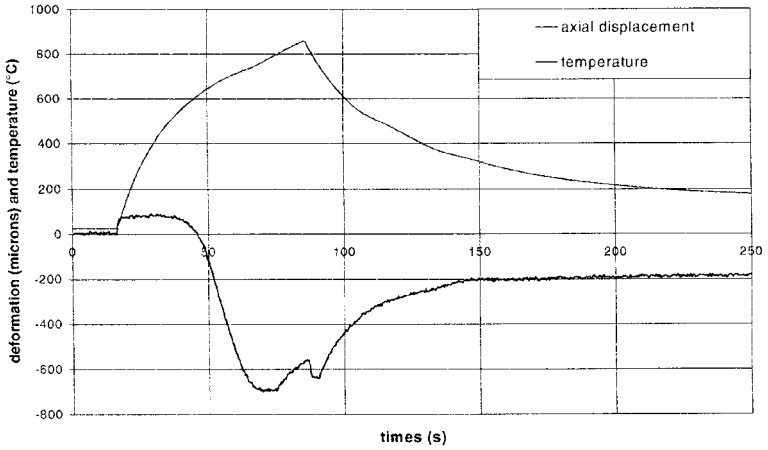

Figure 3 :Temperature and displacement measured at 10 mm from the centre on the back side

Figure 4 presents the main directions estimated by the correlation method of the front side of the disk. The grey level and the crosses represent the direction of the main deformation : they show the strain load is axisymmetric. The Figures 5 shows

the loads of the plane main strains. Main strain ε_{11} and ε_{12} are estimated to be equal to the circonferential and radial ones because of the principle directions.
All the measurements done enable to validate each step of the calculation : thermal, metallurgical and mechanical (displacements, strains and stresses).

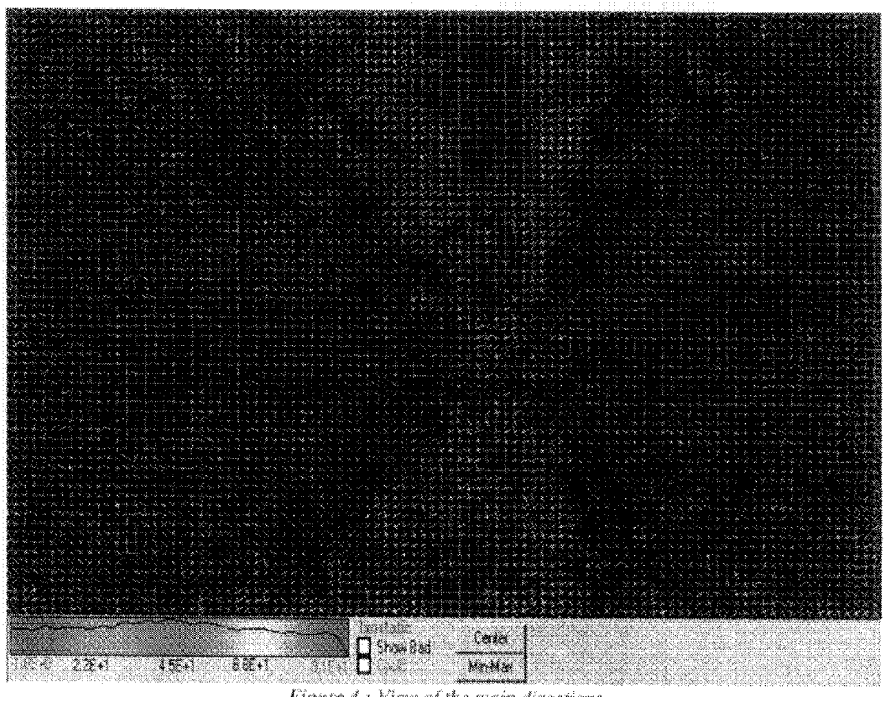

Figure 4 : View of the main directions

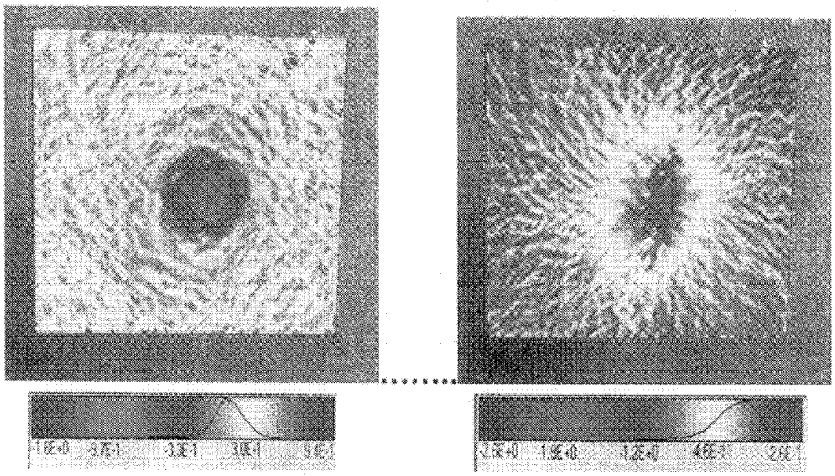

Figure 5 : Plane main strains

4. Conclusion

The experimental developed permits the application of an axisymmetric thermal load on a disk to measure :

- during the test, temperature and axial displacements along a diameter of the back side of the disk
- after the test, residual stresses, microstructures and final geometry and the residual plane strains on the front side by a new use of the correlation method

All the measurements permit the validation of each calculation step and particularly the capacities of codes to estimate residual strains and stresses in the case of phase transformations. This test can also be used with various loads corresponding to the thickness of the disk and the power of the laser. H.A.Z. gradients can also be reproduced and multicycles can be applied as in the H.A.Z. to validate the stresses relaxation estimated by models.

Acknowledgements

Authors wish to thank Electricité de France and le Bureau de Contrôle des Chaudières Nucléaires for financial et technical supports.

5. References

Cavollo, N., Taleb, L., Jullien, J.F., Wadier, Y., Waeckel, F., Moche, L., Dubois, D., Devaux J. (1997-I) Phase transformation effects on mechanical behaviour of steel vessel, SMIRT Lyon, August 97, **1** pp.698-1_698-3

Cavollo, N., Taleb, L., Jullien, J.F., Wadier, Y., Waeckel, F., Moche, L. (1997-II) Thermomechanical behaviour of a carbon manganese steel under martensitic transformations. The Firth International Conference on Residual Stresses, edited by T. Ericsson, M. Odén and A. Anderson, **2,** pp. 283-243

Blanc, G., Raynaud, M., Schau, T.H. (1998) A guide for the use of the function specification method for 2D inverse heat conduction problems, *Int J. of Heat and Muss Transfer,* **3,** pp. 703-716

Mguil-Touchal, S., Morestin, F., Brunet, M. (1997) Various experimental applications of digital image correlation method, CNEN97, Rhodes, **4** pp. 45.48

This Page Intentionally Left Blank

IUTAM SYMPOSIUM
ADVANCED OPTICAL METHODS AND APPLICATIONS IN SOLID MECHANICS

POITIERS, FRANCE
August 31, to September 4, 1998

CONCLUSIONS

J.W. DALLY
University of Maryland
College Park, MD 20742, USA

The symposium has been full and rich with a large number of general lectures, papers and posters. Researchers from Europe, North America and Asia have described their new discoveries. Through the symposium we have been able to share the results of the work in many different laboratories and to engage in dialog which extended our understanding both technically and socially.

During the symposium, 16 general lectures of the highest quality were presented. In addition to the oral presentations, the general lectures are available in written format in the Proceedings. A total of 37 lectures were also presented that provided the participants the opportunity to interact with investigators on the latest developments in optical methods in mechanics. As time was limited during the symposium, many excellent papers were relegated to the poster sessions. Twenty four posters were on display for the entire week of the symposium, and the authors described their work during two different poster sessions and during the breaks between the lecture sessions.

1. TECHNICAL OBSERVATIONS

1.1 ROLES OF THE COMPUTER AND THE EXPERIMENT

During the last 50 years, the roles of the computer and the experiment have changed dramatically. In the 1950s, the use of the computer in the study of stresses and strains was limited as indicated in Fig. 1. The computers were mostly analog and digital computers were extremely rare. Most of the studies to verify the adequacy of the design of engineering hardware were conducted using strain gages and photoelasticity. With the advent of the transistor and integrated circuits, digital computers became more common, lower in cost, and more powerful. In the 1960s finite elements were introduced, many different types of elements were developed, and numerical analysis began to replace

A. Lagarde (ed.),
IUTAM Symposium on Advanced Optical Methods and Applications in Solid Mechanics, 659–662.

experimental analysis in more routine engineering studies. During the 1970s the numerical analysis and experimental analysis followed different paths and were essentially competitive methods. However, since the 1980s the computer, numerical techniques, and experimental methods have been progressively integrated. The integration began with the data acquisition and then data analysis. Today many experiments are conducted under computer control where the entire process including loading, data acquisition, load and data control, and on-line real-time analysis is performed with interlocked experiments, instrument systems and the computer.

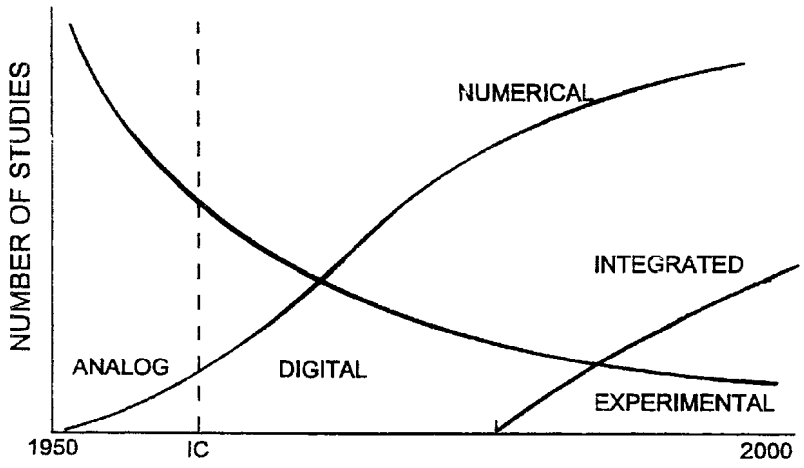

Fig. 1 The number of studies conducted using numerical techniques, experimental methods and integrated computer-experimental techniques during the past 50 years.

1.2 TRENDS

As we observed the many excellent general lectures and papers presented at this symposium and compared it with the last symposium (also held at the University of Poitiers in 1979) it was possible to note some significant differences in the thrust of the research. These include:

There has been a clear change of emphasis from military or defense oriented projects to those with more commercial applications. Instead of seeking high performance at any cost, we study techniques for producing products that are safer, more convenient to use and more cost effective.

Many research papers show a significant integration of disciplines. Rather than describing only optical method for generating data, researchers are integrating techniques from optics, electronics, mechanical systems, computers and displays. The result is powerful approach capable of generating important solutions rapidly in a cost effective manner.

We also recognize a trend toward studies on an unprecedented size scale. As the object of our studies has grown smaller, we have moved from scales dimensioned in

millimeters to micrometers and finally to nanometers. In some studies, we have moved beyond the limits imposed by the wave length of light and are using electron beam to probe features with dimensions of the order of 100 nanometers.

It is becoming necessary to move our equipment from the confines of a clean laboratory to the factory floor. The environment (hot and dirty) on the factory floor is extremely demanding. Vibrations, ever present, cause additional difficulties. However, by reducing the size of the equipment, packaging in air tight containers and using rugged electronics and fiber optics satisfactory systems are available for wide ranging studies.

There is a growing importance of the use of optical methods for non destructive evaluations (NDE). These studies are related to quality control systems employed to insure reliable performance of consumer goods. While the trend toward NDE shows an increase in emphasis, there is clearly a less important role for experimental solutions of boundary value problems. In this regard, the role of photoelasticity is much diminished. Finally, there is a closer coupling of the experimental methods with material science where measurements of strain, stress, stress rate, strain rate, temperature and time is essential in characterizing the non linear behavior of material and developing realistic constitutive relations.

There is a growing reliance on image analysis and phase adjustment in several different optical methods for measuring surface displacement. The new developments in digital cameras, piezoelectric translators, frame acquisition circuits, electronic and magnetic memory, and computers have essentially permitted us to introduce a new approach in conducting experiments and acquiring and analyzing data. Interference fringes are no longer required. Instead, the experimental measurements are processed in nearly real-time to produce whole-field representations of the field quantities in pseudo-color.

Finally, new optical methods under current development show great promise. In this regard, the two papers on photo-refractive crystals were most interesting as they indicated the significant enhancement of holographic interferometry possible with this new optical element. In the area of new methods in optical measurements the French researchers clearly showed the most significant progress.

2. ACKNOWLEDGEMENTS

The Symposium has clearly met the IUTAM criteria of providing of a small group well recognized researchers and promising young scientist an opportunity to interact. The forum was conducive to interaction with pleasant surroundings, excellent facilities, and superb food. Two different social event, both well attended, provided additional venues for discussions in a relaxed atmosphere.

The symposium required a significant level of external financial support. We acknowledge with our appreciation the assistance of the following organizations in this regard:

- International Union of Theoretical and Applied Mechanics
- European Research Office
- Delegation Générale à l'Armement

- Centre National de la Recherche Scientifique
- Association Universitaire de Mécanique
- Université de Poitiers
- Faculté des Sciences Fondamentales et Appliquées de Poitiers
- Mairie de Poitiers
- Conseil Général du Département de la Vienne
- Conseil Régional du Poitou-Charentes
- Peugeot Citroën
- Kluwer Academic Publishers

Finally, our deepest thanks go to the organizers of the Symposium that include the Scientific Committee and the Local Organizing Committee. Professor Alexis Lagarde chaired both Committees and his organizational skills were evident in the excellence of the program and the arrangements. He was supported locally by his able staff including: M. Cottron (secretary), F. Brémand, J. C. Dupré and V. Valle.

LIST OF AUTHORS